Solid Freeform Fabrication Symposium 2001

Proceedings
August 6-8, 2001

Edited by
David L. Bourell, Richard H. Crawford
Joseph J. Beaman, Harris L. Marcus
Kristin L. Wood, and Joel W. Barlow

The University of Texas at Austin
Austin, Texas

REPORT DOCUMENTATION PAGE

Form Approved
OMB No. 0704-0188

Public reporting burden for this collection of information is estimated to average 1 hour per response, including the time for reviewing instructions, searching data sources, gathering and maintaining the data needed, and completing and reviewing the collection of information. Send comments regarding this burden estimate or any other aspect of this collection of information, including suggestions for reducing this burden to Washington Headquarters Service, Directorate for Information Operations and Reports, 1215 Jefferson Davis Highway, Suite 1204, Arlington, VA 22202-4302, and to the Office of Management and Budget, Paperwork Reduction Project (0704-0188) Washington, DC 20503

PLEASE DO NOT RETURN YOUR FORM TO THE ABOVE ADDRESS.

1. REPORT DATE *(DD-MM-YYYY)*	2. REPORT DATE	3. DATES COVERED *(From - To)*
04/02/2002		06/01/01 to 12/31/01

4. TITLE AND SUBTITLE
Solid Freeform Fabrication Symposium - 2001
Report and Proceedings

5a. CONTRACT NUMBER

5b. GRANT NUMBER
N00014--01-1-0637

5c. PROGRAM ELEMENT NUMBER

6. AUTHOR(S)
D. L. Bourell and J. J. Beaman, Jr.

5d. PROJECT NUMBER

5e. TASK NUMBER

5f. WORK UNIT NUMBER

7. PERFORMING ORGANIZATION NAME(S) AND ADDRESS(ES)
The University of Texas at Austin
Solid Freeform Fabrication Symposium
Department of Mechanical Engineering C2200
Austin, TX 78712-1063

8. PERFORMING ORGANIZATION REPORT NUMBER

9. SPONSORING/MONITORING AGENCY NAME(S) AND ADDRESS(ES)
Ralph F. Wachter ONR 361
Ballston Centre Tower One
800 North Quincy Street
Arlington, VA 22217-5660

10. SPONSOR/MONITOR'S ACRONYM(S)

11. SPONSORING/MONITORING AGENCY REPORT NUMBER

12. DISTRIBUTION AVAILABILITY STATEMENT
approved for public release

20020405 057

13. SUPPLEMENTARY NOTES

14. ABSTRACT

The Twelfth Solid Freeform Fabrication Symposium, held at The University of Texas in Austin on August 6-8, 2001, was attended by over 125 national and international researchers. Papers addressed SFF issues in computer software, machine design, materials synthesis and processing, and integrated manufacturing. A total of 78 presentations were made, 61 oral presentations and 17 poster presentations. Of these, 69 are included in the proceedings volume. The diverse domestic and foreign attendees represented industrial users, SFF machine manufacturers, universities, and government. The attendance was up this year from previous years.

15. SUBJECT TERMS
Freeform Fabrication, Symposium, Proceedings

16. SECURITY CLASSIFICATION OF:			17. LIMITATION OF ABSTRACT	18. NUMBER OF PAGES	19a. NAME OF RESPONSIBLE PERSON
a. REPORT	b. ABSTRACT	c. THIS PAGE			David L. Bourell
unclass-ified	unclass-ified	unclass-ified	UL	650	19b. TELEPONE NUMBER *(Include area code)* (512) 471-3170

End of Fiscal Year Letter - ONR Grant **N00014-01-1-0637**
Solid Freeform Fabrication Symposium -2001
David L. Bourell, PI

A. Description of the Technical Research or Development Goals: This grant helped to underwrite the publication expenses associated with the Twelfth Solid Freeform Fabrication (SFF) Symposium. The symposium took place on August 6-8, 2001 in Austin, Texas at the University of Texas.

It included papers on computer interfaces with SFF, materials processing and properties associated with SFF and machine design and requirements for SFF.

B. Significant Research or Development Results During the Past Year: The Twelfth Solid Freeform Fabrication Symposium, held at The University of Texas in Austin on August 6-8, 2001, was attended by over 125 national and international researchers. Papers addressed SFF issues in computer software, machine design, materials synthesis and processing, and integrated manufacturing. A total of 78 presentations were made, 61 oral presentations and 17 poster presentations. Of these, 69 are included in the proceedings volume. The diverse domestic and foreign attendees represented industrial users, SFF machine manufacturers, universities, and government. The attendance was up this year from previous years. The Symposium organizers look forward to its being a continuing forum for technical exchange among the expanding body of researchers involved in SFF.

The Symposium was again organized in a manner to allow the multi-disciplinary nature of the SFF research to be presented coherently, with various sessions emphasizing computer issues, machine topics, and the variety of materials aspects of SFF. The three-day event was completely composed of individual oral presentations (no panel discussions/presentations) to accommodate the demand for this dissemination format. The afternoon parallel sessions were split into two sessions, and the poster session was reduced to give preference to presenters desiring to give oral presentations at the meeting. We believe that documenting the constantly changing state of SFF art as represented by these Proceedings will serve both the people presently involved in this fruitful technical area as well as the large flux of new researchers and users entering the field. This year is the second year of production of a CD proceedings. Available in November 2001, this medium allows enhancements such as higher resolution photos and figures, color presentation and whole-document searching in place of a keyword index. The attendee list is included, and the table of contents has hyperlinks to the articles. Page numbering is sequential to facilitate citation. A hard-copy print-out of the entire document is also available to those desiring that format.

The Organizing Committee hosted a special morning plenary session on the State of SFF. Five keynote talks were given by world experts. Joe Beaman (U Texas) gave a historical perspective, Ely Sachs (MIT) talked about SFF in manufacturing, Phill Dickens (De Montfort U, now Loughborough U) spoke on integration of SFF into the design process, Kevin Lyons (NIST) gave a presentation on computational issues in SFF and Fritz Prinz (Stanford U) wrapped up with a presentation on the Future of SFF.

We are pleased to report that the SFF Symposium attracted a large number of young scientists this year. We had 42 students attend this year, almost 30% of the entire meeting. Participants represented 38 universities (13 international universities), 24 industries (8 international) and 6 national labs and government agencies. The Organizing Committee has always valued the role of technical meetings as a venue for graduate students in research. We strive to make the conference affordable and therefore accessible to students. The 2001 meeting registration cost of $100 for students reflected this. Non-student cost was $350.

Information on the SFF Symposium was made available through the worldwide web at http://lff.me.utexas.edu/. On-line registration forms, hotel information, general information

brochure, proceedings order forms, maps, and previous years' talk titles are all available. The symposium email address is sffsymp@uts.cc.utexas.edu.

C. Plans for Next Year's Research or Development: Plans are currently underway for organization of the Thirteenth Solid Freeform Fabrication Symposium. The dates are tentatively August 5-7, 2002.

Solid Freeform Fabrication Proceedings

August 2001

Solid Freeform Fabrication as an important and totally integrated approach to design, materials processing and manufacturing research results related to it is contained in this proceedings of the SFF Symposium held in Austin, Texas on August 6-8, 2001

SFF Topics covered in the Symposium include:

Machine Design
Computer Sectioning
Reverse Engineering
Materials Processing
Applications

David L. Bourell , Joseph J. Beaman,
Richard H. Crawford, Harris L. Marcus,
Kristin L. Wood and Joel W. Barlow, Editors

© 2001 The University of Texas at Austin
All rights of reproduction in any form are protected by U.S. Copyright Laws.
Permission to copy all or portions of the proceedings contents must be obtained
from the authors and The University of Texas at Austin.
Library of Congress ISSN 1053-2153

DISTRIBUTION STATEMENT A
Approved for Public Release
Distribution Unlimited

this page intentionally blank

PREFACE

The Twelfth Solid Freeform Fabrication (SFF) Symposium, held at The University of Texas in Austin on August 6-8, 2001, was attended by over 130 national and international researchers. Papers addressed SFF issues in computer software, machine design, materials synthesis and processing, and integrated manufacturing. The diverse domestic and foreign attendees included industrial users, SFF machine manufacturers, university researchers and representatives from the government. The Symposium organizers look forward to its being a continuing forum for technical exchange among the expanding body of researchers involved in SFF.

A special plenary session on the state of SFF was organized to present overview talks on various aspects of the field. Invited speakers were Joseph Beaman (University of Texas) who gave a historical perspective, Emanuel Sachs (MIT) who related SFF to manufacturing, Phill Dickens (DeMontfort University) who gave a presentation on the role of SFF in design, Kevin Lyons (NIST) who spoke on software developments and Fritz Prinz (Stanford) who discussed the future of SFF.

The Symposium was again organized in a manner to allow the multi-disciplinary nature of the SFF research to be presented coherently, with various sessions emphasizing modeling, process development, and materials. We believe that documenting the changing state of SFF art as represented by these Proceedings will serve both those presently involved in this fruitful technical area as well as new researchers and users entering the field.

The papers are stored individually on the CD in pdf format by primary author last name, and Adobe® Acrobat® Reader™ installers for the Macintosh (OS 9.x) and PC (Windows 2000) are included which may be used to view and search the pdf files. The Table of Contents file has links to all the papers. We have sequentially numbered the pages of the papers to facilitate citation. Some versions of Reader™ do not have search capabilities which are necessary to keyword search the SFF Symposium Proceedings. If you have problems with searching, you might consider installing the version of Reader™ from the CD. The Adobe website (http://www.adobe.com/) also has versions of Acrobat Reader which may be downloaded free of charge.

The editors would like to extend a warm "Thank You" to Rosalie Foster for her detailed handling of the logistics of the meeting and the Proceedings, as well as her excellent performance as registrar and problem solver during the meeting. We would like to thank the Organizing Committee, the session chairs, the attendees for their enthusiastic contributions, and the speakers both for their significant contribution to the meeting and for the relatively prompt delivery of the manuscripts comprising this volume. We look forward to the continued close cooperation of the SFF community in organizing the Symposium. We also want to thank the Office of Naval Research (N00014-01-1-0637) and the National Science Foundation (DMI-0117072) for supporting this meeting financially. The meeting was co-organized by the University of Connecticut at Storrs, and the Mechanical Engineering Department, Laboratory for Freeform Fabrication and the Texas Materials Institute at The University of Texas at Austin.

The editors.

this page intentionally blank

Organizing Committee

Joel Barlow	University of Texas at Austin
Joseph Beaman	University of Texas at Austin
David Bourell	University of Texas at Austin
Richard Crawford	University of Texas at Austin
Harris Marcus	University of Connecticut at Storrs
Kris Wood	University of Texas at Austin

Advisory Committee

David Alexander	Pratt & Whitney
Amit Bandyopadhyay	Washington State University
Ian Campbell	Loughborough University
Joe Cesarano	Sandia National Labs-NM
Richard Chartoff	University of Dayton
Stephen Danforth	Rutgers-The State University of New Jersey
Phill Dickens	Loughborough University
Steve Fishman	Office of Naval Research
Kesh Narayanan	National Science Foundation
Fritz Prinz	Stanford University
Eli Sachs	Massachusetts Institute of Technology
Brent Stucker	University of Rhode Island
Ralph Wachter	Office of Naval Research

this page intentionally blank

Table of Contents

Page

Preface ---------- ix

Organizing/Advisory Committee ---------- xi

Process Development

Study on Selective Laser Sintering Components with Electrically Conductive Channels
F. P. Y. Ting, I. Gibson, W. L. Cheung, The University of Hong Kong ---------- 1

Design and Integration of a Laser-Based Materials Deposition System
J. Laeng aka Jamaluddin Abdullah[a], Frank Liou[b], M. N. Mohamad Ibrahim[a], W. M. Wan Muhammad[a], [a]Universiti Sains Malaysia, [b]University of Missouri-Rolla ---------- 11

Skeleton-based Geometric Reasoning for Adaptive Slicing in a Five-axis Laser Aided Manufacturing Process System
Kunnayut Eiamsa-ard, Jun Zhang, F. W. Liou, University of Missouri-Rolla ---------- 20

Surface Roughness Enhancement of Indirect-SLS Metal Parts by Laser Surface Polishing
J. A. Ramos, J. Murphy, K. Wood, D. L. Bourell, J. J. Beaman, The University of Texas-Austin ---------- 28

SLS Powder Life Study
J. Choren, V. Gervasi, T. Herman, S. Kamara, J. Mitchell, Milwaukee School of Engineering ---------- 39

High-Speed Curtain Recoating for Stereolithography
M. Gilio, J.-P. Kruth, P. Vanherck, Katholieke Universiteit Leuven ---------- 46

Effective Cooling Method for Spin Casting Process
Yong-Ak Song, Sehyung Park, Yongsin Kwon, Korea Institute of Science and Technology KIST ---------- 55

Fabrication of Multi-Layered Carbon Structures Using LCVD
Ryan W. Johnson, Scott N. Bondi, Daniel L. Jean, Chad E. Duty, Ming Xuan Jiang, W. Jack Lackey, Georgia Institute of Technology ---------- 61

Homogeneous Metal Parts by Infiltration
Adam M. Lorenz, Emanuel M. Sachs, Samuel M. Allen, Michael J. Cima, Massachusetts Institute of Technology ---------- 69

Accuracy Improvement in Rapid Prototyping Machine (FDM-1650)
A. Gregorian[a], B. Elliott[a], R. Navarro[a], F. Ochoa[a], H. Singh[a], E. Monge[a], J. Foyos[a], R. Noorani[a], B. Fritz[b], S. Jayanthi[c], [a]Loyola Marymount University, [b]Northrop Grumman, [c]3D Systems ---------- 77

On Some Physical Aspects of Process Control in Direct Selective Laser Sintering of Metals Part I
Suman Das, University of Michigan-Ann Arbor ---------- 85

On Some Physical Aspects of Process Control in Direct Selective Laser Sintering of Metals Part II
Suman Das, University of Michigan-Ann Arbor ---------- 94

On Some Physical Aspects of Process Control in Direct Selective Laser Sintering of Metals Part III
Suman Das, University of Michigan-Ann Arbor---------- 102

New Way of Process Parameters Optimization in SFF Based on Deposition by Welding
Z. Jandric, R. Kovacevic, Southern Methodist University---------- 110

Controlled-Depth Laser Cutting of Aluminum Sheet for Laminated Object Manufacturing
Gene Zak, Matthew Shiu, Queen's University---------- 120

Closed Loop Control of 3D Laser Cladding Based on Infrared Sensing
D. Hu, H. Mei, G. Tao, R. Kovacevic, Southern Methodist University---------- 129

Research and Development of a Hybrid Rapid Manufacturing Process
F. W. Liou, J. Choi, R. G. Landers, V. Janardhan, S. N. Balakrishnan, S. Agarwal, University of Missouri-Rolla---------- 138

Material Movement and Fusion Behavior of TrueForm and TrueForm/SiO_2 during Selective Laser Sintering
K. M. Fan, W. L. Cheung, I. Gibson, The University of Hong Kong ---------- 146

Design of a Micro-Hopper Array for Multi-Material Powder Deposition
Suman Das, James Santosa, University of Michigan-Ann Arbor---------- 155

Materials

SALDVI of SiC into Metal and Ceramic Powders
James E. Crocker, Haoyan Wei, Leon L. Shaw, Harris L. Marcus, University of Connecticut-Storrs ---------- 163

Spot Joining of Si_3N_4 and SIC Ceramics using Selective Area Laser Deposition (SALD) Technique
Ibrahim M. Ghayad[a], Erik Geiss[b], James E. Crocker[b], Harris L. Marcus[b], [a]Central Metallurgical Research and Development Institute, [b]University of Connecticut-Storrs ---------- 170

Robocasting of Photonic Band Gap Structures
James E. Smay[ab], Joseph Cesarano III[b], Shawn Y. Lin[b], John N. Stuecker[b], Jennifer A. Lewis[a], [a]University of Illinois-Urbana-Champaign, [b]Sandia National Laboratory-NM---------- 175

Mechanical Properties of Laser-Deposited Ti-6Al-4V
P. A. Kobryn, S. L. Semiatin, Air Force Research Laboratory ---------- 179

Composite Modeling and Analysis of FDM Prototypes for Design and Fabrication of Functionally Graded Parts
Longmei Li, Q. Sun, C. Bellehumeur, P. Gu, University of Calgary---------- 187

Microstructure Evaluation for Laser Densification of Dental Porcelains
Xiaoxuan Li[a], Jiwen Wang[a], Alvin Augustine[a], Leon L. Shaw[a], Harris L. Marcus[a], Thomas B. Cameron[b], [a]University of Connecticut-Storrs, [b]Degussa-Ney Dental Inc.---------- 195

Freeform Fabrication of Ti_3SiC_2 Structures
D. J. Dcosta, W. Sun, T. El-Raghy, Drexel University---------- 203

Slurry-Based 3DP and Fine Ceramic Components
M. J. Cima, M. Oliveira, H. R. Wang, E. Sachs, R. Holman, Massachusetts Institute of Technology ---------- 216

Fused Deposition of Ceramics (FDC) and Composites
Seyi Onagoruwa, Susmita Bose, Amit Bandyopadhyay, Washington State University ---------- 224

Solidification Modeling and Microstructural Characterization of Alloy IN718 Deposited by Laser Engineered Net Shaping
J. N. DuPont[a], J. G. Nawrocki[a], M. L. Griffith[b], [a]Lehigh University, [b]Sandia National Laboratory-NM ---------- 232

Experimental Study of Selective Laser Sintering of Parmax®
Jagan R. Rajan[a], Kristin L. Wood[a], Nick Malkovich[b], [a]University of Texas-Austin, [b]Mississippi Polymers Technologies Inc. ---------- 242

Effects of Aging on Epoxy-Based Rapid Tooling Materials
Xavier Ottemer, Jonathan S. Colton, Georgia Institute of Technology ---------- 256

Limits of Loose Metal Powder Density in the Sinterstation
Klas Boivie, The Royal Institute of Technology ---------- 264

Direct Metal Laser Re-Melting (DMLR) of 316L Stainless Steel Powder Part 1: Analysis of Thin Wall Structures
Rhys Morgan, Adam Papworth, Chris Sutcliffe, Pete Fox, Bill O'Neill, University of Liverpool ---------- 276

Direct Metal Laser Re-Melting of 316L Stainless Steel Powder Part 2: Analysis of Cubic Primitives
Rhys Morgan, Adam Papworth, Chris Sutcliffe, Pete Fox, Bill O'Neill, University of Liverpool ---------- 283

Modeling

A Study of Functional Testing with SFF Parts
Alan J. Dutson, Kristin L. Wood, Joseph J. Beaman, Richard H. Crawford, David L. Bourell, University of Texas-Austin ---------- 296

STL-based Finish Machining of Rapid Manufacturing Parts and Tools
Xiuzhi Qu, Brent E. Stucker, University of Rhode Island ---------- 304

A System Approach in Extrusion-Based Multi-Material CAD
Cheng-Tiao Hsieh, Noshir A. Langrana, Rutgers-The State University of New Jersey ---------- 313

Maximum Visibility Building Direction for Layered Manufacturing of Jewel Rings
Y. Y. Young, K. M. Yu, C. K. Kwong, The Hong Kong Polytechnic University ---------- 322

Thermal and Stress Modeling of Laser Fabrication of Multiple Material Components
K. Dai, L. Shaw, University of Connecticut-Storrs ---------- 330

Manufacturing of Instrumented Prototypes
Moss Shimek, Nachiket Patwardhan, Kristin L. Wood, Joseph Beaman, Richard Crawford, University of Texas-Austin ---------- 338

Compensation of Non-Linear Shrinkage of Polymer Materials in Selective Laser Sintering
K. Manetsberger[a], J. Shen[a], J. Muellers[b], [a]DaimlerChrysler Research Center, [b]Dornier Research ---------- 346

A Model of Laser-Powder Interaction in Direct Selective Laser Sintering of Metals
Suman Das, Haseung Chung, University of Michigan-Ann Arbor---------- 357

Thermal Stresses in Direct Metal Laser Sintering
Haiko Pohl[a], Abdolreza Simchi[ab], Munther Issa[ac], Hugo Calefi Dias[ad], [a]Fraunhofer Institute for Manufacturing and Advanced Materials IFAM, [b]Sharif University of Technology, [c]University of Bremen, [d]Universidade Federal de Santa Catarina---------- 366

Thermal, Fluid, and Mass Transport Modeling of a Gas-Jet Reagent Delivery System for Laser Chemical Vapor Deposition (LCVD)
Chad Duty, Ryan Johnson, Daniel Jean, Scott Bondi, W. Jack Lackey, Georgia Institute of Technology---------- 373

Finite Element Structural Analysis of Prosthesis Sockets for Below-the-Knee Amputees Manufactured Using SLS
Mario Faustini[ac], Mahendra Lokhande[a], Richard Crawford[a], William Rogers[b], Andrew Gitter[b], Gordon Bosker[b], [a]University of Texas-Austin, [b]University of Texas Health Science Center-San Antonio, [c]National Council of Scientific and Technological Development---------- 381

Modeling of Selective Area Laser Deposition Vapor Infiltration (SALDVI) of Silicon Carbide
K. Dai, J. Crocker, L. Shaw, H. Marcus, University of Connecticut-Storrs---------- 392

Computer Integrated Adaptive Slicing and Vision Technologies for High Performance Rapid Prototyping System
Jia-Chang Wang, Jun-Ming Wang, Tsung Te Lin, Jeng-Ywan Jeng, National Taiwan University of Science and Technology---------- 400

A Slicing Procedure for 5-Axis layered Manufacturing
R. Sundaram, J. Choi, University of Missouri-Rolla ---------- 408

Voxel-based Modeling with Multi-resolution Wavelet Transform for Layered Manufacturing
Soonkyu Yim, Hae Chang Gea, Rutgers-The State University of New Jersey---------- 416

Rapid Prototyping using Fractal Geometry
S. C. Soo, K. M. Yu, The Hong Kong Polytechnic University---------- 424

Melt Pool Size Control in Thin-Walled and Bulky Parts via Process Maps
Aditad Vasinonta, Jack L. Beuth, Raymond Ong, Carnegie Mellon University ---------- 432

On-line Monitoring of Epoxy Resin Cure using Infrared Spectroscopy
F. Fouchal, J. A. G. Knight, P. Dickens, N. Garrington, DeMontfort University ---------- 441

Empirical Modeling and Vision Based Control for Laser Aided Metal Deposition Process
Mallikharjuna R. Boddu, Srinivas Musti, Robert G. Landers, Sanjeev Agarwal, Frank W. Liou, University of Missouri-Rolla ---------- 452

Control of Laser Cladding for Rapid Prototyping--a Review
Mallikharjuna R. Boddu, Robert G. Landers, Frank W. Liou, University of Missouri-Rolla---------- 460

Physical Modeling for Dynamic Control of Melting Process in Direct-SLS
S. Ahn, J. Murphy, J. Ramos, J. J. Beaman, University of Texas-Austin ---------- 468

Software for the Interactive Configuration of RP Based Process Chains
Stefan Dreher, Fraunhofer IPK Berlin ---------- 479

Simulation of the Electrochemical Machining Process
R. Temur, T. Coole, C. Bocking, Buckinghamshire Chilterns University College---------- 486

Applications

Automated Construction using Contour Crafting
B. Khoshnevis, H. Kwon, S. Bukkapatnam, University of Southern California---------- 497

Clinical Evaluation of Prosthetic Sockets Manufactured by Selective Laser Sintering
Bill Rogers[a], Andrew Gitter[a], Gordon Bosker[a], Mario Faustini[b], Mahendra Lokhande[b], Richard Crawford[b], [a]University of Texas Health Science Center-San Antonio, [b]University of Texas-Austin---------- 505

Testing of Compliance in a Prosthetic Socket Fabricated Using Selective Laser Sintering
Mahendra Lokhande, Richard Crawford, University of Texas-Austin---------- 513

Rapid Prototyping Assisted Design and Development of Inter-Vertebral Implants
J. Chiang, M. Lehmicke, D. Dcosta, X. Hu, F. Lin, W. Sun, Drexel University ---------- 527

Custom Fabrication of Hard Tissue Reconstructive Frameworks
R. V. Nambiar, R. E. Jones, J. R. Gomez, University of Texas-Pan American ---------- 539

Powder Delivery in Dental Restoration Rapid Prototyping Process
Jiwen Wang[a], Xiaoxuan Li[a], Leon L. Shaw[a], Harris L. Marcus[a], Thomas B. Cameron[b], [a]The University of Connecticut-Storrs, [b]Degussa-Ney Dental Inc. ---------- 546

Manufacturing of a Heterogeneous Flywheel on a LENS Apparatus
Stephane Morvan[a], Georges Fadel[b], James Love[a], Dave Keicher[a], [a]Optomec Inc., [b]Clemson University ---------- 553

Robocasting Periodic Lattices for Advanced Filtration
John N. Stuecker, Joseph Cesarano III, James E. Smay, Sandia National Labs-NM---------- 561

Synthesis of a Compact Tetralattice Heat Exchanger using Solid Freeform Fabrication and Comparison Testing Against a Tube Heat Exchanger
James R. Heidrich, Vito Gervasi, Subha Kumpaty, Milwaukee School of Engineering ---------- 567

Applications of Solid Freeform Fabrication at the Naval Research Laboratory
J. P. Thomas[a], B. A. Bender[a], A. Pique[a], K. P. Cooper[a], R. J. Rayne[a], A. C. Richardson[b], [a]Naval Research Laboratory, [b]National Naval Medical Center ---------- 576

State of Solid Freeform Fabrication

Solid Freeform Fabrication: An Historical Perspective
Joseph J. Beaman, University of Texas-Austin---------- 584

Manufacturing by Solid Freeform Fabrication
Emanuel Sachs, Massachusetts Institute of Technology ---------- 596

Integration of Solid Freeform Fabrication in Design
R. Hague[a], I. Campbell[b], P. Dickens[a], P. Reeves[c], [a]DeMontfort University, [b]Loughborough University, [c]Edward Mackenzie Ltd.---------- 619

Laser Fusion Coatings of Functional Parts
J. A. Ramos[a], D. L. Bourell[a], M. R. Govindaraju[b], [a]University of Texas-Austin,[b]Karta Technologies, Inc.---------- 628

Author/Attendee List---------- 637

Study on selective laser sintering components with electrically conductive channels

F.P.Y. Ting, I. Gibson, W.L. Cheung

Department of Mechanical Engineering, The University of Hong Kong, Pokfulam Road, Hong Kong

Abstract

Electrically conductive channels were created using conductive carbon cement (CCC) by a simple non-contact continuous deposition method on sintered DuraForm™ Polyamide parts. The deposition system consisted of a drive circuit, a Micro Inert Solenoid Valve (MIV), a nozzle head and two liquid material reservoirs. Effect of CCC/solvent ratio, speed of deposition head and sintering condition of the Polyamide base material on the electrical properties of the conductive channels were investigated. The paper will then go on to discuss how these results relate to potential applications of Selective Laser Sintering (SLS) components with electrical property.

Keywords: SLS; electrically conductive channels; non-contact deposition

1. Introduction

SLS is a rapidly developing technology and its applications are no longer limited to conceptual testing but it is also used in building functional prototypes and even for rapid manufacturing [1,2]. Traditionally, commercial SLS only produces models with single materials or homogeneous mixtures. Previous work has demonstrated that it is possible to create SLS prototypes with different properties in desired positions. Ling and Gibson [3] tried to create colour RP components in which a secondary material, i.e. colour ink, was delivered. In view of this, if an electrically conductive material is chosen as the secondary material, it is possible to create SLS components with electrically conductive channels. In this study, Commercial Leit-CCC™ (Conductive Carbon Cement) was chosen as the secondary material in creating the electrically conductive channels. A non-contact deposition method has been developed for delivering the CCC and it will be introduced in this paper.

Since SLS parts are porous, it is possible for CCC to infiltrate through the layers of a SLS component. One possible advantage of the phenomenon is that a conductive channel can be built through the layers. On the other hand, diffusion of CCC may adversely affect the electrical properties of the conductive channels within the layer. Previous study has shown that penetration of CCC into polyamide substrate at high temperature increased the resistance of CCC channels [4]. Apart from temperature, other parameters such as ink composition, feed rate of ink as well as porosity of the SLS component will all have an effect on the performance of the conductive channels. The objective of this study is to investigate the effects of ink concentration, deposition speed and the sintering condition of base material on the resistance of the CCC channels created on sintered DuraForm™ Polyamide. Finally, some potential applications of SLS components with electrical property will also be discussed.

2. Experimental

2.1 Materials

Commercial Leit-CCC™(Conductive Carbon Cement) was used as the primary ingredient for formulating the electrically conductive ink used to create the electrically conductive channels. A typical composition of CCC consists of graphite, acrylic and organic solvents in which graphite is the conductive ingredient while acrylic serves as a binder. The organic solvents include acetone, methoxypropylacetate, xylene and butylacetate. Thinner was added to lower the viscosity of the conductive ink and extra amount of graphite powder was added to enhance the conductive nature of the ink. Four compositions of the ink were tested in this study and the details are shown in Table 1. The substrates, onto which the conductive channels were deposited, were sintered from DuraForm™ Polyamide, Fig. 1, which has a melting point of 184°C [5].

Table 1 Compositions of the blended conductive ink

Type	CCC/graphite ratio	Paint*/thinner□ ratio
I	½	1/3
II	½	1/5
III	½	1/7.5
IV	½	1/10

*Paint: mixture of commercial CCC and graphite powder
□thinner: mixture of organic solvents xylene, methoxypropylacetate, acetone and butylacetate in equal weight.

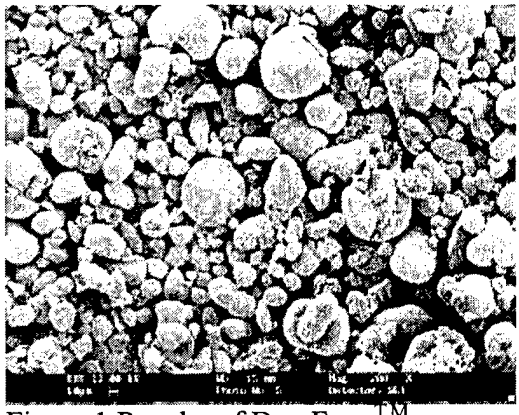


Figure 1 Powder of DuraForm™ Polyamide

2.2 Sintering of DuraForm™ Polyamide substrates

The sintering process was carried out using a DTM Sinterstation™ 2000. The sintering condition can be varied by the fill laser power (P), beam speed (BS), scan spacing (SCSP) and the part bed temperature (T_b). When studying the effects of ink composition and deposition speed, DuraForm™ Polyamide substrates were sintered at P = 8%, BS = 1257.3mms^{-1}, SCSP = 0.15mm and T_b = 167°C. The value of P was lower than the nominal setting but was still chosen as it could give acceptable physical properties for creating electrically conductive paths in SLS DuraForm™ Polyamide samples. This setting gave a higher porosity than the normal setting but at the same time, the part was strong enough for handling. In studying the effect of sintering condition of DuraForm™ Polyamide substrates on the performance of the CCC channels, the sintering process was carried out at P = 6% to 16% corresponding to ED = 0.01 J/mm^2 to 0.06 J/mm^2 according to the equation derived by Nelson [6].

2.3 Deposition of CCC

An experimental non-contact deposition system was developed for depositing the conductive ink (CCC) onto the polyamide substrates. It consists of a typical drive circuit, Fig.2, a Micro Inert Solenoid Valve (MIV), Fig.3, a nozzle head with diameter 0.328mm and two liquid material reservoirs. Fig.4 shows a schematic diagram of the set-up. The 3-way MIV was operated at 24Vdc.

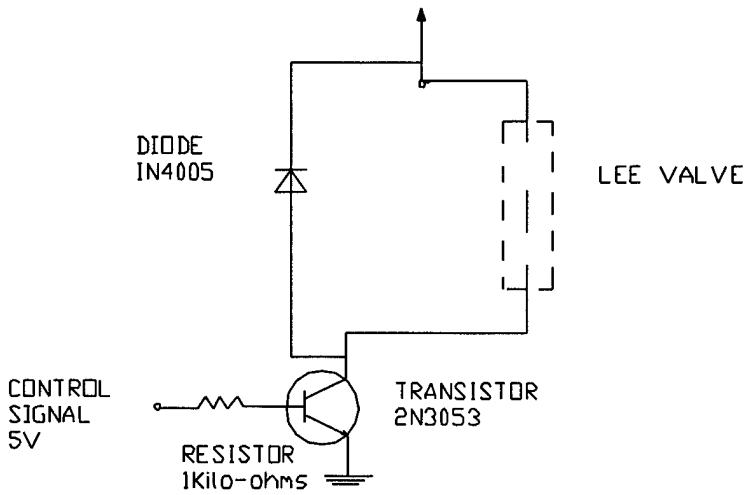


Fig. 2 Schematic Diagram of the typical drive circuit

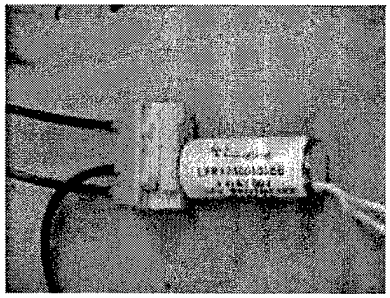


Fig. 3 Micro Inert Solenoid (MIV)

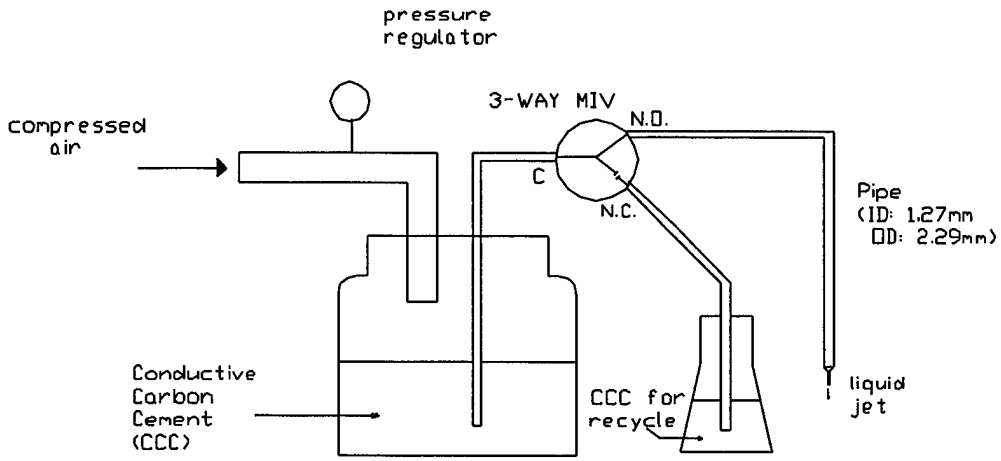


Fig. 4 Schematic Diagram of non-contact deposition system

Compressed air was first passed through a pressure regulator before entering the conductive ink reservoir. The air pressure in the ink reservoir was controlled at 10psi. The CCC

was squeezed out through the outlet pipe (internal diameter = 1.27mm and external diameter = 2.29mm) and then through the 3-way MIV which was controlled by the typical drive circuit. Upon energising of the MIV solenoid, CCC was ejected from the nozzle head. When not energised, CCC was collected for recycling. The nozzle head was mounted on a computer controlled X-Y plotter.

For a constant feed rate from the nozzle, speed of movement of the deposition head will affect the amount of ink deposited per unit length. This would undoubtedly affect the electrical properties of the CCC channels created. To study the effect of deposition head speed, Type II ink was used. For the X-Y plotter, 100% speed setting equals to $1016 mms^{-1}$. Five deposition head speed settings (10%, 30%, 50%, 80% and 100%) were chosen for creating the CCC channels on the base material.

2.4 Resistance measurement of CCC channels

Resistance of the CCC channels created on the sintered DuraForm^{TM} Polyamide substrates were measured using a multimeter. The two electrodes were placed on the surface of the channels and the distance between the electrodes was 90mm. Five readings were taken for each measurement.

2.5 Scanning electron microscopy (SEM)

The SEM was conducted on a Cambridge Stereoscan 440 scanning electron microscope at operating voltages below 20kV. Specimens were dipped into liquid nitrogen before they were split to give the cross-sectional views. Samples were sputter coated with gold-palladium to avoid charging.

3 Results and Discussion

3.1 Performance of the non-contact deposition system

Non-contact deposition methods are more suitable to be employed during the SLS process because of the following reasons. In order to avoid curling, the chamber temperature within the DTM Sinterstation^{TM} 2000 is high, usually at the melting threshold of the polymer powder used [5]. The component inside the chamber is in a soft state and direct contact between the deposition head and the component will easily scratch or deform the component. Meanwhile, non-contact deposition methods can preserve the original surface morphology and the profile of the parts. The operation of a non-contact deposition system does not rely on the physical state of the material on which CCC is being deposited. No matter the base material is in solid state or molten state, non-contact deposition can still be applied.

Basically, there are two deposition modes for non-contact deposition, namely, continuous deposition and drop-on-demand [7]. With the present setup, preliminary experiments had demonstrated that continuous deposition gave a promising result for drawing conductive channels of simple geometry and it was therefore chosen in this study. However, there are some problems associated with the setup. The liquid jet emanating from the nozzle into an ambient gas is unstable [8]. The phenomenon is believed to be associated with a number of factors such as

fluctuation of air pressure in the ink reservoir and the intrinsic property such as viscosity of the ink. Viscosity tends to reduce the jet breakup rate and increase the droplet size. Apart from these, sedimentation of graphite particles was also a problem but this could be solved by adding a magnetic stirrer in the ink reservoir.

3.2 Effect of deposition speed

Fig. 5 shows the CCC channels created on DuraForm™ Polyamide substrates at different deposition speeds. When the deposition speed was low, CCC channels were wider as more material was delivered per unit length. The resistance of the CCC channels was found to increase almost linearly with the deposition speed, Fig.6. This is probably because of the reduction in the cross-sectional area of the channels deposited. There is always a trade off between the electrical performance and the geometric requirement of the CCC channels. Usually, the narrower the CCC channels, the higher is the resistance. Therefore, deposition speed can be one way of varying the electrical properties of a conductive channel within a part.

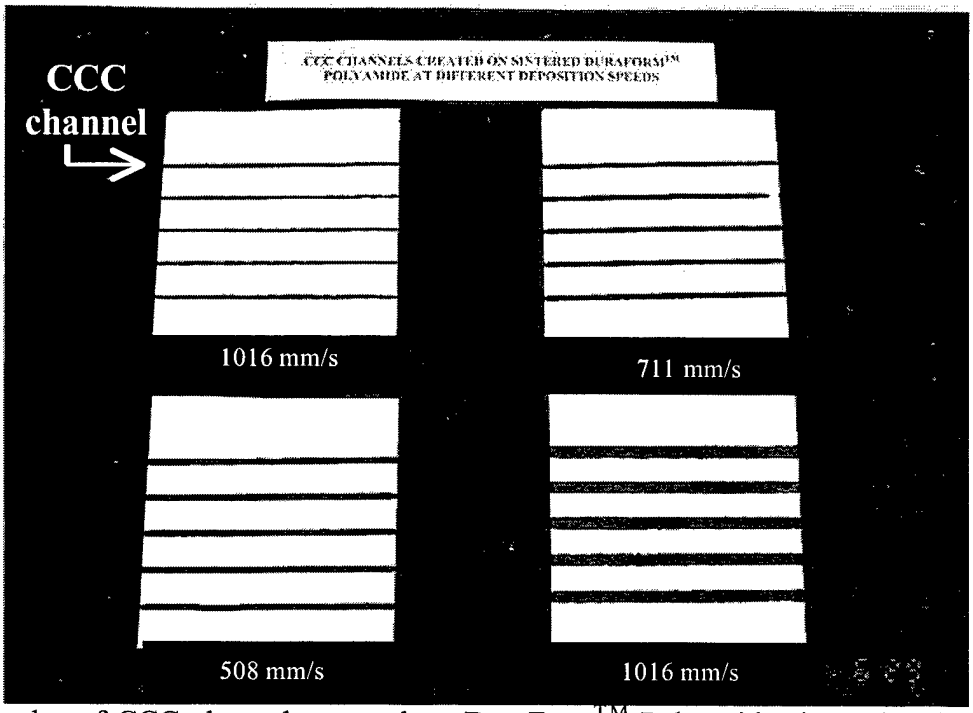


Fig. 5 Samples of CCC channels created on DuraForm™ Polyamide sintered at 0.0212J/mm^2 using Type II conductive ink at different deposition speeds

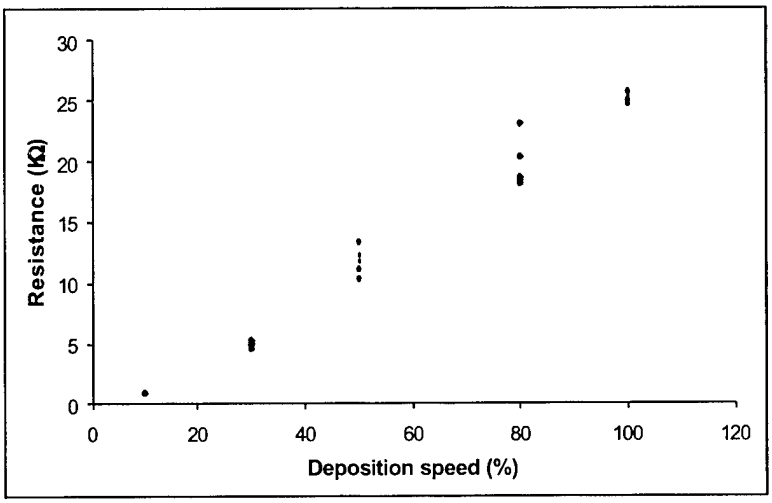


Fig. 6 Resistance of the CCC channels created at different deposition speeds

3.3 Effect of CCC/solvent ratio

Variation of resistance of the CCC channels created from Type I, II, III and IV conductive inks is shown in Fig. 7. The resistance increased when the paint/thinner ratio decreased. This can be attributed to the fact that when the paint/thinner ratio was low, there were less graphite particles in the conductive ink. This could also be seen by the lighter colour of CCC channels created from inks of low paint/thinner ratio. There was a significant increase in resistance when the paint to thinner ratio dropped from 1/7.5 to 1/10. This suggests that further reduction in the paint/thinner ratio would greatly affect the electrical conductive behaviour of the CCC channels.

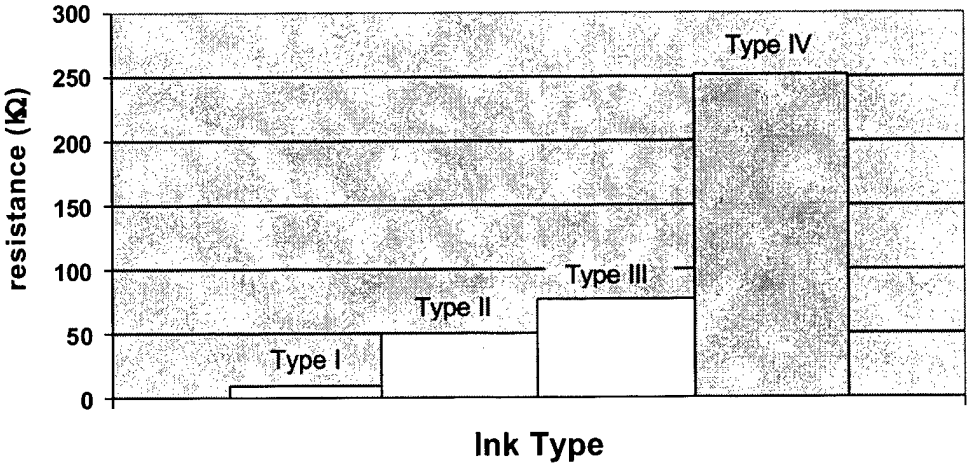
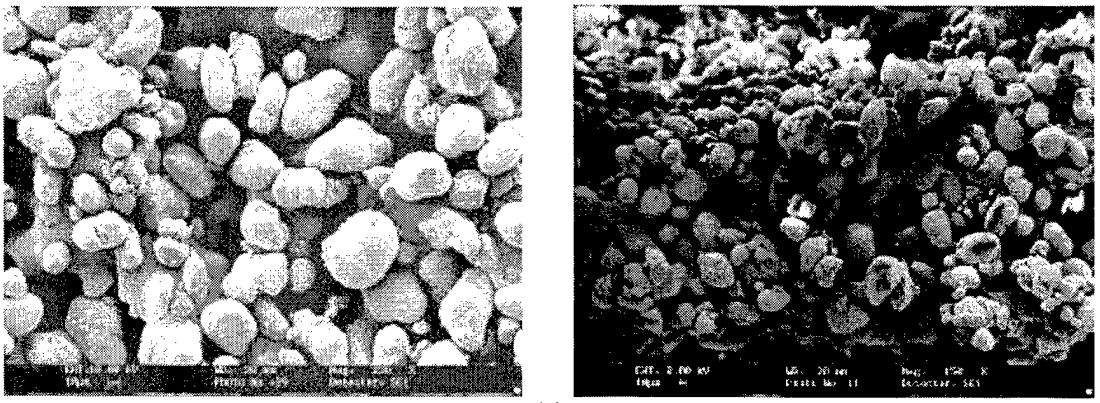


Fig. 7 Variation of the resistance of CCC channels created using different compositions of conductive ink on DuraForm^{TM} Polyamide substrate built under ED = 0.0212J/mm^2, ink deposition speed 1016ms^{-1}

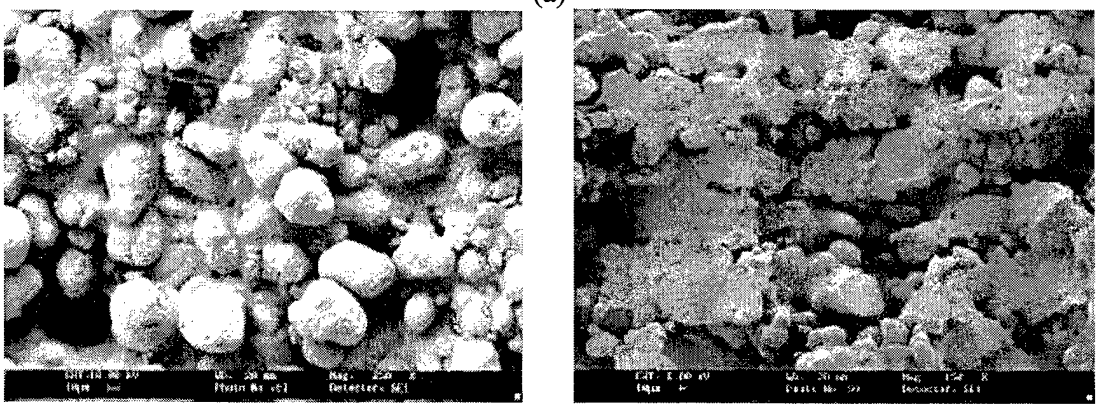
3.4 Effect of sintering condition of the base material

In building a SLS component with electrically conductive channels, ink composition and method of deposition of CCC are certainly not the only considerations. Since SLS parts built under different laser energy densities will have different physical densities, this effect was studied in relation to the process of creating SLS components with electrically conductive channels. Even though semi-crystalline materials like DuraForm^{TM} Polyamide have a limited range of usable energy density values in terms of tensile properties, such a range does exist. Also, parts may be fabricated using smaller energy densities in selected regions, providing suitable conditions for accommodating conductive materials. The variation in ED values and the effect on CCC channels was therefore studied.

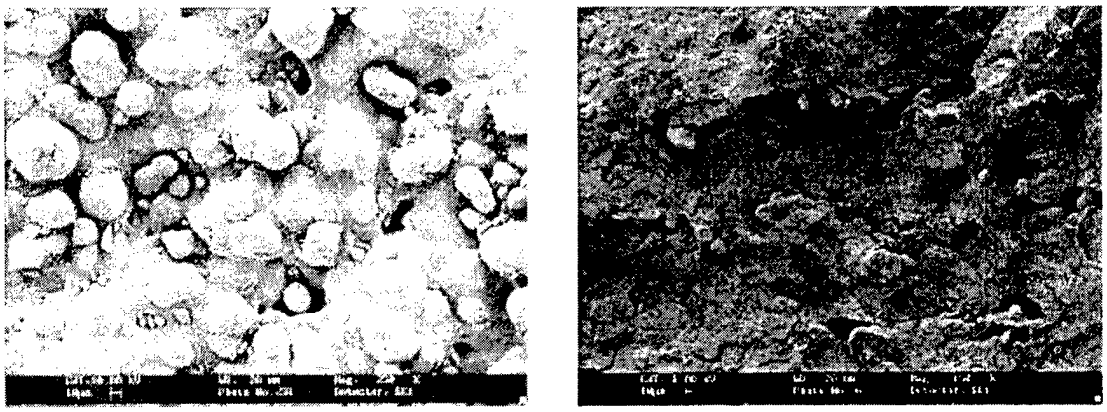
Fig. 8 shows the SEM micrographs of the surface and cross-sectional morphologies of DuraForm^{TM} Polyamide sintered at different ED. At ED = 0.0146J/mm^2, the polymer particles did not fuse well (Fig. 8a) and the surface morphology resembled that of unsintered DuraForm^{TM} Polyamide (Fig. 1), except some of the particles were slightly fused together. In this case, penetration of CCC through the layers was likely, Fig. 9. At a higher ED, better fusion of the powder was observed and the samples were less porous. A layered structure was observed in the cross-section of the sample built under ED = 0.0212J/mm^2 (Fig. 8b). Nevertheless, holes were still present through the layers and penetration of CCC might still be possible. However, it is difficult to distinguish individual layers from the sample processed at ED = 0.0371 J/mm^2 (Fig. 8c) and penetration of CCC is highly unlikely.



(a)



(b)



(c)

Fig. 8 Surface morphologies (left) and cross-sectional morphologies (right) of DuraForm^{TM} Polyamide sintered at different energy densities: a) 0.0146; b) 0.0212 and c) 0.0371 J/mm^2

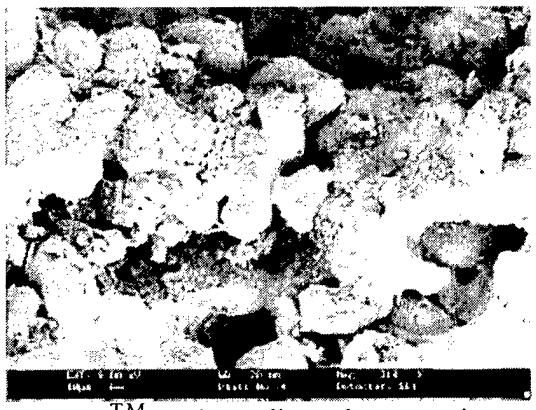


Fig. 9 Cross-section of DuraForm^{TM} Polyamdie substrate sintered at ED = 0.0212 J/mm^2, showing penetration of CCC

The variation of resistance of the CCC channels deposited on DuraForm^{TM} Polyamide sintered at different ED is shown in Fig. 10. There was a 29.4% drop in resistance when the ED increased from 0.016J/mm^2 to 0.053J/mm^2. This is related to the change of morphology of the substrates as described in the previous paragraph. At low ED, the porosity of the sintered component was high. Consequently, CCC would penetrate deeply into the substrate and this would adversely affect the performance of the conductive channels.

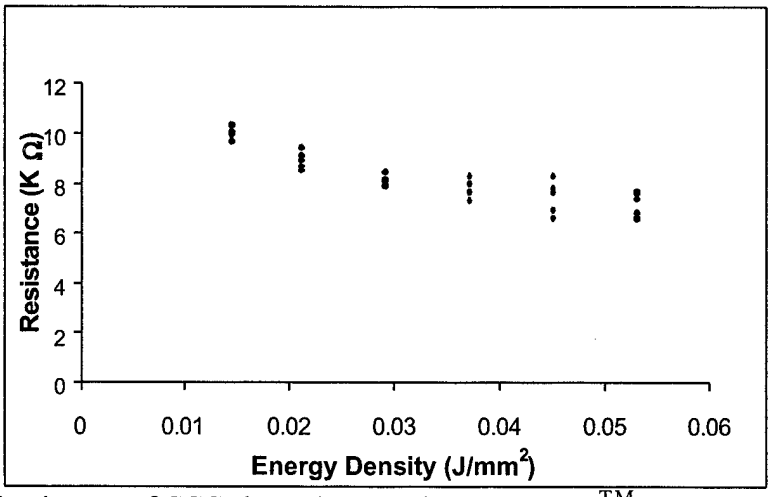


Fig.10 Variation of resistance of CCC channels created on DuraForm^{TM} Polyamide sintered at different energy densities, ink deposition speed 1016mms^{-1}, conductive ink used: Type I

3.5 Potential applications of SLS components with electrical property

EMI shielding

With an increasing use of plastic materials in electronic product design, conductive coatings for EMI shielding has become an important potential developing field. The increase in popularity of plastics is attributed to their non-conductive nature and the fact that they are transparent to electromagnetic waves. For digital electronic products manufactured using plastic enclosures, conductive coating becomes an important method of providing EMI shielding. With further development of the non-contact deposition system and a suitable choice of conductive ink, it is believed that plastic enclosure and conductive coating can be built at one time.

Heating elements and strain gauges

In this study, conductive ink is used in creating electrically conductive channels and these channels provide a passage for resistive components such as strain gauges. It is, however, believed that the application of this system can be expanded to a wider area. If the secondary materials being delivered possess different heat transfer coefficients, thermal properties of the SLS component can be altered as well. Heating elements can be built in any desired locations within the component by depositing materials with different heat transfer properties.

For such applications, CCC may not be the best material candidate. The main concern of this study is to examine the general trend of the effect of different parameters on the electrical performance of electrically conductive channels rather than the absolute values of the resistance measured. In this aspect, CCC has served the purpose. It may be necessary to deposit other materials with different electrical properties such as silver ink because of its good electrical conductivity. Further work is being carried out to improve the non-contact deposition system as well as to identifying a more suitable conductive ink.

4 Conclusion

The setup and operation of a simple non-contact deposition method was described. With further development of the system, it is possible to be employed during the SLS process. Effects of CCC/solvent ratio, deposition speed and morphology of the base material on the resistance of the conductive channels were evaluated. It was found that too a low CCC/solvent ratio would increase the resistance of the CCC channels. In addition, a lower resistance of the CCC channels could be achieved by either lowering the deposition speed or sintering the polymer substrate at a higher ED. Among the three factors that affect the performance of the CCC channels, CCC/solvent ratio was found to play a major role as it greatly affected the resistance of the CCC channels.

Reference

1. S. Das, J.J. Beaman, M. Wohlert and D.L. Bourell, "Freeform Fabrication of high performance Titanium Components Via SLS/HIP", Mat. Res. Soc. Symp. Proc. Vol. 542, 1999, pp45-50
2. H.M. Zaw, J.Y.H. Fuh, A.Y.C. Nee, L. Lu, "Formation of a new EDM electrode material using sintering techniques", Journal of Materials Processing Technology Proceedings of the 1999 4th Asia Pacific Conference on Materials Processing, 1999, v89-90, pp182-186
3. Ling Wai Ming and Ian Gibson, "Colour Rapid Prototyping based on SLS process", Proc., Solid Freeform Fabrication Symp., Austin, Texas, US, Aug 2000, pp227-234
4. F.P.Y. Ting, I. Gibson, W.L. Cheung, "A study on electrically conductive channels in selective laser sintered components", Journal of Materials Science, in press
5. DTM Materials Handbook The Sinterstation® system, Guide to Materials: DuraForm™ Polyamide pp2, 42-44
6. J.C. Nelson, in PhD dissertation "Selective Laser Sintering: A Definition of the Process and an Empirical Sintering Model", (1993) pp 21-24, 153
7. Wei Zhang, Ming C. Leu, Zhiming Ji, Yongnian Yan, "Rapid freezing prototyping with water", Materials and Design 20 (1999) 139-145
8. S.P. Lin and R.D. Reitz, "Drop and spray formation from a liquid jet", Annu. Re. Fluid Mech. 1998, 30:85-105

Design And Integration Of A Laser-Based Material Deposition System

J. Laeng@Jamaluddin Abdullah*, Frank Liou**, M.N. Mohamad Ibrahim♣ and W.M. Wan Muhammad*

*School of Mechanical Engineering, Universiti Sains Malaysia - Engineering Campus, 14300 Nibong Tebal, Seberang Perai, Penang, MALAYSIA
♣School of Chemical Sciences, Universiti Sains Malaysia, 11800 Penang, MALAYSIA
**Department of Mechanical Engineering, University of Missouri-Rolla MO 65409-1350, USA

ABSTRACT

This paper aims to demonstrate the design process of an integrated five-axis Laser-Based Material Deposition (LBMD) system for rapid prototyping application. Several design evaluation methods are selected and applied to the design of the system. A three-dimensional graphical simulation software package was used as a decision making aid and as an analysis tool in the design process. Hardware integration of a five-axis computer numerical controlled (CNC) vertical milling machine, a 2.5 KW Nd:YAG laser and a linear table is discussed. A brief introduction to the system software and control architecture is also summarized. Some important design issues and considerations specific to Laser Based Material Deposition process are suggested.

Keywords: *Design methodology, System Design and Integration, System Simulation, Laser Based Material Deposition, Collision Detection, Tool Path Verification*

1. INTRODUCTION

Since the introduction of the first commercial stereolithography apparatus in 1986, many rapid prototyping (RP) systems have been developed for the ever growing industrial demands for shorter product development cycle time and at significantly reduced costs [1]. Most of the commercial RP units at that time however, were either limited to non-metal fabrication with minimal accuracy and precision or constraint to produce relatively simple parts for physical visualization of design concepts. Some of the developing systems were capable of producing direct metal prototypes. However, the commercial units still require polymer RP molds from which metal castings are formed [2].

The increasing complexity of certain parts geometry imposed by many advanced applications making the production of highly accurate functional model directly from CAD data very difficult or impossible using the available RP systems. Arising from this, many systems have been proposed. The LENS (Laser-Engineered Net Shaping) process has demonstrated the feasibility to produce near net shape metal part [3,4]. Others have tried to utilize the existing laser cladding technique, an established laser surface coating of metallic parts, to produce metal parts by layer additive approach [2,5].

This paper describes the design and integration process at the early development stage of a Laser Based Material Deposition process at the University of Missouri-Rolla, USA. A few design evaluation methods, including a graphical simulation software were employed to assist in decision making. The LBMD system consists of a 5-axis CNC machine, Nd:YAG laser and a linear table put together to work as an integrated system.

2 DESIGN AND INTEGRATION PROCESS

A survey on Laser Based Material Deposition was conducted in order to understand the process and other related issues [6]. Three design concepts were proposed as shown in figure 1, figure 2 and figure 3. The first design as shown in figure 1, integrates a 3-axis CNC milling (X,Y and Z), a 2-axis rotary table (tilting about X, rotating about Z) and a single axis linear actuator (slide up and down along Z axis) that carries the laser and powder delivery nozzle. A rigid support structure is constructed above and spans across the CNC assembly. The laser powder nozzle is attached to this support bar. This design concept provides a stable and rigid support for laser and powder assembly and thus minimizes vibration.

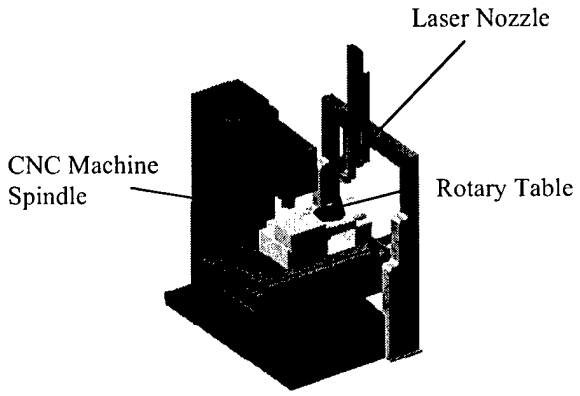


Figure 1 : Design Concept I.

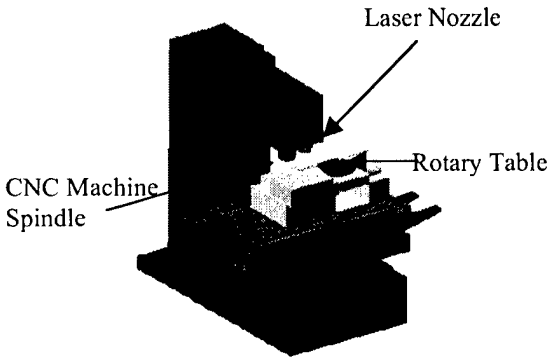


Figure 2: Design Concept II.

In design concept II as shown in Figure 2, a different design concept is proposed. The laser and powder delivery nozzle is attached to the CNC machine head assembly besides the machine spindle. This design integrates a 3-axis CNC milling machine, 2-axis rotary table and a single axis laser and powder nozzle. No support structure as in design I need to be constructed. Initially, this design is thought to be better because it eliminates the support structure for the laser and powder nozzle and does not require additional motion axis for the system. However, the cost of putting the laser nozzle to the CNC machine head assembly will be significantly large. Vibration from the machine spindle during machining process could cause misalignment of laser optic just next to it. Laser optics are also exposed to contamination from metal chips and also coolant. Chances of collision between work piece and the machine spindle and also between work piece and laser nozzle increases during rotation or tilting of work piece.

In concept Design III as shown in Figure 3, a cantilevered support with retraction and

extension arm, where laser and powder nozzle is attached to, is proposed for the system. The laser and powder nozzle can be extended to the work area during metal deposition and they can be retracted to a safe location during machining process. This feature is hoped to protect the laser optics from metal chips and contaminants within the vicinity of the work area. However, accuracy could be jeopardized due to deflection in the cantilever arm and cumulative displacement error from the frequent retraction and extension of the cantilever arm. Also, to have this feature, two linear actuators are needed and considering the load and moment the beam will carry, achieving a higher displacement accuracy (0.001") becomes impossible. With the design configuration in concept design III, the total axis of control would be increased to 7. This is not desirable because it makes integration and controls of the system more complex. Synchronization and motion control of all the individual components is critical to part quality. Therefore, a simple system, but capable of good motion control is desirable.

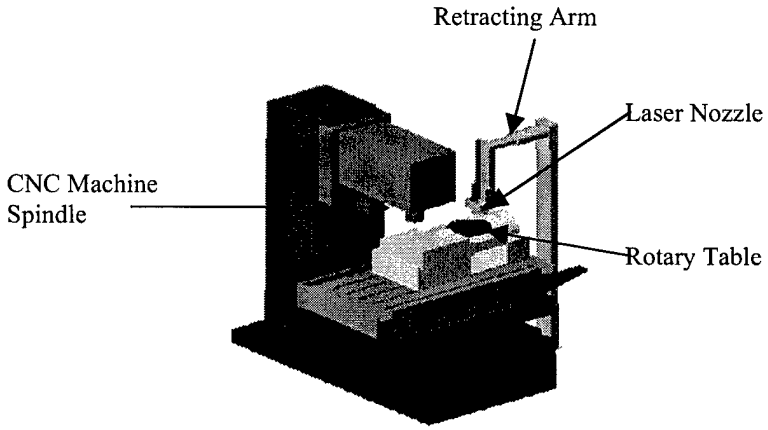


Figure 3: Design Concept III

Two methods were used in design evaluation process. The first method utilizes concept evaluation matrix to compare each design to a selected datum concept. This method provides three levels of comparison: "better than (+) ", "the same as (S) " or "less/worst than (-)" the datum. A set of evaluation criteria was established. Table 1, Table 2 and Table 3 shows the evaluation matrix for each concept. Based on this evaluation, design concept I is the most feasible option. The second method uses a scale from 1 to 5 to further evaluate the design. Table 4 shows the scores for each design. This method assigns quantitative score to each concept and we can rank the concept, as well as each criterion from the highest to the lowest score. The highest score means the best and the lowest is the least/worst. From the second evaluation method, concept I carries the highest score. Concept design I is finally selected for further analysis. The LBMD system would fabricate parts by combination of material addition (laser material deposition) and material removal (CNC milling to correct deposition errors).

Table 1: Concept Evaluation Matrix Using Conceptual Design I as DATUM

	Concept		
Criteria	**1**	**2**	**3**
Positioning accuracy of the system	D	S	_
Repeatability of the system	A	S	_
Ease of system operation	T	+	S
Ease of maintenance of laser and powder	U	_	S
Protection of laser alignment from vibration	M	_	+
Protection of nozzle and laser from		_	_
Simplicity of Integration	D	+	S
Simplicity of Synchronization	A	+	S
User safety from Laser	T	S	S
Ergonomics (user movement and interaction)	U	S	S
Minimum axis of control	M	+	S
Working volume		S	_
Rigidity and stability of nozzle support	D	+	_
Overall estimated cost for the system	A	_	S
Adaptability to multi material deposition	T	_	_
Online process control implementation	U	+	_
Score	M	6+, 5-, 5S	1+, 7-, 8S

Table 2: Concept Evaluation Matrix Using Conceptual Design II as DATUM

	Concept		
Criteria	**1**	**2**	**3**
Positioning accuracy of the system	S	D	_
Repeatability of the system	S	A	_
Ease of system operation	_	T	_
Ease of maintenance of laser and powder	+	U	+
Protection of laser alignment from vibration	+	M	+
Protection of nozzle and laser from	+		+
Simplicity of Integration	_	D	_
Simplicity of Synchronization	_	A	_
User safety from Laser	S	T	S
Ergonomics (user movement and interaction)	S	U	S
Minimum axis of control	_	M	_
Working volume	S		S
Rigidity and stability of nozzle support	_	D	_
Overall estimated cost for the system	+	A	S
Adaptability to multi material deposition	+	T	+
Online process control implementation	S	U	_
Score	5+, 6S, 5-	M	4+, 4S, 8-

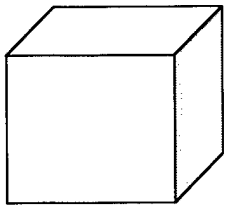
Table 3: Concept Evaluation Matrix Using Conceptual Design III as DATUM

	Concept		
Criteria	**1**	**2**	**3**
Positioning accuracy of the system	+	+	D
Repeatability of the system	+	+	A
Ease of system operation	+	+	T
Ease of maintenance of laser and powder	S	–	U
Protection of laser alignment from vibration	S	–	M
Protection of nozzle and laser from contaminants	S	–	
Simplicity of Integration	S	+	D
Simplicity of Synchronization	S	+	A
User safety from Laser	S	S	T
Ergonomics (user movement and interaction)	S	S	U
Minimum axis of control	+	+	M
Working volume	S	S	
Rigidity and stability of nozzle support structure	S	+	D
Overall estimated cost for the system	+	–	A
Adaptability to multi material deposition	+	–	T
Online process control implementation	S	+	U
Score	6+, 10S	8+, 5-, 3S	M

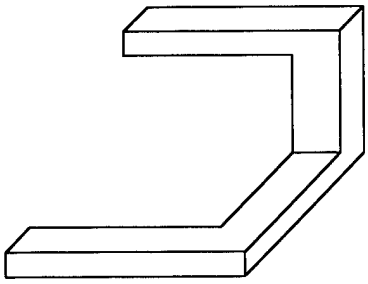
Table 4: Concept Evaluation Using Quantitative Scale (scale 1 – 5)

	Concept		
Criteria	**1**	**2**	**3**
Positioning accuracy of the system	3	5	2
Repeatability of the system	3	4	2
Ease of system operation	4	3	3
Ease of maintenance of laser and powder	4	2	3
Protection of laser alignment from vibration	5	1	4
Protection of nozzle and laser from contaminants	5	2	3
Simplicity of Integration	4	2	3
Simplicity of Synchronization	4	5	3
User safety from Laser	3	4	3
Ergonomics (user movement and interaction)	3	4	3
Minimum axis of control	4	4	2
Working volume	4	2	3
Rigidity and stability of nozzle support structure	4	3	2
Overall estimated cost for the system (least is best)	5	2	4
Adaptability to multi material deposition	4	2	3
Online process control implementation	4	3	4
Score	58	49	47

To further refine the selected design, a three-dimensional graphical simulation software was used to identify the suitable working volume for the system for two different fabrication situations; (i) simple fabrication with no part rotation and tilting and system is required to do vertical buildup only, (ii) more complex fabrication requiring part rotation and tilting and the system is depositing in the vertical direction. For both conditions, work perimeter of 12" x 12" x 12" and 8"x 8"x 8" were simulated. CNC codes were written to instruct the system to perform tool movement to cut the peripheral of the specified work perimeter, and any obstruction or collision was recorded. Simple movement is represented by a cube, while a more complex movement is represented by a part with overhang as illustrated in figure 4(a) and figure 4(b).



(a) Cube representing simple vertical buildup



(b) Part requires rotation and tilting

Figure 4: Representative objects for tool path and work volume verification

From the simulation results, the 12" x 12" x 12" work perimeter had demonstrated some collisions for rotating and tilting movement, while the 8" x 8" x 8" work perimeter had shown no collision for both simple and rotate-tilt movements. The results are presented in Table 5. Major hardware components of the system is shown in Table 6

Table 5: Simulation Results for 12" x 12" x 12" and 8" x 8" x 8" work volume

Work Envelope Representations	**Deposition Process**	**Milling Process**
Perimeter (12" X 12" X 12")	• No collision	• No collision
With rotation and tilt (12" X 12" X 12")	• Collision between part and rotary table base	• Collision between part and rotary table base • Collision between part and machine column.
Perimeter (8" X 8" X 8")	• No collision	• No collision
With rotation and tilt (8" X 8" X 8")	• No collision	• No collision

Table 6: Major Hardware Components of LBMD System

Component	Sub-Components	Primary Functions
5-axis CNC Machine	2-Axis Rotary Table	• Rotation and tilt motion • Work table for the system
	3-Axis milling machine	• X, Y and Z motion • Controls all axes motion
Powder and Laser Delivery System	Powder Storage Hopper	• Store metal powder • Releases powder to powder feeder unit
	Powder Feeder Unit	• Feeds powder into nozzle • Controls powder flow rate
	Powder and Laser Nozzle	• Deliver powder to melt pool • Deliver protection and carriage gas
	Laser Head	• Holds laser focus lenses
	Gas Supply System	• Provide Protection and Carriage gas
	Fiber Optic Cable	• Deliver laser beam to focus lenses
1-axis Linear Table	Way cover	• Protect Linear table from contaminants (dust and moisture)
	Motor and Encoder	• Provide Linear table motion • Closed loop control for linear table

4 SOFTWARE AND CONTROL SYSTEM

Typical software architecture for a Laser Based Material Deposition includes the modeling of a three-dimensional CAD model in standard Stereolithography (STL) format, generation of layer representation of the object which is equal to the deposition thickness, and creation of CNC codes for the tool path that are understandable by the machine controller [3,4,7]. The system architecture for the LBMD system is illustrated in Figure 5.

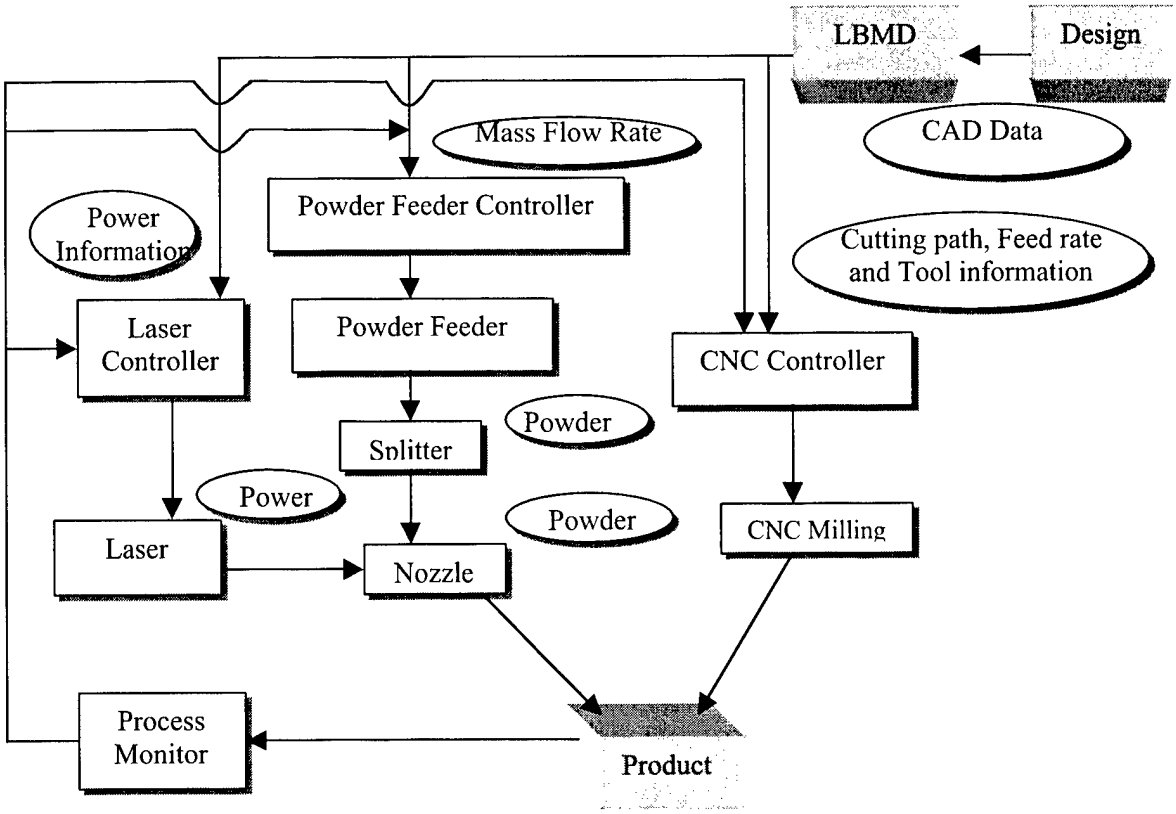


Figure 5: System Architecture [8].

5 CONCLUSIONS

Design and integration process of a Laser Based Material Deposition System have been presented and a LBMD system is proposed. A three-dimensional graphical simulation has been applied and proven to be a useful tool in the development of the LBMD system. A few important considerations in the design and integration of the system include the following: (i) system performance – high accuracy and precision, stable powder and power delivery, online control and monitoring. (ii) high temperature working environment – nozzle made of high temperature material and equipped with cooling system. (iii) protection of optical lenses or any sensitive components from moisture and dust or easily cleaned and replaceable. (iv) safety – laser radiation, metal powder, coolant mist and dust. (v) maintenance – laser alignment check should be minimize, ventilation system is needed to properly disposed contaminants (metal powder, coolant mist, dust) out of the system

ACKNOWLEDGEMENTS

The support from the National Science Foundation Grant No. DMI 9871185 is appreciated. The contributions from the RP group at UMR and the support from Research and Development Unit, Universiti Sains Malaysia is also noted here.

REFERENCES

1. Jacobs, P.F., *Rapid Prototyping & Manufacturing: Fundamentals of Stereolithography*, Society of Manufacturing Engineer, 1st edition, pp.1, 18-20, 1992.
2. Koch, J.L. and Mazumder, J., *Rapid Prototyping By Laser Cladding*, The International Society For Optical Engineering, vol. 2306, pp. 556-eoa, 1993.
3. Keicher, D.M., Miller,W.D., Smugeresky, J.E. and Romero, J.A., *Laser Engineered Net Shaping (LENS): Beyond Rapid Prototyping to Direct Fabrication,* Proceeding of the 1998 TMS Annual Meeting, San Antonio, Texas, USA, p. 369 – 377.
4. Beardsley, Tim, *Making Light Work: Blasting Metal Powder with Lasers to Make Precision Parts*, Scientific American, August 1997.
5. Kreutz, E. W., Backes, G., Gasser, A. and Wissenback, K., *Rapid Prototyping with CO_2 Laser Radiation*, Applied Surface Science, vol. 86, 1995, p. 310-316.
6. J. Laeng, J. G. Stewart and F. W. Liou, *Laser Metal Forming Processes For Rapid Prototyping- A Review,* International Journal of Production Research, Vol 38, No.16, 3973-3996, 2000.
7. McLean, M. A., Shannon, G. J. and Steen, W. M., *Laser Generating Metallic Components*, SPIE, Vol. 3092, 1997, p. 753-756.
8. Laser Aided Material Deposition System, Rapid Prototyping Group, University of Missouri-Rolla.

this page intentionally blank

Skeleton-based Geometric Reasoning for Adaptive Slicing in a Five-axis Laser Aided manufacturing Process System

Kunnayut Eiamsa-ard, Jun Zhang, and F.W. Liou
Department of Mechanical and Aerospace Engineering and Engineering Mechanics/
Intelligent Systems Center, University of Missouri – Rolla, Rolla, MO 65409

Abstract

Multi-axis Laser Aided Manufacturing Process (LAMP) is an additive manufacturing process similar to laser cladding. This process can produce full functional parts [1]. Traditional Layered Manufacturing processes produce parts with limited surface quality; and also the build time is often long due to the deposition of sacrificial support structure. The multiple degrees of freedom endow the LAMP system a capability to build parts without support structure. An algorithm for adaptive slicing based on skeleton is presented in this paper. The skeleton is useful for many applications such as feature recognition, robot path planning, shape analysis, and etc [2]. The near optimal build direction can be generated using information provided by the part skeleton, which is a 2D (or less) "surfaces" embedded 3D space containing the general form of the object.

1. Introduction

The focus of layered manufacturing has shifted to building functional metal parts [3]. Even though, Solid Freeform Fabrication (SFF) has taken the manufacturing industry to new heights, there are still some problems remain unsolved. These problems are addressed and reduced by our process – LAMP. The detail of the LAMP system was described in earlier work. [1] For the sake of completeness, however, the system architecture is described briefly here.

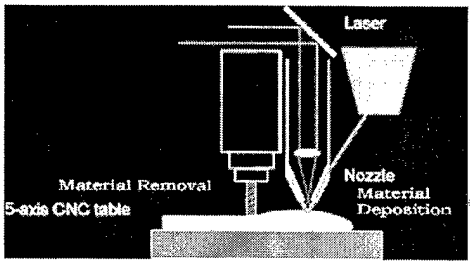


Figure 1. Five-axis LAMP system

The system consists of two major subsystems – laser deposition subsystem including the powder feeder, and CNC milling subsystem. (Figure 1) These 2 subsystems share a common X-Y translators as well as a rotary table. (4 DOF 's totally – 2 translations and 2 rotations) The deposition module takes care of the material deposition. The CNC machining module removes unwanted material. LAMP is a novel layered manufacturing process in which the support will be gotten rid of as much as possible in the deposition process. In LAMP system, each layer is "truly" 3D in nature using the combination of material addition and subtraction processes by exploiting the presence of five-axis motion. In some cases, the hollow parts or the parts containing overhang

(undercut faces) features may need the support material unavoidably. Variable build direction and variable depth of slices increase the surface quality as well as the possibility of material deposition without support structure. Also, by combining the 5-axis machining in the system improves the surface quality and accuracy [1,4].

2. Background

2.1 Face Classification:

Following the earlier work done by Ramaswami [4], let **V** is the normal vector of a face **F** and **Z** is the normal of a slicing plane or the slicing direction. If the inner product <**V**, **Z**> is greater than or equal to **0** then face **F** is a non-undercut face. On the other hand, if the inner product <**V**, **Z**> is less than **0** then face **F** is an undercut face. (Figure 2)

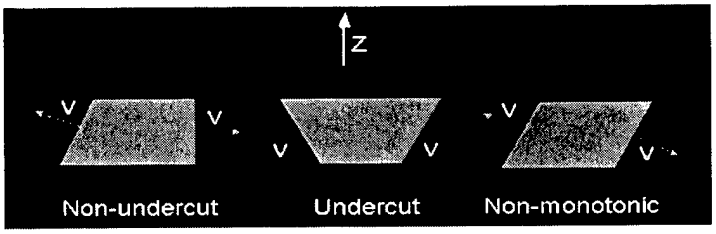


Figure 2. Face Classification [4]

2.2 Edge Classification:

Convex Edge: The solid angle between two facets sharing the edge is between 0 and 180 degrees [1].

Concave Edge: The solid angle between two facets sharing the edge is between 180 and 360 degrees. In Figure 3, the concave edge is shown; the rests are convex edges.

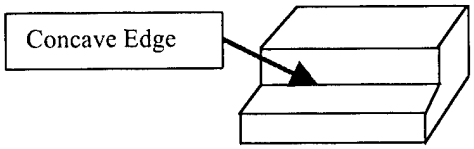


Figure 3. Edge Classification

2.3 Distance Calculation:

The idea for computing the distance to boundary faces is adapted in an inverse sense from a work done by Choset and Burdick [5]. In their work, the skeleton is computed for an unknown connected free space for robot path planning; but in this paper, the skeleton is computed for a known connected space of the part filled with the material. The distance ($\mathbf{d_i(x)}$) and its gradient ($\mathbf{\nabla d_i(x)}$) from a point "x" to a face from the face set $\mathbf{\{C_i: i = 1, 2, 3, \ldots, n\}}$ can be computed by

$$\mathbf{d_i(x) = \min \|x - c_o\|} \quad \textbf{(1)}$$

$$\mathbf{\nabla d_i(x) = (x - c_o) / \|x - c_o\|} \quad \textbf{(2)}$$

respectively; where as $\mathbf{d_i(x)}$ basically is the normal distance to the face if the closest point in the interior of the face, and $\mathbf{c_o \in C_i}$. In the case of the closest point is on a boundary edge or a point, the faces (which share that common edge or point) are considered as one as if there were only one face. Also, the distance is just the closest distance from the point "x" to that closest point or edge. The vector $\mathbf{\nabla d_i(x)}$ is a unit vector in the direction from $\mathbf{c_o}$ to point "**x**" [5]. Note that we do not fill the spaces with any convex polyhedrons or objects like in their work. The advantage of this compared to their method is: we do not lose line of sight to a face of a pair of faces whose solid angle between them is greater than 90°.

2.4 Skeleton Structures:

Our skeleton extraction algorithm is based on earlier work done by Choset et al [5, 6]. For the sake of completeness, a brief review of the ***Generalized Voronoi Graph*** and its incremental construction is described here.

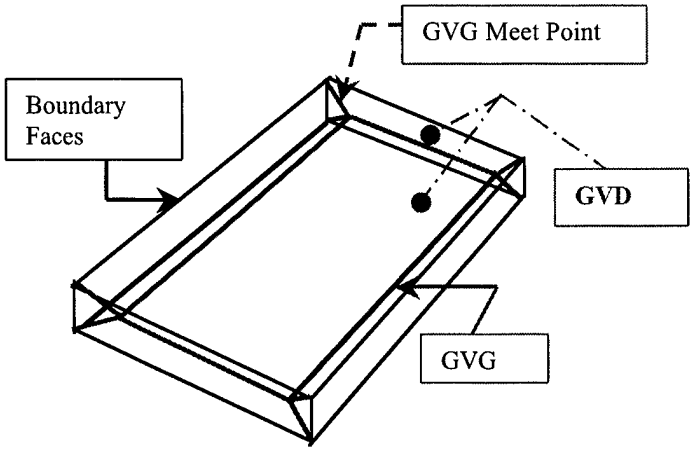


Figure 4. Equidistant Faces and GVG edges

(a) Generalized Voronoi Diagram (GVD): GVD is defined as a set of points equidistant to two closest sets C_i and C_j which called the two-equidistant "surface" (also called **skeleton;** see [7] for detail). GVG is usually "2D - surfaces" embedded in 3D space; and defined mathematically as.

$$\{\mathbf{x \in part : d_i(x) = d_j(x)} \quad \textit{or} \quad \mathbf{d_i(x) - d_j(x) = 0}\} \tag{3}$$

(b) Generalized Voronoi Graph (GVG): GVG can be thought of a boundary of the GVD since GVG is a set of points which GVD surfaces intersect (Figure 4); defined as following

$$\{\mathbf{x \in part : d_i(x) = d_j(x)\ ) = d_k(x) = \ldots = d_n(x)},\quad n = \textit{closest equidistant faces}\} \tag{4}$$

2.5 Incremental Constructions:

The algorithm starts at one of the *seed* points, which actually are the set of all vertices where only convex edges intersect, in the part. The common prediction-correction scheme borrowed from [5] is used in marching along these edges. In the

prediction step, the marching point is moved a small step, $\Delta\lambda$. Usually, the prediction steps take the marching point off the edge. Next, the correction steps bring the marching point back on to the edge. The marching point marches along the edges until all of the seed points have been explored. While exploring, if a meet point is detected when a sudden change in distance gradients has been encountered, that meet point will be marked as a seed point. Note that in 3D, this type of seed points has more than or equal to 3 closest faces, therefore at these seed points, the traces are branched out to the combinations of equidistant faces. Basically, the incremental construction is to generate the roots of function **"$G(y,\lambda)$"** which is specifically defined for each of GVG as follows:

$$G(y,\lambda) = \begin{bmatrix} (d_1 - d_2)(y,\lambda) \\ (d_1 - d_3)(y,\lambda) \\ \cdot \\ \cdot \\ \cdot \\ (d_1 - d_m)(y,\lambda) \end{bmatrix} \quad (5)$$

$$\nabla G(y,\lambda) = \begin{bmatrix} \nabla d_1(y,\lambda) - \nabla d_2(y,\lambda) \\ \nabla d_1(y,\lambda) - \nabla d_3(y,\lambda) \\ \cdot \\ \cdot \\ \cdot \\ \nabla d_1(y,\lambda) - \nabla d_m(y,\lambda) \end{bmatrix} \quad (6)$$

If the edge has non-zero curvature, the prediction step will take the marching point off the graph [6]. Hence, correction procedure is invoked on a hyper plane "Y" orthogonal to the tangent to correct the marching point back on to the edge as follow.

$$y^{h+1} = y^h - (\nabla_Y G(y^h,\lambda^h))^{-1}\, G(y^h, \lambda^h) \quad (7)$$

3. Algorithm for Finding a Build Direction

Each build direction is determined from the information given by the skeleton. *First*, a preprocessor is used to reduce the excess faces for a given STL file. The simple idea behind this preprocessor is that the common edges of adjacent faces are deleted if their normal vectors are the same (Figure 5).

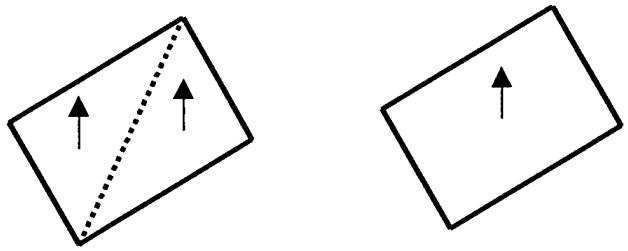


Figure 5. Preprocessor is used to reduce the unnecessary edges

Second, the skeleton is extracted from the part using GVG incremental - construction. An example of the skeleton extracted from the part is shown in Figure 6.

Third, after the skeleton is extracted, the candidates for the base face can be determined. Only the faces not containing any concave edges are considered. The faces in which all of the seed points are encountered while tracing the GVG edges are the candidates to be selected as the base for deposition procedure. Thus, the back face, two side faces, two front faces, top and bottom face are the candidates in the following example (Figure 6).

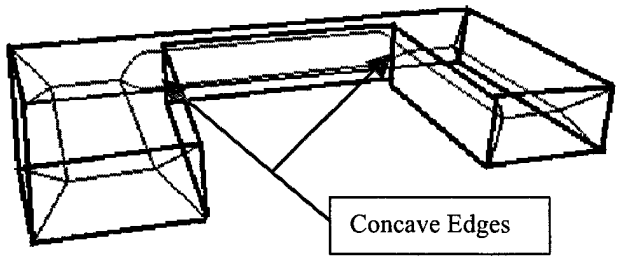


Figure 6. An example of skeleton extracted from the part

Fourth, some of the candidates for the base face can be eliminated since some of the faces are considered undercut surfaces if one of the normal vectors of the candidates is selected to be our slicing direction. Therefore, in the above example, only the back face, top face, and bottom face are the remaining candidates. In case that there is no face that passes the forth criteria described above, the half plane criteria will be perform to check if there is solid material only on one side of our face candidates. If the test is passed, the face is still be our candidate, delete it from the candidates otherwise.

Fifth, user defined objective functions will be used to select one face from the candidates. For example, user might think that the bigger the face is, the stronger the base is. Thus, in the example, the top and bottom faces have highest priority to be selected as our base face. Either one of the remaining 2 faces can be picked.

4. Examples

Case 1: In case that the skeleton is a point (case of a sphere), there should be no different choosing a slicing direction. In this case, the support structure will be needed.

Case 2: In case that the skeleton is a point with some spokes, any face could be the base.

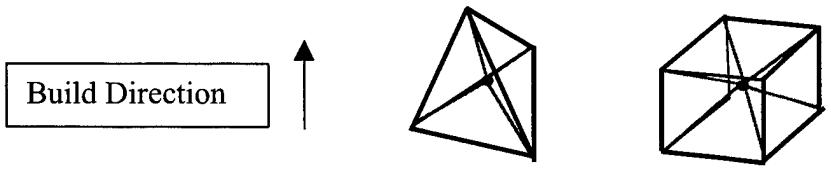


Figure 7. Examples for case 2

Case 3: In the case of tubes, the side faces have more priority to be chosen as our base if there is no undercut surface appeared shown in Figure 8 a, b. Otherwise one of ending faces is chosen as the base and the build direction will follow the saturated GVG edge,

which is the edge that does not contain the seed points (shown as a dash line Figure 8 c).

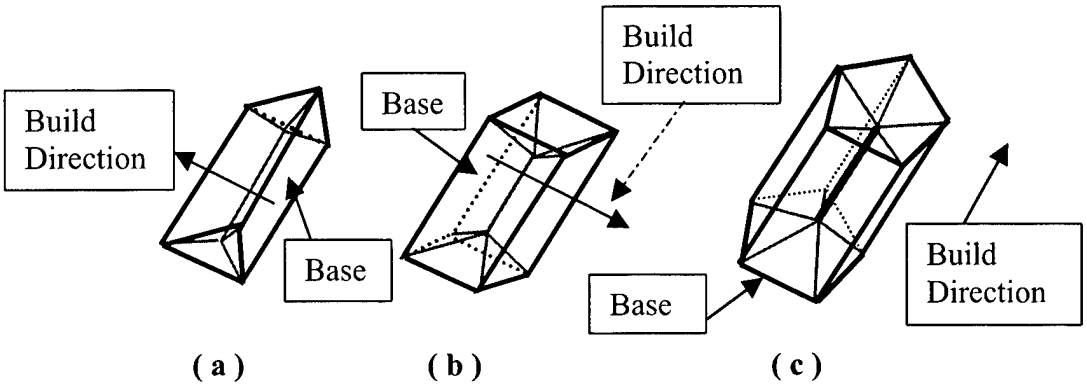


Figure 8. Examples for case 3

Case 4: In this example, GVD structure has one plane or a combination of planes such as T-shape part, the example part in Figure 6, and also the one in Figure 9. In Figure 9, there are initially 3 candidates for the base. However from the fifth criteria, the top or the bottom will be chosen as the base.

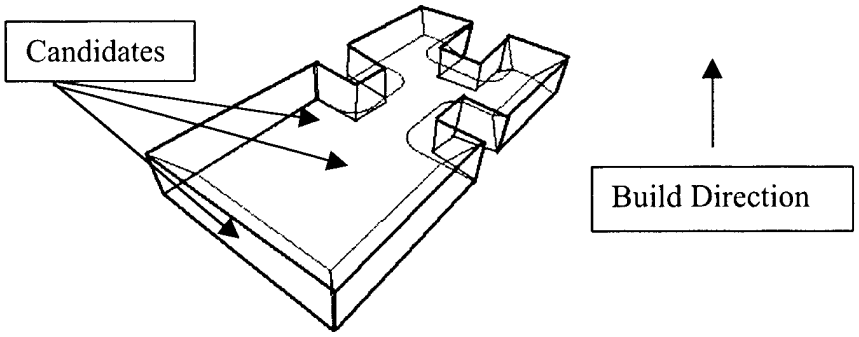


Figure 9. Examples for case 4

Case 5: This case is classified as bended tubes. The flat ends of the tubes are usually selected by our algorithm and the slicing directions will be tangent to the skeletons. There is possible that the side face might be selected instead of the flat ends such as bended rectangular-cross sectioned tubes.

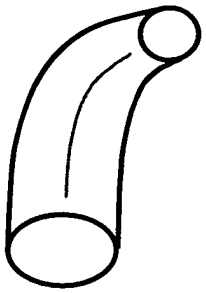


Figure 10. Examples for case 5

Case 6: This case and the following case are the cases that there is no candidate left from the fourth criteria. *Obviously, addition criterions are required.* In these cases, all of the deleted candidates from the fourth criteria will be undeleted. Next, the fifth criteria will be used to find the base face and build direction as in the previous cases. Given the base and the build direction, the half plane technique is used to divide the part into subpart that does not contain any undercut surfaces. The face that occurs from the intersection of the one of the subparts and the cutting plane will be used as our next base face. This step will be repeated until there is no subpart left. (Note that the surface occurs from the intersection in this case is same as the face in which the intersection face resides.)

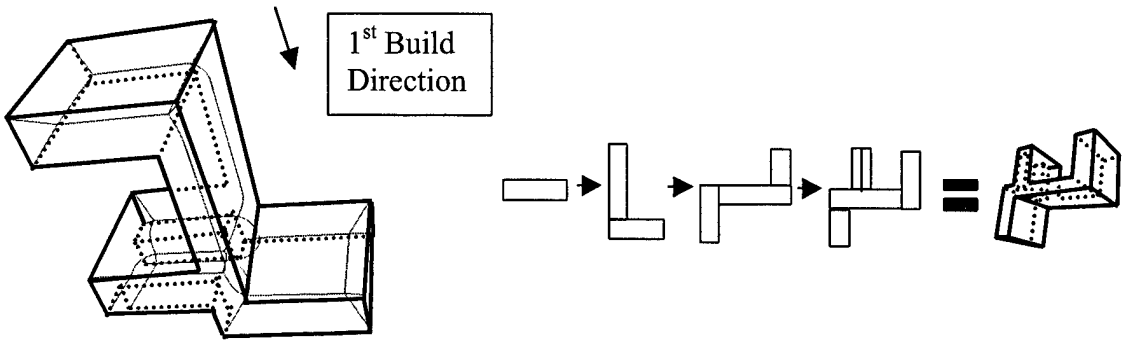


Figure 11. Examples for case 6

Case 7: This case is different from the previous one since the surface occurs from the intersection in this case is not same as the face in which the intersection face resides as shown in Figure 12. In this case, we definitely need the support structure. We have not come up with an automatic way to create the support structure for each selected base face. However, the steps of decomposing the part are the same as in the previous case. This case is one of the limitations of our algorithm described in the next topic.

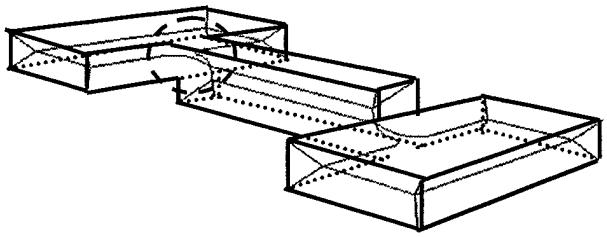


Figure 12. Examples for case 7

5. Conclusion and Future Work

In this paper, an algorithm for finding "near" optimal slicing direction for LAMP system has been described. (It can be applied to any SFF systems.) There are some advantages of our algorithm. First, our algorithm is complete and do not need any pre-specified parameters to start with. By complete, we mean all of the candidates can be found. (Therefore, the users can leave the decision to the computer by user-defined

parameters or the users can make the decisions themselves by using the results from this algorithm.) Our approach currently has the following limitations:

1. Only parts with planar surfaces are considered.
2. Since the exhaustive searches are performed in some steps, this algorithm does not work well in the part that contains too many surfaces. (Especially, the parts that contain approximated faces of highly curvature surfaces.)
3. The parts that definitely do not need the support structures are considered.

We are working toward relaxing these limitations.

6. Acknowledgments

This research was supported by the National Science Foundation Grant Number DMI-9871185, Missouri Research Board, and a grant from the Missouri Department of Economic Development through the MRTC grant. Their support is appreciated.

7. References

[1] Jun Zhang and Frank Liou, to be appeared in Proceedings of the 2001ASME Design Automation Conference, 2001.

[2] H. Blum, "Transformation for extracting new descriptors of shape", Wathen-Dunn, W (Ed.) Models for Perception of Speech and Visual Form, MIT Press, Cambridge, MA, 1967, pp.362-380.

[3] P. Singh and D. Dutta, "Multi-Direction Slicing for Layered Manufacturing" Proceedings of DETC'00, ASME 2000 Design Engineering technical Conferences and Computers and Information in Engineering Conference, September 10-13, 2000.

[4] Krishnan Ramaswami, "Process planning for shape deposition manufacturing", Ph.D. Thesis, Stanford University, November 1996.

[5] Howie Choset and Joel Burdick, "Sensor-Based Exploration: The Hierarchical - Generalized Voronoi Graph", The International Journal of Robotics Research, Vol. 19, No. 2, February 2000, pp. 96-125.

[6] Howie Choset, Sean Walker, Kunnayut Eiamsa-Ard, and Joel Burdick, "Sensor-Based Exploration: Incremental Construction of the Hierarchical Generalized Voronoi Graph", The International Journal of Robotics Research, Vol. 19, No. 2, February 2000, pp. 126-148.

[7] Kunnayut Eiamsa-ard and Howie Choset, "Sensor-Based Path Planning: Three - Dimensional Exploration and Coverage", 1999 Mechanical Engineering Graduate - Technical Conference, Carnegie Mellon University, April 16, 1999, Pittsburgh, PA.

Surface Roughness Enhancement of Indirect-SLS Metal Parts by Laser Surface Polishing

J.A. Ramos, J. Murphy, K. Wood, D.L. Bourell, J.J. Beaman

Mechanical Engineering Department
Laboratory for Freeform Fabrication
The University of Texas at Austin, Austin, TX 78712

ABSTRACT

Laser polishing by means of shallow surface melting of indirect-SLS metal parts was achieved using high power CO_2 and Nd:YAG lasers raster scanned at high speed. This was an effective technique for reducing surface roughness. The fast moving laser beam provides just enough heat energy to cause melting of the surface peaks. The molten mass then flows into the surface valleys by surface tension, gravity and laser pressure, thus diminishing the roughness. Surface roughness R_a data were obtained by profilometry measurements of the polished samples. An analytical model was developed based on the assumption that the surface of an SLS part consists of semi-spherical caps. The model was used to predict the R_a values as a function of laser power, scan speed and precursor powder particle size. The modeled results fit the empirical data within a 15% error.

Introduction

For more than a decade the SFF community has acknowledged that the transition from Rapid Prototyping towards Rapid Manufacturing of functional parts requires adequate treatment of surface roughness [1-3]. From a survey carried out by the Laboratory for Freeform Fabrication (LFF) at University of the Texas at Austin, answers from 20 different sources related to RP technology were gathered, indicating that surface finishing is a critical issue when SFF parts need to serve functional purposes. This result was further confirmed in an interview of key people in the RP world published by Time Compression Technologies magazine [4]. On the latter, all interviewed agreed that surface finishing is a major barrier to overcome to achieve functional parts by means of RP.

SLS parts, regardless of the material system used, inherently present a grainy surface finish, which is rough due to powder particle size, layer-wise building sequence and to some degree to the spreading of the powder by the roller mechanisms [5]. The RP

survey carried out by the LFF also indicated that among the finishing techniques used today to reduce roughness of SFF parts, surprisingly, hand polishing and abrasive flow grinding were the most commonly used. These are tedious and time consuming, although effective in reducing surface roughness. Less commonly used techniques are electro-polishing, shot-peening, ultrasonic and vibratory finishing [6]. A more sophisticated approach currently used is robotic arm polishing; however, the trajectory of the polishing tool must be determined a priori by 3D profilometry or some other means thus increasing the complexity and cost of this post process [7].

Laser Polishing of Silica Rods

For over 30 years lasers have been excellent tools for material surface modification [8-10]. Depending on the laser processing parameters (i.e., power density and interaction time) several modification regimes can be attained, namely: transformation hardening, melting, glazing, ablation and shock wave generation. Previous work done in the LFF indicated that the surface of silica rods could be polished from 2.0 μm to 0.05 μm (i.e. peak-to-valley distance) by means of a 25 W CO_2 focused c.w. laser [11]. The polishing mechanism is laser melting of a very thin layer of material that flowing under the action of surface tension. A wide laser polishing operational window from 900 to 1300 J/cm^2 existed for this type of material.

Laser Polishing of Indirect-SLS Metal Part

The latter positive results obtained in semiconductor materials encourage pursuing laser polishing of metallic surfaces of SFF parts as made by indirect-SLS technology. High power Nd:YAG and CO_2 lasers (c.w. mode) were successfully used in polishing 420 stainless steel-40 wt.% bronze indirect-SLS parts. Table 1 shows the operation window that provided considerable reduction in roughness R_a values. Figure 1 indicates that the operation window falls inside a melting-welding zone [9].

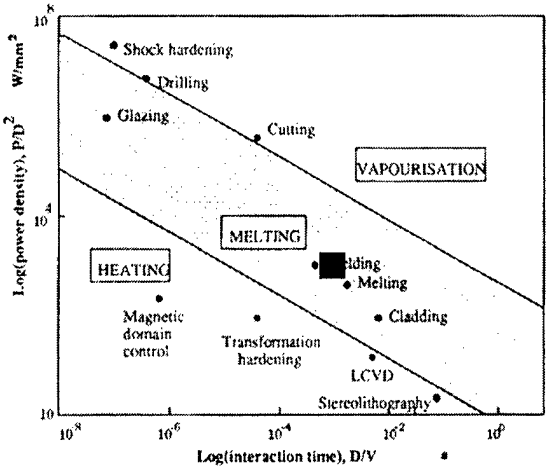


Figure 1. Operational window for several laser processes. Adapted from Steen [9]. The dark box near "Welding" and "Melting" indicates the polishing operational window.

	Max	Min
P [W]	420	220
V_S [m/min]	45	16
P/D^2 [W/mm2]	2.7*10^3	1.4*10^3
D/V_t [s]	10-3	6.5*10-4

Table 1. Operational window used in laser polishing of indirect-SLS parts. The material system was 420 stainless steel-40 wt.% bronze.

Simplistically, a rough SLS surface can be envisioned as consisting of spherical peaks and valleys. When the laser beam impinges on a rough surface, a peak will have higher probability of reaching the melting temperature before a valley does. A fraction of the molten peak will then flow into the valley by the action of Marangoni forces, gravity and laser pressure [9]. This "partial-melting" mechanism effectively reduces the peak-to-valley height, thus reducing the surface roughness. On the other hand, if the speed of the laser beam is too slow, the peaks may become "over-melted". The surface then becomes completely molten, and it is likely that low frequency - high amplitude surface waves may develop on cooling, thus potentially increasing the roughness.

Experimental Setup

Samples were provided by DTM Corp. and consisted of rectangular slabs made using DTM powder and process development called LaserForm^{TM} ST-100. It consists of a 420 stainless steel mixed with a 2 wt.% polymer binder that is shaped into a green pre-form by means of SLS. The pre-form is then placed inside a N_2 atmosphere furnace to burn off the binder and proceed with a 40 wt.% bronze (5 wt.% Sn) infiltration of the part. This material system is aimed towards tool making for the injection molding industry. The minimum surface roughness achieved is 2.4 μm, but some samples were showing values of up to 9.0 μm depending on the process parameters. Phonak A.G. (Switzerland) has applied this materials system to produce tooling for a hearing aid transmitter housing. However, machining and finishing operations were needed to achieve the specified tolerances [12].

CO_2 and Nd:YAG lasers were used in c.w. mode to laser polish the surface of the samples. The focal spot size of the CO_2 laser was 0.35+/-0.05 mm whereas for the Nd:YAG the real spot size was 0.25+/0.05 mm. High speed galvanometer motor driven rotating mirrors provided scanning speeds of up to 45 m/min raster speed and 2.0 mm/s traverse speed. The processing chamber was evacuated to 200 mTorr and then back filled with a inert gas reducing atmosphere of 4.5%H_2+Ar.

After the samples were treated, the surface roughness of the polished samples was measured using an automated profilometer device. The arithmetic average roughness value (i.e. R_a), was used to quantify this feature. This is the average displacement of the peaks and valleys measured with respect to a mean line.

Empirical Results and Discussion

Figure 2 shows an optical macrograph of multiple CO_2 laser polished tracks. These were made using 220 W and a traverse speed of 2.2 mm/s. The surface roughness R_a value of the as-received sample was 2.1 μm. The achieved surface roughness was

brought down to R_a = 1.6 μm (traverse-direction) and R_a = 3.2 μm (scan-direction). The latter value is higher than the as-received because at the overlapped regions a hump is formed. In Figure 3 the transition from the as-received surface to a polished one can be observed. A Nd:YAG laser was used at 220 W and a traverse speed of 1.7 mm/s. The as-received surface roughness R_a value was reduced from 9.0 μm down to a R_a value of 2.40 μm.

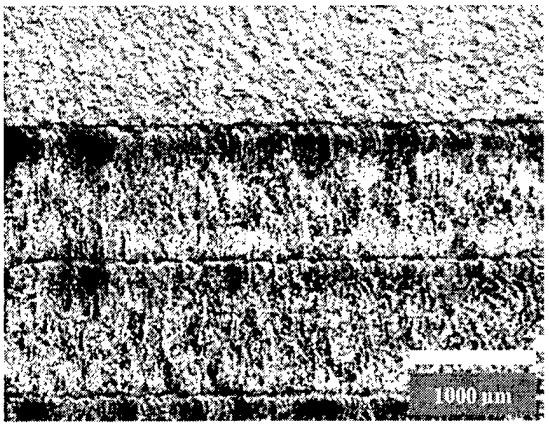


Figure 2. Optical macrograph of multiple CO_2 laser polished tracks on a 420 stainless steel–40 wt.% bronze indirect-SLS slab, 50x.

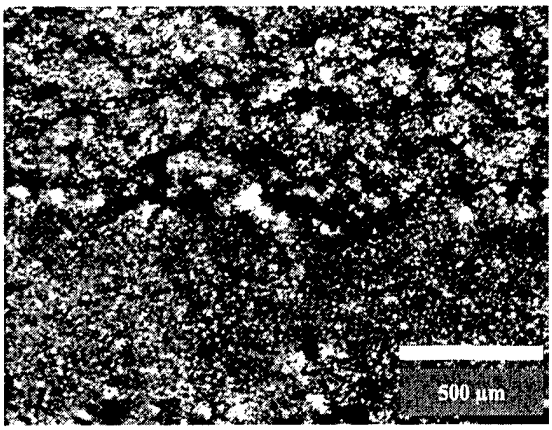


Figure 3. Optical macrograph of Nd:YAG laser polished 420 stainless steel–40 wt.% bronze indirect-SLS slab, 100x.

Figure 4 shows an SEM image of the previous sample, from which it can be clearly seen that the as-received surface is made up of overlapping spherical caps, corresponding to bronze coated 420 stainless steel powder particles and clusters, forming peaks and valleys. Where the laser beam has raster scanned through the sphere caps, these seem to have collapsed down, smoothing the surface. Figure 5 illustrates this better, as it can be seen that at the interface of the as-received and polished zone some sphere caps became semi-melted.

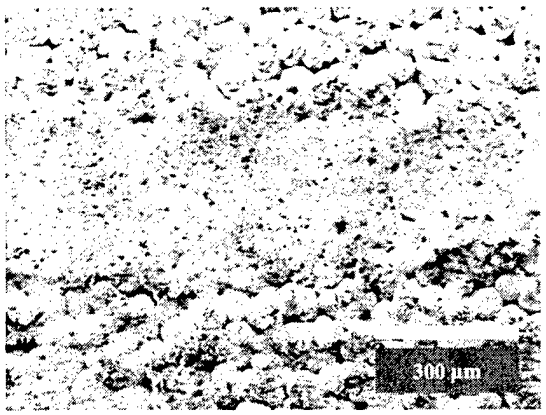


Figure 4 SEM image of Nd:YAG laser polished 420 stainless steel–40 wt.% bronze indirect-SLS slab, 60x.

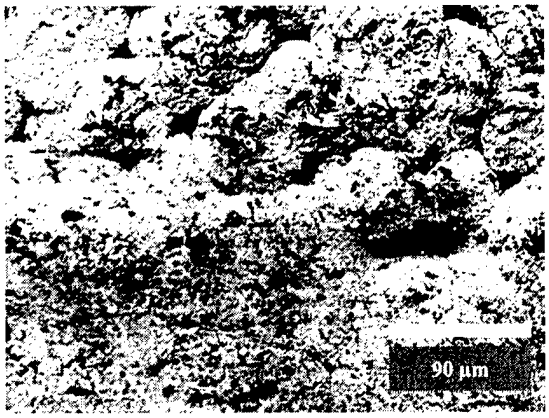
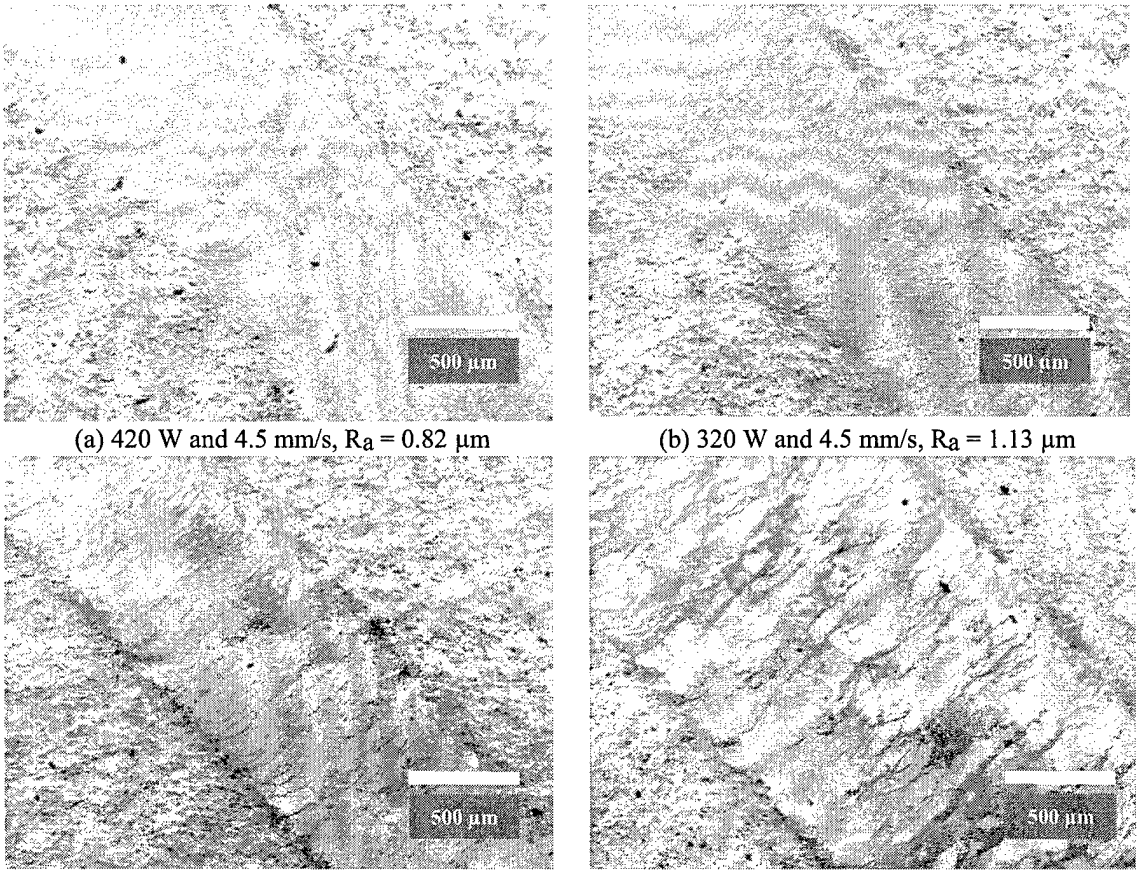


Figure 5 SEM image of interface zone of previous sample, 200x.

Figures 6 (a)-(d) show SEM images of laser polished tracks having widths ranging from 1.8 to 2.9 mm. The difference in resulting track widths is due to the various power and

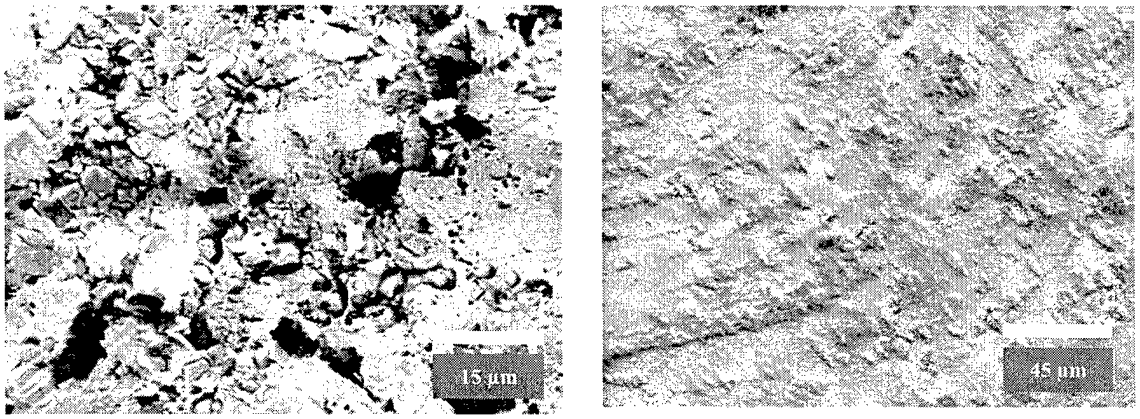
speeds used. The as-received roughness value R_a was 2.38 μm, while the obtained R_a values after polishing were (a) R_a = 0.82 μm, (b) R_a = 1.13 μm, (c) R_a = 2.56 μm and (d) R_a = 4.18 μm. From Figures (a) and (b) in can observed that a higher power provides better polishing results when the traverse speed is fixed. However, Figures (c) and (d) show that for a given laser power, too low a traverse speed produces over-melting with an increase of the R_a value above the as-received level.



(a) 420 W and 4.5 mm/s, R_a = 0.82 μm (b) 320 W and 4.5 mm/s, R_a = 1.13 μm

(c) 220 W and 4.5 mm/s, R_a = 2.56 μm (d) 220 W and 1.8 mm/s, R_a = 4.18 μm

Figure 6. SEM of CO_2 laser polishing of 420 stainless steel–40 wt.% bronze indirect-SLS slab, 50x.



(a) As-received surface, 1500x (b) CO_2 laser polished surface, 500x

Figure 7. SEM of as-received and polished 420 stainless steel–40 wt.% bronze indirect-SLS samples.

Figure 7 shows a sequence of SEM images of the surface morphology of laser polished samples. Figure 7a corresponds to the as-received surface having a R_a value of 2.38 μm. Here, powder particles are clearly seen embedded in a bronze matrix. Figure 7b shows a close-up of a polished zone, obtained using 320 W and a traverse speed of 4.5 mm/s. The periodically distributed minuscule humps may have been caused by surface tension and oxidation effects; these contribute to the 1.13 μm roughness R_a measured.

Figure 8 is a plot of the R_a values for Nd:YAG laser polished 420 stainless steel–40% bronze indirect-SLS samples. The power was 220 W at five traversing speeds: 1.46, 1.47, 1.73, 1.74 and 1.76 mm/s. The as-received R_a value of the surface was 9.0 μm, and for the five sets of parameters, a considerable reduction in R_a value was achieved. However, as the speed is increased, the R_a values increase from 3.0-3.3 μm to 3.7-4.1 μm. Higher speed at constant power level implies less melting of the sphere caps and therefore less mass flow into the sphere valleys.

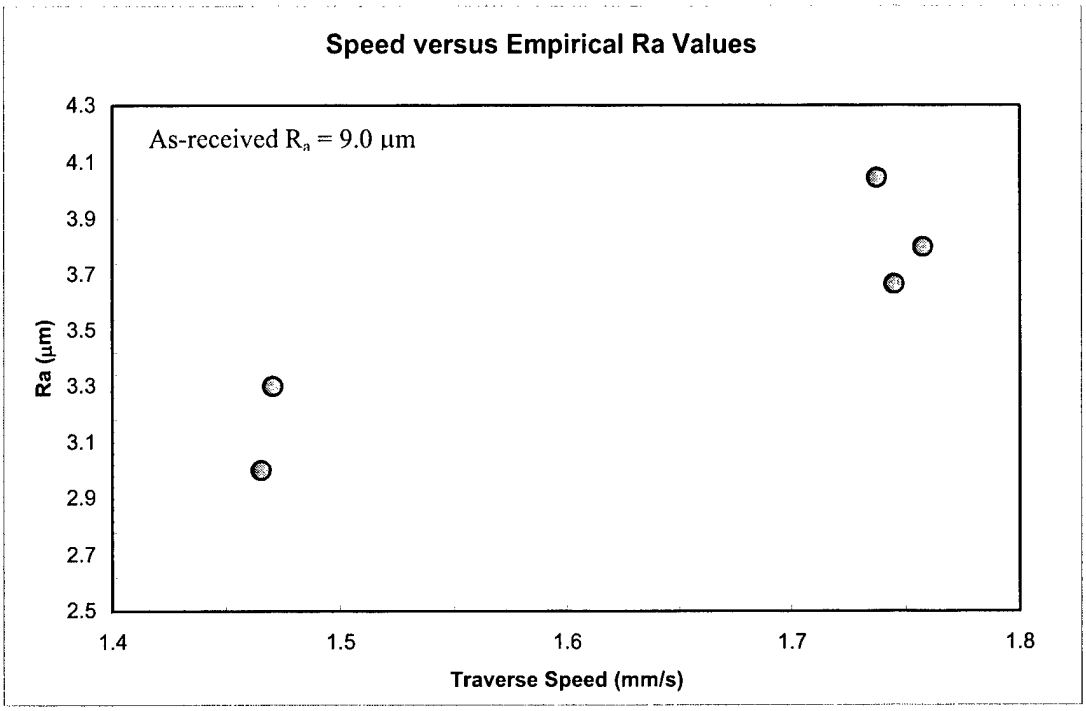


Figure 8. R_a values for Nd:YAG laser polished 420 stainless steel–40 wt.% bronze samples, 220 W.

Figure 9 is a plot of the R_a values for CO_2 laser polishing done at 320 W as a function of traverse speed. In these samples, the as-received R_a value is 2.38 μm, lower than in the previous case. The data show a "U-shape" trend for the R_a values, all below the as-received R_a value, as a function of increasing traversing speed with a minimum R_a of 1.65 μm at 1.19 mm/s. The increase of R_a value with decreasing speed from 1.19 to 0.65 mm/s is attributed to the over-melting mechanism; i.e. the sphere caps are melted completely and surface tension effects and oxidation may possible induce low frequency - high amplitude waviness morphology on the treated surface. In the speed range from

1.19 to 1.89 mm/s the increase in achieve R_a values is due to the partial-melting mechanism as described in Figure 8.

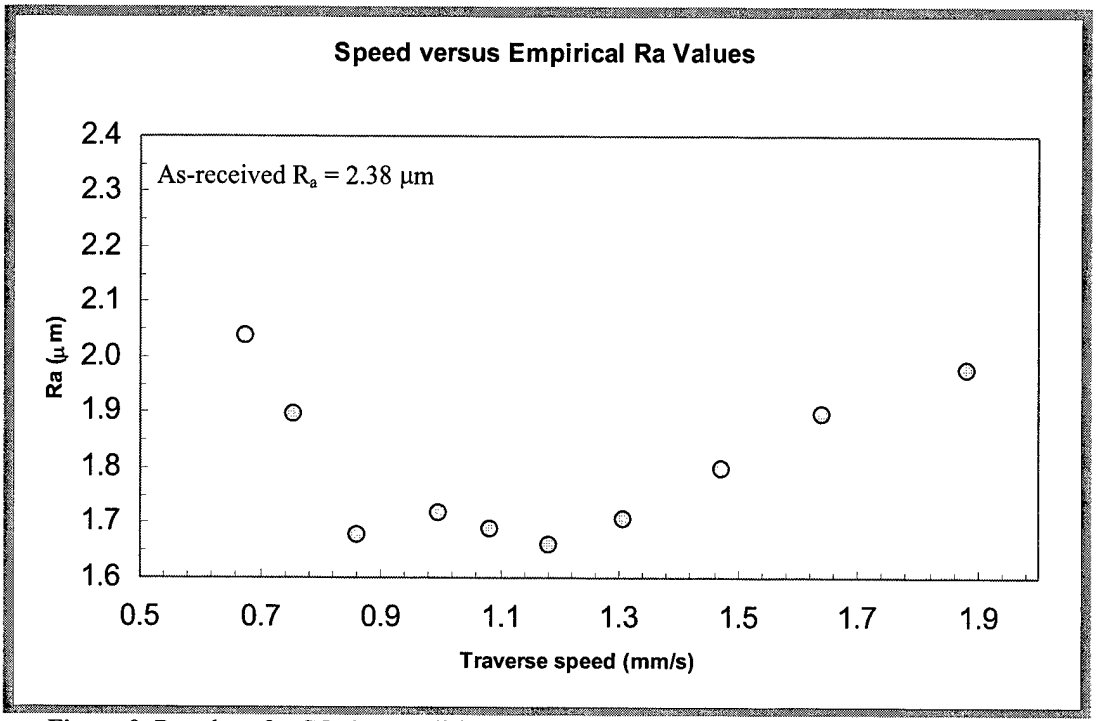


Figure 9. R_a values for CO_2 laser polished 420 stainless steel–40 wt.% bronze samples, 320 W.

Summary of Results

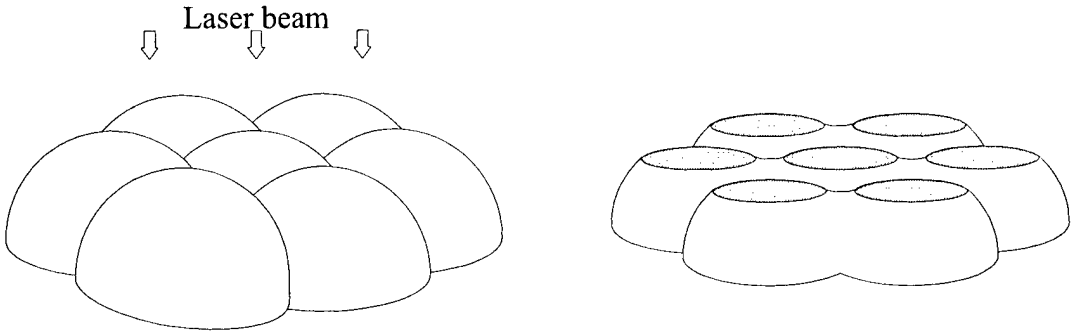
The results obtained indicate that a reduction in R_a roughness has been achieved in 420 stainless steel - bronze infiltrated SLS parts by means of CO_2 and Nd:YAG laser polishing. The best results are: (i) R_a reduction from 2.1 μm to 1.6 μm at 220 W and 2.2 mm/s (ii) R_a reduction from 2.38 μm to 1.65 μm at 320 W and 1.19 mm/s and (ii) R_a reduction from 2.38 μm to 0.8 μm at 420 W and 4.5 mm/s. By means of Nd:YAG laser polishing the best result is a R_a reduction from 9.0 μm to 2.40 μm at 220 W and 1.7 mm/s.

Analytical Modeling

Melting Spherical Cap Model

As confirmed by the SEM images, the surface of indirect-SLS metal parts consists of spherical 420 stainless powder particles of different radii that have been coated with bronze during the infiltration process. The surface roughness is then related to the height between the particle peaks and valleys formed in between them. This observation allows us to develop a simple model assuming that the surface is made of tangent semi-spheres as shown in Figure 10a. The impinging coupled laser energy heats up the spherical caps

to their melting point with subsequent flow of the melt into the valleys as shown in Figure 10b. The model must be able to determine the newly established surface morphology of the melted caps and filled valleys.



(a) Schematic of spherical cap surface prior to laser impingement on the surface.

(b) Schematic of the surface after the laser has melted the spherical caps.

Figure 10. Assumed sequence of events during laser polishing.

The first step is to write a lumped energy balance, Eq.1, taking into account surface melting and superheating due to a flux of energy (i.e., a stationary laser beam). The energy balance is expressed in terms of the melted volume of one semi-spherical cap, i.e. V_{MELT}. It is then necessary to introduce two parameters f_1 and f_2 (see Figure 11a) to account for the relationship between the thermally affected volume underneath the laser beams, f_1, and the total volume of spherical caps that is melted and superheated by ΔT_l at the surface only, given by f_2.

$$P(1-\Re)\cdot\Delta t_{INTERACTION} = \left[\rho_s Cp_s \Delta T_s \cdot f_1 + (\rho_s L + \rho_l Cp_l \Delta T_l)\cdot f_2\right]\cdot V_{MELT} \qquad (1)$$

$$f_1 \propto \left[\frac{\alpha_s \cdot \Delta t_{INTERACTION}}{R^2_{PARTICLE}}\right]^{\frac{3}{2}} \qquad f_2 \propto \frac{D^2_{LASER}}{4\cdot R^2_{PARTICLE}} \qquad (2)$$

The time a moving laser beam impinges over a spherical cap, is determined by its own spot diameter and scan speed and is given by Eq.3. This expression is a good approximation for the time a stationary laser beam is heating up the cap surface. Table 2 lists and defines the variables used in equations 1-3.

Variable	Definition	Variable	Definition
P	Laser Power	α_s	Thermal diffusivity of solid phase
$\Re$	Reflectivity	D_{LASER}	Laser spot diameter size
ρ_s	Density of solid phase	$R_{PARTICLE}$	Powder particle radius size
ρ_l	Density of liquid phase	$\Delta t_{INTERACTION}$	Laser interaction time
Cp_s	Heat capacity of solid phase	ΔT_l	Max. temperature above melting
Cp_l	Heat capacity of liquid phase	ΔT_s	Avg. temperature below melting
L	Heat of fusion	$v_{TRAVERSE}$	Traverse speed of laser beam

Table 2. Melting Spherical Cap Model definition of variables.

$$\Delta t_{INTERACTION} = \frac{D_{LASER}}{v_{TRAVERSE}} \tag{3}$$

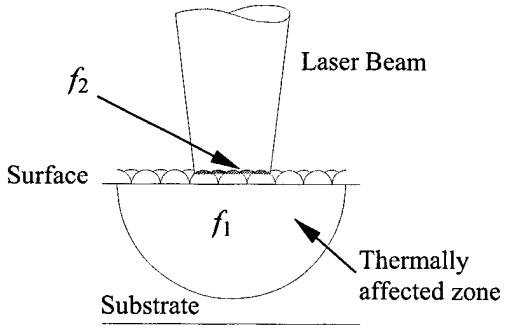
The volume of a spherical cap expressed as a function of the height, z, measured from its cusp to the basal plane, is given as Eq.4. If this expression is set equal to V_{MELT}, from Eq.1, then the depth of melt, z_m, can be calculated by solving a cubic polynomial on z.

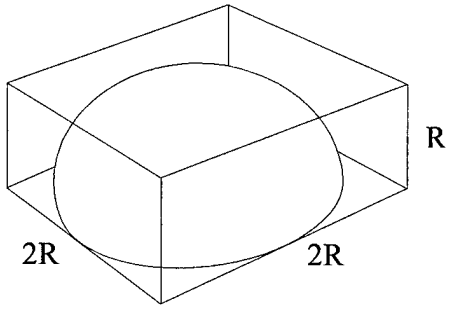
$$V_{CAP}(z) = \frac{1}{3}\pi z^2 \cdot (3R - z) \tag{4}$$

The volume of a sphere segment, $V_{SEGMENT}(z)$ is given as Eq.5. The expression for the volume of a valley to be filled by V_{MELT} is given by Eq.6. The latter was obtained by subtracting the volume of a sphere segment of height z, Eq.5, from the volume of a parallelepiped (i.e. base $4R^2$ and height z), as shown in Figure 11b. To find the filled valley height, z_f, Eq.6 is set equal to Eq.4., the latter evaluated at z_m; this is illustrated in Figure 12a. Again a third order polynomial must to be solved for z_f.

$$V_{SEGMENT}(z) = \frac{1}{6}\pi z \cdot (6R^2 - 2z^2) \tag{5}$$

$$V_{FILLED}(z) = 4R^2 \cdot z\text{-}V_{SEGMENT}(z) \tag{6}$$



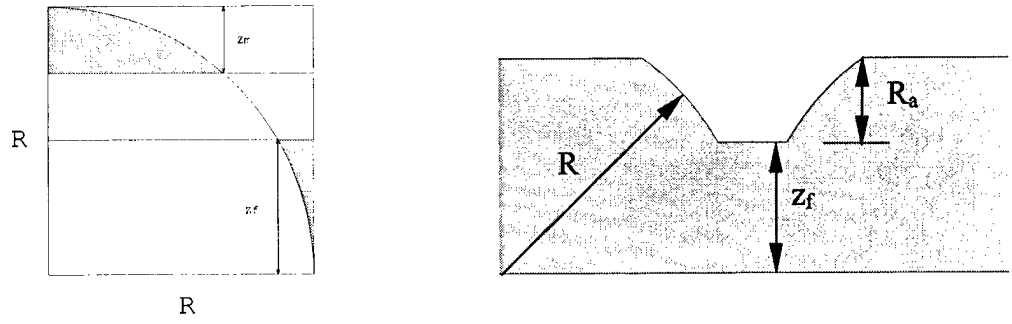


(a) Domain used in lumped energy balance. (b) Sphere cap embedded in parallelepiped.

Figure 11. Schematics of the Melting Spherical Cap Model.

Equation 7 gives the expression for the arithmetic average surface roughness as a function of the sphere radii, R_i, corresponding to specific powder particle sizes. This expression computes an arithmetic average between the peak-to-valley distances (i.e. R_i-z_m-z_f) for N different particle sizes (see Figure 12b).

$$R_a \approx \frac{\sum_{i=1}^{N} \frac{(R_i - z_m) - z_f}{2}}{N} \tag{7}$$



(a) Relationship between melt depth - filled height. (b) Idealized cross section after laser polishing.

Figure 12. Schematic drawings for the determination of the surface roughness R_a value.

From Figure 13 it can be observed that the proposed model fits the empirical data well in the region corresponding to the partial-melt mechanism, i.e. increase in R_a value (below the as-received value) with increasing speed. Particle radii of 10, 15, 20 and 25 μm were considered when computing the R_a values. The model can predict changes in R_a roughness within a 15% error inside an operating window of 1.1 - 1.9 mm/s and 320 W.

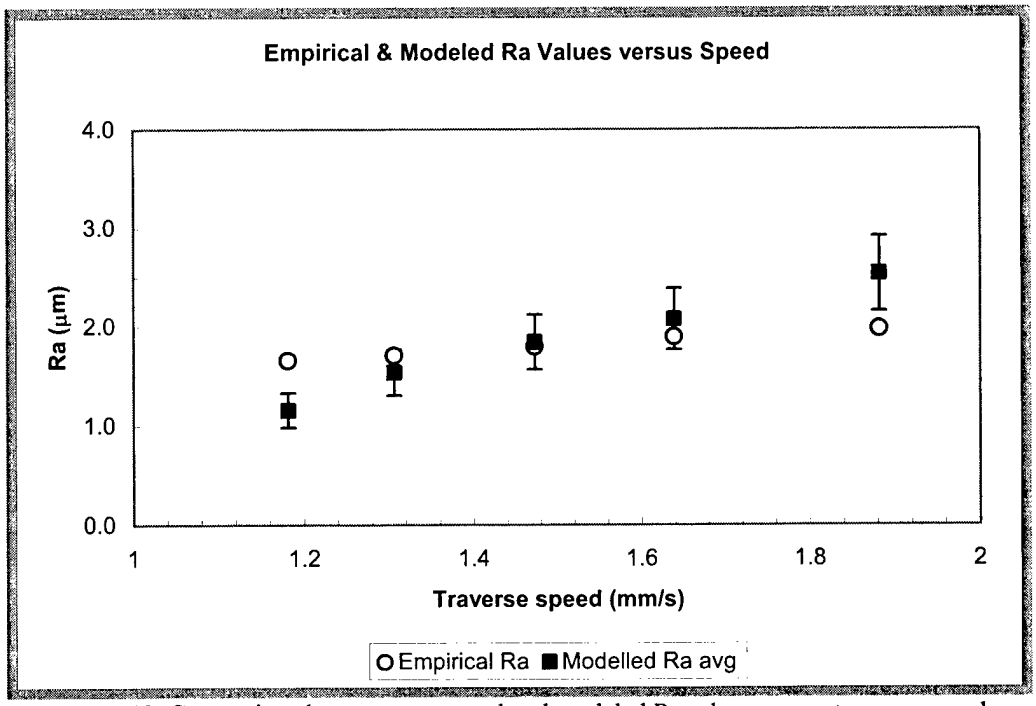


Figure 13. Comparison between measured and modeled R_a values versus traverse speed.

Conclusions

1. Reduction in surface roughness has been achieved by means of a high laser power polishing technique using either CO_2 and Nd:YAG lasers at high scanning speed. Two polishing mechanisms are observed: (a) partial-melting with increase in R_a values with increasing speed, (b) over-melting with decrease in R_a values with increasing speed.

2. As-received surface roughness values affect the reduction in roughness.
3. Surface integrity of the treated part remains to be assessed; however, an increase in the surface microhardness is expected to occur.
4. Laser power and speed control need to be implemented as the parts to be treated have finite dimensions.

References

1. J.J.Beaman, J.W.Barlow, D.L.Bourell, R.H.Crawford (1997): Solid Freeform Fabrication: A New Direction in Manufacturing. Kluwer Academic.
2. M. Burns (1993): Automated Fabrication: Improving Productivity in Manufacturing. Prentice-Hall.
3. J.A. McDonald, C.J. Ryall and D.I. Wimpenny (2001): Rapid Prototyping Casebook, Professional Engineering Publishing.
4. J. Connolly, "Direct Rapid Manufacturing – Is it Possible?", Time Compression Technologies, May, pp. 46-47, 2001.
5. I.Y.Tumer; D.C.Thompson, K.L.Wood and R.H. Crawford, "Characterization of Surface Fault Patterns with Application to a Layered Manufacturing Process", Journal of Manufacturing Systems, Vol. 17, No.1, 1998.
6. J.D. Spencer, R.C. Cobb and P.M. Dickens, "Vibratory Finishing of Stereolithography Parts", Proceedings of the 4th Solid Freeform Fabrication Symposium, Austin, Texas, 1993.
7. D.Shi and I.Gibson: "Surface Finishing of Selective Laser Sintering Parts with Robot", Proceedings of the 9th Solid Freeform Fabrication Symposium, Austin, Texas, pp. 27-35, 1998.
8. J.F. Ready, Ed. (1979): Lasers in Modern Industry. Society of Manufacturing Engineers.
9. W.M. Steen (1994): Laser Material Processing, 2nd edition, Springer Verlag.
10. J.F. Ready, D.F. Farson T. Feeley Eds.(2001): LIA Handbook of Laser Materials Processing, Laser Institute of America, Magnolia Publishing Inc.
11. H.Wang, D.L.Bourell and J.J.Beaman, "Laser Polishing of Silica Rods", Proceedings of the 9th Solid Freeform Fabrication Symposium, pp. 37-45, Austin, Texas, 1998.
12. DTM-Corporation, "Housings for hearing aid transmitter created within two month window". Horizons Q3, pp.5-7, 2001.

Acknowledgments

The Laboratory of Freeform Fabrication gratefully acknowledges the support of the Office of Naval Research for funding the project "Surface Engineering for SFF Processes", Grant N°: N00014-00-1-0334 and DTM Corporation for providing LaserForm™ ST-100 samples for testing.

this page intentionally blank

SLS POWDER LIFE STUDY

J. Choren, V. Gervasi, T. Herman, S. Kamara, and J. Mitchell
Rapid Prototyping Center, Milwaukee School of Engineering
1025 N. Broadway, Milwaukee, WI 53202

ABSTRACT

Producing acceptable models on the Selective Laser Sintering (SLS) machine involves adjusting machine parameters relative to powder age. Typically, a fraction of the powder is used and the remainder of the unused powder is recycled. After 5-7 recycles, this method leads to a powder inventory with inconsistent characteristics. The goal of this study was to apply a new recycling program to extend powder life, reduce powder inventory, and improve part quality. This study looks at various material properties of processed powder over its lifetime, including: surface quality, toughness, impact strength, elastic modulus, tensile strength, and shrinkage. A new approach to powder recycling and machine parameter adjustment will be recommended.

INTRODUCTION

Since build parameters vary for different machines and powders, this study focused on the Sinterstation 2000 using DuraForm™ Polyamide powder. Previously, during model building, a fraction of the powder is used and the remainder of the unused powder is re-processed (recycled). Recycling DuraForm™ powder involves mixing 33% unused (or new) powder and 67% used (or old) powder through a sifter with a 50/70 Mesh Screen. After 5-7 recycles, this method leads to a powder inventory with inconsistent characteristics that will produce unacceptable models using default machine parameters – *as defined by the manufacturer*. It became expensive building models over 4 inches high on a consistent basis, considering the amount of powder required for recycling. This method also failed to accurately indicate the number of recycles possible before the powder was unusable.

OBJECTIVE

The main objective of this study was to determine when powder is no longer usable. Primarily, start with enough powder so that it will provide 300 hours of build time without running short. Explore the effect on mechanical and physical properties if laser power, glaze, and crack point are determined and adjusted before each build. Determine optimal laser power and glaze point as a function of powder age and desired property.

APPROACH

Part Geometry

The part was designed to capture several characteristics of parts produced using SLS nylon. As shown in figure 1, the overall part is composed of three smaller parts joined together. The tensile sample captures mechanical properties such as, tensile strength, modulus of elasticity, percent elongation, and toughness. The smaller, rectangular part captures un-notched impact strength. The tensile and impact samples capture process shrinkage and warpage. The

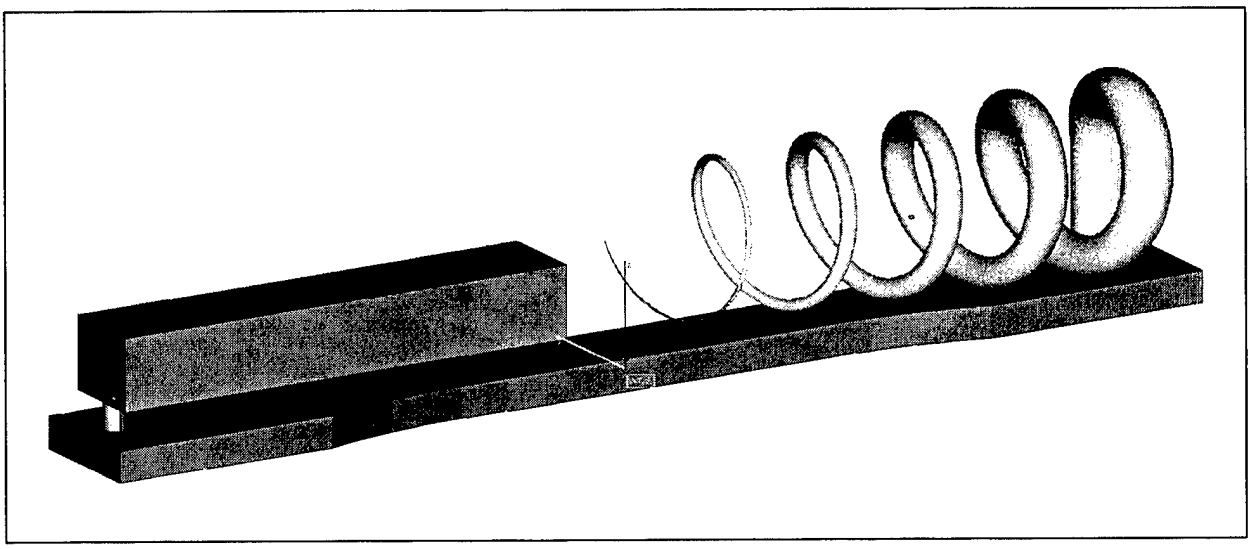


Figure 1. Test Sample Geometry

tapered helix provides information on minimum cross-sections and non-vertical surface finish. The combination of all parts provide information on sharpness of edges and surface quality.

Part Processing

Five drums of powder were used for the experiment, all verified to be from the same lot of powder. As shown in figure 2, powder samples were taken at the start of each run. The same powder was reused during the entire series of runs. The glaze and crack point were determined and used for optimal settings before building each set of test parts. The glaze point is the temperature at which powder on the part bed begins to melt. The crack point is the temperature at which powder on the feed heaters begins to melt. Before each run, small disks were built to determine the laser power range of the aging powder. The disks were not removed from the machine, but were visually inspected to determine upper and lower limits. After the range was determined, three sets of two samples were produced with low, medium, and high power. For the

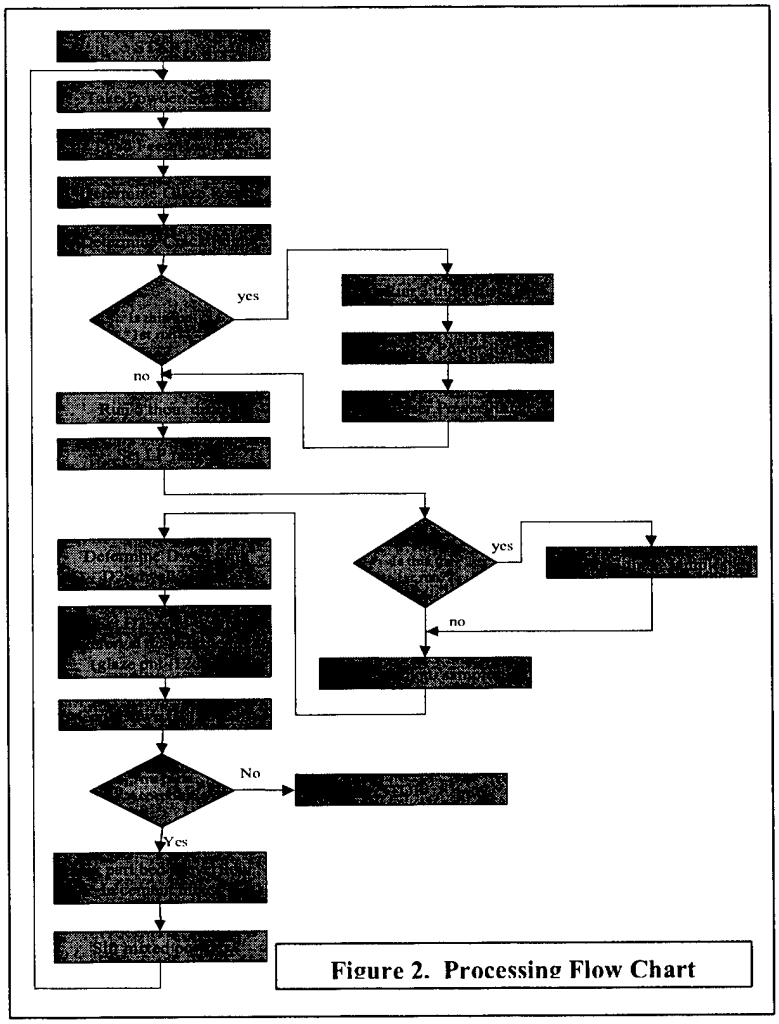


Figure 2. Processing Flow Chart

first run, one set of 0.003 inch layer thickness parts was included followed by 0.005 layer thickness parts. After the first run all test parts were produced in 0.005 inch layer thickness. The z-height of the test parts produced was not large enough to use up all the powder in the feed heaters. All powder in the feed heaters needed to be used in order to age the powder at the same temperature by passing it through the part bed, which is at about 65°C degrees above the temperature of the feed heaters. To better simulate a taller build and age all the powder in the feed heaters, each 5-6 hour run was stretched to 24 hours. This was necessary to realistically age the powder until it degraded to the point where it is no longer useful. A method was created to age the powder at the same temperature by utilizing the cool down process on the Sinterstation to simulate the build process. Typically, the cool down process starts when the laser has scanned the last part in the part bed. This process cools the part bed and lowers the temperatures of the feed heaters in a controlled manner while spreading the powder from the feed heaters onto the part bed. We revised this process to maintain the same temperatures experienced during part building in order to age the powder uniformly. The average scan time of each layer was used as the time interval between layers during the revised cool down process, until most of the powder in the feed heaters was used and enough remained to allow for the normal cool down process. After each run, the parts were visually inspected for physical defects, characteristic of fully degraded powder, to determine when to end the experiment. Powder degradation has a direct impact on the surface finish of the parts. It is important to note that mechanical properties did not determine the number of runs, appearance was the deciding factor in when to stop. All remaining powder from the part bed, feed heaters and overflows was thoroughly blended and sifted before the start of each run.

Testing

Testing can be divided into three categories, including tensile testing, impact testing, and physical testing. After samples were processed on the SLS they were stored under the same conditions until all samples were complete and ready for testing. All samples were tested within a two-day period under the same test conditions.

RESULTS & DISCUSSION

Glaze & Crack Point

Glaze point, shown in figure 3, was fairly constant to around 150 hours at which point it declined up to 192 hours. It should be noted that before the final run the IR sensor failed and was replaced. Actual temperature was higher (by a constant factor) than set temperature in the runs before 216 °C. Crack Point was steady at 96 °C.

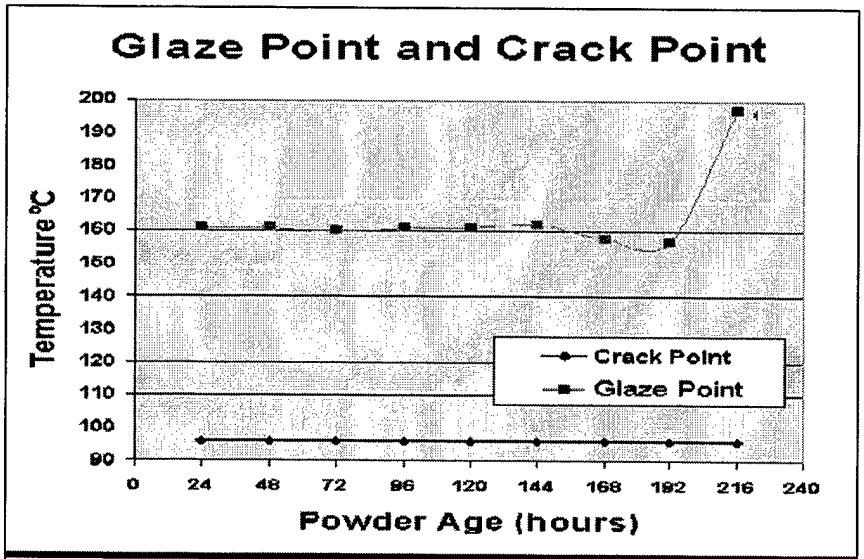


Figure 3 *glaze point increase on last run is due to IR sensor change

Laser Power

Low, medium and high laser power were increased as needed before each build. Figure 4 illustrates an increase in laser power settings from a range between 3 and 5 watts in the first run to a range between 6.5 and 8.5 watts in the final run. This study shows the importance of increasing laser power relative to powder age to maintain part quality.

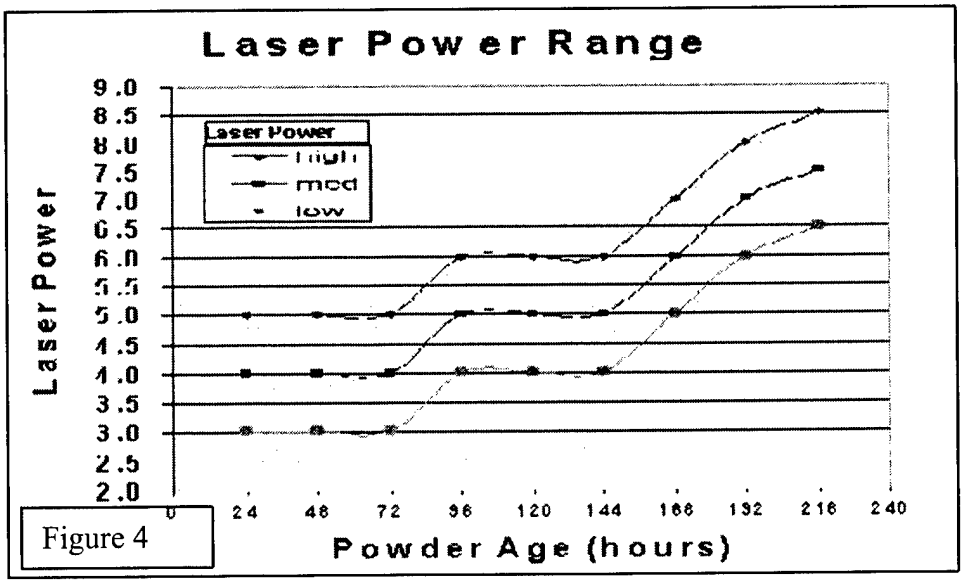


Figure 4

Tensile Strength

As shown in figure 5, the ultimate tensile strength is higher for the high power setting and steadily declines below the low and medium powder settings, at around 150 hours of powder age. A combination of higher than needed power and older powder may tend to chemically degrade the powder. Typical UTS fell between 5000 to 7000psi, which corresponds with vender's claim of 6400psi.

Young's Modulus of Elasticity

Modulus of elasticity was fairly stable averaging around 250 Ksi, as shown in figure 6.

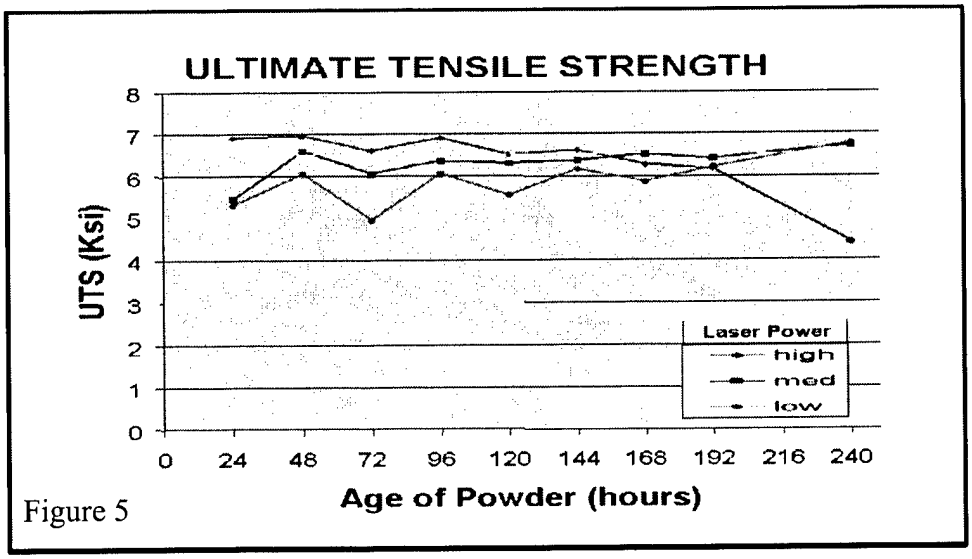


Figure 5

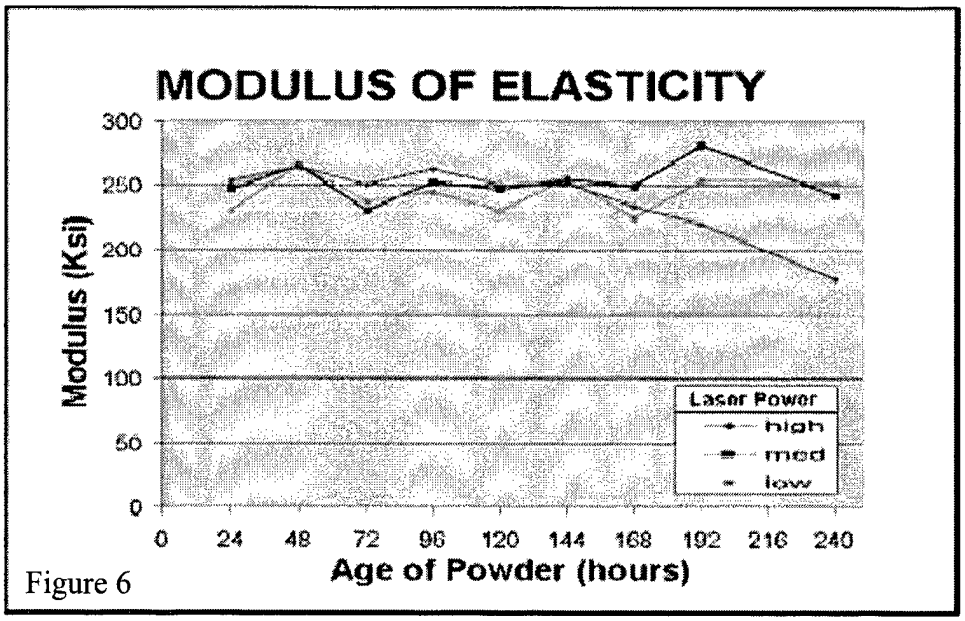


Figure 6

For the samples with high laser power modulus declined after 150 hours. The modulus corresponds with the vender's claim of 232 Ksi.

Toughness

Toughness is determined by calculating the area under the stress strain curve on each specimen. As shown in figure 7, the toughness increases to a point around 168 hours and then declines for med and high laser settings. The low laser setting increases to a high in toughness at 240 hours. Figure 7 suggests that toughness has much to do with the amount and intensity of heat the powder has been exposed to over its lifetime, reaching a threshold at around 160 hours for the medium and high laser power.

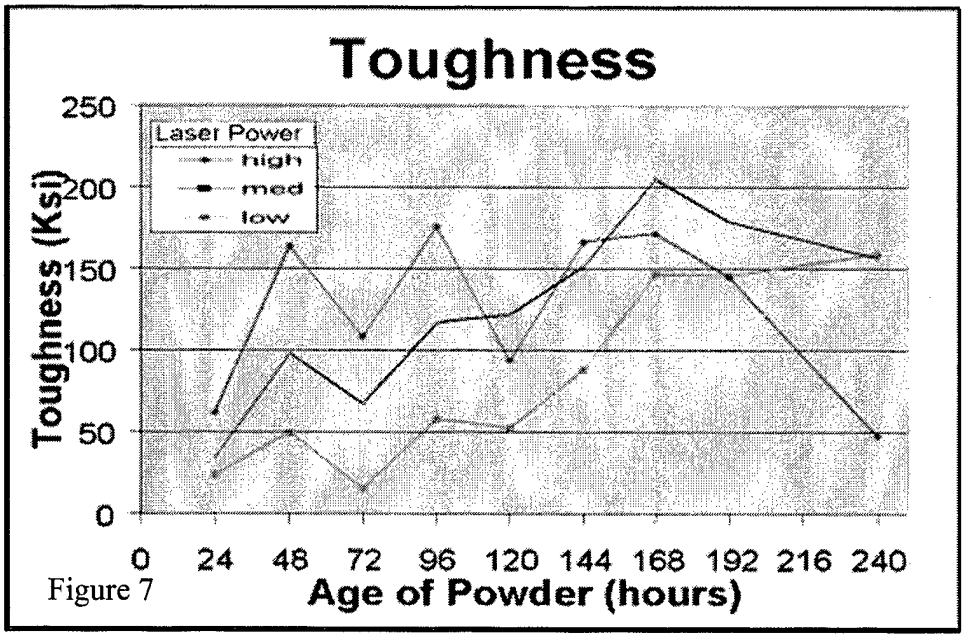


Figure 7

Impact Strength

Impact strength, shown in figure 8, follows a pattern comparable to the toughness results, in the previous graph, with impact strength declining after 150 hours. In this test all three samples decline at the same age, suggesting that impact strength declines due to powder age more than the combination of laser power and powder age.

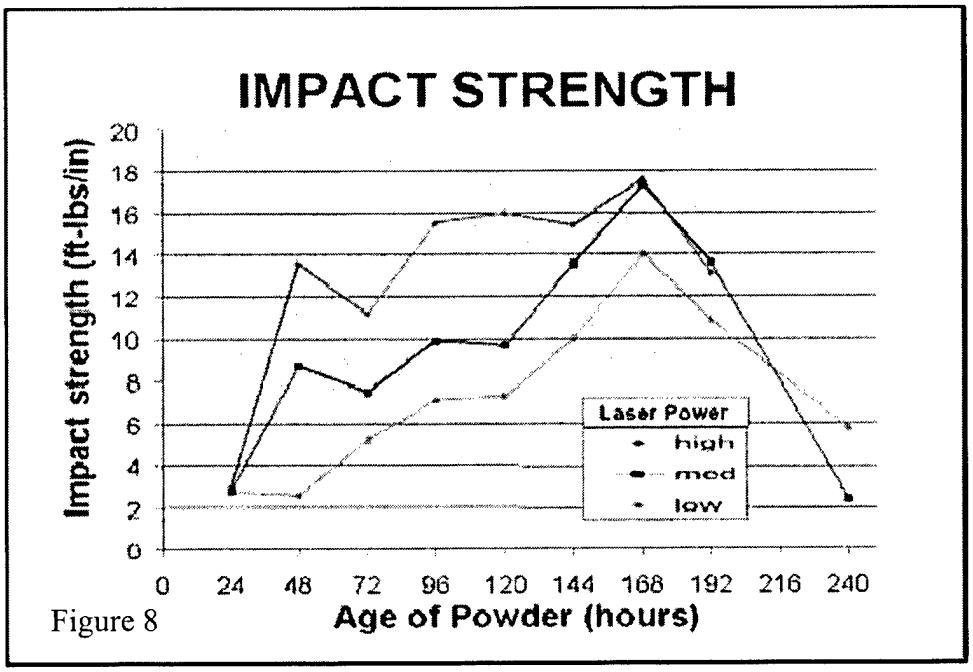


Figure 8

Shrinkage

Shrinkage as shown in figure 9, was not constant in this study. Shrinkage was least effected by laser power on the first run, holding steady at 3.8%. After 24 hours the powder shrinkage became more sensitive to laser power and held steady to 144 hours. At around 168 the shrinkage was very small at around 1%. After the powder aged past 168 the shrinkage again increased. From these results, average shrinkage as a function of laser power and powder age could be estimated. This change in shrinkage has not been verified with an additional study.

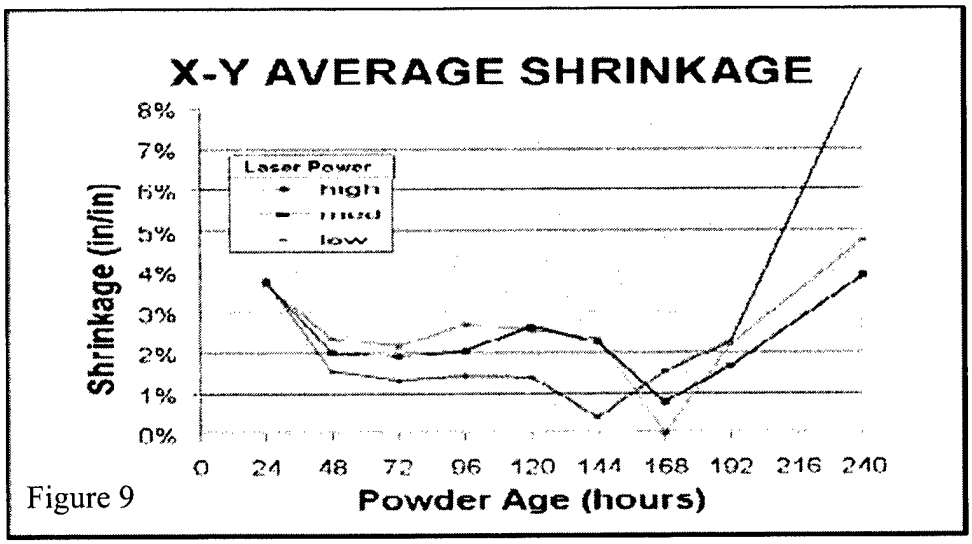


Figure 9

CONCLUSIONS

Glaze point and crack point are fairly stable as the powder ages while laser power must continually be bumped up.

Mechanical properties such as tensile strength and modulus of elasticity are fairly stable up to and past 192 hours of powder age. Toughness and impact strength generally improve up to around 168 after which they tend to decline.

Shrinkage decreases after the first powder usage and stabilizes around 2%. After the powder is older than 150 hours shrinkage decreases and then rises above 2%.

The SLS powder life study proved a tremendous success since we averaged 215 hours per 4 drums before the study and now averaging 315 hours. Using the experimental results, consider storing the used powder in separate bins based on the amount of hours spent on the machine instead of the number of builds. In the case of varying build times, which is inevitable, only mix and sift powders within a 5-hour age difference. This will ensure average powder characteristics.

Experimental results show a significant laser power change every 75 hours, therefore the NY Scale and laser discs should be built every 75 hours to determine the new shrinkage values and appropriate laser power. Although the glaze point show a minimum increase from the experimental results, it should be determined after150 hours to verify the experimental results.

ACKNOWLEDGEMENTS

We gratefully acknowledge the support of the National Institutes of Health (SBIR 2R44RR/GM14983-02, "Physical Models for Proteins by Rapid Prototyping")

The authors would like to thank Julie Schweiger and Chris Boll of the Milwaukee School of Engineering.

Special thanks to DTM Corporation and the Rapid Prototyping Consortium

SELECTED REFERENCES

Forderhase, Paul, "SLS Prototypes From Nylon," 1994 Solid Freeform Symposium Proceeding, pp 102-109

Nelson, Christian, "Improvements in SLS Part Accuracy," 1995 Solid Freeform Symposium Proceeding, pp 159-168

Pang, T.H.,"Stereolithography Epoxy Resins SL 5170 and SL 5180: *Accuracy, Dimensional Stability, and Mechanical Properties,"* 1994 Solid Freeform Symposium Proceeding, pp 204-224

this page intentionally blank

HIGH-SPEED CURTAIN RECOATING FOR STEREOLITHOGRAPHY

M. Gilio, J.-P. Kruth, and P. Vanherck

Division of Production Engineering, Machine design and Automation
Katholieke Universiteit Leuven, Belgium 3001 Heverlee

Abstract

The University of Leuven uses a liquid curtain recoating system for resin deposition in stereolithography. This system deposits new liquid layers of photo-polymer by means of a liquid curtain travelling over the build vat. Experiments have been carried out to increase the speed of the liquid curtain while depositing a layer. Speeds up to 1.2 m/s, and accelerations up to 1 g have been tested successfully, meaning that it is possible to coat high-quality layers of 75 μm thickness with this recoating technique. However, the curtain restores too slowly after acceleration. This paper discusses possible reasons and tries to formulate adequate solutions. Possible solutions consist in controlling small pressure differences in the curtain's neighbourhood. A solution to this problem is necessary, as to make the travelling length of the curtain, and so the machine length acceptable with respect to the dimensions of the build vat.

Introduction

The process of *curtain coating* consists of pumping a coating liquid from a reservoir into a precision extrusion head, which has a narrow slot along its lower face. The liquid is extruded out of the slot, and in flowing downwards under the influence of gravity it forms a liquid sheet, also called a *liquid curtain*. The liquid curtain then hits a substrate. This substrate moves relative to the curtain, and by so doing a liquid film is coated onto it. Liquid sheets are often employed to deposit uniform liquid layers on a moving substrate as, for example, in the coating of photographic film. For more applications, the reader should consult Finnicum [4] and the references of Brown [2]. Typically, the liquid curtain is long and thin, and can be up to several metres wide. Because of their technological and theoretical interest, the flow in a liquid curtain has been extensively studied, addressing both the shape of the curtain [4, 5], and instability issues [8, 7, 2].

In our application the extrusion head is displaced, rather than the substrate. The substrate, consisting of a build vat filled with liquid photo-polymer and a partially built stereolithography part, is not moving. In order to apply a new liquid layer in the stereolithography process, the extrusion head together with the liquid curtain is moved over the build vat. As several subsequent layers are coated during the process of fabricating a part with stereolithography, we refer to this coating technique as *curtain recoating* [9, 6]. Curtain recoating is one of the fastest coating techniques,

able to coat a new liquid layer for stereolithography in about two seconds. Considered the appreciable amount of layers a stereolithography product usually consists of, curtain recoating enables a substantial reduction of part build times.

Basically, a build vat with moving platform is used as depicted in figure 1. Before coating a new layer of liquid photo-polymer, the platform is lowered over a distance equal to the layer thickness. Hereafter, the coating head, and thus the liquid curtain is moved over the build vat. As a result, the liquid level in the build vat after each newly coated layer remains at constant height. A basin around the build vat collects the excess of resin and feeds it to a supply reservoir which, in turn, feeds a metering pump. In a sense, this application of curtain coating is unique with respect to all previously published studies, because of the coating head, rather than the substrate, is moving. The problem of seeking optimal operating conditions, necessary to coat layers of good quality is described in the following section. The subsequent sections discuss the experiments that have been performed in order to gain a better understanding of the curtain's dynamic behaviour, a necessary prerequisite for process improvement.

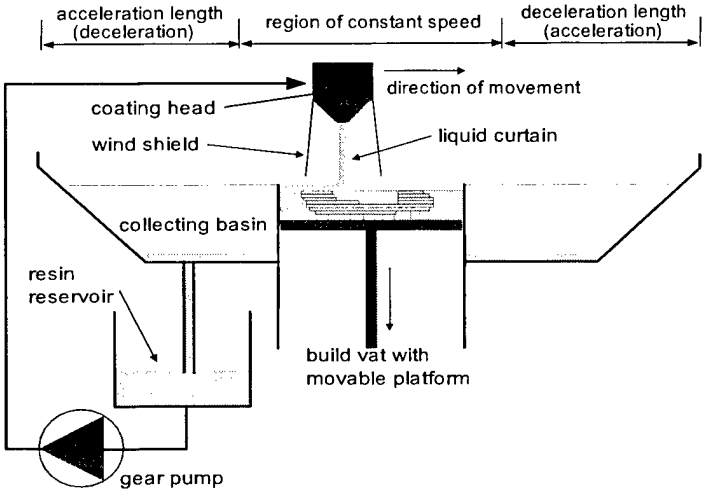


Figure 1: *Curtain recoating for stereolithography: coating of a new liquid layer*

Problem description

The thickness d of a coated liquid layer relates to the flow rate q through the extrusion head's slot per unit slot width [m^2/s], and the speed of the coating head U [m/s], according to:

$$d = \frac{q}{U}. \tag{1}$$

In order to coat a layer of uniform thickness, q must be constant along the width of the curtain, and U must remain constant while the head crosses over the build vat. There exists a minimum value for q for good operation, based on a stability issue for the liquid curtain. Below this minimal q the liquid curtain breaks and no intact liquid layers can be coated. Hence, in order to further decrease the thickness of a coated layer, U has to be increased. A typical value for q = 90 mm^2/s for our coating head, meaning that in order to coat a layer of d = 100 μm, U must be 0.9 m/s; for d = 60 μm, U = 1.5 m/s.

Actually, decreasing the layer thickness is not the primary goal of high-speed curtain recoating. The deposition of a liquid layer of good quality is a more stringent problem to be solved. If the recoating speed U is equal to the fluid velocity V in the curtain at a point where it impinges onto the substrate, then the thickness d of the coated layer will be equal to the thickness h of the curtain at its lower end. When U is smaller than V, d will be larger than h, and a kind of 'heel' will form where the curtain hits the substrate [1, 3]. Figure 2 depicts this phenomenon. Recirculating flows will develop in this heel, thereby entrapping air in tiny bubbles. These bubbles will, eventually, be trapped in the liquid layer. At present, the curtain in our machine is 125 mm long, and the velocity of the fluid at the lower end of the curtain is about 1.4 m/s [2]. The maximum achievable speed U in our machine is 0.7 m/s, meaning that the thickness of the coated layer d is about two times the curtain thickness h at its lower end. Thus, our primary goal in this research is seeking better operating conditions than the ones presently used.

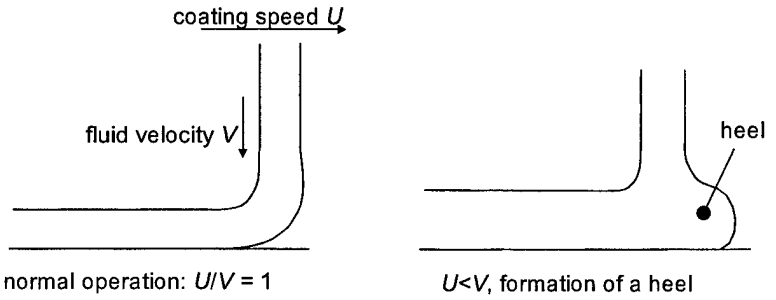


Figure 2: *Formation of a heel at the lower end of a liquid curtain when the coating speed is substantially smaller than the fluid velocity in the curtain*

In order to coat a liquid layer, the coating head has to be accelerated from rest to the desired coating speed U. Throughout this paper the distance travelled by the head during acceleration will be called the *acceleration length* (fig. 1). A section of constant speed U follows next. In the beginning of this constant speed section, the curtain has to reassess from acceleration. Subsequently, a liquid layer is coated. Finally the coating head decelerates in order to be at rest at the end of its stroke. When coating the subsequent layer, the head starts at this latter position and moves towards the former rest position, thus necessitating a symmetrical machine.

Some problems that are encountered in high-speed curtain recoating are now discussed. Firstly, the machine dimensions have to remain within reasonable proportions. It would be unacceptable to have a machine of more than 3 m long with a build vat of only 250 mm diameter. The acceleration length should thus be limited. When increasing the coating head's speed U, the *peak acceleration* should be increased, rather than the acceleration length. Secondly, inertia forces during acceleration will bend the liquid curtain backwards. Vertical rods at both lateral ends of the curtain are needed to maintain a straight curtain, as surface tension would otherwise contract it. The curtain is pinned at these rods, also called 'edge guides' (fig. 3). Thus, when bending backwards the curtain will curve also in a horizontal plane, remaining pinned at the edge guides and assuming a maximal bending in its middle. This situation is depicted in figure 4. After reaching the desired coating speed U, the curtain slowly returns to its original, planar shape. This planar shape has to be reached before beginning to coat the layer, otherwise the contact line between curtain and

substrate will be curved. Since, in this case, the curtain is still in a transient state, its velocity is not equal to the constant speed U, and the thickness of the coated layer will not be uniform. A number of experiments have been performed in order to investigate the feasibility of using high-speed curtain recoating for stereolithography. The following section describes the set-up that has been used for the experiments.

Experimental set-up

A number of experiments have been performed in order to investigate the possibility of high-speed curtain recoating. In the context of curtain recoating for stereolithography, *high-speed* means coating speeds U higher than 1 m/s. The coating head was mounted on a linear drive, having a total stroke of 900 mm. This linear drive was chosen because of its ease of programming different acceleration profiles, and because of the high accelerations the drive can achieve. Degraded Somos 7100^{tm} resin with a viscosity of 1.1 Pa.s @ 34$°C$ was used for the experiments. The curtain was 400 mm wide and 125 mm long. Figure 3 shows the set-up. A Sony digital video camera was mounted next to the coating head, moving together with the head and slide. Video frames were recorded at a rate of 50 Hz during motion.

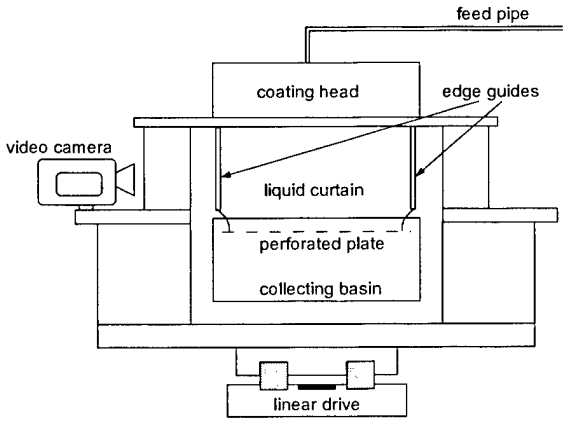


Figure 3: *Experimental set-up for the investigation of the curtain's behaviour during acceleration to high speeds of the coating head.*

Different acceleration profiles were tested, among these a 2nd order polynomial, having a discontinuous jerk profile at the beginning and end of the acceleration section, and a 4th order polynomial, having a continuous jerk profile throughout the entire trajectory of the drive. For a given acceleration length, the 2nd order profile gives the lowest peak acceleration. For a given peak acceleration, the 2nd order profile gives the shortest acceleration length. No substantial difference has been observed in the curtain's response to both mentioned profiles. This observation is also supported by the results of a simulation of the curtain's behaviour during acceleration of the coating head. As a liquid curtain possesses a very low stiffness, a shield is mounted at both sides of the coating head to protect the curtain from aerodynamic forces during motion. Figure 5 and 4 show cross-sections of a backwards bent curtain. The following section covers the performed experiments in more detail, and discusses the results.

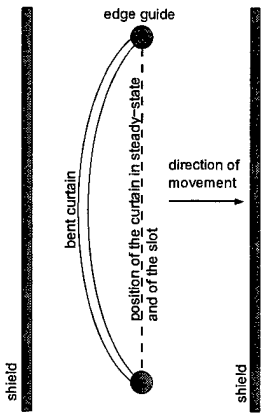


Figure 4: *Horizontal cross-section of a liquid curtain bending backwards during motion. The shields are protecting the curtain from aerodynamic influences.*

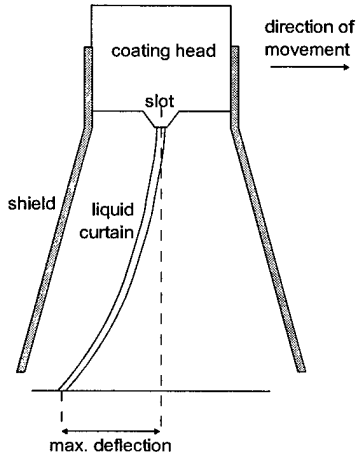


Figure 5: *Vertical cross-section of a falling liquid curtain bending backwards during motion.*

Results and discussion

A first issue in the experiments was to observe up to which maximum peak accelerations the curtain could resist without breaking. A higher peak acceleration shortens the acceleration length needed to achieve a desired speed U, thus making the machine shorter. The coating head and curtain were subjected to a peak acceleration of 1g (9.8 m/s^2), both with a 2nd and 4th order polynomial acceleration profile to reach a speed U of 0.9 m/s only after an acceleration length of respectively 62 mm and 77 mm for the 2nd and 4th order polynomial profile. During acceleration, maximum backwards bending of the curtain, as defined by figure 5, was 42 mm. No breakage of the curtain was observed. These observations show that high accelerations are no limiting factor for high-speed curtain recoating. Secondly, the feasibility of letting the curtain move at speeds higher than 1 m/s was investigated. Due to the limited stroke of the linear drive, the maximal speed tested was U = 1.2 m/s. To reach this speed, a peak acceleration of 9.0 m/s^2 was used and the acceleration length was respectively 120 mm and 150 mm for the 2nd and 4th order polynomial profile. No breakage of the curtain was observed, and the curtain's maximum backwards bending was 52 mm with respect to the slot's position.

However, in restoring towards its flat shape after acceleration to a speed U, the curtain takes a much longer time than would be expected. As the curtain must return to its flat shape before actual coating can start, the observations show that extra length has to be added to the travelling length of the coating head, in order to give the curtain sufficient time to reassess. It is the purpose of this paper to investigate the reasons of this unwanted slow reassessment of the curtain, and to formulate a possible solution. The behaviour of the curtain during acceleration of the coating head has been simulated. A two-dimensional model of the curtain has been used for simulation, thus assuming a curtain of infinite width. As the curtain in reality, is pinned laterally to the edge guides, it reaches its maximal bending in the middle. This pinning of the curtain at its lateral ends will undoubtedly influence the amount of bending in the middle, as the curtain is not free to deflect

as a whole. Therefore, the simulation will always yield a higher deflection than experimentally observed. It is not a purpose of this paper to describe the simulation in detail. What does matter in this stage of analysis, is that the model is able to qualitatively predict the experimentally observed behaviour of the curtain.

The curtain's shape is governed by the equations of Navier-Stokes for viscous flow, suitably transformed to be used for liquid sheets. External forces acting on the curtain are: gravitation, inertial forces due to the acceleration, and aerodynamic forces induced by the air between the curtain and the two shields. The influence of viscosity and surface tension was also modelled. The aerodynamic forces, that act as a pressure difference between the curtain's front and back side, are most subject to uncertainty. The reason for this uncertainty is due to the fact that, although the shields indeed protect the moving liquid curtain from still air, an amount of air still enters the space between curtain and shield through a gap between the lower edge of the front shield and the substrate. The shields may not contact the liquid substrate. Therefore the shields are mounted such that a gap of 2 mm is left between them and the substrate. When the curtain is moving, air enters through this gap into the space between curtain and shield. The liquid curtain will subsequently have to deflect the inflowing air toward its lateral ends, where the air is free to escape. Since in this case the curtain is moving at a speed U, while the air can be considered to be at rest, the aerodynamic forces have been modelled as a stagnation pressure, acting as a pressure difference between the curtain's front and back side. The modelled stagnation pressure relates to the coating speed U according to:

$$p_s = \frac{\rho_{air} U^2}{2} \tag{2}$$

with ρ_{air} the density of air. This pressure is very low ($\approx$ 1 Pa when U = 1.2 m/s), but its influence on the curtain dynamics is nevertheless tremendous, because the bending stiffness of the curtain is also very low. According to our model, and considering a steady state, a constant pressure difference of 1 Pa between the curtain's front and back side causes the curtain to deflect by 70 mm at its lower end, measured from the slot's position. The reader should bear in mind that the length of the curtain in this case is only 125 mm.

With this in mind, and in order to qualitatively predict the experimentally observed behaviour, the reader should notice from figures 6 and 7 that during the motion at constant speed U, the curtain shows a relaxation towards its planar shape. The relaxation obviously suggests that the pressure difference across the curtain slowly vanishes. This means that the stagnation pressure in our model should be subject too to a relaxation, which was implemented as an exponential decay of the stagnation pressure. As the dynamics of the experimentally observed relaxation are not clear yet, the relaxation constant of the modelled exponential decay of the stagnation pressure is found such that a best fit between the experimental data and the model's results is achieved. A relaxation constant $\tau \approx 0.2$ sec is found to agree best with all data, as can be seen in figures 6 and 7.

The introduction of a *stagnation* pressure is open for discussion; what is important though, is that the experimental data shows that the curtain first deflects, due to inertial and aerodynamic forces, the latter ones increasing with increasing speed U. The deflection shows afterwards a kind of relaxation. This relaxation is mainly caused by a pressure in front of the curtain, that has built up during acceleration and is now disappearing slowly. A first possible explanation for the dynamics

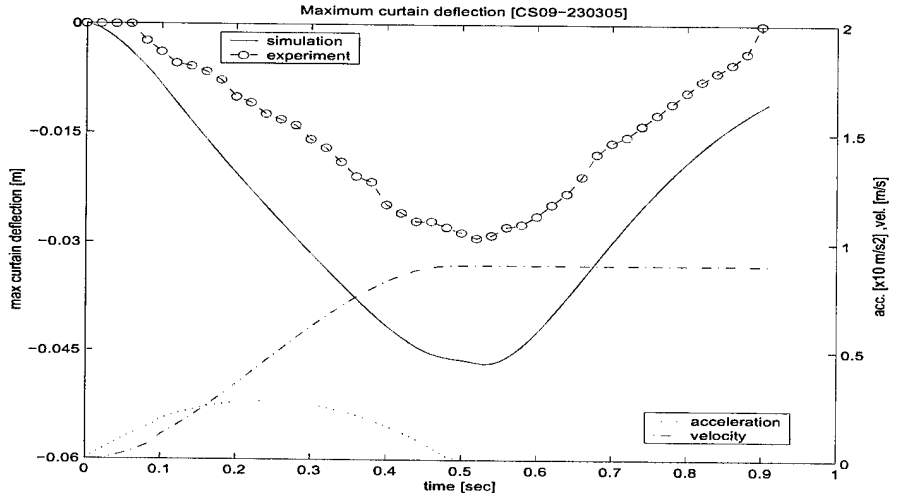


Figure 6: *Plot of the curtain's deflection measured at its lower end with respect to the slot's position. Both experimental data and simulation results are plotted; values refer to left y-axis. The applied acceleration (2^{nd} order polynomial profile, a_{max} = 2.7 m/s^2) is plotted, together with the speed of the coating head U_{max} = 0.9 m/s (right y-axis).*

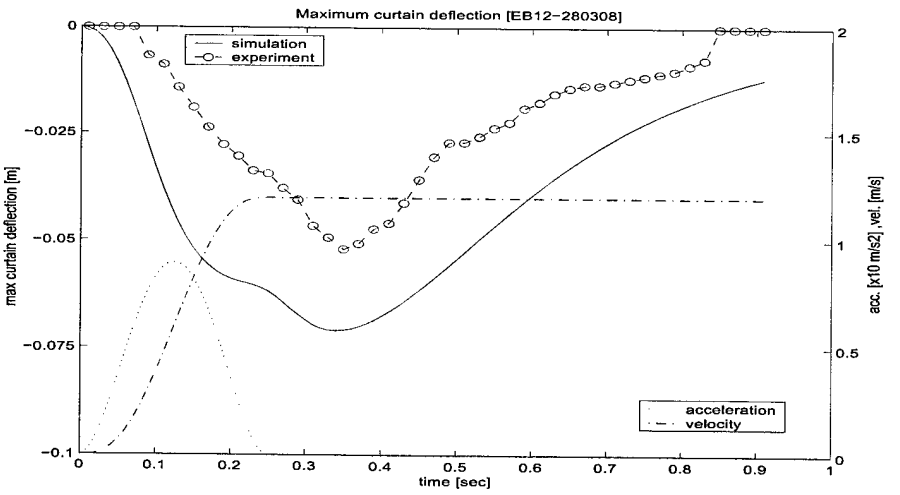


Figure 7: *Plot of the curtain's deflection measured at its lower end with respect to the slot's position. Both experimental data and simulation results are plotted; values refer to left y-axis. The applied acceleration (4^{th} order polynomial profile, a_{max} = 9.0 m/s^2) is plotted, together with the speed of the coating head U_{max} = 1.2 m/s (right y-axis).*

of the relaxation is a rearrangement of the air flow in the space between the curtain and the air shield. Once a constant speed U has been achieved, a rearrangement of the air flow could drop the pressure in the direct vicinity of the curtain's front. A second possible explanation is a pressure building up behind the curtain, thereby balancing the pressure in front of the curtain. The dynamics of this pressure build-up could reasonably be slower than the ones accounting for the curtain's front pressure. The pressure differences occurring in this problem are very low (magnitude 1 Pa). Since pressure differences are the driving force behind flows, the flow rate of air is minimal too, thereby serving as a possible explanation for the slow relaxation. Moreover, the compressibility of air certainly affects the curtain's dynamics, because the speed of propagation of a pressure disturbance is finite in a compressible medium. The relaxation constant τ, that has been introduced in our simulation is thus a generic parameter, accounting for all physical effects that influence the observed relaxation.

A validation of these assumptions is difficult, since the pressure measurements are difficult to perform because of their small magnitude and because of the occurring accelerations that will influence the measurements. Another approach consists in visualising the streamlines of air around the curtain in a wind tunnel. Such a test would be incomplete though, due to the inability to simulate inertial forces acting on the curtain. Actually, the assumptions could be tested by experiments aiming at influencing the relaxation. If the relaxation is dependent upon a presumed pressure difference between the curtain's middle and its lateral ends, the speed of relaxation could be increased by increasing the mentioned pressure difference. A second solution could be accomplished by increasing the pressure at the back of the curtain, thereby balancing in a much faster way the stagnation pressure that has built up in front of the curtain. Anyway, it is clear that there are methods to dynamically control the curtain's deflection during acceleration. These ideas have not been implemented yet, but will be a research topic in the future. They are needed for implementing high-speed curtain recoating for stereolithography while maintaining the length of the coating head's drive, and thus the machine length within reasonable proportions.

Conclusion

This paper has discussed preliminary experiments for the implementation of high-speed curtain recoating for stereolithography. Curtain recoating is a fast technique to coat even very thin liquid layers. The terminology 'high-speed' is used in this application to refer to coating speeds higher than 1 m/s. Speeds up to 1.2 m/s and accelerations up to 1g have been tested successfully, without breakage of the curtain. A main problem to be solved is the curtain's slow returning to its flat shape after bending due to acceleration. In this respect, the curtain's dynamics have to be made faster. Possible solutions to this problem have been mentioned, all consisting in controlling small pressure differences in the curtain's neighbourhood. A solution is necessary as to make the machine length acceptable with respect to the dimensions of the build vat.

Acknowledgements

The present research is financed by the Institute for the Promotion of Innovation by Science and Technology in Flanders (IWT).

References

[1] T.D. Blake, A. Clarke, and K.J. Ruschak. Hydrodynamic assist of dynamic wetting. *AIChE Journal*, 40(2):229–242, 1994.

[2] D.R. Brown. A study of the behaviour of a thin sheet of moving liquid. *J. Fluid Mechanics*, 10:297–305, 1961.

[3] A. Clarke. Recirculating flows in curtain coating. In *1st European Coating Symp. Med. Thin. Films*, pages 32–41, 1995.

[4] D.S. Finnicum, S.J. Weinstein, and K.J. Ruschak. The effect of applied pressure on the shape of a two-dimensional liquid curtain falling under the influence of gravity. *J. Fluid Mech.*, 255:647–665, 1993.

[5] S.F. Kistler. *The fluid mechanics of curtain coating and related viscous free surface flows with contact lines*. PhD thesis, University of Minnesota, 1984. University Microfilms International.

[6] J.P. Kruth, I. Meyvaert, P. Vandormael, and K. Renap. Curtain coating for depositing layers in stereolithography. In *Proc. of the 7th Int. Conf. on Rapid Prototyping*, pages 218–228, 1997.

[7] S.P. Lin, Z.W. Lian, and B.J. Creighton. Absolute and convective instability of a liquid sheet. *J. Fluid Mech.*, 220:673–689, 1990.

[8] L. De Luca and M. Costa. Instability of a spatially developing liquid sheet. *J. Fluid Mech.*, 1997.

[9] K. Renap. Curtain recoating. Materialise NV, 1997. international patent WO97/29901.

this page intentionally blank

Effective Cooling Method for Spin Casting Process

Yong-Ak Song, Sehyung Park, Yongsin Kwon

Korea Institute of Science and Technology KIST, CAD/CAM Research Center
P.O. Box 131, Cheongryang, Seoul, Korea

Abstract

Spin casting has been widely used in prototyping industry as a secondary process to convert a master model into a functional metal or plastic part. The main problem of the spin casting process consists in the poor thermal conductivity of silicone rubber as mold material which leads to a long cooling time between each casting processes and also to a short life time of mold. To solve this problem, different cooling methods have been developed and compared to each other experimentally. First, air cooling channel has been integrated into the spin casting mold to enhance the heat removal. Secondly, the silicone rubber has been mixed with different metal and ceramic powders to increase its thermal conductivity. The results so far prove an applicability of the developed cooling methods.

1. Introduction

Spin casting is a secondary process to produce metal and plastic parts quickly from an existing master model. It is especially suitable for the manufacture of die casting parts since the manufacture of dies is normally very time-consuming and expensive. In spin casting, a silicone rubber material is used. Since the silicone rubber is a flexible material before vulcanizing, it can be easily formed around the master model, thus making the mold manufacture fast and easy to learn.

Although the silicone rubber material can withstand a temperature of 420 °C and thus allowing the use of low-melting alloys such as tin and zinc for casting, it has a low thermal conductivity. A typical value for the thermal conductivity of rubber is _=0.2 W/Km [1]. This low thermal conductivity leads to an increasing mold temperature in the course of casting process. The constant heating-up of the mold has a damaging effect on the mold surface since it can be worn off due to the thermal stress or even burned off. To avoid such a damage, it is necessary to cool down the mold surface between each shots with compressed air or just with natural convection. This, however, increases the total cycle time. Also, according to [2], the deviation increases with higher mold temperature. For this reason, it is necessary to cool down the mold during spin casting, thereby keeping the mold temperature constant.

2. Development of cooling methods

In the experiment, a spin casting equipment of Tekcast is used. Since the mold rotates during the casting process, it is rather difficult to supply a constant flow of coolant from the outside into the mold as it is mostly done in conventional injection molding. A closed loop of coolant flow also imposes a serious problem regarding the proper sealing of the mold. Under the circumstances, air seems preferable to water. Also in view of easier integration into the existing spin casting equipment, air cooling seems a better choice than water cooling. To realize an air cooling system, the center of the shaft coaxial to the pneumatic cylinder is modified to let the air flow into the inside of the mold, as shown in **Fig. 1**. To connect the lower and the upper mold, a plastic tube is used. By this means, the air flows from the lower part of the mold to the upper part.

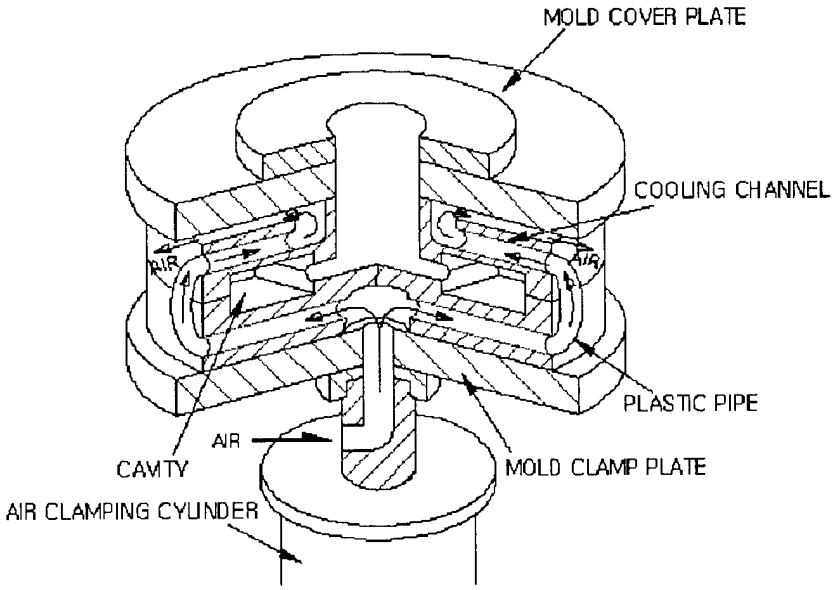


Fig. 1: Flow of cooling air through the mold

The way how the mold is fabricated offers a great flexibility to design the cooling channel into the inside of the mold. According to the thickness of a master model used, an appropriate number of silicone rubber discs are stacked on each other. To implement an internal cooling channel in the mold, the copper pipes are then inserted between those silicone rubber discs, preferably directly beneath the cavity surface, **Fig. 2**. The copper pipes can be bended prior to the insertion and in this way different shapes of the cooling channel can be realized. After vulcanizing of the silicone rubber discs, the pipes are then firmly included in the mold. With regard to a high thermal conductivity around the cooling channel, it is recommendable to let the copper pipes in the inside of the mold.

In order to enhance the cooling effect in the mold during air cooling, it is tried to increase the thermal conductivity of the mold locally around the cavity. A commonly used method for this purpose is to add a high thermal conductivity material to the mold material. For example, a high thermal conductivity metal powder such as aluminum is added to the UV-curable resin which is then used in SLA process to make a mold for low temperature molding process [3, 4]. Two metal powders, copper (_=350 W/Km) and aluminum(_=221 W/Km), as well as two ceramic powders, alumina (_=27.6 W/Km) and silicon nitride (16-33 W/km), are used in the experiment. Although ceramics have lower thermal conductivities compared to those of metals, ceramics offer a higher heat resistance, thus protecting the mold surface better than metals at higher casting temperature. The powder size of used powder materials is between 15-40 _m.

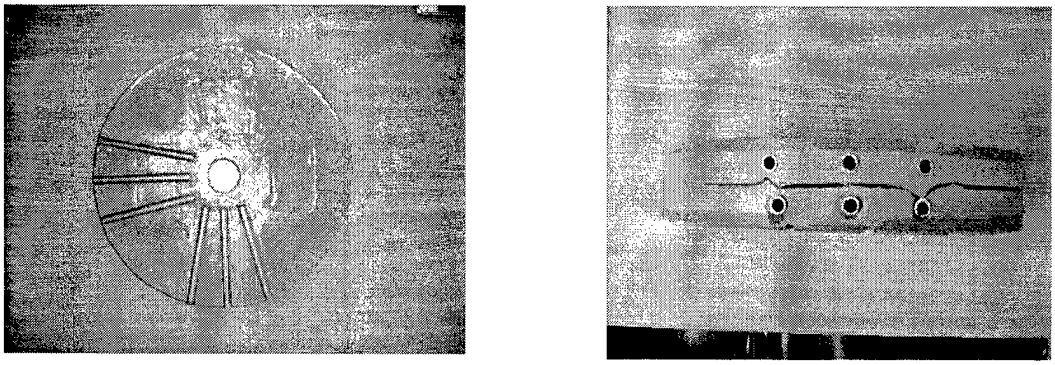


Fig. 2: Copper-mixed cavity and cooling pipes in the spin casting mold

3. Comparison of different cooling methods

To measure how effective each cooling methods are, molds with and without internal cooling channel are compared to each other regarding their surface temperatures. The experimental parameters are as follows:

Clamping pressure:	4000 PSI
Rotating speed:	500 rpm
Melting temperature of zinc:	410 °C
Pouring time:	1 min.
Flow rate of cooling air:	140-150 l/min

In case of in-process cooled molds, the cooling effect of the combination of air cooling with the copper-mixed cavity is compared to that of the solely air cooled mold as well as to that of the copper-mixed cavity without air cooling. The weight mix ratio of silicone rubber to copper is 3:2. After each shot, the surface temperature of the molds is measured. As shown in **Fig. 3**,

the surface temperature of a mold without any cooling reaches 140 °C after 20 shots and then remains almost constant at that temperature. If air is supplied to the mold, the surface temperature is reduced to 110 °C. This result means that even a simple air supply into the mold is an effective cooling method.

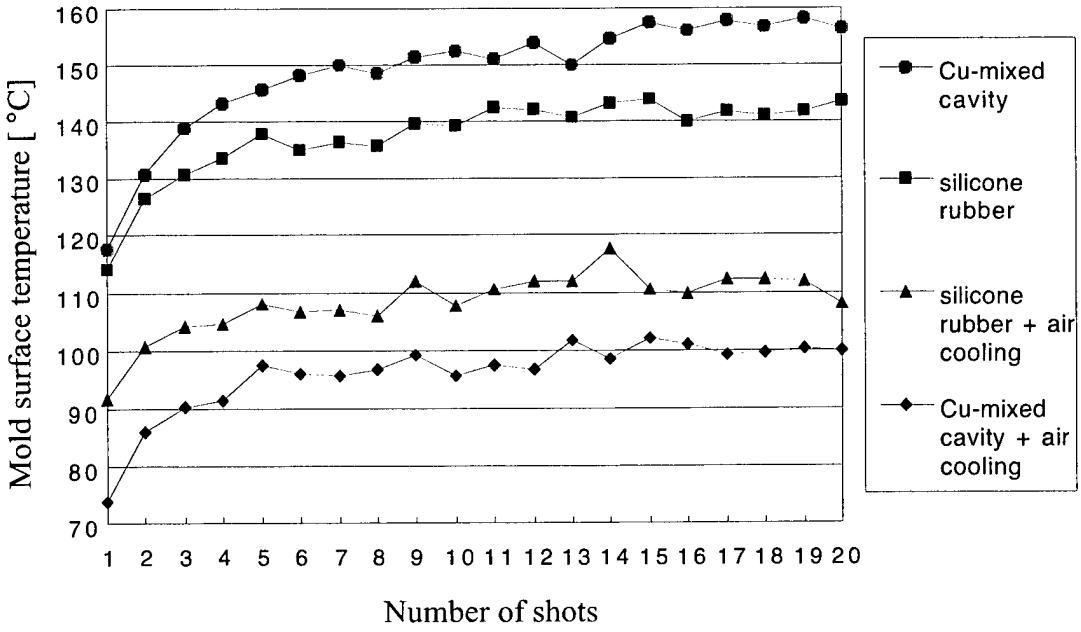


Fig.3: Surface temperatures of molds cooled with different cooling methods

The high surface temperature of the copper-mixed mold around 160 °C proves that the addition of copper to silicone rubber increases the thermal conductivity of the cavity and thus making it a heat sink. When cooled with air, the surface temperature drops to 100 °C, which is around 10 °C lower than that of the pure silicone rubber mold cooled with air. This result implies that the combination of copper-mixed mold with air cooling can be used if air cooling of silicone rubber mold alone is not sufficient enough.

In case of aluminum-mixed molds, the surface temperature also increases to around 160 °C if no air cooling is additionally used, **Fig. 4**. When air is supplied, the surface temperature decreases to around 120 °C. Compared to that of the pure silicone rubber mold, however, this is no distinct temperature difference, the reason being that the mix ratio of silicone rubber and aluminum is not optimal yet. The ceramic-mixed molds also show no distinct cooling effect compared to that of the pure silicone rubber mold. However, the ceramic-added molds show less surface burn after several shots. Therefore, in terms of the surface protection, the addition of ceramic powder gives a distinct advantage over the use of pure silicone rubber mold.

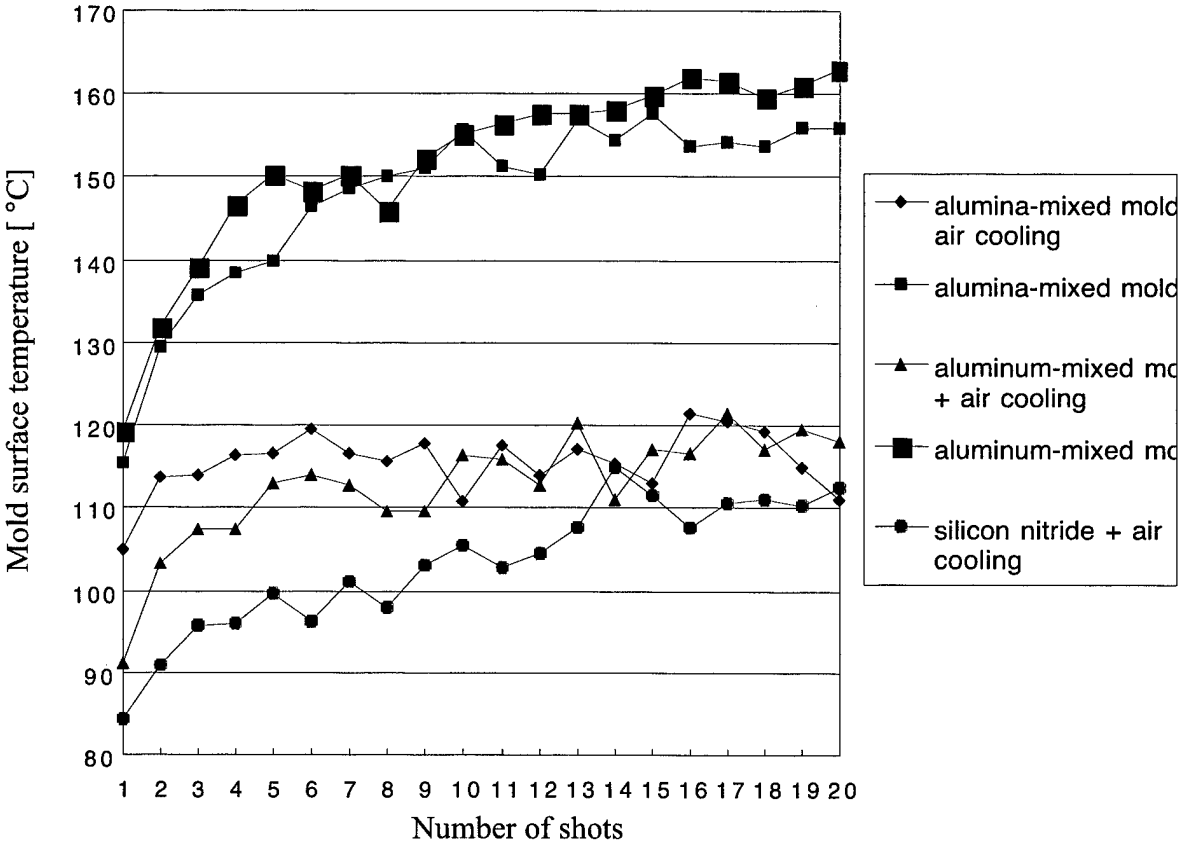


Fig. 4: Surface temperatures of molds mixed with different materials

4. Conclusion

It was aimed to develop an in-process cooling method for spin casting process. Two cooling methods are proposed: First, an insertion of internal cooling channel with copper pipe for air cooling and second, an increase of thermal conductivity of mold by mixing the silicone rubber with a high thermal conductivity material. The result of the investigation shows that a cooling effect can be already achieved when compressed air is supplied into the mold through the copper cooling pipes. By this means, the surface temperature can be decreased by around 30 °C. The cooling effect can be enhanced if materials of higher thermal conductivity such as copper are added to the silicone rubber in the cavity area. Among the tested materials, copper shows the best cooling effect. In case of the copper-mixed mold with air cooling, the surface temperature is even reduced by around 40 °C. This result clearly indicates the effectiveness of the developed cooling methods. Regarding the surface protection during spin casting, ceramic materials offer a distinctive advantage over metals and pure silicone rubber mold. In future work, the influence of mold cooling temperature on the part accuracy has to be investigated in detail.

5. References

[1] http://www.mininglife.com/Miner/general/thermalconductivity.htm

[2] Barnard, L.J., "Spin casting as a tool in rapid prototyping", Solid Freeform Fabrication 1999, The University of Texas at Austin, 9-11 August 1999, pp. 719-725

[3] Girouard, D., "Molds for low temperature molding processes using rapid prototyping", The Fourth International Conference in Rapid Prototyping, 14-17 June 1993, Dayton, Ohio, p. 61-66

[4] Nakagawa, T., "Rapid Prototyping in Japan", The Eighth International Conference on Rapid Prototyping, 12-13 June 2000, Tokyo, pp. 1-16

Fabrication of Multi-Layered Carbon Structures Using LCVD

Ryan W. Johnson, Scott N. Bondi, Daniel L. Jean,
Chad E. Duty, MingXuan Jiang, and W. Jack Lackey

Rapid Prototyping and Manufacturing Institute
Woodruff School of Mechanical Engineering
Georgia Institute of Technology
Atlanta, GA 30332

act

Others have used Laser Chemical Vapor Deposition (LCVD) to create 3-D fibrous structures and helical springs. Current research efforts focus on the creation of more advanced three-dimensional carbon objects through the use of multi-layered deposition. Multi-layered structures require an understanding of interlayer adhesion and the propagation of geometric anomalies through multiple layers. An important aspect in minimizing these shape anomalies is the implementation of closed loop temperature control. Several laminated carbon structures are presented with discussions and observations about the fabrication process and visual characteristics of each. The major issues in using LCVD to create multi-layer carbon structures are addressed.

Introduction

Numerous previous attempts at constructing layered deposits using LCVD have been made. Such efforts have typically produced non-uniform periodic deposits or dimensionally unstable structures. There is a belief that the general nature of the LCVD process is responsible for these irregularities. The existence of substrate protrusions and the creation of abnormalities in one layer of a deposit are thought to be amplified in each successive layer. This behavior stems from localized heating of surface irregularities causing increased local deposition rates. Online monitoring and control of the reaction is necessary to enable consistent and uniform deposition.

Recent efforts have been made to determine the feasibility of building multi-layered pyrolytic carbon structures using a temperature controlled LCVD process. All structures built for this objective were created using a multiple pass process whereby the substrate was either translated along one axis in alternating directions of travel or in a continuous circular pattern. The resulting structures were multi-layered carbon walls or cylinders conceptually similar to those presented by Messia, et al.[2] Theoretically, this construction technique will create layers that are intimately bonded producing a final structure that could exhibit either bulk solid or laminated solid properties. Many observations were made during the construction of the walls with regard to a new temperature control system and the general nature of the deposits. Some deposits were cut and polished so as to provide a view of the cross section of the walls and thus allow inspection of their integrity. Analysis of the cross sections and other features of the walls provide insight into the use of LCVD to create multi-layered structures.

Experimental Setup

Georgia Tech's LCVD reactor is powered by a 100 W CO_2 laser with a 200 μm diameter spot size. The system incorporates a fixed laser and reagent supply nozzle with several motion stages enabling the reactor to create three-dimensional objects by traversing and rotating the substrate.[3,4] The control of the plane geometry of the structures was accomplished by programming the substrate stages to move in the desired patterns. The most typical deposits that have been made in this manner at Georgia Tech have been of pyrolytic carbon; using the reagent gases methane and hydrogen at or below atmospheric pressure. All experiments described here used 75% CH_4, 25% H_2. The pressure in the reaction zone was held at 1 atm and the reagent nozzle flow was set to 300 sccm CH_4 and 100 sccm H_2.

Layered line growth using the LCVD process is dependant on several environmental variables that can greatly affect the rate and type of deposit that is produced. The most important of these is temperature. Some of the experiments presented below utilized a precision temperature control system. The temperature control was accomplished through use of a thermal imaging camera capable of resolving the temperature in the region of the laser spot to 3.5 μm per pixel. The camera's software allows for the creation of one or more 'Regions Of Interest' (ROIs) within which the average temperature can be calculated. The average ROI temperature is fed back to a PID controller for the laser power so as to maintain a target temperature as set by the operator. ROIs for these experiments were typically areas of about 0.246 mm^2 and temperature set points for the regions were varied between 1600 and 1700°C. Note that the ROI temperature does not necessarily correspond to the substrate temperature, but is a useful means for controlling the LCVD reaction.

Another factor in building layered structures is the speed at which the substrate is traversed beneath the laser spot, i.e. the scan speed. Many different speeds have been tested, and the tendency for heat to conduct away through the substrate during the initial stages of a wall enforces an upper limit on the initial scan speed. A lower limit is also imposed on the scan speed below which deposits may begin growing away from the substrate into fibers.[2,5] The fastest speed that has been used thus far with successful initiation under the given conditions has been about 42.3 μm/s and thus was used for these experiments.

A final factor in making deposits is the substrate material.[6] The Georgia Tech system uses a sacrificial substrate system, and these particular experiments used two graphite disk substrates with different levels of porosity.

Results

Experimentation with deposition of multi-layered carbon structures without a means of automatically controlling temperature and laser power yielded some interesting results that are consistent with the findings of others.[2] The procedure was typically to bring the reactor to running conditions and simultaneously begin translating the substrate and initialize the laser to a specific power level. Sometimes, the laser power was not altered throughout the course of the experiment while other experiments involved some systematic manual reduction in laser power as the wall height and number of layers increased.

The deposits exhibit non-uniform morphology and size. In particular, the laminated walls tend to develop large obtrusions on their ends while the center regions maintain a more uniform height as is shown in Figure 1.

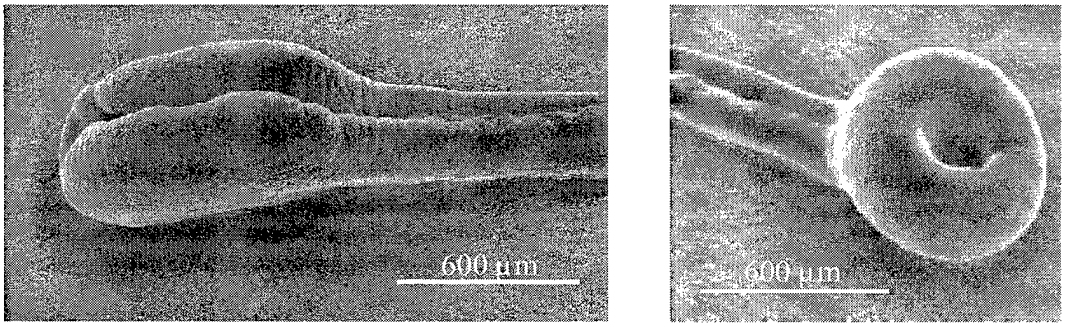


Figure 1. Carbon walls made without process control.[7]

The end obtrusions are likely related to several factors. One possible factor is the tendency for the linear translating stage to decelerate upon completion of a pass causing the end of the line to be exposed to higher temperatures.[7] A related factor involves the possibility of the stage pausing at the end of a pass causing the same phenomenon. In order to study the stage deceleration and pause factors, a control program was implemented to turn off the laser prior to the end of linear movement and restart the laser at the same position on the next pass. Figure 2 illustrates the concept of this control program. The implementation of the stage translation program had no significant impact on the end irregularity.

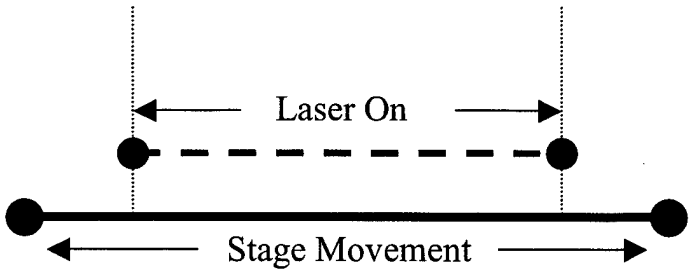


Figure 2. Diagram of stage control program used to study relationship between stage movement and line end irregularities.[7]

Another possible source of the obtrusions is related to heat transfer within the deposit and substrate. Initially, residual heat from the preceding laser pass leads to higher local substrate temperatures and an increased deposition rate. As the wall height increases, the nature of the heat conduction path changes such that the heat at the ends of the wall can conduct easily along the wall in only one direction, whereas the heat in the center region of the wall can conduct in two directions along the wall. During the deposition of such laminated structures as discussed above, observations were made through the thermal imaging camera as to the behavior of the temperature within the laser spot. It was observed that the ends of the lines exhibited higher temperatures earlier in the deposition process as is consistent with the shape of the resulting deposits. Active temperature control can eliminate these undesirable end effects.

Also noteworthy in Figure 1 is the appearance of a crevice in the center of the deposit. This 'volcano effect' could be detrimental to the use of LCVD in producing precise geometric objects, but has been shown to be a temperature or power density related phenomena.[8] According to Jean, the volcano effect for carbon using a methane precursor appears when maximum deposit zone temperatures exceed 2500°C.[7] This effect reiterates the need for a suitable temperature control system in the LCVD process.

Two grades of graphite substrates were tested for carbon deposition and the best results have been produced using the higher porosity graphite. It is theorized that low porosity graphite is more conductive and allows the heat generated by the laser spot to conduct away faster leading to longer deposit initiation times. Use of porous graphite would seem to encourage the creation of irregularities due to surface roughness; however, there were no apparent morphological differences between the deposits produced on the different substrates.

The implementation of automatic temperature control has allowed for significant advances in the ability to deposit uniform multi-layer carbon structures. The setup of the temperature control system used in these experiments was presented above. Figure 3 presents an image from the thermal imaging and control system during wall deposition.

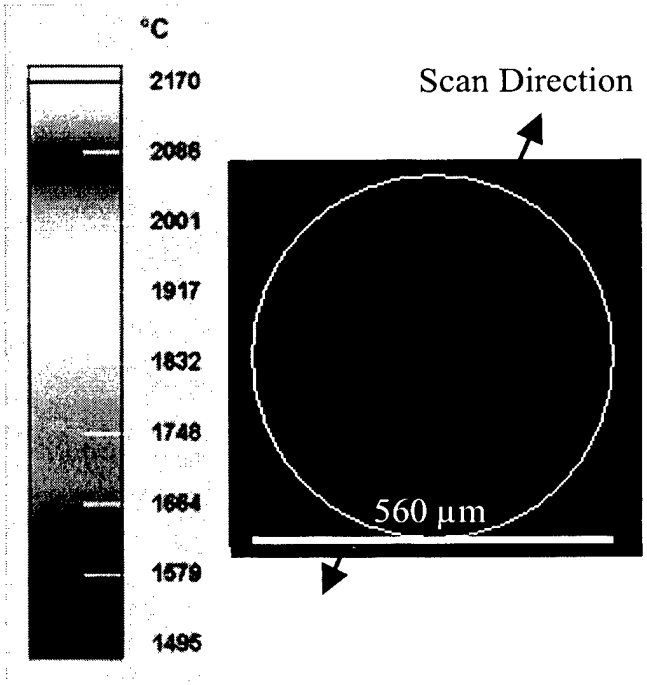


Figure 3. Thermal image captured during deposition with temperature control.[7]

Laminated deposits created using the temperature control system exhibited reduced occurrences of end obtrusions and the volcano effect. The elimination of the end effects with temperature control is due to the system's ability to automatically compensate for the increased local temperatures on the line ends by reducing laser power. Experimentation showed that the volcano effect could be eliminated by maintaining a temperature set point below 1700 °C for the given ROI. Figure 4 illustrates a typical laminated carbon wall built using the stated conditions.

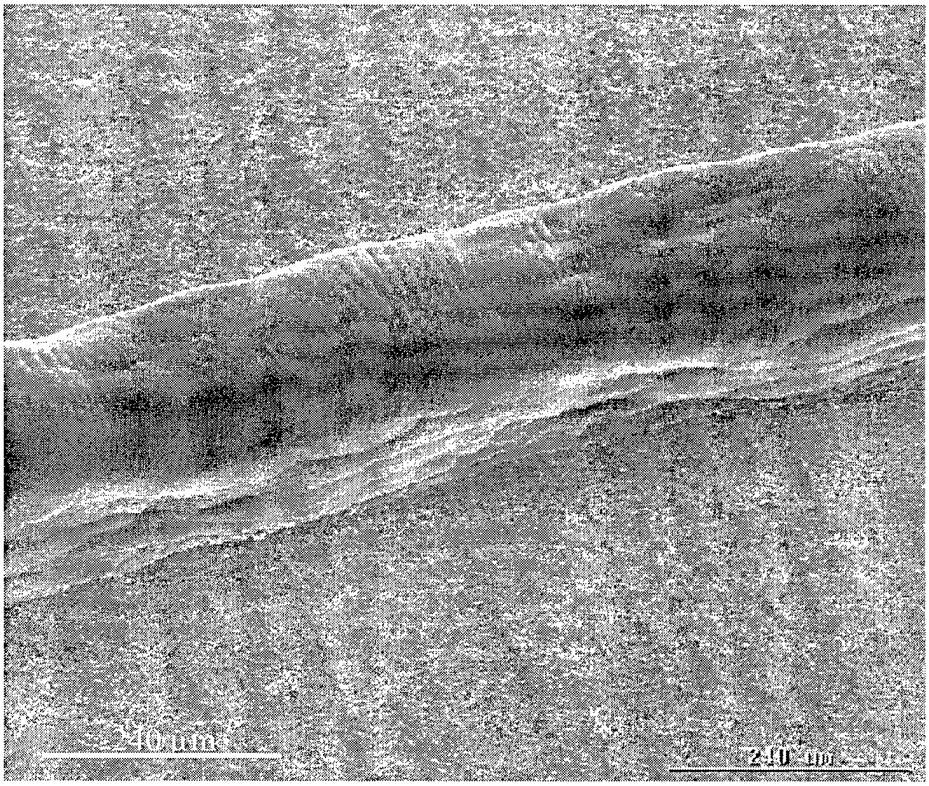
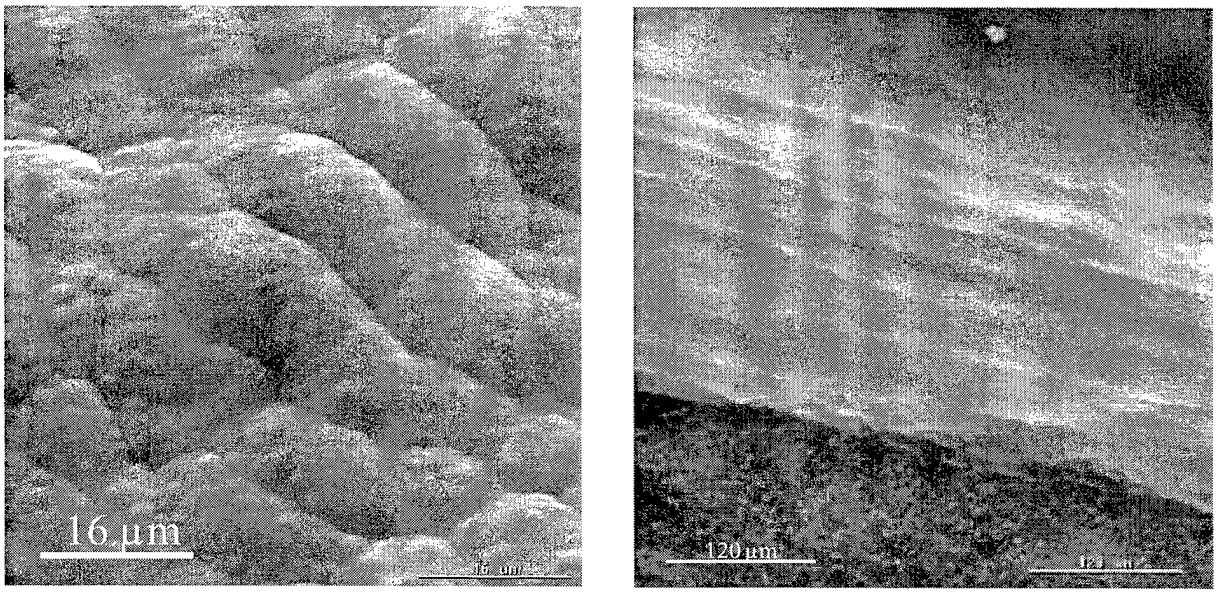


Figure 4. Twenty pass wall deposited using temperature control.[7]

The surface morphology of the walls was examined using a scanning electron microscope (SEM). Figure 5a illustrates a view of the top surface of a wall showing a rippled form. Figure 5b depicts the side of a wall. The side appears homogenous yet slightly stratified in accordance with the individual number of wall layers.



(a) (b)

Figure 5. Surface appearance of carbon walls.

Examination of Microstructure

Internal analysis of the structures produced in these experiments yielded some interesting findings. Several samples were mounted in epoxy, cut, and polished to allow for examination of the cross section of the walls. Figure 6 is an example of such a cross section.

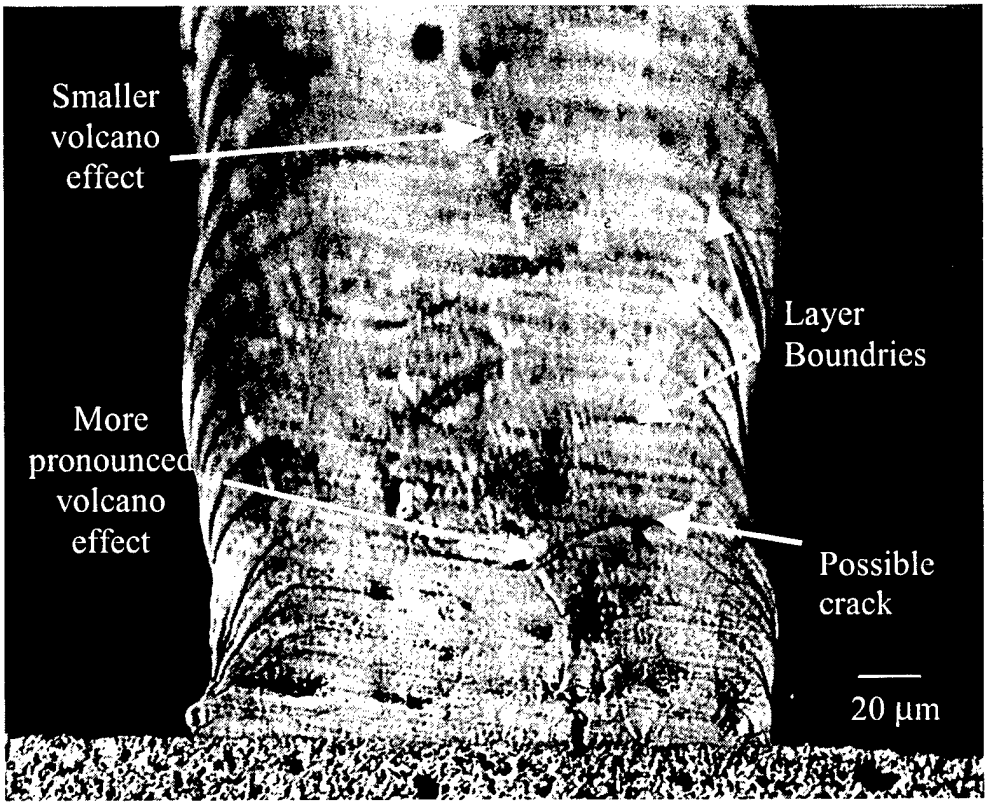


Figure 6. Cross-section of multi-layer carbon wall.[7]

One should first note the uniform density of the deposit. Individual layers of the wall can easily be seen in Figure 6. It is believed that some of the less defined black marks in the photo are artifacts of sample preparation such as residue from the polishing operation. The basic form of the deposit has the characteristic volcano shape, which appears to diminish with increasing numbers of layers. The diminishing of the volcano effect with height is evidence that a temperature controlled process can eliminate sizeable interlayer voids. An important feature observed in the cross section are cracks believed to be related to thermal stress between layers of deposit. One proposed method for addressing these cracks involves using a substrate heater to bring the substrate temperature closer to the reaction temperature and reduce the thermal gradients within the deposited structure. A substrate heater has been implemented into the reactor, but experiments to determine its effectiveness have not yet been conducted.

Some features of the deposit likely stem from a lack of robustness in the existing LCVD system. For example, the variation in the horizontal position of the layers as the height of the wall increases could be due to straightness error associated with the linear stage specified to be ±2.5 μm/25 mm. This can be seen in Figure 6, where the layers offset the width of the deposit

by up to 10 μm. The variations could also be caused by lack of rigidity in the mounting design for the stages.

Figure 7 is another wall cross section that illustrates the integrity of the multi-layer carbon walls. This sample does not show evidence of the volcano effect. The lower layers of the structure have a more rippled interface than the upper layers which again illustrates the importance of the temperature control process in dampening the effects of local abnormalities. This structure does not have the horizontal oscillations shown in Figure 6.

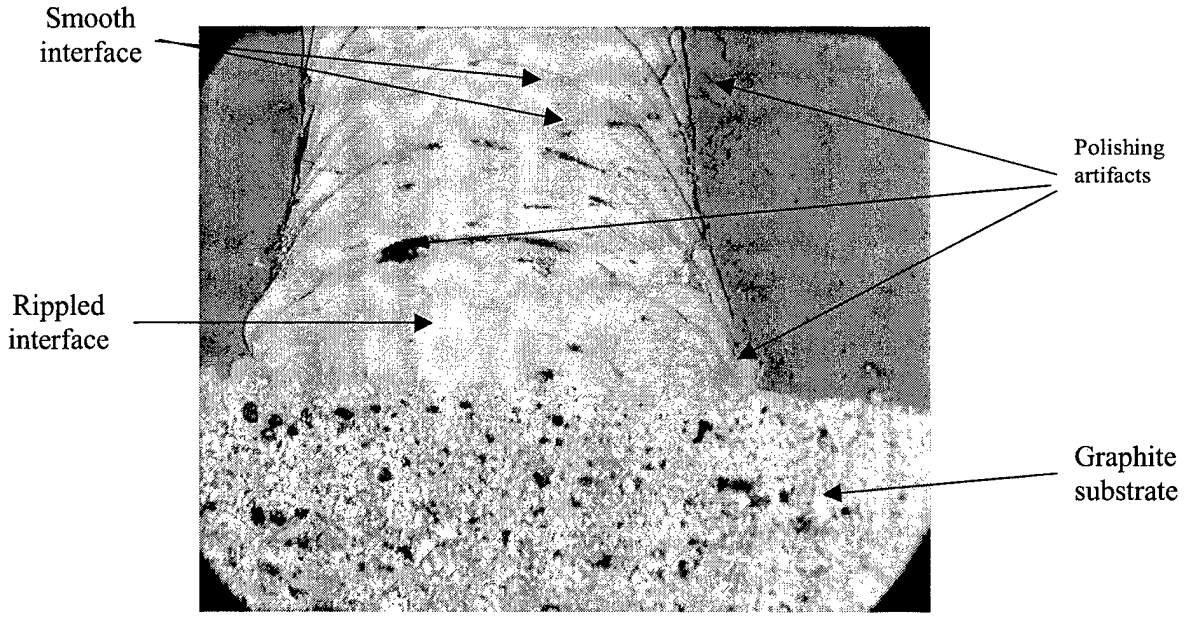


Figure 7. Cross section of wall without any volcano effects.

Conclusions

Experiments have shown that a temperature controlled LCVD process is capable of growing multi-layered pyrolytic carbon structures. The propagation of irregularities through the structures is reduced by the control process, resulting in a uniform deposit with a flat top and straight side walls. Viewing of the wall cross sections indicates a generally solid internal structure, free of large voids or defects. The interlayer bonding may be adversely affected by the thermal stresses associated with the laser heating. These thermal stresses could be the source of cracks shown in Figure 6. More testing is required to determine the extent of this apparent cracking and its impact on the functionality of LCVD multi-layered structures. In conclusion, we believe this work to be an important building block for the future creation of more complex 3D layered structures.

Acknowledgements

This work is supported by the National Science Foundation and the Georgia Institute of Technology.

References

1. C. Duty, D. Jean, and W. J. Lackey. "Laser Chemical Vapor Deposition: Materials, Modeling, and Process Control," Accepted for publication in *International Materials Reviews,* 2001.
2. D. Messia, J. Pegna, W. H. Lee, D. DeAngelis. "Layered Micro-Wall Structures from Gas Phase," *Solid Freeform Fabrication Symposium Proceedings*, 1997, 231-239.
3. D. Jean, C. Duty, B. Fuhrman, W. J. Lackey. "Precision LCVD System Design with Real Time Process Control," *Solid Freeform Fabrication Symposium Proceedings*, 59-65, 1999.
4. C. Duty, D. Jean, and W. J. Lackey. "Design of a laser CVD Rapid Prototyping System," *Ceramic Engineering and Science Proceeding,* 20 (4), 347-354, 1999.
5. N. Arnold, P. B. Kargl, and D. Bauerle. "Modeling of pyrolytic direct writing: Noncoherent structures and instabilities," *J. Appl. Phys.,* 82 (3), 1997.
6. Guisheng Zong. "Solid Freeform Fabrication Using Gas Phase Selective Area Laser Deposition," Ph.D. Dissertation, The University of Texas at Austin, 1991.
7. Daniel Jean. "Design and Operation of an Advanced Laser Chemical Vapor Deposition System with On-Line Control," Ph.D. Dissertation, Georgia Institute of Technology, 2001.
8. J. Han, K. Jensen. "Combined experimental and modeling studies of laser-assisted chemical vapor deposition of copper from copper(I)-hexafluoroacetylacetonate trimethylvinylsilane," *J. Appl. Phys.,* 75 (4), 2240-2250, 1994.

HOMOGENEOUS METAL PARTS BY INFILTRATION

Adam M. Lorenz[1], Emanuel M. Sachs[1], Samuel M. Allen[2], and Michael J. Cima[2]
[1] Department of Mechanical Engineering
[2] Department of Materials Science and Engineering
Massachusetts Institute of Technology, Cambridge, MA 02139

Abstract

Infiltration of powdered metal parts made by SFF processes enables densification with negligible dimensional change, but typically uses a dissimilar infiltrant material resulting in poor corrosion resistance, machinability, and a heterogeneous composition inconducive to certification for critical applications. A new approach called transient liquid-phase infiltration is described using an infiltrant composition similar to that of the powder skeleton, but containing a melting point depressant. Upon infiltration, the liquid undergoes diffusional solidification at infiltration temperature and eventually the composition becomes homogeneous. Parts over 20 cm tall have been fabricated through careful selection of skeleton and infiltrant compositions, skeleton powder size, and infiltration technique. The work presented in this paper uses a nickel-silicon alloy to infiltrate a skeleton of pure nickel powder.

Introduction

Several Solid Freeform Fabrication technologies use powdered metal as the raw material to produce a net shape part skeleton that is less than 70% dense. The skeleton must then undergo further processing to achieve full density and the desired mechanical properties. The densification is typically done either by light sintering and infiltration with a lower melting temperature alloy or by high temperature sintering alone. In the first method of densification, the part's dimensional change is typically only ~1%, making it suitable for fairly large (~0.5 m on a side) parts. However, the resulting material composition is a heterogeneous mixture of the powder material and the lower melting temperature infiltrant, often with poor machinability and corrosion resistance. In critical applications such as structural, aerospace and military, a material of homogeneous composition is preferable for certification. Sintering the powder to full density will result in a homogeneous final material, but a part will undergo ~15% linear shrinkage if it starts out at 60% density. For this reason, full density sintering is typically only used for smaller (< 5 cm on a side) parts.

This paper describes a process for making large, homogeneous parts from a powder skeleton using an infiltrant material similar in composition to the skeleton material, with the addition of a small amount of melting point depressant. The liquid infiltrant fills the void space in the skeleton, then undergoes diffusional solidification to achieve a homogeneous final part composition. The process is shown schematically in Figure 1 and is referred to here as Transient Liquid-phase Infiltration (TLI) due to the phase transition of the infiltrant. In some cases the diffusional solidification can prevent the infiltrant from filling a part skeleton. Determination of conditions that allow complete infiltration is a major focus of this work.

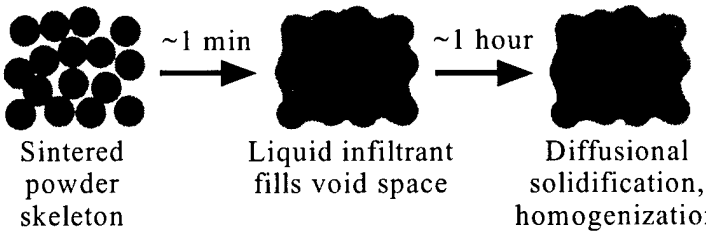


Figure 1: Transient Liquid-phase Infiltration

A nickel-based material system was chosen for development of the TLI concept because transient liquid-phase nickel brazing alloys are commonly used in the aerospace industry and nickel alloys are of interest in some DoD applications. Silicon was chosen as the melting point depressant primarily because it has a lower diffusivity than boron and phosphorous, the other common melting point depressant in nickel brazing alloys. In addition, silicon has a high enough solubility in nickel to allow complete solidification at the infiltration temperature. Figure 2 shows the nickel-rich side of the binary Ni–Si phase diagram[1] and points out the composition of the skeleton and infiltrant as well as the resulting homogenized composition at an infiltration temperature of 1180°C. The diffusivity of the melting point depressant affects the amount of time the liquid has to fill the skeleton before it freezes. The diffusivity of Si in Ni is ~10^{-13} m^2/s at 1200°C, resulting in a characteristic diffusion distance of $\sqrt{4D \cdot t} = 5$ μm after 1 minute. This is a sufficiently small distance to allow infiltration of nickel powders greater than 50 microns in diameter.

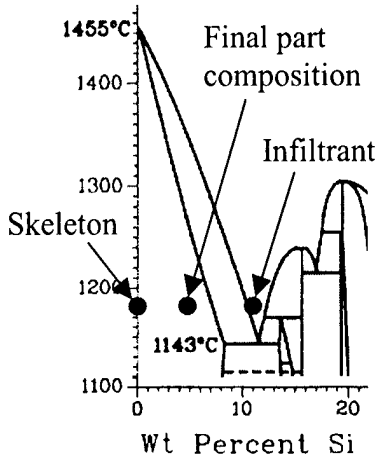


Figure 2: Ni–Si phase diagram.

Study of Fluid Flow and Infiltration Rate

Infiltration is the result of capillary induced pressure driving the fluid into the skeleton. In a non-reactive system, fluid will continue to flow into the skeleton until the gravitational head, *pgh*, balances the capillary force. The maximum capillary rise height can be calculated accordingly:

$$h_{\max} = \frac{1}{\rho g}\left(\frac{\gamma_{LV} \cdot \cos(\theta) S_p}{V_p}\right) = \frac{6\gamma(1-\varepsilon)}{D\varepsilon\rho g} \qquad (1)$$

where h is fluid height, ρ is the fluid density, g is gravity, γ_{LV} is the liquid/vapor interfacial energy, θ is the contact angle of the liquid to the solid, S_p is the surface area of the pore space and V_p is the volume of the pore space.[2] The right most term in the equality lumps the wetting angle into the surface energy term $\gamma = \gamma_{LV} \cdot \cos(\theta)$, and assumes the powder bed is composed of uniform spheres of diameter D with a void fraction ε to substitute for the ratio of surface area to volume. Due to the high surface energy of most liquid metals, a skeleton of 100 μm powder will typically result in capillary rise heights greater than 1 meter. In TLI, this equilibrium condition may not be reached before the infiltrant freezes.

Because the liquid has a limited amount of time available to fill the skeleton, it is necessary to study the fluid flow behavior. Darcy's Law describes the flow of viscous fluid through porous media, stating that the pressure gradient will be directly proportional to the volume-averaged velocity of the fluid:

$$\nabla P = -\frac{\mu}{K} V \qquad (2)$$

where μ is the fluid viscosity and K describes the permeability of the porous body. The permeability of various powder skeletons was determined by measuring the flow rate of oil (Multitherm 503) through the skeletons at room temperature under known pressure conditions as shown in Figure 3 at right.[3] Skeletons for these and all subsequent experiments were composed of hydrometallurgically processed nickel powder sintered at 1200°C for 1 hour. Skeletons of 90–125 μm and 212–300 μm powder resulted in permeabilities of 5.0×10^{-12} m^2 and 1.7×10^{-11} m^2 respectively.

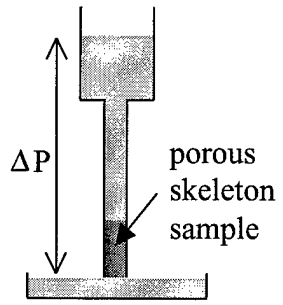


Figure 3: Permeametry.

The rate of infiltration into the skeleton was measured experimentally and compared to a model of the fluid flow based on Darcy's Law. The model uses the same assumptions as Equation 1 for the capillary driving force with an extra term for the head losses due to gravity:

$$\frac{dh}{dt} = \frac{K}{\varepsilon\mu}\left(\frac{6\gamma(1-\varepsilon)}{D\varepsilon h} - \rho g\right) \qquad (3)$$

Experiments were conducted at room temperature with oil and the results are shown in Figure 4. The measured permeability predicted a slightly faster infiltration than that observed experimentally, so a second curve is shown with permeability selected to match the experimental data. This permeability was 40% less than that measured by permeametry.

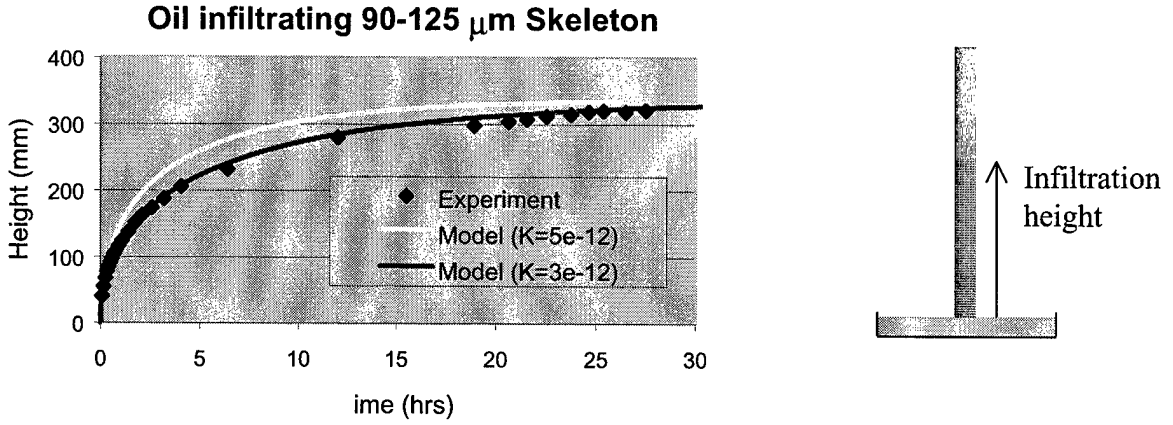


Figure 4: Infiltration rate experiments with oil at room temperature.

Measurements of the infiltration height of liquid metal inside the furnace was not directly observable, so the rate of infiltration was calculated based on mass increase. Figure 5 schematically shows the apparatus used to measure the mass of the skeleton during a transient liquid phase infiltration of a similar skeleton, along with experimental results. The skeleton was suspended from a 0.010" diameter molybdenum wire and the force on the wire was measured via

a load cell and a datalogger at 0.05 second intervals. The contribution due to surface tension was subtracted from the measured force, and the resulting value was converted to infiltration height by dividing by the density of the liquid and the cross-sectional area and void fraction of the skeleton. The model of the fluid flow is shown for the same skeleton permeability values as Figure 4, with the fluid properties of the liquid metal substituted for those of oil.

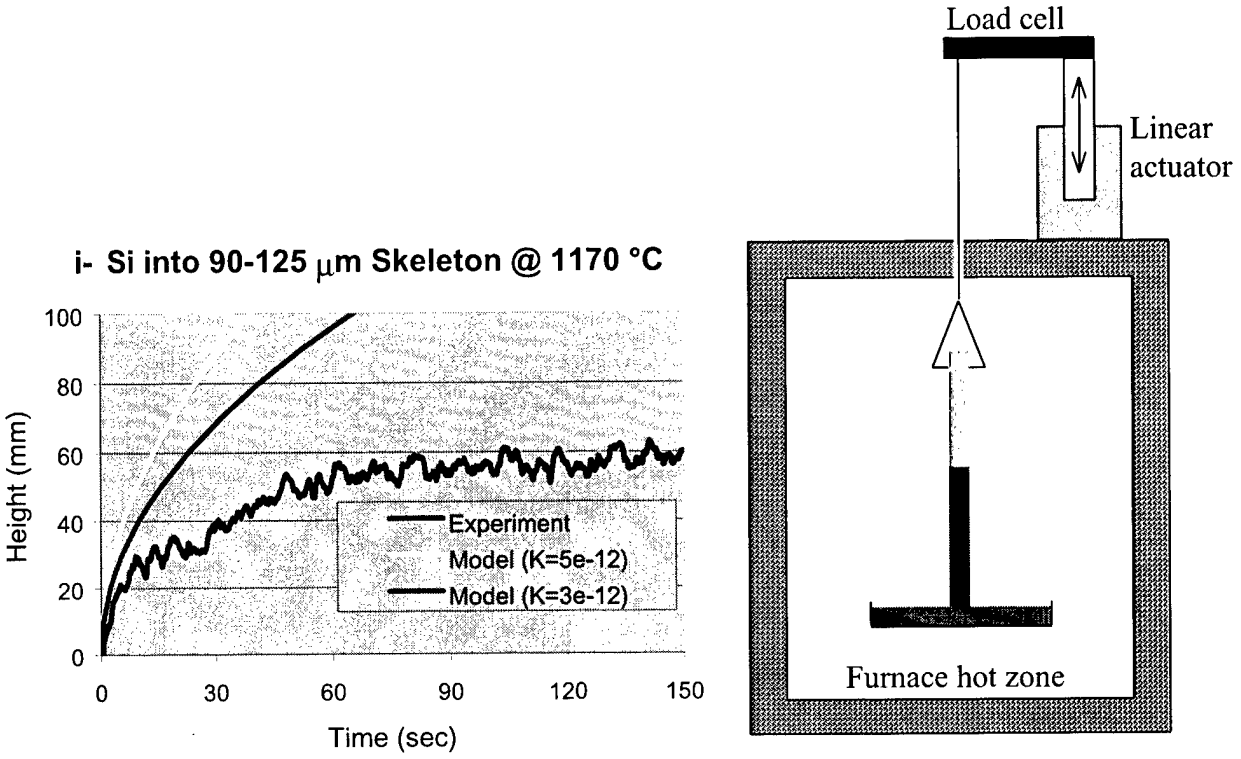


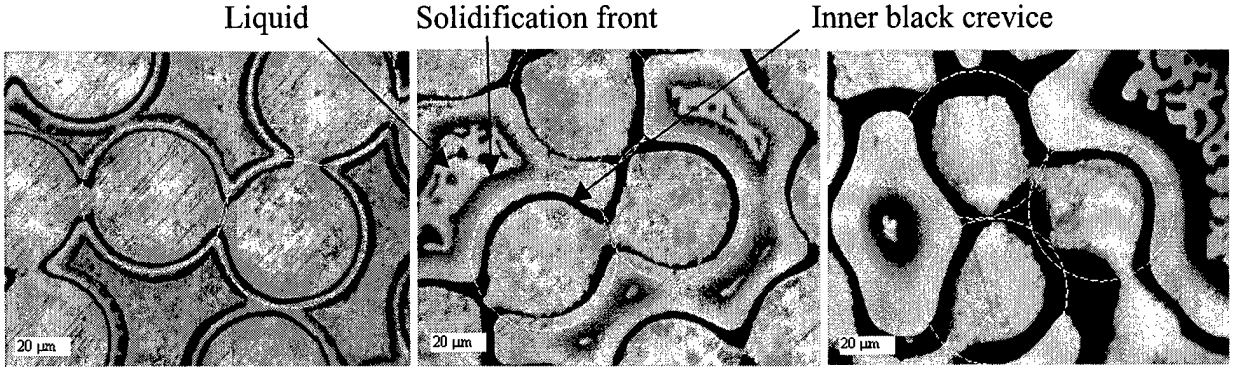
Figure 5: Infiltration rate experiments with molten metal and mass measurement setup.

Comparison of Figures 4 and 5 demonstrates that the time scale of the liquid metal infiltration is much faster than for infiltration with oil. This difference arises because the surface tension is ~50 times greater for the liquid metal. The significant deviation of the experimental results in Figure 5 from the model prediction can be explained by the "choking" effect of the infiltrant solidifying as it flows into the part. The next section will describe the attempt to characterize this solidification behavior.

Solidification Quenching Experiments

The solidification rate was measured experimentally through a series of quenching experiments. A bundle of 50 μm diameter nickel wires was sintered and then the bundle was dipped into a bath of molten Ni–10Si infiltrant. After holding at the infiltration temperature for variable time periods, the samples were air quenched. The samples were then sectioned and electropolished to reveal the microstructures shown in Figure 6 below. Wire was used instead of powder so that the motion of the solidification front could be referenced to the initial wire diameter and all motion would be perpendicular to the cross-sectioned view. Dashed white lines have been superimposed on the images to show the initial wire diameter. The outward progression of the solidification front can be seen by comparing the pictures in sequence. The

area with a eutectic microstructure reveals the part of the sample that was liquid at the time of the quench, and is bordered by the solidification front. The black crevice that appears within the dashed white circle is an effect of the electropolishing used to reveal the microstructure. The crevice corresponds to the distance to which silicon diffused into the initially pure nickel powder. A planar diffusion couple would result in a compositional profile of an error function with characteristic diffusion distance $\sqrt{4D \cdot t}$. For a diffusivity of silicon through nickel of 7.85 x 10^{-14} m^2/s at 1180°C,[4] this distance would be 1.8, 5.6 and 9.7 microns for 10, 100 and 300 seconds respectively. These expected diffusion distances correspond reasonably well with the observations in Figure 6, especially considering the difference in geometry.



After 10 sec at 1180°C After 100 sec at 1180°C After 300 sec at 1180°C

Figure 6: Optical micrographs showing sequence of infiltrated bundles of 50 µm nickel wire.

Infiltration Distance Limits

In order to maximize the distance the infiltrant can reach before freezing in TLI, a gating mechanism is used to prevent the infiltrant from contacting the skeleton prior to infiltration. Premature contact would allow diffusion to occur and the infiltrant to freeze just as it begins to melt. Other problems could arise if liquid begins to flow before the system has reached thermodynamic equilibrium. Several gating mechanisms have been used in practice such as dipping a suspended part into the melt or initial confinement of the melt followed by opening up a path for the melt to flow out and contact the skeleton.

The particle diameter of the powder affects both the fluid flow and the amount of time before the infiltrant freezes. Equation 3 describes the fluid flow behavior and because the permeability of a skeleton (K) is proportional to the square of the powder diameter the net result of using larger powder is faster liquid flow. Further, the larger powder decreases the surface area for diffusion and provides more time for liquid to flow before the porous network is closed off by solidification. Figure 7 clearly shows how the infiltration distance (in this case height) is affected by the powder size of the skeleton. The capillary rise limit shown corresponds to the maximum height in Equation 1 with liquid metal properties of γ= 1.2 N/m and ρ = 8 g/cc and a void fraction of ε = 0.4. The rise limit will remain fairly consistent with different materials because many liquid metals have similar surface tension and density. The premature freezing limit shown corresponds to the experiments shown to the right using various powder sizes. Through the use of progressively larger powder size, infiltration heights as tall as 22 cm have been achieved. The freezing limit will vary significantly for different material systems because

it is affected by other properties such as the diffusivity of the melting point depressant in the skeleton, which can vary by several orders of magnitude.

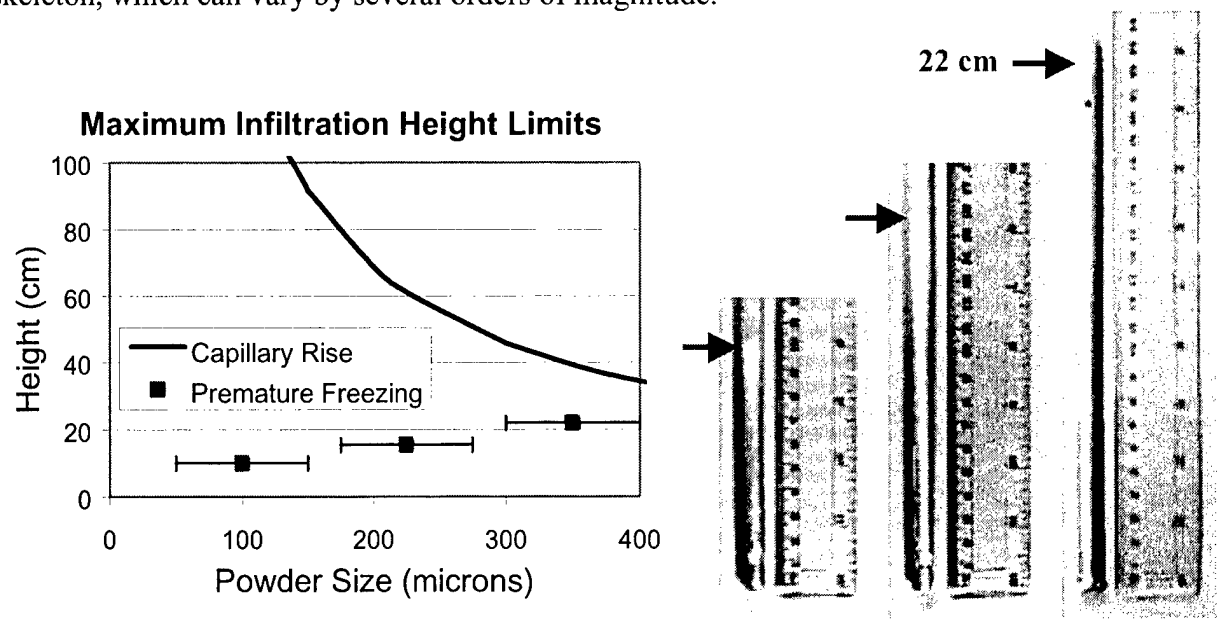


Figure 7: Limitations on infiltration height. Images at right show heights achieved with skeletons of 50–150μm, 150–300μm, and 300–400μm powder (left to right).

Uniform bulk composition throughout the part

Due to mass transport occurring simultaneously with the fluid transport within a part during transient liquid-phase infiltration, there exists the possibility of non-uniform bulk composition in a final part, with a higher concentration of silicon expected near the point of liquid entry. In order to prevent this variation, the liquid infiltrant can be maintained at a liquidus composition. This will ensure that any liquid present in the skeleton will be the same composition — any loss of silicon must result in solidification. Further, the liquid is already saturated with nickel and has no driving force for dissolution of the skeleton, preventing erosion.

Several techniques have been used to hold the composition of the infiltrant at its equilibrium liquidus composition and prevent it from dissolving the skeleton. Excess Ni powder was added to the melt in sufficient quantities that the bulk composition would be a mixture of saturated liquid and solid at the infiltration temperature. The supply of infiltrant was then soaked at a temperature slightly above the infiltration temperature to dissolve the excess nickel. A ceramic impeller was used to stir the melt and ensure the infiltrant supply was well mixed as the temperature was decreased again for the infiltration. The composition of parts infiltrated with infiltrant at its liquidus composition show no signs of erosion and have a bulk composition that does not change along the path of infiltration. This is further illustrated in Figure 8, showing a capillary infiltrated with infiltrant at its

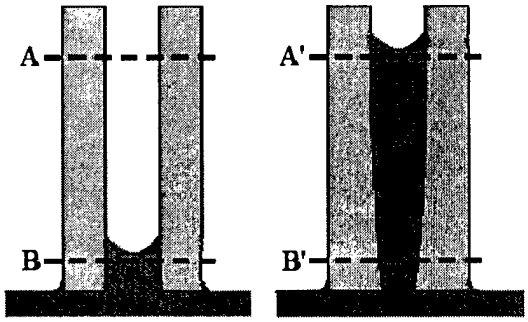


Figure 8: Uniform bulk composition along path of infiltration

liquidus composition. The composition profile at a point just behind the infiltration front (cross-section B) would consist of pure nickel and infiltrant at its liquidus composition because very little time has elapsed to allow for diffusion. After the liquid has continued to fill the capillary, a similar location just behind the infiltration front at cross-section A' would have an identical composition profile to B. Even though some diffusional solidification will occurr at B' while the liquid is still infiltrating, the fixed composition of the liquid ensures that the bulk or average composition will be the same at point B, A', and B' — constant with time and position.

Homogenization and mechanical properties

The time necessary for homogenization of a final part will depend strongly on the diffusivity of the melting point depressant and the geometry or powder size. Figure 9 shows cross-sections of a skeleton of ~300 μm diameter powder that was infiltrated with Ni–10Si at 1170°C. The three sections of the infiltrated skeleton shown were heat treated at 1200°C for 1, 5 and 12 hours (left to right). Compositional analysis was conducted using an electron microprobe. The dark regions of the initial image correspond to high silicon content (>6%). After 5 hours of heat treatment, the compositional profile was nearly uniform, but regions of localized porosity are visible in the image — perhaps due to differential mass transport (Kirkendall effect). After 12 hours of heat treatment, the composition is uniform and any remaining porosity is evenly distributed.

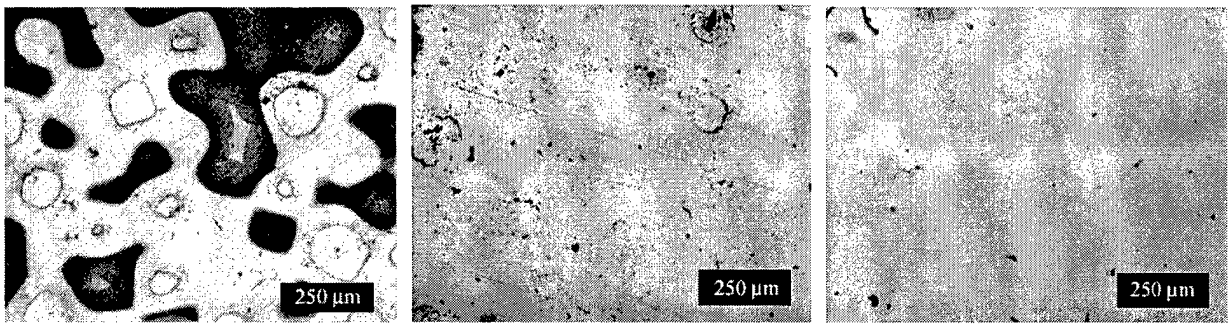


Figure 9: Homogenization of infiltrated 300μm powder after 1, 5, and 12 hours at 1200°C.

The binary Ni–Si alloy used for these experiments is not available commercially and expectations for mechanical properties were not high. Comparison of an infiltrated specimen to a casting of identical composition showed that the transient liquid-phase infiltration process could produce a final material with similar properties. Tensile specimens were machined from an infiltrated bar homogenized for 12 hours and from a cast bar cooled at 5 °C/min from 1400°C. The tensile test results are shown in Figure 10 along with an image of the infiltrated specimen after failure. The elastic behavior and yield strength of both materials were nearly identical. The elongation of the infiltrated specimen was moderate at 6%, but still much less than that of the cast specimen. The mechanism causing the different behavior under high strain is not yet understood, but could be due to differences in porosity.

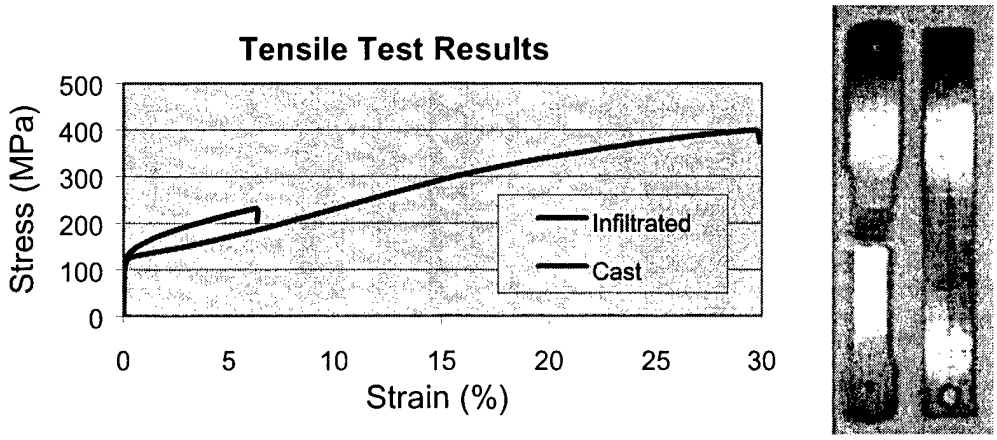


Figure 10: Tensile properties for infiltrated and cast specimens of the Ni – 4wt% Si. Image at right shows the infiltrated tensile specimen after failure.

Summary

Transient liquid-phase infiltration of a PM skeleton has been shown to achieve homogeneous final part composition without the dimensional change associated with full-density sintering. This densification concept is broadly applicable to any of the SFF processes that produce green PM skeletons, as well as more traditional PM processes such as Metal Injection Molding. A binary Ni–Si alloy was used to explore the important tradeoff between infiltration and diffusion rate that can prevent the liquid from filling the part due to diffusional solidification. Using infiltrant at a liquidus composition ensures uniform bulk composition throughout the part. Through gated introduction of the liquid infiltrant to the skeleton and control of powder size within the skeleton, parts greater than 20 cm tall were infiltrated to full density. Subsequent heat treatment achieved a homogeneous final composition and the mechanical properties compared favorably to a cast specimen of the same composition.

Acknowledgments

This research was sponsored by the Office of Naval Research, Contract #N00014-99-1-1090. The measurements of permeability and infiltration rate with oil were conducted by Vinay Prabhakar, a graduate student in the 3-D Printing research lab at MIT.

---

[1] Alloy Phase Diagrams. ASM Handbook Vol. 3. Metals Park, Ohio: American Society of Metals, 1992. pp 2·318

[2] Scherer, George W. "Theory of Drying" *J. Am. Ceram. Soc.*, Vol 73, No. 1, 1990. pp 3–14.

[3] Heinzer, Peter J. "Permeametry." Powder Metallurgy. ASM Handbook Vol. 7. Metals Park, Ohio: American Society of Metals, 1984. pp 263-265.

[4] Smithells, Colin J. Smithells Metals Reference Book. 6th Edition. London, UK: Butterworths, 1983.

ACCURACY IMPROVEMENT IN RAPID PROTOTYPING MACHINE (FDM-1650)

A. Gregorian*, B. Elliott*, R. Navarro*, F. Ochoa*, H. Singh*, E. Monge*
J. Foyos*, R. Noorani*, B. Fritz[1], and S. Jayanthi[2].

*NSF Research Experiences for the Undergraduates (REU)
Loyola Marymount University, Los Angeles, CA - 90045

[1]Northrop Grumman, El Segundo, CA - 90245

[2]3D Systems, Valencia, CA - 91355

ABSTRACT

Over the past few years, improvements in equipment, materials, and processes have enabled significant improvements in the accuracy of Fused Deposition Modeling (FDM) technology. This project will investigate the present in-plane accuracy of a particular FDM machine using the benchmark "User Part" developed by the North American StereoLithography User Group (NASUG) and show the effect of optimal Shrinkage Compensation Factors (SCF) on the accuracy of the prototyped parts.

The benchmark parts were built on the FDM-1650 prototyping machine and a total of 46 measurements were taken in the X and Y planes using a Brown & Sharpe Coordinate Measuring Machine (CMM). The data was then analyzed for accuracy using standard formulas and statistics, such as mean error, standard deviation, residual error, rms error, etc. The optimal SCF for the FDM-1650 machine was found to be 1.007 or 0.7%.

INTRODUCTION

Rapid Prototyping (RP) is the f abrication of a physical, three-dimensional part of arbitrary shape, directly from a numerical description (typically a CAD model) by a quick, highly automated, and flexible process. RP technology has made many contributions to the manufacturing industry mainly by reducing the time to produce prototype parts and improving the ability to visualize part geometry. The physical prototype allows for earlier detection and reduction of design errors and the capability to compute mass properties of components and assemblies [1,7]. Also, it is very advantageous to present a design in client presentations, consumer evaluations, bid proposals, and regulation certification. This concept was first introduced in 1988, and since then the growth of Rapid Prototyping has been exponential every year.

RP also has some challenges that must be improved upon and one of the main challenges is part accuracy. This is the main concern of countries like Japan, which are not willing to incorporate RP to there manufacturing process [1-3]. The parts produced tend to warp and/or shrink from its given dimensions forcing the user to run several trials of a part to reach its ideal dimensions or settle for a slightly inaccurate part. Another concern is the build time; it can often take several days to prototype certain parts depending on the size.

When Rapid Prototyping was first introduced, the materials used to produce the parts had low yield strength. Through the advancement in material science, the photopolymers and thermoplastics used now have much higher yield strength. The strength of RP materials is sufficient for some applications, but does not always satisfy the strength requirements for wind tunnel testing. The use of stronger materials in the future such as metal-based powders will enable RP to produce parts to satisfy these requirements.

The purpose of this engineering research project is to make a contribution towards the accuracy improvement of Rapid Prototyping machines. This can be accomplished by finding the most optimal shrinkage compensation factor (SCF). The Shrinkage Compensation Factor determines the amount an object should be enlarged so that it can approach the desired dimensions of the user during the shrinking process.

THEORY AND ANALYSIS

In this engineering project, the rapid prototyping technology used was a Fused Deposition Modeling machine (FDM –1650), built by Stratasys. The machine uses a 3D CAD drawing that is converted to a Stereolithography file (.STL) and then it is sliced into a series of closely spaced horizontal planes [2,7,8]. The file is then sent to the machine as a build file and production of the part begins. The machine has a build area of 10x10x10 in. and produces hard solid prototypes that may be used in many applications.

The FDM technology uses a spool of ABS thermoplastic filament with a diameter of .070 inches to build a part. The filament is heated to above its melting point and then extruded through a nozzle on a delivery head and onto a build platform. When one layer is finished the platform is lowered and a new layer is formed on top of it.

The overall inaccuracy of the parts being built by RP technology has been one of the major challenges that need to be overcome. Errors due to shrinkage and warpage dominate the inaccuracy of the part. The thermoplastic ABS material used in FDM machines experiences a volume change when it is heated and then extruded onto a build platform. "Each prototype made is slightly smaller than its designed dimensions"[3,5,8]. SCF is one of the variables that can be controlled by the operator to influence the overall accuracy of the part. When prototyping, the shrinkage is compensated by multiplying the dimensions by a SCF through the build software. Through research, the optimal SCF can be found and the prototype can be built within the specified build accuracy of the machine.

To test the build accuracy of a prototyping machine, a user part was developed by the North American StereoLithography User Group (NASUG). It is an in-plane benchmark part, which covers the extent of the build platform and allows for the measurement of the part's X and Y dimensions. This particular part (Fig. 1) was chosen because of: (1) its large amount of independent surfaces, (2) a variety of balanced measurements ranging from .125 to 9.5 inches, and (3) an almost equal amount of inside and outside measurements. These three characteristics made the part ideal for performing measurements because it reduced biases on certain measurements, making all of the factors in producing the part just as important [4-5].

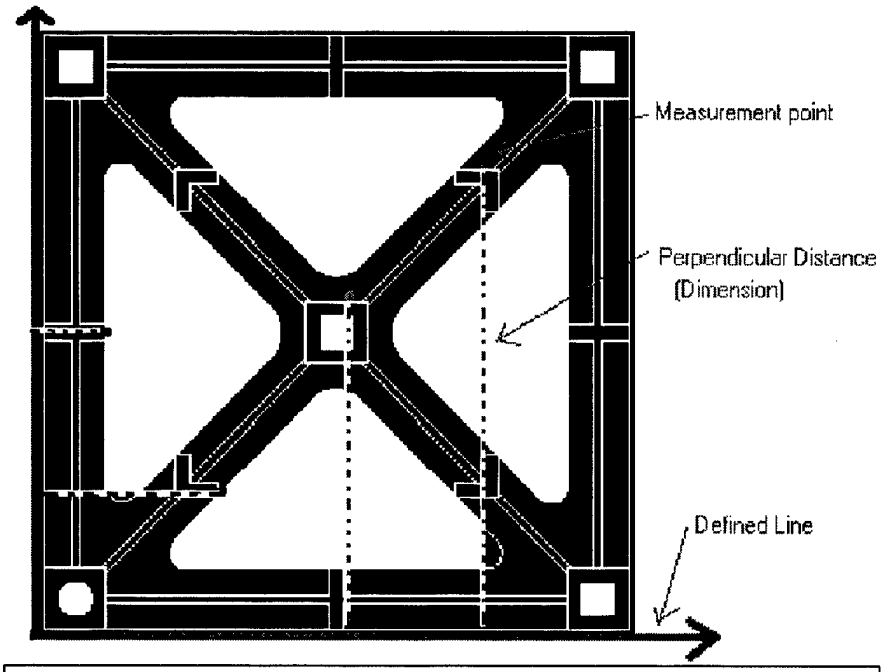


Figure:1NASUG "User Part" and the CMM measurement technique

To calculate the SCF, 46 measurements were taken in the X and Y plane [9]. These measurements were input into an Excel program and from these points, 27 outside and 21 inside dimensions were calculated. After obtaining this data, statistical equations were used to determine the overall accuracy of the part.

First the dimensional data is converted to the differences relative to the CAD dimensions. The error in each of the dimensions is calculated by,

$$Actual\ error = a - c \qquad (1)$$

where a is the measured dimension and c is the CAD Dimension.

Many statistical data analysis computations were derived from the 21 inside dimensions and 27 outside dimensions. The slope of the best-fit regression line of actual error vs. ideal dimension was calculated to get an idea of the accuracy of the part and to determine the new SCF. The slope is determined by,

$$Slope = \frac{(42+54)*(A+B) - (C-D)*(E-F)}{Constant} \qquad (2)$$

where A = Σ(Inside Ideal Dimension)*(Error), B = Σ(Outside Ideal Dimension)*(Error), C = Σ(Outside Ideal Dimension), D = Σ(Inside Ideal Dimension), E =Σ(Error Outside Dimensions), and F = Σ(Error Inside Dimensions). The constant is determined by,

$$Constant = (42+54)*(\Sigma(G^2)+\Sigma(H^2)) - (\Sigma(H) - \Sigma(K))*(\Sigma(M) - \Sigma(K)) \qquad (3)$$

where G = Inside Measured Dimension, H = Outside Measured Dimension, K =Inside Ideal Dimension, and M = Outside Ideal Dimension.

Next a y-intercept value must be determined to complete the equation for the least-square regression line for which the slope was found above. This equation is used to find the expected error in each of the dimensions and when that value is compared to the actual error, we can determine the residual error in the part. The equation for the intercept is given by,

$$Intercept = \frac{(\Sigma(A)^2 + \Sigma(C)^2)*(\Sigma(E) - \Sigma(G)) - (\Sigma(I) + \Sigma(L))*(\Sigma(C) - \Sigma(A))}{Constant} \qquad (4)$$

where I = (Outside Ideal Dimension)*(Error), L = (Inside Ideal Dimension)*(Error), C = Outside Ideal Dimension, A = Inside Ideal Dimension, E = Outside Error, and G = Inside Error.

Now with the slope and intercept defined, the predicted value for the error, given an ideal dimension, can be found by the equation,

$$y\ (predicted) = mx + c \quad (5)$$

where m = slope, x = ideal dimension, and c = intercept.

This process of finding the slope, constant, and intercept is performed for both the x and y dimensions and the two results are averaged at the end.

The predicted value of error is used to determine the residual square, which squares the difference between the measured dimensions and the predicted value:

$$Residual\ Square = (Difference - Predicted)^2 \quad (6)$$

With the result from equation 6, the residual error in the part can be calculated. The residual error defines the overall difference of the measured values from the predicted error values [6]. The equation for residual error is defined by,

$$Residual\ Error = \sqrt{\frac{(M + N + O + P)}{121}}$$

where M = Residual Square (Inside Y Dimensions), N = Residual Square (Outside Y Dimensions), O = Residual Square (Inside X Dimensions), and P = Residual Square (Outside X Dimensions).

Finally the SCF can be derived. The SCF is an indication of the numerical percentage of how small or large the user part is compared to the actual CAD dimensions. The SCF equation incorporates the initial shrinkage compensation factor, which was used in the beginning of the build process. The equation to determine the SCF is,

$$SCF\ (X) = 1 - (1 - (Slope))*(1 + SCF(X)\ OLD) \quad (8)$$

$$SCF\ (Y) = 1 - (1 - (Slope))*(1 + SCF(Y)\ OLD) \quad (9)$$

RESULTS & DATA ANALYSIS

After several trials of making the "User Part", FDM-1.007 [1] exhibits the lowest Mean, RMS, and Residual Error indicating that so far, a SCF of 1.007 gives the lowest error and the most accuracy for the user part.

A scatter graph of the difference between the measured and desired dimension (error) plotted against the desired (CAD) dimension was used in the calculation of the SCF and the Total Shrinkage (TS) for the "User Part". The Total Shrinkage is the slope of a "least squares" regression line of the Error vs. Ideal (CAD) dimension graph. It gives an indication of how far off the SCF that was used to create the part is to the SCF that will produce the most accurate part. A negative TS means the part was made too small and a positive TS means the part was made too big. The lowest TS value is desired for the most accurate part. FDM-1.008-P2[2] had the lowest Total Shrinkage value, but it was not the most accurate part as indicated by further statistical calculations performed on it. As Figure 2 summarizes, the greatest total shrinkage of

[1] FDM refers to the build method, 1.007 is the SCF, and I (if used) refers to the first measurement for the part

[2] This is the second part made with a SCF of 1.008, due to questionable results given by the first part

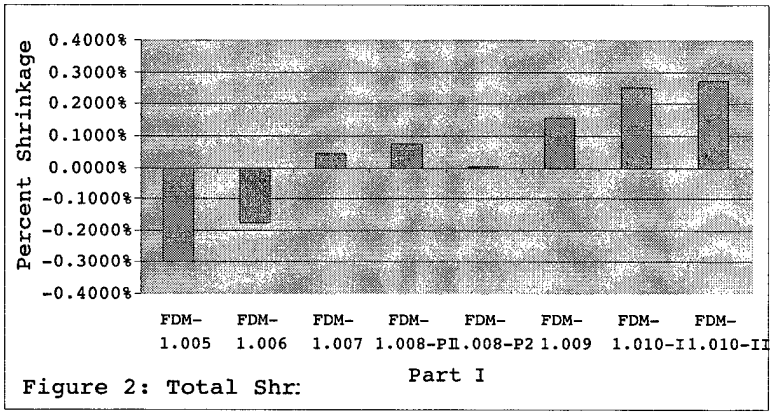


Figure 2: Total Shr:

-0.2966% and 0.2744% was achieved from parts FDM-1.005 and FDM-1.010-II, which indicates that the optimum SCF is not close to those SCF. Part FDM-1.007 showed the second least shrinkage of 0.0453%, but further calculations proved this was the most accurate part.

The Shrinkage Compensation Factor (SCF) is related to Total Shrinkage because the value for Total Shrinkage is subtracted from the initial SCF, to get a new, more accurate SCF. As Figure 3 illustrates, calculations performed on the measurements revealed that a new SCF that should improve the accuracy for a part made on a FDM machine lies between 0.65% and 0.75%. Part FDM-1.007 was the only part that could be made in this range and it was this part that turned out to be the most accurate.

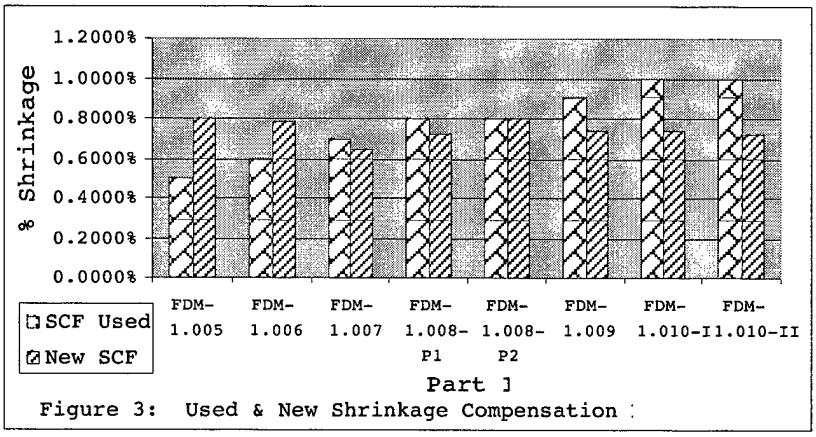


Figure 3: Used & New Shrinkage Compensation

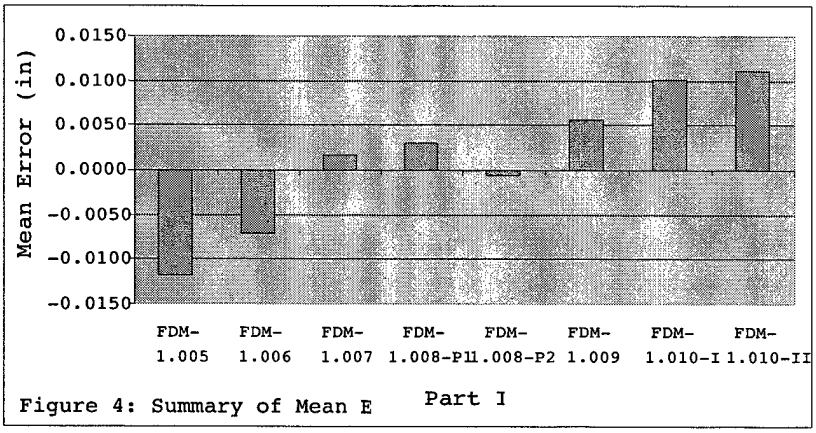


Figure 4: Summary of Mean E

The mean error is calculated to get an indication of the error in the part and to determine whether the dimensions were within the machine specified accuracy **[6]**. The graph for mean error shows a similar trend to the Total Shrinkage graph and thus gives similar information. A positive mean error indicates that most of the measured dimensions were greater than the CAD dimensions, and a negative mean error indicates that most of the measured dimensions were smaller than the CAD dimensions. The FDM parts with shrinkage factors set from 1.005 to 1.010 had mean errors ranging from –0.0119 inches to 0.0110 inches, giving an even spread about zero. As Figure 4 shows, FDM-1.007, FDM-1.008-P1, & FDM-1.008-P2, produced mean errors, which satisfied the machine specified accuracy of $\pm$0.005 in. However, the mean error can be influenced by negative and positive error values, and needs to be used in conjunction with other statistical calculations to find the best part.

The standard deviation was also calculated to get an indication of the spread of errors around the mean and really understand the meaning for the value of mean error [6]. A low mean error and a low standard deviation will provide a good indication of the accuracy of a user part. The standard deviation data varied from 0.0096 inches to 0.0246 inches with the full results represented in Figure 5. Parts FDM-1.007, FDM-1.008-P1, and FDM-1.008-P2 all had mean errors very close to zero. However, when these values were matched with the standard deviation values, FDM-1.007 had the lowest spread of errors around the mean and this is another reason for the high accuracy of this part.

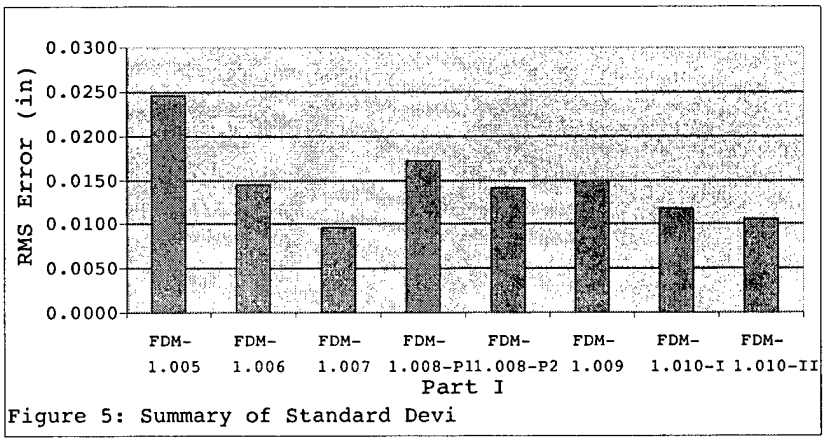


Figure 5: Summary of Standard Devi

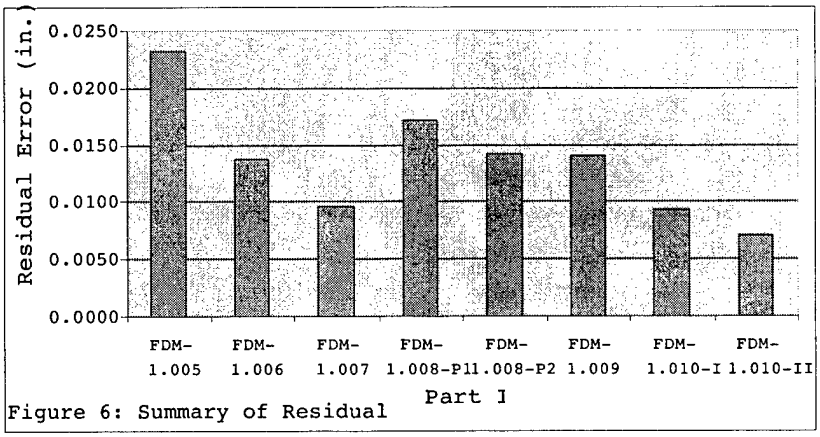


Figure 6: Summary of Residual

Calculating Residual Error for the user part allows the measurement of the errors in the part, which are not caused by shrinkage. These are random errors in the machine, material, and measurement that are much harder to measure and control. Overall, the Standard Deviation and Residual Error (Figure 6) for each user part had similar values, indicating that the error in the part due to shrinkage is very small and it is the random errors, which contribute greatly to the inaccuracy of the part. The lowest Residual Error of 0.0096in. for FDM-1.007 was the same as its Standard Deviation, indicating the error in the part due to shrinkage was extremely small and all the errors were random errors that are harder to control.

The most important of all the data calculated is the RMS Error (Figure 7) as it gives a better indication of the size of the error in each part. It is a better approximation than the mean error, which can be influenced by positive and negative error values [6]. The lowest RMS Error would indicate the most accurate part. It is FDM-1.007, which gives the lowest RMS Error value indicating its greatest accuracy and verifying the previous results, which indicated that it was the most accurate part. Part FDM-1.008-P2 had lower Total Shrinkage and Mean Error values than FDM-1.007, but its Standard Deviation, Root Mean Square Error and Residual error values verified its inaccuracy.

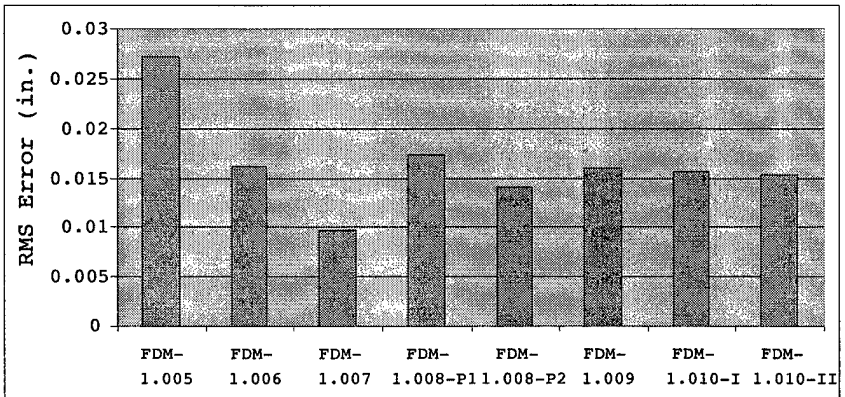


Figure 7: Summary of RMS Er Part I

Part ID	Slope	SCF Used	New SCF	Mean Error (in.)	SD (in.)	Residual Error (in.)	RMS Error (in.)
FDM-1.005	-0.2966%	0.5000%	0.7981%	-0.0119	0.0246	0.0232	0.0272
FDM-1.006	-0.1752%	0.6000%	0.7800%	-0.0071	0.0145	0.0137	0.0160
FDM-1.007	0.0453%	0.7000%	0.6500%	0.0017	0.0096	0.0096	0.0097
FDM-1.008-P1	0.0739%	0.8000%	0.7253%	0.0030	0.0172	0.0172	0.0174
FDM-1.008-P2	0.0006%	0.8000%	0.7993%	-0.0006	0.0142	0.0142	0.0141
FDM-1.009	0.1551%	0.9000%	0.7442%	0.0057	0.0150	0.0141	0.0159
FDM-1.010-I	0.2543%	1.0000%	0.7400%	0.0102	0.0118	0.0093	0.0156
FDM-1.010-II	0.2744%	1.0000%	0.7200%	0.0110	0.0107	0.0071	0.0153

Table 1. Summary of FDM-1650 Results

Conclusions and Recommendations

The objective for this research project was to find the optimal shrinkage compensation factor for the FDM-1650 prototyping machine and produce the most accurate part. From the data that was analyzed, the best SCF for the FDM-1650 was:

SCF = 1.007, or (0.7%)

There are a few recommendations arrived upon for future accuracy research on the FDM-1650. Firstly, varying temperature and build speed during the build process could affect the accuracy of the parts. These parameters might help minimize the amount of warpage that the part undergoes due to the amount of time it is exposed to heat. Also, building different percent sizes of the part can be used as a test to compare the effects of shrinkage on a small and a large part. Another recommendation is for more accurate SCF inputs, which contain 4 to 5 decimal places. This would allow for accuracy research of parts with SCF's between 1.0065 to 1.0075, the region where the results point to as having the best SCF. The machine should also allow for inputs in both the X and Y direction instead of the one shrinkage factor that can presently be input into the

build software. The addition of these inputs and added accuracy in the decimal place should produce a more accurate part that is even closer to its desired dimensions. Finally, the support material that is currently in use with this machine should be changed because it is difficult to remove. A water-soluble support material would make it easier to remove and clean the part, saving valuable time.

ACKNOWLEDGEMENT

This work was funded by a National Science Foundation (NSF) grant to Loyola Marymount University for their Research Experience for Undergraduates program. The authors also appreciate the support provided by Northrop Grumman and 3D Systems.

REFERENCES

1. Noorani, R. Rapid Prototyping Lectures, Los Angeles, CA: Loyola Marymount University, 2000.
2. Gargiulo, E.P (E.I. DuPOnt de Nemours and Co., Wilmington, DE) & Belfiore, D.A (Pennsylvania State University, State College, PA) "Stereolithography Process Accuracy User Experience", 1995.
3. Noorani, R., et al. "Calculation of Shrinkage Compensation Factors for Rapid Prototyping". Computer Applications in Engineering Education, Vol. 7, No. 3, Oct. 1999.
4. Gargiulo, E.P., and Belfiore, D.A., "Photopolymer Solid Imaging Process Accuracy", Intelligent Design and Manufacturing for Prototyping, ASME PED-Vol.50, Dec. 1991.
5. Gargiulo, E.P (Dade International Inc.) & Jayanthi, Suresh S. (Dupont Company) "Current State of Accuracy in Stereolithography"
6. Freedman, D., et al, Statistics. W.W. Norton & Company, 2nd ed., 1991.
7. Jacobs, P., PhD, Stereolithography and other RP&M Technologies. Society of Manufacturing Engineers., 1996.
8. Stratasys inc. FDM System Documentation 1996.
9. Brown & Sharpe, MicroMeasure II+ and III USER'S MANUAL @ 1996 Brown & Sharpe Manufacturing Company.

On Some Physical Aspects of Process Control in Direct Selective Laser Sintering of Metals—Part I

Suman Das
Department of Mechanical Engineering
University of Michigan
Ann Arbor, MI 48109-2125
USA

1 Introduction

Selective laser sintering (SLS) of metals is a complex process exhibiting multiple modes of heat, mass and momentum transfer, and chemical reactions. The strong interplay between these physical mechanisms directly impacts the SLS process, determining whether a given material can be processed and if so, how the microstructure and properties of the processed material are influenced. In order to understand the complex nature of these mechanisms, their interplay and impact on process control in SLS, it is appropriate to first understand them at a fundamental level. The next step should involve developing simple models that can quantitatively reveal the influence of these mechanisms as functions of processing conditions. Following this step, increasingly detailed models that take into account the coupling between different mechanisms should be developed.

In this review paper, a first step is taken towards identifying and understanding some of the important physical mechanisms in direct SLS. This study not only provides an insight into phenomena observed during direct SLS of a variety of metallic materials, but also helps in selecting materials that are most amenable to processing by direct SLS. Physical mechanisms discussed include oxidation, wetting, epitaxial solidification, elemental vaporization, melt flow instabilities and powder bed caking. Understanding these physical mechanisms is essential for the design of direct SLS machines and their process control.

2 Wetting

2.1 Effect of Processing Atmosphere on Wettability

Direct SLS of metals is far more demanding than SLS of polymers or indirect SLS of metals. Oxidation is a serious problem at the higher processing temperatures necessary for melting metals of interest (typically exceeding $> 1000°C$). Since selective laser sintering is a layerwise additive process, oxidation of laser processed powder is a severe impediment to interlayer bonding and causes defects such as balling. Balling occurs when the molten metal does not wet the underlying substrate due to an oxide layer being present on the substrate and on the surface of the melt. Oxidation also causes delamination induced by poor interlayer bonding in combination with thermal stresses. These phenomena severely degrade material properties and part geometry.

Poor wetting of an oxide substrate by a liquid metal is explained by the interfacial thermodynamics involved. The equilibrium of a liquid in contact with non-interacting solid

and gaseous phases is shown in Figure 1. The equilibrium of interfacial free energies γ_{ij} is governed by

$$\gamma_{SV} - \gamma_{SL} = \gamma_{LV} \cos\theta \tag{1}$$

The liquid will wet the substrate as $\cos\theta \to 1$ or equivalently, if $\gamma_{LV} < \gamma_{SV} - \gamma_{SL}$. This corresponds to the case on the left. The difference $\gamma_{SV} - \gamma_{SL} - \gamma_{LV}$ is termed the spreading coefficient S. Large, positive S favors spreading. Surface free energies of metal oxides are much lower than the corresponding liquid-vapor surface free energy. Thus, in the absence of a chemical reaction between the liquid and the substrate, liquid metals do not wet surface oxide films, preferring to minimize surface area by balling instead.

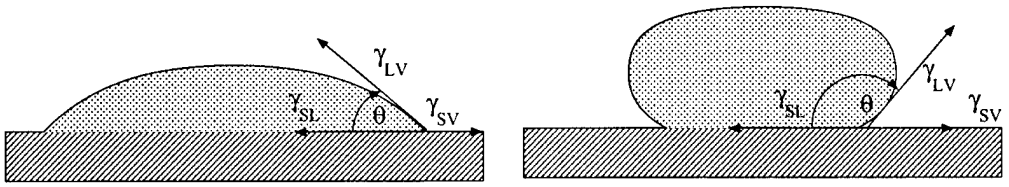


Figure 1: Three phase equilibrium for wetting and non-wetting systems.

To ensure good wetting and successful layer-by-layer consolidation direct SLS of metals, processing must be conducted in a vacuum or protective atmosphere using high purity inert gases. An Ellingham diagram [1] of common oxides shows that at the melting points of Nickel (1454.4°C), Chromium (1857°C) and Titanium (1704.4°C), the equilibrium partial pressure of oxygen must be less than 10^{-5}, 10^{-12} and 10^{-16} atm. respectively to prevent the oxidation reaction. Therefore, some oxidation cannot be avoided under normal operating conditions. In traditional furnace brazing operations for metals and alloys conducted under pure hydrogen atmosphere, it is important to consider the dew point or moisture content of the atmosphere against the most stable oxide forming element. A chart of metal-metal oxide equilibria under pure hydrogen at 1 atm is available in the literature [2]. This chart, calculated for a variety of metal oxides shows the temperature and water

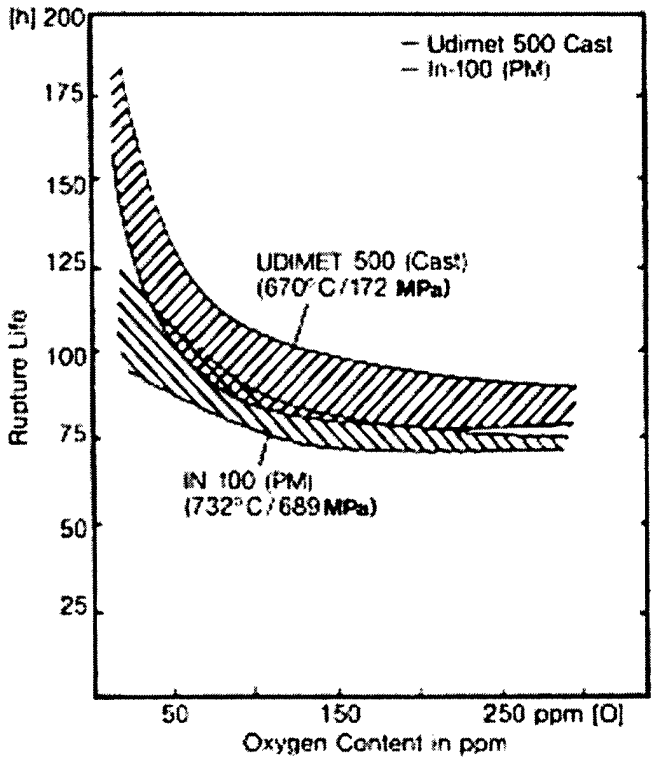


Figure 2: Influence of Oxygen on rupture life, after Choudhry (1990)

vapor partial pressure combinations under which the reaction is reducing or oxidising. For good wetting to take place, reduction of surface oxides is necessary to provide a clean metal-metal interface. Conventional practice involves providing a continuous flow of hydrogen to maintain the water vapor partial pressure levels favorably. It has been noted that the same chart is equally applicable for continuous flow inert gas atmospheres with similar oxygen content.

Some extremely reactive metals such as titanium cannot be processed under hydrogen atmospheres for two reasons. First, it is difficult to obtain hydrogen of the necessary purity at the processing temperature of interest (*i.e.* the melt temperature) . Second, titanium and its alloys are extremely sensitive to hydrogen embrittlement. Thus, traditional high temperature sintering and vacuum brazing is conducted in the 10^{-4}–10^{-6} Torr vacuum range. Although processing under these vacuum levels yields satisfactory results with regards to wetting, volatilization of alloying elements at high temperatures under reduced pressure can be a serious concern.

Oxidic cleanliness is also of paramount importance while processing high performance metals, especially superalloys and titanium with extremely high strength, high creep resistance properties at elevated service temperatures approaching the solidus temperature. Figure 2 shows the detrimental influence of increasing oxygen content on the rupture life of superalloys. Commercially pure titanium (CP Ti) has a specification of 1400 ppm maximum acceptable level of oxygen. The titanium alloy Ti-6Al-4V has specification oxygen limits in the final product ranging from 0.1% to 0.40% weight depending on the particular application. Molybdenum is classified as a "superclean" metal [3] and is typically purified by electron beam melting at 10^{-5}–10^{-6} Torr. When compared to cast or wrought product, powders have higher degree of contamination due to their much higher surface area per unit volume. As-received powders are known to harbor moisture, organics, adsorbed gases, oxide and nitride films on particle surfaces depending on the production method and shelf life. These contaminants not only inhibit successful wetting and densification of the melted powder but also degrade mechanical properties of the consolidated product. Therefore, processing under high vacuum ($< 10^{-5}$ Torr) or ultra high purity inert environments is necessary for successful direct SLS of high performance metals.

2.2 Homologous Wetting

Most of the work on wetting reported in the literature is based on isothermal wetting of dissimilar substances, *e.g.* wetting of a liquid on a solid substrate of chemical composition different than the liquid. An excellent review of the physical mechanisms governing this wetting regime is given by de Gennes [4]. The wetting behavior of a molten liquid on a substrate of its own kind was investigated only recently by Schiaffino and Sonin [5, 6, 7] This particular situation is known as "homologous wetting" and is inherently a non-equilibrium phenomenon involving simultaneous heat transfer, fluid flow and solidification.

In SLS, laser induced melting of powder and subsequent solidification onto a previously formed layer constitutes homologous wetting. Experiments were conducted by laser melting droplets onto prepared substrates of the same material to investigate homologous wetting in SLS. Stainless steel 304L was chosen as the material for investigation due to its ready availability in both powder and plate form. Stainless steel plate 0.125 inches thick was

prepared by polishing with 120, 240, 400 and 600 abrasive grits, followed by $3\mu m$ diamond paste and a final polish with $0.05\mu m$ alumina slurry, followed by ultrasonic cleaning in acetone. This preparation technique was necessary to provide as clean and smooth a surface as possible since the presence of surface oxides will cause the material to spread poorly [8] and surface roughness can drastically alter wetting behavior [4].

Two types of experiments were conducted. In the first type of experiment, stainless steel powder placed on the stainless steel substrate was melted by a stationary Nd:YAG laser beam incident on the powder. In the second type of experiment, a strip of stainless steel, 1 mm wide and 4 mm long was placed on the substrate and melted by the same laser beam. Each type of experiment was conducted under high vacuum ($< 10^{-5}$ Torr) with no preheat, 350° C preheat and 900° C preheat to document the influence of preheat on the wetting behavior (analogous to the Stefan number in the studies of Schiaffino and Sonin [5]). The dynamics of melting, droplet formation, wetting and solidification were captured by video microscopy. The objective in these experiments was to visualize and qualitatively understand the wetting behavior of a metal melt on a substrate of its own kind. Therefore, no attempt was made to carefully control the temperature of the superheated melt. Such an arrangement could be implemented by controlling the laser power via feedback from a pyrometer aimed at the melt pool.

All the experiments revealed that after melting and droplet formation, the molten metal showed no tendency to spread and wet the underlying substrate. Instead, it formed a nearly spherical droplet having a point like contact with the substrate. The influence of preheat temperature on the wetting behavior was minimal and could not be distinguished visually. Sequential frames from video microscopy of one such experiment conducted with stainless steel strip on stainless steel plate is shown in Figure 3. The image at 1s shows the point of incidence of the laser beam, approximately at midlength of the strip. At 33s, the ends of the strip begin to lift off the substrate and fold in rapidly towards the center. The laser beam is turned off at 49s, revealing a very nearly spherical molten droplet and by 54s, the droplet has solidified.

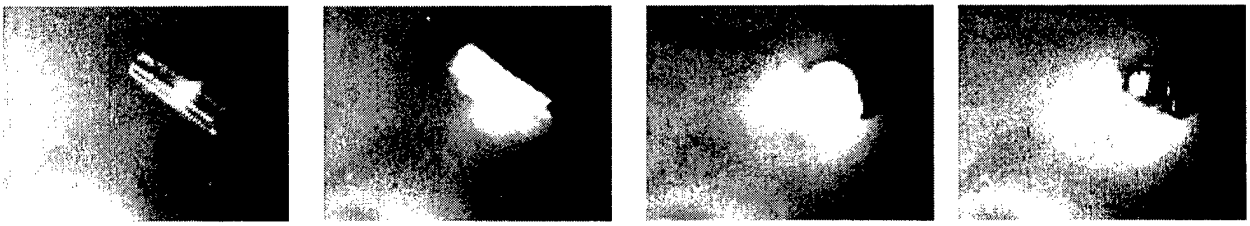
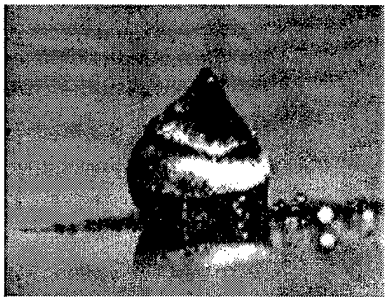


Figure 3: Homologous wetting experiment at 1s, 33s, 49s, and 54s (right).

The solidified droplets (with largest dimension typically 2mm) exhibited different shapes for powder and solid strips. In the case of "powder on plate" type experiments, the solidified droplets, shown on the left in Figure 4 had an elongated peaked feature at the top and a finite contact area with the plate. On the other hand, the solidified droplets of "strip on plate" type experiments, shown on the right in Figure 4 exhibited a much higher degree of sphericity, and a very small area of contact with the plate. The typical length scale in the photos is 2 mm.



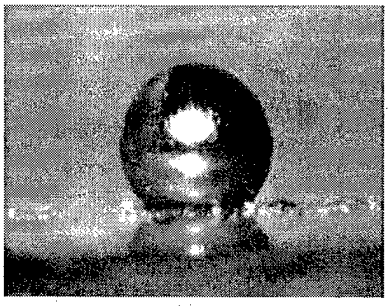


Figure 4: Solidified droplets in "powder on plate" experiment (left) and "strip on plate" experiment (right).

Very poor metallurgical bonding was observed between the solidified droplet and the substrate in each of the homologous wetting experiments conducted on stainless steel. The solidified droplets were easily detached from their respective substrates. In addition, the substrates did not exhibit any evidence of melting at the droplet-substrate interface. Despite excellent atmosphere control (down to 10^{-6} Torr), poor wetting observed in these experiments resulted due to a lack of substrate remelting and ensuing epitaxial solidification. As shown in the following section, remelting of the underlying substrate is necessary to break down surface contamination (*e.g.* oxide films) in order to provide a clean interface at the atomic level between the solid and the liquid.

2.3 Epitaxial Solidification in Direct SLS

Direct SLS of metals is very similar to fusion welding. In fusion welding, the base metal and the weld metal may have similar but not necessarily the same composition whereas in direct SLS of monolithic metallic materials, the base metal and weld metal are necessarily the same. Some dilution of the base metal is known to occur in all types of fusion welding. Dilution refers to partial localized remelting of the base metal during welding and is necessary to provide a continuous interface free of oxide films or other contaminants between the solidifying liquid weld metal and the base metal. Dilution is deemed extremely important to ensure good weld integrity. The most important implication of dilution or "meltback" is that during solidification, grain growth will occur at the solid-liquid interface between the base metal and the liquid in contact with it. Grain growth is important because it has been well established by metallographic inspection that initial solidification in fusion welding occurs by epitaxial solidification [9]. Due to the signicant similarities between fusion welding and direct SLS, it is instructive to understand the implications of epitaxial solidification on SLS process control.

Epitaxial solidification is a process of heterogeneous nucleation. In heterogeneous nucleation, a solid nucleus "nucleates" from the liquid onto a substrate with which the liquid is in contact. The shape of the nucleus is governed by the balance of interfacial free energies between the nucleus, solid and the liquid. It can be shown that the total interfacial free energy of this system is minimized when the nucleus assumes the shape of a spherical cap as shown in Figure 5.

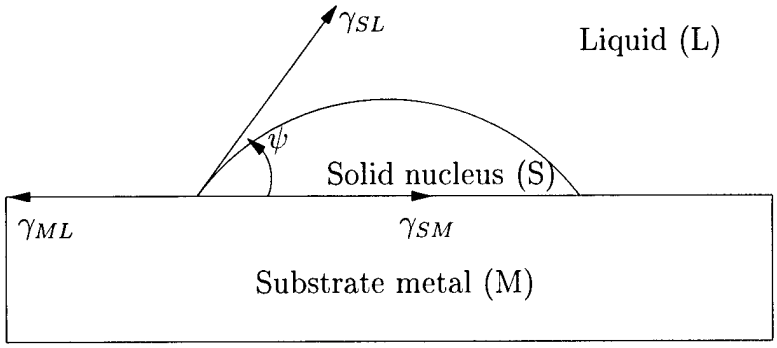


Figure 5: Heterogeneous nucleation of a solid nucleus at the solid-liquid interface.

At equilibrium, the balance of interfacial forces is given by

$$\gamma_{ML} = \gamma_{SM} + \gamma_{SL} \cos\psi \tag{2}$$

where the interfacial free energies are γ_{ML} between the substrate metal and the liquid, γ_{SM} between the solid nucleus and the substrate metal, and γ_{SL} between the solid nucleus and the liquid. The contact angle of the nucleus is ψ. Rearranging equation 2 gives

$$\cos\psi = \frac{\gamma_{ML} - \gamma_{SM}}{\gamma_{SL}} \tag{3}$$

In the context of direct SLS, the compositions of the solidified nucleus and the solid substrate are the same. Thus the interfacial energy between the nucleus and the solid substrate should be negligible while the interfacial energies between the nucleus and the liquid, and the solid substrate and the liquid should be about the same. This leads to the following approximations:

$$\gamma_{SM} \approx 0 \tag{4}$$

$$\gamma_{ML} \approx \gamma_{SL} \tag{5}$$

$$\psi \rightarrow 0 \tag{6}$$

The change in free energy associated with the formation of a solid "spherical cap" nucleus with radius of curvature r is given by

$$\Delta G_{het} = -V_S \Delta G_v + A_S \gamma_{SL} \tag{7}$$

$$= \left(-\frac{4}{3}\pi r^3 \Delta G_v + 4\pi r^2 \gamma_{SL}\right) S(\psi) \tag{8}$$

where ΔG_v is the free energy change per unit volume associated with formation of the nucleus, V_S is the volume of the nucleus, A_S is the surface area of the new interface created between the solid nucleus and the liquid, and $S(\psi)$ is a shape factor dependent on the contact angle given by

$$S(\psi) = \frac{(2+\cos\psi)(1-\cos\psi)^2}{4} \tag{9}$$

By differentiating equation 8 with respect to r and setting the result equal to zero, the critical radius $r^\star$ to promote heterogeneous nucleation is given by

$$r^\star = \frac{2\gamma_{SL}}{\Delta G_v} \tag{10}$$

By substituting the expression for $r^\star$ into equation 8, the associated nucleation energy barrier for heterogeneous nucleation to proceed is

$$\Delta G^\star_{het} = \frac{16\pi}{3}\frac{\gamma^3_{SL}}{\Delta G^2_v} S(\psi) \tag{11}$$

It is of interest to note the dependence of $\Delta G^\star_{het}$ on $S(\psi)$. From equations 4-6, it apparent that in epitaxial solidification, $S(\psi) \to 0$. This result implies that the energy barrier for heterogeneous nucleation to proceed during epitaxial solidification is vanishingly small. This is in stark contrast to coventional casting processes in which ψ is finite, and hence $S(\psi)$ and $\Delta G^\star_{het}$ are finite due to mold and cast materials being dissimilar, as illustrated by Grong [10] in Figure 6.

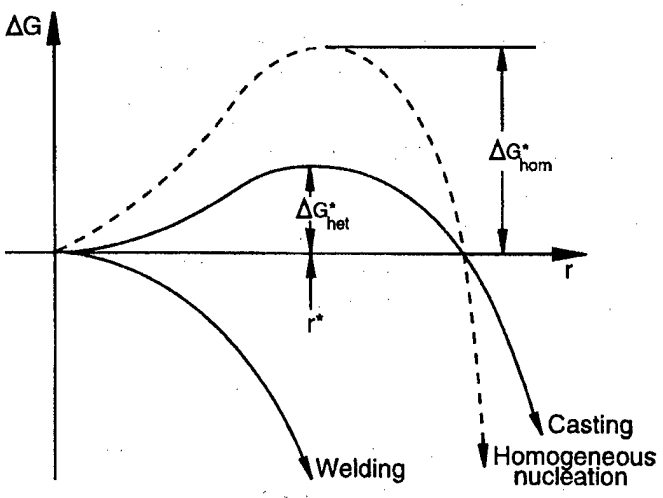


Figure 6: Schematic of free energy change associated with heterogeneous nucleation in casting and welding juxtaposed with free energy change in homogeneous nucleation (after Grong, 1994).

Nucleation proceeds immediately in epitaxial solidification by virtue of the negligible energy barrier. For this mode of solidification to occur, the substrate must be partially melted back to promote growth from the prior grains of the substrate. Epitaxial solidification by heterogeneous nucleation is indeed the mode of solidification in direct SLS processing to full density. Evidence of epitaxial solidification was confirmed by microstructural examination of sections of SLS processed material encompassing several layer thicknesses.

A cross-section of specimen 102097, shown on the left in Figure 7 is an example of incomplete homologous wetting and solidification. In this case, the melt front from above barely propagated down to the surface of the previous layer. The uniformity of layer thickness is particularly notable. In contrast, the fabricated layers in the cross-section of specimen 102497 produced at a higher laser power density, shown on the right in Figure 7, are completely indistinguishable indicating continuous grain growth across the layers. This indicates that sufficient meltback of the previous layer took place tp induce epitaxial solidification. It should be noted that these micrographs on traverse approximately three layer thicknesses.

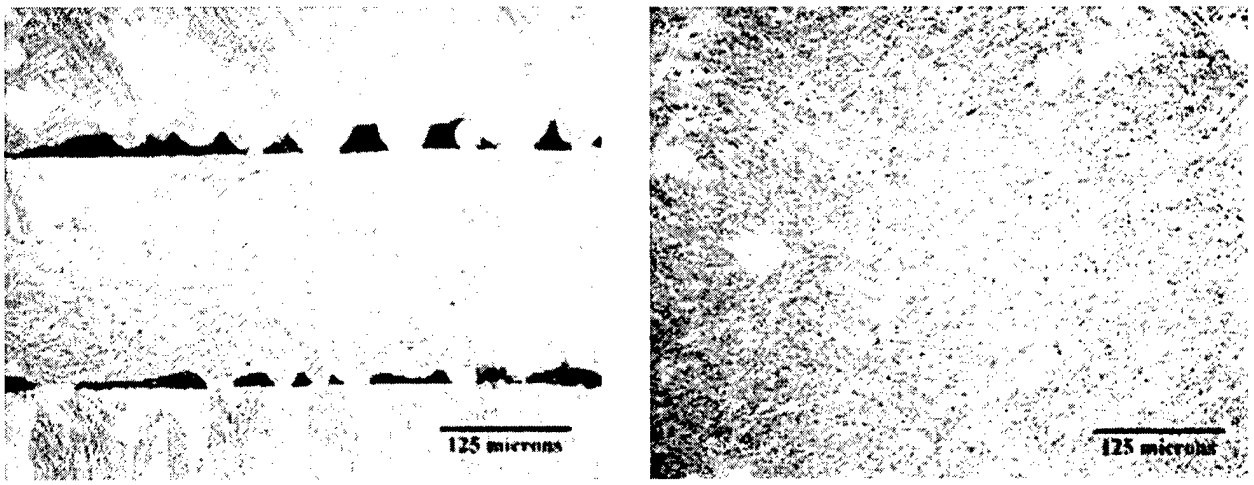


Figure 7: Etched microstructure of Ti-6Al-4V specimen 102097 (Kroll's reagent).

Another benefit resulting from epitaxial solidification is fine grain size resulting in improved mechanical properties. Equation 10 shows that for heterogeneous nucleation to proceed, the critical radius of the nucleus $r^\star$ depends on the solid-liquid interfacial free energy γ_{SL}. However, in SLS, the solid and liquid are of the same composition (assuming negligible contamination or segregation). Thus, γ_{SL} is very small implying that $r^\star$ is very small. Since SLS is a localized solidification process, this means that under identical processing conditions (temperature gradients at the solid liquid interface, cooling rates, etc), the "as SLS processed" material will exhibit finer and more uniform grain size compared to conventional casting. This hypothesis was also confirmed by examining the etched microstruture of SLS processed Ti-6Al-4V which revealed finer grain size than conventionally cast Ti-6Al-4V.

Thus, the mechanism for "good wetting" in direct SLS is epitaxial solidification by heterogeneous nucleation. As an analogue to fusion welding [9], in SLS, remelting of the previous layer is necessary to ensure full density. Remelting the previous layer removes surface contaminants, breaks down oxide films, provides a clean solid-liquid interface at the atomic level and allows epitaxial grains to grow heterogeneously. Laser processing parameters in direct SLS should be chosen so as to ensure that sufficient meltback of the previous layer takes place and continuity of the solid-liquid interface under the moving laser beam is maintained.

References

[1] David R. Gaskell. *Introduction to the Thermodynamics of Materials*, page 370. Taylor and Francis, 1995.

[2] N. Bredzs and C. C. Tennenhouse. Metal-Metal Oxide-Hydrogen Atmosphere Chart for Brazing and bright Metal Processing. In Melvin H. Schwartz, editor, *Source Book on Brazing and Brazing Technology*, pages 86–90. ASM, 1980.

[3] A. Choudhry. *Vacuum Metallurgy*, page 101. ASM International, Materials Park, OH 44073–0002, 1990.

[4] P. G. de Gennes. Wetting: statics and dynamics. *Reviews of Modern Physics*, 57(3): 827–863, July 1985.

[5] Stefano Schiaffino and Ain A. Sonin. Motion and arrest of a molten contact line on a cold surface: An experimental study. *Physics of Fluids*, 9(8):2217–2226, August 1997.

[6] Stefano Schiaffino and Ain A. Sonin. On the theory for the arrest of an advancing molten contact line on a cold solid of the same material. *Physics of Fluids*, 9(8):2227–2233, August 1997.

[7] Stefano Schiaffino and Ain A. Sonin. Molten droplet deposition and solidification at low Weber numbers. *Physics of Fluids*, 9(11):3172–3187, August 1997.

[8] A. J. Wall and D. R. Milner. Wetting and Spreading Phenomena in a Vacuum. *Journal of the Institute of Metals*, 90:394–402, 1961.

[9] Kenneth Easterling. *Introduction to the Physical Metallurgy of Welding*, chapter 2, pages 66–69. Butterworth-Heinemann, 2nd edition, 1992.

[10] Øystein Grong. *Metallurgical Modeling of Welding*, chapter 3, pages 222–227. The Institute of Materials, 1994.

this page intentionally blank

On Some Physical Aspects of Process Control in Direct Selective Laser Sintering of Metals—Part II

Suman Das
Department of Mechanical Engineering
University of Michigan
Ann Arbor, MI 48109-2125
USA

3 Volatilization of Elements in Direct SLS

Volatilization of elements is a well known phenomenon in vacuum metallurgy [1], welding [2, 3], electron beam processing [4, 5] and thin film technology [6]. Evaporation and condensation of metals has been noted in direct SLS as well. The evaporation process from a metal melt is governed by four distinct regimes: mass transport of atoms from the interior of the melt to its surface, phase change to gaseous state at the surface, mass transport in the gas phase above the melt and finally condensation.

3.1 Evaporation of a Pure Metal

The molecular (or atomic) rate of evaporation per unit area and time for a liquid in equilibrium with its vapor was derived first by Hertz and later modified by Knudsen [6] to give

$$\frac{dN_e}{A_e dt} = \alpha_v \left(\frac{1}{2\pi mkT}\right)^{\frac{1}{2}} (P_v - P) \qquad (s^{-1}) \tag{1}$$

where m is mass of an individual molecule, k is Boltzmann's constant, T is the absolute temperature, P_v is the vapor pressure at the liquid's surface temperature and P is the hydrostatic pressure acting on the liquid surface. The coefficient α_v accounts for the fraction of vaporized molecules that are ejected and not resorbed back into the evaporating surface, hence, the maximum evaporation rate is attained when $\alpha_v = 1$.

Langmuir showed that the Hertz-Knudsen equation was also applicable to vaporization from free solid surfaces. In addition, he demonstrated that for pressures below 0.1 Torr ($\approx 10^{-4}$ atm), the vaporization rate is independent of residual gas pressure due to the negligible resistance offered. This resulted in the Langmuir equation for the maximum vaporization rate expressed in mass flux form as [6]

$$\Gamma = \left(\frac{m}{2\pi kT}\right)^{\frac{1}{2}} P_v \tag{2}$$

The Clausius-Clapeyron equation describes the change of equilibrium vapor pressure as a function of temperature and is given by

$$\frac{dP_v}{P_v} = \frac{LdT}{RT^2} \tag{3}$$

where L is the molar latent heat of vaporization and R is the molar gas constant. If the latent heat of vaporization is assumed constant for the temperature range of interest, equation 3 can be integrated to give the relation

$$P_v(T) = P_0 e^{-\frac{L}{RT}} \tag{4}$$

For most materials, in the range of vapor pressures below 1 Torr (1.315×10^{-5} atm), it has been observed experimentally [7] that the vapor pressure is indeed related to the temperature in the form of equation 4. Substituting equation 4 into equation 2 for the evaporation rate yields the form

$$\Gamma = P_0 \left(\frac{m}{2\pi kT}\right)^{\frac{1}{2}} e^{-\frac{L}{RT}} \tag{5}$$

showing the near exponential dependence of the vaporization rate on the vaporization temperature.

3.2 Alloy Melting and Vaporization Under Vacuum

In the melting of alloys under vacuum, volatile solute and impurity atoms are vaporized in addition to base metal atoms. Therefore, mass transport of the solute from the interior to the surface must be considered in addition to evaporation from the surface. Both processes contribute to the overall transfer of metal atoms into the gas phase and it is therefore important to determine the rate limiting step.

The average mass transfer coefficient in an stirred metal melt is described by [8]

$$k_{m,l} = 2\left(\frac{D}{\pi\theta}\right)^{\frac{1}{2}} \tag{6}$$

where D is the diffusion coefficient (m^2/s) of the solute in the liquid and θ is the "residence time" (s), which is given by the melt pool characteristic length divided by the surface velocity of the flowing melt.

Thus, the flux to the surface from the bulk liquid is

$$j_A = k_{m,l}(C_{A\infty} - C_A^s) \tag{7}$$

where j_A is the flux (mol $m^{-2}s^{-1}$), $C_{A\infty}$ and C_A^s are volumetric concentrations of the solute in the bulk and at the surface respectively.

Evaporation from the surface of a pure metal was described earlier. In the case of an alloy, the evaporation rate or flux of an alloying component is given by [8]

$$j_A = \frac{\gamma_A P_A^0 C_A^s}{\rho\sqrt{2\pi MRT}} \tag{8}$$

where γ_A is the activity coefficient of the component, P_A^0 is the vapor pressure of the pure component at the temperature under consideration, ρ is the molar density of the alloy and M is the alloy's molecular weight. From equation 8, the mass transfer coefficient for surface evaporation is

$$k_{m,e} = \frac{\gamma_A P_A^0}{\rho\sqrt{2\pi MRT}} \tag{9}$$

When the melting and vaporization takes place under vacuum better than 0.1 Torr, the resistance to mass transport in the gas phase is negligible, as was indicated earlier. Under this condition, the liquid phase mass transfer and evaporation fluxes are in equilibrium. Therefore,

$$k_{m,l}(C_{A\infty} - C_A^s) = k_{m,e}C_A^s \tag{10}$$

Subsituting for C_A^s from equation 10 into equation 7, the expression for the flux is given by

$$j_A = \left(\frac{k_{m,e}k_{m,l}}{k_{m,l} + k_{m,e}}\right) C_{A\infty} \tag{11}$$

$$= KC_{A\infty} \tag{12}$$

where K is the overall mass transfer rate constant which can be rewritten as

$$\frac{1}{K} = \frac{1}{k_{m,l}} + \frac{1}{k_{m,e}} \tag{13}$$

By evaluating the magnitudes of the "resistances" $\frac{1}{k_{m,l}}$ and $\frac{1}{k_{m,e}}$ offered by each step, once can determine whether they are the same order of magnitude or one is clearly the rate limiting step. The higher the degree of stirring or convection in a melt, the higher the value of $k_{m,l}$ and the smaller its effect on the overall mass transfer rate. Conversely, the lower the vapor pressure P_A^0 of the solute, the smaller the value of $k_{m,e}$ and the greater the resistance offered by surface evaporation to mass transport.

For example, it has been reported [5] that for electron beam processing of a wide variety of liquid metal systems, $k_{m,l}$ falls in the range $1\times10^{-4} - 5\times10^{-4}$ m/s. In the refining of silver from liquid copper at 1920 K by electron beam melting in a water cooled hearth, the rate constants reported were $k_{m,e} = 6.1\times10^{-4}$ m/s, $K = 1.4\times10^{-4}$ m/s to yield $k_{m,l} = 1.9\times10^{-4}$ m/s. Given that the hearth area was 0.16 m^2 and typical surface velocity observed in this experiment was 7×10^{-2} m/s, the residence time θ is of order $3s$. This value is of the order of the time expected in an inductively stirred melt [8]. If this system is considered for full density SLS processing (where a continuous melt pool would be maintained), as a first approximation we can assume that the laser scan speed is representative of the surface velocity in the melt pool and the melt pool size is on the order of the beam diameter. For a typical scan speed of 5.08 cm/s (2 in/s) and a beam diameter of 0.05 cm, the value of θ is 0.01s. Due to the high surface velocity for the pool size under consideration, it is expected that stirring is even more vigorous in SLS and that $k_{m,l,SLS} \approx 10k_{m,l,EB}$. This calculation is based on a very conservative estimate of flow velocity at the pool surface. Surface velocities induced by surface tension gradients that are 2 to 3 orders of magnitude higher than the velocity of the moving heat source have been observed and predicted [3]. This indicates very good mixing in the melt pool and that the rate limiting step for mass transfer is volatilization at the pool surface.

Evaporation of alloying elements from the melt pool also causes loss of input laser power. The power loss due to evaporation of an alloying element is given by [2]

$$P_{L,A} = \Gamma_A(L_A - \Delta H_A) \tag{14}$$

where $P_{L,A}$ is the power lost due to evaporation of element A, Γ_A is the evaporation rate of element A, L_A is the heat of vaporization of pure component A and ΔH_A is the partial molar heat of mixing of A in the alloy. The evaporative power loss affects the peak temperature attainable in the melt pool.

3.3 Vaporization Characteristics of Elements Relevant to SLS

Empirical data obeying the form of equations 4 and 5 have been used by Dushman [7] to tabulate data for a wide variety of elements. The vapor pressure data for selected elements of relevance to SLS are shown in Table 1.

Element	T_m (° C)	T_b (° C)	Vaporization Temperature (° C) At Pressure (Torr)					
			10^{-5}	10^{-4}	10^{-3}	10^{-2}	10^{-1}	1
Al	659	2447	882	972	1082	1207	1347	1547
B	2027	3927	1687	1827	1977	2157	2377	2657
Co	1495	2877	1162	1262	1377	1517	1697	1907
Cr	1903	2665	1062	1162	1267	1392	1557	1737
Cu	1084	2578	942	1032	1142	1272	1427	1622
Fe	1539	2857	1107	1207	1322	1467	1637	1847
Mg	650	1104	287	330	382	442	517	612
Mn	1244	2051	697	767	852	947	1067	1227
Mo	2577	4827	1987	2167	2377	2627	2927	3297
Ni	1452	2839	1142	1247	1357	1497	1667	1877
Pb	328	1751	487	551	627	719	832	977
Si	1415	2787	1177	1282	1357	1547	1717	1927
Ti	1660	3287	1321	1431	1558	1703	1877	2083
V	1857	3377	1432	1551	1687	1847	2037	2287
W	3377	5527	2547	2757	3007	3297	3647	n/a
Zn	420	906	208	246	290	342	405	485
Zr	1852	4405	1837	2002	2187	2387	2647	2977
T_m=Melting point T_b=Normal boiling point								

Table 1: Vaporization temperature of selected elements as a function of pressure.

Some important observations can be made in this table with regard to SLS process control. For example, in the $10^{-4} - 10^{-5}$ Torr vacuum range, all elements in the table except Al and Pb have vaporization temperature lower than their respective melting points. Hence, all these elements will show a very high tendency to vaporize when processed under this vacuum range. The vaporization temperature approaches and exceeds the melting point in

the $10^{-2} - 10^{-3}$ Torr range. In the $1 - 10^{-1}$ Torr range, most vaporization temperatures are in excess of the melting points but not significantly. This range allows melt superheat by a few hundred degrees Centigrade before the vaporization temperature is attained. However, it should be noted that even at 1 Torr, Cr, Cu, Mg, Mn will all vaporize. Therefore, it is apparent that to inhibit vaporization, SLS processing under partial pressure rather than high vacuum is necessary.

3.4 Partial Pressure Processing—Reducing Mean Free Path

Volatilization of alloying elements has been observed during SLS processing under high vacuum. The most deleterious effect of this phenomenon is condensation of volatilized elements on the laser window, severely affecting consistency of laser energy delivery. Condensation of volatilized elements also takes place on chamber interior surfaces that can cause contamination during subsequent processing of other materials. Volatilization can also cause depletion of alloying elements resulting in alteration of alloy chemistry.

In the absence of laser spot temperature control so as to regulate the temperature of the melt zone, some degree of superheat is likely to occur. Therefore, it is necessary to select the operating pressure based on the elemental constituents that have the highest vaporization tendency. In order to maintain purity of the processing atmosphere, this entails evacuating the chamber to high vacuum followed by back fill to partial pressure with an ultrahigh purity inert gas such as 99.999% purity Argon or Helium ($<$ 2 ppm oxygen, $<$ 3 ppm moisture, $<$ 1 ppm hydrocarbons and $<$ 6 ppm nitrogen [9]). It is necessary implement inert gas partial pressure processing to decrease the mean free path of gaseous element atoms so that condensation on the laser window is inhibited. In addition, if a continuous flow of inert gas is maintained to provide "dynamic" partial pressure processing, volatilized material will tend to be flushed away from the processing zone and out of the vacuum system.

The mean free path is defined as the average distance between successive collisions of gaseous molecules and is given by [6]

$$\lambda = \frac{kT}{\sqrt{2}P\pi\sigma^2} \tag{15}$$

where k is Boltzmann's constant, T is the absolute temperature, P is the pressure and σ is the molecular diameter. Assuming $\sigma = 5$ Å, $T = 298K$ and P is expressed in Pa, equation 15 reduces to

$$\lambda = \frac{3.642 \times 10^{-3}}{P} \quad (m) \tag{16}$$

Table 2 shows the mean free path as a function of pressure over 10 decades. Upon inspection of table 2, the reason for substantial condensation of elemental volatiles on the laser window is clear. The distance, r, from the laser window to the scanned powder surface is typically less than 0.5 m. At 10^{-7} Torr, the mean free path is about 35 m. Therefore, at 10^{-7} Torr vacuum levels, volatilized metal atoms travel unimpeded to the laser window and processing chamber walls. At an order of magnitude lower vacuum, *i.e.* 10^{-6} Torr, the mean free path of 3.59 m is still an order of magnitude larger than r. It is only at 10^{-5} Torr that the mean free path is of same order of magnitude as r. Thus, if the arrival rate of volatilized metal

Pressure (atm)	Pressure (Torr)	λ (m)
1	760	3.59×10^{-8}
10^{-1}	76	3.59×10^{-7}
10^{-2}	7.6	3.59×10^{-6}
10^{-3}	7.6×10^{-1}	3.59×10^{-5}
10^{-4}	7.6×10^{-2}	3.59×10^{-4}
10^{-5}	7.6×10^{-3}	3.59×10^{-3}
10^{-6}	7.6×10^{-4}	3.59×10^{-2}
10^{-7}	7.6×10^{-5}	3.59×10^{-1}
10^{-8}	7.6×10^{-6}	3.59
10^{-9}	7.6×10^{-7}	35.9

Table 2: Mean free path for various pressures.

atoms at their condenation on the laser window is to be substantially curtailed, it is necessary to operate at still higher pressure levels. We assume that the arrival rate is substantially reduced by decreasing the mean free path to two orders of magnitude lower than r. This hypothesis suggests that the desired operating vacuum (pressure) level is in the neighborhood of 7.6×10^{-3} Torr. This hypothesis was indeed confirmed by experiment. While substantial condensation was observed at 10^{-4} Torr partial pressure processing, condensation on the laser window was nearly completely eliminated at 10^{-3} Torr levels, allowing the fabrication of large complex parts spanning several hundred layers and several tens of hours build time.

3.5 Alloy Melt Refining by Evaporation of Suboxides

Melting of high performance alloys under high vacuum or ultrahigh purity inert gas partial pressure enviroments can provide the added benefit of alloy refinement by volatilization of oxides, impurities and non-metallic inclusions. Refining of alloy melts during SLS processing under vacuum can occur by mechanisms very similar to those in vacuum induction melting (VIM), vacuum arc remelting (VAR) and electron beam cold hearth refining (EBCHR). The techniques VIM, VAR and EBCHR are presently well established for production of aerospace and specialty alloys including nickel base superalloys and alloys of titanium [10]. From the perspective of SLS process control, it is important to consider the refining mechanisms and their impact on the chemistry of the processed material.

If the stoichiometric form of the metal oxide is M_xO_y, then the atomic ratio of oxygen to metal in the vapor is given by

$$\frac{O}{M} = \frac{\Sigma y P_{M_xO_y}}{\Sigma x P_{M_xO_y}} \tag{17}$$

where P is the partial pressure of the M_xO_y gaseous species.

The oxygen to metal ratio in the metallic phase is defined as the ratio of mole fractions of oxygen and metal. At low concentrations of oxygen, this ratio reduces to the mole fraction X_0 of oxygen in the metal. The ratio R is defined as [11]

Element	Evaporating oxide	T (K)	P_M (atm)	X_0 (sat)	R (low X_0)
Oxygen alloys of 4th group metals					
Si	SiO	1685	$10^{-6.3}$	$10^{-3.7}$	10^{8}
Ge	GeO	1210	10^{-9}	$10^{-2.5}$	$10^{9.5}$
Sn	SnO	1000	10^{-10}	10^{-2}	$10^{6.3}$
Pb	PbO	1000	$10^{-4.8}$	$10^{-3.1}$	$10^{2.6}$
Oxygen alloys of transition metals					
Ti	TiO	1940	$10^{-5.2}$	0.3	1
V	VO	2190	$10^{-4.4}$	0.3	10
Cr	CrO	2171	$10^{-2.2}$	10^{-2}	$10^{0.5}$
Mn	MnO	1516	$10^{-2.8}$	10^{-2}	10^{-4}
Fe	FeO	1810	$10^{-4.5}$	$10^{-2.2}$	$10^{0.4}$
Co	CoO	1765	$10^{-5.1}$	$10^{-2.1}$	10
Ni	NiO, O	1726	$10^{-5.4}$	$10^{-2.1}$	10
Oxygen alloys of refractory metals					
Zr	ZrO	2125	$10^{-7.7}$		10
Nb	NbO	2740	$10^{-5.8}$		10^{3}
Mo	Mo_3O_9, MO_3, MO_2, O	2880	$10^{-4.3}$		10^{6}
Ta	TaO	3250	10^{-5}		10^{5}
W	W_3O_9, WO_3, WO_2, O	3650	10^{-4}		10^{6}

Table 3: Vaporization behavior of selected elements, after Brewer and Rosenblatt (1962).

$$R = \frac{\left(\frac{O}{M}\right)_{vapor}}{\left(\frac{O}{M}\right)_{metal}} \tag{18}$$

If $R > 1$, vaporization of the metal phase will lower the oxygen content of the base metal. Brewer and Rosenblatt [11] state that substantial purification (>50%) will only occur if $R > 10$ since for $R = 10$, vaporization of 10% of the metal results in 50% reduction of oxygen impurity. Their data for various metals is shown in Table 3.

Inspection of Table 3 reveals that the elements Si, Ge, Pb and Sn will undergo high purification by evaporative loss of oxide. However, the second group of metals which are of most interest to SLS (consituents of steel, titanium and alloys) will not undergo substantial deoxidation. Therefore, in order to meet specifications on the chemistry of such alloys while processing by SLS under vacuum or ultrahigh purity inert gas partial pressure environments, it is important to monitor not only the initial chemisty of the feedstock material but also the leak integrity of the processing environment to prevent further contamination. On the other hand, the refractories except Zr all have very high values of R and will thus undergo very good purification.

References

[1] O. Winkler and R. Bakish. *Vacuum Metallurgy*, chapter III. Elsevier, 1971.

[2] A. Block-Bolten and T. W. Eagar. Metal Vaporization from Weld Pools. *Metallurgical Transactions B*, 15B, September 1984.

[3] M. M. Collur, A. Paul, and T. Debroy. Mechanism of Alloying Element Vaporization during Laser Welding. *Metallurgical Transactions B*, 18B:733–740, December 1987.

[4] Robert Bakish. *Introduction to Electron Beam Technology*, chapter 6. Wiley, 1962.

[5] J. Herbertson and R. Harris. Composition Changes in Liquid Metals During E.B. Processing. In R. Bakish, editor, *Electron Beam Melting and Refining-State of the Art 1985*, volume 2, pages 26–38. Bakish Materials Corporation, 1985.

[6] Reinhard Glang. Vacuum Evaporation. In Leon I. Maissel and Reinhard Glang, editors, *Handbook of Thin Film Technology*, chapter 1. McGraw-Hill, 1970.

[7] Saul Dushman. *Scientific Foundations of Vacuum Technique*, chapter 10. Wiley, 2nd edition, 1962.

[8] D. R. Poirier and G. H. Geiger. *Transport Phenomena in Materials Processing*, chapter 15, pages 560–567. TMS, 1994.

[9] Wilson Oxygen. Certificate of Analysis, Helium, Ultra High Purity, July 1996.

[10] *JOM*, pages 12–35. TMS, March 1998.

[11] Leo Brewer and Gerd M. Rosenblatt. Thermodynamics of Suboxide Vaporization. *Transactions of the Metallurgical Society of AIME*, 224:1268–1271, 1962.

On Some Physical Aspects of Process Control in Direct Selective Laser Sintering of Metals—Part III

Suman Das
Department of Mechanical Engineering
University of Michigan
Ann Arbor, MI 48109-2125
USA

4 Surface Tension Driven Instabilities

Surface tension plays an important role in localized melting processes such as welding and direct SLS. For instance, it is well known that the surface tension of pure metals is a decreasing function of temperature. Therefore, temperature gradients in a melt pool can give rise to surface tension gradients and associated Marangoni convection. It is also well known that small amounts of impurity elements can drastically alter the surface tension values and surface tension gradients, changing the direction of flow in the melt pool. Even under isothermal conditions, capillary instabilities are known to occur in the flow of jets, rivulets and planar bodies of fluids. These instabilities result from disturbances giving rise to surface waves whose amplitude can get large enough so that the fluid breaks up into smaller volumes to minimize surface free energy. Two aspects of surface tension driven effects influenced by the scan speed and scan spacing in SLS are addressed with their implications on the geometry of the laser processed and subsequently solidified melt.

To investigate the effect of scan speed on the shape of the solidified melt, single line scan experiments were performed by scanning 0.5 inch long lines on Alloy 625 powder at 80 Watts Nd:YAG laser powder, under high vacuum ($< 10^{-5}$ Torr) and without powder preheat (powder at ambient temperature). The flow and solidification behavior of the melt was captured by video microscopy at 30 frames/s. Testing at a variety of scan speeds confirmed that the flow behavior of the melt was very similar to the jet instability. At high scan speeds, the melt tended to be broken up or "atomized" into a number of droplets, whereas at slower scan speeds, the melted line tended to form regularly spaced beads or undulations whose size grew with decreasing scan speed, eventually tending towards jet break-up at very slow speeds. Figure 1 shows three scan lines Alloy 625. From left to right, the lines were scanned at 1.4 in/s, 0.7 in/s and 0.35 in/s respectively, showing the relative differences in line width, bead geometry and bead frequency as a function of scan speed.

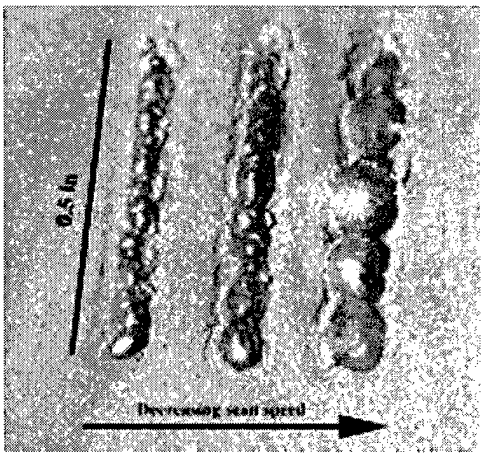


Figure 1: Single line scans on Alloy 625 at 1.4, 0.7 and 0.35 in/s.

Two types of instabilities were observed during raster scanning in SLS of metals. The first type, termed the starting edge instability occurs at the edge where raster scanning is

initiated. The molten material at the starting edge exhibits a tendency to break up or tear into smaller pieces. Under a wide variety of laser processing conditions, the tendency of the melt to break up was noted to attenuate after the first four or 5 lines were scanned. The flow behavior of the starting edge instability is very similar to the behavior of single line scans illustrated in the previous section. The second instability, termed surface instability pertains to the formation of ripples on the surface of a solidified layer. At fixed laser power, scan speed and scan vector length, this instability is strongly attenuated by decreasing the scan spacing.

Single layer raster scan experiments were performed by scanning 0.5 inch long lines at 11.2 in/s on Alloy 625 powder (-325 mesh) at 80 Watts Nd:YAG laser powder, under high vacuum ($< 10^{-5}$ Torr) and without preheating the powder. The flow and solidification behavior of the melt was captured by video microscopy at 30 frames/s. Testing at a variety of scan spacings confirmed that the flow and solidification behavior of the melt was very strongly influenced by the scan spacing. A progressive transition from a highly rippled surface to a very smooth surface occurs with decreasing scan spacing.

Shown in Figure 2 are selected video frames of a single layer raster scanned at 0.005 inches scan spacing. The tendency of the melt produced by the first scanned line to break up is apparent in frame 1. Frame 2 reveals that with progressive scanning, the break at the middle of the starting edge stabilizes and does not propagate. However, the starting edge attains a highly irregular definition, while the trailing edge is well defined. Frame 3 shows the poor surface finish of the entire layer.

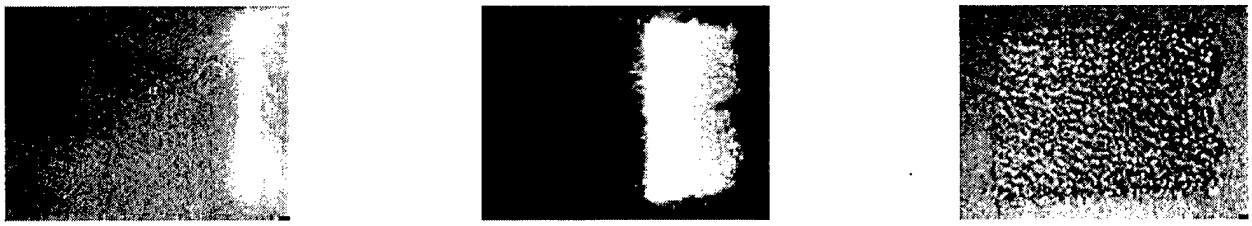


Figure 2: A layer of Alloy 625 scanned at 0.005 inches scan spacing

A raster scan spacing of 0.0005 inches is about the smallest scan spacing available on the scanning apparatus used for these experiments. By inspecting layers scanned with scan spacings ranging from 0.005 to 0.0005 inches, it was clear that while the starting edge instability manifests itself across all cases, as scan spacing decreases, the surface instabilities are damped out resulting in progressively smoother solidified surfaces. The starting edge instability is associated with the short interaction time of the moving laser beam with the powder, causing it to locally melt coupled with the inherent tendency of a liquid stream to break up into smaller pieces. In raster scanning mode, if the time for the laser beam to return to a previously scanned location is longer than the local solidification time, then that portion of the layer has already solidified and possibly substantially cooled below the melt temperature. It has been observed experimentally that the laser beam operating in continuous wave (CW) mode is typically unable to substantially remelt the soldified material. The scan spacings used in the above cases were all smaller than the laser beam diameter (of order 0.020 inches). Therefore, during raster scanning, each point on the scanned surface was

overlapped multiple times by the laser beam, the degree of overlap increasing with decreasing scan spacing.

To qualitatively understand the effect of scan spacing on the temperature history, constant vector length raster scanning can be idealized as an infinite medium moving at a constant speed U past a strip heat source of fixed width equal to the beam diameter at the scan plane. Only pure conduction is considered in this analysis. In SLS, if the scan vector length is l and the scanning speed of the rastering laser beam is v, then the time taken to scan one vector is t_v given by

$$t_v = \frac{l}{d}$$

After scanning a vector, the laser beam is indexed over to the starting position of the next vector by a distance equal to the scan spacing δ. This movement takes place very rapidly and hence the time taken to index the beam is negligible compared to t_v. Therefore, we can assume for all intents and purposes that the total time to index the beam by a distance δ in the transverse direction is t_v. Therefore, the transverse velocity of the idealized moving line source is given by

$$U = \frac{\delta}{t_v}$$

It is readily apparent that for a fixed scanning speed v and fixed scan vector length l (as was maintained in the experiments described above), The transverse speed U is directly proportional to the scan spacing δ. If Q is the heat emitted per unit time per unit area over the strip, the steady state temperature distribution at a point (x, y, z) in the medium for a infinite strip source $-b < x < b$, $-\infty < y < \infty$ in the plane $z = 0$ is given by [1]

$$T(x,y,z) = \frac{Q}{2\pi K}\int_{-b}^{b} e^{-U(x-x')/2\kappa} K_0\left\{U[(x-x')^2+z^2]^{\frac{1}{2}}/2\kappa\right\} dx' \tag{1}$$

where K is the thermal conductivity, κ is the thermal diffusivity and K_0 is the modified Bessel function of the second kind of order 0. By defining the dimensionless variables

$$X = \frac{Ux}{2\kappa}, \qquad Z = \frac{Uz}{2\kappa}, \qquad B = \frac{Ub}{2\kappa} \tag{2}$$

the integral of equation 1 at the surface (z=0) becomes

$$T(x,y,0) = \frac{\kappa Q}{\pi K U}\int_{X-B}^{X+B} e^{-u} K_0\{|u|\} du \tag{3}$$

The generic form of the integral in equation 3 is given by [2]

$$\begin{aligned} I(a) &= \int_0^a e^{-u} K_0\{|u|\} du = a e^{-a}\{K_0(a) - K_1(a)\} + 1, \quad a > 0 \\ &= -\int_0^a e^{u} K_0\{|u|\} du = 1 - a e^{a}\{K_0(a) + K_1(a)\}, \quad a < 0 \end{aligned} \tag{4}$$

where K_0 is as defined before and K_1 is the modified Bessel function of the second kind of order 1.

Therefore, equation 3 can be rewritten as

$$T(x,y,0) = \frac{\kappa Q}{\pi K U}[I(X+B) - I(X-B)] \tag{5}$$

Plots of the steady-state temperature (scaled by $\frac{\pi K}{\kappa Q}$) as a function of strip source location x (scaled by $\frac{1}{b}$) for various values of δ are shown in Figure 3, with each successive value of δ half the previous value, as was selected in the experiments. The instantaneous location of the strip heat source center line is at $x = 0$. As expected, from the plots of Figure 3, it is apparent that the steady state temperature is inversely proportional to scan spacing. Therefore, in the real situation where melting and solidification are taking place in addition to heat conduction, it is expected that scanned regions will remain at higher temperatures for longer times. Thus, it is conceivable that under certain conditions of laser power and scan speed, as scan spacing is decreased, local regions could remain molten (or in the mushy state) during successive passes of the laser (i.e. for a number of contiguous vectors). Thus, increasing the solidification time for a strip like region parallel to the direction of the scanning laser beam, while maintaining uniformity of temperature along its scan length could allow for surface tension driven instabilities in the melt to be damped out, resulting in improved surface flatness or smoothness, as observed experimentally.

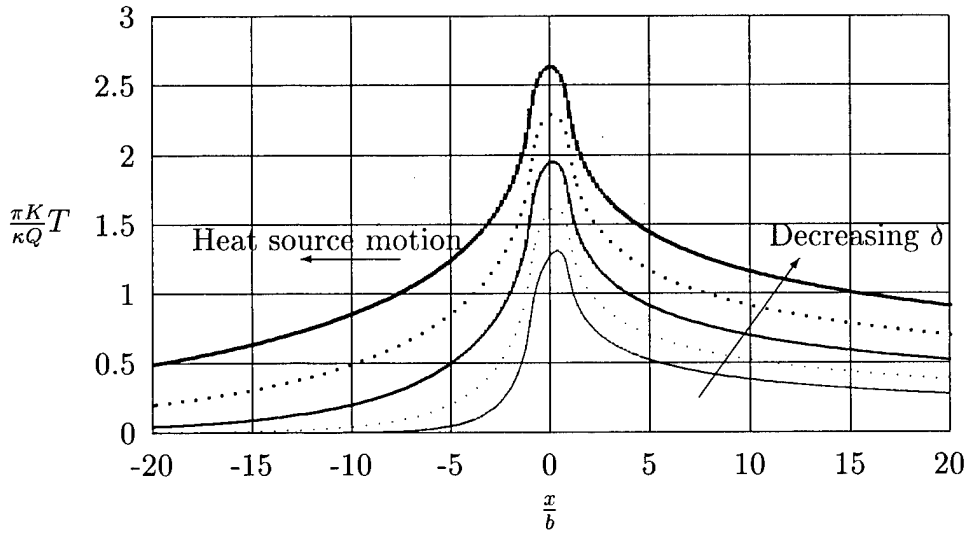


Figure 3: Steady state temperature vs. coordinate for a strip heat source.

One method of eliminating the starting edge instability is to displace the starting edge into the interior of the layer while minimizing the length of the starting scan vectors. In the extreme case, the starting scan vector can be reduced to a point. This technique can be easily applied by starting the scan at the center and tracing concentric patterns of increasing dimension towards the edges. An example of this technique for a circular cross-section is

shown in Figure 4. In this case, the laser starts at the center of the circle and traces an Archimedean spiral. As can be seen in frames 1, there is no balling or beading of the melted and resolidified material. Frames 2 and 3 show not only a flat solidified layer surface but also excellent edge definition at the outward propagating solidification front. In addition to eliminating the starting edge instability, with the absence of abrupt changes in scan direction, this type of scanning ensures that continuity of the solid-liquid interface is maintained at the instantaneous location of the moving laser beam. Maintaining continuity of the moving solid-liquid interface is essential to avoid macro-porosity and other defects in materials processed by direct SLS.

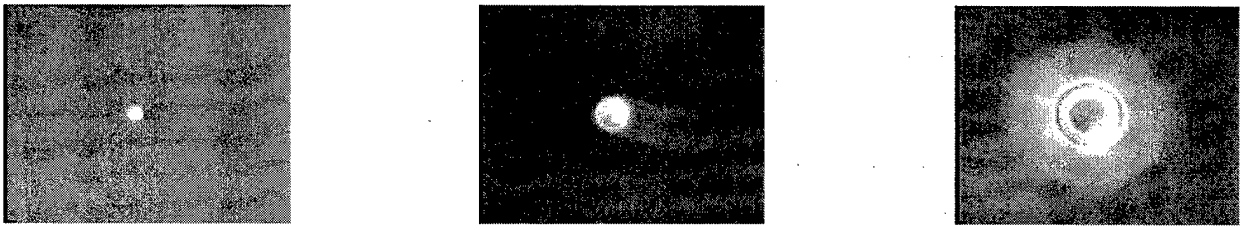


Figure 4: Archimedes spiral, scanned at 0.00125 inches scan spacing

5 Powder Caking

Powder bed caking has been observed while preheating powder during SLS processing. For Alloy 625 and Ti-6Al-4V, 450° C and 350° C respectively were the threshold preheat temperatures at which substantial powder caking was noted to occur. It was also noted that despite Ti-6Al-4V having a 250° C higher melting temperature range and twice the particle size as that of Alloy 625, its tendency was to cake more vigorously. Therefore, a study was undertaken to understand the low temperature (with respect to melting temperature) sintering characteristics of metal powder materials and their effects on powder morphology.

Powder caking is the result of sintering (necking and densification) between adjacent powder particles. Sintering is initiated by thermally activated mass transport between powder particles and is typically observed to consist of three stages, namely initial stage sintering, intermediate stage sintering and final stage sintering.

During initial stage sintering, surface transport and bulk transport are the primary modes of mass transport contributing to necking and densification. In surface transport, surface diffusion and evaporation-condensation are the two most significant mechanisms, while for bulk transport volume diffusion, grain boundary diffusion, plastic flow and viscous flow are the most significant. The distinction between the two primary modes is that surface transport leads to neck formation and neck growth without net volume change (*i.e.* densification), whereas bulk transport results in shrinkage.

German [3] states that surface diffusion dominates low temperature sintering in many metals. For bulk transport, he states that plastic flow is important for sintering of compacted powders with high dislocation density while viscous flow must be considered when a liquid phase appears at the grain boundaries. It is also stated that grain boundary diffusion is quite

important in the densification of most crystaline materials. In view of the above arguments, only surface diffusion, volume diffusion and grain boundary diffusion were considered for the investigation of low temperature sintering to explain the caking behavior of loosely packed preheated powders in SLS.

To study powder caking as a result of powder preheat in SLS, we restrict ourselves to initial stage sintering. The general equation for initial stage sintering (final fractional density $< 70\%$) is given by [3]

$$\left(\frac{X}{D}\right)^n = \frac{Bt}{D^m} \tag{6}$$

where X is the neck diameter, D is the powder particle diameter, B is a parameter governed by the dominant sintering mechanisms, t is the time and the exponents n and m are also determined by the specific sintering mechanisms. Equation 6 is generally valid for the range $0 \leq \frac{X}{D} \leq 0.3$. The form of the parameter B and its dependence on material properties for each of these mechanisms is listed by German [3]. The forms of the parameters B, m and n for volume diffusion, grain boundary diffusion and surface diffusion are shown in Table 1, where γ is the surface energy, D_v, D_b and D_s are the temperature dependent (Arrhenius form) diffusion constants for volume, grain boundary and surface diffusion respectively, Ω is the atomic volume, δ is the grain boundary width, k is Boltzmann's constant and T is the temperature.

Mechanism	n	m	B
Lattice (volume) diffusion	5	3	$80D_v\gamma\Omega/(kT)$
Grain boundary diffusion	6	4	$20\delta D_b\gamma\Omega/(kT)$
Surface diffusion	7	4	$56D_s\gamma\Omega^{4/3}/(kT)$

Table 1: Sintering parameters for volume, grain boundary and surface diffusion.

Initial stage sintering curves incorporating the cumulative effect of mechanisms in Table 1 for titanium (α and β), nickel, MARM200 (a nickel base superalloy) and stainless steel 304L are shown in Figure 5 for 300° C. Several sintering characteristics are readily discernible from these graphs. At the same particle size and temperature, the alloys (MARM200 and SS304L) show lesser sintering activity than the pure elements. At 300° C and 0.5 hours, the neck radius exceeds 5% and 2% of the particle diameter for the pure elements and the alloys respectively. At 450° C at 0.5 hours, the neck radius for pure elements is more than about 18% of the particle diameter for the elements and approaching 10% for the alloys. The sintering activity rises dramatically at 600° C such that at 0.1 hours, the sintering curves for the elements are out of the range of validity of equation 6.

These results explain the caking behavior as a result of preheat observed for Alloy 625 and Ti-6Al-4V. It is expected that the caking behavior of Alloy 625 (a nickel base superalloy) will be similar to that of MARM200 while the caking behavior of Ti-6Al-4V (an $\alpha - \beta$ alloy) will lie between that of α titanium and β titanium. Powder caking due to preheat is highly undesirable in SLS. For successful delivery and laser consolidation of powder layers, it is vitally important to maintain free flowing characteristics of the feedstock powder. The initial stage isothermal sintering model predicts that significant inter-particle necking and

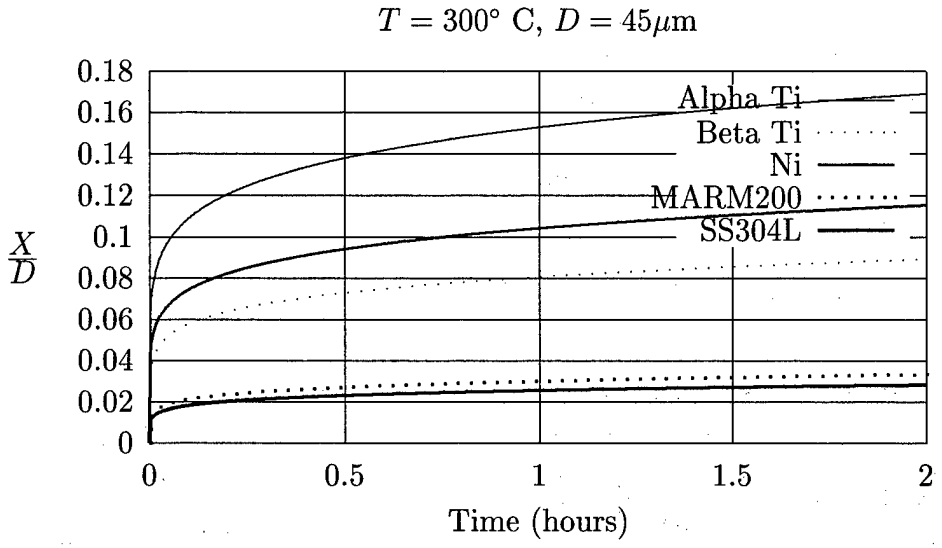


Figure 5: Neck diameter vs. time at 300° C.

associated powder caking will occur at preheat temperatures as low as 300° C. Therefore, preheat at lower temperatures (100° C to 200° C) could be used for *in situ* dynamic degassing of adsorbed contaminants from feedstock powder while being able to avoid caking. However, tremendous cost benefits are achievable by eliminating the need for a heating system in a SLS machine. The ability to fabricate full density components by SLS without any external powder bed preheat has been demonstrated for Ti-6Al-4V [?] and is expected for other materials as well. A heaterless SLS machine for metals will require having an off-line powder degas apparatus with appropriate "clean handling" procedures to transfer degassed powder to the SLS chamber without contamination or exposure to air. The advantages of having such a combination far outweigh the advantages of having an integral low temperature heating system in the HTW.

6 Conclusions

An understanding of some of the important physical mechanisms in SLS processing of metals was achieved. This understanding is crucial to machine design and process control development. The following conclusions can be made with respect to successful direct SLS processing of metals.

1. Processing atmosphere control using high vacuum or low oxygen partial pressure ultrapure environment is necessary to prevent surface contamination, poor wetting and internal oxidation.

2. Poor wetting can occur even with good atmosphere control. The mechanism for "good wetting" in direct SLS of metals is epitaxial solidification by heterogeneous nucleation.

In order to obtain full density, partially remelting previously formed, underlying layers is necessary to induce epitaxial solidification.

3. SLS processing under vacuum results in volatilization of alloying elements to due reduction of vaporization temperatures. Volatilization and subsequent condensation on the laser window causes inconsistent laser energy delivery while condensation on chamber internal surfaces can potentially contaminate other materials processed subsequently. Partial pressure processing with a continuous flow of ultra-pure inert gas increases the vaporization temperature, reduces the mean free path, alleviates elemental volatilization and flushes away volatilized material from the processing zone.

4. Surface tension driven instabilities in raster scanning occur at the starting edge and on the processed surface. In raster scanning, the starting edge instability persists while surface instabilities are alleviated by using a fine scan spacing. Both instabilities can be eliminated by starting the scan at a point and progressing outward in a continuous path to fill the area to be consolidated.

5. Preheating metal powders at low to moderate temperatures leads to solid state sintering, caking and poor powder flow. Preheating and associated caking are detrimental to SLS processing and are not recommended.

References

[1] H. S. Carslaw and J. C. Jaeger. *Conduction of Heat in Solids*, chapter X, page 267. Oxford University Press, Inc., 1959.

[2] J. C. Jaeger. Moving Sources of Heat and Temperature at Sliding Contacts. *Proceedings of the Royal Society of New South Wales*, 76:203–224, 1943.

[3] Randall M. German. *Powder Metallurgy Science*, chapter 7. MPIF, 1994.

NEW WAY OF PROCESS PARAMETERS OPTIMIZATION IN SFF BASED ON DEPOSITION BY WELDING

Z. Jandric and R. Kovacevic
Research Center for Advanced Manufacturing (RCAM), Southern Methodist University
1500 International Pkwy. Suite 100, Richardson, TX 75081

Abstract

To successfully control the welding process and to make it appropriate for solid freeform fabrication (SFF), it is necessary to fully understand the influence of the welding parameters and the geometry of the substrate on the resulting weld bead dimensions. Extensive experiments with different welding parameters and complex geometrical features such as edges and corners have been designed and completed. The experimental data show a clear correlation between the heat input, the weld bead dimensions, and the two dimensional (2D) geometrical features. This correlation may be used for on-line welding process control. It is found that the geometry of the molten pool is directly related to the heat transfer conditions determined by surrounding mass of material. A machine vision system based on a high-resolution CCD camera coaxially integrated with a gas tungsten arc welding (GTAW) torch is used to acquire the images of the molten pool. The results demonstrate the capability to adjust GTAW process parameters according to complex external and internal geometrical features of the substrate. The heat loss affected by the surrounding mass of material will be used to determine the optimal energy input.

Introduction

In the last decade, it has been shown that solid freeform fabrication (SFF) through layered material deposition is an attractive method for 3D-object generation. Common to all layered forming techniques is the incremental nature of the material build up. The quality of each deposited layer as well as the quality of the bond between the layers determines the quality of a built part [1]. The goal of any SFF technique is the fast construction of precise parts directly from CAD drawings, or as it is often called "from computer to component" process. While most of the SFF systems still make parts from non-metallic materials, not specified by the designer of the parts, SFF based on deposition by welding overcomes this disadvantage. Several research-teams [1 – 8] have shown that this technique is capable of making diverse part shapes. Spencer et al. made a vertical wall and a hollow box. Ribeiro et al. made a 'chimney' shape, a 'bow tie' shape, and a 'pint glass' shape. Kovacevic et al. also made a thin vertical wall, cylinders, cubical 3D parts with straight channels, a 3D part with complex geometry and a 3D network of the conformal channels.

Relatively small changes to the welding parameters dramatically influence welding quality during the building of 3D parts by welding. So, an intelligent control system that controls the process parameters has to be developed. There are a number of parameters in GTAW which have a significant impact on the weld (i.e. bead) quality, such as: filler metal feeding speed, welding current, arc voltage, welding speed, shielding gas flow rate, electrode to substrate angle, type of shielding gas, shape of the tungsten electrode etc. Also, it should be noted that some of these parameters are non-linear and have transient-dependent and temperature-dependent

natures. In recent years statistical design for experiments, linear regression modeling, neural network, etc. have been used to model the effects of the welding process parameters on the weld bead geometry, and it has been shown that a strong correlation between them exists [9-11].

The goals in welding based SFF are significantly different than those in metal joining. During normal welding, large depths of penetration and/or fast material deposition are desirable [12]. Some of the usual goals in the SFF based on deposition by welding are to keep the heat input as low as possible, to control the heat input in the real time, to have a small depth of penetration, to maintain uniform bead build-up, etc. Additionally, when the weld bead is deposited in the vicinity of sharp corners, heat input should be significantly lower, since the heat sink, determined by the surrounding mass of the material, is small [13]. If the heat input do not follow the conditions driven by the part geometry, unnecessary melting of already-deposited material will occur. In welding handbooks, one can find how welding parameters are related to the weld bead geometry, but all those data are intended for normal welding and can not be successfully applied to the SFF based on deposition by welding.

In this paper, extensive experiments with different welding parameters and complex geometrical features, such as edges and corners, have been designed and completed. From the experimental results, it can be observed that the heat-affected zone depends on the geometry of the substrate. In order to show the influence of the geometry on the heat transfer conditions in the vicinity of the molten pool, a new parameter called the geometrical factor is introduced. A machine vision system, based on a high-resolution CCD camera coaxially integrated into a GTAW torch, is capable of acquiring images of the molten pool in real time. A newly-developed controller uses the geometrical factor to determine the status of the mass of material around the molten pool.

Background

The SFF based on deposition by welding (SFF – DBW) under development at Southern Methodist University is a hybrid technique – a combination of welding and cutting. The whole process of making the 3D part can be considered as relatively slow. However, if the welding parameters could be optimized, than the surface of each deposited layer would be smooth enough and many, if not all, of the layers could be deposited without introducing the milling operation, and the major disadvantage of this process could be eliminated.

To produce a flat surfaces using a dynamic process, such as GTAW, welding parameter control must be introduced. Two kind of controls can be implemented here: open-loop and closed-loop control. When closed-loop control is used, it is necessary to have an experimental database for comparing the feedback value with the optimal one. According to their difference, a controller should then react accordingly. When open-loop control is used, one should know in advance what are the most appropriate process parameters at each point (again according to a suitable database).

All of experimental data that could be found in the welding handbook [12] and in published papers are obtained by performing the experiments over a semi-infinite solid. In the semi-infinite solid (Fig.

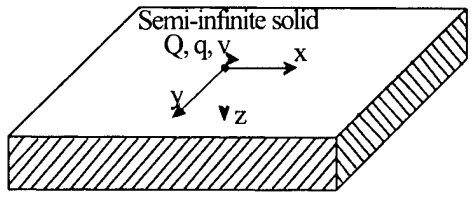


Fig 1. Schematic presentation of semi-infinite solid

1), the heat is propagating isotropically, since heat transfer conditions are constant during the welding. However, the building of 3D parts by welding is characterized by non-uniform heat transfer conditions (welding along edges, corners, thin substrates, etc.). It is evident that these conditions will require a new effort to form a database of optimal welding parameters as a function of the geometry of the substrate.

Experimental Set-up

The experimental set-up of the gas tungsten arc welding process with the addition of filler metal is shown in Fig. 2. A non-consumable tungsten electrode, shielded by the inert gas (pure argon in this case) is used to strike an electric arc with a substrate. Heat generated by the electric arc is used to melt the substrate (or workpiece) and the filler metal. Filler metal is fed directly into the molten pool. Step motor (1) is used to ensure that the wire is always fed in front of the moving arc. Step motor (2) is used to control the filler metal feeding speed. A PC-based data acquisition system synchronizes the control of the step motors with a CNC machine controller, which provides precise motion of the workpiece in the X-Y plane. A machine vision system based on a high-resolution CCD camera is coaxially integrated with a GTAW torch (Fig. 3) which is capable of acquiring the images of the molten pool in real-time.

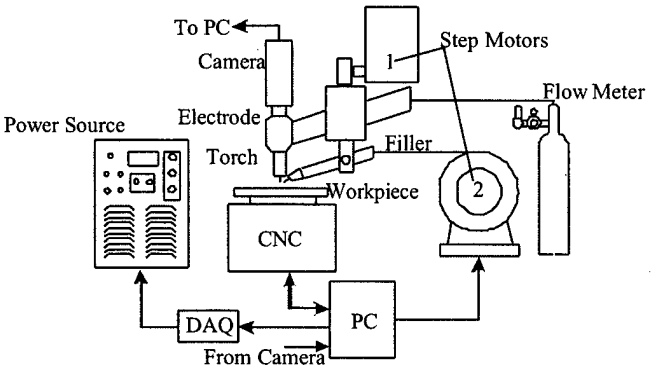


Fig. 2 Experimental set-up for GTAW

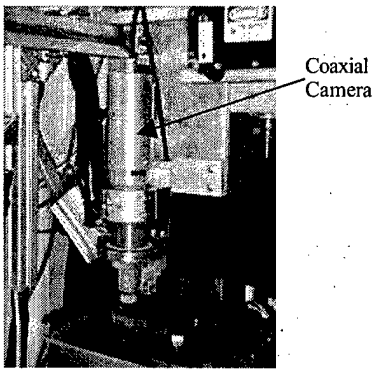
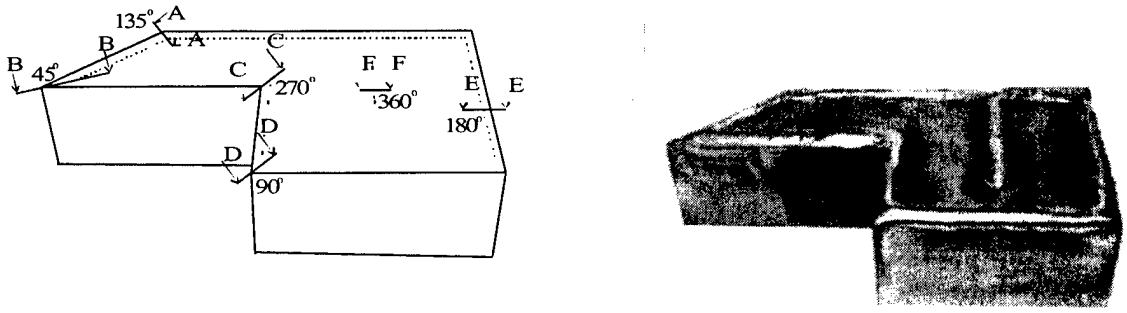


Fig. 3 Coaxially integrated camera with torch

Experimental Procedure

In order to simulate different heat transfer conditions during the deposition by welding, a workpiece as a substrate is designed with different 2D geometrical features, as shown in Fig. 4. The weld beads placed along the boundary of substrate, Fig. 4b, simulate different heat sinks, from 100% for the bead placed at the flat top surface (360°) down to 12.5% for the bead placed at the 45° corner. It is evident that the welding parameters have to be controlled in order to achieve uniform weld bead geometry under different heat sink conditions.

The heat source has finite dimensions that cannot be neglected, so the distance between the edge and the electrode should be approximately half of the heat source width, which changes with the heat input [15]. In order to provide uniform heat transfer conditions during the experiment, the



a) Schematic presentation *b) after experiment*

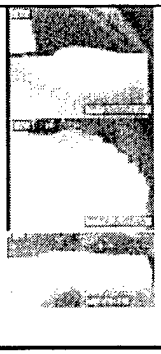
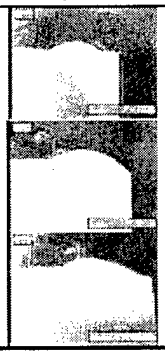
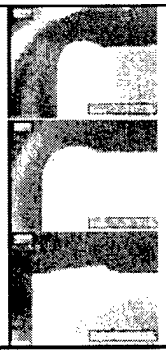
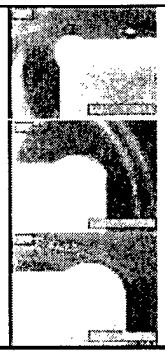
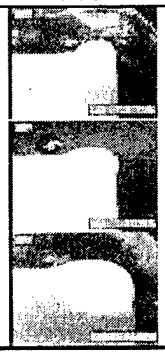
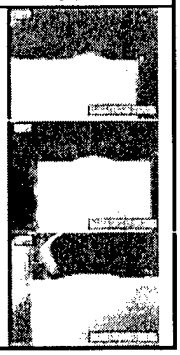
Fig. 4 The shape of workpiece

workpiece is first preheated. Experience and experimental results [14] showed that the welding current and the wire feeding speed have the largest influence on the quality of the bead. Nine experiments are performed in order to analyze the affect of the welding current, the wire feeding speed, and the geometry of the substrate on the weld bead geometry. Mild steel welding wire with a diameter of 0.9 mm is used. The welding current is changed from 80 A to 160 A, with increments of 40 A. The wire feeding speed is changed from 40 cm/min to 120 cm/min, with increments of 40 cm/min.

Experimental Results

Table 1 presents some of the experimentally obtained results. After weld beads are applied under different welding conditions, workpieces are cross-cut along the lines A-A, B-B, C-C, D-D, E-E and F-F (see Fig. 4a) in order to obtain information about the weld bead geometry. After polishing and etching the cross-sections, bead widths are measured and their relationships with respect to the welding parameters and geometrical factor are presented in Figs. 6a, 6b and 6c.

Table 1. The bead cross-sections

I[A]/ v_f [cm/min]	Angle of bead location					
	45°	90°	135°	180°	270	360°
80/40						
120/40						
160/40						

Experimental data are approximated with the linear functions. Each line corresponds to the bead location, such as: 45°, 90°, 135°, 180°, 270° and 360° from top-to-bottom, respectively. Increasing the welding current, while wire-feeding speed is kept constant enlarges the bead

width. Also, it can be noticed that the reduction in the angle also contributes to the increase in the bead width.

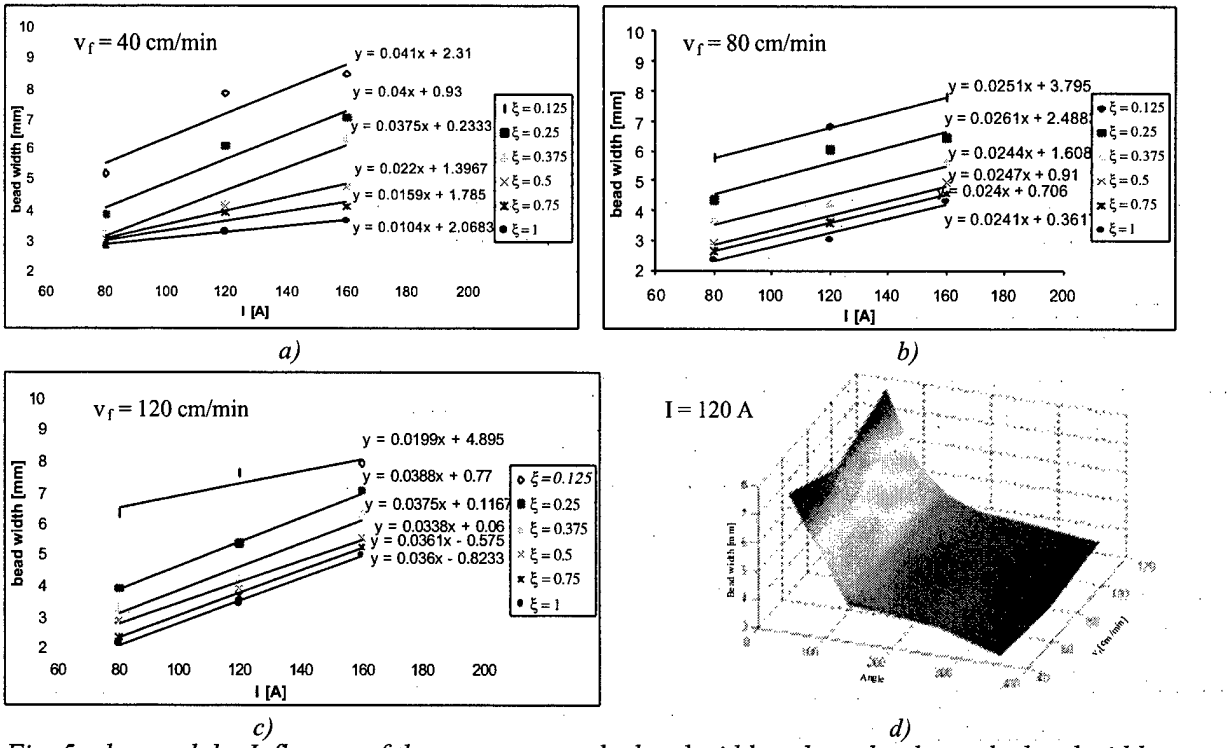


Fig. 5a, b, c and d – Influence of the geometry on the bead width. a, b, and c shows the bead width vs. current for three different wire feed speeds and for six different bead locations, d shows the change of the bead width when the wire feeding sped and heat sink are changed

In order to better demonstrate the influence of the geometry of substrate on the bead width, all the experimental data obtained for an unique welding current of 120 A is presented in a three-dimensional manner (Fig. 6d). How significant this influence is can be seen if a single curve of bead width vs. angle is observed while wire feeding is kept constant. The reduction in the angle of the corner means that less surrounding material in the vicinity of the molten pool exists. By changing the angle from 360° to 45° the bead width is increased more than twice. So, an accurate model of GTAW has to take this influence into account. An outcome of this analysis is the off-line heat input planning model.

Off-line Planning and On-line Control of Heat Input

Experimental results proved that local substrate geometry, i.e. vicinity of the molten pool, has the greatest impact on the bead dimensions. Since the geometry of the part to be built is known in advance, the amount of the material around an arbitrary point could be calculated. If that calculated value is provided to the controller, the heat input can be appropriately adjusted. Basically, this is the idea behind the developed off-line planning model.

In order to define the '*local geometry*', the 3D-part geometry and the net heat energy delivered to the workpiece are analyzed. Net heat energy is divided into three portions. A portion of the energy is used to melt the workpiece, the second portion is used for melting the feeding wire, and

the third portion is lost to the adjacent base metal outside of the melting zone, primarily by thermal conduction. The energy lost to the base metal outside the fusion zone contributes to the formation of the heat-affected zone and to the heating of the rest of the base metal. It can be observed from the experimental results that the heat-affected zone also depends on the geometry of the substrate. Logically, when the heat input is kept constant, the greater the amount of the surrounding material, the smaller will be the heat-affected zone. The goal here is to deposit material with a constant bead height and with a uniform heat affected zone. This could be achieved by adjusting the welding parameters (mostly current) in real-time.

Heat input is the relative measure of the energy transferred per unit length of weld [14]. Typically it is calculated as the ratio of the power to the velocity of the moving heat source as follows:

$$H = \frac{60EI}{1000 \cdot S} \tag{1}$$

where, H = heat input [kJ/mm], E = arc voltage [V], I = current [A] and S = travel speed [mm/sec]. During the experiment, the arc voltage and the welding speed are kept constant, so the heat input, and therefore heat affected zone, depend only on the current. To establish the relationship between the heat input and the part geometry, the '*geometrical factor*' ξ_G is introduced.

In order to define the geometrical factor, ξ_G, the 3D part should be represented by the 3D matrix which is generated according to the coordinates of the exterior points of the 3D solid-model. The 3D matrix consists of ones and zeros; the ones represent solid voxels and zeros represent empty voxels in the scope of the 3D solid part. The matrix is defined with the 'matrix resolution', which is the number of points per unit length. It is determined that 100 points per one inch (25.4mm) provides satisfactory results. Since all of these calculations are performed off-line, much higher resolutions can be used.

Next, the shape and the size of the heat affected zone have to be determined. It is found theoretically [15] and experimentally (Table 1) that the shape of the heat affected zone can be approximated as a half-sphere, whose radius was found experimentally to be approximately 3 mm.

The geometrical factor can be defined as:

$$\xi_G = \frac{V}{V_{max}} \tag{2}$$

where, V_{max} represents maximum possible number of 'ones' in the half-sphere and V is the counted number of 'ones' within the same volume. The center of the half-sphere is the point for which the welding current should be determined. So, the geometrical factor multiplied by 100 gives the percentage of the surrounding mass of the material in the vicinity of the molten pool. The accuracy of the calculated geometrical factor depends on the chosen 'matrix resolution'.

Once the geometrical factor is determined, the welding current can be selected from the experimental data-base. The results presented at Fig. 5 are particularly useful for this application. The relationship between the bead width and the welding current is approximated with the linear function. Each linear function is defined with its coefficients k and n ($y = kx + n$) and their values are given in Figs. 5a, b and c.

Combinations of Two Controllers

A number of published results [15-19] showed that monitoring the size of the molten pool is a valuable source of information in welding. The reason why it can not be used as the sole feedback variable in SFF by welding could be demonstrated in the example shown in Fig. 6. From Fig. 6 it can be seen that welding over the channels demands three different welding-currents values in time. In the zone I, the maximal current value, I_{max}, should be applied in order to provide enough energy to melt the feeding wire and substrate. In the zone II, the heat input is coming close to the channel's edge. The reduction in the surrounding mass of the material necessitates a reduction in the energy needed for melting the substrate. In the zone III, the heat input is located above the channel, where the thin sheet metal is placed, and only energy for melting feeding wire is needed such that I_{min} must be used. It should be noticed that decreasing the current from I^* to I_{min} has to be done instantaneously in order to avoid burning-through the thin sheet metal. The monitoring of the shape of the molten pool in the condition where the mass of surrounding material around the molten pool is changed abruptly will not be useful for the feedback control. However, it is shown that monitoring the molten pool under conditions of more uniform change of the surrounding mass of material around the molten pool could be successfully used as a feedback in the control of the uniformity of the bead height. The welding process is highly dynamic and depends on the many transient and temperature dependent parameters that are difficult to predict. These parameters are considerably less influential than the part geometry, but they still affect the quality of the bead. So, the need for an additional 'independent' controller that will provide more uniform quality of deposition by welding is necessary. Fig. 7 shows the images of the molten pool obtained for the constant welding current and constant wire feeding speed, but still, the size as well as the shape of the molten pool fluctuates significantly.

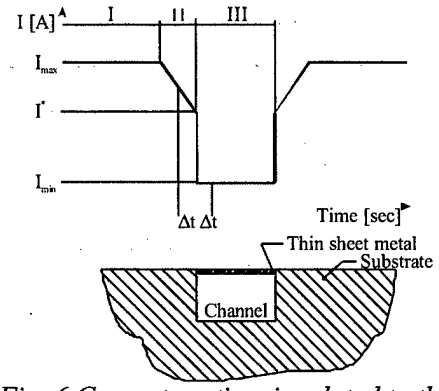
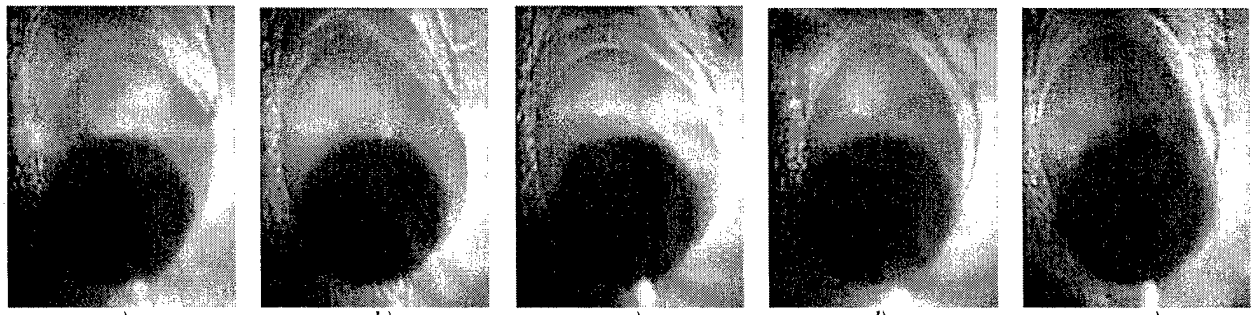


Fig. 6 Current vs. time is related to the part geometry



a) *b)* *c)* *d)* *e)*

Fig. 7 Images of the fluctuating molten pool obtained for the same welding parameters

Architecture of the developed controller to control welding current for SFF - DBW is showed in Fig. 8. Before the controller updates the welding current, data about the heat transfer conditions in the vicinity of the molten pool has to be provided, and this information is inherent in the value of the geometrical factor. Each time the calculated geometrical factor is referenced (Fig. 8). From the definition of the geometrical factor it follows that, if the geometrical factor is less than one, the selection of the corresponding welding current has to be made off-line. If it is one, monitoring of the size of the molten pool by machine vision is used to control the uniformity of the bead height. Overall performance of the designed control strategy is shown in Fig. 9, where welding current vs. time, and voltage vs. time diagrams are presented.

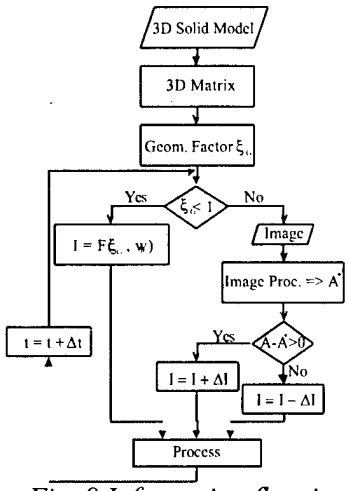


Fig. 8 Information flow in the designed controller

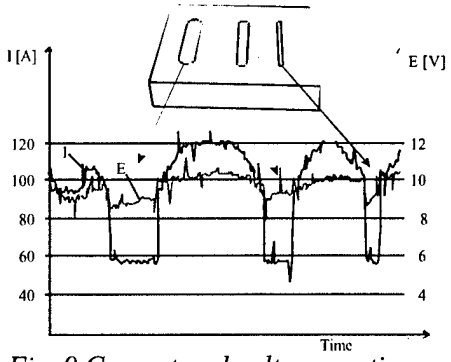
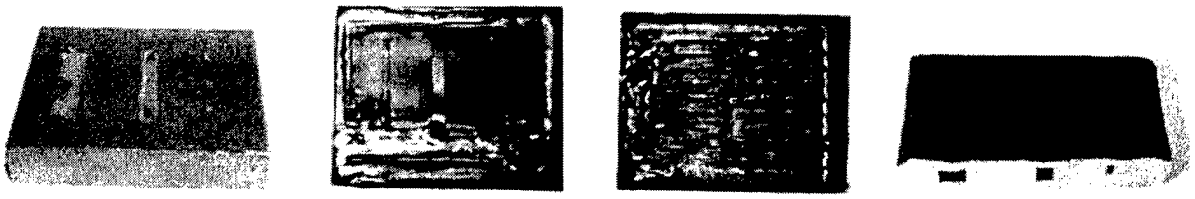


Fig. 9 Current and voltage vs. time

The verification of the designed controller is performed on the samples shown in Fig. 10. Three grooves with different widths (6.5 mm, 3.8 mm, and 1.7 mm) are milled in the block of mild steel with sizes of 63.8 mm × 50.6 mm × 12.7 mm. The depth of the grooves is 7.8 mm. The grooves are filled up with casting sand and covered with 1mm thick steel sheet metal. The goal is to make a build up of material over the top surface of this sample by depositing material in the form of layers by SFF – DBW. In the case of welding without a controller or any pre-selected welding parameters will generate excessive heat and the thin sheet metal covers will burn through, as it is shown in the Fig. 10b. Fig. 10c shows the results of the build up in the case when the selection of the welding current is done in advance based on the geometry, along the torch path. The burn-through is avoided but the uniformity of the build-up layer is not achieved. Fig. 10d shows the results of the control strategy shown in Fig. 8. In the case when the geometrical factor along the torch path is less than one, the welding current is selected in advance. However,



a) *b)* *c)* *d)*

Fig. 10 Weld deposition over the channels

if this factor is equal to one, then the welding current will be selected on-line based on the area of the molten pool obtained in real-time by incorporated machine vision. The outcome of this control strategy is a very uniform height of built layer over the channels. The same strategy will be applied to the building of a layer with specified external and internal boundaries of material which are deposited by welding. The results of building a part consisting of very sharp corners are shown in Fig. 11.

Building a Test Part

The controller is challenged with depositing filler metal over a complex geometry (Fig. 11). A 3D part with sharp corners is successfully built. Building this part can be divided into several stages: a) making 3D solid model, Fig. 11a, b) slicing it, Fig. 11b, c) automatically generating G-code for the planned torch path Fig. 11c, d) depositing material along the external boundary of the layer where the welding current is selected in advance based on the value of the geometrical factor along the torch path, Fig. 11d, e) depositing material inside of the border contour, therby activating the machine vision system that will feed the data into the controller for selecting the welding current in real time, Fig. 11e, f) final shape of the part after end and face milling is done, Fig. 10f.

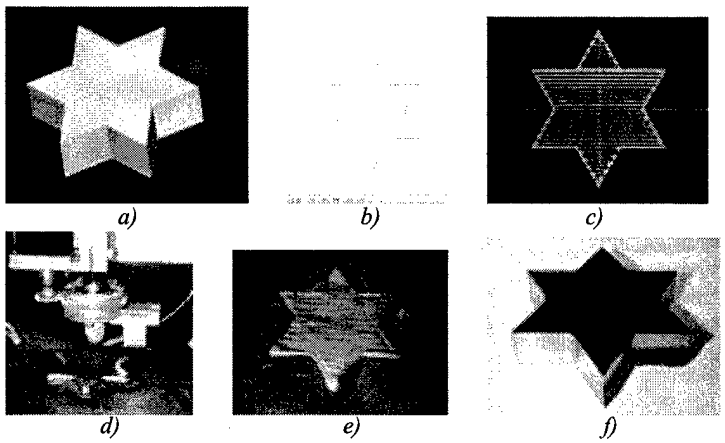


Fig. 11. Building a Test Part

Conclusion

Extensive experiments with different welding parameters and complex geometrical features such as edges, corners, and channels have been designed and completed, and an experimental database has been created. A new parameter, named the geometrical factor, is introduced, that reflects on the local geometry of the substrate. A machine vision system based on a high-resolution CCD camera which is integrated into the GTAW torch is used for monitoring the size of the molten pool. The heat input controller is developed and tested. The controller is characterized by two branches. The off-line control branch is activated when the torch is following the external and the internal boundaries of the layer. In that case, the welding current is specified in advance based on the known shape layer boundary. The other branch of the controller, the on-line branch, is activated during the filling of the surface surrounded by the external and the internal boundaries. In this case, the shape of molten pool captured by the machine vision system is used as feedback for selecting the corresponding welding current.

Acknowledgment

This work was financially supported by THECB, Grant N$_o$. 003613-0022001999, NSF, Grants N$_o$. DMI – 9732848 and DMI – 9809198, and the U.S. Department of Education, Grant N$_o$. P200A-80806-98.

References

(1) Spencer, J.D., Dickens, P.M., and Wykes, C.M., (1998). Rapid prototyping of metal parts by three-dimensional welding, *ImechE Proc. Part B, Journal of Engineering Manufacture*, Vol. 212, pp. 175-182.

(2) Dickens, P., Cobb, R., Gibbson, I., and Pridham, M., (1993). Rapid Prototyping Using 3D Welding, *Journal of Design and Manufacturing*, Vol. 3, No. 1, March, pp. 39-44.

(3) Merz, R., Prinz, F., Ramaswami, K., Terk, M., and Weiss, L., (1994). Shape Deposition Manufacturing, *Proceedings of the Solid Freeform Fabrication Symposium*, University of Texas, Austin, Texas, August 8-10.

(4) Karunakaran, K., Shanmuganathan, P., Roth-Koch, S., and Koch, K., Direct Rapid Prototyping Tools, *Proc. of the SFF Symposium*, University of Texas, Austin, TX, August 1998, pp. 105-112.

(5) Ribeiro, A. F. M., Norrish, J., (1996). Rapid Prototyping Process using Metal Directly, *Proceedings of Solid Freeform Fabrication, Symposium*, 12-14 August, Austin, pp. 249-256, ISSN 1053-2153.

(6) Kovacevic, R., (2001). Rapid Manufacturing of Functional Parts Based on Deposition by Welding and 3D Layer Cladding, *Proc. of the MoldMaking Conference*, April 3-5, Rosemont, IL, presented by the MoldMaking Technology Magazine, pp. 263-276.

(7) Kmecko, I., Hu, D., and Kovacevic, R., (1999). Controlling Heat Input, Spatter and Weld Penetration in GMA Welding for Solid Freeform Fabrication, *Proceedings of the 10th Solid Freeform Fabrication, Symposium*, August, Austin.

(8) Kmecko, I.S., Kovacevic, R., and Jandric, Z., (2000). Machine Vision Based Control of Gas Tungsten Arc Welding for Rapid Prototyping, *Proceeding of the 11th Solid Freeform Fabrication, Symposium*, August, pp. 578-584.

(9) Starling, M.D., Marques, V., and Modenesi, J., (1995). Statistical modeling of narrow gap gas tungsten arc welding with magnetic arc oscilation, *Journal of Material Processing*, 51, pp. 37-49.

(10) Zeng, X.M., Lucas, J., and Fang, M.T.C., (1993). Use of neural networks for parameter prediction and quality inspection in tungsten inert gas welding, *Transaction of the Institute of Measurement and Control*, 15(2), pp. 87-95.

(11) Million, K., Datta, R., Zimmermann, H., (1986). Method of manufacture of a design piece by form creating deposition welding and a design piece manufactured by this method, *European Patent Office*, Publication number: 0 172 309 A1.

(12) Welding Handbook – Part 1, eighth edition, volume 2, American Welding Society, Miami, 1996.

(13) Radaj, D., (1992). Heat Effects of Welding – Temperature Field, Residual Stress, Distortion, *Springer-Verlag Berlin Heidelberg*, printed in the USA.

(14) Scot, R., (1999) A Look at Heat Input, *Welding Innovation*, Vol. XVI, No. 1, pp. 8-11.

(15) Kovacevic, R., Zhang, Y.M., (1995) Real-Time Image Processing for Monitoring of Free Weld Pool Surface, *Journal of Manufacturing Science and Engineering*, Vol. 119, pp. 161-169.

(16) Kovacevic, R., Zhang, Y.M., Ruan, S., (1995). Sensing and Control of Weld Pool Geometry for Automated GTA Welding, *Transaction of the ASME*, Vol. 117, pp. 210-222.

(17) Richardson, R.W., Gutow, D.A., Anderson, R.A. and Farson, D.F., (1984). Coaxial Arc Weld Pool Viewing for Process Monitoring and Control, *Welding Journal*, March 1984, pp. 43-51.

(18) Brzakovic, D., Khani, D.T., Awad, B., (1992). A Vision System for Monitoring Weld Pool, *Proceedings of the 1992 IEEE, International Conference on Robotics and Automation*, Nice, France, May, 1992, pp. 1609-1614.

(19) Chen, S.B., Lou, Y.J., Wu, L., Zhao, D.B., (2000). Intelligent Methodology for Sensing, Modeling and Control of Pulsed GTAW: Part I – Bead-on-Plate Welding. *Welding Research Supplement*, June 2000, pp. 151-s, 163-s.

CONTROLLED-DEPTH LASER CUTTING OF ALUMINUM SHEET FOR LAMINATED OBJECT MANUFACTURING

Gene Zak and Matthew Shiu

Centre for Automotive Materials and Manufacturing
Department of Mechanical Engineering, Queen's University, Kingston, ON, Canada K7L 3N6

Abstract

Replacing paper with metal in laminated object manufacturing would bring improvements in terms of part's longevity, and its mechanical and thermal properties. In fabricating laminated parts, a challenging step is blind cutting of the metal sheet. Challenges to overcome are (1) maintaining consistent depth of cut, (2) achieving good surface quality of the cut groove walls, and (3) minimizing the formation of recast. Results are presented of an experimental investigation into controlled-depth laser cutting of aluminum sheet. Thin (0.12-mm) aluminum sheet specimens were cut with a 10-W Nd:YLF laser while varying scan speed and laser power. To accurately observe the cut profiles, specimens were mounted in resin and sectioned. Special handling procedure was developed to handle thin sheet material while avoiding damage. Relationship between cut profile and process parameters was established and shown to conform to established theoretical models.

Introduction

Using laminations (i.e., material in sheet form) for layered manufacturing (LM) avoids phase transformations with attendant shrinkage (e.g., in powder sintering) and allows easy process scale-up. Number of researchers have explored this approach to fabrication of functional parts. Adams et al. [1] produced working tools from steel laminations 1-3 mm thick, but had resort to a finishing milling step to achieve acceptable surface quality. Himmer et al. [2] proposed to fabricate injection moulds by (1) joining flux-coated 2.5-mm-gauge aluminum through heat treatment near the flux melting temperature and (2) finish milling. Walczyk and Dolar [3] present results of tests on several epoxy and alumina-based adhesives used to bond aluminum laminations. All of these papers adopt the "cut-stack-bond" approach (Fig. 1a), meaning the process sequence is (1) cut out the desired part's profile at each layer's height; (2) assemble (stack) the profiles, and (3) bond them (mechanically with fasteners, adhesively, or by welding). The main disadvantage of the "cut-stack-bond" approach is the complexity of handling the cut-out profiles between the cutting and stacking steps, requiring indexing, transporting, and alignment. This complexity makes *automation* of the process highly impractical.

An alternative approach exists which is more amenable to automation. It is characterized by a "stack-bond-cut" sequence (Fig. 1b). This method has been applied in a commercial LM process, Laminated Object Manufacturing (LOM), but the sheet materials have been limited to paper or polymers [4]. Replacing soft materials with metals is a challenge, however, due to difficulties with "blind" cutting of metals (i.e., cutting only to the depth of the sheet's gauge).

This paper presents results of experimental investigation into controlled-depth blind laser cutting of aluminum sheet. Before presenting these results, background information on laser-machining of metals is provided.

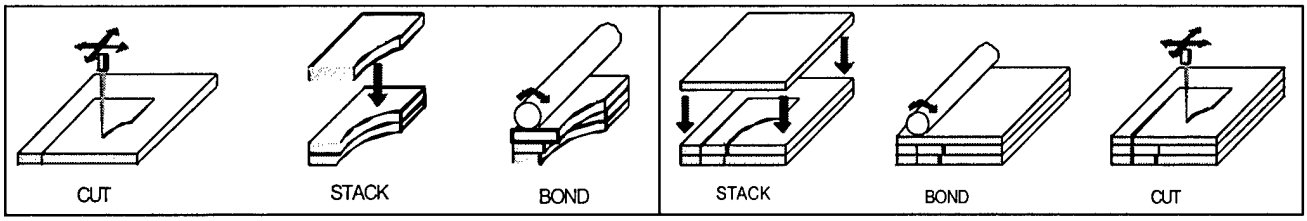


Figure 1. Two alternative sequences for producing laminated objects: (a) cut-stack-bond and (b) stack-bond-cut.

Laser Machining of Metals

Laser machining of metals is accomplished by achieving a sufficiently high power density (W/cm^2) at the focal point to melt or evaporate the material. The molten material is likely to resolidify, and thus, if most material in the groove is molten, it can produce poor-quality cut, making vaporization the preferred mode.

Through cutting vs. blind cutting: In through cutting, the molten and vaporized material can escape through the cut slot; on the other hand, in blind cutting, this material has to be evacuated through the groove's top opening. Pressurized gas is often used to assist cutting. With through cutting, the gas helps the debris to escape through the cut slot. The role of gas assist in blind cutting is not as significant (and potentially detrimental, pushing the material back into the groove). When cutting metal *laminations*, the situation more closely resembles blind cutting, since there is no escape route for the molten material and gases through the bottom of the cut. However, there is a difference as well since the groove is being cut not in a bulk material but through a thin sheet with a layer of adhesive below

Laser and optical system considerations: To achieve the high power density required for cutting aluminum (10^6 - 10^9 W/cm^2) [5], we need to deliver the laser energy over a short time interval (on the order of tenth of nanoseconds) and into a very small area (diameter of 5-20 μm). Most suitable laser beam mode for metal machining is the fundamental (or Gaussian) mode TEM_{00} because it can be focused to a smallest spot and has the greatest depth of focus compared to other modes. The focal spot diameter is theoretically given by:

$$d = \frac{4 \lambda f}{\pi D} \tag{1}$$

where λ is laser light wavelength, f is the focal length of the focusing lens, and D is the diameter of the incident beam. Depth of focus is another important factor to be aware of. It is defined as the distance within which the power density is greater than 90% of its peak value at the focal point. It can be calculated by:

$$Z = \frac{8 \lambda f^2}{\pi D^2} \tag{2}$$

If Z were too small, even slight surface irregularities and misalignment of specimen surface and X-Y translation plane may cause significant variations in power density. On the other hand, if Z were to be made larger by increasing f or decreasing D, it would also increase the focal spot diameter (Eq. 1), and therefore decrease power density. Thus, given the initial beam diameter and laser wavelength, the appropriate choice of beam expansion ratio (affecting D) and focal length involves a trade-off between minimizing the focal spot diameter (d) and maximizing the depth of focus (Z).

Laser grooving theoretical models: While much research has been conducted in the area of through cutting of metals [6, 7], the more relevant subject for our work is that of blind cutting (or *laser grooving*). For example, Modest [8] developed a 3-D conduction model to predict the transient effects in laser machining of ablating/decomposing materials. The model predicts not only the depths but also the shape of a developing groove formed by ablation of material (e.g., aluminum). Chryssolouris [9] developed a simpler closed-form generalized model to address cutting, drilling, and grooving processes. The model is derived by considering the heat-transfer balance at the constant erosion front produced by the moving laser beam. It predicts the groove depth as:

$$L_d = \frac{2aP}{\pi^{1/2} \rho V d \, (C_p(T_s - T_o) + L)} \qquad (3)$$

where a is the material absorptivity ($0<a<1$), P is the incident laser power, ρ is the material density, V is the beam scanning speed, d is the focal spot diameter, C_p is the specific and L is the latent heat, and T_s and T_o are the vaporization and room temperatures, respectively. The relationship implies that the groove depth L_d is directly proportional to the laser power and inversely proportional to the scanning speed. The model assumes that the material is isotropic and its properties are constant; the material changes phase from solid to vapour in one step at a single evaporation temperature; the evaporated/ejected material does not interfere with the beam reaching the erosion front; multiple reflections of the beam within the groove are neglected; and material is removed by vaporization (sublimation cutting).

Laser cutting experiments

Objectives: Experiments were conducted with the overall objective of finding suitable processing parameters for controlled-depth cutting of the aluminum sheet material in laminated object manufacturing. The primary controllable process parameters are laser power and scan speed. The primary measured characteristic is the groove depth. The primary interest in groove depth is due to the need to cut the sheet laminations precisely to the depth of one sheet without significant damage to the underlying stack. A second objective was to determine the effect of changing the material being cut from a (relatively) thick aluminum plate (3.2 mm) to a stack of thin laminated sheets (sheet thickness 0.12 mm). Laser grooving is normally performed on relatively thick material and theoretical predictions would normally also be made for such materials. On the other hand, the material to be cut in our case consists of a sandwich of polymeric adhesive and aluminum sheet. Aluminum is an excellent heat conductor (thermal conductivity 210 W/m C) while a typical adhesive acts as an insulator, with very low conductivity (0.2-0.5 W/m C). Thus, the solid plate represents a "reference" case while the laminated sheet specimens approximates the special material combination to be encountered in the laminated fabrication process.

Specimen Preparation: Two types of specimens were used: solid plates or laminated sheets. The plates were prepared by cutting 2"×1/8" (50.8 mm×3.2 mm) aluminum alloy bar stock (ASTM B221 6061 T6511) into 95 mm lengths. These plates were used either directly or as supports for three laminated sheets bonded to them. The latter were cut from a rolled aluminum sheet stock (6061, 0.05" or 0.12 mm gauge) into 90 mm by 20 mm strips. To bond the sheet strips to the support plates, (1) the plates were sanded, (2) plate and sheet surfaces were cleaned by chemical etching, (3) adhesive was applied to the sheets, and (4) using the heat sealer, the strips were bonded one on top of another starting with the support plate. To bond the sheets, a film adhesive was used (Scotch 467MP from 3M consisting of 200MP high-performance acrylic adhesive (50 microns) with polycoated Kraft paper liner).

Laser Machining Equipment: The experimental setup consisted of a laser light source, a beam delivery system, and a motion system[1]. The platform carrying the specimen moved in X-Y plane (with accuracy of ±1 μm) while the optical system remained stationary. The light source was a GSI Lumonics Sigma-400 diode-pumped Nd:YLF laser operating at a wavelength of 1054 nm (near infrared), capable of up to 12W average power and (Q-switched) pulse frequency up to 20 kHz.

The optical path from the laser to the specimen surface consisted of five-time beam expander/collimator, three mirrors, and a 55-mm apochromat triplet lens. Given the light wavelength, initial beam diameter (1.3 mm), beam expansion ratio, and the focal length, the theoretical focal spot diameter is estimated by Eq. (1) to be 11.3 μm. The depth of focus is estimated using Eq. (2) to be only 112 μm, which implies that care must be taken to make sure the specimen surface is parallel with the plane of X-Y motion and that the beam is properly focused. Assuming actual focal spot diameter to be approximately 15 μm (larger diameter is expected due to optical aberrations of the non-ideal focusing lens), the power density at the specimen's surface during a single pulse can be estimated to range from 2.3 to 6.8×10^9 W/cm^2 for laser power outputs of 4W to 12W and pulse frequency of 10 kHz used in the experiments. Therefore, our experimental setup was capable of producing sufficient power density to vaporize the aluminum.

Test Procedure: For each specimen, four groups of seven parallel 3.7-cm lines were scanned, with two groups scanned for each power setting (Figure 2). The scan directions in the two groups were reversed with the intention to ascertain absence of any directional effects. (Due to experimental error, for Set 1, both sets of lines for 4 and 7W were drawn in the same direction. Since no significant difference between directions was observed for the two higher powers of Set 1, this error is not expected to affect the results.) Within each group, the scan speed increased from right to left as viewed in the figure, from 1500 to 4500 in 500 mm/min increments. Four power settings were used: 4, 7, 10, and 12W, all at pulse frequency of 10 kHz and pulse duration of 100 ns.

Data Collection: After experimenting with other examination techniques (SEM and vertical scanning interferometry, i.e., profilometry), it was found that the only reliable way to obtain the desired information was via metallography. The difficulties with examining the specimens are caused by the narrow width of the grooves (as little as 15 μm), their fragility, high height to width ratio (up to 8 to 1), and presence of recast and other debris within the groove cut obscuring the groove bottom from non-destructive optical

[1] Experiments were conducted at the Laser Micromachining Facility, Toronto, Ontario.

examination. The drawbacks of the metallographic examination are that it is destructive and labour-intensive.

To make sure that the fragile sheets are completely immobilized, a two-stage mounting process was developed. In the first stage, a 25-mm segment of the support plate with the sheet layers attached was cut away from each side of the specimen (see Figure 2). Each piece was placed in a rectangular rubber mould (85L × 53W × 30H mm), and set in epoxy (Araldite GY502). This epoxy block was cut into two pieces, each containing one line group, and, in the second mounting stage, these two pieces were mounted in epoxy within a one-inch diameter cylindrical mould. After polishing to 0.5 μm finish, gray-scale images of sections (256-level, 975×975 pixels) were captured through an optical microscope and used subsequently to measure the groove cross-section features with a resolution of 0.25 μm/pixel.

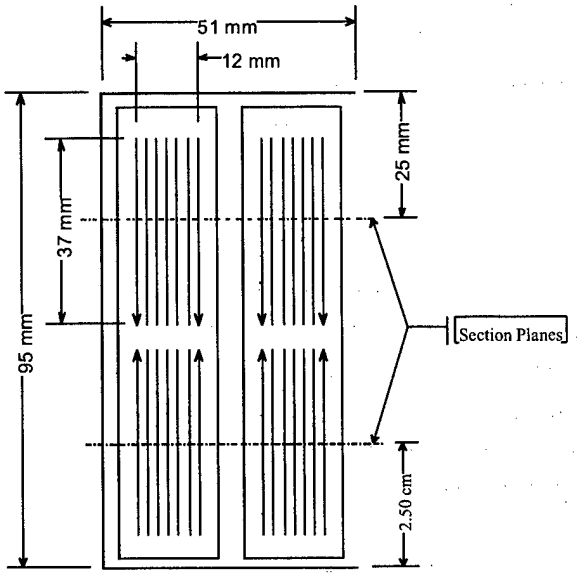


Figure 2. Geometry of specimens and line scans (same line pattern was used for all specimens).

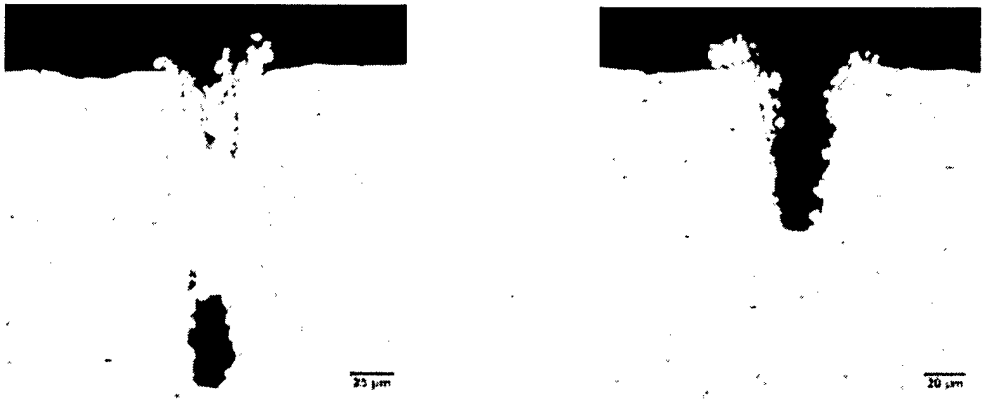
Results and Discussion

The observed features of groove cross-sections were groove depth (L_d) and recast area fraction (A_r). The amount of recast within the groove indicates how successful the laser was in severing the sheet. A_r is defined as a percent fraction of profile cross-section area occupied by recast. The areas were measured with the aid of Scion Image image-processing software.

Set 1: Solid-plate Specimens: Figure 3 shows two examples of groove cross-sections, one with significant recast present and another showing a successful (clean) groove. Both figures show upward molten material flow pattern which developed as the vaporized and molten metal escaped vertically. Recast occurs when molten and vaporized metal resolidifies upon coming in contact with the relatively cool walls of the groove. Under certain process conditions, there is enough resolidification to form a "bridge" across the groove.

Figure 4(a) shows the groove depths (L_{d1}) averaged from two observations. As expected, the groove depth decreases with scan speed and increases with laser power. Also shown on the same plot are the results of fitting the model in Eq. (3) to our data. The parameter values used for the model were:

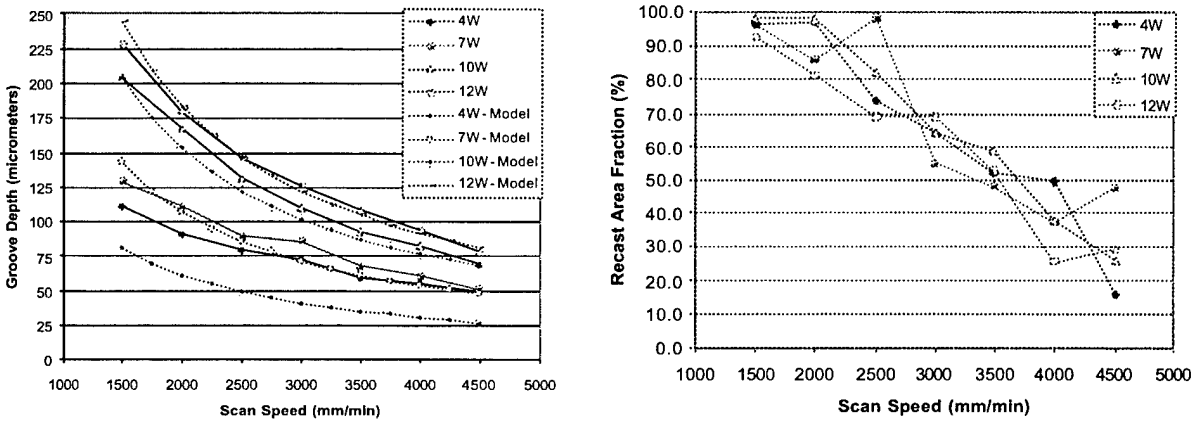
ρ = 2700 kg/m^3, d = 30 μm, C_p = 896 J/kgC, latent heats of fusion 395 kJ/kg and vaporization 10.5 MJ/kg, T_s = 2467°C. The model curves were "fitted" by adjusting the absorptivity value (a). The resultant plots are for a = 0.48. Even though this value is higher than the rated absorptivity of aluminum (0.2-0.25), it is well-known that a rises at elevated temperatures [5]. An excellent fit was obtained for all but the lowest power setting. It is possible that the model fails at this setting since it assumes that the material removed from the groove is completely vaporized (i.e., all absorbed incident energy is used to vaporize the groove material). At the lowest power, this assumption may not be valid.



(a) (b)

Figure 3. Examples of groove cross-sections for solid-plate specimens: (a) recast-filled groove (12W, 2000 mm/min); (b) clean groove (12W, 4500 mm/min).

Figure 4(b) shows how recast area fraction (averaged from two observations) decreases linearly with scanning speed. The value falls quickly from nearly 100% at 1500 mm/min to, on average, about 30% for 4500 mm/min. There is no significant dependence on the laser power.



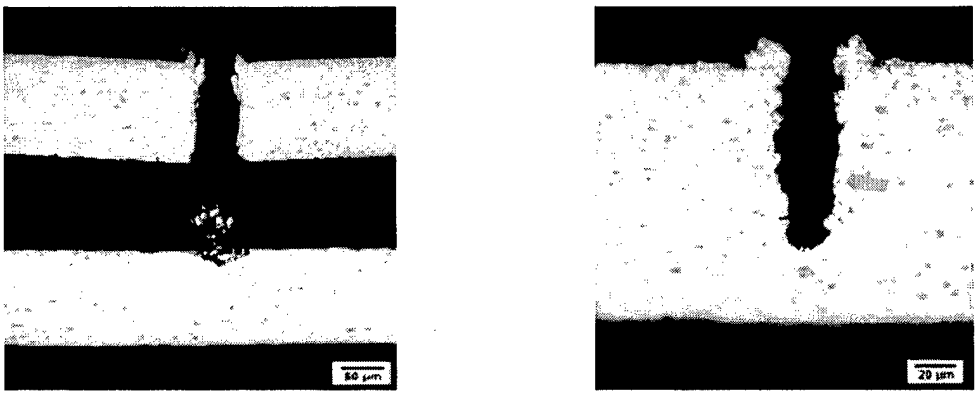
(a) (b)

Figure 4. (a) Groove depths (experiment and model) and (b) recast area fraction for solid-plate specimens as a function of scan speed.

Set 2: Laminated-sheet Specimens: For laminated-sheet specimens, some combinations of speed and power resulted in successful through cutting of the aluminum sheet (Fig. 5a) while others produced grooves, similar to the solid-plate specimens (Fig. 5b). The trends for the groove depth values (L_{d2})

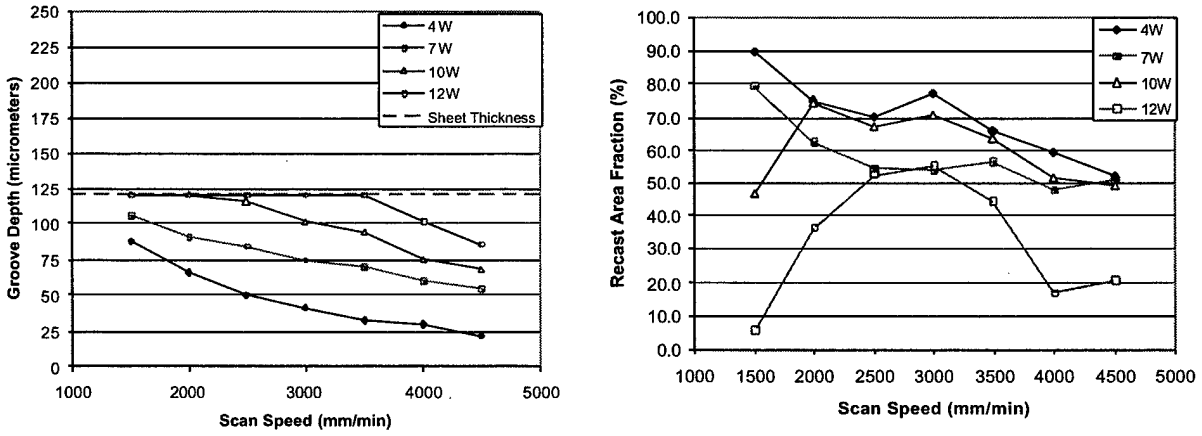
shown in Figure 6(a) are similar to those observed for the solid-plate specimens except for the upper limit of 120 μm (sheet thickness).

Recast area fraction for laminated-sheet specimen (A_{r2}) displays some of the trends of the solid-plate specimens, but also has some different features (Fig. 6b). In a trend similar to that for the solid-plate specimens, for speeds above 2000 mm/min, the recast area decreases with speed. One important difference, however, is a significant decrease in recast formation at 1500 mm/min for the two highest powers (10 and 12W). These are also the powers and speeds at which a through-cut was observed (see Fig. 5a). It is conjectured that at these higher powers and lower speeds, sufficient energy is delivered through the cut groove to the adhesive below to increase the pressure from vaporized material to the point where the material is removed from the groove before it is able to resolidify.



(a) (b)

Figure 5. Examples of groove cross-sections for laminated-sheet specimens: (a) through-cut sheet (12W, 1500 mm/min); (b) recast-free groove (12W, 4500 mm/min).



(a) (b)

Figure 6. Groove depths (a) and recast area fraction (b) for laminated-sheet specimens as a function of scan speed.

Comparison of Set 1 and 2 Results: Figure 7 shows the ratio of groove depths for laminated sheet over those for solid plate: $\psi_d = L_{d2}/L_{d1}$. For example, values of ψ_d less than one would indicate that, for equivalent power and speed parameters, shallower grooves were produced in the laminated-sheet

specimens. It is interesting to observe that there is a consistent decline in this ratio with speed for the lowest power (4W), from 0.79 to 0.44, but, for all other (higher) powers, the ratio increases linearly with speed, reaching nearly unity at the highest speeds. Also, at the lowest speeds (1500 and 2000 mm/min), laser power does not appear to affect the ψ_d ratio.

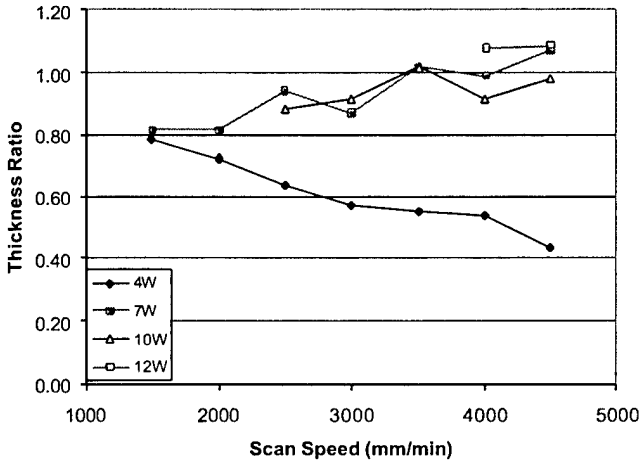


Figure 7. Ratio of groove depths for laminated sheet vs. solid plate ($\psi_d = L_{d2}/L_{d1}$).

Conclusions

From laser-cutting experiments on solid aluminum plates and laminated sheets, the relationship between the process parameters (scan speed and laser power) and groove depth was determined and found to agree well with the established theory. Additionally, a consistent relationship between the groove depths in the solid plate and in the laminated sheets was found. A novel method of metallographic examination of fragile laminated-sheet specimens was developed. Process parameter settings were found which resulted in recast-free through cut of uppermost sheet without significant damage to underlying stack.

Acknowledgements

We gratefully acknowledge the financial support of Centre for Automotive Materials and Manufacturing and Canada Foundation for Innovation. Our appreciation to Laser Micromachining Facility, Toronto, Canada, and to Marc Nantel for his advice. We also wish to express our thanks for assistance with specimen sectioning to Ms. W. Clapp and for microscope imaging to Ms. S. Hinchcliffe, both of Alcan Research Centre Labs.

References

[1] C. Adams, B. Bryden, D. Wimpenny, "Rapid laminated tooling – making the technology work," *8th European Conf. Rapid Prototyping and Manufacturing*, Nottingham, UK, Jul 1999, pp. 511-527.

[2] T. Himmer, T. Nakagawa, M. Anzai, "Lamination of metal sheets," *Computers in Industry*, V. 39, 1999, pp. 27-33.

[3] D. Walczyk, N. Y. Dolar, "Bonding methods for laminated tooling," *Solid Freeform Fabrication Symp.*, Austin, TX, Aug 1997, pp. 211-221.

[4] M. Feygin, "Apparatus and method for forming an integral object from laminations," US Patent No. 4,752,352.

[5] J. F. Ready, **LIA Handbook of Laser Materials Processing**, Laser Institute of America, Magnolia Pub., 2001.

[6] K. A. Bunting and G. Cornfield, "Toward a General Theory of Cutting: A relationship Between the Incident Power Density and the Cut Speed", *Transactions of ASME-Journal of Heat Transfer*, 1975, pp. 116-122.

[7] H. Kaebernick, D. Bicleanu, and M. Brandt, "Theoretical and Experimental Investigation of Pulsed Laser Cutting", *Annals of the CIRP*, V. 48, N. 1, 1999.

[8] M. F. Modest, "Three-dimensional, transient model for laser machining of ablating/decomposing materials", *Int. J. Heat Mass Transfer*, V. 39, N. 2, 1996, pp.221-234.

[9] G. Chryssolouris, **Laser Machining-Theory and Practice**, Springer-Verlag, 1991.

this page intentionally blank

CLOSED LOOP CONTROL OF 3D LASER CLADDING BASED ON INFRARED SENSING

D. Hu, H. Mei, G. Tao, R. Kovacevic

Research Center for Advanced Manufacturing,
Southern Methodist University
1500 International Parkway, Suite 100, Richardson, TX, 75081

Abstract

In this paper, a heat input closed-loop control system based on infrared image sensing for 3D laser cladding is introduced. A high frame-rate (up to 800 frames/s) camera is installed coaxially on the top of the laser-nozzle setup. Complete of the infrared images of the molten pool can be acquired with a short nozzle-substrate distance in different scanning directions, eliminating the noise from the metal powder. The characteristics of the images show a clear relationship with the parameter variations of the cladding process. A closed-loop control system is built based on the feedback of the infrared image sensing. The control results show a great improvement in the geometrical accuracy of the part being built.

Keywords: SFF, Laser Cladding, Infrared Image Sensing, Control.

1. Introduction

Solid Freeform Fabrication (SFF) is a novel manufacturing technology that could be used for the rapid creation of models, prototypes and patterns and for limited-run production. Nowadays, several SFF methods have been developed, such as 3D welding [1,2], micro-casting [3], selected laser sintering [4], Laser Engineered Net Shaping (LENS) [5], Shape Deposit Manufacturing (SDM) [6], Directed Light Fabrication (DLF) [7], 3D laser cladding [8] and some hybrid methods [9-11]. Among these SFF methods, 3D laser cladding has been considered to be very suitable for building metallic parts. A laser beam could be easily delivered and controlled and could be focused on a very small area, so that the interaction zone of a laser process can be accurately positioned and the bead track could have a small width (< 1 mm). This means that higher geometrical accuracy and surface quality of the final part can be achieved. Moreover, because of the powder delivery feature in 3D laser cladding, no inert-gas protection chamber is required. So, a larger part can be produced, and a more complicated cladding path can be traced, including four-dimensional and five-dimensional paths. By controlling the mass flow rate of the metal powders from different powder feeders, a composite material or alloy with a functionally gradient distribution can also be produced.

When laser cladding is used for SFF, it builds parts by adding powder material (e.g. layer by layer) and in a way that it resolves a complicated manufacturing process into a series of simple and repetitive layer procedures. A stable and repeatable layer procedure is therefore crucial for the quality of the part produced. However, the laser cladding process is governed by a large number of parameters [11]. Some of the parameters are sensitive to the environment variations and some of them affect the other laser cladding parameters. In order to perform successful 3D laser cladding operations, an on-line closed-loop control of the process is necessary.

Several previous research works [12-18] have been done to control the laser cladding process. Some of them are focused on controlling the powder delivery in order to achieve more stable powder delivery [12,13], or study the powder stream distribution and laser-powder interaction [14,15]. Others deal with the optimization of the laser cladding process by a closed-loop control, using a CCD camera [16-18] or a phototransistor [19] as the sensing device. However, the CCD camera or the phototransistor is installed usually from one side of the nozzle. This installation is not practical for SFF 3D cladding. The distance between the nozzle and the substrate is very small (~5mm), so the viewing area of the cladding is limited. The images are deformed due to the angle between the optical central line of the camera and the laser-nozzle setup. Also, the images acquired from an asymmetrically installed camera will vary according to the scanning direction, which is always changing in SFF processes.

This paper discusses the control of the heat input in 3D laser cladding for SFF. A closed-loop control system based on infrared image sensing is developed. A high frame-rate (up to 800 frame/s) camera is installed coaxially on the top of the laser-nozzle setup. Complete infrared image of the molten pool and surrounding area can be easily acquired with a short nozzle-substrate distance and different scanning directions, eliminating the noise from the metal powder. The characteristics of the images vary with the cladding process parameters and have a clear relationship with variations of those parameters. A series of laser cladding experiments were conducted with and without the closed-loop control. The experimental results show a great improvement in the geometrical accuracy of the part being built.

2. Development of closed-loop control system

The 3D laser cladding system is comprised of four subsystems: a 1 kW Nd:YAG laser source, a powder delivery system, a 3-axis positioning system and an infrared image acquisition system. The complete system is shown in Figure 1. The 3D metal part is produced layer by layer by synchronizing the X-Y motion, the Nd:YAG laser and the injection of metal powder. The infrared image acquisition system takes the images of the molten pool in real time and calculates the dimensions of the molten pool. It compares the recorded information to the preset value and creates a feedback control value to modify the output of the laser source. In this way, a stable molten pool with desired dimensions is obtained, and thus it will be possible to produce stable and repetitive layers if stable powder delivery is ensured.

The difficulties of image sensing in 3D laser cladding arise from several problems. The distance between the cladding nozzle and the substrate is short (~5 mm). This distance blocks the sight if the observation is from the sides of the nozzle. In order to observe the molten pool of cladding from one side, the camera is usually installed at a large angle with respect to the central line of the nozzle setup. The image acquired will be distorted due to that angle as well as to the direction of the motion. This problem will be exaggerated when the scanning path is multi-dimensional where the part could come in collision with the camera or could obstruct the direction of observation. Other problems of image sensing come from the intense light produced by laser cladding. The metal powder adds to the difficulty of image processing as well.

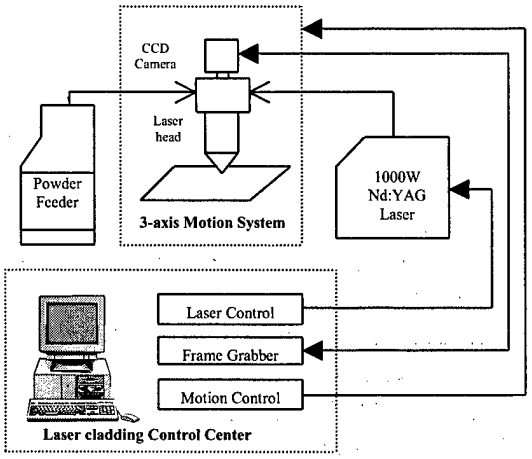


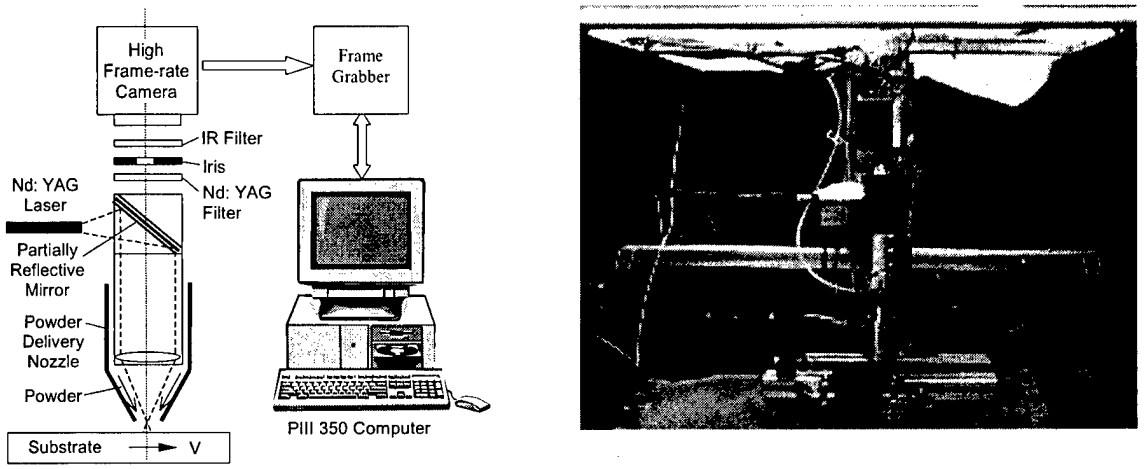
Figure 1 System Integration of 3D laser cladding.

A coaxially installed image sensing setup with respect to the laser beam is developed to solve the problems mentioned above. The optical part of the laser head (Figure 2(a)) provides another optical path for the observation of the laser processing. A high frame-rate (up to 800 frames/s) camera is installed on top of the laser head, taking gray-scale images with a size of 128×128 pixels. The radiation from the molten pool produced by the laser cladding passes through the partially reflective mirror and an infrared filter, forming an image on the CCD chip of the camera. A Nd: YAG laser blocking filter (~1.06 μm) is utilized to protect the camera from laser damage. An iris is used to adjust the intensity of the radiation received by the camera to prevent over-exposure. In order to get the infrared image of the molten pool, which reduces the high intensity light from the molten pool and eliminates the image noise from the metal powder, an infrared filter is selected (>700 nm) and installed between the iris and camera. During the laser cladding process, the camera acquires images of the cladding process in a frame rate of 200 frames/s. Images are transferred to the frame grabber installed on a PC computer that carries out the sensing and control process. The real system setup is shown in Figure 2(b).

Figure 3 provides an infrared image acquired by the coaxially-installed camera under practical laser cladding condition. Because the observation is directly from the top of the molten pool, a full view image of cladding can be acquired without any blocking. With the correct combination of the Nd: YAG filter and the IR filter as well as the right iris aperture, a clear

image of the molten pool can be obtained without the noise from the metal powder. The radiation wavelength received by the camera is between 0.7 and 1.06 μm.

Meriaudeau and Truchetet [16] calibrated the CCD camera with an IR filter, and concluded that the gray level of the pixels has a linear relationship with the temperature. So, the infrared images acquired reflected the temperature distribution around the molten pool. Due to the temperature range in laser cladding, the wavelength region of 0.7-1.06 μm occupies the part of the electromagnetic spectrum in which most radiometric surface temperature measurements are made. Figure 3(b) shows the gray level isotherms of the unprocessed infrared image shown in Figure 3(a). In a closed loop control of 3D laser cladding process, an absolute temperature measurement is not necessary, as only the relative difference is necessary for generating the feedback.



(a) Schematic presentation

(b) Close-up

Figure 2 Infrared image acquisition system



(a) unprocessed

(b) processed

Figure 3 Acquired infrared image

3. Laser cladding experiments

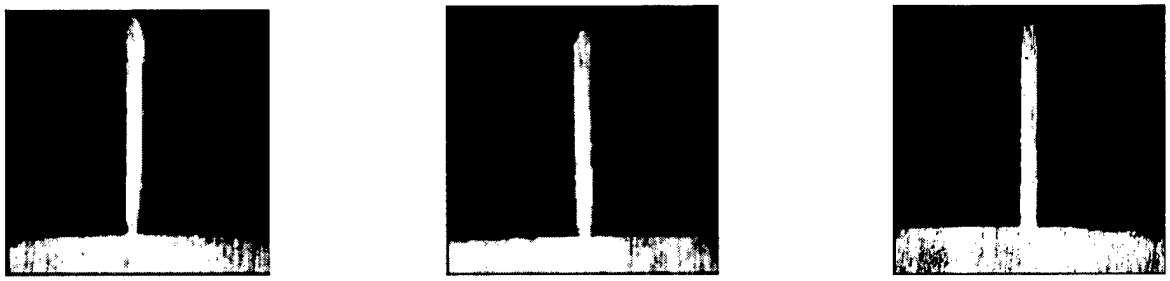
A set of laser cladding experiments have been performed to test the control effect of the developed closed-loop control system based on infrared image sensing. The substrate material utilized in the experiments is mild steel, and the metal powder is an H13 tool steel powder with a -100/+325 mesh size. The powder delivery rate is kept constant at 5.2 g/min. The experiments are carried out at a constant scanning speed of 8 mm/s, but at different laser powers.

To compare the processing results, single-bead walls are built under the following three varied processing conditions. The first type of samples are built with no pre-heating of the substrate and no closed-loop control for the heat input. The second type of samples are built with pre-heating but no control, and the third type of walls are built utilizing the closed-loop control function. The walls are produced in a repetitive manner. The nozzle moves along the positive direction of the X axis first to build one layer, moves up a small increment along the Z axis after the layer is built up, and then moves back along the negative X direction for the next layer's deposition. During the wall building process, the area of the thermal field with a threshold of 50 is recorded continuously with an image-processing rate of 10 frames/second.

A typical group of single-bead-wall samples built by laser cladding at the same laser power (290 W) is shown in Figure 4. It can be observed that, when no heat input control is utilized, the root of the wall is obviously narrower than the upper part of the wall, as shown in Figure 4(a) or (b). Moreover, this trend is even more pronounced within the wall built without preheating (Figure 4(a)). The geometrical change of the uncontrolled 3D laser cladding process results from the variation in heat loss. At the beginning of the wall building, due to the large heat conduction of the substrate, the created beads are narrower. As the wall grows up, there is less heat conduction along the built wall, and the bead becomes wider until it reaches a new equilibrium value. For the wall with preheating, the initial heat loss conducted into the substrate is reduced because of the high temperature of the substrate, and thus more energy is used to create the molten pool, which results in a wider wall than that without preheating. The role of the closed-loop control system in laser cladding is just to overcome the effect of heat variation. At the initial stage of wall building, because a lot of heat is conducted into the substrate, a small molten pool is created. The control system reacts by increasing the laser power in order to produce a molten pool with the preset dimensions. As the wall grows, heat conduction loss is reduced and the laser power output returns to a normal level. With this feedback control function, the size of the molten pool could be kept nearly constant, resulting in the constant wall width along the entire height of the wall.

This process can be more clearly explained with the use of the recorded infrared images recorded during laser cladding. As was mentioned before, the pixel number of the infrared image reflects the temperature distribution of the laser cladding as well as the size of molten pool. It can be observed from Figure 5(a) that, when neither preheating or heat input control is applied, the pixel number of the thermal field area starts with about 1,000 for the first layer, and it gradually increases up to 5,000 and stays there for the rest of the buildups. However, when a preheating procedure is applied, the pixel number of the infrared images at the beginning is relatively high compared to the case without preheating, as shown in Figure 5(b). This fact corresponds to the

geometrical comparison of the walls built under these two conditions. Figure 5(c) shows the pixel numbers of the images acquired from the laser cladding of a single-bead wall with heat input control. Apparently, a very stable pixel number is obtained which corresponds to a uniform width of the wall. Contrary to the stability of the pixel number, the laser power fluctuates greatly (Figure 5(d)), showing the obvious control function of the closed loop control system.

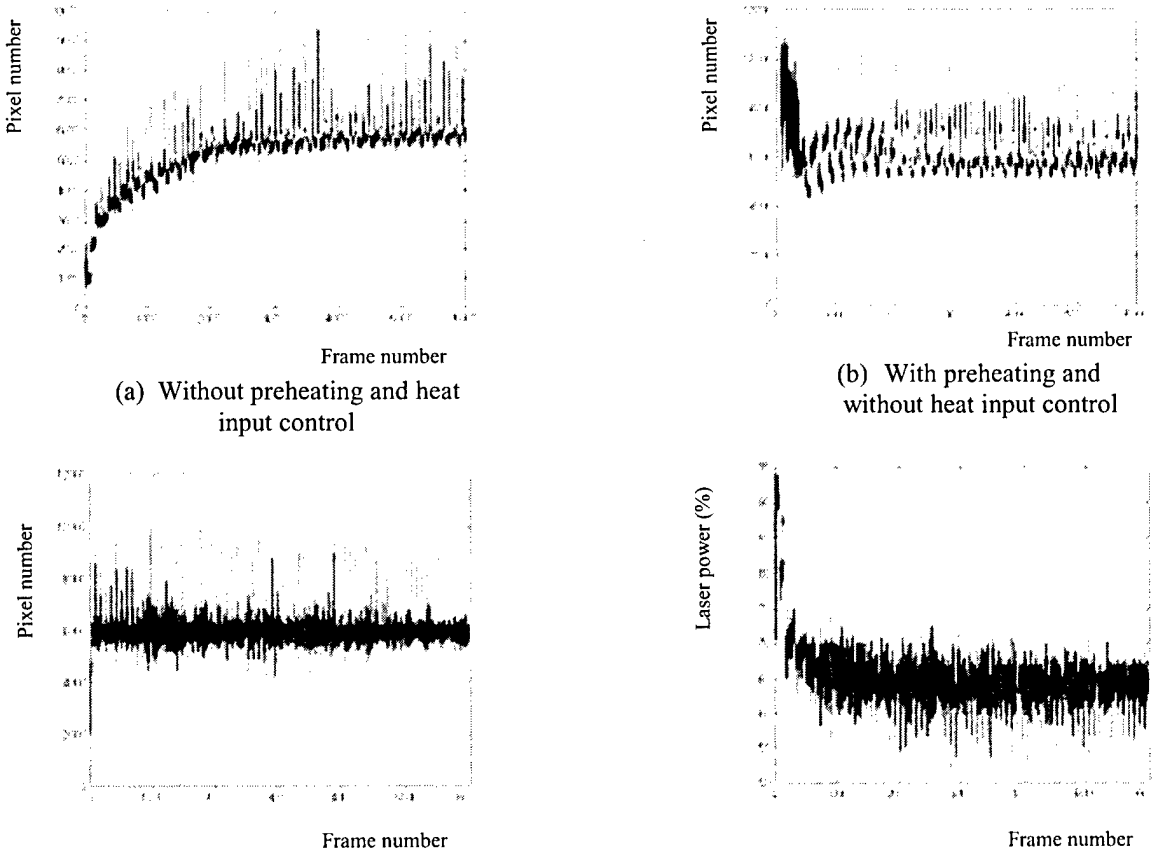


(a) Without preheating and without heat input control

(b) With preheating and without heat input control

(c) With heat input control

Figure 4 Single-bead walls built by 3D laser cladding process.



(a) Without preheating and heat input control

(b) With preheating and without heat input control

(c) With heat input control

(d) Power level corresponding to (c)

Figure 5 The area of thermal field in 3D laser cladding.

The geometrical parameters of cross-sections of the walls built under different processing conditions are given in Table 1. The average width of the wall w_a is calculated by averaging 10 width measurements taken at 10 evenly spaced heights from the substrate surface. w_{min} means the minimum width of the wall, which normally corresponds to the root of the wall. A geometrical accuracy η is introduced to express the width variation of each wall sample, which is calculated by the following formula:

$$\eta = \left| \frac{w_a - w_{\min}}{w_a} \right| \times 100\%$$

Table 1: Geometry of the walls built under different conditions

Power Level (W)	Without preheating and without control			With preheating and without control			With control **		
	Average width w_a (mm)	Minimum width w_{min} (mm)	Geometrical accuracy η (%)	Average width w_a (mm)	Minimum width w_{min} (mm)	Geometrical accuracy η (%)	Average width w_a (mm)	Minimum width w_{min} (mm)	Geometrical accuracy η (%)
290	0.95	0.45*	53%	0.95	0.62	35%	0.91	0.90	1%
370	1.33	0.58	56%	1.26	0.9	29%	1.02	1.01	1%
450	1.48	0.79	47%	1.5	0.94	37%	1.35	1.15	15%
540	1.61	0.945	41%	1.60	1.0	38%	1.58	1.29	19%
620	1.7	0.99	42%	1.75	1	43%	1.67	1.31	22%

*: The bonding of the wall with the substrate surface is not continuous.
**: The laser powers listed are transformed from the calibrated pixel numbers

The geometrical change of the walls with laser power is shown in Figure 6. When no heat input control is applied, a preheating procedure contributes to improve the geometrical accuracy of the wall, especially when the laser power is less than 500W. With the increase of laser power, the influence of preheating becomes of less importance. This is because a higher laser power could compensate for the difference in heat loss due to the different thermal conditions

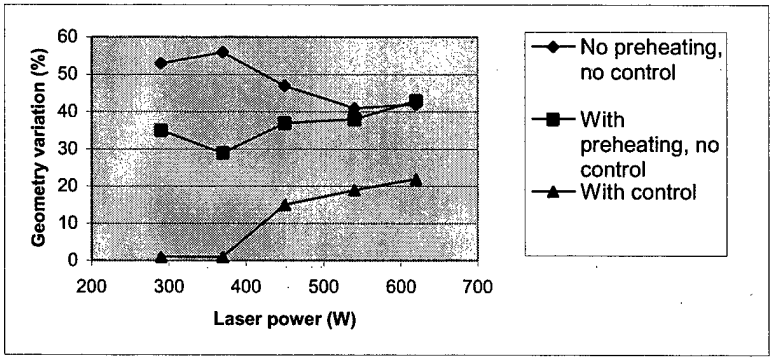


Figure 6 Geometrical accuracy Vs laser power

It can also be observed that, under all laser power levels, the geometrical variation of the cross sections of the walls built with heat input control is much lower than those without control. When the laser power is below 400W, there is almost no width variation along the wall height if a control function is applied. Even at higher laser power levels, the geometrical accuracy gradually goes down, but it is still far superior to that without any control function.

4. Conclusions

Infrared image sensing is an efficient sensing method for 3D laser cladding for SFF. Clear infrared images of the molten pool generated by the laser beam can be acquired easily by a coaxial camera even in the case of a short nozzle-substrate distance and in different scanning directions. The infrared image reflects the temperature information that is a significant parameter affecting the cladding result. The closed-loop-controlled 3D laser cladding based on the infrared image sensing can overcome the effects of thermal variation and thus achieve a consistent processing quality of 3D laser cladding.

5. Acknowledgement

This work was financially supported by THECB, Grant 003613-0022-1999, NSF, Grants No. DM1-9732848 and DM1-9809198, and the U.S. Department of Education, Grant No. P200A80806-98.

6. References

1. Spencer, J. D., Dickens, P. M., and Wykes C. M., 1998, "Rapid Prototyping of Metal Parts by Three-Dimensional Welding," *Proceedings of the Institution of Mechanical Engineers, Part B: Journal of Engineering Manufacture*, Vol.212, No.B3, pp.175-182.
2. Ribeiro. F., Norrish. J., and McMaster. R S., 1994, "Practical Case of Rapid Prototyping Using Gas Metal Arc Welding," *Proceeding of Conference on Computer Technology in Welding*, Paris, Paper 55.
3. Rangel, R. H., Bian, X., 1996, "Metal-Droplet Deformation and Solidification Model with Substrate Remelting," *Proceedings of the 1996 ASME International Mechanical Engineering Congress and Exposition*, Atlanta, Vol.336, pp. 265-273.
4. Das, S., Fuesting, T. P., Danyo, G., Brown, L. E., Beaman, J. J., Bourell, D. L., and Sargent, K., 1998, "Direct Laser Fabrication of Gas Turbine Engine Component-Microstructure and Properties," *Solid Freeform Fabrication Proceedings*, Marcus, H. L. et al, ed., Austin, pp. 1-18.
5. Griffith, M. L., Keicher, D. M., Atwood, C. L., Romero, J. A., Smugeresky, J. E., Harwell, L. D., and Greene, D. L., 1996, "Free Form Fabrication of Metallic Components Using Laser Engineered Net Shaping (LENS)," *Solid Freeform Fabrication Proceedings*, Bourell, D.L. et al, ed., Austin, pp. 125-131.

6. Link, G.R., Fessler, J., Nickel, A., and Prinz, F., 1998, "Rapid Tooling Die Case Inserts Using Shape Deposition Manufacturing," *Materials and Manufacturing Processes*, Vol.13, No.2, pp.263-274.

7. Milewski, J. O., Lewis, G. K., Thoma, D. J., Keel, G. I.; Nemec, R. B., Reinert, R. A., 1998, "Directed Light Fabrication of a Solid Metal Hemisphere Using 5-Axis Powder Deposition," *Journal of Materials Processing Technology*, Vol. 75, No. 1-3, pp. 165-172.

8. Yevko, V., Park, C. B., Zak, G., Coyle, T. W., and Benhabib, B., 1998, "Cladding Formation in Laser-Beam Fusion of Metal Powder," *Rapid Prototyping Journal*, Vol. 4, No. 4, pp.168-184.

9. Kovacevic, R., 2001, "Rapid Manufacturing of Functional Parts Based on Deposition by Welding and 3D laser Cladding," *Proceedings of the Mold Making 2001 Conference,* presented by *Mold Making Technology Magazines*, pp. 735-742.

10. Song, Y. A., Park, S., Jee, H., Choi, D., and Shin, B., 1999, "3D Welding and Milling-A Direct Approach for Fabrication of Injection Molds," *Solid Freeform Fabrication Proceedings*, Beaman, J. J., et al, ed., Austin, pp. 793-800.

11. Verret, P.-A., Engel, Th., Fontaine, J., 1998, "Laser Cladding: the Relevant Parameters for process Control," *SPIE*, Vol. 2207, pp. 452-462.

12. Li, l. and Steen, W. M., 1993, "Sensing, modelling and Closed Loop Control of Powder Feeder for Laser Surface Modification," *ICALEO (1993)*, pp. 965-974.

13. Grunenwald, B., Nowotny, St., Henning, W., Dausinger, F., and Hugel, H., 1993, "New Technology Developments in Laser Cladding," *ICALEO (1993)*, pp. 934-944.

14. Jeng, J.-Y., Quayle, B., Modern, P. J., and Steen, W.M., 1992, "Computer Control of Laser Multi-Powder Feeder Cladding System for Optimal Alloy Scan of Corrosion and Wear Resistance," *Proceedings of LAMP'92*, pp. 819-824.

15. Vetter, P. A., Engel, Th., and Fontaine, J., 1994, " Laser Cladding: the Relevant Parameters for Process Control," *SPIE*, Vol.2207, pp.452-462.

16. Meriaudeau, F., Truchetet, F., Dumont, C., Renier, E., and Bolland, P., 1996, "Acquisition and Image Processing System Able to Optimize Laser Cladding Process," *Proceedings of ICSP'96*, pp.1628-1631.

17. Hofmeister, H.W., MacCallum, D.O., Knorovsky, G.A, "Video Monitoring and Controlof the LENS Process," *NIST Special Publication 949*, Edts. T. Siewert and C. Polloch, May 2000. *9th International Conference on Computer Technology in Welding.*

18. Hu, D., Wu, Y, and Kovacevic, R., 2001, "Heat Input Control in 3D Laser Cladding Based on Infrared sensing," accepted for *the 2001 International Mechanical Engineering Congress*, Nov. 11-16, New York.

19. Koch, J., and Mazumder, J., 2000, "Apparatus and methods for monitoring and controlling multi-layer laser cladding," U.S. Patent #6,122,564.

20. Tikare, V., and Griffith, M., 1997, "Simulation of coarsening during laser engineered netshaping," *Proceeding of the Solid Freeform Fabrication Symposium*, August 11-13, Austin, TX, pp.699-707.

21. Sankaranarayanan, S., Guo, W., and Kar, A., 1998, "Characteristics of laser-fabricated metal structures," *Materials and Manufacturing Processes*, Vol.13, No.4, pp.537-554.

this page intentionally blank

Research and Development of A Hybrid Rapid Manufacturing Process

F. W. Liou*, J. Choi*, R. G. Landers*, V. Janardhan*, S. N. Balakrishnan*, and S. Agarwal**

*Department of Mechanical & Aerospace Engineering & Engineering Mechanics
** Department of Electrical and Computer Engineering
University of Missouri – Rolla

Abstract

This paper presents the research and development of a hybrid rapid manufacturing process being developed at the University of Missouri-Rolla. This process includes a laser deposition and a 5-axis CNC milling system. By combining laser deposition and machining processes, the resulting hybrid process can provide greater build capability and better accuracy and surface finish. The hybrid process can build some features that are difficult to build in using a purely deposition processes. The issues and related approaches in the research and development of the hybrid deposition-machining process, including laser deposition process, system design and integration, process planning, and sensor selection and control, are discussed.

Introduction

This paper summarizes an interdisciplinary approach to design and develop a hybrid rapid manufacturing process to build functional metal parts. This process uses laser deposition for material deposition and CNC milling for material removal as shown in Figure 1. This five-axis laser deposition/CNC machining process has been developed at the Laser Aided Manufacturing Processes (LAMP) Laboratory in the University of Missouri at Rolla (UMR). It includes two major systems: a laser deposition system (Rofin–Sinar 025) and a CNC milling machine system (Fadal VMC-3016L). The laser deposition system and CNC milling machine work in shifts in a five-axis motion mode. The laser deposition system consists of a laser and a powder feeder.

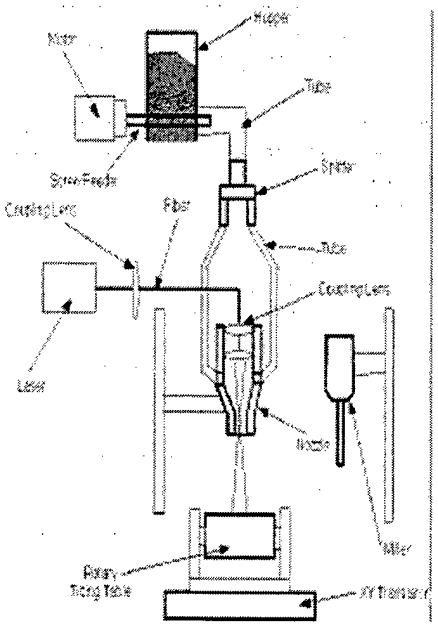


Figure 1. Schematic diagram of the hybrid system at UMR

In conventional 2.5-D laser deposition process to create three-dimensional parts, overhang and top surfaces of hollow parts need be supported. Often support materials for functional metal parts are not feasible. Moreover, deposition of the support material for metals leads to poor surface quality at the regions in contact with the support structure. Moreover, it increases the build time of the part and necessitates a time-consuming post-processing. Additionally use of support increases the build time of the part and necessitates a time-consuming post-processing. With a five-axis deposition process integrated with five-axis machining, these obstacles can be removed. This paper summarizes the issues and related

approaches in the research and development of the hybrid deposition-machining process, including laser deposition, sensor selection, system control, and process planning.

Laser Deposition

For successful deposition, the Direct Laser Deposition, or DMD, process should be well designed and controlled. The scientific challenge is how to accurately control the physical dimension and material properties of the part. Close control of dimension will result in substantial savings in post process machining cost. Substantial cost reduction is possible, if desired properties can be achieved through process control thus minimizing post-process heat treatment. Control of the melt pool size and solidification time can offer both desired dimension by limiting the melt pool volume and desired properties through microstructure manipulation by controlling the cooling rate. This will require quantitative understanding of the relationship between independent process parameters (laser power speed, powder deposition rate etc.), and dependent process parameters (dimension, microstructure and properties, etc.). Issues related with these parameters and possible approaches are discussed below:

A. Independent process parameters

The major independent process parameters for the laser aided DMD process include the following: (1) incident laser beam diameter, (2) process speed, (3) laser beam power, (4) powder feed rate, and (5) laser beam path width (path overlap) as shown in Figure 2. Other parameters such as nozzle to surface distance (standoff distance), nozzle gas flow rate, absorptivity, and depth of focus with respect to the substrate also play important roles.

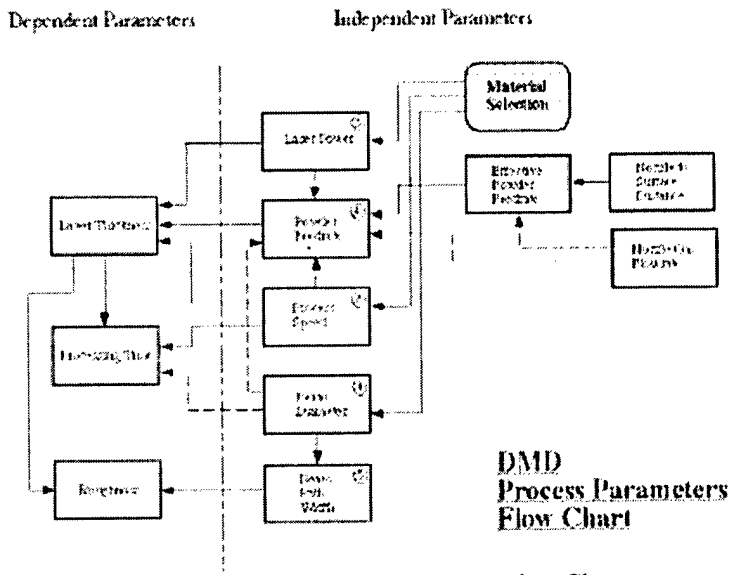


Figure 2. DMD Process Parameters Flow Chart

(1) Laser beam diameter

This parameter is one of the most important variables because it determines the power density. However it is very difficult to measure for high power laser beams. This is partly due to the nature of the beam diameter and partly due to the definition of what is to be measured. Many techniques have been employed to measure the beam diameter, but most are unsatisfactory in some respect or another. Single isotherm contouring techniques such as charring paper and drilling acrylic or metal plates suffer from the fact that the particular isotherm they plot is both power and exposure time dependent. Multiple isotherm contouring techniques overcome these difficulties but are tedious to interpret.

(2) Process speed

In general, decreasing process speed increases the layer thickness. However there is a threshold to reduce process speed since too much specific energy may cause previous layers

tempered or secondary hardened (Mazumder, 1997). Process speed for DMD process should be well chosen since it has strong influence on microstructure.

(3) Laser beam power

The layer thickness during laser cladding process is directly related to the power density of the laser beam and is a function of incident beam power and beam diameter. Generally, for a constant beam diameter, the layer thickness increases with increasing beam power provided corresponding powder feed rate. It was also observed that the cladding rate (deposition rate) increased with increasing laser power (Weerasinghe, 1983).

(4) Powder mass feed rate

Powder mass feed rate is another important process parameter to decide the layer thickness. However effective powder feed rate, which includes powder efficiency during the DMD process, was turned out to be more important (Lin, 1998; Mazumder, 1999). Also the factor that most significantly affected the percent powder utilization was laser power. The powder nozzle is set up to give a concentric supply of powder to the cladding melt pool, and due to the nature of the set-up, the powder flow is hour glass-shaped. As shown in Figure 3, the powder flow initially is unfocused as it passes through the powder delivery nozzle, but the nozzle guides the powder concentrically towards its center, and essentially "focuses" the beam of powder.

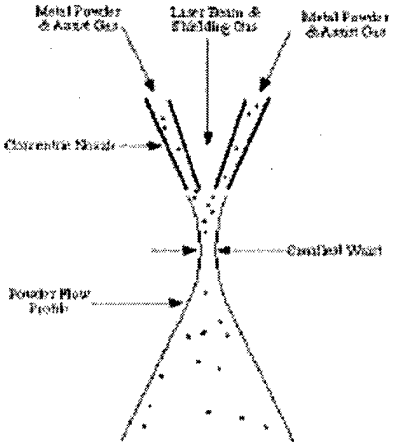


Figure 3. Powder Delivery Flow Profile

The smallest diameter focus of the powder "beam" is dependent upon the design of nozzle. If the laser beam diameter becomes too small as compared to the beam diameter, e.g., 100μm, much of the supplied powder may never reach the cladding melt pool. Thus, there will be unacceptably low powder utilization.

(5) Beam path width (Beam width overlap)

Beam width overlap has strong influence in top surface roughness. The reason for this decrease in surface roughness is depicted in Figure 4. As the cladding pass overlap increases, the valley between passes is raised due to the overlap therefore reducing the surface roughness. In order to obtain the best surface quality, the percent pass overlap should be increased as much as possible. On the other hand, in order to decrease the wall surface roughness, the cladding layers should be kept as thin as possible.

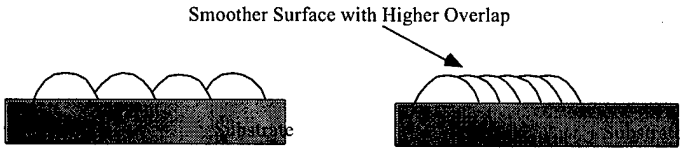


Figure 4. Surface Profile Change from Increase in Percent Overlap

B. Dependent process parameters

The major dependent process parameters are considered to be (1) layer thickness, (2) surface roughness, and (3) process time. Other dependent parameters such as hardness, microstructure, and mechanical properties, etc should be also considered, but in this paper we will focus only on the parameters related with physical dimension.

(1) Layer thickness

There is a large range of layer thickness as well as deposition rates that can be achieved using laser deposition. However, part quality consideration put a limit on optimal deposition speeds. Both the layer thickness and the volume deposition rates are affected predominately by the specific energy and powder mass flow rate. Here, specific energy (SE) is defined as: SE = p/(Dv), where p is the laser beam power, D is the laser beam diameter and v is the process speed. Also it has been well known that actual laser power absorbed in the melt pool is not same as nominal laser power measured from laser power monitor due to reflectivity and other plasma related factors depending on the materials (Duley, 1983). The use of adjusted specific energy is thus preferable. Considering the factors, it was reported that there is a positive linear relationship between the layer thickness and adjusted specific energy for each powder mass flow rate (Mazumder, 1999).

(2) Surface roughness

Surface roughness was found highly dependent on the direction of measurements with respect to the cladding (Mazumder, 1999). In checking the surface roughness, at least four directions should be tested from each sample; the length and width direction on the top surface, and the horizontal and vertical directions on the walls. Since the largest roughness on each sample is of primary interest, measurements should be only taken perpendicular the clad direction on the top surface and in the vertical direction on the walls, based on our preliminary experiments.

(3) Process time

The overall deposition processing time is mainly dependent upon the layer thickness per slice, process speed and laser beam diameter. As an example, if the layer thickness is 250 μm/slice, and process speed is 12.7 mm/s, and laser beam diameter is 1 mm, the process volume deposition rate is about 0.2 cm^3/min. However, the processing conditions need to be optimized prior to optimize the processing time, since the processing time is directly influenced by the conditions. If the laser beam diameter is increased, the specific energy and power density will be decreased under the same process condition, that means, less deposition rate unless the laser power and powder mass flow rate are correspondingly increased. Similarly when the process speed is increased, all other process parameters including laser power and powder mass feed rate, etc should be optimized.

Sensor Selection

The temperature of the melt pool, the thickness of the deposited layer and the physical dimensions and characteristics of the melt pool should be determined for feedback control. Since molten metal is deposited in very thin layers on a steel substrate, the temperature range of the melt pool is between 1000°C and 1500°C but less than 2000°C. The layers are deposited with a minimum thickness of 10μm. The diameter of the laser beam would typically be a little less than 1 mm.

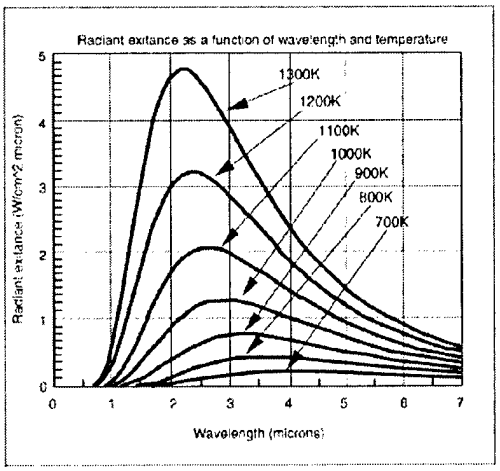


Figure 5. Radiant exitance as a function of wavelength and temperature

A. Temperature Sensors

Due to the nature of DMD process, the temperature sensor should be a non-contact sensor and must work with the Nd:YAG laser. *Infrared*

Thermometry is best suited for non-contact application.

Every object emits radiant energy and the intensity of this radiation is a function of its temperature. Radiance in the visible range is quite low. The radiance at every wavelength increases with increasing temperature as shown in Figure 5 and the determination of the radiance at any wavelength serves to establish the emitters' temperature. Because of this fact, temperature-measuring devices that are based on a single wavelength do not give the absolute temperature. Hence, *two-color infrared thermometry* is preferred.

The *two-color infrared thermometry* utilizes the two-color principle, in which the temperature measurement is made by *ratioing* the radiation intensities of two adjacent wavelengths rather than from absolute intensity as with single band (or single color) instruments as shown in Figure 6. Thus, these sensors are: independent of emissivity, unaffected by dust and other contaminants in the field of view, independent of target size, and can take accurate readings with only 10% of the target area within the field of view.

Most of the sensors work with wavelengths around 1μm. Since the Nd:YAG laser operates at 1,06μm wavelength, it might interfere with the temperature sensor being used. One possible solution is to shut off the laser for a relatively small period of time, about 20 to 50ms (typical response time of the temperature sensor) every 2s, to facilitate sensing. The disadvantage of opting for this method was that the feed-rate could not exceed 0.01 m/s for a proper deposition layer without discontinuities. Hence, temperature sensors working with wavelengths around that of the primary laser could not be used. A *Williamson Corporation* temperature sensor working with wavelengths around 1.5 μm was chosen for this particular application.

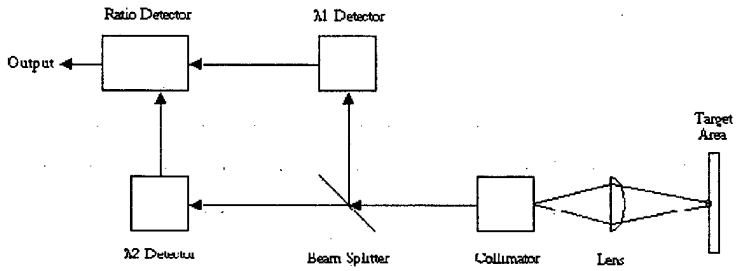


Figure 6. Block diagram of two-color infrared temperature sensor

B. Displacement Sensor

The main criteria for choosing a displacement sensor is the measuring range, resolution and spot size, which is unique to each laser-based direct metal deposition system. Since the displacement sensor has to be a non-contact sensor and cannot be mounted vertically on top of the spot to be measured, a laser displacement sensor (LDS) has to be used which can be mounted at an inclination. The laser displacement sensor is not focused on the melt pool, but rather with a little offset, to measure the thickness of the deposited layer. The laser displacement sensor emits a beam of laser and detects the deflection in the reflected beam. The thickness of the deposited layer is proportional to the deflection of the beam. The deflection of the beam is detected by a laser detector, which outputs a voltage that is proportional to the thickness of the deposited layer. An *Omron Laser Displacement Sensor* was chosen for this particular system.

C. Imaging Sensor

An imaging sensor is mounted on top of the nozzle with a beam bender so that it can "look" at the melt-pool from nadir. The melt-pool images can be processed to monitor bean width and melt-pool quality. Since real-time processing was a concern a camera with embedded DSP processor was favored. The conventional camera technology is based on CCD sensors, however CCD sensors have low dynamic range so that the bloom of the laser processing saturates the

sensor. One possibility was to shut the laser for a few milliseconds while the image is captured, however it the thought to interfere with the deposition processes. Thus a camera based on new CMOS technology is opted. Due to self-adaptive gain feature, these sensors can achieve very high dynamic range so that it is possible to "see through" the bloom. Moreover this camera affords random access to any region of interest.

Control

The implementation of process control for deposition processes is scarce. Parameters such as melt pool profile, melt pool temperature, and overlap factor must be regulated while each layer is being placed to indirectly control the part microstructure and layer bonding. The bead width and height should also be regulated such that removal processes are not unduly required to even the surface, as this will decrease productivity dramatically. Powder catchment efficiency is always an important parameter to maximize, too, as it directly affects the system cost.

Since the deposition process is relatively new, it is not surprising that advanced control theory has not been utilized. The state–of–the–art still utilizes classical control theory where the gains are not chosen systematically and the different phenomena (e.g., melt pool temperature) are regulated separately. Also the models are typically static. The empirical relationships do not account for inherent process variability, and the process and servomechanism dynamic effects have not been taken into account. In the LAMP Lab, we are developing system theoretic, dynamic models of the laser metal deposition process for simulation and controller development. A schematic of the control architecture is shown in the Figure 7. The three major components that affect the laser metal deposition process are the powder feeder, laser, and CNC traverse velocity. The dynamics are inherent in these components as well as in the deposition process. Note that the communication with the CNC via an RS232 port induces delays. There are also physical transport delays in the powder feeder system. The process control system will utilize a Smith Predictor–Corrector algorithm to account for these delays, multivariable control techniques is used to account for multiple control inputs and outputs, and parameters estimation is employed to account for process variability.

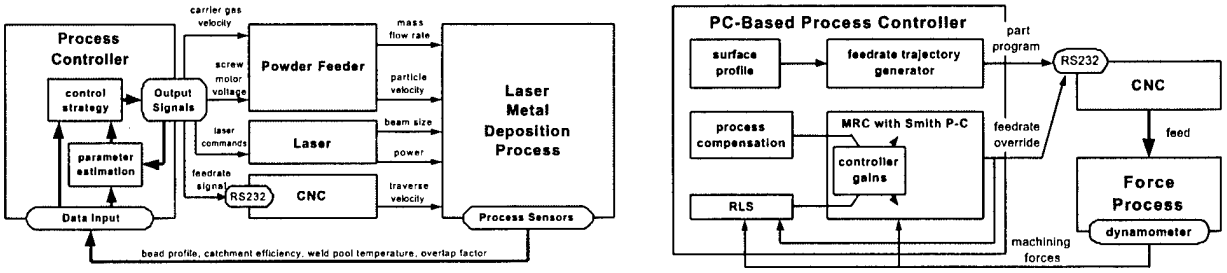


Figure 7. Deposition (left) and Structural Deflection (right) Process Control Architectures

As opposed to the literature in deposition process control, the literature in removal process control is immense and will not be reviewed in this paper. In the hybrid process, the main concern of the machining process is to remove excess material as quickly as possible while meeting the part geometry constraints. If the part is damaged during the removal process and must be scraped, the cost will be tremendous, as machining is the finishing process. The parts built by the hybrid process typically have thin sections and complex geometries, and the material to be removed will typically have an uneven distribution over the surface from which it will be removed. The removal process is required before the part is reoriented, or when access to a

surface to be machined may be blocked by further deposition. For the removal process, the issues are to ensure that the structural deflections are not excessive, that regenerative chatter, excessive tool wear, and tooth chippage do not occur, and that the machine's geometric and thermal errors are compensated.

Structural deflections will be the first issue addressed in the LAMP Lab. A schematic for a structural deflection control system is shown in the figure above. During the deposition process, the bead profile will be monitored; therefore, the profile of the excess material to remove off of each surface will be known. Using a mechanistic model of the machining process, an optimal feedrate trajectory can be calculated such that a constant machining force, and hence structural deflection, may be maintained. This feedrate profile will be embedded in the part program. However, due to model inaccuracies and unknown changes in the force process, a feedback loop will also be required to maintain a constant force while machining the surface. A Model Reference Controller (MRC) with a Smith Predictor–Corrector algorithm (to account for the communication delay with the RS232 port) will be implemented. Using the surface profile, process compensation will be used to adjust the controller gains to account for known process changes, while a Recursive Least Squares (RLS) algorithm will be utilized to estimate variations in model parameters due to unknown process changes. These compensation schemes will adjust the controller gains allowing for a robust control scheme.

Process Planning

Process planning, simulation, and tool path generation for the LAMP allow the designer to visualize and perform the part fabrication from the desktop. The Laser Aided Manufacturing Process Planning uses STL models as input and generates a description that specifies contents and sequences of operations. The objective of the process planning is to integrate the five-axis motion and deposition-machining hybrid processes. The results consist of the subpart information and the build/machining sequence. Basic planning steps involve determining the base face, extracting the skeleton, decomposing a part into subparts, determining build sequence and direction for subparts, checking the feasibility of the build sequence and direction for the machining process, and optimization of the deposition and machining.

(1) Skeleton Computation

An algorithm for computing the skeleton of 3-D polyhedron is needed. The algorithm is based on a classification scheme for points on the skeleton computation (Sherbrooke, 1995) in which the continuous representation of the medial axis is generated with associated radius functions. Because it is used as a geometric abstraction, the skeleton is trimmed from the facets that touch the boundary of the object along every boundary edge for which the interior wedge angle is less than π rad.

(2) Part Orientation

The determination of the base face from which the building process of the part starts is very important. The base face functions as the fixture in the machining process. Therefore, when in the machining process, it must provide enough resistance against the cutting force. The maximal resistance force depends on the area of the base face. The base faces have to satisfy the following conditions: 1) Located on the convex hull of the part, and 2) Certain amount of contact area.

(3) Part Decomposition and Building Direction

The objective of part decomposition is to divide the part into a set of subparts, which can be deposited and machined. The topology of the part can be obtained from the skeleton. Each

branch of the skeleton corresponds to a subpart. One of the partitions that are preformed is along a non-planar surface. Therefore, close to the partition area, 3-D layers are needed to build the connection between two subparts. The build direction of a subpart may not be constant. It changes when the part is built layer by layer so that for two adjacent layers, the later layer can be deposited based on the early layer without any support structures. To achieve the non-support build, the build directions need to be along the skeleton.

(4) Building Sequence

The results of decomposition are recorded in an adjacency graph where nodes represent subparts, and edges represent the adjacency relationship between connected nodes. After considering part building order, a directed graph that represents the precedence relationship among subparts can be constructed. From the precedence graph, one can identify in what order the subparts can be built. With the precedence graph, a set of alternative building plans can be generated. Each plan represents a possible building sequence on the decomposed geometry and can be chosen optimally depending upon machine availability or other criteria such as minimum building time.

(5) Machinability Check

The main purpose of machinability check is to choose an optimal building sequence from the sequence set. Local and global collision checks are operated first to choose acceptable sequences since the building direction is different in each sequence. If any kind of collision happens or an under cut plane appears, the corresponding sequence will be discarded. For the rest of the building sequences in set, the buildability check and machining time computation is performed to find an optimal building sequence.

Conclusion

The research and development of a hybrid material deposition and removal system is summarized in this paper. It outlines some issues and approaches to establish this system.

Acknowledgments

This research was supported by the National Science Foundation Grant Number DMI-9871185, Missouri Research Board, and a grant from the Missouri Department of Economic Development through the MRTC grant. Their support is appreciated.

References

Darling, Charles R., "Pyrometry. A Practical Treatise on the Measurement of High Temperatures." Published by E. & F. N. Spon Ltd. London. 1911.

Duley W. W., "Laser Processing and Analysis of Materials", Plenum Press, New York, 1983, pp69-78.

Harry, J. E., "Industrial Application of Lasers", McGraw-Hill, 1974.

Lin J. and W. M. Steen, "Design characteristics and development of a nozzle for coaxial laser cladding", J. of Laser Applications, 10(2), 1998, pp55-63.

Mazumder J., J. Choi, K. Nagarathnam, J. Koch, and D. Hetzner, "The Direct Metal Deposition of H13 Tool Steel for 3-D Components", JOM, 49(5), 1997, pp55-60.

Mazumder J., Schifferer A., and Choi J., "Direct Materials Deposition: Designed Macro and Microstructure", Materials Research Innovations, 3(3), 1999, pp118-131.

Sherbrooke, E.C., N.M. Patrikalakis, and E. Brisson, Computation of the medial axis transformation of 3-D polyhedra. Symposium on Solid Modeling and Applications, pp187-200, 1995.

Weerashinghe V. W. and W. M. Steen, "Laser Cladding with Pneumatic Powder Delivery", 8301-016, in Proceedings of Conference on Lasers in Materials Processing, 1983, pp166-175.

Material Movement and Fusion Behavior of TrueForm and TrueForm/SiO_2 during Selective Laser Sintering

K. M. Fan, W. L. Cheung and I. Gibson

Department of Mechanical Engineering, The University of Hong Kong, Pokfulam Road, Hong Kong, China.

Abstract

Different material systems, TrueForm and TrueForm/SiO_2 composites, were sintered under similar conditions. A microscope equipped with a CCD camera was utilized to examine the material movement near the laser beam. Powder movement of the blends was found to start at different ranges ahead of the line of scan. For TrueForm, the polymer particles were found to undergo fusion ahead of the laser beam and form a band, 0.5-0.7mm wide, which then moved as a single block towards the sintered area. The dry mixed TrueForm/SiO_2 composites (dry blends) exhibited a short-range material movement in the form of small agglomerates. Meanwhile, the TrueForm/SiO_2 composite powder prepared by melt extrusion (melt blend) showed a range of material movement between those of TrueForm and the dry blends. The discrepancy is believed to arise from changes in heat transfer properties and fusion behavior after blending. The surface temperature of the powder bed was monitored during sintering. Generally, the dry blends exhibited a higher surface temperature. Apparently, both the particle size of SiO_2 and the blending method had an effect on the temperature and material movement, and hence on the final morphology of the sintered components.

Keywords: Selective laser sintering; TrueForm/SiO_2; material movement.

1. Introduction

During the SLS process, the polymer powder melts and shrinks under the influence of the laser beam. This causes movement of the powder just ahead of the line of scan. The extent of material movement will affect the morphology as well as the dimensional accuracy of the component. Basically, the dimensional accuracy is dependent upon three factors: (1) design of software such as the CAD model and slicing algorithm, (2) resolution of the sintering facility and (3) material formulation. Different methods have been suggested and used to reduce problems associated with shrinkage and to improve surface finish. Most of these methods are processing parameter based, such as thermal control via control of the laser scan[1]; calibration of shrinkage and beam offset[2] and post-process to improve the surface finish.[3] Another approach is through improved material formulation, for example, glass microspheres filled composites.[4] However, much has yet to be learnt about the actual influence of a solid additive on heat transfer properties

and fusion behavior of the powder bed. In this paper, TrueForm was blended with SiO_2 of different particle sizes by either dry mixing or melt blending. The composite powders were then sintered under similar conditions. The movement of the powder materials during the sintering process was investigated *in situ* by a microscope setup. The surface temperature of the powder bed was monitored by a non-contact infrared thermometer. The results provided some useful information about the influence of the additive and of the blending methods.

2. Experimental

2.1 Materials and blending processes

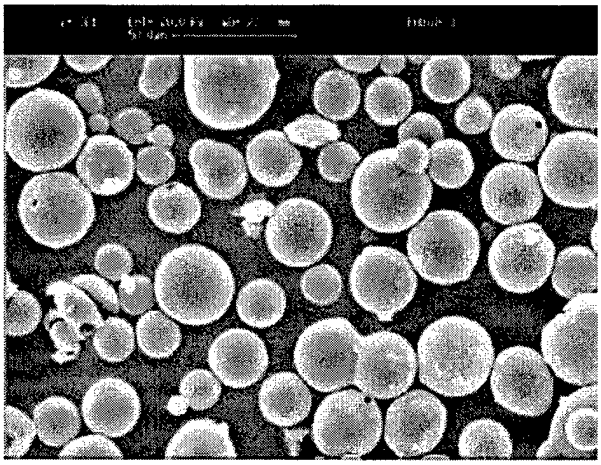
TrueForm, supplied by DTM, was used as the base polymer, figure 1a. It is acrylic based and has a T_g of 69°C. The SiO_2 powder was supplied by Fisher Scientific, figure 1b. Its original mean particle size is approximately 32μm. Depending on blending requirements, some SiO_2 powder was ball milled and treated with silane to improve the adhesion with the polymer. The silane coupling agent used was Dow Corning z-6040. All TrueForm/SiO_2 blends used in this study had a SiO_2 volume fraction of 30% and their details are shown in Table 1. For the melt blend, the extrusion process was carried out using a Prism TSE 16TC co-rotating twin screw extruder. The extrudate was first pelletised and then ground into a powder using a Philips blender. The powder was sieved to eliminate particles larger than 250μm.

Table 1. Details of powders used in the sintering process

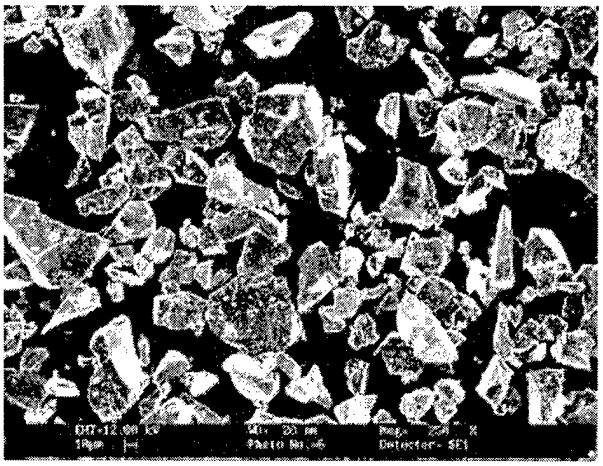
Blend Type	Mean SiO_2 particle size (μm)	Silane treatment	Blending method	Powder density / Solid density
TrueForm (TF)				0.48
Dry Blend I (DBI)	32 (as received)	No	Dry mixing	0.47
Dry Blend II (DBII)	<10 (ground)	No	Dry mixing	0.46
Dry Blend III (DBIII)	<10 (ground)	Yes	Dry mixing	0.47
Melt Blend (MB)	<10 (ground)	Yes	Melt blending	0.49

2.2 Sintering process

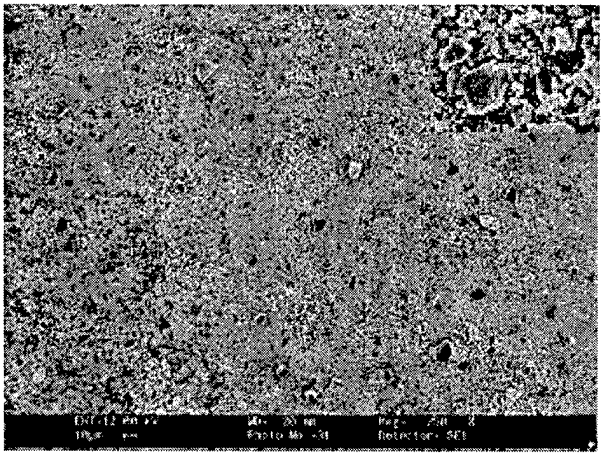
Sintering was carried out on a M25e Universal Laser Engraving Machine, which is equipped with a 25 watt CO_2 laser. The laser beam has a spot size of 0.32mm at focus and it is driven by a x-y table mechanism. The laser power (P) was set at 30% and the beam speed (BS) at 50%, equivalent to 500mm/s. The distance between adjacent parallel scans was 0.0508mm. Sintering was performed in air and at room temperature.



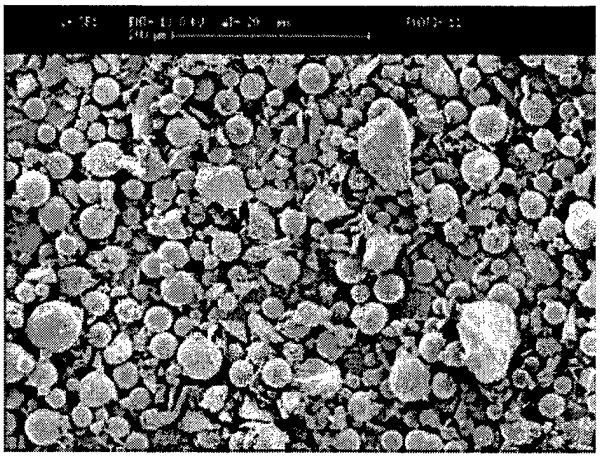
(a) TrueForm powder



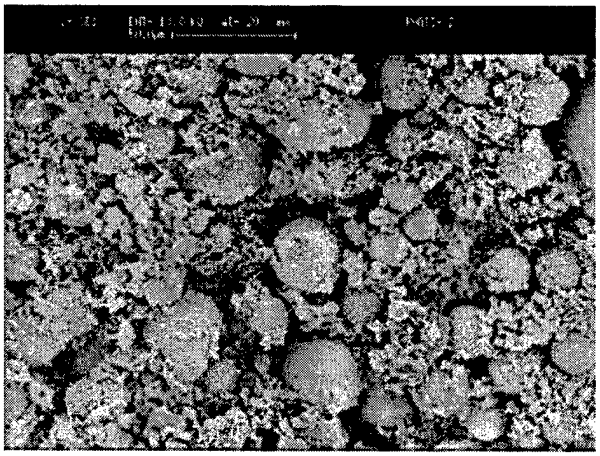
(b) SiO_2 powder (as received)



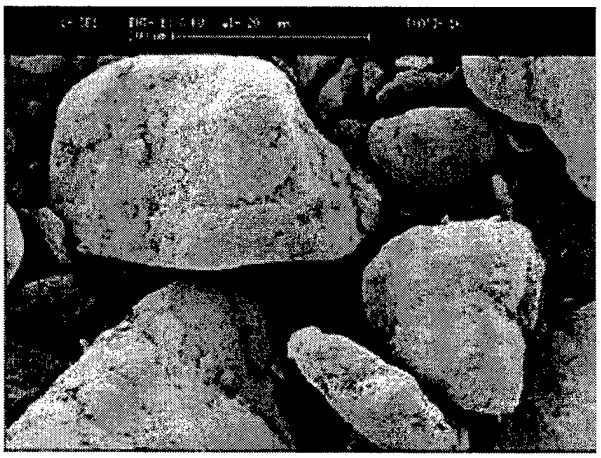
(c) SiO_2 powder (ground)



(d) TrueForm/SiO_2 (dry blend I)



(e) TrueForm/SiO_2 (dry blend II)



(f) TrueForm/SiO_2 (melt blend)

Figure 1. SEM micrographs of (a) TrueForm powder; (b) as received SiO_2 powder; (c) ground SiO_2 powder and (d-f) TrueForm/SiO_2 blends.

2.3 *In situ* microscopy and surface temperature measurement

In situ observation of material movement during sintering was conducted using a microscope setup as shown in figure 2. The surface temperature at a point (diameter 3mm) within the scan area was monitored during the sintering process by a Mikron M67s non-contact infrared thermometer. The details of the thermometer setup has been reported earlier.[5]

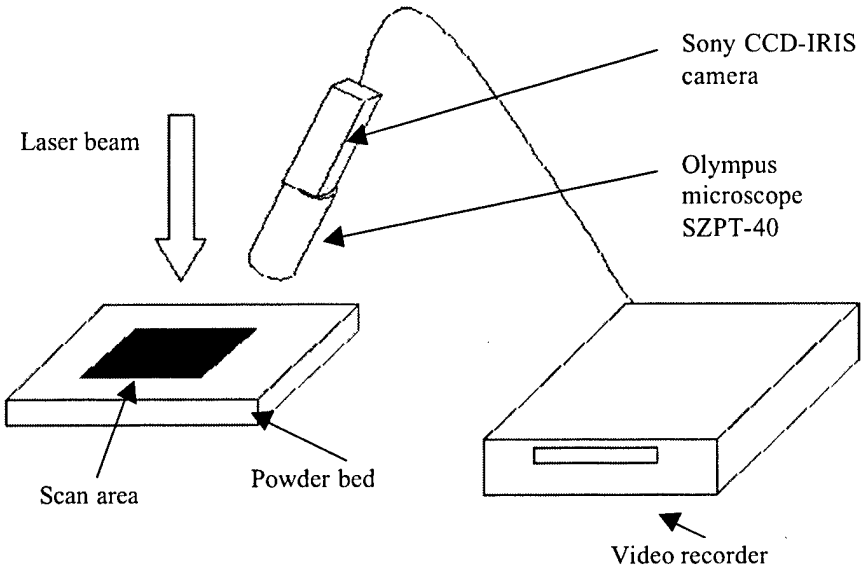


Figure 2. Microscope setup for *in situ* observation of material movement during sintering process

3. Results and Discussion

Material movement

Figure 3 shows the material movement of the blends ahead of the line of scan during the sintering process. For pure TrueForm, the polymer particles adhered together and moved as a single block towards the sintered area as a result of material shrinkage. The width of the block or band was about 0.5 to 0.7 mm and its formation was likely due to slight fusion of the polymer powder in the laser affected zone. The band collapsed and densified under the influence of the advancing laser beam. The leftover powder front remained more or less stable for a number of scans until the laser beam had advanced and made contact with it. Then, another powder band would form shortly afterward and break away from the unsintered region of the powder bed. For DBI, no powder band formation was observed. Only agglomerates were formed slightly ahead of the line of scan and moved towards the sintered area. DBII and DBIII showed very limited range of powder movement next to the line of scan. One possible explanation is that the polymer particles in DBII and DBIII are fully surrounded by fine SiO_2 powder, figure 1e, and fusion between the polymer particles under moderate heat is unlikely. Therefore, there is no bonding between the material at a distance from the laser beam and the shrinking material at the line of scan. For MB, the range of material movement lay between those of TrueForm and the dry blends. No distinctive band structure was seen and the material also moved as agglomerates.

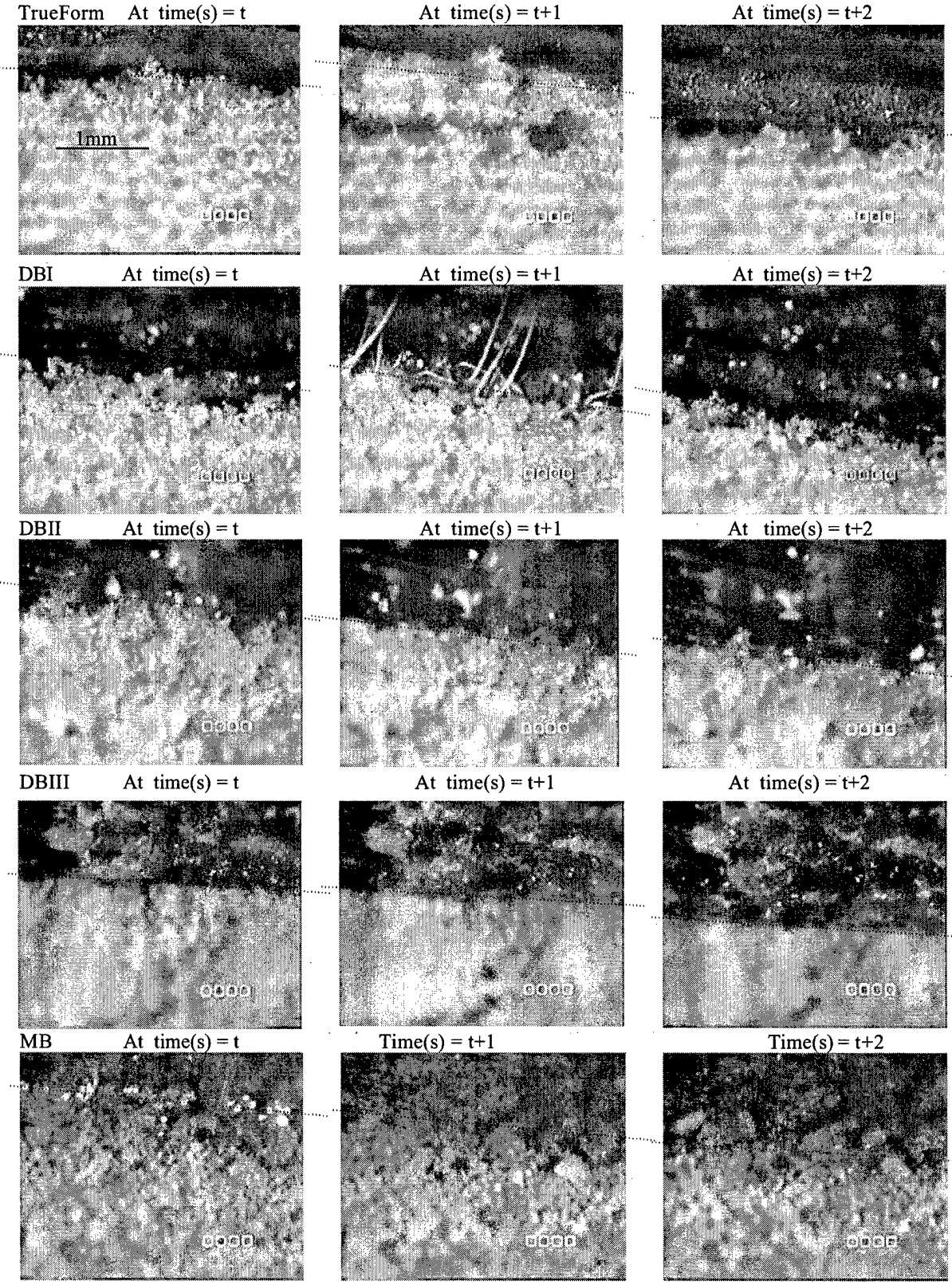
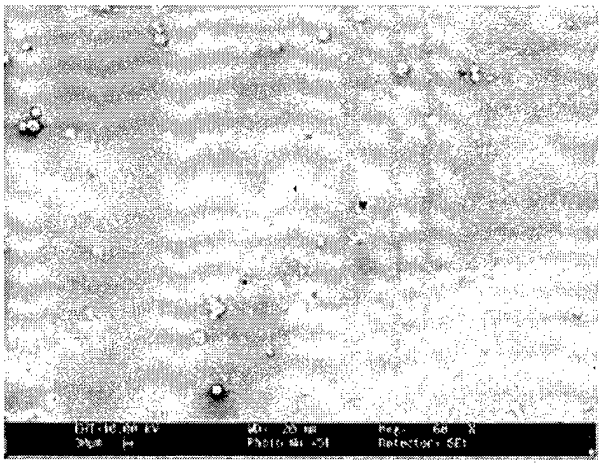


Figure 3. *In situ* observation of material movement during sintering process. There are about 10 parallel scans within 2 seconds, the dotted line in each figure roughly indicates the line of scan.

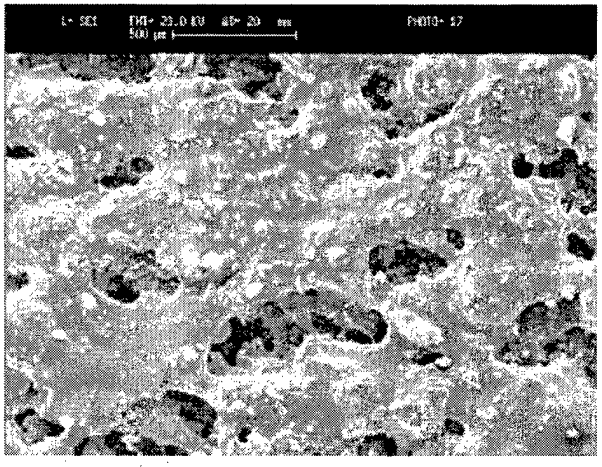
It is believed that the different material movement characteristics were due to changes in heat transfer properties and fusion behavior after blending. In dry blends DBII and DBIII, agglomeration of SiO_2 powder was found and this would affect the packing characteristics of the powder bed.[6] Also, the presence of a large number of very fine SiO_2 particles was likely to obstruct contact between the polymer particles. Meanwhile, the polymer particles were in close contact in TrueForm and fusion was much easier in regions well ahead of the laser beam where the temperature was moderate. Also, smoke and sparks were observed during sintering of the dry blends. These were signs of excessively high temperature.

The surface morphologies of the sintered specimens are shown in figure 4. The pure TrueForm specimen, figure 4a, gives a smooth and fully dense structure. This indicates that the molten polymer flowed easily under the sintering condition. Among the dry blends, figure 4b-d, DBI exhibits a higher degree of fusion than that of DBII and DBIII. The latter two samples had a larger number of very fine SiO_2 particles, which would obstruct contact and hence fusion between the polymer particles. Nevertheless, in areas of high polymer concentration, significant flow of polymer material is apparent, giving rise to some well-fused patches. In contrast, the melt blend only exhibits a limited flow of material and the structure remains highly porous. This is probably due to the fact that the embedded SiO_2 particles in the composite powder has significantly increased the viscosity of the material. Furthermore, the strength of DBII was the lowest among the blends and it tended to fall apart very easily after sintering. The phenomenon can be attributed to the weak boundaries between bare SiO_2 particles.

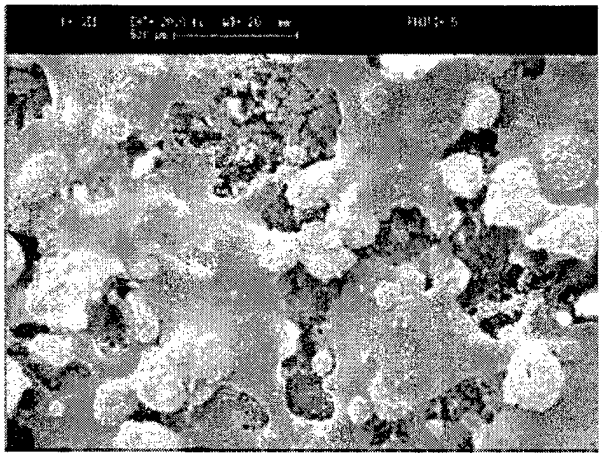
The surface temperature variation of a particular area, 3 mm in diameter, of the powder bed was monitored with respect to its distance from the line of scan. The temperature measurement results are shown in figure 5a-c, whilst, the schematic representation of the relative distance between the monitored area and the line of scan is shown in figure 5d. The hidden lines on each graph represent the boundaries of the focused area by the infrared thermometer. The distance between the hidden lines is 3 mm because the diameter of the focused area was 3mm during the experiment. When the laser beam hits the left boundary, the distance is designated as 0 mm. When the laser leaves the monitored area from the right boundary, the distance is 3 mm. From figure 5a, SiO_2 shows the highest temperature profile. However, it is not certain whether it really reflects the true surface temperature of the powder bed or it is partially due to the highly reflective nature of the SiO_2 particles. Among the blends (i.e. TF, DBII and MD), DBII generally gives a higher temperature. This is in agreement with the fact that smoke and flashes were seen during sintering of the dry blends. It is noteworthy from figure 5b that particle size of the SiO_2 powder also affects the temperature, the smaller the particle size, the higher the temperature. Again, it is not known if the increased total surface area of the ground SiO_2 powder has a role to play and further investigation is underway.



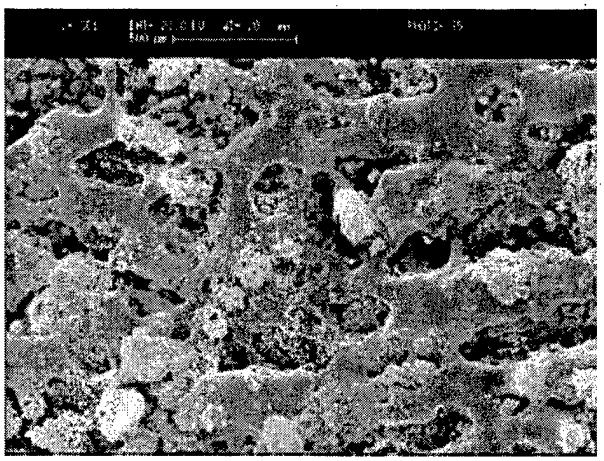
(a) TF



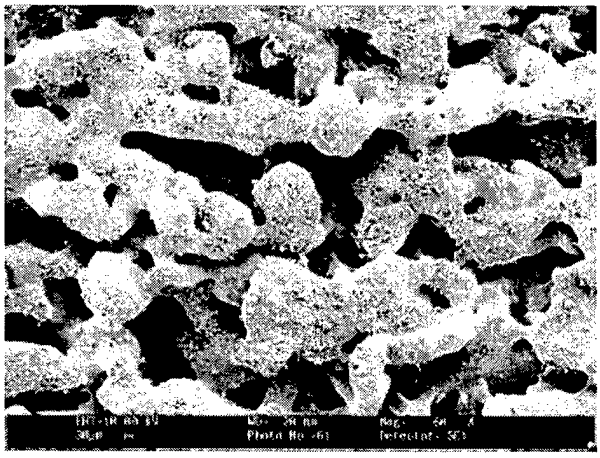
(b) DBI



(c) DBII

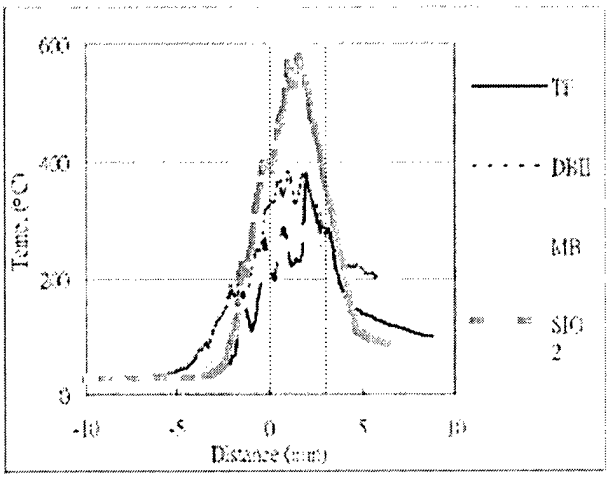


(d) DBIII

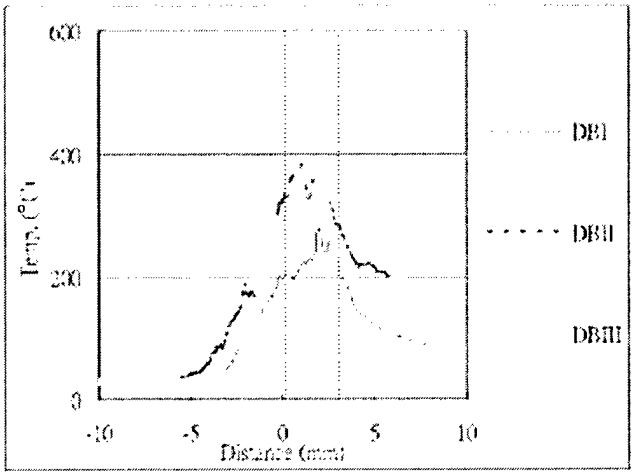


(e) MB

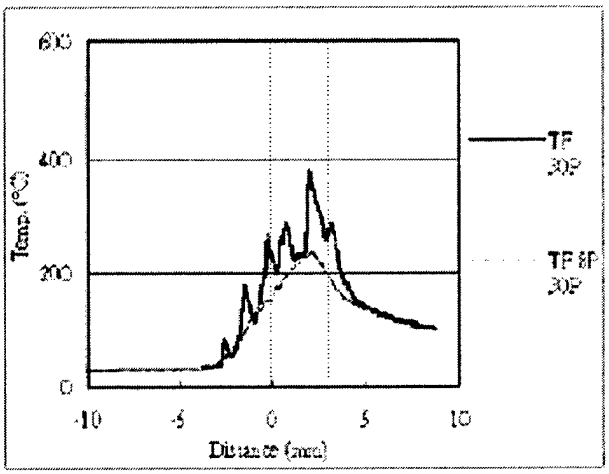
Figure 4. Surface morphologies of specimens laser sintered at P=30% and BS=50%



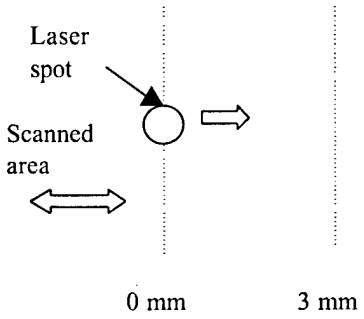
(a) TF, DBII, MB and SiO_2



(b) DBI, DBII and DBIII



(c) TrueForm sintered at P=30% (TF 30P); TruForm pre-sintered at P=8% then at P=30%(TF 8p 30p)



(d) Schematic representation of the relative distance between the line of scan and area monitored by the non-contact infrared thermometer

Figure 5. Surface temperature variation of different powder systems during laser sintering at laser powder P=30% and beam speed BS=50%.

Furthermore, a large fluctuation is found in the temperature profile of Truefrom, figure 5a, despite the fact that its temperature profile is not the highest among the materials tested. It was suspected that the large-scale powder movement of Truefrom during the laser sintering process might affect the temperature profile. In order to verify the hypothesis, a two-step sintering process was carried out. First, the powder bed was sintered at a very low power P=8% to slightly bond the polymer particles together without changing the surface morphology of the powder bed significantly. This would eliminate the large-scale powder movement during the

second sintering process at P=30%. The temperature profile for the second sintering process was recorded and shown in figure 5c together with that extracted from figure 5a. It is clear that material movement during the sintering process does affect the temperature measurement result from the non-contact infrared thermometer. This is probably due to the fact that when the powder band is tilted at a certain angle, direct reflection of laser beam to the infrared thermometer is possible and this will greatly increase the reading. The temperature profiles of the other blends did not show such a large temperature fluctuation because the scale of the powder movement was not so large.

4. Conclusions

This study has shown that material movement at and near the fusion zone during selective laser sintering affects the morphology and properties of the sintered product. Adding a solid additive such as SiO_2 powder will obstruct contact between the polymer particles and hence change the material movement characteristics. For a given volume fraction of the additive, a smaller particle size of the additive would obstruct fusion of molten polymer particles more significantly and result in a weak component. The blending method also plays an important role in the properties of the composite powder. Although melt blending enhances polymer/polymer contact between the composite particles, the embedded SiO_2 powder increases the viscosity of the material and hence adversely affects the densification of the powder bed. Also, degradation becomes more apparent, especially in the dry blends.

5. References

1. Beaman, Joseph J.; McGrath, Joseph C. "Thermal control of selective laser sintering via control of the laser scan." US Patent, US5352405, (1994).

2. Wang, Xiangwei, "Calibration of shrinkage and beam offset in SLS process", Rapid Prototyping Journal, v 5, n 3 (1999) 129-133.

3. Shi, D.; Gibson, I., "Improving surface quality of selective laser sintered rapid prototype parts using robotic finishing", Journal of Engineering Manufacture, v214, n3 (2000) 197-203.

4. McAlea, Kevin P.; Forderhase, Paul F. "Selective laser sintering with composite plastic material", US Patent, US5733497, (1998).

5. Ho, H. C. H.; Gibson, I.; Cheung, W. L. "Effects of graphite powder on the laser sintering behavior of polycarbonate", submitted to Rapid Prototyping Journal.

6. German, R. M. "Particle packing characteristics", Metal Powder Industries Federation, (1989).

this page intentionally blank

DESIGN OF A MICRO-HOPPER ARRAY FOR MULTI-MATERIAL POWDER DEPOSITION

Suman Das and James Santosa
Department of Mechanical Engineering
The University of Michigan
Ann Arbor, MI 48109-2125

Abstract

We present a concept for creating patterned beds of multi-material powder particles using an array of small-scale hoppers. Using this technique, we propose that to place fine particles of multiple fluidized powders discretely in a thin layer as opposed to depositing an entire powder layer of uniform composition using a roller device or doctor blade. Processing and consolidation of multiple, patterned powders can enable fabrication of composite objects with spatially varying structural and multifunctional characteristics. Although theory on the design of small-scale hoppers is lacking, our design for a hopper, its valving, and its particle delivery system are guided by background theory for large hoppers. A hopper array configuration is proposed, and a calculation for deposition time is presented. Delivery of powder was achieved on a prototype hopper. Experimentally measured mass flow rates were used to justify the use of this hopper with SLS and to guide further design improvements.

INTRODUCTION

The variety of applications for multi-material composite structures is both well established and growing rapidly. However, a present obstacle to continued growth lies in the approaches to manufacturing these types of artifacts. The development of new approaches for fabricating multi-material components is in part dependent upon developing SFF techniques capable of depositing and consolidating multiple materials. In particular, the selective laser sintering (SLS) process is well suited to this challenge. A means of incorporating the delivery of multiple powders in SLS may enable the production of complex, multi-functional and intelligent components.

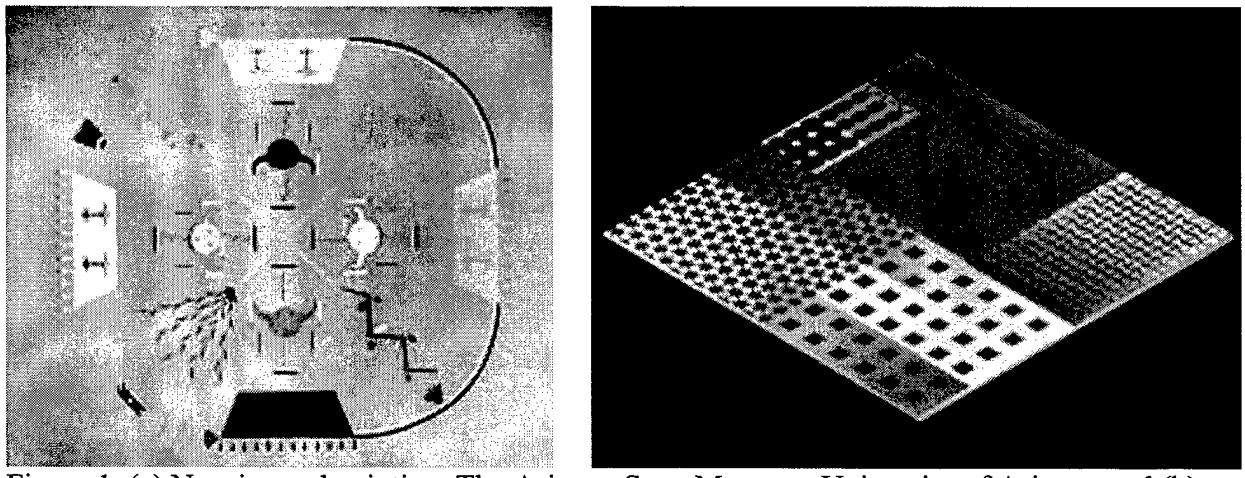


Figure 1. (a) Navajo sand painting, The Arizona State Museum, University of Arizona and (b) Conceptual design of a multiple material, patterned, powder layer for building multifunctional components by SLS.

The concept of 2-D deposition for multiple powders is by no means a new idea. In fact the greatest model for this idea is based on the art form of sand painting as shown in Figure 1a and first described in the context of SFF by Pegna et al [7]. The Navajo and Tibetan monks of earlier centuries have shown that detailed patterning of fine powders can be achieved manually. These artists typically spent several weeks working patiently on a single-layer design. However, the challenge from a layered manufacturing perspective is in successively depositing thin layers of multiple powders quickly and with high placement accuracy. By allowing the consolidation of multi-materials as shown in Figure 1b, SLS has the potential to launch a new manufacturing paradigm that enables fabrication of complex, multifunctional, intelligent components that cannot be fabricated by existing methods. The following sections provide background on the use of hoppers with fine powders, the theory guiding the design of a single hopper and standpipe to an array of these devices, and results of preliminary experiments conducted on a prototype hopper design.

BACKGROUND

In current selective laser sintering machines, powder is leveled over the part-build area by a counter-rotating roller mechanism or a doctor blade. A bed of powder may be quickly rolled over the build area in layers of consistent thickness. Currently the SLS process is limited to fabricating components of only a single composition. However, SLS is capable of simultaneously sintering a variety of powdered materials (metals, ceramics, polymers). This makes depositing and processing two or more different powdered materials side-by-side on the bed feasible. With this in mind, the development of hoppers for delivering dots, sharp lines and prescribed patterns of powder is desirable for use in the SLS process. In fact, those who practiced the art of sand painting used a tool that is essentially a hopper releasing powder to a surface by vibration. A multi-powder deposition device for adaptation to SLS should have more stringent requirements. For the design of our hopper, a number of design specifications were established. According to these specifications, the device should be able to:

1. Deposit arbitrary patterns of multiple powder material (i.e. points, lines, regions) for particles with diameters ranging from 0.1 to 100 μm.
2. Achieve a minimum in-plane feature size of 100 μm.
3. Achieve layer thickness ranging from 25 to 250 μm.
4. Regulate hopper mass flow rate, start and stop flow with minimal time delay.
5. Handle multiple materials with real time composition control.

In an attempt to meet some of these goals, the background research focuses on 3 areas: the relevant properties of powder particles, the design of hoppers, and, flow control and valving techniques.

Relevant Powder Properties

The characteristics of powdered material that must be considered are the size, shape (sphericity), cohesion properties, bulk density, and porosity (voidage). These are most critical to understanding the bulk flow of the solid material, from how it is packed to how it is transported (Shamlou [8], Woodcock and Mason [11]). Cohesive properties can be described as the ability of the bulk material to freely flow based on inter-particle forces (Jenike [3]). One of several methods to measure cohesion property that is of special concern to SLS is the angle of repose

(a.k.a. angle of internal friction) of a deposited powder. This is useful for understanding the ability of a poured powder to remain in a stable pile (Stepanoff [10]) i.e. when the deposited lines are settling on the substrate.

For applications over a wide variety of materials, it is important to have a practical method for classifying powders without depending on extensive experiments. The Geldart classification [2] is an appropriate and well-used system for grouping powders by their ability to fluidize. Fluidization is the ability of a uniform bed of particles to expand when an upward stream of gases is distributed from beneath. A bulk material that is well fluidized will have an expanded volume, where particles seem to be floating in the fluid stream, separate from other powder particles. This is advantageous because of reduced inter-particle friction and ability to circulate powders within the bed.

SLS applications require fine powder particle diameter between 0.1 μm to 100 μm, and the bulk material is largely considered non-cohesive (fair to free-flowing in nature). These types of powders would typically fall into the Geldart A classification [2]. An attempt to fluidize such powders relies upon the knowledge of minimum fluidization velocity. This is the velocity of introduced gas at which incipient fluidization occurs in the powder bed or chamber. There are many approaches to gaining values for minimum fluidization velocity, but equation (1) is the rule of thumb for particles in air (Woodcock and Mason [11]).

$$U_{mf} \cong 420 \rho_p d_v^2 \qquad (1)$$

where U_{mf} = minimum fluidization velocity (m/s)
ρ_B = bulk density of the powder (g/m^3)
d_v = mean particle diameter based on volume (m)
and 420 is an empirical value for particles in air ($m^2/g\text{-}s$).

Hopper Design

A hopper can be described as the lower converging section of any vertical bin for discharging bulk materials. Hoppers can have conical, wedge-shaped, or even asymmetrical designs. Hoppers can also have circular, square, or rectangular orifices. Evidently, the geometry of a hopper design is essential in achieving desired flow properties of the discharged material. The delivery of particles may happen under core flow (first in-last out) or the more desirable mass flow (first in-first out). For the design of a conical hopper, the hopper half-angle, α, and the orifice diameter, D_0 are the most important dimensions to be considered in preventing arching (bridging of particles that blocks flow) and rat-holing (an empty tunnel over the orifice due to core-flow). Jing and Li [5] provide useful information on hoppers for fine powders, stating an effective hopper half-angle of 10.2° or less for maintaining mass flow.

One of the most frequently used theories on flow from hoppers is W. A. Beverloo's modified correlation [1] for mass flow rate in conical hoppers. While there are other similar theories for mass flow rate, e.g. the hourglass theory, these do not take into account the effects of particle diameter. The modified Beverloo correlation is

$$G_s = C\rho_b \sqrt{g + \left(\frac{dp}{dz}\right)_0 \frac{1}{\rho_b}} (D_0 - kd_p)^{5/2} \qquad (2)$$

where G_s= mass flow rate of particles (g/s)
C = empirical constant (usually .58) dependent on hopper angle and angle of internal friction
ρ_B= bulk density of the powder (g/m^3)
g = gravitational constant of acceleration ($9.8 m/s^2$)
D_0= hopper orifice diameter (m)
k = empirical constant for particle shape (1.6 for spherical particles)
d_p = mean particle diameter (m).

The term $1/\rho_B (dp/dz)_0$ is a modification of the gravitational acceleration term to include the interstitial pressure gradient. Beverloo's correlation states that as particle size decreases, there is an increase in the mass flow rate. Empirical results agree for particle sizes down to 500μm, where actual mass flow rate takes on much lower values than predicted.

An article by Spink and Nedderman [9] presents an experimental and theoretical study on the rate of discharge of fine particles (diameters between 50 μm and 500 μm) under gravity in air from a hopper. These size particles are small enough to be retarded by air resistance when passing through the hopper orifice, but not too small so as to be subject to cohesive effects. In this work, it is believed that the air pressure gradient opposed to the downward flow reduces the flow rate of the particles under 500 μm, and it is also presumed that change in voidage as the hopper converges has a slowing effect as well. The work by Spink and Nedderman used first principles (stress equations for different regions in the hopper) to come up with a theoretical model. They experimentally measured the voidage and interstitial fluid pressure distribution with external probes around the hopper and used these to account for the drop. The result was a downward sloping set of data points for the mass flow rate of particles having less than 500 μm diameter (always higher than actual, but generally following the reducing trend). This is a good basis for the kind of experimentation needed to understand the behavior (voidage changes and pressure distribution) in much smaller hoppers. Our challenge in designing a micro-hopper based powder deposition system for SLS will be to adapt these types of experiments to small scale hoppers.

At the present, most theoretical predictions relate to large, coarse particles on the order of 500 μm diameter that are cohesionless and insensitive to drag. Beverloo's equation is known to be inaccurate for particles under 500 μm diameter. Most hopper theory is valid for large-scale bulk materials handling only. However, the existing theory provides a useful basis on which empirical models, and eventually a working theory for powders under 500μm and orifices around 100μm can be developed.

Flow Control and Valving

There are a number of techniques to starting/stopping flow, from the use of physical barriers such as gate valves, to fitting a hopper with flow aids like vibrating plates. Considering the small particle and hopper sizes we are compelled to modify or combine existing techniques for application to an array of hoppers.

Pegna et al [7] conducted an experiment using a non-mechanical L-valve [6], where powders come to rest in the elbow portion due to their angle of repose. Flow was started by introducing air from an aeration point. The flow rate was proven to be unstable considering the size of the particles. However, this design did not feature a hopper, and the orifice was simply the end of the downcomer. The concept of a hopper valve for Geldart A powders is presented in an article by Jing and Li [4]. In this setup, the flow regime and flow stopping are controlled by maintaining a negative pressure gradient from the hopper orifice to the standpipe. It is our belief that combining the design of a standpipe with L-valve and hopper dimensions according to the Jing and Li criteria can be a strong combination for use with a greater variety of powders.

EXPERIMENTS

Figure 2 shows our prototype hopper design. Some of the features include:

1. A 60mm I.D. glass Buchner funnel and coarse fritted glass disk used as a chamber for fluidizing particles and delivering them to the standpipe.
2. Two angled aeration points at the base of the funnel to fluidize the powder above the fritted glass disk. Fluidized powder travels down the standpipe originating at a hole in the fritted disk.
3. Adjustable tube lengths for the glass standpipe and elbow in 10 mm increments. Glass pieces are joined using photosensitive UV curing resin. The prototype shown has a 150mm long standpipe and 40mm long elbow, both 4mm I.D.
4. An L-valve aeration point angled at 45° to the elbow. The position of the aeration point can also be varied along the standpipe with the use of adjustable tube lengths.
5. Bio Plas, Inc. pipette tips used as micro-hoppers, which feature a half angle < 10.2° and 5mm orifice that can also be trimmed for larger diameters (.75 and 1mm).
6. 100 μm glass beads used for powder for initial testing (bulk density 2480000g/m^3),120 grit sandpaper used as the substrate (depositing surface).

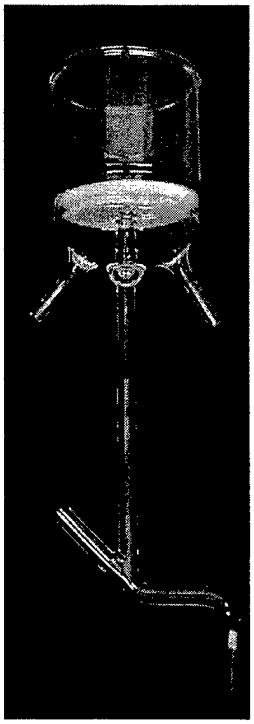


Figure 2. Prototype micro-hopper

RESULTS

Ten trial runs for mass flow rate were conducted on the prototype hopper under both gravity flow and air assisted flow for orifice diameters of 0.5, 0.75, and 1 mm. Our preliminary trials show that the standpipe with L-valve design is fully capable of stopping the flow of powders. The powder will come to rest at the angle of repose (approximately 23°) when the elbow portion of the L-valve remains horizontal. Particles just over the nozzle will continue to flow through until this portion is emptied. Air introduced from the aeration point prefers to fluidize the column of particles in the standpipe rather than push particles over the elbow. Although a higher flow of air will move the powder through the elbow, we avoid interfering with flow settings that may make the powders in the standpipe entrain (bubble out). To restart flow, we preferred to slightly tip the L-valve down – a technique that may possibly be incorporated into later designs.

Nozzle diameter(mm)	Gravity flow or Air assisted	Average mass flow rate (g/s)	Volume delivered per second (m^3/s)	Time to draw a 250 μm high, 6in.(.1524m) line
0.5	G	0.0283	$1.9X10^{-8}$	0.79 seconds
0.5	A	0.045	$3.0X10^{-8}$	0.50 seconds
0.75	G	0.0316	$2.1X10^{-8}$	0.71 seconds
0.75	A	0.0616	$4.1X10^{-8}$	0.37 seconds
1.0	G	0.0717	$4.81X10^{-8}$	0.32 seconds
1.0	A	0.1	$6.7X10^{-8}$	0.22 seconds

Table 1. Results from prototype hopper tests for 100 μm glass beads (bulk density 2480 kg/m^3).

Our mass flow rate results in the third column of Table 1 show that flow rates of a single powder increase with larger orifice diameters. Trials with air entry from the aeration point were conducted at the velocity just below where entrainment in the standpipe was observed. It is believed that the position of the aeration point primarily allows the standpipe's particles to be fluidized, while slightly counteracting the pressure gradient at the nozzle and increasing the flow rate. Flow rate for all diameters were improved by approximately 0.025g/sec with air. Further experiments may reveal whether there is proportional relationship between air-assisted flow and orifice diameter.

Array Theory

Using basic information such as mass flow rate, it is possible to calculate the deposition times of our prototype hopper design its suitability for use with SLS. To compete with the speed of current roller mechanisms for laying powder on a bed, a successful design should be able to deposit a complete layer in a matter of seconds. The following assumptions characterize the ability of our prototype hopper (and eventually a hopper array) to achieve deposition times appropriate for SLS:

Assume that the volume of material deposited per second in m^3/s is:

$$\dot{V} = \frac{G_s}{\rho_B(1-\varepsilon)} \qquad (3)$$

where G_s = mass flow rate of particles (g/s)
ρ_B = bulk density of the powder (g/m^3)
ε = voidage of powder particles, assumed to be 0.4, based on 60% packing density

Also assume that a stationary orifice is capable of depositing a disk of material with the same diameter as the orifice. Therefore, the volume of the disk (m^3) to be filled is:

$$V = \frac{\pi D_0^2}{4} \bullet h \qquad (4)$$

where D_0 = hopper orifice diameter (m)
h = desired height of a disk of material (m)

Therefore the time (s) to deposit a single disk of material with height h is:

$$\frac{V}{\dot{V}} = t = \frac{\pi D_0^2 h \rho_B (1-\varepsilon)}{4G_s} \tag{5}$$

A series of these deposited disks laid side-by-side can be thought of as collectively forming a line. With knowledge of the diameter of the disks, the number of disks that compose a line of desired length is the ratio l/D_0. The overall time,T, required to deposit a line is:

$$T = t\frac{l}{D_0} = \frac{\pi D_0 l h \rho_B (1-\varepsilon)}{4G_s} \tag{6}$$

The last two columns of Table 1 show that the volumetric flow rate and the time required for drawing a 0.010 inches (250 μm) high, 6 inches long line (an estimated minimum length for a powder bed) would be feasible for use with SLS. Even though delivery times for potentially smaller orifice diameters are above 1 second for gravity flow or air-assisted, an array of nozzles that produces a complete layer in a similar amount of time will be faster than current roller or doctor blade techniques. Shown in Figure 3 are two array concepts to be explored for minimizing delivery time to the bed.

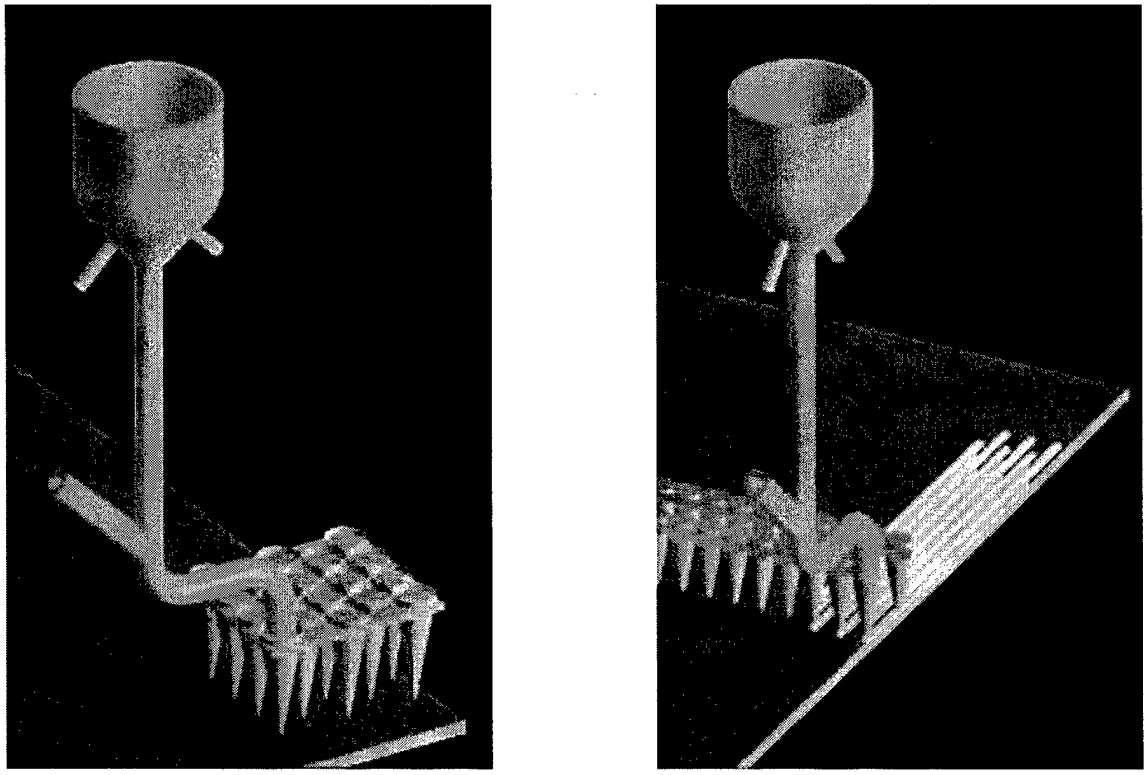


Figure 3. (a) A 4x5 staggered array, and (b) A array covering the entire bed length.

FUTURE WORK

There are many challenges for future work on a micro-hopper array. It is our aim to determine experimentally and eventually theoretically a prediction for mass flow rate in micro-hoppers. Theory should apply to a variety of powders, so a single highly compatible hopper

design and model for fluidization with dispensing adjustments can be achieved. Visually, the micro-hoppers are delivering powder with consistent flow rate. However, techniques to aid in understanding all of the phenomena, i.e., determining the pressure at the aeration point and minimum fluidizing velocity in the particle delivery system, need to be determined. Incorporating an XYZ positioning system will yield valuable information on whether our desired minimum feature size for lines and patterns is feasible. Once these goals are achieved, work will focus on the design and control of the array and powder supply system. We look forward to experiments on mixing and depositing powders in gradient fashion with the ability to draw two or more powders from a reservoir supply system

CONCLUSIONS

Existing theory on large hoppers was used to guide the design of prototype micro-hoppers for powder delivery. Information on relevant particle properties and flow control techniques was noted. A prototype micro-hopper design was completed and tested with 100 μm glass beads for both gravity flow and gas assisted flow conditions. Mass flow rates were noted to increase with air-assistance, and measured delivery times were found to be appropriate for use with SLS.

REFERENCES

[1] Beverloo, W.A., H.A. Leniger and J. van de Velde, "The Flow of Granular Solids through Orifices", Chemical Engineering Science. Vol. 15, pp. 260-69 (1961).
[2] Geldart, D., "Types of Gas Fluidization", Powder Tech. Vol.7, pp. 285-92 (1973).
[3] Jenike, A.W., "Gravity Flow of Solids", Trans. Instn Chem. Engrs. Vol. 40, pp. 264-71 (1962).
[4] Jing, S., and H. Li, "Hopper Valve for Fine Powders in a Moving-bed Standpipe", Powder Technology. Vol. 114, pp. 252-54 (2001).
[5] Jing, S., and H. Li, "Study on the Flow of Fine Powders from Hoppers Connected to a Moving-Bed Standpipe with Negative Pressure Gradient", Powder Technology. Vol. 101, pp. 266-278 (1999).
[6] Knowlton, T.M. and I. Hirsan, "L-valve Characteristics for Solids Flow", Hydrocarbon Processing. Vol 57, pp. 149-56 (1978).
[7] Pegna, J., S. Pattofatto, R. Berge, C. Bangalan, H. Herring, M. LeSaux, J. Engler, "The Sand Painter: Two-dimensional Powder Deposition", Proceedings on the Solid Freeform Fabrication Symposium, Austin, TX, pp. 695-709 (Aug. 1999).
[8] Shamlou, P.A. *Handling of Bulk Solids - Theory and Practise*, Butterworth & Co. Ltd. London, pp. 1-88 (1990).
[9] Spink, C.D. and R.M. Nedderman, "Gravity Discharge Rate of Fine Particles from Hoppers", Powder Technology. Vol. 21, pp. 245-61 (1978).
[10] Stepanoff, A. J., *Gravity Flow of Bulk Solids and Transportation of Solids in Suspension*, John Wiley & Sons. New York, Ch. 1-8. (1969).
[11] Woodcock, C.R. and J.S. Mason, *Bulk Solids Handling,* Chapman and Hall. New York, Ch. 1-4. (1987).

SALDVI OF SiC INTO METAL AND CERAMIC POWDERS

James E. Crocker, Haoyan Wei, Leon L. Shaw, and Harris L. Marcus
Institute of Materials Science, Department of Metallurgy and Materials Engineering
University of Connecticut, Storrs, CT 06268

Abstract

Selective Area Laser Deposition Vapor Infiltration (SALDVI) is the SFF technique using gas phase precursors to locally infiltrate a powder bed into a desired shape. Experiments were performed with a CO_2 laser and the silicon carbide forming gas precursor $Si(CH_3)_4$. This paper will report on the microstructural aspects of SiC into a variety of metal and ceramic powders including Mo, SiC, ZrO_2, and WC.

Introduction

SALDVI is a layer-by-layer approach to SFF in which porous layers of loose powders are densified by depositing solid material from gas precursors into the pore spaces using laser chemical vapor infiltration (CVI)[1]. Because the CVI process can deposit a variety of desirable materials in pure form, SALDVI is capable of building ceramic and composite net shapes and shapes with functionally graded compositions such as embedded devices[2] in a single machine. The nanocrystalline nature of the solid material deposited from the $Si(CH_3)_4$ gas precursor by laser CVD on solid ceramic substrates has also been well characterized on the micro and atomic scales[3]. SALDVI using ceramic powders and the SiC-forming gas $Si(CH_3)_4$ has been previously investigated for single line bar geometries with single and multiple layers[4]. The laser induced processing temperature distribution, gas precursor pressure, laser scanning speed, and the particle size of the starting powder were found to affect the densification rate and mechanical properties. In this paper we examine some SALDVI processing issues related to the fabrication of multiple layer rectangular geometries.

Experiment

The SALDVI workstation consists of a vacuum chamber, a powder delivery system, a 50 watt continuous wave CO_2 (10.6 μm wavelength) laser beam, an xy table with scanning mirrors, and an optical pyrometer temperature probe. All components are computer controlled. In these experiments the surface temperature measured by the optical pyrometer is used in a feedback loop to adjust the laser output power as necessary to maintain a constant surface temperature, termed the target temperature, throughout the experiment. The target temperature in this work is 1000°C, the $Si(CH_3)_4$ gas pressure is 10 Torr, and layer thickness is 120 μm. The laser beam spot size was nominally 1 mm in diameter and Gaussian in shape. The rectangular sample has dimensions 10 mm long by 3 mm wide and is obtained by rastering the beam with a scan spacing of 0.75 mm. Figure 1 shows two scan patterns used to generate the rectangular shape, one in which the major scan direction is horizontal (a) and one vertical (b). In order to obtain a more uniform structure, the scan direction is alternated from horizontal to vertical on alternating layers.

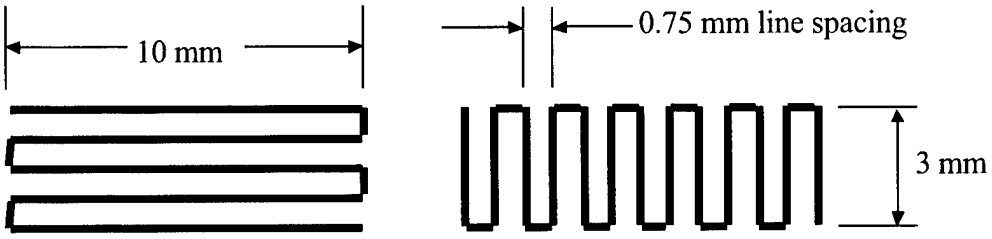


Figure 1. Scan patterns for 10 mm by 3 mm rectangle with 0.75 mm line spacing and (a) horizontal and (b) vertical major scan direction.

Results and Discussion

A. Effect of starting powder

Rectangular samples containing at least four layers were processed by SALDVI using SiC, ZrO_2, Mo, and WC powders and 1000°C target temperature, 10 Torr $Si(CH_3)_4$ gas pressure, and 120 μm layer thickness. Figures 2a-5a show the surface of the samples just after processing, and Figures 2b-5b show a polished cross-section through the thickness direction for SiC, ZrO_2, Mo, and WC powders, respectively. The arrows indicate the location of each cross-section.

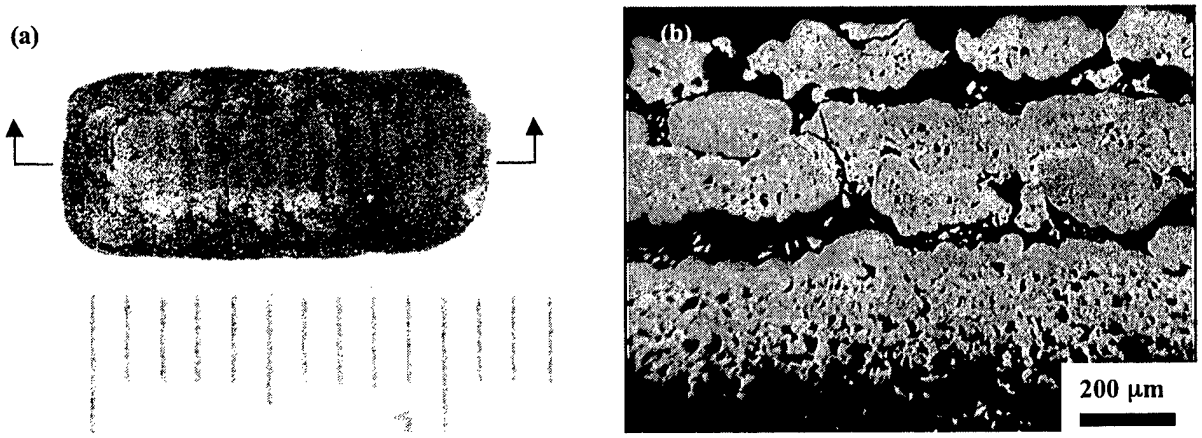


Figure 2. SiC powder/SiC matrix rectangle with 4 layers (a) as-fabricated and (b) cross-section across layers.

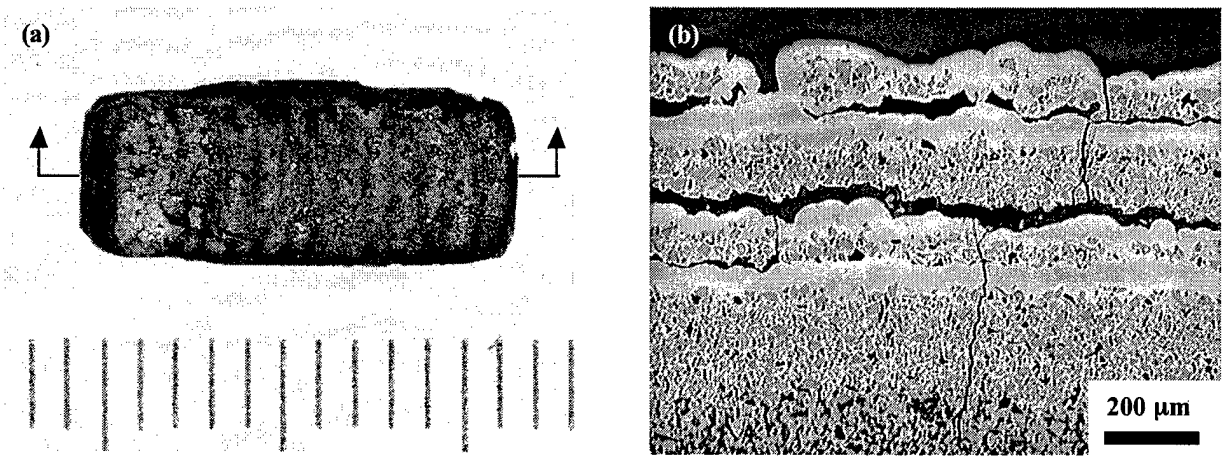


Figure 3. ZrO_2-Y_2O_3 powder/SiC matrix rectangle with 4 layers (a) as-fabricated and (b) cross-section across layers.

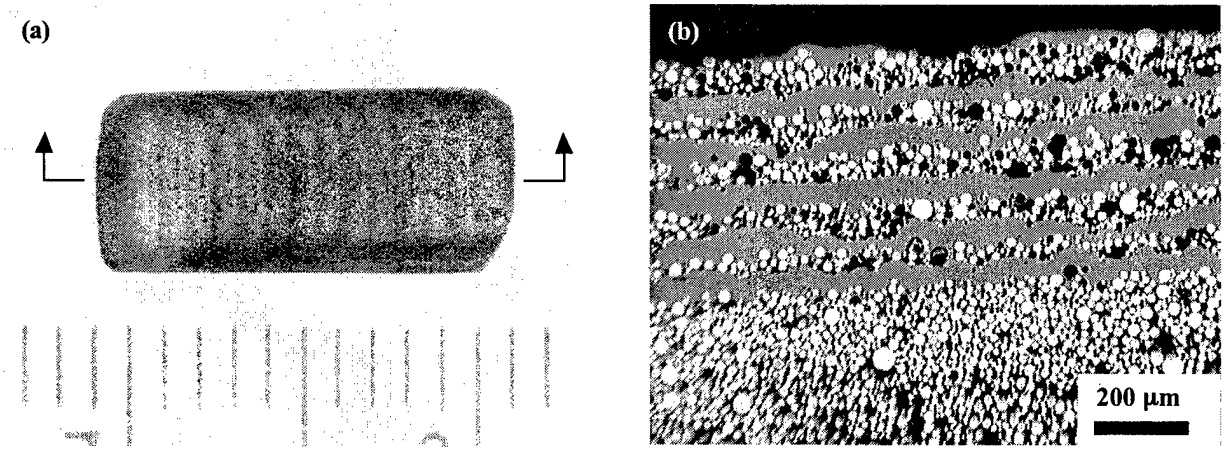


Figure 4. Mo powder/SiC matrix rectangle with 6 layers (a) as-fabricated and (b) cross-section across layers.

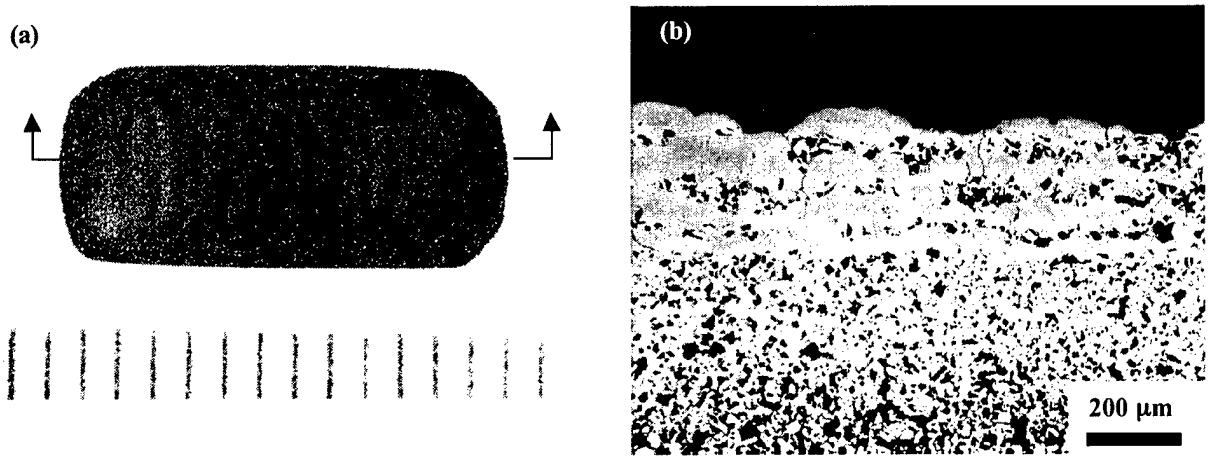


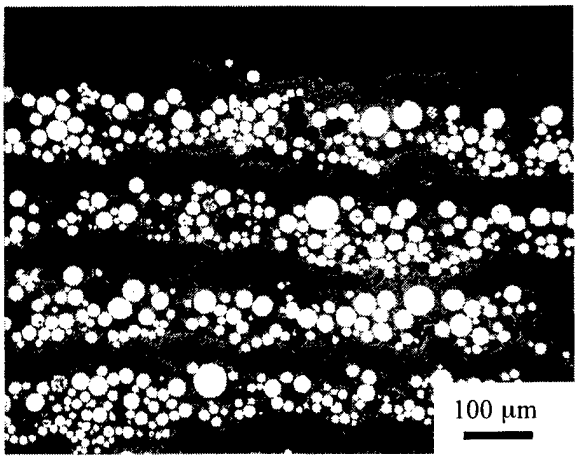
Figure 5. WC powder/SiC matrix rectangle with 4 layers (a) as-fabricated and (b) cross-section across layers.

The SiC powder/SiC matrix and ZrO_2 powder/SiC matrix samples show a rougher as-fabricated surface appearance than the Mo powder/SiC matrix and WC powder/SiC matrix samples. Also there are delaminations between adjacent layers for the SiC and ZrO_2 powder samples while the Mo and WC powder samples have continuous solid material with no delaminations across the layers. The rough surface appearance shown by the SiC and ZrO_2 powder samples appears to be due to a local absence of powder, giving the surface a porous appearance. This absence of solid material is also observed in the cross-sections in the form of gaps between adjacent laser scan lines in the surface layer. These gaps are more pronounced for the SiC powder and less so for the ZrO_2 powder sample. The Mo and WC powder samples show no such gaps at the surface in the cross-sections. We know from in-situ observations of the powder surface during processing that each new powder layer appears smooth and completely covers the previous layer prior to laser heating. It is only after laser heating that the surface gaps appear in the SiC and ZrO_2 powder samples. The reason for the absence of powder in the SiC and ZrO_2 powder samples is likely due to their lower density (3.1 gm/cc for SiC and 5.7 gm/cc for ZrO_2) compared to Mo and WC (10.2 gm/cc for Mo and 15.8 gm/cc for WC). The force to displace the powder likely comes from the gas. Upon the decomposition of the $Si(CH_3)_4$ gas molecule in forming SiC at equilibrium conditions, three methane molecules are released and there is a corresponding increase in local gas pressure. The local gas pressure can also increase due to the local rise in temperature. Assuming the pressure is trapped below the powder, it provides sufficient force to overcome the weight of the loose powder particles and even the weight of the infiltrated layer. This could produce the surface gaps and layer delaminations observed in the SiC and ZrO_2 powder samples. The weight of the Mo and WC powder seems to be sufficient to resist the levitating force of the gas.

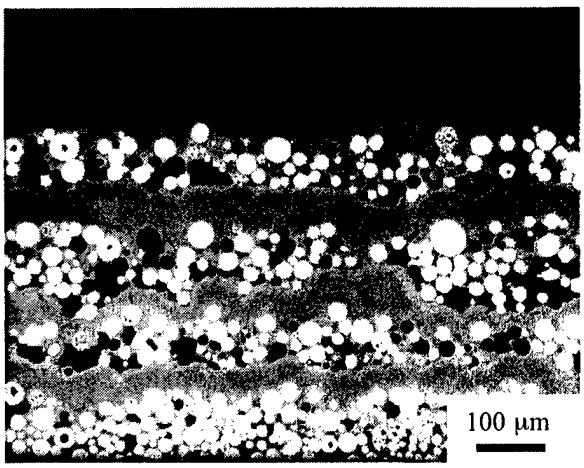
B. Effect of laser scan speed

In SALDVI the amount of local vapor deposition and infiltration depends on the reactant gas concentration and the temperature history, where the temperature history depends on the target temperature and the laser scan speed. It is desirable to achieve parts with both a high

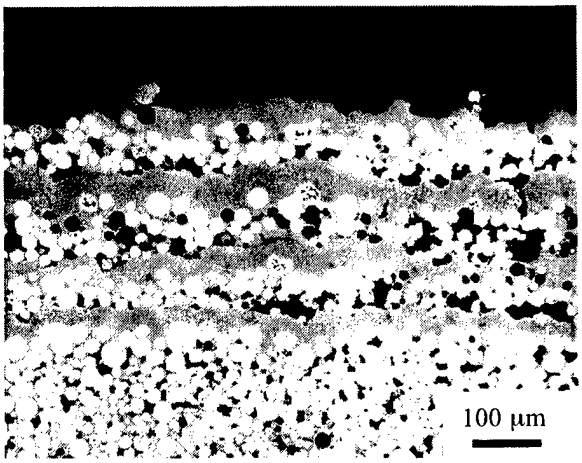
infiltration density and a uniform structure. The Mo powder/SiC matrix sample in Figure 4b shows a non-uniform structure. In addition to the vapor infiltrated powder, each layer also contains a layer of pure vapor deposited SiC at the surface of each powder layer. Here the scan speed is increased to reduce the time at temperature and examine the effect on reducing the thickness of the purely vapor deposited layer at the surface of each powder layer. Figures 6a-e show cross-sections of Mo powder/SiC matrix rectangle samples with four layers processed at 1000°C target temperature, 10 Torr $Si(CH_3)_4$ gas pressure, 120 μm layer thickness, and with scan speeds of 2.5, 3.8, 5.0, 7.5, and 10 μm/s, respectively. As the scan speed increases, the thickness of this vapor deposited layer decreases, from about 75 μm thick for a scan speed of 2.5 μm/s to about 10 μm thick for a scan speed of 10 μm/s. However, at some point decreasing the heating time will also cause the density in the infiltrated powder to start to decrease. The infiltration density begins to decrease when the scan speed increases to 10 μm/s. So there is a compromise between obtaining parts with high infiltration density and uniform distribution of vapor infiltrated powder.



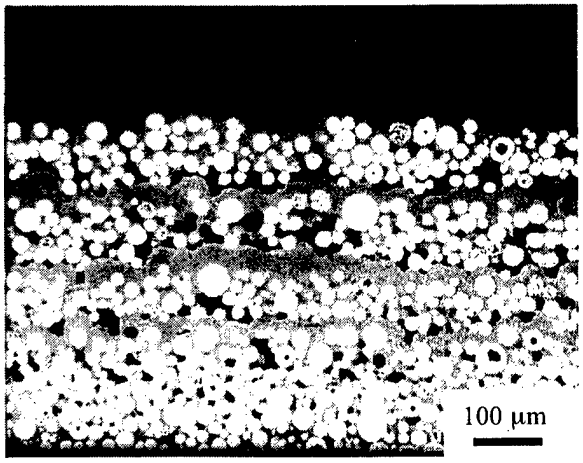
(a) 2.5 μm/s scan speed



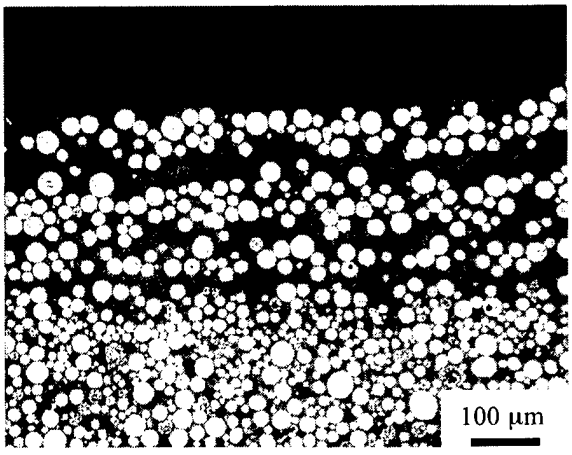
(b) 3.8 μm/s scan speed



(c) 5.0 μm/s scan speed



(d) 7.5 μm/s scan speed



(e) 10 μm/s scan speed

Figure 6. Mo powder/SiC matrix rectangles with 4 layers.

Conclusions

The type of powder was found to affect the surface appearance and internal structure of SiC matrix multiple layer SALDVI rectangles. Samples with SiC and ZrO_2 powder show a porous surface appearance due to displacement of the powder during processing. Mo and WC powder samples have a dense surface and continuous solid material across adjacent layers. The lower density of the SiC and ZrO_2 powders and convective effects in the gas are the likely cause of their poor structure.

The laser scan speed affects the distribution of vapor deposited SiC in Mo powder/SiC matrix multiple layer SALDVI rectangles. Higher scan speeds increase the uniformity of the microstructure of each layer by reducing the amount of pure vapor deposition that occurs at the surface of the powder layer. However, at higher scan speeds the infiltration density in the interior of the powder layer begins to decrease.

Acknowledgement

The authors acknowledge the support for this research by the Office of Naval Research (grant #N00014-95-1-0978).

References

1. B.R. Birmingham and H.L. Marcus, "Silicon Carbide Shapes by Selective Area Laser Deposition Vapor Infiltration," Proceedings of the Solid Freeform Fabrication Symposium, The University of Texas at Austin, 1994, pp. 348-355.
2. J.E. Crocker, S. Harrison, L. Sun, L.L. Shaw, and H.L. Marcus, "Using SALDVI and SALD with Multi-Material Structures," *JOM*, **50**, 21-23, December, 1998.
3. J.E. Crocker, S.L. Harrison, L. Sun, L.L. Shaw, and H.L. Marcus, "Localized CVD and the Ultrafine Grain Structure," Proceedings of TMS Ultrafine Grained Materials Symposium, Nashville, TN, March, 2000.
4. J.E. Crocker, L. Sun, H. Ansquer, L.L. Shaw, and H.L. Marcus, "Processing and Characterization of SALDVI Ceramic Structures," Proceedings of the Solid Freeform Fabrication Symposium, The University of Texas at Austin, 1999, pp. 495-501.

this page intentionally blank

SPOT JOINING OF Si_3N_4 AND SIC CERAMICS USING SELECTIVE AREA LASER DEPOSITION (SALD) TECHNIQUE

Ibrahim M. Ghayad*, Erik Geiss , James E. Crocker, and Harris L. Marcus
Institute of Materials Science, University of Connecticut, Storrs, Connecticut
*Central Metallurgical Research and Development Institute, Cairo, Egypt

Keywords, Silicon Nitride, Silicon Carbide, Laser Spot Joining of Ceramics

Introduction

An important approach to forming difficult and intricate ceramic products is the joining of simple ceramic shapes together to build up to the desired design and hence the economic and technological barriers in manufacturing complex ceramic designs could be avoided. The traditional manner of metal welding by melting the base material is extremely difficult with the typical ceramic high melting temperature or impossible due to thermal decomposition. Brazing of an intermediate material to stick two objects together at a seam also has complications because ceramics are poorly wet by most metals and the resulting operating temperature is lowered (1).

A new, promising manufacturing path involves a gas-phase decomposition approach, known as Selective Area Laser Deposition (SALD) joining. SALD is a gas-phase Solid Free Form (SFF) process in which a specific gas mixture decomposes either thermally or photolytically from the energy input of a laser beam to form a solid reaction product (1,2,3,4). The chemical process is similar to Chemical Vapor Deposition (CVD) but the product is selectively deposited locally under the laser spot, which can be scanned, and therefore controlled.

The present paper focuses on deposition of silicon nitride or silicon carbide filler materials to spot join silicon nitride and silicon carbide ceramic materials. Chemical and structural characterization of joints was performed.

Experimental

The SALD work-station consists of a vacuum chamber, a 150 watt continuous wave Nd:YAG (1.06 micron wavelength) laser beam, an xy table, scanning mirrors, and an optical pyrometer temperature probe. During SALD experiments the surface temperature was measured by an optical pyrometer and was used in a feedback loop to adjust the laser output power to establish the conditions to maintain a constant surface temperature throughout the experiment. These laser power conditions were then used in the spot joining experiments. The laser beam spot size is nominally 1 mm in diameter and approximately Gaussian in shape.

Specimens of fully dense silicon nitride from Norton (NBD 200), 0.8 x 0.8 x 0.2 inch samples were used for joining experiments. Other experiments were carried out using silicon carbide infiltrated Mo powder specimens prepared using the Selective Area Laser Deposition Vapor Infiltration (SALDVI) technique which shares many attributes of SALD. The main difference is that SALDVI uses the pyrolytic products of gas precursor decomposition to infiltrate into layers of powder rather than forming a completely free standing shape associated with SALD (2). The

specimens were held together with a clamp (Fig. 1) prior to exposing them to laser. The precursor gases as well as the processing parameters are summarized in Table 1. These conditions were used in the previous work of Shay Harrison (1) for the deposition of SiC and Si_3N_4 whose XRD patterns are shown in Figures 2 and 3. Metallographic cross-sections of the formed joints were investigated using an Environmental Scanning Electron Microscope (ESEM).

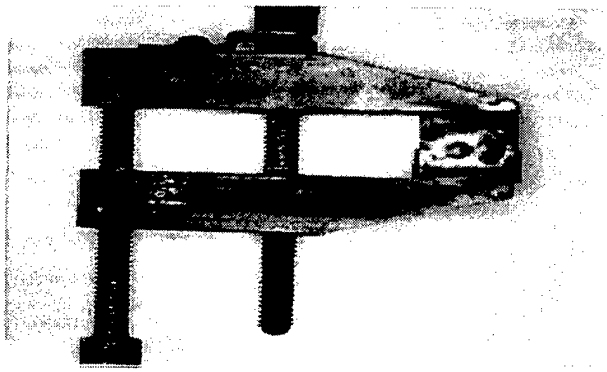


Figure 1: The clamp used to hold the samples.

Table 1: Precursor gases and the processing parameters of experiments

Deposited Material	Gas Precursors	Pressure (torr)	Temperature, °C
Silicon Carbide	Tetramethylsilane (TMS) and H_2	20 TMS and 20 H_2	800-1000
Silicon Nitride	TMS and NH_3	20 TMS and 30 NH_3	900-1100

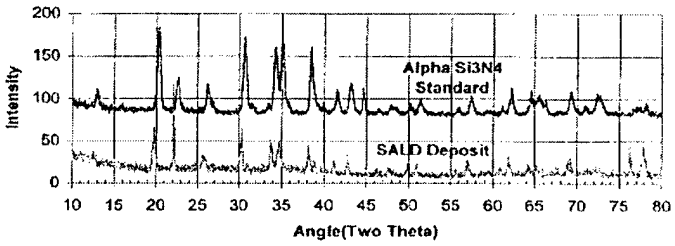


Fig. 2: X-Ray diffraction of SALD Si_3N_4 compared to standard alpha silicon nitride.

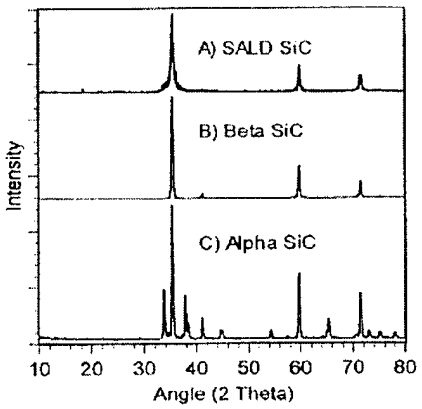


Fig. 3: X-Ray diffraction of SALD SiC compared to commercial alpha and beta SiC

Results

Specimens of SALDVI silicon carbide/Mo composite were held together and exposed to the laser under conditions of silicon carbide deposition. A tight spot joint (Fig. 4) was formed through the deposition of silicon carbide.



Figure 4: SiC joint formed over SiC/Mo composite sample.

When thin specimens of fully dense silicon nitride materials were exposed to the laser a successful spot joint was formed under the conditions of either silicon carbide or silicon nitride deposition (Figs. 5, 6). Thick fully dense silicon nitride samples were exposed to the laser under the above experimental conditions. Unfortunately no joining could be obtained with these specimens. Deposition occurred on one side of the joint but not the other. Several experiments were carried out with exposing the samples to the laser in different geometries without forming a spot joint.

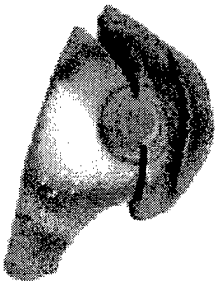


Figure 5: SiC joint formed over Si_3N_4 samples.

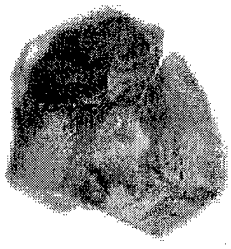


Figure 6: Si_3N_4 joint formed over Si_3N_4 samples.

The microstructures of the silicon carbide and silicon nitride spot joints, as well as the silicon nitride substrate, are shown in Figures 7, 8, and 9.

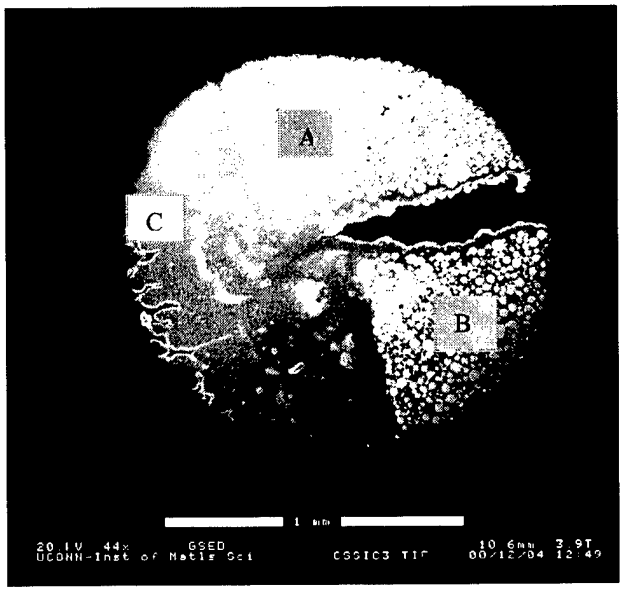


Fig. 7: A cross section of SiC joint over SiC/Mo composite. A, B: Substrate C: Deposit

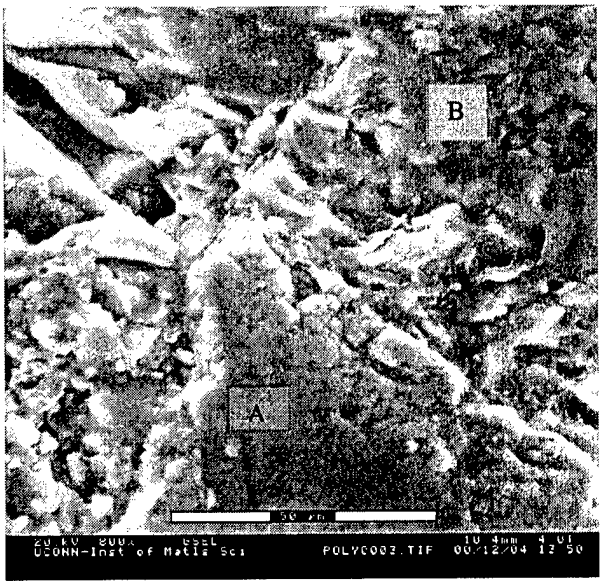


Fig. 8: Si_3N_4 deposition over Si_3N_4 substrate. A: Substrate B: Deposit

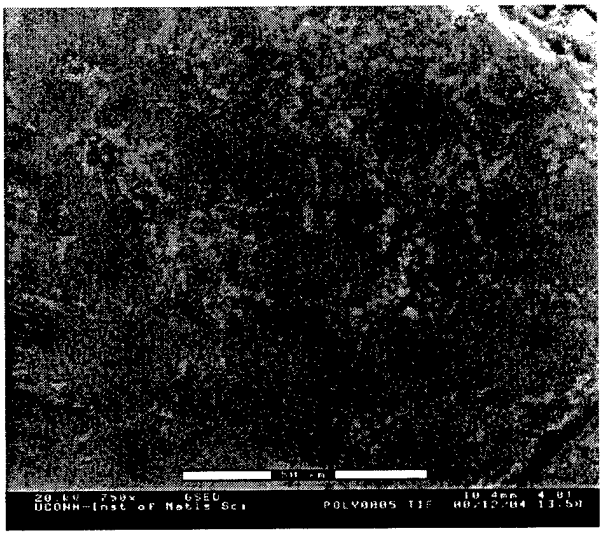


Fig. 9: Microstructure of Si_3N_4 substrate

Discussion

The results of this study demonstrate that spot joining of silicon nitride and silicon carbide using the SALD joining process is possible. A question that arose is; why did the thin specimens spot join while the thicker specimens did not? The answer to this question is related to the thermal conductivity of the sample and the available laser power. The heat sink and resulting thermal gradient of the thinner specimens is much smaller than that of thicker specimens. The laser was able to uniformly heat the thinner specimens effectively, allowing deposition to occur on both sides of the joint at the same time with same deposition rate leading to a successful joint. For the thicker

specimens, heating and therefore deposition occurred preferentially on one side resulting in a poor spot joint.

Future work will concentrate on the formation of a complete joint between silicon nitride flat samples and silicon nitride tubes. Other factors that influence joining will be studied, including the laser scan speed and laser wavelength.

Conclusions

1. Spot joints were obtained for the thin fully dense silicon nitride samples and for SALDVI silicon carbide samples.
2. The factors that affect the successful spot joining process are the laser power, the thermal conductivity of the substrate, and the substrate size.

References:

1. Selective Area Laser Deposition (SALD) Joining of Silicon Carbide With Silicon Carbide Filler, Shay L. Harrison, Ph.D. Dissertation, 1999.

2. In Situ Thermocouples in Macro-Components Fabricated Using SALD and SALDVI Techniques, I. Evaluation of Processing Parameters, Lianchao Sun, Kevin J. Jakubenas, James E. Crocker, Shay Harrison, Leon L. Shaw, and Harris L. Marcus, Materials and Manufacturing Processes, vol. 13, No. 6, p 859-882, 1998.

3. In Situ Thermocouples in Macro-Components Fabricated Using SALD and SALDVI Techniques, II. Evaluation of Processing Parameters, Lianchao Sun, Kevin J. Jakubenas, James E. Crocker, Shay Harrison, Leon L. Shaw, and Harris L. Marcus, Materials and Manufacturing Processes, vol. 13, No. 6, p 883-907, 1998.

4. Gas-Phase Solid Freeform Fabrication of SiC Ceramics Using SALDVI, James E. Crocker, Leon L. Shaw, and Harris L. Marcus, Solid Freeform Fabrication Symposium Proceedings 2000, p 168-175.

this page intentionally blank

Robocasting of Photonic Band Gap Structures

James E. Smay[*†], *Joseph Cesarano III*[†], *Shawn Y. Lin*[†],
John N. Stuecker[†], *and Jennifer A. Lewis*[*]

[*]*Materials Science and Engineering Department*
University of Illinois at Urbana-Champaign, Urbana, IL 61801

[†]*Sandia National Laboratories*
Albuquerque, NM 87106

Introduction

Photonic band gap (PBG) materials[1] exhibit characteristic frequency bands in which the density of states for electromagnetic wave propagation approaches zero. This behavior has great potential for efficient bending of light, increased efficiency of lasers by inhibiting unwanted modes, and a variety of other applications where control of photons is important. The length scale, symmetry, and dielectric constant contrast of the crystal structure define the domain and directionality of this band gap. Solution of the Maxwell equations for periodic dielectric structures reveals that the PBG scales with the feature size of the crystal. Thus, while the ultimate application of PBG's may target a 1.5 μm wavelength, fabrication routes that can create periodicity on the millimeter length scale can be used to rapidly screen new structures and materials with direct correlation to higher frequency applications. Our motivation was to demonstrate that a solid freeform fabrication technique, known as robocasting[2, 3], could be used to rapidly produce PBG structures on a mm length scale.

Robocasting, was invented at Sandia National Labs to utilize colloidal ceramic slurries in the rapid, moldless fabrication of components. The process starts by formulating a well-controlled, weakly flocculated colloidal suspension at high solids loading. The suspension is then extruded through a deposition nozzle onto a mobile *x-y* translation stage. A computer controls the *x-y* stage, allowing the extrudate to be deposited in 2-dimensional patterns derived from slices of a 3-dimensional CAD model. After each layer is drawn, the deposition nozzle is incremented in height and the next layer is deposited until the 3-D part is finished.

Robocasting of alumina slurry was used to construct self-supporting, spanning lattice structures that display a PBG. The symmetry of the rods forming the lattice resembled a face centered tetragonal stacking pattern. In addition to model lattices, intentional defects were introduced by periodically omitting rods from the lattice with the aim of producing allowed transmission modes in the PBG. Example transmission spectra are given for three lattices to highlight the frequency dependant attenuation in the 80 to 100 GHz regime.

Experimental Procedure

Materials System

The ceramic chosen for this study was AKP-30 aluminum oxide (Sumitomo Chemical Co., Osaka, Japan). AKP-30 is a high purity α alumina (>99.99%) with a particle size of ~0.3 μm and BET surface area of 7 m^2/g. α alumina has a refractive index of n = 1.765. A poly(electrolyte), the ammonium salt of poly(acrylic acid) (Darvan 821A, R.T. Vanderbilt Company Inc., Norwalk, CT), was used as a dispersing agent. Darvan 821A provides electrosteric stabilization of the colloidal alumina particles by adsorbing on their surface at a

concentration of ~0.2 to 0.4 mg/m^2. In the robocasting suspensions, the concentration was 2 mg of active polymer per gram of alumina. Darvan 821A behaves similarly to poly(acrylic acid), as described by Cesarano *et. al.*, [4, 5] in acidic and alkaline conditions. Potentiometric titration of Darvan 821A solutions of known concentration revealed that approximately 75% of the monomer groups were ionized at a pH of >8.0. The colloidal stability of the suspensions was tailored through pH and ionic strength adjustments[6]. Hydroxypropyl methylcellulose (Methocel F4M, DOW Chemical Co., Midland, MI) was added as a binder/thickener.

Fabrication of Lattices

The first step in the robocasting process is to formulate a suspension with sufficient yield stress to form the spans of the lattice structure. An aqueous suspension of 55% alumina by volume was achieved by initially dispersing the ceramic powder with the aid of the Darvan 821A and ultrasonication. After dispersion, the methylcellulose was mixed into the suspension from a stock solution. Next, the ionic strength and pH were adjusted to promote weak flocculation. The details of suspension rheology and shape evolution during robocasting are the subject of a future publication[7], however, the shear yield stress of these suspensions has been measured in the range of 50 to 150 Pa.

Next, the suspension was loaded into the robocaster and deposited at a speed of 8 mm/s through a 0.84 mm orifice. The robocaster was programmed to build lattices with the symmetry illustrated in Figure 1 where, *d* is the pitch, *a* is the rod diameter, and *c* is the height of the four layer repeat unit. Similar lattices with this symmetry on the micron length scale have shown PBG's at much shorter wavelengths[8].

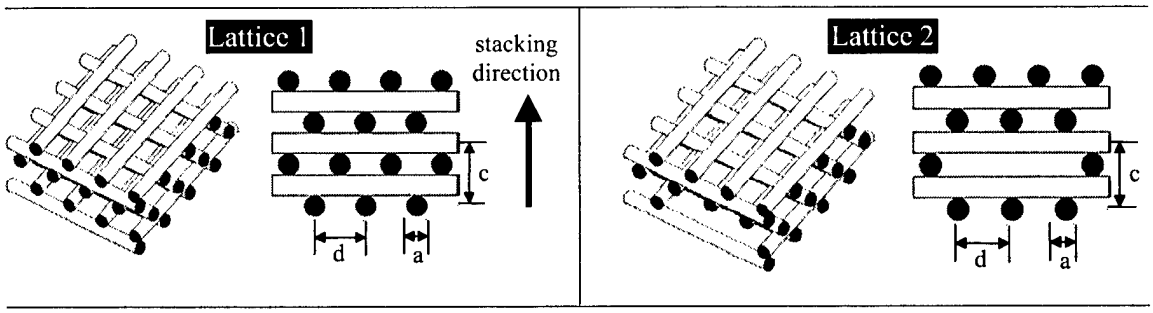


Figure 1 Schematic illustration of robocasting models where lattice 1 has no missing rods and lattice 2 has a pair of rods removed.

The filling fraction of dielectric rods is thus defined as *a/d*. Lattice 1 contained all the rods while pairs of rods were periodically removed from lattice 2. After deposition, the dried lattices were sintered at 1650°C for 2h.

Measurement of Photonic Band Gap

The transmission spectra of the lattices was probed through a frequency range of 80 to 110 GHz using a HP8510C network analyzer and mm wavelength test set (Agilent Technologies, Palo Alto, CA). The lattices were mounted on a sapphire substrate using small dots of glue at the corners and placed on a stage between the emitter and receiver of the test set. The microwaves were transmitted through the lattices in the stacking direction (see Fig. 1). The attenuation of each lattice as a function of frequency was determined by comparing their transmission spectra to that obtained for a sapphire window alone. The attenuation in decibels (dB) was therefore

calculated as 20 log (I/I_o) where, I is the transmitted microwave intensity with the sample present and I_o is the reference intensity.

Results and Discussion

Two lattices were successfully robocast and sintered without (Figure 2(a)) and with (Figure 2(b)) periodic line defects.

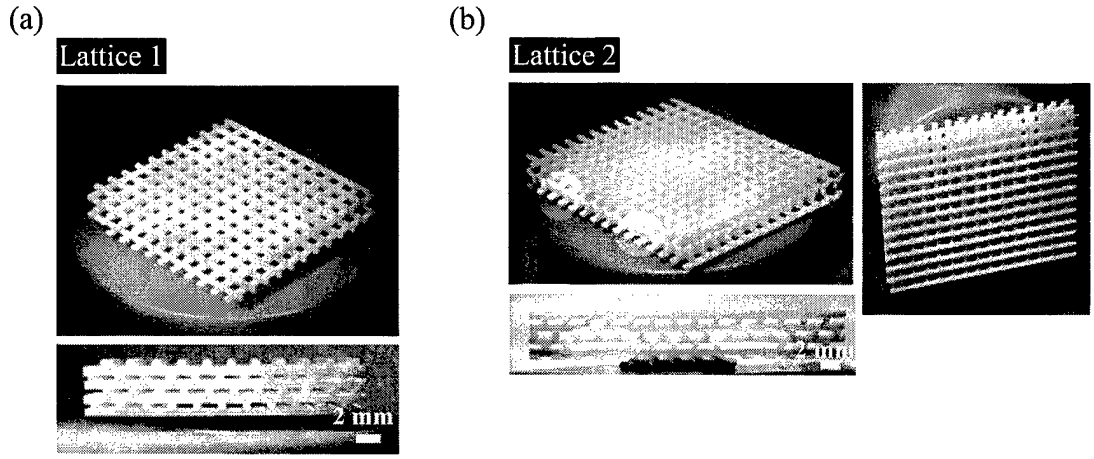


Figure 2 Aluminum oxide lattices with 8 layers (2 unit cells) having parameters (a) d = 2.25 mm, a = 0.64 mm, filling fraction ~ 0.28 and (b) d = 2.3 mm, a = 0.68 mm, filling fraction ~ 0.29.

In each lattice, the filling fraction was ~28 to 29% based on optical microscopy observation of the rod diameters and pitch. Lattice 1 was fabricated without defects and lattice 2 contained two line defects consisting of pair of missing rods.

The attenuation spectra for lattices 1 and 2 are plotted in Figure 3 for microwaves transmitted in the stacking direction.

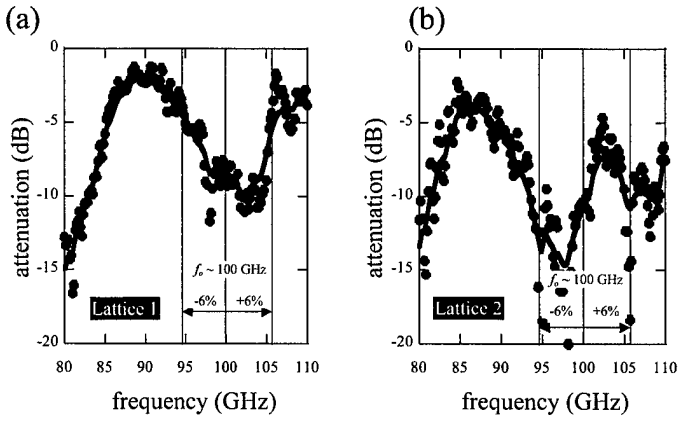


Figure 3 Attenuation spectra of (a) lattice 1 and (b) lattice 2. The smooth line through the data is simply an aid to guide the eye.

An attenuation of ~ -10 dB was observed around a center frequency of f_o = 100 GHz in lattice 1. In Figure 3(a) the center frequency is denoted by a vertical line and the +/- 6% markers give the bandwidth of the PBG (*i.e.*, ~12% of the center frequency). Lattice 2 displayed a similar center frequency around 100 GHz. Again, the +/- 6% markers denote the band edges for comparison to lattice 1. The feature in this spectrum occurring at ~103 GHz is assumed to be associated with transmission modes allowed by the periodic defect states. Conclusive proof of this hypothesis, however, is impossible from these initial measurements and the limited data set.

Summary

We have demonstrated the ability to construct periodic lattices of aluminum oxide rods using robocasting. The lattices have good definition of the rods and spacing in both the *x-y* plane and the stacking direction. The filling fractions achieved were on the order of 0.28 to 0.29. Initial PBG transmission measurements indicate an attenuation of -10 dB for the defect free lattice and -15 dB for lattice 2 containing periodic line defects. The bandwidth for both lattices was approximately 12% of the center frequency. Lattice 2 appeared to display transmission modes commensurate with the inclusion of the periodic line defects. Further characterization of PBG lattices needs to be performed to verify the effects of engineered defect states on their transmission behavior. Robocasting provides a facile method to produce periodic dielectrics in the mm length scale. Current efforts are focusing on refining the scale of such lattices to reach into the low THz regime.

1. Joannopoulos, J.D., Meade, R.D., and Winn, J.N., "Photonic Crystals." 1995, Princeton, New Jersey: Princeton University Press.
2. Cesarano III, J., Segalman, R., and Calvert, P., *Ceramic Industry*, 1998, 148 [4], 94-102.
3. Cesarano III, J. and Calvert, P., US *Patent No.* 6,027,326,
4. Cesarano III, J. and Aksay, I.A., *Journal of the American Ceramic Society*, 1988, 71 [12], 1062-67.
5. Cesarano III, J., Aksay, I.A., and Bleier, A., *Journal of the American Ceramic Society*, 1988, 71 [4], 250-55.
6. Channell, G.M. and Zukoski, C.F., *Aiche Journal*, 1997, 43 [7], 1700-1708.
7. Smay, J.E., Cesarano III, J., and Lewis, J.A., *Langmuir*, 2001, in preparation.
8. Lin, S.Y., *et al.*, *Nature*, 1998, 394 [16], 251-253.

Mechanical Properties of Laser-Deposited Ti-6Al-4V

P.A. Kobryn and S.L. Semiatin

Air Force Research Laboratory, AFRL/MLLMP,
Wright-Patterson Air Force Base, OH 45433-7817

Abstract

Laser additive manufacturing is a solid-freeform-fabrication process which is being investigated for titanium-component manufacturing and repair based on its cost-reduction potential and flexibility. Laser additive manufacturing also has the potential to improve mechanical properties due to the high cooling rates involved. However, the effect of the layered manufacturing process and any lack-of-fusion porosity and texture on the magnitude and anisotropy of mechanical properties is of concern. Hence, a preliminary effort was undertaken to assess these effects for bulk Ti-6Al-4V deposits manufactured using the LENS™ process. Tension, fatigue, and crack-growth tests were performed on both stress-relieved and HIP'ed deposits in three primary directions. The results were compared to published data for conventionally processed Ti-6Al-4V castings and forgings.

Introduction

Laser additive manufacturing is a solid-freeform-fabrication method which can be used to manufacture solid metallic components directly from CAD files. During laser additive manufacturing, powder is fed into a melt pool which is produced by a sharply-focused laser beam. Parts are built in a layer-by-layer fashion by rastering the laser and powder source across the substrate. Laser additive manufacturing has many potential applications, including production of functional prototypes, short-run component fabrication, component repair, and fabrication of functionally-graded materials.

Laser additive manufacturing is particularly attractive for the fabrication of titanium aerospace components because it can greatly reduce the buy-to-fly ratio and lead time for production, two factors which impact cost. Thus, a number of recent efforts have been undertaken to develop titanium laser-additive-manufacturing processes [1,2,3,4,5]. Much of the focus of this prior research has been on equipment development and mechanical property measurements [1,2]. Acceptable processing parameters have been determined largely through trial-and-error approaches. On the other hand, only limited work has been done to establish the relationship between process parameters and the structure of deposits [3,4,5]. Such an understanding is critical for both process design and control.

The work reported here is part of a larger effort to establish the effect of process parameters and input materials on deposit structure, texture, and mechanical properties. The results of efforts to characterize the effect of process parameters on structure have been described elsewhere [4,5]. The results of an initial investigation of mechanical properties in bulk Ti-6Al-4V deposits formed using the LENS™ process are described here with a focus on the relationship between properties and structure.

Materials and Procedures

Materials: The materials used in this investigation consisted of gas-atomized prealloyed Ti-6Al-4V powder made by Crucible Research and 13.23-mm-thick hot-rolled Ti-6Al-4V plate with an equiaxed-alpha microstructure. The powder had a composition (in weight percent) of 6.24 aluminum, 3.92 vanadium, 0.104 oxygen, 0.006 hydrogen, 0.007 nitrogen, 0.038 carbon, 0.047 iron, balance titanium and a mesh size of -100, +325 (particle sizes between 45 and 150 μm). The plate had a composition (in weight percent) of 6.19 aluminum, 3.89 vanadium, 0.20 oxygen, 0.0074 hydrogen, 0.01 nitrogen, 0.02 carbon, 0.12 iron, balance titanium. Prior to deposition, the plate was lapped on both sides to a surface finish of 12 to 14 μm and degreased using acetone and alcohol.

Test Material Fabrication: Two 76 mm x 76 mm x 76 mm cubes were formed in a LENS™ system using the powder and substrate material described in the previous section and the operating parameters recommended by the system manufacturer. One cube was stress relieved in vacuum for 2 hours at 700 - 730°C, while the other cube was hot isostatically pressed (HIP'ed) for 2 hours at 900°C and 100 MPa. Six cylindrical dogbone tension specimens (total length = 76 mm; gauge length = 13.5 mm; gauge diameter = 5 mm) and two ASTM E 399 compact tension specimens were extracted from each cube in each of the three primary deposition directions (Figure 1).

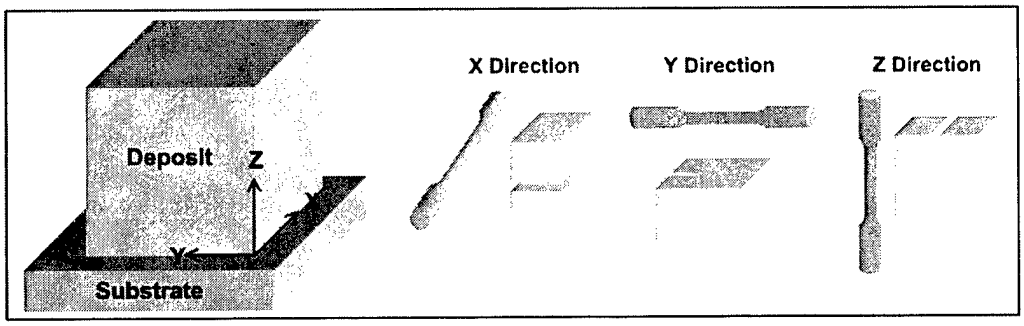


Figure 1. Illustration of the deposit geometry and the corresponding primary deposition and test-specimen directions.

Material Characterization: Remnants from each cube were sectioned, mounted, and polished using standard metallographic preparation techniques. The macrostructures and microstructures were characterized via light microscopy to assess the extent of porosity, the prior-beta grain morphology and grain size, and the morphology and scale of the transformed-beta microstructure. The crystallographic texture of the Ti-6Al-4V material produced via LENS™ was measured at a distance of approximately 6 mm from the substrate-deposit interface. It was determined using a scanning electron microscope (SEM) equipped with an electron-backscatter-diffraction (EBSD) analysis system [6].

Mechanical Testing: Standard tension tests were performed on three of the six dogbone specimens from each direction in each cube to determine the tensile yield and ultimate stresses, total elongation, and elastic modulus. The remaining dogbone specimens were used to perform fatigue tests for use in constructing an S-N fatigue curve. The compact tension specimens were used to determine fracture toughness values (i.e., $K_{I,C}$ or K_q). The fracture surfaces of all of the specimens were examined to establish the gross failure modes.

Data Analysis: The measured mechanical properties were analyzed to determine differences between different material conditions (i.e., stress-relieved vs. HIP'ed) and test directions (X, Y, and Z). The resulting tension data were also compared to published A-basis design properties for wrought, mill-annealed Ti-6Al-4V plate [7], while the fatigue and fracture-toughness data were compared to published scatterbands for cast and for wrought Ti-6Al-4V product forms [8]. Similarities and/or differences were reconciled based on the observed microstructures and texture.

Results

Microstructure/Texture: Both the stress-relieved material and the HIP'ed material contained columnar prior-beta grains with a grain size of approximately 155 μm (Figure 2a,b). A macroscopic banding (similar to that observed in previous Ti-6Al-4V material produced via LENS™ [4]) was also evident in both materials. However, the stress-relieved material contained significant lack-of-fusion porosity while the HIP'ed material contained none. This result indicated that the selected processing conditions did not produce fully consolidated material, but that porosity which did form was closed to the surface and therefore healed during HIP.

Both materials also possessed a Widmanstätten transformed-beta microstructure (Figure 2c,d); however the alpha laths in the stress-relieved material were finer than those in the HIP'ed material. This difference was expected because the higher temperature used during HIP allows the alpha phase to coarsen, while the lower temperature used for stress relief does not. Such a difference in coarseness of the alpha phase would be expected to have a noticeable effect on mechanical properties, particularly tensile strength [8].

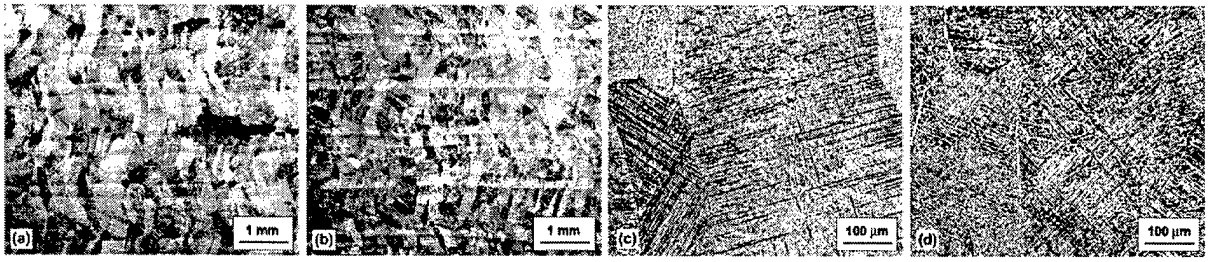


Figure 2. Photographs showing the (a,b) macrostructures and (c,d) microstructures of the (a,c) stress-relieved and (b,d) HIP'ed deposits.

The measured crystallographic texture was consistent with that which would form as a result of epitaxial growth of *columnar* beta grains from the substrate (i.e., showing the influence of both a solidification-induced <100> fiber texture and the texture of the beta-annealed substrate), However, the texture was found to be relatively weak (i.e., maximum of 2.5 times random in the alpha phase) [10].

Static Tension Test Results: The tension-test results provided insight into the effect of the deposition process and post-deposition HIP on mechanical properties (Table 1). For example, the deposits exhibited significant yield-strength anisotropy in both the stress-relieved and the HIP'ed conditions. The X- and Y-direction yield strengths were higher than those in the Z direction. However, this anisotropy was much greater in the stress-relieved condition than following HIP.

Table 1. Average Tensile Properties of Bulk Ti-6Al-4V Produced via the LENS™ Process.

Condition	Test Direction	Yield Strength (MPa)	Ultimate Strength (MPa)	Total Elongation (%)	Elastic Modulus (GPa)
Stress Relieved	X	1065	1109	4.9	116
Stress Relieved	Y	1066	1112	5.5	116
Stress Relieved	Z	832	832	0.8	112
HIP'ed	X	946	1005	13.1	118
HIP'ed	Y	952	1007	13.0	118
HIP'ed	Z	899	1002	11.8	114

The large anisotropy in the stress-relieved deposit was a direct result of the distribution of lack-of-fusion porosity in the material. Due to the layered nature of the LENS™ process, lack-of-fusion porosity tended to form primarily along the *planar* inter-layer boundaries (Figure 2a). Hence, the effective load-bearing area in tension tests perpendicular to the layer boundaries was significantly reduced, and the measured yield stress (which assumes full-density material) was correspondingly reduced. While additional lack-of-fusion porosity can also form at the inter-line boundaries *within* each layer, such porosity appeared to occur less frequently (Figure 2a). Additionally, because the line direction was alternated by 90° with each subsequent layer, inter-line porosity would be expected to have been distributed more evenly throughout the deposit and therefore have had a much smaller effect on strength. The amount of porosity and deformation observed in the fractured specimens (Figure 3) supported these conclusions. While the X- and Y-direction specimens exhibited large amounts of deformation and little porosity, the Z-direction specimens exhibited very little deformation and extensive porosity. The relative ductility of each of the three directions was further illustrated by the relative values of ultimate strength and total elongation in Table 1. While the X and Y directions had significant differences between their yield and ultimate stresses and had approximately 5% total elongation, the Z direction had no measurable difference between its yield and ultimate stresses and less than 1% total elongation.

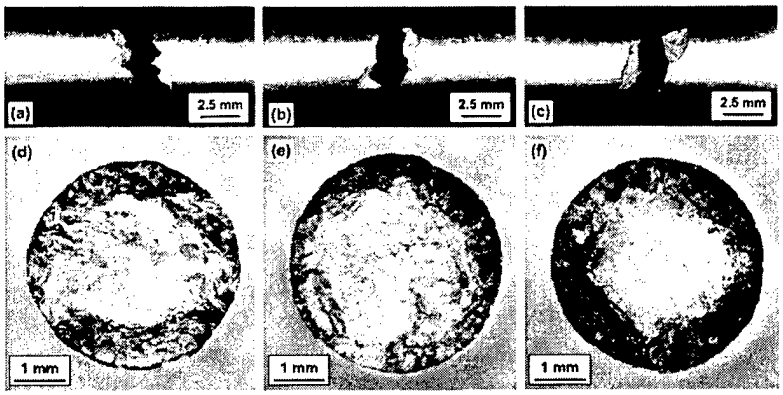


Figure 3. Macrographs of (a,b,c) broken specimens and (d,e,f) fracture surfaces of tension-test specimens cut from the stress-relieved deposit in the (a,d) X direction, (b,e) Y direction, and (c,f) Z direction.

Because the HIP'ed deposit was essentially porosity free (Figure 2b), a much smaller yield-strength anisotropy was observed. The specimens from all three directions exhibited significant ductility, as illustrated by the large amount of deformation observed in the fractured specimens (Figure 4) and the large, similar values of ultimate strength and total elongation. Hence, the yield-strength anisotropy is most likely *not* a result of porosity which might have remained incompletely healed after HIP. Instead, it is probably due to some form of mechanical

or crystallographic texture. While further research is required to determine the precise effect of various forms of texture on properties, some general comments can be made. One potential cause of the observed anisotropy is the mechanical texture due to the columnar grain morphology. In lamellar titanium microstructures, the effective slip length (which has a large, inverse effect on yield strength) is determined by the alpha colony size which, in turn, is limited by the prior-beta grain size [10]. In a columnar microstructure, the effective grain size is much smaller in directions perpendicular to the columnar grains than in the direction parallel to them. Hence, one would expect the yield strength to be lower in the direction parallel to the columnar grains (which in this case is the Z direction). Another possible cause of anisotropy is crystallographic texture [11]. Due to the high anisotropy of the hexagonal crystal structure, texture can greatly affect mechanical properties in titanium alloys. Because the texture of Ti-6Al-4V LENS™ deposits is markedly affected by the <100> fiber texture which forms during columnar solidification, a difference in texture between the Z direction and the X and Y directions would be expected and was indeed observed [9]. However, the effect of this texture on properties is not straightforward and requires further investigation.

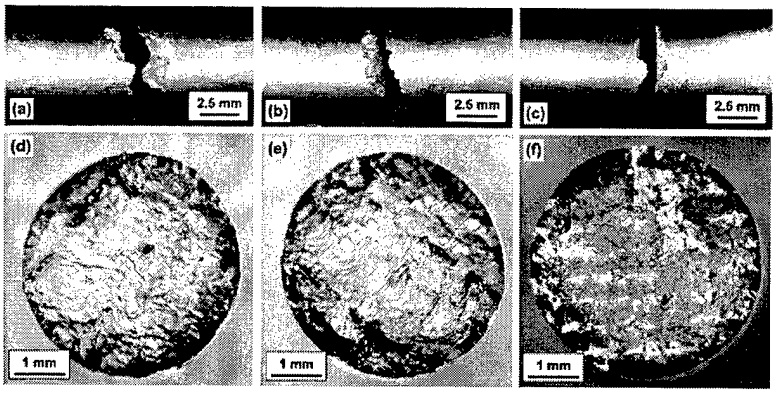


Figure 4. Macrographs of the (a,b,c) broken specimens and (d,e,f) fracture surfaces of tension-test specimens cut from the HIP'ed deposit in the (a,d) X direction, (b,e) Y direction, and (c,f) Z direction.

Another interesting observation was the significant difference in strength and ductility for the stress-relieved and HIP'ed material conditions. Focussing on the X- and Y-direction results, the stress-relieved material was stronger yet less ductile than the HIP'ed material. The difference in strength was likely a result of the difference in alpha-platelet thickness between the two materials with the coarser HIP'ed material being weaker. The difference in ductility was probably due to the presence of porosity in the stress-relieved material.

The Z-direction tension properties of these materials showed interesting comparisons to published design properties for wrought, mill-annealed Ti-6Al-4V (Table 2). While the strength and ductility of the stress-relieved material were severely limited by porosity, the yield strength was not particularly low when compared to the wrought material. Considering the much higher strengths and ductilities observed in the X and Y directions, it appears that the LENS™ process actually may offer improvements in tensile strength provided that the material can be fabricated *without* porosity. However, even if HIP is required to heal porosity, a modest improvement in strength relative to wrought properties can be achieved without a significant loss of ductility.

Table 2. Measured Z-Direction Tension Properties of Bulk Ti-6Al-4V Produced via the LENS™ Process versus Published A-Basis Design Properties for Wrought, Mill-Annealed Ti-6Al-4V Plate [7].

Condition	Yield Strength (MPa)	Ultimate Strength (MPa)	Total Elongation (%)	Elastic Modulus (GPa)
Stress Relieved	832	832	0.8	112
HIP'ed	899	1002	11.8	114
Wrought	827	896	10	110

Tensile Fatigue Test Results: The tensile fatigue test results revealed the expected trends in view of the distribution of porosity in the deposits (Figure 5). The stress-relieved material had much lower fatigue strengths than the HIP'ed material and also displayed an anisotropy. The Z-direction fatigue strengths were significantly lower than those in the X and Y directions. When compared to alternate product forms, the fatigue strength of the HIP'ed material was similar to that of wrought product, indicating that no debit in fatigue strength would need to be considered in component design.

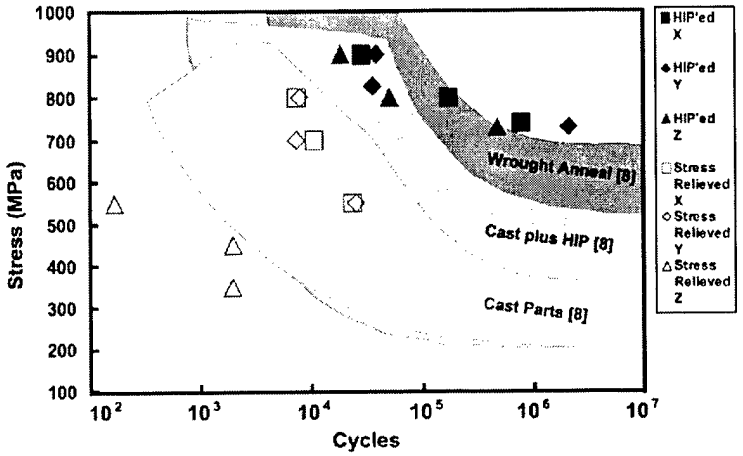


Figure 5. Comparison of measured fatigue strengths for Ti-6Al-4V deposits in both the stress-relieved and HIP'ed conditions to published scatterbands for Ti-6Al-4V castings and forgings (Reference 8).

Compact Tension Test Results: The compact tension results further demonstrated the effect of lack-of-fusion porosity on mechanical behavior. In the stress-relieved specimens, a strong anisotropy was again observed (Figures 6 and 7). In the X-direction specimens (Figure 6a,d), the crack did not begin at the notch tip, but instead at the nearest layer of lack-of-fusion porosity. From there, the crack grew rapidly with little plastic deformation thus resulting in a very low fracture toughness (Figure 7). In the Y and Z directions, the porosity layers were not in the same plane as the crack; thus, larger fracture toughnesses were obtained (Figure 7). In addition, an unusual phenomenon occurred in the Z-direction specimens (Figure 6c,f). The crack propagated along the original plane for a significant distance and then began to propagate along the layers of porosity at an angle 90° from the original plane. Nevertheless, these specimens exhibited the *highest* toughness values for the stress-relieved material (Figure 7).

In contrast, the HIP'ed specimens exhibited a much smaller level of anisotropy (Figures 7 and 8). The Z-direction toughness was slightly higher than that for the other directions. Significant ductility and nominally planar cracks were observed in all three directions (Figure 8).

Hence, the cause of the observed anisotropy is likely related to the same source as the observed yield-strength anisotropy.

Finally, upon comparing the toughness of these materials to those of other product forms, the toughness of the stress-relieved material fell below published values for wrought and cast product forms, while that of the HIP'ed material lay within the range of published values.

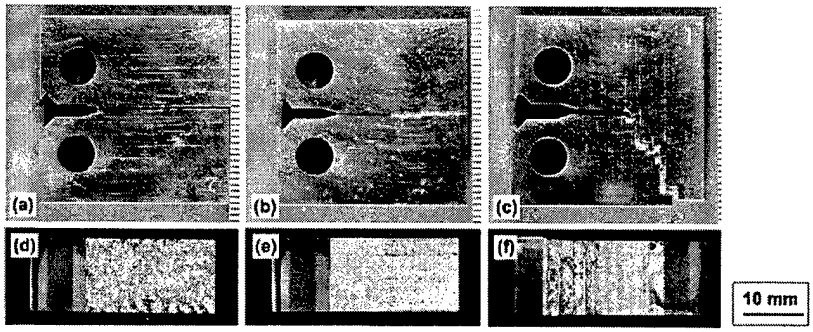


Figure 6. **Macrographs showing the (a,b,c) broken specimens and (d,e,f) fracture surfaces of the compact-tension specimens from the stress-relieved deposits in the (a,d) X direction, (b,e) Y direction, and (c,f) Z direction.**

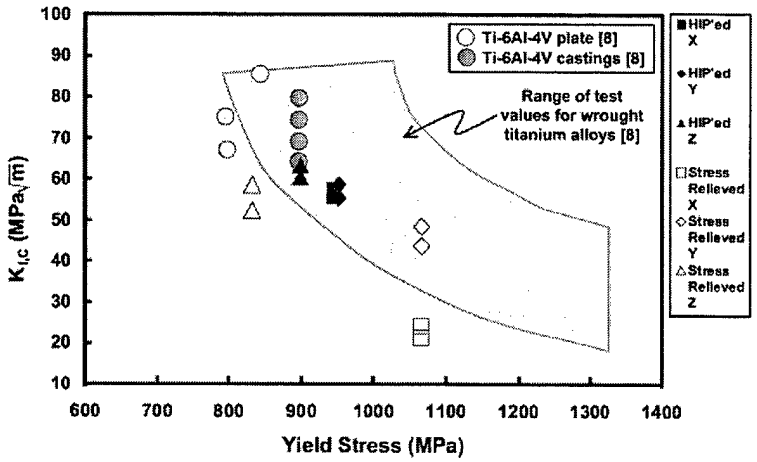


Figure 7. **Comparison of measured $K_{I,C}$ and yield-strength values for Ti-6Al-4V deposits in both the stress-relieved and HIP'ed conditions to a published scatterband for wrought Ti-6Al-4V (Reference 8).**

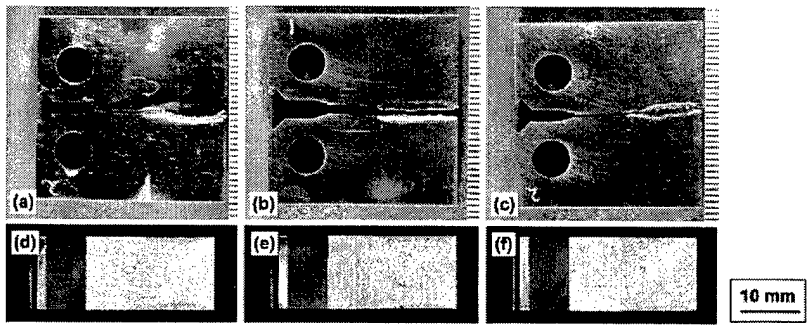


Figure 8. **Macrographs showing the (a,b,c) broken specimens and (d,e,f) fracture surfaces of the compact-tension specimens from the HIP'ed deposits in the (a,d) X direction, (b,e) Y direction, and (c,f) Z direction.**

Summary and Conclusions

The effect of microstructure and texture of laser-deposited Ti-6Al-4V on mechanical properties was investigated by conducting tension, fatigue, and fracture toughness tests. From this work, the following conclusions were drawn:

1. Lack-of-fusion porosity has a significant effect on both the levels and anisotropy of mechanical properties.
2. HIP appears to be effective in healing lack-of-fusion porosity.
3. The yield strength can show a noticeable anisotropy due to residual deposition porosity (in the stress-relieved condition) and mechanical and/or crystallographic texture (in both conditions).
4. The static tensile strength and ductility, fatigue strength, and fracture toughness of HIP'ed Ti-6Al-4V produced via LENS™ compare favorably to those of wrought products.

Acknowledgements

This work was conducted as part of the in-house research activities of the Metals Processing Group of the Air Force Research Laboratory's Materials and Manufacturing Directorate. The support and encouragement of the Laboratory management and the Air Force Office of Scientific Research (Dr. C.S. Hartley, program manager) are gratefully acknowledged. The assistance of P. Gorman of Optomec Design Co. and W. Capshaw of ICE Prototyping in fabricating the deposits, D. Maxwell in performing the mechanical tests, S. Short, J. Vann, and R. Lewis in preparing and analyzing the metallographic specimens, and M. Glavicic in performing the OIM analysis is also much appreciated.

References

[1] Schriempf, J.T., Whitney, E.J., Blomquist, P.A., Arcella, F.G., *Advances in Powder Metallurgy and Particulate Materials*, v. 3, Princeton, NJ: Metal Powder Industries Federation, 1997:21-51.

[2] Keicher D.M., Miller, W.D., *Hard Coatings Based on Borides, Conference: Carbides & Nitrides: Synthesis, Characterization & Applications*, San Antonio, TX, USA, 16-19 Feb. 1998, Warrendale, PA: TMS, 1998: 369.

[3] Brice, C.A., Schwendner, K.I., Mahaffey, D.W., Moore, E.H., Fraser, H.L., *Proceedings of the 10th Solid Freeform Fabrication Symposium*, University of Texas at Austin, Austin, TX, USA, Aug. 1999.

[4] Kobryn, P.A., Moore, E.H., and Semiatin, S.L., *Scripta Materialia*, v. 43, no. 4, 2000.

[5] Kobryn, P.A. and Semiatin, S.L., *Proceedings of the 11th Solid Freeform Fabrication Symposium*, University of Texas at Austin, Austin, TX, USA, Aug. 2000.

[6] Adams, B.L., Wright, S.I., and Kunze, K., *Metall. Trans. A*, v. 24A, 1993: 819.

[7] MIL-HDBK-5H, Battelle's Columbus Labs, Columbus, OH, 1998.

[8] Donachie, M. J. Jr., ed., *Titanium: A Technical Guide*, ASM International, 1988.

[9] Kobryn, P.A., Glavicic, M.G., and Semiatin, S.L., AeroMat 2001, Long Beach, CA, June 13th, 2001.

[10] Lütjering, G., *Mater. Sci. Eng. A*, v. A243, 1998: 32.

[11] Williams, J.C. and Starke, E.A. Jr., in: G. Krauss, ed., *Deformation, Processing, and Structure*, ASM, 1984: 279.

Composite Modeling and Analysis of FDM Prototypes for Design and Fabrication of Functionally Graded Parts

Longmei Li, Q. Sun, C. Bellehumeur[1], and P. Gu [2]
Department of Mechanical and Manufacturing Engineering
[1]Department of Chemical and Petroleum Engineering
The University of Calgary, Calgary, Alberta, T2N 1N4, CANADA

Abstract

Solid Freeform Fabrication technologies have potential to manufacture parts with locally controlled properties (LCP), which would allow concurrent design of part's geometry and desired properties. To a certain extent, Fused Deposition Modelling (FDM) has the ability to fabricate parts with LCP by changing deposition density and deposition orientation. To fully exploit this potential, this paper reports a study on the mechanical properties of FDM prototypes, and related materials and fabrication process issues. Both theoretical and experimental analyses of mechanical properties of FDM parts were carried out. To establish the constitutive models, a set of equations is proposed to determine the elastic constants of FDM prototypes. An example is provided to illustrate the model with LCP using FDM.

Key words: Fused Deposition Modeling, Composite Mechanics, Locally Controlled Properties.

1. Introduction

With recent advances in Solid Freeform Fabrication (SFF) technologies, it is possible to use these technologies to produce parts with desired mechanical properties. The ability to fabricate parts with locally controlled properties (LCP) would create opportunities for manufacturing of a whole new class of parts with graded compositions [Jackson *et al.*, 99] and [Cho *et al.*, 01]. Fused Deposition Modeling(FDM) has the potential to produce parts with LCP by changing deposition density and deposition orientation. A few examples with LCP are shown in Figure 1 b), c), d), e).

FDM processes fabricate prototypes by extruding a semi-molten filament through a heated nozzle in a prescribed pattern onto a platform layer by layer, as in shown Figure 1 a). After the semi-molten material is deposited onto the worktable it begins to cool and bond to the neighboring material diffusely. The bonding between the individual roads of the same layer and of neighboring layers is driven by the thermal energy of semi-molten material. FDM processes use several types of materials, such as Acrylonitrile-butadiene-styrene (ABS) and wax, to build conceptual and/or functional prototypes.

Most of the existing research work in FDM is primarily directed towards the development of new materials or techniques for material deposition [Agarwala *et al.*, 96] [Gray IV *et al.*,98], [Yardimci *et al.*, 96]. The mechanical properties of ABS filament and FDM parts were also investigated by researchers such as [Comb *et al.*, 94], [Kulkarni and Dutta, 99] and [Rodriguez Matas, 99].

ABS parts made by FDM processes essentially consist of partially bonded ABS filaments. Mechanical properties of FDM prototypes are governed by their meso-structures that are determined by manufacturing parameters. By selecting manufacturing parameters, such as deposition directions in layers and gap sizes between filaments, FDM processes can achieve LCP and produce prototypes with desired properties. To fully exploit this potential, issues concerning the mechanical properties of FDM parts and the fabrication process parameters, should be investigated. This paper describes a study on the mechanical properties of FDM prototypes.

[2]To whom all correspondences should be addressed: gu@enme.ucalgary.ca

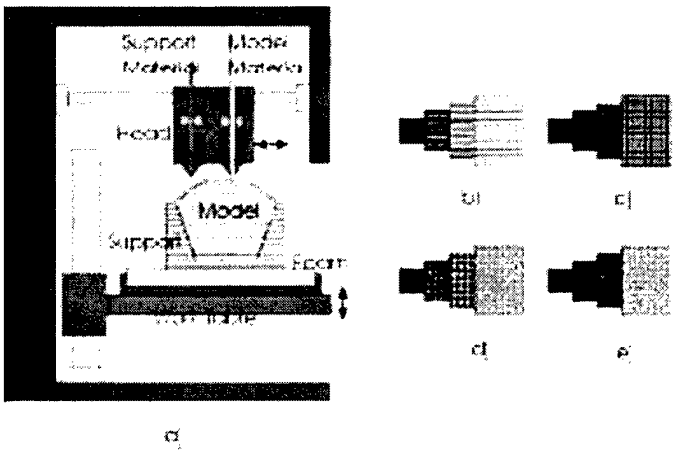


Figure 1: FDM process and the parts fabricated with graded mechanical properties

The remaining sections of this paper consist of the following parts: Section 2 is devoted to the modeling of the mechanical properties for design of FDM parts; experimental validation is given in Section 3. Section 4 provides an example of the prototypes with graded mechanical properties using LCP. The final section summarizes the main conclusions.

2. Modeling and Analysis of Mechanical Properties of FDM Prototypes

The FDM prototypes are orthotropic composites of ABS filaments, bonding between filaments and voids. They can be viewed and analyzed at different levels and on different scales. At macro level, they are studied as laminates of bonded laminars. At micro level, the properties of each laminar are functions of properties of filaments and void density.

2.1 Lamination Analysis of FDM Parts. To concurrently design mechanical geometries and properties, it is important to determine the effective stiffness so that the model can be used to predict the mechanical behaviors of the parts. Filament orientation θ is defined as the angle between the loading direction and longitudinal direction of filaments of each lamina. The in-plane constitutive relations for the case of *specially orthotropic*, where $\theta = 0(or 90^o)$, the constitutive relation reduces to form of Equation 1:

$$\begin{bmatrix} \sigma_{11} \\ \sigma_{22} \\ \sigma_{12} \end{bmatrix} = \begin{bmatrix} Q_{11} & Q_{12} & 0 \\ Q_{12} & Q_{22} & 0 \\ 0 & 0 & Q_{66} \end{bmatrix} \begin{bmatrix} \epsilon_{11} \\ \epsilon_{22} \\ \epsilon_{12} \end{bmatrix}. \quad (1)$$

where $[\sigma_{ij}]$ and $[\epsilon_{ij}]$ are the in-plane stress and strain respectively. $[Q]$ is the stiffness matrix. Four independent elastic constants, namely, longitudinal Young's modulus E_{11}, transverse Young's modulus E_{22}, major Poisson's ratio ν_{12}, and shear Modulus G_{12} are required to describe the in-plane elastic behavior of a lamina. All elements in matrix $[Q]$ are functions of these constants. *General orthotropic* lamina refers to a lamina with fiber orientation other than 0^o or 90^o. Although, the stiffness matrix for general orthotropic lamina is fully populated with 6 elements. These six elements are functions of the four independent elements in matrix $[Q]$ [Mallick, 93].

A laminate is constructed by stacking a number of laminas in the thickness direction. The

overall properties can be modeled by the Lamination Theory [Mallick, 93]. As such, in macromechanical approaches, the stiffness matrix of a laminate is composed by properties of every lamina according to the Lamination Theory, while the in-plane elastic behavior of a unidirectional lamina may be fully described in terms of four elastic lamina properties including E_{11}, E_{22}, G_{12} and ν_{12}. For the design purpose, it is desirable to have reliable predictions of lamina properties as a function of constituent properties and geometric characteristics. One of the objectives of micromechanics is to obtain such relationships.

2.2 Micromechanics of Material with Voids. A variety of methods have been used to predict properties of composite materials as functions of constituent volume ratio and geometric packing parameters. Tsai [Tsai, 64] conducted an analysis based on variational principles in which contiguity of the fibers and fiber misalignment were considered. The filament contiguity was incorporated in theoretical prediction E_{22}, and the fiber misalignment was considered in E_{11}. The set of the equations, when being reduced to material with voids, is depicted below.

The longitudinal Young's modulus can be described by the equation:

$$E_{11} = k(1 - \rho_1)E \tag{2}$$

where E is the Young's modulus of the polymer, ρ_1 is the void density in Plane 1 (normal to the fibers), and k is an empirical factor that takes into account the fact that the filament may not be exactly parallel or perfectly straight. The prediction of transverse modulus, E_{22}, takes form:

$$E_{22} = (1 - C)\frac{[1 - (1 - \rho_1)\nu](1 - \rho_1)}{1 + 2\rho_1 - \nu(1 - 2\rho_1)}E \tag{3}$$

where ν is the Poisson's ratio of the polymer. The effective in-plane shear modulus, G_{12}, is given by:

$$G_{12} = (1 - C)\frac{1 - \rho_1}{1 + \rho_1}G \tag{4}$$

where G is shear moduli of the polymer. And the in-plane Poisson's ratio, ν_{12}, is given by the following relation:

$$\nu_{12} = (1 - C)\nu \tag{5}$$

Only the void density in the plane perpendicular to the fibers is required to compute the effective properties. The value of fiber contiguity factor C can be assigned to two extreme cases, (1) all filaments are isolated, $C = 0$; (2) all fibers are contiguous, $C = 1$. The effective Poisson's ratio, ν_{12}, is found to be the same as that of polymer when $C = 0$. It is the same as Hashin and Rosen's conclusion [Hashin and Rosen, 64].

Tsai's equations may be suitable for materials with cavities, but they could be used for FDM parts only under the assumption of perfect bonding among filaments. However, this assumption is not valid for the FDM process according to the ABS sintering experiments that were conducted in this research.

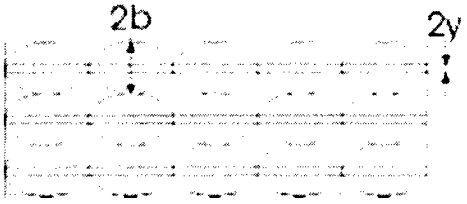


Figure 2: Fiber volume fraction in the transverse direction

2.3 Modeling of Elastic Constants for FDM Prototypes. The previous section demonstrated that FDM prototypes are composites of partially bonded ABS filaments and voids. Because of imperfect bonding, A new set of equations is proposed to calculate the elastic constants.

When loaded in longitudinal direction, a unidirectional FDM part is an aggregate of ABS filaments. Longitudinal Young's Modulus can be predicted well by the rule of mixtures. Therefore, Longitudinal Young's Modulus is:

$$E_{11} = (1 - \rho_1)E \tag{6}$$

where E is Young's Modulus of P400 filament, and ρ_1 is the area void density in the plane normal to filaments. In the case of transverse normal loading, the bonding among the filaments is the load carrier. The following equation is proposed for Transverse Modulus:

$$E_{22} = \zeta(1 - \rho_2)E \tag{7}$$

where ζ is an empirical factor that takes into account the bonding strength. ρ_2 is linear void fraction along the transverse direction. Refer to Figure 2, the definition of ρ_2 is:

$$\rho_2 = \frac{b - y}{b}. \tag{8}$$

Term $(1 - \rho_2)$ is the ratio of bonding length to overall dimensions. Similarly, the prediction of the in-plane shear modulus takes form:

$$G_{12} = \zeta(1 - \rho_2)G, \tag{9}$$

where G is the Shear Modulus of P400 filament, and the in-plane Poisson's ratio, ν_{12}, is same as that of ABS filaments, ν:

$$\nu_{12} = \nu \tag{10}$$

Comparing Equations 6 through 10 with Equations 2 to 5, the significant differences are in the predictions of E_{22} and G_{12}. Void density ρ_2 is introduced to count the potential load carrying dimension, whereas $\zeta(1 - \rho_1)$ results in the ratio of the effective load carrying media. Since the estimation of these elastic constants requires the void density in the plane perpendicular to filaments ρ_1 and bond length ratio ρ_2, the calculations of the void densities are the topic of the next section.

2.4 Micro-scopic Images Analysis. Theoretical calculations of strength, modulus, and other properties for a FDM part are based on the the void densities ρ_1 and ρ_2. Therefore the cross-sections of FDM specimens are studied under a microscope. Unidirectional cubic specimens of dimension $10 \times 8 \times 20mm$ were made with different gap sizes. They were cut in the middle plane

Table 1: Results of digitized image analysis

Gap Size(μm)	ρ_1	ρ_2
-50.0	0.0343	0.2776
-25.4	0.0434	0.3419
0	0.0799	0.4038
100	0.1990	1

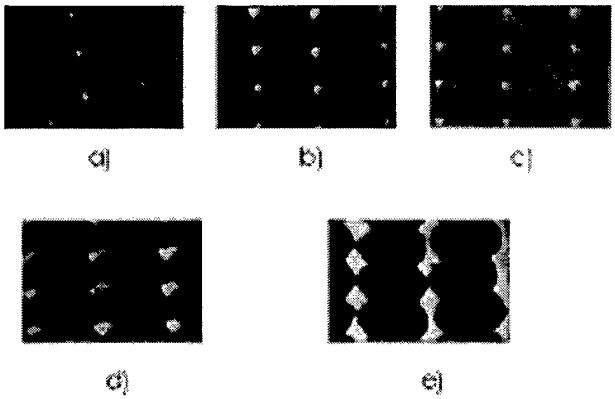


Figure 3: Meso-structures of different gap settings. a) $g = -0.100mm$; b) $g = -0.050mm$; c) $g = -0.0254mm$; d) $g = 0.0mm$ and e) $g = +0.100mm$

which is normal to filaments. Then the photos of meso-structures were taken under a microscope, as shown in Figure 3. They were analyzed by using image processing software. Void densities ρ_1 and ρ_2 were calculated, and the results are listed in Table 1. From the observation and the image analysis, it can be concluded that the voids appear periodically when the negative gap is small. When the negative gap reaches $-0.1mm$, the dimensional accuracy and surface quality of the specimen become very poor, and the periodicity can rarely be observed.

3. Experimental Validation

The theoretical stiffness model developed previously is a function of deposition densities and deposition orientations. To validate the model and method, the experimental analysis was carried out. The experiments tested the orthogonal-ply specimens, and the experimental results were compared with those of constitutive modeling described in Section 2. All specimens were manufactured by the FDM2000 machine. The elastic constants of P400 filaments were cited from work of Rodriguez Matas [Rodriguez Matas, 99], listed in Table 2, as the inputs of the theoretical calculations.

Table 2: Elastic Properties of P400 filament

Elastic Constant	Value
Young's Modulus, E	$2230 \pm 15MPa$
Shear Modulus, G	$833 \pm 7.6MPa$
ν	0.34 ± 0.02

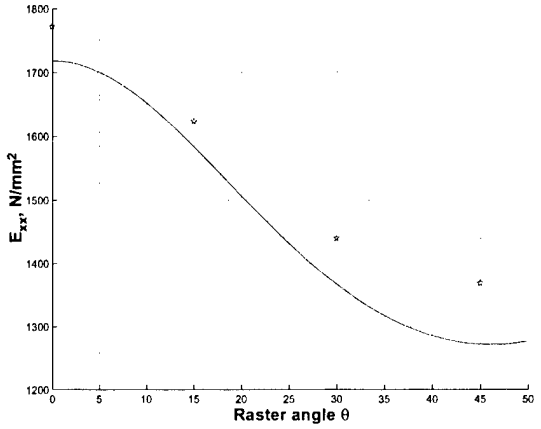


Figure 4: Young's modulus vs deposition Orientation in orthogonal-ply specimens

Table 3: Orthogonal-ply specimen test results

Specimen	Young's Modulus MPa		Difference
	Experimental	Theoretical	Percent
[0/90]	1772.9	1718.7	3.1
[15/-75]	1623.4	1584.7	2.4
[30/-60]	1440.4	1368.2	5.0
[45/-45]	1369.6	1272.7	7.1

The stiffness matrix of orthogonal-ply specimens can be constructed according to the procedure described in Section 2. As a result of the laminate modeling, the in-plane Young's modulus of the orthogonal-ply symmetric laminates with different $[\theta/(\theta - 90^o)]$ fiber orientations is a non-linear function of the deposition angle, as shown in Figure 4. It can be observed from the figure that the laminate with raster angles of approximately [45/-45] yields the minimum modulus of elasticity. The laminate with raster angles of [0/90] has the highest Young's Modulus. The experiments with the orthogonal-ply symmetric specimens were tested to determine the same in-plane moduli. The specimens with raster angles of [0/90], [30/-60], [45/-45], and [15/-75] were manufactured with the same thickness of 11 layers. These experimentally determined values were then compared with the theoretically predicted values to evaluate the effectiveness of the proposed laminate modeling approach, in Table 3 and marked as "$*$" in Figure 4. The experiment data were in good agreement with the results of laminate modeling.

4. Example

The purpose of the study of mechanical behaviors of FDM prototypes is to establish the models for design and fabrication of the parts with the desired mechanical properties through local composition control. This can be carried out with FDM process by changing deposition density and orientations to obtain the requried properties.

The design of the example part with graded mechanical properties is shown in Figure 5a). Assume that the geometrical and functional constraints require the smaller section with equal or higher stiffness than that of the larger section areas. Therefore, the properties are gradient along

Table 4: Configuration of the axis

	l_1	l_2	l_3
Length(mm)	20	20	20
Deposition strategy^o	[0/0]	[0/90]	[45/-45]
Gap (μm)	-25.4	-25.4	-25.4
E^i_{xx}	2137.7	1718.7	1272.7

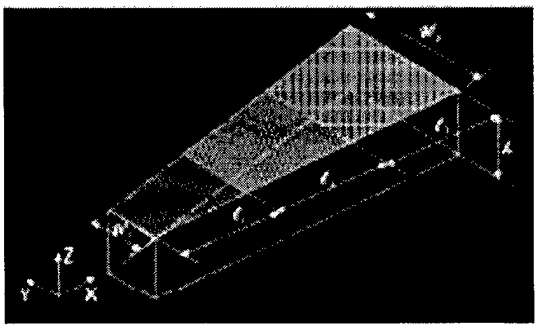


Figure 5: An axis with gradient property.

Axis X. Different deposition strategies and deposition densities were used for different sections of the part to meet the requirements as listed in Table 4. Young's modulus E_{xx} of each section calculated according to the stiffness modeling are listed in the table. If an external axial force P is applied at each end, the overall elongation ΔL is calculated using the following equation:

$$\Delta L = \sum_{i=1}^{3} \int \frac{PL_i}{E^i_{xx} A_i(x)} dx. \tag{11}$$

where L_i is the length of each section, E^i_{xx} is the Young's Modulus of the sectoin, and $A_i(x)$ is the cross-sectional area of the section. With locally controlled deposition density and deposition orientation, it is possible to make the section with smaller cross-sectional area as stiff as, or even stiffer than, the section with bigger cross-sectional area.

5. Concluding Remarks

The design and fabrication of products with LCP would make it possible to create a new class of products with desired mechanical and material characteristics. This paper reported a study on modeling of in-plane mechanical properties of FDM prototypes relating to fabrication parameters. Based on both the theoretical and the experimental analyses, a set of new equations of calculating the elastic constants were proposed and validated, which were used to determine the constitutive models of FDM parts. An example was presented to illustrate the design and fabrication of the FDM prototypes with required mechanical properties by locally controlled deposition density and orientations. Different deposition densities, angles and their combinations can be employed in producing the required stiffness properties of manufactured parts. The further study is currently underway in investigating void geometry and density with more manufacturing parameters.

Acknowledgements

The financial support for this research was provided by the National Sciences and Engineering Research Council of Canada (NSERC) through Research Grant OGP0192173. The authors would like to thank Brandon Furguson and Art Moehrle for their assistance with experiments performed in the research.

References

[Agarwala *et al.*, 96] M. K. Agarwala, A. Bandyopadhyay, R. van Weeren, N. A. Langrana, A. Safari, and S. C. Danforth, *Fused Deposition of Cerameics (FDC) for Structural Silicon Nitride Components*, Solid Freeform Fabrication Symposium, Austin, TX, Aug. 8th, 1996.

[Gray IV *et al.*,98] Robert W. Gray IV, Donald G. Baird and Jan Helge Bohn, *Effects of processing conditions on short TLCP fiber reinforced FDM parts*, Rapid Prototyping Journal, Vol. 4, No. 1, pp. 14-25, 1998.

[Cho *et al.*, 01] W. Cho, E. M. Sachs, N. M. Patrikalakis, M. Cima, T. R. Jackson, H. Liu, J. Serdy, C. C. Stratton, H. Wu, and R. Resnick, *Methods for Distributed Design and Fabrication of Parts with Local Composition Control*, Proceedings of the 2001 NSF Design and Manufacturing Grantees Conference, Tampa, FL, USA, January 2001.

[Comb *et al.*, 94] Comb, J. W., Priedeman, W. R., and Turley, P. W.,*Layered Manufacturing Control Parameters and Material Selection Criteria* Manufacturing Science and Engineering, PED-Vol. 68-2, Nov. 6-11, pp. 547-556, 1994.

[Hashin and Rosen, 64] Zvi Hashin and B. Walter Rosen, *The Elastic Moduli of Fiber-Reinforced Materials*, Transactions of ASME: Journal of Applied Mechanics, Vol. 86, pp. 223-232, June 1964.

[Jackson *et al.*, 99] T. R. Jackson, H. Liu, N. M. Patrikalakis, E. M. Sachs, and M. J. Cima. *Modeling and Designing Functionally Graded Material Components for Fabrication with Local Composition Control* Materials and Design, June 1999, Vol. 20, No. 2/3, pp. 63-75.

[Kulkarni and Dutta, 99] P. Kulkarni and D. Dutta, *Deposition Strategies and Resulting Part Stiffnesses in Fused Deposition Modeling*, ASME Transictions: Journal of Manufacturing Science and Engineering, Vol. 121, pp. 93-103, February, 1999.

[Mallick, 93] P. K. Mallick, *Fiber-reinforced Composites: materials, manufacturing, and design*, Second Edition, Marcel Dekker, Inc, 1993.

[Rodriguez Matas, 99] Jose F. Rodriguez Matas, "Modeling the mechanical behavior of fused deposition acrylonitrile-butadiene styrene polymer components", Ph. D Dissertation, Department of Aerospace and Mechanical Engineering, Notre Dame, Indiana, 1999.

[Tsai, 64] Stephen W. Tsai, *Structral Behavior of Composite Materials*, NASA CR71, 1964.

[Yardimci *et al.*, 96] M. Atif Yardimci, S. I. Guceri, S. C. Danforth, and M. Agarwala, "Part Quality Prediction Tools for Fused Deposition Processing", Proceedings of the Solid Freeform Fabrication Symposium, Austin, TX, pp. 539-548, Aug. 1996.

Microstructure Evaluation for Laser Densification of Dental Porcelains

Xiaoxuan Li, Jiwen Wang, Alvin Augustine, Leon L. Shaw, Harris L. Marcus
Institute of Materials Science
University of Connecticut
Storrs, CT 06269

Thomas B. Cameron
Degussa-Ney Dental Inc.
Bloomfield, CT 06002

ABSTRACT

The feasibility of dental restorations has been investigated using a multi-materials laser densification (MMLD) process, where dental alloy and porcelain powders are laser densified layer by layer to form solid bodies. The present study focuses on the densification behavior of dental porcelain powders in response to a moving laser source. Effects of the laser processing temperature and the green density of the powder bed on microstructure, distortion, macro-cracks, porosities and phase contents of the laser densified porcelain have been investigated. The condition to generate continuous porcelain bodies from powder compacts have also be studied. It is found that the geometry, composition and density of densified porcelain bodies are strongly affected by the laser processing temperature and the green density of the powder compact.

INTRODUCTION

Dental porcelain-fused-to-metal (PFM) restorations are fabricated by fusing the porcelain to the metal at high temperatures. PFM restoration is a very time consuming and labor intensive work because PFM restoration requires a multi-stage process using multiple materials (both ceramics and metals) and each stage involves multiple processing steps [1]. Typically, 4 – 8 labor hours are needed to make the dental restoration of a three-unit bridge. As such, labor costs account for about 90% of the final cost to the patient while dental materials occupy only less than 5%. The current project is to develop a novel multi-materials laser densification (MMLD) process for dental restorations. This process utilizes laser-assisted solid freeform fabrication (SFF) to fabricate artificial dental units layer-by-layer directly from a computer model without part-specific tooling and human intervention. As such, the labor cost will be substantially reduced, and better and faster dental restorations will be achieved.

To develop a robust MMLD process for dental restoration, the densification behavior of dental alloys and porcelains in response to a moving laser source needs to be investigated. Some investigation results on dental nickel alloys have been reported in a previous paper [2]. The present study focuses on laser sintering of the dental porcelain delivered in both loose powder and paste form. Effects of the laser processing temperature and the green density of the powder bed on microstructure, distortion, macro-cracks, porosities and phase contents of the laser densified porcelain have been investigated. The condition to generate continuous porcelain bodies from powder compacts have also been studied. The results are presented below.

EXPERIMENTAL

Starting Materials – The dental porcelain powder was provided by Degussa-Ney Dental Inc., Bloomfield, CT. The chemical composition of the porcelain is confidential; however, it is within 5% of the nominal composition of the Weinstein patent [3], which has the following composition (wt%): 63.40% SiO_2, 16.70% Al_2O_3, 1.50% CaO, 0.80% MgO, 3.41% Na_2O, and 14.19% K_2O. The typical morphology and microstructure of the porcelain powder are shown in Figure 1 and its main properties are summarized in Table 1. It can be seen that the as-received dental porcelain material is composed of two phases, one being the feldspar-based glass matrix and the other the crystalline leucite ($K_2O{\cdot}Al_2O_3{\cdot}4SiO_2$). Leucite has a high coefficient of thermal expansion (CTE) and raises the inherently low CTE of the feldspathic glass matrix to match that of the PFM dental alloys, typically 13.8 ~ 16.9 x 10^{-6} K^{-1}. The CTE is one of the most critical issues regarding dental restorations because the potential for micro-cracking due to mismatch in CTE between the dental alloy and porcelain cannot be overlooked. From Table 1 it can be seen that the CTE of the dental porcelain is close to that of the dental alloy (13.8 ~ 16.9 x 10^{-6} K^{-1}).

Table 1. Properties of Dental Porcelain Powder

Particle Size	Particle Shape	Glass Transition Temperature	Softening Point	Coefficient of Thermal Expansion
1 – 50 microns	Angular	~ 580°C	~ 650°C	14.4~14.9 x 10^{-6} K^{-1}

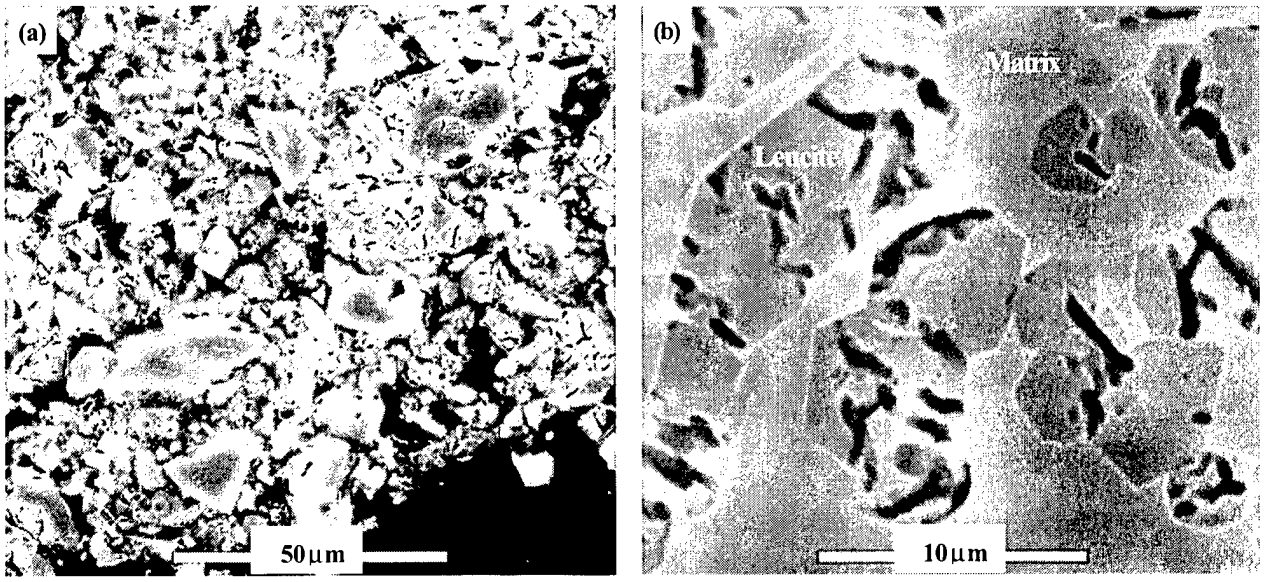


Figure 1. The as-received dental porcelain powder contains crystalline leucite before PFM and MMLD process: (a) an overview of several porcelain particles, and (b) the microstructure of the porcelain powder, showing leucite particles dispersed in the feldspathic glass matrix.

Laser Densification Process - An integrated SFF system was used for the laser densification process during which a continuous wave laser beam was emitted from a 50W CO_2 laser, and steered into a atmosphere-controlling chamber by a series of motion-controlled mirrors, hitting and sintering the desired areas of the powder bed surface. The whole sintering process was closed-loop-temperature controlled through a pyrometer by comparing the pyrometer reading with a user-defined target surface temperature. The effect of the target surface temperature on the quality of laser densified porcelain bodies was evaluated. The dependence of the quality of laser densified

porcelain bodies on green density of powder compacts was also investigated by comparing the results obtained from a dry powder bed and a dried powder paste. The dry powder bed was a loose powder compact. However, the paste was prepared by dispersing the porcelain powder in de-ionized water, then delivered on a steel substrate, and finally dried on an electric plate before laser densification.

Microstructure Characterization – Densified porcelain bodies were mounted with epoxy and finish-polished with one-micron diamond suspension. The polished coupons were subsequently etched in 1% hydrofluoric (HF) acid for 20 seconds and then gold sputter-coated before characterized using an environmental scanning electron microscope (PHILIPS ESEM 2020), or examined using a digital optical microscopy. The x-ray energy-dispersive spectrometry (EDS) was used to evaluate the chemical composition.

RESULTS AND DISCUSSION

Effects of the Green Density of Porcelain Powder Compacts – Typical microstructures of laser densified porcelain bodies using a dry powder bed and a dried powder paste are shown in Figure 2. It is obvious that the densified porcelain body derived from the dried powder paste has a better quality than that derived from the dry powder bed. Specifically, the dried powder paste has led to smooth surfaces at both the top and bottom of the densified body, whereas the dry powder bed has resulted in the densified part that contains substantial amounts of porosities and voids. The marked difference is believed to be due to the high green density achieved via the dried powder paste. Thus, it can be concluded that the high powder packing density in the dried paste is beneficial for obtaining laser-densified bodies with good surface finish and low porosities.

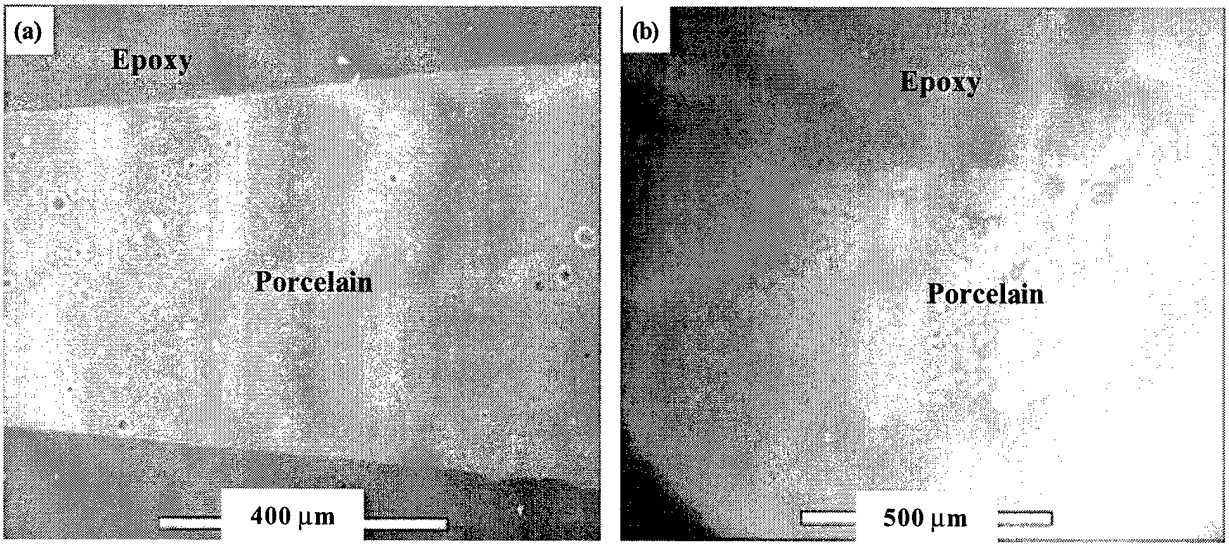


Figure 2. Typical morphology of laser processed porcelain bodies from (a) a dried powder paste and (b) a dry powder bed.

Temperature Dependence of the Quality of Densified Bodies – The effect of the laser sintering temperature was evaluated by comparing the parts laser processed with single line scanning under different target surface temperatures. Shown in Figure 3 are the overall morphology and microstructures of the laser densified bodies using different target surface temperatures. The top

micrographs in Figures 3(a), (b) and (c) are the microstructures before etching and the bottom micrographs after etching. The micrographs before etching can reveal the presence of porosities and microcracks with relative ease, whereas the micrographs after etching can show the morphology and size of the crystalline leucite in the densified bodies. The dark spots emerged after etching in the bottom micrographs of Figures 3(a), (b) and (c) are the images of leucite particles. The morphology of these leucite particles can be revealed clearly under high magnifications, as shown in Figure 3(d). Note that the morphology of leucite particles is similar to that in the as-received porcelain powder (Figure 1b).

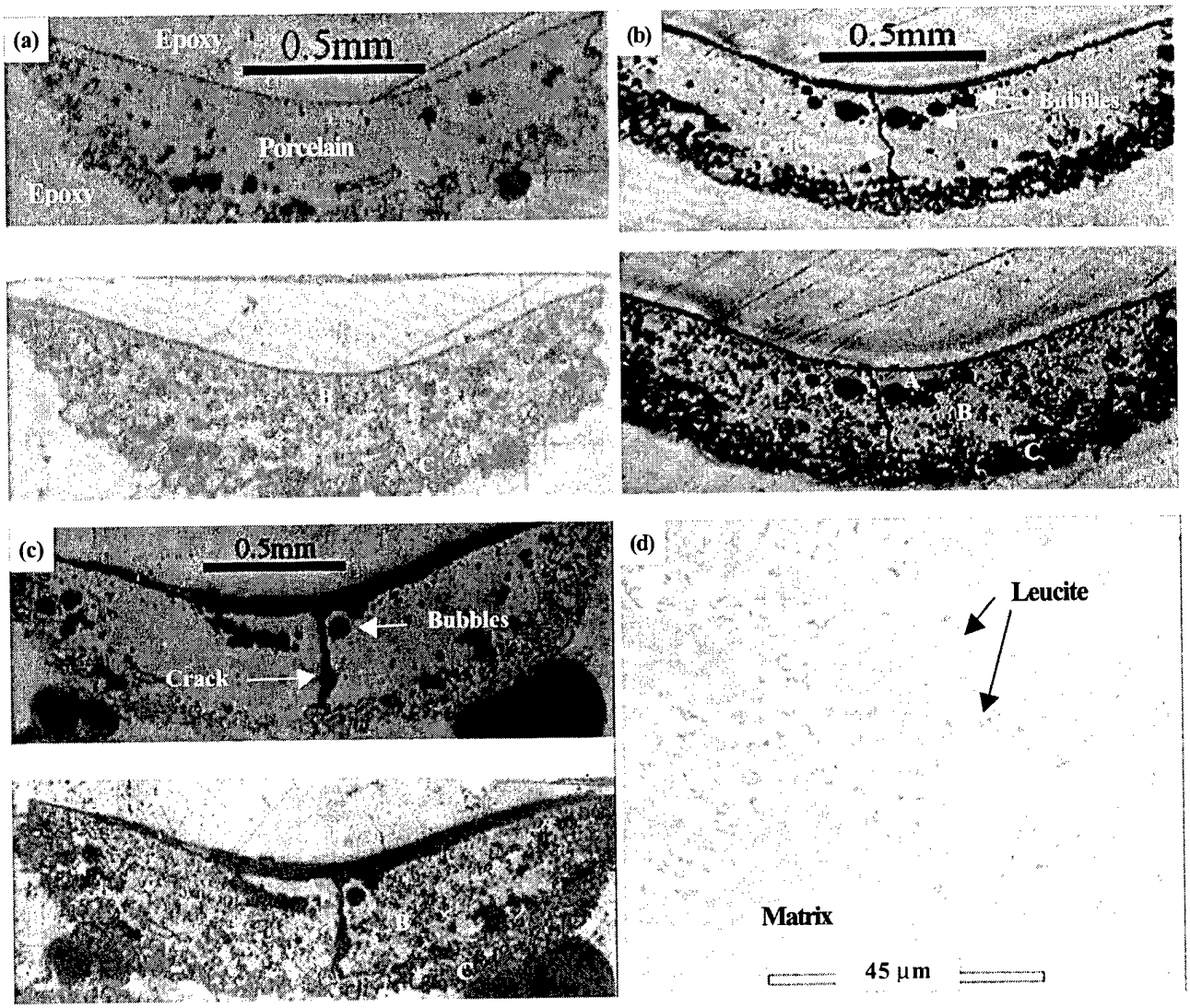


Figure 3. Morphology of laser densified porcelain bodies with scanning speed 0.24 mm/s and the target surface temperature of (a) 900°C, (b) 1000°C, and (c) 1050°C. The top micrographs of (a), (b) and (c) are obtained before etching and the bottom micrographs after etching. (d) is a high magnification micrograph of Zone B shown in (a).

A close examination of Figure 3 reveals that a laser processed body can normally be divided into three distinct zones, A, B and C. Furthermore, the processed body may contain macro-cracks and bubbles as marked in Figures 3(b) and (c). Zone A is the region that appears featureless even after etching (Figure 4), suggesting that this zone does not contain leucite particles. Zone B is the

region where leucite particles are finely dispersed in the feldspathic glass matrix (Figure 3d), and it has a similar microstructure as the as-received porcelain powder (Figure 1b). Zone C is the area with little laser sintering.

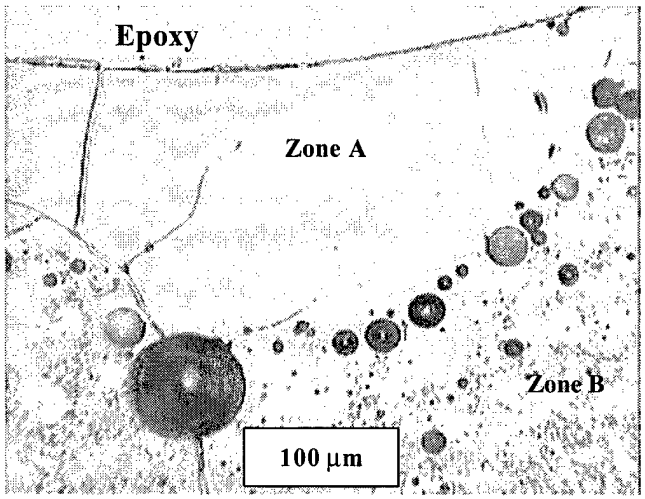


Figure 4. The typical appearance of Zone A.

It is noted that Zone A appears at the location where the laser beam center has traveled through. Thus, Zone A has been exposed to a much higher temperature than the surrounding area because of the Gaussian power distribution of the laser beam. In order to understand the appearance of Zone A, the various zones in Figure 3 have been examined using the energy-dispersive spectrometry. The results are shown in Figure 5. For comparison, the EDS results of the traditional PFM dental body feldspathic matrix and leucite precipitates are also included in the figure.

As expected, the EDS of the traditional PFM body shows that the glass matrix contains lower potassium concentration than the leucite particles [3,4]. Furthermore, the matrix contains sodium and calcium both of which are not found in the leucite particles, again consistent with the porcelain and leucite compositions [3,4]. A comparison between the traditional PFM porcelain body (Fig. 5(a) and (b)) and the laser densified body (Fig. 5(c) and (d)) indicates that both the matrix and leucite in the laser processed body have lower potassium concentrations than the counterparts in the traditional PFM porcelain body. This suggests that some of the potassium, a volatile element, has evaporated in the laser densification process. The loss of the potassium is especially severe at the locus of the laser beam center where the temperature is the highest. It is also noted that Zone A always appears at the locus of the laser beam center (Figure 3) and has the lowest potassium concentration (Figure 5(e)) among all the regions measured in this study. It has been well established that the feldspathic porcelain needs a minimum amount of potassium to form leucite precipitates [5,6]. Thus, the disappearance of leucite particles in Zone A is due to the substantial loss of the potassium element in that particular area. Since the appearance of Zone A is associated with the loss of potassium, Zone A is then expected to increase with increasing the target surface temperature. This is exactly what we observed in the experiment. As shown in Figure 3, there is no Zone A when the target surface temperature is low (e.g., 900^0C). Zone A appears when the target surface temperature is set at 1000^0C and becomes larger when the target surface temperature is 1050^0C.

Macro-cracks, Bubbles and Distortion – The integrity of the densified porcelain body is one of the important criteria for determining what laser processing conditions should be. Figure 3 reveals three major defects that degrade the integrity of the laser densified porcelain body. These

are (i) macro-cracks, (ii) bubbles and (iii) distortion. Macro-cracks appear only when the laser processing temperature is high (e.g., 1000 and 1050^{0}C of the target surface temperature). Further, the higher the target surface temperature is, the larger the macro-crack is, as exhibited by Figures 3(b) and (c). These results suggest that macro-cracks are caused by thermal shock. Higher laser processing temperatures lead to higher temperature gradients between the top and bottom of the densified porcelain body, thereby producing more severe thermal shock and larger macro-cracks. Thus, to avoid macro-cracks the target surface temperature should not be too high. 900^{0}C appears to be appropriate for the porcelain used in this study. Preheating of the substrate may be a useful approach to combat the macro-cracking problem especially when a high target surface temperature is required for densification of the porcelain body.

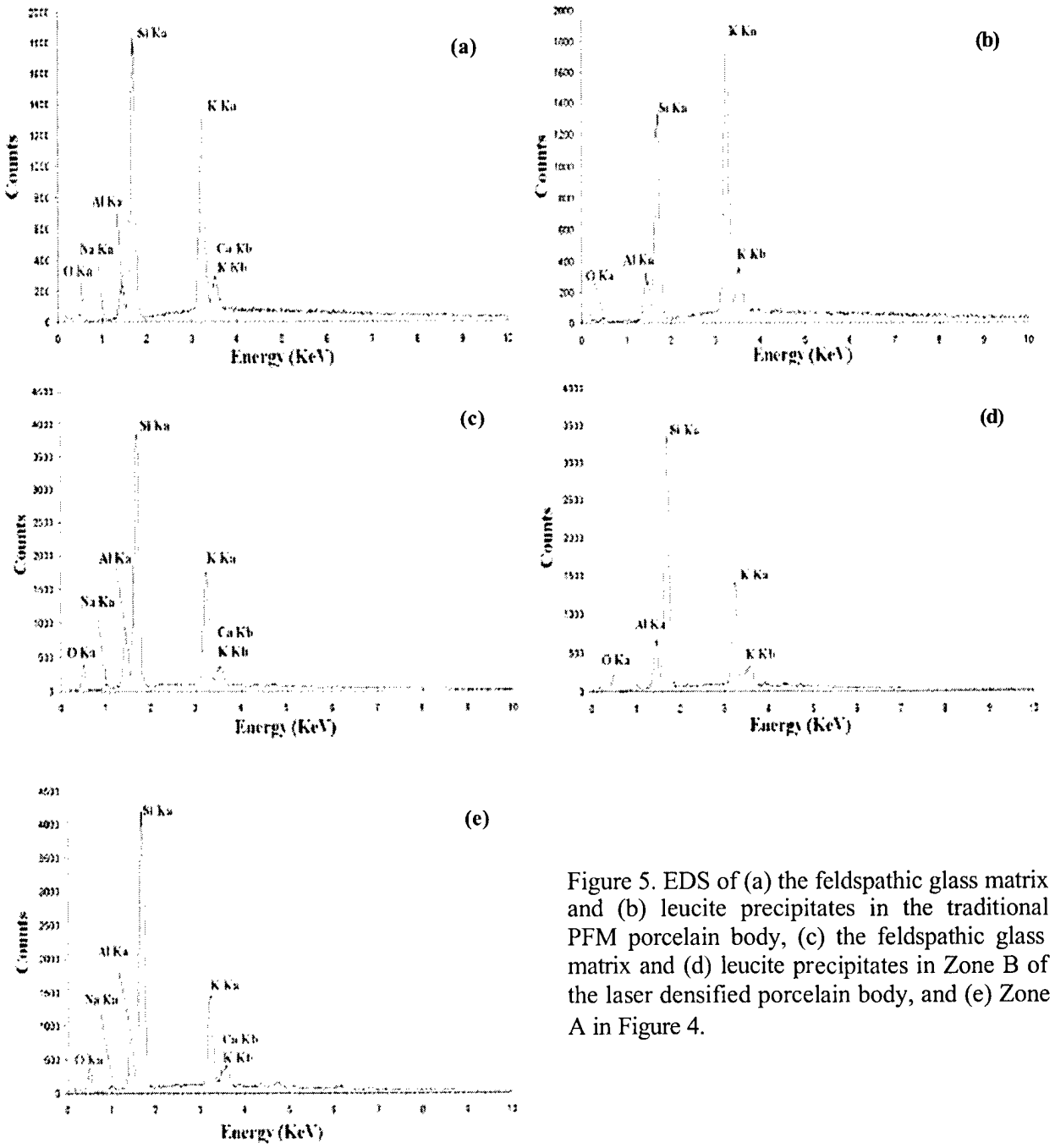


Figure 5. EDS of (a) the feldspathic glass matrix and (b) leucite precipitates in the traditional PFM porcelain body, (c) the feldspathic glass matrix and (d) leucite precipitates in Zone B of the laser densified porcelain body, and (e) Zone A in Figure 4.

The appearance of large bubbles in the densified porcelain body also appears to be associated with high laser processing temperatures. As shown in Figures 3(b) and (c), most of the large bubbles gather around Zone A. The formation of the bubble clusters around Zone A is clearly undesirable and efforts are currently under way to identify the exact mechanism and prevent its formation.

Finally, it is noted that regardless the laser processing temperature, the laser densified porcelain body always exhibits substantial distortion, showing a severe concave upward warping (Fig. 3). Our recent thermal and stress analyses of laser processing using finite element modeling [7] have indicated that such distortion is caused by the temperature gradient between the top and bottom surfaces of the densified body. One of the methods to eliminate warping is having the same temperature for the top and bottom surfaces [7]. Although this is hard to achieve, warping can be minimized by preheating of the substrate so that the temperature gradient can be reduced.

Continuity of Laser Densified Porcelain Bodies – Another important issue for laser densification of porcelain bodies is whether or not laser densified bodies are continuous macroscopically. The continuity issue covers a wide range of laser scanning conditions. The simplest case is the continuity issue when a single-track laser scan is performed. The more complicated cases are the continuity issues when multi-track laser scans to form a solid plate or a single-track laser scan to form a ring, a rectangle or a triangle is needed. The present study shows that continuity is not a problem for a single-track laser scan. However, continuity becomes a problem when fabrication of a ring-shaped porcelain body is desired. Figure 6 shows a porcelain ring produced using a single-track laser scan with the end point of the scan overlapping with the starting point. It can be seen that there is a groove near the starting point, i.e., the ring is not smoothly connected at the starting point even though the end point of the scan overlaps with the starting point. The appearance of the groove is related to the volume shrinkage of the porcelain powder changing to a dense body and spheroidizing of the molten porcelain under the surface tension during the laser melting and solidification process. The attempt to eliminate the groove by overlapping the starting point of the scan with the end point by a 45 degree additional scan was not successful. Efforts are currently under way to identify a suitable approach to eliminate the groove.

Concluding Remarks

The present study has investigated the densification behavior of dental porcelain powders in response to a moving laser source. Based on this investigation, the following conclusions can be made.

(a) The high powder packing density is beneficial for obtaining laser densified bodies with good surface finish and low porosities.
(b) The potassium content in the laser densified porcelain body is lower than that of traditional PFM body because of the volatile nature of potassium and the high local temperature at the center of the laser beam.
(c) When the target surface temperature is higher than 1000°C, the leucite content at the locus of the laser beam center is substantially reduced. As a result of this large loss of potassium, a leucite-free zone is formed. The size of the leucite-free zone increases with increasing the target surface temperature.
(d) Thermal shock-induced macro-cracks appear when the laser processing temperature is too high (e.g., the target surface temperature greater than 1000°C). The higher the target surface temperature is, the more severe the cracking phenomena.

(e) Regardless the laser processing temperature, the laser densified porcelain body always exhibits substantial distortion, showing a severe concave upward warping. Such distortion is caused by the temperature gradient between the top and bottom surfaces of the densified body.
(f) The macroscopic continuity of laser densified porcelain bodies may become a problem when fabrication of a porcelain body with a shape having macroscopic connectivity such as rings and triangles are performed.

Acknowledgement – The authors gratefully acknowledge financial support provided by the National Science Foundation under Grant No: DMI-9908249.

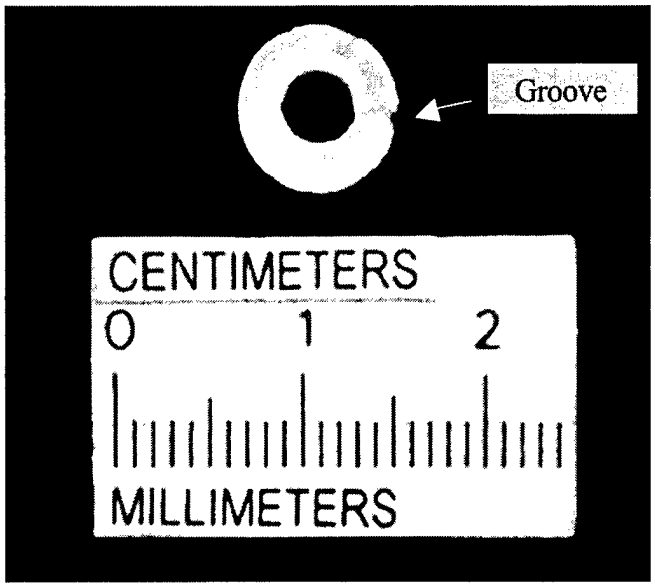


Figure 6. Top view of a ring-shaped porcelain body fabricated using a single-track laser scan with the end point of the scan overlapping with the starting point, showing the presence of a groove near the starting point.

References

1) X. Li, J. Crocker, E. Geiss, L. Shaw, H. Marcus and T. Cameron, "Evaluation of Microstructure and Properties for Multi-Materials Laser Densification of Dental Restorations," in the proceedings of the 11th Annual SFF Symposium, edited by D. L. Bourell, et al., The University of Texas, 2000, pp. 159 – 167.
2) X. Li, J. Crocker, L. Shaw, H. Marcus and T. Cameron, "Laser Densification of Nickel Powder for Dental Restorations," to appear in the proceedings of the 2001 NSF Design, Manufacturing & Industrial Innovation Research Conference, Tampa, Florida, 2001.
3) M. Weinstein, S. Katz and A. B. Weinstein, "Fused Porcelain-to-Metal Teeth," U.S. Pat. No. 3 052 983, Sept. 11, 1962.
4) J. R. Mackert, Jr., M. B. Butts, R. Morena and C. W. Fairhurst, "Phase Changes in a Leucite-Containing Dental Porcelain Frit," J. Am. Ceram. Soc., 69 [4] C-69-C-72 (1986).
5) L. Hermansson and R. Carlsson, "On the Crystallization of the Glassy Phase in Whitewares," Trans. J. Br. Ceram. Soc., 77, 32-35 (1978).
6) M. A. Rouf, L. Hermansson and R. Carlsson, "Crystallization of Glasses in the Primary Phase Field of Leucite in the K_2O-Al_2O_3-SiO_2 System," Trans. J. Br. Ceram. Soc., 77, 36-39 (1978).
7) K. Dai and L. Shaw, "The Size Effect on Stresses and Distortion of Laser Processed Multi-Material Components," unpublished research.

Freeform Fabrication of Ti_3SiC_2 Structures

D.J. Dcosta and W. Sun[1]
Department of Mechanical Engineering and Mechanics

T. El-Raghy
Department of Materials Engineering

Drexel University
Philadelphia, PA 19104

This paper introduces a three-stage process to fabricate highly dense Ti_3SiC_2 structures. The properties of Ti_3SiC_2 material, the synthesis of the ceramic powder, the procedure involved in the 3-stage fabrication process and the preliminary results on fabricating fully dense Ti_3SiC_2 structures are presented. The characterization and microstructure evaluation of the mechanical, morphological and structural properties covering the compressive strength, Vickers micro hardness, damage tolerance, thermal shock, shrinkage and porosity of Ti_3SiC_2 structures printed using the 3-stage process are presented.

1. Introduction

Quite a few researches have used freeform fabrication techniques to directly prototype functional ceramic parts in order to obtain more freedom in the design and utilization of ceramic structures [1]. Studies include photopolymer resin curing by ultraviolet light employing SLA and solid ground curing [2], thermal fusion of powders by laser scanning used in the SLS process [3], adhesion of powders by disbursal of binder through an ink-jet used in three-dimensional printing [4-6], compacting and sintering of powders as demonstrated in the freeform powder molding technique [7], extrusion of thermoplastics through a fixed diameter nozzle in the FDM process [8], using an extension of the 3D Printing technique to build objects of variable density by controlling microstructure and composition [9], and Multiphase Jet Solidification (MJS) [10]. Another technique involved a further development to the technology of Inkjet Printing, wherein, the binder in the printing cartridge was replaced by a ceramic suspension, pressurized in a continuous ink jet printer [11,12]. Similar techniques such as Robocasting [13], involving a computer-aided deposition of highly concentrated ceramic colloidal slurries directly forming complex shapes without the use of molds or dies have also been researched upon. Additionally, other similar techniques relying on the basic inkjet printing technology are the overprinting technique [14] using inkjet printing of electro ceramics such as lead zirconate titanate (using a piezoelectric actuator to eject the ink); electro photographic powder deposition [15] technique employing the deposition of charged powder particles layer-by-layer, resulting in the precise deposition of particles to the desired shape; electromagnetic ink jet printing [16] employing the ejection of ceramic inks via an electromagnetic valve printing head and dispersion of ceramic inks onto a substrate using an ultrasonic vibrating horn have also been experimented upon.

[1] Corresponding author, Tel: 215-895-5810; Fax: 215-895-2094; Email: sunwei@drexel.edu

The objective of this paper is to present our preliminary studies on using Layered Printing, compacting, and sintering processes to fabricate fully dense functional Titanium Silicon Carbide (Ti_3SiC_2) structures with the comparable properties to the Ti_3SiC_2 bulk reported in [17-20]. The contents of this paper are presented as follows. Section 2 briefly reviews the properties of Ti_3SiC_2 and the ceramic powder preparation. Section 3 describes the 3-stage process. The fabricated samples are presented in Section 4. The results of structural characterization, such as the compressive strength, Vickers micro hardness, damage tolerance, thermal shock, shrinkage and porosity and microstructure evaluation, of Ti_3SiC_2 structures are presented in Section 5. Summary, conclusion and discussions are presented in Section 6.

2. Ti_3SiC_2 - Properties and Powder Preparation

Titanium Silicon Carbide, a layered ternary ceramic compound was processed in bulk, by Dr. M. W. Barsoum and Dr. T. El-Raghy at Drexel University. Polycrystalline bulk samples of Ti_3SiC_2 were synthesized by reactively hot pressing Titanium, Graphite (Carbon) and Silicon Carbide powders at a pressure of 40 MPa and temperature of 1600 °C for 4 hours at a temperature rate of 10 °C/min. [18 - 20]. The bulk sample obtained as a result of the solid phase reaction was milled to obtain a ceramic powder. As a part of the powder preparation process pure Ti_3SiC_2 powder is thoroughly mixed with a water-soluble binder and dried to form clinker. The resulting clinker is crushed in a powder mill. As a result of this entire process fine Ti_3SiC_2 powder particles coated with a film of binder are obtained. Further, the powder was sifted through a –325 mesh sieve to obtain an average grain size of less than 40 μm. This batch of powder was used as the build powder in our study.

Ti_3SiC_2 possesses a unique combination of mechanical, electrical and thermal properties of both metals and ceramics. Like metals it is an excellent electrical and thermal conductor, easily machinable, relatively soft, good thermal shock resistance and behaves plastically at higher temperatures, and like ceramics it is oxidation resistant and refractory in nature[18,19]. It has an electrical conductivity of 4.5×10^6 ohm^{-1} m^{-1} that is twice that of pure Titanium (2.3×10^6 ohm^{-1} m^{-1}). The thermal expansion coefficient, in the temperature range of 25 to 1000 °C, the room temperature thermal conductivity and heat capacity are 9.2×10^{-6} °C-1, 43 W/m K and 588 J/kg K respectively, these being similar to that of Titanium namely, 31 W/m K and 523 J/Kg K. Its density of 4.5 gm/cc is roughly half the density but almost double the stiffness of Nitrogen based super-alloys. Ti_3SiC_2 is relatively soft with Vickers Hardness of 2-5 GPa but elastically stiff and easily machinable.

A remarkable property of Ti_3SiC_2 carbide is its easy machinablility in spite of its high stiffness. The layered structure of material and its ductility contributes to direct machinability to close tolerances without any post machining sintering, whereas in other cases the ceramic needs to be sintered after machining resulting in an additional shrinkage. Ti_3SiC_2 is the only carbide that can be cut manually using a hacksaw. Due to its good electrical properties it is also easily shaped and cut using Electric Discharge Machining. In addition, Ti_3SiC_2 retains its mechanical properties at high temperatures and is stable at temperatures of 1800 °C with excellent high temperature mechanical properties [20]. There is no effect on the bend strength of Ti_3SiC_2 when heated to 1400 °C and quenched. This ceramic actually increases in strength and exhibits excellent resistance to thermal shock, whereas other ceramics have a drastic reduction in strength

when subjected to the same conditions of quenching. The structural properties of samples developed using the 3-stage integrated process have been evaluated in Section 5.

3. The Three-Stage Fabrication Process

The fabrication of Ti_3SiC_2 structure is divided into three primary stages [21]: 1) solid freeform fabrication, 2) pressure compacting, and 3) Sintering. Flow chart of the 3-stage process is described in Figure 1. In the first stage, the part is built using the layered Printing technique employing the powder deposition and liquid binding technique to print the part as a layered structure, wherein the Ti_3SiC_2 powder is used as the build material. In this process the STL file generated from the corresponding CAD model is inputted to the prototyping system to generate the process path. The green part is built by deposition of Ti_3SiC_2 powder and binder spray (as per the cross-section at the particular slice) layer by layer till the entire part is built. At this stage the green part has been freshly developed and has a low structural strength. The second stage is to compact the green part by applying a high pressure on the green part to increase the density and the strength of the green part. The last stage of the process is to sinter the compacting part in an electric tube furnace at high temperature in a flowing Argon atmosphere (inert atmospheric conditions are specified to prevent any oxidation).

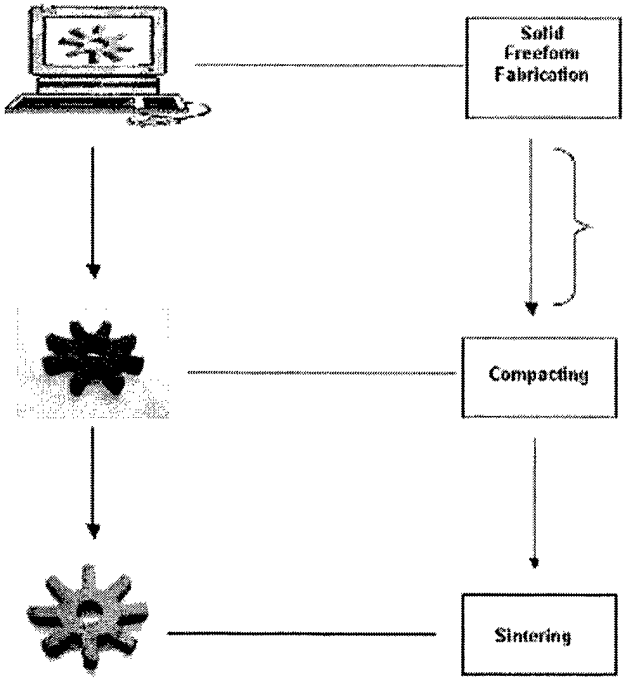


Figure 1: Three-stage fabrication process for Ti_3SiC_2 structures

4. Fabrication of Ti_3SiC_2 Samples

To understand the effect of the compacting pressure on the structural properties of the Ti_3SiC_2 samples, two sets of samples were processed. One set of samples was fabricated using the integrated 3-stage process, i.e., SFF, Compacting, and Sintering. While the other set was sintered directly without Compacting after SFFP. The samples without the compacting process

were fabricated with layer thickness of 0.0035", 0.007" and 0.01" and the binder concentration of 7 – 40%. Standard procedures were used to prepare samples for structural and optical characterization.

Figure 2 shows different Ti_3SiC_2 samples fabricated through the 3-stage process, such as a 6-tooth sprocket, turbine wheel and hollow tube (Figure 2), and the master sample for test and characterization (Figure 3). Figure 2a to 2c show the samples at different process stages, namely, SFF green parts (2a), compacted parts (2b), and sintered parts (2c). The master sample shown in Figure 3 was used as the test specimen. Test samples for mechanical property evaluation were derived from the master sample. The layer thickness for fabricating the master sample was fixed at 0.0035". The densities achieved for samples fabricated using the 3-stage technique were over 99%.

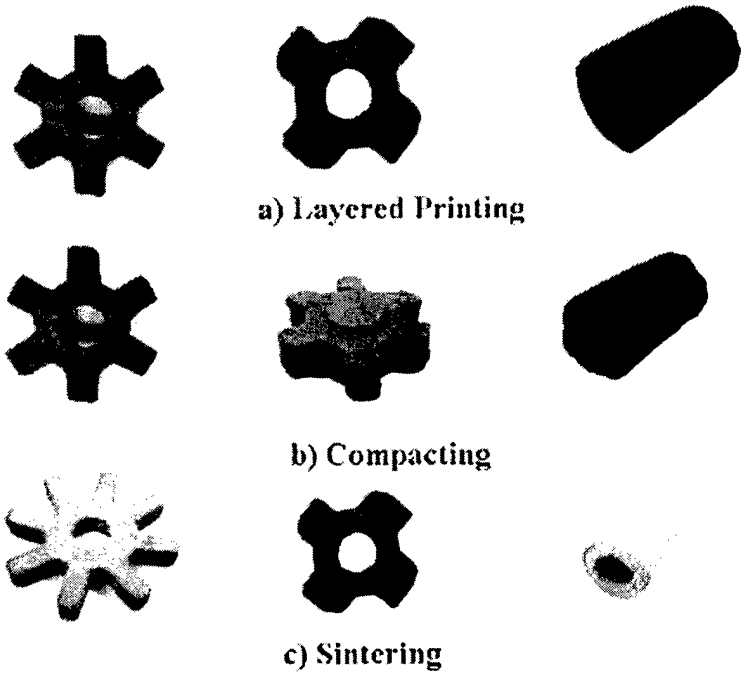


Figure 2: Parts fabricated using the 3-stage process

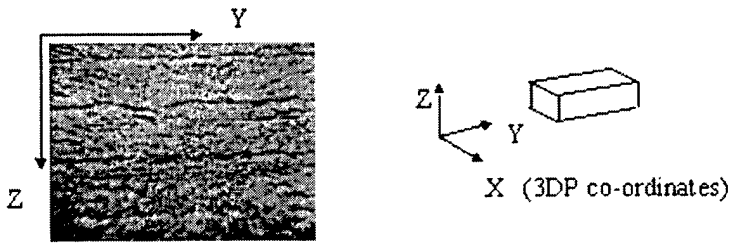


Figure 3: Master sample (layered structure) fabricated using the 3-stage process

5. Mechanical Testing and Microscopic Evaluation

The mechanical testing and microscopic evaluation of the prototyped Ti_3SiC_2 samples were conducted to evaluate the compressive strength, Vickers micro hardness, damage tolerance, thermal shock, shrinkage and porosity (Figure 4). A summary of the results is presented in this section. Comparisons have been made with the available data reported in the references. It needs to be pointed out that the Ti_3SiC_2 powder batch used in our samples contained about 30 – 40% more TiC (Titanium Carbide) than the powder used in reference [20], and hence the results reported here are higher than the reported data due to the presence of the excessive amount TiC.

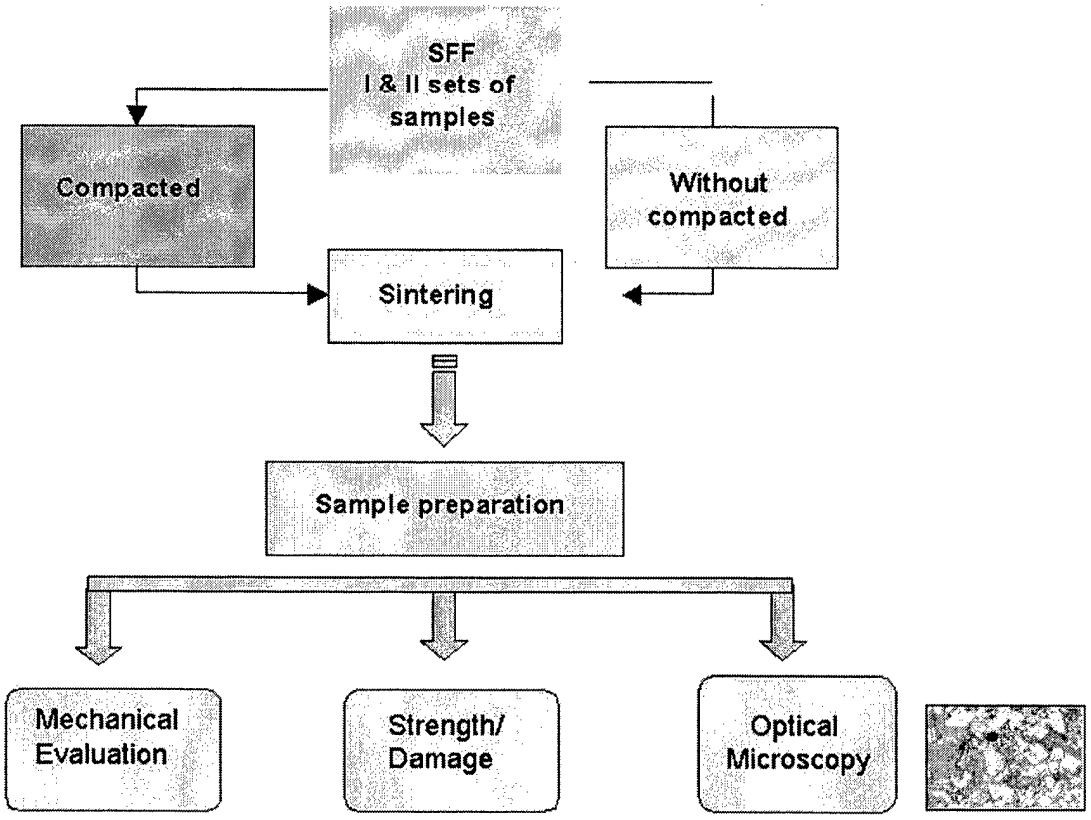


Figure 4: Mechanical characterization and microscopic evaluation of Ti_3SiC_2 test samples

The test specimens were cut from the master sample (Figure 3) using an EDM. Parallel machining was ensured to minimize any irregularities in dimensions of the test samples. For the evaluation of micro hardness and optical microstructure, samples cut from the master sample. were subjected to a grinding sequence of 300, 500 and 1200 grit Silicon Carbide paper and later polished to a mirror finish on 3 μm and 1 μm diamond suspension using a Struers Rotopol automatic polishing machine.The specimens for compression testing were cut from the master sample in the X and Z axes of the printing development, and for damage tolerance and thermal shock in the X and Y axes of the printing development. The sides of the specimen were ground on 800 and 1200 grit Silicon Carbide paper to remove burrs and flashes. This was done to minimize the possibility of error during the four point bend test. The specimens for the damage tolerance tests were marked with an indentation using a Vickers Indenter, on the tensile side of the specimen with indentation loads of 100, 200 and 300 N. It was ensured that the indentation

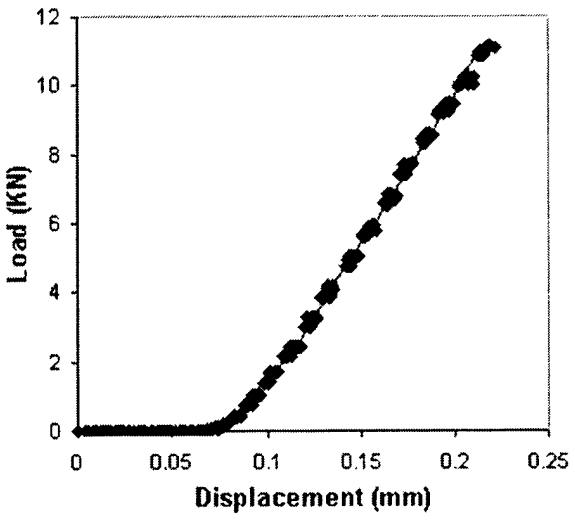
was in the region of maximum bending of the specimen. The samples for the thermal shock tests were heated upto pre-quench temperatures of 400 °C, 800 °C and 1200 °C.

5.1 Compression Strength

The compression tests were conducted on test specimens measuring 3mm x 3mm x 6mm cut along the X and Z axes of the printing using a servo-hydraulic testing machine (MTS System, Eden Priarie, MN) at a constant crosshead speed of 0.01 mm/s. Friction and mutual sliding between the Testing Machine platens and the specimen surfaces was minimized by the application of anti-friction grease. The breaking stress in compression was calculated as:

$$\sigma = \textbf{Load / Area}$$

The Load – Displacement curve is presented in Figure 5. It is observed that the deformation in compression of the test specimen is linear to failure and does not exhibit any plastic deformation behavior, with the failure being that of a brittle fracture. The results of the compression tests were calculated based on an average of five measurements. The average breaking strength in compression at a breaking load of 10.3 KN was found to be 1144.44 MPa in the XY plane of the printing, and at a breaking load of 11.03 KN was 1225 MPa in the Z plane, both at a strain rate of 0.0016/s. The observed difference in strength along the two independent planes or axes leads us to believe that the strength property is anisotropic due to the Layered Printing process. Although the micrographs (presented later) do not reveal any texture in the specimen, we believe that there is a process-induced anisotropy in the printed structure. The reported compressive strength of compacted and sintered (without SFF) coarse-grained Ti_3SiC_2 samples at room temperature is 720 MPa [20]. The test results conform to the reported compressive strength values for compacted (without SFF) and sintered coarse-grained Ti_3SiC_2 samples, with a proportional increase observed due to the presence of 30 – 40% of TiC.



Direction of Compressive Force : 3DP X Axis

Sample No.	Breaking Load	Breaking Strength
	KN	MPa
1	9.88	1097.78
2	11.28	1253.33
3	9.30	1033.33
4	10.68	1186.67
5	10.36	1151.11
Average	10.30	1144.44

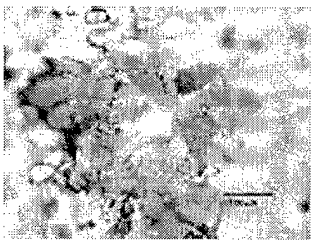
Direction of Compressive Force : 3DP Z Axis

Sample No.	Breaking Load	Breaking Strength
	KN	MPa
1	11.09	1232.22
2	10.89	1210.00
3	11.23	1247.78
4	10.89	1210.00
Average	11.03	1225.00

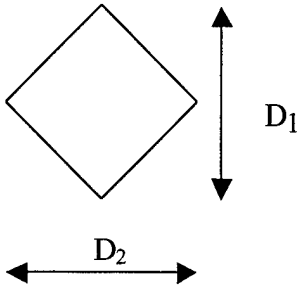
Figure 5: Load - Displacement curve and compressive strength

5.2 Vickers Micro Hardness

The micro-hardness test was conducted on polished sample surfaces using a Leco M-400 (St. Joseph, MI) diamond indenter at loads of 1, 3, 5 and 10 N. The diagonal values of the indentations were measured, an average of the diagonal lengths (Figure 6) was calculated and a conversion was obtained from the corresponding Vickers charts to derive the Vickers Micro Hardness.



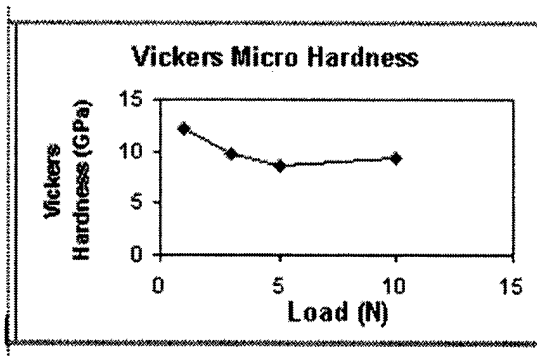
Micrograph



Schematic

Figure 6: Indentation obtained using Leco M400 Micro Hardness Tester

The micro hardness values have been presented as an average of five measurements. The hardness obtained for the samples was in the range of 12.3 – 9.4 GPa for an indentation load of 1 – 10 N (Figure 7). Further, the hardness seemed to have stabilized at 9 GPa, i.e, Vickers Hardness at increased loads will result in the stabilized value. The Vickers hardness of compacted and sintered (without SFF) Ti_3SiC_2 samples has been reported to be in the range of 8 - 4 GPa for samples obtained from fine grained Ti_3SiC_2 with load increasing from 1 N to 100 N, and for coarse-grained samples the reported range is 5 - 4 GPa for the same range of indentation load [20]. The hardness value asymptotically stabilizes at 4 GPa for loads greater than 100 N. This corresponds to the similar trend observed in the SFF samples. The results obtained conform to the established values for Ti_3SiC_2 . An increase in VHN, as we believed, is due to the presence of excessive 30 – 40% of TiC imparting greater hardness to the samples.



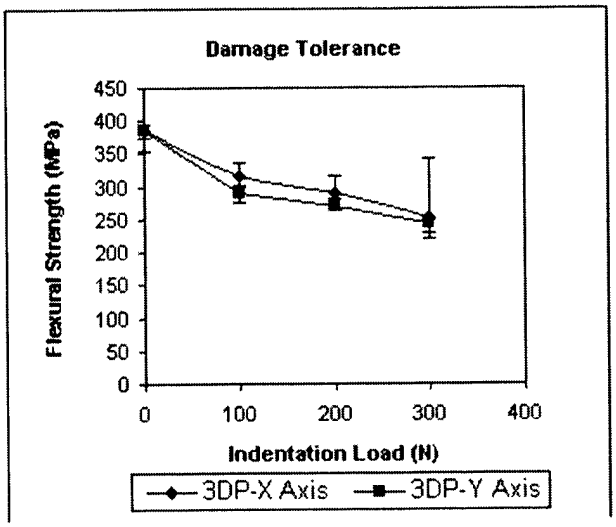
Load (N)	VHN
1	12.26
3	9.74
5	8.62
10	9.41

Figure 7: Vickers Micro Hardness for Ti_3SiC_2 samples

5.3 Damage Tolerance

For the damage tolerance tests the specimens were prepared as per ASTM C1161 type A (25mm x 1.5 mm x 2 mm) along the X and Y directions of SFF Layered Printing. Indentations on these specimens were performed using a Vickers indenter under loads of 100, 200 and 300 N, with one diagonal of the indenter parallel to the length of the specimen. The flexural strength after indentation was determined by a four point bend test as per the procedure in ASTM C 1161 and ASTM C 1211 using a four point flexural fixture. The cross head speed was set for 0.01 mm/s, this corresponds to an average strain rate of 0.0066/s. To remove any surface defects that could act as a crack initiation site under load, the tensile surfaces of the specimens were polished with 1200 grit Silicon Carbide prior to the indentation.

The results for damage tolerance are reported as an average of five measurements taken for each indentation load. The results reported here are for indentation loads of 100, 200 and 300 N. Damage tolerance was recorded as a measure of the breaking strength in a four-point bend test. The retained flexural strength as a result of indentation decreases from 387.33 MPa at no load to 251.67 MPa at 300 N for the sample length along the X-axis of the printing dierction, and decreases from 385 MPa to 242.92 MPa for the sample length along the Y-axis, as shown in Figure 8. The flexural strength of compacted and sintered (without SFF) Ti_3SiC_2 samples has been reported to be in the range of 300 MPa at no load to 240 MPa for a 300 N indentation load in the case of coarse-grained samples [20]. The flexural strength decreased steadily with the increase in the indentation load. This trend is reflected in SFF samples, and the results conform well to the reported data for coarse-grained Ti_3SiC_2.



Direction of 4 point bend test : 3DP - X Axis

Indentation Load (N)	MOR(MPa)
0	387.33
100	317.50
200	289.17
300	251.67

Direction of 4 point bend test : 3DP - Y Axis

Indentation Load (N)	MOR (MPa)
0	385.00
100	290.67
200	270.67
300	242.92

Figure 8: Damage Tolerance for Ti_3SiC_2 samples

5.4 Thermal Shock

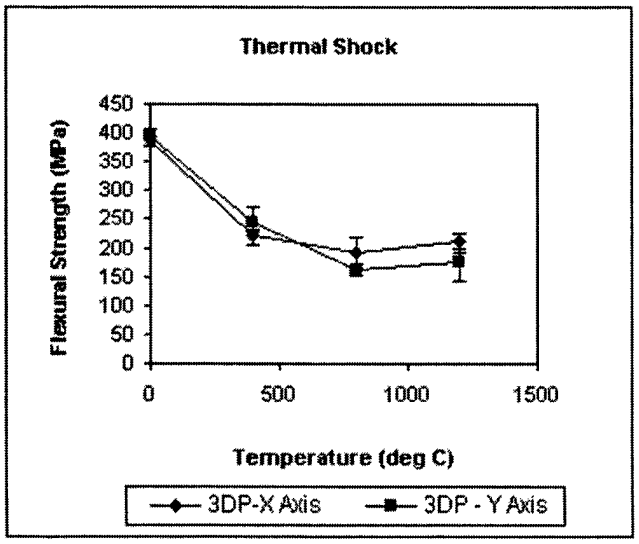
For the thermal shock resistance, specimens conforming to ASTM C1161 type A (25mm x 1.5 mm x 2 mm) along the X and Y directions of the printing were placed in a furnace at the pre-quench temperatures of 400, 800 and 1200 °C, under flowing argon (to prevent the formation of any oxide layers) for 10 minutes. The samples were then immediately quenched into an

ambient temperature water bath. The quenched samples were tested according to the ASTM C1161 and ASTM C 1211 using a four point flexural fixture. All four point bend tests were conducted using a servo-hydraulic MTS Systems testing machine running at a cross head speed of 0.01 mm/s, corresponding to a nominal strain rate of 0.0066 /s. In both cases, thermal shock resistance and damage tolerance, the flexural strength was calculated using the following formula:

$$\sigma = 3\,P\,(l_1 - l_2) \;/\; (2\,B\,W^2)$$

where P is the load at fracture, l_1 and l_2 are the outer and the inner span, respectively, B is the specimen width (2 mm), and W is the specimen thickness (1.5 mm). The four-point bend fixture used had an outer span of 20 mm and inner span of 10 mm. The fixture rollers were free to rotate, but constricted laterally in this setup. The mutual friction between the sample and the rollers was eliminated by the application of a very thin film of anti-friction oil on the roller interface.

The results for thermal shock are reported as an average of five measurements taken for each temperature condition. Thermal shock has been reported as a measure of the flexural strength of the sample under the four-point bend test. The tests were conducted at room temperature, 400 °C, 800 °C and 1200 °C. The retained flexural strengths for the sample length along the X-axis of the printing are in the range of 387.33 – 211.67 MPa and 395 – 174.58 MPa for the sample length along the Y-axis of the printing. The test samples thermally shock up to 400 °C and the Module of Rapture further stabilizes and is retained up to 1200 °C. Beyond 800 °C, an increase in post quench strength is observed in both sample sets, as shown in Figure 9. The flexural strength of compacted and sintered (without SFF) Ti_3SiC_2 samples subjected to thermal shock are about 260 MPa for a temperature of 1400 °C for coarse grained samples and ranging from 560 – 170 MPa over a temperature range of 500 °C to 1100 °C for fine grained samples [20]. It is observed that coarse grained samples retain flexural strength up to a temperature of 1400 °C and are thus thermal shock resistant, whereas fine grained samples thermally shock between 750 °C and 1000 °C [20].



Direction of 4 point bend test: 3DP - X Axis

Temperature deg C	MOR MPa
0	387.33
400	222.08
800	190.67
1200	211.67

Direction of 4 point bend test: 3DP - Y Axis

Temperature deg C	MOR MPa
0	395.00
400	246.25
800	161.25
1200	174.58

Figure 9: Thermal Shock Resistance for Ti_3SiC_2 samples

The test results reflect the reported results of thermal shock resistance and the increasing trend of post quench strength at temperatures of 800 °C for coarse-grained Ti_3SiC_2. Additionally, it is also observed that the flexural strength along the X-axis of the printing is greater than that along the Y-axis. This is mainly due to the layered nature of the Layered Printing technique. The published results of the Module of Rapture for damage tolerance and thermal shock for Ti_3SiC_2 samples are as per tests conducted without regard for the axis of development. The presented values as per this research demonstrate the anisotropy in strength arrived at as a result of the Layered Printing process.

5.5 Porosity and Shrinkage

The physical shrinkage of each of the samples was measured and calculated as a function of the linear dimensions D, of the individual parts. The shrinkage was calculated as a percentage after each process, namely, Layered Printing, Compacting, and Sintering.

$$\textbf{Shrinkage} = (D_{\text{pre-process}} - D_{\text{post-process}}) / D_{\text{pre-process}}$$

The percentage porosity is an average of 5 independent representative regions of the sample surface under test. The sample that was derived form the master sample (subjected to the post RP processes of compacting and sintering) had a density of greater than 99%. For the samples developed by varying the binder concentration and layer thickness during the Layered Printing process and directly sintering without compacting, the porosity obtained from the surface calculations of the micrographs show an average porosity of 50 – 60%. This shows that compacting is the dominant process in improving the density of the part. This is quite noticeable comparing the micrographs between Figures 10 and Figure 12. The optical microscope was used to measure the cross-sectional porosities of each sample. The supporting software provides image capture, threshold and density slice tools by which percentage of black and white phases are measured directly. The average porosity for each sample is calculated as a mean value for the data retrieved by the random choice of at least 5 representative points on each sample surface.

The shrinkages after each stage of the integrated process were calculated as a percentage for the sprocket, turbine wheel and tube as listed in Table 1. The average shrinkage measured after the compacting was in the range of 15% and after sintering was about 30%.

Table 1: Shrinkage data for parts developed using the integrated 3-stage process

Sprocket / Turbine:

Geometric Features	Pre-Compact	Post-Compact	Compact	Post Sintering	Compact & Sintering
	inches	inches	% change	inches	% change
Length	1.52	1.33	12.50	1.06	30.07
Width	1.52	1.33	12.50	1.06	30.07
Height	0.50	0.42	16.00	0.36	27.30

Tube:

Geometric Features	Pre-Compact	Post-Compact	Compact	Post Sintering	Compact & Sintering
	inches	inches	% change	inches	% change
Length	1.00	0.81	19.00	0.69	30.70
OD	0.62	0.49	20.97	0.42	31.61
ID	0.30	0.30	0.00	0.22	28.33

5.6 Optical Microscopy

Micrographs of the various samples representing dense and porous structures were acquired using the Olympus PM-3G Optical Microscope. From the micrographs shown in Figures 10, we observe that the part density is in excess of 99% in the planes XY, XZ and YZ through the 3-satge process. The sample structures exhibiting greater than 99% density show a homogeneous distribution of grains without any texture within the powder matrix as shown in Figures 11. The main cause of high density and structural homogeneity is due to the compacting process. In the case of the samples exhibiting porous structure it is observed that the average porosity measured is about 50 - 60% as shown in Figure 12. From the micrographs we observe that the sintering without compacting leads to binder burnout and results in the part being porous. This explains the voids (dark regions) on the micrographs as shown in Figures 12. Further, the increased binder concentration increases the possibility of sintering of a lower quality.

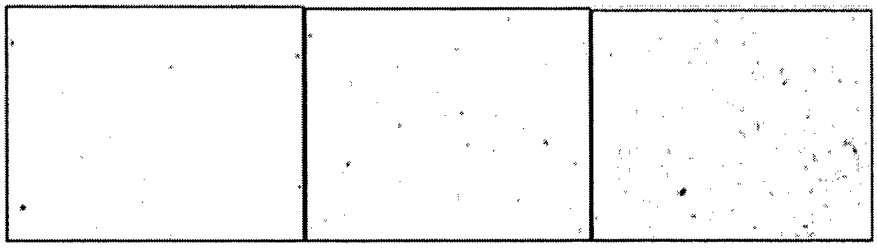


Figure 10: Micrographs of XY, XZ and YZ planes of the master sample
With density greater than 99% (200 μm)

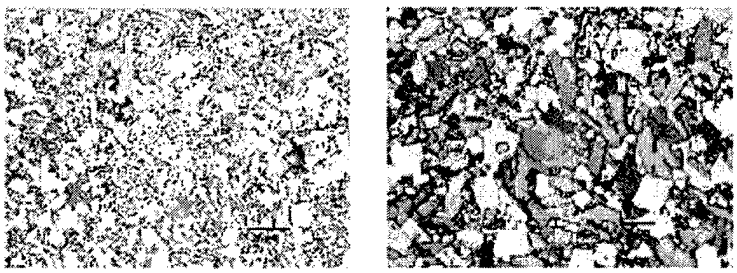


Figure 11: Micrographs of the cross-section of the master sample with density greater than 99% at X 500 and X 1000 magnification

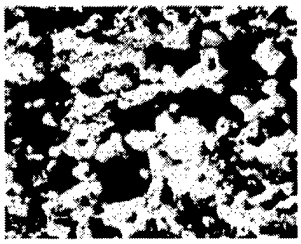


Figure 12: Micrograph of sample with porosity at 60% (porous structure) (200 μm)

6. Summary and Conclusions

This paper introduces an integrated process of Layered Printing, Compacting, and Sintering to fabricate highly dense Ti_3SiC_2 structures. Experiments were conducted to study the mechanical characteristics and the effect of the processing parameters on the morphological and structural properties of the fabricated Ti_3SiC_2 structures. The results of the mechanical characterization and the microstructure evaluation of Ti_3SiC_2 structures have been presented. The resulting sintered parts were achieved with a density of greater than 99%. As a post processing surface finishing the parts can be subjected to a grinding and polishing sequence to obtain a mirror finish. As a demonstration of the machinability of the SFF parts, EDM was used to cut the test samples and polished them to obtain required 1μm surface finish. This integrated process was used to freeform fabricate structures with complex shapes, as shown in Figures 2. A density of greater than 99% was achieved for each of these parts.

The Load – Displacement curves show a linear to failure deformation behavior of the Ti_3SiC_2 specimens. The results of the mechanical characterization for the Ti_3SiC_2 samples also reveal an anisotropy in the mechanical properties, for example, the compressive strength, damage tolerance and thermal shock properties are greater along a certain axis of the printing development. Although the SEM micrographs show a homogeneous grain distribution of Ti_3SiC_2 powder without any texture within the part matrix, we believe that the layered printing process contributes to the anisotropy in the prototyped structure. The results from the tests for compressive strength, hardness, damage tolerance and thermal shock are comparable to the reported data for Ti_3SiC_2, considering the effect of the presence of excessive 30 – 40% TiC in the Ti_3SiC_2 powder used in the fabrication of samples under test.

The samples fabricated using the 3-stage process achieved a density of greater than 99%, while samples without the compacting had a porosity in the range of 50 – 60%. This shows that compacting is the dominant process leading to the high structural density. The average shrinkage measured after compacting was in the range of 15% and after sintering was 30%. The main cause of high density and structural homogeneity is due to the compacting process. A certain amount of warpage was observed after the printing. We believe that this is mainly due to the capillary forces distributed in the powder matrix during the printing process. The maximum warpage occurred along the Y-axis (longest dimension) of the printing and was further enhanced after the compacting process.

In comparison to other Solid Freeform Fabrication methods for prototyping dense and functional structure, the developed 3-stage process is simplicity and cost-effective. However, the process of a larger scale and complicated geometry needs to be developed further to possibly eliminate the compacting process, thus to avoid the part collapse and to retain the designed geometry. The process-induced anisotropy and its relation with the processing parameter and part geometry need also to be further investigated.

References

1. J. G. Heinrich: "New developments in the solid freeform fabrication of ceramic components", *Ceramic Forum International*, Vol. 76, No. 5, 1999, pp. 29-35.

2. B.K. Paul, S. Baskaran : "Issues in fabricating tooling using powder-based additive freeform fabrication", Journal of Materials Processing Technology 61(1996) pp. 168-172.
3. D. Bourell, H. Marcus, J. Barlow, and J. Beaman, "Selective Laser Sintering of Metals and Ceramics", The International Journal of Powder Metallurgy, Vol. 28, No. 4, 1992, pp. 369-381.
4. E. Sachs, M. Cima, P. Williams, D. Brancazio, and J. Cornie, "Three Dimensional Printing: Rapid Tooling and Prototypes Directly from a CAD Model", Journal of Engineering for Industry, Vol. 114, November 1992, 481-488.
5. J. Moon, J. Grau, P.J. Baker, M. Caradonna, M.J. Cima: "Binder-powder bed interactions in the slurry-based 3-dimensional printing process", *Proceedings of Solid Freeform Fabrication Symposium*, University of Texas, Austin, Texas, 1997.
6. J. Grau, J. Moon, M.J. Cima: "Structural ceramics fabricated by 3-dimensional printing", *Proceedings of Solid Freeform Fabrication Symposium*, University of Texas, Austin Texas, 1997.
7. S. Rock and C. Gilman, "A New SFF Process for Functional Part Rapid Prototyping and Manufacturing: Freeform Powder Molding," *Proceedings of Solid Freeform Fabrication Symposium*, University of Texas, Austin, Texas, 1995.
8. M. Agarwala, et al, "Structural Ceramics by Fused Deposition of Ceramics", *Proceedings of Solid Freeform Fabrication Symposium*, University of Texas, Austin, TX, 1995.
9. S. Uhland, R. Holman, B. DeBear, P. Saxton, M. Cima, E. Sachs, Y. Enokido and H. Tsuchiya: "Three-dimensional printing, 3DP™, of electronic ceramic components", *Proceedings of Solid Freeform Fabrication Symposium*, University of Texas, Austin, TX, 1999, pp. 865-872.
10. M. Greul, T. Pintat, M. Greulich : "Rapid Prototyping of Functional Parts", Advances in Powder Metallurgy and Particulate Materials. 3, 1997. Metal Powder Industries Federation, Princeton, NJ, USA. p 18-153-159.
11. P.B. Blazdell, J.R.G. Evans: "Application of continuous ink jet printer to solid freeforming of ceramics", *Journal of Materials Processing Technology*, Vol. 99, 2000, pp. 94-102.
12. M. Mott, J.-H. Song and J. Evans: "Microengineering of ceramics by direct ink-jet printing", *Journal of American Ceramics Society*, Vol. 82, No. 7, 1999, pp. 1653-58.
13. J.Cesarano, "Robocasting: Direct fabrication of ceramics from colloidal suspensions", *Proceedings of Solid Freeform Fabrication Symposium*, University of Texas, Austin, TX, 1997.
14. J. Windle, B. Derby: "Ink jet printing of PZT aqueous ceramic suspensions", *Journal of Materials Science Letters*, Vol. 18, 1999, pp. 87-90.
15. A.V. Kumar and H. Zhang: "Electro photographic powder deposition for freeform fabrication", *Proceedings of the 11th Solid Freeform Fabrication Symposium*, University of Texas, Austin, 1999, pp. 647-653.
16. M.J. Wright, R.G. Evans: "Ceramic deposition using an electromagnetic jet printer station", *Journal of Materials Science Letters*, Vol. 18, 1999, pp. 99-101.
17. D. J. DCosta. S. D. Dimovski, F. Lin, T. El-Raghy, M. W. Barsoum and W. Sun: "Three Dimensional Printing of Layered, Machinable, Ductile Carbide", *Proceedings of the 11th Solid Freeform Fabrication Symposium*, University of Texas, Austin, August 2000.
18. T. El-Raghy and M. W. Barsoum: "Synthesis and Characterization of a Remarkable Ceramic: Ti_3SiC_2", *Journal of American Ceramics Society*, Vol. 79, No. 7, 1999, pp. 1653-58.
19. T. El-Raghy and M W. Barsoum: "Processing and mechanical properties of Ti_3SiC_2, Part I: Reaction Path and Microstructure Evolution", *Journal of American Ceramics Society*, Vol. 82, 1996., pp. 1953-56.
20. T. El-Raghy, M. W. Barsoum, A. Zavaliangos and S. R. Kalidindi: "Processing and mechanical properties of Ti_3SiC_2, Part II: Mechanical properties", *Journal of American Ceramics Society*, Vol. 82, 1999., pp. 2855-60.
21. W. Sun, D. J. Dcosta, and T. El-Raghy, "Fabrication of Three-dimensional Fully Dense Ti_3SiC_2 Structures," US Patent, (pending).

this page intentionally blank

Slurry-Based 3DP and Fine Ceramic Components

M.J. Cima, M. Oliveira, H.R. Wang, E. Sachs, and R. Holman

Department of Materials Science and Engineering, Massachusetts Institute of Technology, Cambridge, MA, 02139.

Abstract

Slurry-based 3DP™ (S-3DP™) is a solid freeform fabrication technique developed at MIT for production of fine ceramic components with complex geometries and fired densities in excess of 99% of theoretical density. Current research involves identification of the factors controlling minimum feature size in S-3DP™. The ink-jet printed binder droplet size is the primary factor controlling the minimum feature dimension when deposited on the powder layers. For a given droplet size, however, a balance between spreading of the binder solution on the surface of the S-3DP™ powderbed and infiltration determine the feature size, while interactions between the polymeric binder and the powder surface (polymer adsorption) control the minimum feature cross-section. Droplet-on-demand printing of the binder solution has been introduced to improve resolution, decreasing the minimum feature width from 300 μm to less than 150 μm.

Introduction

Three Dimensional Printing (3DP™) is a Solid Freeform Fabrication (SFF) technique developed at MIT. As with other SFF techniques it is a process based on using sequential 2D slices of an image to build up a 3D component. Presently there are two main approaches to 3DP™, traditional 3DP™ and S-3DP™. The difference between the two lies in the method used to form the sequential layers in which the 2D slices are deposited. Previous research has focused on dry powder spreading methods such as shown in Figure 1 where a vibrating roller spreads dry powder from a reservoir over a piston to form a layer. A 2D image of the component cross section is generated from a CAD file, and this image is deposited into the powder layer using inkjet printing. The powder particles are bound together in only the areas where printing occurs. The process is repeated until a complete 3D part is formed within the bed. Powder in the areas where binder is not deposited is excess and provides support to the part being generated.

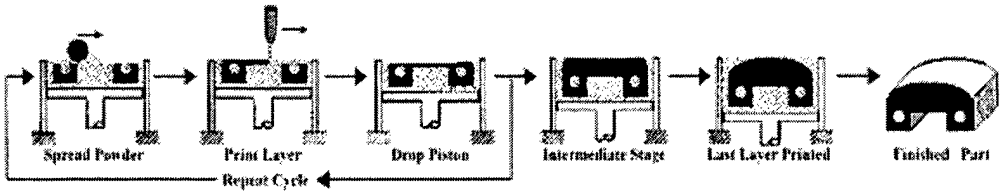


Figure 1: Schematic of the traditional (dry-powder) 3DP™ process.

3DP™ and S-3DP™ use the same methods for depositing binder. Each layer is, however, formed in S-3DP™ by slip casting a slurry of ceramic powder onto a porous substrate which is mounted on a piston. S-3DP™ has been described in detail by Grau[1] and is shown schematically in Figure 2. Individual green layers are formed by rastering a jet of ceramic slurry (typically ~30 vol.% ceramic in a water, water-alcohol, or alcohol vehicle) over a porous substrate. The individual jetted beads slip cast and stitch to one another and to the previous layer. The slurry

solids loading, the volumetric flow rate of slurry, the spacing between raster lines, and the cast (green) density of the layer determine the green layer thickness. A drying step removes the excess solvent/dispersing medium. Binder is then printed in a manner that is identical to that used in traditional (dry powder) 3DP™. Continuous ink-jet printing is practiced by pressurized flow of an electrically grounded solution through a ruby orifice. The resulting stream breaks up into droplets at the Rayleigh frequency by a piezo and is raster scanned across the surface of the powderbed. The stream off droplets can be turned "on" or "off" to define the part edges by charging the droplets and deflecting them into a catcher, as shown in Figure 3. The surrounding green powderbed acts as a support structure for thin sections and overhangs, as in traditional 3DP™. The binder system currently used is a solution of polyacrylic acid, PAA (MW 60000), from 2 to 5 vol.%, either aqueous or in ethanol. Glycerol is added to the solution to cross link the binder during subsequent curing. The printed green components are contained in the slip cast block of green ceramic (the powderbed) upon completion of the building process. The powderbed is heated to 150°C for an hour in Argon to cure the binder and make it insoluble. The entire block is then submersed in water (or in some cases ethanol), and the un-printed region redisperses, swells, and sloughs off, leaving the printed component. Polyethylene glycol (PEG, MW 400) is added to the ceramic slurry to aid in this redispersion process. Minor sonication removes any residual powder contained in internal structures.

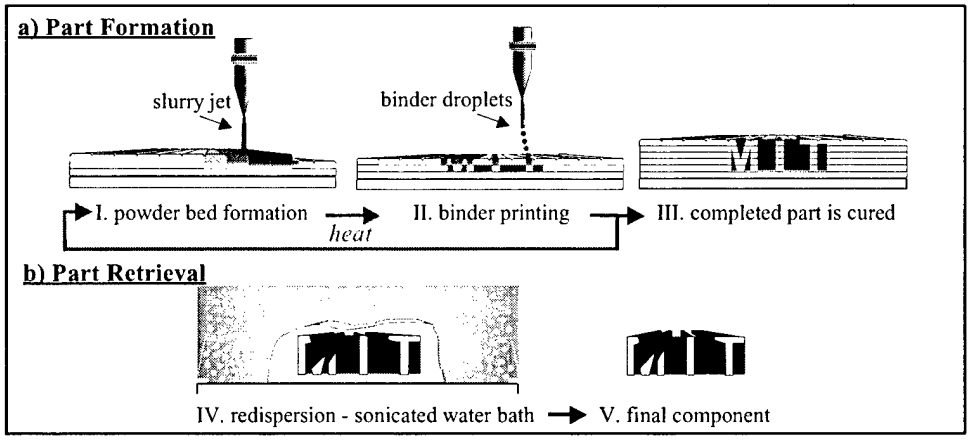


Figure 2: Schematic of the Slurry-Based 3DP™ (S-3DP™) Process.

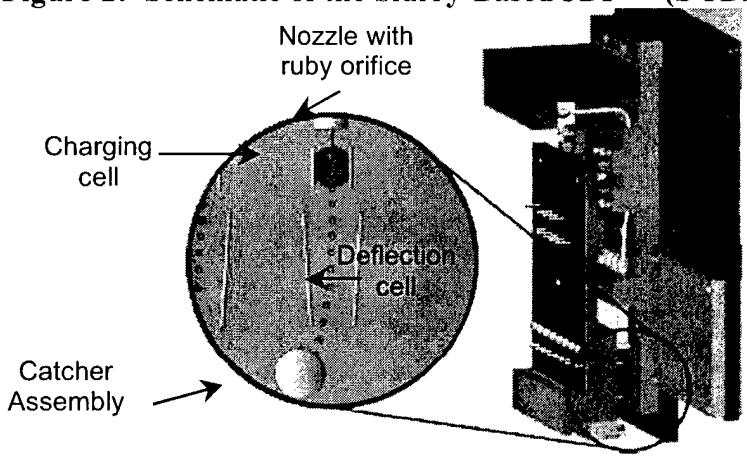


Figure 3: Schematic of continuos jet print-head turned "Off"

Line merging is a new layer forming method that avoids inter-line defects and reduces the line ridges (roughness at the top surface of the bed) seen in rastered powderbeds, while offering the potential for higher production rates. These failings of the conventional jet rastering layer forming method required that a more continuous slurry spreading process be developed to minimize or eliminate the line ridge defects. In the new line merging approach, the nozzle path of conventional jet rastering is maintained, but the inter-arrival time is reduced dramatically through machine design, and the slurry chemistry is adjusted to slow the rate of slip casting. Thus, the jet rastering approach is made to approximate a continuous deposition process, as follows: If the inter-arrival time is reduced enough, line N+1 is deposited before line N is fully slip cast, and the curvatures of the wet lines merge seamlessly together into a uniform "wet front" which advances steadily across the powderbed, as seen in Figure 4. Polito[2] implemented this approach and showed that the resulting powderbed had significantly reduced line ridge and inter-line defects.

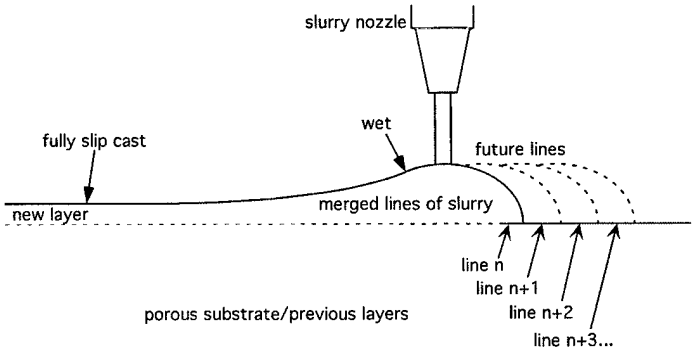


Figure 4: Schematic diagram of line merging concept

Printing style can effect printed part definition. The conventional print style is to raster the binder nozzle across the powderbed surface. Alternatively, a vector approach can be used where the outline of the part is first traced with the binder stream then the interior of the part is printed with the raster-type method. Vector printing the parts in this manner requires a much lower droplet frequency and more control on the placement of each individual drop than CJ printing could offer. Drop on Demand (DoD) printing provides this by generating each drop with a specific electronic waveform applied to a piezo. The waveform expands then contracts the hollow cylindrical piezo around a steel tube carrying the binder, creating one droplet. DoD printing generates droplets in the range of 1kHz while CJ printing operates at 25-60kHz. Figures 5(a) and 5(b) show the difference in droplet placement between raster-style printing and vector-style printing.

a) b)

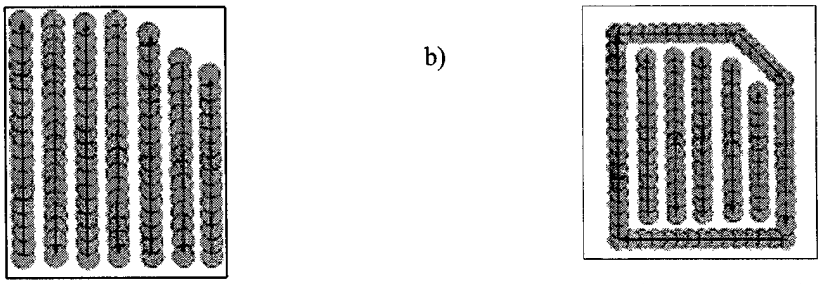


Figure 5: Comparison of drop placement in a) raster style and b) vector style printing[3]

Surface Roughness

The roughness of the top surface of printed parts originates from the layer forming method. Each deposited line of slurry slip casts before the next is deposited and naturally form a rounded shape with conventional slurry jet rastering. This process results in "ridges" along the width of the completed layer which transfer to the printed part. Slurry line merging, described above, attempts to overcome this problem. Figure 6 compares images of two powderbeds as well as laser profilometry measurements made of the beds[2].

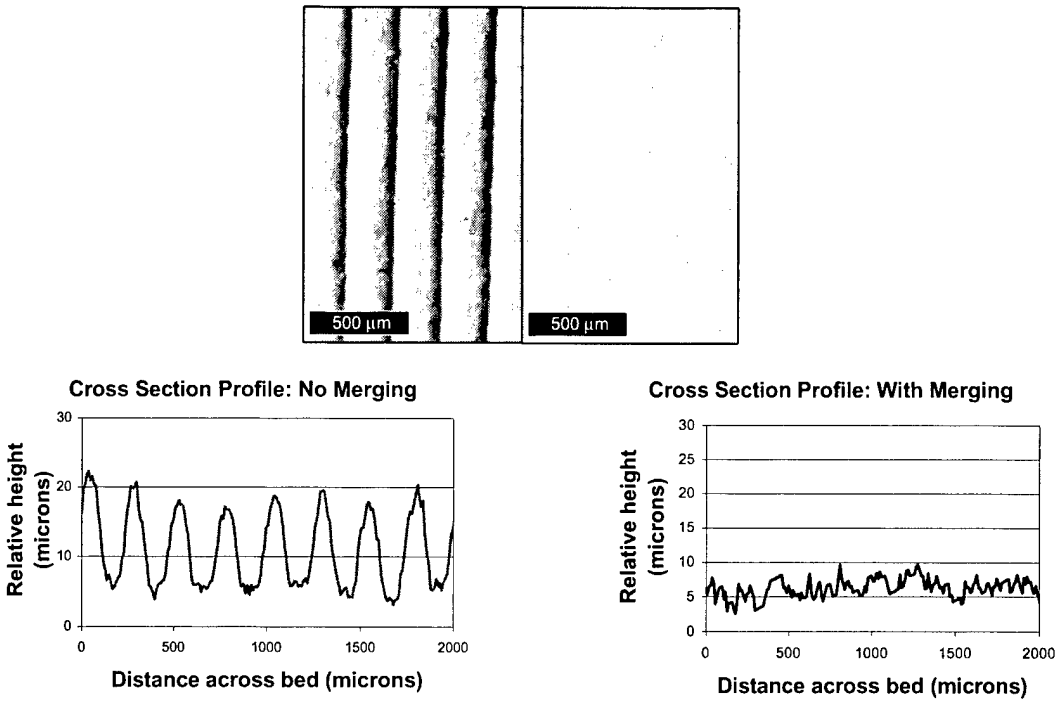


Figure 6: Top: Image of conventional (left) and merged (right) alumina powderbed. Bottom: Profilometry measurement of conventional (left) and merged (right) bed.

The roughness on the vertical sidewalls of a printed is controlled by binder droplet registration and by the shape of the binder primitive. Droplet registration depends on the capabilities of the machine used as well as the stability of the binder stream. The binder primitive is the shape that a single printed line (or droplet) of binder creates in a powderbed and is shown in Figure 7. The aspect ratio of the primitive, the ratio of the width to depth, is controlled by binder adsorption to the particles as well as the liquid infiltration behavior of the binder. A lower aspect ratio primitive allows for lower sidewall surface roughness. The height of each layer and the amount of binder printed must be set to values where the layer height is in the approximate proportion shown in Figure 7[3].

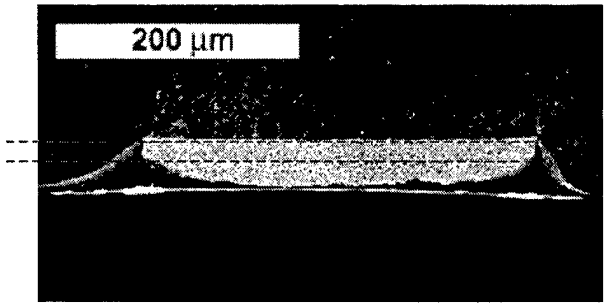
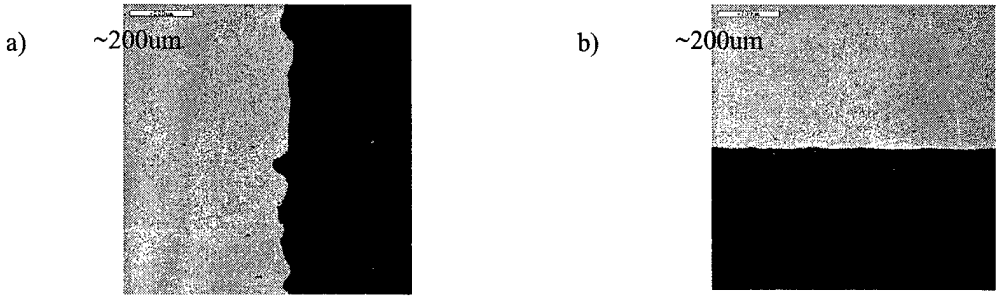


Figure 7: Cross section of binder primitive formed with CJ printing in an alumina powderbed. Hatched lines show proportion of layer height to binder primitive to reduce sidewall roughness.

The roughness of the bottom surface of printed parts can be represented by the image shown in Figure 8(b). Bottom surfaces exhibit low roughness. This can be attributed to the large amount of overlapping of binder primitives that occurs within layers of printed parts[4].



Figures 8: Images showing a) sidewall and b) bottom surface roughness. Images are of S-3DP™ MR2 components.

Layer Height

The controlling parameters for the height of a jetted layer of slurry are the slurry flow rate, nozzle diameter, raster line spacing, nozzle raster speed, and the packing fraction of the slip cast. Presently, the smallest layer height achieved with S-3DP™ is 13µm, using an alumina slurry[5]. The maximum layer height is set by the Critical Saturation Thickness (CST) and is discussed in detail by Grau[1]. The CST defines the maximum thickness that powderbed can be 100% saturated with liquid before cracking of that layer occurs due to drying stresses. The surface tension and pore size both affect the value of the CST, with larger pores and lower surface tension increasing the CST.

Line Width by CJ and DOD Printing

Large area AC plasma display panels (PDP) usually employ a barrier rib structure to separate the sub-pixels of red, blue and green colors. To achieve high image quality, the barrier ribs must have high dimensional accuracy. S-3DP™ offers the potential of producing large size components while retaining high dimensional accuracy. Uniform ribs have been produced by CJ printing using a binder nozzle size of 30 µm[5] and alumina as the material system to demonstrate the capability of S-3DP™. The rib width of 300 µm shown in Figure 9 was obtained after sintering, while the green rib width was about 330 µm. This is still larger than the required

width for PDPs but the rib width can be reduced further by increasing the printhead velocity and by decreasing the size of binder printing nozzle and binder flowing rate. Another method to reduce the printing line width is S-3DP^{TM}-DoD printing. The minimum line width presently achieved with DoD printing in alumina with an average droplet size of 40 μm is 150 μm[6], as shown in Figure 10.

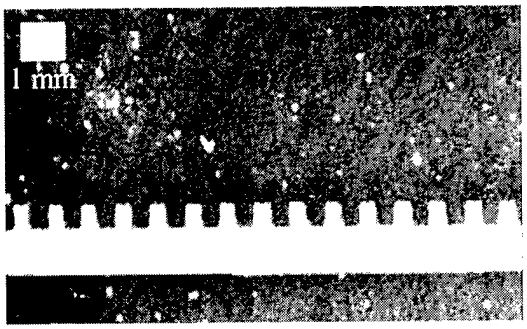


Figure 9: Optical microscope cross section image of the S-3DP^{TM} ribs

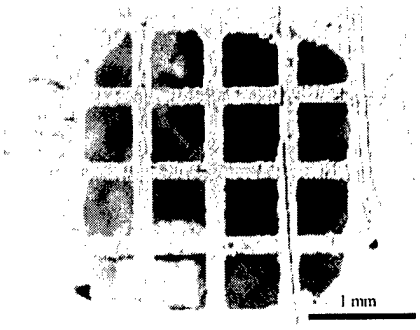


Figure 10: The minimum line width produced by vector DOD printing

Edge smoothness has also been improved with the DoD printing. The cross section of the printed RF filter is shown in Figure 11[7]. The edges in Figure 11 are smooth and show high accuracy of definition. The mm-wave package in Figure 12[7] also shows sharp and accurate edge definitions.

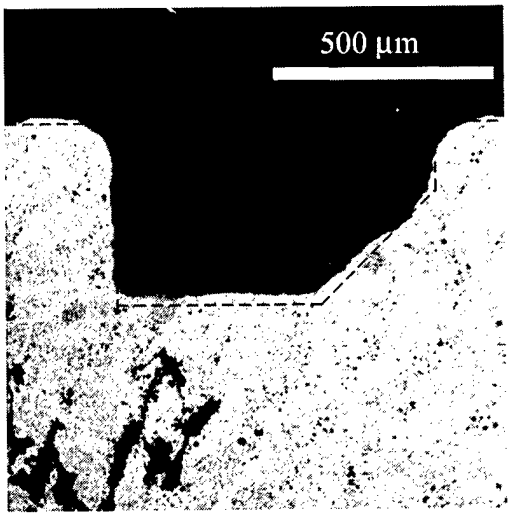


Figure 11: SEM cross section image of the S-3DP^{TM} RF filter

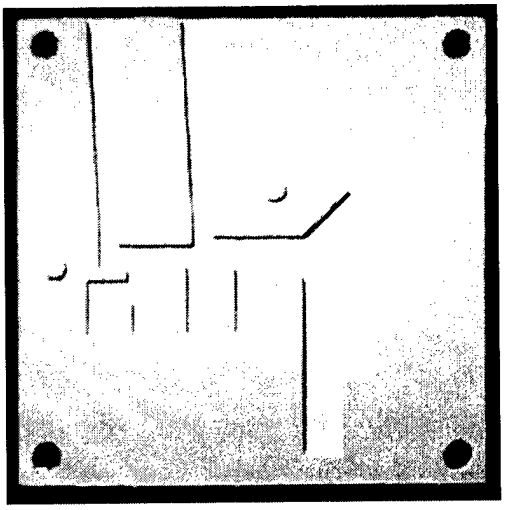


Figure 12: Green S-3DP^{TM} mm wave package

Structures, such as EBG (electromagnetic band gap) devices and RF filters, with through and blind holes have been produced by the DoD printing. Figures 13(a) and 13(b) show the front and rear views of the S-3DP^{TM} RF filter while Figures 14(a) and 14(b) show those of the S-3DP^{TM} EBG device[7].

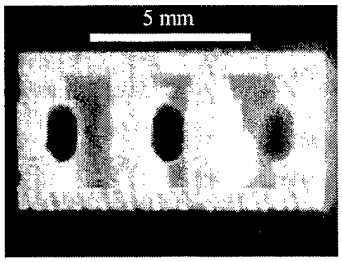


Figure 13(a): The front view of the S-3DP™ RF filter

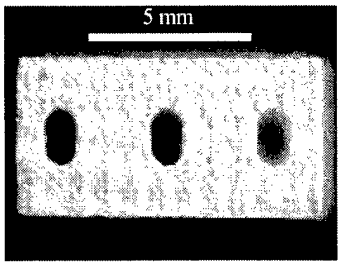


Figure 13(b): The rear view of the S-3DP™ RF filter

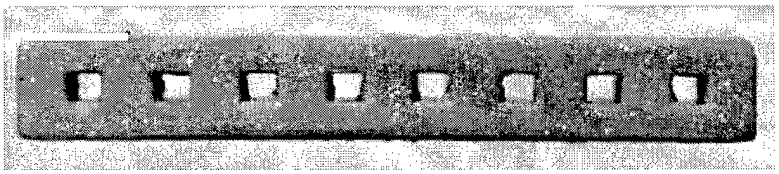


Figure 14(a): The front view of the S-3DP™ EBG device

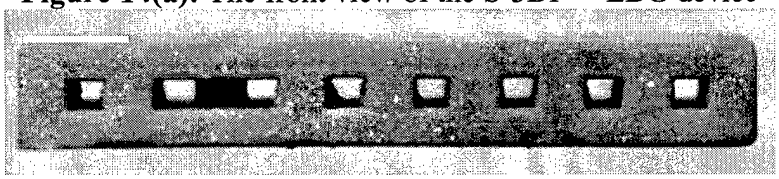


Figure 14(b): The rear view of the S-3DP™ EBG device

Complex structures with higher accuracy for various applications can now be produced using S-3DP, as shown in Figures 15, 16, 17, 18, 19, and 20[3,4,7]. The green packing density of the parts is higher than 58% and therefore the final density with more than 99.9% of the theoretical density after sintering is easily obtained.

Conclusion

Slurry based Three Dimensional Printing has been shown to fabricate high-density ceramic components of complex geometry. S-3DP™ component production has been achieved with alumina, titania, silica, silicon nitride, MR2, and Tungsten Carbide-Cobalt with no foreseeable material limitations. The results presented for the process capabilities can still be optimized for further accuracy or resolution and systems for mass production are under development.

References

1. Grau, J., Fabrication of Engineered Ceramic Components by the Slurry-Based Three Dimensional Printing Process, Ph.D. Dissertation, Department of Materials Science and Engineering, MIT, 1998.
2. Polito, Ben., unpublished work.
3. Holman, R., Effects of the Polymeric Binder System in Slurry-Based Three Dimensional Printing of Ceramics, Ph. D. Dissertation, Department of Materials Science and Engineering, MIT, 2001.
4. Uhland, S., Fabrication of Advanced Ceramic Components Using Slurry-Based Three Dimensional Printing, Ph.D. Dissertation, Department of Materials Science and Engineering, MIT, 2000.

5. Li, Yawen, personal communication.
6. Guo, David, unpublished work.
7. Enokido, Y., Tsuchiya, H., Nakahata, I., Himeno, M., unpublished work.

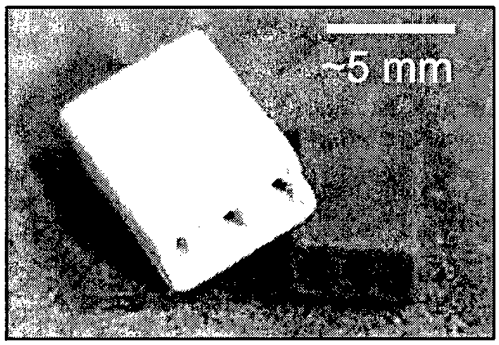


Figure 15: Green and dense $BaTiO_3$-based RF filters

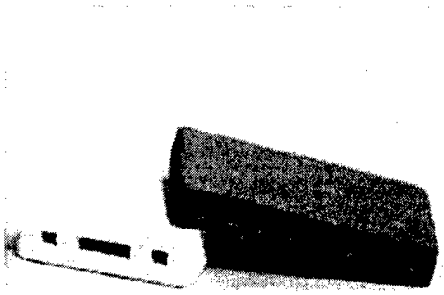


Figure 16: Green and dense $BaTiO_3$-based EBG devices

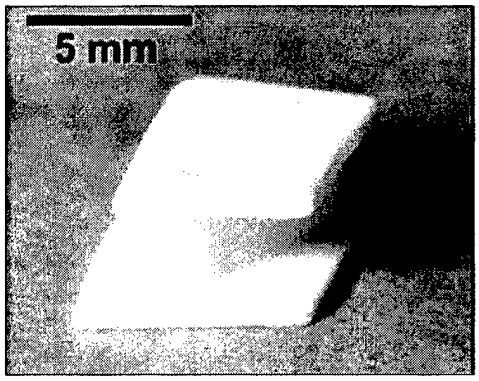


Figure 17: Dense Al_2O_3 stator

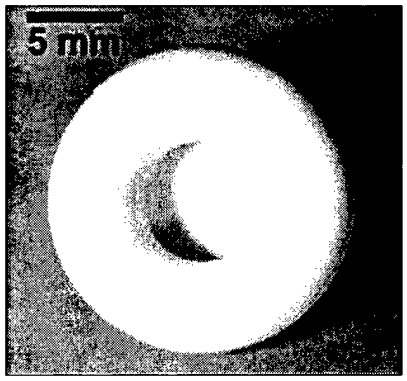


Figure 18: Dense Al_2O_3 toroid

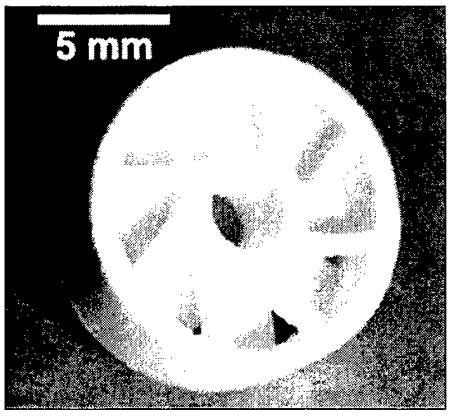


Figure 19: Dense Al_2O_3 rotor

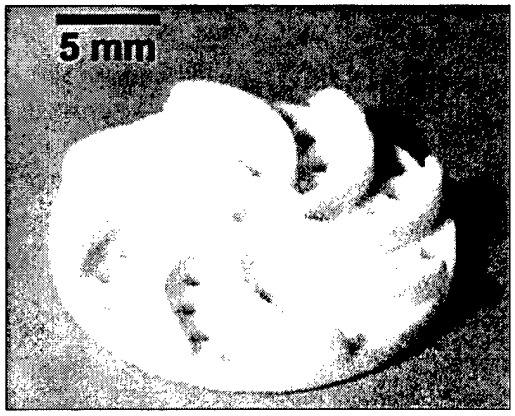


Figure 20: Dense Al_2O_3 sample geometry

Fused Deposition of Ceramics (FDC) and Composites

Seyi Onagoruwa, Susmita Bose and Amit Bandyopadhyay
School of Mechanical and Materials Engineering
Washington State University
Pullman, WA 99164-2920
E-mail: amitband@wsu.edu

Abstract

Fabrication of functional ceramics and composites has been attempted using fused deposition of ceramics process. In this work, first a polypropylene (PP) binder system has been developed for the FDM. The PP binder system was mixed with ceramic powders and then extruded in the form of filament for the FDC. Controlled porosity ceramic parts were directly fabricated using a FDM 1650 machine with mullite, fused silica and titania powder loaded green filaments. The parts were then binder removed and sintered. Some of the porous parts were then infiltrated in Al metal to form the metal-ceramic composites. This article discusses feedstock development, part fabrication and methods to improve the quality of parts during processing.

Introduction

Rapid prototyping (RP) or solid freeform fabrication (SFF) is a technique in manufacturing in which a solid physical model of a part is made directly from a three-dimensional computer-aided design (CAD) file. There are several RP techniques are available. Some of the most common RP techniques include stereolithography (SLA), selective laser sintering (SLS), fused deposition modeling (FDM), 3-D printing and sanders prototyping. Fused deposition modeling (FDM) is the RP technique used in this study.

FDM, a solid-based RP technique, is commercialized by Stratasys Inc. (Eden Prairie, MN). FDM is an extrusion-based layered manufacturing process in which semi-solid thermoplastic polymers gets deposited on a platform through a nozzle fitted into a heated liquifier controlled in X and Y directions. The cold filament at the top of the liquefier acts as a piston, creating a positive pressure to extrude fine roads of molten material through the nozzle. The motion of the FDM head (X-Y direction) and platform (Z direction) is controlled by the computer, based on the CAD design of the prototype been built. After the head has completed the first layer, the platform indexes down set by the slice thickness and the second layer gets deposited on top of the first layer. This process continues until all layers are complete, leaving a solid model of the desired part. There are several variables that controls part quality in FDM. Among the materials related variables critical to FDM include surface chemistry, melt viscosity, stiffness, heat capacity and adhesiveness. Commercially available materials for FDM include wax, ABS and nylon.

Fused deposition of ceramics (FDC) is a modified FDM process where ceramic powder loaded thermoplastic filaments are extruded through the FDM [1-4]. During fused deposition of ceramics, thermoplastic polymers melt carry the ceramic powders along with it. The green ceramic parts are similar to injection-molded parts having 40-45 volume % binder in it. The

parts are then subjected to a binder removal and sintering cycle for densification. The process development for FDC work requires optimization of thermoplastic binder composition, filament fabrication, FDC and binder burn out and sintering cycle development.

Basic requirements for the development of the FDC feedstock filaments include low viscosity, high strength, high strain and high modulus. The high strength enables the filament to act as a piston during the FDC to prevent buckling. Low viscosity would prevent back flow of molten material. Binder system development is a major key to a successful FDC process. The binder system could be viewed as a parent that nurtures a child until the child is able to live on his/her own. Good properties of a binder system such as low viscosity, high strength, high strain, high modulus and easy binder burnout would enable the green filament to be easily fabricated in the FDC process into green structures and the green structures to survive the post processing. The properties of ceramic powders introduced into the thermoplastic binder system are very important too. The most important parameters one needs to consider when choosing ceramic powders are surface area, chemical composition, particle size and their distribution. Fine-grained, wide-size distribution ceramic powders lower the overall viscosity of the FDC mixture during compounding. When developing green filament, it is very desired to have the maximum solids loading of ceramics for reduced problems during post processing.

Fabrication of the FDC feedstock such as mullite ($3Al_2O_3$, $2SiO_2$), fused silica (SiO_2), titanium dioxide (TiO_2), and alumina (Al_2O_3) involves three distinct processing steps. The first step involves the composition formulation of binder system and compounding of binder system and ceramic powder. The second step involves the extrusion of compounded mixtures into filament. The third step involves the FDC to fabricate high quality, structural parts. Binder removal and sintering are the post operations. Other post operations in the FDC process could include trimming or filing of seam lines in FDC parts while in the green state before binder removal and sintering. Good optimization of material and build parameters (e.g. head speed, flow rate, pre-flow, build temperatures) in the FDM software could prevent some of these post-processing operations.

Development of binder system for FDC

A binder system was developed from an in-house polypropylene-based FDM feedstock. The binder system was developed from commercially available thermoplastic materials. The prevalent components of the binder system are polypropylene base polymer, wax, tackifier, plasticizer and elastomer. Table 1 summarizes the role of each constituent material in the binder system and the FDC feedstock.

Binder constituent/s	Characteristics
Base polymer (polypropylene)	Act as the backbone of the filament and gives strength
Tackifier	Enables tackiness and provides flexibility
Elastomer	Provides elasticity and flexibility
Plasticizer	Provides plasticity to filament for spooling
Wax	Reduces viscosity

Table 1: FDC filament constituent/s and their characteristics

The base polymer gives strength to the entire filament. The role of the base binder is to act as the "backbone" or "strength giver" in the overall FDC feedstock formulation. The base polymer is the most difficult to choose, specifically because the other constituents are chosen to modify the properties of the base polymer. It should exhibit low viscosity, high strength, and good flexibility. The wax component in the FDC filament reduces the viscosity of the filament formulation. The tackifying component or tackifier provides tackiness and also increases the flexibility of the filament composition. The plasticizer provides plasticity and flexibility. It also provides some strength to the filament. The elastomer provides elasticity and flexibility. The elasticity in the filament helps to achieve a uniform feed rate during the FDC operation without any breakage of the filament. The elastomer also enables the filament to be spooled without any significant plastic deformation.

Polypropylene, wax, tackifier, plasticizer, and elastomer are general names that represent different groups of materials that behave in a certain way or have almost same characteristics. These materials are produced by different manufacturers with different properties or characteristics. It's the responsibility of the FDC feedstock developer to hand pick the best brand of polymer and additives that would produce a good binder system and eventual FDC feedstock. Mechanical testing was performed on several brands of materials from different groups and manufacturers. The vendor's materials with the highest strength, highest strain, and lowest viscosity were selected as the FDC filament constituent for the composition formulation of the binder system.

Experiment matrix as a technique of the DOE (Design of experiment) was used to organize and evaluate experimentation to obtain the best binder system composition. The matrix helps better understand what and how each constituent influences the base polymer and the binder system. The matrix was also used to understand how volume percent solids loading of ceramic powders influence the binder system and the corresponding FDC feedstock. The matrix contains results of mechanical testing (strength [MPa], strain [mm/mm], rheology torque [Nm]) of strategic compositions. Results of these various compositions and the outcome of sintered parts fabricated from the FDC feedstock were used to tailor a desirable binder system for the FDC.

A binder system has been developed from the above methodology. The binder system has been used to load 55 volume % of mullite, fused silica, and titanium dioxide ceramic powders. The mullite feedstock in volume % comprises of 47.93% mullite powder + 6.85% alumina powder + 0.69% MgO + the developed binder system. The fused silica feedstock comprises of 53% fused silica + 3% MgO + the developed binder system. The titanium dioxide feedstock comprises of 51% titanium dioxide + 4% MgO + the developed binder system. The developed binder system is composed of 44% polypropylene + 13.9% elastomer + 18.7% plasticizer + 7.8% tackifier + 15.6% wax.

Filament fabrication for the FDC

Compounding of binder system and ceramic powders (mullite, fused silica, and titanium dioxide) was done with the aid of a Haake polylab system (Paramus, NJ). All FDC compositions were compounded at 180°C at roller speed of 120 rpm for 80 minutes in a 48.3 cm^3-mixing bowl. The neat binder is first compounded for about 15 to 20 minutes before ceramic powders are added to the binder. Compounded mixtures are allowed to cool down to room temperature before they are

granulated into smaller size particles for extrusion. Ceramic powders especially fused silica tends to absorb moisture from the surroundings, which could reduce the strength of the FDC filament. Granulated compounded mixtures were subjected to moisture removal in a vacuum oven prior to filament extrusion. All the compounded mixtures were extruded at a screw speed of 7 rpm and 170°C (zone1) to 172°C (zone2) to 174°C (zone3) to 168°C (die zone) through a 1.78 mm diameter rod die. A horizontal conveyor belt was attached to the extruder for continuous fabrication of filament and subsequent spooling. The speed of the conveyor belt is very critical in obtaining a filament of 1.78 mm in diameter.

Fused deposition of ceramics

The extruded filaments were used as feedstock for the Stratasys FDM 1650 machine to create high quality parts. A small length of filament was first used to fill the empty FDM liquefier heated to a particular temperature until the filament is extruded in a continuous semi-molten, string-like manner through the liquefier's nozzles. These steps are repeated for all temperatures between 200°C and 265°C until a suitable extrusion rate through the nozzles was attained. Set-point temperatures for building ceramic parts from the filaments of mullite, fused silica, and titanium dioxide were established at 235°C and 237°C for both main and support build temperatures, respectively. Envelope temperature of 48°C and material flow rate of 130% was established for part building.

FDM machines come with some preset parameters for different materials such as pre-flow, start-flow, main flow, roll back and head speed. These values are preset in Stratasys' Quickslice software for filaments such as ICW-06 wax and ABS. The FDC filaments have different material characteristics (such as viscosity, melting points, drag coefficient) from the commercially available FDM filaments. New sets of material-dependent values had to be established for the FDC filaments to improve the quality of parts. Using the DOE as a tool coupled with optimization, a new set of material dependent values was established for the FDC filaments (Table 2). Several parts were build using these parameters with mullite, fused silica and titania powder loaded filaments. Figure 1 and 2 show mullite and fused silica parts processed via the FDC.

Material dependent parameters	Values for FDC feedstocks: mullite, SiO_2 and TiO_2
Pre-flow	79
Start flow	37
Start distance	60
Main flow	150
Roll back	153
Head speed	700

Table 2: Material-dependent parameters for the FDC filaments

Binder removal and sintering

Binder removal and sintering are part of the post processing operations. Binder removal and sintering was done in two stages. In the first stage, all the binders were removed. Different

heating rates were used in various temperature intervals to prevent surface and internal cracking of the samples. At low temperatures (< 200°C), liquid binder component(s) were removed via capillary action to the surrounding setter bed of alumina powder in which FDC parts were embedded. At a temperature over 200°C, evaporation and decomposition of the residual binders remove the remaining binders. The second stage is the sintering or densification stage. This was done at a temperature of 1650°C and hold time of 3 hours. These two stages of binder removal and sintering helped to fabricate high quality ceramic parts. Linear shrinkage after binder removal and sintering for the FDC part was established at 10-12% for mullite parts and 8-12% for fused silica parts. Figure 3 shows three sintered mullite parts.

FDC part quality

Visual inspection and the dimensional accuracy of FDC parts determined the part quality. The dimensional accuracy and tolerance of all the FDC parts were found to be very good in comparison to commercially available FDM feedstock for Stratasys' FDM 1650 machine. Parts created were very close to the net shape and dimension of the CAD/STL files. All part dimensions were measured within +/- 1% of the original dimensions.

Different types of defects in the FDC parts are classified into two main categories: (1) surface defects, (2) internal defects. Surface defects were minimal but visible to the naked eye. Two common surface defects are the staircase and chordal effect. Staircase defect is a common defect of most RP methods and is caused due to layered manufacturing. Reducing the thickness of each layer during operation can reduce this defect. Chordal effect originates in the STL format of the CAD. The STL is very similar to meshing in finite element analysis by approximating the surfaces of the CAD model with triangles. Highly curved surfaces must employ many triangles. The smaller the mesh sizes of curved surfaces, the better the quality of the fabricated model. Chordal effect was reduced by specifying binary mode and smallest chord length when exporting CAD files as STL files to the FDM machine. Similar part quality effects have also been discussed in Reference 5.

Internal defects need to be addressed seriously if the part is going to be used as a functional component. Internal defects are product of hardware and software specifications and their limitations. The most common types of internal defects are sub-perimeter voids, inter-road voids and core voids. Sub-perimeter voids are created by incomplete filing of areas inside the fused deposition part. A void is created due to an insufficient material flow to fill the volume at the tangent path and actual perimeter path intersection. Specifying a negative offset (-0.003) to the perimeter in the Quickslice software rectified this defect. Inter-roads voids are created due to the inconsistent material flow of the FDC filaments. This defect is important because of the void it creates in the interior of the ceramic structure. Extruding the FDC filaments to near net size of 1.78 mm diameter, and increasing the flow rate of the FDC filaments to 130% reduced this defect. Core defects were attributed to parts with concentric circular features and created by improper road selection for the contour fill of an area. Specifying road widths that were ideal to both specified slice thickness and slice interval eliminated these defects. A detailed analysis related to different types of defects and tolerances are presented in Reference 6.

Metal-ceramic composites

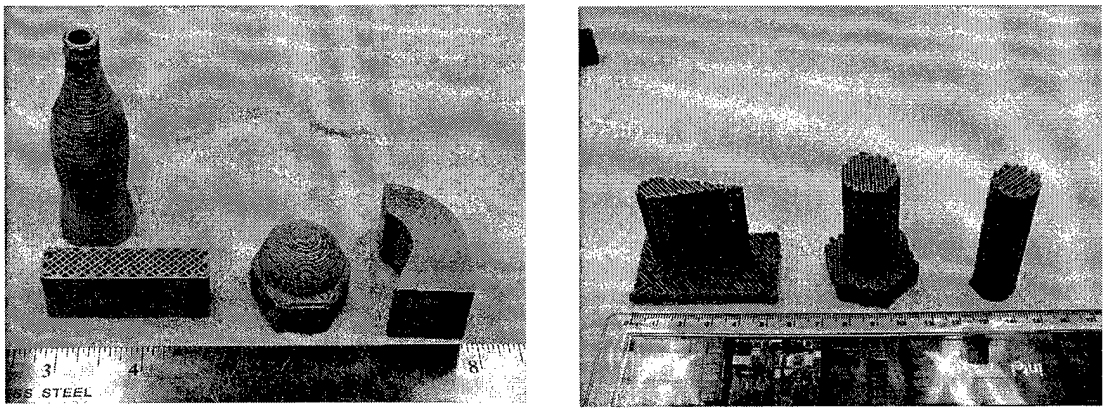
Once the porous ceramic preforms (mullite and fused silica) are fabricated via the FDC process, some of the preforms were infiltrated with molten aluminum metal via pressure-less reactive metal infiltration to form interpenetrating metal-ceramic composite. In these composites, the metal as well as the ceramic phases are connected in all three directions to themselves. Some of the advantages of processing the metal-ceramic composites via the FDC route include: (1) microstructure and macro structures of the part can be designed simultaneously in CAD (2) volume fraction as well as phase distribution can be controlled by controlling the pore architecture. Figure 4a and b show the as-processed and polished microstructures of the mullite-Al composites. The uniformity in the metal phase distribution can be seen from these pictures. Both uniform as well as gradient composites can be fabricated by this method.

Conclusions

This study has demonstrated the process of developing a binder system for the FDC process. The developed binder system has been used in fabricating the FDC filaments for mullite, fused silica, and titanium dioxide. Green FDC parts were created from the filaments with features and appearance similar to those present in FDM processed wax and polymer parts. The green parts were successfully sintered to obtain fully dense ceramic parts with minimal or no defects. Porous ceramic parts of mullite, and fused silica have been infiltrated with aluminum metals to obtain metal-ceramic composites. Properties of these composite are currently being addressed as a function of their structural parameters.

References

1. T. F. McNulty, F. Mohammadi, A. Bandyopadhyay, D. J. Shanefield, S. C. Danforth and A. Safari, "Development of Binder Formulation for Fused Deposition of Ceramics," *Rapid Prototyping Journal*, **4** [4], pp 144-50 (1998).
2. A. Bandyopadhyay, R. K. Panda, T. F. McNulty, F. Mohammadi, S. C. Danforth and A. Safari, "Piezoelectric Ceramics and Composites via Rapid Prototyping Techniques," *Rapid Prototyping Journal*, **4** [1], pp 37-49 (1998).
3. A. Bandyopadhyay, R. K. Panda, V. F. Janas, M. K. Agarwala, S. C. Danforth and A. Safari, "Processing of Piezocomposites by Fused Deposition Technique," *Journal of the American Ceramic Society*, **80**, 1366-72 (1997).
4. M. K. Agarwala, A. Bandyopadhyay, R. V. Weeren, N. A. Langrana, A. Safari, S. C. Danforth, "Fused deposition of ceramic (FDC) for Structural Silicon Nitride Components," Proceedings. Solid Freeform Fabrication Symposium, Austin, TX, 1996.
5. R. van Weeren, M. Agarwala, V. R. Jamalabad, A. Bandyopadhyay, R. Vaidyanathan, N. Langrana, A. Safari, P. Whalen, S. C. Danforth, C. Ballard, "Quality of parts processed by fused deposition," Proceedings. Solid Freeform Fabrication Symposium, Austin, TX, 1996.
6. S. Onagoruwa, MS Thesis, Mechanical and Materials Engineering, Washington State University, August 2001.



(a) (b)

Figure 1: (a) and (b) Mullite parts fabricated via FDC.

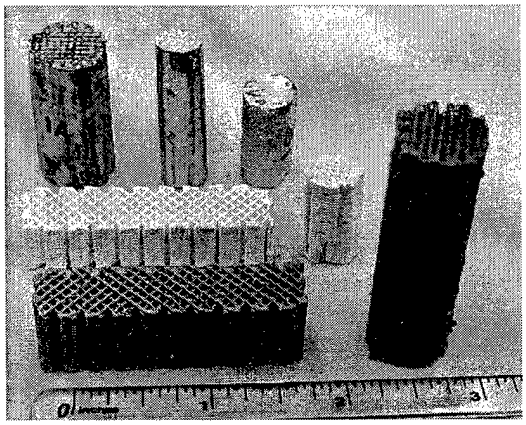


Figure 2: Green, brown and sintered fused silica parts via FDC. Three metal infiltrated parts can also be seen in the back of the picture.

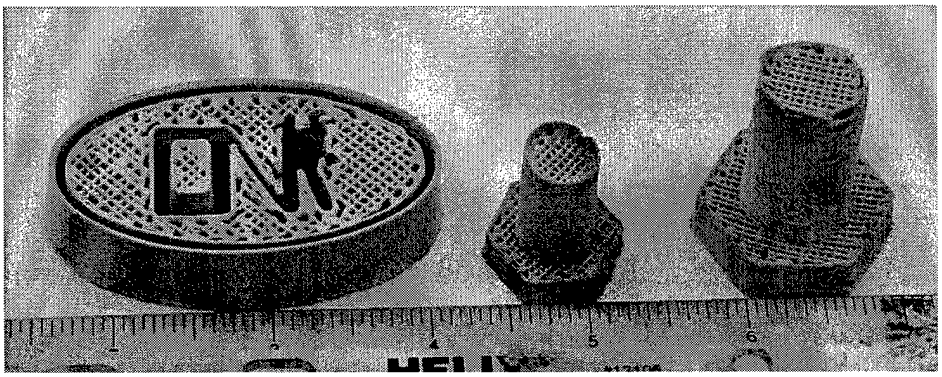
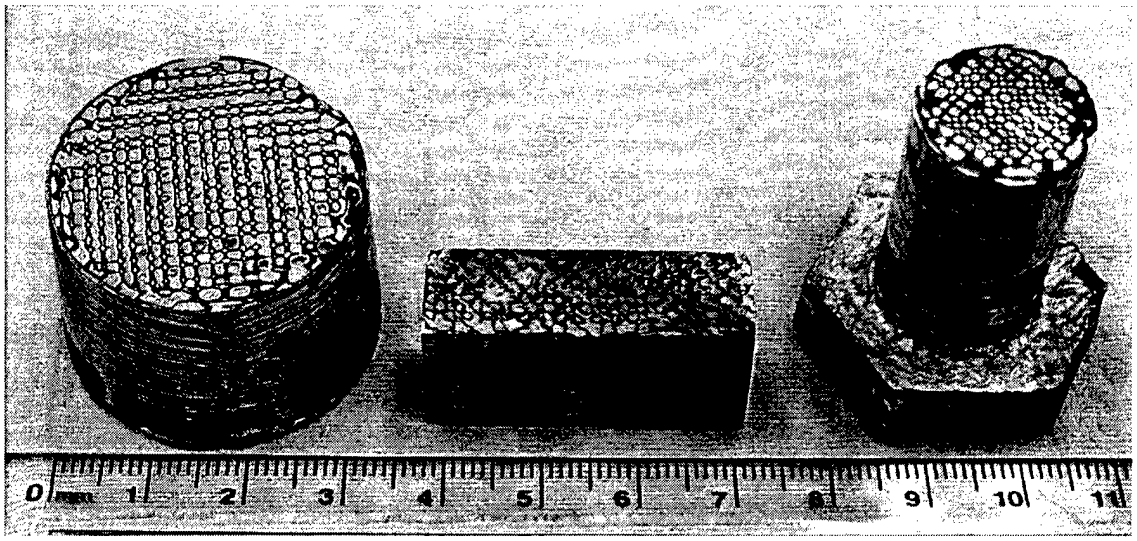
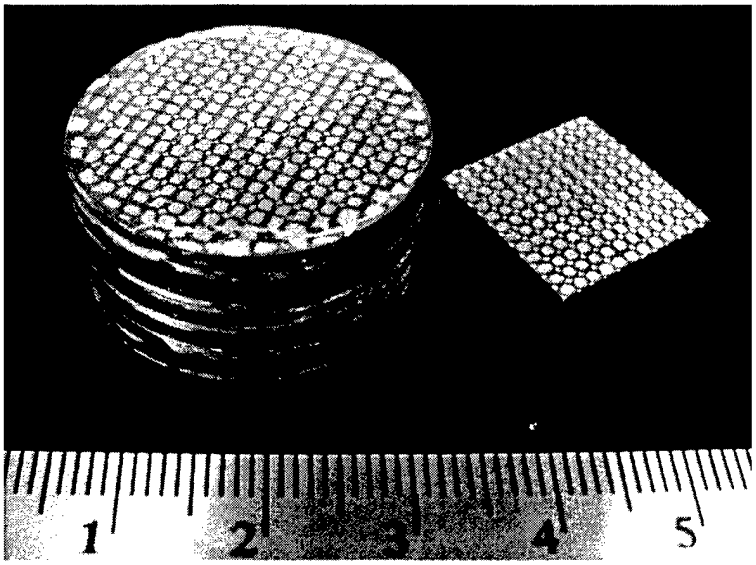


Figure 3: Sintered mullite parts processed via FDC



(a)



(b)

Figure 4: (a) As-processed mullite-Al composites. (b) Microstructures of mullite-Al composites.

Solidification Modeling and Microstructural Characterization of Alloy IN718 Deposited by Laser Engineered Net Shaping

J.N. DuPont [1], J.G. Nawrocki [1], and M.L. Griffith [2]

1. Department of Materials Science and Engineering, Lehigh University, Bethlehem, PA
2. Mechanical Engineering Department, Sandia National Laboratory, Albuquerque, NM

Abstract

Alloy IN718 deposited by the LENS process was characterized using light optical, and scanning and transmission electron microscopy techniques. The as-solidified microstructure contained primary γ–austenite cells with intercellular NbC and Laves phases. Underlying layer microstructures were not altered by the thermal cycles of subsequent passes. Dendrite tip modeling calculations provided a reasonable estimate of cell core compositions measured experimentally by analytical electron microscopy techniques and were used to demonstrate that dendrite tip undercooling was not significant under the deposition conditions employed. Preliminary guidelines on solidification conditions required to suppress microsegregation during LENS deposition of IN718 are provided from the modeling results. A solute redistribution model was employed, which accurately described the solidification reaction sequence and resultant phases present in the final microstructure.

Introduction

Fabrication of superalloy components via Laser Engineered Net Shaping (LENS) is being considered for a variety of applications in the aerospace and defense industries. In these applications, alloy composition and LENS processing parameters will control the microstructure and concomitant properties. In terms of processing parameters, the as-solidified microstructure of a given alloy will be controlled by the travel speed and beam power, which dictate the solidification velocity and temperature gradient, while subsequent solid state reactions will be governed by the thermal history induced from deposition of subsequent layers. In order to accurately model microstructural development of LENS components, it is necessary to know the relative importance of liquid-to-solid and solid-to-solid transformations in determining the final microstructure. In steels where the post solidification γ (austenite) → α (ferrite) solid state transformation occurs and the diffusion rate of carbon and other alloying elements is relatively rapid, it has been shown [Ref. 1] that subsequent thermal cycles after the initial deposition induce significant microstructural modification via solid-to-solid transformations. In this case, accurate microstructural prediction requires both solidification and solid state transformation models. However, in Ni base superalloys such as IN718, the γ phase is stable after solidification and no post-solidification allotropic transformations occur [Ref. 2]. Although precipitation reactions can lead to the formation of γ', γ", and δ phases, these reactions are generally slow due to the low diffusion rates of substitutional alloying elements in the FCC matrix [Ref. 3]. In this case, post solidification reactions under LENS processing conditions may be negligible, in which case only the liquid-to-solid transformation needs to be considered for estimating the microstructure after deposition. However, no experimental information is available to confirm this. In addition, the high solidification rates possible with the LENS process are often viewed as a means for reducing undesirable microsegregation that typically occurs during solidification of superalloys in other fabrication methods such as casting and welding. To this point, there has

been no detailed microstructural characterization conducted on LENS deposited IN718 to determine the extent to which microsegregation can be suppressed under typical deposition conditions. In this research, alloy IN718 was prepared by LENS deposition and characterized using scanning and transmission electron microscopy. The type of phases and distribution of alloying elements that existed between the last pass (which experienced no subsequent thermal cycles) and the underlying passes was compared in order to assess the influence of subsequent thermal cycles on the as-solidified microstructure.

Experimental Procedure

Alloy IN718 was deposited into single line wall builds that were approximately 25 mm wide and 100 mm high. The LENS processing parameters were set at a travel speed of 7.6 mm/s and a powder flow rate of 35.4 mm^3/sec. Samples were then sectioned for microstructural analysis via light and electron microscopy. Samples for light optical microscopy (LOM) and scanning electron microscopy (SEM) were mounted and polished using standard metallographic techniques and electrolytically etched in 10% chromic acid (balance water) solution. A JEOL 6300 field emission gun SEM was used for imaging in the secondary electron mode. Thin foils for transmission electron microscopy (TEM) were prepared by polishing 3mm diameter disks to a thickness of approximately 50um and then ion milling to electron transparency. The SEM and TEM analysis was conducted on the last pass (which experienced no subsequent thermal cycles) and the fifth from last pass, which experienced four subsequent thermal cycles. Microhardness measurements were conducted using a Vickers indenter with a 200 gram load.

Results

Figure 1 contains LOM photomicrographs of the line builds, which shows the last seven passes. The bottom region of each pass contains a light colored area, but microhardness measurements (shown in Figure 1a) indicate there is no significant difference in hardness in any particular region of the sample. The microstructure exhibited a cellular/dendritic substructure with interdendritic secondary phases (Figure 1b). Figure 2 shows higher magnification SEM views of regions of the last pass and the fifth from last pass. The region of the last pass shows two secondary interdendritic phases with different morphologies – a small, equiaxed phase and larger, globular phase (Figure 2a). The fifth from last pass shows essentially identical results (Figure 2b). Figures 3 and 4 show TEM images and electron diffraction patterns of these phases. The small, equiaxed phase was identified as FCC (Ti,Nb)C (Figure 3), while the larger, globular phase was identified as an HCP A_2B Laves phase (A = Fe,Ni,Cr and B = Nb,Mo, Figure 4). These phases have also been observed in IN718 solidified under lower cooling rate conditions found in fusion welding [Ref. 2]. There is no significant difference in the type of phases present between the first and fifth from last passes. AEM compositional profiles were also acquired across these passes to measure the distribution of alloying elements across the cellular substructure. Typical examples of AEM line scans are shown in Figures 5 (last pass) and Figure 6 (fifth from last pass). In each case, the cell cores are depleted in Nb and Mo and slightly enriched in Cr and Fe. This indicates that Nb and Mo segregate to the liquid during solidification while Fe and Cr slightly segregate to the solid. These results also indicate that the solidification velocity used here is not high enough to suppress microsegregation in this alloy system.

Discussion

The microstructural characterization data indicates that there is no significant difference in microstructure between the last pass and underlying passes which have been exposed to subsequent thermal cycles. This suggests that the as-deposited microstructure of IN718 does not change significantly from the thermal cycles induced by subsequent depositions. It is generally known [Ref. 3] that as-cast IN718 will precipitate γ', γ", and δ phases upon heating at elevated temperatures. However, the time required to precipitate these phases is on the order of six minutes at 870 °C, and the times required for precipitation increase significantly at lower temperatures. Thermocouple measurements previously conducted on LENS deposits [Ref. 1] have shown that the peak temperature decreases to ~ 850 °C approximately five layers below the weld pool. More importantly, the time above the peak temperature is extremely short. Thus, based on these considerations, it is expected that precipitation reactions would not occur during deposition, and this was confirmed by the TEM microstructural characterization data. This indicates that the as-deposited microstructure for this alloy can be estimated from solidification models alone.

The main objective of the microstructural modeling described here is to predict the type of phases that form during solidification and the solidification conditions (solidification velocity and temperature gradient) required to suppress microsegregation. One of the major advantages of LENS processing is the potential for minimizing concentrations gradients in the solid, which are often detrimental to mechanical properties and corrosion resistance [Ref. 4]. Under rapid solidification conditions encountered during laser deposition, there can be significant reduction in the cell tip radius and accumulation of solute in the liquid ahead of the solid/liquid interface. Each of these factors leads to dendrite tip undercooling and a concomitant enrichment of solute in the primary solid. However, the AEM data presented in Figures 5 and 6 indicate that microsegregation is still persistent under the current set of deposition conditions. The set of conditions needed to reduce microsegregation can be estimated based on the model presented by Kurz *et al* [Ref. 5], which is given by

$$V^2\left[\frac{\pi^2\Gamma}{P^2 D_l^{\,2}}\right] + V\left[\frac{m_l C_o(1-k)\xi}{D_l[1-(1-k)I(P)]}\right] + G = 0 \qquad (1)$$

$$\xi = 1 - \frac{2k}{[1+(2\pi/P)^2]^{1/2} - 1 + 2k} \qquad (2)$$

where V is the solidification velocity, Γ is the Gibbs-Thomson parameter, P is the Peclet number defined as $VR/2D_l$, (R is the cell tip radius, D_l is diffusivity of solute in the liquid), m_l is the liquidus slope, C_o is the nominal alloy composition, k is the distribution coefficient, G is the mean temperature gradient, k is the equilibrium distribution coefficient, and I(P) is the Ivanstov function. A numerical technique is required to solve equation (1). This model provides information on the cell radius and corresponding cell tip temperature, T_{tip}, as a function of solidification velocity and temperature gradient. Once the cell tip temperature is established, the cell tip composition, C_l^*, can be determined by

$$C_l^* = \frac{C_o}{1-(1-k)I(P)} \qquad (3)$$

Once C_l^* is known, the cell core composition, C_{core} (which was also measured experimentally by AEM) can be determined from knowledge of the equilibrium distribution coefficient. Figure 7 shows the calculated variation in T_{tip}, C_l^*, and C_{core} as a function of solidification velocity for IN718. Following the work of Knorovsky *et al* [Ref. 2], IN718 was modeled as a γ-Nb binary system for these calculations. A temperature gradient of 500 °C/mm was used for the calculations based on previous thermal analysis data conducted on the LENS process [Ref. 6]. Material constants used for the calculations are shown in Table 1. The liquidus temperature for IN718 (i.e., in the absence of undercooling) is ~1360 °C [Ref. 2]. Note that the suppression in the dendrite tip temperature is not significant for this alloy under typical LENS solidification velocities (~ 2 – 10 mm/s). As a result, there is not a large increase in the cell tip composition. The AEM data measured at the cell cores is plotted in Figure 7c assuming that the travel speed of the heat source is equivalent to the solidification velocity. The solidification velocity will approximately reach the travel speed at the weld pool centerline and decrease towards zero at the edge of the weld pool. There is reasonable agreement among the calculated and measured data, providing validation on the accuracy of the calculations. These modeling results can also be used to provide information on the solidification conditions required to suppress microsegregation, i.e., to identify conditions in which C_{core} approaches C_o. Figure 7d shows a plot of C_{core}/C_o (this ratio is numerically equal to k, the distribution coefficient) as a function of solidification velocity. Note that rather high solidification velocities are needed in order to appreciably suppress microsegregation. These results show that effective suppression of microsegregation during LENS deposition requires careful consideration of the processing parameters, most notably the travel speed.

Table 1. Material parameter values used in dendrite tip calculations.

Parameter	Value	Reference
Γ (K-mm)	0.0002	9
D_l (mm^2/sec)	0.02	9
m_l (°C/wt% Nb)	-8.3	10
k (unitless)	0.48	2

Having established that dendrite tip undercooling is not large under the current set of deposition conditions, the solute redistribution stage of solidification can be modeled by the approach previously presented by DuPont *et al* [Ref. 7]. The primary solidification path is given by

$$C_{l,Nb} = C_{o,Nb}\left[\frac{C_{o,C} - k_C C_{l,C}}{(1-k_C)C_{l,C}}\right]^{k_{Nb}-1} \qquad (4)$$

Where $C_{l,Nb}$ and $C_{l,C}$ are the Nb and C concentrations in the liquid during the primary L → γ reaction, $C_{o,Nb}$ and $C_{o,C}$ are the nominal Nb and C concentrations, and k_{Nb} and k_C are the distribution coefficients for Nb and C. A liquidus projection is needed along with the solidification path calculation in order to determine the solidification reaction sequence and

concomitant phases present after solidification. Figure 8 shows the solidification path (according to eq. 4) superimposed on a pseudo-ternary liquidus projection for IN718 that was calculated with Thermo-Calc thermodynamic system [Ref. 8] . These results indicate that solidification starts by a L $\rightarrow$ γ reaction, which rejects Nb and C to the intercellular liquid. This process continues until the primary solidification path intersects the NbC/γ two fold saturation line, at which point γ and NbC start forming simultaneously from the liquid. This process continues as the liquid composition follows the NbC/γ two fold saturation line until the NbC/γ/laves Type II reaction is reached, at which point γ and Laves form as solidification goes to completion. This predicted reaction sequence is in agreement with the NbC and Laves phases observed during microstructural characterization. These results do not account for the presence of cell tip undercooling, since it was previously demonstrated to be negligible under the current set of deposition conditions. However, process optimization studies are underway in order to identify parameters, which induce significant cell tip undercooling and reduce microsegregation. In this case, dendrite tip undercooling calculations must be combined with solute redistribution computations for accurate modeling. This work is currently underway.

Conclusions

Alloy IN718 deposited with the LENS process solidifies by a three step reaction sequence; L $\rightarrow$ γ, followed by L $\rightarrow$ (γ + NbC) and L $\rightarrow$ (γ + Laves). This solidification reaction sequence has been accurately modeled by solute redistribution calculations and the use of a computed pseudo-ternary liquidus projection. Thermal cycles from deposition of subsequent layers have no significant effect on the as-solidified microstructure. Under low travel speed conditions, dendrite tip undercooling is not significant and microsegregation is not suppressed. Dendrite tip undercooling models have been used to estimate solidification velocities required to minimize microsegregation.

Acknowledgements

Prof. DuPont gratefully acknowledges support of this work by the National Science Foundation through a PECASE Award, Grant No. DMI 9983968, made through the Division of Manufacturing and Industrial Innovation and helpful discussions with Dr. Delcie Durham of NSF. The portion of research conducted at Sandia National Laboratory was supported by the U. S. Department of Energy under contract DE-AC04-94AL85000. Sandia is a multiprogram laboratory operated by Sandia Corporation, a Lockheed Martin Company, for the United States Department of Energy.

References

1. M.L. Griffith, M.E. Schlienger, L.D. Harwell, *Materials and Design*, Vol. 20, 1999, pp. 107-113.
2. Knorovsky, G.A., Cieslak, M.J., Headley, T.J., Romig, Jr., A.D., and W.F. Hammetter, *Metallurgical Transactions A*, Vol. 20A, 1989, pp. 2149-2158.
3. A. Oradei-Basile and J.F. Radavich, *Superalloys 718, 625, and Various Derivatives*, TMS, 1991, pp. 325-334.
4. K.R. Luer, J.N. DuPont, A.R. Marder, and C.K. Skelonis, Corrosion Fatigue of Alloy 625 Weld Claddings Exposed to Combustion Environments, *Materials at High Temperatures*, Vol. 18, 2001, pp. 11-19.
5. W. Kurz, B. Giovanola, and R. Trivedi, Acta Materialia, Vol. 34, 1986, pp. 823-830.

6. W. Hofmeister, M. Wert, J. Smugeresky, J.A. Phillibier, M. Griffith, and M. Ensz, *JOM*, Vol. 51, 1999, (e-journal version).
7. DuPont, J.N., Robino, C.V., and A.R. Marder, *Acta Materialia*, Vol. 46, no. 13, 1998, pp. 4781-4790.
8. Saunders, N. *Ni-Data v.3*, Thermotech Ltd., Surrey Technology Centre, The Surrey Research Park Guildford, Surrey GU2 5YG, U.K.
9. W. Kurz and D.J. Fisher, *Fundamentals of Solidification*, 3rd Ed., Trans Tech Publications, 1989.
10. J.N. DuPont, C.V. Robino, and A.R. Marder, Modeling Mushy Zones in Welds of Multi-Component Alloys: Implications to Solidification Cracking, *Science and Technology of Welding and Joining*, 1999, Vol. 4, No. 1, pp. 1-14.

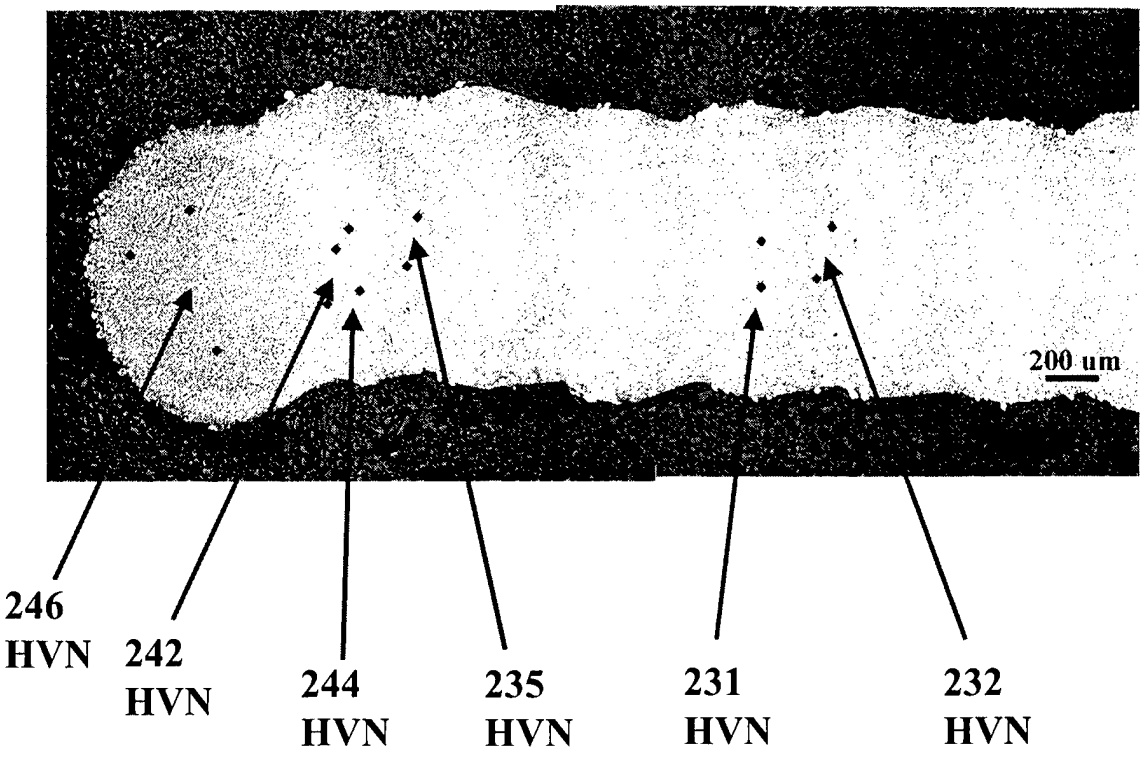


Figure 1a: Macrostructure and hardness of an IN718 LENS deposit.

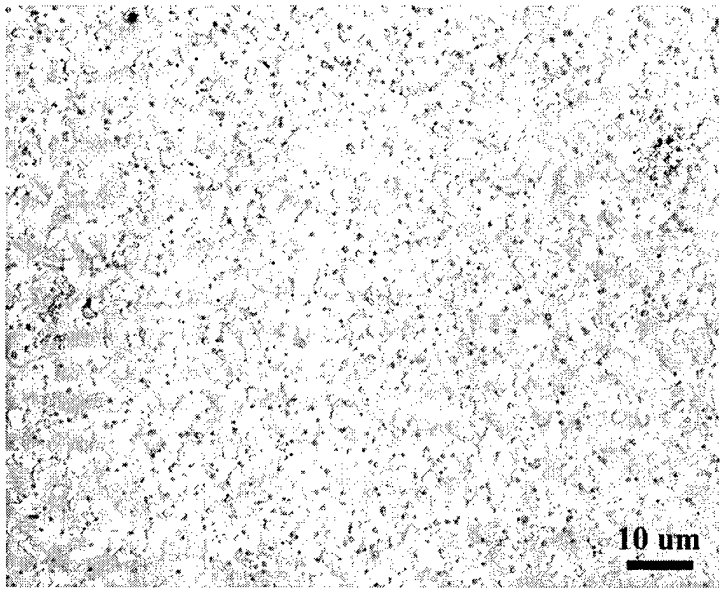
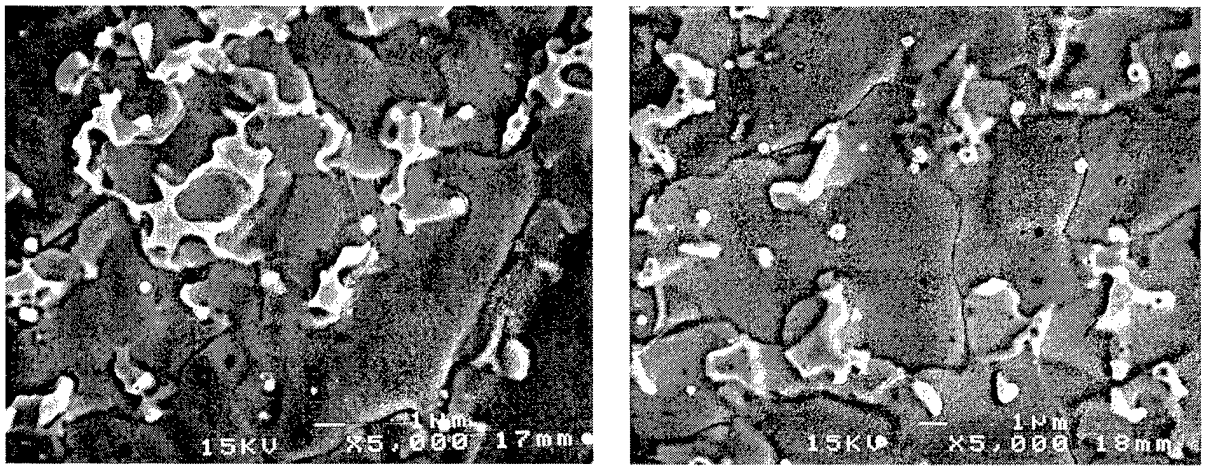


Figure 1b: Representative LOM photomicrograph of an IN718 line build showing a cellular/dendritic substructure and interdendritic secondary phases.



a b

Figure 2: SEM photomicrographs of (a) the last pass and (b) the fifth from last pass of an IN718 line build.

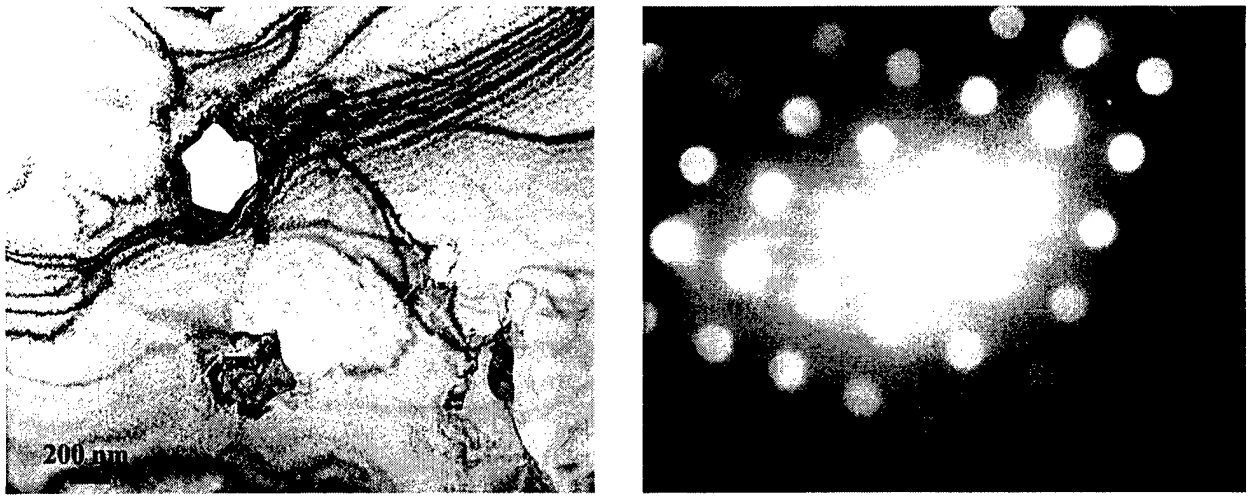


Figure 3: TEM photomicrograph of FCC (Ti,Nb)C and accompanying electron diffraction pattern showing a [011] zone axis.

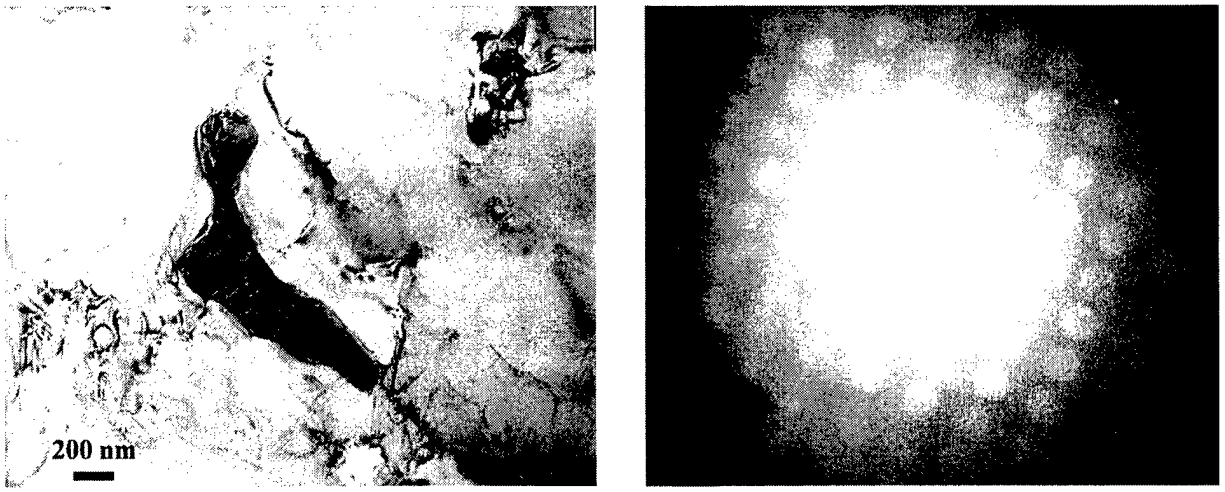


Figure 4: TEM photomicrograph of HCP A_2B Laves phase (A=Fe,Ni,Cr and B= Nb,Mo) and accompanying electron diffraction pattern showing a [311] zone axis.

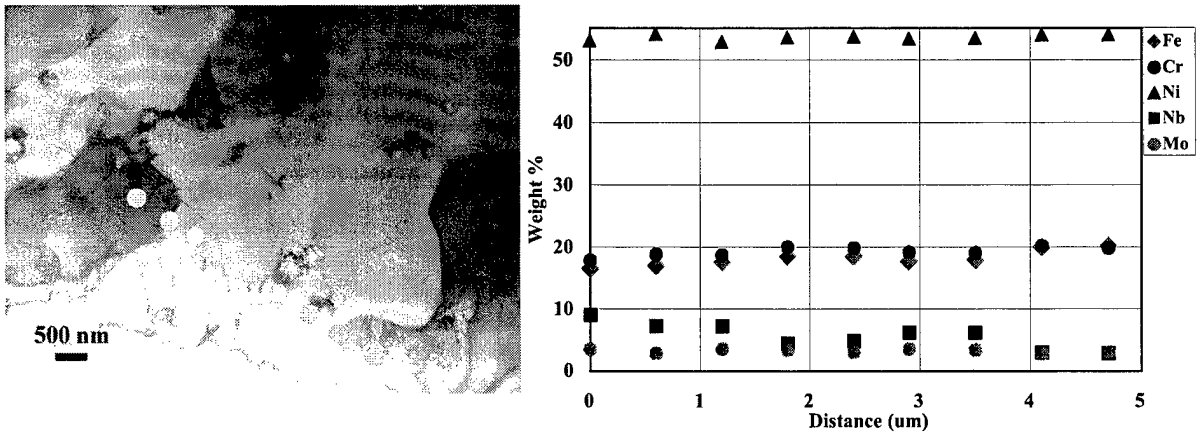


Figure 5: Typical AEM line scan of the last pass in an IN718 line build indicating Nb and Mo segregation. The points shown on the micrograph from the upper left to the lower right correspond to increasing distance on the accompanying graph.

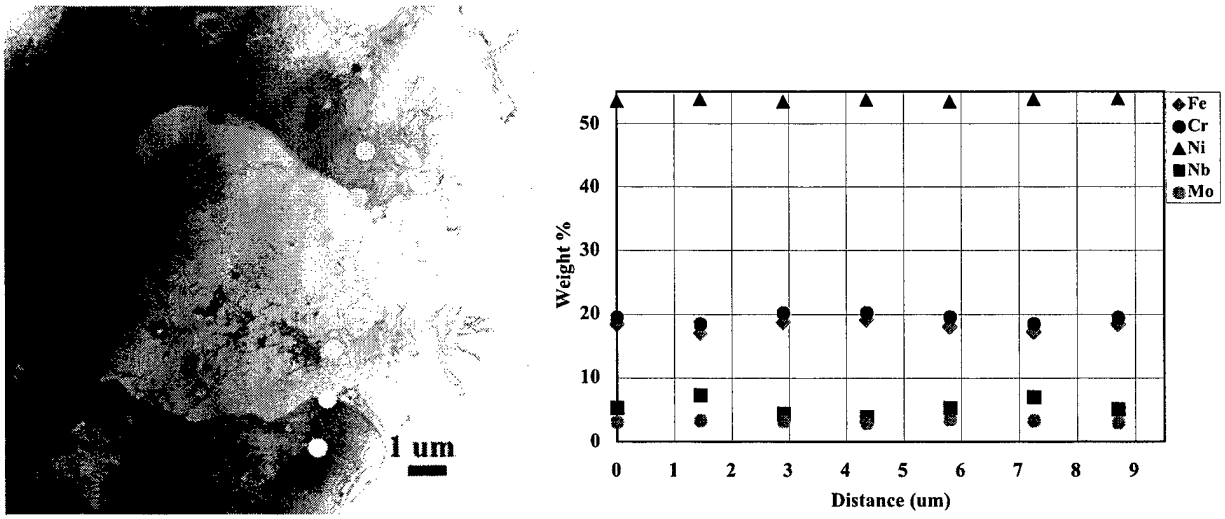


Figure 6: Typical AEM line scan of the fifth pass in an IN718 line build indicating Nb and Mo segregation. The points shown on the micrograph from the bottom to top correspond to increasing distance on the accompanying graph.

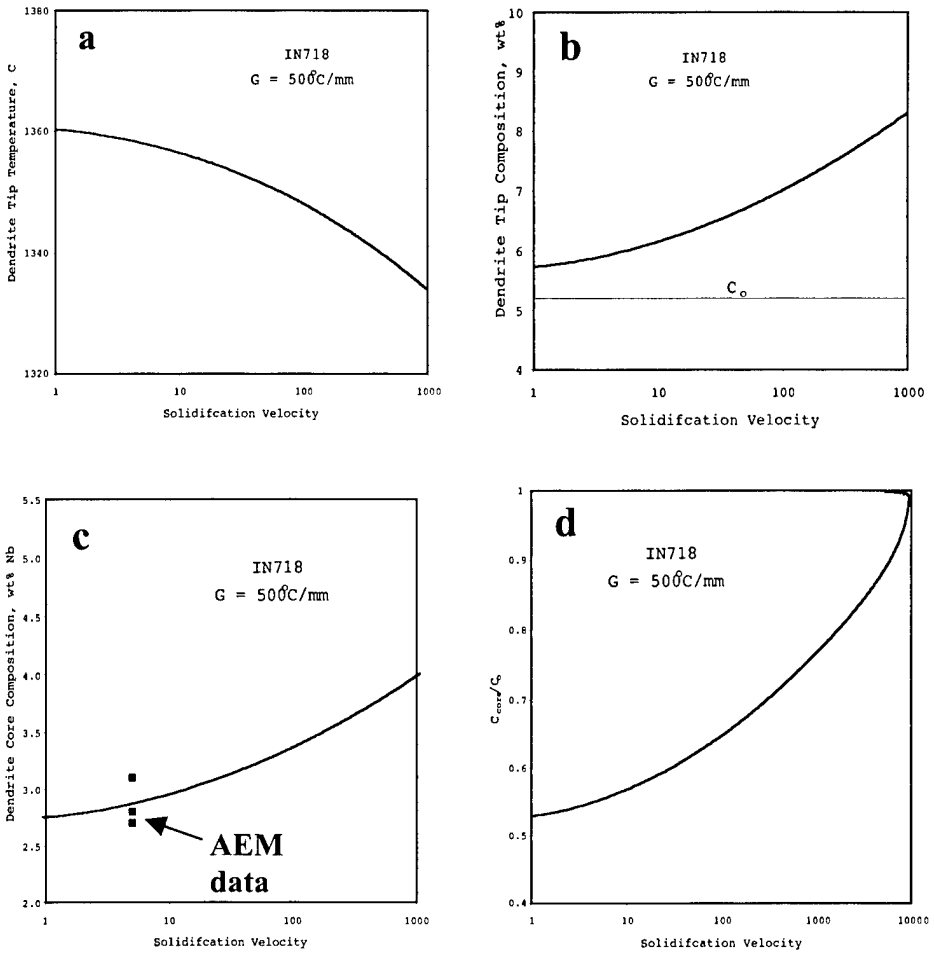


Figure 7. Dendrite tip calculations. a) Dendrite tip temperature as a function of solidification velocity, b) Dendrite tip composition as a function of solidification velocity, c) Dendrite core composition as a function of solidification velocity with AEM data plotted, d) C_{core}/C_o as a function of solidification velocity.

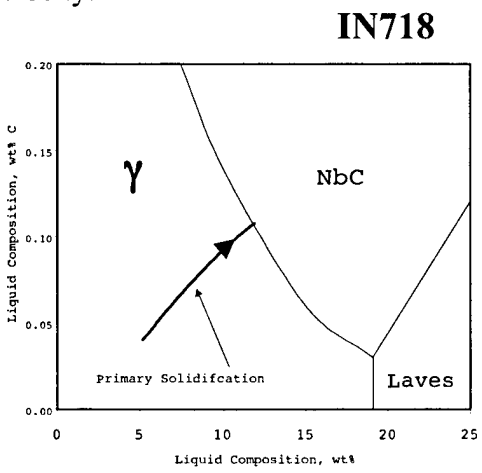


Figure 8. Calculated primary solidification (equation (4)) superimposed on the IN718 pseudo ternary liquidus projection.

Experimental Study of Selective Laser Sintering of Parmax®

Jagan R Rajan, Kristin L Wood
Laboratory of Freeform Fabrication
The University of Texas at Austin
Austin, TX - 78712

Nick Malkovich
Research Engineer
Mississippi Polymers Technologies Inc.
Bay St. Louis, MS - 39520-9078

Abstract

Selective Laser Sintering (SLS) has been used to successfully process crystalline polymers, ceramics and metals. However, wide range of materials available and their applications have acted as an impetus to expand the applications of SLS to different material systems. This paper presents one such experimental study undertaken to explore the application of SLS to process Parmax® polymers – a family of high performance amorphous poly p-phenylenes. As a part of the collaborative study, various process parameters and material formulations were tried out to ascertain the feasibility of the process and the initial results obtained look promising. This paper lists the material formulations tested and process parameters controlled. Also, analysis of the results of the experimental study and the outline of the next phase of research to be undertaken have been described. This study was motivated by the numerous applications of Parmax® in the electronics, defense and aerospace industries as well as the goal to expand the applications and utility of SLS.

Introduction

Rapid prototyping has become an essential tool in dealing with dramatically shortened manufacturing product life cycles. It replaces machine carved prototype models and patterns with machine-built components produced in a few hours, suitable for testing of form, fit and function. Functional testing often places the rapid prototyping part in an operating assembly, requiring high strength materials. Unfortunately, current polymeric rapid prototyping materials such as nylon and polycarbonate, do not offer sufficient mechanical properties for high strength components, restricting functional testing up to this point and thus limiting the overall utility of rapid prototyping.

To overcome this limitation, new materials with higher strength need to processed through Selective Laser Sintering(SLS). One such material, developed at MPT is its novel, high strength class of rigid-rod Parmax® Self Reinforced Polymer (SRP) resins.

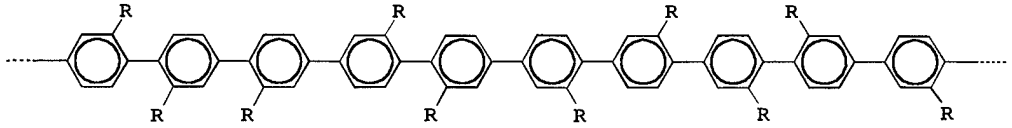


Figure 1. Generalized Structure of Rigid-Rod Parmax® SRPs

The extraordinary hardness, stiffness and strength of Parmax® SRPs make them attractive for a wide range of uses that include molded articles and extruded sheet, stock and profiles for aircraft interiors, electrical and electronic components, surgical instruments, bushings, gears etc.; films and coatings for fiberless printed wiring boards, abrasion resistant coatings etc.; foams for high strength, low moisture absorption core and structural components and in blends and additives in which Parmax® SRPs are used to improve the performance of other polymers. With its application extending into so many different areas, it becomes important to manufacture functional prototypes quickly and cheaply in order to demonstrate its capability and also arrive at optimized material formulations for each application. Thus being able to make Parmax® SRPs compatible to SLS is important from this point of view and this study aims at achieving the same.

The primary objectives of this research effort are to (1) develop sinterable powder formulations based on MPT's high-performance Parmax® SRP resins, (2) determine initial processing conditions for these powders via the Selective Laser Sintering (SLS) rapid-prototyping process, and (3) fabricate initial test coupons to demonstrate the high-integrity components that can result from this combination of material and processing. However, the ultimate goal of the research is to come up with optimized powder and process parameters to produce components with unprecendented mechanical properties, thus paving the way for the commercialization of Parmax® SRP-based SLS formulations.

The selection and development of powder formulations based on Parmax® SRP resins suitable for SLS processing were carried out at MPT under the aegis of an SBIR grant while determination of initial processing conditions and production of test coupons was conducted at the University of Texas.

The paper is organized in the following way. First, a brief description of mechanical and chemical properties of relevant Parmax® SRP resins developed, current resin processing methods as well as the Selective Laser Sintering process are stated. Following this, the process parameters considered, material formulations tested and the initial experimental trials are presented. The results of the experiments are then analyzed. The paper concludes with a section on the contributions of this effort and an outline for the next phase of the research.

Background

Powder Properties:

MPT's Parmax® SRPs, a new family of rigid-rod self-reinforcing polyphenylenes, possess a unique combination of high performance mechanical properties along with good processing capabilities. Research largely inspired and supported by the Air Force Materials Laboratory in the 1970's and 1980's has demonstrated that rigid-rod polymers possess exceptional mechanical properties[1], but most are either intractable or are soluble only in strong acid solvents. Parmax® SRPs have been designed to overcome the processing deficiencies of other rigid-rod polymers via the use of carefully chosen pendant side chains to impart solubility and thermal processability to the normally intractable rigid-rod polyparaphenylene backbone. Thus, Parmax® materials can be dissolved in a variety of common organic solvents (methylene chloride, N-methylpyrrolidinone, phenyl ethers and esters, etc.) and, perhaps most importantly, can be thermally fabricated (compression molded, extruded, injection molded, etc.).

Parmax® SRPs are prepared by proprietary processes that assure the isomeric integrity of the structure. A variety of substituent groups (R) can be utilized, so Parmax® SRP resins comprise a

versatile class of polymers, like polyimides, polyesters, and polyamides, within which a wide range of structural variation is possible. We have surveyed many different derivatives including the thermoplastic rigid-rod Parmax®-1000 (benzoyl side chain structure) and Parmax®-2000 (4-phenoxybenzoyl side chain) homopolymers (Figure 2.) and the "tougher" and more processible Parmax®-1200 series of "kinked" copolymers. Currently it appears that the Parmax®-1000 and Parmax®-1200 derivatives will provide the first commercial Parmax® molding resin products.

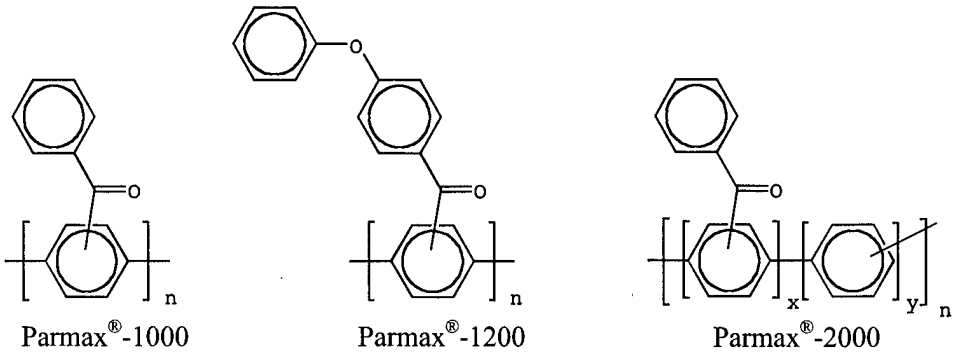


Figure 2. Chemical Structures of Some Thermoplastic Parmax® SRP Derivatives

Parmax® SRP resins demonstrate extraordinary strength, modulus, hardness, and other properties in a combination unrivaled by any other single material (Table 1). Metals are widely used for structural support but are heavy and subject to corrosion and fatigue. Common thermoplastics are inexpensive to fabricate into parts but currently cannot provide enough strength or stiffness for many applications. Fiber-reinforced composites have evolved to offer unprecedented strength-to-weight characteristics but are extremely difficult and expensive to process. As demonstrated in Figure 3, isotropic Parmax® resins possess unparalleled mechanical strength and modulus when compared to other engineering thermoplastics. In fact, on weight basis, Parmax® polymers are extremely competitive with structural metals such as aerospace grades of aluminum and titanium (Figure 4).

Table 1. Selected Properties of Thermoplastic Parmax® SRP Resins

	Parmax®-1000	Parmax®-2000	Parmax®-1200
Specific Gravity	1.21	1.23	1.23
Tensile Modulus (MSI)	1.5	1.2-1.4	1.2
Flexural Strength (KSI)	35-50	20-30	39-46
Rockwell Hardness	K98	K98	K90
Limiting Oxygen Index (1/8" thick)	41%	32%	42%

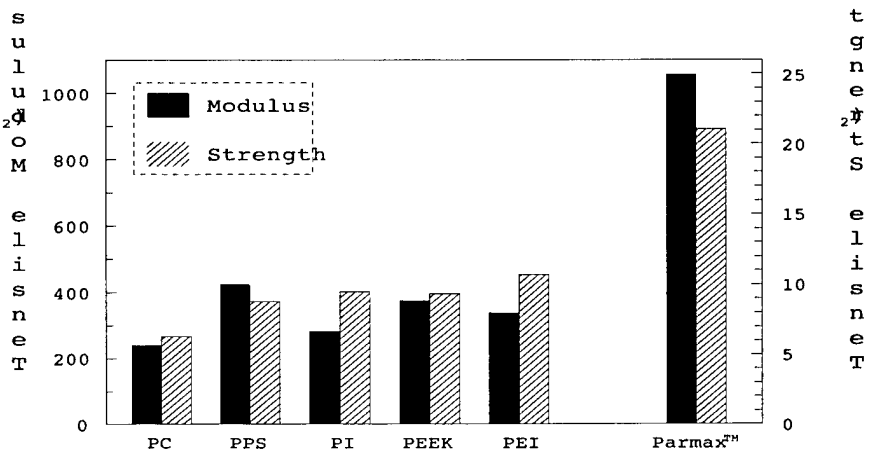


Figure 3. Mechanical Properties of Engineering Plastics and Parmax® SRPs

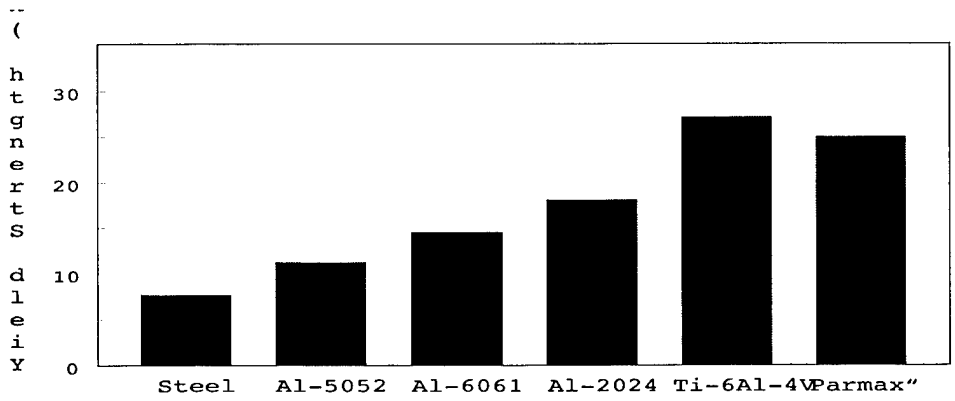


Figure 4. Specific Strength Comparison of Various Metals with Parmax® SRPs

Processing Techniques:

Ultra high performance, isotropic Parmax® SRP polymers are processed utilizing conventional polymer techniques. These include routine extrusion, thermoforming and compression molding operations. Injection molding grades are under development and their availability is anticipated for fourth quarter of 2001. Processing temperatures are in the range of 290 to 340 °C. Within this processing window, Parmax® SRP resins display remarkable stability and do not require any additional stabilizers to facilitate the processing. The excellent solubility of these materials in common organic solvents allow for the facile preparation of films and coatings from solution.

Selective Laser Sintering Process:

Selective Laser Sintering is a rapid prototyping process in which powdered material is melted into the desired shape through the repeated scanning of cross-sectional areas that will eventually form the 3D model[14]. The machine (figure 5) consists of one part piston which translates within the part cylinder; 1 or 2 feed pistons that move within the powder cartridge and act as the powder feeding/collection system; a roller mechanism for spreading powder; heating coils, sensors and controllers for heating and maintaining the powder at the correct temperature;

laser and its accompanying optics to focus the laser beam precisely; blower, sensors and controllers that maintain the process chamber inert(not shown in figure); a computer interface that serves as the communication link between the user and the machine(not shown in figure). The SLS process is accomplished with a CO_2 laser which scans a cross section of the part on the surface of the part bed. After one cross section is scanned, the part piston moves down and the feed pistons, carrying powder above them, move up. Then a roller sweeps across the bed, laying a fresh layer of powder and the whole process is repeated till the whole component is made. Uneven or large temperature gradients need to minimized during the build so as to prevent excessive part curl. This is achieved by preheating the powder in the feed bins as well as the part piston to prescribed temperatures.

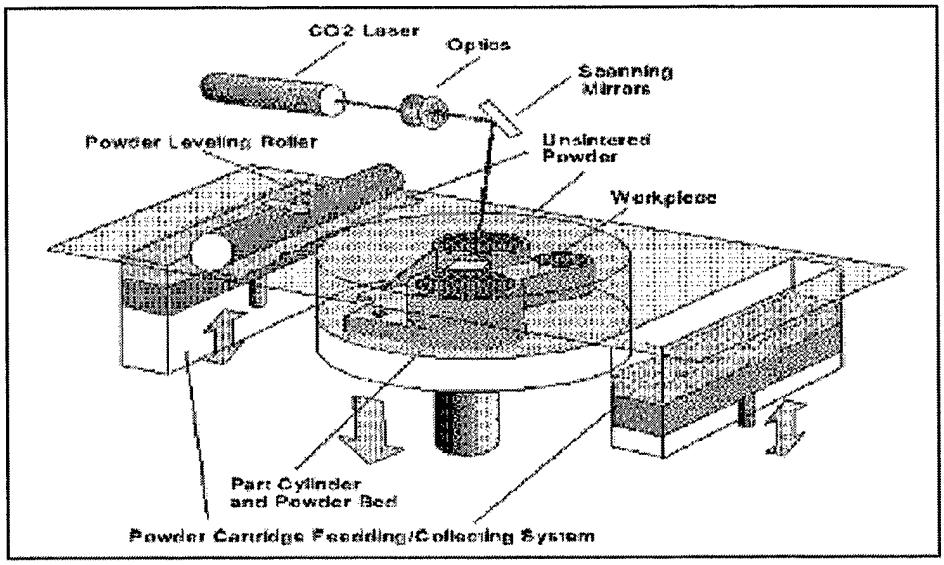


Figure 5: Schematic of the Selective Laser Sintering Process

Approach

The aim of the study, as stated before, is to process Parmax® SRPs using Selective Laser Sintering. There are many powder as well as process parameters that affect the quality of components produced. Hence, to manufacture functional prototypes, these parameters have to be optimized to achieve the desired values of performance variables(responses) such as strength, modulus and dimensional accuracy. Since the SLS process has not been mathematically modeled to the extent desired, a set of experiments need to be performed to identify important parameters and establish mathematical relationships between them that will help optimize the process.

The first step in the research process was to identify the parameters that could affect the process. An initial study revealed 12 SLS process parameters and 4 powder parameters that could be controlled. These are briefly discussed below.

SLS Process Parameters

The 12 SLS parameters are powder age, powder type, part bed temperature, feed piston temperature, part piston temperature, laser power, powder layer thickness, feed rate, chamber atmosphere, part orientation, roller speed and time between layers.

The first parameter to consider in the process is the type of powder to be used. There are currently 12 commercially available powders that can be used with the SLS process. Each of these have different physical properties and chemical properties and produce different results. This study focuses on only Parmax – a family of high performance amorphous poly p-polyphenes.

The designer then has the choice of using either new powder or recycled powder. The powder in the machine is pre-heated very close to its melting or softening temperature causing partial melting. This might cause clumping and hence change the particle size. Therefore, every time the powder is used, different laser power and pre-heating temperatures might be needed. Temperatures of the part bed, part piston and feed pistons have been observed to have a great effect on the properties of the final part. Normally, the feed pistons and part pistons are kept at temperatures below the part bed temperatures. This is to minimize powder clumping that might occur due to prolonged exposure of powder very close to its melting or softening point. The feed piston temperature and the part bed temperature have an effect on part curl, strength of part and on the dimensional accuracy.

The laser power is another important parameter. The laser power can be controlled by varying the incident laser power, the scan speed of the laser and the scan spacing of the laser. However the machine allows the user to change only the incident power. The laser power like the piston and part bed temperatures has a profound effect on the part curl, strength and dimensional accuracy.

The orientation is an important factor in determining the quality of the part. Because the build proceeds in the z direction(upward), taller part take longer to build. Hence the build time can be minimized by orienting the longer dimension of the part in the X or Y direction(parallel to the bed of the machine). Orientation may also effect the part strength because in the Z direction, there is a potential problem with proper bonding between the layers. This is also expected to cause a decrease in strength along the Z direction. Surface roughness is also effected by the part orientation. The layered nature in which parts are produces causes a "stairstep" effect on the surfaces that are not parallel or perpendicular to the part bed surface[14].

Layer thickness is a controllable parameter that effects many part properties. Among these are build time, strength, density and accuracy. The layer thickness is controlled by the movement of the part piston. More the movement of the part piston downward, more is the layer thickness. Coupled with the layer thickness is the feed rate which is determined by the distance moved by the feed pistons upward. The convention used in the process to ensure a uniform layer to be spread across the part piston is to have a feed rate that is twice the layer thickness. However, the particle size may effect the feed rate setting that is needed.

The roller speed and the time between layers are parameters that have an effect on the build time and is suspected to have an impact on the part curl. This is because the roller speed determines the time in which the powder is spread across the part piston and also the force it applies on the sintered part while the time between layers determines the amount of time the freshly laid powder has to attain the part bed temperature. If enough time is not given for the freshly laid powder to attain the part bed temperature, large temperature gradients might occur leading to excessive part curl.

An inert atmosphere in the chamber is required during processing to prevent oxidation that might cause loose powder to solidify. This is achieved by supplying a steady flow of nitrogen to the build chamber. The percentage of oxygen present in the chamber effects post processing and accuracy of the part. Since it is known that a more inert atmosphere would

always be preferred, a steady nitrogen flow is maintained to limit the oxygen content below 5.5%(default machine parameter value).

Powder Parameters

The four important powder parameters are particle size, density, viscosity and chemical structure.

Powder particle size determines the time taken for the powder to melt when sintered. Also it is related to the minimum powder layer thickness and the feed rate. Large particle size causes an increase in the layer thickness and leads to poor consolidation and hence strength. Thus it is important to arrive at an optimum particle size.

The density of the powder is known to have a direct impact on the strength of the processed component and also on the degree of consolidation. Typical densities of powders that have been processed are between 0.4 gm/cm^3 to 0.6 gm/cm^3

Viscosity determines the ease with which the powder flows and it is desirable that the powder exhibits low viscosity at the processing temperatures. However, modification of viscosity often entails a change in the chemical structure.

Chemical Structure of the powder is one of the most important parameters but often its modification is difficult and restricted. The structure of the polymer determines its viscosity, crystallinity and melting temperature.

Performing an exhaustive set of experiments taking all of the 16 variables into account is time consuming and a waste of resources. In order to identify those variables that have a major effect on the response, an initial set of experiments were performed. The work progressed on dual tracks. One was formulation of Parmax® SRP resins suitable for SLS and the other was SLS process optimization.

Initial formulation selection

Research effort executed under the Phase I SBIR Contract initiated with assessment of the critical parameters of the successful SLS formulations and the fit that current Parmax® SRP resin offer. The first parameter examined closely was the effect of the powder particle size. The focus was on the identification of Parmax® SRP resins with a range of particle sizes to bracket the acceptable limits on this parameter. The initial two formulations represented materials with mean particle sizes varying from 8 μm (1200-341) to 60 μm (1200-367). Bulk densities for the two formulations were 0.02 gm/cm^3 for 1200-341 and 0.25 gm/cm^3 for 1200-367 Micrographs of these two formulations can be found in Figures 6 and 7, respectively.

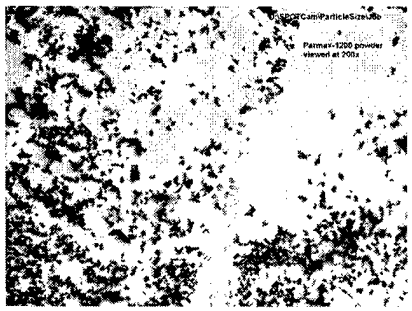


Figure 6. 1200-341 powder structure and size

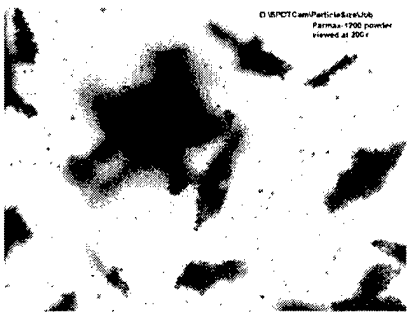


Figure 7. 1200-367 powder structure and size

Both of the formulations utilized in this first SLS iteration are the Parmax® 1200 derivative, the chemical structure of which can be found in Figure 8.

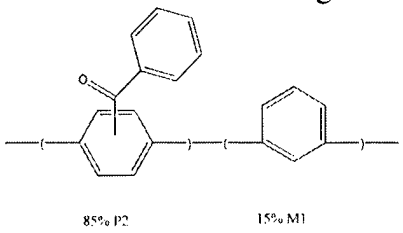


Figure 8. Structure of Parmax® 1200

Parmax® 1200 is a copolymer with about 15% of the flexible meta-phenylene linkages present. This intentional kink introduces a degree of flexibility to the otherwise rigid para-phenylene backbone. This limited flexibility is translated into improved processability and molecular flow above glass transition temperature (T_g), when compared to the completely rigid Parmax® 1000.

Initially, three materials were planned for the first iteration, with the remaining formulation being Parmax® 1200-367 with its particle size further reduced. This was attempted through the use of jet milling at Fluid Energy in Hatfield, PA. This vendor, however, failed to induce any particle size reduction. This was particularly puzzling, since the same vendor previously ground Parmax® 1200 to the 10-20 μm particle size specification. As a result of this failure, only 2 Parmax® SRP formulations were tested during the first iteration of this effort.

Initial sintering trials

Initial experiments were conducted using Parmax® 1200-367 to ascertain the feasibility of the process, reduce the number of process parameters by eliminating variables that had little effect on consolidation and to get the outer bounds on the important parameters. These experiments were driven by intuition and the insights obtained during experimentation and not by following formal experimentation methodologies. This was mainly because an exhaustive set of experiments could not be run with the powder available and the goals of the experiment did not warrant a large set of experiments to be run.

DSC curves of Parmax® 1200 indicated the onset of softening temperature (Tg) as 152 °C. With knowledge gained from processing parts using DuraForm (nylon-based SLS material), the part heater temperature was initially set at 132 °C, the left and right feed pistons were at 60 °C and a laser power of 5.5 watts (default power setting for DuraForm) was used. With these settings the powder did not consolidate. Hence the laser power was increased to 6 watts (at z

(measure of part thickness) = 0.012"). This did not alter the result and subsequently (at z = 0.016) it was increased to 9 watts. This sintered the powder to a greater extent but the sintered powder was turning brown (which at this point was thought undesirable). To minimize the discoloration the part heater temperature was increased to 132 °C (at z=0.02") and various laser powers were tried out. Also, part heater temperature was ramped up by 2 °C and at z = -.524" it was increased further by 4 °C to 142 °C. However, these changes brought about little change in the result. One main reason for not increasing the part heater temperature appreciably was to avoid solidification of all the powder in the part piston leading to wastage of large amounts of expensive powder. An interesting phenomenon that was noticed during the experiment was that at around 0.028", the sintered powder started warping and at 0.056" it was high enough to lead to movement of the part under the roller. Warping could occur due to the following reasons:(1) localized expansion due to uneven temperature gradients while scanning by the laser. (2) Excessive force applied by the movement of roller over the sintered part (3) uneven expansion due to a large difference in temperatures between the feed pistons and part pistons.

Green parts obtained in these first iterations can be seen in Figure 9. Following this stage, the parts were sent to Bodycote IMT for an additional HIP-ing step.

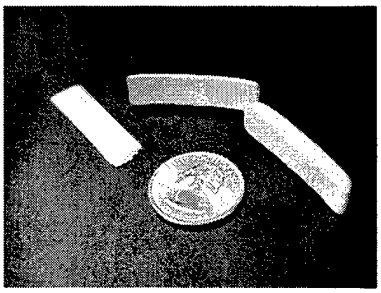


Figure 9. First Parmax® SRP parts produced via SLS

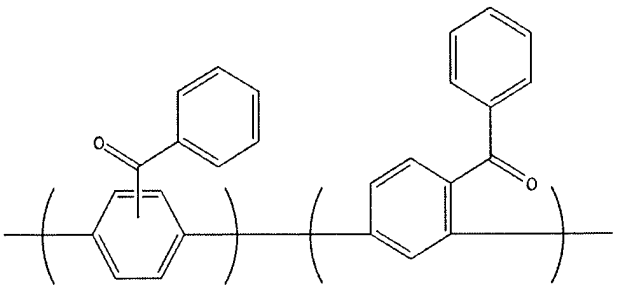
Through this experiment it was established that the grain size of the 1200-367 powder formulation was suitable for the SLS process, at least for the initial levels of consolidation. The roller was able to spread the powder evenly and bulk density variability was minimized. Based on the results of this run, overall powder bulk density and viscosity of the powder at these temperatures might have to be varied to optimize the consolidation. From the point of view of the process parameters, the operating temperatures could be increased, other parameters like roller speed, power layer thickness and feed distance need to be controlled so as to determine their impact on warping and powder consolidation.

The second material formulated for this iteration, Parmax® 1200-341, could not be adequately processed owing to the extremely low bulk density of this powder. Even though it appeared that the small particle size would be beneficial from the standpoint of better surface finish as well as larger particle surface area for laser to operate on, the flocculent nature of this material did not allow the Sinterstation 2000 roller to distribute the powder evenly.

Formulations aimed at viscosity reduction

Based on results obtained during the first half of the effort, a second iteration of materials was formulated for the laser sintering trials. The stated goal during this phase of the effort was an improvement of the molecular flow of Parmax® SRP resins at the Sinterstation operating temperatures. Formulations were as follows:

- Plasticized Parmax® SRP formulation (1200-366), containing 15% of di-octyl phthalate (DOP), an esteric plasticizer commonly used in PVC industry. DOP and Parmax® SRP resin were compounded using a 1" Davis Standard Killion Single Screw Extruder (SSE). Approximately 6 lbs of this formulation was produced and pelletized. Pellets were then sent to Particle Reduction Corp of Elk Grove Village, IL for another attempt at particle reduction. The two processes used were hammer milling and jet milling. Hammer milling successfully ground Parmax® SRP pellets to approximately 500 μm particle size (consistency of beach sand). Unfortunately, further milling, utilizing the jet milling facilities, was again unsuccessful.
- Formulation utilizing a different copolymer of Parmax® SRP materials, Parmax® 1215K (Formulation designation 1215-373), structure of which can be found in Figure 10. This chemical structure modification had a goal of reducing the viscosity of the resulting material at Sinterstation processing temperatures, and also to examine the suitability of chemistry modification as means for optimizing sinterable Parmax® SRP derivatives. Viscosity reduction is achieved through an addition of benzoxy-substituted meta-phenylene linkage. This hinders efficient packing of the rigid rod backbone chains, resulting in increased disorder within the polymer lattice. Resulting free volume increase translates into lower viscosity at processing temperatures of interest. 1215-373 had particle size of approximately 70 μm with bulk density of 0.23 gm/cm^3.



Parmax-1215

Figure 10. Chemical structure of Parmax® 1215K

Sintering studies of 1200-366 and 1215-373

As a baseline for this round of sintering trials, conditions that led to the consolidation of parts in the first iteration were replicated. It became immediately obvious that 1200-366's sand-like powder consistency was unsuitable for laser sintering process, owing to the inability of the Sinterstation roller to distribute the material evenly across the sintering surface. The second formulation, labeled 1215-373 was successfully consolidated using the same parameters utilized in previous successful consolidation, 1200-367. Following the baseline establishment, the remainder of the machine time was devoted to the sintering parameter optimization, utilizing 1200-367 and 1215-373 materials.

Effect of the powder layer thickness on part consolidation and warping

Localized expansion arising from uneven temperature gradients while scanning by the laser might be affected by process parameters such as powder layer thickness, time between layers, feed distance, part heater temperature, laser power used and the left and right feed temperature. The third experiment concentrated on studying the effect of powder layer thickness, feed distance and part heater temperature.

Left and right feed distances were set initially at 0.014" and the powder layer thickness was increased to 0.006". The left and right feed heaters were set at 120°C during the warm up stage and at 145°C during the sintering stage. However, owing to the technical difficulties with Sinterstation 2000, the powder could not be heated beyond 115°C. The part heater was set at 154°C and laser power used was 6 watts. The increase in the powder layer thickness and the feed distance did not seem to have an impact on the warping and so the powder layer thickness and feed distance were decreased to 0.005" and 0.012" respectively (at z=0.18") while the part heater temperature was ramped up to 165°C to aid consolidation of powder. To prevent discoloration of the powder, the laser power was not increased beyond 7.5 watts.

Based on these results, we suspect that powder layer thickness and feed distance were not the primary reasons for uneven temperature gradients and localized expansion leading to warpage. Also, we conclude that the temperature reached by the powder on preheating to 165°C and application of laser power of 7.5 watts is not high enough to sinter it completely.

Impact of roller motion

The next experiment focused on studying the effects of the roller motion over the sintered part and also the time elapsed between laying of fresh powder by the roller and the start of the sintering process. The movement of the roller carrying powder might apply a force on the sintered part that is enough to cause yielding. So in this experiment the roller speed, and the amount of powder it carries, which is directly related to the feed distance, are varied, as is the time between which layers of powder are laid down.

During this run, the left and right feed distances were set at 0.012"; the feed heaters were at 120 °C while the part heater was set at 175 °C (10 degrees more than the previous experiment). The laser power was maintained at 6.5 watts through out the experiment. The roller speed was at the default value of 5 in/sec but the time between layers was set at 50 sec (default value 15sec). At various points in the experiment, the roller speed was varied from a minimum of 3 in/sec to 7 in/sec and the feed distance between 0.012" to 0.035". The effect on warping seemed minimal. The part heater temperature was increased to 180 °C and then to 190 °C. At these high temperatures, the powder in the part piston had started clumping and hence the roller was unable to spread the powder evenly. The clumping might have occurred because the temperature was too high or because of prolonged heating (the powder was at these temperatures for around 3 hours and being amorphous in nature might have started softening and coagulating gradually).

Laser power optimization

Through this experiment we aimed at obtaining the outer bounds for the laser power. The part heater, piston heater and feed heater temperatures were set at 165°C, 130°C and 100°C respectively. Laser power was varied from 6 watts to 30 watts. At values beyond 15 watts, the laser power was high enough to totally degenerate the powder. The powder was getting

completely charred at these high values, establishing the upper bound for the laser power application to Parmax® SRP resins.

From the above experiments, we conclude that the most important parameters that seem to impact sintering as well as warping are the feed piston temperatures, part heater temperature and laser power. Overall, these experiments were successful in eliminating 3 parameters (time between layers, roller speed and piston heater temperature). Also, it helped us obtain the outer bounds of part heater temperature and laser power. This information is going to be crucial in reducing the number of variables to be examined during the next phase of research, therefore speeding up the screening process and allowing us to concentrate on mission critical parameters.

Results

During the first phase of study, we have demonstrated successful processing of Parmax® SRP resins using Selective Laser Sintering (SLS) techniques, offering the prospect of rapid prototyping of components with unprecedented mechanical properties. This phase also elucidated the requirements for development of commercially practical Parmax® SRP SLS materials.

The research performed thus far consisted of these distinct phases:

Materials Formulation: The initial phase involved selection and development of sinterable powder formulations based on Parmax® SRP resins that would be suitable for processing by Selective Laser Sintering (SLS) rapid-prototyping process. Four candidate powder formulations were screened for sintering. Decisions to focus on these four candidate formulations were based on a number of properties of interest, most importantly powder particle size, viscosity, chemical structure and bulk density.

SLS Trials: Following the identification of the candidate formulations by MPT, initial processing studies at The University of Texas at Austin were performed. Following the initial parameter determination, a set of conditions were selected and the initial fabrication of the parts was undertaken. This formulation iteration consisted of 2 formulations, one of which failed due to the low bulk density and tackiness of the powder (Parmax® 1200-341). Using the second formulation, Parmax® 1200-367, with a bulk density an order of magnitude higher than the first attempt, initial test coupons were successfully fabricated. Both of these formulations are based on Parmax® 1200, structure of which is illustrated in Figure 8. Dimensions of the first parts were approximately 30 mm × 7 mm × 1-3 mm. Following a successful consolidation phase, green parts were subjected to Hot Isostatic Pressing (HIP) at Bodycote IMT of London, OH.

Mechanical Properties Assessment: Following this densification step, initial mechanical properties were measured(by standard 3 point bend test) and are reported in Table 2, along with typical properties of nylon and polycarbonate prepared by the SLS process. This data confirms the hypothesis that the intrinsically higher modulus and strength properties of Parmax® SRP resins would translate into higher mechanical properties of the SLS processed components when compared to the current materials in use. This is even more remarkable when considering that the bulk density of Parmax® SRP resin utilized in these experiments is less than 50% of the conventional SLS materials.

Material	Powder Bulk Density	SLS Properties	
		Tensile Strength	Flexural Modulus
Nylon	0.5-0.6 gm/cm^3	5,200 psi	0.13 Msi
Polycarbonate	0.6 gm/cm^3	3,400 psi	0.15 Msi
Parmax®+ 1200	**0.25 gm/cm^3**	**~10,000 psi**	**0.40 Msi**

Table 2. Comparison of mechanical properties of Parmax® 1200 and other SLS materials

Based on the knowledge base acquired during the first effort iteration, a second set of formulations was produced in an attempt to improve on the sintering characteristics observed during the initial trials. These included a structurally modified component, Parmax® 1215-373 (Figure 10), and a plasticized formulation to reduce the viscosity (Parmax® SRP 1200-366). One of the formulations, Parmax® 1200-366, underwent particle reduction via a hammer mill in order to obtain the powder necessary to attempt laser sintering. The second iteration of the sintering trials succeeded in fabricating parts of comparable quality to 1200-367 using Parmax® 1215-373, while the plasticized Parmax® 1200-366 proved very difficult to feed, owing to the very coarse grain structure resulting from the particle reduction operation. Optimization of the laser sintering conditions was relatively limited owing to the small supply of candidate resins, as well as some machine limitations with Sinterstation 2000 at University of Texas. However, preliminary sintering condition optimization successfully eliminated several variables, thus rendering the next phase optimization effort a much less time intensive task.

Conclusion and Future Work

In summary, this research effort was successful in demonstrating that Parmax® SRP resins can be consolidated utilizing the SLS process. Sintered components were tested for mechanical properties and, as expected, far exceed mechanical properties obtainable with conventional SLS polymeric materials, even in their current un-optimized state, thus fulfilling all three of the objectives. Work performed on a structurally modified Parmax® 1215-373 also opens up new and exciting possibilities for optimizing the sinterability of Parmax® SRP resin even further through judicious chemistry and structure manipulation. This reinforces the promise that these materials hold for Rapid Prototyping applications following the optimization during the next phase of research. Commercial potential of this development will be especially significant in laser sintering of a wide variety of low-volume, high integrity components for many possible commercial and industrial prototype needs, as well as prototyping needs in aerospace, military and tooling areas. The ultimate goal of this project is to produce materials strong enough to be utilized as fully functional prototypes, not only visual design aides, and thus fulfill one of the most vexing needs of the laser sintering community. Parmax® SRP materials appear ready to be the materials the rapid prototyping community relies on to achieve these ambitious goals.

+ Properties measured after Hot Isostatic Pressing

Recommendations for further work involves continuing focus on optimization of Parmax® SRP materials that were initially processed by laser sintering techniques during the current study as well as the optimization of the Laser Sintering processing parameters. Therefore, a dual track approach is recommended:

Optimization of resin molecular architecture and composition (e.g., molecular weight and distribution, melt rheology, additives, co-monomer selection, degree of crystallinity etc.) and powder characteristics (e.g., particle size and distribution, bulk density, etc.) to enable effective sintering with high retention of mechanical properties. This work will be performed under a rigorously designed experimental matrix in order to maximize the efficiency of the research effort.

An optimal set of laser sintering conditions will be established. This will draw on the preparation of initial test coupons fabricated at the University of Texas at Austin during the Phase I effort, and will be performed on statistically based Design-Of-Experiments (DOE) principles. This work will be performed at University of Texas' Laboratory for Free Forming (where the technique was invented) to insure successful Laser Sintering parameter establishment.

References

1. Adams, W.W.; Eby, R.K.; McLemore, D.E.; Editors "The Materials Science and Engineering of Rigid-Rod Polymers," *Mat. Res. Soc. Symp. Proc.* **1989**, Volume *134*.

2. Beaman J. J.; Barlow J. W.; Bourell, D. L.; Crawford R. H.; Marcus, H. L.; McAlea, K. P.; *Solid Freeform Fabrication: A new direction in Manufacturing: With research and applications in Thermal Laser Processing.* Kluwer Academic Publishers, **1997**.

3. Konstandakopoulou, F. D.; Gravalos, K. G.; Kallitsis, J. K. *Macromolecules* **1998**, 31, 5264-5271.

4. Nieuwhof, RP; Marelis, A. T. M.; Sudhoter, E. J. R.; Picen, S.J.; de Jeu, W. H. *Macromolecules* **1999**, 32, 1398-1406.

5. Puciarello, R.; Angioletti, C. *J. Polym. Sci.Part B: Polym. Phys.***1999**, 37, 679-689.

6. Kodaira, T.; Endo, M.; Kurachi, M. *Macromol. Chem. Phys.* **1998**, *10*, 2329-2339.

7. Kricheldorf, H. R.; Domschke A. *Macromolecules*, **1996**, 29, 1337-1344.

8. Grob, M. C.; Feiring, A. E.; Auman, B. C. *Macromolecules*, **1996**, *29*, 7284-7293.

9. Ge, J. J.; Guo, M.; Zhang, A.; Honigfort, P. S.; Mann, I. K.; Wang, S.; Harris, F. W.; Cheng, S. *Marcromolecules* **2000**, *33*, 3983-3992

10. Lindsay Smith, J. R.; McKeer, L. C.; Taylor, J. M. *J. Chem. Soc.; Perk. Trans. 2* **1989**, 1529-1537.

11. Oberhauser, T. *J. Org. Chem.* **1997**, 62, 4504.

12. Grob, M. C.; Feiring, A. E.; Auman, B. C. *Macromolecules*, **1996**, *29*, 7284-7293.

13. Percec, V., Zhao, M., Bae, J. Hill, D. *Macromolecules*, **1996**, *29*, 3727-3735.

14. Watson, D.A., *Process Optimization for Selective Laser Sintering Through the Use of Design Rules and Constraints*, Master's Thesis, The University of Texas at Austin, **1999**

15. Sutherland, J.W., DeVor, R.E., Chang, T., *Statistical Quality Design and Control*, Prentice-Hall, Inc, **1992**

16. Montgomery, D.C., *Design and Analysis of Experiments*, John Wiley and Sons, **1991**

EFFECTS OF AGING ON EPOXY-BASED RAPID TOOLING MATERIALS

Xavier Ottemer and Jonathan S. Colton
Center for Polymer Processing, Rapid Prototyping and Manufacturing Institute, and
School of Mechanical Engineering
Georgia Institute of Technology, Atlanta, GA 30332-0405 USA

Abstract

This study shows the effects of aging on epoxy-based rapid tooling materials. Two epoxy-acrylate resins used for stereolithography and one aluminum powder-filled epoxy used for the high speed machining of plastic injection molds were selected to investigate their aging behavior in different environments. Four different conditions, each characterized by a specific relative humidity, were used to perform a seven week long aging study. Temperature was kept constant at 30°C. Both stereolithographic resins showed a drop in mechanical properties and in their glass transition temperatures in wet environments, whereas aging time showed little influence on these properties. Moisture uptake is mainly responsible for that drop and coefficients of water diffusion were determined. On the other hand, the aluminum powder-filled epoxy showed little humidity-dependent drop in mechanical properties and in its glass transition temperature during aging. This result correlates well with the very low moisture absorption of this material.

Introduction

Prototype tooling for injection molding applications needs to have a long lifetime regardless of storage conditions. Many RP's materials are polymer-based. It is imperative therefore that test methods be developed in order to predict the long-term durability of these materials in different environments. This study (Ottemer, 2001) focuses on three materials that can be used for soft tooling for injection molding applications: Somos SL7110, Ciba SL7510, and Vantico Renboard Ren Shape-Express 2000. Both SL7110 and SL7510 are epoxy-acrylate photopolymers for stereolithographic systems manufactured by 3D-Systems. Ren Shape-Express 2000 is an extremely fast milling aluminum powder-filled epoxy for prototype and short run tooling. These three materials are representative of the current trend in polymer-based rapid tooling materials.

Aging of polymers

Aging is the term given to various processes that degrade polymers over time. During aging, one or more environmental stress factors act on the bulk polymer. The effects of these stress factors are translated to the microscopic/molecular level where changes occur in the polymer network or chain. Allred (1981) used the glass transition temperature as an indicator of any physical changes in the resin due to aging.

Hydrolytic aging is the greatest concern as contact with water is almost unavoidable. Moisture has the most significant effect on the reduction in the properties of these materials. Moisture exposure has two important components:

- Diffusion of water into the sample: the moisture absorption of a resin can be attributed to the water's affinity for the highly polar functional groups in the cured resin.
- Plasticization of the resin: on a molecular level the effect of water associating with polar groups is to decrease the hydrogen bonding between polymer chains which causes plasticization of the resin (Roe, 1991).

Time-humidity superposition principle

Moisture accelerates the aging process in the same way as temperature. A time-moisture principle has been proposed by Knauss and Kenner (1980) where the effect of moisture could be explained by the time-humidity superposition principle using a shift factor as shown in Equation 1.

$$\log(a(c)) = -\frac{B_1(c - c_0)}{B_2 + c - c_0} \tag{1}$$

Where a(c) is the shift factor; B_1, B_2 are constants determined by regression; c, c_0 are the moisture concentrations at time t, and at an arbitrary reference time, respectively.

Sample Preparation

Samples made of SL7110 for tensile, diffusion, and DMA tests were built with 3D-Systems's stereolithography machine SLA250. Samples made of SL7510 were built with a SLA3500. Parts were all built vertically on the platform. After part formation, the excess resin was removed by rinsing with tripropylene glycol monomethylether, followed by a rinse in isopropyl alcohol. Then the parts were post-cured for 60 minutes with UV light and for 120 minutes in a thermal oven at 80°C. RenBoard was shaped into samples using a conventional milling machine.

Study of Moisture Diffusion

Time dependence of coefficient of diffusion

The diffusion behavior of glassy polymers cannot be described adequately by a concentration-dependent form of Fick's law with constant boundary conditions. Deviations from Fickian behavior are considered to be associated with the finite rates at which the polymer structure changes in response to the sorption or desorption of penetrant molecules. This viscous behavior of the polymer makes the diffusion time-dependent. Three different equations were used to fit the data because the diffusion behavior of the resin systems did not strictly follow any well-known model. Coefficients of diffusion were determined by plotting the short-time, average, and long-time diffusion data using equations from Crank (1975). For short times, Equation 2 was used.

$$\frac{M_t}{M_\infty} = \left(\frac{16 D_s t}{\pi L^2}\right)^{\frac{1}{2}} \quad (2)$$

Where M_t is the mass uptake at time t, M_∞ is the mass uptake at infinite time, D_s is the coefficient of short-term diffusion, t is the time, and L is the thickness of sample. Coefficients of long-time diffusion were computed using Equation 3, where D_l is the long term diffusion coefficient.

$$\frac{M_t}{M_\infty} = 1 - \frac{8}{\pi^2}\exp\left(\frac{-D_l \pi^2 t}{4L^2}\right) \quad (3)$$

Then, assuming that the coefficient of diffusion is independent of solvent concentration, an estimated average of this coefficient can be derived with an error being about 0.001 percent using Equation 4 where the value of (t/L^2) for which $M_t/M_\infty = 1/2$ is defined as the half-time, $(t/L^2)_{1/2}$.

$$D_{av} = \frac{0.049}{(t/L^2)_{1/2}} \quad (4)$$

Moisture uptake measurements:

ASTM D-570 is a standard test practice for water absorption. Eight standard specimens of each material were made. The dry weights of the samples were recorded with an accuracy of 0.1 mg. Then half of each kind of sample were put in pure water (humidity=100% and T=30°C) and the remaining half in saturated salt-water. This aqueous solution has an equivalent relative humidity of 75.1±0.1% at 30°C, according to the ASTM E104. However, this solution is not totally equivalent to a 75.1% RH environment because the osmotic pressure created by Na^+ and Cl^- ions will affect the leaching out of the polymer.

The samples were weighed at 2 hrs, 4 hrs, 6 hrs (RenBoard), 8 hrs (RenBoard), 24 hrs, one week, and every two weeks until they absorbed less than 1% of the total weight gain or 5 mg per two weeks, whichever was greater. After all the test samples reached the termination criteria, they were placed in a dessicator overnight, and then reweighed in order to observe any leaching out of the materials. Figure 1 shows the weight gain versus time of the three materials. By comparing the main trends of the mass uptakes for the three materials, it appears that SL7510 absorbs the most water and RenBoard the least. Also, the infinite moisture absorption for both SL7110 and SL7510 is lower when immersed into salt-water, equivalent to a 75.1% RH environment, than in distilled water. That was not observed with RenBoard.

The coefficients of diffusion are shown in Table I. These values are consistent with values of coefficients of diffusion of water in other commercial resins (Becker and Colton, 2000). RenBoard shows an odd behavior - the coefficients of diffusion for salt-water immersion are higher than those for water-immersion. This may be due to a chemical interaction between ions (Na^+,Cl^-) and the aluminum filler. Moreover a change of color from gray to brown has also been observed after 1 week of salt-water immersion and after 3 weeks of water-immersion. Only SL7510 immersed into water has shown some significant leaching out (3% of material loss).

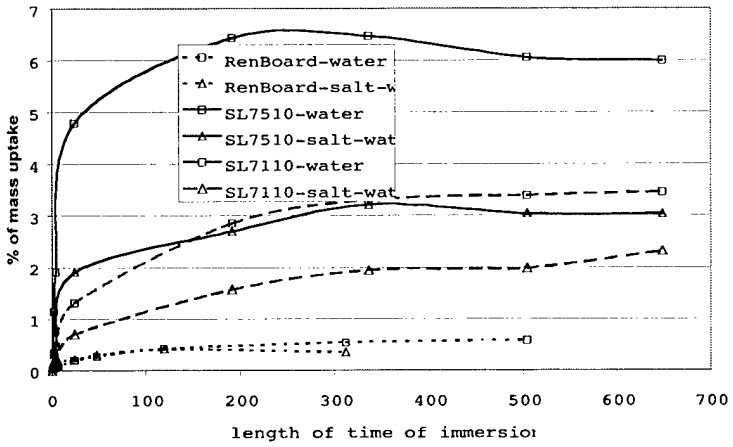


Figure 1: Water uptake

Table I: Coefficients of diffusion

mm^2/s	D short	D average	D long
SL7510 - 100%RH	10.0E-7	21.8E-7	13.8E-7
SL7510 - 75%RH	3.1E-7	9.2E-7	8.6E-7
SL7110 - 100%RH	3.3E-7	9.4E-7	2.3E-7
SL7110 - 75%RH	2.1E-7	5.4E-7	1.4E-7
RenBoard - 100%RH	2.1E-7	8.5E-7	2.5E-7
RenBoard - 75%RH	10.7E-7	20.7E-7	7.4E-7

Aging study

Eighty-four samples of each material were immersed in distilled water at 30°C. The same number of samples were put in a bath of saturated aqueous salt solution, equivalent to a 75.1% RH environment at 30°C. Another set of samples were exposed to ambient atmosphere kept at 30°C (dry-bulb temperature) by the use of a ventilated thermal oven. The RH of the environment varied other time due to weather conditions. It was 30±5% at 30°C during the aging study on SL7510, 23±5% at 30°C during the study of SL7110, and 20±6% at 30°C during the study of RenBoard. Finally, a dessicator placed in the oven provided dry conditions for the last set of samples.

Mechanical properties:

At specified aging times, two sets of three samples of each material were removed and dynamical mechanical analysis (DMA) and tensile test were performed.

Storage modulus E' and Glass Transition Temperature T_g.

These characterizations were made with DMA testing (DMA 2980, TA Instruments, New Castle, DE) in the single cantilever flexural mode at a frequency of 1Hz and an amplitude of deformation of 20 _m. E' and T_g were recorded during a temperature ramp of 3°C/min from 30°C to 130°C for both SL7110 and SL7510 and from 30°C to 270°C for RenBoard. T_g was measured at the peak of tan_=E"/E'.

Young's modulus and ultimate tensile properties

Standard ASTM D638 was used as a guideline for the mechanical testing procedure. A tensile testing machine (Instron 4466, Canton MA) with a 10 kN load cell was used, and an extensometer was mounted on the sample. The cross head speed was 0.25 cm/min. Both strain and load were recorded.

Aging behavior of SL7510 and SL7110:

The evolution of the glass transition temperature is a good indicator of the aging behavior of a material. Figure 2 shows the evolution of the T_g of SL7510. After an induction period of around 400 hr due to diffusion of water inside the materials (area I on Figure 2), the T_g becomes time-independent and shows a marked decrease with RH due to the effect of moisture uptake on the material (area II on Figure 2). From 96°C for the dry environment, the T_g of SL7510 drops down to 55°C for the wet environment. This drop is an indication that the resin is being plasticized by moisture uptake.

The results of the mechanical tests are similar for both SL resins, showing a drop in properties in wet environments, except for the yield strain which remains mostly unaffected and constant, whatever the aging time or the RH of the environment.

After a 400 hr induction period, aged SL7510 samples show a 66% decrease in ultimate tensile strength from dry to wet environments. Initial properties were UTS = 54.5 MPa, E = 2407 MPa, E' = 2200 MPa, and ultimate strain = 5.75%. On the other hand, the tensile strength remains constant for the dry environment, with a slight increase observed. The storage modulus, E', and the Young's modulus, E, of SL7510 also reveal the same behavior (Figure 3): first an induction period followed by a time-independent, RH-dependent stage. It also is observed that the ultimate and yield strengths of SL7510 decrease with RH in the same way as T_g, E', and E.

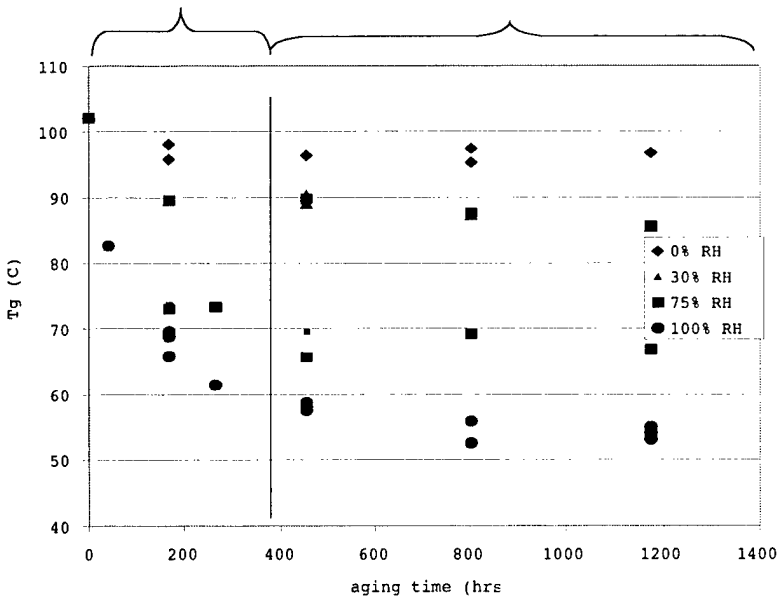


Figure 2: Tg of SL7510

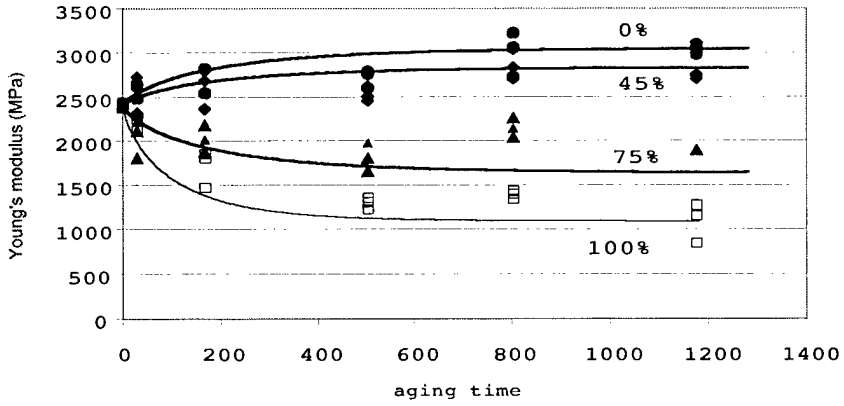


Figure 3: Young's modulus of SL7510

The same overall behavior is observed for SL7110, but to a lesser extent. Its initial values were UTS = 52 MPa, E = 2450 MPa, E' = 2000 MPa, and ultimate tensile strain = 4.6%. After an induction period of around 400 hr, the T_g becomes more time-independent and shows a marked decrease with RH (Figure 4). From 108°C for the dry environment, the T_g drops down to 75°C for the wet environment. The mechanical test results indicate the same, showing a drop in properties in wet environments, but here the properties are ruled by a 200 hr induction stage. The ultimate tensile strength is 25.3% higher than initially in dry and ambient environments, remains constant when immersed into the 75.1% RH environment, and drops 12% from its unaged value when submitted to the wet environment.

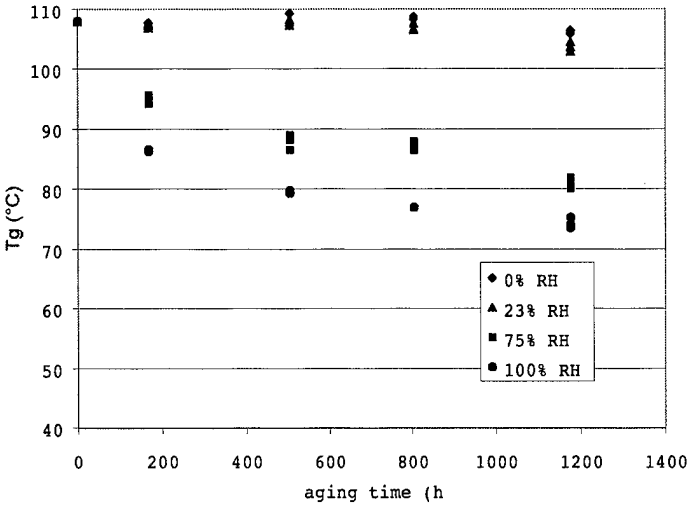


Figure 4: Tg of SL7110

Aging behavior of RenBoard:

RenBoard does not behave like the two other materials. The initial values were UTS = 52 MPa, E = 15000 MPa, E' = 6026 MPa, and the ultimate tensile strain = 0.83%. Figure 5 shows the evolution of the T_g of RenBoard with aging time. The variations observed are not significant. The T_g remains quite constant at 248°C whatever the aging time or the RH of the environment. The mechanical results indicate the same, showing almost no significant variations. Whatever the aging time or the RH, the material failed in a brittle manner. This is different from the behavior of SL7510 and SL7110.

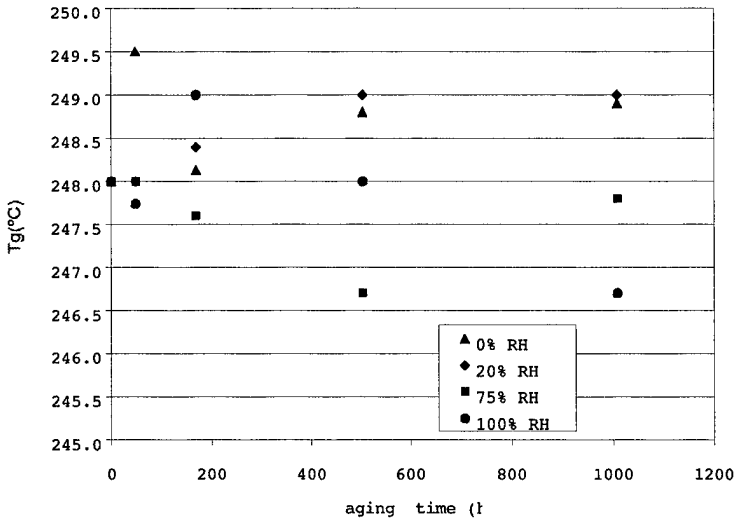


Figure 5: Tg of Renboard

Conclusions

The aging behaviors of three epoxy-based rapid tooling materials were investigated under four different moisture environments at 30°C over seven weeks. Two were stereolithographic resins and showed a drop in mechanical properties and in their glass transition temperatures in wet environments, whereas aging time had no significant influence on these properties. The magnitude of the drop of mechanical properties was found to be related directly to the magnitude of the moisture uptake by the material. The properties (T_g and mechanical properties) first undergo an induction period led by moisture absorption and then reach asymptotic values, which are functions of the infinite mass-uptakes. The higher the moisture absorption, the more affected are the properties. The third material, an aluminum-filled epoxy, did not show significant humidity-dependent drops in mechanical properties and in its glass transition temperature. This result correlates well with the very low moisture absorption ability found for this material.

Acknowledgments

This work has been made possible thanks to the National Science Foundation (DMI-9618039) and the Rapid Prototyping and Manufacturing Institute, whose member companies include 3D-Systems, 3M, Baxter, Ciba, Club Car, Durden Enterprises, Ford, Kodak, Lucent Technologies, Pratt&Whitney, and Siemens.

References

Allred, R.E. (1981), Journal of Composite Materials, Vol. 15, No. 2, 117-132.

Becker, K. and Colton, J.S. (2000), Polymer-Plastics Technology and Engineering, Vol. 39, No. 4, 667-682.

Crank, J. (1975), The Mathematics of Diffusion, 2nd Edition, Oxford: Oxford University Press.

Knauss, W.G., and Kenner, V.H. (1980), Journal of Applied Physics, Vol. 51, No. 10, 5131-5136.

Kelen, T., (1983), Polymer Degradation, New York: Van Nostrand Reinhold.

Ottemer, X. (2001), Effects of Processing and Environmental Conditions on the Properties of Epoxy Materials, M.S. thesis, Georgia Institute of Technology, Atlanta, GA.

Roe, R.J., and O'Reilly, J.M., Eds. (1991), Structure, Relaxation, and Physical Aging of Glassy Polymers, Pittsburgh, PA: Materials Research Society.

imits of Loose Metal Powder Density in the Sinterstation

Klas Boivie
Woxéncentrum, KTH, The Royal Institute of Technology
Sweden

Abstract

The possibility to increase the density of applied metal powder in the Sinterstation has been investigated by successive addition of smaller sized particle fractions to a base powder. The optimal composition for each blend was determined experimentally, and their apparent densities were compared to the densities after Sinterstation application. The principal limiting factors for the density of metal powder in the Sinterstation were found to be the interparticle friction and the small sized particles' tendency to form a suspension in the air. Finally, based on the evaluation of the different powder compositions' behavior, a practical upper limit of loose metal powder density was estimated to 86%, when applied by a Sinterstation. The highest applied powder density in this investigation was a binary blend with 68.60% relative density.

1. Introduction

Some of the major challenges facing the SFF technology today are concerned with the manufacturing of tools and other objects in metal. Several technologies have been developed, but despite rapid progress there are still many more challenges to meet and properties to be improved. The commercial direct tooling and metal applications of SFF technology are dominated by different powder based techniques, such as DTM's SLS, EOS' DMLS and ProMetal. In all these approaches, the materialization of objects starts by the spreading of loose powder layers over a processing area. The particles are then either fused by a melting fraction of the compound with the laser, and thus densify by pointwise liquid phase sintering (EOS), or glued together for sintering and infiltration in a separate furnace (DTM, ProMetal). Both strategies does somewhat limit the possible material systems and no manufacturer has yet marketed a hardenable tool steel material. However a combined approach, using liquid phase sintering of the whole object during a separate furnace cycle, could probably be used to overcome this gap [1], [2].

In all these approaches a crucial point is the density in the applied powder layers. For the furnace requiring approaches, 50% density is a minimum to avoid distortion during processing [3]. An increased loose powder density would, apart from improving green strength, also have a positive impact on precision and surface quality as well as decrease the need for liquid phase or infiltrant in order to reach the desirable density It is the purpose of this present work to investigate the practical possibility to increase the density and improve the quality of the loose powder mass applied by a Sinterstation, by the addition of finer powder grades. Thereby indicate what the main limiting factors are, and whether there is an upper practical limit, for the loose metal powder density in the current Sinterstation system.

2. Background

The packing of particles is a field of importance not only within the area of metals SFF, but in a vast range of areas. Needless to say, it has, in different forms been the subject of research several times before. In a fundamental work Mc Geary [4] investigated the basic scientific laws for the packing of spherical particles, and an arrangement with 95.1% of theoretical density was reported. To achieve this, a four component packing composition was used, where each finer grade was vibrated into the voids of a matrix formed by the larger sized grains. Powder densities of that magnitude are usually found only in compressed green bodies prior to sintering. Even though such reports are encouraging, the set up was idealized, and the results could probably not be duplicated on a practical SLS system.

In the field of SFF, Karapatis et. al. [5] used an idealized experimental set up to investigate the effect of relative size ratio on the density of a single applied layer of a binary powder blend, and thereby achieved binary layers with 63% relative density. However the size range used for the particles (up to 150 μm) was but a bit outside what could be used in a practical SFF system with acceptable precision. Furthermore, only single layers were used which gave a large influence to wall effects, which may not be as important in a real powder spreading process. In particular as the spreading procedure used was not similar to the counter-moving roller used in the Sinterstation.

This work takes a practical approach to powder application. The powders were experimentally applied in a Sinters station, and powder grades were primarily selected in respect to:

1. Size range; for optimal packing of a loose powder mass, it is necessary that the finer powder grains are filling the voids between the larger grains. From a theoretical analysis it has been found that suitable proportions would be 1:7:49:343…[6]. The largest grain size is determined by maximum acceptable layer thickness, which, in respect to precision, is 0.1 mm. The smaller grain sizes are limited by availability in the suitable size range.

2. Shape; smooth spherical shape is superior in respect to internal friction and packing properties [6],[4].

3. Availability; all powders used should be available as commercial grades.

4. Handling; since the current Sinterstation systems requires manual powder handling, it should be possible to handle the powders without damaging the equipment or the health of the operator.

These aspects taken in respect, suitable iron base alloyed powders were selected, Due to limited availability in the smaller size ranges, the number of components in the powder blends are limited to three. If the wall effects are a dominant limiting factor also in reality, then the applied powder density should in all cases be smaller compared to apparent density. To investigate this, each powder compound was prepared with an experimentally determined composition, and the apparent density prior to Sinterstation application was measured to be compared to the density of the applied powder mass.

3. Experimental

3.1 Experimental procedure

A Sinterstation 2000 was used in these experiments. The apparent density of each powder prior to Sinterstation application was measured by a simple procedure with a graduated cylinder and a precision scale. A generic build file was used to apply a sufficient amount of powder in the Sinterstation's part cylinder. After termination of the build, the powder in the build chamber was removed in level with the chamber floor, and the position of the part piston was noted $_2$). The powder in the part cylinder was removed by subsequently raising the piston 0.5 mm, and scraping off each layer with a straight edge blade. This was repeated until all the applied powder was collected in a container, and the second position of the part piston was noted (h_1). The powder mass in the container (m) was weighed on a precision scale and the density of the applied powder $(\rho_{app.})$ as well as relative density $(\rho_{rel.})$ was calculated by relation with part cylinder volume (V) and theoretical density of the massive material (ρ_m).

$$\rho_{rel} = \frac{\rho_{app}}{\rho_m}; \text{ where } \rho_{app} = \frac{m}{\left[\frac{d_{cyl.}}{2}\right]^2 \pi[h_1 - h_2]} \qquad \textbf{Eq. 1. \& 2.}$$

Each powder went through several experimental cycles in order to establish the powder mass' behavior in the Sinterstation under varying powder application conditions, such as feed rate and roller speed. Following this procedure the behavior of powders, consisting of one, two and three components were examined in respect to general powder behavior and applied powder density. To ensure comparability between the different powders, each composition was made by adding a smaller grained fraction to the previous powder compound.

3.2 One Component

3.2.1 The Powder

Large sized grains: For bulk material, a highly alloyed, gas atomized tool steel powder, Anval 60, from Dynamet Anval, was selected, see **Fig. 1.** The chemical composition and size range of this powder can be found in **Tables 1 & 2.**

Table 1

lement	C	Si	Mn	P	S	Cr	N	Mo	Co	V	W	N	Fe
%	2.39	0.54	0.47	0.022	0.047	4.29	0.19	6.86	10.2	6.52	6.6	0.053	Bal.

Table 1. *The chemical composition of Anval 60.*

Table 2.

Micron	90	75	63	45
Mesh	170	200	230	325
%<	96	76	43	8

Table 2. *The sieve analysis, (ASTM-E11) of Anval 60.*

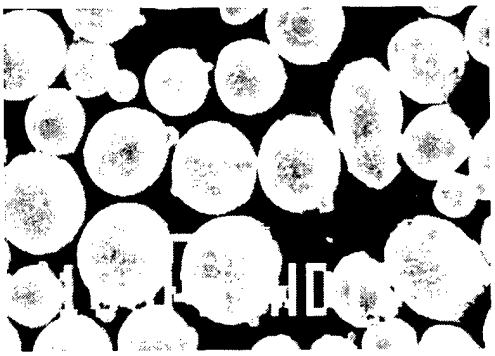


Fig. 1. Anval60. A highly alloyed tool steel material, with the characteristic spherical shape of gas atomized metal powder. The spherical shape is known to have the lowest interparticle friction and thus the best possible flowing behavior and packing. As in all commercial powders a size range interval is hardly avoidable. The apparent density was experimentally found to be 4.68 g/cm^3, or 57.16 % relative density. The density of solid Anval 60 alloy is calculated to 8.1874 g/cm^3.

3.2.2 In the Sinterstation

The powder was cycled twice through the experimental procedure, no visible differences in powder behavior was observed. The powder had excellent free flowing behavior. The applied powder densities found was $\rho_{rel.} = 60.82\%$, and $\rho_{rel.} = 60.09\%$.

3.2.3 Conclusion

The apparent density of this powder may seem rather low, but considering the size range interval, it is reasonable to find a lower density compared to more narrow size intervals. Still, the considerably higher relative density when applied by the Sinterstation indicates that the powder grains are being distributed in a favorable manner, and that the wall effects are not a significant limiting factor in the Sinterstation applied powder mass.

3.3 Two Components

3.3.1 The Powder

Intermediate sized grains: To fit into the voids between the larger particles, the powder of intermediate particle size should not be larger than 1/7th of that grain size. Since a particle size interval for both coarse and fine powders seems unavoidable, a fine powder where the larger part of the grains could fit into the voids of the larger part of the coarser grain mass was selected, in this case Carbonyl Iron CL from BASF, see **Fig. 2**. The chemical composition and size range of this powder can be seen in **Tables 3 & 4**.

Table 3.

Element	Fe	C	N	O	Ni	Cr	Mo
Unit	g/100g	g/100g	g/100g	g/100g	mg/kg	mg/kg	mg/kg
Limit	Min. 99.5	Max. 0.05	Max. 0.01	Max. 0.2	Max. 50	Max. 50	Max. 50

Table 3. *The chemical composition of BASF Carbonyl Iron Powder CL.*

Table 4.

Size Distr.	D10	D50	D90
Unit	µm	µm	µm
Limit	<5	<10	<30

Table 4. *The particle size distribution (Microtrac X100) of BASF Carbonyl Iron Powder CL.*

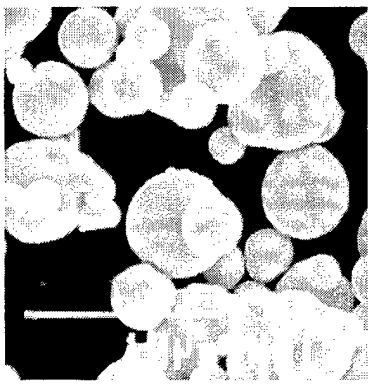


Fig.2. *Carbonyl Iron CL. Almost pure iron, with the spherical shape typical of carbonyl metal powder. In this size range the interparticle friction associated with Van der Waals and electrostatic forces are of increasing importance. Nevertheless the spherical shape still is the best possible considering flow and packing properties. As in all commercial powders a size range interval is unavoidable. Tap density, given by the manufacturer, is 3.8–4.5 g/* cm^3*, ASTM B527 (analog). The chemical composition suggests that it is reasonable to estimate the density of the solid material to be the same as pure iron: 7.86 g/* cm^3*.*

Optimal composition in terms of weight fraction large particles X^* can, according to [6] be calculated by: $X^* = f_L / f^*$, **Eq. 3.**, where f_L is the fractional packing of large particles. f^* is the packing density at optimal composition, given as $f^* = f_L + f_S(1 - f_L)$, **Eq. 4.**, where f_S is the fractional packing of small particles. f_L has been determined experimentally to 0.60, and the tap density interval was used to find f_S. Tap density: $\rho_{CL} = 3.8 - 4.5\ g/cm^3$; $\rho_{Fe} = 7.86\ g/cm^3 \Rightarrow \rho_{rel.} = 48.35\%$-57.25%, thus, $f_S = 0.4835$-5725. **Eq. 3.** & **Eq. 4.** => $X^* = 0.7245$-0.7569. Compensated for the difference in specific mass this gives that the optimal composition would include 25.30-28.65 weight % Carbonyl Iron Powder CL. Such a compound could give a theoretical maximum packing density, f^*, of 79.39-82.94% of the solid material. Several compositions with weight fraction Carbonyl Iron CL varying from 21.8% to 32.24% was mixed in a horizontally rotary type-blender, and the densities were measured. With higher fraction fine particles, the free flowing properties decreased, as the interparticle friction and the tendency to form agglomerates in the powder blend increased. This made the measurement of apparent densities more uncertain. The variation of the achieved densities can be seen in **Fig. 3.**

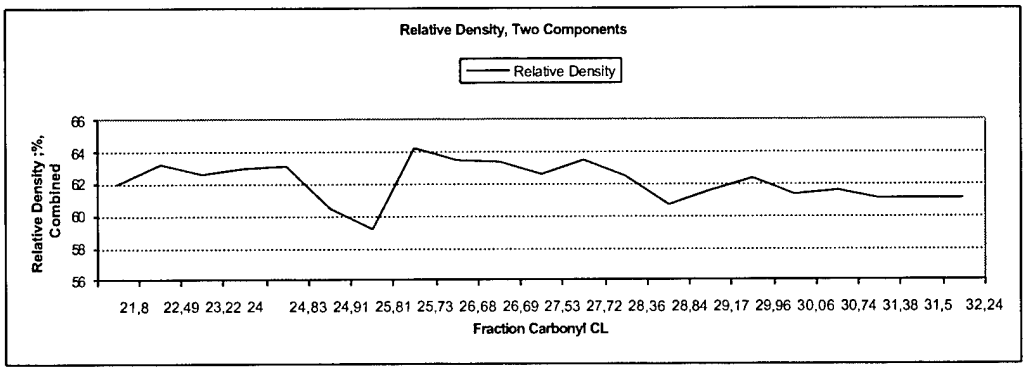


Fig. 3. *Relative densities of the binary blend of Anval60 and BASF Carbonyl Iron Powder CL.*

With compensation for some divergent values the trend is obvious in **Fig. 4.**

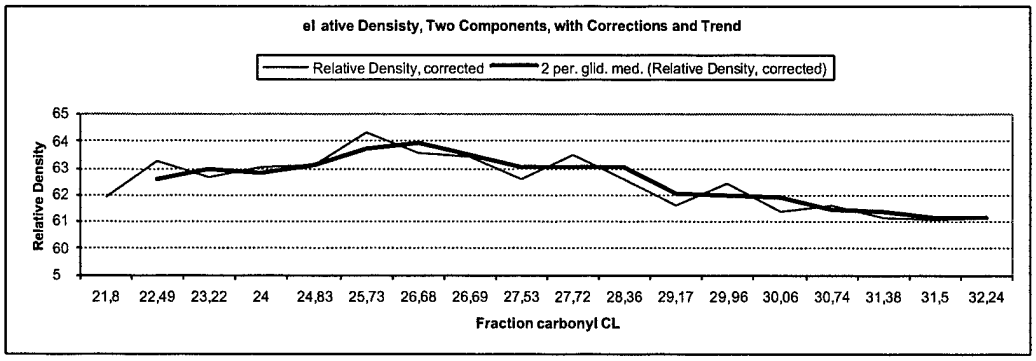


Fig. 4. *Corrected relative densities of the binary blend with trend inserted.*

In conclusion of these experiments, a powder compound was composed by blending 26% Carbonyl Iron CL into a base of Anval 60. This binary blend has a relative apparent density experimentally found to be 63.88%. The solid density is calculated to 8.1 g/cm^3.

3.3.2 In the Sinterstation

The powder properties were examined according to the experimental procedure. The powder body's consistency was similar to moist sand, and apart from a tendency to form agglomerates and a general decreased free flowing behavior, the powder showed a disposition to raise dust in the air during handling. Still, the powder spread well and showed no visible signs of powder segregation during the application of layers in the part cylinder. Obtained densities related to roller speed and feed rate can be seen in **Fig. 5. & 6.**

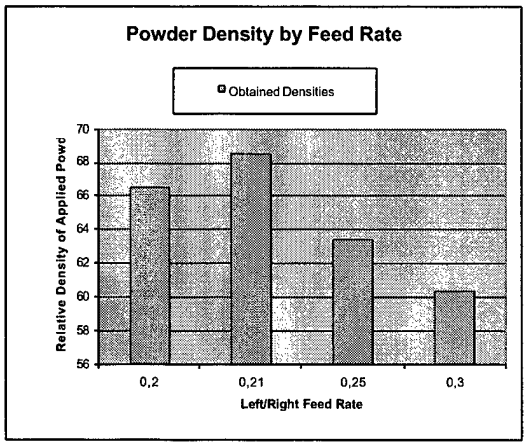


Fig. 5. *Powder densities obtained by variation of feed rate. At feed rate 0.20 the amount of powder was insufficient to fill the layer of the part cylinder. Roller speed is set to 100.*

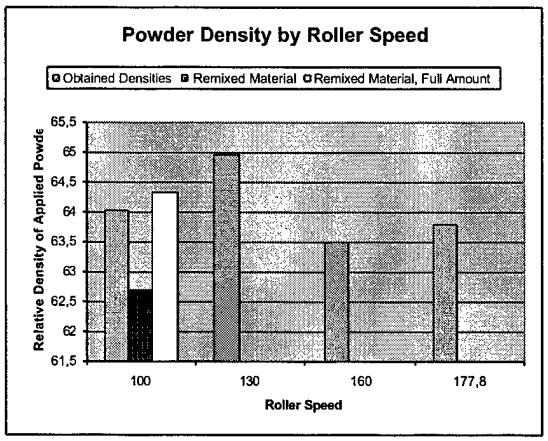


Fig. 6. *Powder densities obtained by variation of roller speed. The two extra runs at roller speed 100, was made to find out whether the lower densities in this test series was caused by powder segregation. Left/right feed rate is set to 0.21.*

Since the second test series concerning roller speed gave a considerable lower density at conditions identical to the most favorable, it was suspected that a segregation in the powder mass had occurred. However, after recycling the powder in the mixer, a smaller sample of powder obtained an even lower density, and the full amount of powder showed only a slight increase. Evidently segregation was not the problem.

3.3.3 Conclusion

The addition of a second, smaller sized powder gave a distinct increase in powder density. The densities obtained were however, not in the range of the theoretically achievable. Increased roller speed had, if any, a small, and possibly negative effect on the powder packing. Feed rates above the necessary to complete the new powder layer showed a distinct negative effect on the obtainable powder densities. The apparently increased interparticle friction in the powder compound could explain this. A free flowing powder forms a rolling wave in front of the roller during the spreading of each new layer. With the interparticle friction, the free flowing behavior is reduced and the powder partially forms a "wedge" of agglomerates that is being pushed along by the roller. An increase in mass of such a wedge would induce a higher pressure, and thus higher frictional shear in the applied powder bed below, causing cracks and poor packing in the applied layer. The counter rotation of the roller does lift and transport some powder, but only grains in direct contact with the rollers moving surface. There is only a limited rolling motion in this powder blend during the application of new layers.

Densities above the measured apparent density of this powder composition were obtained in the Sinterstation. This could be explained by the strong effect friction has on the used method for the measurement of apparent density, but in the Sinterstation does the powder motion probably also have an influence. The counter rotating motion of the roller is likely to have a vibratory effect on the upper surface of the applied layer, as well as exerting slight downward pressure on the last thin "edge" as the powder is being moved ahead. These conditions are not entirely unlike those idealized conditions used in McGeary's experiments, [4], mechanically inducing percolation of fine powder in each layer. These results confirm that the influence of the powders' interparticle friction dominates over the influence of wall effects on the density of Sinterstation applied powders.

The lower densities obtained by the repetition of early experimental runs was a mystery with separation ruled out as an explanation. However by re-weighing the powder mass it was found that a significant amount of powder had been lost during handling. There are no obvious leaks, except for the powder's tendency to raise dust in the air. Given a moderate estimation, that 75% of thereby lost powder is fine sized Carbonyl Iron CL, that would leave a blend with only 23.75% Carbonyl Iron CL. Such a composition had a relative apparent density of approximately 63% (**Fig. 4.**). In that case, the densities obtained in the last experimental runs follow the pattern of the earlier in respect to the obtained densities. Therefore this assumption is being made for the continued experiments.

3.4 Three Components

3.4.1 The Powder

Smallest sized grains: The third size range is supposed to fit into the voids between the grains in the binary powder blend. As both previous components show a size range interval, the prediction of the actual sizes of these voids is hardly possible. However, by selecting the smallest available powder, with an average particle size, within the range to fit into the matrix of the intermediate sized powder, it was estimated that this addition would give an increase in loose powder density. The selected powder was Carbonyl Iron Powder HQ from BASF, see **Fig. 7.** The chemical composition and grain size distribution can be seen in **Tables 5 & 6.**

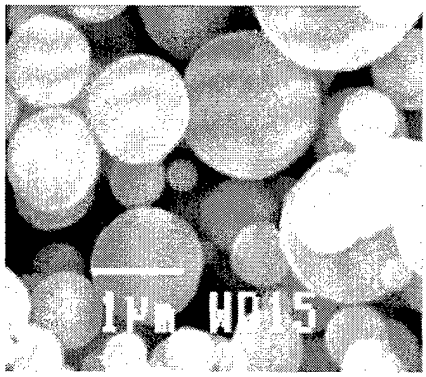


Fig. 7. *Carbonyl Iron HQ. Almost pure iron, with the spherical shape typical of carbonyl metal powder. In this size range, the friction is associated with Van der Waals and electrostatic forces, and is thus increasingly independent of particle shape. Nevertheless, the spherical shape still is the best possible considering the achievable packing properties. As in all commercial powders a size range interval is hardly avoidable, and with smaller particle size, the relative size interval increases. Tap density, is given by the manufacturer, to 3.8–4.5 g/cm^3, ASTM B527 (analog). The chemical composition suggests that it is reasonable to estimate the density of the solid material to be the same as pure iron: 7.86 g/cm^3.*

Table 5.

Element	Fe	C	N	O
Unit	*g/100 g*	*g/100 g*	*g/100 g*	*g/100 g*
Limit	Min. 97.5	0.7-1.0	0.7-1.0	0.3-0.5

Table 5. *The chemical composition of BASF Carbonyl Iron Powder HQ.*

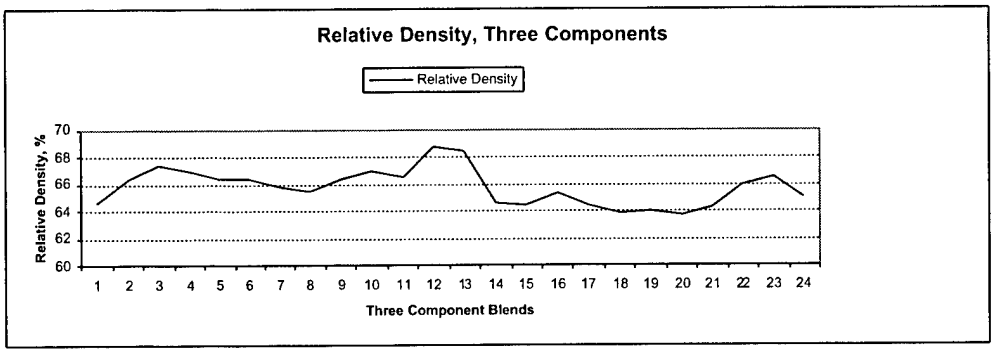
Table 6.

Size Distr.	D10	D50	D90
Unit	µm	µm	µm
Limit	1.2	2.5	4.0

Table 6. *The particle size distribution of BASF Carbonyl Iron Powder HQ.*

To find a suitable composition for the ternary powder an experimental approach was used. Different blends with varying composition was mixed and the apparent density was measured. The variation of the achieved densities for respective composition can be seen if **Fig. 8.**

Considering that the increased interparticle friction in the ternary blends, made the difficulties of apparent density measurement increase with the fraction Carbonyl Iron HQ, and that a different measuring cylinder was used for blends 12 and 13 the difference in density are in general small among these compositions. Nevertheless in conclusion of this experimental series, a powder compound was composed by with 73.35% Anval 60, 14.10% Carbonyl Iron CL, and 12.55% Carbonyl Iron HQ. This ternary blend has a measured relative apparent density of 68.40%. The solid density is calculated to 8.1 g/cm^3.

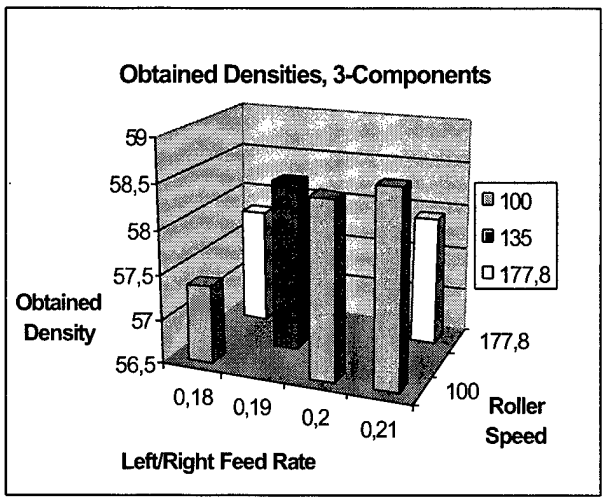


Blend	Anval 60	CL	HQ		Blend	Anval 60	CL	HQ
1	84,27	15,23	0		13	74,86	14,08	11,06
2	83,24	15,54	1,23		14	74,96	14,08	11,06
3	82,23	15,35	2,42		15	74,09	14,51	11,4
4	81,24	15,17	3,59		16	73,27	14,97	11,76
5	80,28	14,99	4,73		17	72,4	15,46	12,14
6	79,34	14,81	5,85		18	71,48	15,98	12,55
7	78,43	14,64	6,93		19	70,48	16,53	12,98
8	77,53	14,47	8		20	69,42	17,13	13,45
9	76,65	14,31	9,04		21	68,28	17,77	13,95
10	75,8	14,15	9,04		22	67,04	18,46	14,5
11	74,96	13,99	9,04		23	65,71	19,21	15,08
12	74,96	13,99	9,04		24	64,26	20,02	15,72

Fig. 8. *Compositions and relative densities of the ternary blends.*

3.4.2 In the Sinterstation

The powder was examined in the Sinterstation according to the experimental procedure. With a body consistency quite similar to wet sand, the powder showed much interparticle friction and was also difficult to handle without raising smoke-like dust. The compound hardly had anything like free flowing behavior and was more likely to form agglomerates than not. Since the powder tended to stick to the roller, scrapers were installed. Several cycles were preformed to investigate the powder compound's spreading behavior and find suitable process conditions. The obtained densities can be seen in **Fig. 9.** In difference from the powder in the part cylinder, the powder distributed around the building area settled to a stable and apparently very dense surface, whereas the powder mass in the part cylinder, remained unstable and shifted with every pass of the roller.



	100	135	177,8
0,18	57,37		57,81
0,19		58,42	
0,2	58,48		
0,2	57,45		

Fig. 9. *Powder densities obtained by variation of feed rates and roller speeds. The powder showed unstable behaviour and the applied layers were uneven and cracked. As the different cycles at 0.20 feed rate/100 roller speed shows, the results are of dubious reproducibility.*

3.4.3 Conclusion

The addition of a third component did increase the apparent density of the powder mass, but in difference to the binary blend that increase could not be observed in the Sinterstation. The obtained densities were on the contrary significantly lower than those obtained with the binary blend. Despite variation in both roller speed and feed rate, a stable behavior in the applied powder mass could not be found. This is explained by the strong disposition to form agglomerates and is in analogy with the explanation of the behavior of the binary powder. A higher interparticle friction in the powder mass causes a stronger frictional shear in the underlying layers. When the shear is too big the powder mass starts to shift. The frictional shear depends on both the inner friction in the powder mass and the pressure applied by the mass of transported powder during spreading.

These phenomena in combination with the general problems of handling extremely fine powder, makes metal powder compositions containing grain sizes in the range of one micron or smaller, unlikely as practical SLS materials.

5. Conclusions

It has been established that the addition of particles of a smaller size range can increase the relative density of a powder mass applied in the Sinterstation. It is furthermore concluded that the principal limiting factors for such an approach to densification of the powder mass are: the availability of suitable powder grades, the inner friction of the powders with smaller particle sizes, and the dusting of fine sized powder grades.

1. Availability: Each additional smaller sized powder component should be of a narrow size interval, and maximum $1/7^{th}$ of the diameter of the larger particles to increase the density of a powder mass. It is obvious that there are limits to how fine powders and how narrow grain size ranges can be obtained at a reasonable cost.

2. Inner friction of fine powders: As particle sizes reach the range of 1-2 microns or smaller, the pure powder shows a dominant tendency to agglomerate, which counteracts the densification as well as separation. This effect could possibly be reduced by addition of some sort of lubricant to the powder. However this lubrication would in it self reduce the powder density, and it is most uncertain how such an addition would influence the behavior during the further processing.

3. Dusting of fine powders: A suspension of metal particles is not an ideal atmosphere for electronic equipment, which must include SFF equipment. Even less so considered that such suspensions are deemed highly flammable and hazardous to the human health. Iron, for example, is probably harmless to ingest, but ill-advised to inhale. Even if the previous limits could be overcome, the dusting of fine powders is hardly possible to address without an entirely new powder handling system.

These points taken in consideration, size range compositions beyond binary are unlikely to become of practical use. The highest theoretical density that thus could be expected to come of use is 86%. Still considering the practical difficulties, any density in a stable powder mass above 70% should be considered an achievement. In this work, the highest achieved applied powder density was 68.60%.

These limits of applied loose powder density, makes further densification a necessity to build full density objects. This, in turn, will have a limiting effect on the material choice, achievable green strength, and also influence the process precision. It is unlikely that these issues could be fully addressed successfully to their full extent without designing an entirely new machine.

References

1. Boivie, K., "SLS Application of the Fe-Cu-C System for Liquid Phase Sintering," Bourell, D.L., et al., editors, Proceedings of the Solid Freeform Fabrication Symposium 2000, The University of Texas at Austin 2000.

2. http://www.rsc.rockwell.com/structuralmaterials/index.html

3. Beaman, J.J., et al. "Solid Freeform Fabrication: A New Direction in Manufacturing," Kluwer Academic Publishers, 1997.

4. McGeary, R.K., "Mechanical Packing of Spherical Particles," J. Am. Ceramic Soc., 1961, vol. 44, pp. 513-522.

5. Karapatis, N, et al. "Optimization of Powder Layer Density in Selective Laser Sintering," Bourell, D.L., et al., editors, Proceedings of the Solid Freeform Fabrication Symposium 1999, The University of Texas at Austin 1999, pp. 255-263.

6. German, R.M., "Powder Metallurgy Science," MPIF 1994.

Direct Metal Laser Re-Melting (DMLR) of 316L Stainless Steel Powder
Part 1: Analysis of Thin Wall Structures

Rhys Morgan, Adam Papworth, Chris Sutcliffe, Pete Fox, Bill O'Neill
Research in Advanced Technologies Group
Faculty of Engineering, The University of Liverpool, UK.

Abstract

Direct Metal Laser Re-Melting is a process variant of Selective Laser Sintering, whereby 316L stainless steel powder fractions are melted by a high power Nd:YAG laser. Layers are built up as a series of single lines to produce thin walled structures in the range ≈0.3-1.0mm thick. The structures exhibit a periodic, angular roughness to the wall surfaces. The samples also display a wave-like pattern on their upper surfaces. Further investigations reveal the angled 'wave' pattern exists on a macroscopic level in the microstructure. The pattern is fully formed by the third or fourth layer. Fern-like grain structures follow the orientation of the surface roughness and exist across many layers. This is believed to be the effect of grain orientation within the samples. The microstructure reveals long, needle, cell structures. The uni-axial needles grow epitaxially from previous layers. The samples have been shown to exhibit very little or no thermally induced residual stresses.

Introduction

Selective Laser Sintering has three main production routes for the processing of metallic components. The first two, Indirect Metal Sintering and Binary Phase Sintering involve, at some stage in the process, the use of alloy materials with properties poorer than that of the high strength, high temperature material in order to increase density or to improve melting and wetting characteristics (Tobin 1993; Bunnell, 1994). The parts produced, however, will not reproduce the exact materials characteristics of a similarly machined component.

The third route utilises only a single phase powder of the engineering material required for the fabricated end component. In this process, a high power laser beam directly melts and fuses the high temperature powder particles. There are, however, very significant problems associated with direct illumination of engineering alloys in this way. Firstly, large thermal gradients exist in the layers due to the non-homogenous heating of the powder by the laser. This causes substantial thermal stresses to be generated in the parts (Deckard, 1995). In polymer sintering processes, increasing bulk powder bed temperature reduces these thermal gradients. However, due to the high temperatures involved with direct laser sintering, anchor plates have been used to overcome

the effect of thermal stresses in the laser-sintered part, and can be incorporated into the geometry of the final component (Meiners, 1998).

Final part density is a significant barrier to the success of single phase direct laser sintering. The molten volume is shaped through surface energy minimisation, driven by surface tension. There is also a possible effect of free convective "Marangoni" forces, as experienced in melt pools during laser welding (Lampa, 1997). These effects act to shape the volume into strings of connected melt beads, which are inherently difficult to tessellate and therefore create areas of porosity. Also, surface tension forces act to drag surrounding particles into the melt, causing local depleted areas of material (Song, 1997). Furthermore, high temperature oxidation of the material reduces wetting at the interface between layers and causes a greater degree of balling. These factors must be overcome for the successful production of fully dense, engineering alloy components for heavy duty, functional use. Research at the University of Liverpool is investigating Direct Metal Laser Remelting (DMLR) of stainless steel with Nd:YAG laser to achieve this goal.

DMLR Experimental Arrangement

The DMLR test facility consists of a Rofin Sinar 90W flash Q-Switched, Flash Lamp Pumped Nd:YAG Industrial Laser Marker and an atmospheric control chamber built in-house at the University of Liverpool. The Q-Switch of the Laser Marker facilitates pulsing of the output beam, with Pulse Repetition Frequencies (PRF) in the range 0 – 60kHz, where 0kHz is a Continuous Wave Output (CW). The Nd:YAG laser is preferred over CO_2 output beam, due to the improved coupling with the 1.064μm wavelength compared with 10.64μm, and hence greater absorption with metals (Tolochko, 2000); This reduces the input energy requirement and hence induces less thermally distortive effects. The integrated scanning mirrors enable a maximum scanning speed of up to 500mms^{-1} over an 80x80mm square area. Minimum beam diameter at the focal length is measured as approximately 100μm.

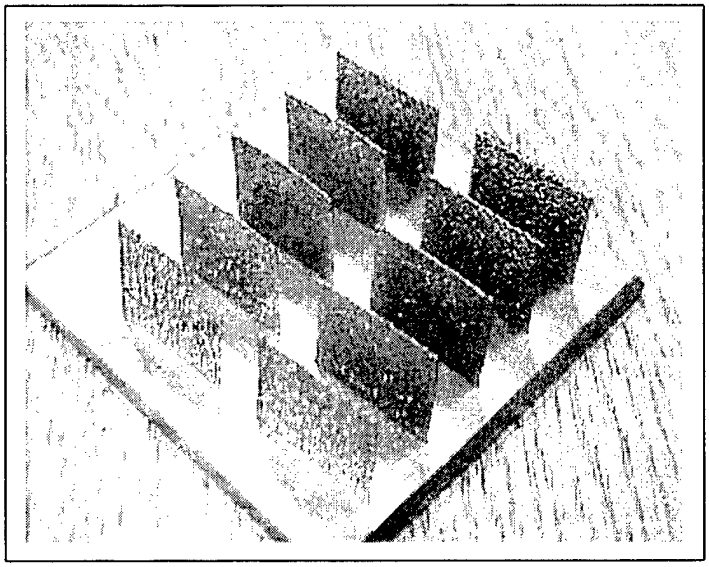


Figure 1: Array of thin wall structures produced at varying scan speeds

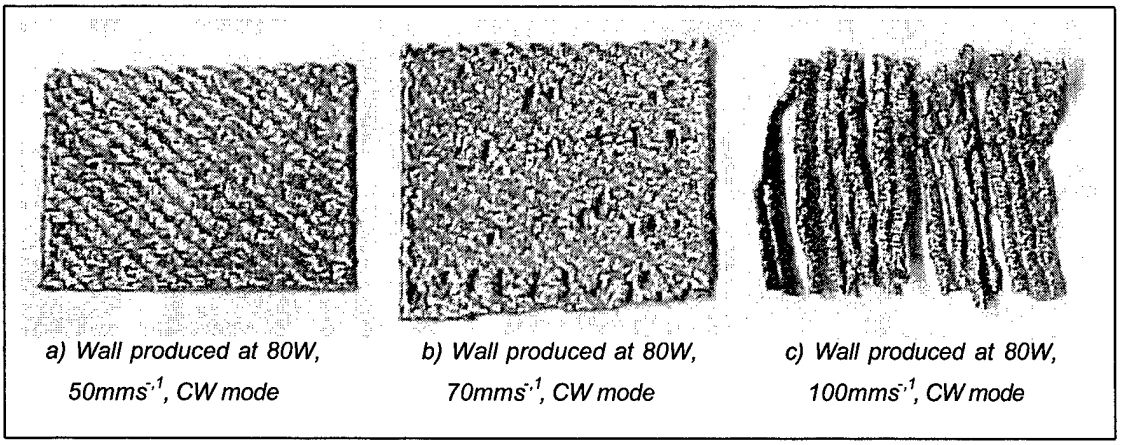
The Atmospheric Control Chamber is of typical SLS process chambers. It has a single powder feed cylinder with counter rotating roller mechanism for powder deposition onto the build platform. Layer thickness is controlled by stepper motors, whose minimum linear step size is 1μm. The process is controlled by in-house software for full automation and communication between the system and laser marker. The system is enclosed to allow for evacuation of ambient environment and re-fill with Nitrogen process gas. No heaters are used before or during the process.

The material under investigation is Stainless Steel 316L. The powder is gas atomised (spherical), specified as 80%<22μm, with a distribution approximately -<1μm <ϕ< 60μm. It has the composition: 16.73Cr, 13.19Ni, 0.017C, 0.710Si, 2.69Mo, 1.6Mn, Fe balance (%wt).

Samples were ground and polished to 1μm, and etched with standard austenitic (40% HCl, 20% HNO_3, balance H_2O) etch. A further "coloured" etch was employed to establish variations in composition within the austenite (4% Ammonium Hydrogen Difluoride, 16% Potassium Metabisulfite, balance H_2O). This etchant highlights microstructures, which are chromium rich in blue, while nickel rich regions are shown in brown.

Experimental Study

Initial experiments were undertaken to assess the effect of laser and scanning variables on cold, loose powder beds of arbitrary depth. Detailed results can be seen elsewhere (Morgan, 2001). A significant effect of scanning on loose powder layers, was the significantly increased beam absorption during the first scan lines, leading to increased volume of the coalesced melt beads, previously recognised as First Line Scan Balling (Hauser, 1999). The increased volume of these first scan lines causes problems when applying further powder layers. In order to overcome this effect, multiple layer experiments are undertaken on 3mm substrate plates of the same material.



a) Wall produced at 80W, 50mms^{-1}, CW mode

b) Wall produced at 80W, 70mms^{-1}, CW mode

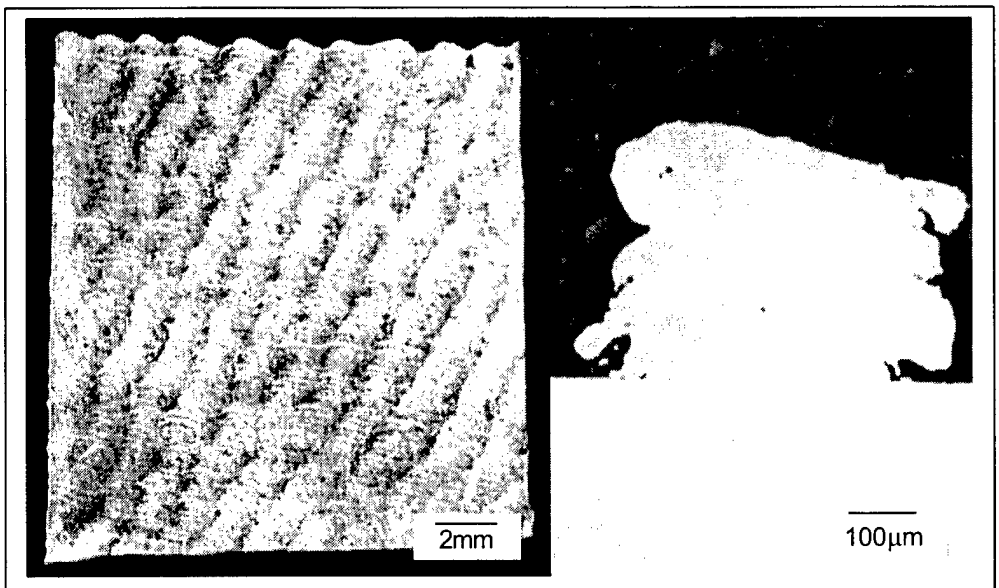
c) Wall produced at 80W, 100mms^{-1}, CW mode

Figure 2: Thin Wall Structures Produced at Varying Scan Speeds

Ten single scan-line walls, of length 15mm, were produced per plate. The layer thickness was a constant 100μm. A hundred layers were produced during each experimental run. Due to the increased conduction effects from the substrate, power was kept at a maximum to ensure sufficient fusion between the powder layer and the plate. Average power was measured at 80W. Scan Speeds were varied in the range 10-500mms^{-1}. For this study, the samples were produced using CW mode scanning. The beam was set at the focal position, with a diameter of 100μm.

Results and Discussion

Figure 1 shows a typical plate with thin wall structures. Each wall is produced with a different scan speed, incremented by 10mms^{-1}. Walls produced in the range 10-60mms^{-1} exhibit full density, with a diagonal pattern emerging in the surface as shown in Figure 2a. A threshold speed of 70mms^{-1} creates a step in the diagonal pattern resulting in areas of porosity within the structures (Figure 2b). Above 90mms^{-1}, the walls become a series of weakly connected vertical branches; the thickness of each branch reducing with increasing scan speed (Figure 2c). At scan speeds above 140mms^{-1}, there is insufficient energy imparted to the powder to affect bonding with the underlying layer, resulting in failure of the build. The thickness of the samples varies with scan speed. Increased thickness at the lower scan speeds is attributed to increased energy incident on the powder layer, resulting in radial conduction to the local surrounding powder, causing an increase in lateral melt volume and hence thicker walls. Also, there is a tendency for wall thickness to increase slightly with build height. This is due to the decreasing conduction

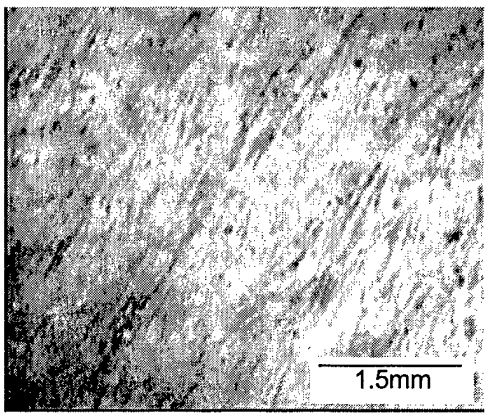


a) Diagonal structure in polished sample

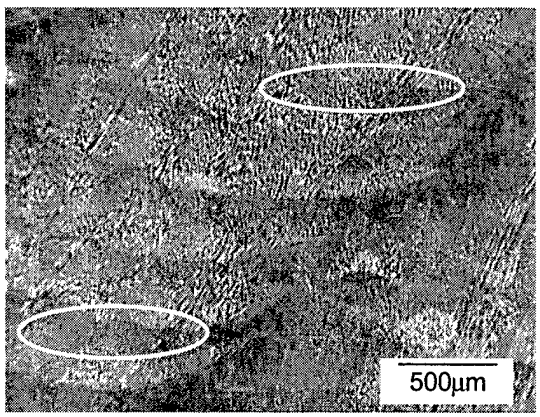
b) Cross Section of thin wall (4 layers)

Figure 3: Formation of wave pattern in thin wall structures

effect from the substrate with increasing build height. The samples show no sign of deformation or residual stress; this was borne out when samples were annealed at 500°C for 4 hours and retained their form.



a)'Fern' Grain structure in thin wall sample

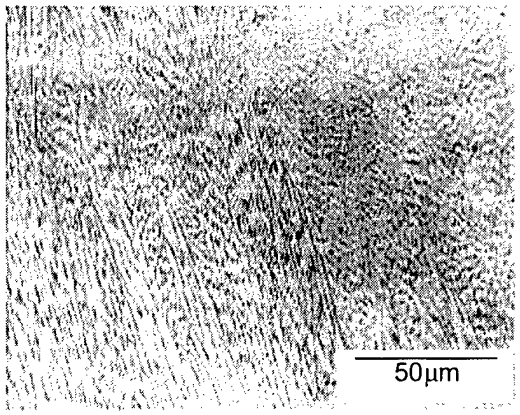


b) Ni rich regions on upper surface of each layer (circled). Bulk of layer appears Cr rich

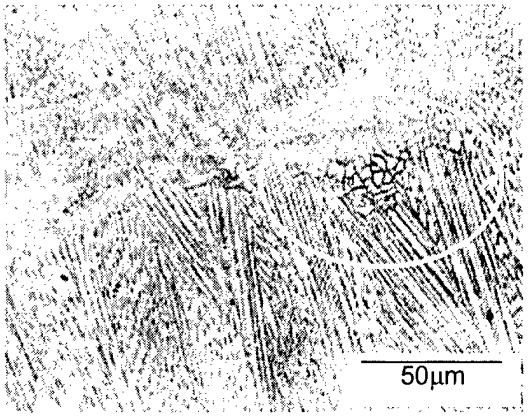
Figure 4: Analysis of microstructure with colour etch

Macroscopic analysis of the polished samples reveals the pattern on a macro-scale within the microstructure, while the upper surface of the samples exhibit a wave-like form (Figure 3a). The wave pattern has a periodicity of approximately 1.5mm. The wave structure evolves from the second or third layer; by the fourth layer it is fully established. A cross sectional view of the first three layers shows that a possible cause of the structure is due to the melt volume falling over the side of the wall (Figure 3b).

On closer examination of the polished samples, fern-like structures exist running along the diagonal pattern. These structures were initially thought to be the formation of nitrides. However, thermodynamically, this is not likely, as it is doubtful that there will be sufficient energy, in the time available, to disassociate the nitrogen to form a nitride. Also, replacing the Nitrogen process gas with Argon yielded the same grain structures. Using the colouring etch, the fern structures appear brown surrounded by light blue regions, suggesting regions of nickel rich grains (Figure 4a). However, it is more likely that the ferns are due to grain orientation within the microstructure. Further analysis of the samples with the colouring etch reveals the upper surface of each scan line is rich in nickel compared with the chromium rich bulk material of each layer (Figure 4b). This may be due to the differences in freezing temperatures between the chrome and nickel rich grain.



a) Micrograph of Cellular Structure across layers



b) Termination of cellular structure due to insufficient melting of the previous boundary substrate, shown in circled area, causes chill crystals to form and subsequent new orientation of the cellular structure

Figure 5: Microstructure of Direct Metal Laser Remelted Thin Wall Structures

High magnification microstructural analysis reveals, long needle shaped grains. These grains are due to the rapid solidification, where the formation of dendrite branching is restricted, resulting in a cellular structure (Figure 5a). Upon the passing of the beam, the underlying substrate (previous layer) is re-melted, causing the cellular structure to exhibit uni-axial, epitaxial growth. The columnar growth will continue throughout subsequent layers unless terminated by insufficient melting of the boundary substrate (previous layer) as marked in Figure 5b.

Conclusions

The Direct Laser Re-Melting process has shown to produce full density thin walls (<1mm) at scan speeds < 70mms^{-1}. The thin walls exhibit a wave-like pattern visible in the microstructure. This pattern is believed to be due to melt dynamics. Within the wave pattern, there appears a fern-like grain structure. This is believed to be due to grain orientation. The microstructure has shown full melting of the powder layers with no occurrence of unmelted particles. Grains exist along many layers, confirming melt metallurgic bonding between layers. Surprisingly, there appear to be no residual stresses in the walls. Scanning Transmission Electron Microscopy analysis is currently being undertaken to further assess the material structure.

References

Tobin, J.R., Badrinarayan, B., Barlow, J.W., Beaman, J.J., Bourell, D.L., Indirect Metal Composite Part manufacture using the SLS process. Solid Freeform Fabrication Symposium. The University of Texas at Austin, Texas. Vol 4. 1993.

Bunnell, D.E., Bourell, D.L., Marcus, H.L., Fundamentals of Liquid Phase Sintering Related to Selective Laser Sintering. Solid Freeform Fabrication Symposium, The University of Texas at Austin, Texas. 1994 pp. 379-385.

Deckard, C., Miller, D., Improved Energy Delivery for Selective Laser Sintering
Proc Solid Freeform Fabrication Symposium. The University of Texas at Austin, Texas. Vol. 6. 1995 pp. 151-158.

Meiners, W., Wissenbach, K., Poprawe, R., Direct Generation of Metal Parts by Selective Laser Powder Remelting (SLPR). Proceedings of the International Congress on Applications of Lasers & Electro-Optics (ICALEO) 1998. Section E. pp. 31-36.

Lampa, C., Kaplan, A. F. H., Powell, J., Magnusson, C., Analytical thermodynamic model of laser welding Journal of Physics D: Applied Physics, Vol. 30, No 9, (May 7 **1997**), pp. 1293-1299.

Song, Y.A., Experimental study of the basic process mechanism for direct selective laser sintering of low-melting metallic powder. CIRP annals – Manufacturing Technology. 1997 46(1) pp. 127-130.

Tolochko, N. K., Laoui, T., Khlopkov, Y. V., Mozzharov, S.E., Titov, V. I., Ignatiev, M. B., Absorbtance of powder materials suitable for laser sintering. Rapid Prototyping Journal. Vol. 6, No 3, 2000 pp. 155-160.

Morgan, R., Sutcliffe, C.J., O'Neill, W., Experimental Investigation of nanosecond pulsed Nd:YAG laser Re-Melted Pre Placed Powder Beds. Rapid Prototyping Journal. Vol. 7, No 3, 2001.

Hauser, C., Childs, T.H.C., Dalgarno, K.W. (1999, b) "Selective Laser Sintering of Stainless Steel 314S HC Processed Using Room Temperature Powder Beds", Proc Solid Freeform Fabrication Symposium, The University of Texas at Austin, Texas. Vol. 10, pp. 273-280.

this page intentionally blank

Direct Metal Laser Re-Melting of 316L Stainless Steel Powder
Part 2: Analysis of Cubic Primitives

Rhys Morgan, Adam Papworth, Chris Sutcliffe, Pete Fox, Bill O'Neill
Research in Advanced Technologies Group
Faculty of Engineering, The University of Liverpool, UK.

Abstract

The paper reports the production of cubic primitives by Direct Metal Laser Re-Melting (DMLR) a process variant of Selective Laser Sintering. Stainless steel powder fractions are melted and fused by a high power Nd:YAG laser in a room temperature, inert environment. Research in DMLR has paid particular attention to the Q-switch pulsed laser interaction with the powder bed. High peak powers (as a result of controlling Q-switch pulse repetition frequencies) cause vaporisation and re-distribution of the melt through recoil forces acting towards the powder layer. Through a variety of density measurements, cubes have exhibited densities between 30% and 89%. Results show that in certain lasing regimes, Q-switch pulsing within a certain frequency range can yield increased densities compared with Continuous Wave (CW) produced samples. The results also show, in terms of the Andrew Number, the effect of scan speed and scan spacing on part densities. Optical analysis of porosity has exposed angular, periodic porosity in the plane normal to the scan direction and random porosity along the scan direction. Causes of this and methods of its removal are discussed. Scan strategies have been developed to produce densities in excess of 99%.

Introduction

Research in Rapid Prototyping (RP) technologies is moving towards the development of processes that will enable tool-less Rapid Manufacturing. A significant drawback to the success of these processes gaining popularity in a mass-manufacturing environment, is the lack of adequate materials characteristics of components compared with traditional manufacturing processes *(i.e. machining operations, injection molding etc).* Particularly, in the case of Selective Laser Sintering of metal parts, the density and hence mechanical characteristics of components produced by the process, is in question. Current commercial systems require the use of mechanically inferior alloys with low melt temperatures to effect densification by improved wetting during the process, or infiltration following the process. Thus the components produced will never achieve the same mechanical or material characteristic as those produced conventionally.

A number of research institutions and companies alike, have been investigating the possibility of direct laser fusion of single component powders with a view to achieving full density, high

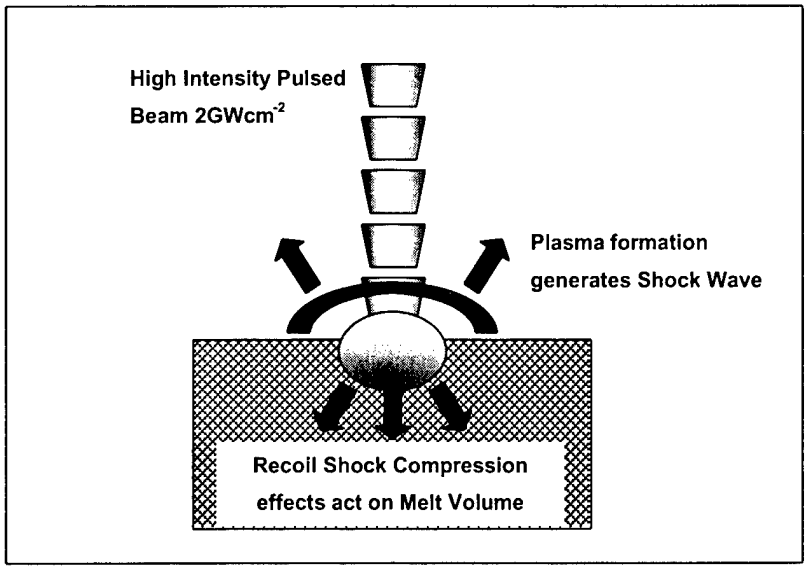


Figure 1: Interaction of Pulsed Laser with Powder Bed

mechanical strength parts for heavy duty industrial use, without the requirement of binders or infiltrants. There exist significant problems with such systems, particularly with melt dynamics and high temperature oxidation (Meiners 1997; Hauser, 1999). The existence of large thermal gradients inherent in laser sintering processes has been previously reported (Deckard 1995). These reduce the wetting characteristics of the melt and also lead to thermal stresses in the solidified layers, causing curl and deformation. Further effects of Marangoni convective flow within the melt volume cause cylindrical shaping of the melt bead (Pericleous, 1995; Lampa 1997) resulting in areas of porosity between scan lines. High temperature oxidation of the re-solidified powder layer also reduces wetting and can prevent bonding between layers (Carter, 1993). A fundamental problem arises with density of components in pre-placed powder processes such as these due to the inherent low density of the powder bed.

It has been argued that, as interaction times are several orders of magnitude shorter in SLS than in conventional sintering processes, rearrangement of particles in liquid phase sintering is essentially the only operative densification mechanism (Karapatis 1999). However, this assumes a partial melting of the powder layer. In order to achieve the mechanical characteristics of conventionally manufactured components, full melting of the powder layers must be achieved.

This paper reports on research in Direct Metal Laser Remelting (DMLR), utilising high power Nd:YAG laser to achieve full density components. The research has investigated, in particular, the effects of pulsed laser interaction with the powder bed.

Pulsed Laser Interactions

Pulsed lasers have been used in a variety of process to utilise the non-thermal photodisruption effects of the laser/material interaction (Asmus. 1986). Q Switching (rapid shuttering of the laser cavity) enables low energy pulses to be emitted over nanosecond timescales. With small beam diameters, this generates Peak Power Densities in excess of $2GWcm^{-2}$ (Sano, 2000). The material quickly melts and evaporates. The fast expanding vapour ejected from the surface produces a shock wave, which propagates radially from the interaction area. This causes a recoil force to impinge on the liquid substrate as shown in Figure 1. This has been shown, in laser welding, to overcome Marangoni forces acting on the melt volume (Ohmura, 1997). These effects have been investigated in DMLR with a view to overcoming the forces acting on the melt, to form a flatter, wider profile of the melt bead so as to increase final part density.

Experimental Arrangement

The experimental test facility consists of a Rofin Sinar 90W, Q-Switched, flash lamp pumped, Nd:YAG Industrial Laser Marker. Pulse Repetition Frequencies (PRF) are in the range 0 – 60kHz, where 0kHz is Continuous Wave (CW) mode. Pulse energies and pulse widths are in the range 1-30mJ and 80-200ns respectively. Maximum output power is measured at 80W with a minimum beam diameter of 100μm. Scanning is accomplished by an integrated galvo-scanner head over an $80mm^2$ area, where scan speeds up to $500mms^{-1}$ can be achieved.

The build chamber has been constructed in-house; it is typical of SLS build chambers. The chamber has a single powder feed cylinder. Platform control is by way of linear stepping actuators, controlled by pc based microstep controller, to enable 1μm linear step size. A counter-rotating roller is used to deposit powder over the build area. The whole system is enclosed in an atmospheric control chamber to enable evacuation of atmosphere and refill with inert process gas. The system is controlled by in-house software, which provides full communication and automation between laser and process chamber.

Gas atomised, austenitic stainless steel 316L was used during the study. The powder is generally spherical in form and has a wide distribution. Particle diameters are in the range <1-56μm with 80% <22μm. The elemental composition of the alloy powder is: 16.73Cr, 13.19Ni, 0.017C, 0.71Si, 2.69Mo, 1.69Mn, Fe bal. The powder bed was measured for density by fabricating a hollow box on a stainless steel plate using the DMLR process. The insides of the box being filled with the unmelted loose powder delivered to the build area. This gave a realistic assessment of the density as the powder was deposited into the box (layer by layer) in exactly the same way as the

Laser / Scanning Parameter	Values
Average Power, P (W)	80W Constant
Pulse Repetition Frequency, f (kHz)	10, 20, 30, 40, 50, 60
Scan Speed, v (mms^{-1})	50, 100, 200, 300, 400, 500
Scan Spacing, s (%)	25, 50, 75, 90, 100, 110, 125

Table 1: Laser / Scanning Parameter Ranges

powder was deposited for the cube fabrication during for the experiments. Three measurements of powder bed density were taken with the average density being recorded as 48% of full density.

Experimental Procedure

Cube Fabrication

Preliminary studies on loose powder beds revealed an increase in volume of the melt tracks during the scanning of the first line compared with the rest of the layer, which produces First Line Scan Balling (Hauser 1999, Morgan 2001). To overcome this effect, all cubes were built on a substrate plate of 316L stainless steel.

Cubes were fabricated at a variety of scan speeds, scan spacings (the distance between two adjacent scan lines) and PRF. Due to conduction effects of the substrate, maximum power was maintained throughout the builds. The build platform was adjusted such that the beam remained at the focal position with a diameter of 100μm. A Nitrogen shroud gas was used during the process. Nitrogen gas has shown to reduce porosity in stainless steel in laser welding processes (Katayama, 2000). A series of seven cubes were produced during each build. Pulse frequency was varied for each cube, while the scan speed and scan spacing remained constant for each experiment. The cubes are produced with a simple bi-directional raster scan strategy with scan spacing dictating the distance between consecutive scans.

Density Measurements

Cube densities were measured by two methods. The first was a simple mass/volume measurement. Mitutoyo digital callipers (500-171) were used to measure five points for x,y,z measurements, while mass was measured by digital balance (Oertling RB300, to 4 decimal places). The second method of density analysis was by Xylene impregnation technique (Arthur 1954). The cubes are immersed in xylene and placed under vacuum. The xylene is impregnated into interconnected pores during this process. Following the evacuation, the samples are weighed in air and water. The xylene, being non-miscible in water, does not allow it to penetrate into the

open pores. The respective densities of xylene and steel are known, and therefore, the difference in weighting using given formulae enable open, closed and total porosity to be calculated.

Samples were prepared for optical examination by typical metallographic techniques. A simple histogram technique was used on b/w images for optical analysis of density (for cross-reference purposes), however optical analysis was mainly concerned with pore shape and size.

Results and Discussion

Density Measurements

Figure 2 shows a typical set of density measurements of cubes produced at 80W and with 75μm Scan Spacing, measured by mass/volume and xylene impregnation techniques. The two sets of have good correlation, with the xylene technique providing slightly higher values. Measurements in the Mass/Volume technique accounts for the inaccuracies as the cubes were not square.

The graphs show the effect of pulse frequency on the resulting density of the samples. CW mode and high PRF lasing regimes produce the highest densities at 89%. There is a significant reduction of the resulting part density at 10-20kHz pulse frequency. This is due to the detrimental effects of the high peak powers as the beam impacts the powder bed; the plasma formed during the illumination of the bed and its resulting shock wave visibly blasts powder from the interaction site. The density of samples produced at the higher speeds (400-500mms^{-1}) are actually less than the loose powder bed density. Cube density continues to increase throughout the 30-40kHz

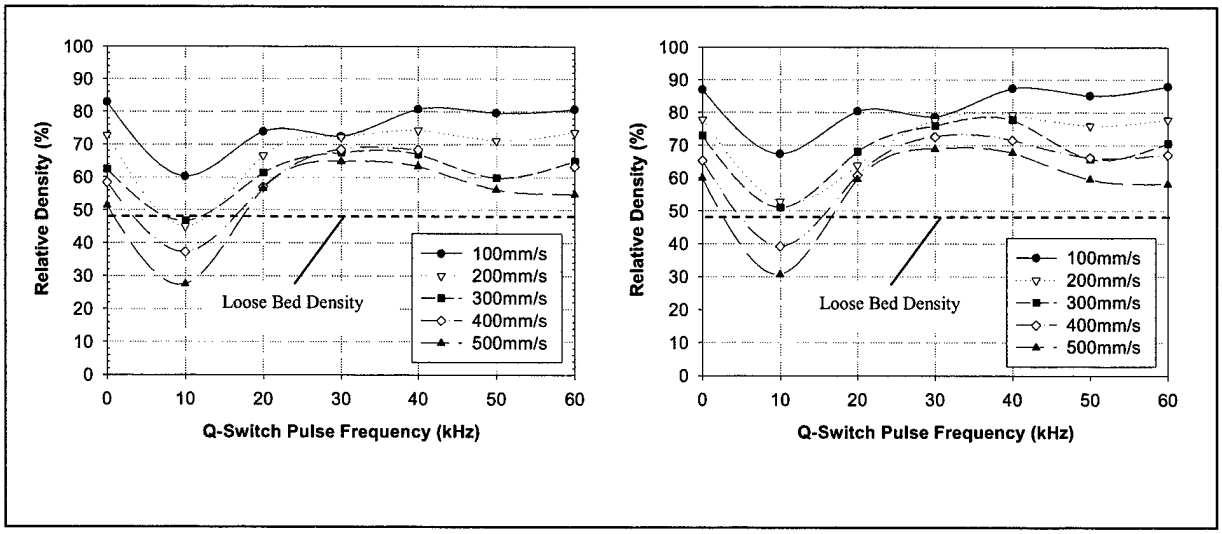


Figure 2: Density Measurements of DMLR Cubes produced at 80W Average Power and 75μm Scan Spacing by Mass/Volume and Xylene Impregnation Techniques

range, and at high pulse frequencies (>50kHz) the resulting densities are very similar to those produced during the CW lasing regime.

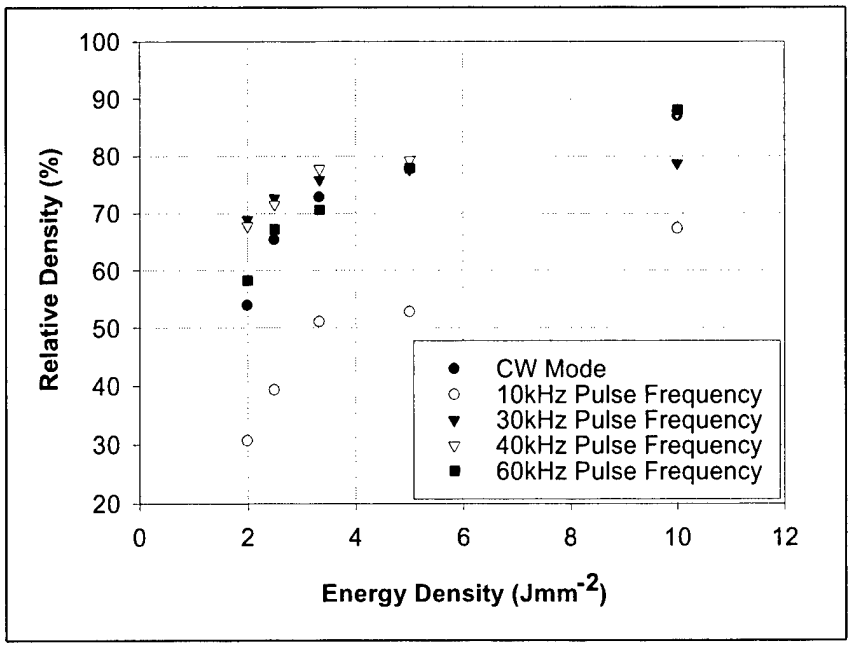


Figure 3: DMLR Cube Density as a function of Andrew Number (Energy Density)

A clearer view of the effect of scan speed and scan spacing is achieved when representing the results in terms of the Andrew number (Jmm^{-2}); a measure of the total incident energy density of a layer scan: $A_N = P / vd$, where: P, Power (W), v Scan Speed (mms^{-1}), d Scan Spacing (mm). Figure 3 shows density as a function of Andrew Number for varying pulse frequencies. At high scan speeds and large scan spacing (i.e. low Andrew Number), the results show an increase in part density for pulse frequencies in the range 30-40kHz, compared with CW and 60kHz PRF. As energy to the powder layers is increased (by reduction in speed), the overall densities of the cubes increase. The CW and 60kHz PRF cubes now exhibit the greatest density. Any further increase in energy density beyond $10Jmm^{-2}$ does not yield increased cube density. Reductions in scan speed to $50mms^{-1}$ for a scan spacing of 25μm resulted in excessive heat input to the build layers causing deformation of the layers and failure of the build.

Figure 4 shows the effect of scan spacing on part density. The results show that; at high scan speeds, the part density decreases with increasing scan spacing. However, at low scan speeds, this effect is reduced and, at $100mms^{-1}$, the resulting part density increases with scan spacing. Additional cubes were produced with further reduction in scan spacing, to the point where there

was negative overlap between consecutive scan lines. At 110μm Scan Spacing, the density is at a maximum 92% at 110μm and decreases at 120μm scan spacing, or –20% scan overlap.

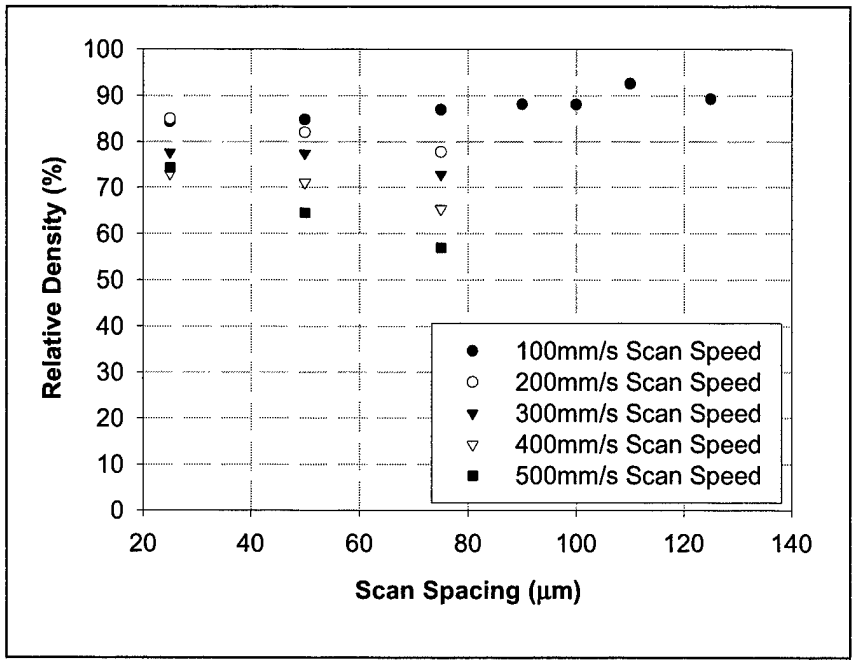


Figure 4: DMLR Cube Density as a Function of Scan Spacing(Beam Diameter 100μm)

Optical Analysis

Optical analysis of the samples supports, qualitatively, the findings of the density measurements. Figures 5 and 6 show cross sections of samples produced at the varying laser parameters. The images show cross sections in two planes: normal to the laser scan direction and in line with the scan direction. Figure 5a-c shows the cubes produced in CW mode. The in-plane sections show diagonal porosity occurring across many layers, while the sections normal to the scan direction exhibit random porosity. The extent of porosity increases with decreasing scan spacing and increasing scan speed. The cube produced at $500mms^{-1}$ reveals a flash melting of the powder bed. The diagonal porous structure is still visible. The phenomenon of angular porosity also occurs in the pulsed samples. Figure 6a-c shows sections of cubes produced at a variety of pulse frequencies and scanning parameters. The 60kHz pulsed sample displays the angular voids very prominently in the plane of scan direction. The areas of material exhibit smooth undersides, while their upper surfaces appear circular or spherical. The 30kHz sample produced at $500mms^{-1}$

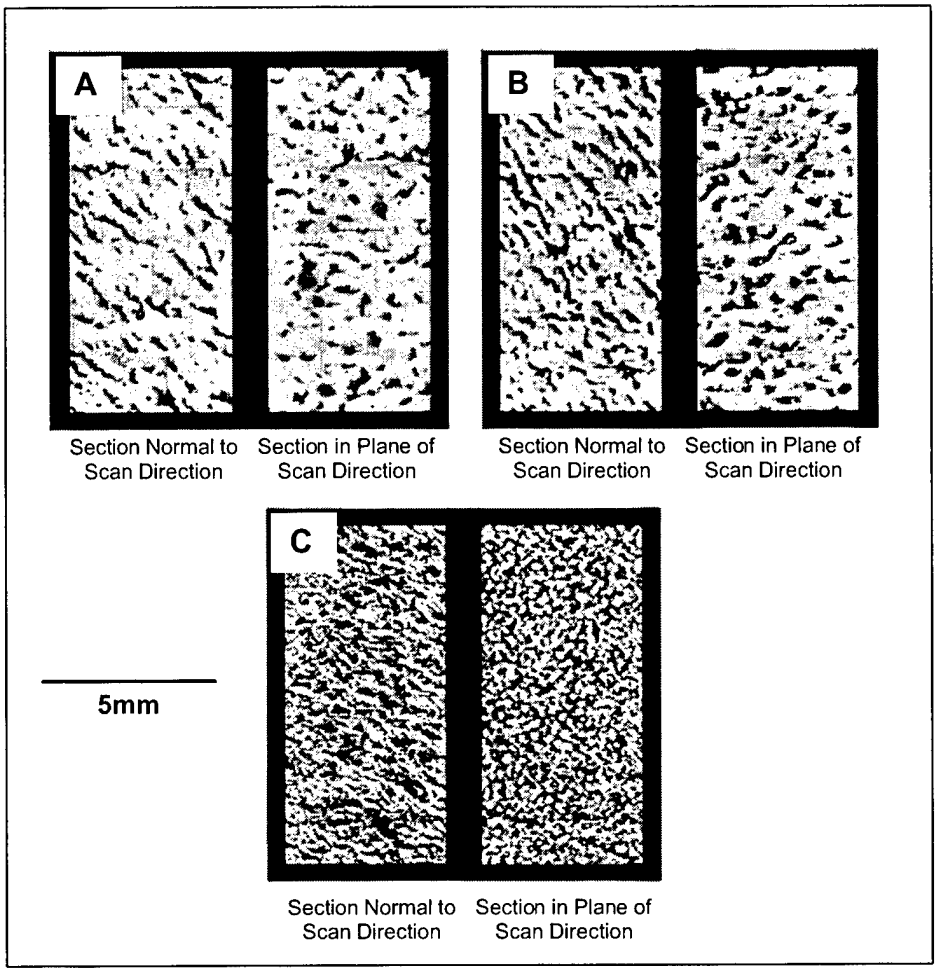


Figure 5: a) 80W, CW, 100mms^{-1}, 75µm Scan Spacing
b) 80W, CW, 100mms^{-1}, 50µm Scan Spacing
c) 80W, CW, 500mms^{-1}, 75µm Scan Spacing

demonstrates, like the CW sample, the effect of flash melting. However, the extent of porosity is certainly less. Figure 6c shows the cube produced at 10kHz pulse frequency. The sections show large, flat areas of melt in each layer, but very little inter-layer bonding. This occurs in both sections of the sample.

The cause of angular porosity is attributed to a diagonal wave pattern (as a result of melt dynamics) visible on single scan-line thin wall structures as discussed in part 1 of this paper (Morgan, 2001). The pattern produces a roughness to the wall. When two adjacent walls are produced, the periodic roughness of the adjoining scan lines causes porosity corresponding to the angular pattern.

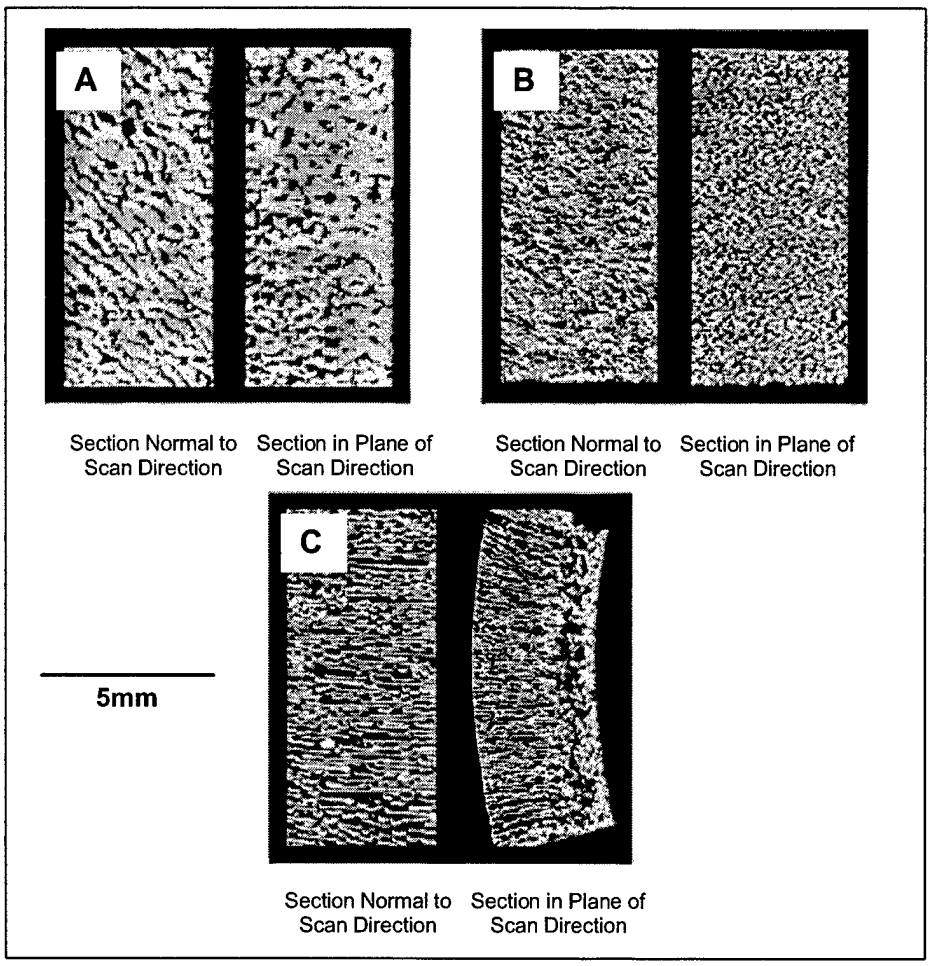


Figure 6: a) 80W, 60kHz Pulsed, 100mms^{-1}, 50μm Scan Spacing

b) 80W, 30kHz Pulsed, 500mms^{-1},75μm Scan Spacing

c) 80W, 10kHz Pulsed, 100mms^{-1}, 75μm Scan Spacing

Scan Strategies

Scan strategies were developed to remove the angular structure from the walls, in an effort to increase part density. From the previous results for optimum density, laser power and scan speeds were set at 80W and 100mms^{-1} respectively. The laser was run in CW mode. The scan strategy involved the creation of a bi-directional rasterscan 'tracks' whose widths were less than that of the periodicity of the wave formation; a 0.75mm scan length was chosen. The scan spacing between successive scan lines in a track was varied and optimised at 115μm for a 100μm beam diameter, thus creating a negative (-ve) 15% overlap (Figure 7a).

Trials were undertaken to devise optimum quilting strategies. It was found that regardless of overlap between adjacent rasterscan tracks, porosity remained in the solidified layers due to the inherent lack of powder in the low-density bed. The strategy was modified such a powder refill cycle was introduced between the scanning of alternate odd/even tracks, as illustrated in figure 7.

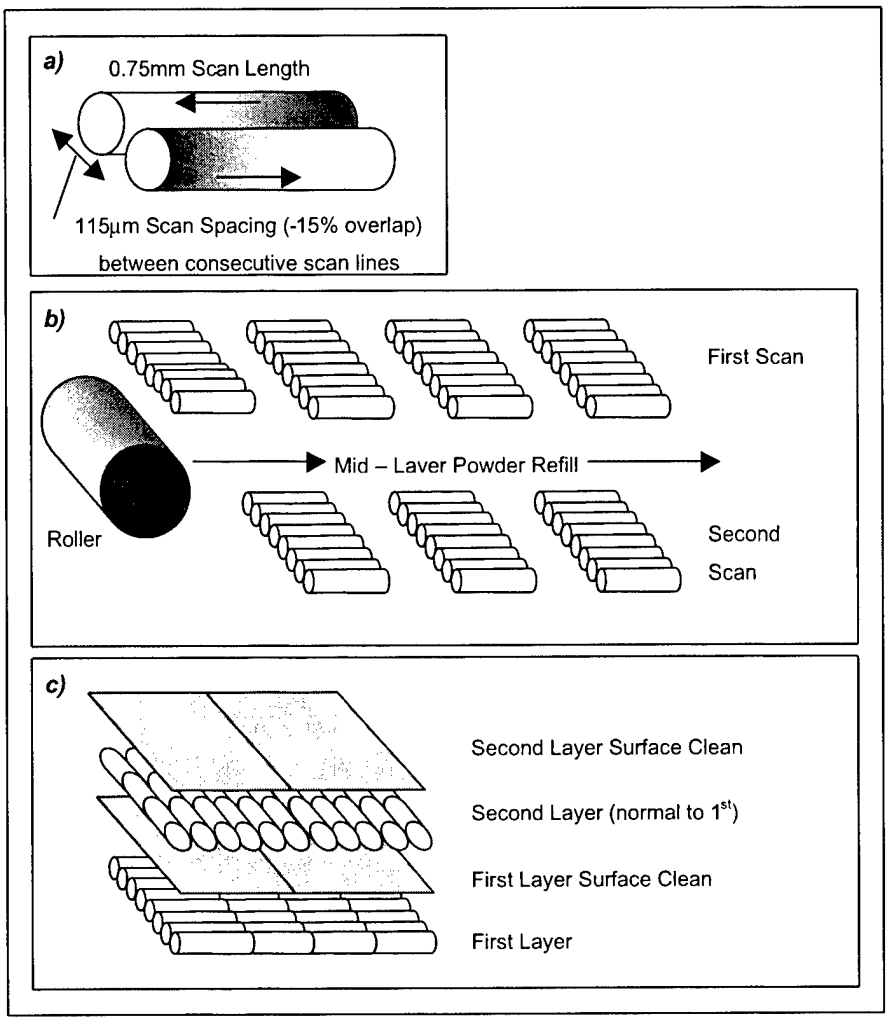


Figure 7: Scan Strategy for Production of >99% Dense DMLR Cube

a) Two consecutive Scan Lines,

b) Construction of a Single Layer

c) Multiple Layers inc. Cleaning Process Steps

The powder refill cycle increased density, measured by optical analysis, to 98%. However, inter-connected porosity remained across several layers. The cause of the voiding was attributed to gas entrapment upon deposition of new layers on rough laser re-melted surfaces. The strategy was further developed to scan each layer normal to the preceding layer to avoid interconnected porosity (Figure 7c). An additional cleaning step was introduced to scan over the re-solidified surface to reduce surface roughness. Minimal re-melting takes place due to the reduced absorption coefficient of the highly reflecting surface.

Though the addition of powder refill and surface clean incur time penalties, density measurements by Xylene impregnation technique show an increase to 99.65% of full density.

With the new scan strategies, pulsed mode is being investigated, and further developments to the scan strategy are currently being undertaken to reduce the build time. Figure 8 shows a polished cube produced by the DMLR technique.

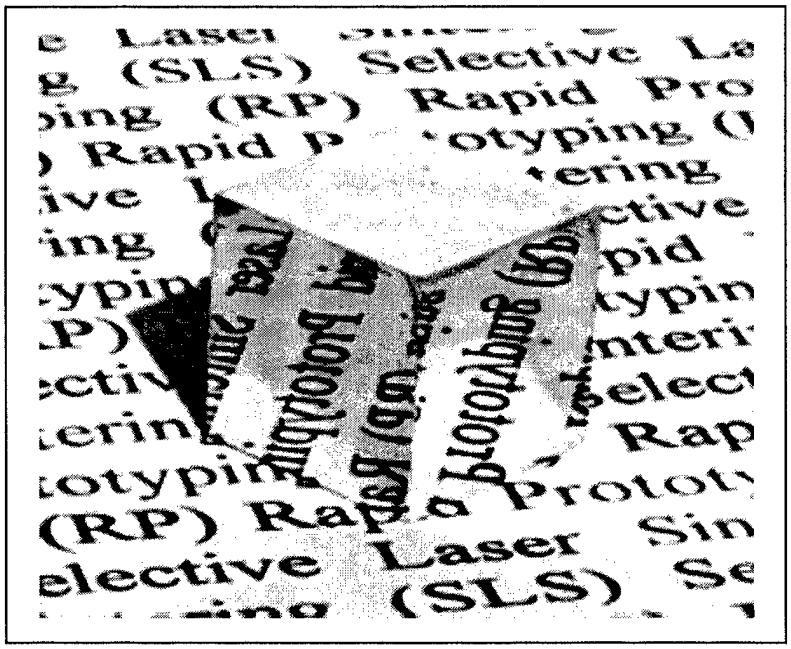


Figure 8: Stainless Steel 316L Cube Produced by DMLR (Density >99%)

Conclusions

The work has shown the development of the DMLR process as a one-step route for the production of high-density stainless steel components. Pulsed interactions with the material have shown to vary the density of cubes produced. Pulsed interactions with the powder layer have shown to be beneficial for certain parameters, though CW mode scanning has produced the greatest density. Certain pulse repetition rates are detrimental as shock waves blast the powder from the bed. There is a strong possibility that pulsed scanning may enable graduated porosity in the construction of objects, this is being investigated. Optical analysis of cross sections of the cubes revealed periodic diagonal porosity throughout the samples. This is attributed to melt dynamics and observed on thin wall structures. To remove the porosity, scan strategies were developed, resulting in part densities in excess of 99%.

Acknowledgments

The authors would like to thank Mr Lawrence Bailey, experimental officer, for the construction of the experimental apparatus. Rhys Morgan is approaching the culmination of his PhD research and would like to take this opportunity to thank the other authors and Mr Bailey for their continued support and efforts during the project.

References

Meiners, W., Wissenbach, K., Propawe, R., Direct Selective Laser Sintering of Steel Powder. Laser Assisted Net shape Engineering 2, Proc. LANE 1997 pp. 615-622

Hauser, C., Childs, T.H.C., Dalgarno, K.W., Eane, R.B., Atmospheric control during Selective Laser Sintering of Stainless Steel 314S Powder. Proceedings of the Solid Freeform Fabrication Symposium, University of Texas at Austin, Texas. Vol. 10, pp. 265-272

Deckard, C., Miller, D., Improved Energy Delivery for Selective Laser Sintering Proc Solid Freeform Fabrication Symposium. The University of Texas at Austin, Texas. Vol. 6. 1995 pp. 151-158

Pericleous, K. A., Bailey, C., Study of Marangoni phenomena in laser-melted pools Meeting: Proc 1995 7th Conf Model Casting Welding Adv Solid Process, Sep 10-15 1995

Lampa, C., Kaplan, A. F. H., Powell, J., Magnusson, C., Analytical thermodynamic model of laser welding Journal of Physics D: Applied Physics, Vol. 30, No. 9, (May 7 1997), pp. 1293-1299

Carter, W.T., Jones, M. G., Direct Laser Sintering of Metals. Proc Solid Freeform Fabrication Symposium. The University of Texas at Austin, Texas. Vol 4. 1993 pp. 51-59

Karapatis, N.P., Egger, G., Gygax, P.E., Glardon, R., Optimisation of Powder Layer Density in Selective Laser Sintering Proceedings of the Solid Freeform Fabrication Symposium, University of Texas at Austin, Texas. 1999 pp. 255-263

John Asmus More light for art conservation IEEE Circuits and Devices Magazine No. 2, Vol. 2. 1986 pp. 6-15

Sano, Y., Kimura, M., Mukai, N., Yoda, M., Obata, M., Ogisu, T., Process and application of shock compression by nano-second pulses of frequency doubled Nd:YAG laser. Proc. SPIE 2000, (3888) pp. 294-306

Ohmura, E., Hayashi, H., Fujimori, S., Miyamoto, I., Thermohydrodynamics Analysis of Fusion Phenomena Accompanied with Evaporation due to Laser Irradiation. Proc. LIA ICALEO 1997. Section G pp.9-15

Morgan, R., Sutcliffe, C.J., O'Neill, W., Experimental Investigation of nanosecond pulsed Nd:YAG laser Re-Melted Pre Placed Powder Beds. Rapid Prototyping Journal Vol. 7, No. 3, 2001

Katayama, S., Seto, N., Mizutani, M., Matsunawa, A., Formation mechanism of porosity in high power YAG laser welding. Proc. ICALEO 2000, Section C pp. 6-24

Arthur, G., Porosity and permeability changes during the sintering of copper powder. Journal of the Institute of Metals 1954-55 (83) pp. 329-336

Rhys Morgan, Adam Papworth, Chris Sutcliffe, Pete Fox, Bill O'Neill, Direct Metal Laser Re-Melting (DMLR) of 316L Stainless Steel Powder Part 1: Analysis of Thin Wall Structures. Proceedings of the Solid Freeform Fabrication Symposium, University of Texas at Austin, Texas. (Submitted 2001)

this page intentionally blank

A Study of Functional Testing With SFF Parts

Alan J. Dutson, Kristin L. Wood, Joseph J. Beaman, Richard H. Crawford, David L. Bourell

Department of Mechanical Engineering
The University of Texas at Austin

Abstract

A study of functional testing with SFF parts is presented. The study includes the use of traditional similitude methods as well as advanced similitude methods for predicting product performance through prototype testing. Cantilever beams created from the selective laser sintering process are used to predict the static deflection of both aluminum and polycarbonate beams. The results of 20 experiments using various geometric, loading, and material configurations are presented. Results of the study suggest that a coupling between geometry and material properties exists in SLS parts. Possible sources for the coupling are discussed. An approach for establishing the functional relationship between material and geometry is outlined.

I. Introduction

Advances in virtual prototyping techniques, including numerical modeling and simulation tools, have increased the engineer's ability to quickly analyze a product's performance early in the design cycle. Improved simulation tools have been key in reducing cycle times and improving product quality. Virtual prototypes can often be used in place of physical prototypes in certain stages of the design process, thus saving tremendous time and cost during product development.

Despite advances in virtual prototyping techniques, however, the range of physical phenomena that can be accurately modeled and simulated numerically is still limited. For example, the steady-state temperature of a thermal system, composed of heat sinks and cooling fans, is often difficult to predict using virtual methods only (Nadworny, 1995; Fisher, 1997). Such limitations in virtual modeling require that physical models be used to refine and validate numerical models. Physical models are also important in capturing unique physical behaviors or anomalies that are not accounted for in virtual models. Virtual prototyping techniques, while maturing rapidly, have still not advanced to the point of replacing physical prototypes entirely. In this light, the research presented in this paper is centered on *experimental* methods that are intended to be used as a compliment to, rather than as a substitute for, virtual prototyping techniques.

A serious drawback to functional testing with physical prototypes is the extensive time and cost involved in building and testing the physical part. The fabrication effort for physical parts can be reduced dramatically through solid freeform fabrication (SFF) techniques. While the "fit" and "form" of a product can be accurately evaluated with SFF parts, the amount of functional information that can be obtained is still limited. The limited functional information available

from SFF parts is due primarily to the limited number of materials that can be used in SFF processes.

Figure 1 shows a conceptual representation of the current capabilities of SFF in evaluating products along three primary axes: Fit, Form, and Function. The goal of the research presented in this paper is to increase the functional information that can be obtained from SFF parts. By increasing the functional information available from SFF parts, physical prototypes can be constructed with SFF techniques and tested in a fraction of the time that is required for traditional approaches.

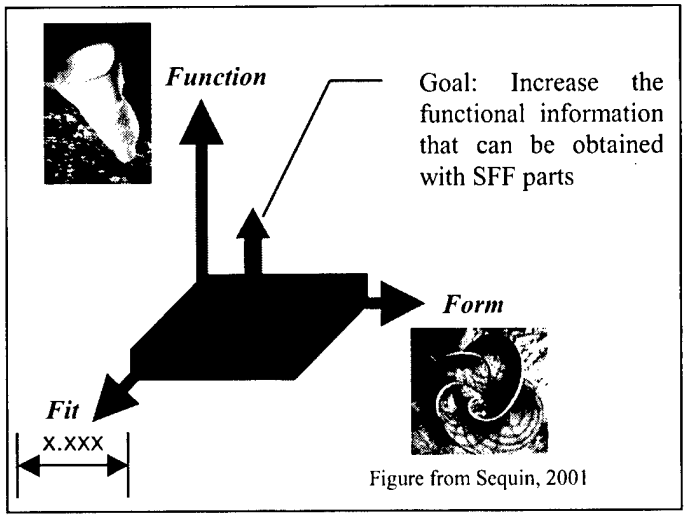


Figure 1. Current capabilities of SFF in evaluating products

Products that contain complex geometry are especially suited for this approach to functional testing because of the extensive fabrication effort that is required from traditional prototyping techniques, such as NC machining. The advantage of SFF techniques over traditional methods increases as part geometry becomes more complex, as illustrated in Figure 2.

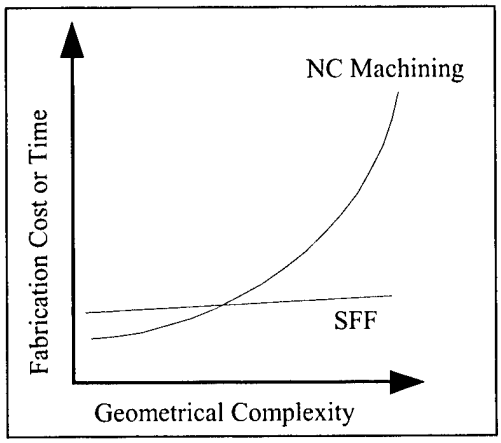


Figure 2. Geometric Complexity vs. Cost

Two main approaches exist for obtaining better functional information from SFF parts:

1. Improve the base materials and/or processes in order to obtain the same properties as those of the part.
2. Correlate properties of existing materials to those of the part in order to predict product behavior.

Significant research has been dedicated to both of the approaches mentioned above. The first approach deals with improving and expanding SFF systems, while the second approach seeks to utilize what is already in place. The second approach is more flexible in its ability to predict behavior for a wide range of parts with different materials, and is the approach taken for the research presented in this paper.

II. Background

Correlating the behavior of two systems can be accomplished by using either dimensional information from the systems or by using empirical data, as described in the following sections.

2.1 Traditional Similarity Method, TSM

The traditional similarity method (TSM), also known as dimensional analysis, is based on the Buckingham Pi theorem. The Pi theorem (Bridgman, 1931) states that a complete equation written in terms of dimensional system parameters d_j, $j = 1, \ldots, n$, can be recast in terms of dimensionless parameters π_i, $i = 1, \ldots, N$, where $N < n$. In equation form,

$$g(d_1, d_2, \ldots, d_n) = 0 \;\Rightarrow\; f(\pi_1, \pi_2, \ldots, \pi_N) = 0 \tag{1}$$

Two systems that are governed by the same set of dimensional parameters can be correlated by considering corresponding sets of dimensionless parameters. For two systems (a product, p, and a model, m) the dimensionless parameters can be represented as

$$\begin{aligned} f(\pi_{p,1}, \pi_{p,2}, \ldots, \pi_{p,N}) &= 0 \\ f(\pi_{m,1}, \pi_{m,2}, \ldots, \pi_{m,N}) &= 0 \end{aligned} \tag{2}$$

or, in terms of a particular parameters of interest, say X, as

$$\begin{aligned} \pi_{p,X} &= f(\pi_{p,1}, \pi_{p,2}, \ldots, \pi_{p,N-1}) \\ \pi_{m,X} &= f(\pi_{m,1}, \pi_{m,2}, \ldots, \pi_{m,N-1}) \end{aligned} \tag{3}$$

For these two corresponding systems, the TSM states that $\pi_{p,X} = \pi_{m,X}$ if $\pi_{p,i} = \pi_{m,i}$ for all $i = 1, 2, \ldots, N\text{-}1$. (Many references exist which show systematic derivations of dimensionless parameters from sets of dimensional parameters. See for example Barr, 1979 or Langhaar, 1951.)

As a simple example, consider the cantilever beam shown in Figure 3. Suppose we are interested in the deflection of the beam under a static load. A relationship among dimensional parameters can be written as

$$\delta = g(E, t, w, L, F) \tag{4}$$

where δ = static beam deflection
E = Young's modulus
F = applied load
t, w, L = beam dimensions, as shown in Figure 3

Equation (4) can be recast in dimensionless form as

$$\frac{\delta}{t} = f\left(\frac{w}{t}, \frac{L}{t}, \frac{F}{t^2 E}\right) \tag{5}$$

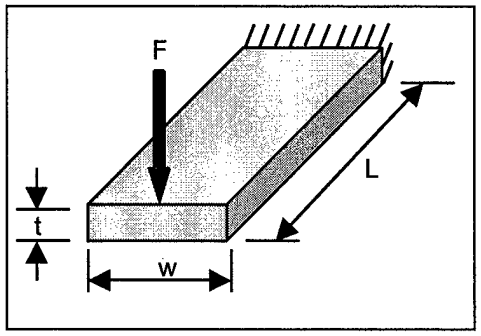


Figure 3. Cantilever Beam

Note that this set of dimensionless parameters is not necessarily unique, but is just one of several possible sets.

A model beam (m) that is similar to the product beam (p) (i.e. is governed by the same set of dimensional parameters) can now be used to predict the deflection of the product beam as

$$\frac{\delta_p}{t_p} = \frac{\delta_m}{t_m} \tag{6}$$

if

$$\frac{w_p}{t_p} = \frac{w_m}{t_m}, \quad \frac{L_p}{t_p} = \frac{L_m}{t_m}, \quad and \quad \frac{F_p}{t_p{}^2 E_p} = \frac{F_m}{t_m{}^2 E_m} \tag{7}$$

Equation (6) is known as the TSM *prediction equation*, and Equation (7) is known as the *similarity constraints*. The model beam must be constructed so that all of the similarity constraints are satisfied in order for the prediction equation to be valid. Note that scale factors derived from the similarity constraints are assumed to be constant over the range of interest. For example, the scale factor for the applied force on the model ($F_m = \frac{t_m{}^2}{t_p{}^2}\frac{E_m}{E_p}F_p$) assumes constant ratios for beam thickness and for Young's modulus. If these ratios are not constant, the system is said to be *distorted*. A model beam that does not have a constant value for Young's modulus, for example, will cause the system to become distorted. The behavior of a distorted system cannot be predicted accurately with the TSM.

2.2. Empirical Similarity Method, ESM

The empirical similarity method, ESM, provides a means of correlating distorted systems. The fundamental concept of the ESM is shown in Figure 4. Unlike the traditional method, which relies solely on dimensional information to correlate systems, the ESM utilizes a simplified specimen pair to construct an empirical correlation between systems. The model specimen (*ms*) is a geometrically simplified version of the model, while the product specimen (*ps*) is a geometrically simplified version of the product. The ESM uses measured values from the model specimen, the product specimen, and the model to predict the behavior of the product. In other words, $x_p = f(x_m, x_{ms}, x_{ps})$. The ESM assumes that:

1. The model and the model specimen can be tested to determine the state variation caused by pure geometric changes (G).
2. The model specimen and the product specimen can be tested to determine the state variation caused by pure non-geometric (material and loads) changes (M).

The state of the product can be predicted by multiplying the state of the model by M or by multiplying the state of the product specimen by G, as shown in Figure 4. A basic assumption of the ESM is that M and G are independent.

The transformation matrices G and M can be determined with either a circulant matrix approach or with a pseudoinverse approach (since one cannot take the inverse of a vector directly). The pseudoinverse approach for determining M and G can be summarized as follows:

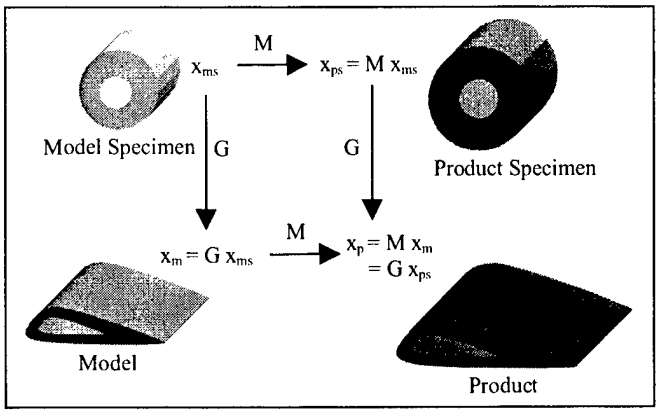


Figure 4. Empirical Similarity Method.

$$x_{ps} = Mx_{ms} \quad \Rightarrow \quad M = x_{ps}x_{ms}^{+}$$
$$x_m = Gx_{ms} \quad \Rightarrow \quad G = x_m x_{ms}^{+} \tag{8}$$
$$where \quad x_{ms}^{+} = (x_{ms}^{T}x_{ms})^{-1}x_{ms}^{T}$$

The advantage of the ESM approach over the TSM is that system distortions due to material properties are captured in the material transformation matrix (M) and system distortions due to geometry are captured in the geometry transformation matrix (G). This procedure is contrasted with the TSM which relies solely on dimensional information to correlate systems, with no means of compensating for system distortion.

The position of the ESM in functional testing of products is between the TSM and Direct Product Tests, as shown in Figure 5. The ESM is presented as a more accurate approach, in general, than the TSM. The ESM is also presented as a better approach for correlating systems with complex geometry whose governing parameters may not be well known, as required by the TSM. Continuing areas of research include identifying the boundaries of the ESM as well as expanding the boundaries of the ESM to replace direct product testing.

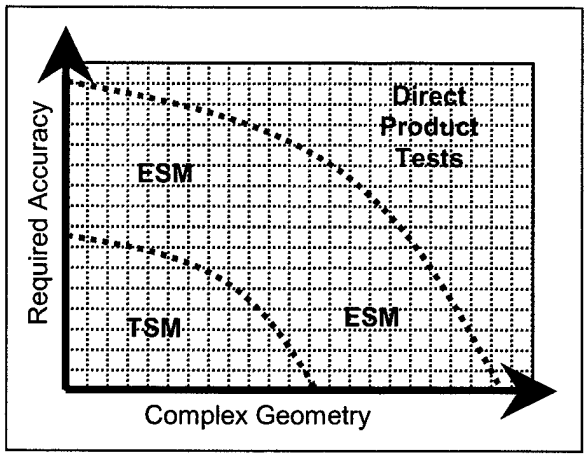


Figure 5. ESM vs. TSM

The ESM approach was validated with a simple cantilever beam example taken from (Cho, 1997). The beams used in the experiment are shown in Figure 6. The product is an aluminum beam with holes. The model is a scaled polycarbonate beam with holes. The model specimen and product specimen are straight beams with no holes, with dimensions and materials as shown in Figure 6. Both the TSM and the ESM were used to predict the deflection of the beam under an applied load. In order to evaluate the different methods, the actual product was also built and tested. (The purpose of both the TSM and the ESM is to predict product performance *without* having to build the product; in this case, the product was built simply to evaluate the accuracy of the predictions). The actual displacement of the beam, along with the ESM and TSM predictions, are shown in Figure 7. The geometric nonlinearities introduced by the holes in the beams cause the TSM to give inaccurate results. The ESM, however, gives a very accurate prediction of the beam deflection.

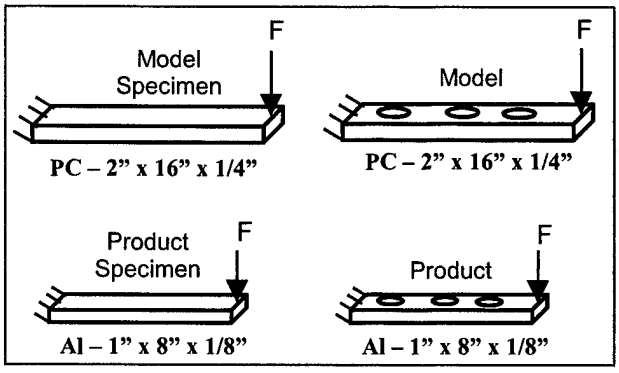


Figure 6. Cantilever Beam Example.

III. Application of ESM to SFF Parts

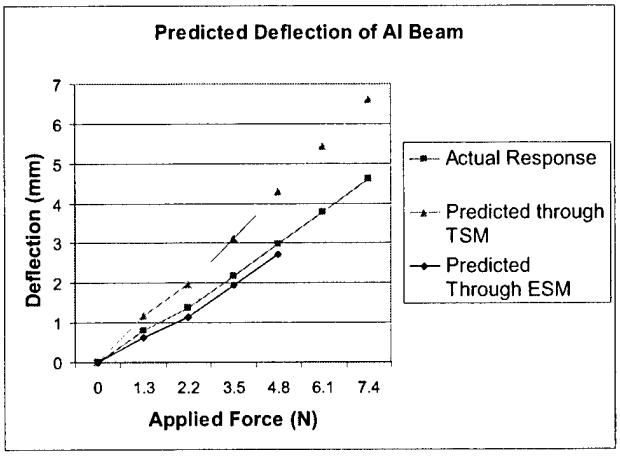


Figure 7. Cantilever Beam Results.

The feasibility of using the ESM approach with SFF parts was evaluated with a similar cantilever beam experiment. Using SFF techniques to fabricate the model and the model specimen for the ESM introduces additional complexities to the problem, including orthotropic material structures and process-dependent material properties. The initial experiment used a tapered aluminum beam with holes as the product, and a straight aluminum beam without holes as the product specimen (see Figure 8). The model and model specimen were fabricated with DuraForm™, a polyamide-based powder, using the selective laser sintering (SLS) process. The behavior of interest is static deflection under a load applied 10" from the clamped end of the beam. Both the TSM and the ESM were used to predict beam deflection under the load. Again, the actual product was constructed and tested in order to evaluate the accuracy of the predicted results. The results of the test are shown in Figure 9. As shown in Figure 9, the ESM underpredicts the beam deflection by nearly the same amount as the TSM in this case (22% error).

In order to isolate the source of the ESM error, additional experiments were conducted with the following variations:

- Product and specimen geometry were varied
- Product material was varied (aluminum and polycarbonate)
- Loading conditions were varied (load applied at both 4" and 10" from the clamped end of the beam)

A total of 20 experiments were conducted with different combinations of the variables described above. Results of the experiments are shown in Table 1.

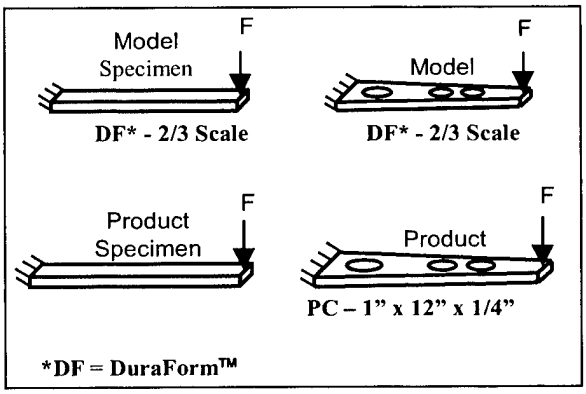


Figure 8. Beam Experiment with SLS Models.

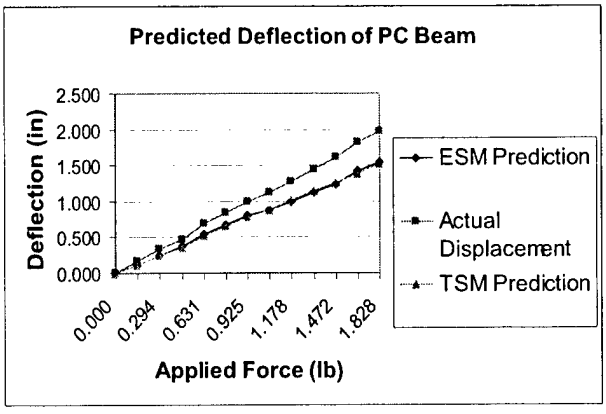
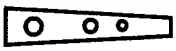
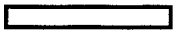
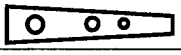
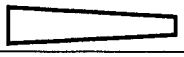
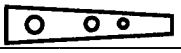
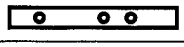
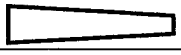
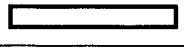
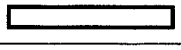


Figure 9. Experimental Results.

Table 1. Experimental Results.

Test	Product/Model Geometry	Specimen Geometry	ESM Prediction Error* (%)			
			PC @ 4"	PC @ 10"	Al @ 4"	Al @ 10"
1			-19	-22	-17	-25
2			+23	+22	+15	+28
3			+23	+22	+32	+21
4			-34	-38	-24	-41
5			-34	-39	-37	-38

*** A negative value indicates a prediction less than the actual value; a positive value indicates a prediction greater than the actual value.**

A review of the experimental results in Table 1 indicates that the predicted values are very sensitive to changes in geometry, but rather insensitive to changes in product material and application of load. The conclusion that can be drawn from these results is that the material and geometry transformations that are used in the ESM approach are not independent when DuraForm™ SLS models are used. In other words, a coupling appears to exist between material and geometry in SLS parts such that M(G), which violates the fundamental assumption of the ESM.

The SLS process was evaluated for clues as to the source of the coupling between material and geometry. Although many processing parameters could contribute to a coupling between material and geometry, the process evaluation led to the following primary hypothesis:

- Geometric size and complexity affects scan time and, consequently, exposure time between layers of sintered powder to part bed temperature.
- Exposure time of sintered powder to heat may affect the elastic properties (e.g. Young's modulus) of a sintered beam.
- Elastic properties of a beam directly affect static deflection under an applied load.

The hypothesis is to be tested by setting up a secondary experiment in which the effect of scan time, or exposure time of sintered powder to heat, on elastic properties of sintered parts is evaluated. The results of the secondary experiment will then be used to establish the functional relationship between material and geometry, or M(G). The ESM approach can then be expanded to account for such couplings between material and geometry.

IV. Conclusions

The potential benefits of using SFF parts to obtain functional information on products are tremendous. Replacing direct product tests with tests on SFF models could cut development costs and cycle time significantly. Using SFF techniques to obtain functional information more quickly can also provide more time for product refinement, thus leading to higher product quality.

Similitude methods provide a means of overcoming the current limitations of functional testing with SFF parts. The empirical similitude method has been demonstrated as an effective means of correlating distorted systems that are not compatible with the traditional similarity method. The empirical similitude method, however, operates under the assumption of independence between geometry and material properties. The study presented in this paper suggests that a coupling can exist between material and geometry when SFF parts are used as the model and model specimen.

Future work will include a secondary study aimed at isolating the source of the coupling between material and geometry and establishing the functional relationship M(G). Results from the secondary study can be used to expand the ESM to make it applicable to functional testing with SFF parts.

References

Barr, D. I. H. 1979. "Echelon Matrices in Dimensional Analysis," *International Journal of Mechanical Engineering Education*, Vol. 7, No. 2, pp. 85-89.

Bridgman, P. W. 1931. *Dimensional Analysis*, Yale University Press, New Haven.

Cho, U. and Wood, K. 1997. "Empirical Similitude Method for the Functional Test with Rapid Prototypes," In *Proceedings of the 1997 Solid Freeform Fabrication Symposium*, Austin, TX, pp. 559-567.

Fisher, T. S. et al. 1997. "Analysis and Optimization of a Natural Draft Heat Sink System," *IEEE Trans. On Components, Packaging, and Manufacturing Technology. Part A*, Vol. 20, No. 2, pp. 111-119.

Langhaar, H. L. 1951. *Dimensional Analysis and Theory of Models*, John Wiley & Sons, New York.

Nadworny, E. B. 1995. "High Power CPU Cooling Experiment," In *Proceedings of the Computers in Engineering Conference and the Engineering Database Symposium*, ASME, Boston, MA, pp. 1057-1066.

Sequin, C., Scherk-Collins Sculpture Generator [online], [cited 2001-8-17], Available from Internet: <URL:http://www.cs.berkeley.edu/~sequin/SCULPTS/scherk.html>

STL-based Finish Machining of Rapid Manufactured Parts and Tools

Xiuzhi Qu, Brent E. Stucker
Department of Industrial and Manufacturing Engineering
University of Rhode Island
Kingston, RI 02881

Abstract

Accuracy and surface quality problems when utilizing layered manufacturing technologies have limited its use in tooling areas. Therefore, in some situations a CNC machine is still necessary for finish machining of rapid manufactured parts and tools. This paper presents a STL-based CNC machining technique for automating the finishing of RP tools and parts to obtain CNC accuracies and surface finishes. Preprocess operations, such as rotate and scale, are used to change the part orientation and compensate for shrinkage in the whole process. An offset algorithm is developed to add "skin" to the original STL file to make sure enough material is left for finish machining after the rapid manufacturing process. The machining strategy of adaptive raster milling of the surface, plus hole drilling and sharp edge contour machining, is proposed to finish the RP parts and tools. Corresponding algorithms of adaptive tool path generation for raster milling, automatic hole recognition and drilling tool path generation, and automatic sharp edge detection and tool path generation are developed. Finally, a designed benchmark is machined successfully by using the above mentioned machining strategies and tool paths generated by developed software.

1. Introduction

In order to compete in today's global market, products must be developed and brought to market at an ever-increasing rate. This has led to the wide use of rapid prototyping and manufacturing technologies in industry. Until now, almost all rapid manufacturing techniques use layered manufacturing methods. Layered manufacturing processes, decomposing the 3D CAD model into 2D layers and building part layer by layer, have limitations on surface quality and accuracy. Therefore, in some situations CNC machining is still necessary for finish machining of rapid manufactured parts and tools to increase accuracy and to smooth the surface.

When using CNC machining to finish the parts, pre-processing of the original 3D model and quickly and correctly generating tool paths and machine code from a 3D model are very important issues. To a certain degree, this will determine the success of applying milling to Rapid Prototyping and Rapid Tooling (RP/RT). Thus, a CAM system is being developed to accomplish this purpose.

Today, many CAD systems are being used and each of them uses a different kernel to describe the geometry. It is not possible to read all of these different data formats using one software package. A standard format that can be output by most commercial CAD systems should be used as the input for this CAM system. When looking at standard formats for describing and transferring geometrical data, it was found that the STL format is readily available and can provide great accuracy when created

properly. In addition, the STL format is being widely used in rapid prototyping systems that use layered manufacturing technology. It has been shown that this format works very well and reliably for tool path generation [1,2]. Thus, the STL format is a good choice for CAM systems focusing on the application of machining to RP/RT.

The accuracy and surface quality of parts manufactured by RP technology are material and process dependent. In order to obtain high quality parts or tools, some pre-processing of the 3D model is necessary. Translation and rotation operations are used to optimize the part position and orientation. Scaling of the model is used to compensate for the overall shrinkage during the manufacturing process and finish machining is used to improve part accuracy and smoothness. In order to make sure there is enough material left on the surface to be machined, a 3D offset method is developed to add "skin" to the original model.

Considering both accuracy and machine efficiency, the machining strategy of adaptive raster milling of the surface, plus hole drilling and sharp edge contour machining, is applied to finish the RP parts and tools. According to surface curvature information, a stepover distance is calculated adaptively to maintain a minimum cusp height during raster milling of the model surface. This adaptive stepover distance increases machining efficiency while maintaining accuracy and surface quality. Sharp edges are normally the definition curves of features. By machining along these edges, the dimensional accuracy of critical features can be improved. The strategy of recognizing holes from the STL model and drilling them using the appropriate drilling tools reduces machining time and improves part accuracy. For finish machining of rapid manufactured parts or tools, the degree of automation and the total time used to generate tool paths from the model are important criteria. It is more important to generate tool paths automatically and quickly than to generate high efficiency machine code. The latter is more important for mass production, but for this application one, or at most a few, parts will be produced with the same geometry. So an automatic tool-path generation algorithm is developed, which requires very little user interaction.

2. Pre-process of 3D model

In most situations, pre-processing of the original 3D model is required before utilizing a rapid manufacturing process. These operations include changing the part orientation for optimization of building time or surface quality, scaling and offsetting the original model to compensate for part shrinkage and for other kinds of dimensional variations during the manufacturing process.

2.1 Translate, rotate and scale

For most layered manufacturing processes, the building position and orientation will influence part accuracy, surface smoothness and total build time. Thus translate and rotate operations are applied to the original model to optimize the part position and orientation. In addition, shrinkage usually occurs at some point during the manufacturing process. For example, using a SLS machine and a furnace to make cermet parts, it was found that shrinkage would occur during furnace cycles as well as during the SLS

process. Preprocess operations on the original model will allow a scale factor to be used to compensate for the overall shrinkage.

The implementation algorithms for these basic operations are first simply translating, rotating or scaling each vertex of triangles of the 3D model, and then recalculating the model size information. For rotate operations, one more calculation is needed to modify the unit normal values of all triangles.

2.2 Offset

In order to make sure there is enough material left on the surface to be machined, adding "skin" to the original model is necessary. From experiments performed in the Rapid Manufacturing Center (RMC) at the University of Rhode Island (URI) [3], it was shown that the shrinkage level varied, even for the same SLS and furnace parameter settings. This variation also requires offsetting of the original model to guarantee that even the features with the largest shrinkage levels still have material left for machining.

The algorithm developed for offset includes first offsetting all of the individual vertices of the model by using the normal information of all triangles, then reconstructing the triangles by using new vertex values. Normally each vertex is shared by several triangles whose unit normal vectors are different. When offsetting the model, the new value of each vertex is determined by the unit normal values of its connected triangles.

Suppose $\vec{V}_{Offset}$ is the unit vector from the original position to the new position of the vertex, and $N_1, N_2, ...N_n$ are the unit normal vectors of corresponding triangles. $\vec{V}_{Offset}$ can be calculated by the weighted mean of those unit normal vectors,

$$\vec{V}_{Offset} = \sum_{i=1}^{n} W_i * \vec{N}_i \tag{1}$$

where W_i are coefficients whose values are determined to satisfy the equation,

$$\vec{V}_{Offset} \bullet \vec{N}_i = 1 \qquad (i = 1,2...n) \tag{2}$$

After solving for $\vec{V}_{Offset}$, the new position of the vertex is given by the equation,

$$P_{new} = P_{original} + \vec{V}_{Offset} * d_{Offset} \tag{3}$$

where $\boldsymbol{d_{Offset}}$ is the offset dimension.

The above procedure is repeated until the new position values for all vertices are calculated. The model is then reconstructed using the new triangle information.

3. Machining Strategy

Machining strategy is very important for the finishing of rapid manufactured parts and tools. Considering both accuracy and machine efficiency, adaptive raster milling of the surface, plus hole drilling and sharp edge contour machining is applied in this paper.

3.1 Adaptive Raster Milling

Isoparametric curve machining, parallel plane-surface intersection curve machining, constant cusp height machining and space-filling curve machining are several very popular machining strategies used for freeform surface machining [4-6]. Through

analysis, it was found that parallel plane-surface intersection machining (raster machining) is the most suitable for 3D models represented by triangular planar facets (STL format).

When raster machining is used for milling operations, stepover distance is a very important parameter that controls the machining accuracy and surface quality. It is known that higher accuracy and surface quality require a smaller stepover distance. Normally the cusp height of material left after the model is machined is used as a measurement of the surface quality.

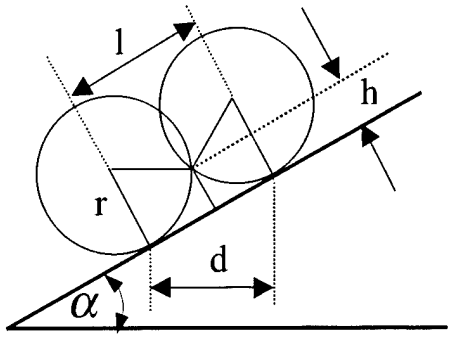


Figure 1. Illustration of determining stepover distance

Fig. 1 shows a triangle face being machined with a ball endmill. The relationship between cusp height h, cutter radius r, stepover distance d, and inclining angle α can be given in the following equation:

$$d = 2.0 * \sqrt{r^2 - (r-h)^2}\cos\alpha \tag{4}$$

α is determined by the triangle surface normal and stepover direction. Suppose $\vec{N}_{Triangle}$ is the unit normal vector of triangle surface, $\vec{N}_{Stepover}$ is the unit vector along stepover direction, then

$$\cos(\frac{\pi}{2} - \alpha) = \sin\alpha = \left|\vec{N}_{Triangle} \bullet \vec{N}_{Stepover}\right| \tag{5}$$

From Equations (4) and (5), the following equation is derived,

$$d = 2.0 * \sqrt{h(2r-h) * (1 - (N_{Triangle} \bullet N_{Stepover})^2)} \tag{6}$$

When machining the model, the cutter radius and milling direction are the same for all triangle surfaces. If given the required cusp height h, d is only related to the triangle normal vector. For surfaces with different normal vectors, the stepover distance obtained will be different. In order to guarantee a machining tolerance, a minimum d should be chosen for the whole raster milling step if a constant stepover distance is used.

Smaller stepover distances, however, will lead to longer programs and machining times. Therefore, an adaptive stepover distance for milling operations according to local geometry is used to allow for both accuracy and machine efficiency. It means that stepover distances are calculated dynamically for each just-finished tool pass, using the maximum cusp height to determine the stepover distance for the next tool pass.

3.2 Sharp Edge Contour Machining

Sharp edges are often the intersection curves between features and surfaces. Normally these edges define the critical dimensions. When using raster milling, the edges parallel to the milling direction can be missed and cause large errors. As shown in Fig.2, the stepover distance d is used to machine a part with a slot. Even when the CNC machine is perfectly aligned (i.e. ignoring machine positioning errors), the slot width error will be at least,

$$W_{Error} = 2d - \delta_1 - \delta_2 \tag{5}$$

When δ_1, δ_2 become 0, $W_{Error} = 2d$. It means that the possible maximum error is approximately two times the stepover distance. A machining experiment performed running tool paths generated by using constant stepover distance on a 3-axis CNC machine to make wax benchmark parts, when measured, also showed this result.

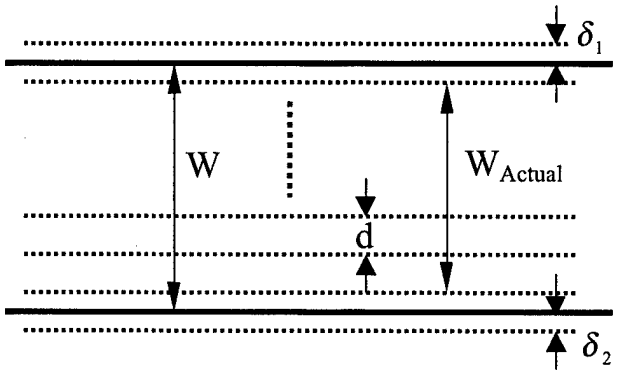


Figure 2. Influence of stepover distance on dimensional accuracy

For complicated edges not parallel to the milling direction, raster milling is ineffective for creating smooth edges. In addition, this will make the adaptive tool path generation algorithm less efficient. A method of milling along recognized sharp edges (contours) is developed to solve this problem.

3.3 Hole drilling

Circular holes are common features in parts and tools. Using milling tools to create holes is inefficient and the circularity of the holes is poor. Therefore, a machining strategy of drilling holes using the correct sized drilling tool is developed. The most challenging aspect is to recognize holes in all directions automatically. In the STL data format, the 3D geometry is represented by a collection of unordered triangular planar facets. Thus all feature information is lost. The algorithms used in the next section allow for reconstructing the holes and determining their diameters, orientations and depths.

4. Automatic Tool Path Generation

One of the essential tasks of finish machining is to generate the tool paths automatically from the 3D CAD model. Based on the machining strategies proposed above, the corresponding algorithms for adaptive tool path generation for raster milling, automatic hole recognition and drilling tool path generation, and automatic sharp edge detection and tool path generation have been developed.

4.1 Tool Path Generation for Raster Milling

For tool path generation using raster milling, the most widely used method is to first calculate the cutter contact point on the model, then use normal direction and cutter size information to find the cutter location. This method normally requires gouge detection algorithms to adjust cutter location data in order to avoid overcuts for some complex surfaces. Gouge detection development is time consuming and complex. An alternative, offset surface method can generate gouge-free tool paths [7], and offset algorithms were developed for the above-mentioned skin addition operation. Therefore, offset surface milling algorithms are used for tool path generation.

Fig. 3 shows a flowchart for this tool path generation program. It is designed for use with ball endmills. The original facet model is offset by the cutter radius. This new model represents the cutter location points. Because not all triangular surfaces can be accessed by the cutter in a 3 axis machine using one setup, only the triangles who have positive z-components of their normal vectors are picked to generate a machinable triangles list. Taking into account the milling direction given and relevant 3D model information, a starting cutting plane is defined. For example, if the milling direction is along the x axis and the minimum y value of model is $y_{\min}$, then the plane $y = y_{\min}$ is defined as the starting plane. By calculating the intersections between the cutting plane and the triangle facets in the machinable list, many line segments will be defined. These segments are sorted, checked and linked to identify the top envelope lines that will become the tool paths. By using equation (6), the required stepover distance can be calculated for each line segment, or tool pass. The minimum distance is used as the stepover distance to update the cutting plane. The above procedure is repeated until the cutting plane lies outside of the model.

4.2 Tool Path Generation for Sharp Edge Contour Machining

In order to machine along sharp edges, all sharp edges must be identified from the STL model first. The normal vector information of each triangle is used to check the property of the edge. The angle between normal vectors of two neighboring triangles is calculated. If this angle is larger than a specified angle, the edge shared by these two triangles will be marked as a sharp edge. If edges are not accessible by a cutter, they are eliminated, and leaving only the "nearly-straight" walls of interest for machining. Thus, hidden edges and edges not belonging to vertical surface are removed from the sharp edges list. Overlaps of edge projections in the XY plane will cause redundant tool paths, they are also eliminated before tool paths are calculated. By offsetting the edges by the cutter radius, the x, y location of the endmill is obtained. The z value is determined by calculating the intersection with the 3D model and finding the corresponding maximum z value. Fig. 4 shows a flowchart of the process.

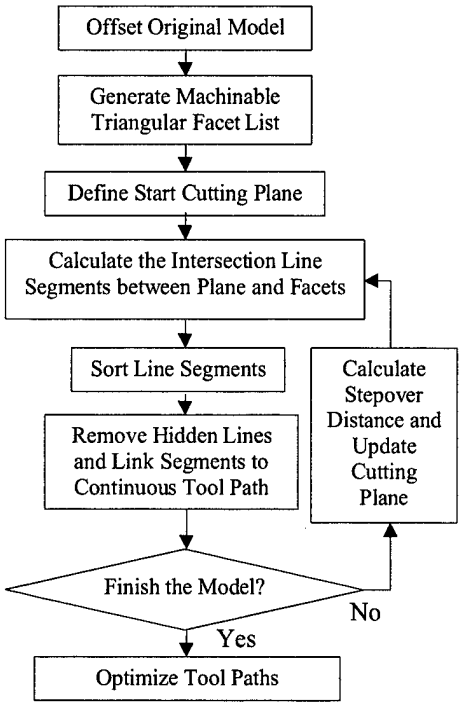


Figure 3. Flowchart of Tool Path Generation for Raster Milling

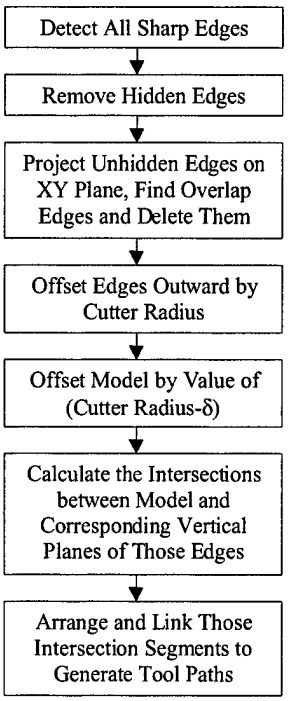


Figure 4. Flowchart of Tool Path Generation for Sharp Edges

4.3 Hole Drilling Tool Path Generation

The intersection curve between a hole and a surface is typically a closed loop. Thus, closed loops are constructed using sharp edges from the entire model. However, these closed loops will not necessarily be the intersection curves between holes and the model surface. A hole checking method is used to remove the loops that do not correspond to a drilled hole. The remaining loops and hole geometry are used to determine the diameter, axis position and direction, and depth for drilling. Finally, the tool path can be easily generated using information. Fig. 5 summarizes this procedure.

The hole checker algorithm shown in Fig 6 illustrates how to determine if loops represent drilled holes in the surface. In most situations, more than 10 triangular facets are needed to reconstruct hole surfaces in order to meet accuracy requirements. This criterion is used to quickly remove unsatisfactory loops. The cross product of two different normal vectors of the inside surface of the hole will give a vector that is parallel to the hole axis direction. Based on this information, 3 evenly distributed edges in each loop are selected. For each edge, there will be two corresponding triangular facets, only one of which belongs to the hole surface. By calculating the cross products of normal vectors of these triangles, the hole orientation is obtained. By projecting all of the edges inside the loop onto the plane that is perpendicular to the hole axis direction, passing through (0,0,0), the circularity of the loop is checked. Center and diameter information is obtained if it meets circularity conditions.

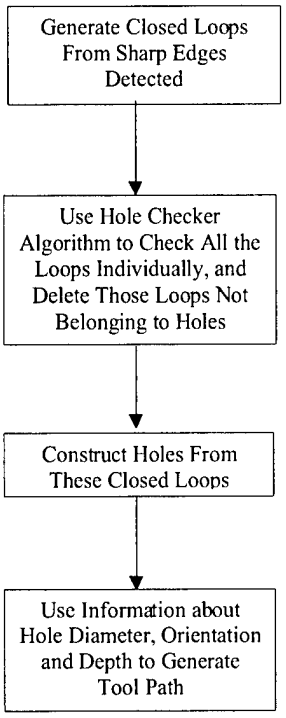


Figure 5. Hole Recognition and Tool Path Generation

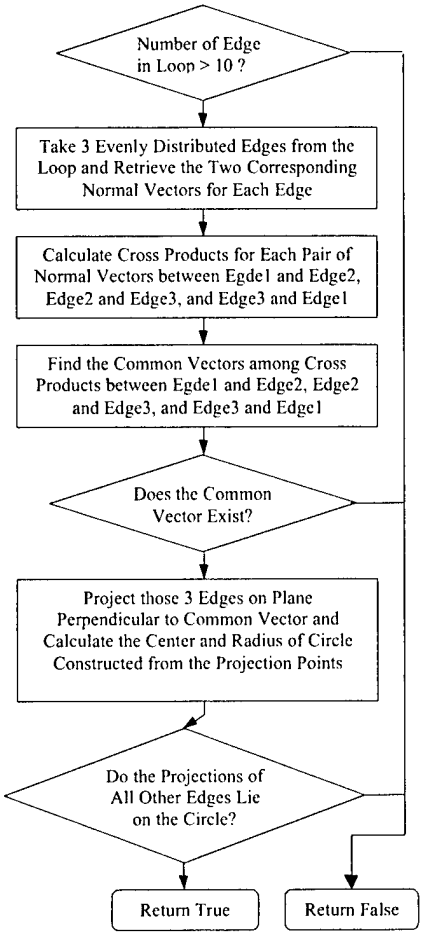


Figure 6. Flowchart of Hole Checker

5. Application

A benchmark shown in Fig.7 is designed to efficiently verify the proposed machining strategies and automatic tool-path generation algorithms developed. This benchmark includes a variety of features, such as different types of surfaces, complicated sharp edges and holes in different orientations. The part is successfully machined using G code generated by the developed software on a 3-axis CNC machine.



Figure 7. Designed Benchmark

6. Conclusion

The overall objective of this project is to develop techniques for finish machining of rapid manufactured parts and tools. The work focuses on the issues of original STL file preprocessing and STL-based automatic tool path generation for CNC machining.

Preprocess operations, such as rotate and scale, are used to change the part orientation and compensate for shrinkage in the entire process. An offset algorithm was developed to add "skin" to the original STL file to ensure material is left for finish machining after the rapid manufacturing process.

Layered manufacturing techniques have many benefits over traditional tooling manufacture methods. Accuracy and surface quality problems, however, have limited its use in tooling areas. Therefore, in some situations a CNC machine is still necessary for finish machining. Considering the popularity and reliability of the STL format, it was chosen as the input file type for CAM software development. The machining strategy of raster milling of the surface, plus hole drilling and sharp edge contour machining, is proposed and automatic tool path generation has been developed.

Future work on pre-processing will be aimed at adding reference fixture features to the original 3D model to facilitate easy and accurate mounting of the part on a CNC machine. To improve machining efficiency, a surface splitting algorithm will be developed to divide the model into several regions using sharp edge information. These different types of surfaces can be machined by using different strategies and cutters which are more optimum for each type of surface identified.

References

[1]. J.W. Gunnick, Multi-Axis High Speed Milling: How to Speed up Prototyping & Tooling Process by Using STL Technology, Proceedings TCT Conference 1998, Nottingham, Oct 1998:43-65.

[2]. Lex Lennings, Selecting Either Layered Manufacturing or CNC Machining to Build Your Prototype, Rapid Prototyping and Manufacturing Conference 2000, Rosemont(Chicago), April 2000.

[3]. Muni Malhotra, Rapid Manufacture of Zirconium Diboride/Copper & Dimensional Stability of RapidSteel® 2.0, MS thesis, University of Rhode Island, RI, May 2000.

[4]. C.G. Jensen, D.C. Anderson, A review of numerically controlled methods for finish-sculptured-surface machining, IIE Transaction, Vol. 28, pp. 30-39,1996.

[5]. D. Dragomatz and S. Mann, A classified bibliography of literature on NC milling path generation, Computer Aided Design, 29(3), pp. 239-247, 1997.

[6]. Chih-Ching Lo, CNC machine tool surface interpolator for ball-end milling of free-form surfaces, International Journal of Machine Tools and manufacture, 40(3), pp. 307-326, 2000.

[7]. K.I. Kim, K. Kim, A new machine strategy for sculptured surfaces using offset surface, International Journal of Production Research, 33(6), pp.1683-1697, 1995.

this page intentionally blank

A System Approach in Extrusion-Based Multi-Material CAD

Cheng-Tiao Hsieh and Noshir A. Langrana

Department of Mechanical & Aerospace Engineering
Rutgers - The State University of New Jersey
98 Brett Road, Piscataway, NJ 08854

Abstract

For extrusion based multi-material Layered Manufacturing (LM) processes, a CAD system has been developed for the Fused Deposition of Multiple Ceramics (FDMC) hardware. This closed loop CAD system includes solid model design & multi-material slicing, multi-material toolpath generation and virtual simulation modules. Intelligent features and an adaptive roadwidth optimum toolpath generation algorithm compute void sizes & their location and generate a void free toolpath [1][2]. The present study focuses on a comprehensive approach, which includes a format that contains the information on the geometry of the multi-material components, the build materials and the necessary fabrication process information. Multi-CAD utilizes computer graphics techniques to visualize the fabricated part. The slicing algorithm is utilized to create multi-material contours, which then are integrated into our previously developed intelligent tool-path system.

Introduction

As we know, there are many advantages to introducing layered manufacturing systems into current manufacturing environments. These include the capability to fabricate parts with complicated geometry, shorter process time and the elimination of assembly of components. The above advantages dramatically reform the economics of current industry to satisfy the needs of the competitive market. Unfortunately, a big drawback of most LM systems is that constraints in handling multi-material products. A major reason is that their computer models do not contain material information. Without material information, LM systems are unable to distinguish the multi-material models and always treat them as single-material models. To overcome this drawback, developing a multi-CAD system to recognize multi-material models is needed. The developments in fabricating multi-material parts include two parts, the development of multi-material LM systems and the development of multi-material CAD system. Examples of the recent developments include the Shape Deposition Manufacturing (SDM) developed at Stanford University and Fused Deposition of Multiple Ceramics (FDMC) built at Rutgers University. Of multi-CAD systems, Vinod Kumar proposed an approach to modeling multi-material objects in 1997 [3]. Dan Qiu presented a multi-material tool path generation in 2000 [4][5].

1. The Configuration of Multi-CAD System

Figure 1 shows the configuration of our multi-material CAD system. This multi-CAD system is based on the Fused Deposition Method (FDM) - an extrusion based LM system. The FDM system includes a liquefier to heat up the filaments and a two-dimension table to drive the liquefier along the tool path to deposit the molten filaments layer by layer to build up the part.
The multi-CAD system requires component STL models from available CAD modelers such as I-DEAS, Pro/E and AutoDesk. The CAD systems allow us to position the STL models in the

desired locations. After all STLs are made, we use Multi-CAD to indicate the building material for each STL model separately and then assemble them into a new multi-material model [1][2]. This new multi-material model includes not only geometry information, but material information as well. The above information enables the multi-CAD system to display multi-material models on the screen and to proceed with LM multi-material fabrication processes (slicing process and tool path generation process). Because the LM fabrication processes applied in the Multi-CAD system all are based on a multi-material model, the model slicer and tool path generator must be able to recognize the multi-material model to accomplish their tasks.
The model slicer slices a multi-material model into a slice model (a set of contours) and then the tool path generator executes its job according to the slice model. The tool path generator is designed to create void free FDM parts.

In previous studies at Rutgers, we had found numerous defects in fabricating multi-material FDM parts [1][2][4]. To eliminate the defects, we have introduced a material library into our Multi-CAD system [5]. The material library stores the control parameters for all of the building materials; the parameters guide the LM system to avoid the defects. Greater detail on the material library will be addressed later in this paper.

The multi-CAD system also provides fabrication simulation to make virtual FDM parts. It applies computer graphics technology to assist us in evaluating the FDM parts (especially the insides of the parts). This road shape simulator also links with the road shape library, which assists us in selecting the right shape of nozzle to fabricate void free parts.

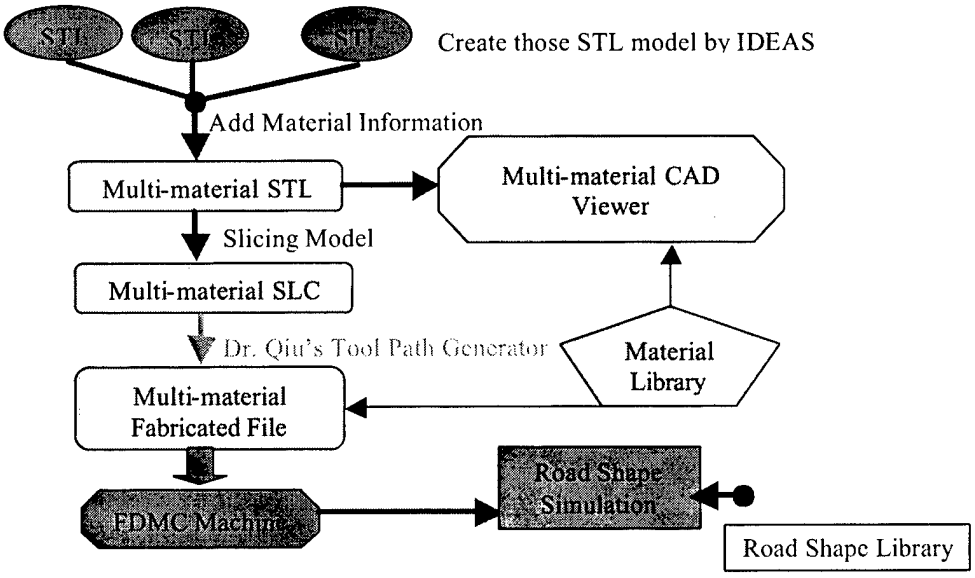


Figure 1 The Configuration of Multi-CAD System

2. Assembly STLs to Multi-material Model:

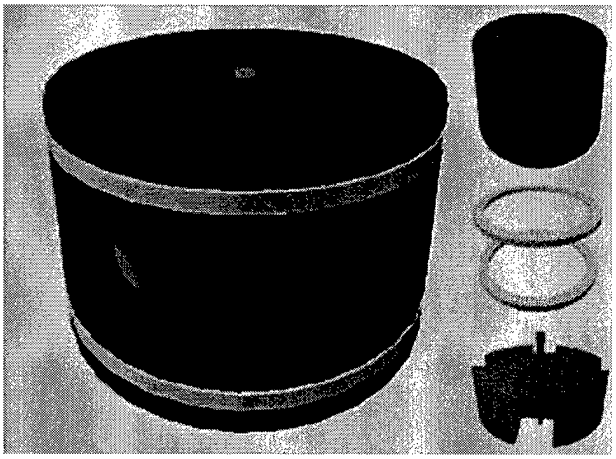
STL is the most common solid model format used in the LM industry. For this reason, we chose it for the components of the multi-material model. It describes its surface by a set of triangular facets; it is also known as a surface solid model. The format includes a file-name and a collection of triangular facets. Every facet is defined by a normal vector and three vertices. The normal

vector, a normalized vector, is used to indicate the outward direction of the surface. The most important task of this vector is to allow the computer to distinguish between the inside and outside of the solid model. In addition, it offers instant data for lighting effects in computer visualization. The vertex coordinates of the triangular facets play an important role in fabricating an accurate part by determining the shape and scale of the model.

2.1 Prepare STLs by Commercial Modelers:

STL contains only geometry information; this information is inadequate for supporting our multi-CAD system. The issues to be resolved in order to accomplish the preparation of STLs for a multi-material model are summarized as follows:

(1) Scale or Unit Issue:
Our goal is to fabricate an accurate multi-material part, so the scale and unit of the model is very important to us. Unfortunately, STL does not include information on its unit system. To handle this disadvantage of STL, it is necessary to know the type of unit system used in commercial modelers since they are the original sources of the STLs. In our investigation, we have found that STLs converted from I-DEAS are based on the INCH system. This means that the scale of such STLs is 1:1 with the INCH system of I-DEAS. Once the STL is generated, it can be treated as a standard and then scaled to other unit systems.



```
solid  MATERIAL1
  facet normal VX VY VZ
    outer loop
      vertex X Y Z
      vertex X Y Z
      vertex X Y Z
    endloop
  endfacet
:
:
endsolid  MATERIAL1
solid  MATERIAL2
  facet normal VX VY VZ
    outer loop
      vertex X Y Z
      vertex X Y Z
      vertex X Y Z
    endloop
  endfacet
:
:
endsolid  MATERIAL2
:
:
```

(a) (b)

Figure 2 (a) Solid Multi-material Model (b) Multi-material STL Format

(2) Assembly Issue:
Since it is required that the componential STLs are created independently, we have to carefully create each component in its exact position to provide for perfect matches during the assembly process. Fortunately, most commercial modelers are good at translation and rotation. Using these functions, the STLs can be easily located to the desired positions and then assembled to the multi-material model. Our multi-CAD system does not have the

function to optimize the building orientation, so the building orientation should also be considered when componential STLs are created.

2.2 Multi-material Model Format:

Our multi-material model is a set of STLs, as shown on Figure 2(a). The title name of STL following the word "solid" is redundant data, so we replaced it with a material index (used to indicate the building material of the STL). The material index is a standard in our material library. Users continuously load the STLs and define their building materials by the multi-CAD system. Multi-CAD will automatically generate the multi-material model. The format of multi-material models is shown in Figure 2(b). It contains a material index, normal vectors of the facets, and the coordinates of the vertices.

For visualization, we treat the material index as a material color index because we would like to distinguish materials by color. In order to visualize multi-material models, it is necessary to store all OpenGL color parameters of the available FDM building materials in the material library. The material index in the multi-material format will guide the multi-CAD system to find its color parameters from the material library. The color parameters are then applied in OpenGL view functions to display the models appropriately.

2.3 Efficient Data Structure:

Many researchers have investigated the use of efficient data structures to speed up the slicing process [6][7][8]. Including topology information in data structures is one such method [9]. Based on this technique, the data structure shown in Figure 3 was developed to fulfill our need. Our data structure includes two sets of data: one set stores the coordinates of all vertices while the other set stores the instant data containing the topology (facet, the minimum points and maximum points in XYZ directions of componential models, normal vectors of facets, and the number of facets of componential models). The instant data were calculated from original STL data and stored in computer memory to await calling from our processes. The processes can immediately obtain them from computer memory without re-calculation, dramatically speeding up execution. The instant data offers good advantage, but unfortunately we cannot extend them without limit. Huge instant data will occupy enough computer memory to affect the ability of Multi-CAD systems to handle large models. In order to avoid this problem, we need to determine the optimal size of instant data.

Because the capability to handle large-sized models is one of our goals, we introduced the "INDEX" algorithm to reduce redundant instant data and save memory. The "INDEX" algorithm uses a 2-dimension integer variable type matrix to indicate the connection of facets and vertices, *facets[#facets][4]* storing three vertex indexes of the facet and one register for the slicing process. All of the vertex coordinates will be 2-dimension float variable matrix, *points[#points][3]* storing a point index and 3-D coordinates. As we know, the size of the variable *Integer* is 16 bits, and the size of variable *float* is 32 bits. The size of *integer* is just half that of *float*, so we can eliminate redundant instant data and shrink the size of instant data at same time.

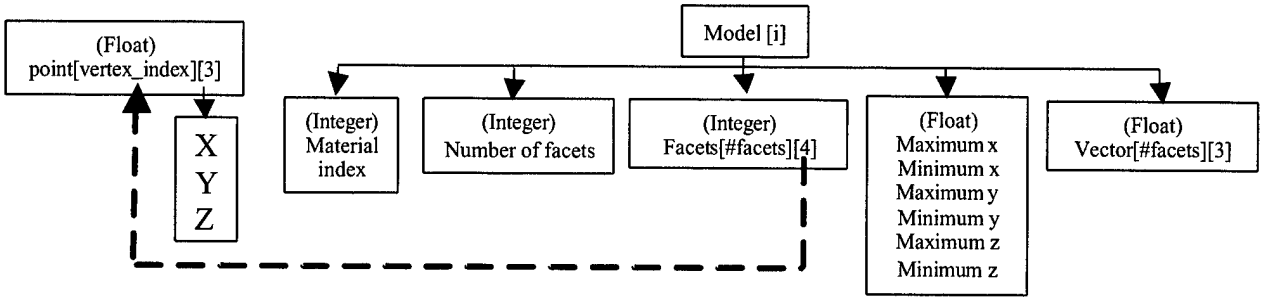


Figure 3 Data Structure Used in Multi-CAD System

3. A Slicing Process for Multi-material Model:

The slicing process includes three stages: search for appropriate edge to begin slicing, generating intersection points, and determining slicing direction [10]. The key to slicing multi-material models is to slice componential STLs independently and to indicate their building material on their contours at same time. In this study, the slice thickness is kept constant. The details of slicing a multi-material model are shown in the following chart, Figure 4.

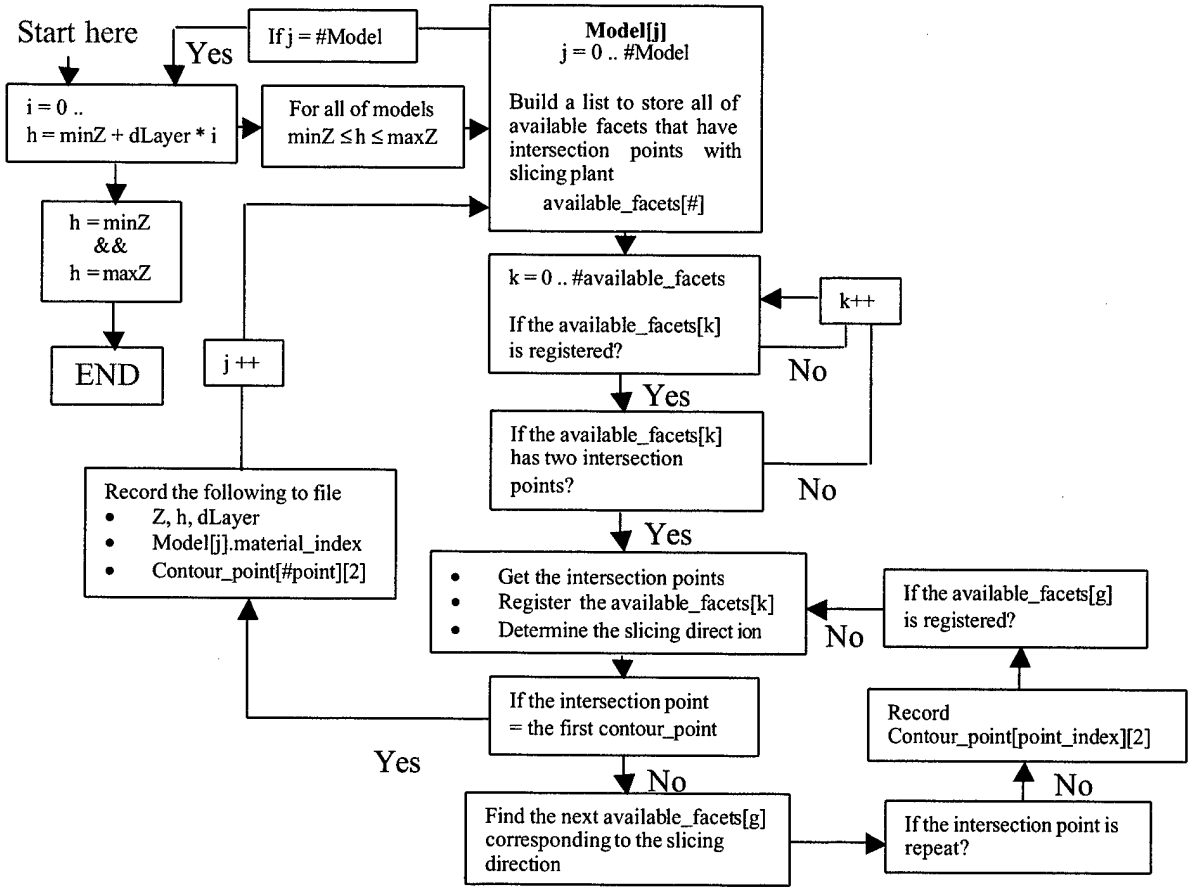
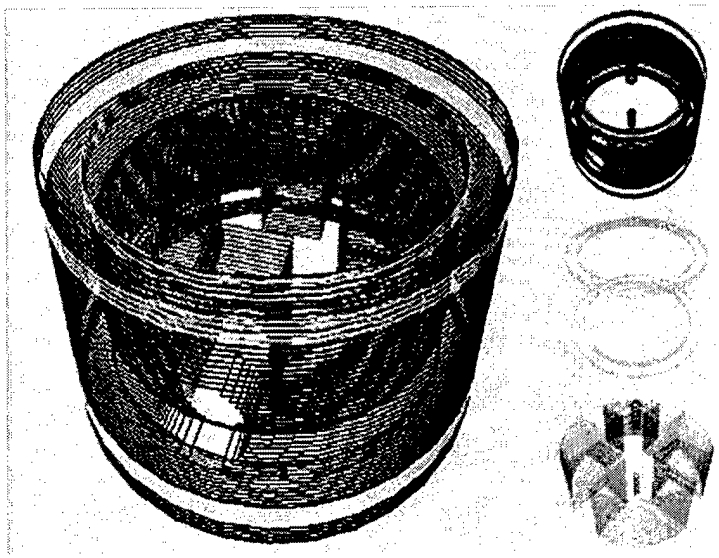


Figure 4 The Flow Chart of Multi-material Slicing Process

The sliced model visualization is the same as that of a solid model Figure 2, the material index guides the multi-CAD system to its OpenGL color parameters in material library and contours are displayed appropriately as shown in Figure 5(a). Since there is no standard format for slice files, the format of our multi-material slice file is similar to the Stratasys SSL file format shown in Figure 5 (b) [11].



(a)

Z z-coordinate z-step
Material index
Number of contour points
X0 Y0
X1 Y1
X2 Y2
:
:
:
Z z-coordinate z-step
Material index
Number of contour points
X0 Y0
X1 Y1
X2 Y2
:
:
:
END

(b)

Figure 5 (a) Multi-material Contour Model (b) Multi-material Contour Format

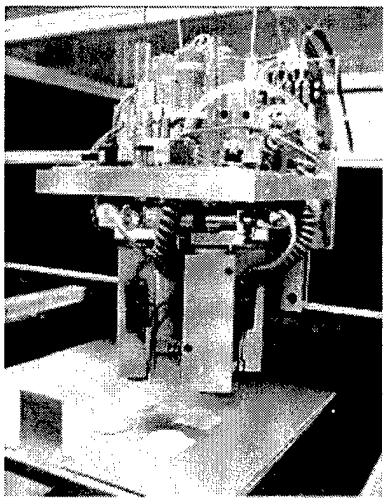
4. Tool Path Generation:

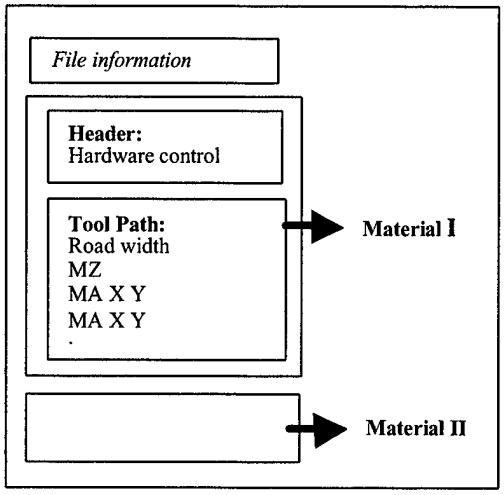
Because our model is a multi-material model, it may include many contours with various materials at the same level. In addition, contours can also be classified as outside and inside contours. It is necessary to classify such contours group by group to allow the tool path generator to correctly process its task. Contour orientation is the way to distinguish between outside and inside contours. The orientation of outside contours is counterclockwise, and that of inside contours is clockwise. The multi-CAD slicer slices the multi-material model component by component, so contours with various materials can be easily classified. At this stage, the previously developed intelligent tool path generator [4] can be used to create defect free virtual parts.

5. The Generation of FDM Fabricated File:

The process to generate a FDM fabricated file is to put the tool path and hardware control parameters together. The hard control parameters include start flow, main flow, head speed, liquefier temperature, and the size and shape of nozzle. These control parameters are sensitive to the building material. In other words, the setups of control parameters will be different if the

building material is changed. To address this need, we introduced the material library into our multi-CAD system. It contains all of the control parameters for each building material. The multi-CAD system will choose the appropriate control parameters from the material library according to the material index of the multi-material model. Once the control parameters are defined, the multi-CAD follows the format of the fabricated file shown in Figure 6 to put them together with the tool path. The process is repeated for each building material in the multi-material model to complete the fabricated file for the multi-material model.





(a) (b)

Figure 6 (a) Fused Deposition of Multiple Ceramics (FDMC)
(b) The Format of Multi-material Fabricated File

6. Road Shape Simulation:

Based on our experimental study at Rutgers, we know that the size and the shape of the deposited roads are dependent on the material and the processing parameters. The purpose of building the road shape simulator shown on Figure 7 is to simulate the fabrication process of FDM (Fused Deposition Manufacturing). The simulation program using computer graphics technology allows us to detect errors and to remove the errors from the FDM fabrication process easily and quickly. Generating a virtual FDM part by the simulator requires little time; it is much faster than the time to generate a physical FDM part. This methodology reduces product cycle time and enhances the quality of products.

Conclusions

In this paper, we have demonstrated a systematic approach to fabricating multi-material products by a FDM system. The approach includes a new multi-material model, a multi-material slicing process, multi-material tool path generation, and multi-material fabricated file generation. In addition, we have also introduced a virtual manufacturing simulator to remove errors from the fabrication process. This system has demonstrated great benefit by shortening the product cycle and reducing cost.

Acknowledgement

The research reported here has been performed towards the partial fulfillment of requirements for PhD thesis of the first author. The authors would like to thanks the Office of Naval Research (ONR) Drs. R. Wachters, G. Spanos and K. Cooper for financial support under #N00014-96-1-1175 Multidisciplinary Research Program of Univ. Research Initiative (MURI).

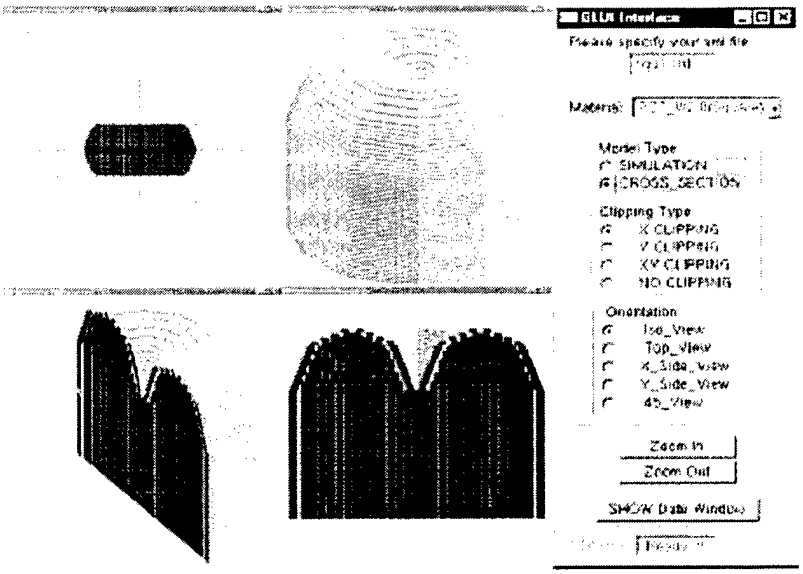


Figure 7 Road Shape

References

1. Langrana, N.A., Qiu, D. et al. (2000). "Virtual simulation and video microscopy for fused deposition method", Journal of Materials & Design, **21**: 75-82.
2. Langrana, N.A., Qiu, D. et al. (2000). "Design, Simulation and SFF Techniques for Functional Components", in the CD-ROM Proceedings of ASME 2000 Design Engineering Technical Conferences, DETCC00/MECH-14205, Baltimore, MD.
3. Kumar, V. and Dutta, D. (1997). "An Approach to Modeling Multi-Material Objects", pages 336-345, in the Proceedings of the 4th Symposium on Solid Modeling and Applications. Atlanta, GA.
4. Qiu, D. and Langrana, N.A., (2001), "Void elimination algorithm for extrusion based layered manufacturing", in the CD-ROM Proceedings of ASME 2001 Design Engineering Technical Conferences, DETC2001/DFM-21197, Pittsburgh, PA.
5. Langrana, N.A., Qiu, D. et al, (2000) "Design tools for Multi-material Layered Manufacturing System", in the Proceedings of 24th Annual Cocoa Beach Conference and Exposition, The American Ceramic Society.
6. Kulkarni, P. and Dutta, D. (1996). "An accurate slicing procedure for layered manufacturing." Computer-Aided Design **28**(9): 683-697.
7. Rock, S.J. and Wozny, M.J., (1991). "Utilizing topological information to increase scan vector generation efficiency", Proceedings of the Solid Freeform Fabrication Symposium, University of Texas at Austin.
8. Rock, S.J. and Wozny, M.J., (1992). "Generating Topological Information from a Bucket of Facets", Proceedings of the Solid Freeform Fabrication Symposium.

9. Tata, K., Fadel, M.G., et al. (1998). "Efficient slicing for layered manufacturing." Rapid Prototyping Journal, **4**(4): 151 - 167.
10. Sabourin, E., Houser, S.A., et al. (1996). "Adaptive slicing using stepwise uniform refinement." Rapid Prototyping Journal, **2**(4): 20 - 26.
11. http://www.Stratasys.com (personal communications)

this page intentionally blank

Maximum visibility building direction for layered manufacturing of jewel rings

Y. Y. Young, K. M. Yu, C. K. Kwong

Department of Manufacturing Engineering, The Hong Kong Polytechnic University
Hung Hom, Hong Kong

Abstract

Rapid prototyping is used in jewelry production since the introduction of Stereolithography Apparatus into the market. However, the building orientation is mainly decided by the experience of the operator rather than by any systematic analysis. A theory is therefore needed to analyze the best orientation of jewelry in rapid jewelry production. In this paper, a new orientation methodology is applied to jewel ring models to properly orient them for layer manufacturing. Jewel ring model built is then demonstrated to have better quality and less error. A case study is presented to illustrate the theory.

Introduction

There are a number of researches being done in the past about part orientation in rapid prototyping or layered manufacturing. In 1994, Dietmar and Georges [1] proposed an expert system tool for determining the preferred part building orientation for stereolithography processes. An expert system was used to interact with the user to assess the most critical issues for deciding the optimal part building position. Three aspects were concerned in the expert system: surface finish, build time and support structure. Surface finish is considered as the most important, then the build time and finally, the support structures. The research defines specific geometric features such as a hole or a plane. Characterristic feature axis is defined and orientation of specific geometric features is described. In 1994, Allen, Dutta and Arbor [2] determined the best direction to build an object by layered manufacturing processes. The object was constructed with minimal support structures and was stable, and rested on a planar base. Ray-structure computation was used for each orientation in analyzing the support structure. The object intersects with rays will produce intersection points. The intersection points are then classified by the direction of normals. For face with normal pointing upwards, the corresponding point on the object does not need support, otherwise, the boundary points on the object may need support. For the latter, they will be further classified as supported or unsupported. If the angle between the face normal and the negative z-axis (building direction) is smaller than the user specified angle, support will be added. Otherwise, the points are unsupported. In 1995, Cheng, Fuh, Nee, Wong, Loh and Miyazawa [3] developed a multiple objective-function as a formulation to derive the optimal orientation for stereolithography process. Two objective functions are defined. The primary objective function considers the part accuracy. The influence by the types of surfaces on the accuracy will be represented by a weighting. The secondary objective function deals with the build time. The build time of the orientation obtained from primary objective function is checked. In 1997, Ng and Tan [4] optimized the part orientation in rapid prototyping processes by using feature-based functions. Three factors were used to

determine the optimal orientations: part accuracy, build time and support structures. Two functions: feature weight and feature objective value were used to analyze the part accuracy and to determine the potential candidates for optimal part orientation. Optimal orientation was then chosen from the potential candidates based on minimal building time using minimum number of layers. In 1997, Xu, Wong, Loh, Fuh and Miyazawa T. [5] sliced a CAD model directly by introducing an adaptive variable thickness slicer implemented on a solid CAD modeller and obtain an optimal building orientation by considering building time, part accuracy and part stability in SLA systems. The building time is measured in terms of the number of layers to be built. In building parts using SLA, part accuracy can be improved by minimizing the overhang area. Overhang area is calculated by using a function. If the projection of the mass center falls within the convex hull of the base geometry, the part is assumed to be in a stable building direction. If not, the part is unstable in that building direction.

In general, the previous researches concern mainly with part accuracy, build time, support structure and part stability of the prototype to be built in the RP machine. However in jewelry production, aesthetic quality is the main concern. In layer manufacturing of jewelry, the building orientation will definitely affect the quality of the prototype. Thus, a new methodology is introduced in this paper to give the best-built orientation for jewelry production.

Maximum Visibility Building Orientation

Inherently, layered manufacturing is an approximation process even though direct slicing and adaptive slicing is used. As an aesthetic product (rather than a functional product), the staircase approximation error is better minimized from the observer. In layer manufacturing of jewelry, the best build orientation is the direction with least error visible instead of build time, accuracy, or minimization of support. In this paper, a new methodology, **maximum visibility building orientation** is introduced to find the best orientation of jewel ring in layer manufacturing.

For any three-dimensional object, different viewing direction will give different boundary information to the viewer. Except for highly symmetric objects, some viewing directions will provide the maximum information. The maximum visibility direction of an object is the direction in which maximum visible surfaces can be observed. In other words, it is the one giving the maximum projection area.

To obtain maximum visibility building orientation, two steps are needed. First, the orientation information is extracted from the CAD model. Second, the maximum visibility direction is determined using the projection area criterion. For step one, Gaussian image is used to represent the orientation information of the CAD model. For the second step, the Gaussian image is extended to include the local area associated with a particular viewing direction. Figure 1 shows the flowchart of the whole process.

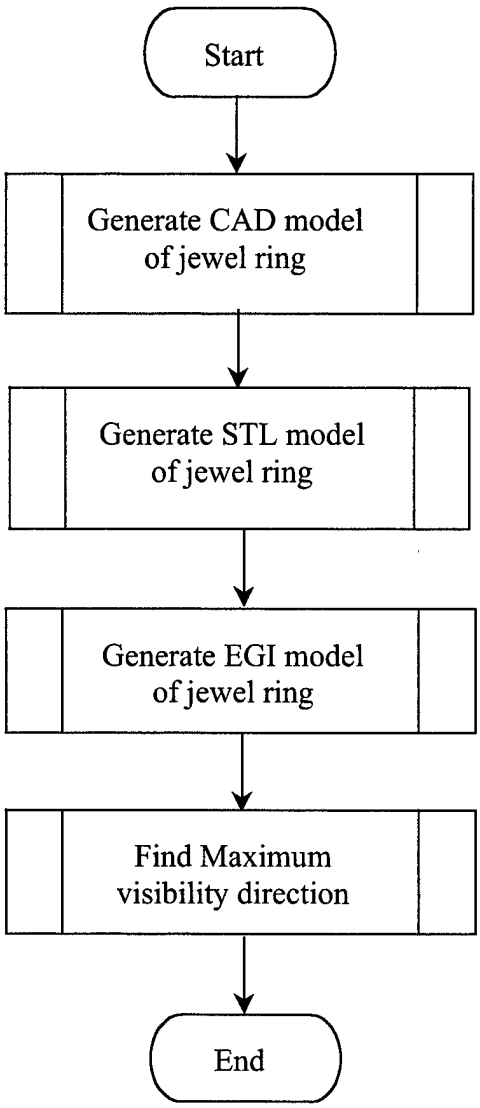


Figure 1. Complete process of maximum visibility orientation.

A CAD model of a jewel ring is first constructed. Then the STL file of the jewel ring is created to obtain approximated model with triangular facets. Next, the extended Gaussian image (EGI) model of the jewel ring is generated.

The Gaussian image of an object is obtained by associating with each point on its boundary surface a point on the Gaussian sphere which has the same surface orientation as shown in Figure 2. For convex object with positive Gaussian curvature everywhere, no two points have the same surface normal. Thus, the mapping from the object to the Gaussian sphere is invertible. However, if the convex surface has patches with zero Gaussian curvature, curves or even areas on it may correspond to a single point on the Gaussian sphere [6]. The many-to-one mapping encapsulates only the orientation information of the object. Other geometric information, like size, surface type, is not considered.

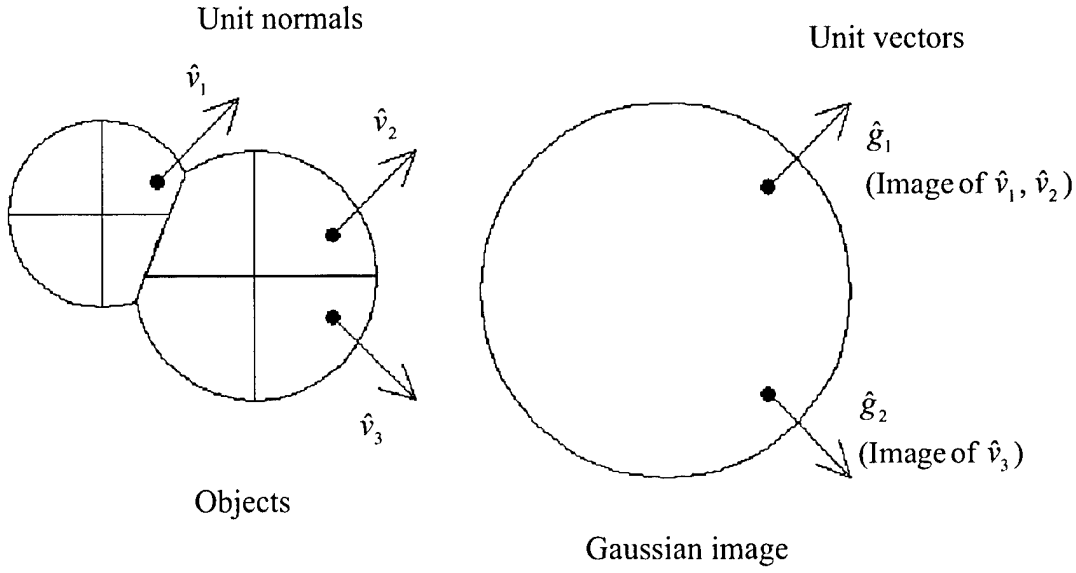


Figure 2. Gaussian image of an object.

The Gaussian image will only give a collection of directions. In other words, all elements have unit length. To extend the Gaussian image to rapid jewellery production, regions of the jewellery product visible in the same direction will be quantified as area. The EGI for rapid jewellery production use will thus have elements of Gaussian image weighted by area. In other words, elements in EGI may have different lengths. If a lot of boundary points in the object have the same outward normal, the corresponding image in EGI will be longer. The EGI of an object is independent of the position of surfaces and it represents the distribution of the surface normals. In general, it is difficult if not computationally expensive to find the EGI of non-convex object. A polygonal approximation is therefore used. In particular, triangular facetted approximation in STL file format is employed to obtain the EGI. Figures 3a – c shows an example of using EGI to represent an ellipsoid. Each arrow in Figure 3a represents a surface normal direction. The length of each arrow in the Gaussian sphere represents the area of facets with the same direction in Figure 3b. The tails of each arrow in Figure 3c are pointed from the center of the sphere.

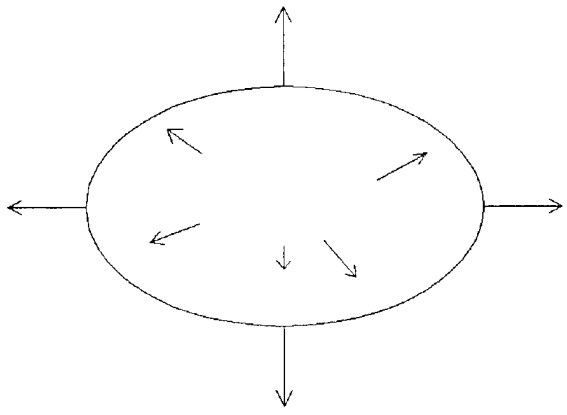


Figure 3a. Ellipsoid with its surface normals.

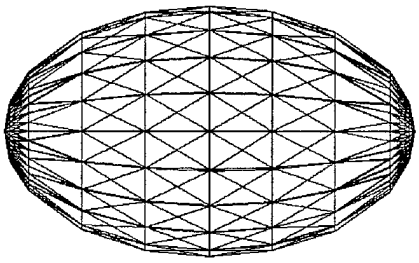


Figure 3b. Facet approximated model of the ellipsoid.

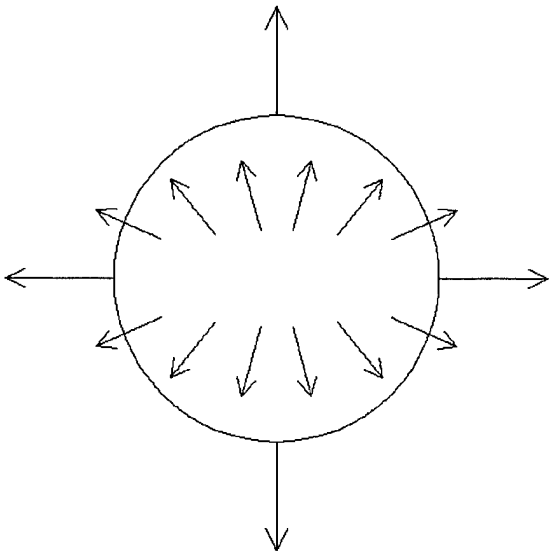


Figure 3c. EGI model of the ellipsoid.

For any object, there exists a direction in which maximal surfaces are visible. If the object is built by aligning maximum visibility direction with the building direction, the rapid prototype of jewel ring model will have the best quality.

Using the EGI model, the maximum visibility direction for a jewel ring model can be easily found. Each element in the EGI model has direction $\hat{n}_i$ and magnitude ΣA_i. The maximum visibility direction is the resultant vector $\sum_{i=1}^{m} A_i \hat{n}_i$.

However, a jewel ring has a through hole. If all the vectors $A_i \hat{n}_i$ are summed, the resultant vector $\sum_{i=1}^{m} A_i \hat{n}_i$ will be equal to zero. Thus, the component of all unit normals $\hat{n}_i \bullet \hat{i}$, $\hat{n}_i \bullet \hat{j}$ and $\hat{n}_i \bullet \hat{k}$ will take the absolute value before the summation.

Case study

A jewel ring model in Figure 4 is used for illustration. Figure 5 shows the facet model of jewel ring. Figure 6 is the EGI model. Figure 7 shows the maximum visibility direction obtained.

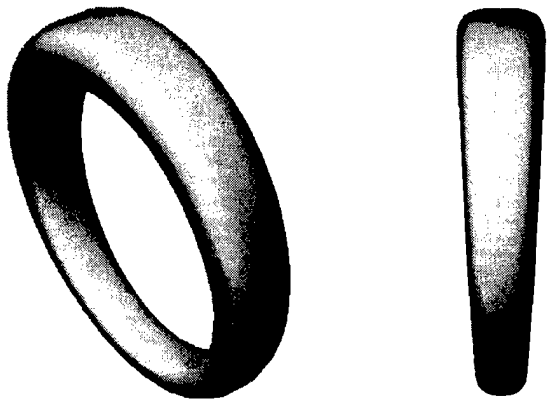


Figure 4. A simple jewel ring in isometric view and side view.

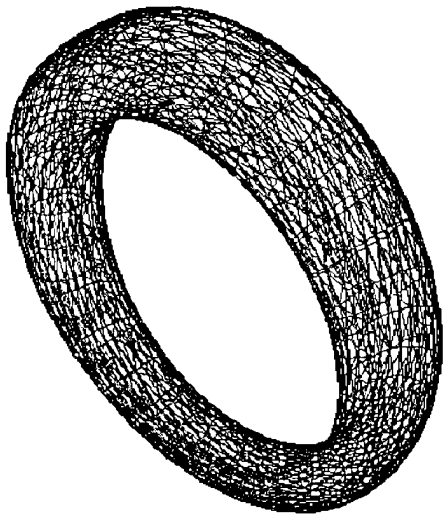


Figure 5. Facet model of jewel ring.

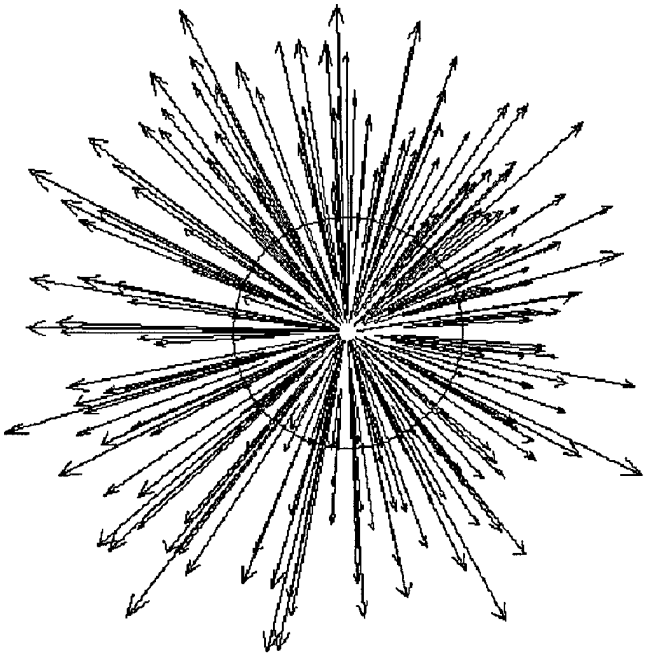


Figure 6. EGI of the jewel ring.

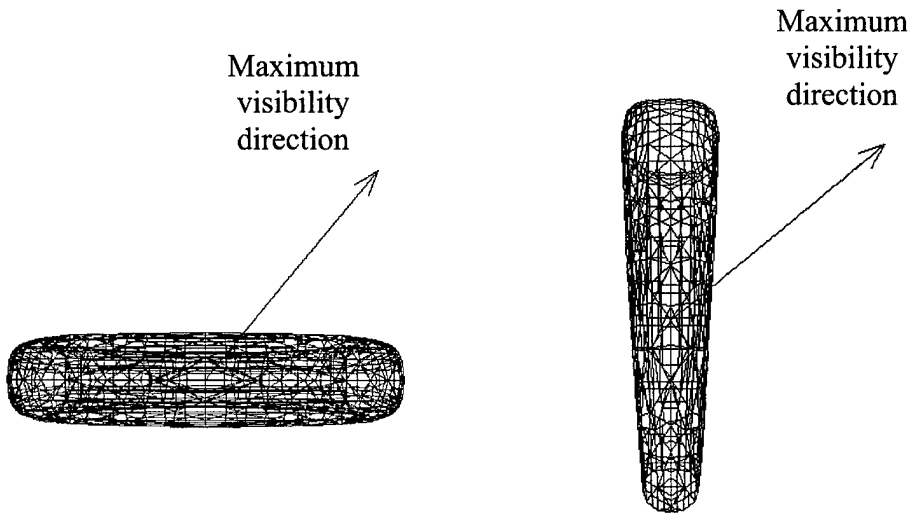


Figure 7. Maximum visibility direction in front view and side view.

Conclusion

In this paper, EGI is used for determining the maximum visibility direction of the jewel ring model. However, EGI of STL model is used instead of EGI of smooth surface model or EGI of polygonal approximated model. If EGI of smooth surface model is used, an infinite number of normal needs to be computed. Alternatively, sampling may be needed for choosing characteristic points. If EGI of polygonal approximated model is used instead of EGI of facetted model, the data storage and computational time will increase as there are three vertices in a STL file facet but more than three vertices in a polygon.

In the case study, the maximum visibility building orientation is applied. If there is no systematic methodology for proper orienting the jewel ring model, the model will be built vertically (Figure 7) by experienced operator and the resulting quality may not be the best. Jewel ring model built has largest visible area. In fact, the method has potential to be applied to industry other than jewellery. This can be studied further in the future.

Acknowledgement

The work described in this paper was supported by a grant from the Hong Kong Polytechnic University (Project No.: G-V617).

References

1. Dietmar F. and Georges F., "Preferred Direction of Build for Rapid Prototyping Processes", The Fifth International Conference on Rapid Prototyping, 1994, pp. 191-200.
2. Allen S., Dutta D. and Arbor A., "On the Computation of Part Orientation Using Support Structures in Layered Manufacturing", Proceedings of the Fifth Solid Freeform Fabrication Symposium, Austin, Texas, 1994, pp. 259-269.
3. Cheng W., Fuh F.Y.H., Nee A.Y.C., Wong Y.S., Loh H.T. and Miyazawa T., "Multi-Objective optimization of part-building orientation in stereollithography", Rapid Prototyping Journal, Volume 1, Number 4, pp. 12-23.
4. Ng W.M. Micky and Tan S.T., "Feature Based Optimization of Part Orientation for Rapid Prototyping", International Conference on Manufacturing Automation Proceedings, HKU, 1997, pp. 434-442.
5. Xu F., Wong Y.S., Loh H.T., Fuh F.Y.H. and Miyazawa T., "Optimal orientation with variable slicing in stereolithography", Rapid Prototyping Journal, Volume 3, Number 3, 1997, pp. 76-88.
6. Horn Berthold K.P., "Extended Gaussian Images", Proceeding of the IEEE, Volume 72, Number 12, December 1984, pp. 1671-1686.

Thermal and Stress Modeling of Laser Fabrication of Multiple Material Components

K. Dai and L. Shaw
Department of Metallurgy and Materials Engineering
Institute of Materials Science
University of Connecticut, Storrs, CT 06269

ABSTRACT

Solid freeform fabrication (SFF) is an automated manufacturing process that builds three-dimensional complex-shaped structures layer-by-layer directly from CAD data without part-specific tooling and human intervention. In many cases multiple materials are involved in fabricating one component using SFF approaches. Porcelain-fused-to-metal (PFM) restoration for permanent fixed prosthodontics is an example of this kind. In this study 3-dimensional finite element modeling has been carried out to investigate the temperature and stress field in processing of multiple material components using a moving laser beam. Effects of fabrication sequences, laser scanning patterns and scanning rates on residual stresses have been investigated. Implications of these results on laser fabrication of multiple materials have been discussed.

Keywords: Solid freeform fabrication, Dental restoration, Laser processing, Finite element modeling, Thermal and stress analyses.

INTRODUCTION

Solid freeform fabrication (SFF) is an emerging manufacturing technology that creates 3-dimensional components directly from a CAD design without part-specific tooling and human intervention [1]. The development in SFF has offered opportunities to make the dental restoration using a SFF process with laser-assisted densification of multiple materials, or in short, multi-material laser densification (MMLD) [2]. In this process, dental restorations are built driectly from 3-D computer solid models through two steps. First, dental ceramic and metallic powders are delivered through slurry approaches point-by-point to the desired location. Second, once a layer (or a layer segment) is delivered, the layer is densified using a laser beam scanning in the desired pattern and with adjusted input power density depending on which powder material is under densification. After densification, a new layer of powders will be deposited as described in the first step, which will then be followed again by the second step. This layer-by-layer fabrication process continues until dental restoration is completed. The automation of the MMLD process offers opportunities to reduce the labor cost and increase the dental restoration rate.

For a specific restoration, many experiments are needed to optimize the fabrication process so that the maximum strength, minimum residual stress and distortion can be achieved. Such an experimental trial-and-error approach will inevitably lead to a high cost of the dental restoration through the MMLD process. Instead of using experimental trial-and-error approaches, this study uses finite element modeling (FEM) to investigate the effect of various processing parameters and to provide guidance for intelligent selection of various parameters in the MMLD process.

Finite element models were developed before to optimize several SFF processes for minimal residual thermal stresses and distortion in the final component fabricated. These efforts [3-11] provide substantial insights into how thermal gradients, thermal transient stresses and residual stresses in the fabrication of complex-shaped components using SFF processes. However, most of these models are limited to 1D or 2D cases [3-9] and all of them only deal with processing of single material [3-11]. In contrast, the present study provides 3-dimensional analyses of laser processing of components made of multiple materials. Furthermore, although the principal motivation for this work is to provide guidance for minimizing residual thermal stresses and distortion in the component fabricated via the MMLD process, the understanding developed in this work is expected to be applicable to other SFF processes that are involved with multiple materials. The result of this study may also be applied to conventional fabrication processes that are involved with heating of multi-material components using a moving laser source.

MODEL DESCRIPTION

To develop fundamental understanding on how temperature and stress gradients develop during laser processing of multiple materials and to evaluate the dependency of the thermal and stress fields on various laser processing parameters and material properties, bi-material laser processing with simple geometry has been investigated in this study. All of the models investigated have the same geometry. One of the models investigated is shown in Figure 1.

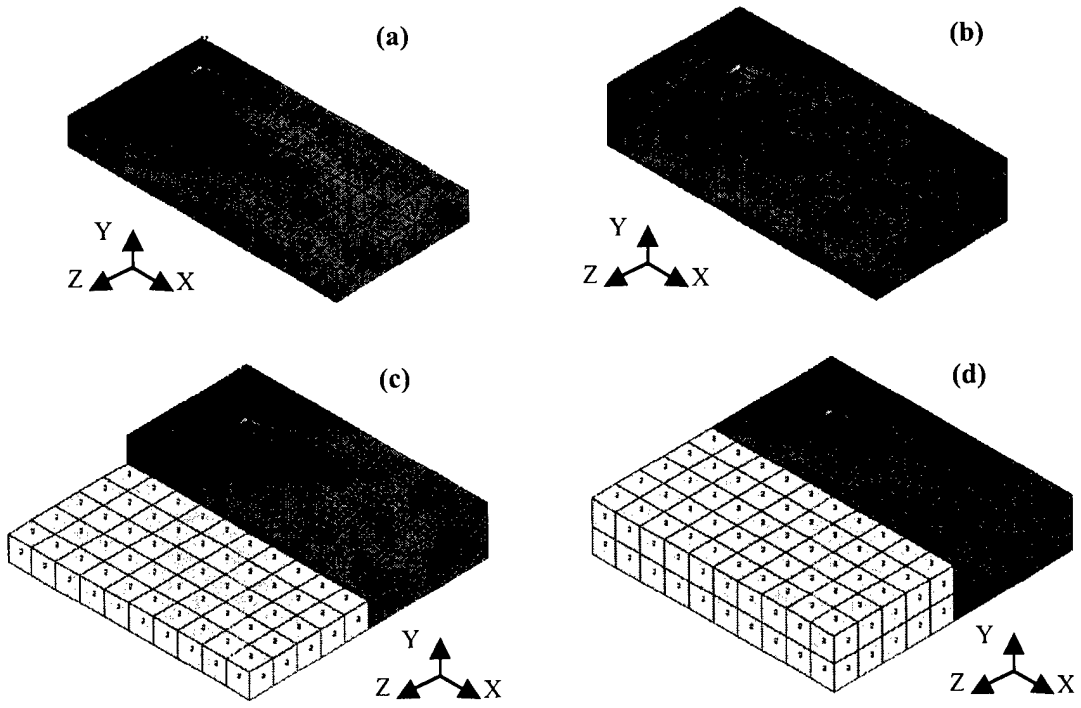


Figure 1. Schematic of fabrication sequence I. The dental alloy section (in dark color) is first fabricated in (a) and (b) steps, whereas the porcelain section (in gray color) is fabricated in (c) and (d) steps.

The model consists of a dental porcelain section (shown in gray color) and a dental nickel alloy section (shown in dark color). The final size of the part is 20×20×4 mm and the size of

every element in the mesh is 2×2×2 mm. The part is built layer-by-layer with two different laser fabrication sequences. Fabrication sequence I fabricates 3-dimensional bi-material bodies via buildup of the dental alloy section first, followed by buildup of the dental porcelain section, as shown in Figure 1. In contrast, fabrication sequence II entails fabrication of a 3-dimensional bi-material body through buildup of the bi-material layer-by-layer, as shown in Figure 2. For both fabrication sequences, all the elements in one layer are added simultaneously as the first layer, or onto the previous layer, or adjacent to the neighboring section built in the previous step depending on which step it is in the fabrication sequence. These elements are then subjected to laser processing (i.e., laser melting and solidification). After laser processing, a new layer of elements is added, which is then followed by laser processing. This element-adding and laser-processing procedure is to mimic the MMLD process described in the Introduction section.

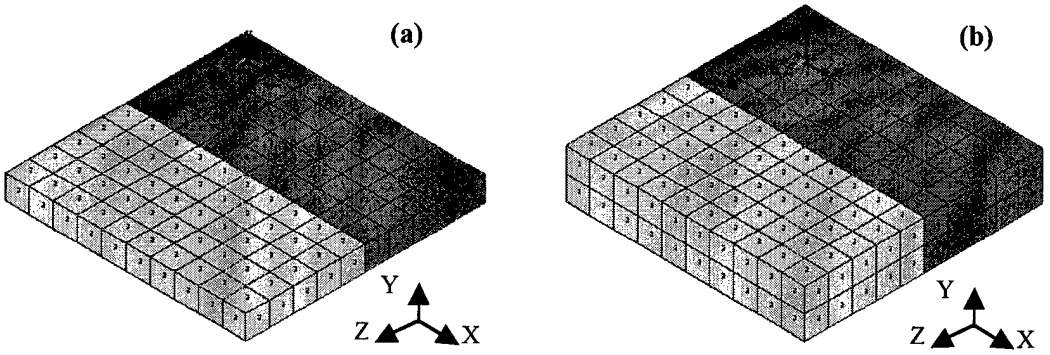


Figure 2. Schematic of fabrication sequence II. The first bi-material layer is fabricated in step (a), and the second bi-material layer is built in step (b).

For each fabrication sequence, two laser scanning patterns and two scanning rates have been investigated. The two scanning patterns for each fabrication sequence are shown in Figure 3. Note that scanning pattern A has its major scanning direction (i.e. the long scanning direction) parallel to the interface of the bi-material, whereas scanning pattern B has its major scanning direction perpendicular to the interface of the bi-material. The two scanning rates investigated are 10 and 100 μm/s. The combination of two fabrication sequences, two scanning patterns and two scanning rates results in a total of eight laser fabrication conditions all of which have been investigated and are complied in Table 1.

In simulation the dental nickel alloy is assumed to be pure nickel, while the dental porcelain is composed of 63.40% SiO_2, 16.70% Al_2O_3, 1.50% CaO, 0.80% MgO, 3.41% Na_2O, and 14.19% K_2O (wt%). The nickel has plastic deformation capacities and simulated using the bilinear kinematic hardening behavior. Furthermore, this bilinear kinematic hardening behavior is a function of temperature. The porcelain is assumed to be an elastic material below its melting point (1373K) and no fracture is considered. Above the melting temperature the behaviors of both the nickel and porcelain are approximated using plasticity with extremely low elastic moduli, tangent moduli and yield strengths. Such approximation maintains the fluidity of the molten nickel and porcelain although time-dependent properties (e.g., creep and viscous flow) are ignored. The numerical simulation is carried out using the ANSYS code [12]. The simulation approach, which has been crosschecked with analytical solutions for relatively simple geometry [13], has been used in this study. Every element in the model is assumed to be initially solid. The

latent heat of fusion is not considered in the model, nor is the volume change associated with melting and solidification. The latent heat of fusion and the volume change, especially those associated with powder densification, are expected to have influence on the transient and residual stresses and will be investigated in future studies. The model does not include the convection of liquid in the molten pool. This approximation is quite reasonable because the present simulation shows that the size of the molten pool generated under the assumed processing condition is similar to the size of the laser beam (~ 2 mm) and thus liquid convection if any will be very limited in such a small liquid pool.

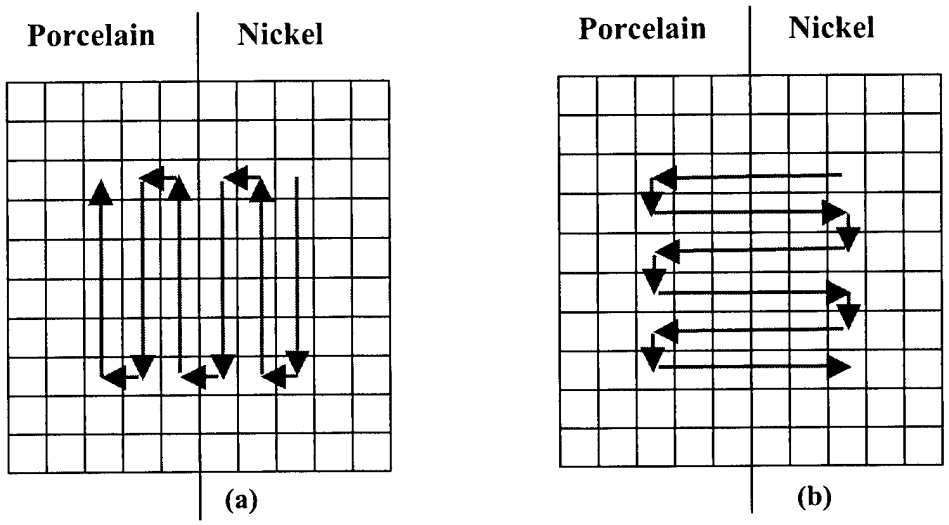


Figure 3. The two laser scanning patterns: (a) scanning pattern A and (b) scanning pattern B.

Table 1. Laser Densification Conditions Modeled

Model ID	Model 1	Model 2	Model 3	Model 4	Model 5	Model 6	Model 7	Model 8
Densification Sequence	I	I	I	I	II	II	II	II
Scanning Pattern	A	A	B	B	A	A	B	B
Scanning Rate (μm/s)	10	100	10	100	10	100	10	100

The boundary conditions for modeling are set as follows. The part being built is assumed to be in contact with air and the heat loss through air is approximated through the inclusion of a convection heat transfer coefficient (6×10^{-5} w/mm^{2}K) between the part and the ambient air. The ambient air is assumed to be 300K and the temperature dependence of the convection heat transfer coefficient is neglected. The laser beam heating is modeled as a fixed temperature and moves from a group of surface nodes within the laser beam size of 2×2 mm to the next group of surface nodes as defined by the fabrication sequence, the scanning pattern and the scanning rate. Such a heating condition mimics the temperature close-loop control used in the MMLD process [2]. The input temperature is set at 1740K when the laser beam scans in the nickel section and 1380K in the porcelain section and at the bi-material interface. To avoid rotation and translation of the part during simulation, the node at one of the bottom corners of the part is fixed in the x, y and z directions. Furthermore, the node next to the fixed node and located at the x-axis is fixed in the y and z directions, while the node next to the fixed node and located at the z-axis is fixed in the x and y directions. Fixing only one corner allows the part to respond to thermal transient and

residual stresses with minimum interference from the boundary condition, and thus stress and distortion analyses can be carried out with reasonable accuracy.

SIMULATION RESULTS AND DISCUSSION

Effects of Laser Scanning Patterns: The simulation results of Models 1 to 8 are summarized in Table 2 from which the effect of the scanning pattern can be found. For example, comparisons can be made among models with fabrication sequence I (Models 1 to 4). By comparing Models 1 (pattern A, 10 μm/s) with 3 (pattern B, 10 μm/s) and 2 (pattern A, 100 μm/s) with 4 (pattern B, 100 μm/s), we can conclude that pattern B generates larger residual stresses and thus larger distortion than pattern A. Recall that pattern A has the major laser scanning direction parallel to the interface (Figure 3a), while pattern B has the major laser scanning direction perpendicular to the interface (Figure 3b). The multiple heating and cooling cycles at the interface caused by scanning pattern B have resulted in large residual stresses and thus large distortion of the part. In contrast, for scanning pattern A the interfacial region is only heated once. Furthermore, such heating is followed by relatively slow cooling because of the subsequent laser processing of the neighboring porcelain region away from the interface. The slow cooling at the interfacial region has resulted in a small temperature gradient and thus low residual stresses and distortion.

Table 2. Summary of Simulation Results

Model ID	Temperature range of the part when the laser beam is scanning the final point (K)	Stress range of the part after cooling down to room temperature (MPa)		
		X-direction	Y-direction	Z-direction
1	379 ~ 1380	-288 ~ 543	-250 ~ 314	-319 ~ 67
2	463 ~ 1380	-310 ~ 552	-293 ~ 353	-346 ~ 109
3	565 ~ 1380	-336 ~ 548	-325 ~377	-486 ~ 95
4	494 ~ 1380	-350 ~ 563	-338 ~ 385	-460 ~ 112
5	379 ~ 1380	-447 ~ 579	-453 ~ 455	-431 ~ 152
6	464 ~ 1380	-439 ~ 614	-407 ~ 460	-425 ~ 184
7	927 ~ 1740	-441 ~ 593	-513 ~ 467	-480 ~ 236

Effects of Laser Scanning Rates: Effects of laser scanning rates can also be found in Table 2. For example, a comparison can be made between Models 1 and 2. Model 1 has a laser scanning rate of 10 μm/s, whereas Model 2 is 100 μm/s. Both of these models have the same scanning pattern (i.e., pattern A). The comparison indicates that both residual tensile and compressive stresses increase with scanning rate. More specifically, depending on which stress is concerned, the maximum tensile stress has risen by 2 to 62% and the maximum compressive stress has increased by 8 to 17% when the scanning rate increases from 10 to 100 μm/s. Corresponding to the increase in residual stresses, the distortion of the part has also increased by about 10%. However, when the comparison is made between Models 3 and 4 that have scanning pattern B, the result becomes more complex. Although the maximum residual tensile stress also increases with scanning rate (2 to 18% increase in the stress for a 10-times increase in the scanning rate), the maximum compressive stress may increase or decrease depending on which stress component is concerned (see Table 2). Such a complicated situation is also found in the comparisons between Models 5 and 6 and between Models 7 and 8. Thus, whether residual

stresses increase or decrease with increasing scanning rate depends on the scanning pattern and the stress component under consideration. No general rule can be made.

A close examination of Table 2 further reveals that the dependence of residual thermal stresses on scanning rates is also affected by the fabrication sequence. As will be discussed in the next section, the fabrication sequence II is not an acceptable fabrication sequence. Thus, as far as the fabrication sequence I is concerned, the x-stress, which is dominated by the CTE mismatch between the dental alloy and porcelain, always increases with scanning rate. This is related to the phenomenon that there is less time for the interface porcelain to expose to high temperatures when the scanning rate is high. As a result, the interface porcelain has shorter time in the molten state and thus less compressive permanent deformation. Such a smaller permanent compressive deformation of the porcelain in the molten state leads to a higher residual compressive x-stress in the porcelain and a higher tensile x-stress in the nickel because the nickel has a larger CTE and is constrained by the porcelain that has a less compressive deformation in its molten state. The same reasoning can be applied to the residual y-stress because the y-stress is also predominately controlled by the thermal mismatch between the dental alloy and porcelain.

Effects of Fabrication Sequences: The fabrication sequence has the largest effect on residual stresses and distortion among all the parameters we have evaluated. It also has substantial impacts on the transient stresses and temperature. It is noted from Table 2 that for fabrication sequence II with scanning pattern A (i.e., Models 5 and 6), the final temperature range of the part before it cools down to room temperature is close to that for fabrication sequence I with scanning pattern A (Models 1 and 2). However, if the transient temperature is examined (not shown in Table 2), it immediately becomes obvious that fabrication sequence II is not acceptable for fabricating a part with controlled shape and dimensions.

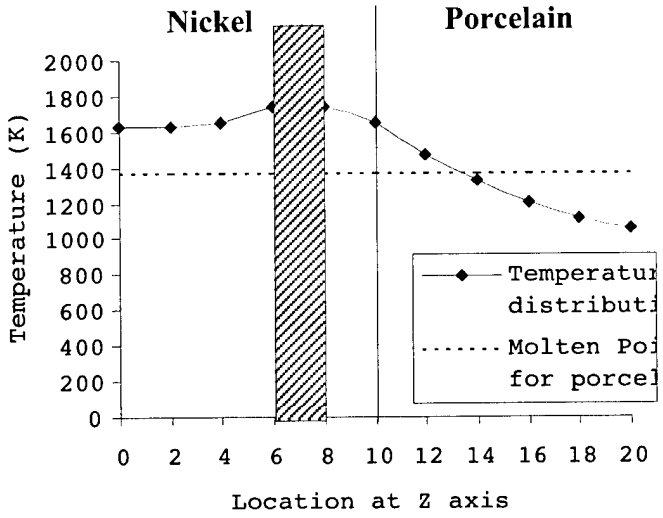


Figure 4. The temperature distribution along the nodal points with y = 4 and $0 \le z \le 20$ at the y-z plane with x = 10 for Model 5 (i.e., fabrication sequence II, scanning pattern A and scanning rate 10 μm/s) when the laser beam is scanning the nickel alloy section. The hatched area indicates the location of the laser beam.

The point made above can be well illustrated using Figure 4 that shows the temperature distribution along the nodal points with y = 4 and $0 \le z \le 20$ at the y-z plane with x = 10 for an

intermediate step of fabrication sequence II with scanning pattern A and a scanning rate of 10 μm/s (Model 5). It can be seen that the porcelain near the interface has temperatures higher than its melting point even though the laser beam is scanning at the neighboring nickel section before it reaches the porcelain section. Clearly, this is due to the high thermal conductivity of the dental nickel alloy and the high fabrication temperature (slightly higher than the melting point of the dental nickel alloy) used to process the nickel section. This result suggests that if fabrication sequence II is used for dental restoration, the shape and dimension of the porcelain section would be very difficult to control because the porcelain section have become liquid and led to substantial distortion of the shape even before the laser beam reaches the porcelain section. Models 7 and 8 suffer from the same problems as Models 5 and 6. Thus, when the melting points of the two materials are substantially different, fabrication sequence II is not an acceptable fabrication sequence.

CONCLUDING REMARKS

Processing of bi-material parts via a moving laser beam has been investigated using finite element modeling in this study. The effects of various processing parameters, including the fabrication sequence, laser scanning pattern and scanning rate, on the transient temperature, transient stresses, residual stresses and distortion of the part have been evaluated. Based on these investigations, the following conclusions can be offered.

1) Fabrication sequence I, which fabricates the section of the high melting temperature material (e.g., the dental nickel alloy) first and then the section of the low melting temperature material (e.g., the dental porcelain), is the appropriate sequence to fabricate the part made of two materials with the substantially different melting points. Fabrication sequence II, which fabricates the entire bi-material layer one after another, offers little control over the shape and dimension of the section of the low melting temperature material, and thus is not an acceptable fabrication sequence.
2) The transient thermal stresses generated using fabrication sequence I are relatively small and will not impose threats to the mechanical integrity of the part being fabricated (i.e., cracking in the dental porcelain section).
3) Thermal residual stresses are large in the direction along which shrinkage is strongly affected by the CTE mismatch between the two materials, and small in the direction along which shrinkage can take place with little influence from the CTE mismatch.
4) In general, using the fabrication sequence I the thermal residual stress and distortion increase with the laser scanning rate because the faster the scanning rate, the less permanent compressive deformation occurs to the molten porcelain. As a result of the less compressive deformation of the porcelain in its molten state, higher residual thermal compressive stresses appear in the interface porcelain and higher residual tensile stresses occur in the interface nickel.
5) Scanning pattern A with the major scanning direction parallel to the interface of the bi-material generates lower residual thermal stresses than scanning pattern B that has its major scanning direction perpendicular to the interface.
6) Effects of the fabrication sequence, laser scanning pattern and scanning rate are interrelated. The optimal combination of these parameters for fabricating bi-material parts with minimum residual stresses and distortion is fabrication sequence I, scanning pattern A and fast scanning rate.

Acknowledgements – The authors gratefully acknowledge financial support provided by the National Science Foundation under Grant No: DMI-9908249.

REFERENCES

1. Beaman, J.J., Barlow, J.W., Bourell, D.L., Crawford, R.H., Marcus, H.L. and McAlea, K.P., "Solid Freeform Fabrication: A New Direction in Manufacturing," Kluwer Academic Publishers, MA, 1997.
2. Li, X., Crocker, J., Geiss, E., Shaw, L., Marcus, H. and Cameron, T., "Evaluation of Microstructure and Properties for Multi-Materials Laser Densification of Dental Restorations," in the proceedings of the 11th Annual SFF Symposium, edited by D. L. Bourell, et al., The University of Texas, 2000, pp. 159 – 167.
3. Chin, R.K., Beuth, J.L. and Amon, C.H., "Thermomechanical Modeling of Molten Metal Droplet Solidification Applied to Layered Manufacturing," Mech. Mater., Vol. 24, 1996, pp. 257-271.
4. Amon, C.H., Beuth, J.L., Merz, R., Prinz, F.B. and Weiss, L.E., "Shape Deposition Manufacturing with Microcasting: Processing, Thermal and Mechanical Issues," J. Manufact. Sci. Eng., Vol. 120, No. 3, 1998, pp. 656-665.
5. Ong, R., Beuth, J.L. and Weiss, L.E., "Residual Stress Control Issues for Thermal Deposition of Polymers in SFF Processes," in the proceedings of the 11th Annual SFF Symposium, edited by D. L. Bourell, et al., The University of Texas, 2000, pp. 209-218.
6. Vasinonta, A., Beuth, J.L. and Griffith, M.L., "Process Maps for Controlling Residual Stress and Melt Pool Size in Laser-Based SFF Processes," in the proceedings of the 11th Annual SFF Symposium, edited by D. L. Bourell, et al., The University of Texas, 2000, pp. 200-208.
7. M. Kandis and T. L. Bergman, "A Simulation-Based Correlation of the Density and Thermal Conductivity of Objects Produced by Laser Sintering of Polymer Powders," J. Manufact. Sci. Eng., Vol. 122, No. 3, 2000, pp. 439-444.
8. Steinberger, J., Shen, J., Manetsberger, K. and Muellers, J., "The Simulation of the SLS Process as the Basis of a Process Optimization," in the proceedings of the 11th Annual SFF Symposium, edited by D. L. Bourell, et al., The University of Texas, 2000, pp. 377-385.
9. Zhang, Y and Faghri, A., "Melting of a Subcooled Mixed Powder Bed with Constant Heat Flux Heating," Int. J. Heat Mass Transfer, Vol. 42, 1999, pp. 775-788.
10. Childs, T.H.C., Hauser, C., Taylor, C.M. and Tontowi, A.E., "Simulation and Experimental Verification of Crystalline Polymer and Direct Metal Selective Laser Sintering," in the proceedings of the 11th Annual SFF Symposium, edited by D. L. Bourell, et al., The University of Texas, 2000, pp.100-109.
11. Bugeda, G., Cervera, M. and Lombera, G., "Numerical Prediction of Temperature and Density Distribution in Selective Laser Sintering Process," Rapid Prototyping J., Vol. 5, 1999, pp. 21-26.
12. ANSYS User's Manual, Vol. I-VI, Swanson Analysis Systems, Inc., Houston, PA, 1992.
13. Dai, K., Klemens, P. and Shaw, L., "Numerical Simulation of Bi-Materials Laser Densification," in the proceedings of the 11th Annual SFF Symposium, edited by D. L. Bourell, et al., The University of Texas, 2000, pp. 386-392.

Manufacturing of Instrumented Prototypes

Moss Shimek, Nachiket Patwardhan, Kristin. L.Wood, Joseph Beaman, Richard Crawford.
Department of Mechanical Engineering, The University of Texas at Austin.

Abstract

The research for the Cybernetic Physical project at UT Austin has the goal of producing instrumented prototypes, using selective laser sintering (SLS) that can be used in concert with similarity methods to update virtual models. The SLS process builds prototypes sintering powder in a 2-D cross-section, layer by layer, with a CO_2 laser. Accomplishing this goal could significantly reduce cycle times and costs associated with traditional prototyping methods. Strain gages and thermocouples are chosen as the first sensors to be embedded. Experiments have been carried out to determine the feasibility of embedding sensors both after the manufacturing process as well as during the SLS process. These experiments have yielded data that will serve as a set of design requirements for the embedding process. The results from the post-embedded prototypes closely matched the theoretical results in one case. Hence a design of experiments will be carried out to study the effects of various factors on these sensors. Embedding thermocouples during an SLS build cycle uncovered issues that must be addressed in the design process, such as keeping the sensor and lead wires flat on the cross-section and managing the extra lead wires. A 1-D heat source, pin fin model was used to accurately predict the temperature reading of the thermo couple in the sample. The error was approximately 3.3%.

Introduction

The objective of this research is to manufacture instrumented prototypes in order to integrate rapid prototyping technology with virtual prototyping, so as to improve engineering design. Currently functional tests are performed on prototypes instead of full-scale models in very limited problem domains. Traditionally production prototypes are produced from the virtual designs. Results from the prototyping tests are used to modify the design parameters to achieve optimum design and thus higher quality. Iterations have to be carried out till all the functional requirements are satisfied and then the final product is manufactured. But with the help of instrumented prototyping it will be possible to measure the states at the interior and also on the surface of a prototype, which is often necessary. To achieve this objective of manufacturing instrumented prototypes two approaches could be taken –

1) In-situ manufacturing of sensors
2) Embedding off the shelf sensors in prototypes manufactured by selective laser sintering technique.

As a first step towards instrumented prototyping it was decided to adapt the second approach of embedding off the shelf sensors.
The sensors could be embedded in two ways a) Mono-layer access b) multi-layer access.

Monolayer access means that the sensor thickness is same or less than that of a layer thickness, which is about 0.005in. To comply with the monolayer approach it was decided to choose strain gages (thk 1 mil) and thermocouples as the candidates for embedding.

Further the sensors can be embedded in two ways, either post embedding them i.e. placing the sensor at the desired location after the prototype has been manufactured using SLS process or in process embedding, which means placing the sensors while the prototype is being manufactured on the SLS machine.

We hypothesized that it is possible to embed sensors in either manner but that conducting tests would help uncover the difficulties involved in doing so. Before going into the details of the tests, let us briefly review the basics of selective laser sintering. Figure 1. is a schematic of the SLS process in action. A computer controls the scanning mirrors that trace a 2-D cross-section of a 3-D solid model onto the surface of the powder bed. The part and powder pistons are sequentially lowered and raised respectively for

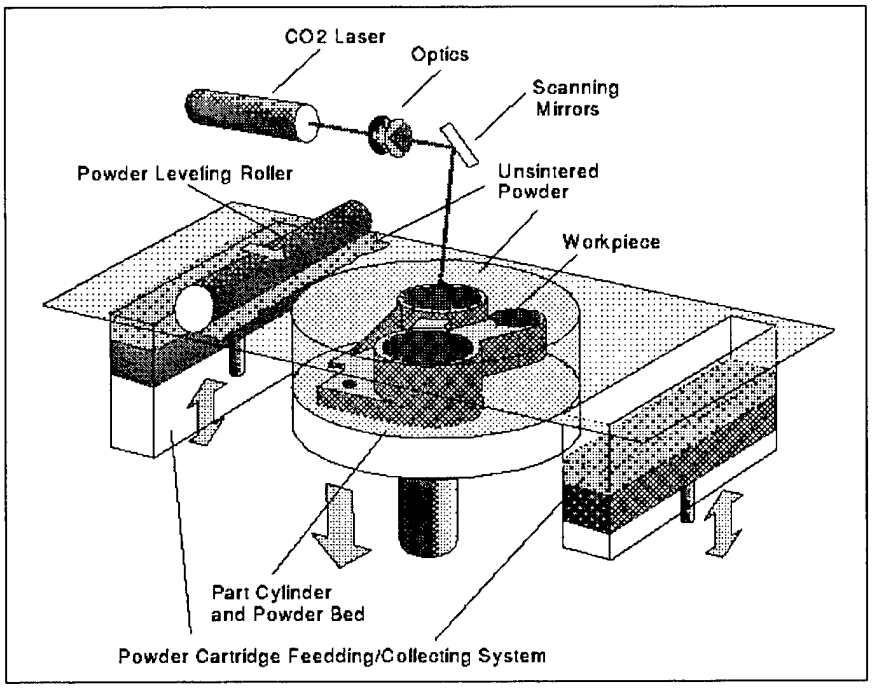


Figure 1. A schematic of the SLS Process

each new layer.

Post Embedding Concepts

As a first step it is decided to pursue the post embedding concept approach to learn the obstacles that might arise in the embedding process. This approach consists of post embedding strain gage in prototypes using various concepts. The prototype chosen is a simple cantilever beam since it is a simple to verify the results obtained.

Concept 1

A cantilever beam having dimension 5" x 0.8" x 0.5" is manufactured with a cavity for the sensor, using SLS process. Strain is measured at 3 in from the load and at a distance of 0.05" from the neutral axis. So the cavity for a strain gage is located at the desired location. After the part is manufactured strain gage (EA –06-125TA-120) is mounted on the cantilever beam at that particular location using standard strain gage mounting techniques. Now in order to fill the cavity a small rectangular piece that corresponds to the size of the cavity is bonded in to the cavity using an epoxy. Thus the first instrumented prototype is manufactured. To test the performance of the sensor the cantilever was loaded with known loads and the output from the strain gage is recorded using a Wheatstone's bridge network.

Concept 2

A cantilever beam having dimension 5" x 0.8" x 0.5" is manufactured with a cavity of 0.5" x0.5"x 0.15". A sensor is mounted in a mold the size of which corresponds to the size of the cavity made in the cantilever. The mold with the sensor is then snapped into the cavity and the opening is shut of with an epoxy. Again the strain gage is at a distance of 0.05" from the neutral axis. Thus we have an instrumented cantilever beam

$$\sigma_c = M\,c\,/I$$
$$I=b\,d^3/12$$

Where ,
σ_c = stress at the particular location (MPa)
M = bending moment due to the applied load (N-mm)
c= distance from the neutral axis of the beam (mm)
I = moment of inertia (mm^4)
b= breadth of the beam (mm)
d= depth of the beam (mm)

Theoretical results:

Load N	Distance from NA c mm	Strain
5	1.27	8.71877E-05

Experimental results:

Load N	Distance from NA c mm	Strain
5	1.27	7E-5

The result of one of the instrumented prototype matched closely with the theoretical results. In the second case the strain measured is way off from the theoretical value. This might be due to the curing of epoxy that might have induced stresses on the gage. Hence a design of experiments will be carried out to study the effects of different factors on the performance of the sensor. Also the initial experiments revealed the design requirements of the system. Based on these design requirements, important functions were realized and a function structure is developed. Fig 2 shows a preliminary function structure.

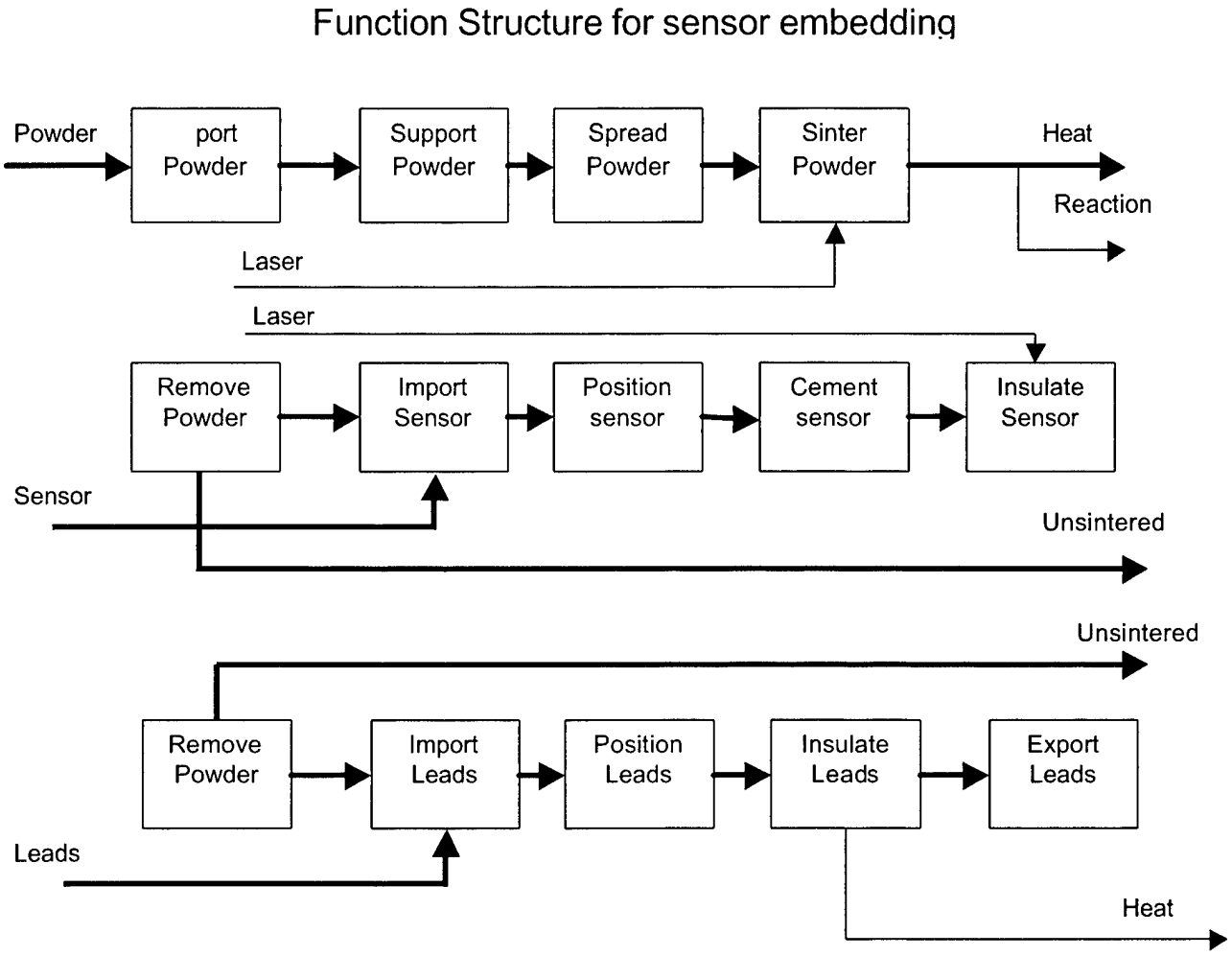


Fig 2. Function Structure

In Process Embedment

The Laboratory for Solid freeform Fabrication at the University of Texas at Austin has taken the first steps toward embedding sensors in SLS parts during the build process. Mono-layer access describes the case where the sensor to be embedded is small enough to fit within a single layer of and SLS part. The SFF lab at UT Austin is pursuing a process that will result in instrumented prototypes using mono-layer sensors.

Determining whether or not embedding monolayer sensors during the build cycle is feasible is the first challenge in developing this process.

Experiment and Results

There were two possibilities for placing the sensors such that they would be completely embedded within the finished part. The first attempts involved placing the sensor on top a layer that was just sintered in the hopes that the surface would still be molten and the sensor would stick. The second proposed method was placing the sensors in a layer of unsintered powder. Once the laser scans the new layer, the sensor is adhered to the part. Both methods were tested on the 21st of June 2001 using K type thermocouples with 0.003" bead diameters.

The experiment was conducted on a prototype SLS machine referred to as "tool 4". This machine was used to develop the commercial SLS machines. Tool 4 is valuable to the students in the SFF lab due to the lack of safety features required on a commercial product. For this experiment, it was necessary to open the process chamber doors during the build cycle. Attempting to place the thermocouples on the newly sintered surface proved futile because it was not tacky enough hold the sensor. Two thermocouples were lost when the roller swept across the surface and carried the sensors away. Placing the sensor in unsintered powder, using the laser to fuse the powder and sensor, was successful but not without its difficulties. We placed the thermocouples by hand which illustrated the need to have the sensors perfectly still while the laser is scanning. The lead wires are very thin and hard to control. This made flat, accurate placement very difficult as well as creating an unanticipated challenge. Once the sensor has been adhered to the part the lead wires seem to have a mind of their own. As the roller swept across the part bed it would bend the wires back and forth with each pass. In one sample this even lead to the part shifting. Figure 3 is a picture of the three cylinders with embedded monolayer thermocouples.

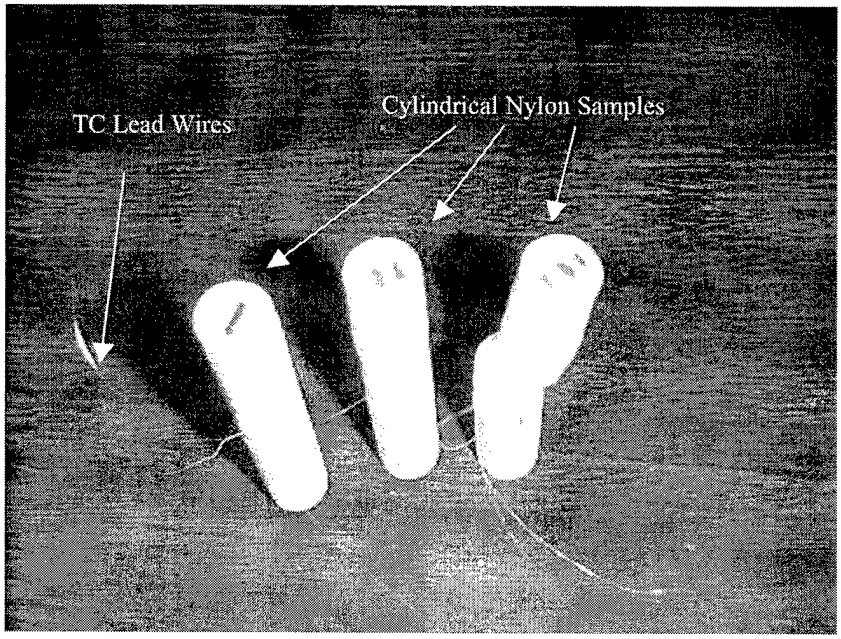


Figure 3. In process embedment samples

Verification

In the future, instrumented prototypes will be used to update virtual and analytical models of parts. For this test, we used an analytical model of a pin fin to verify the results of the thermocouples. This model can give us the temperature as a function of distance from a 1-D heat source with natural convection.

$$T - T_\infty = (T_S - T_\infty) * e^{-mx}$$

Where

$$m = \sqrt{\frac{hP}{kA_C}}$$

And

$$m * L >> 1$$

P is the perimeter of the fin, A_C is the cross-sectional area, and L is length of the fin. The values used for this test are listed below:

$T_S = 89$ °C
$h = 5$ W/m^{2}K
$P = 0.040$ m
L = 0.075 m

$T_\infty = 31$ °C
$k = 0.025$ W/mK
$A_C = 1.267$ e -4 m^2

The thermocouples were embedded at a height of 0.043m. The pin fin model predicts that, at this distance, the pin will have the same temperature as T_∞. This was confirmed by a reading of 30 °C from the embedded sensor, a difference of 3.3% from the predicted value. This verifies our assertion that instrumented prototypes can be used in conjunction with virtual and analytical models to aid in the design process.

Design Requirements

Conducting the test described above was a complete success for two reasons. It established the feasibility of monolayer access as well as uncovering critical issues concerning the design of a system to embed sensors during the SLS build cycle. Obviously, we want to accurately position the sensor for placement. It is also important to have the sensor and lead wires flat within a single layer. Effective management of the loose lead wires is also critical to prevent breakage and part shifting. These requirements and others such as operating temperatures and volume limitations will drive the design of an effective sensor placement system.

Design of the Process

The students in the SFF lab at UT are using design techniques developed by Drs. Kevin Otto & Kristin Wood. The basic idea behind this design process is to develop a detailed set of customer needs that must be satisfied. Functional modeling, concept generation, and concept selection techniques are used to develop possible solutions but the determining factor is how well the solutions satisfy the customer needs.

Functional Modeling

These design requirements are the foundation of a set of "customer needs" that must be further developed by this research team. Functional modeling will translate these needs into a set of functions and sub-functions and organized into a function structure. A function structure serves as a road map for generating conceptual solutions for the various functions. Each function has many possible embodiments that could be overlooked if we try to solve the larger problem all at once. Currently, we have identified the primary or global functions for our system but these must be broken down into individual functions. These primary functions are:

Import/export sensor
Move sensor
Position sensor
Manage lead wires

Positioning the sensor refers to the accurate placement of the sensor. Managing the lead wires is necessary to prevent shifting of parts as well as ensuring the wires do not compromise the structure of the part. We will form a detailed function structure using these global functions and the design requirements as guidelines.

Future work

There are two approaches for embedding sensor in the prototypes-a) Monolayer access and b) multi-layer access. Future work will deal with the design of processes to embed sensors using the above-mentioned approaches with a focus on monolayer embedding approach.

It is proposed to develop a more refined function structure that will more closely represent the design intent and will cover all the functions of the process in more detailed manner. To develop a detailed function structure it would be required to realize the functions and sub-functions that would be necessary to fulfill the desired process of embedding. Once a detailed function structure has been developed concept solutions will be discussed for each of the function using structured methods like brainstorming and 6-3-5-sketch method. Instrumented prototypes will be manufactured based on these concept solutions on the SLS 2000 machine. Finally we envisage an automated system to be incorporated in the machine, that will carry and place the sensor at the desired location.

References

1. Joseph J. Beaman ... (et al.). Solid freeform fabrication: a New Direction in Manufacturing.
2. Measurements Group Inc. Micro- measurements catalogue for strain gages.
3. Wood and Otto. Product Design and development.
4. C.C. Perry and H.R. Lissner, The Strain gage primer.
5. Incropera, Frank P. and David P. De Witt. *Fundamentals of Heat and Mass Transfer*. John Wiley & Sons. New York, 1990.

Compensation of Non-Linear Shrinkage of Polymer Materials in Selective Laser Sintering

K. Manetsberger, J. Shen, J. Muellers*

DaimlerChrysler Research Center, Ulm, Germany

* Dornier Research, Friedrichshafen, Germany

Abstract

Inaccuracies in the selective laser sintering (SLS) process using polymer materials are typically caused by inhomogeneous shrinkage due to inhomogeneous temperature distribution in the powder bed of the SLS machine. These shrinking effects lead to stress in the sintered parts, causing the part to distort. The inhomogeneous shrinkage of benchmark parts has been compensated empirically in a former work. The results cannot been transferred to all geometries, because each geometry requires a specific temperature for laser sintering and, thus, has its own related shrinkage distribution. In a new theoretical approach, shrinkage behavior is to be integrated in a thermal simulation of the SLS process and the thermal shrinkage calculated prior to the building process. In the following, experimental data of the temperature- and pressure-dependent shrinkage of laser-sintered powder samples is presented. Possible theories for a physical model of thermal shrinkage are discussed. In particular, these models have to consider granular characteristics such as internal friction, particle sliding, and powder compaction.

Introduction

Today rapid prototyping, rapid tooling and rapid manufacturing processes are counted as established means of accelerating the product development cycle in the automobile and aeronautics industries. Thus we see more and more prototype parts, which in the past were traditionally produced using high-cost, time-consuming milling and joining techniques, being replaced by investment cast parts. And the master forms deployed in investment casting are now typically plastic forms produced by means of selective laser sintering (SLS). In addition SLS processes are used to generate plastic functional prototypes for both the automobile and aeronautics industries. Yet the above applications alone are not what makes SLS techniques so interesting for industry: the growing demand for customized automotive products and the resulting small lots needed for low-volume production has caused a commensurate demand for the fabrication of volume-produced parts using generative processes. As a key manufacturer of premium cars, DaimlerChrysler is driving research in these direct-to-product technologies to accelerate product development and reduce costs. Thus, an essential part of our work focuses on the very strict requirements for accuracy in the SLS process to achieve the desired high quality of the parts produced.

Typically inaccuracies in the selective laser sintering process using polymer materials occur due to inhomogeneous shrinkage during the building and cooling processes, which causes stresses and results in distortion of the laser-sintered part. Temperature measurements [1] performed within an SLS machine showed a strong temperature gradient in the x-y plane of a layer, thus making the shrinkage of a geometry dependent on its x and y positions in the build room. Yet part shrinkage does not only depend on the temperature at which the part is subjected to laser sintering, it is also impacted by cooling, i.e. the length of time the powder bed retains heat, and by the thickness of the powder layer (causing pressure on the part). Experiments previously performed on sample geometries consisting of hollow rectangular parallelepipeds with equidistant measuring points placed at various x-y locations in the build room showed non-linear shrinkage of the height. We thus follow that a linear scaling of a geometry is not sufficient. A subsequent real geometry scaled non-linear in accordance with the empirical data generated resulted in a greatly improved accuracy of the laser sintering process

The temperature distribution within a build room and the changes in temperature during the building and cooling processes differ with the geometry of each part to be produced. The reason for this lies in the variation in the energy applied by the laser. The energy generated by the laser heats the powder and causes the sintering effect, finally dispersing into the powder bed. And due to the very low thermal conductivity of the polymer powder deployed, the build room retains heat over a relatively long period of time. Moreover, shrinkage in geometries which take up a large part of the build area is very different from that occurring in single, smaller parts since shrinkage in large geometries tends to be retarded owing to internal stresses. Hence, the related non-linear scaling function needs to be determined separately for each part to be laser sintered. So, the process has to be run twice: the geometry is built, shrinkage ascertained, the related scaling data generated, and the upscaled geometry compensating shrinkage then built. To save build time and the related costs, it would therefore seem sensible to calculate shrinkage before laser sintering and update the data model, thus doing away with the need to replicate the building process.

The Procedure

Experiments performed with sample geometries have shown that shrinkage occurring in the SLS machine is dependent on time, temperature, and pressure, i.e. the weight of the powder in which the part is embedded. Hence, to be able to calculate and compensate shrinkage, we must first ascertain the values of these three factors. The basis for any workable shrinkage compensation must therefore be an SLS process simulation that allows calculation of thermal distribution within the build room during the building and cooling processes.

We laid the experimental foundation for the quantification of shrinkage by carrying out dilatometer measurements as a function of time, temperature, and pressure. We measured the changes in height of laser-sintered, cylinder-shaped PMMA samples at temperature and pressure conditions identical to those in the laser-sintering equipment over a period of time of 10 hours. The measured curves were then mathematically set out as fit functions. However, transfer of idealized dilatometer measurements to the real conditions in the SLS machine, e.g. under consideration of temperature-dependent friction between the part and the bulk powder, will necessitate a more exact examination of the granular characteristics of the material used. Here,

we provide a possible theoretical description of particle sliding under consideration of temperature-dependent cohesion, friction, and sintering.

Thermal Simulation as a Basis for Shrinkage Compensation

We decided to compensate shrinkage by means of an FEM simulation which replicates the thermal conditions prevalent within the build room during the building and cooling processes. The heat-conductivity model used for determining heat distribution is described in a previously published work [2]. As shrinkage is a long-term effect, the highly dynamic effects of sintering may be neglected when calculating the heat balance. Exposure of the part and the sintering process itself are instantaneous, i.e. time is not a factor in the transition from the initial density of the powder bed to the final density of the part. This simplification allows us to select suitably large values for both the distance between nodes for the FEM simulation and the time intervals for the FEM calculation, thus greatly minimizing computation time.

Initially, we were only able to compute very simple geometries; yet creating an STL interface to the simulation seemed promising for calculation of parts whose geometries are more complex. As the exposure time for each layer and, thus, the resulting overall time needed for the building process are greatly dependent on the geometry of the part to be sintered, the interface to STL allows specification of the time each layer is subjected to a certain temperature. And the pressure to which each layer is subjected due to the weight of the bulk powder lying on top may easily be ascertained via the current z position of the layer.

Figure 1 depicts isothermal distribution inside the build room using the example of a hollow rectangular parallelepiped. For reasons of symmetry, only one-fourth of the build room need be displayed in the figure.

Of course, the results of the shrinkage compensation are only as accurate as the thermal simulation itself, i.e. the actual temperature conditions in the build room must be simulated as closely as possible. For this reason we compared the results of the simulation with empirical data. However, as we were not able to measure the exact temperature within a part, the temperatures within the powder bed near a sintered geometry were compared.

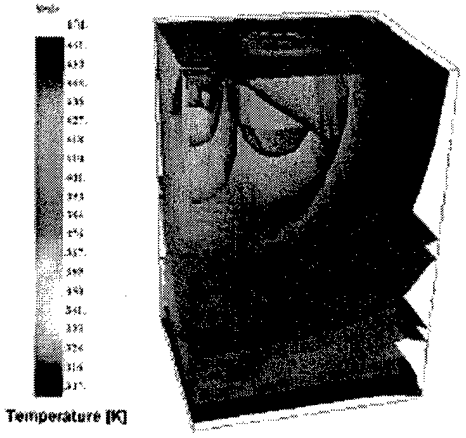


Figure 1: Isothermal distribution within the build room for a hollow rectangular parallelepiped.

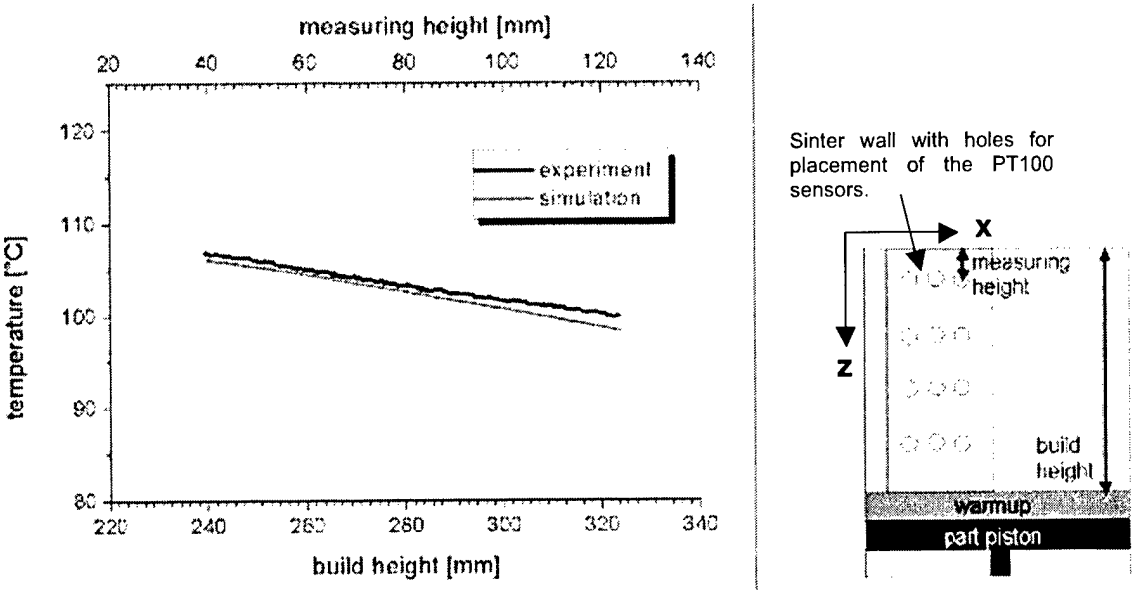


Figure 2: Comparison of the temperatures measured during experiments and the results of the thermal simulation.

Figure 2 compares the measured temperatures with data from the thermal simulation. In the experiment, we inserted PT100 temperature sensors into holes in a sinter wall and measured the temperature in the powder bed. The temperature curve illustrates the cooling of the powder effected by lowering the build platform. Comparison with simulation data showed excellent consistency.

Ascertaining Experimental Data for the Shrinkage Model

To quantify shrinkage of PMMA parts during the selective laser sintering process, we performed dilatometer measurements of the change in height of the samples as a function of time, temperature, and pressure. The resulting data served as the foundation for a physical shrinkage model.

Samples and measuring conditions: The samples used in the experiment were cylindrical in shape with a height of 5mm and a diameter of 7mm. At isothermal conditions, the height of the samples was measured over a period of time of 10 hours: temperatures under T_G (T_G = 123° C) and over T_G (T_{max} = 160° C) were applied. Pressure on the samples that would occur from the weight of the powder in the SLS machine was simulated during measuring by the application of various weightloads. A stamp was used to ensure that pressure was distributed equally over the entire surface of the sample. Measurements were performed at four different loads and at no fewer than five different temperatures for each load applied. A very slight bulging of the samples was registered at the highest temperature and the greatest pressure but, as this was negligible, it was disregarded. For all samples, heat-up time was 4 K/min, so that we were able to assume even heating of the small samples. The samples were placed into the dilatometer under two different conditions:

1.) Friction-free shrinkage: the samples did not come into contact with the quartz walls of the device.

2.) Retarded shrinkage: to be able to estimate the impact of friction between the sample and the powder bed on shrinkage behavior. As we were unable to achieve selective heating between the powder bed and the sample, polyamide powder was scattered between the sample and the quartz walls of the dilatometer to simulate the different flow and cohesive properties of the PMMA powder and the sample at the different temperatures.

Qualitative description of the shrinking curves: *Figure 3* illustrates the shrinking curve of a PMMA sample over a period of time of 10h at a temperature of T=140°C and a pressure of p=18.5g/cm^2, which corresponds to the weight of a powder bed that is approx. 30cm deep. During the heat-up phase, the sample initially expands due to thermal expansion. Yet, when a certain temperature is reached, shrinkage begins. As thermal expansion is not yet fully complete at this point, the sample is in a mixed state between expansion and shrinking. To more exactly define this state, we subtracted the thermal expansion of the sample from the curve which shows the change in height (red line): this curve thus shows greater shrinkage then the measured curve where thermal expansion is considered.

The largest degree of shrinkage (>50%) occurred for all samples within the first 100 minutes with a sharp decrease in the height of the samples registered. After this length of time, shrinking seems to change over to a state of saturation. This is best explained if we see shrinkage as the effect of particles or particle clusters sliding from their original positions to fill empty spaces. This happens when sinter contacts are thermally activated by the temperature applied, which reduces the friction between the individual particles, causing them to slide. The particles which are the first to slide into vacancies or vacancy clusters are those whose sliding planes are tilted in the direction of the space to be filled out (*Figure 4*), as this is the path of the least resistance. This explains why the degree of shrinkage is greatest at the beginning of isothermal densification. The directions of the sliding planes in the samples are distributed statistically and, over time with more and more particles filling vacancies, the concentration of those particles able to slide into vacancy clusters decreases so that shrinkage approaches a saturation value for longer periods of time.

Temperature- and pressure-dependency of the final values of shrinkage: As expected, the height of the cylinder-shaped samples after shrinkage can be expressed as a function of the temperature and the pressure applied to the samples. When the final values of shrinkage and the temperature applied are expressed in the form of an Arrehnius plot, it becomes evident that the two values are linear dependent. Thus, the dependency between temperature T and shrinkage s_{fin} may be expressed as follows:

$$S_{fin} \propto e^{-\frac{E}{cT}}, \qquad \textbf{(Eq. 1)}$$

with c=const.

E may be understood as a thermal energy of activation: the higher the temperature, the greater the number of particles contacts which are thermally activated with the result that a greater number of particles become active, sliding to fill the empty spaces. This increases shrinkage and subsequently the final density.

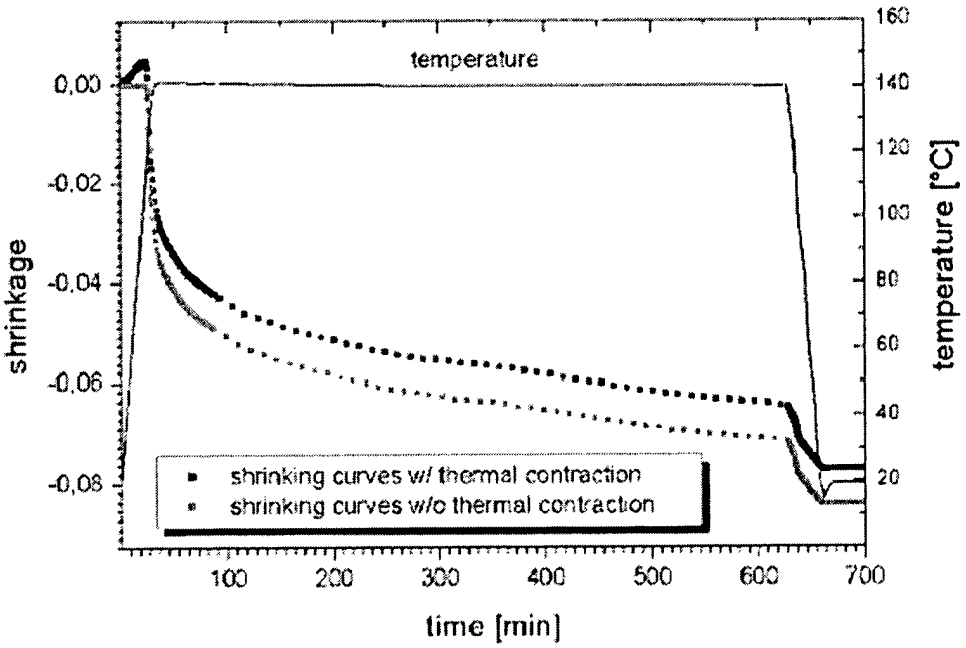


Figure 3: Shrinking curves of a PMMA sample sintered at T=140°C and p=18.5g/cm^2. Note that, in the red curve, thermal expansion of the sample during the heating process has been subtracted. The temperature curve for the overall process is included.

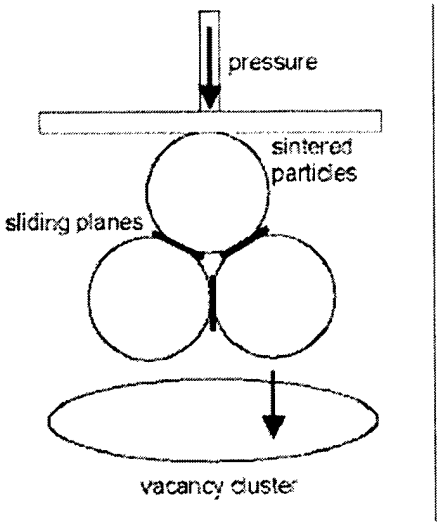


Figure 4: Schematic sketch illustrating the shrinkage mechanism for laser-sintered polymer samples.

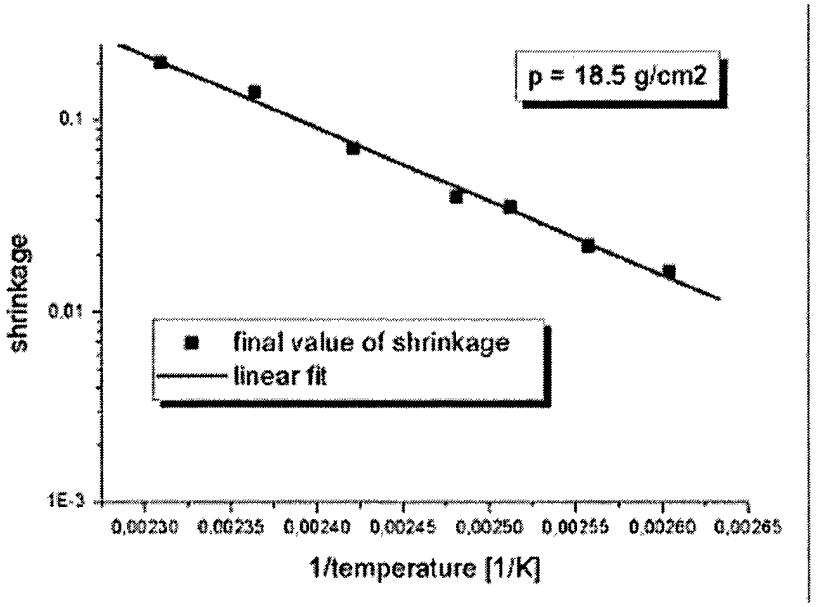


Figure 5: Temperature-dependency of the final values ascertained for shrinkage.

The dependency between the final values of shrinkage and the pressure applied is also linear *(Figure 6)*. However, increasing mass, i.e. the weight applied, does not have as great an impact on the degree of shrinkage as increasing the temperature. The linear dependency between these two values – shrinkage and pressure – may best be explained as follows. When the contact surfaces between the particles are thermally activated, cohesive strength is reduced. Similar to Hooke's Law for elastic bodies, pressure causes the particles to be compressed like a spring. Yet unlike a spring, where the compression of the coils is instantaneous, compression of the particles takes much longer. The internal stresses are relieved when the powder particles slide along their planes to fill any available empty spaces. Therefore, after pressure is removed, the samples – again unlike a spring - do not regain their original shape. This process is, in contrast, a relaxation process.

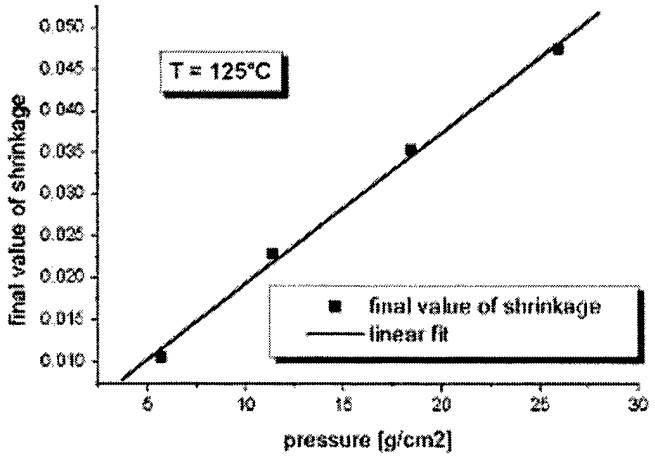


Figure 6: Pressure-dependency of the final values ascertained for shrinkage.

Impact of particle friction on shrinkage: To estimate the impact of friction between the bulk powder and the sinter geometry, we carried out the above-described shrinkage experiments using PA powder. *Figure 7* depicts shrinkage measured at three different temperatures: first without friction and then retarded through friction due to particle contact. For all three temperatures, retarded shrinkage is less than friction-free shrinkage by the same absolute value (1%). This behavior would indicate that, within the temperature range considered, contact friction between the bulk PA powder and the PMMA sample is not temperature dependent. At the temperatures selected here, the PA powder is neither cohesive nor flowable enough to significantly increase friction at the contact surfaces. It naturally remains to be examined in future work whether this behavior holds true for PMMA samples laser-sintered in a PMMA powder bed.

Integration of shrinking curves in the simulation: To be able to incorporate shrinkage in the thermal simulation, we must first express the change in height of the samples in mathematical form as a function of time, temperature, and pressure. When the shrinking curves are shown on the log-log scale, it becomes apparent that the curve, for most of its run, follows a line (*Figure 8).* Hence, according to a power law, the change in height and, thus, the density of the sample, may be expressed as a function of time for longer time periods. Adding the linear dependency of shrinkage s to pressure p renders the following equation:

$$s \propto t^{\alpha(T)} \cdot cp\,, \qquad \textbf{(Eq. 2)}$$

with c=const.

The exponents of the exponential function and the temperature are linear dependent *(Figure 9):*

$$\alpha(T) = c_1 T + c_2\,, \qquad \textbf{(Eq. 3)}$$

with c_1, c_2 = const.

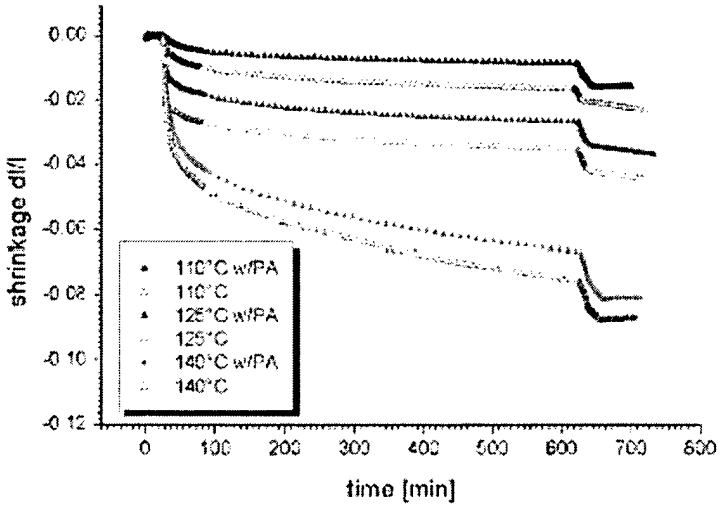


Figure 7: Comparison of shrinkage of pre-sintered PMMA samples tested first friction-free and then using PA powder to enhance cohesive strength.

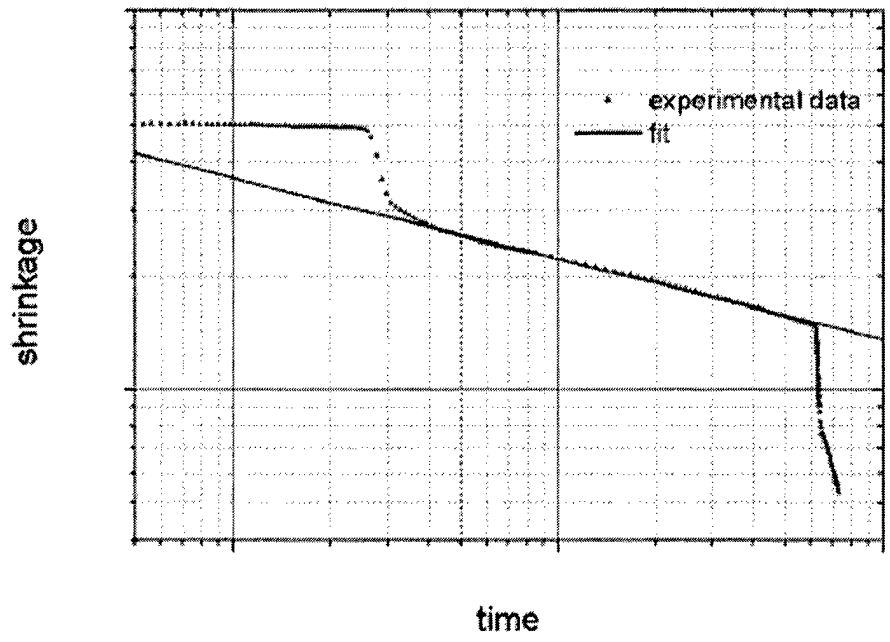


Figure 8: Time-dependency of shrinkage on a log-log scale.

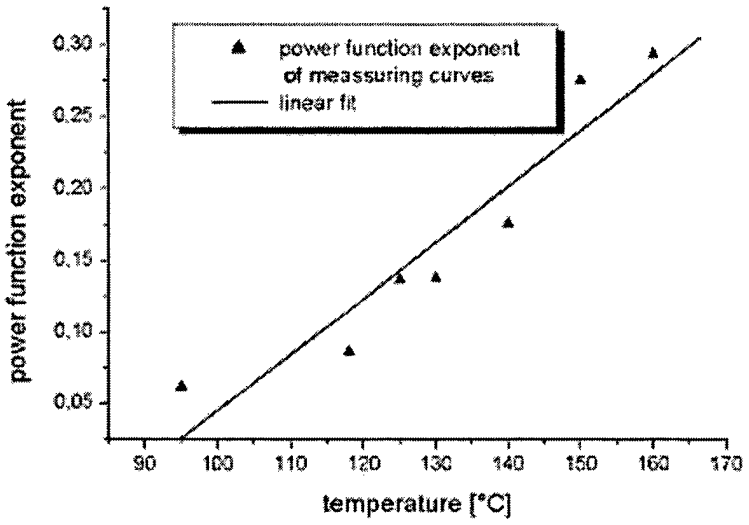


Figure 9: Temperature-dependency of the power function exponents.

Physical Shrinkage Models

Modeling and simulation of shrinkage can be done on two scales: at a microscopic level which tracks an amount of distinct interacting particles, the so-called Distinct Element Model (DEM), and at a macroscopic level. The latter applies special laws for the plastic flow of cohesive granular matter. [3] With respect to the cohesive strength, relevant sintering laws [2] which may

be extended by a pressure dependence need to be found. This can be done, for instance, if the driving surface tension is enhanced by a value proportional to the local pressure and the particle diameter.

A simple version for the DEM system is given through an elastic contact model which consists of two different stiffnesses for loading and unloading in order to incorporate plasticity [3]. Also, cohesion strength has to be considered. The tangential motion of the particles is controlled by a Coulomb-type frictional law. Due to the history- and temperature-dependence of the sintering process, both the cohesion and the friction parameters need not be constant.

In principle, this microscopic simulation together with a certain averaging procedure leads to effective macroscopic dynamic laws. In practice, however, the number of particles is limited for computational reasons. Moreover, most current DEM simulations are restricted to two dimensions. Therefore, it is reasonable to try to directly find some macroscopic constitutive equations.

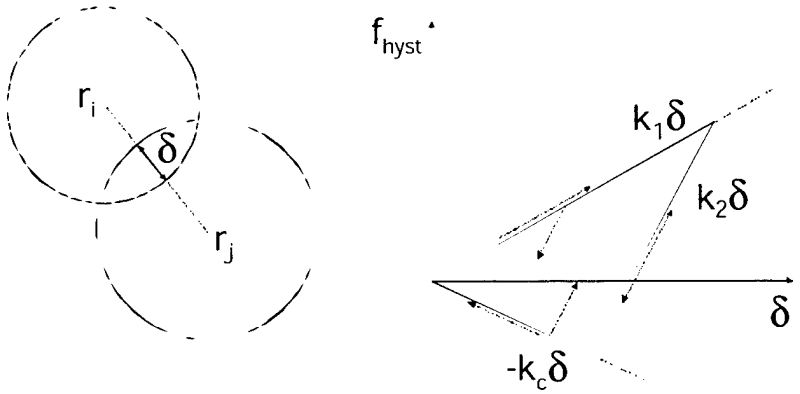


Figure 10: Two-particle contact with overlap d (left), elastic force law with hysteresis and cohesion (right).

Several authors have considered macroscopic stress-strain behavior in the context of soil mechanics. We may start here from a Drucker-Prager formulation of plasticity, which has to be generalized to include cohesion, for instance [3]. However, the resulting model still needs to be extended to make cohesion history- and temperature-dependent. This has not yet been done.

For low stresses, i.e. if no external pressing is carried out, a viscoplastic formulation of the constitutive equations would be more appropriate. The related viscosity coefficients will then depend on the density, leading to a non-linear model [4]. Finding the related sintering laws for the polymer powder remains an area for future work.

Summary and Future Work

Laser-sintered polymer parts shrink during the building and cooling processes. Shrinkage, which may be expressed as a function of time, temperature and pressure, is to be computed before sintering and compensated by upscaling the requisite datasets. The basis for shrinkage compensation as set out here is given through a thermal simulation of the SLS process, which replicates the temperature distribution in the build room very accurately. Data from dilatometer examinations of laser-sintered sample geometries serve as the foundation for a shrinkage model. In experiments, the samples demonstrated a change in height which, given longer periods of time, behaves in accordance with a power law with time. The exponents of the exponential function and the temperature proved to be linear dependent. In addition, the final values of shrinkage can be expressed in the form of an Arrehnius plot as a function of temperature and also show a linear dependency to the pressure applied. The former function results from the necessary thermal activation of the particle contacts, whereas the latter is explained as a stress-strain relationship similar to Hooke's Law, where internal stresses caused by applying pressure to the particles are relieved by the particles sliding into available vacancy clusters. If particle friction is generated through the addition of bulk powder, shrinkage is reduced significantly. Transfer of the experimental results achieved under the idealized measuring conditions prevalent in the dilatometer to the real conditions in SLS machines will require further work. However, this work offers various theoretical approaches for such transfer. While the resulting shrinkage model will need to consider friction and cohesion between the particles at the microscopic level, relevant macroscopic equations for shrinkage are required to significantly minimize computation time.

References

1. J. Shen, J. Steinberger, J. Göpfert, R. Gerner, F. Daiber, K. Manetsberger, S. Ferstl, "Inhomogeneous Shrinkage of Polymer Materials in Selective Laser Sintering", SFF 2000, Austin, Texas
2. J. Steinberger, J. Shen. K. Manetsberger, J. Muellers, "Simulation of the SLS Process as the Basis of a Process Optimization", SFF 2000, Austin, Texas
3. Vermeer, P.A, Diebels, S., Ehlers, W., Herrmann, H.J., Luding, S., Ramm, E., University of Stuttgart, Germany, "Continuous and Discontinuous Modelling of Cohesive-Frictional Materials" 2001. XIV, 307 pp. Hardcover
4. Riedel. H., "A constitutive model for the finite-element simulation of sintering distortions and stresses" in: G.L. Messing et al. (eds.): "Ceramic Powder Science III", American Ceramic Society, Westerville (1990) 619-630

this page intentionally blank

A Model of Laser-Powder Interaction in Direct Selective Laser Sintering of Metals

Suman Das and Haseung Chung
Department of Mechanical Engineering
University of Michigan
Ann Arbor, MI 48109-2125

Abstract

We present a simple one-dimensional model that describes the physical mechanisms of heat transfer, melting and resolidification taking place during and after the interaction of a laser beam with a bed of pure metal powder. The physical model describing this situation is based on the classical Stefan problem with appropriately chosen boundary conditions to reflect direct selective laser sintering of metals. A numerical model based on the finite volume method is developed to perform computations for two beam diameters, three beam speeds and for constant, step and ramp laser power input profiles. The results of these computations show the influence of laser beam diameter, laser power input rate and input duration on the melt interface velocity and location, and temperature. Scaling laws for time to reach maximum melt depth and total melt-resolidification time are derived. Comparisons of the temperature histories for the three power input profiles are described.

INTRODUCTION

Selective laser sintering (SLS) is a solid freeform fabrication [1] technique that creates three-dimensional freeform objects directly from their CAD models. An object is created by selectively fusing thin layers of a powder using a computer-controlled scanning laser beam that scans patterns corresponding to slices of the CAD model. Direct selective laser sintering of metals [2] is a process in which a high-energy laser beam directly consolidates a metal powder or powder mixture to full density. Direct selective laser sintering of metals is a complex process exhibiting multiple modes of heat, mass and momentum transfer, and chemical reaction mechanisms. The strong interplay between these mechanisms directly impacts the SLS process, determining whether a given material can be processed and if so, how the microstructure and properties of the material are impacted. The inherent complexity of this process imposes serious constraints on the complexity of the models that can be constructed to enable a fundamental understanding of the important physical mechanisms in SLS. This understanding is essential to implement effective process control.

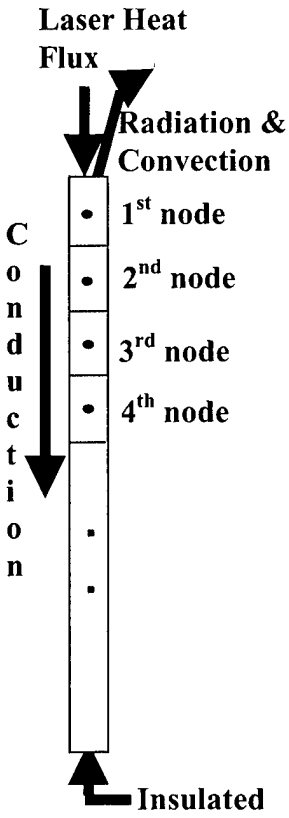
Previous work on modeling SLS of metals includes finite element modeling for metal powder densification [3] and three dimensional models for two-component metal mixtures [4]. With the goal of developing process understanding for control purposes, we present a simple one-dimensional model that describes the physical mechanisms of heat transfer, melting and resolidification taking place during and after the interaction of a laser beam with a bed of pure metal powder. The physical model describing this situation is based on the classical Stefan problem with appropriately chosen boundary conditions to reflect direct selective laser sintering of metals. A numerical model based on the finite volume method was developed to perform computations for two beam diameters, three beam speeds and for constant, step and ramp laser power input profiles. Properties of nickel were used for the numerical computations. The results of these computations show the influence of laser beam diameter, laser power input rate and input duration on the melt interface velocity and location, and temperature. Scaling laws for time

to reach maximum melt depth and total melt-resolidification time are derived. Comparisons of the temperature histories for the three power input profiles are described.

PHYSICAL MODEL

We consider one-dimensional heat conduction in a solid of length L. Heat flux from the laser flows in through the surface at x=0 at a rate q" per unit area during heat up while the surface at x = L is assumed insulated. If heating continues long enough, the surface at x = 0 reaches the melting temperature T_m, melting commences and the melt interface moves inward. This is the well documented Stefan problem [5,6]. During cool down, heat is lost from the surface at x=0 by convection and radiation. We aim to determine the temperature distribution, the velocity and the location of the melting interface within the domain of interest. The following assumptions are made for developing the model:

1. Powder is treated as a solid, no densification occurs during the process.
2. Laser beam intensity distribution is uniform across the beam diameter.
3. Constant material properties.
4. No convective heat transfer at top surface (process occurs in a vacuum).
5. No melt pool convection, no convective heat transfer at melt interface.
6. Planar propagation of melt interface.
7. No evaporative heat loss and no evaporative mass transfer at top surface.
8. Top surface is diffuse gray, top surface cools by radiative cooling.



The governing heat equation describing the process is as follows:

$$\frac{\partial}{\partial x}\left(k\frac{\partial T}{\partial x}\right)+\frac{\partial}{\partial y}\left(k\frac{\partial T}{\partial y}\right)+\frac{\partial}{\partial z}\left(k\frac{\partial T}{\partial z}\right)+\dot{q}=\rho c_p\frac{\partial T}{\partial t}$$

The one-dimensional form of this equation with constant properties is

$$k\frac{\partial^2 T}{\partial x^2}=\rho c_p\frac{\partial T}{\partial t} \quad (1)$$

During heat up and melting, the heat flux boundary condition at the top surface is

$$-k\frac{\partial T}{\partial x}=\alpha_a q'', x=0 \quad (2)$$

During cool down, the general convection and radiation boundary condition at the top surface is

$$-k\frac{\partial T}{\partial x}=h(T_\infty-T)+\varepsilon\sigma(T_\infty^4-T^4), x=0 \quad (3)$$

The bottom surface is assumed insulated, therefore the boundary condition there is

$$-k\frac{\partial T}{\partial x}=0, x=L \quad (4)$$

The Stefan condition describing the heat flux balance at the planar melt interface is

$$k\frac{\partial T}{\partial x}\bigg|_s-k\frac{\partial T}{\partial x}\bigg|_l=\rho V\lambda, x=x_f \quad (5)$$

NUMERICAL MODEL

The finite volume method [7] is employed to develop the numerical model. The computational domain is divided into 2N cells and a node is placed at the center of each cell. Symmetry is used to accommodate the insulation boundary condition. Using symmetry, computation is done only for the first N+1 nodes. The 1st node and (N+1)th node are used to satisfy the boundary conditions. The temperatures computed at each node represent average temperatures for the cell (finite volume element) corresponding that node.

Temperature computation at an interior node not adjacent to the melt interface is given by

$$\rho c \delta x \frac{dT_i}{dt} = \frac{k}{\delta x}(T_{i-1} - T_i) + \frac{k}{\delta x}(T_{i+1} - T_i) \tag{6}$$

which can be rewritten as

$$\frac{\delta x^2}{\alpha}\frac{dT_i}{dt} = (T_{i-1} - T_i) + (T_{i+1} - T_i) \tag{7}$$

The time derivative of temperature can be approximated as $(T_i^{new} - T_i)/\delta t$. Substituting this into (7) and re-arranging leads to an algorithm for computing the new temperature at each node by

$$T_i^{new} = T_i + \frac{\alpha \delta t}{\delta x^2}(T_{i-1} - T_i) + \frac{\alpha \delta t}{\delta x^2}(T_{i+1} - T_i) \tag{8}$$

Temperature computation at the surface node during heat up is given by

$$\rho c \delta x \frac{dT_i}{dt} = \alpha_a q'' + \frac{2k}{\delta x}(T_{i-1} - T_i) + \frac{k}{\delta x}(T_{i+1} - T_i) \tag{9}$$

Using the time derivative of temperature approximation, (9) can be rewritten as

$$T_i^{new} = T_i + \frac{\delta t}{\rho c \delta x}\alpha_a q'' + \frac{2\alpha \delta t}{\delta x^2}(T_{i-1} - T_i) + \frac{\alpha \delta t}{\delta x^2}(T_{i+1} - T_i) \tag{10}$$

By combining the heat transfer resistances for convection, radiation, and conduction for half of δx, the temperature computation at the surface node during cool down is given by

$$\rho c \delta x \frac{dT_i}{dt} = \frac{T_{i-1} - T_i}{\dfrac{1}{h + \varepsilon\sigma(T_{i-1}^2 + T_i^2)(T_{i-1} + T_i)} + \dfrac{\delta x}{2k}} + \frac{k}{\delta x}(T_{i+1} - T_i) \tag{11}$$

which again using the time derivative of temperature approximation can be rewritten as

$$T_i^{new} = T_i + \frac{T_{i-1} - T_i}{\dfrac{1}{h + \varepsilon\sigma(T_{i-1}^2 + T_i^2)(T_{i-1} + T_i)} + \dfrac{\delta x}{2k}}\frac{\delta t}{\rho c \delta x} + \frac{\alpha \delta t}{\delta x^2}(T_{i+1} - T_i) \tag{12}$$

By symmetry, temperature computation at the end node is given by T(N+1)=T(N). Hence, after T(N) has been computed, we simply set T(N+1)=T(N). To satisfy the Stefan condition, heat fluxes due to conduction in the solid and liquid at the previous time step are approximated by

$$k\left.\frac{\partial T}{\partial x}\right|_s = k\frac{T_{i+1} - T_m}{x_{i+1} - x_f} \text{ and } k\left.\frac{\partial T}{\partial x}\right|_f = k\frac{T_m - T_{i-1}}{x_f - x_{i-1}} \text{ respectively} \tag{13}$$

while the melt front velocity is approximated by

$$V = \frac{x_f^{new} - x_f}{\delta t} \tag{14}$$

These approximations lead to an algebraic version of the Stefan condition given by

$$k\frac{T_{i+1}-T_m}{x_{i+1}-x_f}-k\frac{T_m-T_{i-1}}{x_f-x_{i-1}}=\rho\lambda\frac{x_f^{new}-x_f}{\delta t} \tag{15}$$

that can be rewritten to yield the new location of the melt interface via

$$x_f^{new}=x_f+\frac{\delta t}{\rho\lambda}\left(k\frac{T_{i+1}-T_m}{x_{i+1}-x_f}-k\frac{T_m-T_{i-1}}{x_f-x_{i-1}}\right) \tag{16}$$

A different set of equations is employed for computation in nodes adjacent to cells containing the melt interface. The discretized heat flux balance for such nodes is given by

$$\rho c\delta x\frac{dT_i}{dt}=\frac{k}{\delta x}(T_{i-1}-T_i)+\frac{k}{x_f-x_i}(T_m-T_i) \tag{17}$$

The corresponding temperature computation is given by

$$T_i^{new}=T_i+\frac{\alpha\delta t}{\delta x^2}(T_{i-1}-T_i)+\frac{\alpha\delta t}{\delta x}\frac{1}{x_f-x_i}(T_m-T_i) \tag{18}$$

When the melt interface is in the second cell, a special case arises for the first node. The temperature computation for the first node during heat up and melting is given by

$$T_i^{new}=T_i+\frac{\delta t}{\rho c\delta x}\alpha_a q''+2\frac{\alpha\delta t}{\delta x^2}(T_{i-1}-T_i)+\frac{\alpha\delta t}{\delta x^2}\frac{\delta x}{x_f-x_i}(T_m-T_i) \tag{19}$$

while its temperature during cool down and re-solidification is given by

$$T_i^{new}=T_i+\frac{T_{i-1}-T_i}{\frac{1}{h+\varepsilon\sigma(T_{i-1}^2+T_i^2)(T_{i-1}+T_i)}+\frac{\delta x}{2k}}\frac{\delta t}{\rho c\delta x}+\frac{\alpha\delta t}{\delta x^2}\frac{\delta x}{x_f-x_i}(T_m-T_i) \tag{20}$$

The discretized heat flux balance at an interior node adjacent and to the right of the melt interface is given by

$$\rho c\delta x\frac{dT_i}{dt}=\frac{k}{x_i-x_f}(T_m-T_i)+\frac{k}{\delta x}(T_{i+1}-T_i) \tag{21}$$

The corresponding temperature computation is given by

$$T_i^{new}=T_i+\frac{\alpha\delta t}{\delta x}\frac{1}{x_i-x_f}(T_m-T_i)+\frac{\alpha\delta t}{\delta x^2}(T_{i+1}-T_i) \tag{22}$$

Finally, temperature interpolation at a node after the melt interface has passed by it is given by

$$T_i=T_{i-1}+(x_i-x_{i-1})\frac{T_m-T_{i-1}}{x_m-x_{i-1}} \tag{23}$$

The parameter values used for the computations are shown in table 1.

Domain size	Number of nodes	Time step	Laser beam power	Beam diameter
2 mm	100	4 x 10^{-6}s	500 W	100 μm, 250 μm

Table 1. Parameters used for numerical computations.

The concept of beam-material interaction time is used to simulate the temporal action of a moving laser beam over a surface area corresponding to one beam diameter. The beam-material interaction time is defined as the time taken by the beam to traverse one beam diameter, and can be used to set the duration for step power input and ramp power input experienced by an area of the surface corresponding to one beam diameter. Three typical beam speeds in SLS processing of

metals [6] were chosen to determine beam-material interaction times for each of the 100 μm and 250 μm beam diameters used in the computations, as shown in table 2.

Beam speed (in/s)	t_f=d/v (100 μm beam)	t_f=d/v (250 μm beam)
5 (12.7 cm/s)	7.87×10^{-4} sec	1.97×10^{-3} sec
10 (25.4 cm/s)	3.94×10^{-4} sec	9.84×10^{-4} sec
50 (127 cm/s)	7.87×10^{-5} sec	1.97×10^{-4} sec

Table 2. Beam-material interaction times for step power input and ramp power input

RESULTS AND DISCUSSION

Numerical computations were conducted for three types of laser power input; constant power input (laser beam always on), step power input (constant laser power for the duration of beam-material interaction time followed by a drop to zero power) and ramp power input (laser power linearly ramps from zero to full power during beam-material interaction time, followed by a drop to zero power), for two beam diameters (100 μm and 250 μm). For the step and ramp power inputs, computations were carried out for three beam-material interaction times with durations equal to five times beam-material interaction time. Plots of interface velocity, interface location, surface temperature and center node temperature were obtained. The results for each case are described in the following sections.

Case I: Constant Power Input

Figure 1 shows the interface velocity and location as a function of time for constant power input with a 100 μm beam. The interface velocity initially peaks to nearly 4 m/s but then drops sharply to nearly zero in 5×10^{-3} s. The interface location continues to penetrate deeper into the solid during this time as is expect for constant heat flux input, reaching a final value of 460 μm.

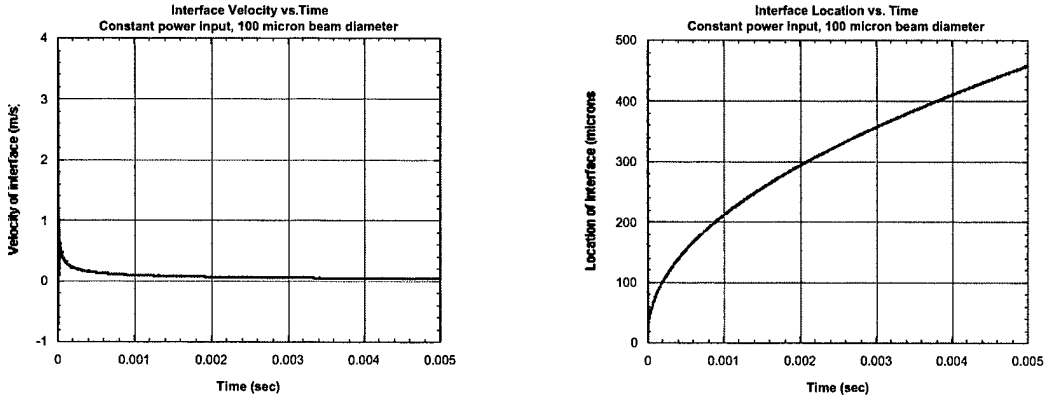


Fig.1. Interface velocity and location for 100 μm beam and constant power input.

Figure 2 shows surface and center node temperatures for constant power input. The computed peak surface temperatures for 100 μm are very high (much higher than the melting point of nickel), which are attributed to unmodeled effects (e.g. evaporation and melt pool convection). At 5 ms, the temperature half-way (1 mm) into the computational domain is lower than the surface temperature by a factor of about 3, yielding a temperature gradient of about 4000 K/mm.

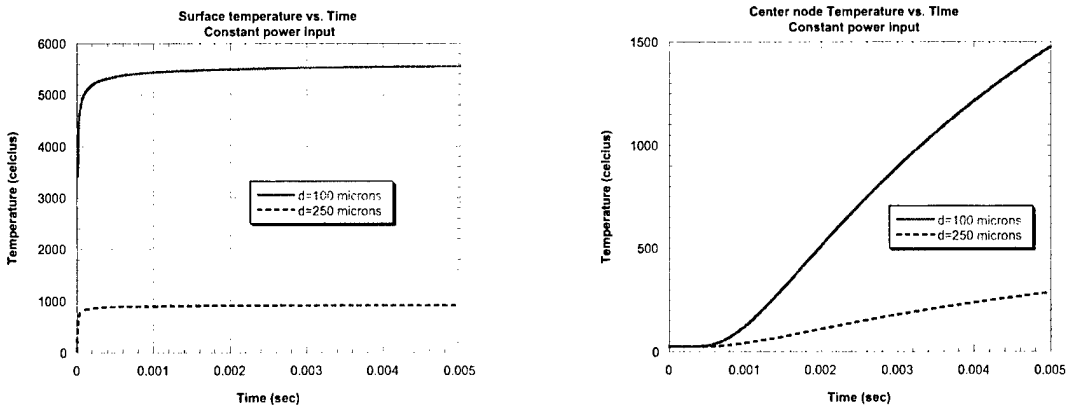


Fig. 2. Surface and center node temperatures for 100 μm beam and constant power input.

Case II: Step Power Input

Figure 3 shows interface velocity and location for 100 μm beam for the three beam-material interaction times and step power input. The variation of interface velocity with time is not significantly different for the three cases. However, the maximum melt penetration depth and time at which the interface velocity changes sign are proportional to beam-material interaction time. The time to reach maximum melt depth scales with the beam-material interaction time by a constant factor of about 2. Estimates for the total melt-resolidification times can be obtained by linearly extrapolating the downward (resolidifiction) portions of the interface location curves to intersect the X-axis. By these estimates, the total melt-resolidification time scales with the corresponding beam-material interaction time by a constant factor of about 10, i.e. about one order of magnitude.

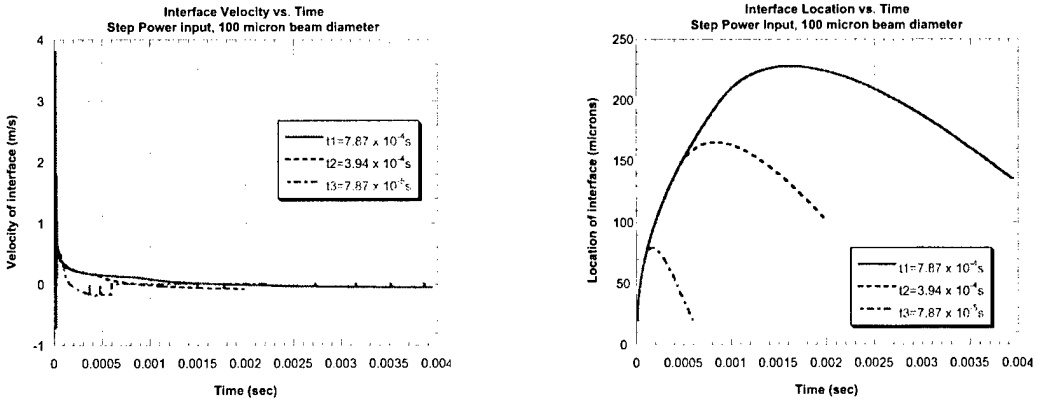


Fig. 3. Interface velocity and location for 100 μm beam and step power input.

Figure 4 shows the surface and center node temperatures for 100 μm beam diameter for the three beam-material interaction times and step power input. As in the case of constant power input, the computed peak surface temperatures are very high, reflecting unmodeled effects. The peak temperature is proportional to the beam-material interaction time. Surface cooling begins almost instantaneously as the power is turned off, and the associated cooling rate is inversely proportional to beam-material interaction time. At the end of beam-material interaction, the temperature half-way (1 mm) into the computational domain has barely risen from ambient and the temperature gradient relative to the surface is about 5000 K/mm for all three instances of beam-material interaction time.

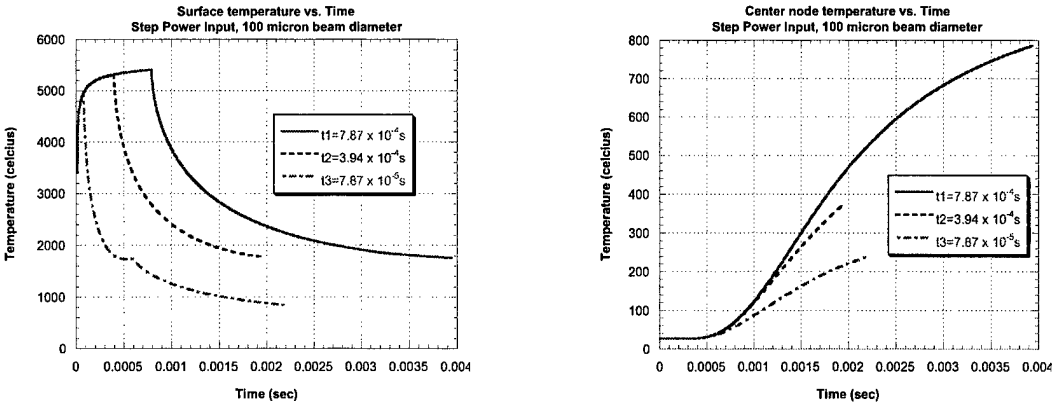


Fig. 4. Surface and center node temperatures for 100 μm and step power input.

Case III: Ramp Power Input

Figure 5 shows interface velocity and location for 100 μm beam for the three beam-material interaction times and ramp power input. The peak interface velocity is inversely proportional while the time to reach the peak velocity is directly proportional to beam-material interaction time respectively. The maximum melt penetration depth and time at which the interface velocity changes sign are proportional to beam-material interaction time. The time to reach maximum melt depth scales with the beam-material interaction time by a constant factor of about 1.4. Estimates for the total melt-resolidification times can be obtained by linearly extrapolating the downward (resolidifiction) portions of the interface location curves to intersect the X-axis. By these estimates, the total melt-resolidification time scales with the corresponding beam-material interaction time by a constant factor of about 4.

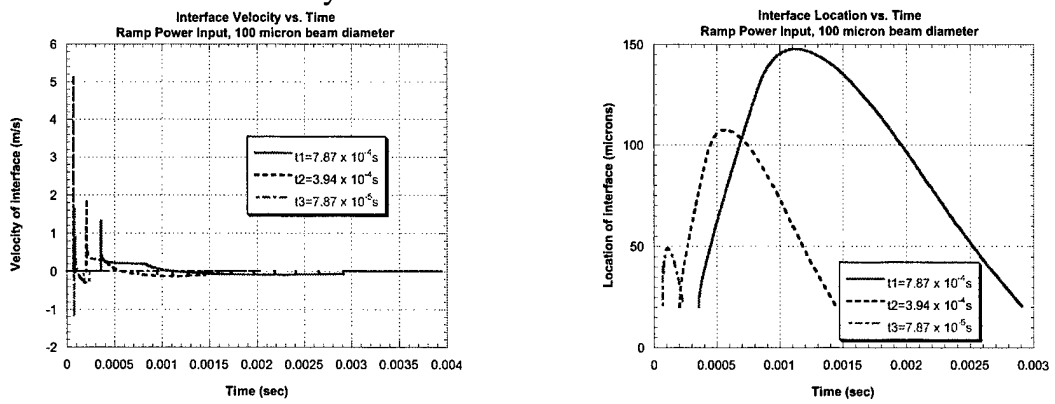


Fig. 5. Interface velocity and location for 100 μm and ramp power input.

Figure 6 shows the surface and center node temperatures for 100 μm beam diameter for the three beam-material interaction times and ramp power input. The peak temperature is proportional to the beam-material interaction time while the rate of surface temperature rise is inversely proportional to beam-material interaction time. Surface cooling begins almost instantaneously as the power is turned off, and the associated cooling rate is inversely proportional to beam-material interaction time. The predicted peak temperatures are comparable to those predicted for constant power and step input power, but are again high, reflecting unmodeled effects. At the end of beam-material interaction, the temperature half-way (1 mm) into the computational domain has barely risen from ambient and the temperature gradient

relative to the surface is between 4000 K/mm and 5000 K/mm for all three instances of beam-material interaction time.

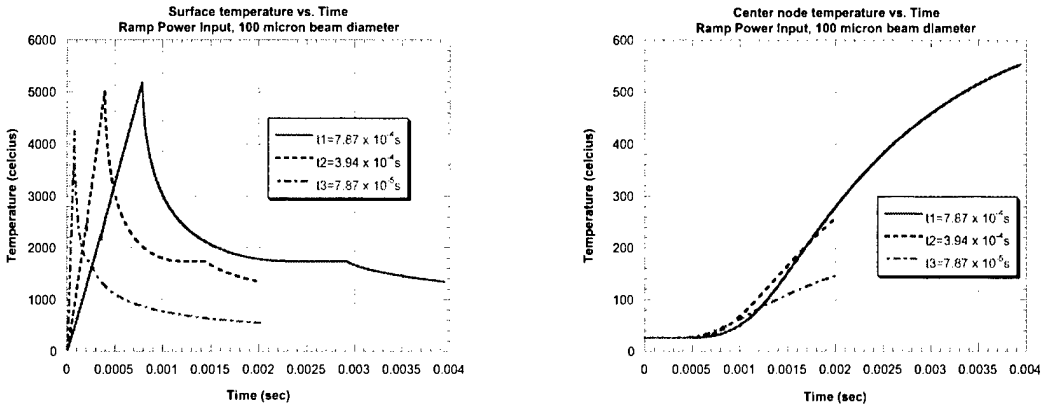


Fig. 6 Surface and center node temperatures for 100 μm and ramp power input.

Figure 7 shows comparisons of surface temperature for constant, step and ramp power inputs with respect to beam diameter for a beam-material interaction time corresponding to 12.7 cm/s (5 in/s) beam speed. No melting is predicted for a 250 μm beam in all cases. The predicted peak temperatures for all three types of power input are nearly the same with constant power input providing the highest temperature as expected, followed by step power input and ramp power input. The rate of temperature rise for ramp power input is more gradual versus step power input as expected. However, the cooling curves are nearly identical for both step and ramp power input.

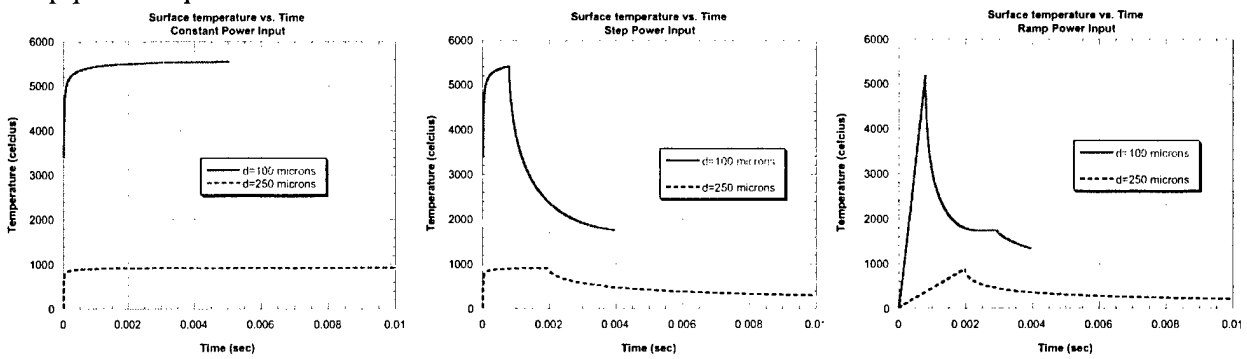


Fig. 7. Surface temperature comparisons for constant power, step power and ramp power at 5 in/s.

SUMMARY AND CONCLUSIONS

The results from this preliminary model can be summarized as follows:

1. No melting is predicted for the 250 μm beam for all cases. The predicted surface temperatures, especially for 100 μm beam are very high, reflecting unmodeled effects (e.g. evaporative heat loss, melt pool convection, temperature dependent properties).
2. For the same beam-material interaction time (same beam speed), peak temperatures for both step and ramp power inputs are inversely proportional to beam diameter.
3. For both step and ramp power input, the peak interface velocity and surface cooling rate after terminating laser power input are inversely proportional to beam-material interaction time while the time to reach peak interface velocity is directly proportional to beam-material interaction time.

4. Peak temperatures for both step and ramp power inputs are attained at the end of beam-material interaction time.
5. For step and ramp power inputs, the maximum melt penetration depth and time at which the interface velocity changes sign (start of resolidification) are proportional to beam-material interaction time.
6. For the same beam-material interaction time, beam diameter and laser power, the maximum melt depth for step power input is higher than that for ramp power input.
7. For step power input, the time to reach maximum melt depth scales with the beam-material interaction time by a factor of about 2 while the total melt-resolidification time scales with the corresponding beam-material interaction time by a factor of about 10.
8. For ramp power input, the time to reach maximum melt depth scales with the beam-material interaction time by a factor of about 1.4 while the total melt-resolidification time scales with the corresponding beam-material interaction time by a factor of about 4.

REFERENCES

1. Beaman, J. J., Barlow, J. W., Bourell, D. L., Crawford, R. H., Marcus H. L., and McAlea, K. P., *Solid Freeform Fabrication: A New Direction in Manufacturing*, Kluwer Academic Publishers, 1997.
2. Suman Das, *Direct Selective Laser Sintering of High Performance Metals-Machine Design, Process Development and Process Control*, Ph.D. dissertation, The University of Texas at Austin, 1998.
3. Shiomi, M., Yoshidome, A., Abe, F., and Osakada, K., "Finite element analysis of melting and solidifying processes in laser rapid prototyping of metallic powders", International Journal of Machine Tools & Manufacture, Vol. 39, 1999, pp. 237-252.
4. Zhang, Y., Faghri, A., Buckley, C. W., and Bergman, T. L., "Three-Dimensional Sintering of Two-Component Metal Powders With Stationary and Moving Laser Beams", ASME J. Heat Transfer, Vol. 122, 2000, pp. 150-158.
5. Cohen, M. I., 1967, "Melting of a Half-Space Subjected to a Constant Heat Input", Journal of The Franklin Institute, Vol. 283, 1967, pp. 271-285.
6. Landau, H. G., "Heat Conduction In a Melting Solid", Quarterly of Applied Mathematics, Vol. 8, 1950, pp. 81-94.
7. Patankar, S. V., *Numerical Heat Transfer and Fluid Flow*, 1980, Taylor & Francis.

NOMENCLATURE

Symbols

c_p = specific heat (J/kgK)
d = beam diameter (m)
h = convective heat transfer coefficient (W/m^2K)
k = thermal conductivity (W/mK)
$\dot{q}$ = internal heat generation (W/m^3)
q'' = heat flux (W/m^2)
T_m = melting temperature (K)
T_{oo} = ambient temperature (K)
T_i = temperature at node (K)
x_i = location of node (m)
x_f = location of interface (m)
v = beam speed (m/s)
V = melt front velocity (m/s)

Greek Letters

α_a = absorptivity of surface (assumed 0.8 for nickel)
α = thermal diffusivity (m^2/s)
δt = interval time (s)
δx = distance between nodes (m)
ε = emissivity of surface (assumed 0.8 for nickel)
λ = latent heat of fusion (kJ/kg)
ρ = density (kg/m^3)
σ = Stefan-Boltzmann constant

this page intentionally blank

Thermal Stresses in Direct Metal Laser Sintering

Haiko Pohl[1], Abdolreza Simchi[1,2], Munther Issa[1,3] and Hugo Calefi Dias[1,4]

1. Fraunhofer Institute for Manufacturing and Advanced Materials IFAM, Bremen, Germany
2. Department of Materials Science and Engineering, Sharif University of Technology, Tehran, Iran
3. Department of Production Engineering, University of Bremen, Bremen, Germany
4. LabMat - Laboratório de Materiais, Universidade Federal de Santa Catarina, Florianópolis – SC, Brazil

Abstract

In Direct Metal Laser Sintering objects are created by sequential sintering loose metal powder particles by means of laser technology. When the laser sintering process involves temperature gradients, thermal stresses develop. Corresponding residual stresses induce warping of the densified structure leading to unacceptable tolerance losses. This paper examines the role of laser beam scan patterns on the resulting stresses and warpage of direct metal laser sintered plate-shaped specimens. The effects of a large variety of laser sintering parameters are described. It can be shown that the optimization of process conditions and material aspects results in a significant reduction of thermal stresses.

Introduction

Direct Metal Laser Sintering is one of a few Rapid Prototyping technologies which possesses the capability to produce metal parts and prototype tools directly from powders. The high laser power supplied by a cw CO_2 laser binds effectively metal powder particles together. Such laser sintered objects then exhibit high densities in the range of 95% theoretical density. Due to the high thermal energy which is required to promote all steps of material re-arrangement and densification during sintering within an extremely short period of time [1], thermal gradients exist in the densified structure. Thermal stresses and corresponding residual stresses induce warping and/or cracking of the object. Warping normally leads to tolerance losses but cracking results in a more detrimental loss of quality.

Various authors have discussed the role of thermal stresses in layered manufacturing, for example in Stereolithography by Jayanthi [2], and Ullet [3], in Selective Laser Sintering by Karapatis [4], and Dalgarno [5], in Shape Deposition Manufacturing by Chin [6], Klingbeil [7], and Nickel [8]. From all those contributions can be predicted that both material properties of the laser sintered system and process parameters such as power intensity, scan rate, thickness of layer etc., control the appearance of thermal stresses. In order to reduce the level of warpage in laser sintered objects, a detailed examination on the role of process parameters was performed. The

variation of process parameters is described on two different powder systems, namely pure iron (Hoeganaes ASC 300) and a commercial steel-based powder DirectSteel 50-V1 (EOS GmbH, Germany).

Experimental

The powder systems were sintered layer by layer to the required shape using EOSINT M250X^{tended} laser sintering machine. The machine consists of a powder handling system, a continuous wave CO_2 laser source with related optics and a process computer. When a part is to be built, the CAD file is sliced into a stack of thin layers. The powder is deposited on a steel platform using a doctor blade. The layer thickness can be varied from 0.05mm to 0.2mm. Then, the laser beam is scanned on the bed surface. The maximum output power is around 200W. The scan rate can be in the range of 50 to 175mm/s for the mentioned materials. The building process was performed under nitrogen atmosphere. The build plate temperature can be set to 80°C.

Two different material systems were used. Pure iron powder type ASC 100 (d_{90} = 45µm) from Hoeganaes was used to study the effects of process parameters on a one-component powder system. DirectSteel 50-V1 (d_{90} = 35µm) is a commercial steel-based powder from EOS GmbH for the direct part production or rapid tooling applications. The powder system consists of a low melting phase which promotes liquid phase sintering.

A steel sheet 1.1403 (1mm thickness) was fixed using screws onto the build plate. A test part with dimensions 60mm x 14mm (variable height) was then laser sintered on top of the steel sheet. The residual stresses in the laser sintered test part result in a deflected steel sheet. After removing the steel sheet from the build plate, the amount of deflection was measured pointwise along the axes on the backside of the steel sheet in x- and y-direction. The precision of the dial gauge was within 1/100 millimeter (Fig. 1).

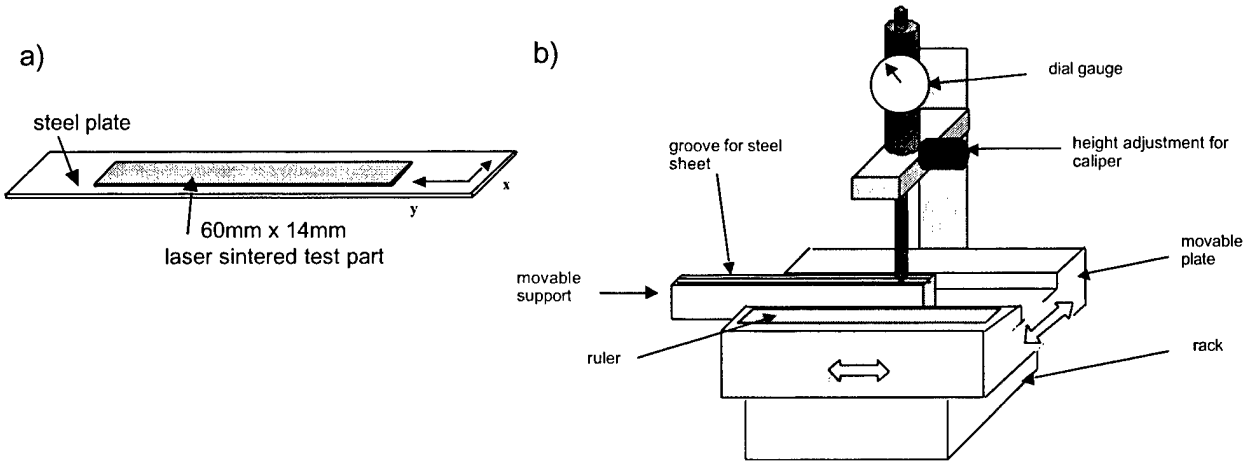


Figure 1: Steel sheet with laser sintered test part (a) and device for deflection measurement (b)

Laser power intensity, scan rate, hatch distance, layer thickness, and number of layers were varied to examine their influence on the amount of residual stresses. Additionally, several scanning patterns were applied. Here, the main target is the variation of the thermal gradient by using different laser scan lengths. An overview of the scanning patterns is given in figure 2.

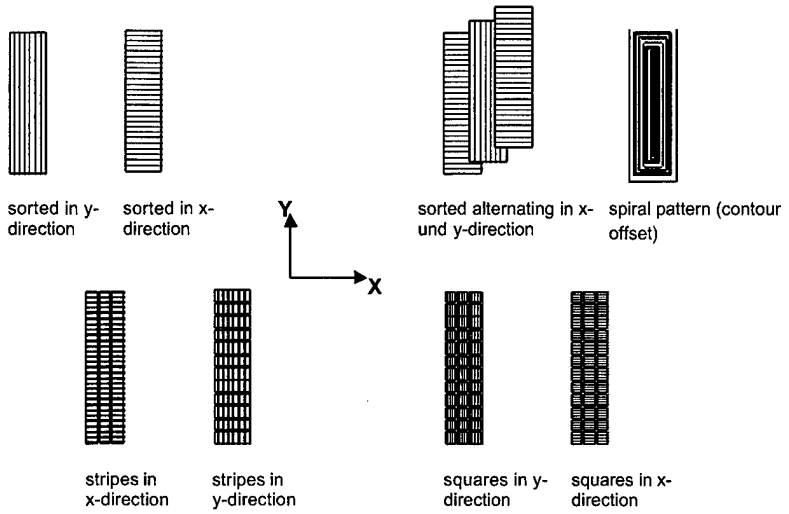


Figure 2: Scanning patterns used in Direct Metal Laser Sintering

The scanning pattern "Sorted" is a typical raster pattern with a short raster pattern in x-direction and a long raster pattern in y-direction. This type can be alternating from layer to layer, starting with a short raster pattern for the first layer. In the spiral pattern, first the laser scans the contour continuously in a single line scan. According to the hatch distance, the contour is offset towards the center of the part and repeated when a new single line scan follows. Scanning pattern "Stripes" is a combination of short and long raster patterns. Here, a short raster pattern determines the width of the stripes. Stripes can overlap each other. "Squares" normally are not attached to each other after scanning. The gap is then closed by a single line scan.

Deflection Measurements

Thermal stresses and corresponding residual stresses develop in the densified structure during laser sintering. The three dimensional stress state is characterized by their components in x-, y-, and z-direction. The deflection of the steel sheet is a result of the stress state in the densified structure. Measurements of the deflection can give a description of preferred process conditions in order to minimize warpage.

Generally, the steel sheet deflects in a bell shape. When the steel sheet is removed from the build plate, the edges bend up whereas the center remains in its original position. Figure 3 depicts the influence of the hatch distance on the deflection for the scanning pattern "Sorted". Keeping all other process parameters constant, the reduction of the hatch distance clearly leads to an increase of deflection.

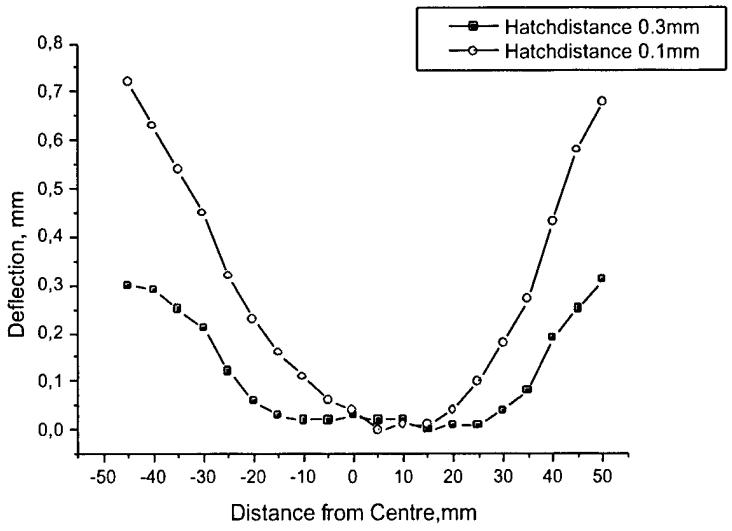


Figure 3: Effect of hatch distance on the deflection of a steel sheet with laser sintered test part, pure iron, sorted with long raster pattern, 50mm/s scan speed

Decreasing the hatch distance is equivalent to increasing the overlap between consecutive laser scan lines. Practically, a lower hatch distance results in a more localized heating of the powder bed by the laser source. In this case, temperature gradients must be more pronounced and bring about more thermal stresses compared with a more homogeneous heating.

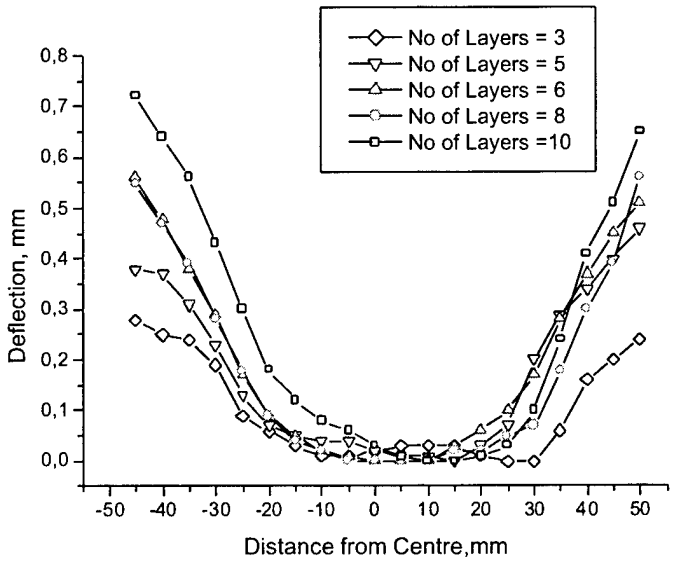


Figure 4: Effect of sample height on the deflection of a steel sheet, pure iron, sorted with long raster pattern, 50mm/s scan speed

Changing the number of layers was used to vary the height of the laser sintered test part. From figure 4 it can be noted that the amount of deflection in longitudinal direction increases with more layers. In contrast, the amount of deflection in transversal direction decreases with more layers. When new powder is spread onto the previous layer and densified by the laser beam, thermal stresses pile up. Neither annealing effects nor a saturation of this pile up was not found. However, the increasing deflection in longitudinal direction restricts the deflection in transversal direction.

The effect of material composition on the deflection of the steel sheet was examined by laser sintering two different powder systems. Figure 5 compares the results for pure iron and a commercial steel-based powder DirectSteel 50-V1. Although laser sintering of iron powder seems to result in less deflection compared with DirectSteel, it must be considered that iron is densified only up to 75% theoretical density (TD) but DirectSteel up to 95% TD. A higher degree of densification seems to promote the formation of residual stresses. Additionally, during laser sintering of DirectSteel material, a considerable amount of liquid phase should exist in order to generate liquid phase assisted sintering. During the solidification of the liquid and the accompanied volume shrinkage, further stresses may be induced into the adjacent densified structure.

In order to minimize thermal stresses, optimized process conditions should be chosen. However, some process parameters may be contradictory with one another. For example, in figure 6 the amount of deflection is compared between different types of scanning patterns using various scan speeds. While a high scan speed clearly leads to a significant reduction of residual stresses and, therefore, should be preferred, it also lowers the energy input and decreases the densification.

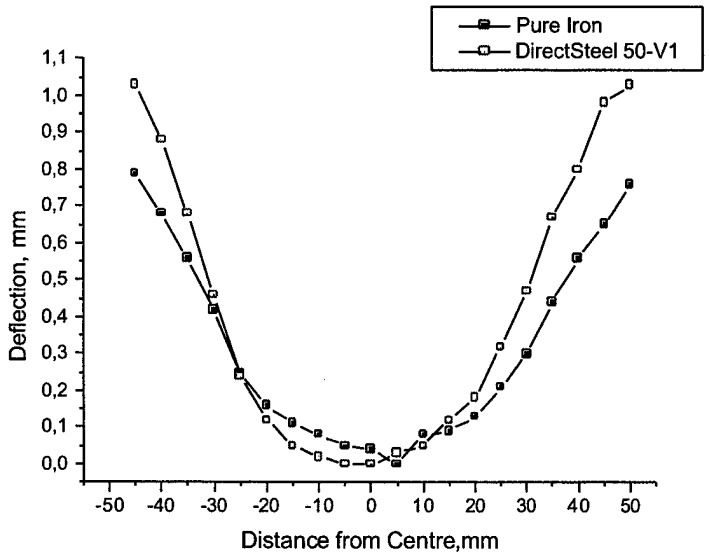


Figure 5: Effect of material composition on the deflection of a steel sheet, sorted with long raster pattern, 50mm/s scan speed

If the applications are such that high densities and corresponding good mechanical properties are required, a lower scan speed must be used. On the other hand, there is still a high potential to exploit as the differences in various scanning patterns are relatively high. The highest amount of deflection was detected for the spiral pattern. Due to the long scan vector length, temperature gradients are very high. The difference for low and high scan speeds is relatively small. Here, the spiral patterns seems to have a positive effect on a homogenized sample heating as soon as the outer contour scans are finished.

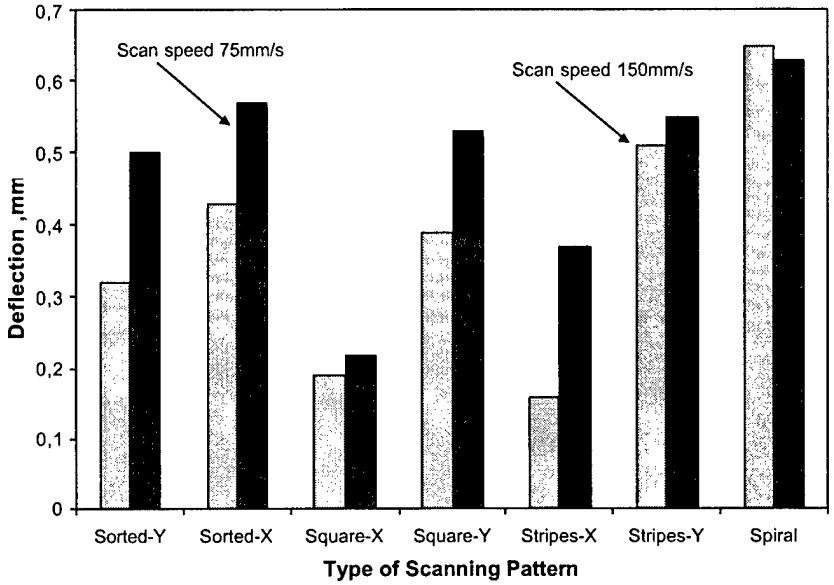


Figure 6: Effect of various scanning patterns on the deflection of a steel sheet at different scan speeds, pure iron (X = short raster pattern, Y = long raster pattern)

The lowest amount of deflections were detected for "square" and "stripes" type pattern with short vector lengths (x-direction). But the residual stresses increase significantly when a long vector length (y-direction) is applied for those types. The difference between short and long raster pattern for type "sorted" is quite small. In contrast to the stripes pattern, the preheating of the powder and substrate might not be well enough by just one progressing laser line. In stripes pattern, the preheated area is mostly determined by the width of the stripe. If the width of the stripes was set at an appropriate rate to the overall dimensions of the laser sintered structure, a significant reduction of residual stresses can be expected.

Conclusions

This study contributes deflection measurements in order to achieve assessments for thermal stresses and corresponding residual stresses in laser sintered test parts. From the results it can be noted that several factors including processing conditions and material aspects play an important role. To minimize residual stresses, a optimum process parameters should be chosen. However, some parameter sets which are essential to other properties such as density or strength

of the laser sintered structure may be contrary to the goal of reduced stresses. It was found that such process conditions leading to a higher densification by increasing the energy input bring about a higher deflection and, thus, higher residual stresses. Whenever a slightly lower final density is acceptable, faster scan speeds, larger hatch distances, less layers with higher layer thickness are recommended.

For different scanning patterns, the lowest deflection was measured for scanning patterns type "Stripes" and "Squares". However, the improvement highly depends on the direction of the line scan. The deflection can be minimized if a short raster pattern is applied. For example, due to the width of the stripe, the laser beam more efficiently preheats the unsintered powder and the substrate material. This results in a more homogeneous temperature gradient and reduced thermal stresses.

Acknowledgements

One of the authors (A. Simchi) is indebted to the Alexander von Humboldt Foundation (AvH) for a research fellowship. This author also acknowledges Sharif University of Technology, Tehran, Iran for permission to reside in Germany as a visiting scientist at the Fraunhofer Institute IFAM.

References

[1] Simchi, A., Petzoldt, F. and Pohl, H.: Direct Metal Laser Sintering: Material Considerations and Mechanisms of Particle Bonding. *Int. J. Powder Metall.* Vol. 37, No. 2, 2001.

[2] Jayanthi, S. et al.: Proc. Solid Freeform Fabrication Symposium, 250-258, 1997.

[3] Ullett, J. et al.: Proc. Solid Freeform Fabrication Symposium, 242-249, 1994.

[4] Karapatis, N. et al.: Proc. Solid Freeform Fabrication Symposium, 79-87, 1998.

[5] Dalgarno, K. et al.: Proc. Solid Freeform Fabrication Symposium, 721-728, 1998.

[6] Chin, R. et al.: Proc. Solid Freeform Fabrication Symposium, 221-228, 1995.

[7] Klingbeil, N. et al.: Proc. Solid Freeform Fabrication Symposium, 125-132, 1997.

[8] Nickel, A. H., Barnett, D. M. and Prinz, F. B.: Thermal Stresses and Deposition Patterns in Layered Manufacturing. *Materials Science and Engineering*. Vol. 317, 2001.

this page intentionally blank

Thermal, Fluid, and Mass Transport Modeling of a Gas-Jet Reagent Delivery System for Laser Chemical Vapor Deposition (LCVD)

Chad Duty, Ryan Johnson, Daniel Jean, Scott Bondi, and W. Jack Lackey
Rapid Prototyping and Manufacturing Institute
Woodruff School of Mechanical Engineering
Georgia Institute of Technology
Atlanta, GA 30332

Abstract

A gas-jet reagent delivery system for laser chemical vapor deposition (LCVD) is modeled with respect to heat transfer, fluid flow, and mass transport. A commercial package was used to model the geometry and flow field surrounding an LCVD reaction zone. The deposition temperature was analyzed for various materials and flow conditions. The forced flow environment was compared against buoyancy-driven flow, which is more typical of a statically filled chamber. A finite difference code was also developed to analyze the effect of the gas-jet on the concentration gradients above the deposition zone.

Introduction

The current study involves the development of a thermal and fluid flow model of Georgia Tech's gas-jet LCVD system, which uses a localized gas-jet to deliver reagent gases directly to the deposition zone. This system is described in detail elsewhere.[1,2] No prior research, excluding our earlier efforts,[3] has analyzed the effect of an angled gas-jet on a laser heated, non-isothermal surface.

Successful operation of an LCVD system demands that the fundamentals of the process are well understood. Since CVD is a thermally activated process, the most important process variable is temperature. In a laser-heated process such as LCVD, the temperature field is restricted to a micron scale and can vary by several hundred degrees over the diameter of the laser spot. Deposition rates typically follow an Arrhenius relationship that is exponential with respect to temperature, so it is critical to understand these two-dimensional temperature variations.

The deposition rate for a given material can be limited by either the chemical kinetics of the reaction or by diffusion and mass transport of reagent gases to and away from the deposition zone. The gas-jet reagent supply for the LCVD system was designed to remove the latter constraint by directing a high velocity stream of reagent gases at the area heated by the laser beam. However, the need and impact of such a system has yet to be determined. Therefore, a two-dimensional concentration model was developed to estimate the effects of the gas-jet with respect to local concentration variations and reaction rates.

Background

Since temperature is such an important variable in LCVD, a number of analytical and numerical attempts have been made over the years to model the temperature variations within and around the laser heated zone.[4,5] The majority assumed a Gaussian distributed laser beam and emphasized conduction as the primary heat transfer mode. Conduction has been stressed because the temperature distribution is typically calculated for an infinite or semi-infinite flat substrate. In this case, the pathways available for conduction are relatively large compared to the surface area that is available to convection and radiation losses. When more complicated geometries were considered, such as during fiber growth,[6] conduction was restricted by the small fiber diameter and a larger surface area became available for convection and radiation losses.

A few thermal models have included the effect of forced flow convection on a laser heated substrate.[3] As early as 1977, Steen[7] developed a finite element model that included a non-reacting gas jet that was coaxial with the laser beam and normal to the substrate surface. He found that forced convection and radiation heat transfer losses were indeed significant for a temperature sensitive process. More recently, Lovell[8] mapped the local heat transfer coefficient on an isothermal substrate subjected to forced flow at various angles of impingement.

Some LCVD thermal models have been extended to include the mass transport of reagent gases and the prediction of deposition rates. Kinetic models for deposition near the substrate have been proposed by Han and Jensen[9] for copper deposition, and by Mazumder and Kar[4] for titanium and titanium nitride deposition. Zhang and Faghri[10] recently proposed a three-dimensional model of the SALD process that included heat transfer, mass transport, and the loss of reagents to the deposition reaction. However, no model has addressed the viscous flow contribution of an impinging gas-jet to the mass transport of reagent gases.

Model Development

Physical System Description

Georgia Tech's LCVD system is a dual chamber design that protects the high precision stage assembly in the lower chamber from the LCVD reactions in the upper chamber. A cross section of the upper chamber is shown in Figure 1. A Gaussian distributed CO_2 laser beam enters vertically through the top of the chamber and heats a 200 μm diameter zone on the circular graphite substrate. A resistive heating element inside a ceramic housing is located just below the substrate to provide global heating. Reagent gases are delivered locally through a high velocity gas jet that impinges the substrate at a 45° angle. Patterned deposits are created by rotating and translating the substrate via the stage assembly.

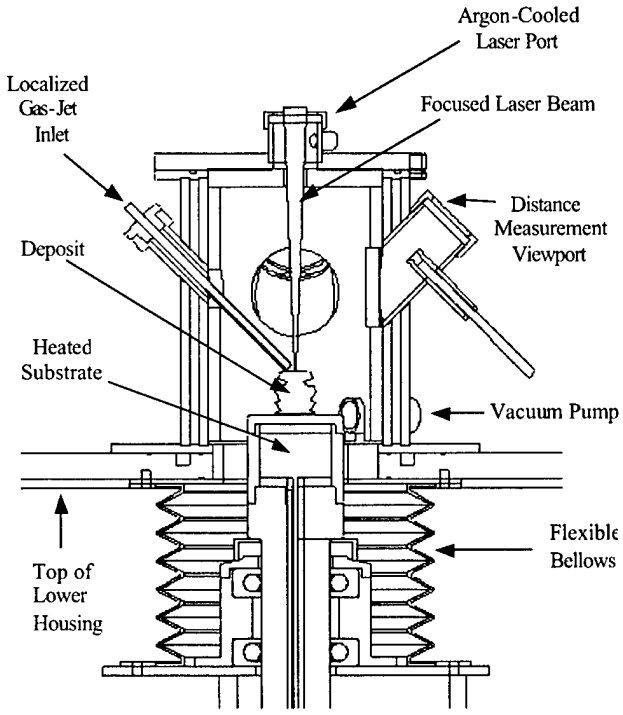


Figure 1. Cross Section of LCVD Chamber.

Thermal and Fluid Flow Models

Both two-dimensional and three-dimensional thermal and fluid flow models were developed using a commercial CFD package called FLUENT. The basic geometry and boundary conditions for each of the models are illustrated in Figures 2 and 3. For both cases, a user-defined function simulated laser heating as a Gaussian distributed energy source in the uppermost layer of elements of the substrate volume, according to Equation 1.

$$P(r) = \frac{2P_o(1-\rho)}{\pi r_o^2 t} e^{\frac{-2r^2}{r_o^2}} \qquad \textbf{(Eqn. 1)}$$

where P_o is the laser power, ρ is the substrate reflectivity, r_o is the nominal laser radius, t is the penetration depth, and r is the variable radius. For our setup, r_o was 100 μm, P_o varied up to 100 W, and t was typically < 5 μm.

The two dimensional model served as a platform for comparing the thermal behavior of various substrate materials when heated by a Gaussian laser beam. Figure 2 shows the basic system setup, in which the top of the graphite shaft serves as the initial substrate. For further comparisons, a given thickness of an alternate substrate material covers the top surface of the graphite substrate. The thermal and optical properties of the substrate materials were considered constant with respect to temperature, excluding thermal conductivity.

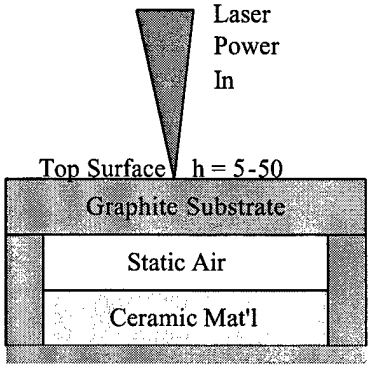


Figure 2. 2D Thermal / Fluid Model.

The two dimensional model was axisymmetric and did not account for fluid movement. Instead, the convection cooling effects associated with the gas jet were approximated by a constant heat transfer coefficient across the top surface of the substrate. The substrate was modeled as a circular piece of graphite with a diameter of 75 mm and a thickness of 6.4 mm. The side wall of the substrate holder was also composed of graphite and was 19 mm tall with a thickness of 6.4 mm. The third component of the substrate base was a ceramic heater material 13 mm thick. The bottom surface of the model was thermally insulated, while the side surfaces had a heat transfer coefficient of 5 W/m^2K. Radiation effects were included for each exterior surface, assuming a view factor of 1 to the chamber walls. Contact resistance was ignored.

The three-dimensional model was extended 25 mm above the graphite substrate to include the gas-jet inlet. The upper and outer boundaries of the gas volume were modeled as pressure outlets. The 1 mm diameter gas-jet was inclined at a 45° angle to the substrate with a standoff distance of 10 mm. The reagent flow was specified at the inlet as a normal velocity corresponding to mass flow rates of 0 to 5000 sccm. Since a 3D model focuses more on fluid interactions with the substrate surface, the geometry of the substrate holder was reduced to a solid graphite cylinder 25 mm thick and 75mm in diameter. This was shown to result in less than a 1% error in temperature predictions. Thermal boundary conditions matched the two dimensional case, excluding the constant heat transfer coefficient

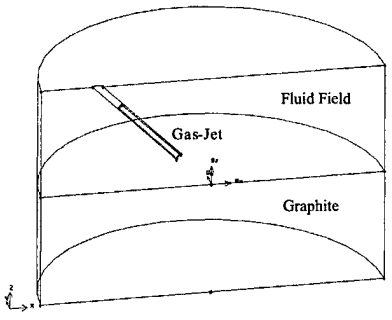


Figure 3. 3D Geometry

across the top surface of the substrate. A vertical plane of symmetry along the axis of the gas-jet was utilized, as demonstrated in Figure 3.

Transport and Concentration Gradient Model

A gas-jet delivery system is expected to aid mass transport of reagent gases to the deposition zone, thus increasing the deposition rate. In order to judge the effectiveness of such a system, a steady state, two-dimensional finite difference code has been developed. The governing equation for mass transport includes macroscopic fluid flow, diffusion, and a sink term that represents the consumption of reagents at the surface. The temperature and fluid velocity throughout the domain were accepted as input from the 3D thermal and fluid flow model previously described. The diffusion term was calculated at each node using the Chapman-Enskog method. At the surface, the sink term was nonzero and equal to kC^n, where k is the rate constant according to the Arrhenius equation, C is the local concentration, and n is the order of the reaction. After applying the boundary conditions in Figure 4, the governing equation was solved iteratively for the concentration throughout the domain. Although this model is simplistic in nature, it is a valuable qualitative tool for estimating the effects of the gas-jet on the deposition process.

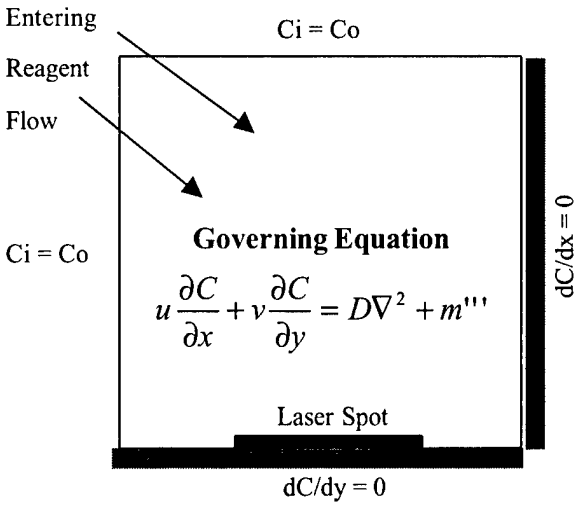


Figure 4. Concentration Model Conditions

Model Evaluation and Results

2D Thermal Model

The two-dimensional thermal model was evaluated for three different substrate materials: graphite, silicon, and tungsten. The model was empirically verified for the first two materials over a range of flow rates. Only a rough agreement was achieved at high flowrates due to exothermic reactions or poor alignment of the gas-jet. Figure 5 shows the peak temperature on each substrate as a function of laser power. Note that peak temperature increases as thermal conductivity decreases, from 108 W/mK for tungsten to 23 W/mK for silicon at 1400 K.

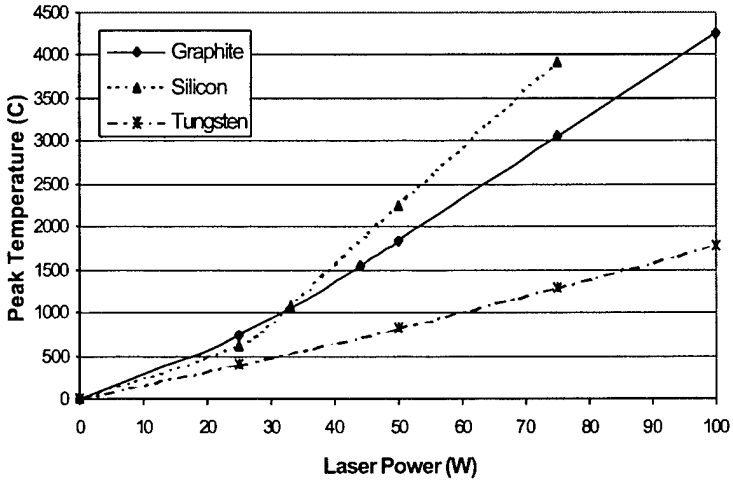


Figure 5. Substrate Peak Temperature vs. Laser Power

Not only does the peak temperature change due to the material properties, but the shape of the temperature distribution changes as well. Note in Figure 6 how the temperature profile for silicon is much more narrow than that of tungsten. For LCVD, this means that it is more difficult to achieve high resolution deposits on highly conductive substrates such as tungsten. The cooling effect of the gas-jet is approximated in Figure 7 by changes in the heat transfer coefficient. A drop of 150° C from h = 5 to 50 W/m^{2}K is roughly equivalent to increasing the flow rate from 100 to 1500 sccm.

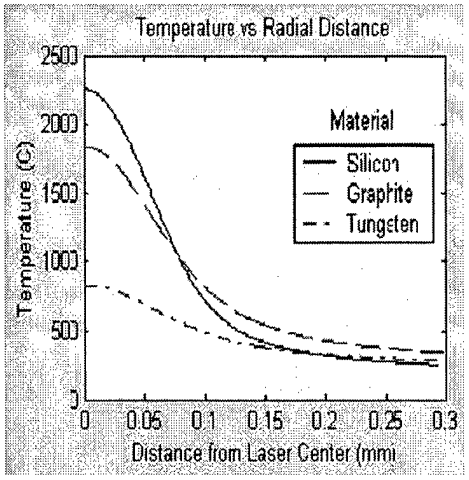


Figure 6. Temperature Distribution (50W)

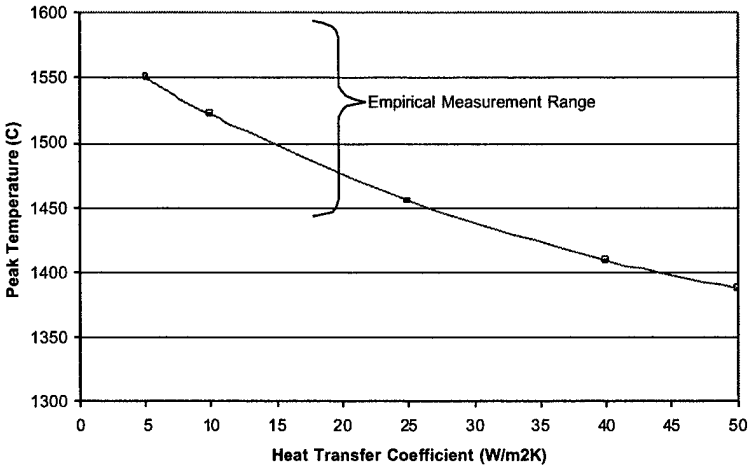


Figure 7. Graphite Temperature vs. Heat Transfer Coefficient

3D Thermal and Fluid Flow Model

The three-dimensional case models the fluid flow in the volume above the deposition zone. Substrate temperature profiles and peak temperatures correlated well with the two-dimensional models. Once again, verification experiments provided a rough guideline for peak temperatures and cooling trends. Figure 8 demonstrates a typical velocity magnitude profile for the gas-jet along the vertical symmetry plane of the model. The effects of flow rate on the temperature profiles for a graphite substrate are shown in Figure 9. The flow was composed of 80% methane and 20% hydrogen.

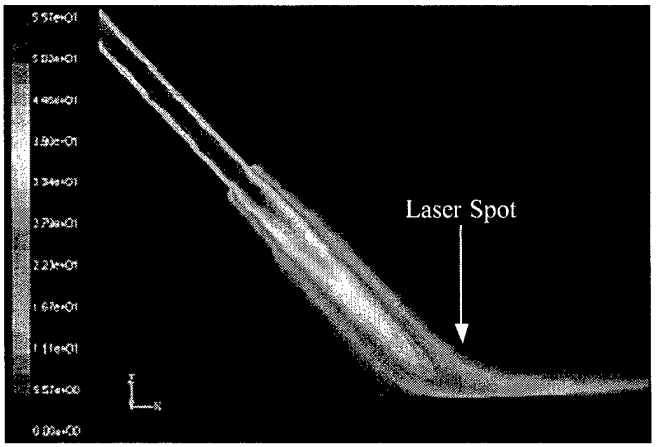


Figure 8. Velocity Magnitude (m/s) Above Substrate.

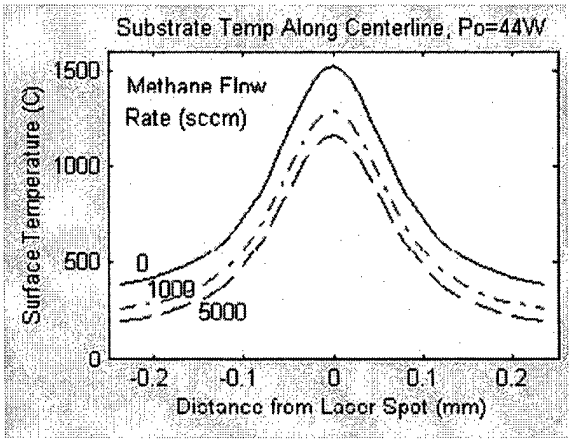


Figure 9. Temperature Profile vs Methane Flow.

Figure 10 quantitatively illustrates the velocity profiles at the center of the laser spot as a function of the vertical distance from the substrate. The height from the substrate is measured directly above the center of the laser spot in each case. Figure 10a shows that the maximum horizontal velocity imparted by the gas-jet occurs less than 400 μm from the surface. The maximum for the vertical component of flow, directed down ward onto the substrate surface, occurs at roughly twice this distance.

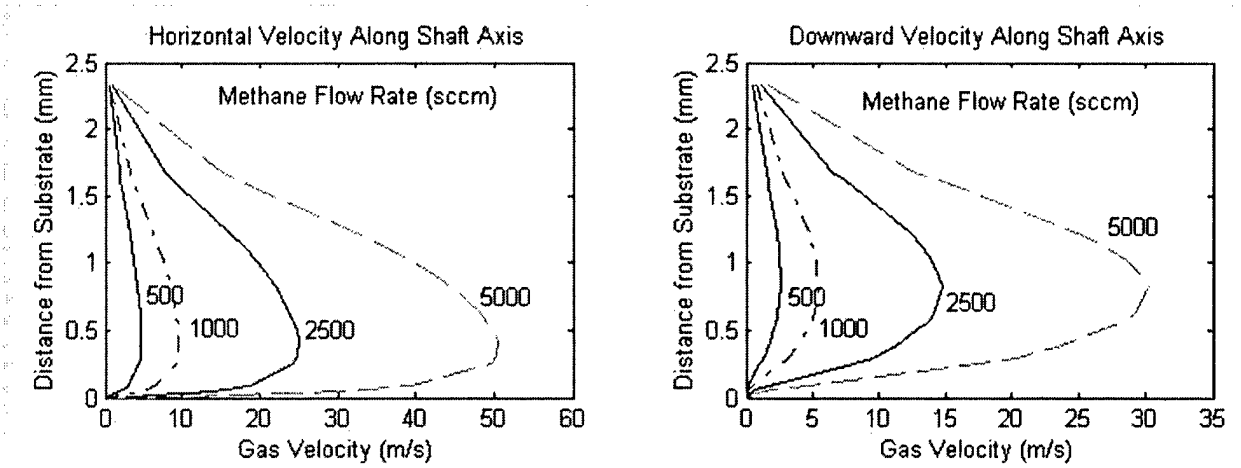


Figure 10. (a) Horizontal and (b) Vertical Velocity vs. Distance Away From Substrate Surface.

Natural Convection

A separate model was developed to investigate the effect of buoyancy-driven upward gas velocity due to density gradients induced by laser heating of the substrate surface. The surface temperature profile for the case of zero flow was applied to the base of an axisymmetric two-dimensional model. The fluid consisted of a methane / hydrogen mixture modeled as an ideal gas. Pressure outlet boundary conditions were applied at the top and side surfaces. Figure 11 shows the axial velocity resulting from buoyancy-driven flow. Notice that the maximum upward velocity also occurs around 400 μm, but is on the order of 1 mm/s -- three orders of magnitude below velocities created by the gas-jet! Although natural convection may be a concern during deposition in an otherwise static atmosphere, the buoyancy effects on the gas-jet LCVD process can be safely ignored when modeling forced flow.

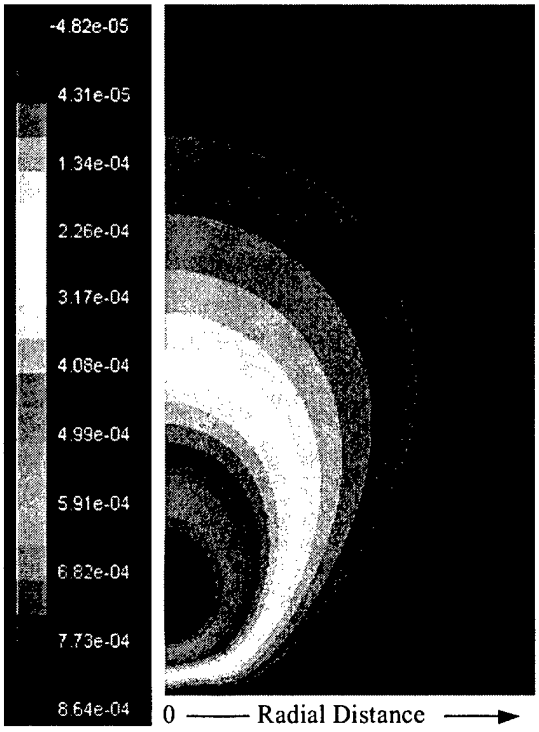


Figure 11. Natural Convection Velocity Above Substrate

Mass Transport Model

At the time of publication, the mass transport model was in the early stages of empirical verification. Preliminary results were in agreement with recent experiments involving the deposition of carbon fibers from a mixture of 80% methane and 20% hydrogen at 1 atmosphere.[11] Both the experimental data and the mass transport model indicated that fiber growth was kinetically limited at peak temperatures around 1500°C. Therefore, the model predicted minimal concentration gradients during steady state growth.

To this point, the transport model results have been very sensitive to the kinetic constants that specify the rate of consumption of reagent gases. For the results just described, the following values were used: activation energy (Q = 176 kJ/mol), pre-exponential constant (k_o = 2.6 x 10^{13} m/s), and reaction order (n = 3.47). Alternate values for these constants, especially the reaction order, lead to significant changes in the concentration gradients predicted by the mass transport model. The binary diffusion coefficient also impacts the model substantially. Therefore, this model may be very useful in future experiments involving the deposition of other materials or of carbon from different reagent sources.

Conclusions

An angled gas-jet has been shown to have a significant impact on both the peak temperature and temperature profile of a laser-heated substrate. The effect of natural convection on fluid flow was shown to be insignificant when modeling forced flow from a gas-jet. The maximum velocity imposed by the gas-jet occurs just 400 μm above the surface and varies proportionally to flow rate. It can be assumed that the fluid in this high velocity zone is composed of fresh reagent gases, supporting the concept that a gas-jet could aid in mass transport and diffusion. Although the effect of the gas-jet on a diffusion-limited deposition process has yet to be determined, the mass transport model has been empirically verified for a kinetic limited process and will serve as a valuable tool in future work.

Acknowledgements

This work was supported by the National Science Foundation, the Engineering Research Program of the Office of Basic Energy Sciences at the U. S. Department of Energy and the Georgia Institute of Technology with significant input from Dr. Andrei Fedorov.

References

1. C. Duty, D. Jean, and W. J. Lackey. "Design of a Laser CVD Rapid Prototyping System." *Ceramic Engineering and Science Proceedings,* **20** (4), 347-354, 1999.
2. D. Jean, C. Duty, B. Fuhrman, and W. J. Lackey. "Precision LCVD System Design with Real Time Process Control." *Proceedings of the Solid Freeform Fabrication Symposium,* 59-65, 1999.
3. C. Duty, B. Fuhrman, D. Jean, and W. J. Lackey. "Heat Transfer Analysis of a Gas-Jet Laser Chemical Vapor Deposition Process." *Proceedings of the Solid Freeform Fabrication Symposium,* 461-468, 2000.
4. J. Mazumder and A. Kar. *Theory and Application of Laser Chemical Vapor Deposition*, New York, Plenum Press, 1995.
5. C. Duty, D. Jean, and W. J. Lackey. "Laser Chemical Vapor Deposition: Materials, Modeling, and Process Control." Accepted to *International Materials Reviews,* January 2001.
6. D. Yu and A. Duncan. "Investigation of Induced Thermal and Fluid Transport Phenomena in Laser Assisted Chemical Vapor Deposition." *Proceedings of the ASME Heat Transfer Division*, **361** (4), 183-191, 1998.
7. W. Steen. "Surface Coating Using a Laser." *Lett Heat Mass Trans*, **4**, 167-178, 1977.
8. B. Lovell. "Local Transfer Coefficients for Impingement of an Axisymmetric Jet on an Inclined Flat Plate." *Master's Thesis*. University of Minnesota. December 1978.
9. J. Han and K. Jensen. "Combined Experimental and Modeling Studies of Laser-assisted CVD of Cu from copper(l)-hexafluoroacetylacetonate trimethylvinylsilane." *J Appl Phys*, **75** (4), 2240-2250, 1994.
10. Y. Zhang and A. Faghri. "Thermal Modeling of Selective Area Laser Deposition of Titanium Nitride on a Finite Slab with Stationary and Moving Laser Beams." *Int J Heat Mass Tran*, **43**, 3835-3846, 2000.
11. D. Jean. "Design and Operation of an Advanced Laser Chemical Vapor Deposition System with On-Line Control." *Ph.D. Dissertation*. Georgia Tech. June 2001.

FINITE ELEMENT STRUCTURAL ANALYSIS OF PROSTHESIS SOCKETS FOR BELOW-THE-KNEE AMPUTEES MANUFACTURED USING SLS

Mario Faustini*‡, Mahendra Lokhande*, Richard Crawford*, William Rogers†, Andrew Gitter† and Gordon Bosker†

*The University of Texas at Austin
†The University of Texas Health Science Center in San Antonio
‡Supported by the National Council of Scientific and Technological Development (CNPq-Brazil)

Abstract

A very attractive application of Solid Freeform Fabrication is manufacture of prosthesis sockets for below-the-knee amputees. The custom geometric design required is very compatible with SFF techniques. The present work focuses on finite element analysis of sockets manufactured by Selective Laser Sintering using Duraform as the material. The objective is to ensure reliability of the sockets for their use by patients. This paper describes the finite element models developed for the sockets, as well as the derivation of realistic boundary conditions that may allow a simulation of the structure under regular workloads.

1) Introduction

The use of Selective Laser Sintering (SLS) in the manufacture of prosthesis sockets for below-the-knee amputees has been recognized as an appropriate potential application of Solid Freeform Fabrication [Rogers et al., 1991]. However, to ensure the reliability of these sockets and their safety for users requires a complete structural analysis of their mechanical behavior during operation. The focus of the current work is a finite element (FE) evaluation of the performance under standard conditions of one sort of socket, the single-wall socket.

This paper is structured as follows: first, the single wall socket design is presented, followed by the development and validation of its FE model. Next, the standard workloads during gait are defined as boundary conditions for the FE analysis. Finally, the results of the simulations of two sockets that were actually manufactured are exhibited.

2) The single wall socket

The single wall socket, as seen in Figure 1, consists of an upper part, where the residual limb fits, and a lower region, which is a hollow cylinder where a pylon is attached with a prosthetic foot at its other end. The first step in the design and manufacture of the socket is fabrication of a mold from the patient's residual limb, from which a copy of the limb is obtained. This copy is digitized with a laser scanning system. From this data, a perfectly fitting model of the socket is designed using computer-aided geometric operations on the data mesh. The thickness of the socket wall is decreased around specific points to provide compliance in those areas. The compliant regions relieve pressure on sensitive spots of the patient's limb, such as the fibular head and distal tibia regions, thereby increasing comfort. Thus, tessellated data file (STL) is generated from this model and transmitted to a Selective Laser Sintering workstation for

fabrication. The material used is Duraform, the physical properties of which are given in Table 1.

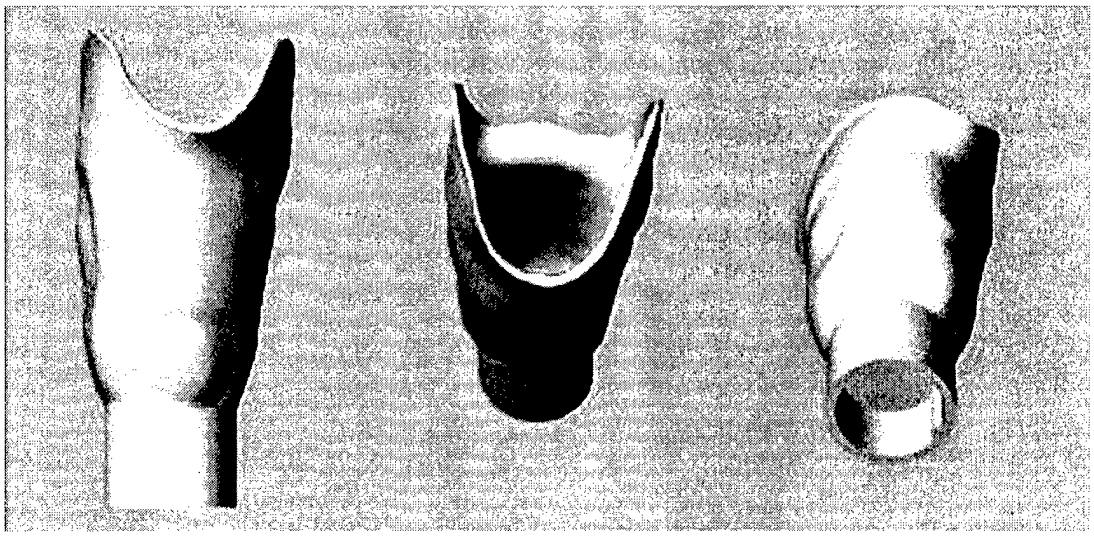


Figure 1. The single wall socket

Table 1. Duraform properties provided by Product Innovation & Development Centre, Liverpool, UK.

	SI units	DuraForm PA
[redacted]		
Specific Density 20°	g/cm_	0.97
Water Absorption	%	0.41
Density	g/cm_	0.59
Average Particle Size	µm	58
Particle Size Range 90%	µm	25 92
[redacted]		
Tensile Strength Break	MPa	44
Tensile Strength Yield	MPa	37
Tensile Modulus	MPa	1600
Tensile Elongation at break	%	9
Flexural Modulus	MPa	1285
Impact Strength		
Notched Izod	J/m	216
Unnotched Izod	J/m	432
[redacted]		
As SLS processed, Ra	µm	8.5
After polishing, Ra	µm	0.13

3) The Finite Element Model

The STL data file of a socket consists of a collection of 48,000 triangular faces that define the socket surface in space. This level of detail would potentially result in unnecessary and time-consuming data preparation and analysis. Thus, the first step to generate the FE model is to apply a reliable mesh decimation algorithm to the STL file. We use Amira[1] to perform the decimation operation. As seen in Figure 2, the decimated version has 2000 faces, but the overall geometric details and features are well preserved (especially the thicknesses of the wall, which is fundamental for the structural analysis).

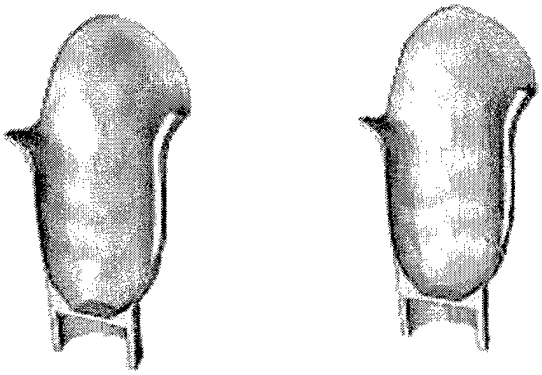


Figure 2. A section of the original STL model (48000+ faces) and the decimated version (2000 faces).

Once decimated, the STL file is loaded into Rhinoceros[2], where the triangular faces of the model are converted to parametric surfaces (NURBS) and exported as an IGES file. The IGES format is readable by SDRC I-DEAS[3] for FE analysis. In I-DEAS, the volume is meshed with solid elements (parabolic tetrahedra), assigned material properties and appropriate boundary conditions, and analyzed.

4) FE Model Validation

In order to validate the results of the FE structural analysis, an actual socket was tested to determine the vertical load that causes mechanical failure. The test is illustrated schematically in Figure 3.

[1] Amira is 3D Visualization package developed by Indeed-Visual Concepts GmbH, Berlin, Germany.
[2] Rhinoceros is a 3D modeling package offered by McNeel & Associates, Seattle, WA.
[3] I-DEAS is a CAD/CAE/CAM package provided by SDRC, Milford, OH.

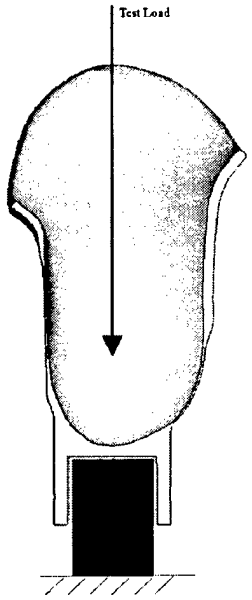


Figure 3. Experimental loading test to determine the maximum vertical load a socket supports.

The results were computed, as the load was gradually increased, in a force–strain graphic, shown in Figure 4. The figure indicates that the socket fails at a test load of 10 kN.

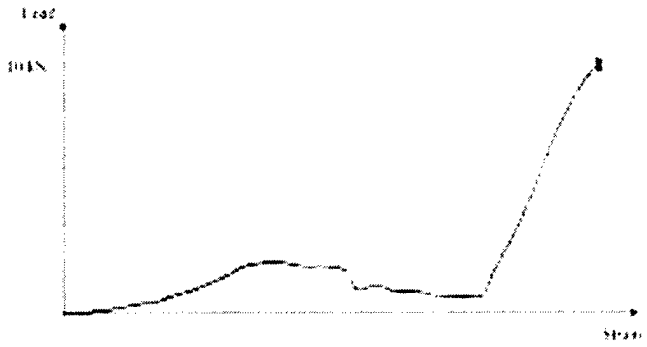


Figure 4. Results of the experimental loading test.

Similarly, a FE model equivalent to the physical model in Figure 3 was analyzed. Using the properties shown in Table 1, it was determined through repeated simulations that the socket reaches the ultimate tensile strength for Duraform (44 MPa) under a load of 6 kN. The simulation results for a 6 kN vertical load are shown in Figure 5.

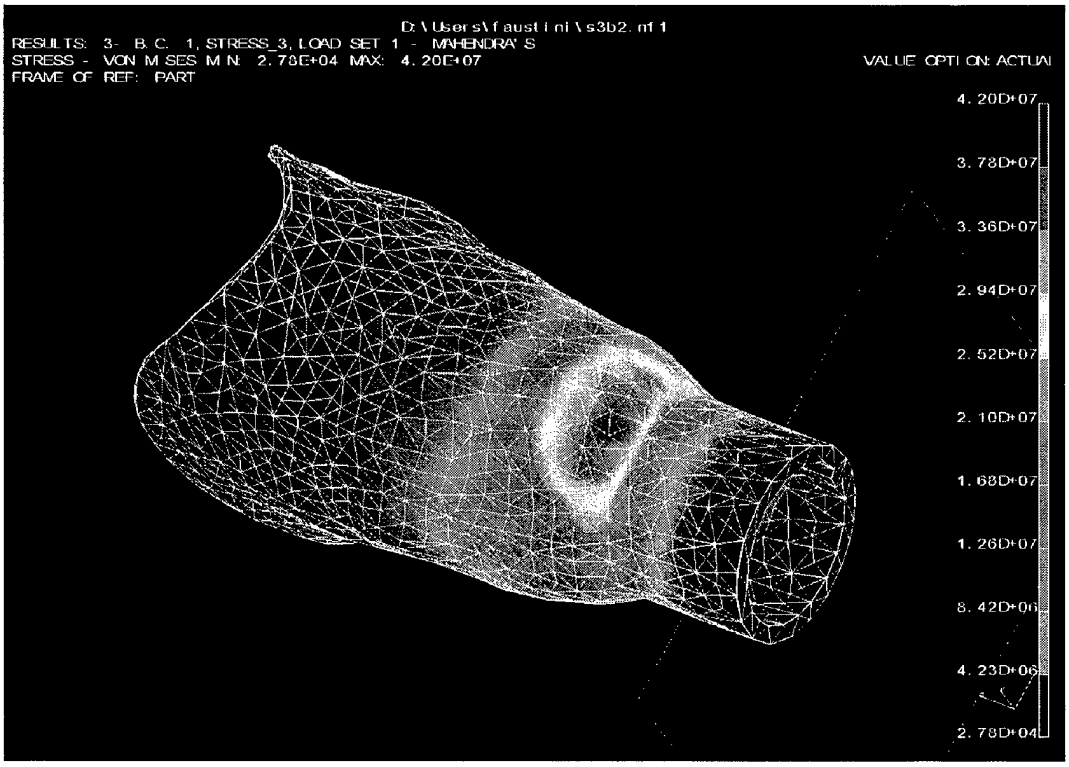


Figure 5. Results for the simulation of the loading test using FE analysis.

The difference between the ultimate load for the empirical test and the FE analysis may be explained by the fact that the socket used on the first one was infiltrated with cyanoacrylate, which increases the tensile strength of the part. Qualitatively, however, the location where the actual socket cracked matched exactly the region of largest stress predicted by the FE analysis.

5) Finite Element Analysis of Gait

In order to simulate the structural behavior of the FE model of the socket during gait, it is necessary to evaluate the loads applied by the residual limb. Figure 6, from Noguchi et al. [2000], shows the components of the ground reaction force of the foot in one stride (with z being the direction of the weight and x the direction of progress) in terms of percentage of body weight. Note that during the double supporting period (between heel contact of one foot and toe contact of the other — when both feet are in contact with the ground), the forces have their greatest values, especially in positions A and B. Therefore, those two positions were analyzed in a worst case scenario, with all forces applied exclusively to the prosthetic foot.

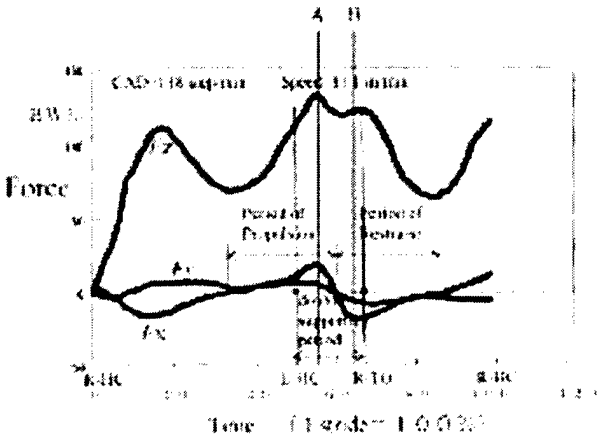


Figure 6. Components of ground reaction force of feet during gait [Noguchi et al., 2000].

The boundary conditions for the FE model were calculated using the values for the forces in both positions A and B, as shown in Figure 7. In the figure, *Fr* is the horizontal resultant force due to F_x and F_y and M_r is the moment needed to balance the forces transferred from the ground to the middle of the socket.

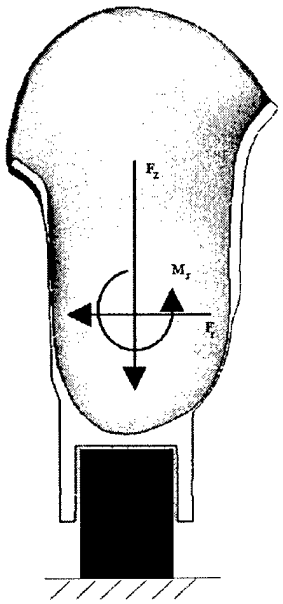


Figure 7. Boundary conditions used in the gait FE simulations.

6) Simulations

Two sockets were simulated for both positions A and B (Figure 6) using the FE analysis procedure described in Section 3. The patient was assumed to have a body mass of 75 kg.

The first socket analyzed had a notch in the junction between the base cylinder and the lower thinner part in the front of the socket, as seen in Figure 8. This socket was actually fabricated and broke while the patient was wearing it. The simulation results for this socket in position A are presented in Figure 9 (stresses are given in Pa). The simulation results for the same socket in position B are presented in Figures 10 (stresses in Pa) and 11 (displacement in meters).

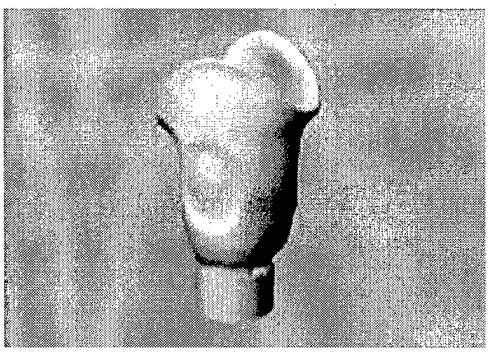


Figure 8. First socket simulated.

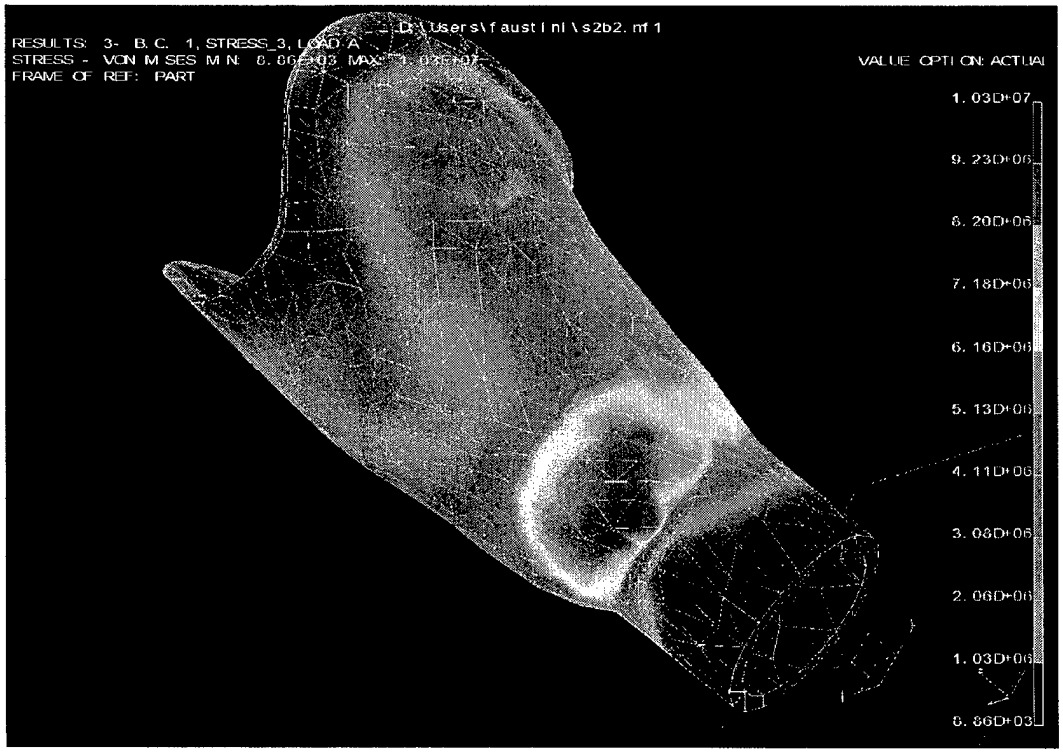


Figure 9. Predicted stresses for first socket in position A.

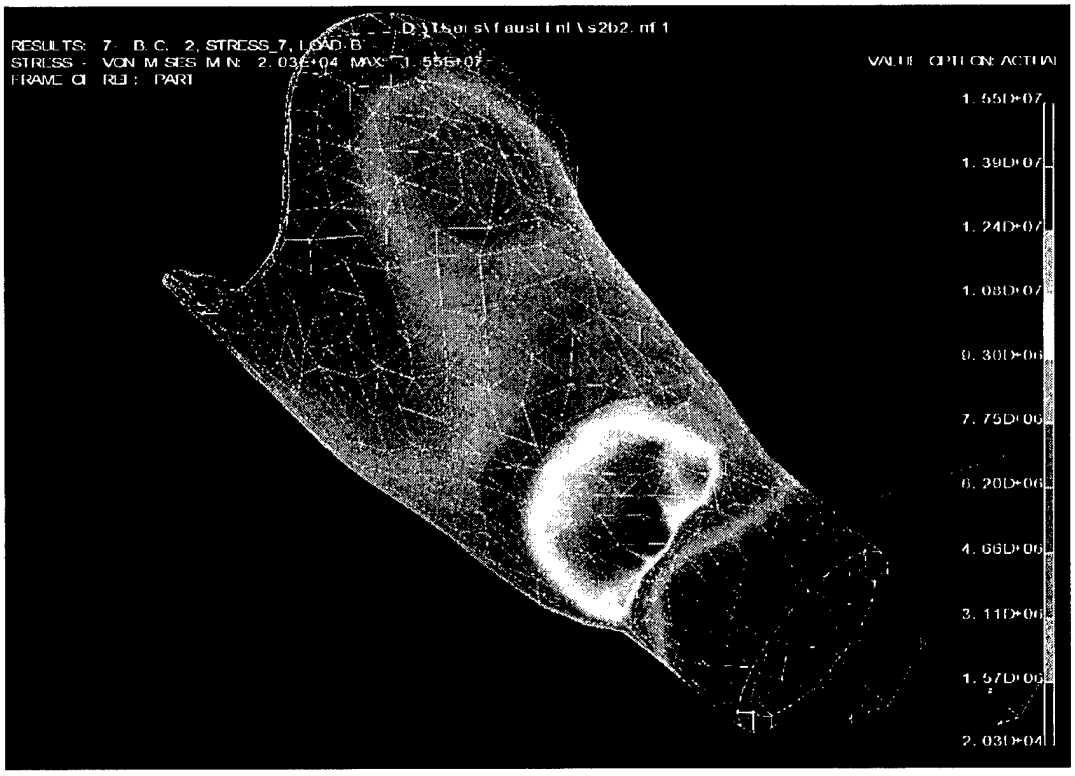


Figure 10. Predicted stresses for first socket in position A.

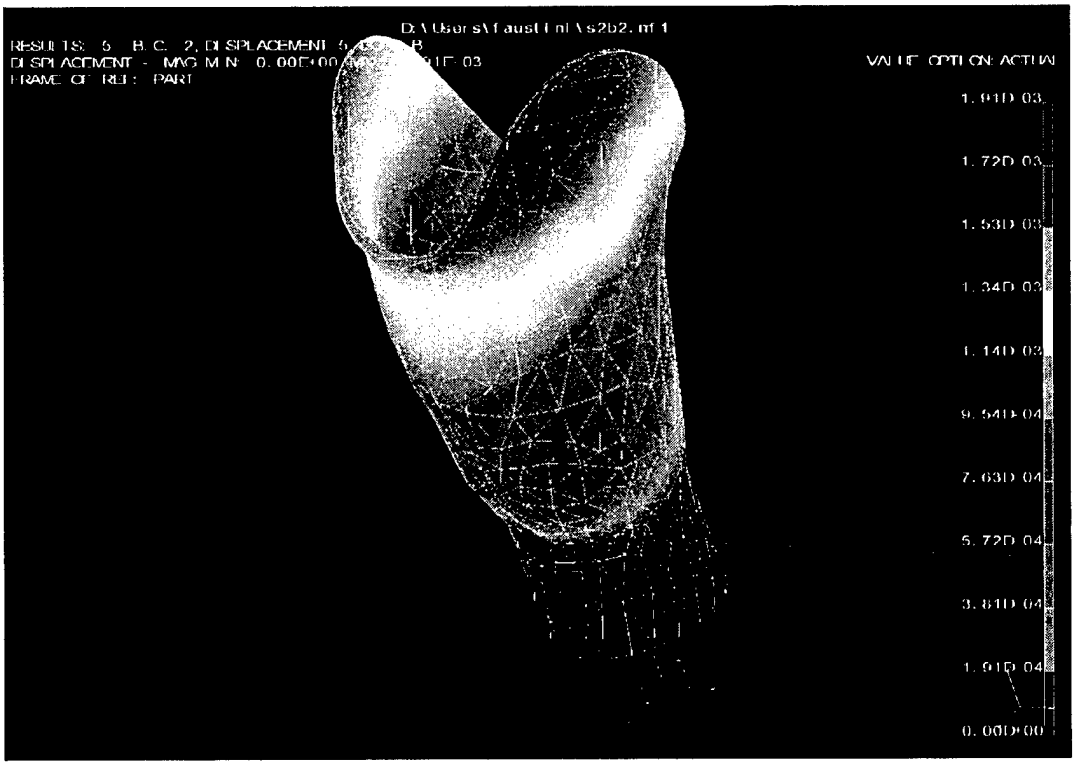


Figure 11. Predicted displacements for first socket in position B.

The second socket analyzed was designed with software with improved smoothing features, and is shown in Figure 12. This socket was also fabricated and has been used by the patient without failure. The simulation results for this second socket in position A are shown in Figure 13 (stresses in Pa). The simulation results for the same socket in position B are presented in Figures 14 (stresses in Pa) and 15 (displacement in meters).

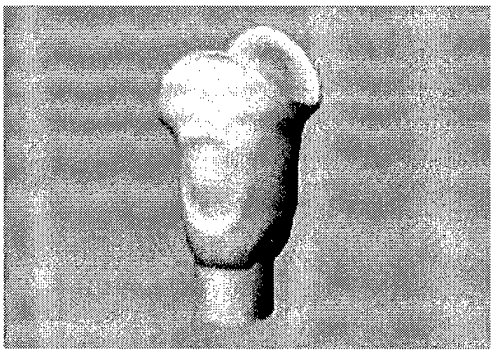


Figure 12. Second socket simulated.

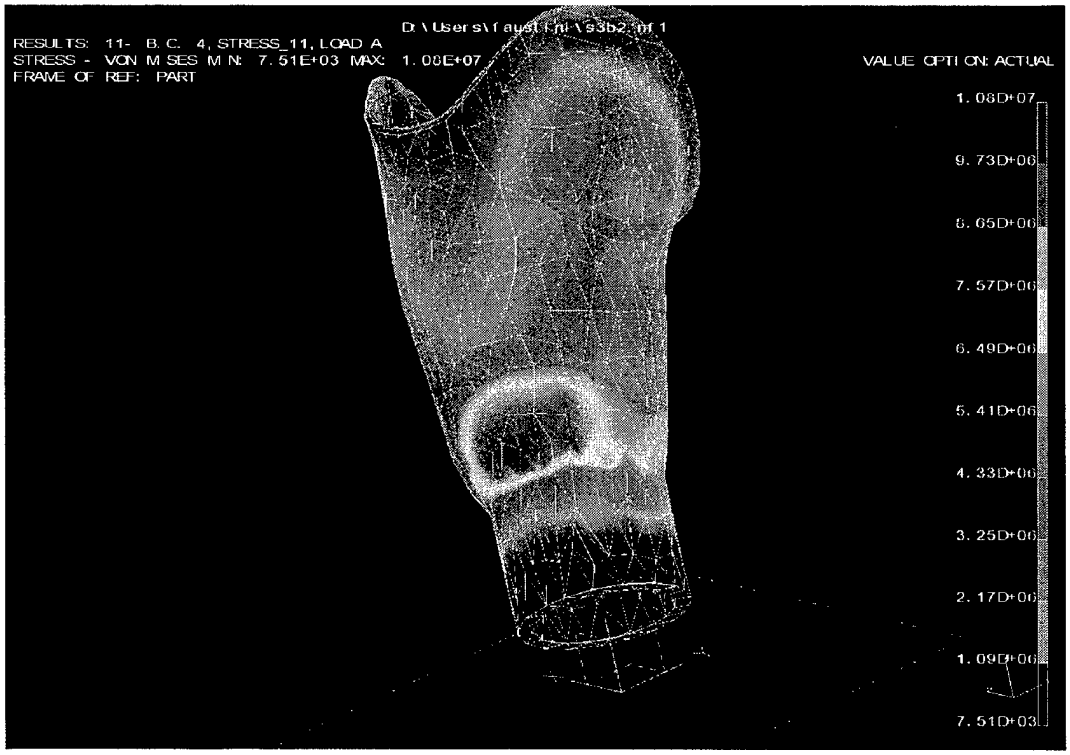


Figure 13. Predicted stresses for second socket in position A.

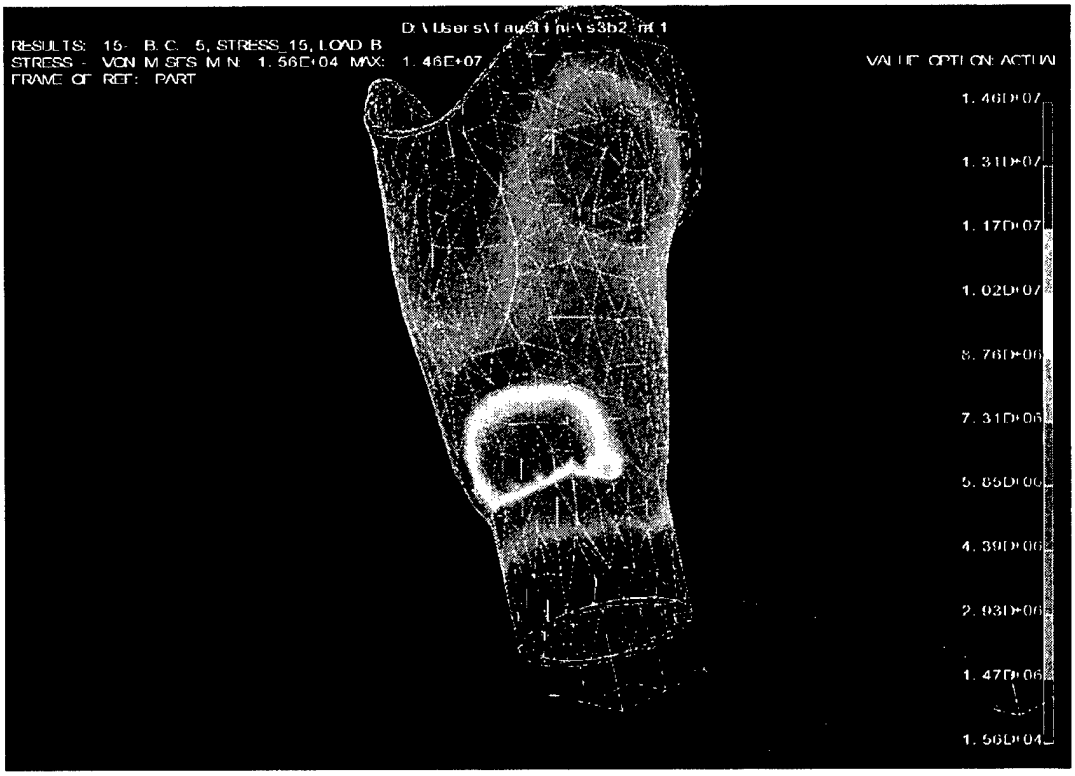


Figure 14. Predicted stresses for second socket in position B – bottom-left-front view.

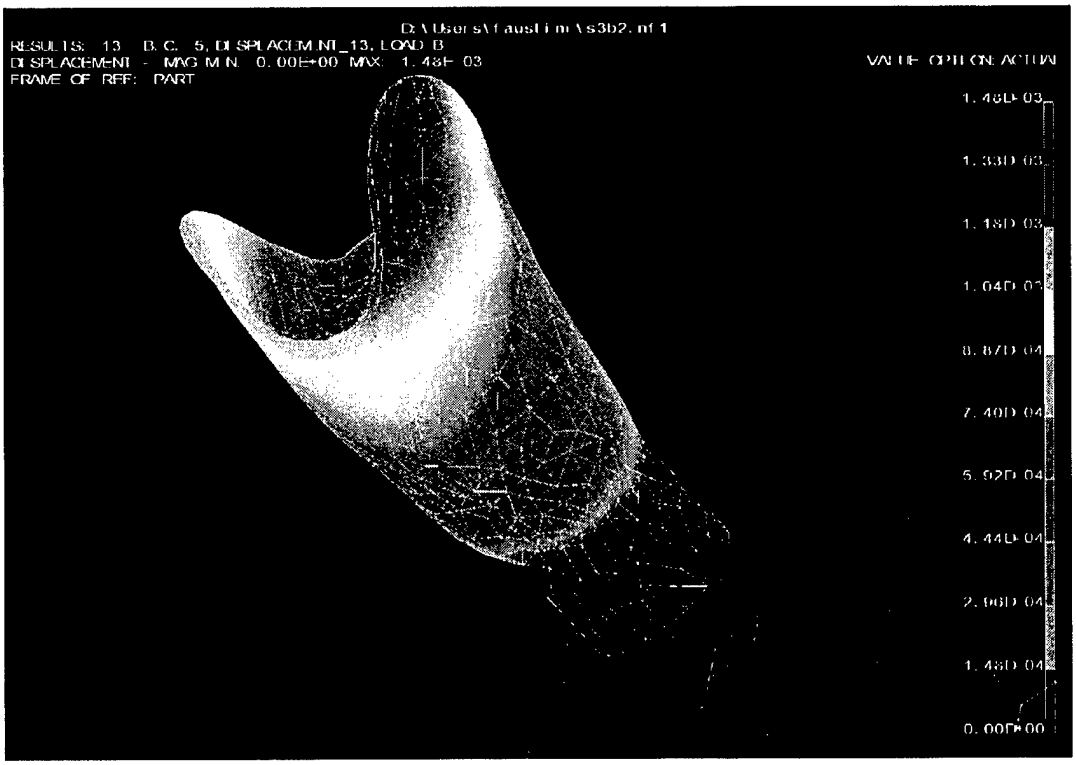


Figure 15. Predicted displacements for second socket in position B.

It should be pointed out that for both sockets the greatest stresses were computed for position B, even though the load values for position A were slightly larger (see Figure 6). Also, the analysis predicted, for position B, greater maximum stress for the first socket (15.5 MPa) than the second socket (14.6 MPa). However, this still does not explain the failure, since this maximum stress is considerably less than the yield strength for Duraform (37 MPa – Table 1). Additionally, the maximum displacement for each socket was less than 2 mm, which preserves the biomechanics of the gait [Stephens, 1999].

7) Conclusion

This paper presents a procedure for finite element based structural analysis for a below-the-knee prosthetic socket. Verification of the FE model and the simulation of two actual sockets are discussed. While the results agree qualitatively, the actual numerical results differ significantly. To address this disagreement, a more precise FE simulation algorithm will be tested (p-adaptive method). Also, more precise material properties for Duraform must be obtained. Both Thompson [1995, 1997] and Watson [1999] illustrated the orthotropic behavior of Duraform, which depends highly on the direction of the parallel layers of the material in the structure (defined during manufacture) with respect to the direction of the stresses applied. Finally, both impact and fatigue studies should be addressed in order to provide a more accurate structural analysis of the socket, as these modes of failure are likely to occur in real sockets.

8) References

1. Rogers, W. E., Crawford, R. H., Beaman, J. J., and Walsh, N. E., 1991, "Fabrication of Prosthetic Sockets by Selective Laser Sintering," *1991 Solid Freeform Fabrication Symposium Proceedings*, Marcus, H. L., Beaman, J. J., Barlow, J. W., Bourell, D. L., and Crawford, R. H., eds., Austin, TX, August 12-14, 1991, pp. 158-163.
2. Noguchi, T., Ochiai, H., Ukai, T., 2000, "Falls from slips in double supporting period gait," Proceedings, *12th Conference of the European Society of Biomechanics*, Dublin, pp. 427.
3. Stephens, S. D., 1999, *Design of a Compliant Socket Fabricated Using Selective Laser Sintering*, Master's thesis, The University of Texas at Austin.
4. Thompson, D. C., 1995, "The Optimization of Part Orientation for Solid Freeform Manufacture," Master's thesis, The University of Texas at Austin.
5. Thompson, D. C., and Crawford, R. H., 1997, "Computational Quality Measures for Evaluation of Part Orientation in Freeform Fabrication," *Journal of Manufacturing Systems*, vol. 16, no. 4, pp. 273-289.
6. Watson, D., 1999, "Process Optimization for Selective Laser Sintering Through the Use of Design Rules and Constraints," Master's thesis, The University of Texas at Austin.

this page intentionally blank

Modeling of Selective Area Laser Deposition Vapor Infiltration (SALDVI) of Silicon Carbide

K. Dai, J. Crocker, L. Shaw and H. Marcus

Department of Metallurgy and Materials Engineering
Institute of Materials Science
University of Connecticut, Storrs, CT 06269

ABSTRACT

Selective Area Laser Deposition Vapor Infiltration (SALDVI) is a developing solid freeform fabrication (SFF) technique in which porous layers of powder are densified by infiltrating the pore spaces with solid material deposited from a gas precursor during laser heating. A 3D finite element model was developed that simulates SALDVI of silicon carbide. The model predicts the laser input power and the distribution of vapor deposited SiC within the powder bed as well as on the surface of the powder bed (SALD). The model considers a moving Gaussian distribution laser beam, temperature- and porous-dependent thermal conductivity, specific heat and temperature-dependent deposition rate. Furthermore, the model also includes closed-loop control of the laser power to achieve a desired target processing temperature on the top surface of the power bed. The simulation results agree fairly well with experimental data for simple geometries and offer guidelines for further experimental studies of the SALDVI process.

Keywords: Finite element modeling, Silicon carbide, Solid freeform fabrication, Selective Area Laser Deposition Vapor Infiltration.

INTRODUCTION

Chemical vapor infiltration (CVI) is a promising process where a vapor-phase precursor is transported into the porous preform, and a combination of gas and surface reactions leads to the deposition of the solid matrix phase and densifies the part. Selective Area Laser Deposition Vapor Infiltration (SALDVI) process which combines the Selective Area Laser Deposition (SALD) process and the CVI process is a developing solid freeform fabrication (SFF) technique aimed at the direct fabrication of ceramic and ceramic/metal structures and composites. SALDVI experiments have shown that the size and geometry of the densified part depend in large part on the temperature distribution in the SALDVI workpiece among other parameters [1]. The understanding of the temperature distribution in the SALDVI process is very important to achieve the insight into the effect of various process parameters on the shape of the SALDVI workpiece. During the SALDVI process the relative density of the workpiece continuously changes with processing time until it reaches near full density. Because of such continuous changes in the relative density and thus the continuous change in thermal conductivity of

the SALDVI workpiece, the transient temperature field of the SALDVI workpiece is too complex to calculate by analytical methods. The development of finite element modeling (FEM) has offered opportunities to solve it. Many efforts of numerical modeling have been carried out to investigate the effect of various processing parameters on the SALD process. However, the SALDVI process has its specific features compared with the general SALD process. The present study provides 3-dimensional thermal analyses of the SALDVI process. It will provide guidance for intelligent selection of various parameters and help to understand other SFF processes involving powder-to-dense-body transition such as selective laser sintering (SLS).

MODEL DESCRIPTION

The goal of this modeling effort is to simulate the SALDVI process in which a porous powder bed is locally densified by laser chemical vapor infiltration. The effect of the laser processing conditions on the size, geometry, and densification history of the workpiece during processing is evaluated. The finite element model used for this purpose is shown in Figure 1 and calculated using the ANSYS 3-dimensional thermal conductive element (Solid70). This model is used to calculate the temperature distribution in the powder bed due to laser heating. The local Chemical Vapor Deposition (CVD) growth rate in the powder bed is calculated from the local temperature and the resulting change in powder bed density is determined. The density-dependent physical properties of the workpiece are updated and are used to calculate the new temperature distribution. In this step-wise manner, the evolution of densification by the Laser Chemical Vapor Infiltration (LCVI) is modeled. The powder bed before densification is assumed to have a dimension of 14-mm length (L=14mm), 4-mm width (W=4mm) and 1.2-mm height (H=1.2mm). Thus, the powder bed in this study is very thick in comparison with the layer-by-layer fabrication technique, which typically has a powder layer thickness less than 0.5 mm. However, the present simulation allows for assessment of building the first solid layer from a thick powder bed rather than from a thin powder layer on the top of a solid substrate or a previously densified layer. Densification of thin powder layer will be modeled in the future effort.

As shown in Figure 1, the SALDVI process is modeled by scanning a laser beam along the surface of a powder bed at a uniform velocity and calculating the resulting temperature distribution. In this model the laser beam is modeled as a heat flux with a Gaussian power distribution as an incoming heat source.

In SALDVI experiments, an optical pyrometer is used to continually monitor the temperature distribution at the surface of the powder bed during laser heating. This pyrometer temperature is used as the feedback parameter in a closed-loop control program that adjusts the incident laser power as needed to achieve a desired constant pyrometer temperature. In the simulation, in order to simulate the closed loop control program used in the experiments, the laser power is modified from one time step to the next if the pyrometer simulation temperature differs from the desired target temperature. This step can make the temperature read by pyrometer approach the desired target surface temperature in the simulation.

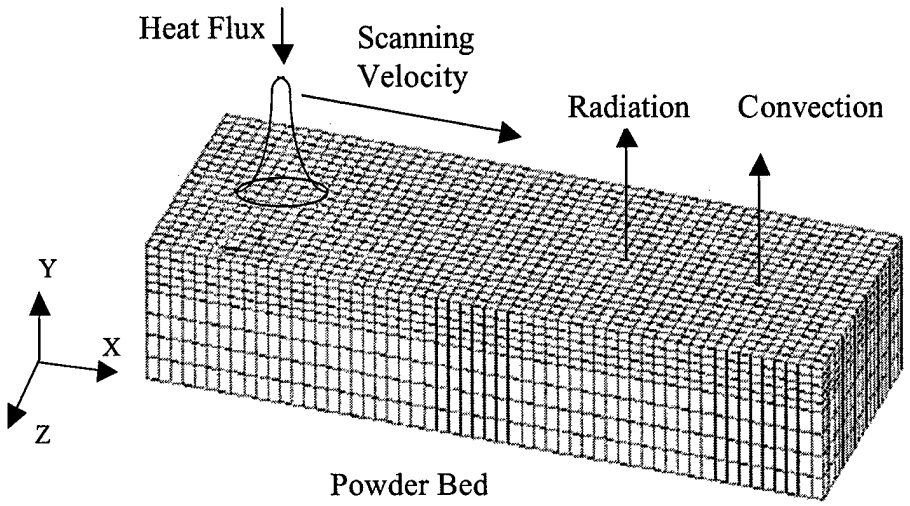


Figure 1. Finite element model of the SALDVI process.

The thermal conductivity, K_T[W/MM-K], is a thermal and solid fraction dependent parameter that is given by equations (1) and (2)

For 42 % dense 15 μm diameter SiC powder [2]:

$$K_T = 3.127 * 10^{-5} T^{0.34196}(1 - P_n)/0.42 \quad \text{when } 1 - P_n \le 0.42 \tag{1}$$

and when sufficient CVI has occurred forming a continuous solid network, there are a upper bound K_{TH} and a lower bound K_{TL} [2-3]

$$K_{TH} = 12.709 T^{-0.89464}(1 - P_n)^{1.5} \tag{2a}$$

$$K_{TL} = 24.7 T^{-1.1896}(1 - P_n)^{1.5} \tag{2b}$$

In this model, the effective thermal conductivity K_T is taken between the upper bound and the lower bound.

$$K_T = 0.2 K_{TH} + 0.8 K_{TL} \quad \text{when } 1 - P_n > 0.42 \tag{2c}$$

where P_n is the porous fraction at step n, and T is the temperature at step n.

The specific heat is given by [4]

$$C_p = (1 - P_n) 90.14428 T^{0.37511} \text{ [J/Kg.K]} \tag{3}$$

SIMULATION RESULTS AND THE COMPARISON WITH EXPERIMENTS

In experiments, a porous SiC powder bed with an initial solid fraction of 0.42 and 15 μm average particle diameter is locally densified by laser chemical vapor infiltration

with 10 Torr $Si(CH_3)_4$ gas at three different laser scanning speeds. The CO_2 laser beam is focused to a diameter of 1 mm and the laser power is continuously adjusted to obtain a surface temperature of 1000°C measured by the pyrometer. The experimental conditions of the three cases that will be simulated in this work are shown in Table 1.

Figure 2 shows the simulation value of pyrometer temperature during the scanning process. The bias is less than 2% of the desired pyrometer temperature, which shows that the closed-loop temperature control in experiment can be adequately simulated in this model. Figure 3 shows the instantaneous temperature distributions in the powder bed for the three scan speeds after the beam has scanned a distance of 12.25 mm. We can see from this figure that the temperature gradient becomes higher with the faster scanning rate.

Table 1. Experimental cases to be simulated

Desired Pyrometer Temperature (K)	Scanning Speed (μm/s)	Powder Packing Fraction	Initial Particle Radius (μm)
1273	1.25, 2.50 and 5.0	0.42	7.5

Figure 4 shows the laser input power history needed to obtain the desired pyrometer surface temperature of 1000°C in the experiment and simulation. Figure 5 shows the distribution of solid material (powder and vapor deposition) in the powder bed after scanning process in the experiment and simulation. All the three different scanning rate cases indicate that a good agreement exists between the experimental and simulation results. From these two figures we can see that as the laser scanning rate decreases, the incident laser power and the infiltration of SiC into the powder bed will increase. As the workpiece becomes denser and larger in size with lower scanning rates, the higher the effective thermal conductivity and the more readily the heat dissipates from the process zone. This is illustrated in Figure 3 where the overall size of the heated zone in the powder bed becomes larger as the scanning rate decreases while the high temperature region (1423 K isotherm) becomes smaller.

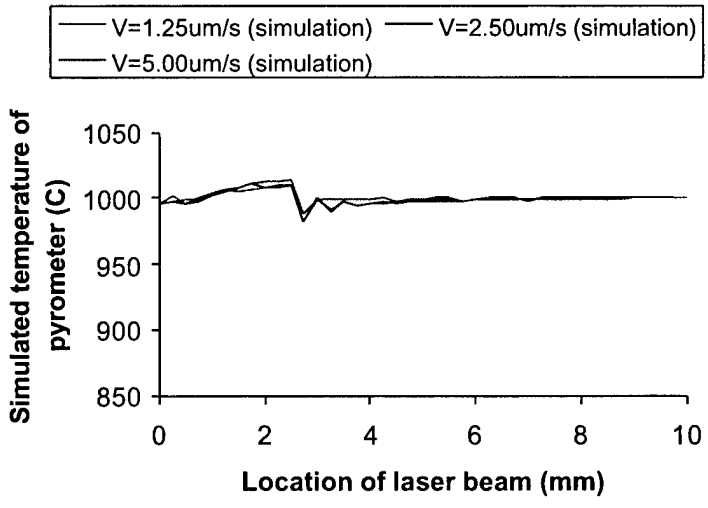


Figure 2. The simulated temperature value of pyrometer during the scanning process

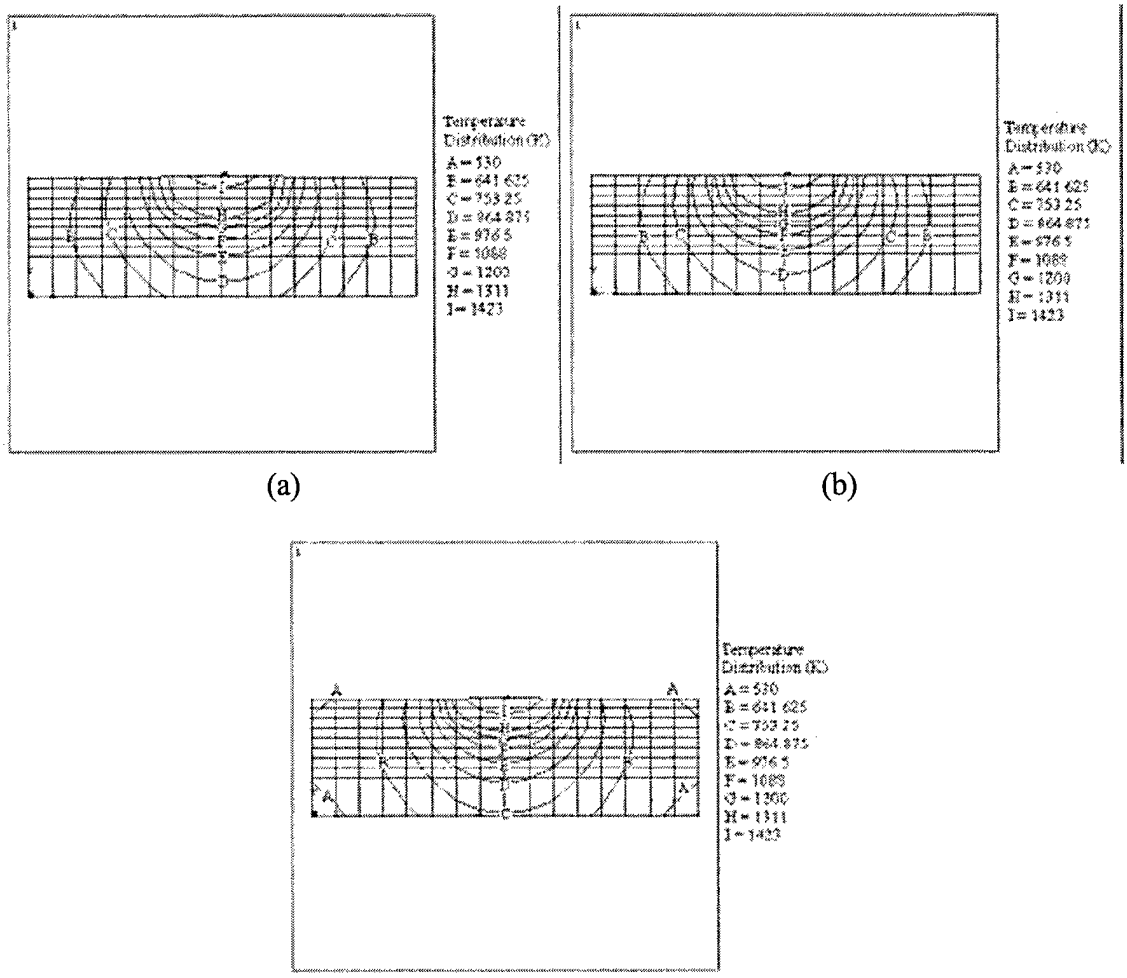


Figure 3. Temperature distribution in the powder bed at the cross section of X= 12.25 mm and scanning rate of (a) 1.25 μm/s, (b) 2.50 μm/s, and (c) 5.00 μm/s.

Comparing Figures 2 and 4, we also can see that uniform temperature on the top surface of powder bed during laser scanning process needs non-uniform laser power at the initial scanning period and nearly uniform laser power beyond this initial period. The reason is that at the beginning of the laser scanning, the laser-heated area is surrounded by powder with a much lower thermal conductivity and heat dissipation is slow. Thus, less laser incident power is needed to heat the powder under the laser beam to the desired pyrometer surface temperature. As the scanning proceeds, the part density and size increases and more heat is dissipated through thermal conduction along the previously densified section with a higher effective thermal conductivity. Thus, the laser incident power will increase with the moving of the laser beam. Finally, a steady state is reached that heat conduction through the previously densified section does not change much with time and the laser incident power reaches a nearly uniform value. Since more heat is conducted away through the previously densifie d section in the steady state region than

that in the initial transient region, the laser incident power in the steady state region is larger than that in the initial transient region.

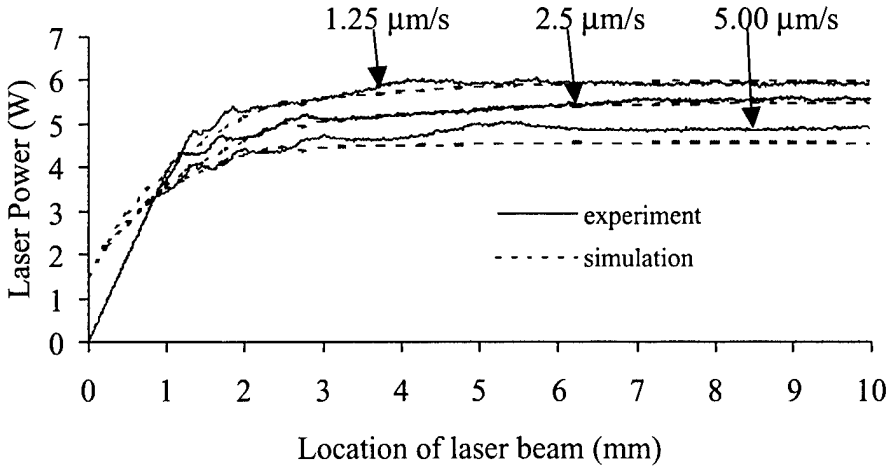


Figure 4. Comparison between the experimental and simulated incident laser power during the scanning process.

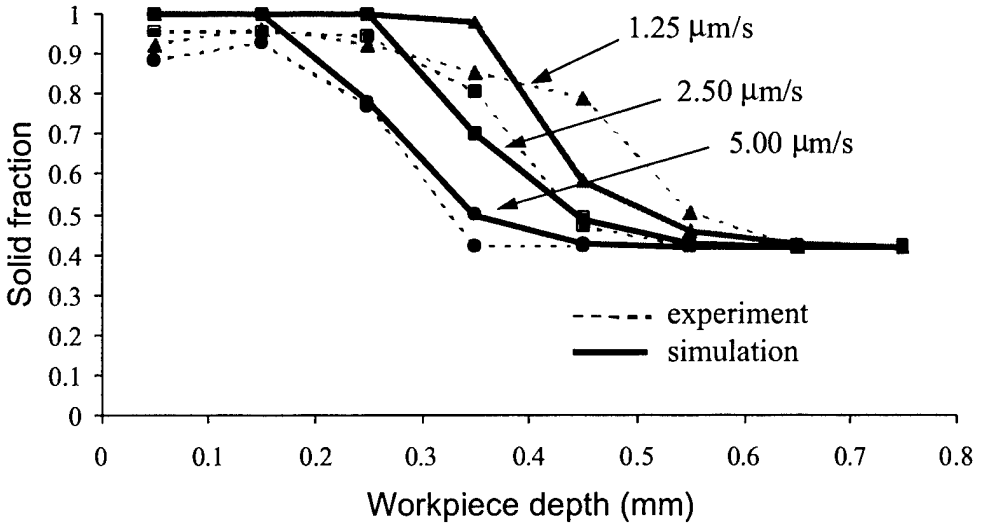


Figure 5. Comparison between the experimental and simulated solid fraction distribution in depth direction under the center of the laser beam after the scanning process at x=7 mm.

The distribution of vapor deposited SiC on the surface of the powder bed (SALD) on the transversal section with different laser scanning rate can be observed in Figure 6. The SALD increases as the laser scanning rate decreases due to the faster scanning rate having less time for SiC to deposit on the surface of powder bed. The height of the SALD is larger at the center region due to the Gaussian power distribution of the incident laser beam. Due to the small SALD (<40μm) when scanning rates are 2.50μm/s and

5.00μm/s, the SALD is hardly to measure. In figure 6, only the SALD with scanning rate 1.25μm/s is measured. The trends between simulation and measurement are consistent.

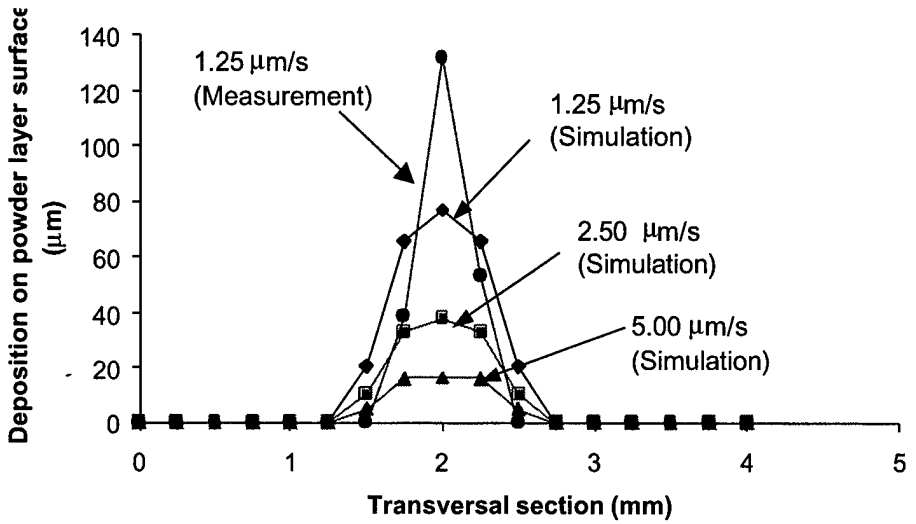


Figure 6. Simulation results of the distribution of vapor deposited SiC on the surface of the powder bed (SALD).

CONCLUSIONS

1) The simulation results of the incident laser power history and the distribution of vapor infiltrated SiC in the powder bed agree fairly well with the experiments.
2) As the laser scanning rate decreases, the incident laser power will increase, the deposition of SiC both within the powder bed as well as on the surface of the powder bed (SALD) will increase.
3) Uniform temperature on the top surface of powder bed during laser scanning process needs non-uniform laser power at the initial scanning period and nearly uniform laser power elsewhere.

Acknowledgements – The authors gratefully acknowledge financial support provided by the National Science Foundation under Grant No: DMI-9908249 and the Office of Naval Research under Grant No: N00014-95-1-0978.

REFERENCES

1. J.E. Crocker, L. Sun, H. Ansquer, L. Shaw, and H.L. Marcus, Processing and Characterization of SALDVI Ceramic Structures, Proceedings of the Solid Freeform Fabrication Symposium, David L. Bourell et al. (eds), The University of Texas at Austin, 495-501:1999.

2. Y.S. Touloukian, R.W. Powell, C.Y. Ho, and P.G. Clemens, Thermophysical Properties of Matter, Volume 2, THERMAL CONDUCTIVITY Nonmetallic Solids, IFI/Plenum, New York, New York, 1970.
3. E. Litovsky, M. Shapiro, and A. Shavit, Gas Pressure and Temperature Dependences of Thermal Conductivity of Porous Ceramic Materials: Part 2, Refractories and Ceramics with Porosity Exceeding 30 %, J. Am. Ceram. Soc., 1996, 79[5] 1366-76.
4. Y.S. Touloukian and E.H. Buyco (Editors), Thermophysical Properties of Matter, Volume 5, SPECIFIC HEAT: Nonmetallic Solids, IFI/Plenum, New York, New York, 1970.

Computer Integrated Adaptive Slicing and Vision Technologies for High Performance Rapid Prototyping System

Jia-Chang Wang, Jun-Ming Wang, Tsung Te Lin, and Jeng-Ywan Jeng

Department of Mechanical Engineering
National Taiwan University of Science and Technology, Taipei, Taiwan

Abstract

This paper discusses the application of adaptive slicing algorithm and computer vision technology on Rapid Prototyping (RP) system to enhance fabrication performance of Model Maker (MM) RP system. Usually, the layer number determines the RP system performance in terms of fabrication time and accuracy. In this research, a new practically adaptive slicing algorithm is developed and easily implemented for RP system, because it only recalculates the scanning path according to the criterion of adjacent profile variation. The experimental results of the proposed adaptive slicing algorithm show that the saving of 54% fabrication time is achieved and the model accuracy is still remained in the same level. MM presents a problem of stability because of tiny nozzle. Computer vision technology is employed in this paper to on line inspect the layer accuracy and defect of a model fabricated by RP system. The results of vision inspection is used to close-loop monitor the process to increase the processing stability and accuracy. These new practically adaptive slicing algorithm and machine vision technology are implemented in the commercial Model Maker (MM) RP system to increase its fabrication speed, accuracy and stability, but not accuracy sacrifice. Hence, the performance of the MM RP system can be significantly enhanced using vision and practically adaptive slicing technologies.

Keywords: Rapid Prototyping, Machine Vision, Adaptive Slicing, Texture Analysis.

Introduction

Rapid Prototyping (RP) technology has been widely applied in all industries to accelerate products into the market, since the first stereolithography machine is commercialized in 1988. However, the RP fabrication speed is still limited by the requirement of model accuracy, although the prototype fabrication has been accelerated using the layer manufacturing and automation technologies. The reason is that the higher the requirement for model accuracy, the smaller the layer thickness, and hence, the more layers required and therefore the slower the fabrication speed. This conclusion is only valid for constant layer thickness, which is employed by most commercial RP systems. Actually, the model accuracy not only depends upon the layer thickness but also the geometrical complexity. If the layer thickness varies with the geometrical complexity, the fabrication speed can be accelerated without accuracy sacrifice. Also, the model accuracy can be improved without sacrifice of fabrication speed, because the total layer number does not increase. In order to accelerate the fabrication speed but not accuracy sacrifice, several researches concentrate on the development of the adaptive slicing algorithm (Hope 1997, Tada 1998, and Sabourin 1996). All of these currently proposed adaptive slicing algorithms need a new slicing engine, which is not practical for or compatible with most of the commercial RP systems.

Although the on-line monitoring of RP is an interesting research topic, there is few documentation concerned with this topic. Reeves and Cobb at the University of Nottingham established a mathematical representation of the surface roughness of stereolithography parts to reduce the surface deviation of stereolithography using in-process techniques (Reeves, 1997). Some Japan researchers used eddy currents to real time measure the stress and strain in the cured photoresin for Stereolithography. In comparison with other RP research topics, the research into on-line monitoring and defect inspection of RP processes is still very limited. In order to monitor the fabrication process and inspect the defect of MM on-line, vision technology is employed in this research. Also, the captured image was processed to identify the defect and feedback to control the process to fix the defect.

The fabrication speed of MM RP system, using the proposed adaptive slicing algorithm, can be significantly accelerated but not accuracy sacrifice. Also, the system is on-line monitored layer by layer using the vision technology to solve the problem of processing stability caused by the adaptive slicing method and the potential blockage of nozzle. Hence, the fabrication performance of the MM RP system is dramatically enhanced and demonstrated by the integrated application of the adaptive slicing algorithm and computer vision technology.

Model Maker RP system

In this research, a practically adaptive slicing algorithm is implemented in the MM RP system, and the layer fabrication process of MM is monitored on-line using a CCD camera. A MM RP system uses two ink-jet type print-heads, one depositing the thermoplastic green building material and the other depositing red supporting wax. The liquefied material cools as it is ejected from the print-head and solidifies upon impact on the model. Wax is deposited to provide a flat, stable surface for the deposition of material in the subsequent layers. After each layer is complete, a cutter planes off the layer's top surface to provide a smooth, even surface for the next layer. The MM RP system is one of the most accurate RP systems, producing layers from 0.0005in to 0.005in. It can produce a model with very small features and fine surface finish.

The .STL file of the fabricated model is loaded into the ModelWorks program, which is a preprocessor of MM, to be sliced and viewed. Then, the .BIN and .BLD files for further model fabrication are generated. The .BLD file is a build process parameter file, which contains the data that describe how the model will be built. The .BIN file contains data describing the physical geometry of the model. It defines the model as a series of cross-section layers. Each layer is defined as a series of individual lines (vectors).

A new practical adaptive slicing method using finest layers stacking

Sabourin et al (1996) proposed an adaptive slicing algorithm to first slice the CAD STL model uniformly into slabs of thickness equal to the maximum available fabrication thickness. Each slab is then re-sliced uniformly as needed to maintain the desired surface accuracy. This adaptive slicing algorithm using stepwise uniform refinement is not practical, because some of the geometrical features may be already lost at the first slicing procedure using the maximum available fabrication thickness. The contradictory concept of Sabourin's adaptive algorithm is used in this study to slice the model uniformly into slabs of thickness equal to the minimum available fabrication thickness. Hence, the best accuracy available in the RP system can be met. Although model fabrication using the minimum available fabrication thickness, i.e. the best

accuracy, is demanded for all RP systems, it sacrifices fabrication speed because of too many layers. In order to compromise between the fabrication speed and accuracy, the number of layers must be reduced to an acceptable range and the model accuracy must not be sacrificed. The profiles of the adjacent finest layers are examined to evaluate whether these adjacent layers can be stacked as a single layer. If the profile variations of these adjacent layers are within the tolerance required, these adjacent layers are stacked as a single layer. Hence, the number of layers can be reduced and the fabrication speed can be accelerated without accuracy sacrifice.

The level of the profile variation is the criterion of the adaptive slicing method using the adjacent finest layers stacking. The level of the profile variation is represented as an angle, which is tangent to the adjacent finest layers. If the profile tangent angle θ is equal to 90 $^{\circ}$, it means that there is no profile variation between the adjacent layers. Or if the profile tangent angle is greater than an acceptable angle, the profile variations between the adjacent layers are within the acceptable tolerance. Hence, these two adjacent layers can be stacked as a single layer without accuracy sacrifice. This stacking procedure repeats until the layer thickness reaches the maximum layer thickness allowed in the RP system. On the other hand, if the tangent angle is less than a critical angle, that means the layer must be fabricated using the finest layer thickness, because the profile variation is too much. These two adjacent layers cannot be stacked together. It is also possible to only stack two, or three, or four, or several layers before reaching the maximum allowed layer thickness, because the profile variation is still within the acceptable tolerance. Therefore, the new fabrication layer thickness depends upon the criterion of the tangent angle. Of course, the fabrication parameters must be adjusted according to the new layer thickness. This adaptive slicing method using the finest layer stacking is implemented in the MM system.

Results and evaluation of the adaptive slicing method using finest layers stacking on the Model Maker system

Table 1 shows the detailed layer information of bench models using both constant layer thickness slicing and the adaptive slicing method on the MM system for three different criteria. As shown in Table 1, the original first 40 layers of bench models, using minimum slicing layer thickness, were stacked as 10 layers, because there is no profile variation at the bottom of the models. The original total layer number of models using the finest layer thickness is 140, but the total layer number of models using the adaptive slicing method is only 66 for the criterion at the tangent angle 30 degrees. For the criterion at tangent angle 60 degrees, the total layer number is only 86, because not only the bottom of the model was stacked as 10 layers from 40 layers, but also the middle of the model was sliced using normal slicing thickness.

As the result the detailed fabrication information of bench models using constant layer thickness and adaptive slicing thickness. It took 6881 seconds to fabricate bench model (a) using the finest layer thickness, 0.1mm, and to fabricate the same model using the maximum layer thickness only took 34% of the fabrication time, in comparison with the finest layer thickness. Of course, the model accuracy using the finest layer thickness is much better than that using the maximum layer thickness. For the criterion of tangent angle at 30 degrees, the fabrication time of bench model (a) using adaptive slicing method is only 62% of that using the finest layer thickness. There are serious steps at the round curves of the original model using constant slicing thickness, but these steps did not exist in the model fabricated using adaptive slicing algorithm. The reason for the better accuracy of the bench model (b) using adaptive slicing method, is that the high level of the profile variation area of bench model B was fabricated using the finest layer thickness

0.1mm. However, the bench model B was all fabricated using the same layer thickness 0.2mm no matter what the profile variation.

In order to quantitatively evaluate the accuracy of the bench models, the roundness error of the model (A) and (B) is measured and tabulated in Table 1. As shown in Table 1, the roundness error of the models, fabricated using adaptive slicing method, is slightly less than that of models fabricated using layer thickness 0.2mm and much smaller than that of models fabricated using layer thickness 0.4mm. Though the roundness error of the models, fabricated using adaptive slicing method, is slightly larger than of models fabricated using finest layer thickness 0.1mm, the fabrication time of the models, fabricated using adaptive slicing method, is much smaller than that of models fabricated using finest layer thickness 0.1mm. Hence, the adaptive slicing method is approved to accelerate fabrication speed of Model Maker RP system and without too much accuracy sacrifice.

Table 1. The result of the bench models test in terms of the fabrication time.

Bench model (A)

Slicing Method		Number of Layers			Total Layer No.	Fabrication Time (s)	Relative Fabrication Time (%)	Roundness Error (mm)
		Tmax = 0.4mm	T=0.2mm	Tmin = 0.1mm				
Constant Layer Thickness	Tmin	-	-	140	140	6881	100	0.205
	T	-	70	-	70	3566	51.82	0.294
	Tmax	35	-	-	35	2358	34.27	0.437
Adaptive Slicing Thickness	Tangent Angle=30	10	44	12	66	4284	62.58	0.276
	Tangent Angle=45	10	34	32	76	5003	72.71	0.248
	Tangent Angle=60	10	24	52	86	5353	77.79	0.229

Bench model (B)

Slicing Method		Number of Layers			Total Layer No.	Fabrication Time (s)	Relative Fabrication Time (%)	Roundness Error (mm)
		Tmax = 0.4mm	T=0.2mm	Tmin = 0.1mm				
Constant Layer Thickness	Tmin	-	-	140	140	5801	100	0.156
	T	-	70	-	70	2958	50.99	0.282
	Tmax	35	-	-	35	1934	33.34	0.435
Adaptive Slicing Thickness	Tangent Angle=30	10	43	14	67	4144	71.74	0.257
	Tangent Angle=45	10	35	30	75	4344	74.88	0.215
	Tangent Angle=60	10	24	52	86	4550	78.43	0.167

Vision monitoring of MM fabrication process

The experimental layout of the on-line layer monitoring and defect inspection is schematically illustrated in Figure 1. The MM machine is controlled by the fabrication commands (.BIN and .BLD files) generated from the process control computer. Another computer is employed to process the captured image from the CCD camera to identify the defect,

calculate the defect coordinate, and generate the compensated program. Also, the sliced profile data obtained from the slicing software, ModelWork, is used to compare with the image profile for further on-line monitoring of the MM system. The coordinates of the layer defect can be calculated and fed back to the process control computer to move the nozzle and deposit new material at the position of the defect. If the profile is oversize rather than defective, the compensated program will raise the platform and move the cutter to plane off the current layer. Only the problem of defect is presented in this paper, because the oversize problem is similar to that of the profile accuracy analysis.

In order to evaluate the feasibility of the on-line monitoring of the MM process, a simple square part of 20X20mm^2 is designed with a rectangular defect in the central area. The image of the defect area is found in the previous layer rather than in the current layer. Hence, the image of the previous layer is an important reference to identify the morphology of the defect. An image difference algorithm is then employed to remove the effect of the previous layer image on the identification of the defect. Also, in order to immediately inspect the layer defect, the image is captured as soon as the build material is deposited rather than after the cutter operation. Since, the surface condition of the material deposition before cutting is very different from that after cutting, the surface texture of the material deposition and the defect can be discriminated. As a result, the defect can be inspected and the process can be further on-line monitored.

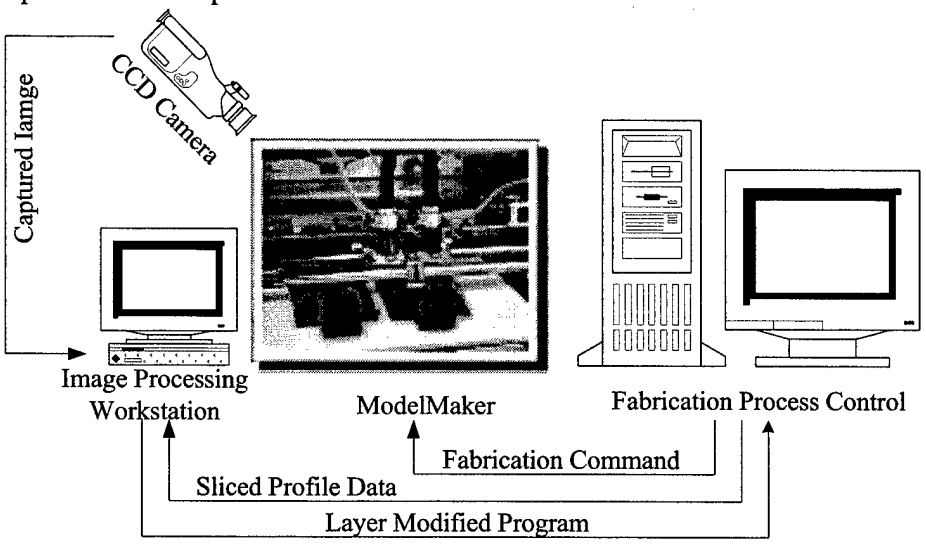


Figure 1. Experimental layout of on line layer monitoring and defect inspection of MM using vision technology.

ON-LINE DEFECT INSPECTION USING AN ADAPTIVE TEXTURE ANALYSIS

The printing path characterizes the build material deposition image, and the defect is characterized by the smooth surface after the cutting operation in the previous layer. The characteristic difference of the deposition and the defect is modeled as adaptive texture analysis to discriminate the defect from the direct image of the current layer, rather than two images captured in the image difference algorithm. The algorithm used in this adaptive texture analysis is the 'adjusted *Texture-Energy-Ratio* approach.' as shown in Figure 2. (Wang, 1998).

Only one image is captured after the deposition of the build material at the current layer, which is different from the two images captured before and after material deposition, respectively.

The captured image of the adaptive filter texture analysis is the target image to identify the defect. The captured image is then processed to identify the defect using an adaptive filter texture analysis. As shown in Figure 3.(b), there are two pattern textures in the image after the build material deposition at the current layer. The first pattern is the texture of the printing path, which is the deposition area of the new build material. The other pattern is the texture of the defect, which is the smooth surface of the previous layer after the cutting operation.

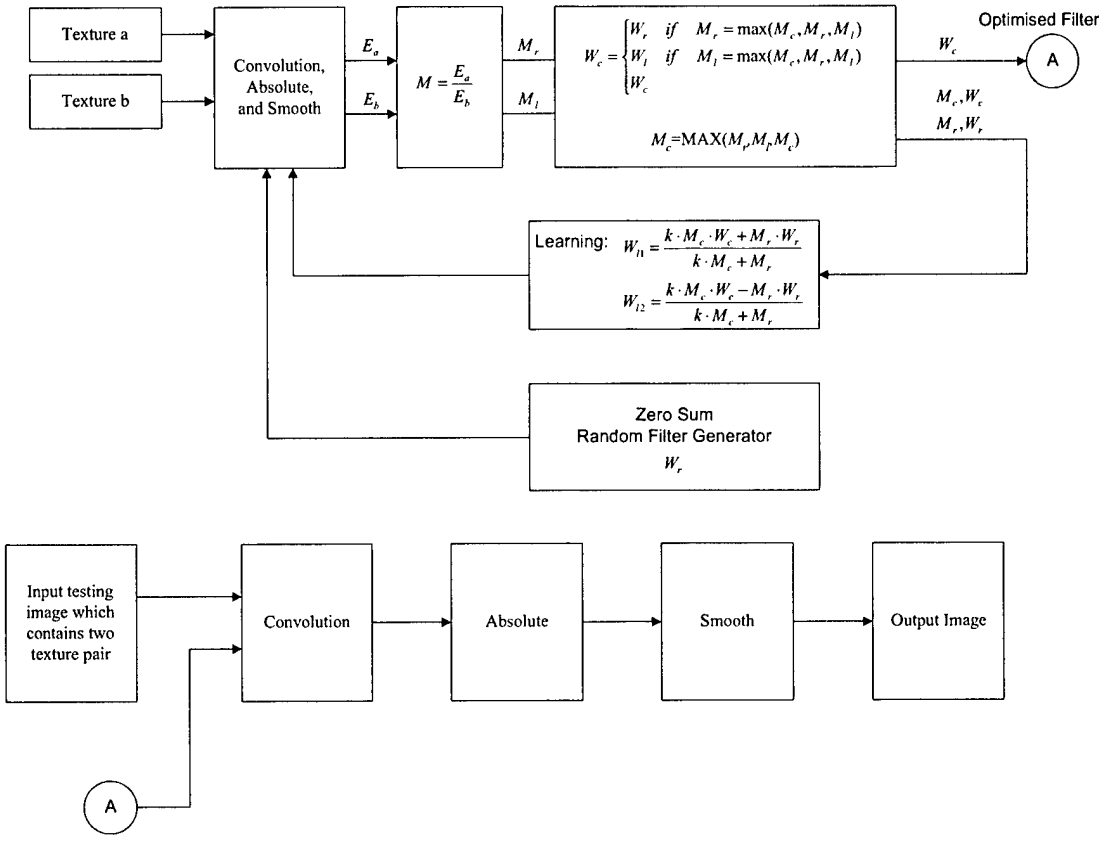


Figure 2. Adaptive texture analysis and inspection using the adjusted *Texture-Energy-Ratio* approach. (Wang, 1998)

In order to analyze the texture of the new printing path and the defect, two masks are employed to extract the characteristics of these two textures as shown in Figure 3.(a). The texture of the printing path for the new build material is extracted using mask "a", and the texture of the defect is extracted using mask "b". The textures from mask "a" and "b" are processed using an adaptive texture algorithm, presented in the next section, to iteratively calculate the resulting filter as shown in Figure 3.(b). This resulting filter is an 11×11 array, and the value of the array distributed from -100 to 100. The equal height of the resulting filter is identified and labeled. The distribution of the resulting filter is regularly repeated like a sine function, and its characteristic is similar to the line by line characteristic of the printing path. It is used to filter out the line characteristic texture of the printing path into one single feature and isolate the defect texture as another single feature. The resulting filter is applied to the image of the current layer to adaptively discriminate the defect feature from the whole image of the current layer. Then, the discriminated image is adjusted for higher brightness and contrast ratio as shown in Figure 3.(c). The smoothing, thresholding, dilating, and eroding operations are then applied to the image to

identify the defect as shown in Figure 3.(d), 3.(e), 3.(f), and 3.(g) respectively, which is the same as that of last four steps in image difference processing. In comparison of defect image processing using image difference and adaptive texture as shown in Figure 3.(f) to Figure 3.(h) and Figure 3.(e) to Figure 3.(g) respectively, the result of the adaptive texture analysis is a little bit better than that of image difference. The reason is that the noisy area of texture analysis is smaller than that of image difference.

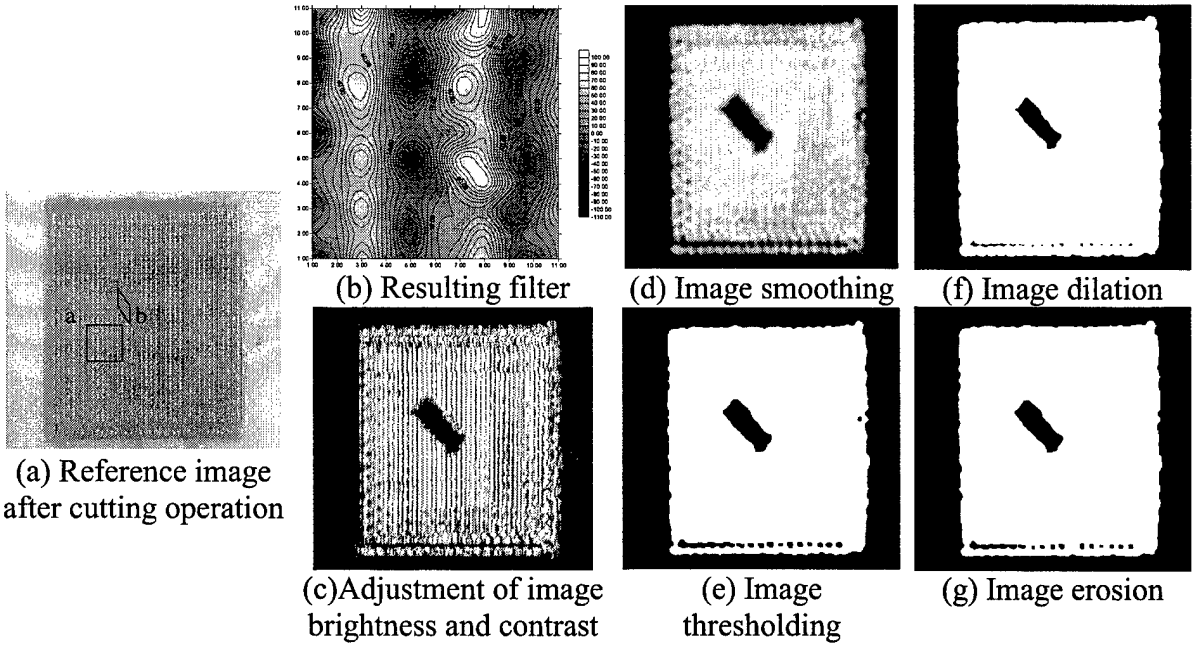


Figure 3. The results of the defect image processing using an adaptive texture filter, smoothing, thresholding, dilation, and erosion algorithms.

Finally, the defect coordinates are calculated from the defect image. If the defect size is within the range of tolerance, the fabrication process continued. However, if the defect size is unacceptable, a compensation program is generated and transferred back to the control program to redeposit build material on the defect area. Hence, the on-line monitoring of MM is achieved.

GENERATION OF DEFECT COMPENSATION PROGRAM FOR ON-LINE MONITORING OF MM RP

Once the defect is identified, a compensated program is generated in the image processing workstation and transferred back to the fabrication process control computer to reprint the defect area for on-line monitoring of MM RP. In order to calculate the defect coordinates, a translated matrix is calculated using simple linear translation and rotation algorithms to transform the image coordinates to the MM coordinate system. Then, the coordinates of the defect are extracted and determined from the image using scanning lines. Once the defect coordinate is determined and transformed into the MM coordinate system using the transformation matrix, a compensated program is generated in .BIN file format and is transferred back to the control computer. Hence, the defect area is redeposit with new build material controlled by the compensation program. Therefore, the fabrication process of MM RP is on-line layer monitored using vision technology.

CONCLUSION

A new practical adaptive slicing method using finest layers stacking for the RP system is presented in this paper. This new proposed adaptive slicing method is easy to implement in the RP system, because it just modifies the profile information after slicing operation and does not involve a new slicing engine. The proposed adaptive slicing method was implemented on the Model Maker RP system to accelerate fabrication speed without accuracy sacrifice. The experimental results show that it only takes 62% of the fabrication time at the similar accuracy to use the new practical adaptive slicing method in comparison with the constant layer thickness.

The detailed image process of defect inspection using the adaptive texture analysis is presented. The defect is on-line inspected and fixed by the reprinting of new build material, layer by layer. Hence, the computer integrated adaptive slicing algorithm and vision technologies enhance the performance of RP system, because it not only increase fabrication speed but not sacrifice with accuracy, but also on-line monitor and stabilize the fabrication process.

Acknowledgement

The support of this research by the National Science Council of Taiwan, ROC under grant NSC-88-2212-E-011-026.

References

Carrion, A., "Technology Forecast on Ink-Jet Head Technology Applications in Rapid Prototyping," *Rapid Prototyping Journal*, Vol.3, No.3, pp.99-115 (1997).

Dolenc, A. and Makela, I., "Slicing procedures for layered manufacturing techniques," *Computer Aided Design*, Vol.26, No.2, pp.119-126 (1994).

Dunn, D., Higgins, W.E., and Wakeley, J., "Texture Segmentation Using 2D Gabor Elementary Functions," *IEEE Transactions on Pattern Analysis and Machine Intelligence,* Vol. 16, No.2, pp.130-149 (1994).

Famieson, R., and Hacker, H., "Direct slicing of CAD models for rapid prototyping," *Rapid Prototyping Journal*, Vol.1, No.2, pp.4-12 (1995).

Hope, R.L., Roth, R.N., and Facobs, P.A., "Adaptive slicing with sloping layer surfaces," *Rapid Prototyping Journal*, Vol.3, No.3, pp.89-98 (1997).

Jeng, J.Y., Mau, T.F., and Leu, S.M., "Gap Inspection and Alignment Using Vision Technique for Laser Butt Joint Welding," Accepted for publication in the *International Journal of Advanced Manufacturing Technology* (1999).

Reeves, P.E., and Cobb, R.C., "Reducing the Surface Deviation of Stereolithography using In-Process Techniques," *Rapid Prototyping Journal*, Vol.3, No.1, pp.20-31 (1997).

Sabourin, E., House, S.A., and Bohn, F.H., "Adaptive slicing using stepwise uniform refinement," *Rapid Prototyping Journal*, Vol.2, No.4, pp.20-269 (1996).

Sternberg, S.J., "High-Performance Cameras Cut Cost of Real-Time Imaging," *Laser Focus World*, Mar., pp.33-38 (1994).

Tata, K., Fadel, G., Bagchi, A., and Aziz, N., "Efficient slicing for layered manufacturing," *Rapid Prototyping Journal*, Vol.4, No.4, pp.151-167 (1999).

Wang, J.C., "The Application of Texture Discrimination to SMT QFP Solder Joint Inspection", Ph.D. Thesis, The University of Liverpool, U.K. (1998).

A SLICING PROCEDURE FOR 5-AXIS LAYERED MANUFACTURING

R. Sundaram and J. Choi
Department of Mechanical Engineering and Aerospace Engineering and Engineering Mechanics
University of Missouri – Rolla, Rolla, MO 65409

Abstract

The 5-axis layered manufacturing technology facilitates fabrication of a part with overhanging features without the use of supports, thereby making a direct-to-use part from the layered manufacturing technology a reality. In this paper we describe a direct slicing procedure for a CAD model, a crucial process planning task for the 5-axis layered manufacturing. The neutral exchange format IGES is used as the slice format. The G and M codes for a CNC 5-axis laser deposition machine are generated from the slice format and the deposition process is simulated. Implemented examples are included to explain the slicing procedure. Exciting possibilities for the future work on the slicing procedure are discussed.

Introduction

Layered manufacturing refers to the fabrication of physical parts layer-by-layer. It involves successively adding raw material, in layers, to create a solid of some predefined shape. The use of layered manufacturing typically results in a significant reduction in the component manufacturing times from the conventional metal forming/cutting technologies. When creating a part layer-by-layer, the geometric complexity of the part has significantly less impact on the fabrication process. Furthermore, manufacturing a component of Functionally Graded Material is very much possible with layered manufacturing technologies. Layered manufacturing includes the processes Solid Freeform Fabrication and Desktop Prototyping.

The use of layered manufacturing technology is currently restricted to prototyping, i.e. creating a physical part for the purposes of analyzing its form, fit or function. The use of layered manufacturing typically results in a significant reduction in the component manufacturing times from the conventional metal forming/cutting technologies. With advances in process planning tasks of layered manufacturing and layered manufacturing technologies such as Directed Light Fabrication (DLF) [1], Laser Engineered Net Shaping (LENS) [2] and Direct Metal Deposition (DMD) [3], manufacturing of a functional metal component that can directly be put to use is not far. In the last few years, enterprises such as Precision Optical Manufacturing in Michigan, Aeromet Corporation near Minnesota and Optomec in New Mexico have began to commercialize these technologies [4]. Advances in the process planning tasks include the increasing use of CAD models instead of faceted STL models, the representation of heterogeneous and functionally graded material objects, the more efficient part orientation algorithms and the more efficient adaptive slicing algorithms to increase the surface quality. However, one impediment to the manufacturing of functional components is the issue of overhanging features and the hollow sections in a component. Present layered manufacturing techniques use sacrificial support structures, of a different material, to support the overhanging and hollow features, which necessitate subsequent post-processing operations apart from poor

surface quality and increased build time. In this paper, we describe a procedure to manufacture a solid functional component without the use of support structures.

5-axis slicing procedure

To motivate the need for this 5-axis slicing procedure, we briefly describe the overhanging features and the use of support structures. The most common need for support structures occurs when material on one layer overhangs the previous layer by more than a specified amount [5]. Figure 1 shows a part with such overhanging features. Regions O_1 and O_2 cannot be deposited without the support structures in the build direction shown.

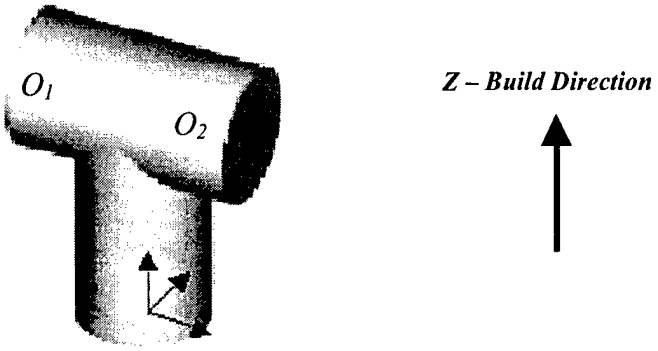


Figure 1. An example part with overhanging features

Since the use of support structures decreases the surface quality and increases the build time a new procedure is required. The 5-axis slicing procedure attempts to build such parts without the use of support structures.

A new generation of layered manufacturing machines has started to emerge in the research domains. A schematic sketch of one such layered manufacturing machine is shown in Figure 2. The machine shown in Figure 2 has 2 additional axes namely, *C*-axis and *B*-axis. *C*-axis allows rotation of the part in the *X*-*Y* plane around the Z-axis in both the directions. *B*-Axis allows the rotation of the part in the *Y*-*Z* plane around the *Y*-axis. These machines eliminate some of the inherent limitations of the existing layered manufacturing such as the overhang issue. The various tasks associated with the 5-axis slicing procedure are:

(1) Model decomposition.
(2) Sequencing the decomposed parts.
(3) Adaptive Slicing and
(4) Tool Path Generation.

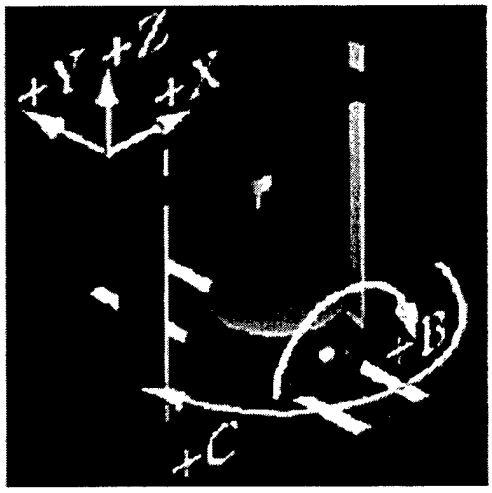


Figure 2. Schematic sketch of a 5-axis layered manufacturing machine

Model decomposition

The build direction is constant and it is assumed to be Z. The solid model with the overhanging features is decomposed into sub-volumes. Each of the sub-volume can be built along the given build direction Z.

The first task in model decomposition is to identify the overhanging features. Surface interrogation [6] is used as a tool to identify the overhanging features. This is accomplished by analyzing the angle θ that the surface normal, at any point on the model surface, makes with the build direction Z. The angle θ is called the overhang angle. At any point p if the overhang angle exceeds the permissible value θ_{max} then we can conclude that point p is a part of the overhanging feature.

Consider a C^1 continuous regular parametric surface $S(u,v)$ and let

$$n(u,v) = \frac{\partial S}{\partial u} \times \frac{\partial S}{dv} \tag{1}$$

be its normal vector field. θ, the angle between the build direction $\vec{Z}$ and the surface normal $n(u,v)$ can then be expressed as:

$$\cos\theta = \frac{\left\langle \vec{Z}, n(u,v) \right\rangle}{\left\| n(u,v) \right\|} \tag{2}$$

θ_{max} is the user specified maximum permitted overhang angle. From equation (2), it is possible to determine the point at which the overhang angle exceeds the maximum permitted value. All the points on the surface at which $\theta > \theta_{max}$ are determined by traversing through the surface. The lowest of all such points p_{min}, in the build direction, is then determined. An intersection section graph is obtained by intersecting the solid model with a horizontal plane at p_{min}. The intersection graph is swept in the build direction to obtain an infinitesimally thin tool body which is open on both the ends. The tool body is then subtracted from the solid model to separate the overhanging features from the solid model as shown in Figure 3. The total number of decomposed parts after the decomposition would be $n+1$, where n is the number of overhanging features. A similar technique with isoclines can also be used to identify the overhanging features [8].



(a) Model to be built (b) Decomposed model

Figure 3. Model decomposition

Sequencing the decomposed parts

The decomposed parts are to be built one-by-one in a sequence. Sequencing includes rotating each of the decomposed parts first around the Z-axis by an angle θ_Z and then around Y-axis by an angle θ_y at the machine origin. θ_Z is the angle between the central-axis of each of the decomposed parts and the $\pm$ X-axis in the X-Y plane at the height of the central-axis of that decomposed part. θ_y is always $\pm$ 90° such that the overhanging parts are built in the positive build direction Z. The decomposed part to which none of the rotation is applied and which can be built in the build direction is always the first in the sequence. This ensures the physical existence of a base surface on which to deposit. The rest of the sequence is determined based on the height of each of the decomposed part exists. The lowest overhanging decomposed part is second in the sequence and so on till the rest of the decomposed parts are built. Sequencing based on the height at which each of the decomposed part exists minimizes the chances of collision with the layers already deposited.

Adaptive slicing

Each of the decomposed parts is then sliced using the adaptive slicing algorithm [7]. Adaptive slicing involves slicing of the CAD model with varying layer thickness. The user can specify a maximum allowable cusp height for the object and also a deposition requirement (excess or deficient). In order to achieve the user specifications, surfaces of high curvature are sliced with thinner layer thickness and surfaces of low curvature are sliced with thicker layer thickness. Adaptive slicing yields better surface quality, as the staircase effect decreases and the variations in the cusp height across the layers are minimized. Adaptive slicing gives the user explicit control over the surface quality. The other advantage of adaptive slicing is a reduction in the build time. The slice is then reverse transformed to get them to their original location. The Figure 4 shows the model after adaptive slicing and reverse transformation of the slices.

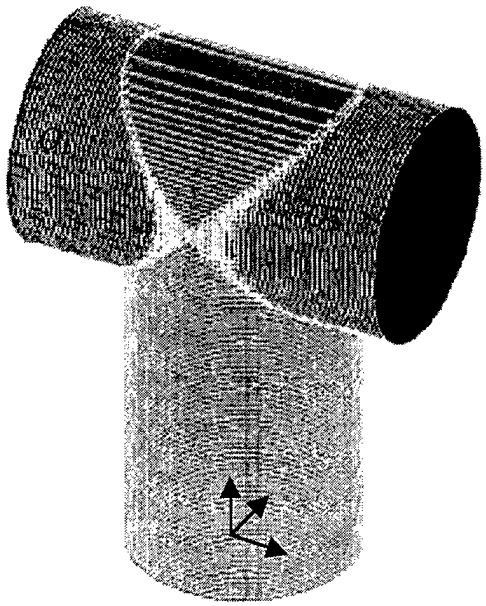
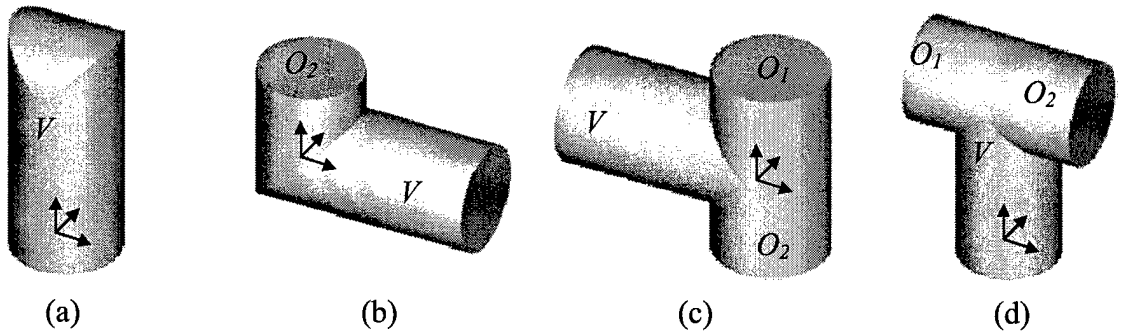


Figure 4. Adaptively sliced model for 5-axis layered manufacturing

Tool path generation

The slice data is obtained from the adaptive slicing procedure in the IGES data format as set of surfaces. Each slice is represented by a planar surface as shown in the Figure 4. These surfaces can be used in any commercially available CAM software with a 5-Axis capability to generate the CNC tool paths. In our case we used SURFCAM®‡. We treated each slice, in a bottom-up approach, as a surface that can be milled and used the 5-axis surface milling option to generate the tool paths that can be used for the 5-axis layered manufacturing machine. This procedure allows us to change the material deposition pattern layer wise giving us the capability to control the physical properties such as residual stresses. Figure 5 shows the steps involved in manufacturing our example.



(a) (b) (c) (d)

Figure 5. Steps involved in 5-axis layered manufacturing: (a) Vertical build-up of V, (b) Rotation of V and build-up of O_2, (c) Rotation of V & O_2 and build-up of O_1, (d) Model recreated

Algorithm

All the bounding surfaces of the model are first extracted along with their defining geometry. These surfaces are then converted into parametric spline surfaces. These surfaces are then analyzed to identify the overhanging features as explained in the earlier section. Once the lowest overhanging location is found then the model is chopped into buildable vertical regions and unbuildable overhanging regions. Each of these regions are then rotated first around the *Z*-axis and then around the *Y*-axis to make them buildable. Each region is adaptively sliced [7] and reverse transformed. The slices are then exported for path generation in IGES format. The algorithm, including the adaptive slicing, is summarized below.

‡ SURFCAM® is a registered CAD/CAM software from Surfware Inc.

Algorithm 5-axis Slicing

Input: 1. Parametric representation of the object *O*.
2. 3-axis or 5-axis
3. Cusp height, δ
4. Slice thicknesses L_{min} & L_{max}
5. Containment requirements: +ve or –ve.

Output: The heights of all the adaptive slices for the layered manufacture of *O* in 3-axis or 5-axis

Set R= decomposed parts of *O*
Set S= all the surfaces that bound each *R*
Set B= blocks obtained by slicing the object through the vertices of each *R*

START

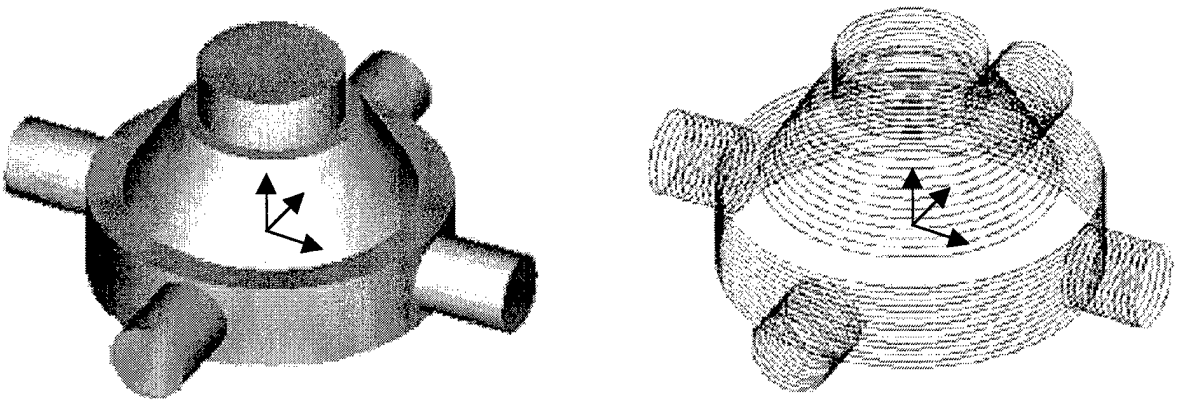
Overhang detection by the surface analysis of *O*
IF (overhang = TRUE)
  Decomposition of the model *O* into *R*
  Overhang detection by the surface analysis and decomposition of each *R* recursively.
  5-axis transformation of each R

WHILE *(R ≠0)* DO
{5-axis transformation applied to *R*
  WHILE *(B ≠ 0)* DO
  { *z*= bottom of block
    WHILE (*z < top of block*)
    { *Si* = no. of surfaces that intersect with slice z
      I=0
      WHILE (*I ≤ Si*)
      { *d = layer thickness (Si, z, δ)*
        IF $d > L_{max}$ THEN height $_i = L_{max}$
        ELSE IF $d < L_{min}$ THEN height $_i = L_{min}$
        ELSE height $_i$ = d;
        I=I+1}
      Slice thickness t= min. height $_i$;
      IF (*sign_normal (z) = TRUE*) containment => TRUE;
    }
    increment z = z+ t
  update B}
update *R* }

END

Implementation and examples

A prototype program has been implemented including the algorithms discussed in the previous sections. Based on the ACIS®[†] solid modeling kernel, the software module is built on a Sun Sparc workstation with an user interface based on Tcl/Tk[‡]. Figure 6(a) shows an example model, which is unbuildable with conventional 2.5-D layered manufacturing techniques without the use of support structures. However the same model can be built with the 5-axis layered manufacturing technique. Figure 6(b) shows the same model sliced for 5-axis layered manufacturing. The 5-axis layered manufacturing of this object is then simulated using the 5-axis surface milling features of the commercially available CAM software SURFCAM® demonstrating the feasibility of 5-axis layered manufacturing. The results are shown in Table 1. From Table 1, it is clear that adaptive slicing decreases the deposition time. Deposition times given are for the 5-axis deposition. Support structures and the associated post processing would only add up the deposition times.



(a) Unbuildable Model (b) Buildable in 5-axis layered manufacturing

Figure 6. 5-Axis adaptive slicing of a model

Table 1. Simulated deposition times (*Process Parameters: Nozzle Speed V = 14.82 mm/sec; Nozzle Diameter = 700 μm; Overlap = 10 %*)

Parameters	Example 1 (Figure 1)		Example 2 (Figure 6)	
Bounding Box Dimension	26×13×36.5 (mm)		30×30×13 (mm)	
Model Volume	6.7017 cm^3		2.7065 cm^3	
	Adaptive Slicing	Uniform Slicing	Adaptive Slicing	Uniform Slicing
Total No. of slices	269	296	123	136
Deposition Time	125 min 3 sec	137min 36 sec	48 min 39 sec	53 min 47 sec

[†] ACIS® is a registered geometric modeling kernel from Spatial Corporation.
[‡] Tcl/Tk is a freely available scripting language with extensions for creating user interfaces.

Conclusions

A procedure was developed for manufacturing an object, with overhanging features, without the use of support structures using 5-axis layered manufacturing process. 5-axis layered manufacturing is a promising new method to manufacture any given part. However, further development of this process is required. In this paper, we have considered only the solid objects with overhanging features. Further work is necessary to manufacture objects with hollow interior. The on-going development of multi-axis deposition machines in the research domains necessitates a more advanced procedure based on the concepts presented in this paper. This paper considered only one of the process planning tasks involved in the process namely the slicing, other process planning tasks such as part-orientation, sequencing and collision avoidance of the deposition nozzle with the object are to be investigated. The algorithm for overhang feature detection can further be optimized using a feature based detection procedure in addition to the surface analysis presented in this paper.

References

1. Milewski J.O., Lewis G.K., Thoma D.J., Keel G.I., Nemec R.B. and Reinert R.A., "Directed light fabrication of a solid metal hemisphere using 5-axis powder deposition", Journal of Materials Processing Technology, vol. 75, 1998, pp. 165-172.
2. Griffith M.L., Keicher D.M., Atwood C.L., Romero J.A., Smugeresky J.E., Harwell L.D., Greene D.L., "Free form fabrication of metallic components using laser engineered net shaping (LENS)", Solid Freeform Fabrication Proceedings, 1996, pp 125-132
3. Mazumder J., Choi J., Nagarathnam K., Koch J. and Hetzner D., "The direct metal deposition of H13 tool steel for 3-D components", JOM, vol. 49, May 1997, pp. 55-60.
4. Mazumder J., "A crystal ball view of direct metal deposition", JOM, December 2000, pp. 28-29.
5. Allen S. and Dutta D., "Determination and evaluation of support structures in layered manufacturing", Journal of Design and Manufacturing, vol. 5, 1995, pp. 153-162.
6. Elber G., "Curve evaluation and interrogation on Surfaces", Accepted paper at GMIP, 2001.
7. Kulkarni P. and Dutta D., "An accurate slicing procedure of layered manufacturing", Computer-Aided Design, vol. 28, no. 9, 1996, pp. 683-697.
8. Singh P. and Dutta D., "Multi-direction slicing for layered manufacturing", Proceedings of DETC'00, ASME, CIE-14626, September 2000.

Voxel-based Modeling with Multi-resolution Wavelet Transform for Layered Manufacturing

Soonkyu Yim and Hae Chang Gea
Department of Mechanical and Aerospace Engineering
Rutgers, The State University of New Jersey, Piscataway, NJ 08854

Abstract

A voxel-based modeling system with multi-resolution for layered manufacturing is presented in this paper. When dealing with discretized data input, voxel-based modeling shows its clear advantages over the conventional geometric modeling methods. To increase the efficiency of voxel data due to its large storage space requirement, multi-resolution method with wavelet transform technique is implemented. Combining with iso-surface generation and lossless polygon reduction, this voxel-based modeling method can easily work with layered manufacturing. To demonstrate these concepts, components with different resolutions are built using Layered Manufacturing and presented in the paper.

Keywords: Layered Manufacturing (LP), Wavelet Transform, Polygon Reduction (PR)

1. Introduction

During the past decade, considerable efforts have been devoted to recreate a meaningful and visible model from three-dimensional scanners and sectional images. In contrast to the conventional geometric modeling that converts 3-D digitized data to many geometric entities for visualization, much research is focused on volumetric modeling that represents digitized data directly from three dimensional discrete units of volume element (voxel). In order to increase the ability of shape control over voxel data, Wu et al. [18] introduced Non-Uniform Rational B-Spline (NURBS) volumetric model with a partial integration between surface and volume graphics. Although volumetric modeling has some clear advantages when dealing with a large set of digitized data, it suffers from its large storage requirement [8]. To reduce the storage size of volumetric data acquired from MRI, Muraki [11] used a wavelet transform that displays models in different resolutions. However, mechanical components modeled by volumetric data still need to be converted to geometric entities before they are fabricated by traditional manufacturing machine tools. Recently, this fabrication bottleneck has been overcome by the advancement of Layered Manufacturing (LM). Because LM fabricates the object layer by layer from the bottom to the top, it is not restricted by the topology of the object or by the orientation of the initial setup. With the development of LM, volumetric data has been suggested as an alternative modeling tool for mechanical components [1][2].

In this paper, a voxel-based modeling with multi-resolution wavelet transform for layered manufacturing is presented. Instead of the Batelle-Lamarie wavelet and the Difference of Gaussian (DOG) wavelet which were implemented in [11][12], the Haar wavelet is chosen in this work. The benefit of the Haar wavelet is that it can be used with integer variables during transform. Therefore, storage size and computation time can be effectively reduced comparing to other wavelets, which use float or double variables. A bit remainder index is applied in this system to accommodate arbitrary data size during the wavelet transform [19]. Primitive voxel editing functions are included for model creation and shape modification. Marching Cube

algorithm and lossless polygon reduction are implemented before building the STereoLithograph (.STL) files. This voxel modeling system is coded in Java and Java3D Application Programming Interface (API) for its portability. To demonstrate these concepts, components with different resolutions built from voxel model creation to LM are presented at the end of this paper.

2. Voxel-based Modeling

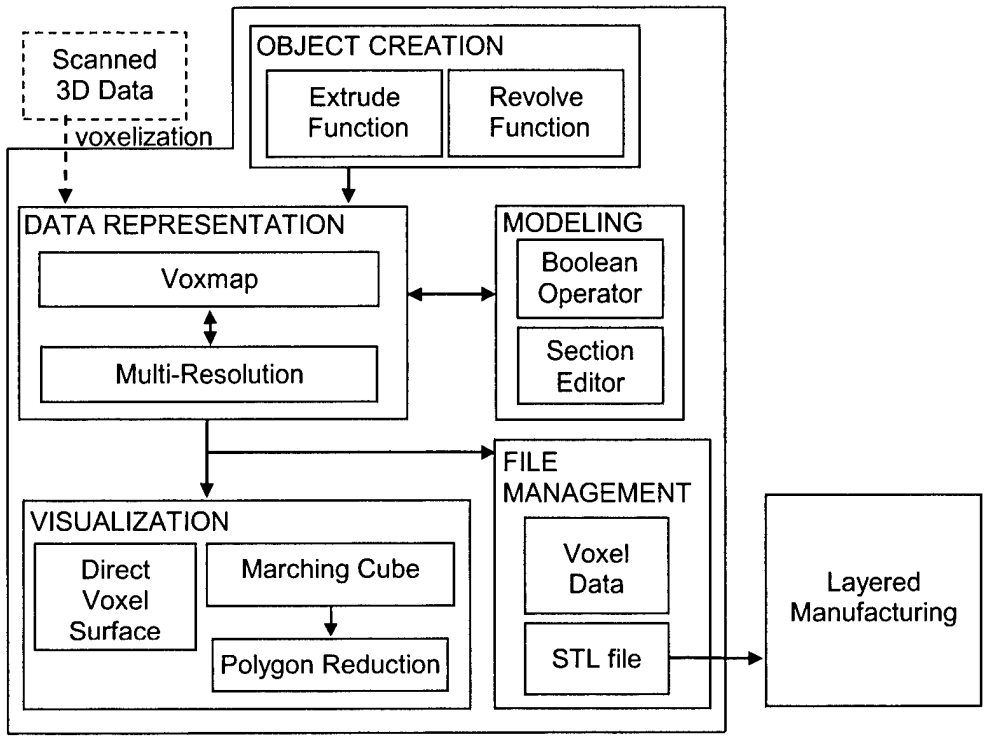


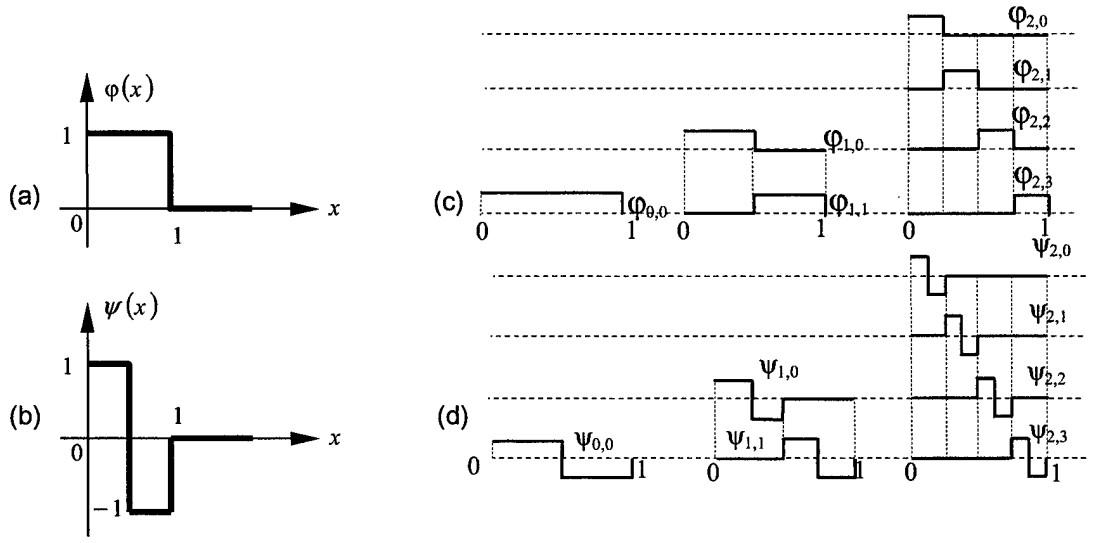
Figure 1: Voxel-based Modeling System.

A voxel-based modeling starts from constructing a voxmap of the object. The voxmap is a three-dimensional data array that is generated through voxelization of an object. To voxelize an object, we first divide the volumetric object into small cubes (voxel) with equal sizes. Then an integer value is assigned to each voxel to describe its property and stored in the corresponding volume buffer (voxmap). Because voxel is a basic atomic unit of a volumetric object, voxel-based model is convenient when representing objects from three-dimensional scanned data, when modeling activity is based on digitized operations, and when the output consists of only discrete values [2][3][7][16][17]. In this paper, a voxel-based modeling system is presented as shown in Fig. 1. First, the object is created from pixel extrusion and revolving operations. It is stored in a voxmap and can be modified by a built-in modeler consisting of various Boolean operations and section editing functions. Direct conversions from 3D scanned image data to voxmap is not implemented here because most scanner vendors support these functions with their hardware. To reduce the storage requirement of the voxmap, a multi-resolution wavelet transform is implemented in the system. Before visualizing the model, inner surfaces are removed and outer surfaces are smoothened by a Marching Cube (MC) algorithm. However, the MC usually generates too many small triangle elements on the surfaces. Therefore, a simple, but loseless Polygon Reduction (PR) is applied to the iso-surfaces before converting to a STL file for LM. Detailed discussion of the system is given in the next few sections.

3. Multi-resolution Wavelet Transform

Although voxmap provides a very simple data structure for digitized models, it suffers from the limitations on resolution and storage. For digitized models, resolution is expressed in terms of the number of pixels (voxels) used in the x, y and z directions. Image with high resolution needs more pixels than that of low resolution. For instance, doubling the image resolution requires eight times more storage space in three dimension. On the other hand, resolution requirements are not the same for all applications. In practice, some applications need higher resolution and others trade higher resolution with faster access speed. To satisfy both demands, a multi-resolution wavelet transform is implemented in our system. The basic idea of multi-resolution wavelet transform is to express functions with a collection of coefficients, each of which has some limited information in both data size and resolution [14][15]. Using multi-resolution wavelet transform, users can easily retrieve both coarse and detail information of the model without heavy computation penalty. The Haar wavelet is chosen in this work. The benefit of the Haar wavelet is that it can be used with integer variables during transform. Therefore, storage size and computation time can be effectively reduced comparing to other wavelets using float or double variables. Next, the Haar wavelet and bit-remainder algorithm used in this system will be discussed.

3.1 Haar Wavelet



(a) scale function (b)wavelet function (c) scale functions for different resolution when n=2 (d) wavelet functions for different resolution when n=3.

Figure 2: Haar wavelet functions

Wavelet transform has two basic functions, scale(φ) and wavelet (ψ) functions as shown in Fig. 2. Before wavelet transform, one dimensional data with 2^n samples are mapped into initial scale functions ($\varphi_{n,j}$), where j varies from 0 to 2^n-1. From wavelet transform, samples are divided into two different regions, coarse and detail data by averaging and subtracting two neighboring samples. This process can be done recursively until there remains one element in the coarse data. Therefore, wavelet transform can be done for maximum n times if the data set

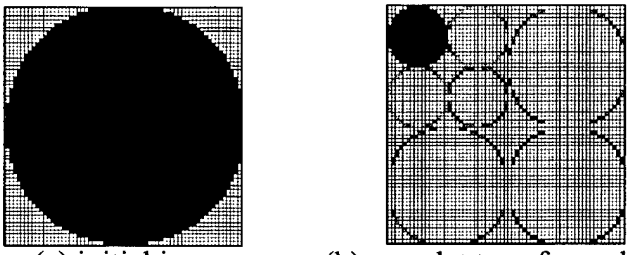
has 2^n samples. During transformation, wavelet and scale functions follow these relations in Eq. (1) through Eq. (3) and their shapes are represented as shown in Fig. 2(c) and (d).

$$\varphi_{i,j} = \varphi(2^i x - j) \tag{1}$$

$$\psi_{i,j} = \psi(2^i x - j) \tag{2}$$

$$\psi_{i,j} = \varphi_{i+1,2j+1} - \varphi_{i+1,2j} \tag{3}$$

where $\varphi(x) = 1$ for $(0 < x \leq 1)$ and 0 otherwise and $\psi(x) = 1$ for $(0 < x \leq 0.5)$, -1 for $(0.5 < x \leq 1.0)$, and 0 otherwise; $i=0,1,...,n-1$ and $j=0,1,\ldots,2^i-1$. If a data set consists of two-dimensional array such as a 2-D image, wavelet transform is applied to both row and column directions. Then, the size of the coarse data ($\varphi(y)\ \varphi(x)$) becomes one quarter of the previous coarse image after one transform. Fig. 3 shows an example when wavelet transform is applied twice in both row and column directions. The black circle in Fig. 3(a) is reduced to its 1/16 size as shown in the top left corner of Fig. 3(b) from two times wavelet transform and rest of the region in Fig. 3(b) indicates detail data



(a) initial image (b) wavelet transformed domain

Figure 3: wavelet transform for an image

3.2 Bit-remainder

After one wavelet transform, data is divided into two regions: coarse and detail data. Both must have exactly the same number of samples. Therefore, it is necessary to have data with 2^n samples in order to keep even numbers for every transform. If an image has an arbitrary size that does not match 2^n, artificial inflation to the nearest 2^n must be done before transforms. For example, an object with 144×128-pixel size image must be expanded to the size of 256×256 before wavelet transformation. Obviously, this artificial inflation increases the size of an image and wastes processing time. This problem is much more serious when we apply wavelet transform to voxmap since it is a three-dimensional array. To reduce this problem, a bit-remainder index is added to the wavelet transform [19]. With the bit-remainder index, images with arbitrary size can be transformed without artificial inflation. The basic idea of bit-remainder index is to keep the size of data in even for every wavelet transform. If the initial data set needs r times wavelet transform, a binary index array with r elements is created first; each index element corresponds to one wavelet transform. For wavelet transform with even array size, '0' is assigned to the index; for wavelet transform with non-even array size, '1' is assigned to the index and one null element is appended to the initial data set. In this way, data set maintains even for wavelet transform and bit-remainder index keeps track how many null elements are added. This process is reversible, i.e. the initial data set can be recovered from a reverse transform. A simple 2-D example can illustrate this method. Suppose a 2-D data set with 140×128 samples needs to have wavelet transforms for five times. Using this method, the

data size after each wavelet transform are: (70×64), (35×32→36×32), (18×16), (9×8→10×8), and (5×4). The second, fourth and fifth transforms produce non-even data size in x direction and null elements are added to the sample in x direction. The x- and y- bit-remainder indices become {0,0,1,0,1} and {0,0,0,0,0}. With the traditional wavelet transform, this data set need to be inflated to 256×256, while this method only adds ten index bits and two null elements (142×128).

4 Model Creation

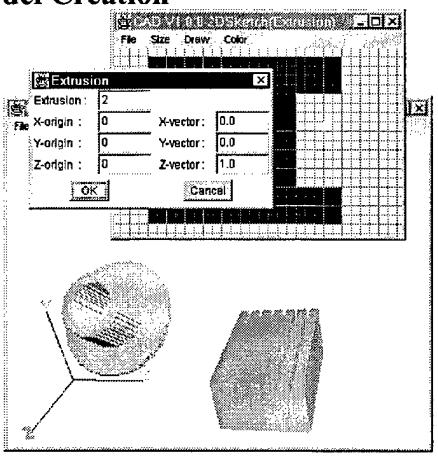


Figure 4: Object Creation

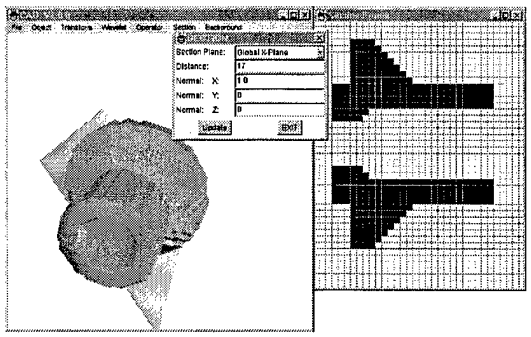


Figure 5: Section view and its local editing

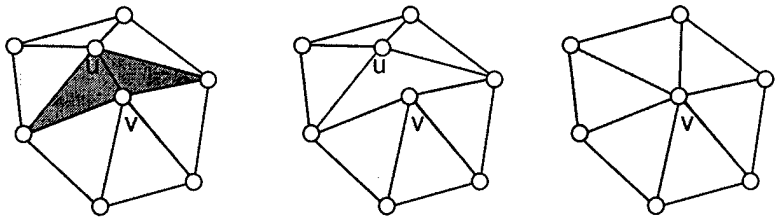
Two basic image operators, extrusion and revolution, are included in this voxel-based modeling system for model creation. A two dimensional canvas is called when designers need to create or modify an object. After designers paint the section shape in the canvas, the Minkowski addition operator is used to extrude the section with a given distance and direction [6][13]. Fig. 4 shows a two-dimensional canvas window, extrusion input dialog and parts created by extrusion and revolution. Model can be modified with the same way: voxels on the intersection plane are extracted to the two-dimensional editing canvas (Fig. 5).

5 Model Visualization

In order to visualize the voxel data, standard MC [9] is used for iso-surface extraction. Because one voxel has eight vertices, the number of different cases of occupied/non-occupied vertices is $2^8 = 256$. With the help of symmetric conditions, they are reduced to fifteen distinct cases. Based on this look-up table, one to four triangles are created in one voxel for the feature's boundary surface. With the MC algorithm, iso-surface generation from voxmap is simple and straightforward. But this algorithm tends to create so many triangles that enormous triangle entities reduce the over-all system performance and increase the time needed for generating StereoLithograph Contour file (SLC) for LM. To reduce the number of polygons from a set of triangles, a simple Polygon Reduction (PR) scheme is implemented in the system. There are many PR algorithms reported in the literature [4][5][10]. Cost of the edges are determined by the normal vectors of the surfaces as defined in Eq. (4) and the less the cost, the little there has geometric changes. Therefore, PR with zero cost is equal to the loseless polygon simplification.

$$\text{cost}(u,v) = \max_{n_u \in T_u} \left(\min_{n_{uv} \in T_{uv}} \left[(1 - n_u \cdot n_{uv}) \right] \right) \qquad (4)$$

where T_u is the set of triangles surrounding vertex u and T_{uv} is the set of two triangles share vertices u and v. n_u and n_{uv} are the normal vectors of the triangles in T_u and T_{uv}. Cost functions, cost(u,v) and cost(v,u), are different from the formulation. Since our goal is to merge unnecessary triangles without altering the shape, we only merge vertices when cost is zero. All the vertices in the voxmap will pass through this polygon reduction test until zero cost exists. Once the PR is completed, STL file can be generated easily because the whole surface of the model is covered with triangles, which matches the native format of STL files. At this point, the part is ready for LM.



(a) detect an edge (b) remove surfaces (c) update vertex

Figure 6: Surface Removal from each edge's cost function

6. Example

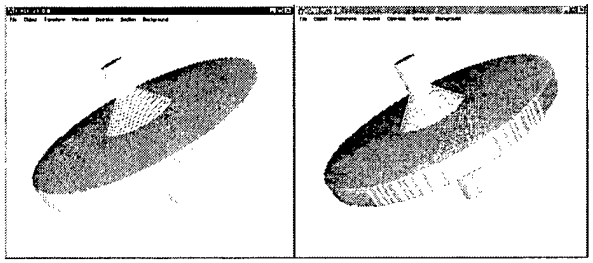


Figure 7: Initial voxel model (117×117×80)

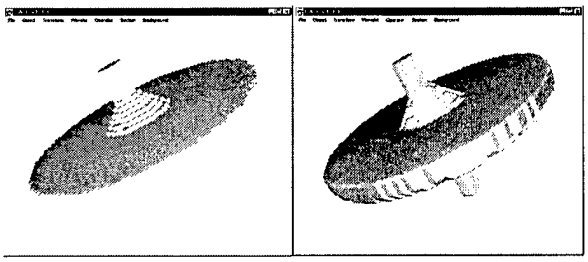


Figure 8: Wavelet transformed voxels(59×59×40)

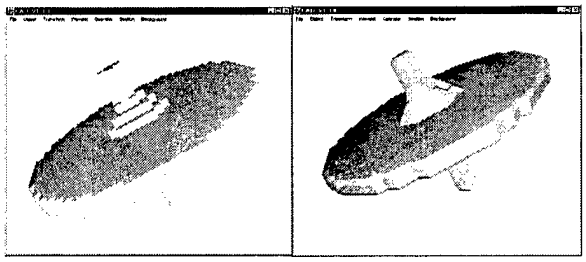


Figure 9: Wavelet transformed voxels (30×30×20)

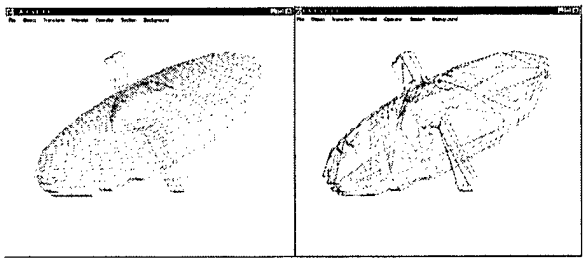


Figure 10: polygon reduction

In this section, simple models created from a voxel-based modeling system and fabricated by SLA-190 are presented. The initial model is created using revolving operator and stored in a 117×117×80 voxmap. Multi-resolution wavelet transform with bit-remainder indices is used twice to reduce the model size to 59×59×40 and 30×30×20. Models with different resolutions are displayed in two ways: voxel surface and iso-surface in Fig. 7 to Fig. 9. In the left hand side, voxel surface models with stair case effect in the center support region are displayed. In the right hand side, iso-surface models with smoothened surfaces are shown. Comparison among different resolutions is listed in Table 1. Due to the multi-resolution characteristics, the number of voxels, vertices, edges and triangles are decreased significantly after wavelet transform. To fabricate this component using LM, we applied polygon reduction to reduce the number of

triangles. As an example, we took the final shape from Fig. 9 and applied the polygon reduction scheme. The results are shown in Fig. 10. In the last row of Table 1, numbers of triangles after polygon reduction for different resolutions are listed for comparison. From triangles and normal vectors generated from PR, STL files are created and parts are built in the SLA-190 machine as shown in Figure 11. The sample ratio among these three objects with different resolution is 1:1, 1:8 and 1:64 due to multi-resolution wavelet transforms. For comparing the difference in resolution, parts are scaled up so that all features have the same dimension as shown in Fig. 11(b).

Table 1. Models with different resolutions

voxmap size	117×117×80	59×59×40	30×30×20
total voxels	1,095,120	139,240	18,000
vertices	29,530	7,600	1,830
edges	88,584	22,794	5,484
triangles	59,056	15,196	3,656
triangles with PR	1,940	1,100	446

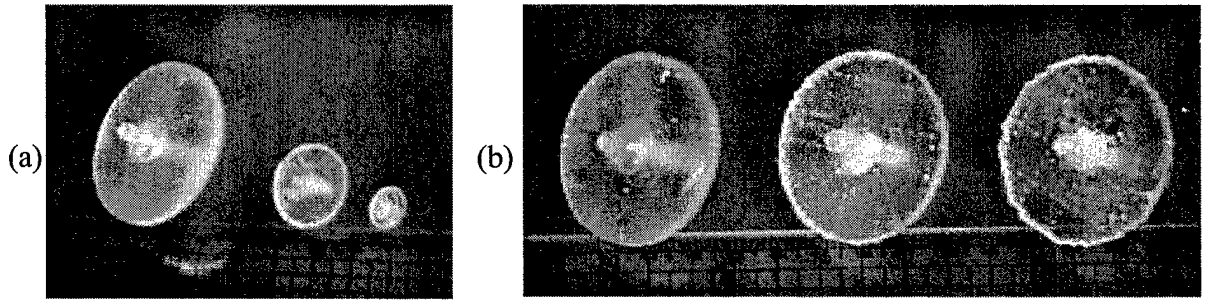


Figure 11: Parts from SLA-190. (a) parts built with same voxel size (b) parts scaled-up to the initial size.

7. Conclusion

Voxel-based modeling system that supports multi-resolution was presented in this paper. This system is programmed with Java and Java3D API. It is portable to any system as long as a Java compiler is presented. To control the size of the data set, wavelet transform and bit-reminder index are applied. We found that multi-resolution function is very useful when the balance between model quality and process efficiency is needed. Simple Boolean operators and section editing functions are implemented in the system but much more need to be done. In addition, model after PR can be easily converted to STL files for LM. To further accuracy improvement to the wavelet transformed model, combination of voxels with different resolution is under development.

8. References

[1] Chandru, V., Manohar, S., and Prakash, G., Voxel-based modeling for layered manufacturing, IEEE Computer Graphics and Applications, pp. 42-47, November, 1995.

[2] Chandru, V., Manivannan, M., and Manohar, S., Minkowski operator and features of voxel models, DETC-99/DAC-8629, September 12-15, Las Vegas, 1999.

[3] Chen, Y., Zhu, Q., Kaufman, A., Physically-based animation of volumetric objects, IEEE Computer Animation '98, pp. 154-160, 1998.

[4] Cohen, J., Olano, M., Manocha, D., Appearance-Preserving Simplification, SIGGRAPH 98, 115-122, Orlando, Florida, July 19-24, 1998.
[5] Hoppe H., Progressive Meshes, SIGGRAPH 96, 99-108, Louisiana, August 4-9, 1996.
[6] Ghosh, P., A unified computational framework for Minkowski Operators, Computer & Graphics, 17(4):357-378, 1993.
[7] Gibson., S., Fyock, C., Grimson, E., Kanade, T., Kinis, R., Lauer, H., McKenzie, N., Mor, A., Nakajima, S., Ohkami, H., Osborne, R., Samosky, J., Sawada, A., Simulating Surgery using Volumetric Object Representations, Real-Time Rendering and Haptic Feedback, MERL technical Report, TR96-16, 1996.
[8] Kaufman, A., Cohen, D., and Yagel, R., Volume Graphics, IEEE Computer, pp. 51-64, July 1993.
[9] Lorensen, W., Harvey, E., Marching Cubes: A High Resolution 3D Surface Construction Algorithm, ACM Computer Graphics, 21(24):163-169, July 1987.
[10] Melax, S., A Simple, Fast, and Effective Polygon Reduction Algorithm, Game Developer, pp. 44-49, November, 1998.
[11] Muraki, S., Volume Data and Wavelet Transforms, IEEE Computer Graphics & Applications, pp. 50-56, 1993.
[12] Muraki, S., Multiscale Volume Representation by a DOG Wavelet, IEEE Transactions on Visualization and Computer Graphics, 1(2):109-116, June, 1995.
[13] Sethia, S., Manohar, S., Minkowski Operator for Voxel-based Sculpting, Computer and Graphics, 22(5):593-600, 1998.
[14] Stollinitz, E., DeRose, T., Salesin, D., Wavelets for Computer Graphics: A Primer Part I, IEEE Computer Graphics and Applications, 15(3):76-84, May, 1995.
[15] Stollinitz, E., Derose, T., Salesin, D., Wavelets for Computer Graphics: Theory and Applications, Morgan Kaufmann Publishers, Inc., 1996, ISBN;1-55860-375-1.
[16] Wan, M., Qu, H., Kaufman, A., Virtual flythrough over a voxel-based terrain, IEEE Virtual Reality Conference, pp. 53-60, March, 1999.
[17] Wright, J., Hsieh, J., A Voxel-based forward projection algorithm for rendering surface and volumetric data, IEEE Visualization '92, pp. 340-348, Los Alamitos, CA, October, 1992.
[18] Wu, Z., Seah, H., and Lin, F., NURBS Volume for Modelling Complex Objects, chapter 9, pp. 159-167, Chen, M., Kaufman, A., and Yagel, R. (Eds), Volume Graphics, Springer 2000, ISBN:1-85233-192-5.
[19] Yim, S., and Gea, H., Development of an Image-based CAD using Wavelet Transform, Proceeding of ASME, DETC00/ DAC-14262, September 10-13, 2000.

RAPID PROTOTYPING USING FRACTAL GEOMETRY

S.C. Soo and K.M. Yu
Department of Manufacturing Engineering, The Hong Kong Polytechnic University, Hong Kong

Abstract

The paper proposes a method for rapid prototyping (RP) fractal geometry represented objects. RP technology has made possible the physical fabrication of solid freeform objects. However, contemporary CAD/CAM/RP systems are developed for Euclidean geometry and are incapable of handling self-similar fractal objects (e.g. jewelry products). To address the problem, a Radial-Annular Tree (RAT) data structure is proposed to represent Iterated Function Systems (IFS) fractal curves. RP toolpaths can then be generated from the RAT data structure. Geometry modeled in the RAT data structure can also be combined with Euclidean geometry from traditional CAD systems to make aesthetic patterns for the jewelry industry.

Introduction

Rapid prototyping (RP) technology has made possible the physical fabrication of solid freeform objects. The input to RP is either a solid model or closed surface model prepared from computer-aided design (CAD) systems. However, the contemporary CAD or RP systems are developed for Euclidean geometry. It is thus beneficial to widen the geometric scope of CAD and RP to non-Euclidean geometry. For instance, many products in jewelry industry will adopt aesthetic appealing patterns existed in nature. In mathematics, natural objects, likes clouds, terrain, trees, can be described by fractal geometry. In order to fabricate jewelry prototype, a CAD model for fractal geometry is needed.

Kerekes [1] is probably the first to generate a fractal tree structure in three dimensions with Stereolithography (SL) RP machine. The example is generated without any help from CAD as the structure is extremely complex. However, Kerekes has not reported much details. Lee [2] has reviewed various commercial CAD systems being used for fractal design. All software have functions for 2-D fractal image generation and processing, but none of them has addressed the 3-D fractal object rapid prototyping. In jewelry making, Lee *et al* [3] has proposed an integrated CAD and RP approach. The discussion is only based on Euclidean geometry domain. In fact, CAD and RP systems available in the market for jewelry making cannot handle fractal geometry yet.

In this research, RP of fractal geometry is achieved indirectly. Fractal geometry is first modeled into some computer understandable format. The information is then imported to Euclidean CAD. Conventional CAD modeling and editing operations are applied before RP tool path is generated for making the physical fractal geometry prototype.

The Fractal Geometry

From the foundation work of Mandelbrot [4], fractal geometry provides a way to describe and to model aesthetic object, especially for those not easily created by Euclidean geometry. Fractal is by definition a set for which the Hausdorff-Besicovitch dimension strictly exceeds the topological dimension. It is used to describe the fragmentation of an object. A

common property of fractal object is self-similar, i.e. a fractal is a shape made of parts similar to the whole in some way. One deterministic approach to generate or to approximate a mathematical fractal object is to use **Iteration function system (IFS)** [5]. An IFS is a family of specified contraction mappings that map a whole object onto the parts, unionize all the parts and iteration of these mappings will result in convergence to an invariant set [6], i.e. a fractal. From the viewpoint of geometric modeling, unionization in IFS is regularized in order to maintain the validity of the operands in further iteration. Thus the equation of **Regularized Iterated Function System** generation is

$$F^k(S) = F(F^{k-1}(S)) = \bigcup_{i=1}^{n} {}^{*} f_i(F^{k-1}(S)) \qquad k = 2, 3, \ldots \quad (1)$$

where S = self-similar segment, F= iterated function, and n=iteration number.

In this research, focus will be put on 2D fractal curves. In particular, the quadric Koch curve will be used to illustrate the methodology. Fractal curves are self-similar and continuous, but they are nowhere differentiable. The quadric Koch curve consists of a *generator* and an *initiator*. The generator is a multi-segment polyline (S) which is also used to derive the IFS. The initiator is a square which is used to derive transformations for replicating other copies. Figure 1 shows an 18-segment quadric Koch curve. The IFS has totally eighteen functions $F=\{f_1, \ldots, f_{18}\}$ that will contribute to a combined transformation from the whole S to each parts $f_i(S)$. According to Equation (1), the number of transformations in the IFS equals to eighteen (i.e. n = 18), such that

$$F^k(S) = F(F^{k-1}(S)) = \bigcup_{i=1}^{18} {}^{*} f_i(F^{k-1}(S)) \qquad (2)$$

The Radial-Annular Tree data structure

In order to represent an IFS generated fractal curve in a computational form, a RAT data structure is developed [7]. The RAT data structure is based on a vertex-link scheme. The data node of RAT consist of three elements, a set of coordinate values, a *sibling* pointer and a *child* pointer. The geometry information of a vertex is its coordinate values. The sibling pointer points to the next node in same level. The child pointer points to the next higher-level node in order to inherit lower level information. Figure 1 also illustrates the RAT levels corresponding to the 18-segment quadric Koch curve. To generate the tool path for RP, the circumferential nodes of the RAT will be traversed.

Capability of RAT data structure

In addition to direct making of fractal curve, the RAT data structure can also combine with Euclidean geometry in traditional CAD systems to model aesthetic patterns for jewelry industry.

Fractal curve on free-form surface

A fractal pattern for engraving or embossing can be prepared by projecting a fractal curve onto a free-form surface. Figure 2 shows an example which parallel projects an 18-segment quadric Koch curve onto a NURBS surface. $\overset{\mathbf{v}}{P}_{Hole}$ denotes a punctured NURBS surface

while $\check{P}_{Trim}$ denotes a trimmed NURBS surface with the projected fractal curve $\check{P}_{fractal}$. $\check{P}_{Hole}$ is formed by subtracting the original NURBS surface with a projected volume of fractal curve while $\check{P}_{Trim}$ is formed by subtracting the original NURBS surface with $\check{P}_{Hole}$. Mathematically,

$$\check{P}_{Hole} = \check{P}_{NURBS} - Vol_{proj}\left(\check{P}_{fractal}\right)$$

$$\check{P}_{Trim} = \check{P}_{NURBS} - \check{P}_{Hole} = \check{P}_{NURBS} - \left[\check{P}_{NURBS} - Vol_{proj}\left(\check{P}_{fractal}\right)\right]$$

The interior of the projected fractal curve $\check{P}_{fractal}$ forms $Vol_{proj}\left(\check{P}_{fractal}\right)$ by intersecting with the modeling work space, W, i.e.

$$Vol_{proj}\left(\check{P}_{fractal}\right) = \left\{(x,y,z) \mid \exists (x,y,z') \in \check{P}_{fractal}\right\} \cap W \quad (3)$$

where z' is arbitrary selected with no duplication. In practice, the coordinate values of the RAT represented $\check{P}_{fractal}$ are translated, scaled and projected onto the NURBS surface. Thus, a variant of the 18-segment quadric Koch curve with piecewise free-form curve segment is generated.

Fractal solid modeling

In order to construct a solid model with fractal boundary, the RAT represented fractal curve can be transformed in Euclidean CAD system. The fractal curve is treated as the operand point set for extrusion, revolution, lofting, sweep, etc. [8]. Figure 3 shows the workflow of embedding the RAT represented fractal curve into contemporary CAD work flow. Figure 4 shows a twist-extruded fractal solid with twice iterated 18-segment quadric Koch curve. Figure 5 shows a twist-extruded fractal solid with offset twisting vector. Figure 4 shows a revolved fractal solid in three quarters turn. Figures 7 and 8 show a lofted fractal solid and a spirally lofted fractal solid respectively. In the above illustration examples, the RAT information of a particular fractal curve level is communicated with Euclidean CAD system via IGES.

Discussion and Conclusion

A workflow for rapid prototyping fractal geometry has been outlined. This is demonstrated with a 2D quadric Koch curve. It can be seen that the RAT data structure plays a central role in bridging the gap between fractal geometry and Euclidean geometry. Figure 8 shows other fractal curves [9] with different generators and/or different initiators that can be constructed using the generation scheme. However, the RAT data structure is applicable for fractal curves that can be formulated in IFS. Other data structure may be needed for non-IFS fractal curve.

The approach also provides a user-friendly way to design jewelry products, such as pendant, button, bangle/bracelet, brooch, medal and cufflinks. To further extend the geometric coverage, true fractal solids like Meger sponge [10] can also be integrated with Euclidean CAD.

Acknowledgement

This work described in this paper has been supported by the Research Grants Council of Hong Kong, China (Project No. PolyU 5141/98E).

References

[1] T. Kerekes, "Stereolithography builds computer-generated models of natural forms", Rapid Prototyping Report, CAD/CAM Publishing, Vol.2, No.4, p.1, 1992.

[2] P.N. Lee, http://home.att.net/~Paul.N.Lee/Fractal_Software.html#top

[3] H.B. Lee, M.S.H Ko, R.K.L. Gay et al., "Using computer-based tools and technology to improve jewellery design and manufacturing", International Journal of Computer Applications in Technology, Vol.5, No. 1, pp.72-80, 1992.

[4] B.B. Mandelbrot, The Fractal Geometry of Nature, W.H. Freeman and Company, 1982.

[5] M.F. Barnsley, Fractals Everywhere, Academic Press, second edition, 1993.

[6] J.E. Hutchinson, "Fractals and Self Similarity", Indiana University Mathematics Journal, Vol.30, No.5, pp.713-747, 1981.

[7] S.C. Soo & K.M. Yu, "Toolpath Generation for Fractal Curve Making", International Journal of Advanced Manufacturing Technology, in press.

[8] I. Zeid, CAD/CAM Theory and Practice, McGraw Hill, 1991.

[9] R.T. Stevens, Understanding Self-similar Fractals, R&D Technical Books, 1995.

[10] S.C. Soo & K.M. Yu, "Rapid prototyping for self-similarity design", Proc. of the 9th International Manufacturing Conference in China, Vol. II, Aug 16-17, 2000, Hong Kong, pp.93-94.

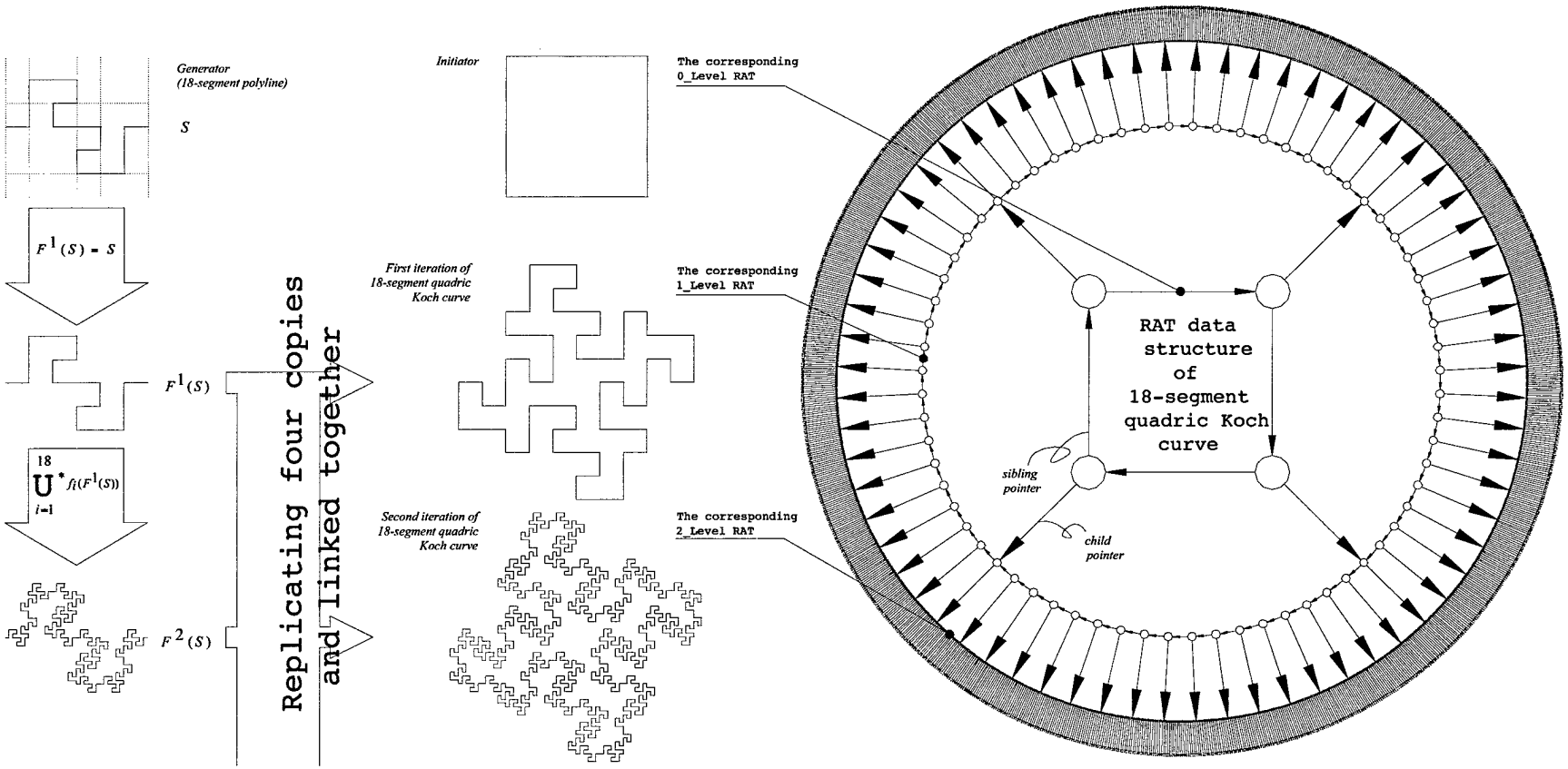


Figure 1. An 18-segment quadric Koch curve and the corresponding Radial-Annular Tree data structure.

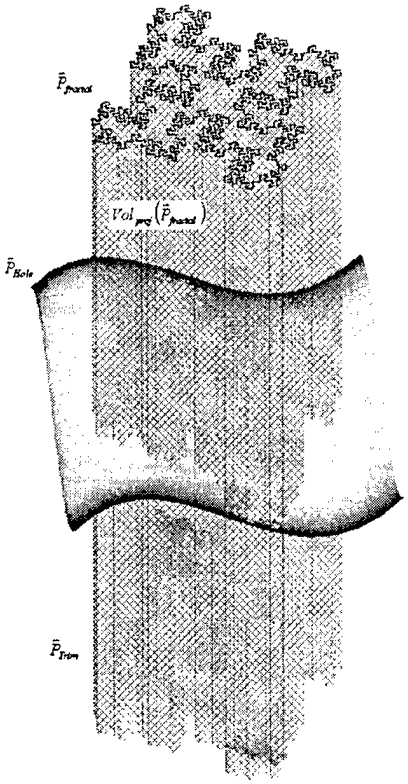


Figure 2. Free-form surface trimmed with a projected Koch snowflake curve.

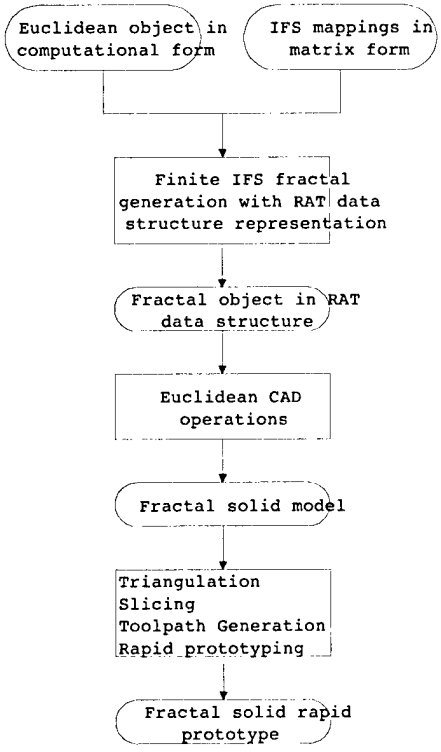


Figure 3. Fractal solid rapid prototyping workflow.



Figure 4. Twisted extrusion with coaxial twisting vector.

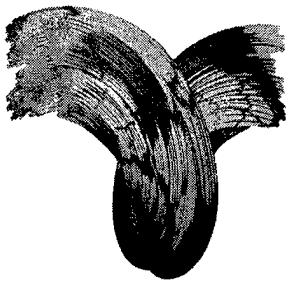


Figure 5. Twisted extrusion with offset twisting vector.

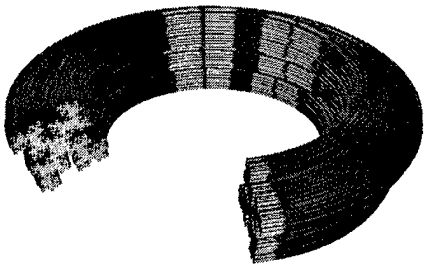


Figure 6. Revolution generated fractal solid.

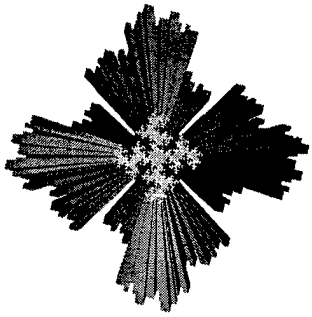
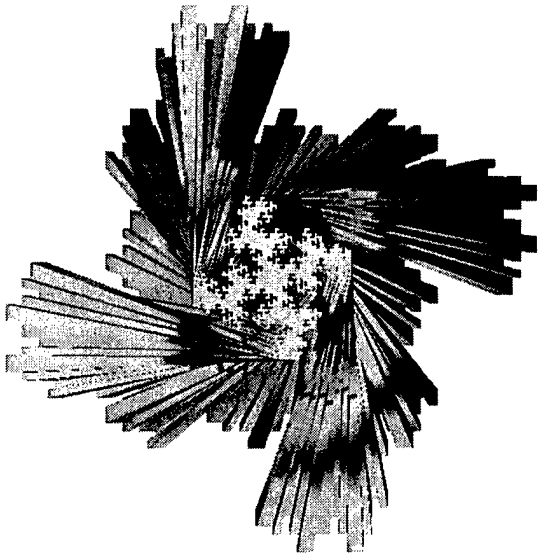
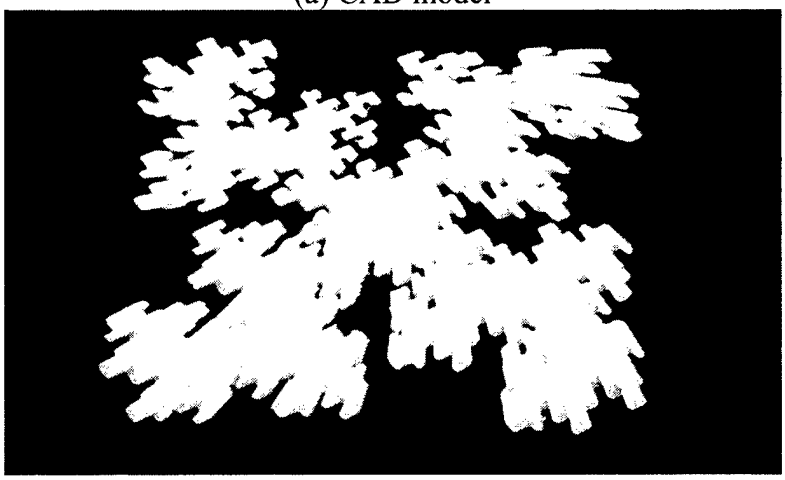


Figure 7. Lofting with cross-sections in different scales.



(a) CAD model



(b) FDM prototype

Figure 8. Lofting with cross-sections in different scales and orientations.

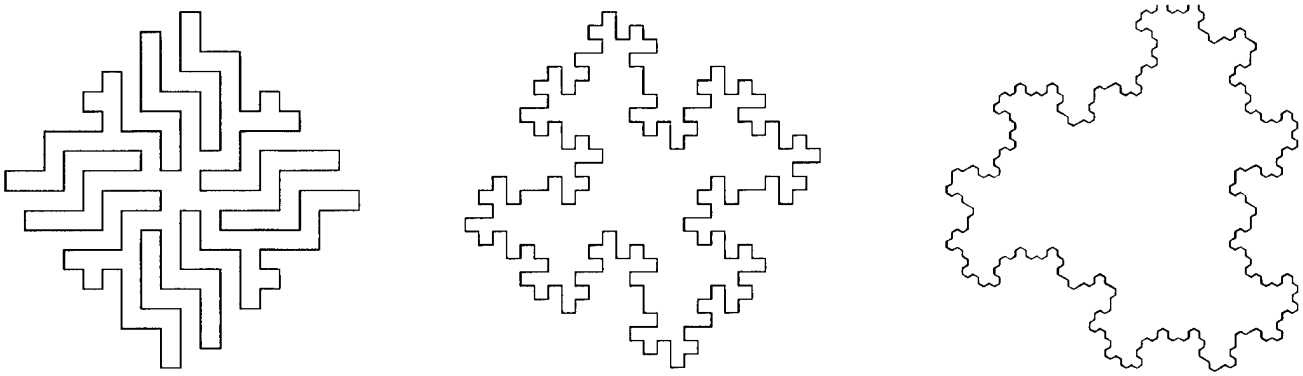


Figure 9. Other quadric Koch curves (a, b) and Fudgeflake boundary curve (c).

Melt Pool Size Control in Thin-Walled and Bulky Parts via Process Maps

Aditad Vasinonta, Jack L. Beuth and Raymond Ong
Department of Mechanical Engineering
Carnegie Mellon University
Pittsburgh, PA 15213

Abstract

Control of melt pool size is critical for maintaining consistent build conditions in the solid freeform fabrication of complex shapes. In this research, melt pool size in laser-based solid freeform fabrication processes is studied for both thin-walled structures and bulky parts. Numerical simulations are used to construct non-dimensional plots (termed process maps) that quantify the effects of changes in part height, laser power, deposition speed and part preheating on melt pool size. Strategies for the control of melt pool size suggested by the process maps are similar for the two geometries. Insights are given as to how transitions between these two extremes in geometry can be managed to maintain a consistent melt pool size. This modeling work is being performed in tandem with process development and melt pool imaging and control research underway on the LENS process at Sandia National Laboratories.

Nomenclature

T	= temperature in degrees Kelvin	T_m	= melting temperature
T_{base}	= base plate and wall preheat temperature	Q	= laser power
α	= fraction of laser power absorbed by the wall	V	= laser velocity
k	= thermal conductivity	ρ	= density
c	= specific heat	t	= wall thickness
L	= part length	h	= part height
W	= bulky part width	d	= melt pool depth
l	= melt pool length	w	= melt pool width

Introduction

A critical issue in developing solid freeform fabrication (SFF) processes as rapid manufacturing techniques is the control of "build conditions," defined as thermal conditions allowing a particular part to be fabricated. Consistency in build conditions is typically defined in terms of a consistent melt pool size during the construction of a part or feature. Previous work by the authors [1-3] has investigated this issue for 2-D thin-walled structures and has presented strategies for controlling build conditions (by maintaining a consistent melt pool size) while also limiting residual stresses (by controlling thermal gradients). The control of melt pool size and thermal gradients in 2-D thin-walled structures was addressed via three-dimensional plots of dimensionless process variables (termed process maps) developed from thermal models of laser-based material deposition.

Current research extends the process map concept developed for 2-D thin-walled structures to 3-D bulky parts. A process map for melt pool size for bulky parts has been

developed through thermal simulations of a simple 3-D structure. It addresses the effect of changes in process variables (laser power, laser velocity and part preheat temperature) and geometry (part height) on melt pool size. Comparing the process maps for thin-walled and bulky structures provides insight into how to control melt pool size for these two extremes in geometry and how to handle transitions between them in a single part. Furthermore, an understanding of these two basic types of structures can form the basis for understanding process control issues in the building of much more complex shapes.

The principal application of this work is to the Laser Engineered Net Shaping (LENS) process currently under development at Sandia National Laboratories [4]. The process maps presented in this paper have been developed to aid in both manual and automated process control efforts currently underway at Sandia Labs [5]. Although this research is directed toward the LENS process, the approach taken is applicable to any solid freeform fabrication process involving a moving heat source. Similarly, although stainless steel (SS304) is treated in the current work, the same approach can be applied to other materials.

In the next section, the 2-D and 3-D structures analyzed in this study are presented, along with details of the finite element models and boundary conditions used. Nondimensionalization schemes used to develop the process maps for both geometries are given. In the succeeding section, the process maps are presented with rules for how results can be applied to the prediction and control of melt pool size. A comparison of melt pool sizes between the two geometries is then presented. Finally, process control-related insights for transitions between the two geometries are discussed.

Geometry Considered, Numerical Model and Analytical Solution

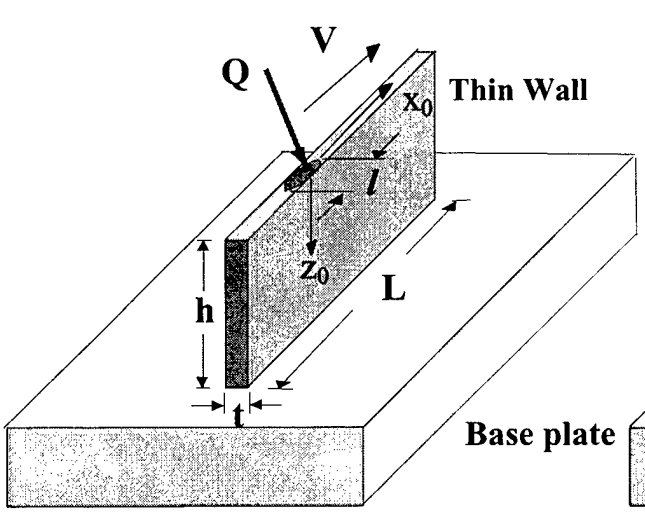


Figure 1a. Thin-Walled Structure

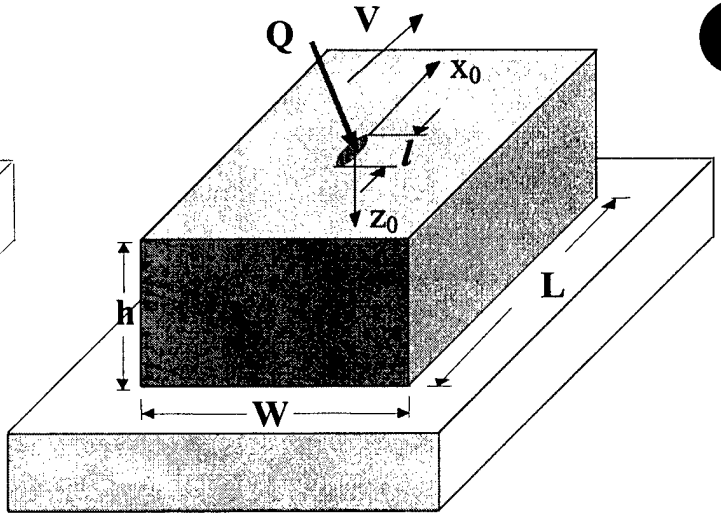


Figure 1b. Bulky Part

Schematics of both the thin-walled and bulky part geometries are shown in Fig. 1. In the LENS process, parts are constructed by focusing a high power laser onto a metal substrate, where streams of metallic powder are simultaneously injected. The laser locally melts the powder to form a molten melt pool on the top surface of the growing part. By moving the laser beam, the material is added to the part and the part is built up line-by-line and layer-by-layer.

In the modeling of this study, it is assumed that both the thin-walled and bulky parts are fabricated on large fixed-temperature metallic substrates, which act as thermal heat sinks. Models are also constructed such that the distance traveled by the laser and the length of the structures in the x-direction are large enough that steady state thermal conditions exist at the melt pool. Numerical models used in this study do not include the effect of convective heat transfer from the wall free surfaces to the surrounding air and do not model convective flows in the melt pool itself. Work by Dobranich and Dykhuizen [6] suggests strongly that the role of these effects in determining melt pool size is not significant. The models of this study also represent the laser as a point source of heat, neglecting the distribution of laser power over the melt pool region. Assuming a point source of power is reasonable given the goal of this study, which is to capture *changes* in melt pool size and other parameters as a function of *changes* in the process variables outlined above. Accuracy in the absolute predictions is of secondary importance. However, comparisons between experimentally determined melt pool sizes for thin-walled structures and model predictions show reasonable agreement [3].

The meshes and boundary conditions used for typical 2-D thin-walled and 3-D bulky part thermal models are shown in Figs. 2 and 3 respectively. For both geometries, a concentrated heat source moves across the top surface of the model, which is initially at a uniform temperature $T = T_{base}$. The finite element models have been created using the ABAQUS software package. Because of high temperature gradients in the region near heat source, the grid of each model is biased toward the region that will surround the heat source at the time when results are to be extracted from the model. In addition to comparisons with analytical solutions valid for large substrates, the convergence of each mesh was checked against a model with roughly half the resolution with no noticeable change in the results.

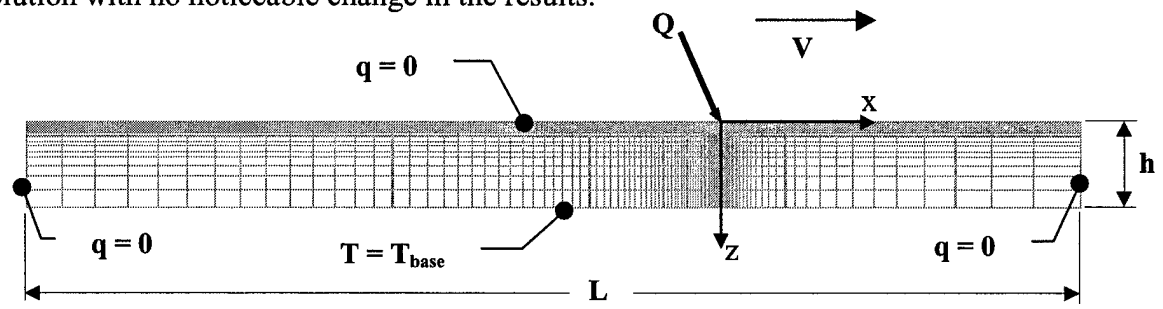


Figure 2. 2-D Thermal Model and Boundary Conditions

For the case of a thin-walled structure, four-noded bilinear thermal elements were used to form the mesh of the 2-D model. It is assumed that the thin wall is fabricated by depositing material along a single row; thus, the thickness of the wall is comparable to the melt pool size. As illustrated in Fig. 2, an insulated boundary condition is imposed on the top and both vertical sides of the substrate. Sensitivity studies have shown that thermal results are not significantly affected by boundary conditions along these surfaces being specified as either insulation or convection. By using a 2-D model, it is also assumed that there is no heat loss through the front and back surfaces. The temperature along the substrate bottom is specified as fixed at the value equal to the temperature of the base plate.

A typical mesh for a 3-D bulky part simulation is shown in Fig. 3, generated using eight-noded linear brick thermal elements. Because of symmetry across the X_0-Z_0 plane, only half of

the 3-D structure is modeled. Analogous to the 2-D model, insulated boundary conditions are imposed on all free surfaces. The heat flux across the symmetry plane (the X_0-Z_0 plane) is set to zero and the temperature of the substrate bottom is held at the temperature of the base plate.

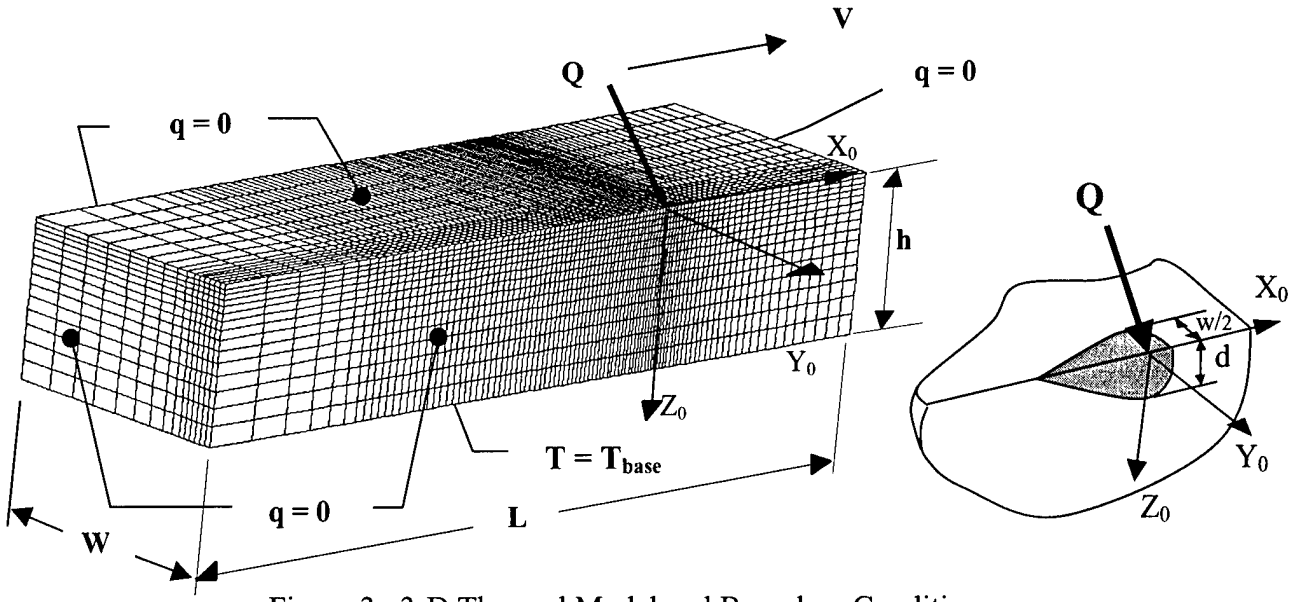


Figure 3. 3-D Thermal Model and Boundary Conditions

Thermal properties of AISI 304 stainless steel (SS304), which is used in the LENS and other SFF metal deposition processes, are used as inputs for the temperature-dependent simulations. Thermal properties were taken from [7] and are also comparable to those used by Chin, et al. [8] and Klingbeil, et al. [9] in thermomechanical modeling of the Shape Deposition Manufacturing process. The properties used in the model that are set to depend on temperature are specific heat and thermal conductivity. The latent heat of the liquid-solid phase transition is also included in the model.

The normalization schemes used to develop process maps in this paper are based on the analytical solutions of conductive heat transfer by Rosenthal [10]. Representation of numerical simulation results in terms of the normalized variables defined below is exact only in the case of temperature-independent thermal properties. The goal of developing process maps for laser-based SFF processes is to use dimensionless variables to collapse a large number of numerical simulations into an easily used format, keeping errors caused by temperature dependent properties within acceptable limits. As suggested by the Rosenthal solution for a point source of heat moving across a 2-D semi-infinite thin substrate, a process map for melt pool size for a thin-walled structure is represented through three dimensionless variables: the normalized melt pool length ($\bar{l}$), the normalized height of the substrate ($\bar{h}$) and the normalized melting temperature ($\bar{\bar{T}}_m$), which are defined as follows:

$$\bar{l} = \frac{l}{2k/\rho cV}, \qquad \bar{h} = \frac{h}{2k/\rho cV} \qquad \text{and} \qquad \bar{\bar{T}}_m = \frac{T_m - T_{base}}{\alpha Q/\pi kt}. \tag{1}$$

Using this normalization scheme, results for normalized melt pool length, $\bar{l}$, are presented as a function of normalized wall height, $\bar{h}$, and normalized melting temperature, $\bar{\bar{T}}_m$.

Analogous to the case of a 2-D thin wall, the 3-D conductive heat transfer solution by Rosenthal suggests that the process map for melt pool size of a bulky part can be represented by three dimensionless variables: the normalized melt pool depth ($\bar{d}$), the normalized height of substrate ($\bar{h}$) and the normalized melting temperature ($\bar{T}_m$). The melt pool depth is chosen to represent the size of melt pool for 3-D bulky parts because it can be related to how well newly deposited material is fused to the top surface of the part. The dimensionless variables for the process map for bulky parts are defined as follows:

$$\bar{d} = \frac{d}{2k/\rho cV}, \qquad \bar{h} = \frac{h}{2k/\rho cV} \qquad \text{and} \qquad \bar{T}_m = \frac{T_m - T_{base}}{\left(\alpha Q/\pi k\right)\left(\rho cV/2k\right)}. \tag{2}$$

Note that the normalized melting temperature ($\bar{T}_m$) for the two geometries is defined differently.

Process Map for 2-D Thin-Walled Structures

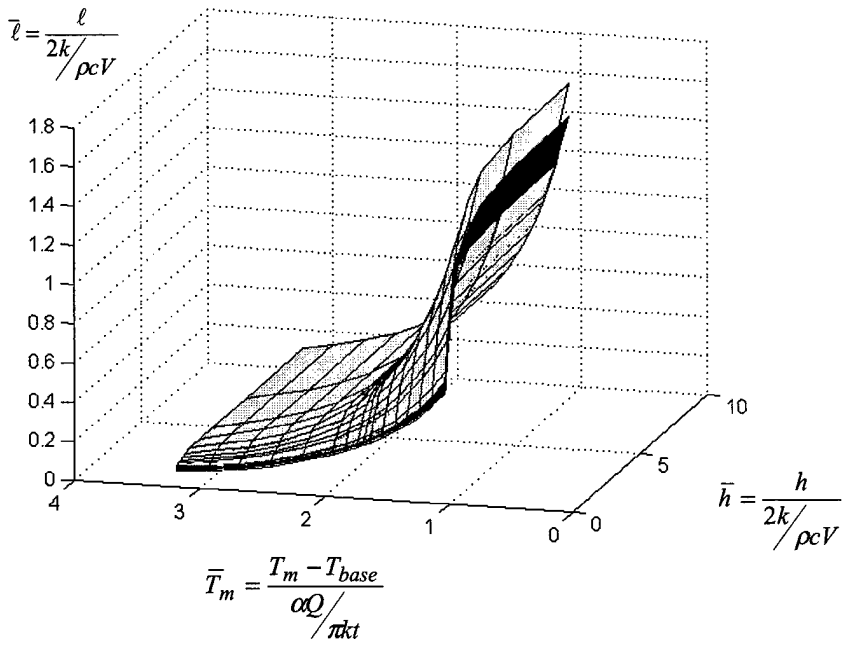


Figure 4. Process Map for Melt Pool Length for 2-D Thin-Walled Structures

A process map for melt pool length for a thin-walled structure with a concentrated laser heat source moving across it has been developed and reported in [1-3]. The work described in [1] uses slightly different normalization rules than the more accurate rules used in [2], [3] and herein. The process map, which is shown in Fig. 4, consists of three surfaces plotted on three coordinate axes. The middle surface was developed from several numerical simulations with temperature-independent properties performed with differing wall heights in order to get the dependence of $\bar{l}$ on $\bar{h}$. The dependence of $\bar{l}$ on $\bar{T}_m$ was then determined from the same simulations by assuming different values of T_m. The results from temperature-dependent simulations are also represented in Fig. 3 by upper and lower surfaces that bound the temperature-independent results. The space between these surfaces reflects the range in results seen when process variables are varied over the range of specific interest in the LENS process.

That range consists of values of αQ from 43.2 to 165 W, V from 5.93 to 9.31 mm/sec and T_{base} from 30° C to 400° C. The maximum range in values of $\bar{l}$ for fixed $\bar{h}$ and $\bar{T}_m$ due to the temperature dependence of properties is less than 13% of the nominal value of $\bar{l}$. Thus if the mean values of $\bar{l}$ for a fixed value of $\bar{T}_m$ are consistently used, the maximum error is ± 6.5%.

The detailed assumptions and procedures for obtaining and using the process map for melt pool length are given in [3]. In brief, the process map of Fig. 4 can be used effectively for SS304 deposition within the range of process parameters of interest in the LENS process by applying the following four rules:

1. Properties of SS304 at 1000 K are used in the normalization;
2. For cases involving a change in preheat, a linear change in thermal conductivity with a preheat temperature is assumed, as given in the following equation,
$$k = 24.3 + 0.013(T_{base} - 30) \quad W/(mK); \tag{3}$$
3. For predicting steady-state melt pool lengths due to a change in process variables, wall thickness is assumed to scale proportionally with melt pool length; and
4. It is assumed that the melt pool length/wall thickness scaling is unaffected by velocity.

Melt pool sizes determined by real-time thermal imaging experiments [5] have been compared with model predictions using the process map of Fig. 4 and the rules outlined above [3]. Reasonable agreement is seen in melt pool length values and the predictions of the process map clearly capture the trends in the measured results.

Process Map for 3-D Bulky Structures

In this section, results are presented from modeling the LENS process for deposition of SS304 to form 3-D bulky parts. The normalization scheme for 3-D structures given in eq. (2) is used. The process map has been developed using concepts similar to those used for 2-D thin-walled structures; however, melt pool depth is chosen to be the parameter representing melt pool size instead of melt pool length. Melt pool depth is chosen because it determines how much of the top of the existing layer is melted by a newly deposited layer. In laser-based SFF processes, controlling melt pool depth as a part is built is important for ensuring fusion at interlayer boundaries. If the melt pool depth is too small, not enough of the top portion of the existing material will be melted during deposition and poor interlayer bonding will result.

Although it is important to control melt pool depth to ensure part quality, it is a difficult parameter to monitor by thermal imaging or other methods. However, the 3-D Rosenthal solution for a point heat source moving across a semi-infinite substrate suggests that, for a tall bulky part, the depth of the melt pool is identical to one half of the width of the melt pool, independent of laser power, laser velocity and preheat temperature. Thus for tall parts, melt pool widths measured via thermal imaging techniques can be compared directly to predicted melt pool depths. Also, it is planned to use thermal model results to quantify the ratio of melt pool width to melt pool depth as a function of part height, to facilitate the use of real-time thermal images of melt pool width to precisely control melt pool depth. It should be noted that it is also possible to relate melt pool areas, which are easily extracted from thermal images, to melt pool depths. However, if changes in laser velocity are allowed, the ratio of melt pool area to

melt pool depth will be a function of laser velocity, laser power and preheat temperature in addition to part height. Because of this, melt pool width is generally a more useful measurable parameter to control as a means for controlling melt pool depth.

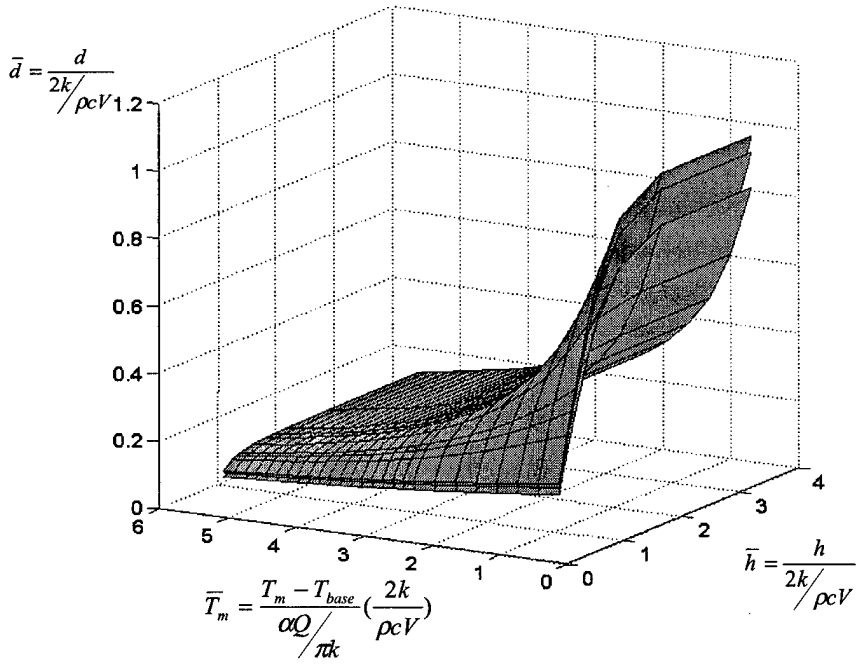


Figure 5. Process Map for Melt Pool Depth for 3-D Bulky Structures

The process map developed for 3-D bulky parts (shown in Fig. 5) consists of three surfaces plotted on three coordinate axes, generated using several numerical models with different part heights. Similar to the process map for 2-D thin-walled structures, the middle surface is generated from simulations assuming temperature-independent properties. Within the limitation of this assumption, this surface is very general and is applicable to any laser-based SFF process involving thermal deposition of any single material. The two bounding surfaces developed from temperature-dependent simulations reflect the range in results seen when process variables are varied over the range of practical use in the LENS process.

As for the process map for thin-walled structures, results from temperature-dependent simulations are normalized using the properties of 304 stainless steel at 1000 K, with the linear change in thermal conductivity as given in eq. (3) applied for cases involving a uniform preheat. The maximum range in values of $\bar{d}$ for fixed $\bar{h}$ and $\bar{T}_m$ is 16% of the nominal value of $\bar{d}$. Thus if the mean values of $\bar{d}$ for a fixed value of $\bar{T}_m$ are used, the maximum error is ± 8%, which is slightly higher than the range of melt pool lengths ($\bar{l}$) for the process map for 2-D thin-walled structures. If properties at 1100 K are used to normalize the 3-D results, maximum errors can be further reduced to approximately ± 6.5%. However, use of the same normalization scheme for both thin-walled and bulky parts offers advantages in comparing melt pool sizes between the two geometries and in understanding transitions between them.

It can be seen in both Figs. 4 and 5 that for a fixed value of $\bar{h}$, melt pool size ($\bar{l}$ for a 2-D thin wall and $\bar{d}$ for a 3-D bulky part) increases with increasing T_{base} or Q (either of which

decreases $\bar{T}_m$). Moreover, a change in T_{base} can be compensated for by a change in Q, to retain a desired melt pool size. When the part is relatively tall, the fixed temperature at the base is not seen at the melt pool, $\bar{h}$ has no significant effect on the size of melt pool, and the results approach those for an infinitely large part. In contrast, $\bar{h}$ has a considerable effect on melt pool size when the part is relatively short, with $\bar{d}$ and $\bar{l}$ dropping rapidly as $\bar{h}$ is reduced.

When comparing melt pool sizes for the two extreme geometries, it is found that, for the same set of process variables, melt pool sizes extracted from the process map for 3-D bulky parts are much smaller than those extracted from the process map for 2-D thin-walled structures. For example, for a tall, thin wall, using typical process variables of αQ = 105 W, V = 7.6 mm/s, and T_{base} = 303 K (and a wall thickness of 1.3 mm) the melt pool length calculated from the process map is equal to 1.4 mm. For the same process variables, the melt pool depth and melt pool length for a tall, 3-D bulky part are found to equal 0.40 mm and 0.85 mm respectively. The considerable difference in melt pool lengths between the two geometries (1.4 mm and 0.85 mm) is due to the fact that there is more material to conduct heat away from the melt pool in the 3-D bulky part.

To keep melt pool size constant while transitioning from thin-walled to bulky features, laser power must be increased. For the case considered above, to obtain a melt pool size of 1.4 mm in a bulky feature, the absorbed laser power must be increased from 105 W to 160 W. Decreasing laser velocity and using part preheating can also increase melt pool size; however, these measures cannot be used alone. Within the practical range of laser velocity and part preheating in the LENS process, melt pool size changes from each of these process changes are not large enough to regain the thin-walled feature melt pool size.

Conclusions

In this paper, process maps have been presented for predicting and controlling melt pool size in the building of thin-walled and bulky stainless steel structures by laser-based SFF processes. For each of the two geometries, all numerical model predictions have been collapsed onto a single three-dimensional plot of dimensionless process variables. The process map for bulky parts could have been made more accurate by developing normalization rules specifically for that geometry; however, both process maps presented herein use the same normalization rules, making a direct comparison between the geometries easier. The process map for bulky parts quantifies values of melt pool depth, which is the key parameter to control for consistent build conditions. Although melt pool area is typically tracked in bulky parts via thermal imaging measurement and control systems, melt pool width is a better parameter to monitor experimentally, due to its more direct link to melt pool depth.

A comparison of melt pool sizes between the two geometries shows that, for the same set of process variables, the size of the melt pool decreases substantially when transitioning from thin-walled to bulky features (decreasing by 39% in the example cited herein). To maintain consistent build conditions, decreasing the laser velocity or base plate preheating alone is not sufficient and a substantial increase in laser power is needed (a 52% increase in the cited example). A detailed comparison of predictions from the two process maps (not presented in this paper) reveals that most process control-related insights and implications relevant to 2-D thin-walled structures also apply to 3-D bulky parts. For example, practical levels of uniform part

preheating, which is pursued as a means to decrease residual stresses, does not increase melt pool sizes significantly for either geometry. Furthermore, any increase in melt pool size can be eliminated by a small decrease in laser power or increase in laser velocity. It is also clear from both process maps that considerably smaller melt pool sizes are seen for short structures. Thus control of melt pool size as a part is built up from a base plate is important. Because it does not significantly change melt pool size, base plate preheating is not sufficient to address this problem.

Acknowledgements

This research has been supported by the National Science Foundation under grant DMI-9700320 and by Sandia National Laboratories under grant BE-0792. The authors would like to than Michelle Griffth of Sandia National Laboratories, Albuquerque, NM, for her substantial collaboration on this research.

References

1. Vasinonta, A., Beuth, J.L. and Griffith, M., "Process Maps for Laser Deposition of Thin-Walled Structures," *Solid Freeform Fabrication Proceedings*, D.L. Bourell, J.J. Beaman, R.H. Crawford, H.L. Marcus and J.W. Barlow, eds., The University of Texas at Austin, August 1999, pp. 383-391.
2. Vasinonta, A., Beuth, J.L. and Griffith, M., "Process Maps for Controlling Residual Stress and Melt Pool Size in Laser-Based SFF Processes," *Solid Freeform Fabrication Proceedings*, D.L. Bourell, J.J. Beaman, R.H. Crawford, H.L. Marcus and J.W. Barlow, eds., The University of Texas at Austin, August 2000, pp. 200-208.
3. Vasinonta, A., Beuth, J.L. and Griffith, M., "A Process Map for Consistent Build Conditions in the Solid Freeform Fabrication of Thin-Walled Structures," *Journal of Manufacturing Science and Engineering*, in print.
4. Griffith, M.L., Keicher, D.M., Atwood, C.L., Romero, J.A., Smugeresky, J.E., Harwell, L.D. and Greene, D.L., "Freeform Fabrication of Metallic Components Using Laser Engineered Net Shaping (LENS)," *Solid Freeform Fabrication Proceedings*, D.L. Bourell, J.J. Beaman, H.L. Marcus, R.H. Crawford and J.W. Barlow, eds., The University of Texas at Austin, August 1996, pp. 125-132.
5. Griffith, M.L., Schlienger, M.E., Harwell, L.D., Oliver, M.S., Baldwin, M.D., Ensz, M.T., Smugeresky, J.E., Essien, M., Brooks, J., Robino, C.V., Hofmeister, W.H., Wert, M.J. and Nelson, D.V., "Understanding Thermal Behavior in the LENS Process," *Journal of Materials Design*, Vol. 20, No. 2/3, 1999, pp. 107-114.
6. Dykhuizen, R.C. and Dobranich, D., "Analytical Thermal Models for the LENS Process," Sandia National Laboratories Internal Report, 1998.
7. Dobranich, D. and Dykhuizen, R.C., "Scoping Thermal Calculation of the LENS Process," Sandia National Laboratories Internal Report, 1998.
8. Chin, R.K., "Thermomechanical Modeling of Residual Stresses in Layered Manufacturing with Metals," Ph.D. Thesis, Carnegie Mellon University, May 1998.
9. Klingbeil, N.W., Beuth, J.L., Chin, R.K. and Amon, C.H., "Measurement and Modeling of Residual Stress-Induced Warping in Direct Metal Deposition Processes," *Solid Freeform Fabrication Proceedings*, H.L. Marcus, J.J. Beaman, D.L. Bourell, J.W. Barlow and R.H. Crawford, eds., The University of Texas at Austin, August 1998, pp. 367-374.
10. Rosenthal, D., "The Theory of Moving Sources of Heat and Its Application to Metal Treatments," *Transactions of the ASME*, Vol. 68, 1946, pp. 849-866.

this page intentionally blank

On-line Monitoring of Epoxy Resin Cure using Infrared Spectroscopy

.Fouchal, J.A.G.Knight, P.Dickens, N.Garrington

Rapid Manufacturing Group, Faculty of Technology and Computing Science
De Montfort University, Leicester, LE1 9BH, UK

Abstract

The method described can be used to observe the cure in epoxy resins, it is a sensor to serve as an on line monitoring system of physical change of the resins during the curing time and the future behaviour of the part built. It is also proposed that the method can be applied in Stereolithography (SL). In this paper the method permits a rapid determination of the state of chemical reaction happening in an epoxy resin diglycidyl ether of bisphenol A (DGEBA) with a curing agent triethylenetetramine stoichiometric mixture. It uses a mid infrared Fourier transform (FT-IR) technique to analyse the mixture via an embedded fibre optic and an FT-IR spectrometer operating in the region of 4000-700 cm^{1}. An accurate concentration versus time of epoxy amine and the hydroxyl groups gave a good estimate of the extent of reaction. The chemical group peaks at 1132cm^{-1} and 3300-3400cm^{-1} where used to follow the disappearance of the epoxy, and the amine respectively, while the peak at 2970cm^{-1} was used as reference peak. A review of a number of techniques used in the study of the curing process of epoxy resins and a number of methods used in an on-line monitoring of thermoset resin cure process is referred to
Keywords: Streolithography, epoxy/amine cure, FT-IR spectroscopy, extent of reaction, fiber optic sensor.

1-Introduction

Epoxy resins have been widely used for adhesives, protective coatings and matrices of many materials used in advanced technologies, they are also used to build rapid prototyping parts via the streolithography process. The other major use is for fiber-reinforced composites made from high strength and high modulus fibers, embedded in a matrix. The curing process of polymers such as epoxy resins entails the conversion of liquid monomers, or prepolymers, which can contain reactive epoxy groups, into three-dimensional polymer networks. The mechanism and kinetics of the curing process determine the polymer network morphology, which in turn determines the physical and mechanical properties of the cured product. For these reasons, a fundamental understanding of the curing process is the first target to optimize the processing of fiber reinforced epoxy composites.

2-1-Litteraure survey

Various techniques have been used to investigate the curing of epoxy resins, and these are briefly reviewed.

Mijovic[1] used calorimetry measurements to investigate the orientation of the dipoles in microwave and thermal fields and compared them to see if this could lead to different network morphology. Two parameters were used to characterise the advancement of the reaction, which were the degree of cure α and the glass transition temperature T_g. These were calculated from the measurements of the heat evolved in the cure. It was found that these parameters increased

faster with temperature and time in the thermal field rather than in the microwave, and that a broader T_g range suggested a broader molecular weight distribution and hence morphological heterogeneity. When Mijovic[2] used High Performance Liquid Chromatography, it was found that three types of hydrogen bond complexes were participating in the reaction of epoxy resin with an amine. This was described by three reaction schemes, epoxy amine complex with amino group, epoxy hydroxyl complex with amino group and epoxy hydroxyl complex with amine hydroxyl complex, which occured only after the hydroxyl complex increased to saturation. The author set out an approach for the calculation of the rate of the reaction, in which some of the associated rate constants were unreliable. However, the reactivity ratio of the consumption of primary amine hydrogen atoms, on the reactivity of the secondary amine hydrogen atom on the same amino group, was used to characterise the polymer cross-linking morphology.

Gonis[3]used differential scanning calorimetry (DSC), to evaluate the activation energies for epoxies of varying chain lengths. It was deduced that as the reaction proceeded, highly branched macromolecules began to form and a step increase in viscosity was indicative of the onset of gelation. In the dynamic mode, only the over-all reaction process could be analysed. In the isothermal measurement, the fractional conversion, α, was determined by dividing the heat evolved during cure by total exothermal energy. The overall kinetics of cure was stated and used to calculate the activation energy and produce the rate equation.

Neilsen[4] used the analytical capabilities of Gel Permeation Chromatography for studying the curing process. He calculated the average molecular weight of various polymer chain lengths, the activation energy and estimated the rate of reaction as a function of temperature and conversion. The author reported that the equation used was not consistent when calculating the activation energy.

Dynamic Dielectric Analysis was used by Maistros[5]; measurements of capacitance and inductance over the curing period of epoxy resin with an amine were carried out. A correlation to the relative permeativity controlled by the ionic character of the different stages of curing was made. Immediately after mixing a high interaction between the reactant induced a high degree of ion in the mixture.

Kozeiski[6] used chemiliminescence (CL) measurements to investigate the curing of epoxy resin with an amine. Some peaks from the plot of intensities of the emitted light against time were assigned to the hydroperoxide reaction and oxidation of the resin. The conclusion was made that a reasonable correlation existed between gelation and CL. However this technique is very sensitive to the increase in the viscosity during the network formation, while gelation is not the only phenomena that occurs in the network construction.

2-2-Conclusion of the literature review

From this investigation it has been concluded that none of these techniques are suitable to describe the development of the chemical reaction between epoxy resin and curing agents. The most consistent technique in monitoring the curing of epoxy amine system was the Fast Fourier Transform InfraRed (FT-IR) spectroscopy, and the results from the DSC technique could be very useful to adjust the FT-IR results.

3-How does Infrared spectroscopy work?

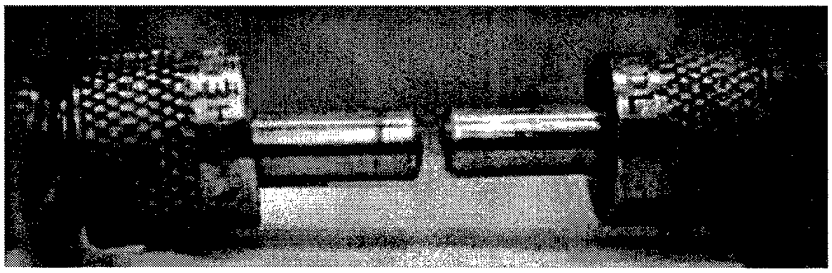
It is intended to concentrate on vibrational spectroscopy, and to use an FT-IR spectrometer to study the Mid-infrared region of electromagnetic spectra. Here the technique will examine the fundamental vibrations of organic and complex inorganic, which covers the region 2.5 to 25μm. The interaction between the electrical component of electromagnetic radiation and the dipolar motion in the molecules is the basis of vibrational spectroscopy. The dipole of the molecule must change during the vibration. CH, NH and OH groups are the most explicit bonds in the mid-infrared region. Heteropolar A-B molecules absorb in the infrared region, but homopolar A-A molecules do not.

FT-IR spectroscopy is a powerful and versatile technique for monitoring transient chemical change during the cure process, and structural change during the deformation process. It offers a unique possibility to obtain detailed information about molecular orientation and relaxation behaviour. The goal is to identify the characteristic Mid-infrared band assignments, monitor their change during the curing process, and use them to evaluate the reaction rate, and deduce the kinetics of reaction and mechanical properties of the products.

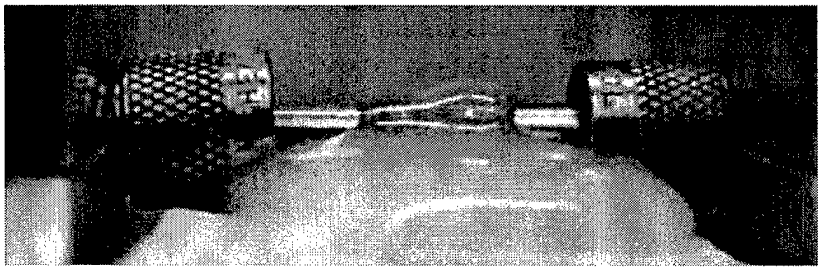
4-Experiment preformed

4-1-The embedding of the sensor in the resin for an on-line monitoring of the cure reaction

An optical interface was made from a set of gold-coated mirrors, a pair of chalcogenide optical fiber cables aligned by means of a micro holder. This was set on the same bench as the spectrometer. It was built to achieve the appropriate alignment of the two fiber optic ends, a micro meter was added as mean of adjusting the gap between the fibers end faces. The embedded fiber optic sensor operating in the mid-infrared band of the electromagnetic spectra, is shown in Figure 1.



-a-



-b-

Figure 1 Two optical fibers axially aligned

(a- not embedded yet), (b- under running experiment, while embedded in the epoxy/amine system)

The setup for the embedding method was linked to a Jasco 410 spectrometer fitted with a powerful fast Infrared HgCdTe detector; coupling two Chalcogenide fiber optic cables via an optical interface carried this out. The described MCT detector was cooled in liquid nitrogen, which provided a high signal to noise ratio. Figure.1 shows also that a mixed resin poured on the fiber optic sensor at the gap between the ends faces, which is already adjusted, by an incorporated micrometer before collecting any data.
Note: (The equivalent set-up in the stereolithography machine is described in Figure 9).

4-2-Sample preparation from DGEBA/TETA reaction and Data collection

A set of frequencies was chosen (1132 cm^{-1}, 3300-3400 cm^{-1} and 2970 cm^{-1}) to follow the development of the reaction. Analysis of the data enabled the information on the rate of reaction at any time during the cure to be obtained.

Their vibrations at frequencies characterized the reactants and products involved in the reaction. The values corresponded to vibrations of the functional groups observed in the curing of DGEBA (diglycidyl ether of 2,2'-bis(4- hydroxypheny) propane) with Triethylenetetramine (The reaction scheme, for this process is shown in Figure 2).

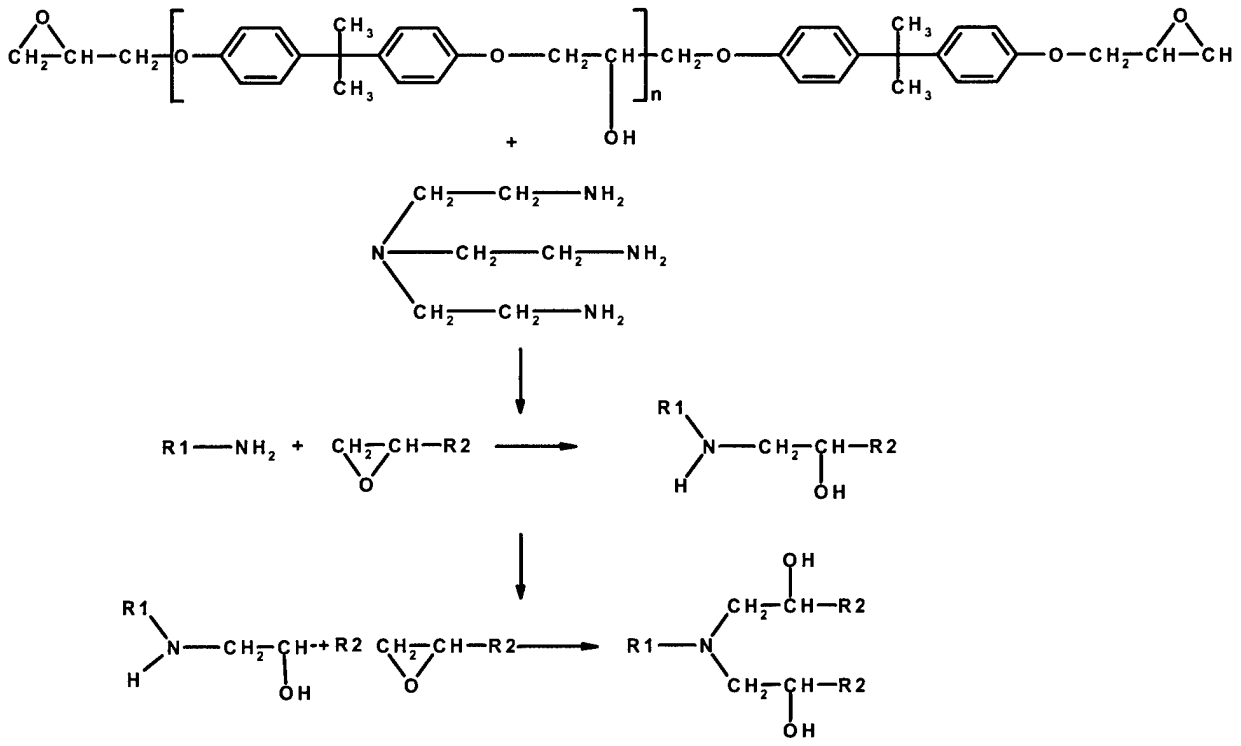


Figure 2. The reaction scheme of the epoxy resin with a tiethylenetetramine

4-3-Results

Peaks were selected from the spectrum (Shown in Figure 3) to determine the state of cure as a function of time. This was achieved by determination of the rates of consumption of the oxirane ring group (Corresponding peak P2 is shown in Figure 4), the primary amine

(Corresponding peak P3 is shown in Figure 5) and appearance of hydroxyl (Corresponding peak P4 is shown in Figure 5), along with the disappearance of secondary amines. The increase of the tertiary amine was determined using mathematical manipulations.

From Figure 4 it can also be seen that the epoxy peak and ether were vibrating at the same frequency and were detected a 1132cm^{-1}. This is supported by confirming the existence of this peak in spectrum of pure DGEBA epoxy resin. However the change recorded at this peak is due only to the disappearance of the epoxy group vibrations as can be seen in the reaction scheme, while the ether group, which was not reacting does not participate to that change

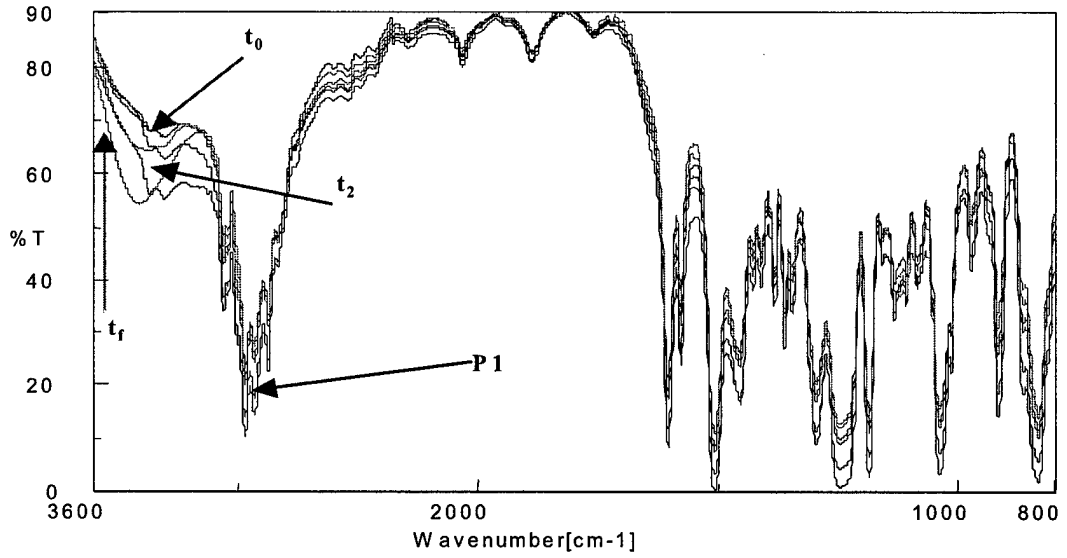


Figure 3. Change in spectrum of the mixture over time as shown, t_0 for initial time and t_f final time

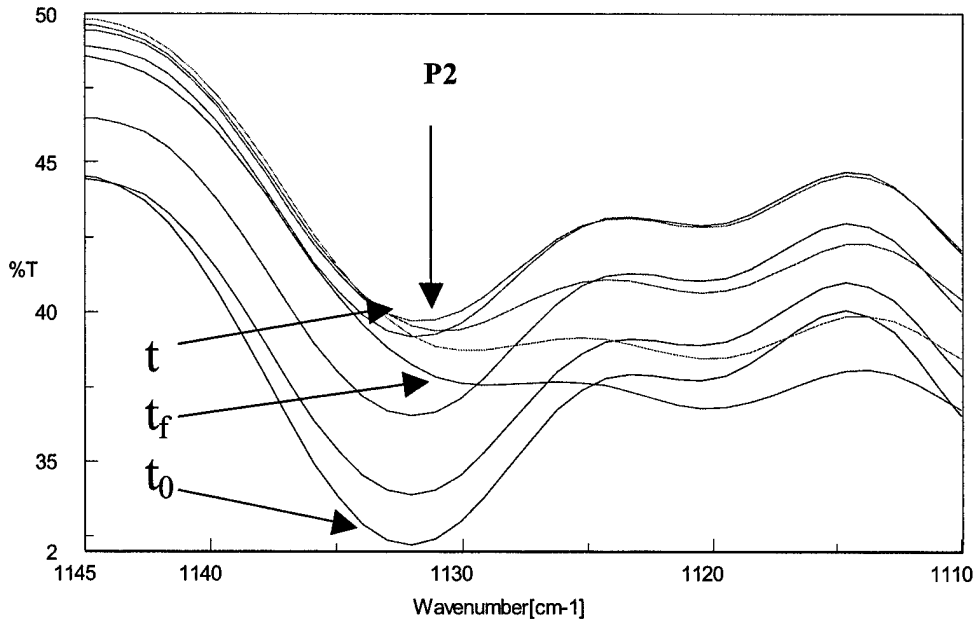


Figure 4. Change in the peak at 1132cm^{-1} with time for oxirane ring of epoxy

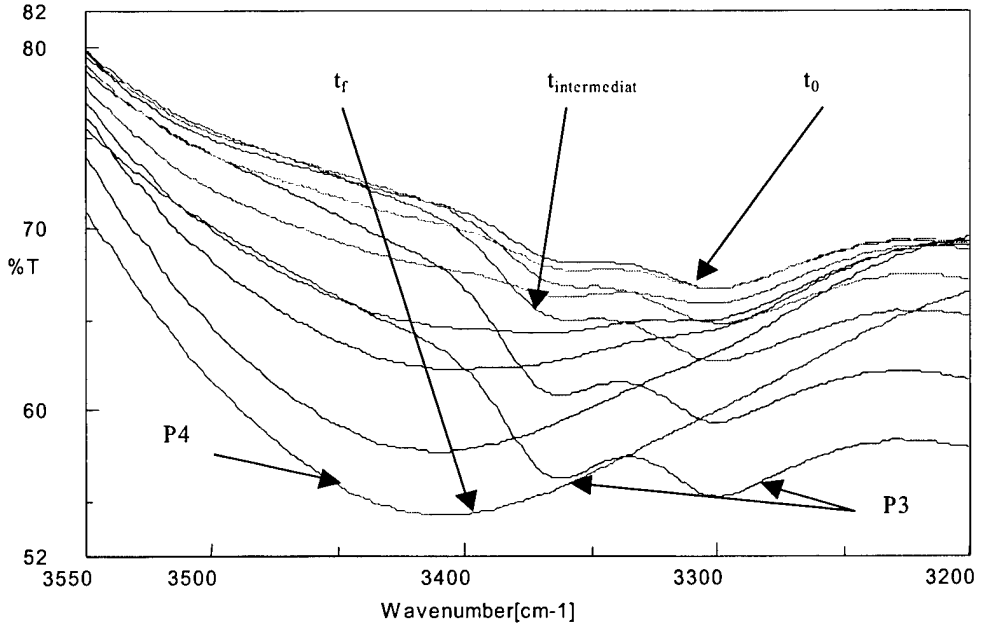


Figure 5. The disappearance of the double peak atat 3300-3365 cm^{-1} and the appearance of the peak at 3400 cm^{-1} over 24hours time

Figure 6 shows the ratio of the area measured under the peak P2 at 1135 cm^{-1} to the area under the selected refrence P1 peak, as can be seen from Figure 4 at 2970 cm^{-1}. This ratio is proved[7] to be directly proportional to the extent of reaction, hence to the concentration of the group causing the vibration. Figure 7 shows the ratio of the area under the peak P3 at 3300-3400 cm^{-1}, characteristic of the used amine as curing agent, to the area under the reference peak P1. This is also directly proportional to the change in the concentration of the amine over the curing period.

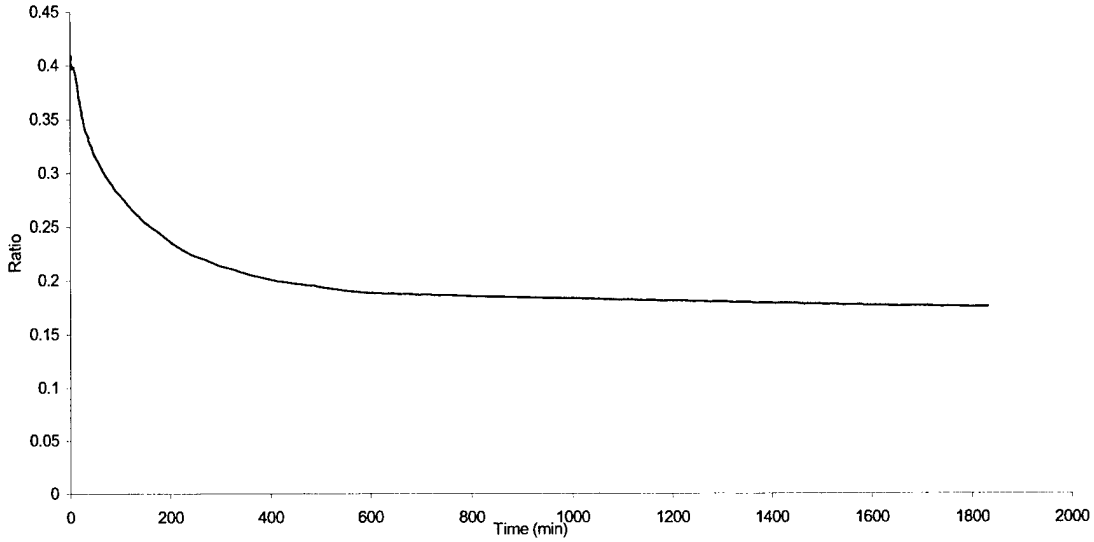


Figure 6. Ratio of area under epoxy group peak to area under reference peak

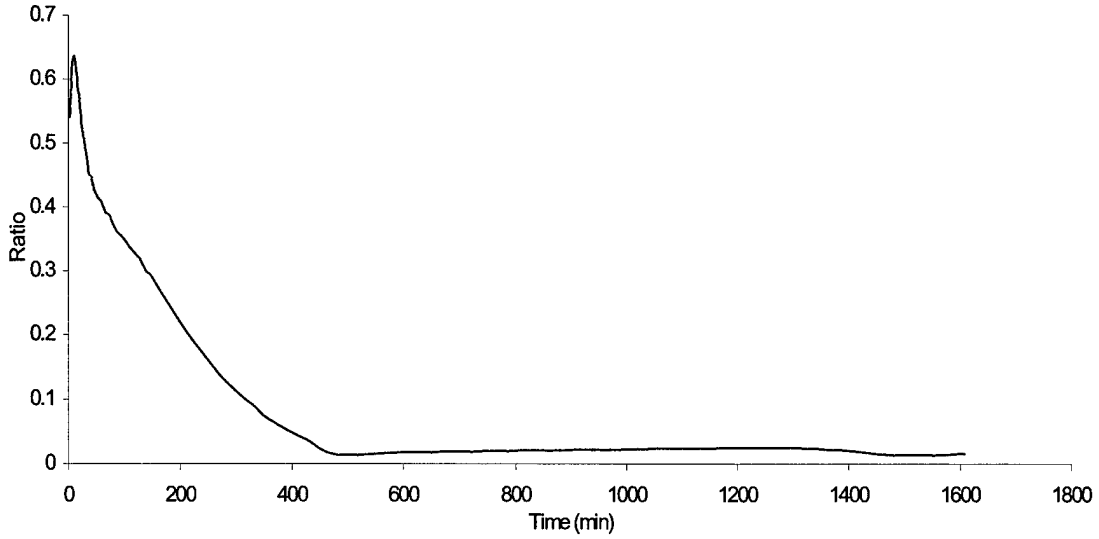


Figure 7.Ratio of area under amine group peak to area under reference peak

5-Data Analysis

5-1-Kinetic Mechanism

The reaction under study was a stoichiometric mixture of Epoxy resin /Amine system prepared at room temperature; DGEBA (Araldite MY 750), which had an average molecular weight < 700, and TETA (Hardener HY 951) were used. These were obtained from Ciba Specialty Chemicals Inc.

The stoichiometric amounts used in this experiment were 46 grams of TETA to 186.56 grams of DGEBA.

This reaction follows the kinetic equations described in (1) and (2).

$$E + P \xrightarrow{K_1} \quad (1)$$

$$E + S \xrightarrow{K2} T \quad (2)$$

k_1 and k_2 define the bi-reaction $R_{1,i}$ $R_{2,i}$ involved in this mixture, which are the reaction of the Epoxy *(E)*with the Primary amine *(P)* and the reaction of the Epoxy with the Secondary amine *(S)*, to end up with a Tertiary amine *(T)*.

Under appropriate kinetic conditions, the following reactions occur in the epoxy-amine mixture, primary amines and epoxy, secondary amine and epoxy. On this basis, the general equations for the rate of epoxy-amine reactions in terms of; the rate of disappearance of epoxy groups, primary amine groups, secondary amine groups and the appearance of tertiary amine as product of the reaction. The system of equations in (3) describes these rates or reactions.

$$\begin{bmatrix} \frac{d[E]}{dt} = -k_1[E][P] - k_2[E][S] --a \\ \frac{d[P]}{dt} = -k_1[E][P] --------b \\ \frac{d[S]}{dt} = k_1[E][P] - k_2[E][S] --c \\ \frac{d[T]}{dt} = k_2[E][S] --------d \end{bmatrix} \quad (3)$$

To solve this set of differential equations, the first step to carry out is translation of the above equations to expressions, which relate the amounts of material of epoxy, primary amine, secondary amine and tertiary amine at any time over the curing period. Further manipulation gives,

$$n_t = n_s + (n_p - n_s)^1 \frac{k_1}{k_1 - k_2}\left[1 - \left(\frac{n_p}{n_p - n_s}\right)^{1-\frac{k_2}{k_1}}\right] \quad (4)$$

Substituting the above equation n_t in the equation b from the system (3) gives the differential equation which represents the studied Epoxy-amine system,

$$\frac{dn_s}{dt} = \frac{k_1}{v}\left(n_e - 2n_s + (n_p - n_s)\frac{k_1}{k_1 - k_2}\left[1 - \left(\frac{n_p}{n_p - n_s}\right)^{1-\frac{k_2}{k_1}}\right]\right)(n_p - n_s) \quad (5)$$

For a numerical solution of the ordinary differential equation (5), a fourth and fifth Runge-Kutta formula was used. These formulas do not use iterative methods to solve the non-linear equation; they are self-starting, not requiring more than immediate past values of n_s. However several function evaluations per integration step were needed.

In this work the ode45 function was used in the Matlab program to solve the above equation. For correlation between the experimental concentration of the reactant and products involved in the studied system and the simulated data estimated by the above model, an extra development is needed. This is based on the a kinetics of reaction mechanism, for which non-linear least squares method was used, it is build on Newton's Gauss method. An application for the studied system is briefly described in the following section.

5-2-Solution of a Non-linear equation by Least Squares

For a function $y(x)$, which is a non-linear function of the coefficient, the following procedure is required, it is based on Newton-Gauss least squares method. Assuming that there exists an initial estimate of these coefficients $a_1, a_2, a_3,\ldots,a_m$ of a polynomial $P(x)$ and that by adding infinitesimal increments $\delta_1, \delta_2, \delta_3,\ldots\ldots,\delta_m$ an improved estimate may be obtained. The new value of y_i is given by,

$$y(x_i)+\sum_{j=1}^{m}\left(\frac{\partial y}{\partial a_j}\right)\cdot\delta a_j \tag{6}$$

Then it is required that the difference between the initial, and the new value is minimum, which then rearranged to give,

$$\left(\frac{\partial S}{\partial \delta a_k}\right)=-2\sum_{i=1}^{n}\left(y_i-y(x_i)-\sum_{j=1}^{m}\left(\frac{\partial y}{\partial a_j}\right)\delta a_j\right)\left(\frac{\partial y}{\partial a_k}\right) \tag{7}$$

$$\therefore\sum_{j=1}^{m}\delta a_j\cdot\sum_{i=1}^{n}\left(\frac{\partial y}{\partial a_j}\right)\left(\frac{\partial y}{\partial a_k}\right)=\sum_{i=1}^{n}\left(y_i-y(x_i)\left(\frac{\partial y}{\partial a_k}\right)\right) \tag{8}$$

The term, $y_i-y(x_i)$, is known as the residual, r_i. The expression above is a set of m simultaneous equations for the m increments δ_1, δ_2, δ_3,....., δ_m.

These equations may be obtained by forming a matrix D that contains as elements $D_{i,j}$, the value of the derivative $\left(\frac{\partial y}{\partial a_j}\right)$, evaluated when $x=x_i$, and a vector r for which the general element $r_i=y_i-y(x_i)$ (10)

The solution to the equation (8) is given by,

$$\delta a=\left((D)^T(D)\right)^{-1}(D)^T r \tag{11}$$

Having obtained the increments δa, they are added to the original a values, $a=a+\delta a$, and the procedure is repeated until $\delta a\cong 0$.

Figure 8. shows a plot of the simulated concentration changes over the curing period, of the epoxy, primary, secondary and tertiary amines. The curve in circles shows the experimental data for the concentration of the epoxy as recorded by FTIR spectroscopy.

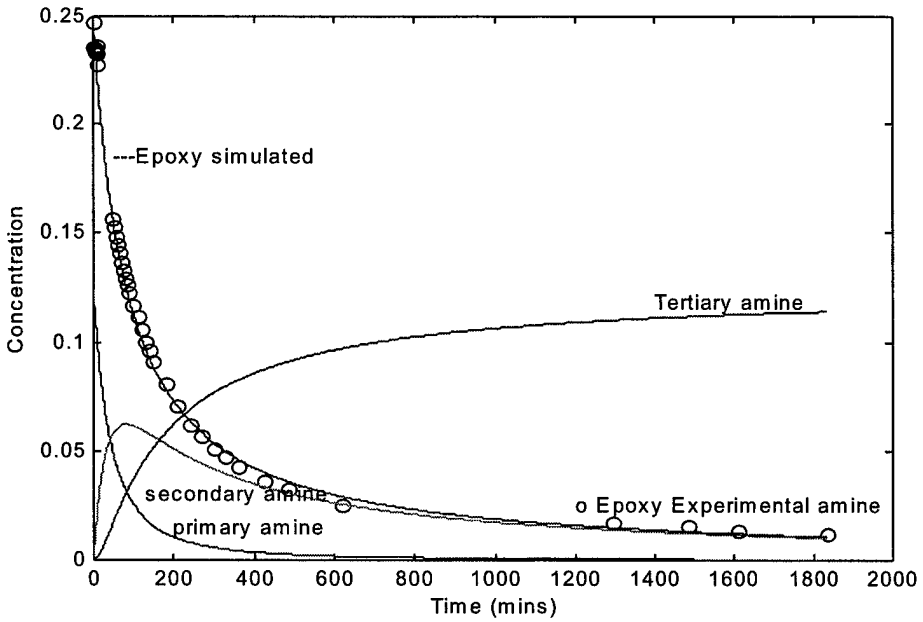


Figure 8. Plotting of concentrations.

7-Conclusion

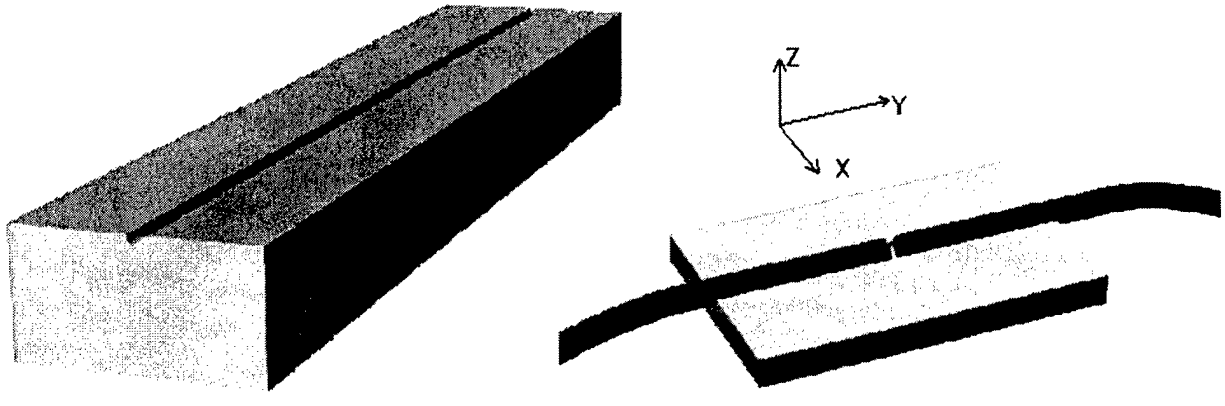
For an optimum processing of epoxy resins in making parts, coating or composite materials, an understanding of the phase transfer from monomers to polymers is needed. The achievement of such a goal may result in a capability to reach the required physical properties by setting the adequate processing schedule.

An optical fiber sensor has been developed and successfully embedded in an epoxy /amine system to monitor the progress of the reaction over its curing period, results of which can be translated in physical parameters. A plan is also given for an implementation of this sensor in streolithography resin, during its curing process in the SLA machine under UV laser. The monitoring will be carried out for the post cure and later for the chemical status of the structure forming the end part over the operating period.

Mid-Infrared spectroscopy is a most suitable technique to follow the curing of the epoxy hardener mixture. It was noticed that many frequencies from the obtained spectra were changing in a significant fashion; these were correlated to a number of reacting groups in the mixture, and their progress was monitored over time. It is clear that this technique provided a direct measurement of the change in concentration over time of any element involved in the reaction. The method developed to process data is capable of calculating all the chemical parameters of the investigated reaction. This is based on converting the measured variations in concentrations over the curing period to two constants of reactions k_1, and k_2, representing the reaction involving the epoxy and the primary amine and the reaction of the epoxy and the secondary amine respectively, which is achieved by minimizing the difference between the experimental data and the result from the simulated model. The values for the reaction DGEBA and TETA of the constants of reaction are, $k_1 = 0.96\ mins^{-1}$ and $k_2 = 0.68\ mins^{-1}$.

7-Recomendation

Figure 9 shows the groove made in the part built in the SL machine. The diameter of the groove is designed to carry the optical fiber sensor, height of one layer in the SL is left inbuilt from the diameter of the groove, this permits the implementation of the optical fiber cable see Figure 9 b.



-a- -b-

Figure 9 Set-up of the optical fiber sensor to be implemented in the SLA machine

Part building is then continued; the next layer is spread until the sensor will be completely immersed, the 30-microns gap as shown in Figure 9 b. will be filled with the resin. When the UV curing laser of 200 microns beam diameter passes over the sensor, at hatch velocity of 525 inches/second, the resin in the gap will cure. A number of spectra can be collected from which the change in the molecular structure of the resin will be measured. The effect of the laser curing the top layers will also be recorded.

The sensor will carry the monitoring process of the reaction progress in the post cure stage of the part under UV light, as well as in the future of the part, where the exterior condition in which the part will operate participate to the degradation of the molecular structure of the material.

8-Refrences

[1] – J.Mijovic, J.Wijaya, *Macromolecules* 1990, vol. 23, p.3671-3674.
[2] – J.Mijovic, S.Andjelic, *Macromolecules* 1995, vol.28, p.2797-2806.
[3] – J.Gonis, G.P.Simon, *J.Apply.Polym.Sci* 1999, vol.72, 1479-1488.
[4] – J.A.Nielsen, S.J.Chen, D.C.Timm, *Macromolecules* 1993, vol.26, p.1369-1993.
[5] – G.M.Maistros, I.K.Partridge, *Composi.Sci.Tech* 1995, vol. 53, p.355-359.
[6] – K.A.Kozielski, N.C.Billingham, *High.perform.polym.* 1995, vol. 7, p.219-236.
[7] – M.C.Finzel, J.Delong, *Journal of polymer science* 1995, vol.33, p.673-689.

this page intentionally blank

EMPIRICAL MODELING AND VISION BASED CONTROL FOR LASER AIDED METAL DEPOSITION PROCESS

Mallikharjuna R. Boddu*, Srinivas Musti[□], Robert G. Landers*,
Sanjeev Agarwal[□], and Frank W. Liou*

*Department of Mechanical and Aerospace Engineering and Engineering Mechanics
[□]Department of Electrical and Computer Engineering
University of Missouri – Rolla, MO 65409

Abstract

This paper gives a brief description of the laser aided manufacturing process. Empirical models describing the process dynamics of the laser aided metal deposition process is developed based on some of the models found in the literature. These models provide the basis for process planning and real time control. An embedded vision system, a two color temperature sensor, and a laser displacement sensor are incorporated for real time monitoring and control of the deposition process. The temperature profile of the surface and geometric characteristics of the melt pool are studied to ensure consistent operation of the process.

Introduction

Lasers have a tremendous impact in manufacturing industries. With laser innovations, the world in now experiencing the use of optical energy in a wide range of applications, from materials processing to Rapid Prototyping (RP). The use of lasers, in conjunction with metal powder, is one of the latest extensions to rapid prototyping, which had earlier involved plastic parts exclusively. Rapid prototyping using lasers has enabled the fabrication of complex, near–net shape functional metal parts directly from a CAD model at a low cost and offers faster turn around. Currently this technology is implemented under a variety of names such as Direct Light Fabrication (DLF), Laser Metal Forming (LMF), Laser Engineered Net Shaping (LENS), Direct Metal Deposition (DMD), Selective Laser Cladding (SLC), etc. Though the system description and specifications of each of these vary, they all rely on the same principle of part fabrication, i.e. layer by layer deposition. A general description of the method of fabricating a part involves utilizing a laser to melt metal powder injected by a nozzle and laying down clad tracks via a positioning system having a controlled motion. In some cases the lasers may be directed along a defined path and tracks are laid down on a stationary table. To control the deposition process it is necessary to understand the process system mechanics for which relations among various parameters need to be studied. The optimization of the process requires the measurements and control of parameters such as the powder feed rate, process speed, melt pool temperature and melt pool quality. During the last few years many sensors have been tried; the high cost of such equipment, the lack of real time or on-line control have led developers to seek other solutions. The use of laser displacement sensor, temperature sensor and CCD matrix camera with embedded image processing tools are sufficient to monitor all relevant process parameters. These sensors with a standard data acquisition card and personal computer enable the operators to interact with the process and processing parameters.

Empirical Modeling of Laser Aided Metal Deposition Processes (LAMD)

The process mechanics describing processes such as Laser Cladding, Laser Forming, Laser Ablation, Laser Welding, Laser Surface Treatment, Laser Metal Deposition etc., are the same, except for certain variations in the control parameters describing these processes. Some of these may include powder deposition, with or without material removal, or the enhancement of metal properties by heat treatment. These processes require certain factors such as dilution, heat-affected zone, porosity, clad dimensions, powder catchment efficiency, etc. to be monitored. Identifying the control parameters and establishing relations to describe these factors forms the basis for empirical modeling. The first step involved is identification of parameters and categorizing them into dependent and independent variables based on certain assumptions. The need for these assumptions arises from the system's flexibility to control certain parameters. Studies have to be conducted by varying these parameters and determining their effect on the part quality and system performance. Figure 1 shows the classification and interaction of different system parameters (dependent and independent) describing the metal deposition process

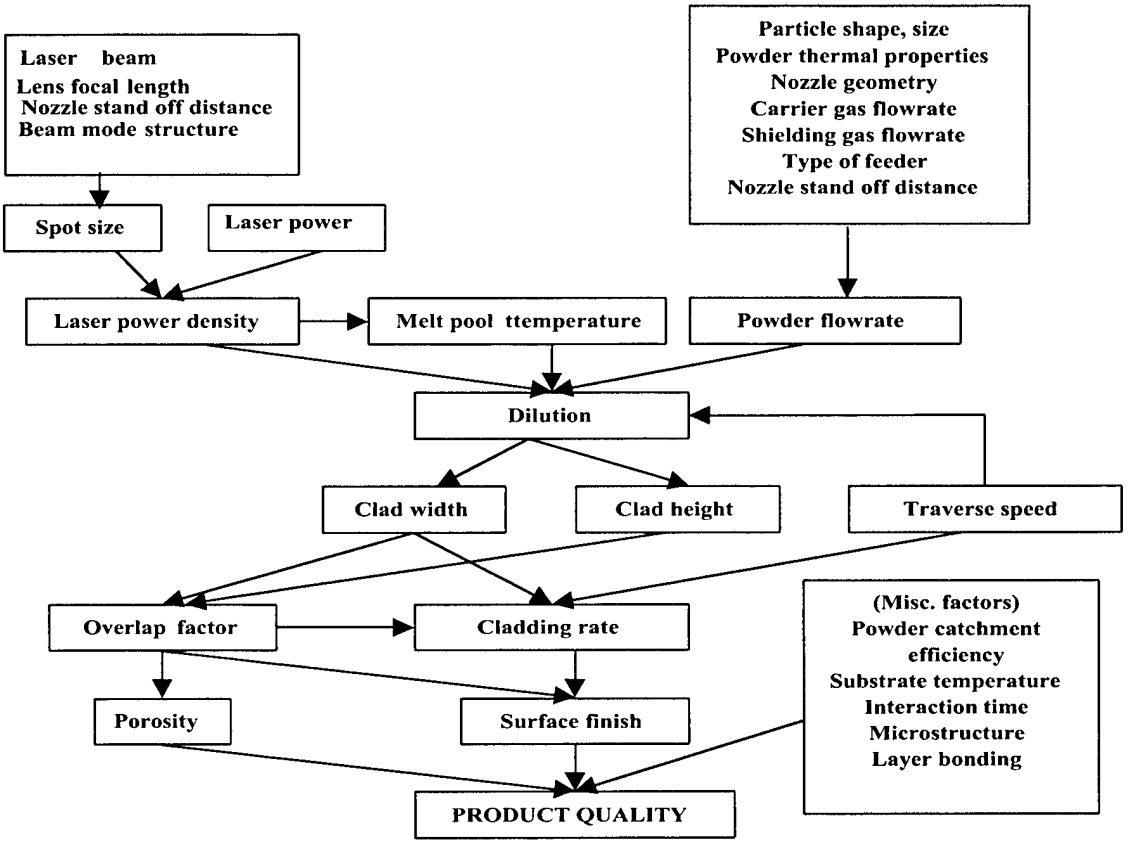


Figure 1. General description of interacting parameters and their effect on quality of part

The second step involves developing analytical/empirical relations of the parameters describing the process. The final step involves fitting these relationships into models, performing specific experiments to evaluate the model constants, and specifying the conditions for which these relations hold.

A. Process Parameters

Powder Feeder: Screw fed powder–feeding systems with a carrier gas is the general powder feeding system used in many deposition processes. The powder fills the screw either by weight or by the pressure of a carrier gas in the hopper. The amount of powder (in weight) being driven by a twin–fluted screw per revolution can be expressed as

$$m = 2\rho A_d r \tag{1}$$

where m is the powder mass per revolution (gm/rev), r is the feed screw helix lead (mm), ρ is the powder density (gm/mm^3), and A_d is the cross sectional area (mm^2) of one flute measured at a right angle to the screw axis. In practice, density depends on the hopper elevation, acceleration (if it is a mobile one), void factor (ratio of the space of air to that of solid), particle size, powder viscosity, and powder level in the hopper. If V_m is the motor speed (rev/sec) then the powder mass flow rate M (gm/sec) can be expressed as (Li *et al.*, 1993)

$$M = mV_m \tag{2}$$

By controlling the amount of powder flowing into the melt pool, the energy input to the substrate can be controlled, thereby governing the amount of dilution that will occur (Blake *et al.*, 1985).

Energy Delivery System: The amount of heat input to a process depends on the system parameters. The heat delivered should be sufficient enough to melt the layers for proper bonding. Overheating results in more dilution and the part may melt back. The laser beam diameter at the laser material interaction is defined as spot size (D) and can be obtained from the relation

$$D = D_b Z / F \tag{3}$$

where D is the laser spot size (mm), D_b is the laser beam diameter (mm), Z is the laser nozzle stand off (mm), and F is the focal length of the focusing lens (mm). Specific energy is defined as

$$E = P / Dv \tag{4}$$

where E is the specific energy (J/mm^2), v is the traverse speed or feed rate (mm/sec), and P is the laser power (W).

Powder Utilization Efficiency (η_p): The powder utilization efficiency is expressed as the ratio of the powder delivered, to the powder deposited on the substrate within the duration of the laser irradiation on the substrate. Powder utilization efficiency also depends on material characteristics such as type, particle size, and shape of powder particles. It can be expressed mathematically as (Hu *et al.*, 1998)

$$\eta_p = W_c / W \tag{5}$$

where η_p is the powder utilization efficiency, W_c is the net clad weight (gm), and W is the total weight of the powder delivered (gm). The total weight of the powder delivered is given by

$$W = \int_0^t M(t)dt \tag{6}$$

where t is the time (sec).

Lin *et al.* (2000) performed experiments to determine the attenuation of optical energy through a focused powder stream and through a columnar powder stream for different nozzle stand off distances. This helps in determining powder utilization efficiency since this depends on the amount of energy being delivered to the substrate.

Dilution: Dilution can be defined mathematically as the ratio of the clad depth in the substrate to the sum of clad height (above the substrate surface) and clad depth. It determines the amount of the liquid layer that needs to be formed on the substrate to ensure proper layer bonding. There are several parameters that determine the amount of dilution. These parameters include the powder flow rate, laser power delivered to the substrate, and table traverse speed. However the dilution mainly depends on specific energy. If specific energy is below a certain value (K_{min}), bonding between the layers does not occur, i.e.

$$E < K_{\min} \quad or \quad P/Dv < K_{\min} \tag{7}$$

Also, if specific energy is more than a certain value (K_{max}), the previous tracks may melt back, i.e.

$$E > K_{\max} \quad or \quad P/Dv > K_{\max} \tag{8}$$

These values of specific energy can be used as indices in determining the range over which other parameters can be varied.

Heat Affected Zone (HAZ): The heat–affected zone is the region beneath the bead which has a different microstructure as compared to the unaffected zone. This may result in cracking and surface distortions due to the hardening mechanism, particularly in steel. The width and depth of the HAZ can also be used as indices in determining the range of variation of other parameters. Specific energy determines the depth of the heat–affected zone. For a given powder feedrate, a higher specific energy indicates more energy will be transferred to the substrate and the depth of the heat–affected zone will increase. Hu *et al.* (1998) performed experiments to show that penetration depth increases almost linearly with increase in the specific energy.

Porosity: Porosity occurs due to cavities between tracks that form from overlapped tracks or due to the evolution of entrapped gases in the clad tracks. Porosity can be avoided if the aspect ratio (ratio of the clad width to clad height) is more than five and the percentage overlap is less than 70% (Steen *et al.*, 1986).

B. Process Model

The quality and surface of finish of the part fabricated by the laser metal deposition process is determined by the clad geometry and its dimensional accuracy. Bead geometry can be defined by clad width and clad height, which depend on a number of other parameters. Empirical relations have to be developed to determine the effect of these parameters on clad geometry. Specific energy can be used to regulate the clad dimensions. For a given powder flow rate, the clad width can be regulated by varying the specific energy delivered to the substrate. Also, the specific energy depends on the laser spot size and traverse speed, which is evident from equation (4).

Williams and Deckard (1998) showed that the average part density at a particular specific energy is greater for a larger laser spot size. The range for which the traverse speed and laser spot size cause a variation in bead width needs to be determined experimentally. Also, the range of traverse speed and spot size is limited by the amount of dilution as seen in equations (7) and (8). Thus, the relationship between bead width and, traverse speed and laser spot size is (Steen *et al.*, 1986).

$$W = D(1 - av) \tag{9}$$

where W is the bead width (mm) and a is an empirical constant. Hu *et al.* (1998) showed that an increase in powder flow rate results in wider cladding tracks provided the other variables are kept constant and there is sufficient energy available to form a clad. The net clad weight can be determined from the relation

$$W_c = \int_0^t \eta_p(t) M(t) dt \tag{10}$$

where W_c is the net clad weight (gm). Assuming the cross section of the clad to be a parabolic arch, clad height can be theoretically defined as

$$H_t = 3A/2W \tag{11}$$

where H_t is the theoretical clad height (mm) and A is cross section area of the clad (mm^2). Hu *et al.* (1998) performed experiments to show that the clad height increases with increased powder flow rate or specific energy, or with a decrease in traverse speed. An empirical relation can be developed to determine height, taking these factors in consideration.

$$H_e = bM/v \tag{12}$$

where H_e is the experimental value of clad height (mm) and b is an empirical constant. The experimental values of clad height can be compared with the theoretical values of clad height using equations (12) and (13).

Aspect Ratio: Aspect ratio is defined as the ratio of clad width to clad height and is expressed as

$$A_r = W/H_e \tag{13}$$

From equations (10) and (13), the aspect ratio can be expressed as

$$A_r = D(1 - av)/(bM/v) \tag{14}$$

Cladding Rate: The cladding rate be expressed in terms of overlap factor (i), clad width (W), and traverse speed (v) as (Manjuluri, 2001)

$$C = (1 - i)Wv = (1 - i)(1 - av)Dv \tag{15}$$

where C is the cladding rate (mm^2/sec) and i is the overlap factor, which is defined as the ratio of the part of the bead overlapped to the overall bead width.

Sensors for LAMD Process

The quality of deposition process using laser aided metal deposition process is controlled by a large number of interrelated parameters. It is important to monitor and control these parameters to ensure consistent and efficient operation of the process. We show in this article, that the use of a two-color temperature sensor, displacement sensor and a standard CCD camera enables us to control and optimize the laser cladding process.

The CCD camera is used to find the geometrical parameters such as the height and width of the track in real time. The camera also provides the temperature profile of the melt pool. This provides the operator with information related to process parameters like dilution factor and melt pool quality. Dual color infrared temperature sensors measure the surface temperature of objects without contact. The sensors work is based on the principle that infrared energy emitted by an object is proportional to its temperature. The temperature output signals can be input into a computer, for process monitoring and control. Displacement sensor uses high precision laser to detect small vertical displacement with 30μm resolution. The advantage with this displacement sensor is that, it has a reasonable stand off distance (80mm) and works efficiently in high temperature environment. Table 1 shows important parameters provided by in-process sensors.

Table 1. Summary of process parameters measured by sensors

Sensors	Dilution	Quality	Geometry	Efficiency
IR Temperature	Absolute temperature	Dilution	-----	Melt pool temperature
Imaging	Thermal profile	Cold spots, thermal contour, melt pool profile, and porosity	Bead width	Melt pool quality
Displacement	-----	Surface finish	Clad height	Track dimensions

A. Shape Measurements

Preliminary experiments were conducted using CCD camera and imaging techniques to extract dimensions, thermal profile and quality of the molten pool in mild steel sample fabricated using the LAMD process. A total of 300 frames/run were recorded at a rate of 30 frames/sec with a CCD camera. The results shown are for mild steel material, at a laser power of 1500W and traverse speed of 10 mm s^{-1}. In order to monitor the bead geometry during the process, the CCD camera is installed right on top of the nozzle head. The image captured in this angle enables us to compute the temperature variation in the melt pool. The images are captured during the off time of the pulsed mode operated laser. Simple algorithm is used to calculate the bead length and width in real-time. The bead height is obtained from the laser displacement sensor. This enables us to check the track dimensions being deposited online. The system is able to detect fluctuations in the mass feed rate. As the mass feed rate increases, the height of the tracks also increases, up to a threshold, after which lack of power prevents the powder to correctly bond to the substrate. This threshold is a function of the laser power and the beam diameter. (Griffith *et al.*, 1998) Figure 2 shows the digital image of the molten pool and the adjacent material created during the processing. The field of view encompasses approximately 4 mm.

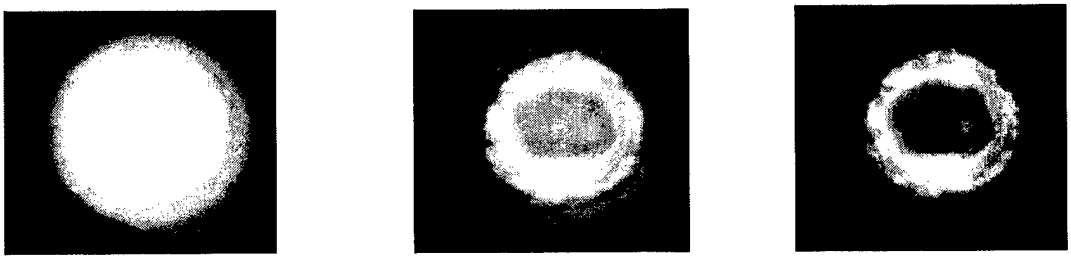


Figure 2. Sequence of images taken at a time interval of 1/60th of a second during laser off time

B. Temperature Measurements

The knowledge of the thermal behavior is critical to reliable and repeatable fabrication during LAMD processing. Our initial experiments show promise in both monitoring as well as understanding the thermal behavior. During the cladding process the camera scans the melt pool and provides information of the temperature distribution within the melt pool. Of the images acquired, we take an average in order to remove unrepresentative features of the distribution like the movements within melt pool and presence of bursting bubbles during the process, which lead to large fluctuations in temperature. (Meriaudeau *et al.,* 1997). By processing the images we obtain two gaussian distributions, the first one (low gray level) is related to the cold areas, the other gaussian centered on the average temperature contains information about temperature distribution within the melt pool. (Truchetet *et al.,* 1996) The study of temperature profile of the melt pool provides us important parameters like dilution and melt pool quality.

Dilution: The powder flow rate and laser power govern the dilution of the melt pool. An uneven distribution of the temperature is the result of unmelted powder particles in the melt pool, due to lower laser power. This introduces porosity and poor mechanical properties. As the laser power increases, the surface temperature increases resulting in higher dilution. This causes the melting of previous tracks and residual stresses may be induced upon solidification (Steen *et al.*, 1986).

Melt pool quality: Thresholding is performed on the averaged image of the melt pool cross section to obtain the geometric characteristics and subsequently the melt pool quality. A well-formed melt pool has a definite boundary with finely distributed powder. An uneven or jagged boundary is a result of uneven distribution of the powder or high laser power. This is one of the important aspects of quality control.

Control Architecture for LAMD Process

A closed loop control system is designed to monitor the bead width, bead height and melt pool temperature during the ongoing process and correspondingly the process parameters are adjusted in order to achieve desired performance. The control architecture to optimize the laser deposition process is shown in Figure 3. Adaptive optimal controller based on empirical process model is used to regulate laser power, feed rate, and powder flowrate to obtain an efficient cladding.

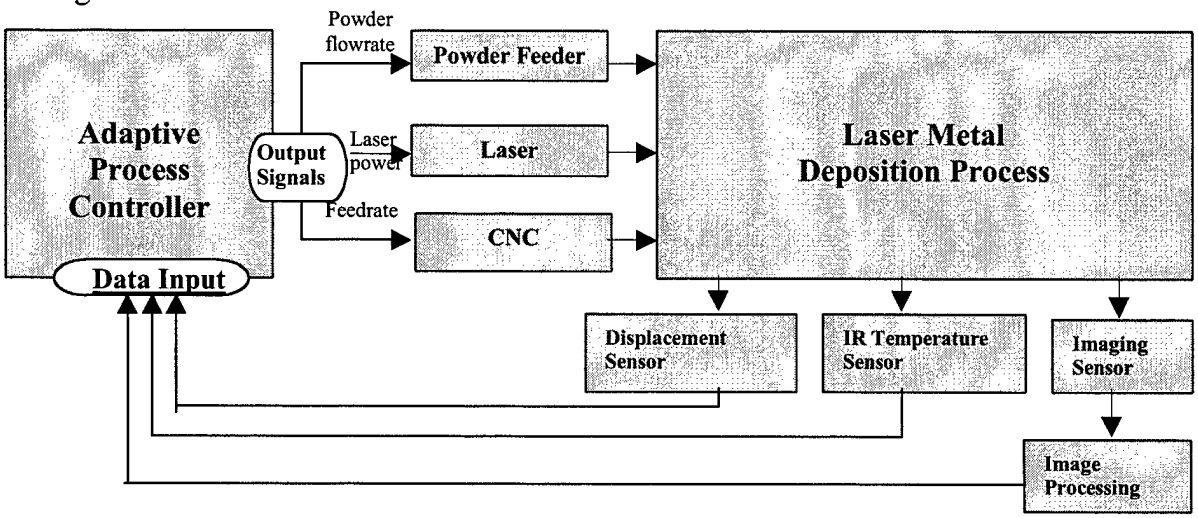


Figure 3. Sensor Control Architecture

The two-color temperature sensor, displacement sensor and a standard CCD sensor, monitor the process in real-time and provide the process parameters (as shown in Table 1) to the adaptive controller. Adaptive controller provides control output in the form of powder flow rate, laser power and feed rate. The imaging sensor obtains sequence of images, which are processed using image processing tools to provide a feedback to adaptive controller. Empirical models, which describe the process dynamics, were used to design the adaptive process controller to optimize the LAMD process.

Conclusion

An empirical model describing the process mechanics is presented for the LAMD process. A low cost system using laser displacement sensor, temperature sensor and CCD matrix camera has been presented which enables the operator to obtain information about laser cladding process. Some information is available in real-time and can be used in a closed loop control. The use of CCD technology enables determination of the clad width and temperature gradient of the melt pool. We showed that the data provided by our system enables us to improve the control of the cladding process through an adaptive process controller. Effects of some controller parameters on material processing are investigated. A statistically designed experimental matrix is used for this study.

References

Blake, A.G. and Eboo, G.M., 1985, "State of the Art Laser Hardfacing Using Dynamic Powder Feed Technology," *Conference on the Laser vs. the Electron Beam in Welding, Cutting and Surface Treatment*, Reno, NV, pp. 196–214.

Griffith, M.L., Schlienger, M.E., Harwell, L.D., Oliver, M.S., Baldwin, M.D., Ensz, M.T., Smugeresky, J.E., Essien, M., Brooks, J., Robino, C.V., Hofmeister, W.H., Wert, M.J., and Nelson, D.V., 1998 "Thermal Behavior In The LENS Process," *Solid Freeform Fabrication Proceedings,* pp. 89-96.

Hu, Y.P., Chen, C.W., and Mukherjee, K., 1998, "Innovative Laser–Aided Manufacturing of Patterned Stamping and Cutting Dies: Processing Parameters," *Materials and Manufacturing Processes*, Vol. 13, No. 3, pp. 369–387.

Li, L. and Steen, W.M., 1993, "Sensing, Modeling and Closed Loop of Powder Feeder for Laser Surface Modification," *Proceedings of ICALEO*, pp. 965–974.

Lin, J., 2000, "Laser Attenuation of the Laser Focused Powder Streams in Coaxial Laser Cladding," *Journal of Laser Applications,* Vol. 12, No. 1, pp. 28–33.

Manjuluri, N., 2001 "Process Modeling, Monitoring and Control of Laser Cladding," *M.S. Thesis,* University of Missouri-Rolla.

Meriaudeau, F., Truchetet, F., Grevey, D., and Vannes, A.B., 1997, "Laser cladding process and image processing," *Lasers in Engineering,* Vol. 6, pp. 161-187.

Meriaudeau, F. and Truchetet, F., 1996, "Control and Optimization of the Laser Cladding Process Using Matrix Cameras and Imaging Processing," *Laser Institute of America,* Vol. 8, pp. 317-324.

Steen, W.M., Weerasinghe, V.M., and Monson, P., 1986, "Some Aspects of the Formation of Laser Clad Tracks," *SPIE*, Vol. 650, pp. 226–234.

CONTROL OF LASER CLADDING FOR RAPID PROTOTYPING – A REVIEW

Mallikharjuna R. Boddu, Robert G. Landers and Frank W. Liou

Department of Mechanical and Aerospace Engineering and Engineering Mechanics, University of Missouri – Rolla, MO 65409

Abstract

Lasers have wide–ranging applications in the manufacturing field (e.g., cladding, welding, cutting, machining, drilling). Extensive work is being conducted to apply laser cladding as a Rapid Prototyping (RP) process. In this paper the authors illustrate various principles of laser cladding in rapid prototyping. Important process parameters for the control of the laser cladding process are discussed as well as the experimental methods adopted, and results obtained by, various authors.

Introduction

The past decade has witnessed the emergence of new manufacturing technologies, where manufacturing time for parts of virtually any complexity is measured in hours, instead of days, weeks or months. This is when Rapid Prototyping (RP) was conceived. Many RP technologies are available in the marketplace; however, these technologies utilize plastic (or similar) material to create parts and, thus, many parts are non–functional. Sterolithography Apparatus was the first commercially available RP system that successfully produced physical prototypes. It enabled the visualization of components produced directly from a CAD model by polymer curing with lasers. Laser–based RP systems have been introduced as a means of creating functional, metal prototypes with near–net shape geometries and development efforts are being conducted in research centers throughout the world (Laeng *et al.*, 2000). The drawbacks to these systems are their low productivity and inability to consistently regulate part quality in terms of mechanical properties and geometry. To overcome these drawbacks, process control strategies have been utilized. This paper provides an overview of this body of research.

Lasers have provided industry with a new form of energy. Their wide application is due to their ability to act as a medium for communication, photography, and medical applications, as well as their ability to evaporate materials at the atomic level. Laser applications in manufacturing industries include welding, cutting, surface treatment, and ablation, and have recently extended their potential to RP. Laser-aided RP is a significant advance in traditional RP techniques due to the direct fabrication of a near-net shape part compared to the two step process involving an intermediate step of mould preparation in conventional RP techniques. Laser aided RP is advancing the state-of-the-art in product design by extending the laser cladding concept to RP. Some of the earlier attempts to build complex parts by layer addition were based on laser cladding principles. Studies have been carried out to determine the effect of process parameters on the quality of the clad layer (Weerasinghe and Steen, 1983). The quality of the clad layer is of importance as it forms the building block of the prototype. The next issue of concern is the bonding (fusion) of layers to build the prototype. Combining these issues together with the

ability of the system to orient the part in the required direction during deposition makes it possible to build parts with complex contours. Experiments were also carried out successfully to develop prototypes based on these principles (Kreutz *et al.*, 1995). Laser Engineering Net Shaping (LENS) has demonstrated the feasibility to fabricate geometrically complex shapes with functional materials directly from a CAD model (Keicher *et al.*, 1998). Integration of layered manufacturing and material removal processes is the latest trend in rapid prototyping. This enables the manufacture of complex geometries with increased accuracy and surface finish. The deposition of each layer is followed by machining of the excess material, which is often referred to as "exterior sculpting" (Kulkarni *et al.*, 2000).

This paper reviews the successful application of Laser Cladding for RP and the control issues for this application. Laser cladding process dynamics and process parameters are studied to determine their importance in real-time control of the laser deposition process.

Previous Work in Laser Cladding for Rapid Prototyping

Laser Cladding is a material processing technique in which a laser is used as a heating source to melt the alloy powder to be cladded onto a substrate. The application of this technique is being extended to obtain layers of deposition of desired height and width with superior properties in terms of pureness, homogeneity and surface finish. Thus, a metal prototype can be generated by selective cladding point–by–point and layer–by–layer. Some efforts have been made to produce metal prototypes by a layer additive approach (Kosh *et al.*, 1993). They have examined building parts in one and two dimensions, taking into consideration the time and cost involved in the process as compared with traditional methods. Direct Light Fabrication (DLF), which is being developed at Los Almos National laboratory, has proven capable of producing metal parts with reasonably good accuracy and improved metallurgical properties (Lewis *et al.*, 1994; Milewski *et al.*, 1998). It is based on the same principle of adding layers until a near net-shape part is obtained. One such application was carried out using a CO_2 laser with inert gas propulsion of material powder into the molten pool generated by laser radiation on the substrate. A specially designed nozzle was used for this specific application. The movement of the substrate in X and Y directions in combination with the movement of the optics in Z direction and a simultaneous change of nozzle angle allowed the generation of arbitrary three–dimensional structures (Kreute *et al.*, 1995). The geometry of the clad was also investigated by metallographic techniques in combination with optical microscopy. Laser Direct Cladding (LDC) and Selective Laser Cladding (SLC) are based on the same principle as laser cladding, where a gas jet containing fine metal powder is directed via a coaxial nozzle through the path of the laser beam, which is focused slightly above the workpiece. The powder heats up to form molten particles and this laser/melt stream is traversed across the workpiece. A small melt–pool is formed on the surface of the workpiece where the molten particles land to form a layer upon cooling, about 0.5 mm thick, after the laser beam has moved on. It is also possible to lay down very narrow tracks in this way (0.8 mm) and multiple layers can be deposited on top of each other, allowing the formation of complex parts in a relatively short time (Morgan *et al.*, 1997; Jeng *et al.*, 2000). Laser Engineering Net Shaping (LENS) is one developing rapid metal forming process that has demonstrated the feasibility of laser metal forming to produce near–net shape metal parts. It utilizes STL file rendition of a CAD solid model to build an object one layer at a time. The file is sliced electronically into a series of layers that are subsequently used to generate

the motion to deposit each layer of the material. These layers are then deposited in a subsequent fashion to build the entire part (Keicher *et al.*, 1998). Direct Metal Deposition (DMD) is being used to fabricate molds and dies and for part repair. Its wide application in aerospace and medical fields is due to its large savings in cost. Mazumder *et al.* (1999) demonstrated the application of laser aided DMD to generate components with dimensional accuracy of 0.01 inch with the required control of process parameters to obtain the desired microstructure.

Relevant Parameters and Factors Effecting Laser Cladding

The characteristics of a built up part using the above–mentioned techniques mainly depends on the clad properties. Therefore, the parameters governing the cladding process have to be studied carefully. These parameters play an important role in determining the clad profile, dilution of the cladding metal, fusion between layers, homogeneity of the layers, surface finish, defects such as porosity, cracking due to thermal stresses, plasma formation, etc. Dilution is an important factor and a desired range should be set to determine various other factors and parameters governing the laser cladding process. It determines the thickness of the liquid layer on the substrate to ensure the bonding of the current layer with the previous layer. It is not possible to predict the influence of an individual parameter on the cladding process. In general, several parameters have to be varied simultaneously to obtain the desired characteristics of the deposited layer. There are also several limitations that restrict the variations of process parameters. Vetter *et al.* (1994) performed experiments to determine the state of powder when it arrives on the substrate surface. This forms an important limitation as the particles of the powder should be hot enough to adhere to the surface and form a layer, but not too hot such that the particles vaporize, followed by ionization and plasma formation. Thus, the energy available per unit length of clad pass per unit mass of powder and interaction time form the key factors in controlling the state of the powder, provided the other parameters such as powder mass flow rate, CNC table traverse speed, etc. are kept constant. The Heat Affected Zone (HAZ) induces surface distortion and residual stress and may be critical when producing small parts. In overlapping of tracks, the HAZ structure of prior tracks may be tempered by subsequent passes. The width and depth of the HAZ have to be used as indices for determining process performance in some cases. Once the conditions are set to control the above factors, the process parameters can be varied in a defined range to obtain the required clad height and thickness, which in turn are determined by bead geometry and overlap factor. These parameters depend on the powder feed rate, power density and CNC table feed rate. Some common surface defects such as the staircase effect (occurs due to part slicing of part), chordal effect (induced when a STL file is generated from the CAD model), support structure burrs and errors due to starting and ending of deposition are to be minimized to eliminate dimensional inaccuracies and improve surface finish. Different control techniques have to be applied to optimize these system parameters to accomplish the required quality and precision in fabricating a part. By exercising on–line control of these parameters, complex metal parts may be built by adding layers. Care should be taken to avoid porosity, which occurs due to cavities between tracks that form from overlapped tracks or the evolution of entrapped gasses in the clad tracks. This can be avoided by proper choice of overlap factor, which also determines the surface finish of the part. Figure 1 shows the process parameters and their interaction in determining the quality of the part.

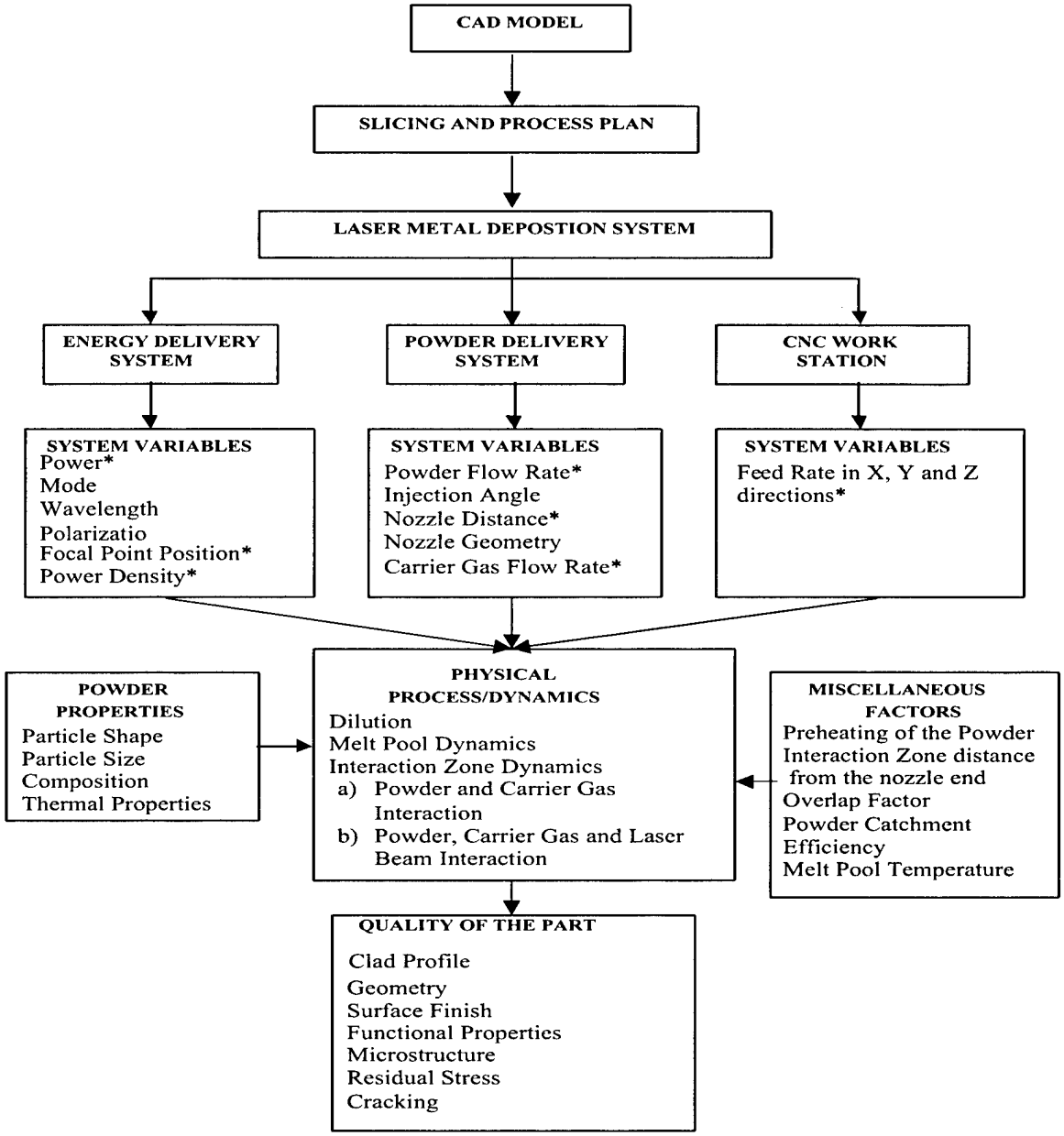


Figure 1: Laser Metal Deposition Process Parameters and Their Interactions. The starred (*) parameters may be varied on–line.

State–of–the–Art in Laser Cladding Control

Rapid Prototyping via lasers requires synchronization of three basic components of the laser deposition system, Powder Feeder System, Energy Delivery System, and CNC workstation. To enhance the part quality, close monitoring and control of the variables of these systems are required. Feedback controllers have to be designed to regulate these variables mainly to control melt pool size, temperature distribution in the melt pool, cooling rate (for microstructure manipulation) and clad height and width. These variables may vary during the operation due to

fluctuations in system parameters such as powder flow rate, beam position and diameter, output power, and CNC feedrate, and pre–setting these operating parameters is not appropriate. They have to be monitored and optimized continuously to obtain the desired conditions. This forms the initial step for real-time process control.

The dimensional accuracy of the part depends on the uniformity and repeatability of the clad height and width being deposited. Mazumder *et al.* (1999) described the application of multiple sensors for closed–loop feedback control of the bead height. The height controller shuts off the laser until it passes the excess built up region, thus preventing the powder from melting. An alternative way to control the bead dimensions is by regulating the powder flowrate, provided the traverse speed of the CNC table is kept constant. Regulation of powder flow rate controls the dilution for a given powder density. Also the carrier and shielding gas flowrate can influence the amount of powder being deposited. By increasing the carrier and shielding gas flowrate, the excess powder can be blown out of the way of the laser beam (Mazumder *et al.*, 1999). Most of the powder feeder systems used for laser cladding were open loop without flow rate sensing. The basic disadvantage of these were their inability to control the flowrate which continuously changes due to variations in powder volume density, with time and level of powder in the hopper although the control settings are kept constant. A small deviation in mass flowrate results in large variations in the geometry and microstructure of the produced tracks. To account for these problems, Li and Steen (1993) designed a closed–loop control system employing Proportional plus Integral plus Derivative (PID) controller with a feed–forward strategy for on-line feedback control of powder flowrate. Carvalho *et al.* (1995) designed a closed loop control system using a (PID) controller for independent delivery of two different powders for variable composition laser cladding. A specially designed coaxial nozzle was used which increased the powder utilization efficiency from approximately 30–50% to values higher than 80% (Hu *et al.*, 1997; Lin and Steen, 1998).

Temperature is another critical factor that requires continuous monitoring and control. It determines the melt pool dimensions and, hence, the dilution. If the temperature is too low, the resulting melt pool catches little powder and if the temperature is too high, it may melt back the workpiece. Morgan *et al.* (1997) described an effective means of controlling the temperature by controlling the laser power via positioning the laser focus relative to the workpiece. It also required a constant adjustment as the height of the structure steadily increases. Experiments were performed to demonstrate the effectiveness of closed–loop over open–loop control of these parameters. Li *et al.* (1987) developed an in–process laser control loop, which is based on an algorithm involving tune currents. The system used a microprocessor based in–process beam control unit using beam sensing via a Laser Beam Analyzer (LBA). Derouet *et al.* (1997) estimated the melt pool depth from the surface width and maximum temperature of the melt pool. This melt pool depth was controlled by a feedback loop using a PID controller. Laser power and scanning velocity were used as the parameters to control the depth of melt pool. Li *et al.* (1987) developed a real-time expert system and a laser cladding control system to determine the optimal operating conditions for a given requirement and for online fault diagnosis and correction. Koomsap *et al.* (2001) presented a simulation–based design of a laser based, free–forming process controller. A simplified model called metamodel was introduced to express the relationship between process characteristics and three process parameters: laser power, traverse speed, and powder feedrate. A dynamic metamodel was obtained and a temperature feedback controller was used to regulate the process. A Proportional plus Integral (PI) controller

was used to regulate the system. Bouhal *et al.* (1999) and Han and Jafari (1999) proposed a tracking controller for positioning and deposition accuracies in part fabrication for fused deposition processes. Fang and Jafari (1999) designed a statistical feedback control architecture integrating Statistical Process Control (SPC) and Automated Process Control (APC) to adjust parameters such as powder flowrate to minimize the possible defects in the next layer. They focused on on–line process parameter adjustment using a layer–to–layer controller. Doumanidis and Skoredli (2000) established a dynamic distributed parameter model with in-process parameter identification to generate a 3D surface geometry. Geometric predictions were made by a real-time model. A controller was designed to regulate the part geometry taking advantage of these predictions. Table 1 shows some of the process control techniques discussed in various papers.

References	Laser Power (kW)	Traverse Speed (mm/sec)	Powder Flow Rate (g/min)	Process Characteristics	Controlling Parameters	Control System	Principle
Morgan et al. (1997)	0.5	8.34		melt pool temperature, clad height	laser focus, melt pool temp	closed loop temperature., laser power	comparison of wavelength of light collected
Hu et al. (1997)	1.3-2.4	3-6	4.8-15	clad zone, interface zone, HAZ	powder flowrate	closed loop powder feeder	fluidized bed metering mechanism
Meriaudeau et al. (1997)			2-3	powder distribution, clad geometry	melt pool temp.		camera used as spectral thermometer
Fang et al. (1999)				overfills, underfills	powder flowrate, traverse speed	layer-by-layer controller for process control	SPC to monitor and APC to adjust variables
Koomsap et al. (2001)	7-14	5-50	6-60	dilution	laser power, traverse speed, powder flowrate	P.I. controller to regulate process parameters	dynamic metamodel was designed
Srivastava et al. (2000)	0.3-0.4	1-24	1-11	clad dimensions, microstructure	scanning rate, laser power	closed loop powder feeder	
Mazumder et al. (1999)	0.7	17	5.6	melt pool size, cooling rate, microstructure	laser power, powder , gas flowrate	closed loop for bead height regulation	
Keicher et al. (1998)	0.18	8.4		surface finish, clad dimensions	laser power, particle size		statistically designed experiment for process control
Derouet et al. (1997)	8-10	5-20		melt pool depth, microstructure, hardness	scanning speed, laser power	P.I.D. controller for melt depth control	
Koch et al. (1993)	0.4	8-12	11	powder utilization efficiency, clad dimensions	melt pool dimensions, laser beam diameter		

Table 1: Process Control Techniques Applied to Regulate Various Parameters.

Summary and Conclusions

Research conducted by various authors in the successful implementation of Laser Cladding for RP has been reviewed, and the impact of the critical parameters in this process has been discussed. Control techniques applied to processes such as dilution, laser power

distribution, powder flowrate, melt pool depth, etc., and on–line control of the parameters governing these processes were discussed.

The study of various works indicates that systematic implementation of process control requires a complete understanding of relation between various parameters and its effect on individual processes and the system as a whole. Most authors have put in efforts in designing closed loop control systems for real-time application of laser cladding for RP. In doing so, many assumptions such as the CNC feed rate and powder flowrate were assumed constant in determining the effect of laser power on processes such as dilution. In real-time application these may not be constant, as the powder flowrate keeps changing as the volume density of powder keeps varying depending on the level of powder in the hopper. Also there might be slight variations in the CNC feedrate, due to accelerations and decelerations while depositing at the edges of the prototype being built. These may lead to overfills and underfills. Hence these deviations need to be taken into consideration and feedback control systems have to be designed to account for these deviations and for process automation and control for optimal operating conditions. Commercial application of laser cladding for RP requires cost oriented design and operating conditions of the laser deposition system, mainly the powder feeder systems, which have to be analyzed to increase powder utilization efficiency which is as low as 30–50% in many of the experimental works.

References

Bouhal, A., Jafari, M.A., Han, W., and Fang, T., 1999, "Tracking Control and Trajectory Planning in Layered Manufacturing Applications," *IEEE Transaction on Industrial Electronics*, Vol. 46, No. 2, pp. 445–451.

Carlvalho, P.A., Braz, N., Pontinha, M.M., Ferreira, M.G.S., Steen, W.M., Vilar, R., and Watkin, K.G., 1995, "Automated Workstation for Variable Composition Laser Cladding – Its Use for Rapid Alloy Scanning," *Surface and Coatings Technology*, Vol. 72, pp. 62–70.

Derouet, H., Sabatier, L., Coste, F., and Fabbro, R., 1997, "Process Control Applied to Laser Surface Remelting," *Proceedings of ICALEO*, Sec. C, pp. 85–92.

Doumanidis, C. and Skoredli, E., 2000, "Distributed-Parameter Modeling for Geometry Control of Manufacturing Processes with Material Deposition," *ASME Journal of Dynamic Systems, Measurement, and Control*, Vol. 122, No. 1, pp. 71-77.

Fang, T. and Jafari, M.A., 1999, "Statistical Feedback Control Architecture for Layered Manufacturing," *Journal of Materials Processing and Manufacturing Science*, Vol. 7, pp. 391–404.

Han, W. and Jafari, M.A., 1999, "Coordinating Control and Deposition Planning for Improving Deposition Accuracy in Layered Manufacturing Process," *IEEE Transactions on Industrial Electronics*, Vol. 46, No. 2, pp. 445–451.

Hu, Y.P., Chen, C.W., and Mukherjee, K., 1997, "An Analysis of Powder Feeding Systems on the Quality of Laser Cladding," *Advances in Powder Metallurgy & Particulate Materials*, Vol. 21, pp. 17–31.

Jeng, J.Y., Peng, S.C., and Chou, C.J., 2000, "Metal Rapid Prototype Fabrication Using Selective Laser Cladding Technology," *International Journal of Advance Manufacturing Technology*, Vol. 16, pp. 681-687.

Keicher, D.M., Miller, W.D., Smugeresky, J.E., and Romero, J.A., 1998, "Laser Engineered Net Shaping (LENS): Beyond Rapid Prototyping to Direct Fabrication," *Proceedings of the 1998 TMS Annual Meeting*, San Antonio, Texas, pp. 369–377.

Koch, J.L. and Mazumder, J., 1993, "Rapid Prototyping by Laser Cladding," *The International Society for Optical Engineering*, Vol. 2306, pp. 556–562.

Koomsap, P., Prabhu, V.V., Schriempf, J.T., and Reutzel, E.W., 2001, "Simulation–Based Design of Laser–Based Free Forming Process Control," *Journal of Laser Applications*, Vol. 13, No. 2, pp. 46–59.

Kreutz, E.W., Backes, G., Gasser, A., and Wissenbach, K., 1995, "Rapid Prototyping with CO_2, Laser Radiation," *Applied Surface Science*, Vol. 86, pp. 310–316.

Kulkarni P. and Dutta, D., 2000, "On the Integration of Layered Manufacturing of Layered Manufacturing and Material Removal Processes," *ASME Journal of Manufacturing Science and Engineering,* Vol. 122, No. 1, pp. 100-108.

Laeng, J., Stewart, J.G., and Liou, F.W., 2000, "Laser Metal Forming Process for Rapid Prototyping – A Review," *International Journal of Production Research*, Vol. 38, No. 16, pp. 3973–3996.

Lewis, G.K., Nemec, R., Milewski, J., Thoma, D.J., Cremers, D., and Barbe, M., 1994, "Directed Light Fabrication," *Proceedings of ICALEO*, pp. 17–26.

Li, L., Hibberd, R.H., and Steen, W.M, 1987a, "In–Process Laser Power Monitoring and Feedback Control," *Proceedings of the 4th International Conference of Lasers in Manufacturing*," pp. 165–176.

Li, L., Steen, W.M., Hibberd, R.H., and Weerasinghe, V.M., 1987b, "Real–time Expert Systems for Supervisory Control of Laser Cladding," *Proceedings of ICALEO*, pp. 9–15.

Li, L. and Steen, W.M., 1993, "Sensing, Modeling and Closed Loop of Powder Feeder for Laser Surface Modification," *Proceedings of ICALEO*, pp. 965–974.

Lin, J. and Steen, W.M., 1998, "Design Characteristics and Development of a Nozzle for Coaxial Laser Cladding," *Journal of Laser Application*, Vol. 10, 55–63.

Mazumder, J., Schifferer, A., and Choi, J., 1999, "Direct Materials Deposition: Designed Macro and Microstructure," *Materials Research Innovations*, Vol. 3, pp.118–131.

Meriaudeau, F., Truchetet, F., Dumont, C.D., and Aluze, D., 1996, "Laser Cladding Process: The Relevant parameters and their Optimization through a Low Cost System," *ICALEO,* Section A, pp. 75-84.

Milewski, J.O., Thoma, D.J., Fonseca, J.C., and Lewis, G.K., 1998, "Development of a Near Net Shape Processing Method for Rhenium Using Directed Light Fabrication," *Journal of Materials and Manufacturing Processes*, Vol. 13, No. 5, pp. 719-730.

Morgan, S.A., Fox, M.D.T., McLean, M.A., Hand, D.P., Haran, F.M., Su, D., Steen, W.M., and Jones, J.C., 1997, "Real–Time Process Control In CO_2 Laser Welding and Direct Casting: Focus and Temperature," *Proceedings of ICALEO*, Sec. F, pp. 290–299.

Munjuluri, N., Agarwal, S., and Liou, F.W., 2000, "Process Modeling, Monitoring and Control of Laser Metal Forming," *Proceedings of the Eleventh Annual Solid Freeform Fabrication Symposium*, Austin Texas, August 7–9.

Srivastava, D., Chang, I.H.T., and Loretto, M.H., 2000, "The Optimization of Processing Parameters and Characterization of Microstructure of Direct Laser Fabricated TiAl Alloy Components," Materials and Design, Vol. 21, pp. 425-433.

Vetter, P.A., Engel, T., and Fontaine, J., 1994, "Laser Cladding: The Relevant Parameters for Process Control," *Proceedings of the SPIE The International Society for Optical Engineering*, Vol. 2207, pp. 452–462.

Weerasinghe, V.M. and Steen, W.M., 1983, "Laser Cladding by Powder Injection," *Proceedings of the 1st International Conference on Lasers in Manufacturing*, pp. 125–132.

PHYSICAL MODELING FOR DYNAMIC CONTROL OF MELTING PROCESS IN DIRECT-SLS

S. Ahn, J. Murphy, J. Ramos, and J. J. Beaman
Department of Mechanical Engineering
The University of Texas at Austin, Austin TX 78712

Abstract

During the melting process by laser irradiation, it is essential to understand the phase change processes to get high quality Direct SLS parts especially when high-order scanning paths are needed. This process is a transient three-dimensional heat conduction problem with a moving heat source and a moving phase boundary. The process can be simplified to a one-dimensional moving boundary model using appropriate assumptions. To implement a real-time control strategy, approximate solutions were found using three methods. Experiments using a CW CO_2 laser were performed on low carbon steel samples to verify the models' results. By using first order differential equations derived from the model, multi-input multi-output (MIMO) control strategies can be applied.

Introduction

Laser fusion based SFF processes need a real time control strategy that incorporates melt depth information.[1] Direct-SLS processes involve accurate melting of powder layers and fusion bonding of that layer with the previously deposited layer. The current process lacks melt-depth control capability. Also when high-order scanning paths are needed, the power or speed of the laser beam must be adjusted along the path to provide sufficient depth of melt. Superheating of the liquid zone must be controlled because melting of the entire powder layer thickness and fusion bonding to the previously deposited layer is required. To understand this process, we need to know the temperature distribution inside the material and the melt depth information. To solve this temperature distribution and melt depth, one-dimensional heat conduction with appropriate assumptions have been used.[2-5]. Three different models were used to compare results with experimental data. Each model used slightly different solution methodology and assumptions.

Physical Models

Transient three-dimensional heat conduction with a moving heat source and a moving phase boundary as shown in Fig. 1 is described by the following general governing equations and boundary conditions. V_s and $S(X_s,Y_s,Z_s,t)$ are the heat source velocity and phase boundary surface, respectively.

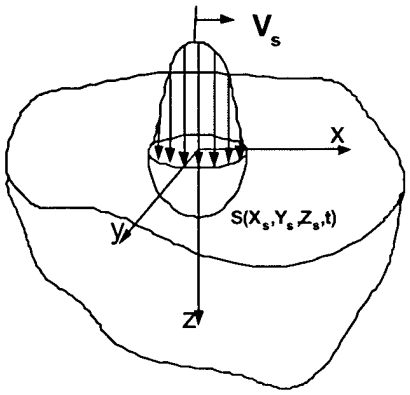


Figure 1: Schematic of a transient three-dimensional heat conduction with a moving heat source and moving phase boundary.

General Heat Diffusion Equation:

$$\frac{\partial}{\partial t}(\rho CT)+\vec{V}\cdot\nabla(\rho CT)=\nabla\cdot(k\nabla T) \tag{1}$$

Equation 1 can be solved separately for the solid and liquid regions with the following boundary and interface conditions.

General Boundary Conditions:

$$-k_l\frac{\partial T}{\partial z}=\varepsilon\sigma(T^4-T_\infty^4)+h_\infty(T-T_\infty)+q_{in} \quad \text{at } z=0 \tag{2}$$

$$T=T_0 \text{ at } t=0 \tag{3}$$

$$T=T_0 \text{ at } x\to\pm\infty \quad y\to\pm\infty \quad z\to\infty \tag{4}$$

Phase Interface Conditions:

$$\left[1+\left(\frac{\partial X_s}{\partial y}\right)^2+\left(\frac{\partial X_s}{\partial z}\right)^2\right]\left(k_s\frac{\partial T_s}{\partial x}-k_l\frac{\partial T_l}{\partial x}\right)=L\left(\frac{\partial X_s}{\partial t}-V_x\right) \tag{5a}$$

$$\left[1+\left(\frac{\partial Y_s}{\partial x}\right)^2+\left(\frac{\partial Y_s}{\partial z}\right)^2\right]\left(k_s\frac{\partial T_s}{\partial y}-k_l\frac{\partial T_l}{\partial y}\right)=L\left(\frac{\partial Y_s}{\partial t}-V_y\right) \tag{5b}$$

$$\left[1+\left(\frac{\partial Z_s}{\partial x}\right)^2+\left(\frac{\partial Z_s}{\partial y}\right)^2\right]\left(k_s\frac{\partial T_s}{\partial z}-k_l\frac{\partial T_l}{\partial z}\right)=L\left(\frac{\partial Z_s}{\partial t}-V_z\right) \tag{5c}$$

Here T, k_i, ρ, ε, σ, L, h_∞ are temperature, thermal conductivity of ith phase, density, emissivity, Stefan-Boltzmann constant, latent heat of fusion, and convention coefficient, respectively. [9]

Assumptions

The general three-dimensional problem can be simplified to a one-dimensional moving boundary problem (e.g. Stefan problem) by using the following assumptions:

- Thermo-physical properties are considered independent of temperature and constant in space within each phase region.
- Velocity of moving beam is replaced by an equivalent interaction time, $\Delta t = \frac{D_b}{V_s}$ where D_b is beam diameter and V_s is scan speed. [13] (See Fig. 2)
- 1-D approximation is enough to predict the maximum depth of melt when the interaction time is less than the radial thermal diffusion time ($FourierNumber \equiv \frac{4\alpha\Delta t}{D_b^2} \leq 1$, α is thermal diffusivity).
- Heat losses by radiation, convection and lateral conduction can be included in an overall absorption coefficient for the surface.

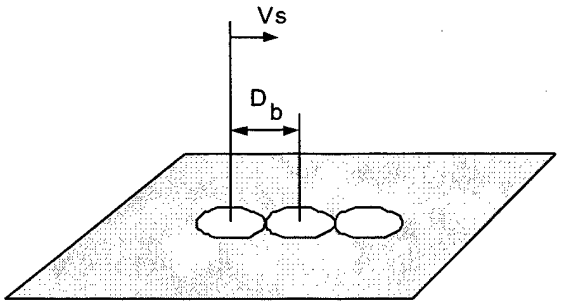


Figure 2: Illustration of interaction time.

Generalized 1-D Model

Using the above assumptions, the general governing equations can be simplified to the equations shown below. Figure 3a shows a cross section of the actual phase boundary. The maximum boundary depth is approximately uniform away from the edges and demonstrates a one-dimensional approximation is reasonable to predict maximum melt depth. Figure 3b shows a schematic of the 1-D model with model parameters included. I, A, z_m, and δ are laser intensity, absorption coefficient, melt depth, and thermal boundary layer thickness, respectively.

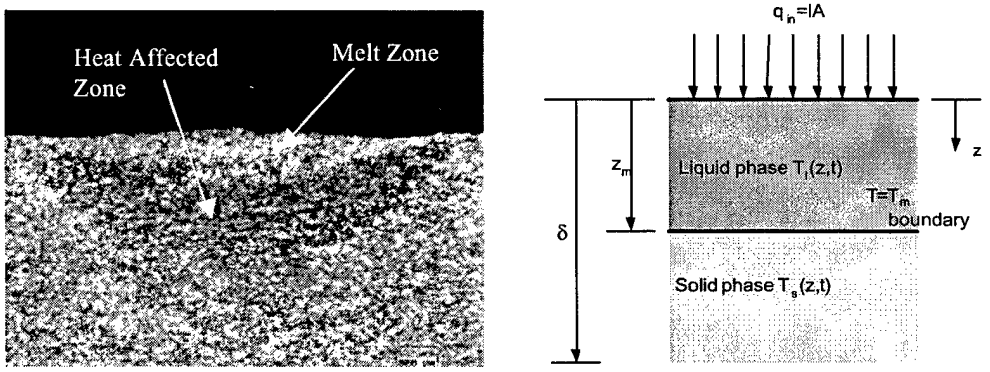


Figure 3: a) Cross section of low carbon steel test specimen scanned at Power = 1.1 kW and Vs = 11 m/min. b) Schematic diagram of one-dimensional moving phase boundary problem.

Heat diffusion equations:

$$\frac{\partial^2 T_l}{\partial z^2} = \frac{1}{\alpha_l}\frac{\partial T_l}{\partial t} \qquad \text{Liquid Phase} \qquad (6a)$$

$$\frac{\partial^2 T_s}{\partial z^2} = \frac{1}{\alpha_s}\frac{\partial T_s}{\partial t} \qquad \text{Solid Phase} \qquad (6b)$$

Boundary conditions:

$$-k_l \frac{\partial T_l}{\partial x} = AI \text{ at } z = 0 \qquad \text{Surface Heat Flux} \qquad (7)$$

$$k_s \frac{\partial T_s}{\partial x} - k_l \frac{\partial T_l}{\partial x} = \rho L \dot{z}_m(t) \qquad \text{Melt Interface Condition} \qquad (8)$$

$$T_l(z,t) = T_s(z,t) = T_m \text{ at } z = z_m(t) \qquad (9a)$$

$$T_s(\infty, t) = T_0 \qquad (9b)$$

$$T_s(z, t_0) = T_0 \qquad (9c)$$

1-D Approximate Integral Model

The approximate integral model was derived using the heat-balance integral solution method. [2] The heat-balance integral is the integral with respect to the space variable of the heat conduction equations. As a result Eqs. (6a) and (6b) become Eqs. (10a) and (10b) shown below. There are two moving boundaries: the melt depth and the thermal boundary layer thickness (see Figure 3b).

$$\left.\frac{\partial T_l}{\partial z}\right|_{z_m} - \left.\frac{\partial T_l}{\partial z}\right|_0 = \frac{1}{\alpha_l}\frac{d}{dt}\left[\int_0^{z_m} T_l dz - \left(T_m z\big|_{z_m} - T_l z\big|_0\right)\right] \qquad (10a)$$

$$\left.\frac{\partial T_s}{\partial z}\right|_{\delta} - \left.\frac{\partial T_s}{\partial z}\right|_{z_m} = \frac{1}{\alpha_s}\frac{d}{dt}\left[\int_{z_m}^{\delta} T_s dz - \left(T_0 z\big|_{\delta} - T_m z\big|_{z_m}\right)\right] \qquad (10b)$$

Solutions were obtained by first assuming the temperature profiles were second order polynomial functions in the space variable, z and fit the given boundary conditions. Next, the profiles were substituted into Eqs. (10a), (10b), and (8). The result was three first order ODE's. The temperature profiles are given in Eqs. (14) and (15) shown below. The first order ODE's are shown below as Eqs. (16) – (18).

Before Melting: $0 \le t \le t_m$

$$T_s(z,t) = T_0 + \frac{AI}{2k_s\delta^2}[z-\delta]^2, 0 \le z \le \delta \qquad (11)$$

$$\delta = \sqrt{6\alpha_s t} \qquad (12)$$

$$t_m = \frac{3k_s^2(T_m - T_0)^2}{4\alpha_s A^2 I^2} \qquad (13)$$

During Melting: $t_m \le t \le \Delta t$

$$T_l(z,t) = T_m + \left(2\lambda z_m - \frac{AI}{k_l}\right)[z - z_m] + \lambda[z - z_m]^2,\ 0 \le z \le z_m \quad (14)$$

$$T_s(z,t) = T_0 + \frac{(T_m - T_0)}{(z_m - \delta)^2}[z - \delta]^2, z_m \le z \le \delta \quad (15)$$

Eq. 16 is the state equation for the melt depth.

$$\dot{z}_m = \frac{AI}{\rho L} - \frac{2k_l \lambda z_m}{\rho L} + \frac{2k_s(T_m - T_0)}{\rho L(z_m - \delta)} \quad (16)$$

Eq. 17 is the state equation for the thermal boundary layer thickness.

$$\dot{\delta} = -\frac{6\alpha_s}{(z_m - \delta)} - \frac{2AI}{\rho L} + \frac{4k_l \lambda z_m}{\rho L} - \frac{4k_s(T_m - T_0)}{\rho L(z_m - \delta)} \quad (17)$$

Eq. 18 is the state equation for the coefficient in the liquid region temperature profile.

$$\dot{\lambda} = \frac{3}{2z_m^2}\left(\frac{AI}{k_l} - 2\lambda z_m\right)\left(\frac{AI}{\rho L} - \frac{2k_l \lambda z_m}{\rho L} + \frac{2k_s(T_m - T_0)}{\rho L(z_m - \delta)}\right) - \frac{3\alpha_l \lambda}{z_m^2} \quad (18)$$

The difference between this solution and classic solution is the assumption is not made that the moving boundaries are only functions of time. Goodman and others use the assumptions, $z_m = \beta\sqrt{\alpha t}$ and $\delta = \gamma\sqrt{\alpha t}$, to reduce the solution to one independent variable, t.[2] The advantage of obtaining first order ODE's is MIMO control schemes can be readily implemented. Figure 4 shows the temperature distribution as a function of depth and time calculated using the approximate integral model. The dark line indicates the melting interface.

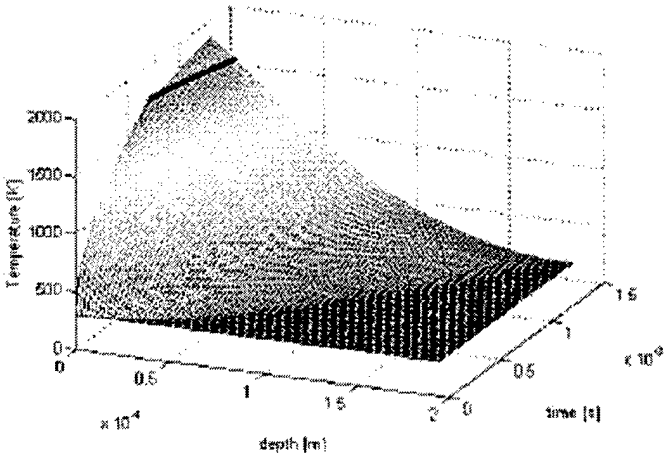


Figure 4: Simulation of 1-D melting using approximate integral model. Power = 230 W, V_s= 0.3 m/s, T_0 = 300K.

Xie & Kar's Model

Based on Sharma and et al.'s an approximate solution for one-dimensional phase-change heat conduction with time-dependent surface temperature [3], Xie and Kar [8] solved the one-dimensional phase-change with heat flux problem given by Eq. (6) by assuming a temperature distribution that satisfies the boundary and interface conditions (7)-(9). For liquid region, they assume a temperature profile which satisfies boundary conditions (7) and (9a) as follows,

For $0 \le z \le z_m(t)$:

$$T_l(z,t) = T_m - \frac{AI}{k_l}[z - z_m(t)] + \frac{AI}{2\alpha_l k_l\left[1+\frac{z_m(t)}{\alpha_l}\dot{z}_m(t)\right]}\dot{z}_m(t)\left[z^2 - z_m{}^2(t)\right] \qquad (19)$$

In the solid region, they assume a temperature profile that satisfies boundary conditions (9), that is:

For $z > z_m(t)$:

$$T_s(z,t) = T_m - (T_m - T_0)\left\{1 - \exp\left[-\frac{1}{\alpha_s}\dot{z}_m(t)(z - z_m(t))\right]\right\} \qquad (20)$$

The melt depth velocity is given below in Eq. 21.

$$\dot{z}_m(t) = \frac{2AI}{\rho\left[C_p(T_m - T_0) + L\right]\left\{1+\sqrt{1+\frac{4AIz_m(t)}{\alpha_l\rho\left[C_p(T_m - T_0)+L\right]}}\right\}} \qquad (21)$$

The time for the surface to reach the melting temperature, t_m, is given by Eq. 22. [7]

$$t_m = \frac{\pi k_s{}^2 (T_m - T_i)^2}{4\alpha_s (AI)^2} \qquad (22)$$

The time required to reach the vaporization temperature, $t_{m\to v}$, can be calculated by using Eq.(21). The melt time, t_m, and the vaporization time, t_v, are used to establish upper and lower bounds on the interaction time, Δt.

Heat ablation model with heat input as function of absorption coefficient and melt depth

Based on the approximation solution for transient heat conduction by Zien [4] and Vujanovic [6], Beaman applied the solution to a vacuum arc remelting model.[10] Here by assuming heat flux is a function of melt depth the model can be applied to the laser melting process.

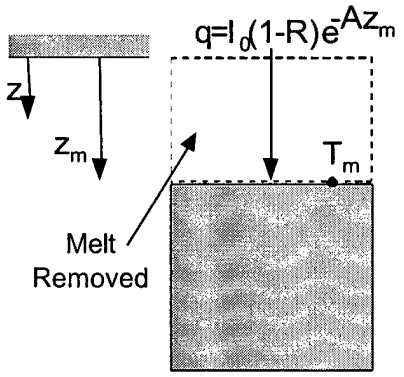


Figure 5: Schematic diagram of one–dimensional heat ablation problem.

The resulting equations are shown below as Eqs. (23) – (26).

$$\dot{\delta} = \frac{C_{\delta\delta}\alpha_r}{\delta} - \frac{C_{\delta p}}{h_m} I(1-R)e^{-Az_m} \qquad (23)$$

$$\dot{z}_m = -\frac{C_{s\delta}\alpha_r}{\delta} + \frac{C_{sp}}{h_m} I(1-R)e^{-Az_m} \qquad (24)$$

where:

$$C_{\delta p} = \frac{32\Lambda^*}{3\Lambda^* + 11} \qquad (25a)$$

$$C_{sp} = \frac{11\Lambda^*}{3\Lambda^* + 11} \qquad (25b)$$

$$C_{s\delta} = \frac{56\Lambda^*}{3\Lambda^* + 11}\left(\frac{1}{2} + \frac{\beta u_m}{3}\right) \qquad (25c)$$

$$C_{\delta\delta} = \frac{224(\Lambda^* + 1)}{3\Lambda^* + 11}\left(\frac{1}{2} + \frac{\beta u_m}{3}\right) \qquad (25d)$$

$$\Lambda^* = \frac{u_m}{u_{sup} - u_m} \qquad (26)$$

Experimental Setup

Experimental specimens were processed using a 1.1 kW CO_2 laser (beam diameter = .4 mm) operated in CW mode. The specimen was placed in vacuum chamber that was evacuated and back filled with argon to prevent oxidation. The power range used was 460 W to 1100 W. Multiple scan speeds were used at each power level to provide a range of interaction times to be compared to simulated results. The laser-scanning program utilizes a raster scan pattern shown in Fig. 7. In Fig. 7, w, L, V_t, and V_s are the scan track width, scan track length, transverse velocity, and scan velocity, respectively. The scan velocity, V_s, was difficult to measure directly, so it was calculated using Eq. 27 shown below. Here S_l is scanning density or scan lines per unit length.

$$V_s = \frac{wV_t}{L} S_l \qquad (27)$$

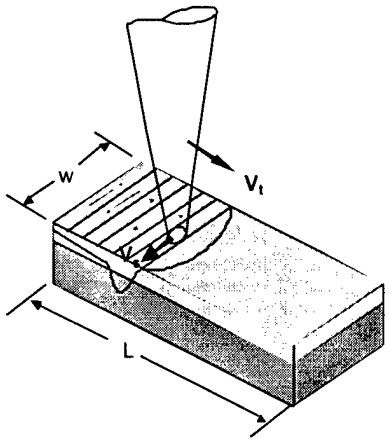


Figure 6: Raster scanning pattern of the 1.1 kW CO_2 laser.

The material used in the experiments was low carbon steel coated with graphite paint to increase the absorptivity of the samples. Two examples of the results are shown in Fig. 7. After processing, the samples were cut, grinded, polished, etched and measured using an optical microscope. The sample in Fig. 7a had the largest melt depth and the sample in Fig 7b had the least.

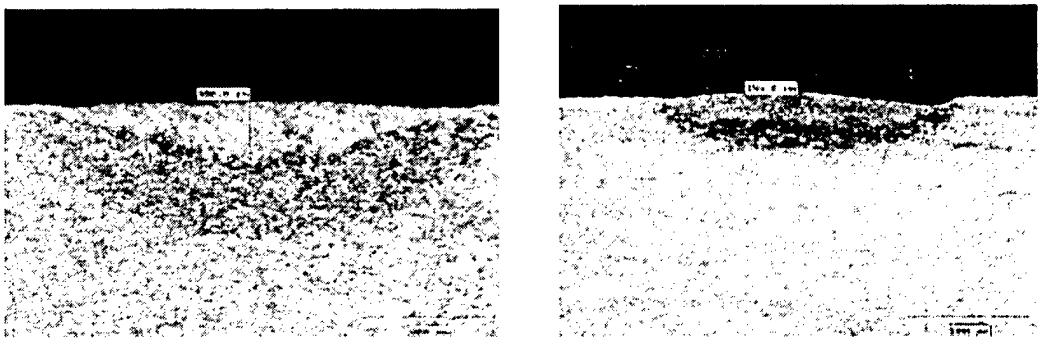


Figure 7: a) Scan track cross section of low carbon steel scanned at Power = 1100 W, Vs = 8 m/min, and melt depth ~ 400 μm. b) Scan track cross section of low carbon steel scanned at Power = 460 W, Vs = 21 m/min, and melt depth ~ 155 μm.

Results and Discussion

The experiments were conducted at three specific power levels: 1100 W, 715 W, and 460 W. The measurements taken from the experimental samples were plotted against the simulated results from all three models. Figures 8 through 10 show the results. The experimental points are indicated by points with error bars protruding. The error in melt depth measurement indicated by the error bars was estimated to be about 10 percent.

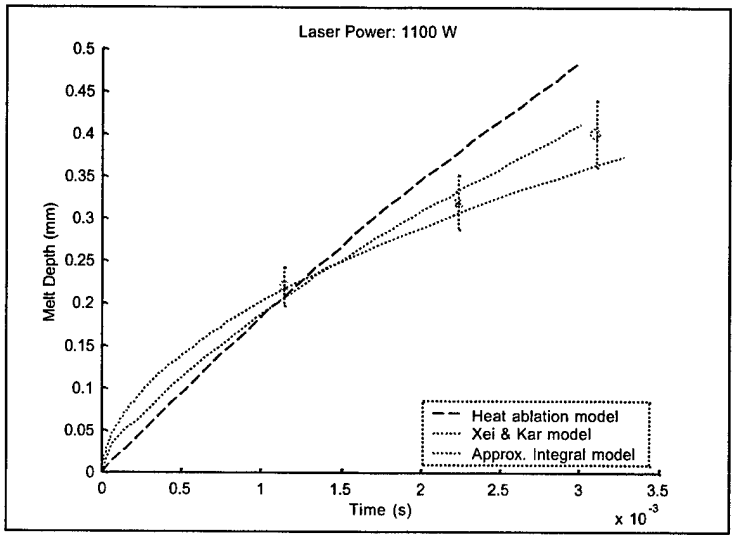


Figure 8: Melt Depth versus Interaction Time. Power = 1100 W.

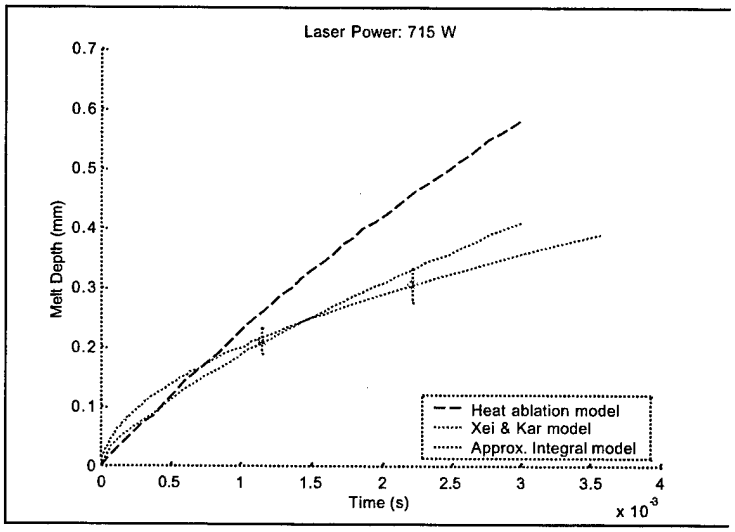


Figure 9: Melt Depth versus Interaction Time. Power = 715 W.

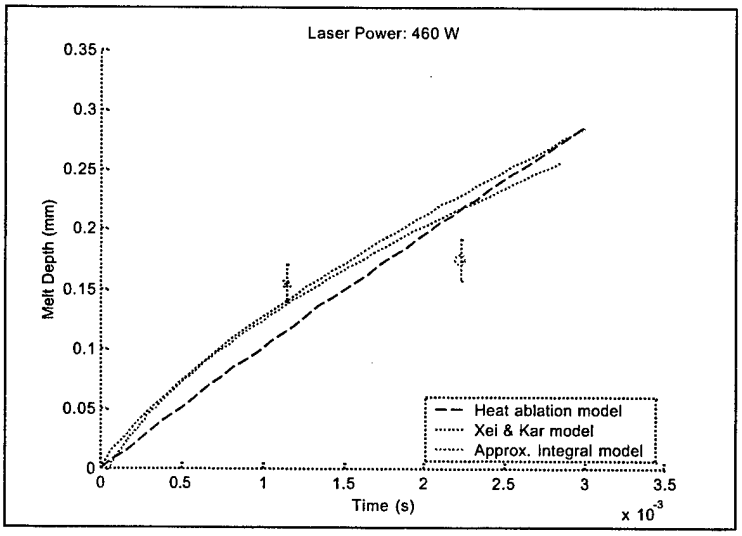


Figure 10: Melt Depth versus Interaction Time. Powe r = 460 W.

Both the Xie and Kar's model and the approximate integral model matched the experimental data well. The heat ablation model overestimates the melt depth as the interaction time increases. The simulated melt depths are highly sensitive to changes in absorption coefficient, so careful calibration must be performed to ensure proper performance. More accurate absorption coefficient data is needed for that process.

All three models can by used for control purposes, but the approximate integral model is more appropriate for MIMO control design. Figure 12 shows a block diagram of a MIMO control design concept.

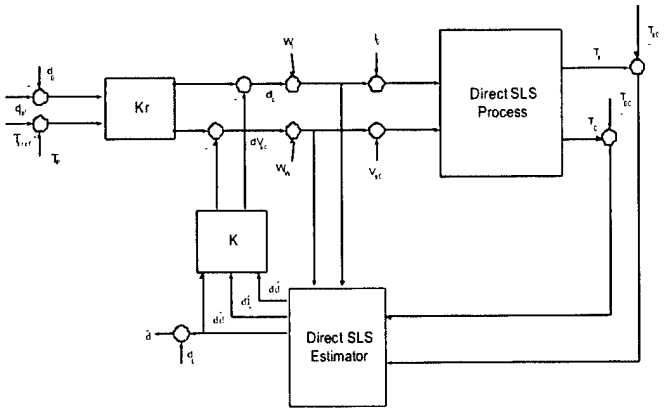


Figure 12: Block diagram of MIMO control design

Conclusions

The comparison between the experimental data and the simulations illustrates the conclusion that the 1-D Stefan problem provides a good approximation for the melt depth when the laser beam velocity is fast enough to make the interaction time less than the radial thermal diffusion time. The 1-D approximation solution can be fitted to the experimental data by adjusting the absorption coefficients of the solid and liquid regions. The models are highly sensitive to the absorptivities and more research must be done to determine how heat losses and material properties affect the overall absorption coefficients. Also for Direct SLS applications, density change during melting of powder-bed will be considered.[12]. Lastly, the approximate integral solution will be investigated further. The solution includes first order ODE's that easily can be adapted to MIMO control design. The design and implementation of the controller will be the future work and final goal of the research.

References

1. S. Das, *Direct selective laser sintering of high performance metals-machine design, process development and process control*, Ph.D Dissertation, The University of Texas at Austin, 1998.
2. T. R. Goodman and J. J. Shea, *The melting of finite slabs*, Journal of Applied Mechanics, Vol.27, pp.16-24, 1960.
3. O. P. Sharma, M. Rotenberg, and S. S. Penner, *Phase-change problems with variable surface temperature*, AIAA Journal, Vol.5, No.4, pp.667-682,1967.
4. T. F. Zien, *Integral solutions of ablation problems with time-dependent heat flux*, AIAA Journal Vol.16, No.12, pp.1287-1295, 1978.
5. M. N. Özisik, *Heat Conduction*, Wiley, New York, 1980.
6. B. D. Vujanovic and S. E. Jones, *Approximate solutions of canonical heat conduction equations*, Transactions of ASME, Vol.112, pp.836-842, 1990.
7. F. P. Incropera and D. P. DeWitt, *Fundamentals of Heat and Mass Transfer*, Wiley, New York, 1990.

8. J. Xie and A. Kar, *Mathematical modeling of melting during laser materials processing*, J. Appl. Phys., Vol.81, No.7, pp.3015-3022, 1997.
9. A. A. Rostami and A. Raisi, *Temperature distribution and melt pool size in a semi-infinite body due to a moving laser heat source*, Numerical Heat Transfer, Part A, Vol.31, pp.783-796, 1997.
10. D. K. Melgaard,R. L. Williamson, J.J. Beman, *Controlling remelting processes for superalloys and aerospace Ti alloys*, JOM, Vol.50, No.3, 1998.
12. Y. Zhang, A Faghri, *Melting of subcooled mixed powder bed with constant heat flux heating*, Int. J. Heat and Mass transfer, Vol.42 , pp.775 -788, 1999.
13. N.Jebbari, M. Jebari, F. Ahdad, A. Tarrats-Saugnac, J. P. Longuemard, *Energy mechanism during machining process by high-power continuous CO_2 laser*, Appl. Phys. B Vol.70(1), pp. 99-103, 1999.

this page intentionally blank

SOFTWARE FOR THE INTERACTIVE CONFIGURATION OF RP BASED PROCESS CHAINS

Stefan Dreher
Department of Virtual Product Creation, Fraunhofer IPK Berlin, Pascalstr. 8-9, 10587 Berlin, Germany

Abstract

In product development, time is one of the most critical factors. By introducing Rapid Prototyping methods, development time can be reduced dramatically. But the required characteristics of the generated prototypes become more and more complex. As a result, a great variety of Rapid Prototyping devices and services have emerged on the market. The product developer may be highly satisfied with the wide range of new potentials, tools and methods but who will give him an orientation about the most suitable process chain to fulfil his demands? To solve this problem, a new software is being developed at the Fraunhofer Institute IPK in Berlin, the iViP-RPSelector.

In a first step, the software tracks a record of the demands to the prototype. These values can be inserted manually, but there is an interface as well connecting the RPSelector to CAD and PDM systems to obtain the design parameters without user interaction. The RPSelector then calculates a complete RP based process chain, which may comprise a layer wise creation, some post processing, a copying process and several finishing processes.

Design Loops

The design and production planning of technical products runs through several phases and each phase is repeatingly performed, using design reviews to allow a loop wise improvement of the product's design and functionality. Within these loops, depending on the maturity of the product, different technologies may be used to produce prototypes rapidly. Since the manufacturing of prototypes is divided into several steps, e.g. generative production, post processing, surface finish, multiplication by means of casting or moulding etc., these process chains have to be configured individually following the requirements.

Today, the configuration of process chains is a task that has to be performed thoroughly in order to obtain the best results in the prototype phase of a product development project. After having defined the requirements concerning all requested prototype characteristics, the product developer needs a partner to execute process selection and process planning interactively. Normally he will contact a 'Rapid Technologies' service bureau. This process can be considered as a brokerage between two or more partners. But when doing so, the product designer is not able to assess neither the selected solution nor the suitability of the promised result.

Software Support for RP manufacturing

Both processes, selection and brokerage of RP process chains, are subject to many error sources in daily business. Firstly, the designer may have omitted to communicate special parameters such as corrosive media that will destroy the surface of the planned prototype, or temperatures occurring during the tests. Secondly, the process planner may omit the influence

of pre-processing or post processing steps. Finally, the service bureau may use sub optimal processes and material, being misinformed about the state of the art.

As a result, the requirements for the software are

- Taking into account the newest technological developments
- Checking the interoperability of individual process steps
- Calculating the impact of individual processes on the manufactured parts
- Make the user competent to assess technologies
- Offering an interface to the brokerage of manufacturing services
- Ability to introduce new processes and materials into the system
- Ability to introduce new rules for the computation of process chains
- Offer the possibility to moderate and control the procurement and logistics

The module has to be designed to assist both, the designer and the production service. It will enhance a much faster and more efficient design review loop. As a result, the quality and circle time of prototype manufacturing are improved significantly.

The software tool „iViP-RPSelector" and the corresponding "RPBroker" have been developed to meet the above described requirements. The development started by collecting the critical factors. This was done by analysing several existing projects in the industry. Existing shortcomings have been documented and converted into software abilities in order to eliminate those gaps.

An object-oriented approach was chosen. Hence all processes and materials could be described as objects having individual properties. As a first step a list of parameters describing the objects used, was exchanged between project partners. System development was then divided into two main tasks:

1. the organization of the database
2. the evaluation functionality

The technological evaluation of the previously defined requirements is based on an object model that describes typical process qualities. Input and output objects are defined for each individual manufacturing step. Input objects of a manufacturing step are e.g. the CAD data of the component or values for shrinkage of predecessor processes. Output objects are output files or the produced components (Fig. 1).

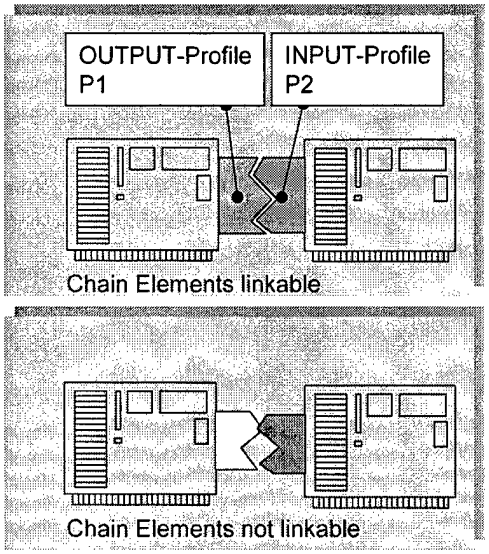


Figure 1: Linking individual process steps

A consistent description of process concatenation alternatives is the outcome. Material cost can be defined easily through a volume calculation of the workpiece. Machine working hours can be calculated approximately by computing the height and volume of the workpiece. Calculation deviations will originate in the workpiece position and amount of parts built, especially when estimating the cost of generative processes. So monetary aspects are reduced to 'technological' costs, that are material and a rough estimation of machine costs.

Evaluation of Requirements

In real life, certain fuzziness underlies the selection and configuration of manufacturing means. Imagine you request a set of four steel prototypes, allowing a delivery time of two weeks. A service bureau you contact is able to produce those four parts within three weeks. If you lower the requested surface quality, the period can be shortened to 16 days. But if you allow 4 weeks, they are able to produce 500 parts. A human being performs the evaluation on the base of his/her experience. The weight/importance is assigned to each requirement by communicating with the customer.

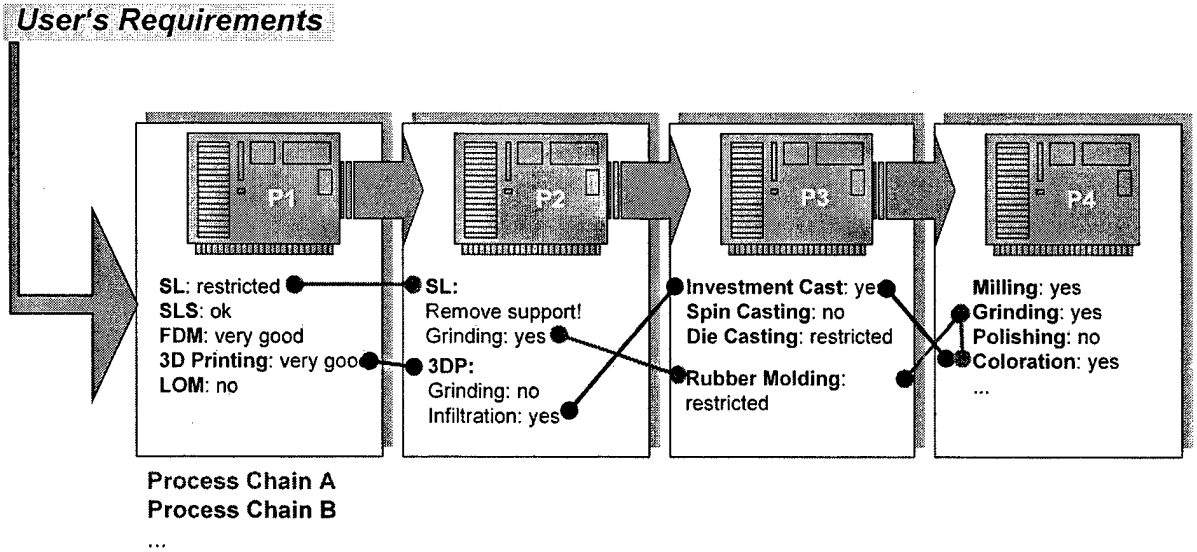


Figure 2: Concatenation of Process Elements

The requirements have to be weighted to enable the system to distinguish between important and less important requirements. The task of the evaluation algorithms is to find a manageable number of approximately ten best fitting manufacturing possibilities, taking into account the requirements and their priority (Fig. 2). The result is then presented to the customer. A reasoning module has been implemented which makes the selection transparent for the customer. For every criterion, the fulfilment degree of the requested characteristic is represented graphically. In the case of unsatisfactory selection results, the customer is able to identify those requirements that represent a weak point in the selection task.Process planning activities can be carried out more efficiently and more precisely based on the described process configuration. The limitations of each single process in the selected chain are listed and the system gives hints to support the machine operator. In addition to the pure technological process planning, the effects of the predecessor and consecutive technologies are considered.

If, for example, a milling process is planned as a following process to the generative production of a component in order to meet tolerances, the iViP-RPSelector adds a reminder to scale the relevant measures. As a result, a sufficient material removal by milling is guaranteed even in the most unfavourable case.

Available Software Architectures

The implementation of a PURE JAVA interface using a JDBC (JAVA Database-Connection)-bridge operating on SQL statements allows the access of database contents and the extraction of specified values regardless what type of database is used. The evaluation functionality is represented schematically in the following figures. Basically four consecutive process elements were defined (Fig. 3). A set of requirements is compared with the capabilities and limitations of every process element. The result is a pre-selection of adequate elements.

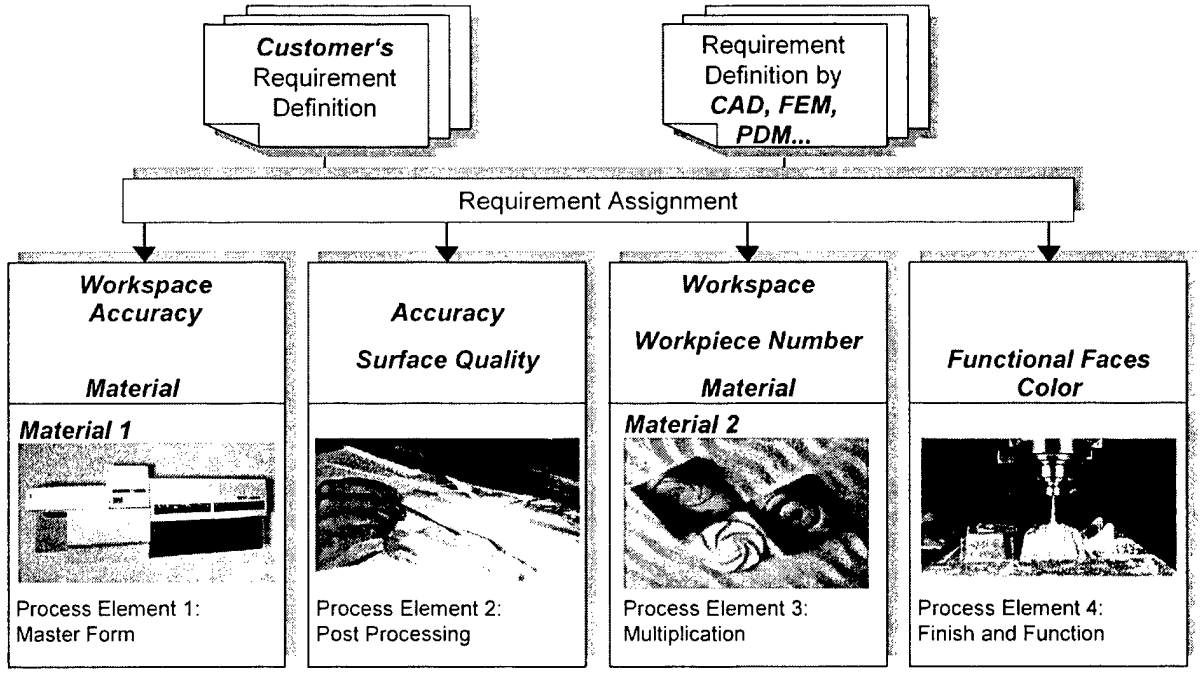


Figure 3: Configuration of process elements due to customer requirements

The planning software is designed to be used by product developers as well as service bureaus. It replaces neither the experience of the experts nor the process planning procedures available at the service bureau's site. The software forms an important bridge between the design and procurement activities on one hand and the subsequent component production on the other hand. The selection module can be used in multiple software environments:

1.1 Stand Alone Application

The selection module can easily be installed on a PC. The database is then stored locally. As a result, external access is not possible. Updating is done manually by inserting new processes or materials that are available at the user's site. Alternatively a complete installation of new versions of the software is necessary when the state of the art has changed.

1.2 Web Access

The selection can be performed by the installation of a web server and accessing it through the World Wide Web. Updates can be realised continuously by experts without end user's interaction. Individual changes of process and material limitations by the user are not available, because the only database is located on the web server.

1.3 Virtual Product Development

The software consists of multiple modules and hence can be integrated into a distributed software architecture like iViP. In this case, the iViP-RPSelector can communicate with other applications in order to retrieve relevant data such as workpiece size, material or prototype functionality. The results are sent to the module iViP-RPBroker, which supports the procurement and manufacturing workflow, following the selected process elements. The architecture of this complex software infrastructure is shown in Fig. 4.

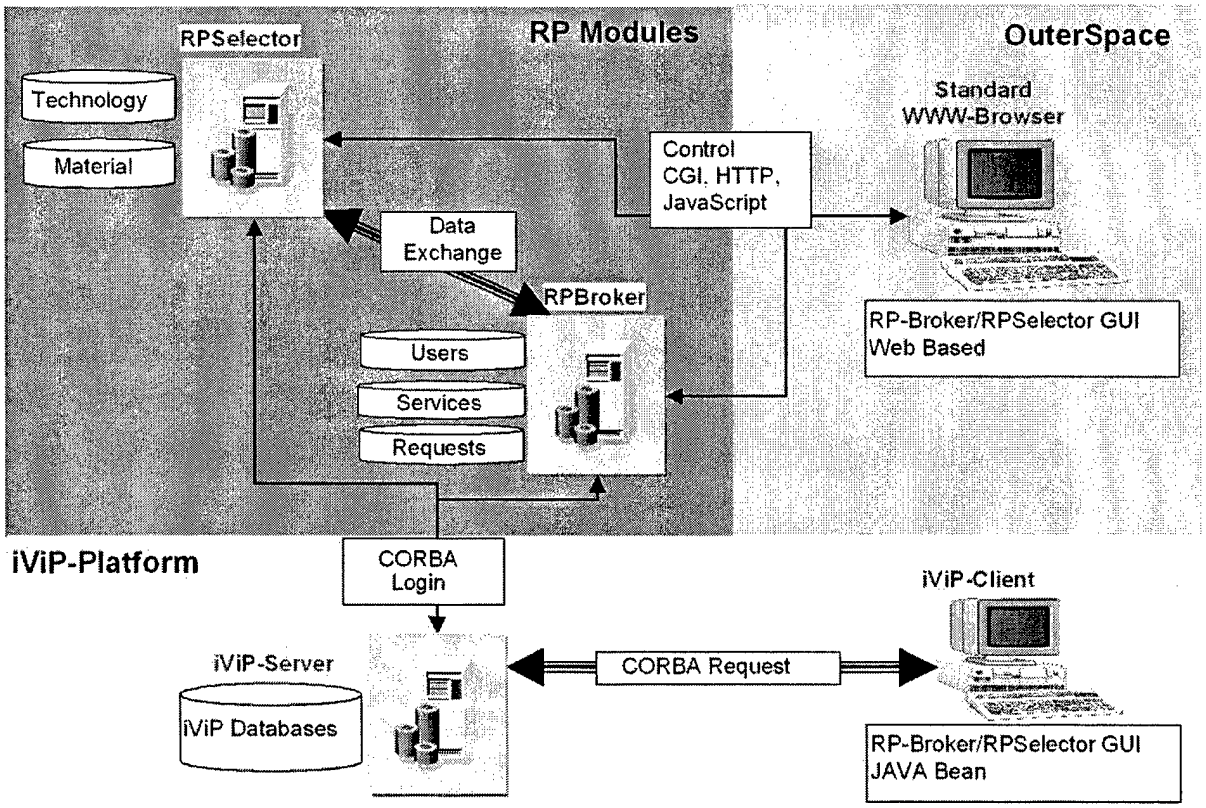


Figure 4: Software Architecture

Case Study

A ground connector bracket (Fig. 5) of an aircraft was used to show the applicability of the software modules.

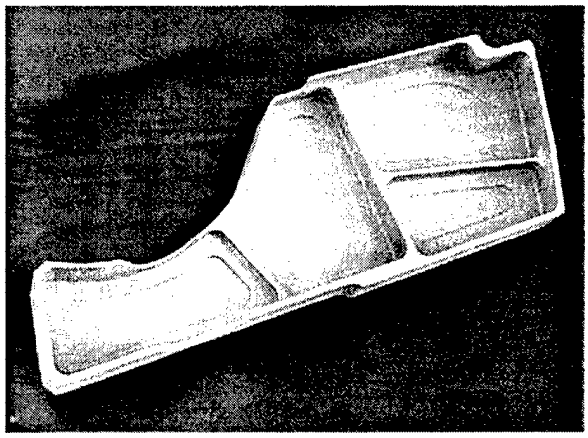


Figure 5: ground connector bracket

For the ground connector bracket, the basic requirements were:

Material characteristics:	aluminium like
Number of parts:	2
Surface Quality:	rough
Accuracy:	0.1 per 100 mm

In this case, the DTM steel 'Laserform' was selected because of its aluminium like characteristics. The only problem here was the specific weight of the part. This shortage of parameter definition was detected by the system and clearly stated.

The alternative presented by the software was generative manufacturing of solvable material and a subsequent employment of investment casting. This process chain requires a longer period, but creates optimal output. Additionally the user received information about shrinkage factors, process capabilities and restrictions. The selected processes, materials and annotations are then transmitted to the RPBroker software module, which accompanied the customer when procuring the corresponding services. The software gave hints regarding the difficulties when breaking out the parts. Several errors and misunderstandings could be eliminated when the complete set of data was transferred to the RPBroker, where procurement of RP services was performed.

Conclusion

It has been demonstrated that the selection of a single process may be an easy-to-perform task, but when a real world environment is considered, the construction of process chains is necessary. Assuming that each process element can be represented by 6 alternatives, the total amount of approximately 1300 process chains have to be tested, taking into account the individual linkage specification of each process and the overall efficiency of the resulting process chain.

Even if an expert could find the best configuration without software support, he/she will appreciate the capability of sorting out unemployable processes rapidly. Additionally, he/she will obtain preselection hints and immediate information about process limitations.

Acknowledgement

The described software was developed within the 'BMBF Leitprojekt' **iViP** and will be available as a product in early 2002. The author thanks Kai Loose and Stefan Ferstl, DaimlerChrysler AG; Thomas Lück, Bertrandt AG; Ralf Nachreiner, CIRP GmbH and Hans Peter Nicolai, TITAL GmbH.

Literature

Krause, F.-L., Bock, Y., Dreher, S.: Design evaluation of virtual clay models using selective laser sintering, Proceedings of Conference on Sculptured Surface Machining, Michigan 1998

Krause, F.-L.; Spur, G.: Das virtuelle Produkt. Carl Hanser Verlag 1997

Krause, F.-L.; Uhlmann, E.; Dreher, S.; Elsner, P.; Frost, T.: Development of a Process Control Strategy for Selective Laser Sintering
WGP-Bericht Vol. VI/1 (1999)

Timm, A.: Decision Support Component for Rapid Prototyping Process Chains. Diplom Thesis, TU Berlin 1997

Kaschka, Uwe; Auerbach, Peter: Selection and evaluation of rapid tooling process chains with Protool.
Rapid Prototyping Journal Volume 6 Number 1 2000 (pp. 60 - 66)

Xu, F. Wong, Y.S.; Loh, H.T.: A Knowledge-based Decision Support System for RP&M Process Selection
Proceedings of SFF Symposium, Austin, Texas 1999

this page intentionally blank

Simulation of The Electrochemical Machining Process

Authors: R. Temur T. Coole and C Bocking

Centre for Rapid Design and Manufacture (CRDM)

Buckinghamshire Chilterns University College

ABSTRACT

Electrochemical machining (ECM) or erosion, is a process for shaping materials by means of the anodic dissolution of a work-piece using suitably shaped cathodes? However, the predictability of the process is poor due to current density variations over the electrode contour leading to poor dimensional tolerances.

This paper describes how the process can be entirely simulated by computer. A model of the electric field during erosion is constructed based on the Laplace equations for the field. From the distribution of the electric field, it is possible to continuously calculate the current density at each point on the work-piece for the whole machining process. In this way, it is possible to predict the final work-piece contour by running the simulation program instead of the real process. Simulations for cylindrical, conical and spherical electrodes were carried out and compared to actual eroded parts.

ADVANTAGES AND PRESENT APPLICATIONS OF ECM

Unconventional machining processes are increasingly being used for manufacturing special steels, ceramics, plastic materials and composites. All these materials generally find applications in aerospace, automotive, electronics and electromechanical industries. In the last 20 years many technological developments have been made in order to improve the potential of unconventional applications and also the knowledge database regarding the electrochemical erosion process [1,2,3,4,5,6,7,8]. Science and engineering development has presented many challenges for the metal processing industry. Today, there is a big need to develop better processing methods and improve on current methods. These methods should reduce the cost of fabrication and should solve many of the difficult processing problems generated by the uses of new materials.

What were once unconventional methods, such electro-discharge machining, and laser processing, are nowadays used to produce high complexity parts in many applications from different processing industry. Using unconventional methods has given a big advantage in reducing the total number of operations needed for complete execution of a part. Also this has given a reduction in reject parts and an easy implementation of computer control.

Although the majority of unconventional methods have a relatively low processing speed, certain factors make them attractive:

- Removal of material is not dependent on the hardness of work-piece
- The tool can be less hard than the work piece
- The wearing of the tool is negligible.
- There is no mechanical contact between tool and work piece and parts free of distortions and internal stresses can be made.
- The secondary products produced during processing can be easily removed
- Self-checking and feedback loops can be easily implemented in the processing system
- Adaptive control strategies can be applied.

The main advantages of electrochemical erosion processing are:

- A easy way to manufacture hard materials
- This method will not produce residual internal stress in the work piece
- The possibility of producing many parts without distortion
- A relatively good speed of processing (~ 1mm/min)
- A good surface finish can be achieved (0.1 up to 10 μm).

DISADVANTAGES

The process of designing tool-electrodes in order to obtain the correct current distribution and thus shape is empirical and a scientific level has yet not been reached. Currently, the design and testing of complex shaped tools is undertaken by "trial and error", a very expensive and time-consuming process. Handling and using a large volume of electrolyte together with the increased probability of corrosion are more problematic for the electrochemical erosion process.

OBJECTIVE OF THIS PAPER

This paper describes the development and verification of a graphical-analytical method for simulating the electrochemical erosion process. This will allow accurate predictions of work piece shape without "trial and error", saving time and cutting costs for research. The big challenge was to identify the mathematical model that described the process and to select those parameters with greatest effect on the process. Finally it was necessary to solve this mathematical model in order to predict the shape of the tool electrode and thus the work piece.

An analytical solution for this problem is complicated by a large number of parameters that are interacting with each other and by a straight interdependence of these parameters. The tool shape required to obtain a final part having a precisely defined profile can be calculated using a number of mathematical models. These existing models simplify the real situation and can lead for inexact results especially when complicated shapes are involved.

A computer based method for the design process, based on the finite element method and using simulation, was recently proposed for electrochemical erosion process [9]. The work presented here builds on this and addresses some of the deficiencies of previous simulations. A computer program was developed which presents a graphic simulation on the screen (two-dimensional or three-dimensional) for specific operations of the electrochemical machining process. This program was developed using C program language and a solid modeller named Silver Screen. The system was divided in three main modules, simulation of the process, design tool electrode and verification of tool designed. The simulation shows on the screen the graphical effects of tool stepping on the work piece. A verification module determines automatically if the processing operation will produce the work piece with the desired dimension and shape.

MATHEMATICAL MODEL OF ECM USED IN THE SIMULATION

For a complete determination, the mathematical model for an ideal electrochemical process has to be written. Thus if f_a = anode shape at any instant during processing then it is possible to establish the evolution of the shape of the work piece:

$$f_a = F(x, y, t)$$

With some simplification assumptions, the evolution of the processed surface is given by [10]

$$\begin{cases} \dfrac{\partial F}{\partial t} = \dfrac{?\cdot\dfrac{K}{?}\cdot ?_e\cdot|grad\ U|}{\cos\ (n, f_a)} - \dfrac{d\ Y_s}{d\ t} \\ \dfrac{\partial^2 U}{\partial x^2} + \dfrac{\partial^2 U}{\partial y^2} = 0 \\ \left.\dfrac{\partial U}{\partial n}\right|_{isol} = 0 \\ F\ (x, y, 0) = F_0 \\ U_{(E)} = 0 \quad , \quad U_{(F)} = U \end{cases}$$

where $U(x, y)$ - is electrical potential in working area

x, y - mobile co-ordinate system with respect to the tool electrode

$?_e$ - electrochemical equivalent

Y_s - dynamic equation for ECM tool, in a fixed co-ordinate system in the case of tool moving with constant speed

$$Y_s = v_s \cdot t$$

F_0 - initial shape of the anode (work piece), all other elements being already defined

K - processing constant.

$?$ - electrolyte density

Applying a discrete approach from a time point of view and assuming that the elementary time interval is Δt, the solution for the equation set is reduced to a sequence of Laplace equation solutions. After solving this set of equations and determining components for the gradient vector of the anode potential, each individual point on the anode is moved accordingly in the processing direction and in this way the evolution of the surface geometry with respect to time is obtained. Subsequently, this initial anode shape will be modified by a correction based on work parameter changes.

This procedure is repeated in order to obtain the final shape for the work pieces using this step by step approach. At the completion of the virtual processing time, if errors exist between the desired shape for work piece and the shape obtained, it is possible to incorporate into the above algorithm a new correction routine to obtain the desired tool profile.

This routine is the basis of the computer simulation program designed for the electrochemical erosion process and tool design program for the cathode.

THEORETICAL CONCEPTS OF ECM SIMULATION

One-dimensional, two-dimensional and three-dimensional mathematical models that were written to describe ECM processing are very difficult to solve analytically. This is because within the solution range, the interface shape between electrolyte and work piece is changing continuously due to erosion. The electrochemical process is different from other machining methods because of the lack of a selective control of erosion process. In addition, this processing takes place continuously with different speeds in all points along work piece surface. Taking in

to consideration these difficulties and characteristics, a combination of a numerical solution and a graphical method was adopted to obtain the final shape of the working cathode.

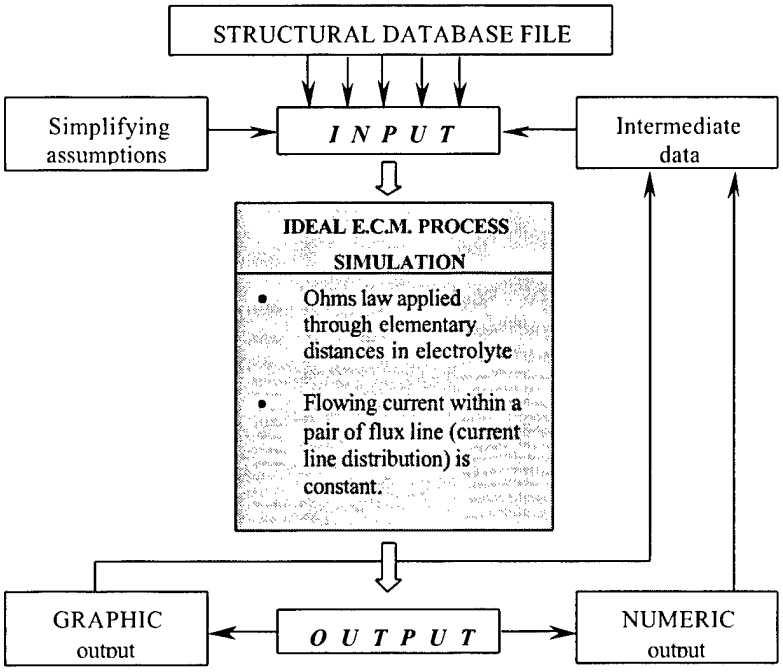


Figure 1. Schematic diagram of the simulation program.

The tool simulation program designed in this work has a main core that operates using an ideal electrochemical process. The data obtained with this base procedure, named SimEcmId was used as input data for connected procedures that translate the process from an ideal situation to a real one. There have been many attempts to use a numerical computer methods to obtain data about ECM processing, for different work conditions, but this new program has a set of improvements that allow results much closer to the real process to be obtained.

The first, general block scheme of the simulation program is presented in figure 1. From this schematic we can see that the simulation program will take input data from a structural database file that contain all the characteristic parameters for a simulation of an electrochemical process. Running this program is carried out under a set of simplification assumptions that are presented below.

Simplification assumption

All the assumptions made for this process were derived after theoretical studies on the electrochemical process. These assumptions have simplified writing and solving the mathematical model for this complex process. The main simplification assumptions were for the electrolyte properties and for the flow type of electrolyte.
Referring to the ideal model for an electrochemical erosion process we can state following assumptions:

- The electrolyte consist of a two phase one-axial flow,
- Hydrogen accumulation does not occur in the electrolyte during processing,
- Hydrogen released in the process obey ideal gases law

- The electrolyte is assumed to be an incompressible fluid
- The effect of secondary products on the electrolyte is neglected
- Two phase flow of the electrolyte is modelled as pseudo-Newtonian fluid, with a turbulent flow in working gap that will produce a complete mixing of the electrolyte.
- Increase of electrolyte temperature is the main result of Joule effect heating. This heating is generated by the electrical current flowing through the gap filled with electrolyte
- Increasing of the electrolyte temperature due to viscous dissipation of energy is neglected
- No heat transfer between electrodes and electrolyte was taken into consideration
- The heating produced by the voltage drop on electrode surfaces, due to over-potential, is considered to be taken by electrolyte
- The surface of the tool-electrode and work-piece are considered equal-potential surfaces

DESCRIPTION OF THE SIMULATION PROGRAM

General principles

The core of the simulation program, SimEcmId, was created starting from two main simplification assumptions for the electrochemical erosion process. If the potential and current distribution within the gap is in accordance with Laplace equations, these two assumptions are:

- Ohm's law applies through the elementary distances in electrolyte
- Flowing current within a pair of flux lines (current line distribution) is constant.

The first assumption eliminates the limitations of previous simulation programs based on "cosines" theory, and the second one asserts continuity of current flowing based on which "Continuity" theory was developed. To see the implementation of above assumption into the simulation procedure of an ideal process, both theories are presented and also the improvements of these theories in the simulation program described in this paper.

For a geometrical configuration of a tool-electrode boundary chosen from the database input file, two elementary columns were considered within the anode with area b and unitary depth. These two columns are positioned with the longitudinal axis parallel to tool feed direction, as is shown in figure 2. For the boundary of the tool-electrode and the work-piece, the following condition is true:

$$U = constant$$

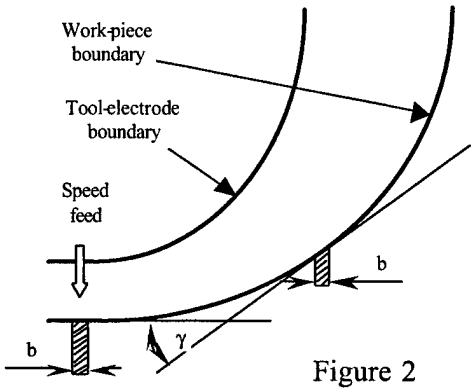


Figure 2

For the case of processing in equilibrium conditions, an ideal electrochemical process, all work-piece boundaries will move down with the same speed. Thus the same metal volume will be removed from both columns. We can say that both columns must have the same current (I). Nevertheless, the area of one column is b and the area of the other column is $b/\cos ?$. Consequently, the current density will be J and $J\cos\gamma$ respectively. Because flux current lines are perpendiculars the results from Ohm law is that also tension normal gradient should obey the same rate as current density. The boundary condition on the surface of work-piece is:

$$\left[\frac{\partial U}{\partial n}\right]_{\gamma} = \left[\frac{\partial U}{\partial n}\right]_{?=o} \cdot (\cos ?)$$

The simulation program SimEcmId uses these boundary conditions and also simplification assumptions that state that Ohm's law is applicable between two corresponding points from work and tool surfaces. Thus, the gap-measured perpendicular on work-piece is inversely proportional with the cosine of angle representing bending of work surface with respect to the feed tool direction – see figure 3.
The Limitation of this approach refers to the bending angle of the work surface, which cannot be greater than 60° and about the radius of curvature of the work surface, which should be at least one order of magnitude greater than the size of inter-electrode gap. These limitations are a direct consequence of the simplification assumption made regarding application of Ohm's law. The effect of this wrong application is that a unitary current flow between the tool and work-piece through a straight conductor of electrolyte with a constant cross section had to be considered.

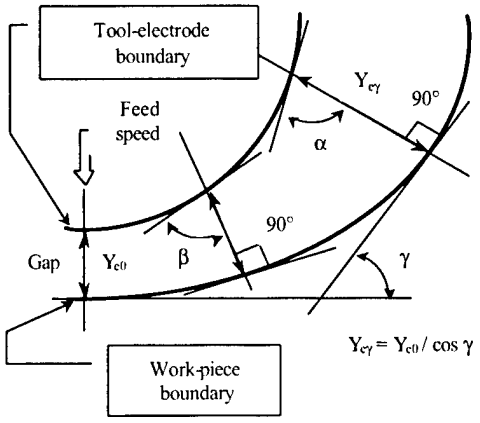


Figure 3

The correct principles on which to construct the potential field between the two electrodes are:

- Equi-potential lines and flux lines are an orthogonal curve set
- The current flowing within a pair of flux lines is constant anywhere in this field

In order to implement above first principle, in the simulation program design, the electrolyte conductor wasn't considered straight but of having a curvature and a variable cross-section. This new shape of electrolyte conductor is described by electric field equations and is an important improvement included in the electrochemical erosion simulation program presented here.
This new approach allows the elimination of simplifications and incorrect determinations presented in figure 3 where the current lines have a correct (90°) angle with only one equal-potential line. This line is the boundary of the work-piece and the remaining equal-potential lines (including here boundary of tool-electrode) have angles different from 90°, as is presented in figure 4.

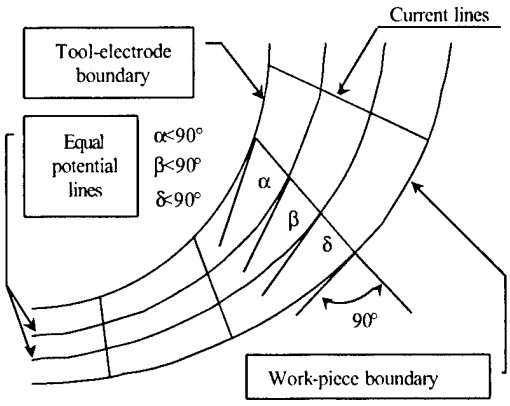


Figure 4

In order to obtain a curved shape of the flux areas with variable cross section, described by the equation $\nabla^2\phi = 0$, a spline graphical primitive type was used. Then this spline primitive had tangency conditions added at both ends: the work-piece surface and the tool-electrode surface. Those tangency conditions were applied for normal lines on the surface of the tool and work-piece as nodes used in the simulation as presented in figure 6.
In this way it was possible to correct α, β, γ angles from figure 4 to 90° angles and keep to the principle which states that current lines and equal-potential lines

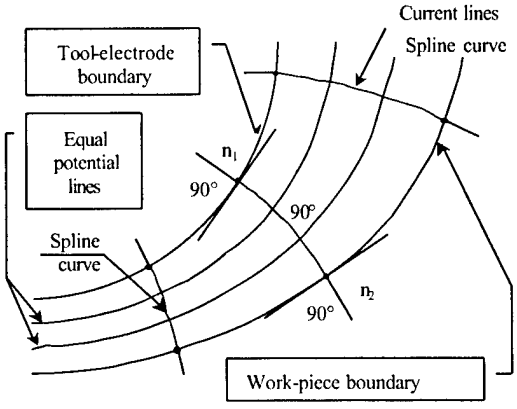


Figure 5

should be orthogonal. Also with this improved approach, the flux section became variable and we can assume that the modelling of electric field between the two electrodes is more accurate and match closer to reality

Determination of work-piece profile

The principle used for the determination of the shape of the processed piece is presented in figure 7 where for each calculation step, a graphical description (for a particular case of a spherical tool electrode) is also given. Input dimensions and parameters assumed at the beginning of the simulation are available for the entire process. The contour defined by the anode surface, cathode surface and isolated side surface represent the starting point for the calculations. For this geometrical configuration, the intensity of electric field on the anode surface is calculated.

Based on this intensity and with the help of electrolyte conductivity at each point considered on anode contour, the current density and effectively the volume of material removed is determined. In the next step the mass of metal removal, in a direction normal to the anode surface and at each node considered, can be calculated for a specific time interval. The next anode contour will be in

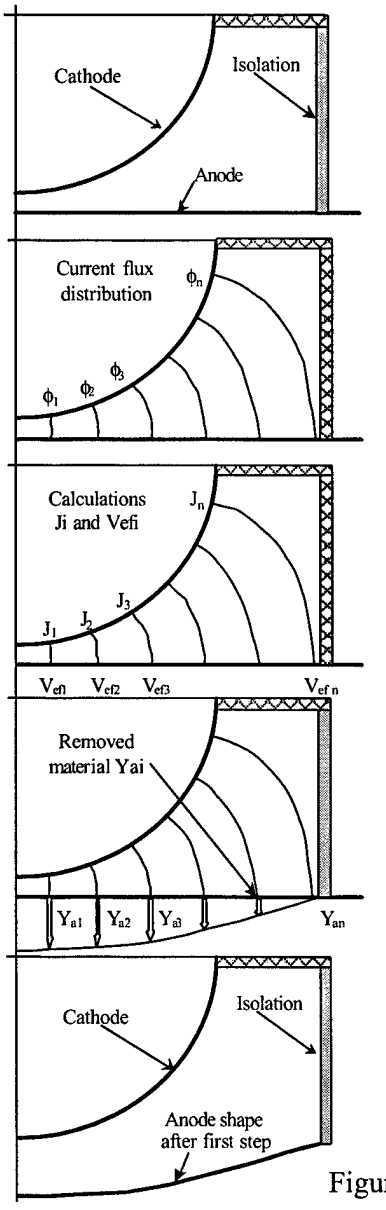
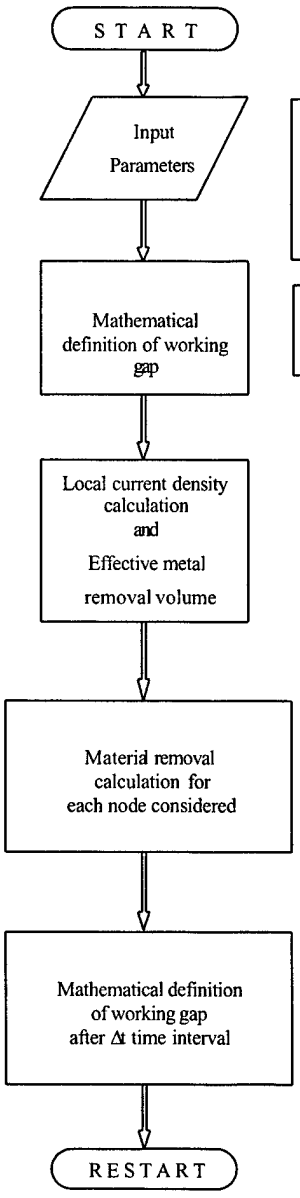


Figure 6



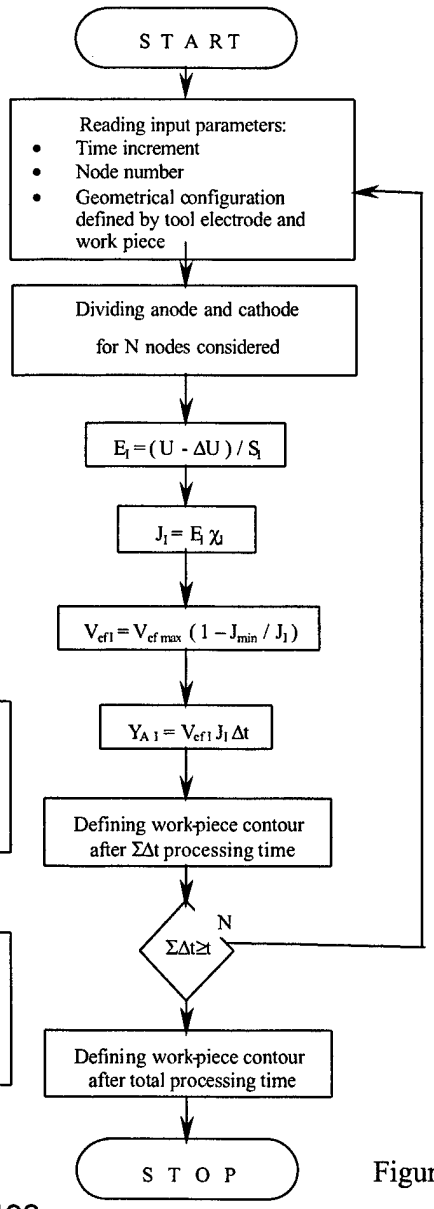


Figure 7

this way described by all n individual points obtained after the metal removal calculation. Once the new position and shape of anode contour is available then mathematical description of inter-electrode area for next simulation step is possible.

Calculation of each point erosion – logical scheme

Based on the principles presented above, the logical scheme shown in figure 7 was developed for a complete solution of work-piece contour calculation. Time interval Δt is given as a fraction of the entire processing time and the number of nodes is dependent on the desired accuracy required for the work-piece contour. After subdividing the inter-electrode gap, based on node number and drawing of current lines normal to the tool and work-piece, calculation of the local surface electric field intensity is carried out. Next, the local current density J_i, is determined and thus the effective anode metal removal volume, V_{ef_i}, together with the magnitude of the metal removal at each node Y_{A_i}, in a normal direction to the work piece. With all points determined by the metal removal calculation, a new anode contour is mathematically described. The last stage is to verify if processing depth was reached or if the processing time is finished. If at least one of these verification fails the new geometric configuration tool-piece is determined by moving the tool towards the work-piece at the appropriate feed speed.

SIMULATION RESULTS

Three elementary tool shapes were used for verification of the simulation procedure described. These shapes are cylindrical, conical and spherical and the parameters set for each simulation are presented below.

Cylindrical tool-electrode

The cylindrical tool-electrode used had following dimensions:

- Radius - 15 mm, Length - 30 mm, Round radius - 2 mm

The gap between cylindrical electrode and the work piece was set to 0.64 mm. For this value, a feed speed of tool electrode corresponded to 1 mm/min. Other input data needed for the simulation were:

- Node number – 20, Total processing time – 30 min, Time increment Δt - 0.5 min

The result of the simulation is presented in figure 8 for a processing depth equal to 25 mm. In figure 9 it is possible to observe a detail of the work-piece obtained for a depth feed of Z=15mm. In this detail it can be seen how the side gap increases, an effect observed in reality.

Conical tool-electrode

The conical tool-electrode used in simulation has following dimensions:

- Top radius – 30 mm, Cone angle - 25°, Length – 30 mm, Round radius – 0.5 mm

The size of gap between the conic electrode and work-piece had a value of 0.42 mm. For this value, a corresponding feed speed of tool electrode equal with 1.5 mm/min is used. The other input data needed to run the simulation was identical with those from the simulation of the cylindrical electrode.

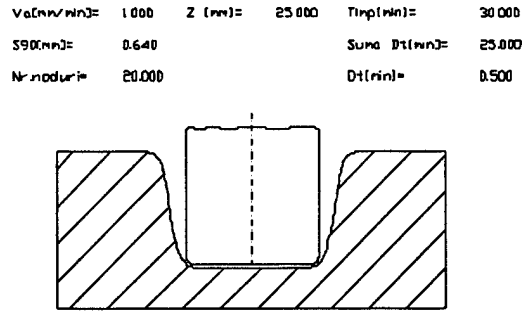


Fig. 8

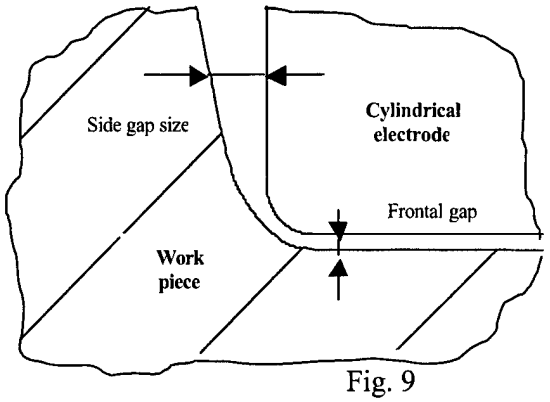


Fig. 9

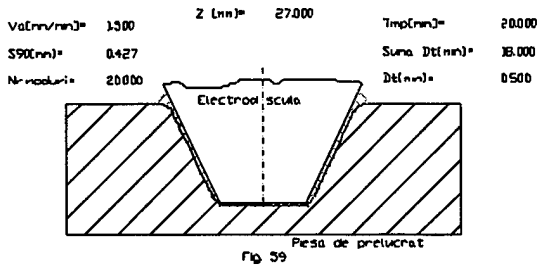


Fig. 10

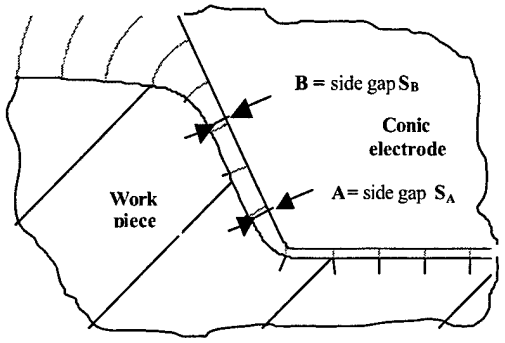


Fig. 11

The evolution of the simulation is presented in figure 10. A detail of the work-piece shape at z=9mm erosion depth is given in figure 11. In this detail it can be seen that a side gap S_A approximately equal with side gap S_B. This behaviour was confirmed in real processing and thus validates once again the simulation program developed.

Spherical tool-electrode

A spherical shape is considered representative for processing complex surfaces by electrochemical erosion. Also, using a spherical shape, a complete verification of the simulation program was possible, because this shape covers regions with angles greater than 60° where "cosines" law cannot be used for the gap determination. Before displaying the graphical simulation window, the following input data is requested:

- The position of the tool electrode centre (the default value is <400,500> and user can accept or change it)
- Tool-electrode radius (default value <30> mm)

The simulation parameters needed:

- Feed speed of tool-electrode – 0.5 mm/min, Nodes number used - 40 nodes, Total processing time – 60 min, Time interval Δt - 0.5 min (this value is connected with tool feed speed in such a way so that a total depth of erosion 30 mm is achieved, which is equal to the tool radius)

This input data and the value for frontal gap size, Y_f = 1.281 mm is displayed in a graphical window for monitoring purposes. The result obtained from this simulation, using a spherical tool-electrode, is presented in figure 12. The final stage is in accordance with erosion depth at

the end of process and the shape of the work-piece at that time. The initial work-piece is assimilated in simulation process with a box with the height 510 mm bigger than maximum erosion depth. The basic electrochemical data used for this simulation are stored in a database connected with simulation procedure. Values extracted from this database are:

- Effective volume of removed material - 2.44 mm3/Amin, Electrolyte conductivity (NaCl solution)– 0.0164 s/mm, Polarisation voltage drop – 2V, Applied voltage – 18V

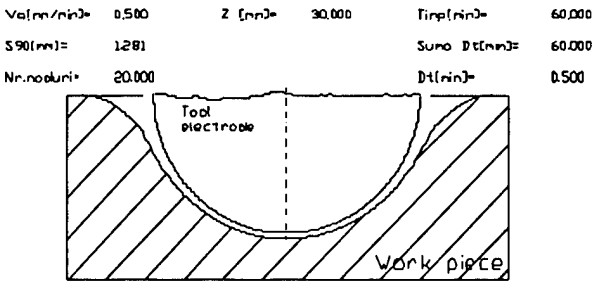


Fig. 12



Fig. 13

RESULTS

The simulation results were compared with real part profiles for each shape presented cylindrical, conical and spherical. The error measured along the contour of the profile was not bigger than 0.15 mm that confirm this simulation program as an good instrument in evaluating the shape of work piece for a given tool electrode. The three parts measured are presented in next figure 13, 14, and 15.

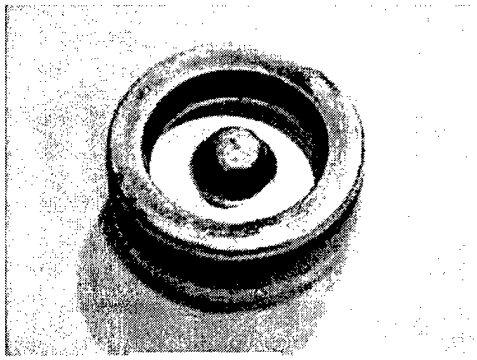


Fig. 14

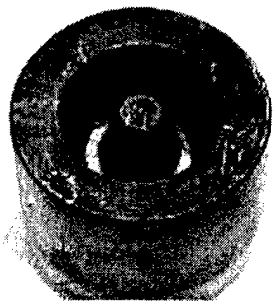


Fig. 15

FURTHER WORK

As can be seen from figure 13, the geometrical shape obtained after processing with a spherical electrode is not good enough from a geometrical and dimensional point of view. The main phenomenon observed is an increasing of gap size between the two electrodes through the tool contour and normal to this contour. This increase resulted in a different work-piece geometry from that desired – a spherical shape. In order to eliminate this phenomenon and thus to increase dimensional and geometrical accuracy in electrochemical process it was possible to extend the simulation to a new stage. This consisted of designing tool electrodes for ECM machines using

this simulation in order to obtain an accurate work-piece profile by appropriately shaping the electrode. The outcome of this part of the work has been presented elsewhere [11].

REFERENCES

1. Kawafune, K., Mikoshiba, T., Neto, K. "Einflus der Einstellbedingungen auf den Bearbeitungspalt beim elektrochemischen Abtragen". CIRP-ANN.18, 1970, 2, s.305.
2. Alekseev, G. a. "Kathoden oberflachenprofil bei der elektrochemischen Bearbeitung". Stanki I Instrument 41, 1970.3.
3. Dietz, H., Gunther, K.G., Otto, K., "Electrochemical Machining: Calculation of Size Gap with Respect to Hydrogen Evolution". Annals of the CIRP, Vol.23/1, 1974, p. 45-56.
4. Konig, W., and Humbs, H.H., "Mathematical Model for the Calculation of the Contour of the Anode in Electrochemical Machining". Annals of the CIRP, 26/1, 1977, p. 83-86.
5. Tipton, H., "The Calculation of Tool Shapes for Electrochemical Machining". Fundamentals of ECM. The Electrochemical Society, Princeton, 1971, p. 87-102.
6. Raju, K.R., Jain, V.K., Lal, G.K., "Cathode Design in ECM: Two Dimensional Analysis". ASME Symposium on Research and Technological Advances in Non-traditional Machining. Vol. PED-34, 1988, p. 89-104.
7. Seimiya, K., "An Approximate Method for Predicting Gap Profiles in Electrochemical Machining". Proceedings of the 5th International Conference on Production Engineering, 1984 p. 389-394.
8. Hewidy, M.S., Rajurkar, K.P. "Computer-Aided Tool Design in ECM". Proc. of the Third Int'l. Conference on Computer-Aided Production Engineering, 1988, p. 371-380.
9. Jain, V.K., Rajurkar, K.P. "An integrated Approach for Tool Design in ECM", Submitted for review to the Precision Engineering, May 1990.
10. L. Dabrowski and J. Kozak, Electrochemical Machining of Complex Shape Parts and holes (Mathematical modelling and practical experiments), Warsaw Technical University, Poland.
11. Temur R., Coole T., Bocking C., "ECM Tool-electrode Construction for Semi-spherical Shapes", Research and Development in Net Shape Manufacturing, Birmingham UK, April 2001.

this page intentionally blank

AUTOMATED CONSTRUCTION USING CONTOUR CRAFTING

B. Khoshnevis, H. Kwon, and S. Bukkapatnam

Industrial and Systems Engineering, University of Southern California
Los Angeles, CA 90089
khoshnev@usc.edu

Abstract

This paper presents some concepts and initial investigation of a novel construction automation approach using the Contour Crafting (CC) layered fabrication process, developed at the University of Southern California. CC uses computer control to take advantage of the superior surface forming capability of trowels, used by craftsmen and builders since ancient times, to create large intricate structures with smooth and accurate surfaces. The potential of CC became evident from the initial investigations and experiments with various materials and geometries. Using this process, a single house or a colony of houses, each with possibly a different design, may be automatically constructed in a single setup.

Introduction

Presently, the construction industry is facing various problems including high project costs, low labor efficiency, high at-site accident rates, vanishing skilled workforce, and poor control of construction projects (Warszawski, and Navon, 1998). Automation has resolved several similar problems in the manufacturing industry. The construction industry, however, largely remains manual and manpower intensive. The few attempts made towards automating certain aspects of construction have aimed only at mechanizing the same manual approach (e.g., use of a brick-laying robot) without introducing any new paradigm (Pegna, 1997). Development of new automation paradigms for whole structure construction may mitigate many of the problems that the industry is facing. In fact, new automation paradigms seem imperative for several applications, including construction of emergency homes and low income housing projects. Furthermore, the development of construction automation technologies is necessary if colonization of other planets is to become a reality in the coming century.

Conventional methods of manufacturing automation do not lend themselves to construction of large structures with internal features. This explains why the evolution of construction automation has been slow. A promising new automation approach is layered fabrication, generally known as solid free form fabrication or rapid prototyping, which uses an additive method and is capable of creating complex internal features. However, most of the current layered fabrication methods are limited by their ability to deliver a wide variety of materials applicable to construction. Additionally, they are severely constrained by the low rates of material deposition that makes them attractive only to the fabrication of small industrial parts.

Contour Crafting (CC) is a layered fabrication technology that uses computer control to exploit the superior surface-forming capability of troweling to create smooth and accurate planar and free-form surfaces (Khoshnevis et al., 2001; Khoshnevis, 1998). Using the layering approach afforded by troweling, an ancient process, a wide range of surface shapes may be created with fewer types of troweling tools than are needed for traditional plaster handwork and sculpting. Some of the important advantages of CC compared with other layered fabrication processes are better surface quality, higher fabrication speed, and a wider choice of materials.

The key feature of CC is the use of two trowels, which in effect act as two solid planar surfaces, to create surfaces on the object being fabricated that are exceptionally smooth and accurate. Artists and craftsmen have effectively used simple tools such as trowels, blades, sculpturing knives, and putty knives, shown in Figure 1, with one or two planar surfaces for forming materials in paste form since ancient times. Their versatility and effectiveness for fabricating complex free-form as well as planar surfaces is evidenced by ancient ceramic containers and sculptures with intricate or complex surface geometries as well as detailed plaster work that have shapes as complicated as flowers, on the walls of rooms.

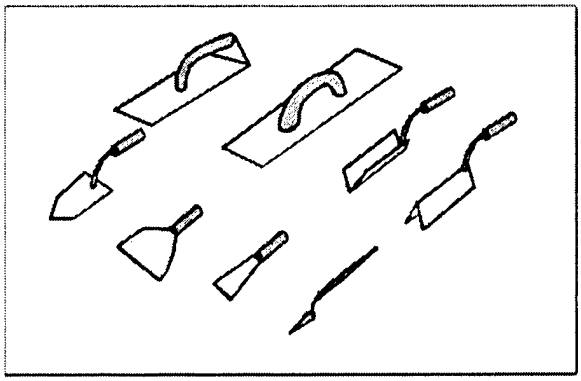


Figure 1. Simple Historical Construction Tools

In CC, computer control is used to take advantage of the superior surface forming capability of troweling to create smooth and accurate, planar and free-form surfaces (Landfoam FAQ, 2000). The layering approach enables the creation of various surface shapes using fewer different troweling tools than in traditional plaster handwork and sculpting. It is a hybrid method that combines an extrusion process for forming the object surfaces and a filling process (pouring or injection) to build the object core. As shown in Figure 2, the extrusion nozzle has a top and a side trowel. As the material is extruded, the traversal of the trowels creates smooth outer and top surfaces on the layer. The side trowel can be deflected to create non-orthogonal surfaces. The extrusion process builds only the outside edges (rims) of each layer of the object. After complete extrusion of each closed section of a given layer, if needed filler material such as concrete can be poured to fill the area defined by the extruded rims.

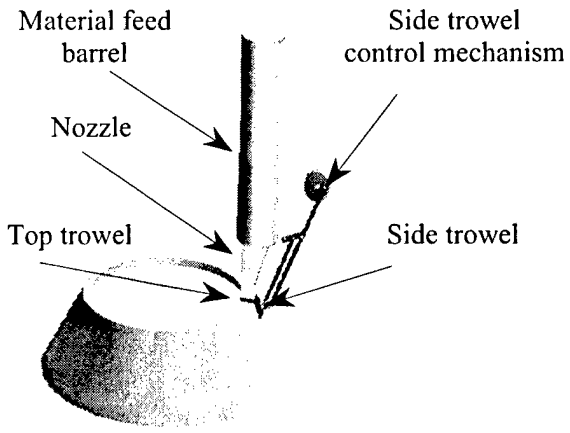


Figure 2. Contour Crafting Process

Some internal walls can be extruded within each layer to create square hatches or other types of hatches (see Figure 3). The hatching process may be required for large objects, since setting or curing can start before the filler material gets a chance to spread over the entire surface of the layer.

However, when hatching is used, each of the small hatches is filled separately, which because of their small size allows more control over the spreading and curing of the filler material. Hatching can also accelerate the forming process because it provides for concurrent extrusion and filling (i.e., as the extrusion nozzle creates new hatches, previously made hatches can be filled).

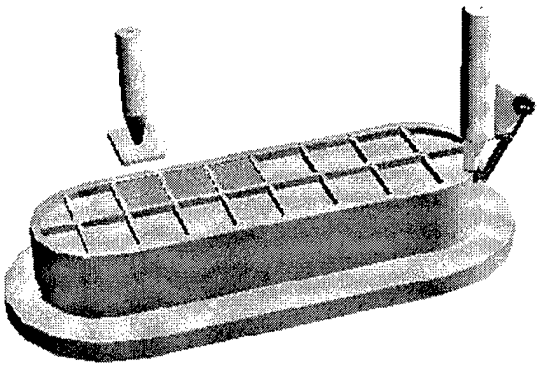


Figure 3. Creation of Internal Walls

Advantages of CC for automated construction

Among all things made by man building structures are those that are fabricated in a layered fashion. This is a clear indication that layered fabrication could be the ideal approach for automating building construction. Although several methods of layered fabrication have been developed in the last two decades (Pegna, 1997), and successful applications of these methods have been reported in a large variety of domains (including industrial tooling, medical, toy making, etc.), only Contour Crafting (CC) is uniquely applicable to construction of large structures such as houses (Khoshnevis, 2000).

The immediate impact of CC will be in the construction of emergency and low income housing structures in various regions by taking advantage of the variety of locally available resources including soil, gravel, lime stone, clay, wood chips, etc. The applicability of CC can possibly be extended to construction applications in regular residential and commercial structures that could utilize functional and exotic architectural geometries, which are difficult to realize using the current manual construction practice. Furthermore, building of structures on other planets using local materials may be achieved using the proposed technology. Such application in building construction is depicted in Figures 4 where a gantry system carrying the CC nozzle moves on two parallel lanes installed at the construction site. A single house or a colony of houses, each with possibly a different design, may be automatically constructed in a single run. Following are some interesting aspects of this automated construction process:

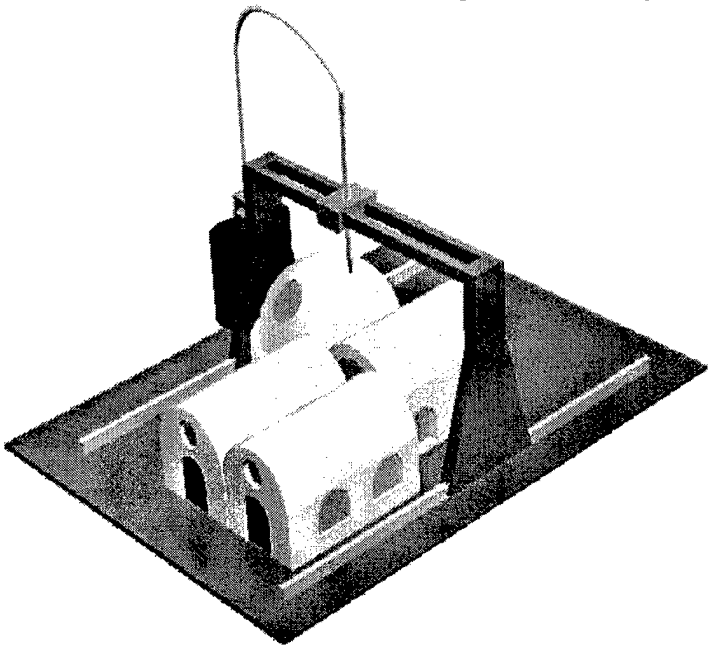


Figure 4.Residential Building Construction

- The process allows architects to design structures with functional and exotic architectural geometries that are difficult to realize using the current manual construction practice. The surfaces produced will be paint-ready, hence an automated painting system may be integrated into the CC system.
- Since deposition in CC is controlled by computer, accurate amounts of selected construction materials, such as smart concrete, may be deposited precisely in the intended locations. This way the electric resistance, for example, of a carbon filled concrete may be accurately set as dictated by the design. Elements such as strain sensors, floor and wall heaters can be built into the structure in an integrated and fully automated manner.

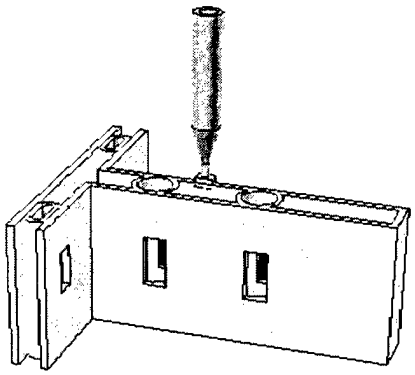


Figure 5. Complex Wall Section

- As shown in Figure 5 utility conduits may be built into the walls of a building structure precisely as dictated by the CAD data.
- The quality of surface finish in CC is controlled by the trowel surface and is independent of the size of the nozzle orifice. Consequently, various additives such as sand, gravel, reinforcement fiber, and other applicable materials available locally may be mixed and extruded through the CC nozzle.
- Multiple materials that chemically react may be fed through the CC nozzle system and mixed in the nozzle barrel immediately before deposition. The quantity of each material may be controlled by computer and correlated to various regions of the geometry of the structure being built. This will make possible the construction of structures that contain varying amounts of different compounds in different regions.
- Methods of imbedding of steel mesh and other forms of reinforcement into each layer may be devised. Note that in this configuration the CC nozzle, the inter-rim filler nozzle, and reinforcement placement mechanisms can all be on the same gantry system. The proposed system can create shapes with smooth outer surfaces and reinforced internal structure automatically and in one setup.
- The lower construction cost and time that CC offers will make frequent reconstruction of buildings a more feasible proposition. This is of special interest in commercial building sector. This possibility is especially appealing if recyclable materials are used.

Experimental investigations

We conducted extensive experiments which show the potential of CC for construction automation. Many of the advantages mentioned in the previous section have been validated through these investigations.

Material used for the experiments

Our examination of the properties of a few ceramic materials and compounds revealed that a type of clay procured from America Ware Co. in Los Angeles did not swell upon exiting

the nozzle orifice. This probably was due to its readiness to shear and virtual absence of an elastic phase (Bardet, 1997; Craig, 1997). We qualified the Bingham characteristics of this material (Fox and McDonald, 1985; Levy and Carley, 1994). Using this material we have been able to create the several geometrical features on our CC machine.

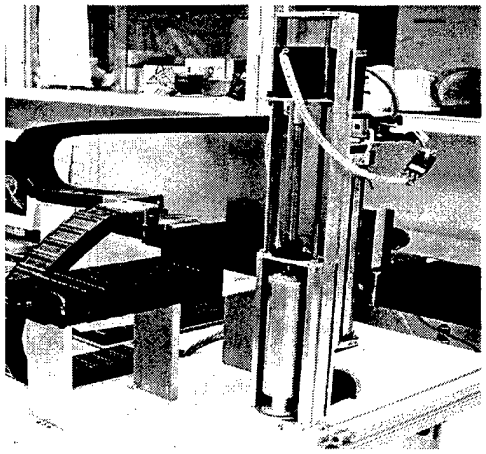


Figure 6. The CC machine for fabricating complex geometries

Description of CC machine

The machine shown in Figure 6 is modified to fabricate the complex geometrical parts for the CC process of uncured ceramic materials, which include the convex, concave, and sharp corner shapes. The machine consists of a trowel rotation system, and a vertical extrusion head capable of linear motion along three coordinate axes.

The trowel rotation mechanism shown in Figure 7 consists of a bevel gear, and a connector. The ratio of the bevel gear is 4 to 1, and is derived by the 5th stepper motor. The connection mechanism allows the raw material to flow continuously from the cylinder to nozzle, and can rotate the extrusion system without disturbing the material flow while fabricating complex curves.

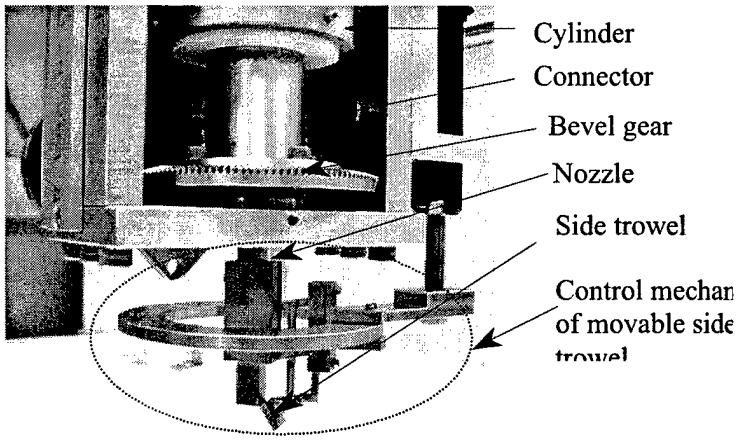


Figure 7. Trowel rotation system of the CC process

The extrusion system consists of a top and side trowel, a cylinder that contains the raw material, and a piston and a threaded feed rod that extrudes the raw material through a nozzle. The process utilizes a Programmable Multi-Axis Controller (PMAC), a high-performance servo motion controller, capable of controlling up to eight axes of motion (Delta Tau Data Systems, 1996 a, b). The eight axes can be all synchronized for completely coordinated motion; each axis can be put into its own coordinate system for eight completely independent operations; any intermediate arrangement of axes into coordinate systems is also possible. Limit switches are used to restrict motion to specified limits.

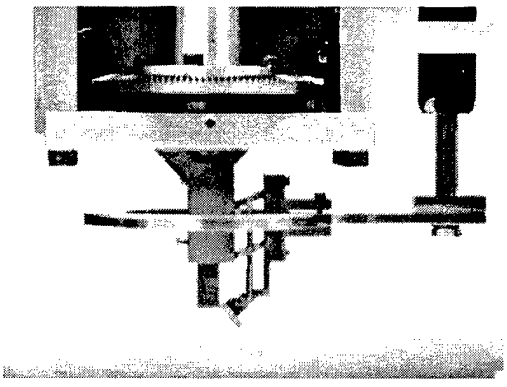


Figure 8.Side view of the movable nozzle assembly

In order to enhance the capability of CC for building certain primitive geometries and hybrid geometries made of these primitives, a nozzle with movable side trowel is designed and assembled into the existing machine as depicted in Figure 8. This nozzle assembly provides for intricate trowel motions to create various complex geometries.

Experimental results

Fabricating complex 3D shapes

Adapting the movable side trowel control mechanism shown in Figure 9 (a), our existing CC fabrication machine has been modified for fabricating a variety of 2.5D and 3D shapes that constitute the primitive construction geometries (e.g. flat floors, straight walls, pyramid, domes, etc.) and hybrid geometries made of these primitives. The primitives have been carefully chosen so that these form the basic shapes for the scaled models of adobe houses (Khalili, 2000). As shown in Figure 9 (b), typical primitives that we have considered thus far are flat floors, straight walls, pyramid, and domes. Hybrid geometries, formed as a direct combination of these primitives, will represent scaled models of adobe houses such as those adopted by CalEarth in Figure 14.

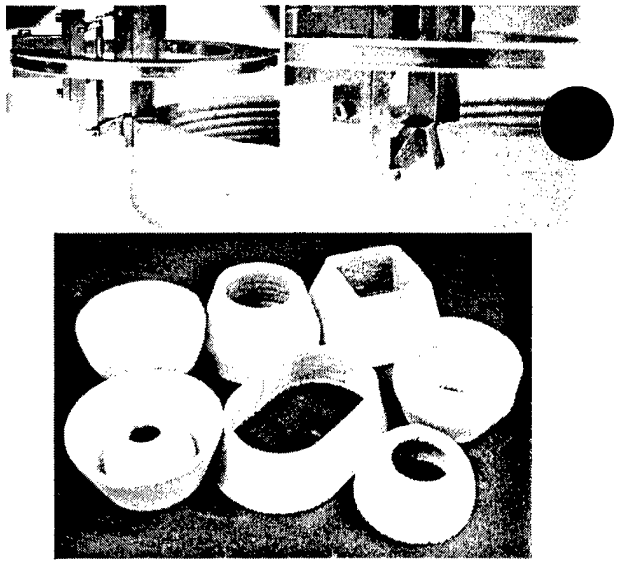


Figure 9. CC process with the movable side trowel: and various primitive parts

Roofs, overhangs, and support structures

Through extensive experimental investigations for the support material, Wax and sand were used as the support materials in order to construct overhang features such as roofs as shown in Figure 10. Note that although this approach is feasible for small parts it may not be so for housing structures. We consider using other means of building overhangs that are more suitable for constructing such structures (one such approach is depicted in Figure 16 for roofing adobe houses).

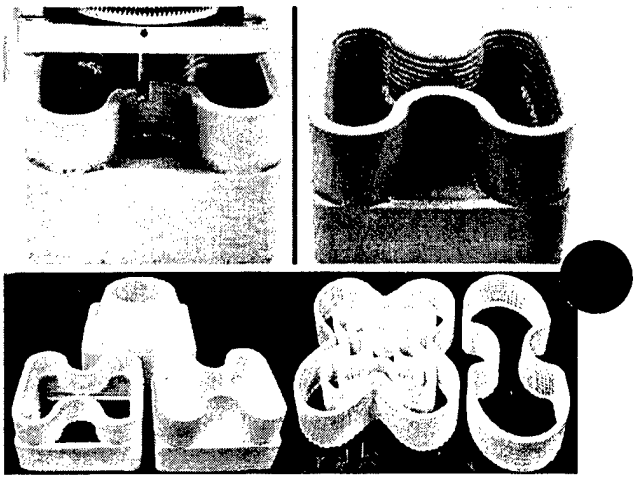


Figure 10. Fabrication of roofs, overhangs, and support structures

Depositions with hollow cavities

In order to investigate co-extrusion of multiple materials using a combination of nozzles, extensive experimentation and a series of design enhancements have been conducted. As shown in Figure 11, we have developed the capability to build layers with hollow depositions using CC. Mandrel of various shapes may be used for creating hollows of various shapes.

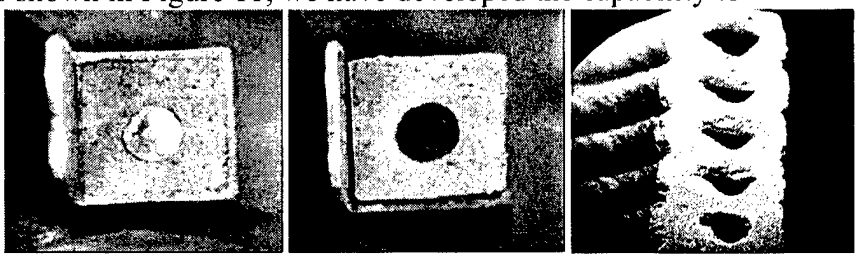


Figure 11. Laying hollow sections through CC: (a) the ceramic material in the nozzle before extrusion, (b) hollow circle formed as the extrudate emerges from the orifice, and (c) cross section of the fabricated part revealing the hollow sections

With these cavities by forcing the material through a nozzle with a central mandrel, various materials may be co-extruded if the mandrel itself is hollow and works as a nozzle to deliver a second material. This

feature will provide the capability to lay base material as well as certain reinforcements simultaneously. These hollow cavities also result in lighter structures.

Furthermore, for constructing walled structures, we will first construct rims using the nozzle system, and will fill the intervening space between wall-rims using a bulk-filling mechanism, a schematic of which is shown in Figure 3.

Reinforcements and impregnation

Towards improving the strength of large housing structures built through CC, we have investigated the use of a variety of reinforcements. For example, Figure 12 shows pictures from our experiments with coil reinforcement. Owing to the high extrusion pressures prevailing in CC compared to other layered free-form fabrication techniques (Zak *et al.,* 1999), the extrudate thoroughly adheres itself around the coils without causing any internal discontinuities. Similar results have been observed from our experiments with sand impregnation.

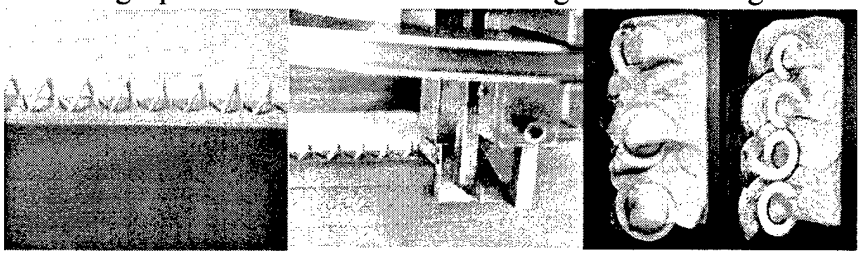


Figure 12. Reinforcement process of CC: (a) metal coil placed on a top layer, (b) a fresh layer of extrudate covers the coil, and (c) cross sections of the fabricated part with the reinforcement coil showing a reasonable adhesion between layers

As shown in Figure 13, two simple modular components may be delivered by an automated feeding system that deposits and assembles them between the two rims of each layer built by CC. Concrete may then be poured between the rims of each layer to contain the steel mesh. The mesh can follow the geometry of the structure. Note that in this configuration the CC nozzle, the steel feeder, and the concrete filler feeder are all on the same gantry system. Thus the use of reinforcements seems promising in our CC process.

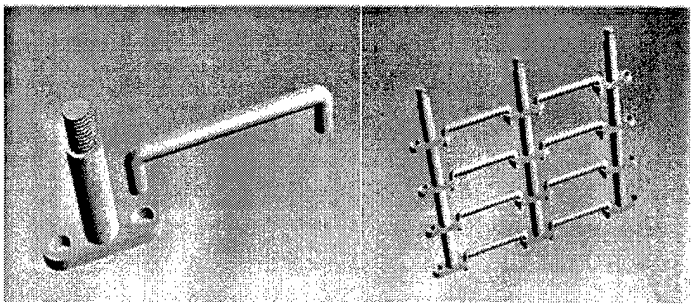


Figure 13. Steel reinforcement modules and mesh

Summary and future work

Preliminary investigation of CC process indicates that the process is feasible and has significant potential in construction automation. The potential of CC became evident from the presented experimental investigations. Experiments with ceramics material show the versatility of the process relative to the use of a variety of fabrication materials. The process seems especially suited for automated construction of emergency structures as well as large scale construction of houses with exotic features such as adobe houses.

In order to facilitate accurate deposition of material and efficient fabrication of the proposed housing structures, we are currently developing a computer control software by modifying our current control software for fabricating both primitive as well as hybrid geometries. The new software will allow for experimenting with various types of trowel motions

and material flow patterns. In devising our construction control software we will benefit from the ancient body of knowledge that is currently being harnessed by CalEarth for building supportless closed structures. An example of a clever and ancient manual method of constructing such supportless structures is shown in Figure 14. Here the vault is constructed by first laying side squinches, and the dome structure is built layer-by-layer. Figure 15 shows a vault structure made of clay bricks using this traditional manual procedure. Our corresponding deposition pattern, inspired by these ancient methods, could be such as the one schematically illustrated in Figure 16.



Figure 14. Manual construction of adobe form structures using clay bricks (Source: Khalili, 2000)

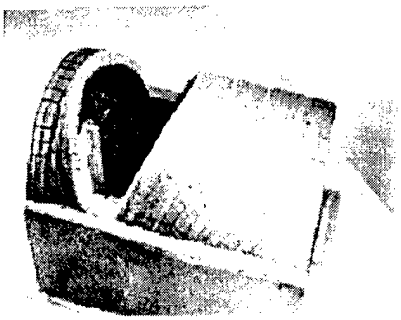


Figure 15. A vault structure made of clay bricks (Source: Khalili, 2000)

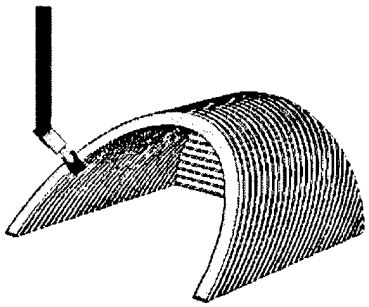


Figure 16. Our approach to fabricate supportless structures

Acknowledgment: We thank the National Science Foundation for support through grants DMI 9634962 and DMI 9522982.

References

1) Bardet, J. (1997), *Experimental Soil Mechanics,* Prentice-Hall.
2) Bukkapatnam, S., Khoshnevis, B., Kwon, H., and Saito, J. (2000), "Effect of orifice shape in contour crafting: A study of extrusion and deposition mechanisms", *Preceding of 52nd Pacific Coast Regional and Basic Science Division Meeting of The American Ceramic Society,* San Francisco, California.
3) Craig, R. F. (1997), *Soil Mechanics,* E & FN Spon.
4) Delta Tau Data Systems Inc. (2000), "PMAC PC ", http://www.deltatau.com, February.
5) Fox, R., and McDonald, A. (1985), *Introduction to fluid mechanics,* John Wiley & Sons, Inc., NY.
6) Khalili, N. (2000) *Ceramic houses & Earth architecture*, Cal-Earth Press, California.
7) Khoshnevis, B., Russell, R., Kwon, H., and Bukkapatnam, S. (2001), "Contour Crafting – A Layered Fabrication Technique", *Special Issue of IEEE Robotics and Automation Magazine*, May (Accepted).
8) Khoshnevis, B., Bukkapatnam, S., Kwon, H., and Saito, J. (2001), "Experimental Investigation of Contour Crafting using Ceramics Materials", *Rapid Prototyping Journal*, Vol. 7, No.1, pp. 32-41.
9) Khoshnevis, B. (2000), "Automated Construction Using The Contour Crafting Layered Fabrication Technique," *8th International Conference on Rapid Prototyping*, Tokyo, Japan, June.
10) Khoshnevis, B. (1998), "Innovative rapid prototyping process makes large sized, smooth surfaced complex shapes in a wide variety of materials", *Materials Technology*, Vol. 13, No. 2, pp. 52-63.
11) Kulkarni, P., and Dutta, D. (1999), "Deposition Strategies and Resulting Part Stiffnesses in Fused Deposition Modeling", *Journal of Manufacturing Science and Engineering*, ASME, No.1, pp. 93-103, February.
12) Landfoam FAQ (2000), "Adaptive-Layer Lamination", http://www.architectural-model.com/adaptive-news.htm.
13) Pegna, Joseph. (1997), "Explorary investigation of solid freeform construction", *Automation in construction*, Vol. 5, No. 5, pp. 427-437.
14) Warszawski, A., and Navon, R. (1998) "Implementation of robotics in buildings: current status and future prospects," *Journal of Construction Engineering and Management*, Vol.124, No.1, pp. 31-41.
15) Zak, G., Sela, M. N., Park, C. B., and Benhabib, B. (1999), "Layered-Manufacturing of Fiber-Reinforced Composites", *Journal of Manufacturing Science and Engineering*, ASME, Vol. 121, pp. 448-455, August.

Clinical Evaluation of Prosthetic Sockets Manufactured By Selective Laser Sintering

Bill Rogers[a], Andrew Gitter[a], Gordon Bosker[a], Mario Faustini[b], Mahendra Lokhande[b], Richard Crawford[b]

[a]The University of Texas Health Science Center at San Antonio
[b]The University of Texas at Austin

Abstract

A pilot study was undertaken to evaluate the clinical acceptance of prosthetic limb sockets manufactured using solid freeform fabrication (SFF). The fabrication of sockets for amputees is a natural application for SFF. The socket is the part of the prosthetic limb that fits onto the amputee's residual limb. Each socket is custom manufactured for each individual amputee. Four amputees were successfully fit with sockets created using selective laser sintering. The scope of the study included software development, finite element analysis, materials testing, and clinical evaluation. This paper discusses socket design issues and clinical testing results.

Purpose

The purpose of this pilot study is to demonstrate the feasibility of Solid Freeform Fabrication (SFF) using Selective Laser Sintering (SLS) to fabricate variable compliant wall prosthetic sockets for trans-tibial amputees. The study includes an engineering design component and a clinical case controlled comparison of variable compliant wall prosthetic sockets with conventionally fabricated prosthetic sockets.

The overall long-term objective of this project is to develop a system to fabricate variable wall compliant prosthetic sockets directly from digital residual limb shape information using freeform fabrication techniques. These sockets are expected to improve prosthetic socket comfort, improve tissue-loading characteristics, reduce skin discomfort and breakdown, and reduce fabrication time and cost compared to conventional socket fabrication techniques.

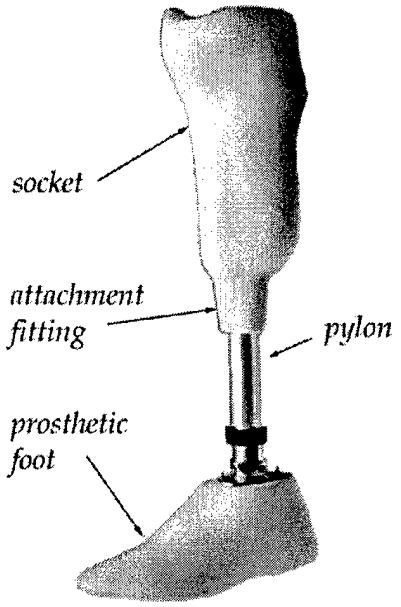


Fig. 1 Prosthetic limb

Introduction

There are approximately 400,000 lower limb amputees in the United States with 60,000 new major lower extremity amputations performed yearly. The majority of these amputees are fit with a prosthetic limb as part of their rehabilitation and return to independence. Because of changes in the shape and volume of the residual limb following amputation, the typical amputee will require a new prosthesis every two or three years.

A prosthetic limb for a transtibial amputee consists of several components (Fig. 1). First there is a socket that fits over the residual limb that is custom fit for each amputee. A fitting is

attached to the lower end of the socket to attach a pylon. The pylon connects to a prosthetic foot and is sized to the proper length for the prosthetic limb.

The most important aspect of a lower extremity prosthesis is socket design. The socket is the interface between the human and the mechanical support system. Ultimately, the design and fit of the socket is what determines patient acceptance, comfort, suspension, and energy expenditure[1]. All of these factors in unison determine the real utility of the final product.

The traditional method for designing sockets requires a skilled prosthetist and time consuming manual steps[2, 3]. First, the patient's residual limb is wrapped with plaster to acquire the shape. The plaster wrap is used to create a plaster positive. The prosthetist empirically modifies the plaster positive of the residual limb to distribute weight bearing to tissues that can tolerate the required forces. The socket is molded over the biomechanically corrected pattern. It is usually necessary to destroy the pattern in order to remove it from the socket. Making a new socket involves repeating all the steps if the pattern is destroyed.

CAD and Computer Assisted Manufacture (CAM) techniques are beginning to be widely used to design and manufacture sockets. A mechanical digitizer, magnetic digitizer, or a non-contact laser scanner[4] inputs the residual limb shape into the computer. The prosthetist then uses specialized software to produce a biomechanically correct socket from the limb shape. A computer controlled milling machine carves the pattern for the socket from plaster or foam. The socket is then made using conventional methods such as vacuum molding or lamination.

A limitation of currently available prosthetic CAD systems is that they only design the shape of the inner wall of the socket, which is all that is necessary for conventional fabrication. These CAD systems do not actually design the three dimensional shape of the socket. The actual wall thickness of the socket and the means of attaching the remainder of the prosthetic limb are determined during manufacturing. This is still largely an artisan process.

SFF techniques are a good match for use in prosthetics. Several artisan steps can be eliminated. These include trimming the final molded socket and the addition of a pylon attachment fitting. Additional features can be included such as variable compliance socket walls and integrated fittings. Due to the nature of the manufacturing process, an increase in socket sophistication does not lead to increased cost. The SFF industry is largely service bureau based which is the mode in which many prosthetic facilities operate.

Previous Work

Over the last ten years there have been several attempts to use SFF in the manufacture of prosthetic sockets for amputees.

Northwestern University working with Baxter Healthcare made a single transtibial socket using Stereolithography (SLA) in 1990[5].

In 1991, The University of Texas at Austin (UTA) and The University of Texas Health Science Center at San Antonio (UTHSCSA) collaborated to make scaled down transtibial

sockets[6, 7]. A full sized socket that incorporated a fitting for attaching the pylon followed this in 1992. An amputee in a supervised setting wore this socket briefly.

In 1992 Rovick from Northwestern developed a rapid prototyping technology called Squirt Shape to address the need for rapidly fabricating prosthetic sockets[8]. The process is a form of Fused Deposition Modeling where a bead of molten plastic is extruded in a continuous spiral to form a single wall socket.

In 1998 Freeman and Wontorcik fabricated check sockets suitable for ambulation though they lacked the durability needed for extended use[9]. The cost of the sockets was deemed to high for use as check sockets.

Also in 1998, Lee et al reported on fabricating two prosthetic sockets for amputees using FDM[10]. Gait analysis was performed comparing conventional and FDM sockets. Minimal variations in gait between the two types of sockets were shown.

In 1999 UTA and UTHSCSA collaborated on a sophisticated double wall socket fabricated using SLS[11, 12]. This work led to the current clinical pilot study.

It is important to note that none of the above work with the exception of the UTHSCSA/UTA collaboration used SFF for anything except replacing the first manual step in socket fabrication. The remainder of the prosthetic limb had to be attached by artisan means and no advanced features such as variably compliant walls were incorporated.

Methods

The previous work involving the double wall socket was extremely complicated and was burdened by the extra weight of the double wall configuration. It was decided to use a simpler approach for this pilot study using a single wall configuration with variable wall thickness. The approach was to vary the wall thickness to provide thinner more flexible socket walls over sensitive areas of the residual limb.

The clinical feasibility of using SLS for socket fabrication was evaluated by comparing conventional and SLS sockets for comfort, stump-socket interface pressures and gait function in four transtibial amputees. Three were vascular amputees and one was a traumatic amputee. Their ages ranged from 31-62 and all would be considered community ambulators. Informed consent was obtained following local institutional review board protocols.

A conventional patella tendon bearing socket was designed for each subject using standard CAD/CAM fabrication techniques. The residual limb of the amputee was cast at the UTHSCSA using a ShapeMate[13] casting sock. This sock hardens in minutes after being put in water. A laser imager was then used to measure the outside shape of the ShapeMate sock. The sock has a uniform thickness so that by measuring the outside of the sock then subtracting the sock thickness, the correct residual limb shape can be calculated. The socket was designed using ShapeMaker[13] prosthetic CAD software. A socket pattern was then milled from urethane foam. The conventional socket was fabricated using carbon fiber lamination. A pylon and prosthetic

foot were added to complete the prosthesis. Final alignment of the prosthesis was performed using visual gait analysis and patient feedback.

Each subject was given at least two weeks to acclimate to the conventional socket before undergoing gait analysis. Reflective markers were placed on the sacrum, bilateral ASIS, knee, ankle, and 2nd metatarsal phalangeal heads. Ground reaction forces were obtained using AMTI[14] force plates embedded into the gait lab floor. Combined joint kinematic and kinetic data was collected at a sampling rate of 60 fps for three representative strides as the subject walked at his self-selected speed. Using VICON Clinical Manager software[15], basic temporal and spatial features of the gait patterns and lower extremity joint angles were determined. Using inverse dynamics, net joint moment (torque) was calculated. For the prosthetic limb hip and knee joints this represented the net muscular generated joint moment that is developed in response to external forces and loads. For the prosthetic ankle, the joint moment is the resultant internal moment developed at the foot/pylon junction that mirrors the location of the intact limb ankle joint.

At the time of the gait analysis each subject filled a questionnaire regarding limb use, wearing schedule and rated socket comfort using a visual analog scale.

The urethane foam pattern used to fabricate the definitive socket was measured using the laser imager and served as the template for SLS socket fabrication. This was to insure that the comparison was between sockets of identical shape. Trim lines, load bearing areas, and pressure sensitive areas were marked in black on the pattern. The laser imager captured these marks. The data including the marked locations were saved in an AAOP data interchange file. This is a non-proprietary file format that is supported by prosthetic CAD/CAM vendors.

In previous efforts at UTHSCSA/UTA[9, 10], the process of taking an AAOP data interchange file and creating a complete 3D socket with an attachment fitting was extremely labor intensive, time consuming and involved several different software packages. In order to produce sockets in a timely manner it was necessary to write custom software to create the final STL file from the AAOP file. This software was written in C++ using the OpenGL graphics API for the Microsoft Windows platform. The software performs four main functions. First it gives thickness to the socket by creating an outer shell from the inner socket shape. The nominal socket wall thickness was set to 6 mm. The socket trimline is set interactively using the mouse cursor to select points on the socket shape (Fig. 2). Areas of variable wall thickness are interactively drawn on the socket shape. These areas are defined relative to pressure sensitive areas marked on the socket pattern. The minimum thickness of regions over sensitive areas was set to 1.3 mm. Finally a fitting for a pylon adapter is added to the bottom of the socket. The fitting has a key that matches a keyway in the pylon adapter. The completed design is saved in an STL file (Fig 3).

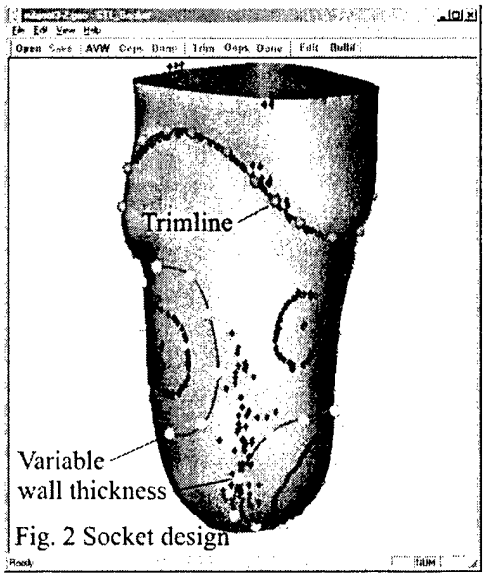
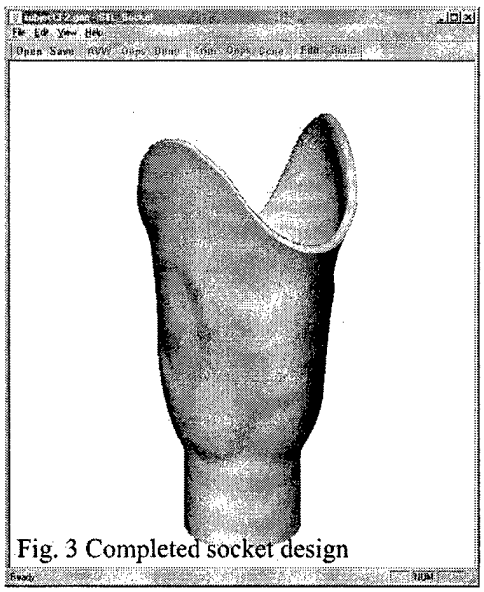


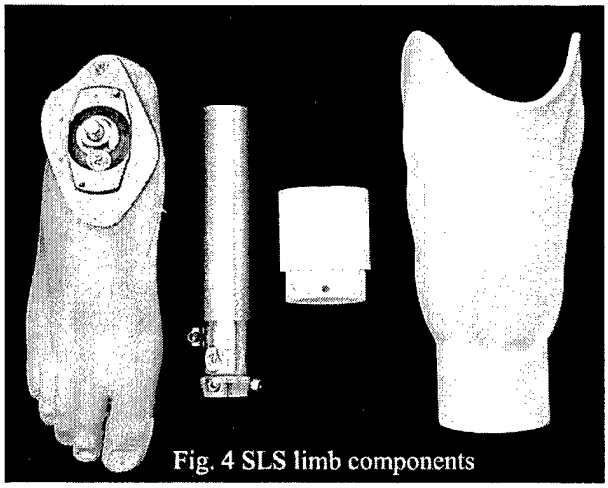
Fig. 2 Socket design

Each STL files was emailed to Accelerated Technologies Inc.[16], a service bureau, for fabrication. The parts were built using Duraform on a Sinterstation 2500[17]. The sockets were coated with cyanoacrylate for a better surface finish after sanding. The finished sockets were sent back to UTHSCSA for final assembly.


Fig. 3 Completed socket design

Epoxy was used to glue the nylon pylon adapter into the keyed fitting on the socket even though there was already a snug fit. The pylon and a prosthetic foot were added to complete the prosthetic limb (Fig. 4). The pylon adapter has two eccentric cylinders that are used to set the proper alignment angle of the pylon relative to the socket.

The gait analysis and subjective evaluation was repeated using the SLS prosthesis. In addition, measurements were made using the FSCAN[18] system to compare stump-socket interface pressures in the conventional socket and the SLS socket. The FSCAN system uses pezioresistive pressure sensitive plastic strips that were attached to the skin of the residual limb at sites that corresponded to the thinned regions of the SLS socket wall. Interfaces pressures were recorded and averaged over 10 strides. Pressure measurements were first conducted while wearing the conventional socket and then repeated with the SLS socket without changing the location of the sensors.


Fig. 4 SLS limb components

A finite element model of the socket was developed at UTA during the same time period though it was not ready to use during the socket design phase. Using IDEAS from SDRC[19] the socket volume is meshed with solid elements (parabolic tetrahedra), generating the final FE model that can be associated with selected material properties, undergo the appropriate boundary conditions and be simulated to generate structural analysis results. This finite element model proved to be valuable during the clinical part of the study.

Materials' testing was also done at UTA. Sample Duraform coupons fabricated at UTA were subject to a uniform pressure and the deflection was measured. It was necessary to verify that the material properties of the parts produced by SLS were the same as used in the finite element model.

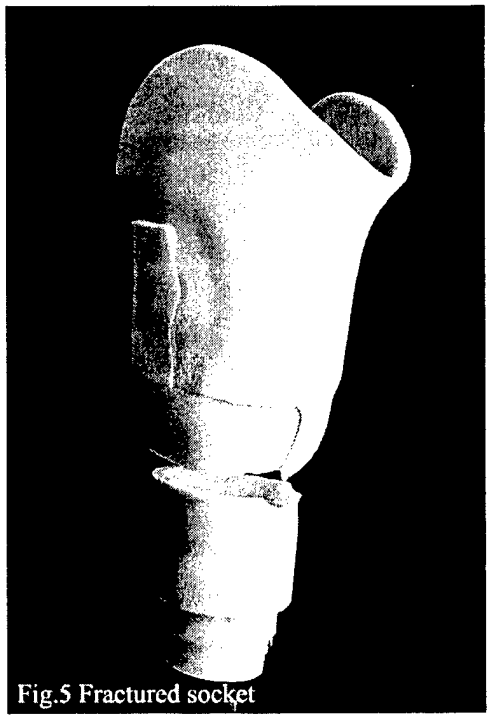
Results

A clinically acceptable fit was achieved in all subjects with both sockets. All subjects were satisfied with the fit of the SLS socket and expressed a willing to use it to meet their ambulation needs. Informal feedback from the subjects suggested that overall socket function was nearly identical in three subjects who had a history of satisfactory socket fit and prosthetic use. The fourth subject had a long history of stump pain and poor tolerance to prolonged prosthetic use. This subject displayed the greatest degree of improvement in comfort and use of his prosthesis when using the SLS socket. Using the visual analog scale (0-10 range) comparison of socket comfort between the sockets ranged from the same to 15% improved with the SLS socket. Average daily wearing time remained the same in three subjects and increased by 5 hours in the fourth subject.

Gait analysis showed no significant differences between SLS and conventional sockets in self selected walking speeds or knee joint torques.

Attempts at measuring interface pressures were problematic. The difficulties were related to sensor movement between test sessions and bucking and wrinkling of the sensors during the loading/unloading cycle associated with each step. The resulting measurements contained spurious errors and the data needs to be interpreted cautiously. Considerable variability in the data existed but some trends were observed. Average peak pressures during the stance phase of gait showed no differences in the lateral aspects of the socket but were decreased by 11 psi in the anterior aspects of the SLS socket compared to the conventional socket.

There was one notable failure where a socket fractured as one of the amputees stepped off of a bus. The socket subsequently broke in two pieces as the amputee continued to walk with the limb (Fig. 5). While this caused great concern about the whole project, it led to greater understanding of the whole process. Upon close examination it was revealed that there were both design and materials components to the failure.


Fig.5 Fractured socket

The materials problem resulted from the way the Sinterstation 2500 was set up. It was previously noticed that the socket material was quite brittle. This was the result of a tradeoff between feature definition and part density. The traditional way of operating an SLS machine is to use a laser power that is less than what would produce the densest possible part. This gives better feature definition and the part is easier to remove from the powder bed. Running the machine at a higher laser power results in a denser part but with a small loss in accuracy. The denser parts are stronger and have material properties that are closer to an extruded part. The socket that fractured was not fabricated at the highest possible density. All succeeding parts were fabricated at a higher laser power and there were no further failures.

The design problem came from the desire to provide the maximum compliance at the distal end of the socket. This resulted in a notch between the pylon adapter and the socket. This was the region where the fracture started. The socket was redesigned to blend the socket and pylon smoothly together.

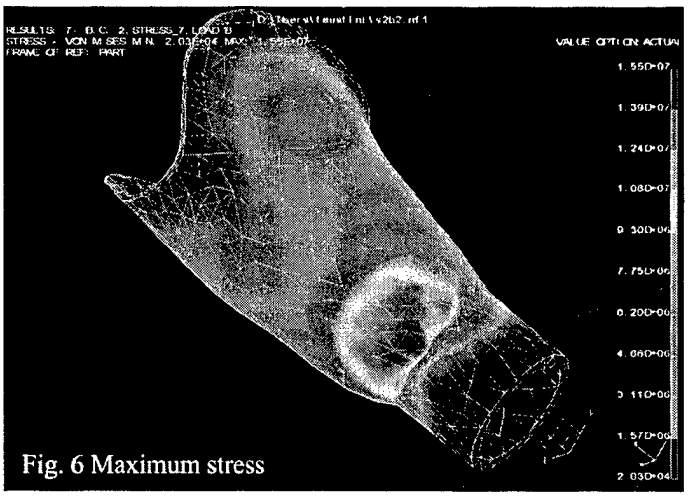


Fig. 6 Maximum stress

The finite element model of the failed socket showed that at the point of failure was the location of maximum stress (Fig 6 in red). The revised socket showed reduced stress at the junction of the pylon and socket. In neither case did the maximum stress in the model approach the (theoretical) ultimate limit of Duraform.

Discussion

This study showed that the SLS sockets were clinically acceptable and that they can be fabricated in a timely manner.

The desired amount of compliance hoped for was not achieved by thinning the socket wall. It was judged that a minimum wall thickness of 1.3 mm was necessary for structural integrity and even at that thickness there was little flexibility.

The pylon adapter chosen for this study presents an obstacle to clinical acceptance. The eccentric cylinder pylon adapter was chosen as it was simple to incorporate into the design. To be accepted by the prosthetics profession it will be necessary to accommodate conventional pyramid adapters.

Future Work

Larger scale clinical studies are planned. In the future, sockets will be designed directly from scan data eliminating the pattern fabrication step. One important addition will be incorporation of industry standard hardware into the socket design. New methods for providing additional compliance for sensitive areas of the residual limb will be employed. It is planned to use finite element modeling of the sockets during the design phase to minimize the possibility of failure as well as testing new methods of varying the socket compliance.

Acknowledgements

The authors wish to acknowledge the Veterans Administration for their support of this study by the VA Research and Development Service Merit Review grant #A1963PA. The authors also wish to thank The DTM Corporation and Accelerated Technologies Inc. for their continued support of this research.

References

1. Foort, J. Et.al., Experimental Fittings of Sockets for Below-knee Amputees Using Computer-aided Design and Manufacturing Techniques, Prosth. & Orth. Int., 9:46-47, 1985.
2. Radcliffe D.F., Computer-Aided Rehabilitation Engineering-CARE. J Med Engin Tech, 10:1-6, 1986.
3. Stokosa J., Prosthetics for Lower Limb Amputees, Vascular Surgery. Principles & Techniques, Ed: H Haimovicci, Norwalk: CN. Appleton-Century-Croft, 1143-1162, 1984.
4. Walsh N.E., Lancaster J.L., Faulkner V.W., Rogers W.E., A Computerized System to Manufacture Prostheses for Amputees in Developing Countries, Journal of Prosthetics and Orthotics Vol. 1 Number 3, p165-181, 1989.
5. Rovick, J.S., R.B. Chan, Van Vorhis, D.S. Childress, Computer-Aided Manufacturing in Prosthetics: Various Possibilities Using Industrial Equipment, Proceedings of the Seventh World Congress of the International Society for Prosthetics and Orthotics (ISPO) Chicago, IL. p. 24, 1992.
6. Rogers WE, Crawford RH, Beaman JJ, Walsh NE, Fabrication of Prosthetic Sockets by Selective Laser Sintering, Proceedings of the Solid Freeform Fabrication Symposium, August 1991, 12-14, p. 158.
7. Rogers WE, Crawford RH, Faulkner VF, Beaman JJ, Fabrication of an Integrated Prosthetic Socket Using Solid Freeform Fabrication, Proceedings of the Seventh World Congress of the International Society for Prosthetics and Orthotics, 1992. Chicago, IL. P. 23.
8. Rovick, J.S., An Additive Fabrication Technique for the Computer-Aided Manufacturing of Sockets, Proceedings of the Seventh World Congress of the International Society for Prosthetics and Orthotics, 1992. Chicago, IL. P. 24.
9. Freeman D., Wontorik L., Stereolithography and Prosthetic Test Socket Manufacture: A cost/benefit analysis, Journal of Prosthetics and Orthotics 10:17-20,1998..
10. PVS Lee, KC Tan, KF Tam, SL Lye, Biomechanical Evaluation of Prosthetic Sockets Fabricated Using Fused Depository Method, The First National Symposium of Prosthetics and Orthotics, Singapore, October 28, 1998.
11. Bill Rogers, Sean Stephens, Andrew Gitter, Gordon Bosker, Richard Crawford, Double-Wall, Transtibial Prosthetic Socket Fabricated Using Selective Laser Sintering: A Case Study Journal of Prosthetics and Orthotics, Vol. 12 Number 3, 2000, 97-103.
12. Sean Stephens, Richard Crawford, William Rogers, Andrew Gitter, Gordon Bosker, Manufacture of Compliant Prosthesis Sockets Using Selective Laser Sintering, Proceedings of the Eleventh Freeform Fabrication Symposium, August 7-9, 2000.
13. Seattle Limb Systems, 26292 Twelve Trees Lane NW, Building One, Poulsbo, WA 98370.
14. AMTI, 176 Waltham St., Watertown, MA 02472.
15. VICON Motion Systems, 15455 Redhill Avenue, Suite C, Tustin, CA 92680.
16. Accelerated Technologies Inc., 12919 Dessau Road, Austin TX 78754.
17. DTM Corporation, 1611 Headway Circle, Building 2, Austin, TX 78754.
18. FSCAN Tekscan, Inc., 307 West First Street, South Boston, MA 02127-1309.
19. SDRC, 2000 Eastman Dr., Milford, OH 45150.

Testing of Compliance in a Prosthetic Socket Fabricated Using Selective Laser Sintering

Mahendra Lokhande and Richard H. Crawford
The University of Texas at Austin

ABSTRACT

Solid freeform fabrication techniques offer potential as manufacturing technologies in applications that require custom design. One such application is the fabrication of prosthetic sockets. This paper reports on research to manufacture compliant below-the-knee prosthetic sockets using selective laser sintering (SLS). Compliance in the socket is a critical factor in the level of comfort the amputee experiences during gait. The ability to control local geometry is seen as an advantage of SLS in fabricating compliant sockets. This paper presents work on developing a model of compliance for sockets constructed of Duraform®. The approach taken here is to provide the necessary compliance by controlling the wall thickness of the socket. To select the right thickness, a study of the wall deflection with respect to contact pressure was performed. An experimental testing device was designed and constructed to test the deflection versus pressure for different thicknesses of test circular discs made of Duraform®. The results were correlated to a finite element model. These results will be used for designing the compliance in the walls of prosthetic sockets fitted to actual patients.

INTRODUCTION

This paper presents results from the on going research to manufacture a compliant transtibial (below-the-knee) prosthetic socket using Selective Laser Sintering (SLS) [Rogers, et al., 1991; Stephens, 1999; Stephens et al. 2000]. This approach has several potential advantages over conventional methods, such as easy duplication of sockets, flexible geometric design and better control on the socket thickness. In particular, SLS offers the potential to increase compliance in the socket in selected locations by controlling the local geometry. Increased compliance relieves excessive pressure on the residual limb tissue, especially in the sensitive bony areas, thereby enhancing the comfort level experienced by the amputee. A socket produced by SLS is shown in Figure 1. The goal of the current research is to develop a model of the compliance of a SLS material. This model will be used to design sockets based on customer needs and feedback from a prosthetist.

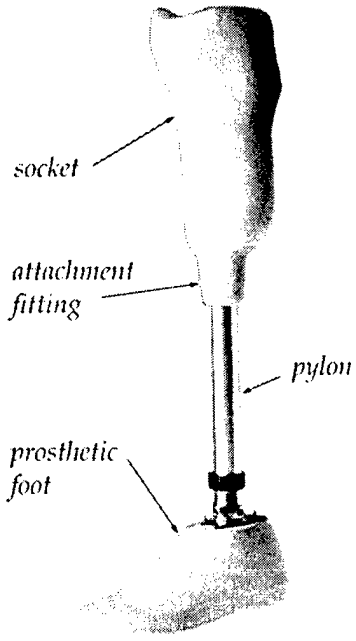


Figure 1. SLS fabricated transtibial socket.

In the present work, a series of experiments was conducted to study the compliance of thin Duraform® discs processed using SFF. The experiments were then used to verify a finite element model of the compliant discs. In this paper we describe the experimental setup and the results obtained from pressure tests on the discs. We then compare the results to finite element simulations of the loaded discs.

PRESSURE-DEFLECTION EXPERIMENTS

The test apparatus is designed to simulate as closely as possible the load conditions on the compliant region of the socket. The design assumes the pressure on the compliant region is uniform. To simulate this, thin compliant discs, such as those shown in Figure 2, were fabricated from Duraform® and subjected to air pressure. The circular disks vary in thickness, being thicker toward the outer diameter and thinner in the middle. The thin middle section has a nominal diameter of two inches. Discs with inner thicknesses ranging from 0.033" to 0.05" were fabricated. Each disc has a diameter-to-thickness ratio of 20, permitting a thin disc assumption for analysis. The discs were subjected to pressures ranging from 0 to 60 psi.

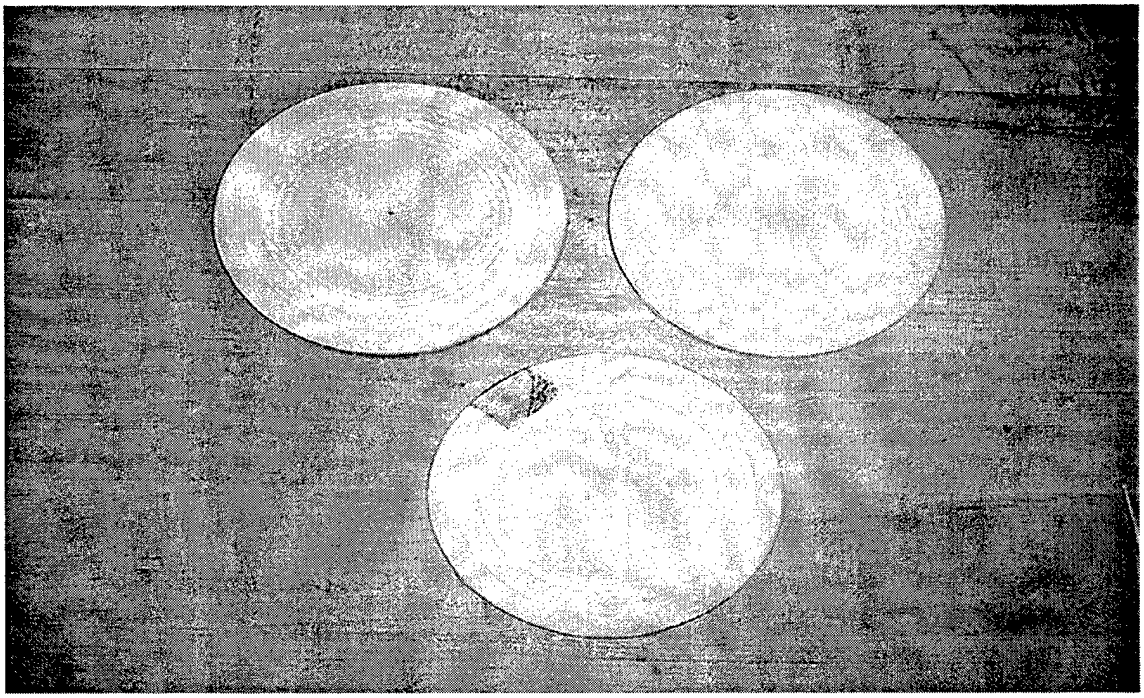


Figure 2. Duraform® specimens.

Experimental Apparatus

A photograph of the test device is shown in Figure 3. The inner diameter of the aluminum cylinder is two inches, corresponding to the thin region of the specimens. Since the Duraform discs were porous and not airtight, a very thin plastic sheet was used to seal the air pressure. Two soft rubber gaskets are also used to make the seal between the support discs airtight. One circular flange is attached to the main cylinder using metal-to-metal glue. The other flange is used to clamp the Duraform disc, which is centrally placed between the flanges and held rigidly on its periphery with four ¼ inch nuts and bolts. Compressed air is supplied using a Schrader valve that is screwed into the other end of the cylinder as shown in Figure 4. It is important to note that this device was designed for static load analysis. The instruments used to measure pressures and deflections were a pressure gauge and a dial gauge. The pressure gauge is attached to a half-inch pipe nipple that is screwed into the side of the cylinder. The resolution of the pressure gauge is 5 psi for the range 0-20 psi, and 4 psi for pressures above 20 psi. The resolution of the dial gauge is 0.001". These were found to be reasonably accurate for these experiments. To avoid disturbance in the dial gauge readings the whole device is rigidly clamped to the table as shown in Figures 4 and 5, with the probe of the dial gauge adjusted so that it touches the center of the disc. The set up can be seen in Figure 5. The maximum pressure of the compressed air supply was 100 psi.

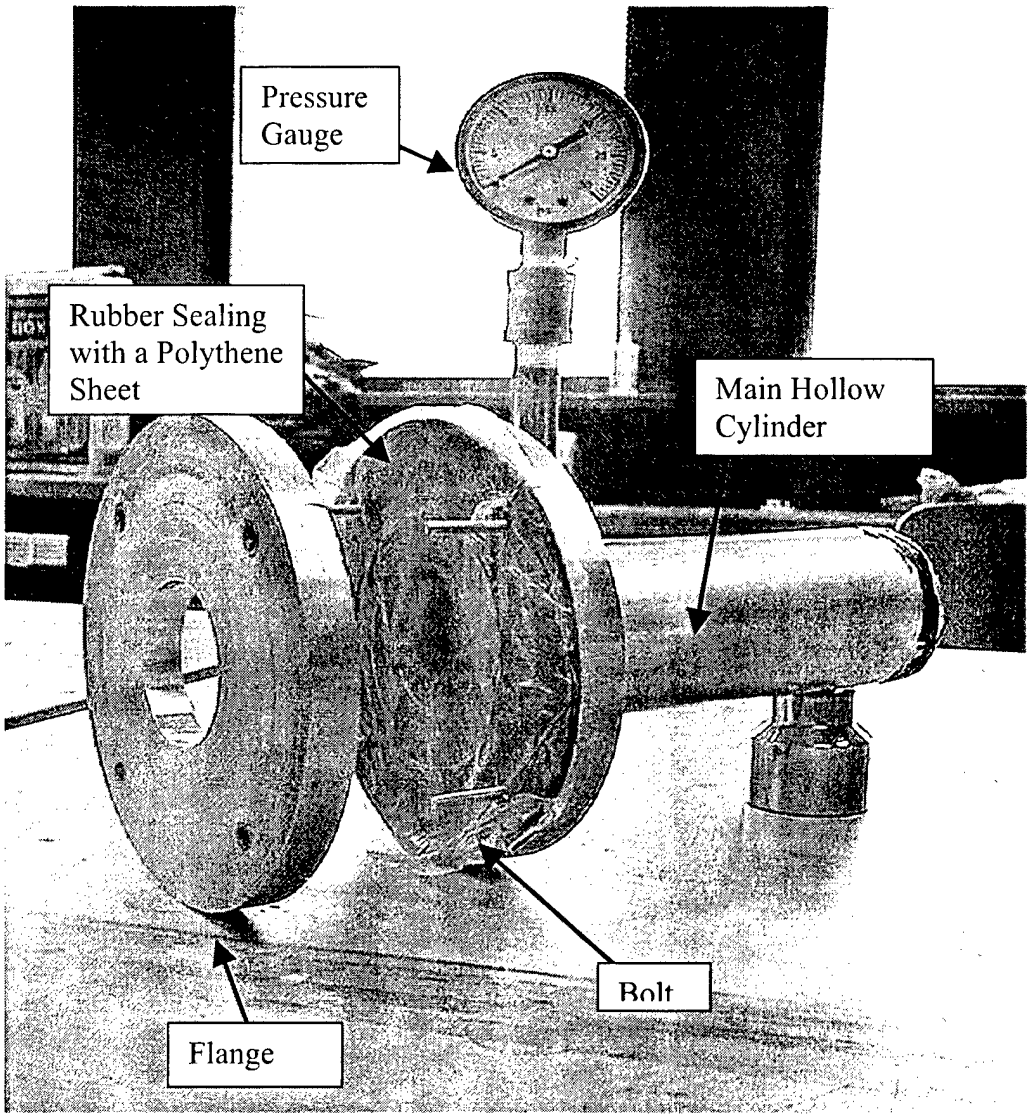


Figure 3. Device used to test compliance.

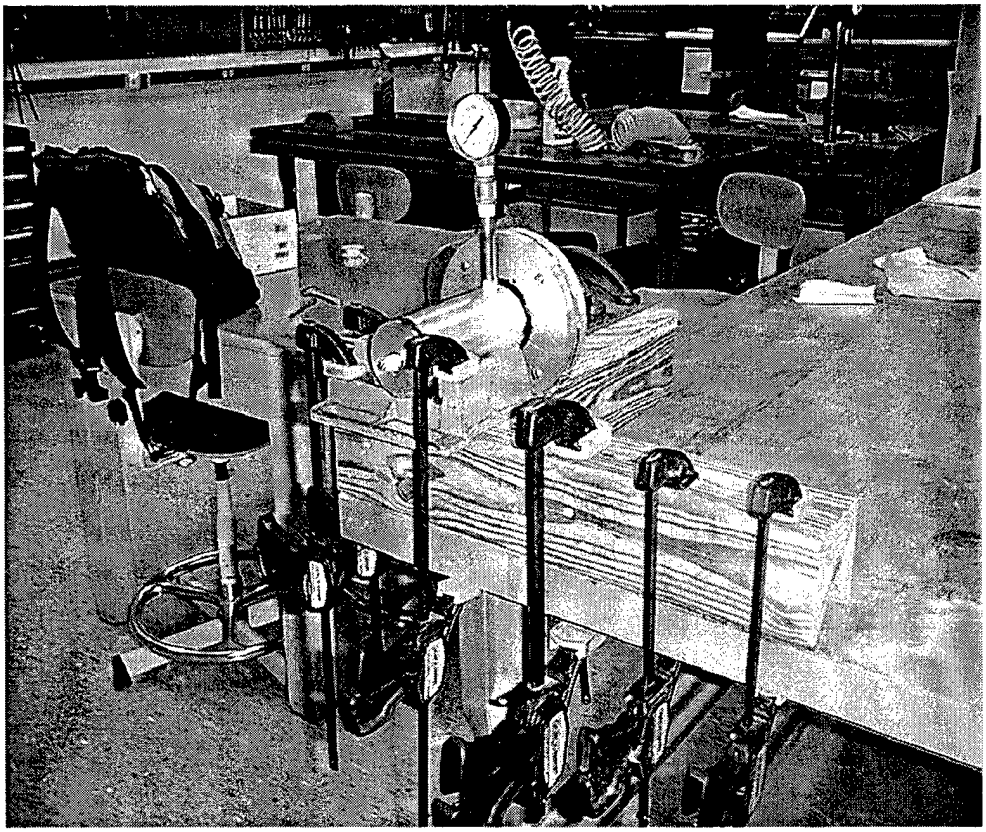


Figure 4. Experimental set up (back view).

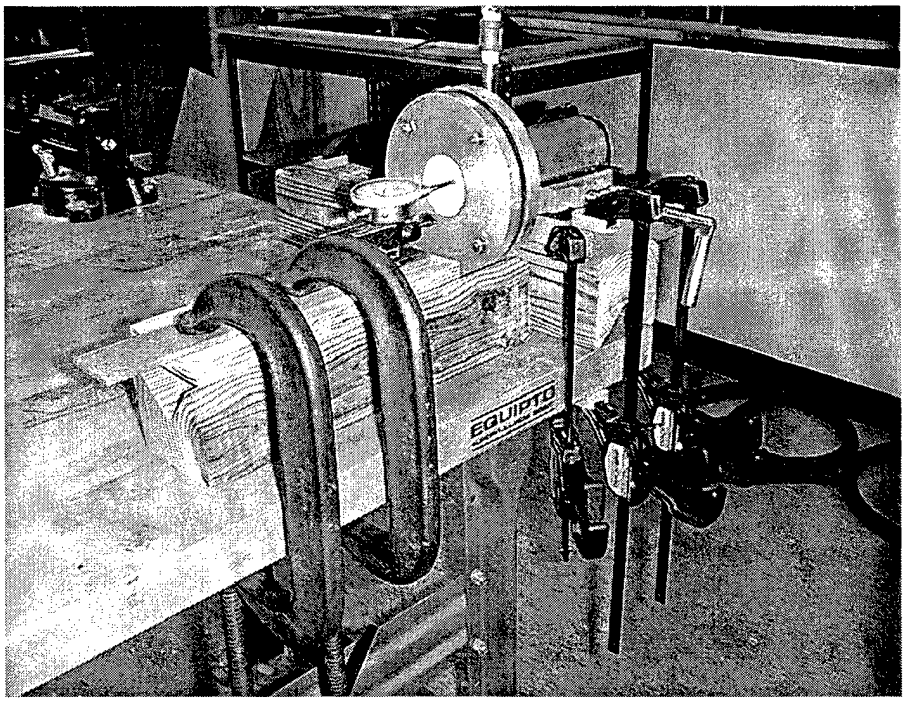


Figure 5. Experimental set up (front view).

Experimental Results

The Duraform discs of varying thicknesses (0.033"-0.05") were made using a Sinterstation 2000. The first set of discs made was of recycled powder. A subsequent set made from virgin powder was tested. As the differences were negligible, we present the results from the recycled powder. Air pressure up to 60 psi was applied to the Duraform, then decreased in steps as the deflection at the center of the disc was recorded. Three sets of readings were taken for each disc. Figure 6 shows the results for the 0.5" disc, and Figure 7 shows the results for the 0.033" disc.

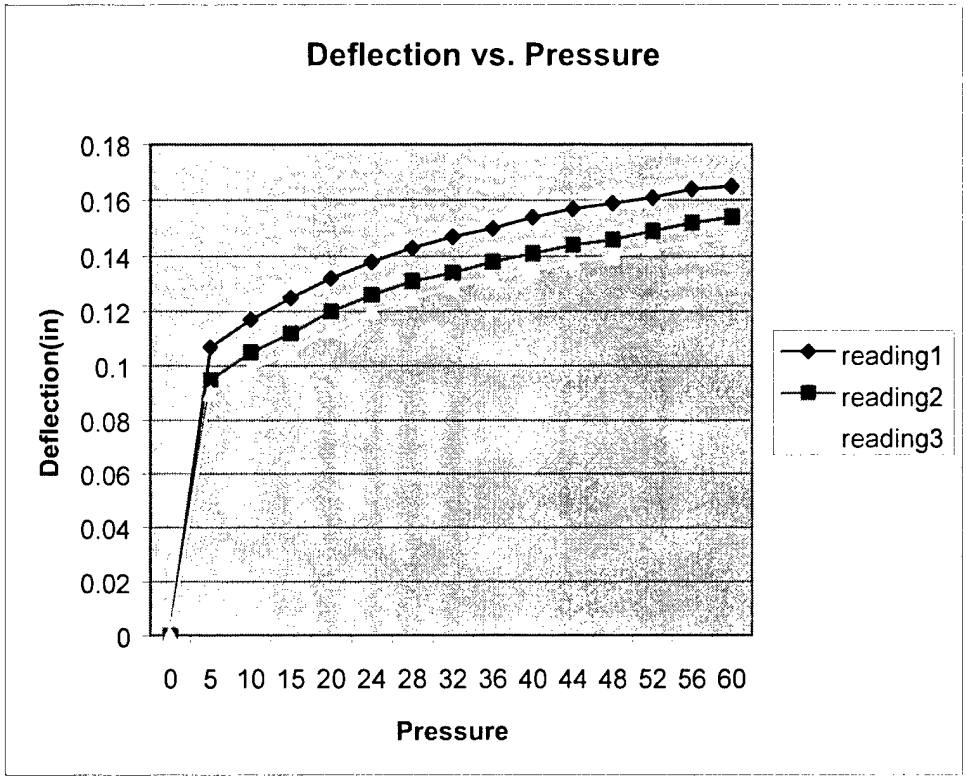


Figure 6. Deflection results for 0.05" disc.

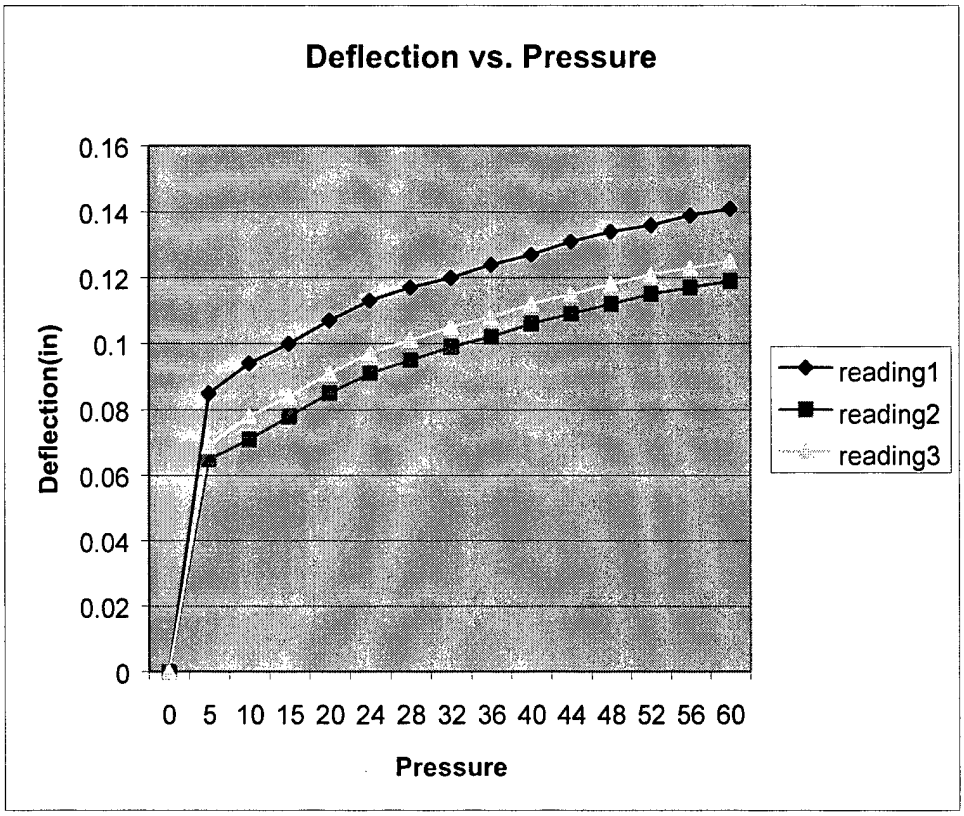


Figure 7. Deflection results for 0.033" disc.

Results and Observations

The graphs above illustrate an unexpected but important result. Each disc experienced some permanent deformation every time a set of readings was taken. Clearly, at some point the disc exceeds the elastic limit. Further evidence of this is given by the visible bulge that remains after the disc is unloaded, giving the initially flat disc a spherical shape (see Figure 8). Also note the general trend of reducing maximum deflection for each consecutive set of readings. Upon sudden reduction in pressure the disc does not regain its original shape instantly. Rather, it tends to regain its new initial state very slowly and gradually. To test the maximum pressure the disc could withstand before cracking, pressure up to 100 psi was applied to both the discs. However, spite of this high pressure, neither disc failed.

Sources of Error

Though the procedure was followed carefully to get the results as accurate as possible there are some sources of experimental errors. The following sources were identified:

1. Use of a tactile measurement instrument (dial gauge-least count is 0.001") to measure the deflection of the disc. This source of error, though very insignificant, reduces the accuracy of the deflection of the disc. Another source of error due to this instrument is the friction between the tip of the probe and the disc. To account for these phenomena,

all readings were assumed to have a general tolerance of about ± 0.005". Three sets of readings were taken for each data point to account for this error.

2. Use of the polyethylene seal. For complete accuracy, the overall disc should be treated as a composite disc (polyethylene + Duraform). However, this is difficult to account for analytically. Thus, measures were taken to eliminate effect of the sheet on the deflection of the disc, such as making the sheet larger in the deflection zone so it is loose and does not provide significant resistance to the applied pressure. It is safe to assume that the pressure recorded is indeed the pressure applied to the disc.

3. There may be a very small amount of error involved in the overall experimental set up. As seen from the figure the set up is very basic with no built-in support structure. Rigidity is provided using clamps, which may not prevent slipping, though care has been taken to ensure no slippage.

4. The test discs are not exactly uniformly thick. This is a definite but unpredictable source of error.

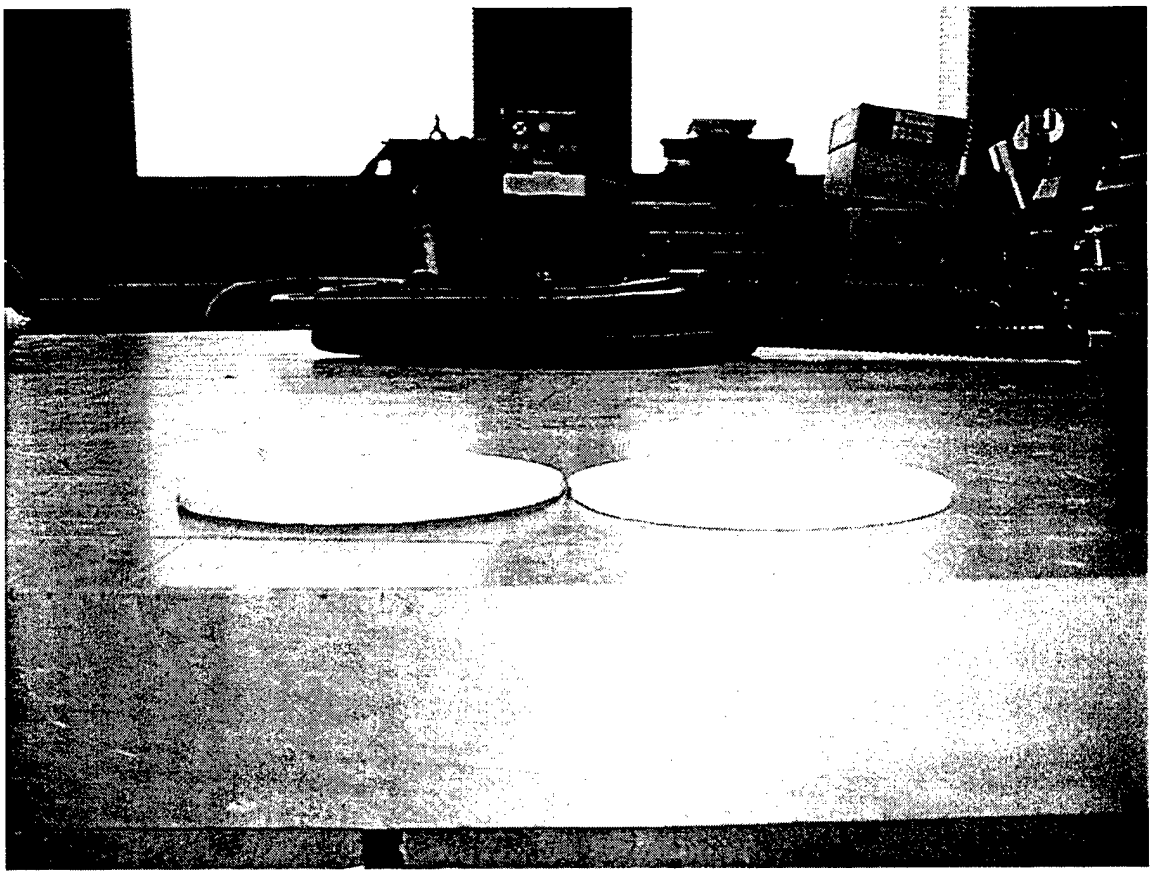


Figure 8. Undeformed disc before experimentation (right) and deformed disc after experimentation (left).

FINITE ELEMENT ANALYSIS OF DURAFORM DISCS

The goal of this research is to develop a finite element (FEA) based compliance model that can be used to design prosthetics sockets. This section describes the model developed and compares the results of the model to the experimental results presented in the previous section. All FEA results were obtained using ANSYS 5.5 from ANSYS, Inc., Canonsburg, PA.

The FEA analysis of each disc assumes that the disc is rigidly clamped at it periphery, thus simulating the experiment performed above. In order to be able to do the FEA, properties of Duraform such as the elastic moduli (E_x, E_y) and Poisson's ratio were needed. Due to layered nature of SLS, the resulting parts and elastic moduli are orthotropic in nature. We used the experimental results from [Watson, 1999] for these properties. In particular, a stress-strain curve was used rather than a single value for the elastic modulus. The curve used is shown in Figure 9, as plotted by ANSYS. The value for Poisson's ration was determined by solving a deflection relationship iteratively to correlate with the experimental results from the previous section. The computed value of Poisson's ratio was 0.406, which agrees well with values published by DTM Corp.

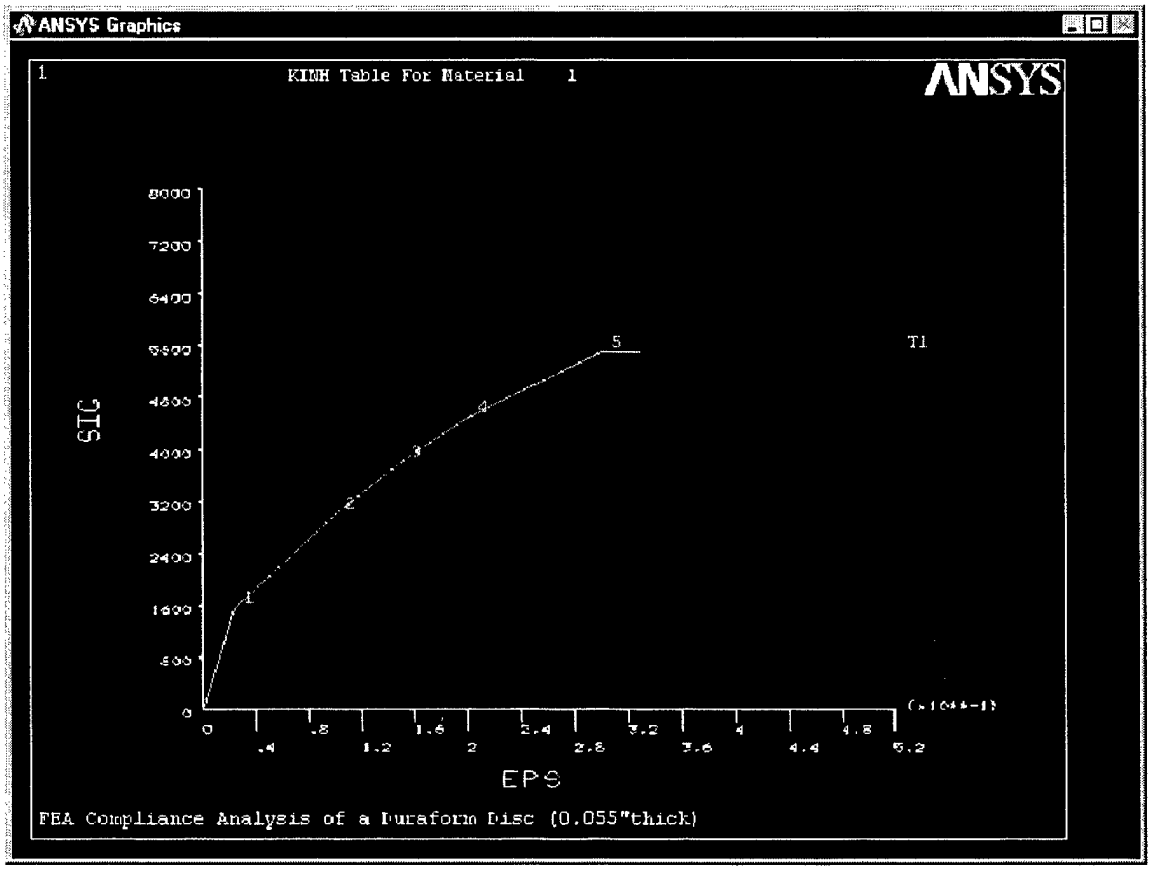


Figure 9. Stress-strain curve used for FEA.

Finite Element Model

The element PLANE42 was used for the analysis. This element assumes the behavior of the disc is axisymmetric and isotropic. Deflections and stresses were analyzed for the disc cross-section. Since the specimens can be considered thin discs, we assumed that E_y has no significant effect on the results. This assumption is confirmed by the stress distribution in the y axis direction, as shown in Figure 10, which shows very low and uniform stresses.

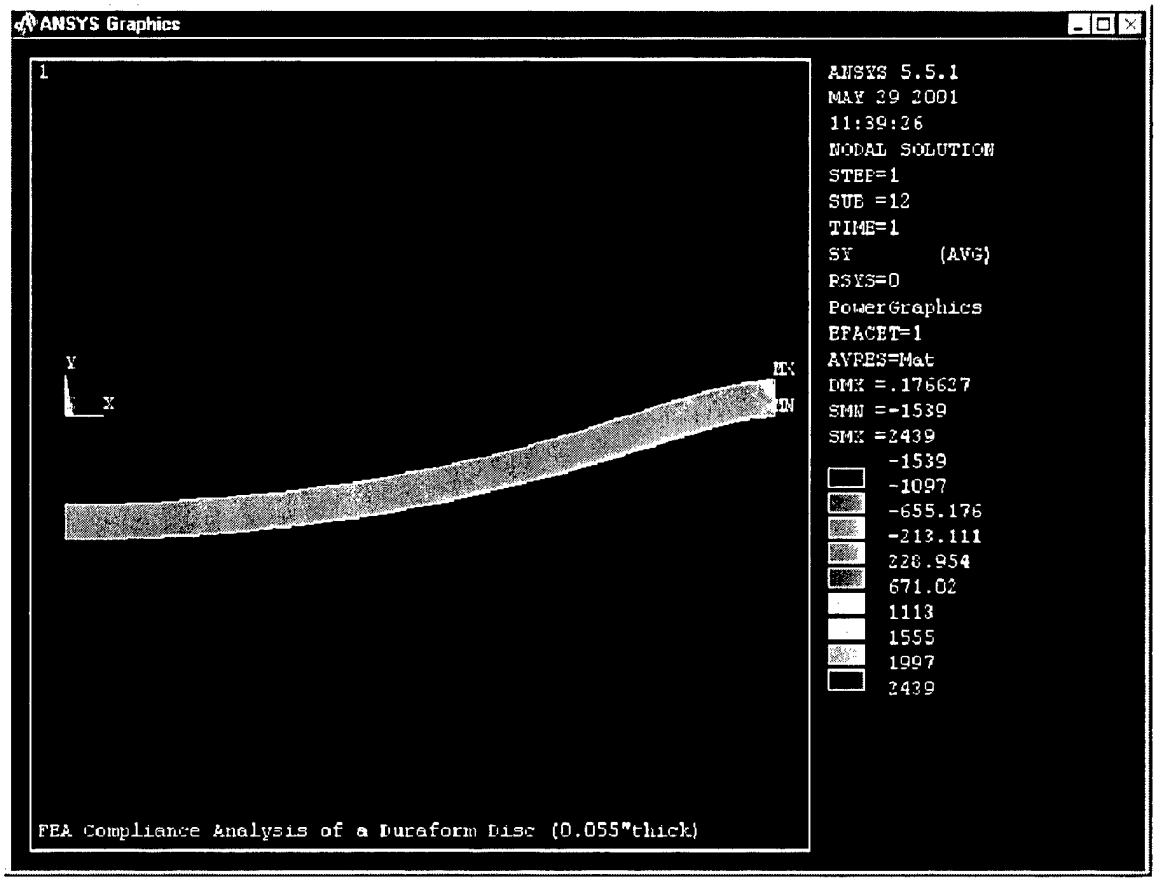


Figure 10. Stress distribution in the y direction.

FEA Results

Using these values for the mechanical properties, the finite element analysis yielded the results shown in Table 1. Figures 11 and 12 show the cross section of the deformed shaped and the stress distribution in the x direction, respectively, for the 0.033" disc. Pressure-deflection graphs for the experimental and analytical results for the 0.033" disc are shown in Figure 13. The figure shows there is good agreement between the two.

Table 1. Deflection vs. pressure results from FEA.

Pressure (psi)	Deflection at the center (in)
0	0
5	0.059988
10	0.083738
15	0.10023
20	0.11351
25	0.12478
30	0.13482
35	0.14409
40	0.15286
45	0.16120
50	0.16923
55	0.17704
60	0.18466

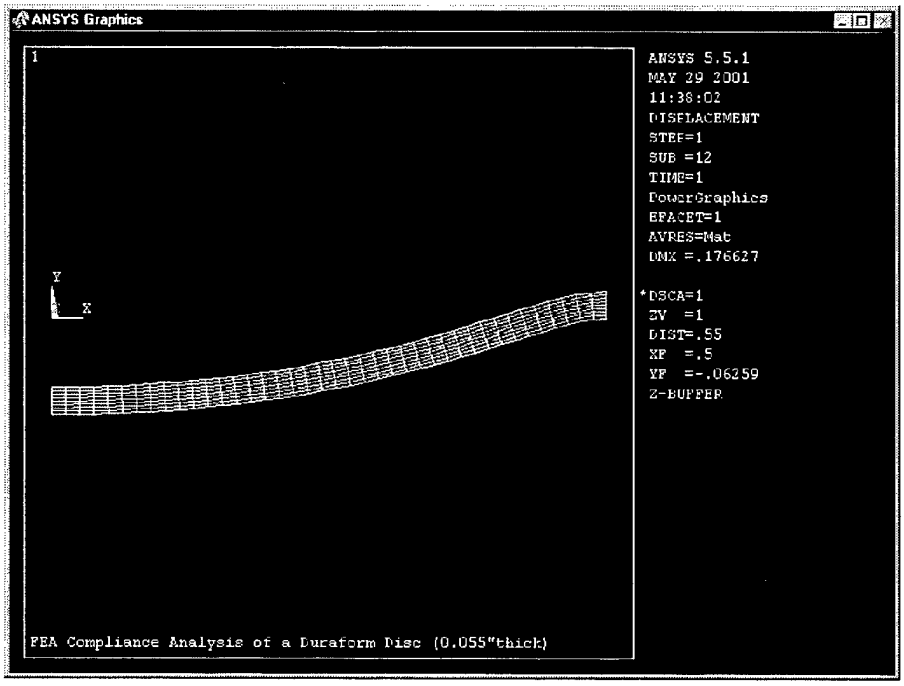


Figure 11. Cross sectional deflection of disc in *x* direction.

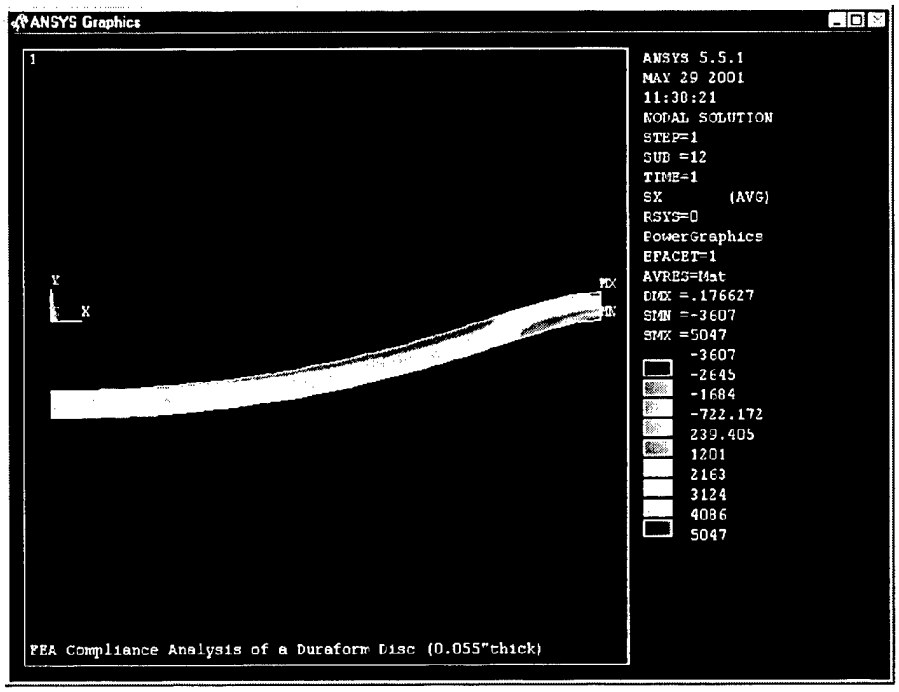


Figure 12. Stress distribution of disc in *x* direction.

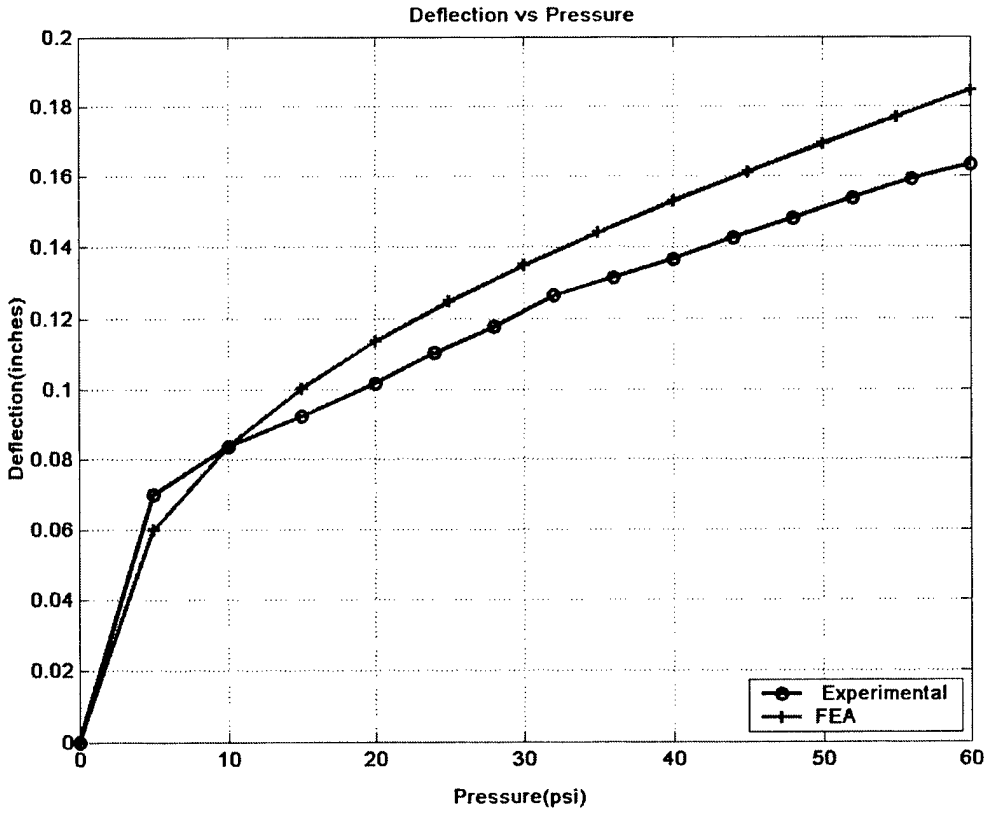


Figure 13. Pressure-deflection relationships from experimental and FEA results.

Analysis of Results

In order to quantify the match between the experimental and FEA results, a Kolmogorov-Smirnov Two Sample Test [Johnson and Leone, 1964] was performed on the two data sets. The two-sample Kolmogorov-Smirnov test determines whether two independent samples come from the same distribution by comparing the two-sample cumulative distribution functions. The test assumes that both samples come from exactly the same distribution.

Using SYSTAT, a statistics package from SSPS Science, Chicago, IL, the Kolmogorov-Smirnov two sample test was preformed with a significance level of 0.05. The results are shown in Table 2. The results show that the two distributions are from the same distribution with a confidence of 96.2 %. Thus, the important step of obtaining similar results from the experiments and FEA was achieved.

Table 2. Kolmogorov-Smirnov two sample test results.

Maximum Difference for Pairs of Variables		
	FEA	Experimental
FEA	0.000	
Experimental	0.2	0.000
Two-Sided Probabilities		
FEA	-	-
Experimental	0.962	-

CONCLUSIONS

The focus of the work reported here is compliance in single walled prosthetic sockets. To quantify the compliance of Duraform®, thin circular discs with varying thicknesses were subjected to pressures corresponding to those that would be experienced during gait by the amputee. The deflections of the discs were recorded as indicators of the degree of compliance. These results were compared to a finite element model of the discs. In order to obtain good agreement between the experimental and analytical models, a non-linear stress-strain curve for Duraform® was used.

The work reported here is part of an ongoing effort to improve the performance of prosthetic sockets using SLS. We have fitted several sockets to patients and performed limited clinical trials, with promising results. The next step is to use the results from the compliance tests to optimize the socket design. We also need to determine the durability of Duraform® sockets made with SLS. Also, more extensive, long-term clinical trials are necessary to prove the durability of these sockets.

BIBLIOGRAPHY

1. Johnson, N., and Leone, F., *Statistics and Experimental Design In Engineering and the Physical Sciences, Vol. 1*, 1964.

2. Rogers, W. E., Crawford, R. H., Beaman, J. J., and Walsh, N. E., "Fabrication of Prosthetics Sockets by Selective Laser Sintering," *Proceedings of Solid Freeform Fabrication Symposium*, Austin, TX, pp. 158-163, August 12-14, 1991.

3. Stephens, S., *Design of a Compliant Prosthetic Socket Fabricated Using Selected Laser Sintering*, Master's thesis, The University of Texas at Austin, August 1999.

4. Stephens, S., Crawford, R., Rogers, W., Gitter, A., and Bosker, G., "Manufacture of Compliant Prosthesis Sockets using Selective Laser Sintering," *Proceedings of the 2000 Solid Freeform Fabrication Symposium*, Austin, TX, August 7-9, 2000.

5. Watson, D., "Process Optimization for Selective Laser Sintering Through the Use of Design Rules and Constraints," Master's thesis, The University of Texas at Austin, May 1999.

Rapid Prototyping Assisted Design and Development of Inter-Vertebral Implants

J. Chiang, M. Lehmicke, D. Dcosta, X. Hu, F. Lin, W. Sun[(1)]

Department of Mechanical Engineering and Mechanics
Drexel University, Philadelphia, PA 19104

Abstract

This paper presents a case study of applying rapid prototyping in assisting in the design and development of inter-vertebral implants for spine fusions. The major process of design and implant development, its biological and mechanical requirements, the approach for developing a 3D reconstructive vertebral anatomy model, the inter-vertebral implant CAD model, and the integration with a finite element analysis for the implant's structural analysis are presented. The process of 3D Printing of the vertebral anatomy and the inter-vertebral implant is described. The application of the prototyping model in assisting in the inter-vertebral anatomic fitting, in guiding the implant's geometric design, in helping with the virtual surgical planning, and in understanding the implant's mechanical properties and structural stability are discussed.

1. Introduction

Over 1 million operations annually involve bone repair and over 200,000 spine fusion procedures are carried out each year in order to cure various back ailments [1, 2]. Pseudoarthrosis occurs in 10 - 40% of single level fusions, and at a significantly higher rate for multiple level fusions [3]. Current standards of care for spinal fusion involve various implants or grafting techniques. However, these techniques or implants are often limited by their biological or mechanical constraints. For example, autograft, the best grafting process, which takes bone from the patient's own body, is limited by its availability and variation in quality (bone from an osteoporotic patient is not strong graft material), and perhaps most significantly, by its host site morbidity. Allograft, processed from cadavers when or where autograft is not available or practical, has a lower success rate compared to autograft in most settings. In addition, it carries the risk of disease transmission. Due to these limitations, implants have been developed specifically for spinal fusions. The most commonly used implants are normally made from titanium, a biocompatible material that has good mechanical properties. The geometries of inter-vertebral implants also vary, from circular threaded implants (placed with the axis perpendicular to the axis of the spine), to mesh implants (placed with the axis parallel to the axis of the spine), and to implants that are rectangular or "dog boned" in shape. Biomechanical studies have demonstrated that rectangular inter-vertebral implants offer increased stiffness in compression as compared to cylindrical ones [4]. Some surgeons believe that the increased contact area offered by a rectangular inter-vertebral implant may also increase the likelihood of fusion.

From a mechanical point of view, any implant for spinal fusion must provide immediate stability under compression. The implant must remain motionless while transmitting

(1) Corresponding author

compressive forces in order for bone healing to occur. Bone will not grow where there are tensional or bending motions, nor will it grow in the absence of stress. Mechanical stability, however, is not the only factor, certain biological factors must also be present. These factors include the osteogenic cells (that remodel bone), osteoinducive factors (that encourage bone growth), and osteoinductive factors (that provide a frame or scaffold for bone growth). Unfortunately, pure titanium made inter-vertebral implants fail to provide any of these biological factors. On the other hand, although hydroxyapatite has been widely used for coating many orthopedic implants due to its osteoinductive behavior [5-7], it is brittle and fractures easily over time, and therefore, hydroxyapatite is difficult to use alone as an ideal implant material. Furthermore, plasma sprayed hydroxyapatite on the surface of metallic implants may change its compositional properties; the coated hydroxyapatite also produces a modulus mismatch, and frequently the hydroxyapatite coating on the newly formed bone will peel off from the metallic implants and the uniformity of the physical and chemical properties as well as the bioactivity could eventually be lost [8-12].

Recently, a Titanium-Hydroxyapatite (TiHA) composite has been considered as a potential biomaterial that can offers a blended biocompatibility, osteoinductive properties, and mechanical properties for implant application. This paper will report a case study of using rapid prototyping technology, along with enabling computer-aided design and computer-aided engineering (CAD/CAE), medical imaging processing and 3D reconstruction to assist in the design and development of TiHA inter-vertebral implants. The presentation of the paper is organized as follows. Section 2 describes the process of the 3D reconstruction in building vertebral anatomy from computed topography images. The CAD modeling and integrated CAD and CAE simulation in the design development and in the structural analysis of the inter-vertebral implant is presented in Section 3, including the studies on the anatomic fitting of the models and the implant's structural stability in spinal fusions. The major procedures of the 3D Printing and post sintering process for prototyping the vertebral physical model and the implant are described in Section 4. A summary and conclusion are given in Section 5.

2. Three-Dimensional Reconstruction

When considering a reconstructive surgery or implantation, it is often difficult to ascertain the exact nature of the affected internal anatomy. Advances in Computed Tomography (CT) and Magnetic Resonance Imaging (MRI) have led to the generation of 3-Dimensional (3D) representations, or views, for internal anatomies through 3D reconstructive techniques. A general process for 3D reconstruction of an anatomic model from CT or MRI data is described in Figure 1. As shown in the process, the CT or MRI data are extracted through 2D segmentation and 3D region growth to form volumetric image which provides more meaningful and derivative 3D anatomic representation. A 3D anatomic representation produces novel views of patient anatomy while retaining the image voxel intensities that can be used for volume rendering and volumetric representation of 3D anatomic structure. The 3D volumetric representation of anatomic structures can be used to generate a contour based, surface based, or volume based computer modeling through CAD techniques, or to be used to directly produce physical prototype. These CAD and prototyping modeling are very helpful when applied to assist in surgical planning, practice, and education [13].

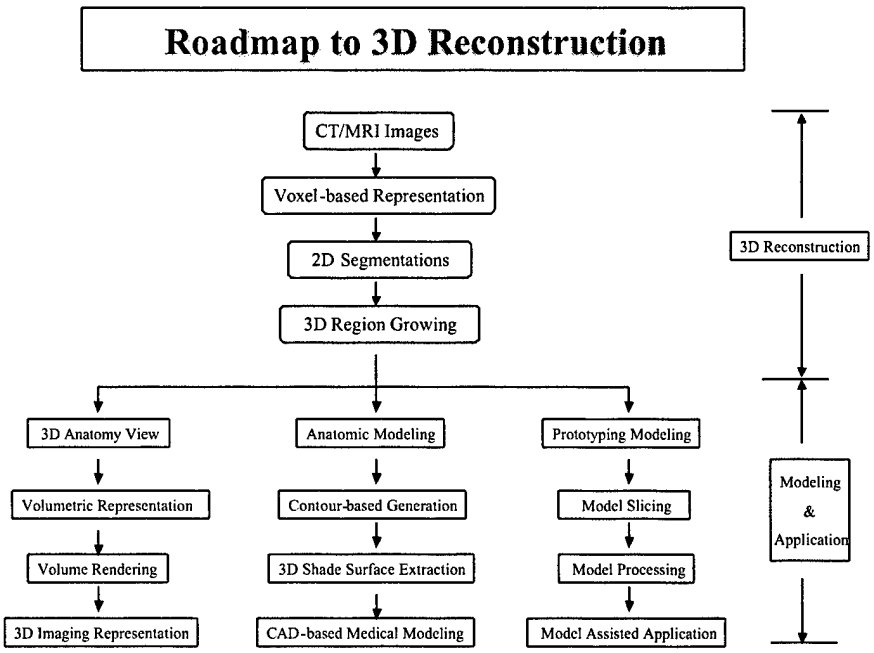


Figure 1: From CT/MRI to 3D reconstruction [13]

In this case study, a CT scan of the spine of an adult human cadaver was used. CT gives excellent resolution of the vertebral bony structures with which the accurate 3D vertebral models can be developed. The geometric and positional accuracy of the vertebral bony structures is critical since the implant will rest between two successive vertebrae and act as an extension of the vertebral bodies. CT data was input into MIMICS, a software package (Materialise Corp., Belgium) used to interface the scanned images and the 3D reconstructive model for vertebral anatomy. MIMICS allows users not only to visualize CT segments but also to edit them as needed, in our case, to create a needed cavity by removing the inter-vertebral disc and to simulate the insertion and placement a suitable implant.

The patient's CT images were imported into *MIMICS*. Factors such as image size, slice thickness, pixel size, and number of images per file were properly defined and the images were organized in order to select the region of interest: two adjacent vertebrae. Directions (anterior, posterior, top, bottom, left, right) were set according to the anatomy. A profile line was drawn transversely across the vertebral body. Based on this profile, a lower threshold value between the value of the cortical wall of the vertebrae and the inside of the vertebral body was set. After setting the threshold, region growing was used to define a yellow mask including the cortical bone regions. A 3D reconstruction of this mask was generated and is shown in Figure 2. Poly-lines were then created and the image was cleaned up to more accurately represent the region of interest. The tubular structure anterior to the vertebral bodies was removed. This structure was probably the aorta or vena cava based on its location. The "filaments" between the vertebral bodies were also removed as these were probably representative osteophytes or the degenerated disc, and in any case, this area would be removed during the surgical procedure. Finally, a clean 3D reconstructive vertebrae representation after removing the soft tissue and the inter-vertebral disc was created as shown in Figure 3. The 3D reconstructive model is further translated into an

stl format to produce rapid prototyping modeling, which will be used to guide the spinal inter-vertebral implant design.

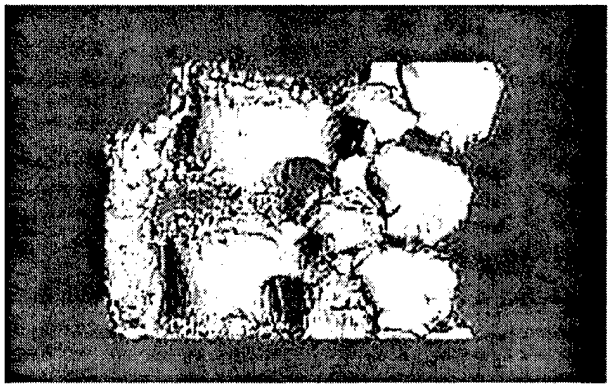


Figure 2: 3D reconstructive vertebrae with soft tissue and inter-vertebrae disc

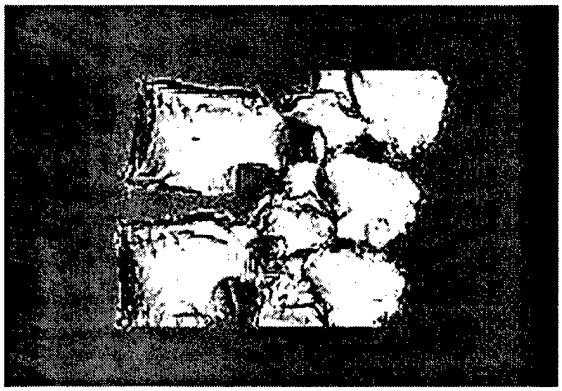


Figure 3: Edited 3D reconstructive vertebrae After removing soft tissue and inter-vertebrae disc

3. Inter-Vertebral Implant Design Modeling and Structural Simulation

The following design considerations were applied in the design and development of the spinal inter-vertebral implant:

1. The inter-vertebral implant must be implantable by using the existing instruments;
2. The size of the implant must anatomically fit within the patient's vertebrae;
3. The implant must be able to withstand the pressures exerted on it by the spine;
4. If needed, allograft or autograft material may be placed inside the implant.

The anatomic compatibility, or the anatomic fit, of the spinal inter-vertebral implant was accomplished by designing the geometry and size of the implant to fit the interior cavity of the vertebrae. The determination of the interior cavity of the vertebrae was achieved by using the 3D reconstructive model developed from the patient's CT imaging. According to the anatomic dimensions, the spinal inter-vertebral implant was designed and the CAD model was generated through Pro/Engineer (Pro/E) 2000i software [Parametric Technology Corporation, Waltham, Massachusetts, 2001]. Using the Pro/E feature and parameteric–based design capability, we defined the implant critical dimensions, such as the height and the contour size of the surfaces, as the parameters which are determined from the patient 3D reconstructive model generated from the CT image, and also on purposely designed the top and bottom surfaces of the inter-vertebral implant with an inclined angle in order to best fit the interior cavity of the customized vertebrae. Representations of the designed implant CAD model and its anatomic fitting are presented in Figure 4 and Figure 5, respectively.

As discussed earlier, titanium is a well-known biomaterial with good mechanical properties, but it is not bioactive, whereas hydroxyapatite is bioactive (osteoconductive), but it is brittle. The combination of hydroxyapatite and titanium, TiHA, may lead to a composite material with desirable biological and mechanical properties. As in any composite material, the properties of TiHA depend on the composition of the constituents. When TiHA is used to make the spinal

inter-vertebral implant, it is important to know its strength and stiffness associated with the given compositions in order to determine whether the designed implant can undertake the applied load after being placed. The analyses to determine the mechanical behavior of the inter-vertebral implant were conducted by using Pro/MECHANICA (Pro/M) [Parametric Technology Corporation, Waltham, Massachusetts, 2001], a finite element analysis software.

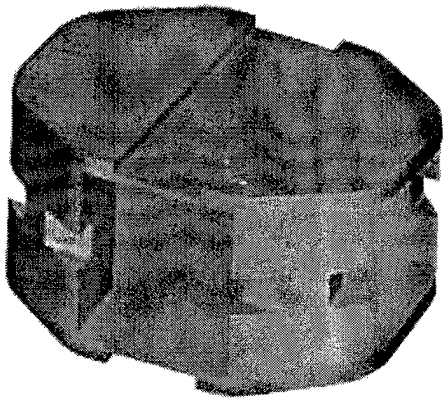


Figure 4: CAD model of the designed inter-vertebral implant

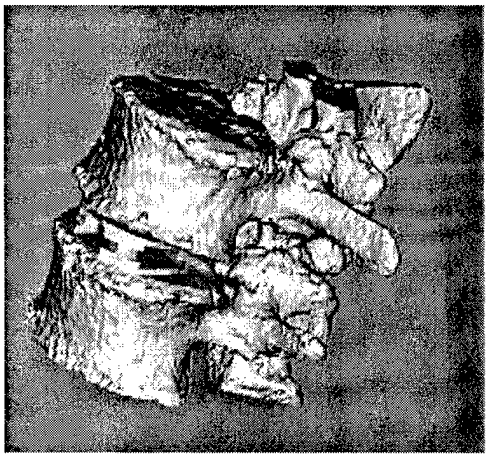


Figure 5: Anatomic fitting of the inter-vertebral implant

The effective Young's module (E_{TiHA}), the Poisson ratio (υ_{TiHA}), and the strength (σ_{TiHA}) of TiHA composite were derived from the composite micro-mechanical model [15], and expressed in Equation (1) to Equation (3), respectively. In which, Equation (1) represents the formula of effective Young's module of composite consisting of titanium particle embedded in the hydroxyapatite matrix. Equation (2) and Equation (3) represent the mathematical formulation of Poisson ratio and strength derived based on the composite's Rule of Mixture.

$$E_{TiHA} = E_{HA}\{\frac{E_{HA} + (E_{Ti} - E_{HA})V_{Ti}^{2/3}}{E_{HA} + (E_{Ti} - E_{HA})V_{Ti}^{2/3}(1 - V_{Ti}^{1/3})}\} \quad (1)$$

$$\upsilon_{TiHA} = \upsilon_{Ti}V_{Ti} + \upsilon_{HA}V_{HA} \quad (2)$$

$$\sigma_{TiHA} = \sigma_{Ti}V_{Ti} + \sigma_{HA}V_{HA} \quad (3)$$

in which, E_{Ti} and E_{HA} denote the Young's modules, υ_{Ti} and υ_{HA} denote the Poisson rations, and V_{Ti} and V_{HA} denote the volume fractions of TiHA composite for titanium and hydroxyapatite, respectively. The material properties of hydroxyapatite and titanium and the results of the calculation are listed in Table 1. The volume factions of both constituents V_{Ti} and V_{HA} in TiHA were all assumed to be 0.5 in the calculation.

It should be pointed out that the model predicted data can only be served as reference data since the actual properties of the TiHA composite are process-dependent and related to the process parameters such as the synthesized temperature, pressure, and the micro-structure of the constituents (shape and size). The realistic TiHA properties should be obtained through experimental tests.

Table 1 - The elastic properties of TiHA composite

Material	E in GPa (Msi)	Poisson ration υ	Strength in compression (MPa)
Hydroxyapatite [14]	34.0 (5.0)	0.28	75
Titanium [12]	117.0 (17.0)	0.33	600
TiHA	65.5 (9.6)	0.305	337.5

In the finite element analysis, Pro/M software first converted the Pro/E implant CAD model into a FEA model. The AUTOMECH module in Pro/M was used to automatically generate a total of 728 tetrahedral elements. The meshing and the elements are shown in Figure 6. The boundary conditions, constraints, and loading were then applied to the FEA model. To simulate the deformation of the implant within the vertebrae, we allowed the top and bottom surfaces of the implant to be free to deform and only completely constrained three individual nodes at the bottom surface to ensure the model stability in the finite element analyses. The pressure loading were applied on the top and bottom surfaces to mimic the pressure imposed by the vertebrae. The constraints and loading conditions for the analysis are schematically shown in Figure 7.

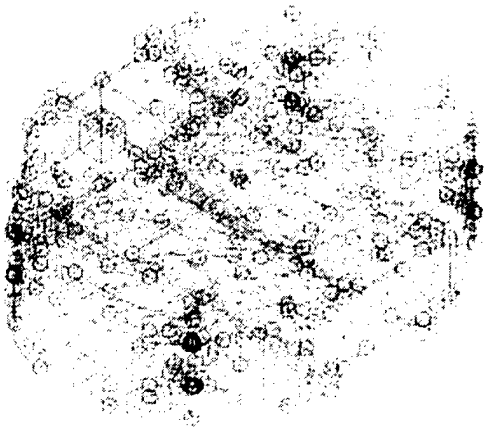


Figure 6: FEA mesh of the implant

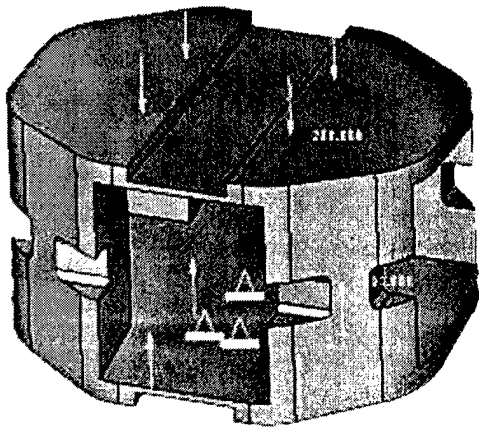
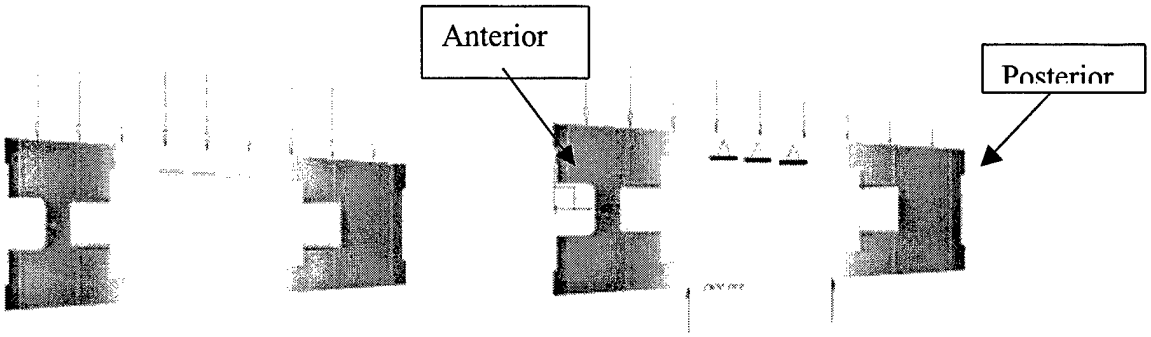


Figure 7: Constraints and loading

Extra care must be exercised in determining the loading imposed on the implant. Anatomically, the vertebrae consist of a thin shell of hard cortical bone surrounding a network of softer trabecular bone. Under normal physiological conditions, most of the load on the vertebral body is slightly anterior to its midpoint. Thus, the cortical bone in this area tends to be denser and stronger [16]. Physiological loads on lumbar vertebrae are difficult to measure. From a design point of view, this does not provide sufficient information to determine the loading applied to the implant from the weight of the body or from a weight that is lifted. The center of gravity in the human body is anterior to the spine, so the resultant moments must be balanced out by muscles such as the spinal erectors. This may result in a higher load exerted on the spine. In a recent landmark experiment, load cells were implanted into the lumbar spine of baboons. In some cases, loads were so high that they were beyond the measuring capacity of the load sensor. For example, standing upright resulted in a load of 690 N for an animal weighing 390 N [17].

In our analysis, we assume that the total pressure load passing through the lumbar vertebrae is applied on both top and bottom surfaces of the implant model as shown in Figure 8. Since we do not know exactly how the pressure is distributed on the surfaces, we studied two possible pressure patterns, as shown in Figure 8. One pattern assumes that the pressure is uniformly distributed on the surfaces. As shown in Figure 8a, $p_{uniform}$ = 4.33 MPa, which is equivalent to 2000 N total pressure load The other assumes that the magnitude of the applied pressure varies linearly with the inclined angle of the surfaces, for example, p_{max} = 7.447 MPa, and p_{min} = 1.242 MPa, which is also equivalent to 2000 N total pressure load, as shown in Figure 8b. The mechanical properties of in vivo vertebrae may vary due to the bone mineral density and the variations in morphology. The maximum pressure applied on the surface, p_{max} = 7.447 MPa, is between the strength of cortical bone (compression strength = 195 MPa) and the strength of cancellous bone (compression strength = 2.8 MPa). Therefore, if the cortical bone is in good condition, we expect it will be able to withstand the applied pressure, i.e., to support the inter-vertebral implant without collapsing the bone.



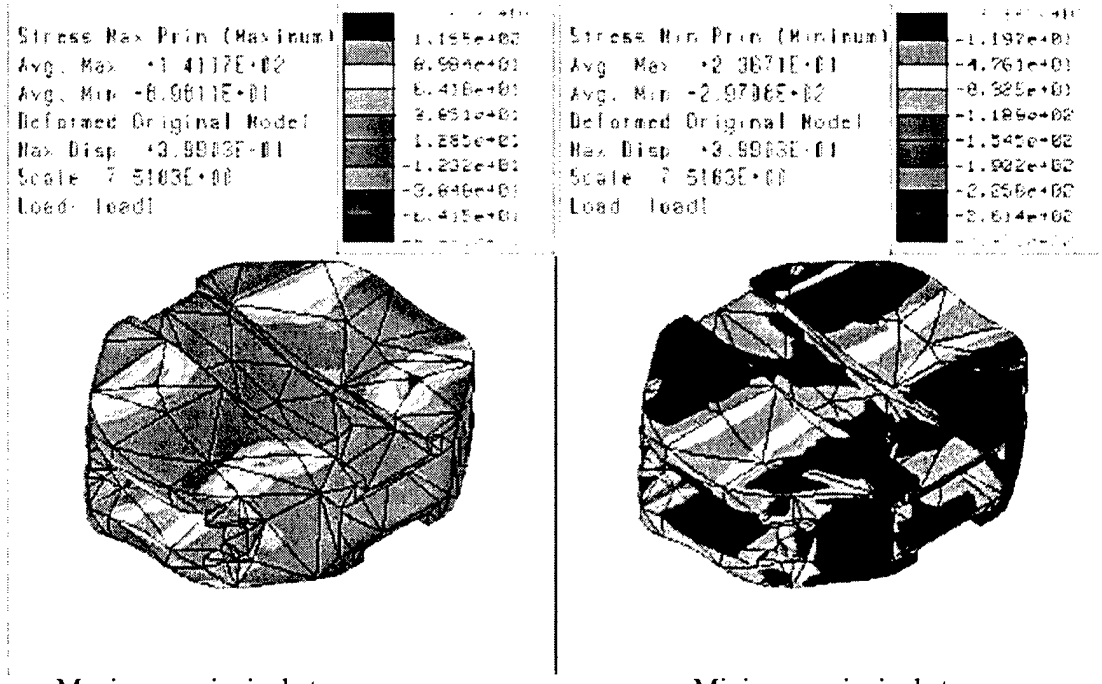
8a): Uniformly distributed pressure pattern 8b): Linearly distributed pressure pattern

Figure 8: - Pressure patterns

In the finite element analyses presented in this study, we assume the mechanical properties of the TiHA to be linearly elastic with the properties listed in Table 1. Using Pro/M, the P-version high order interpolating polynomials was adopted for the solution convergence. In our case studies, 6 p-loop passes were performed before all elements satisfied the convergence condition. The results of the finite element analysis are represented in Figure 9 and Figure 10, respectively. Figure 9 displays a contour representation of the maximum principal stress and minimum principal stress distributed in the inter-vertebral implant subject to a uniformly distributed pressure loading. Figure 10 shows the similar contour representation, but for a linearly distributed pressure-loading condition.

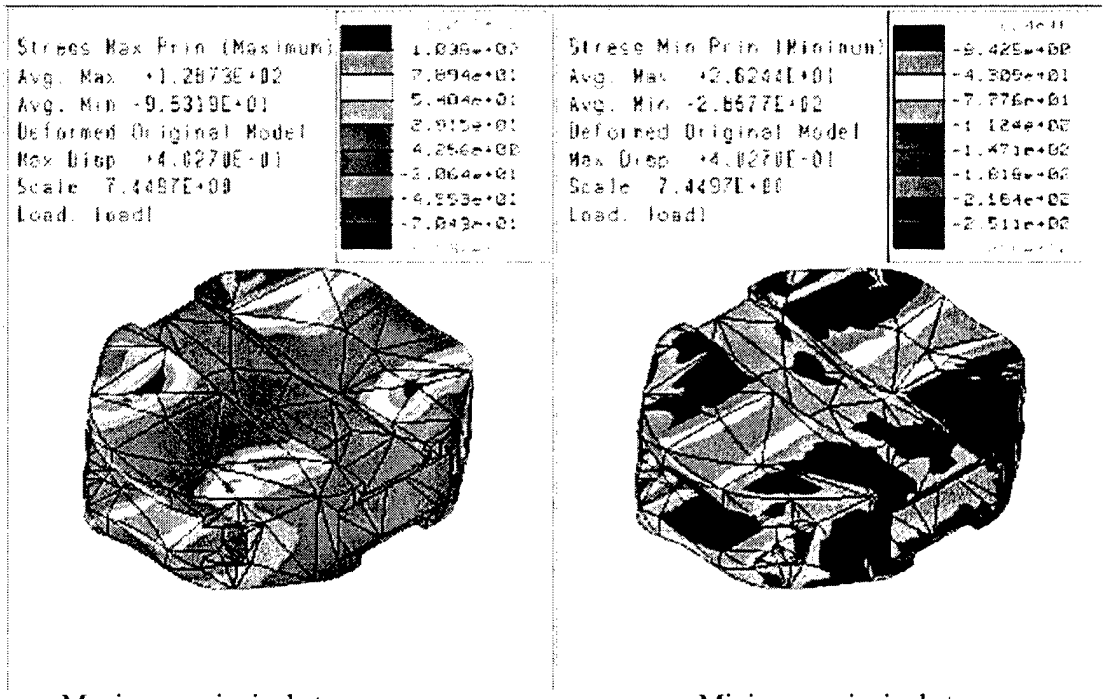
A summary of the maximum and minimum principal stresses calculated from the finite element analyses for the inter-vertebral implant are listed in Table 2. These values are used to verify if the implant satisfies the strength requirement. It can be shown that all calculated maximum stresses in the implant are below the strength of the TiHA composite, for example, σ_{max} (minimum principal) = 297.1 MPa < 337.5 MPa (TiHA strength). With this, we assume that the designed inter-vertebral implant with the TiHA composite at a 50/50 composition will probably be structurally strong enough to withstand the specified loading. However, as discussed

before, the property of the implant is influenced by many processing factors and the important property data should be examined through appropriate experimental testing.



Maximum principal stress Minimum principal stress

Figure 9: Contour representation of the maximum and minimum principal stresses under uniformly distributed pressure loading



Maximum principal stress Minimum principal stress

Figure 10: Contour representation of the maximum and minimum principal stresses under linearly distributed pressure loading

Table 2 – Finite element results in the implant

Load pattern	Total load	σ_{max} (Max. principal)	σ_{max} (Min. principal)
Uniform pressure	2000 N	141.2 MPa	-297.1 MPa
Linear pressure	2000 N	128.7 MPa	-285.8 MPa

4. 3D Printing of Vertebrae and Inter-Vertebral Implants

Titanium and hydroxyapatite can be made into a composite by the powder consolidation method. A volume fraction of 50/50 (titanium and hydroxyapatite powders) is mixed using a ball milling operation. After undergoing an appropriate thermal treatment, the synthesized TiHA composite will provide the hydroxyapatite with more ductility while still providing the osteo-conductive feature of pure hydroxyapatite. In addition to its biological effects, the TiHA composite material will have a higher toughness (less brittle) than pure hydroxyapatite as well as a good fatigue property. This is particularly beneficial for spinal fusion since most spinal implants are damaged due to the fatigue failure.

The rapid prototyping of TiHA implants involves primarily two major processes: 1) 3D Printing of the green part; and 2) Hot Iso-static Pressing (HIP) of the TiHA component. The flow chart of the processes is schematically presented in Figure 11. The work completed in the first process, i.e., 3D printing of vertebrae and inter-vertebral implants, is reported in this study. A general sintering procedure of the HIP post-process will be briefly described. However, research work in the second process, particularly on the binding mechanism of the TiHA particles and the effect of the post-HIP process on the biological and mechanical behavior of the TiHA component are still under investigation and the results will be reported in the future.

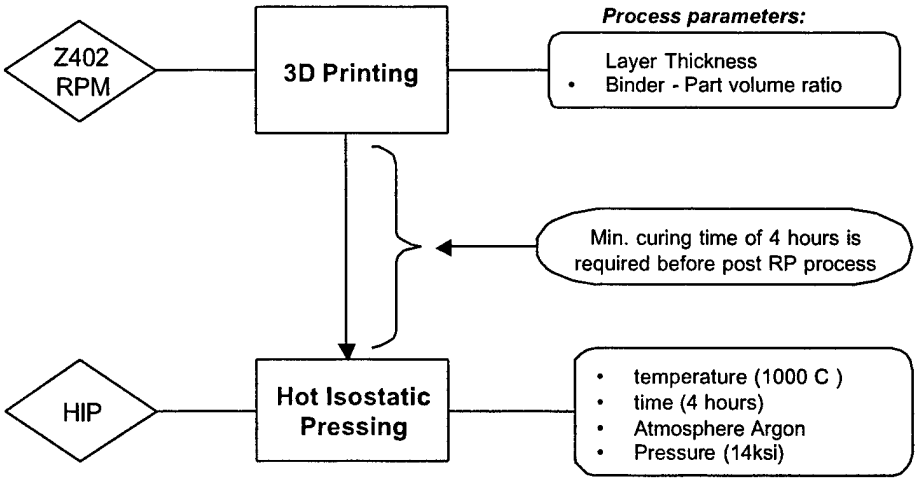


Figure 11: Flow chart of rapid prototyping of TiHA implant

In the beginning of the 3DP process, the *stl* files generated from MIMICS for vertebrae anatomy and from Pro/E for the inter-vertebral implant were converted into a Z402 system Build File (*.bld) and the data was temporarily stored in the form of slices. The slice data were

interpreted and put together by a 3D printing system to produce the prototypes. The Z402 system consists of 2 powder bays, a feed bay, a build bay, and a binder spray head with a cartridge. The slice data, obtained from the Build File, are input into the machine. The binder spray head initially sprays the binder on to the first powder layer (depending on the cross-section of the part at that particular section). As the binder head moves across the 2 bays, it rolls a layer of powder (depending on the specified layer thickness) from the feed bay to the build bay. This process continues, layer by layer, until the entire prototype is built. The printed prototype, or green part, is then removed from the build bay and cleaned using compressed air to remove the excess powder. Furthermore, the green part is subjected to a post-process by infiltrating wax or polymer resin to give additional strength before sending to HIP process to sinter final TiHA component.

The vertebrae were prototyped using zp-11 powder as the build material and zp-07 as the binder. The inter-vertebral implant was prototyped using hydroxyapatite powder as the build material. Both the vertebrae and the implant prototypes were post-processed by infiltrating the model with molten wax and polymer resin to provide additional strength after the printing. The specifications and the process parameters of the 3D Printing are listed in Table 3.

Table 3 - 3D Printing specifications and process parameters

Base material (powder)	Hydroxyapatite / zp-11
Binder	zb-07
Layer thickness (range)	0.01" to 0.0035"
Binder volume (percentage of total volume)	Shell / Core Vertebrae: 14% / 7% Implant: 14% / 14%
Build Speed	1" / hour along z-axis
Accuracy	0.5% along X-Y axes, 1% along Z-axis

The compacted green part is further subjected to sintering by HIP process. The HIP process applies heat and pressure within an enclosed vessel to consolidate or condense materials such as castings. Heat is introduced via molybdenum resistance elements and pressure is supplied by high pressure pumps forcing argon, an inert gas, into the vessel. As the heat softens the castings, the gas pressure exerts a force equally on all surfaces, causing the porous casting to compress to full density. Crucibles HIP vessel and Molybdenum resistance furnaces are used to provide HIP temperatures ranging from 900°F to 2250°F (1230°C) for different metallic alloys, at a gas pressure up to 15,000 psi (103 MPa). In the attempt to sinter TiHA component, the vacuum glass tubes are heated to a temperature of 1000 °C with a pressure of 14ksi for a period of 4 hours in an argon atmosphere. The applied temperature profile of the HIP process is shown in Figure 12.

5. Summary and Conclusion

A case study using the rapid prototyping technology to assist in the design and development of inter-vertebral implants for spine fusion procedures was demonstrated. The process of the design and the implant development, the biological and mechanical constraints, the development of the 3D reconstructive anatomy model and the inter-vertebral implant CAD model, and the application of the models with integrated finite element analysis for implant structural analysis were presented. 3D Printing of the anatomy model and the implant model,

along with the prototyping and post sintering process were described. The application of the prototyping model in assisting in the inter-vertebral anatomic fitting, in guiding the implant's geometric design, and in helping with the virtual surgical planning was demonstrated. Based on the designed implant and anatomic models, finite element analyses were conducted to understand the implant's mechanical properties and structural stability, and the results were also presented.

We were able to generate vertebral anatomy from CT scanned images of a human spine through MIMICS. MIMICS was also used to edit the 3D images and to measure the anatomic geometry of the vertebrae in order to determine the key dimensional parameters for implant design. An *stl* file was created from the edited image to make a prototype of the spine segment. Surface details of the lumbar vertebrae were accurately modeled, but it was not possible to model any of the interior details (such as the trabecular bone) due to the inherent precision of the CT scanner.

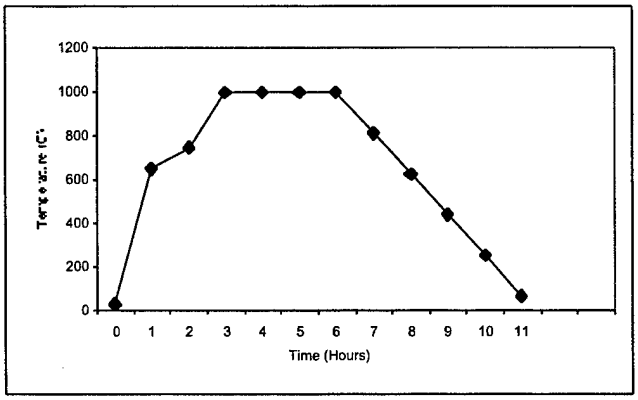


Figure 12: Temperature profile in HIP process

In order to verify the anatomic fitting of the designed inter-vertebral implant, we converted the Pro/E implant model into an *stl* format and input it into MIMICS, as shown in the 3D rendered image in Figure 5. The computer simulation of the positioning and the placement of the designed implant with the patient's vertebrae can be used as an effective tool to help surgeons to make the pre-operative plan and to practice the implantation.

The structural analyses were performed to the TiHA implant structure by using Pro/M software. It was found that the maximum stress (297 MPa) occurred within the implant under the applied loading (2000 N), This value was below the strength (375 MPa) of the TiHA implant. We need to pointed out that for results presented in the analysis and comparison, we used the mechanical properties of the composite obtained from the model prediction, not from the experimental testing. In addition, we were not able to analyze the vertebral anatomy because the CT scanned images were not be able to provide the interior detail of the trabecular structure inside the vertebral body. Without these detail, we can not generate the needed CAD and FEA models.

6. Acknowledgement

We gratefully acknowledge the support from NSF 9980298 project during the course of this study.

References

1. Langer, R. and Vacanti, J. Tissue Engineering. *Science* 260: (1993) 920-925
2. Boden, S.D. Biology of Lumbar Spine Fusion and Use of Bone Graft Substitutes: Present, Future, and Next Generation. *Tissue Engineering* 6(4): (2000) 383-399.
3. Haher, T.R. et al. An *In Vitro* Biomechanical Investigation of Spinal Interbody Fusion Devices. Proceedings of the 14th Annual Meeting of NASS. Chicago: (1999) p. 70-72.
4. Alexander, H. et. al. Classes of Materials used in Medicine. Biomaterials Science. Ed. Ratner et. al. Academic Press; San Diego (1996) P. 74.
5. Bauer, T.W., Geesink, R.C., Zimmerman, R. and McMahon, J.T., "Hydroxyapatite-coated femoral stems, Histological analysis of components retrieved at autopsy," J. Bone Joint Surg., 73: (1991) 1439-52.
6. Cook, S.D., Thomas, K.A., Kay, J.F. and Jarcho, M., "Hydroxyapatite-coated titanium for orthopedic implant applications," Clin Orthop, (1988) 232, 225-43.
7. Klein, C.P.A.T., Patka, P., Wolke, J.G.C., de Blieck-Hogervorst J.M.A., and de Groot K., "Long-term in vivo study of plasma-spray coatings on titanium alloys of tetracalcium phosphate, hydroxyapatite and alpha-tricalcium phosphate," Biomaterials, (1994) 15, 146-50.
8. Yamada, K., Imamura K., Itoh, H., Iwata, H., and Maruno, S., "Bone bonding behavior of the hydroxyapatite containing glass-titanium composite prepared by Cullet method," Biomaterials, 22, (2001) 2207-2214.
9. Bloebaum, R.D. and Dupont, J.A., "Osteolysis from a press-fit hydroxyapatite-coated implant: a case study," J. Arthroplasty, 8, (1993) 195-202.
10. Paschalis, E.P., Zhao, Q., Tucker, B.E., Mukhopadhayay, S., Bearcroft, J.A., Beals, N.B. et al., "Degradation potential of plasma-sprayed hydroxyapatite-coated titanium implants, "J. Biomed Mater Res, 29, (1995) 1499-505.
11. Shen, W.J., Chung, K.C., Wang, G.J., and Mclaughlin, R.E., "Mechanical failure of hydroxyapatite-and polysulfone-coated titanium rods in a weight-bearing canine model," J. Arthroplasty, 7, (1992) 43-49.
12. Moroi, H.H., Okimoto, K., Moroi, R., and Terada, Y., "Numeric approach to the biomechanical analysis of thermal effects in coated implants," Int. J. Prosthodont. 6: (1993) 564-572.
13. Sun, W., Lal, P., "Recent Development on Computer-Aide Tissue Engineering," J. of Computer Methods and Programs in Biomedicine, *in press*.
14. Grenoble, D.E., Katz, J.L., Dunn, K.L., Gilmore, R.S., and Murty, K.L., "The elastic properties of hard tissues and apatites," J. Biomed. Mater., Res., 6(3): (1972) 221-223.
15. Jones, R., "Mechanics of Composite Materials," Taylor & Francis, Philadelphia, PA, 1999
16. White, A., and Panjabi, M. Clinical Biomechanics of the Spine. Lippincott Williams & Wilkins. Philadelphia (1990) P. 43.
17. Ledet, E. et al. Real-Time *In Vivo* Loading in the Baboon Lumbar Spine Using an Interbody Implant Load Cell. Proceedings of the 14th Annual Meeting of NASS. Chicago: (1999) 202-204.

CUSTOM FABRICATION OF HARD TISSUE RECONSTRUCTIVE FRAMEWORKS

R. V. Nambiar, R. E. Jones and J. R. Gomez

The University of Texas-Pan American, Edinburg TX 78539

Abstract

The feasibility of fabricating custom frameworks for tissue regeneration utilizing three-dimensional inkjet printing technology followed by slip casting was investigated. A CAD solid model of mold was created with structures within the mold cavity to provide variable, customized porosity in the cast framework. The polymer mold was printed using a 3D ink-jet printer. The mold was then infiltrated by an aqueous suspension of hydroxyapatite to produce porous frameworks that were tested for mechanical properties.

Introduction

Porous materials have been used as non-resorbable intermediate structures for bone repair and when pore size is properly controlled such repairs can integrate into new bone, even permitting the development of vascularity [1]. A promising approach for hard tissue reconstruction is the integration of a custom mechanical framework with biological agents to promote development of the desired tissue [2]. Such a structure must have three characteristics. It must fit the patient, thus requiring a unique structure for every repair. It must have specified mechanical properties to permit proper function during regeneration. Finally, it must be able to carry the required precursor cells and/or growth factors and direct their development. Thus it will require a controlled internal structure that will probably not be uniform if it is to guide development of all of the subcomponents

of functioning bone or cartilage. These requirements make solid free form fabrication the best hope for cost effective fabrication of the required structures.

Research to date on rapid fabrication of tissue frameworks has utilized either selective laser sintering [3], laminated object manufacturing [4] or fused deposition modeling [5]. In each case, the part must be sintered after the polymer binders are burned out. The ink-jet based rapid prototyping technology proposed for this study is well suited to the fabrication of precision frameworks for reconstruction. The system prints a layer of build material using an ink-jet head and maintains accuracy in the z-direction by milling the layer to a precise height before the next layer is deposited. The result is one of the most accurate and affordable commercially available solid free-form fabrication system. Models with pore feature size of 0.5 mm repeatability accurate to 0.05 mm have been produced. This process is not suitable for very large parts that may be required in orthopedic reconstruction, but it is capable of producing many of the common components needed for maxillofacial work.

In this work, a CAD solid model of a mold is built with the innersurface created using imported surface data from a CT scan. Structures are created within the mold cavity to provide variable, customized porosity in the cast framework. The polymer mold is printed using a 3D ink-jet printer. The mold is then infiltrated by an aqueous suspension of hydroxyapatite mixed with binder. The part is dried then processed in an oven to burn out the polymer binder and then sintered to produce porous framework.

The ability of tissue growth into the framework is requires a well connected network of macropores. A number of different designs for the internal geometry were considered. A repeated hexagonal pattern of axial cylinders interconnected like a honeycomb was found to give the most uniform

mesh as shown in Figure 1. The pattern is repeated at uniform axial increments throughout the structure. Cross section sizes ranging from 0.25 mm^2 to 0.7 mm^2 were used, the smaller sections showing a higher rate of damage in processing. These structures in the wax mold will provide predictable sized pores in the cast structure.

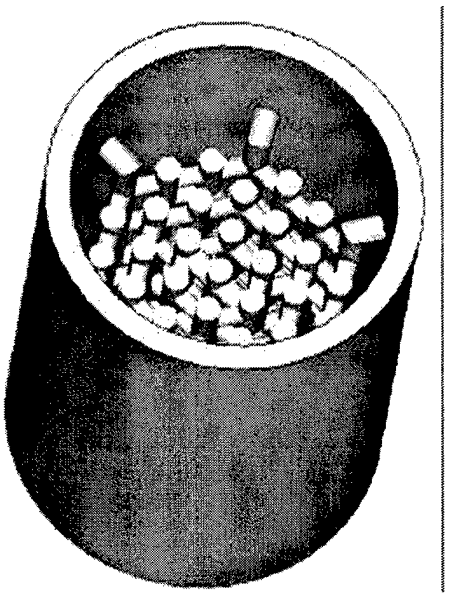


Figure 1. CAD model of mold with internal structure

Processing

Hydroxyapatite powder (Aldrich) was mixed with water and compressed to form coupons. Samples of the coupons were analyzed in a differential thermal analyzer (DTA).

The graph in Figure 2 shows the decrease in weight of the sample as the temperature increases. The initial downward slope is attributed to the loss of water from the specimen up to 600C.

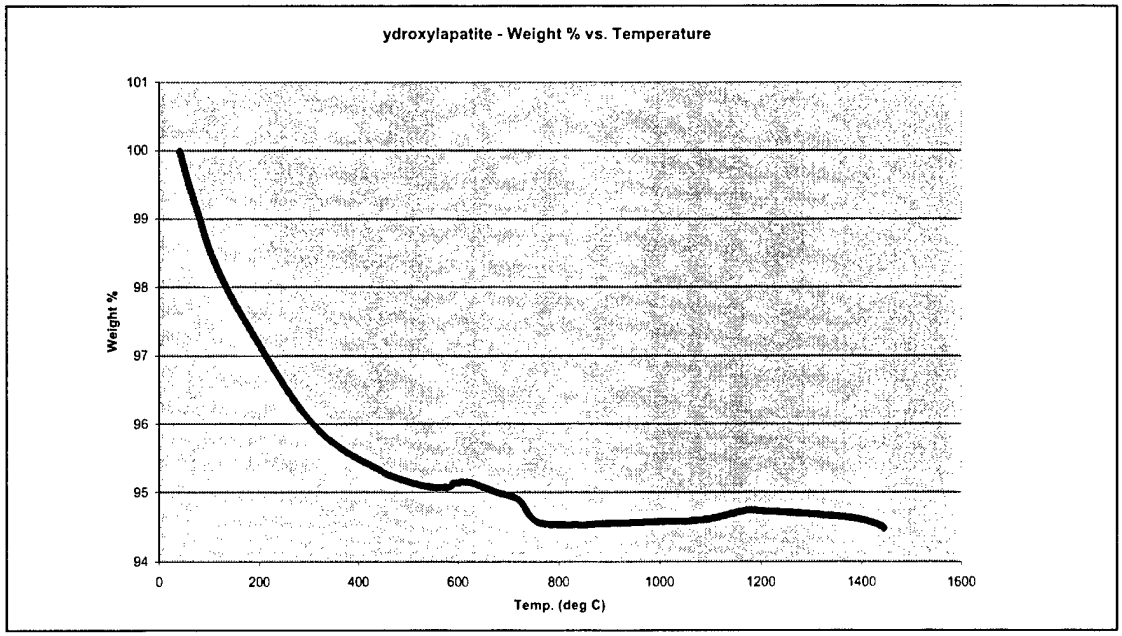


Figure 2. DTA weight loss analysis of HA

The graph in Figure 3 shows the temperature difference of the sample from the control pan in the chamber due to exothermic or endothermic processes. This shows that the loss of the water can be completed at below 600C, but that the sintering temperature can be set below 1200C.

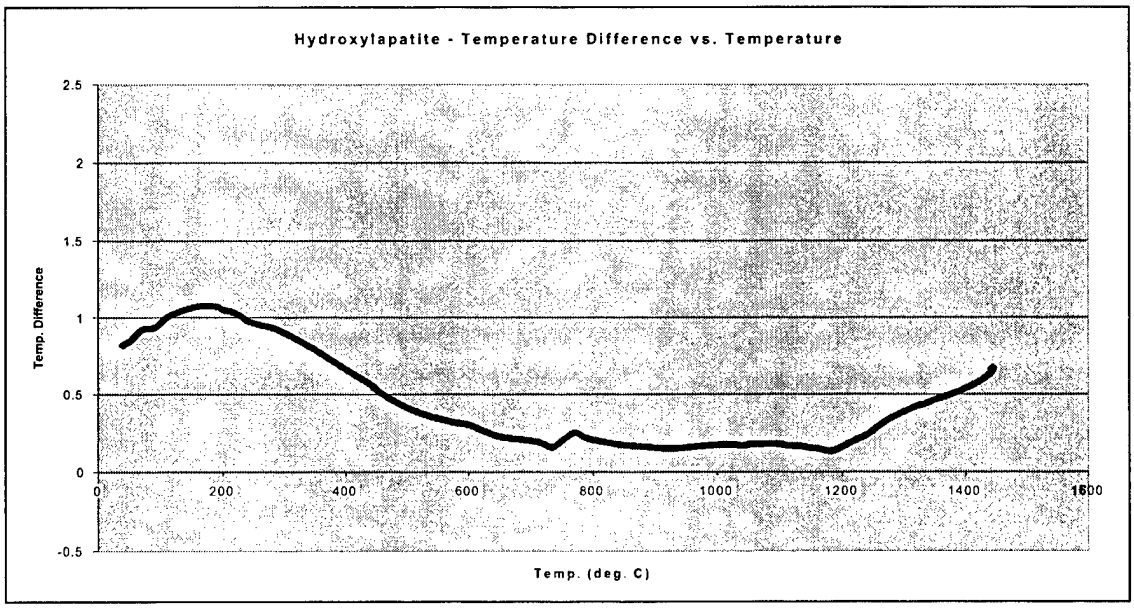


Figure 3. DTA temperature analysis of HA

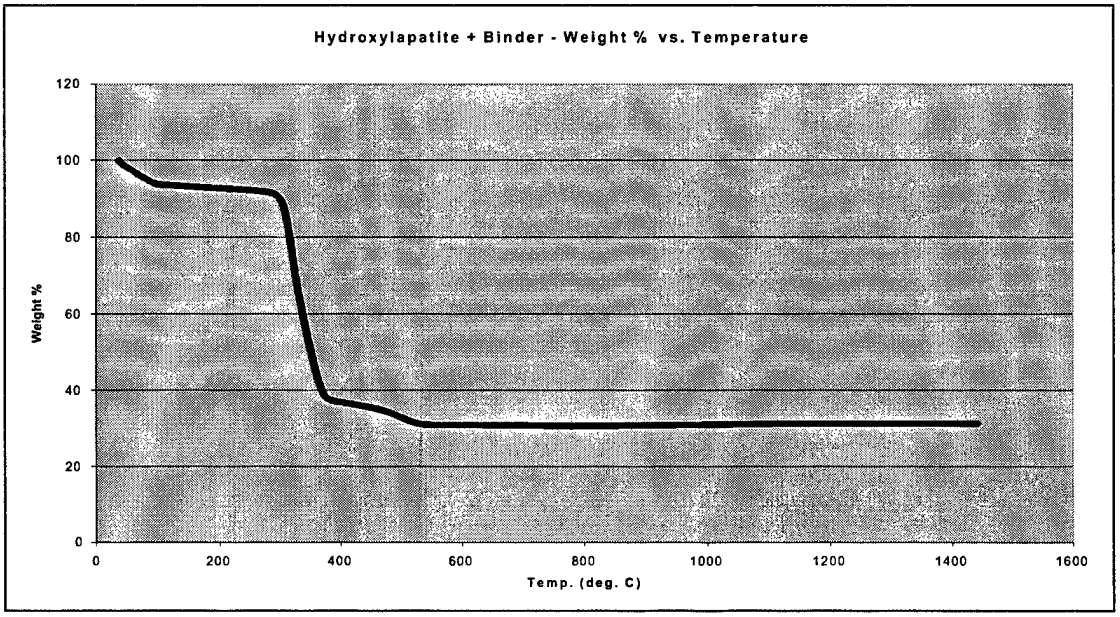


Figure 4. DTA weight loss analysis of HA with binder

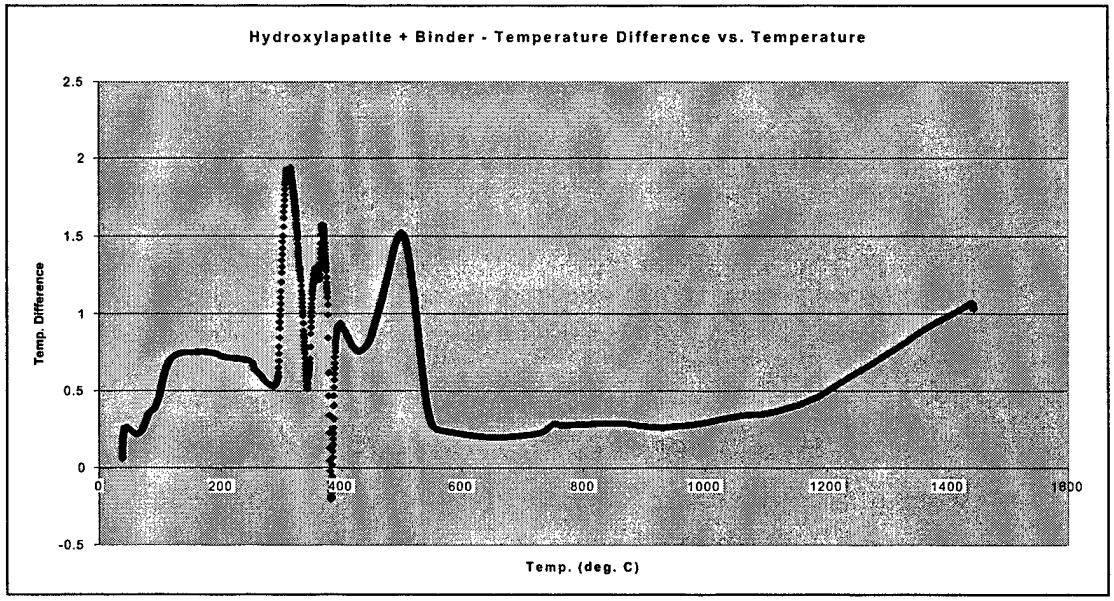


Figure 5. DTA temperature analysis of HA with binder

Figures 4 and 5 show the corresponding graphs for hydroxyapatite mixed withDuramax B-1020 binder. Figure 4 shows the loss of water from the specimen at 500C. The graph in

Figure 5 shows binder is burnt off at 700C. This establishes the burn off temperature at 600C followed by sintering at 1100C, thus the temperatures for processing the specimens have been identified.

Molds with the outer body of the mold and the internal structures for the pores all in one piece were built using the Sanders ink-jet printing machine. Hydroxylapatite powder was combined with Duramax B-1020 organic binder and water to make a slurry. The slurry was poured into the mold and the water allowed to seep out of the base to form solid ceramic specimens.

The specimens fabricated above were all found to have cracks and internal cavities. These make compression strength tests unreliable. The cause of these defects appears to be uneven drying. Experimentation to eliminate these defects by modifying the binder content and controlling the humidity is continuing.

SEM scans of the surface reveal as shown in Figure 6.that the sintering process leads to relatively smooth surfaces. This may indicate that the surface needs to be etched to create micropores to enhance osteoinductivity.

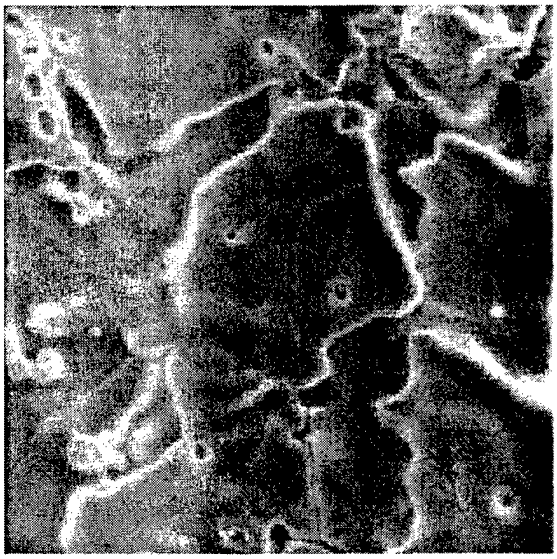


Figure 6. SEM picture of part surface 4000X magnification

Conclusion

The results of the studies conducted this year suggest that we can design molds for frameworks with specified pore size and distribution in a CAD system. These molds can be fabricated using ink-jet printing rapid prototyping technology. The materials to be used for casting of the frameworks in these molds have been selected and analyzed to identify the processing temperatures.

Bibliography

1. C.J. Damien, J.R. Parsons, "Bone graft and bone graft substitutes: a review of current technology and applications," J. Appl. Biomaterials, (1991) 2(3) p187.
2. D.L. Cochran, J.M. Wozney, "Biological mediators for periodontal regeneration," Periodontal 2000 (1999) Feb: 19 p40.
3. G. Lee, J.W. Barlow, "Selective Laser Sintering of Calcium Phosphate Powders," Solid Freeform Fabrication Symposium Proceedings, 1993 UT Austin, TX.
4. Steidle, C., et al., Automated Fabrication of Nonresorbable Bone Implants Using Laminated Object Manufacturing (LOM), M.S. Thesis, Chemical Engineering, University of Dayton, May, 1998.
5. Richter, P.W., Thomas, M.E., Van Deventer, T., Macroporous hydroxyapatite Bioceramics by solid Freeform Fabrication: Towards Custom Implants. South African Journal of Science, vol. 95, 1999.
6. Schenker, R., De Beer, D.J., Du Preez, W.B., Thomas, M.E., Richter, P.W.,Novel Combination of Reverse Engineering and Rapid Prototyping in Medicine. *South African Journal of Science*, vol. 95, no. 8, August, 1999, pp. 327-328.

this page intentionally blank

Powder Delivery in Dental Restoration Rapid Prototyping Process

Jiwen Wang, Xiaoxuan Li, Leon L. Shaw, Harris L. Marcus
Institute of Materials Science
University of Connecticut
Storrs, CT 06269

Thomas B. Cameron
Degussa-Ney Dental Inc.
Bloomfield, CT 06002

ABSTRACT

Rapid prototyping of dental restoration has been investigated for its potential to save time and cost. In this paper, a powder delivery system was developed to deliver dental porcelain powder accurately into 2-D shapes for dental restoration. Aqueous suspension of the porcelain was prepared as the vehicle for the powder delivery. An integrated dry and wet ball-milling process was developed to reduce the particle size and minimize agglomeration. The reduction in particle size and minimization of agglomeration increased the suspension stability. The optimization of the pH value of the suspension also provided an additional means to achieve the stability and reduce the viscosity of the suspension. With the optimization of the particle size, pH value and solid concentration in the suspension, desired powder shapes were successfully delivered.

Key word: Rapid prototyping, dental restoration, powder delivery, ball milling.

INTRODUCTION

There are currently more than 10,000 dental laboratories in the US and a majority of these laboratories use porcelain-fused-to-metal (PFM) restoration for permanent fixed prosthodontics. PFM restoration is a very time consuming and labor intensive work because PFM restoration requires a multi-stage process using multiple materials (both ceramics and metals) and each stage involves multiple processing steps [1]. For example, it normally takes 2-4 weeks to make a three-unit bridge and labor costs account for about 90% of the final cost. This study is part of an overall effort to develop a novel multi-materials laser densification (MMLD) process for dental restorations [1-3]. This process utilizes laser-assisted solid freeform fabrication (SFF) to fabricate artificial dental units layer-by-layer directly from a computer model without part-specific tooling and human intervention. As such, the labor cost will be substantially reduced, and better and faster dental restorations will be achieved.

One of the key issues in the MMLD process is to deliver dental alloy and porcelain powders to the desired locations precisely and accurately point by point, line by line and layer by layer. Point-by-point and line-by-line powder deliveries are essential because there are multiple materials involved in a single plane for dental restorations. This study focuses on how to delivery dental porcelain powder precisely and accurately to the desirable locations in point, line and

layer forms before laser densification of these delivered powder shapes. Powder suspension and paste have been selected as the vehicles to deliver dental powders because wet suspensions and pastes provide a better control on the shape of the powder compact delivered than a dry powder does. Effects of the particle size, the pH value of the suspension and the concentration of solids in the suspension on powder delivery have been investigated. The results are presented below.

EXPERIMENTAL

The dental porcelain powder was provided by Degussa-Ney Dental Inc., Bloomfield, CT. The chemical composition of the porcelain is confidential; however, it is within 5% of the nominal composition of the Weinstein patent [4], which has the following composition (wt%): 63.40% SiO_2, 16.70% Al_2O_3, 1.50% CaO, 0.80% MgO, 3.41% Na_2O, and 14.19% K_2O. The typical morphology and microstructure of the porcelain powder are shown in Figure 1. It can be seen that the as-received powder has angular shapes and their equivalent particle sizes range from 1 to 50 micrometers. To reduce the size of the porcelain powder, ball-milling process was conducted using a SPEX 8000 mill machine. The vial and balls for the ball milling process were all made of alumina, and thus the alumina concentration in the milled powder could be slightly higher than that of the original powder should wear of the alumina vial and balls take place during the milling. The weight ratio of the powder to alumina balls was 2.5 in all of the ball milling experiments.

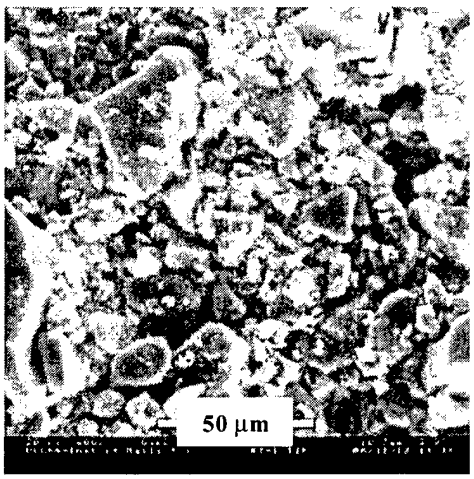


Fig. 1 ESEM image of the as-received dental porcelain powder.

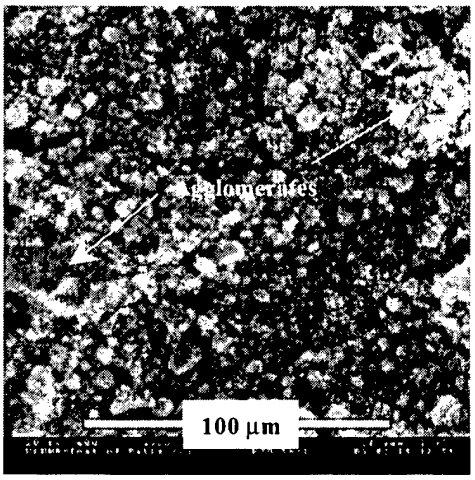


Fig. 2 ESEM image of the porcelain powder after 5 hours of dry ball milling.

Both the as-received and milled powders were used to prepare suspensions with de-ionized water as the liquid media. The suspensions prepared were subjected to the viscosity measurement and suspension delivery evaluation. The porcelain suspension was delivered using a dental restoration machine made in our laboratory. The machine contains a X-Y-Z table controlled by a computer through a DMC-1800 Galil Motion control card. The suspension was held in a barrel at the end of which there was a nozzle for suspension delivery. The diameter of the nozzle can be changed for the evaluation of the nozzle size effect. The sizes of the delivered powder suspension points and lines were measured and compared to the nozzle diameter.

Both the as-received and milled porcelain powders were characterized using an environmental scanning electron microscope (Philips ESEM 2020) to obtain the morphology and size of the powders. Analysis of the specific surface area of the powder was conducted using nitrogen adsorption based on the Braunauer-Emmett-Teller (BET) theory (Quantachrome NOVA 1000). The viscosity of the porcelain suspension was determined using a Brookfield DV II digital viscometer. The zeta potential of the suspension was measured in the National Science Foundation Engineering Research Center for Particle Science and Technology at the University of Florida using a Zeta-Reader instrument.

RESULTS AND DISCUSSION

1. Effect of Ball-Milling Process on Porcelain Powder

As shown in Figure 1, the as-received porcelain particles are substantially larger than 1 μm and thus not suitable for preparing stable colloidal suspensions. To achieve a stable colloidal suspension, the size of solid particles normally needs to be smaller than or about 1 μm. Thus, ball milling was investigated in this study for its potential to reduce the porcelain powder size. Figure 2 shows the ESEM image of the porcelain powder after 5 hours of dry ball milling. When compared with the as-received powder, the size of porcelain particles has been significantly reduced by the ball milling process. After 5 hours of dry milling most of the particles are smaller than 5 μm, whereas 20 μm particles are very common in the as-received powder. The specific surface area of the porcelain powder as a function of the time of dry milling is shown in Figure 3. As expected, the specific surface area of the porcelain powder increases with milling time. At 8 hours of milling, the specific surface area has increased 8 times over the as-received powder, suggesting that the average particle size has been reduced to about 1/3 of the original.

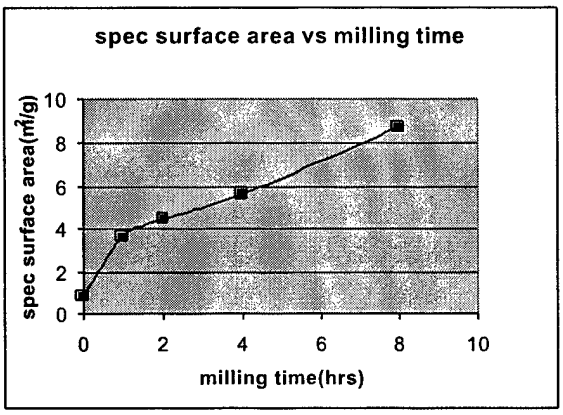


Fig. 3 The specific surface area of the porcelain powder as a function of dry milling time.

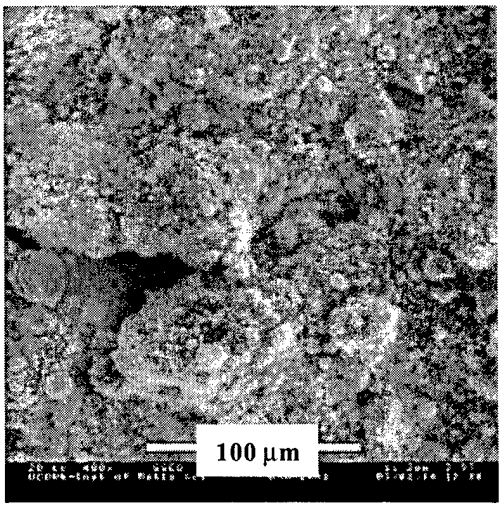


Fig. 4 Particle agglomeration in the porcelain powder with 2 hours of dry milling.

It is also noted from Figure 3 that the increase rate of the specific surface area becomes smaller after 1.5 hours of milling. Detailed SEM examination of the milled powder reveals that the reduced rate for increasing the specific surface area is related to powder agglomeration

during ball milling. Powder agglomeration will degrade the efficiency of the comminution process and is highly undesirable. It is also found that powder agglomeration becomes obvious at about 2 hours of milling, coinciding with the time for changing the increase rate of the specific surface area shown in Figure 3. A typical morphology of powder agglomeration observed in the powder with 2 hours of dry milling is shown in Figure 4. Clearly, to improve the milling efficiency powder agglomeration during milling should be avoided.

In order to overcome the agglomeration problem and obtain a well-dispersed suspension, wet ball-milling process was also investigated. De-ionized water was used as the liquid media for the wet milling process. Figure 5 shows the typical morphology of the porcelain powder after 5 hours of wet milling. It can be seen that there is no agglomeration; however, the particle size is larger than that of the powder dry milled for 5 hours (Figure 2). This is consistent with the well established phenomenon that wet milling is less efficient in particle size reduction than dry milling [5,6]. In order to utilize the advantages of both dry milling and wet milling, we have developed an integrated dry and wet milling process in which the porcelain powder is dry milled for several hours (e.g., 2 to 4 hours) and subsequently wet milled for 1 hour. In such integrated milling process, the dry milling at the early stage of the process reduces the particle size while the wet milling at the later stage of the process breaks down agglomerates and produces a well dispersed suspension. This expectation was confirmed by experiments. Furthermore, the suspension prepared from the integrated milling process was much more stable than without milling or with dry milling only because the suspension from the integrated milling process has fine particles and few or no agglomerates.

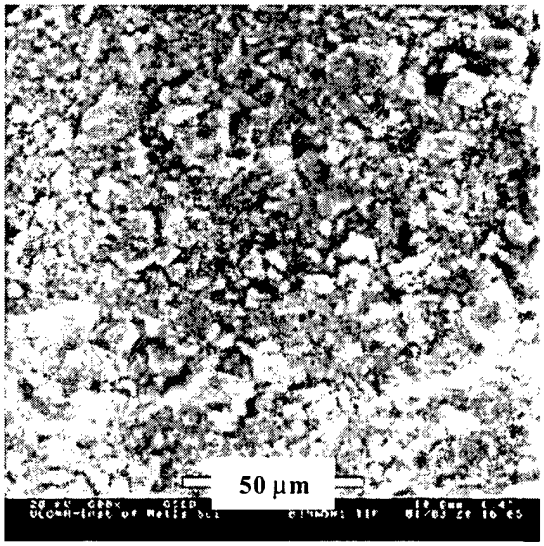


Fig. 5 Morphology of the porcelain powder after wet milling for 5 hours.

2. Influence of pH Value on the Stability and Viscosity of Porcelain Suspension

The stability of a colloidal suspension, according to the DLVO theory [7], is determined by the balance between the repulsive and attractive forces which particles experience as they approach. The repulsive force depends on the degree of double layer overlap. It has long been recognized that the zeta-potential is a good index of the magnitude of the repulsive interaction between particles. Figure 6 shows the zeta potential versus pH value curve of the porcelain

powder suspension. It indicates that the iso-electric point (i.e.p.) of the dental porcelain powder is at about 5.0. It is interesting to note that this number falls between the i.e.p. of Al_2O_3 and SiO_2. The i.e.p. of Al_2O_3 is at 8.7 [8], whereas SiO_2 at 2.0 [9]. Since Al_2O_3 and SiO_2 are the main components of the dental porcelain [4], the zeta-potential of the porcelain powder appears to be controlled by a combined interactive effect of these two compounds.

According to "Eilers and Korff Rule", the onset of instability of a suspension is associated with a rapid decrease in the value of the function ζ^2/κ(ζ: Zeta potential; κ: Debye-Huckel parameter). It can be derived from Figure 6 that between pH value 4 and 6, ζ^2/κ will have a rapid decrease in the value; thus, coagulation of the particles in the suspension will happen quickly in this pH range, leading to an unstable suspension. For suspensions with pH< 3 or pH> 6, the zeta potential of the porcelain powder changes slowly and the surface of powder particles is mainly positive charged (for pH< 3) or negative charged (for pH> 6), which results in relative large repulsive forces between particles and thus stable suspensions.

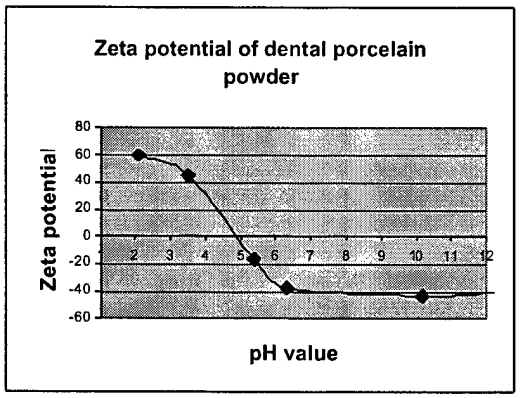


Fig. 6 Zeta potential of the dental porcelain powder as a function of pH value.

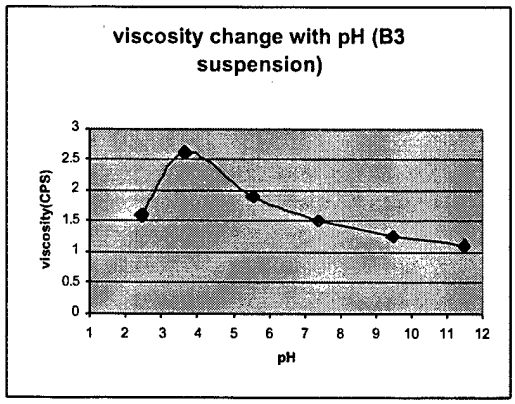


Fig. 7 Viscosity change of the porcelain suspension with pH value (8 vol% solid).

Measurement of the suspension viscosity was also consistent with the finding of the zeta potential measurement. Shown in Figure 7 is the viscosity of the 8 vol.% porcelain powder suspension as a function of the pH value. Note that the viscosity of the suspension peaks in pH range 3 – 6, consistent with the zeta potential curve that predicts the possible coagulation in pH range 3 – 6. Low viscosity of the suspension will translate into high flowability which makes the suspension easy to deal with in powder delivery process. Furthermore, the suspension with pH< 3 or pH> 6 has relatively good stability and thus a long shelf life. Since the suspension with pH range 7– 10 has lower viscosities than the suspension of pH< 3, the suspension with pH range 7 – 10 has been selected for further powder delivery investigation. An additional advantage using the suspension with pH range 7 – 10 over pH< 3 is less corrosiveness offered by the suspension with pH range 7 – 10.

3. Delivery of Dental Porcelain Suspension

Delivery of dental porcelain suspension was done using an in-house designed machine that contains a X-Y-Z table and a barrel used for holding the suspension (Figure 8(a)). At the end of the barrel there is a nozzle the diameter of which can be changed for the evaluation of the nozzle size effect. The delivery of the suspension is controlled by combined effects of the surface tension and the gravity of the suspension. When the nozzle touches the substrate, the suspension

flows out of the nozzle; otherwise, the suspension will be held within the nozzle by the surface tension of the suspension. It was found that successful delivery of dental porcelain suspensions by the aforementioned machine and mechanism relied on the proper selection of the solid concentration and pH value of the suspension, the particle size of the powder, and the diameter of the nozzle. Large particles, small-diameter nozzles and high viscosity suspensions typically resulted in gradual blockage of the nozzle and eventually cessation of the suspension delivery process.

Figure 8(b) shows the porcelain suspension delivered in several 2-D shapes. The suspension shown in Figure 8(b) had a pH value of 10 and a solid loading of 20 vol.%. The diameter of the nozzle used was 0.5 mm. One of the determining factors for the dimensional accuracy of dental restoration is the accuracy of the suspension delivery which, in turn, is determined by the smallest point and line that can be delivered. The present study has revealed that the smallest point and line that can be delivered are affected by many factors. The key factors include the nozzle size, the viscosity and the flowability of the suspension. The smallest point that can be delivered now is 0.5 – 0.8 mm as showed in the middle and right bottom of Figure 8(b). On the upper left, two suspension lines were formed by delivering 30 individual points in each line with 30% overlap between the neighboring points. On the upper right, a square shape was formed by delivering 121 points in 11 lines with no overlap between the neighboring points. Thus, the width and thickness of a single line can be adjusted in the current delivery method by controlling the overlapping distance between the neighboring points.

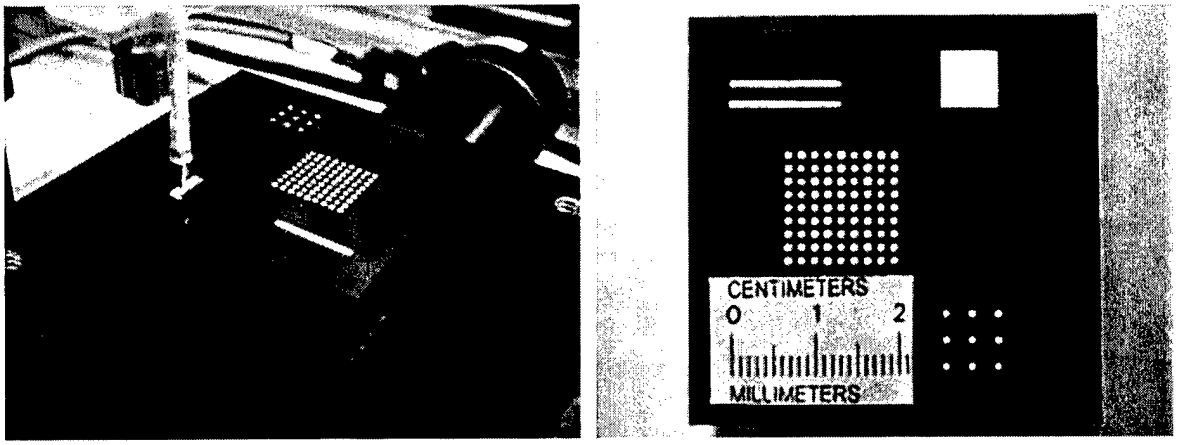


Figure 8. (a) porcelain suspension delivery system, and (b) 2-D samples delivered.

CONCLUSIONS

A delivery process of dental porcelain powder has been developed using a suspension approach. The well-dispersed porcelain suspension is obtained by a newly developed milling process that integrates dry and wet milling processes. The dry milling at the early stage of the integrated process effectively reduces the particle size, whereas the wet milling at the later stage of the integrated process breaks down agglomerates and produces a stable suspension. The viscosity of the suspension strongly depends on the pH value of the suspension. Low viscosity suspensions are obtained when pH is about 10, which coincides with the pH value for obtaining stable suspensions as predicted by the zeta potential measurement. Low viscosity and stable

suspensions are beneficial for suspension delivery. This is especially true when very small points and lines are to be delivered. Without low viscosity and stable suspensions the nozzle for delivering suspensions will be gradually blocked and eventually cease to function. The smallest point delivered that has been achieved in this study is about 0.5 mm in diameter.

Acknowledgement – The authors gratefully acknowledge financial support provided by the National Science Foundation under Grant No: DMI-9908249. The zeta potential measurement carried out in the National Science Foundation Engineering Research Center for Particle Science and Technology at the University of Florida is also greatly appreciated.

REFERENCES

1) X. Li, J. Crocker, E. Geiss, L. Shaw, H. Marcus and T. Cameron, "Evaluation of Microstructure and Properties for Multi-Materials Laser Densification of Dental Restorations," in the proceedings of the 11th Annual SFF Symposium, edited by D. L. Bourell, et al., The University of Texas, 2000, pp. 159–167.
2) X. Li, J. Crocker, L. Shaw, H. Marcus and T. Cameron, "Laser Densification of Nickel Powder for Dental Restorations," to appear in the proceedings of the 2001 NSF Design, Manufacturing & Industrial Innovation Research Conference, Tampa, Florida, 2001.
3) X. Li, J. Wang, A. Augustine, L. Shaw, H. Marcus and T. Cameron, "Microstructure Evaluation for Laser Densification of Dental Porcelains," to appear in the proceedings of the 12th Annual SFF Symposium, edited by D. L. Bourell, et al., The University of Texas, 2001.
4) M. Weinstein, S. Katz and A. B. Weinstein, "Fused Porcelain-to-Metal Teeth," U.S. Pat. No. 3 052 983, Sept. 11, 1962.
5) J. S. Benjamin and T. E. Volin, "The Mechanism of Mechanical Alloying," Metall. Trans., 5, 1929-1934 (1974).
6) P. S. Gilman and J. S. Benjamin, "Mechanical Alloying," Ann. Rev. Mater. Sci., 13, 279-300 (1983).
7) T. F. Tadros, "Solid/Liquid Dispersions," Academic Press, 1987.
8) J. Cesarano III and I. A. Aksay, "Processing of Highly Concentrated Aqueous a-Alumina Suspensions Stabilized with Polyelectrolytes," J. Am. Ceram. Soc., 71 [12] 1062-1067 (1988).
9) L. Shaw and R. Abbaschian, "Fabrication of SiC-Whisker-Reinforced $MoSi_2$ Composites by Tape Casting," J. Am. Ceram. Soc., 78 [11] 3129-3132 (1995).

this page intentionally blank

Manufacturing of a Heterogeneous Flywheel on a LENS Apparatus

Stephane Morvan
smorvan@optomec.com

Georges M. Fadel
gfadel@ces.clemson.edu

Dept. of Mechanical Engineering
College of Engineering and Sciences
Clemson, SC 29634-0921

James Love
jlove@optomec.com

Dave Keicher
dkeicher@optomec.com

Optomec Inc.
3911 Singer Blvd, NE
Albuquerque, NM 87120

Abstract

The design of a 1D gradient component satisfying a particular set of constraints is extended to its manufacturing on a multi-material capable apparatus. The geometry and composition of this flywheel were designed to meet a bi-objective optimum featuring maximum kinetic energy storage and minimal maximum von-Mises stress along its radius. The efforts expanded during the transformation of this design from a computer abstraction into a tangible object are presented. The process-planning step of the manufacturing of this heterogeneous solid, which was dependent on the specifics of a LENS-based Apparatus, required a different approach than that of traditional solids, and proved critical during fabrication.

Introduction

Recent advances (Swann T.A., Keicher D.M. et al. 1998) in the direct deposition of metals have enabled the manufacture of gradient structures and functional materials to provide exciting new alternatives for the design of components. Akin to composites and carbon fibers, these new processes allow the strength and other functional features of a particular material to be used exactly where they are needed within that component, and evade the tradeoffs that are normally made when a particular material is chosen. For example, in the design of a turbine blade, one might find the limited mechanical properties of a ceramic to be problematic in areas where mechanical strength would prevail over thermal properties. Conversely, in that same blade, the thermal properties of a titanium alloy might limit its usefulness in areas exposed to very high temperatures. Using a carefully designed mix of both ceramics and titanium throughout the blade may provide an adequate solution to this problem should the two materials coexist. (König and Fadel, 1999)

When a part is designed from its inception as being composed of multiple materials, the repartition of the material within this solid can be selected using optimization tools such as genetic algorithms ((Goldberg, 1989), (Hajela, 1992), (König, 1999), (Huang and Fadel 1999)). Most optimization tools rely on a discretization of the geometric domain into smaller domains where the material composition can be changed. The difficulty in choosing a particular material distribution grows with the material space available for each subdomain.

From the optimization standpoint, every design variable input to an optimization problem seeks a best value for a mechanical or thermal property given a particular objective to attain (for example: smallest deformation and lightest structure.) The mapping between this property (mechanical or thermal) and a material composition is simplified to be of a linear nature: a part made from 50% Copper and 50% Steel has a strength that is in the same proportions than that of its composition, in that case 50% of Copper strength added to 50% of Steel strength.) Other mixing rules are currently under investigation to fully enable the resolution of the inverse problem (Huang, 2000), Grujicic et al., 2001.)

Heterogeneous Flywheel Optimization

A flywheel is a mechanical component that stores kinetic energy. The mass distribution of a flywheel around its axis of revolution impacts its capacity to store kinetic energy. A high-energy storage is

typically attained whenever the mass is distributed as far as possible, from the axis of revolution (e.g. on the circumference of the flywheel.) Huang (Huang and Fadel, 1999) proposed a novel approach to the design of a flywheel: essentially, since this is a solid of revolution, the problem is reduced to the design of its cross section. The geometry, along with the composition in a cross section is designed by blending two materials with opposed properties (high strength/low weight and low strength/high weight).

The design is therefore treated as an optimization problem; with the following objectives:

- Maximize kinetic energy stored,
- Minimize maximal von-Mises equivalent stress,

The following constraints limit the design:

- Dimensional constraints (maximum height, internal and external radius.)

The composition is represented by way of the volume fractions of Material A with respect to Material B. The geometry and the composition are represented using parametric equations featuring Bezier blending functions:

$$z(u) = \sum_{i=0}^{n} z_i \cdot B_i^n(u)$$

$$v_a(u) = \sum_{i=0}^{n} v_a^i \cdot B_i^n(u)$$

$$r(u) = \sum_{i=0}^{n} r_i \cdot B_i^n(u)$$

$$B_i^n(u) = \frac{n!}{i!(n-i)!} \cdot u^i \cdot (1-u)^{n-i}$$

$$0 \le u \le 1$$

The r_i are set and represent the location of the control points along the radius for the geometry and the composition, z_i and v_i respectively. Both the z_i and v_i represent the design variables. The optimizer computes the optimum values for all $2(n+1)$ design variables, and attempts to meet the objectives presented earlier. The study investigated both continuous and discrete material variations. For the purposes of this study, the gradient material distribution was emulated.

The materials selected are tungsten-carbide (heavy/low strength) and cobalt (light/high strength.) 22 control points are chosen, and a sample result is presented on Figure.1.

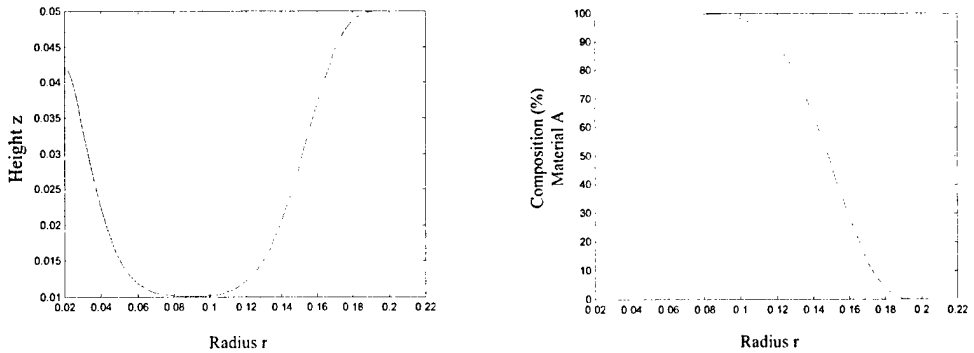


Figure 1. Optimal Geometry and Composition for a Heterogeneous Flywheel

The composition at each point is defined by the volume fractions of Material A and Material B. The previous relation permits to compute the composition at any point based on the composition at every control point. Again, the control composition at each node can be computed by sampling the control composition curves, and by using the sampled points as node points to perform interpolation. Similarly to the geometrical interpolation, the control composition can be used directly in lieu of the node points, and the Bezier blending function can be used as material blending function. The cross section generated so is presented on Figure 2.

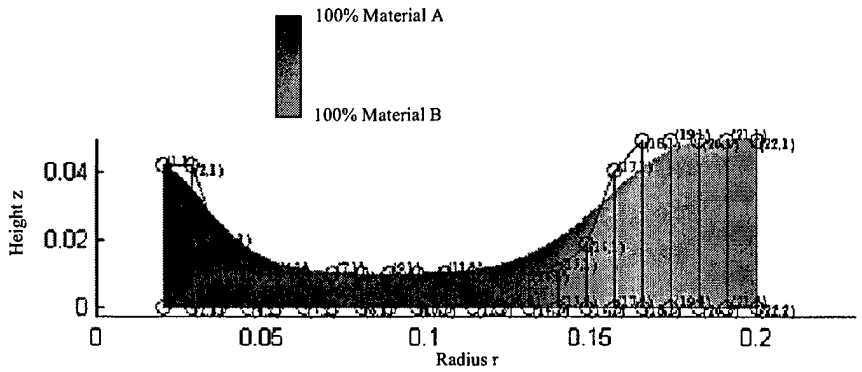
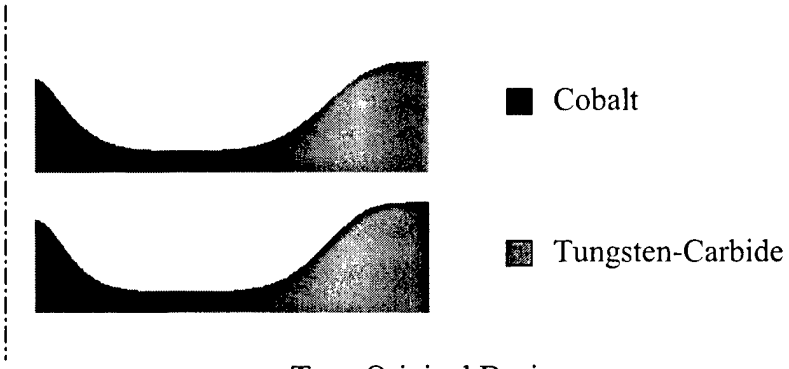


Figure 2. MMa-Rep of Heterogeneous Flywheel Using Bezier Interpolation

In that particular case, and because the optimization was performed directly using Bezier control points, it is suitable to use Bezier blending functions for both the geometry and the material composition. For more general cases, both the profile curve and the material composition must be sampled, and the sampled points can be used as node points in the in a more general type of multimaterial representations (MMa-Rep) presented in (Morvan S. 2001).

Manufacturing

The graded structure is made of two different materials: Cobalt (light/strong) and Tungsten Carbide (heavy/weak). The two sets of design variables are optimized concurrently, generating the profile shown earlier. This profile is then manually refined to exhibit the gradient capabilities available on the LENS apparatus by enclosing the tungsten-carbide located on the periphery, within a *coating* of the cobalt material to make it a 2D Material distribution (in the *r* and *z* direction.) This coating is achieved gradually on the outer surfaces, as show on Figure 3. Furthermore, to provide visual evidence of the graded structure, the constituent materials are changed from cobalt to 320 stainless steel, and from tungsten-carbide to copper coated nickel. The inclusion of a secondary material within the outer part of the flywheel is then more evident in a polished cross section (Figure 4.)



Top: Original Design
Bottom: Modified Design

Figure 3. Original and Modified Flywheel Design

The polished cross section shows cavities (white spots) that result from the insufficient melting of the powder mix. Those cavities are grains of powder trapped in the molten material that were removed during the polishing of the cross section. This porosity can be controlled and practically eliminated if the system parameters (laser power, speed, powder size, powder massflow rate) are appropriately selected and modulated as a function of the material properties. Since the purpose of this work was to show feasibility, these issues were not stressed.

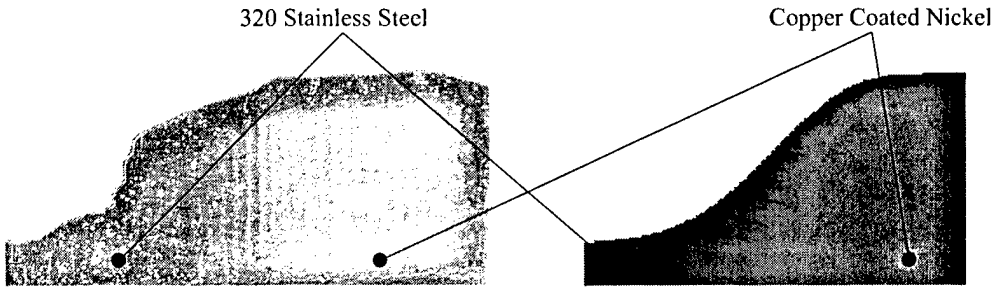


Figure 4. Cross Section of the Gradient Flywheel

Furthermore, from Figure 4 and Figure 5, it is observed that the geometrical accuracy is not adequate as most of the geometrical features are roughly approximated. However, on well calibrated machines, the geometrical accuracy is less of a problem, as can be seen (Figure 5.) This part shows excellent (and uniform) accuracy and improved surface finish when building is achieved on a well-configured LENS apparatus. The constant orientation hatch pattern and the single material greatly contribute to these improvements.

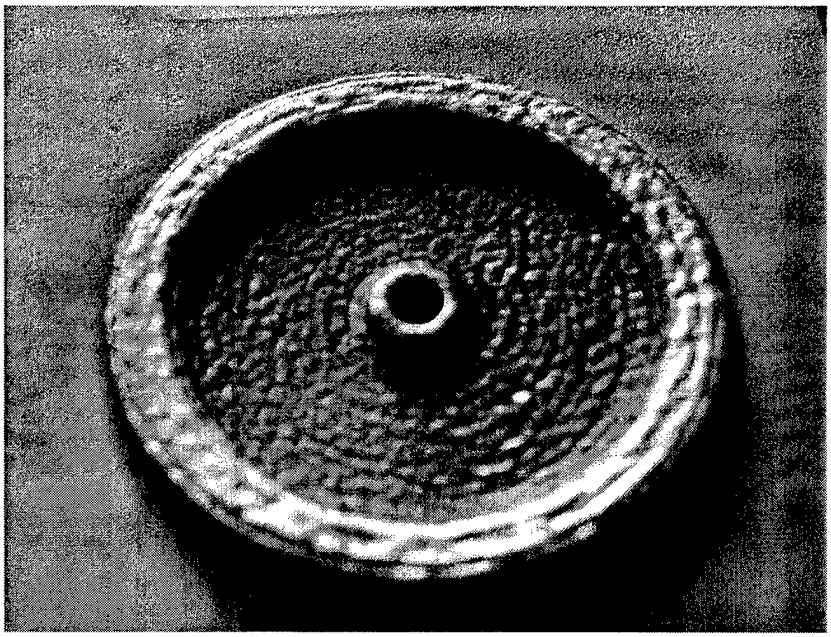


Figure 5. Exterior View of the Gradient Flywheel

The technology used for the control of the material composition does not allow alteration of the powder mix within a single laser stroke. Thus, for the deposition of a set material composition, the powder mix was altered ahead of the actual deposition phase. The time taken to alter the material composition at the nozzle is about 2 or 3 orders of magnitude of the time required to move the head of the apparatus to another location. Therefore the material composition is changed infrequently to minimize the performance hit on manufacturing time, and conversely, laser strokes of similar compositions are generated in sequence.

In its current form, the LENS manufacturing process is akin to a plotter capable of using a set of *inks* mixed upward from the pen. Thus, depositing the material is a combination of four basic operations, comparable to pen up, pen down, pen color and pen move operations:

- A pen up operation consists of shutting the laser off,
- A pen down operation consists of turning the laser on,
- A pen color operation consists of altering the material composition by modifying the powder mix,
- A pen move operation consists of moving the laser to a new location.

Flywheel File Preparation

For single material parts, the traditional process planning stage of the LENS apparatus is essentially to use an .STL file representing the geometry, slice it using adaptive slicing, and convert the slice file in a set of instructions used to program the controlling apparatus (termed a .DMC file.) The heterogeneous nature of this flywheel does not permit its representation in the .STL format (it assumes single material,) therefore the conversion from .STL to slice file is not possible. The .DMC file is instead created directly from the representation presented earlier.

The selection of the hatching pattern is immediately resolved by observing that the constant composition paths are made of concentric rings.

Once the hatching space (0.015 in.) and layer thickness are selected (0.010 in.), the profile is sampled in both r and z direction for composition. The rings are then sorted by z-height, by composition and finally by decreasing radii. Thus, within a given slice, rings of similar composition are deposited at once, minimizing travel time of the head. A flowchart of the essential steps is presented on Figure 6.

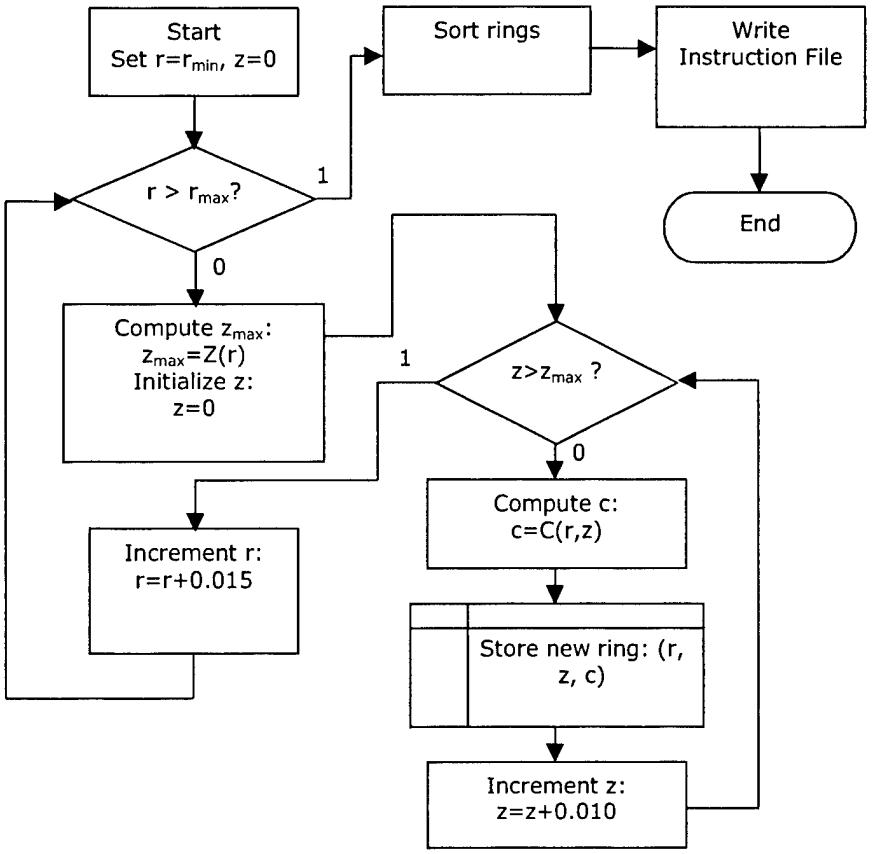


Figure 6. Flywheel File Preparation Flowchart

For rings of different composition, the effects of composition change are somewhat damped, since the transient states that incurred in the powder feeding apparatus are only between neighboring states and exclusively monotonic (e.g. the compositions vary from *10-90* to *15-85*, to *20-80*& in % volume fractions of 320 stainless steel and copper-coated nickel respectively.) A 20 ms wait was sufficient between adjustments to assume that a steady state was reached in the powder feeder. A first trial revealed that as the deposition head repeatedly waits for the powder feeder to reach a steady state at the same location, material was also being deposited at the latter, producing undesired ridges. The creation of the .DMC file was then modified to *randomize* the starting and ending angles used to create the rings, thus alleviating the possible buildup of material.

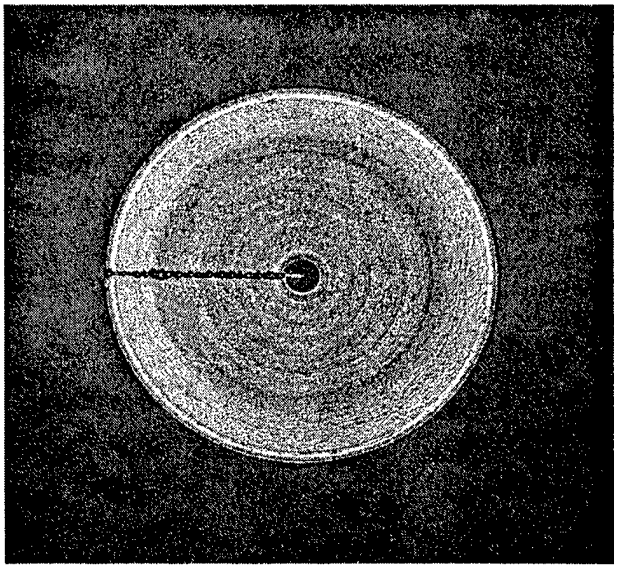


Figure 7. Undesired Buildup

Conclusion

The manufacturing of a graded structure on a LENS Apparatus was accomplished. This approach was novel in that the process planning stage had to be modified to accommodate for the gradient nature of the part, thus outlining a new set of manufacturing constraints. Although many factors influenced the fabrication of this part, they were essentially centered around the choice on the hatching pattern, which actually fills the material inside the contours of the part:

On single material capable rapid prototyping machines, such as the 3D System SLA-250 series, the hatch patterns aims at minimizing laser shut offs and minimizing build time.

On multimaterial, gradient-capable apparatus, the hatch pattern is subject to a different set of constraints, due to the material composition changes. On the LENS apparatus, there is a penalty for altering the material composition. A possible solution to that is to create a deposition sequence featuring strokes of similar composition.

As knowledge about the quality of the materials being manufactured is gained, this set of constraints will be expanded further. Issues such as thermal constraint buildup, resulting from overheating of previously deposited layers might generate other compelling reasons to drastically alter conventional hatch patterns, as the thermal constraint buildup directly influences the metallic structures of the materials fabricated.

The study does however show the potential of the LENS machine to manufacture multimaterial objects. These have been designed taking into consideration manufacturing constraints and then built on a machine that has the potential to brake the paradigm of designing and building homogenous materials.

Acknowledgments

This work was made possible with a grant from Optomec Inc., Albuquerque, NM.

Bibliography

Goldberg D.E. (1989). Genetic Algorithms in Search, Optimization and Machine Learning, Addison-Wesley.

Grujicic, M., Cao, G. and Fadel, G.M.(2001), "Effective Materials properties: Determination and application in Mechanical Design and Optimization", to appear in the Journal of materials, design and applications.

Hajela P. (1992). Stochastic Search in Structural Optimization: Genetic Algorithms and Simulated Annealing. Progress in Astronautics and Aeronautics **150**: 611-637.

Huang J. and Fadel G.M. (1999). Heterogeneous Flywheel Modeling & Optimization. Journal of Materials & Design(Special Issue: Rapid Prototyping and Manufacturing).

Huang J. (2000) "Optimizing material distribution for multi-material Rapid Prototyping" Ph.D. Dissertation, Clemson University.

König O. (1999). Application of Genetic Algorithms in the Design of Multimaterial Structures Manufactured in Rapid Prototyping. Institute for Construction and Design, ETH Zurich, Switzerland - Department of Mechanical Engineering, Clemson University, USA. Zurich, Switzerland, ETH Zurich.

Morvan S. (2001). "MMa-Rep: A Representation for MultiMaterial Solids" Ph.D. Dissertation, Clemson University.

Swann T.A., Keicher D.M., et al. (1998). Laser Engineered Net Shaping (LENS") Technology Commercialization. Rapid Prototyping and Manufacturing 98, Dearborn, MI, Society of Manufacturing Engineers.

Robocasting Periodic Lattices For Advanced Filtration

John N. Stuecker, Joseph Cesarano III, James, E. Smay
Sandia National Laboratories
Albuquerque, NM 87185

Abstract

Ceramic filters used in the casting of molten metals are commonly created by slurry impregnation of polymeric foams, yielding a fired ceramic foam structure. These foam structures have high part-to-part standard deviation in flow rates (~25%) and have weak sections which can fragment into the melt. In contrast, periodic lattice filters (PLF's) made by robocasting have a cross-hatched face-centered-cubic arrangement of rods.. As such, the robocast filters have high strength and may be easily tailored to offer a specific internal pore structure to control the flow rate and pressure drop across the filters. Standard deviation of flow rates among PLF's are less than 1%. This paper describes the methodology of creating PLF's as possible foam filter replacements.

Introduction:

The most commonly used ceramic filters on the market today are thin-walled extruded honeycomb and ceramic foam filters. Extruded honeycomb filters are employed in most automobile exhaust systems and are commonly used as catalyst supports. These filters are made by extruding a plastic ceramic body through a die which yields parallel walled channels. Very well defined pore sizes result from this fabrication method. Ceramic foam filters are made by immersing a polymeric foam into a ceramic slurry. The slurry-saturated foam is then drawn through a set of rollers which displace excess slurry, allowing the pore structure of the foam to become prominent. The polymeric foam is then burned out and the resulting ceramic structure fired to high density. Pore sizes are inherently variable and difficult to reproduce. Non-uniform pore structure leads to inconsistent flow rates for any particular filter. Flow rate control is important when performing metal casting. Further, regions of closed pores occur, as well as regions of very thin/weak ceramic struts. These ceramic foams are most commonly used in filtering oxides from molten metals, with the major issues being variability of porosity resulting in variable flow rates, and fragments of ceramic foam breaking off during filtering, flowing into the casting.

Robocasting of high solids loading slurries allows precise placement of material in three dimensions. By slightly flocculating the slurry, spanning structures can be built and are similar in appearance to stacks of rods with maximum span distances of up to eight times the rod diameter. The rod-like shape of the extruded material is directly created from the circular extrusion orifice. Moving the orifice back and forth in a controlled pattern while extruding the ceramic material allows precise layering of these rods in a periodic lattice and a unique style of ceramic filter to be created. The freshly-extruded slurry melds together with the previously placed rods thereby creating a strong lattice. These filters can have user specified pore size between the solid rods by altering the extrusion path (80 to 3000 μm) as well as having a range of rod sizes by altering the orifice size (80 to 3000 μm). Further, line-of-sight porosity in the flow direction can be eliminated in four build layers by using equal rod size and pore size, and placing the rods in a face-centered cubic (FCC) pattern. This style of filter may be used in applications currently using the extruded honeycomb and ceramic foam structures. This discussion will compare flow properties of ceramic foam and periodic lattice filters.

Experimental:

Alumina ceramic foam filters used commercially in molten metal filtration were generously provided by Selee Corp., Hendersonville, SC (Figure 1a). Standard foams are available in 20, 30, 45, and 60 pores per linear inch (ppi). The foams are present inside a solid, pressed alumina ring, yielding an overall part size of approximately 1" OD, and 0.4" thick through the porous foam.

Periodic lattice filters (PLF's) were fabricated by robocasting an aqueous based 60 vol%, 99.8% purity alumina slurry containing less than 0.5 vol% organic material. Yield stress of the slurry was increased until unsupported lattices could be fabricated. Filters of various pore sizes, rod diameters, and thicknesses were created in attempt to characterize air and liquid flow through the periodic lattices. All PLF's were dried for several hours and fired to 1650°C to near full density. A PLF with 30 ppi is shown in

Fig. 1b. PLF's were created that match first, the geometry of the commercially available foams, and then second, the liquid flow rates. Three of each filter geometry were fabricated and characterized to obtain standard deviations. Table 1 displays a selection of tip sizes used in the robocasting process, the resulting sintered rod diameter, the resulting linear ppi of the FCC lattice, and equivalent surface areas. The surface area data is provided simply for comparison to commercially available extruded honeycomb structures. For example, ultra-thin-walled honeycomb used as a catalyst support with 24.5 ppi yields a surface area of ~98 in^2/in^3, which is very similar to a 25 ppi PLF (99 in^2/in^3).

Air permeability tests were performed by inserting the PLF into a controllable air-flow chamber. Taps just before and after the test specimen allowed monitoring of pressure drop via a digital manometer accurate to ± .1 psi. The air flow rate was adjusted from 1 to 7 cubic feet per minute (cfm) while pressure drop reading were taken. Using the resulting data and Darcy's equation, the permeability constant was calculated:

$$K_d = \frac{QL}{A\Delta P}$$

where Q is the volumetric flow rate, L is the length of the permeate, A is the cross-sectional area, and ΔP is pressure drop across the permeate. Liquid flow rate was measured using water at a constant head of water of 10 psi. The amount of time required to fill a gallon container was timed, and flow rates were recorded in gal/min. It is suitable to use water in the liquid flow tests to get a general idea of the flow rate of molten aluminum due to the very similar Reynolds numbers.

Results and Discussion:

In order to eliminate unimpeded line-of-sight flow channels in the flow direction, PLF's were fabricated with layers of stacked rods with the spacing between the rods equal to the rod diameter. A unit cell consists of four layers. Permeability data for several PLF's are found in Figure 2. The plot contains data for PLF's of 14 to 47 ppi, with one, two, and three unit cells in thickness. The trend in the plot is expected. Decreasing the rod diameter (thus increasing the ppi), restricts flow, increasing the permeability constant K_d. Increasing the number of layers of the PLF for a given pore size also increases K_d, further restricting flow. One notable feature arises from the graph, the permeability constant is not constant. Rather, a decrease in the permeability constant is seen with increasing flow rates. This change in K_d is most likely due to change in gas flow from laminar to turbulent. What parts of the graph are turbulent and what parts laminar? Regardless of laminar of turbulent flow, Fig. 2 may be used as a map to design a PLF with a specified flow rate by selecting the appropriate thickness and ppi values. For example, if a high surface area is needed for a catalyst support, smaller rod sizes yielding larger ppi values are required. However, it may then be necessary to select a small number of layers in order achieve an acceptably high flow rate.

Often, pressure drop across a filter is an important parameter. Figure 3a-c compares the pressure drop across a 45 ppi foam, a 30 ppi foam, and a 47 ppi lattice. The 47 ppi lattice has the same physical geometry as the foam filters (1" OD, 0.4" thick). For the three samples of each filter, it can be seen that the foam structures have lower pressure drop than the PLF. The very low bulk density of the foam structures (~80% porosity) accounts for the lower pressure drop. However, the foam filters show very high part-to-part standard deviations relative to the PLF. From the back-lit foam structure in Figure 1, it is inferred that the inconsistent pore structure inherent in the slurry impregnation process accounts for the standard deviation among samples. The back-lit PLF in Figure 1 conveys the good uniformity and consistency of the internal structure. In conclusion, for a specific ppi value. if it is desired to achieve a low foam-like pressure drop with a PLF then the PLF must be fabricated relatively thinner than the foam. This may or may not pose a problem related to reduced filtration efficiency. It is believed that PLF's may be effective filters even when relatively thin since the flow path is inherently tortuous and line-of-sight flow channels may be completely eliminated in a single unit cell. Conversely, thin foam samples run the risk of exposing straight-through flow channels. The filtration efficiency of PLF's will be an area of future study.

Liquid flow results of the same set of filters are found in Figure 4. Again, it can be seen that although the pore geometries are nearly the same for the foam and PLF, PLF flow rates are lower and more consistent. Standard deviations among the 30 ppi foam filters are on the order of 25%, while PLF's have a standard deviation of less than 1%.

To show the utility of the data mapped in Fig. 2, the flow rate of a 30 ppi foam filter was arbitrarily chosen to be matched with a designed PLF. The data in Fig. 2 was used to predict that a PLF

with 13 ppi should have flow properties similar to a 30 ppi foam of similar dimensions. One such 13 ppi filter was robocast. The robocast filter was created in less than five minutes, dried and fired in 24 hours. The resulting flow rate is recorded in Figure 4. In just one attempt the 13 ppi PLF does in fact lie within the standard deviation of the 30 ppi foam. .

It has yet to be determined if the change in pore size will have a large effect on filtration efficiency. Ceramic filters are used in molten metal filtration for two reasons. First, the high temperatures (>1000°C) rule out most materials. Second, the filters are attempting to filter out oxides. Since the molten metal being filtered is non-wetting to ceramic oxides, including the filter, small oxide particles in the melt are forced onto the ceramic filter, adding a physical adsorption factor to the mechanical entrapment aspect of filtration. Therefore, even though flow rates are matched by enlarging pore size, it is not necessarily detrimental to filtration.

The additional aspect that a SFF method based on a rapid prototyping machine may be used in conventional manufacturing is attractive. As mentioned before, the supplemental PLF may be fabricated in ~5 minutes. It is entirely feasible with this system to build multiple parts in parallel by adding additional tips. Therefore, if 20 parts were built in parallel, 240 parts per hour could be fabricated and fired by the next day, making the step to rapid manufacturing.

Summary:

Periodic lattice filters with good interlayer strength and having a face-centered-cubic structure were robocast. An array of internal pore geometries ranging from 47 to 12.5 ppi were created, and permeability constants were determined for these pore sizes with filter thickness ranging from 4 to 12 layers. Surface areas of these PLF's were calculated and are comparable to extruded honeycomb structures (>100 in^2/in^3). Pressure drops of PLF's were higher than foam structures, most likely due to the higher bulk densities and more tortuous pathways in PLF's. In one attempt, a 13 ppi PLF was designed to match the liquid flow rate of a 30 ppi foam. This example of tailored fabrication was completed by using a data map of known pore sizes and sample thickness, and calculating the filter geometry required for a specific flow rate. Part-to-part standard deviations of PLF's are on the order of 1% while foam filters are closer to 25%. Once filtration efficiency has been determined, the usefulness of PLF's in molten metal filtration will be known. However, it is clear that two shortcomings of foam filters have been addressed; the PLF's are much stronger and have more predictable flow characteristics.

Tables and Figures:

Table 1: Correlation of Fired Rod Diameter to PPI and Surface Area for PLF's.

Tip (μm)	Rod Diameter (μm)	Pores per Linear Inch	Surface Area (in^2/in^3)
410	349	47	134
510	434	25	99
840	714	17.5	60
1190	1012	12.5	42

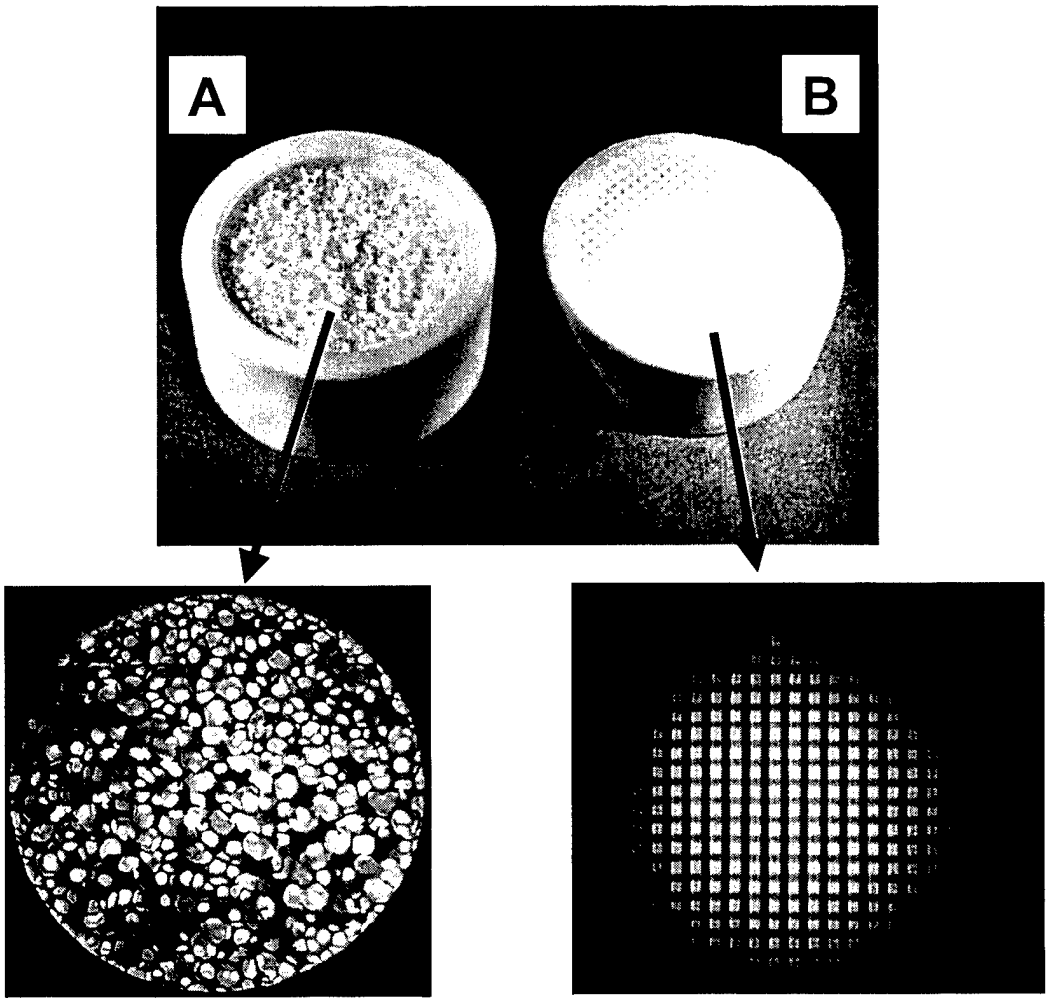


Figure 1: a) 30 ppi ceramic foam filter (courtesy of Selee Corp. SC). b) 30 ppi Robocast PLF. Back-lit images of each show random nature of a) and periodic nature of b).

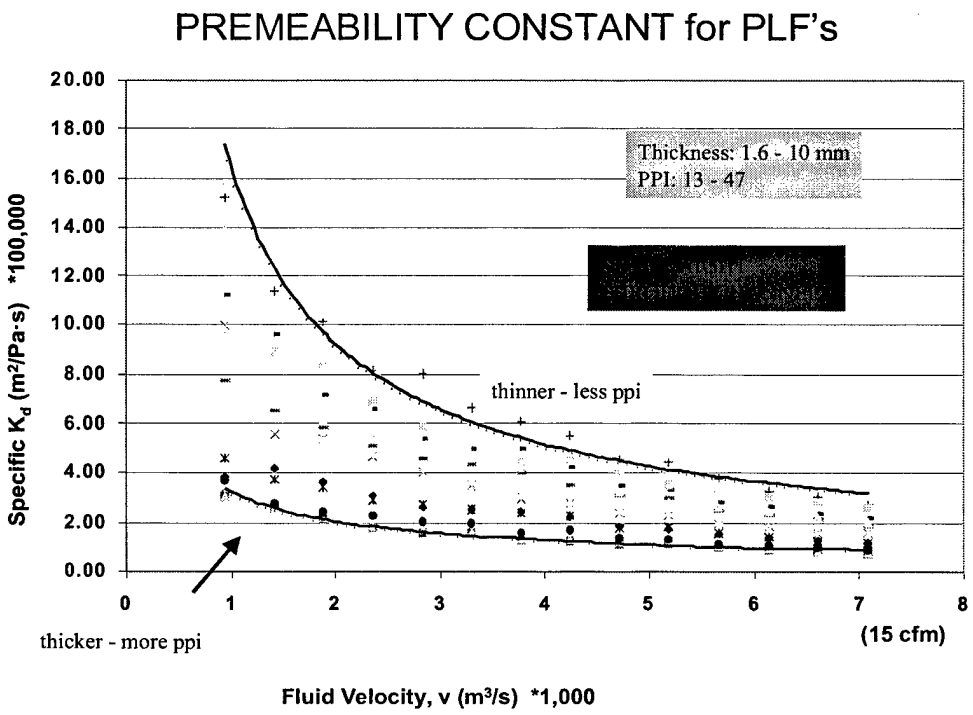


Figure 2: Permeability constants of and array of PLF's. the permeability 'constant' varies with flow rate most likely due to change in flow from turbulent to laminar through the filter.

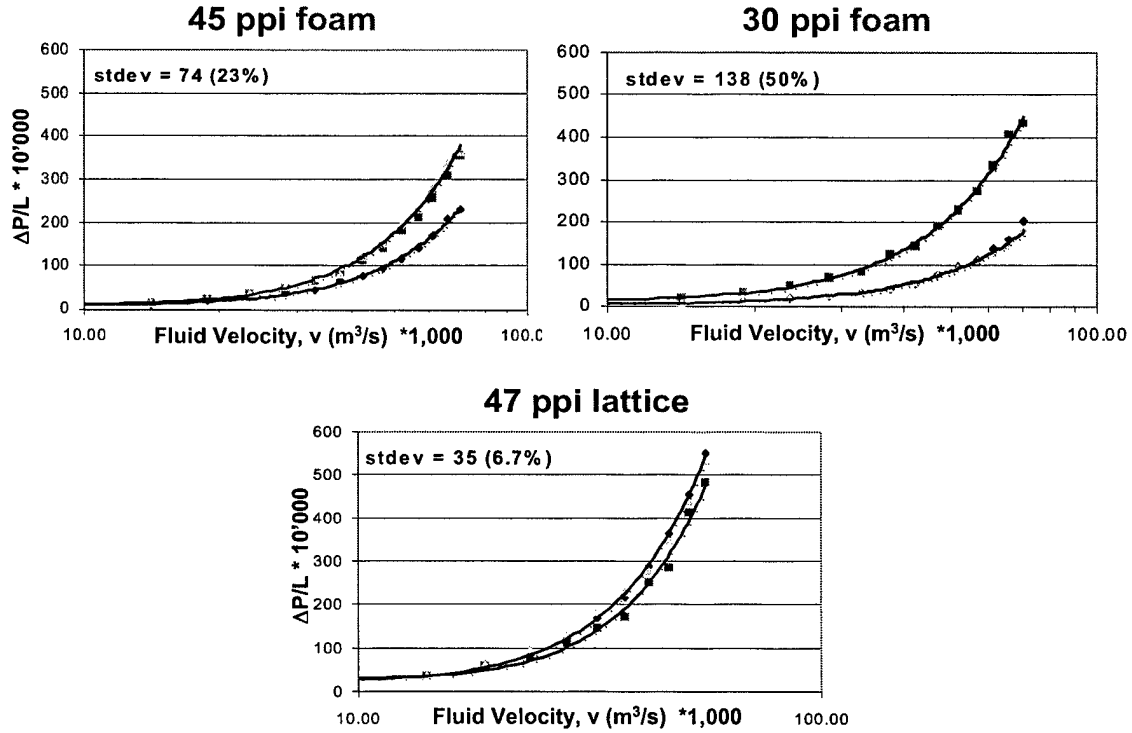


Figure 3: Pressure drop measurements of selected foam and PLF's with high standard deviations being prevalent in foam filters.

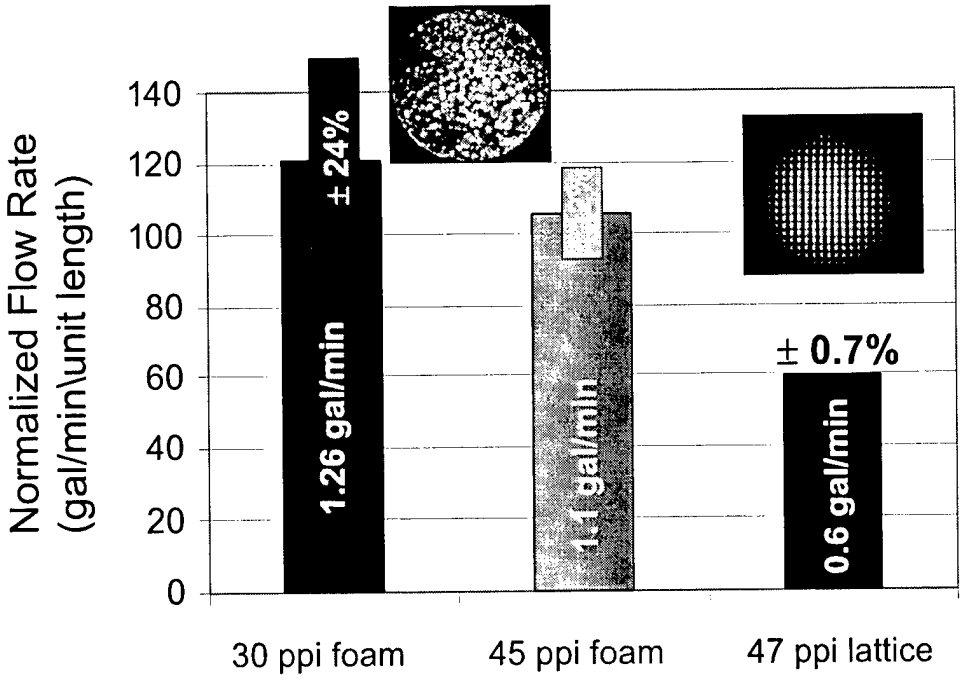


Figure 4: Flow rate measurements of selected foams. The matching PLF has a lower, more predictable flow rate.

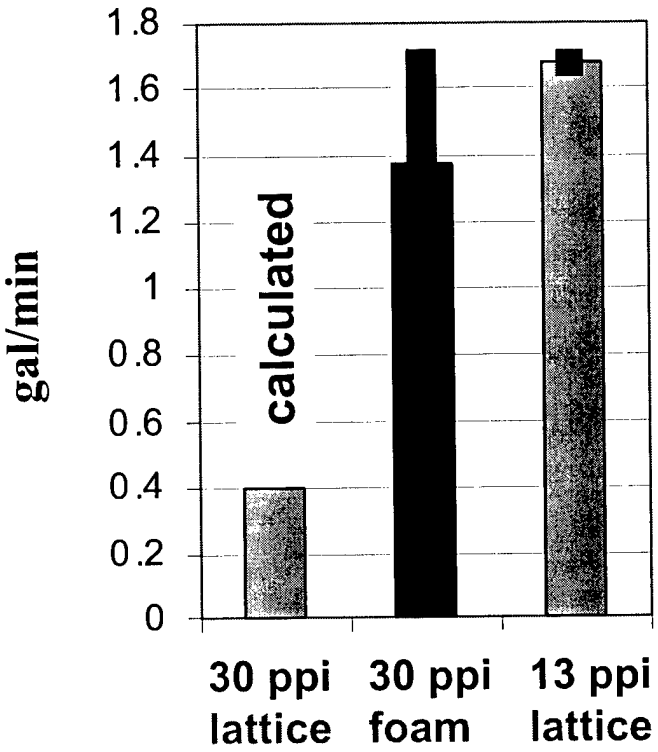


Figure 5: Calculations based on flow rate vs. PLF pore size were employed to match flow rates (in a single attempt) of a PLF to a 30 ppi foam.

SYNTHESIS OF A COMPACT TETRALATTICE HEAT EXCHANGER USING SOLID FREEFORM FABRICATION AND COMPARISON TESTING AGAINST A TUBE HEAT EXCHANGER

James R. Heidrich, Vito Gervasi, and Subha Kumpaty

Rapid Prototyping Research Center
Milwaukee School of Engineering
1025 North Broadway
Milwaukee, Wisconsin 53202

Abstract

The challenge for Solid Freeform Fabrication (SFF) lies in fabricating complex parts that are not possible by conventional manufacturing means. The goal was to apply SFF techniques to complex geometry heat exchangers. The heat exchanger structure is modeled after the covalently bonded carbon atoms of a diamond. The tetrahedron diamond lattice, or Tetralattice, is a repeating lattice unit that forms a network of channels to form the heat exchanger. Electroforming methods creating Tetralattice were applied to synthesize an air-oil compact heat exchanger. After production, the heat exchanger was tested and compared with an industry standard heat exchanger for performance evaluation.

Introduction

A heat exchanger is a device that facilitates transfer of heat from one fluid stream to another [1]. Power generation, heating and air conditioning, aerospace mechanisms, chemical processing, oil refining, and the operation of virtually all types of vehicles depend on heat exchangers of various configurations. This research is intended to develop a compact heat exchanger that is compact, lightweight, and reliable.

A heat exchanger gains the classification of a compact heat exchanger (CHE) if its characteristics include a surface area to volume ratio (β) greater than 212 ft^2/ft^3, or 17.68 in^2/in^3. In the case of an air-oil compact heat exchanger, the flow passage area on the air side must be many times greater than that on the liquid side. One method widely accepted in industry is to employ banks of round tubes with circular disk fins. This arrangement is referred as a Tube-Fin Heat Exchanger. The other classification of a compact heat exchanger is the Tube-Plate Heat Exchanger, where two parallel plates, separated by fins or spacers, define each channel. Both the tube-fin and the plate-fin are formulated from the shell and tube heat exchanger, which was used as the industry standard for the comparison testing stage of this research

Heat exchanger design has been limited due to conventional methods of manufacturing. Traditionally heat exchangers have been manufactured by creating channels for the internal fluids by extruding, stamping, or assembling machined parts with various hardware, such as fins, into a structure that is easy to manufacture. SFF unlocks the imagination to create complex networks for fluid flow and heat transfer, were previously teetering on the realm of impossible.

Objective

This work explores the synthesis of a Tetralattice (TL) air-oil compact heat exchanger (TL AOHE) directly from a CAD design using SFF processing and the Electroforming Process. A tube CHE was also manufactured to do a comparative analysis with the TL AOHE. The following four research objectives will be presented in the subsequent sections of this paper:

- Comparative testing theory
- Approach
  - Air-Oil Tetralattice CHE synthesis
  - Tube CHE synthesis
  - Comparison testing experimentation
- Results from comparison testing
- Discussion of results

Theory

While traditional modes of manufacturing lies in material removal, SFF lies in the additive realm of manufacturing. With this additive philosophy, it is possible to create complex geometries such as three-dimensional lattice structures. Tetralattice (TL) is one such structure, modeled after the covalent carbon bonds that form the tetrahedron characteristic of a diamond [2]. Arrays of TL units form complex structures as well as complex channels within objects. This complexity can result in unmatched characteristics. Recently, TL applications in the areas of gradient materials, conformal heating and cooling, transfer systems, and stress reductions are being discovered [3].

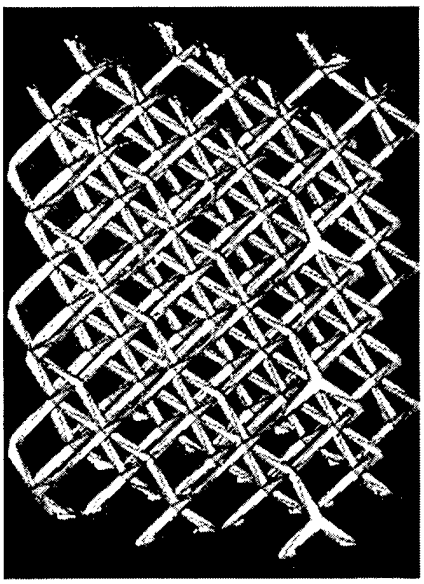


Figure 1. Tetralattice configuration for use in the TL AOHE

The structure shown in Figure 1 is the TL, which was created for the air-oil compact heat exchanger. This geometry is beneficial due to the high surface area to volume ratio (β), which is not the only factor, but an extremely important one when discussing compact heat exchangers.

In the next section of this paper, the TL AOHE is compared to a tube CHE. Both CHEs are manufactured in the exact same fashion. Each prototype of the compact heat exchanger has been designed to have approximately the same volume of internal fluid and was tested under the same conditions. A tube CHE, which is the basis of all CHEs, gives approximations of the overall effectiveness of the TL AOHE verses other compact heat exchangers in industry. The TL AOHE has a very high β ratio, 364.44 in^2/in^3, in comparison to a simple tube compact heat exchanger, 164.56 in^2/in^3, comprised of the same volume.

The hypothesis of this research is that the TL AOHE will have a much greater overall rate of heat transfer (Q) than the tube CHE due to the high β value. The rate of heat transfer (Q) was found through experimentation. The theoretical overall heat transfer coefficient (U) was also calculated to help evaluate the TL AOHE before testing. Through the aid of tables and convection heat correlation equations, the convective heat transfer coefficients (h) for both the inside and outside fluid flow of each compact heat exchanger were calculated. Substituting these values (h_i, h_o) into equation 1 below, the overall heat transfer coefficient (U) for both CHEs were found [4,5].

$$\frac{1}{UA_o} = \frac{1}{h_o A_o} + \frac{\ln(\frac{r_o}{r_i})}{2\Pi kL} + \frac{1}{h_i A_i} \qquad (1)$$

Note: k = Thermal Conductivity & L = specified length

The theoretical heat transfer coefficient (U) for the tube CHE ant TL AOHE are 0.550 KJ/hr*in^2*K and 1.059 KJ/hr*in^2*K respectively. Based on these values, the TL AOHE transfers heat at a rate that is 193% more efficient than the tube CHE. These two pieces of experimental and theoretical evidence help support the hypothesis of a greater rate of heat transfer for the TL AOHE. To verify the afore theory, working models of each heat exchanger were synthesized by various SFF techniques, using a material capable of withstanding high temperatures.

Approach

Utilizing SFF technology, a proprietary process was used to generate a bismuth expendable core. Cerro-bismuth was chosen due to its low melting point, as well as the alloy's high electric conductivity properties. These two factors are imperative in the synthesis of the copper TL AOHE.

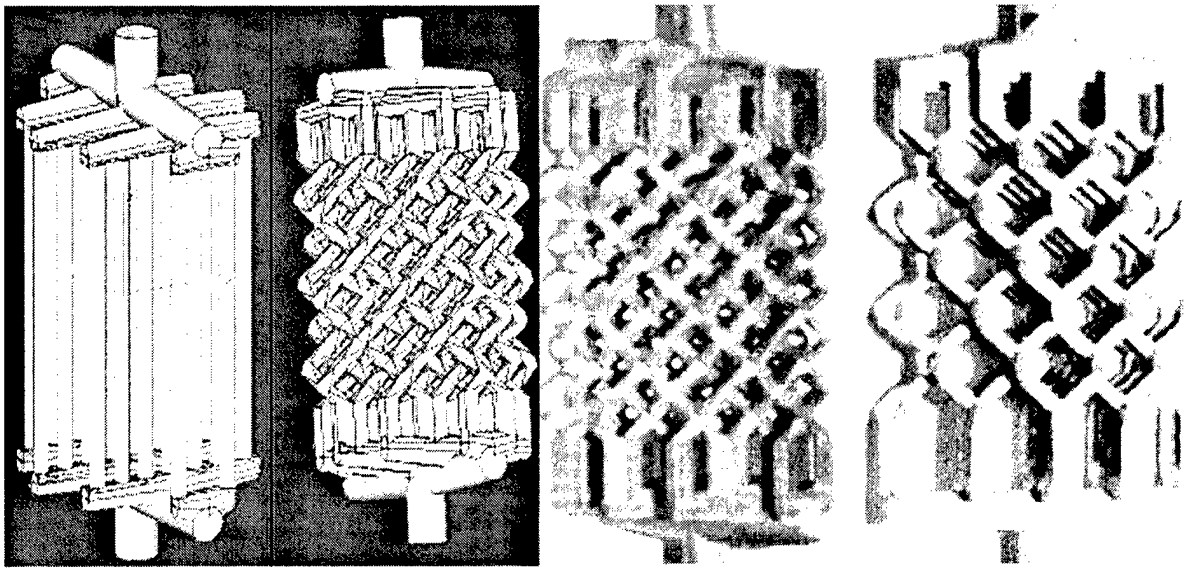


Figure 2. (Right) CAD Drawings of TL AOHE and tube compact heat exchangers, (Left) TL AOHE Bismuth Expendable Cores

To finish the CHEs formation, the electroforming process was used for the production due to its very high dimensional accuracy. The only limitation is the accuracy possible in machining the mandrel (expendable core), which can be in the order of 2.5 micrometers. With the aid of SFF, this process fit the description perfectly.

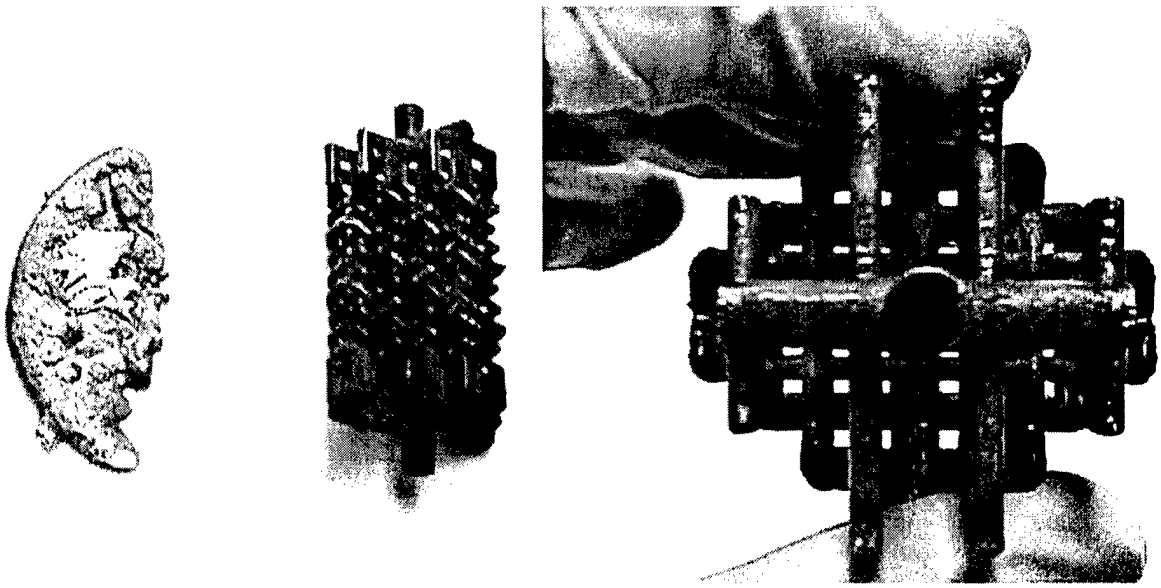


Figure 3. Expendable core removed, fully functional TL AOHE is synthesized

The electroforming process was used to apply a thermally conductive metal (copper) to the complex geometry. Electroforming is defined as the production or reproduction of articles by electrodeposition upon a mandrel or mold that that is subsequently separated from the electrodeposit [6]. A mandrel is a form used as a cathode in electroforming-in this case, it is the Cerro-Bismuth expendable core.

The first step before the actual plating experiment setup was to figure out how to plate the TL AOHE expendable core from a 360-degree range. A copper tube with copper end caps proved to be the best and most cost effective alternative. This configuration also serves as the anode, as well as the container, for the Copper Sulfate solution. The same process was used to manufacture the tube CHE. Both CHEs were electroplated until an average wall thickness of approximately 0.030" was achieved.

The final phase in the TL AOHE synthesis was the removal of the Cerro-Bismuth expendable core. The copper electroform is separated by melting out the expendable core, and at that point in the process, the TL AOHE is a fully functional apparatus. A vacuum process that was enacted at 82 degrees C (355 K), which is slightly above the melting point of the Cerro-Bismuth, removed the expendable core. After steady state temperatures were reached, heated glycerin was forced through the heat exchanger to remove the core. Figure 3 illustrates the results from the glycerol vacuum process.

Now with both CHEs fully functional, it is imperative to test both of these together to see how the TL AOHE scores against industry standards. The first step in testing was to find the rate of heat transfer, as well as the overall heat transfer coefficient for both the TL AOHE and the tube CHE. Knowing the inlet and exit temperatures associated with both fluids involved with the heat exchange process, the rate of heat transfer (Q), as well as the overall heat transfer coefficient (U), can be calculated using the equation below (2).

$$Q = U \bullet A \bullet \Delta T_m = \dot{m} \bullet \Delta T \bullet C_p \quad (2)$$

Where;

Q = rate of heat transfer
U = mean overall heat transfer coefficient
ΔT_m = log mean temperature difference
A = total heat transfer area
$\dot{m}$ = mass flow rate
C_p = specific heat

It is important to test both CHEs exactly in the same manner, since they were manufactured through the same process and for a meaningful comparison of their heat transfer characteristics. A wide variety of testing procedures exist in the advancement of heat exchangers. These range from evaluations of heat transfer, pressure drop, velocity, and

temperature distributions using small models to do acceptance tests of large full-scale units [7]. A medium between the cost of the test, and the value of the information to be obtained, were carefully balanced.

Both CHEs were manufactured to have relatively the same volumes, 0.020 in^3. The surface areas are not the same; this is due to the beneficial characteristics of the Tetralattice. The goal of the testing was ultimately to prove that the Tetralattice geometry is more effective design than that of a tube CHE.

The actual test setup was composed of a flow bench, convection oven, pump, pressure sensors, thermocouples, and a data acquisition unit. The thermocouples were setup at a specified distance from the inlet and outlet sides of both the hot water flow, as well as the cool airflow through the CHEs. Both of the inlet and outlet temperatures were recorded using a Data Acquisition/Switch Unit. The procedure consisted of pumping hot water through the heat exchanger and allowing the temperature to reach steady state, at that point the flow bench had to be initiated to blow cool air across the channels. Once again the temperatures were closely monitored to ensure steady state conditions were reached – of both air and water. Volumetric flow rates of both the air and the water were closely monitored as well. Both the TL and the tube CHEs were tested in the same fashion.

Two sets of experiments were conducted, one using water as the heated fluid, and the SLA CHEs for the test prototypes. The second round of test used glycerin as the heated fluid, and the actual copper CHEs (Refer to the Appendix for a picture of the actual CHEs used, as well as a picture of the testing setup).

Results From Testing

Table 1 illustrates the results from using the SLA prototypes of both CHEs. One outcome of this SLA prototype test is to see the feasibility of using SLA prototypes to get good estimates of heat transfer rate differences between heat exchanger designs. The results were recorded directly off of the data acquisition unit.

Table 1 Results from SLA CHE comparative testing

Tube Heat Exchanger				TL AOHE			
Thermocouple	Degree C	Degree K		Thermocouple	Degree C	Degree K	
Th, in	59.60	332.75		Th, in	59.60	332.75	
Tc, out	20.70	293.85		Tc, out	21.10	294.25	
Th, out	58.30	331.45		Th, out	58.10	331.25	
Tc, in	27.60	300.75		Tc, in	27.80	300.95	
	Qrts	Seconds	Qrt/Sec		Qrts	Seconds	Qrt/Sec
Flow Rate	2	86	0.0233	Flow Rate	2	99	0.0202
density (kg/cm^3)		0.001		density (kg/cm^3)		0.001	
Vol. Flow Rate (cm^3/hr)		79200		Vol. Flow Rate (cm^3/hr)		68933	
Mass Flow Rate (kg/hr)		79.2		Mass Flow Rate (kg/hr)		68.9	
Cp (KJ/Kg*K)		4.184		Cp (KJ/Kg*K)		4.184	

Table 2 shows the setup using the actual copper CHEs and glycerol as the heated fluid. Glycerol was used as the heated fluid in this particular part of the experiment due to the oxidation properties of pure copper.

Table 2 Results from copper CHE comparative testing

Tube Heat Exchanger				TL AOHE			
Thermocouple	Degree C	Degree K		Thermocouple	Degree C	Degree K	
Th, in	84.50	357.65		Th, in	79.00	352.15	
Tc, out	34.60	307.75		Tc, out	33.00	306.15	
Th, out	81.20	354.35		Th, out	74.02	347.17	
Tc, in	24.60	297.75		Tc, in	22.80	295.95	
	Qrts	Seconds	Qrt/Sec		Qrts	Seconds	Qrt/Sec
Flow Rate	2	25.22	0.0793	Flow Rate	2	45.58	0.0439
density (kg/cm^3)			0.00126	density (kg/cm^3)			0.00126
Vol. Flow Rate (cm^3/hr)			270071	Vol. Flow Rate (cm^3/hr)			149434
Mass Flow Rate (kg/hr)			340.3	Mass Flow Rate (kg/hr)			188.3
Cp (KJ/Kg*K)			2.39	Cp (KJ/Kg*K)			2.39
Pressure Drop (psi)			3	Pressure Drop (psi)			12

Note: the pressure drop is significantly higher for the TL AOHE

Analysis and Discussion of Results

The results of the comparison testing did in fact prove that the TL AOHE is a more effective design, but not to the extent that the theoretical values show. The theoretical calculations found the overall heat transfer coefficient to be 193% greater for the TL AOHE. Table 3 shows the rate of heat transfer (Q) values, as well as the overall heat transfer coefficients (U), for both of the CHEs.

Table 3. Heat Transfer Properties for SLA CHEs

Tube CHE	TL AOHE
Q = 430.79 KJ/hr	Q = 432.93 KJ/hr
U = 0.4326 Kj/hr*in^2*K	U = 0.480837 Kj/hr*in^2*K

From these values it is evident that each CHE SLA design has the same rate of heat transfer (Q) and also a relatively equal overall heat transfer coefficient (U). These results are not that surprising considering the low conductive properties of the SLA material. The SLA prototypes were an integral part of setting up the final test setup and establishing a solid testing procedure. Now that the SLA experiment has been conducted, it was necessary to compare the prototypes results against those of the actual copper CHEs. The Copper CHEs values of Q, and U, are shown in table 4.

Table 4. Heat Transfer Properties for Copper CHEs

Tube CHE	TL AOHE
Q = 2683.87 KJ/hr	Q = 4050.20 KJ/hr
U = 1.7554 Kj/hr*in^2*K	U = 1.7560 Kj/hr*in^2*K

Based on the copper CHE testing, the TL AOHE transfer heat at a 150.91% more effective rate than the tube CHE. That difference in heat transfer rates correlates well with theoretical values. The TL AOHE also has a slightly higher overall heat transfer coefficient (U), which confirms the theory, at least qualitatively. Both percentage values of the overall heat transfer coefficients result in values that are 48% different than those calculated theoretically. This difference is contributed to the substantial pressure drop that is associated with the TL AOHE. The mass flow rate for the tube CHE was almost twice that of the TL AOHE. The theoretical values assumed equal mass flow rates. This problem area will have to be compensated for future testing. Future complex geometries for heat exchangers will have to be planned with the increased pressure drop in mind.

Conclusion

Synthesis of complex three-dimensional functional compact heat exchangers is now possible using SFF (expendable core), and the electroforming processes. A Tetralattice air-oil compact heat exchanger was successfully synthesized and compared to a tube CHE encompassing the same internal fluid volume to evaluate its feasibility. Based on a high β value and a high theoretical overall heat transfer coefficient (U), the TL AOHE was thought to be a more effective heat exchanger than the tube CHE. This initial theory was proved correct by comparing both SLA and copper CHEs of both designs. In both cases the overall heat transfer coefficients were slightly higher for the TL AOHE. The copper TL AOHE transfers heat at a 151% more effective rate. Though data from the SLA CHE were inconclusive, they were an essential part of establishing an initial test setup and procedure.

Problems with the TL AOHE include high-pressure drops that result in a lower mass flow rate. This low mass flow rate could explain the 48% difference from theoretical overall heat transfer coefficient (U) values. The pressure drop will have to be accounted for in future complex geometry heat exchangers. The TL configuration could be "stretched" out in the z direction to decrease some of the sharper angles, which could lower significant pressure drops within the heat exchanger.

The next step in the attempt to reach the perfect beta value is to utilize Rapid Prototyping technology to adequately model the lung vasculature. Nature's perfect design has a specific surface that is around two orders of magnitude greater than the best compact heat exchanger designs [8].

Acknowledgements

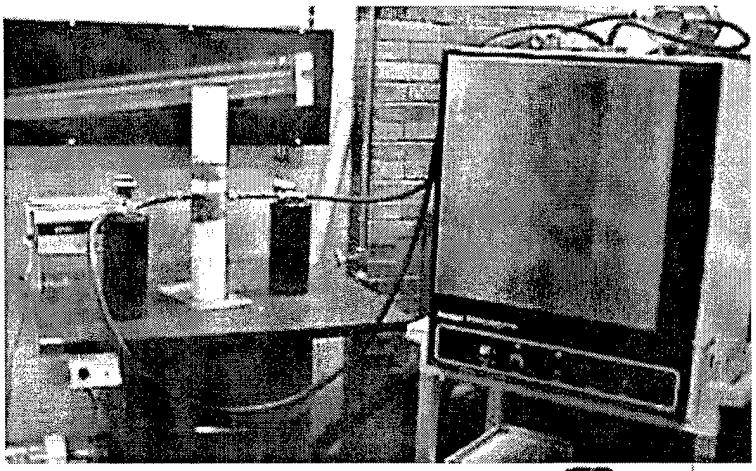
The author would like to express appreciation to the National Science Foundation and the Milwaukee School of Engineering for the opportunity to be a part of the 2000 Research Experience for Undergraduates (REU) program. I would also like to thank Vito Gervasi for

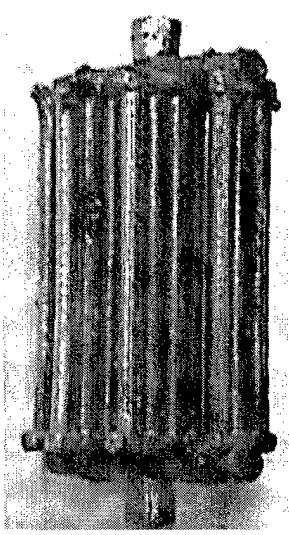
giving me the freedom to take my own research paths; Ann Bloor for support; and to Subha Kumpaty for the advice on Heat Transfer.

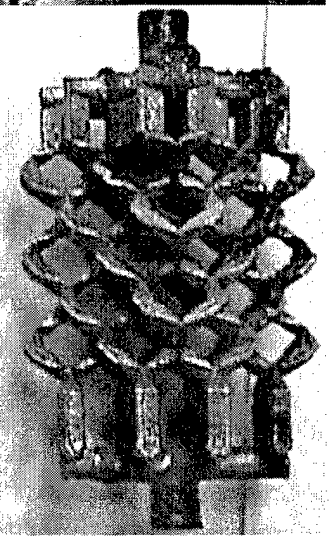
References

(1) Mills, A.F., *Heat Transfer*, 2nd ed., Upper Saddle River, New Jersey: Prentice-Hall, 1999.
(2) "http://www.britannica.com/bcom/eb/article/2/0,5716,118742+24,00.html" (7/01/00).
(3) Gervasi, V.R., Crockett, R.S., "Composites With Gradient Properties From Solid Freeform Fabrication", *1998 Solid Freeform Fabrication Symposium Proceedings*, Austin, Texas 1998.
(4) Rolle, Kurt C., *Heat and Mass Transfer*, 1st ed, Upper Saddle River, New Jersey: Prentice-Hall, 2000.
(5) "http://chemengineer.about.com/science/chemengineer/library/weekly/aa020298.htm"
(6) Gervasi, V.R., "Net Shaped Composites Using SLA TetraCast Patterns", *1997 Solid Freeform Fabrication Symposium Proceedings*, Austin Texas 1997.
(7) Lowenheim, Frederick, A., *Electroplating*, McGraw Hill, Inc., 1978.
(8) Frass, Aurthur R., Heat Exchanger Design, 2nd ed., New York: Wiley-Interscience Publications, 1989.

Appendix: Copper CHE Testing Pictures







this page intentionally blank

APPLICATIONS OF SOLID FREEFORM FABRICATION AT THE NAVAL RESEARCH LABORATORY

J. P. Thomas†, B. A. Bender†, A. Piqué†, K. P. Cooper†, R. J. Rayne†, and A. C. Richardson‡

†: Materials Science and Technology Division, Naval Research Laboratory, Washington, DC 20375
‡: Capt. USN, Department of Radiology, National Naval Medical Center, Bethesda, MD 20889

Abstract

Solid Freeform Fabrication (SFF) and related techniques are used at the Naval Research Laboratory (NRL) for a variety of materials related investigations. Research and applications conducted over the past few years are described including: Helisys Laminated Object Manufacturing System (LOMS) fabrication of: ceramic piezoelectric actuators, tooling for multifunctional materials, and anatomical prototypes for surgical visualization; fabrication of mesoscale electronic and sensor components using a laser forward transfer direct write technique; and visualization of complex, 3-D microstructures using a Stratasys Fused-Deposition Modeler. The paper closes with a brief overview of future SFF related work at the NRL.

Introduction

Solid Freeform Fabrication (SFF) and related techniques are used at the Naval Research Laboratory (NRL) for a variety of materials related investigations. This paper will describe several recent SFF projects conducted using an NRL Helisys Laminated Object Manufacturing System (LOMS Model 2030H) or a custom NRL built laser-based, direct material writing system known as: "Matrix-Assisted-Pulsed-Laser-Evaporation Direct-Write" (MAPLE DW). Use has also been made of the Stratasys Fused-Deposition Modeler (FDM) in some collaborative efforts.

We begin with a description of several LOMS-based applications including: ceramic piezoelectric actuator fabrication, rapid tooling for multifunctional unmanned air-vehicle components, and anatomical prototyping for surgical visualization. Fabrication of mesoscale electronic and sensor components using the MAPLE DW system is described next followed by a description of the use of FDM for creating a physical model for complex, 3-D material microstructures. We conclude with a brief overview of future SFF related work at the NRL.

Laminated Object Manufacturing System Applications

Piezoelectric Actuators

Advancing the development of high authority (i.e., high force and displacement) piezoelectric actuators through the use of innovative designs and advanced fabrication techniques is a critical enabling step for military systems [Wu et al., 1999]. The NRL has been involved in a program to develop the Navy's SFF capability for rapid R&D of novel tailored actuators as a means of accelerating their insertion into fleet applications.

One such novel actuator, the telescoping actuator, patented by Lewis and Kahn [1997] (Figure 1), serves as an active element in machinery mounts for noise (acoustic signature) reduction. The telescoping design provides for displacement amplification with an output force proportional to the cross-section of the smallest element. These actuators are used in constrained spaces of varying size and have varying power/displacement requirements. Another actuator,

designed for active payload vibration suppression during spacecraft launch, consists of a thin ceramic piezoelectric ring with small axial holes along the circumference for weight savings.

Actuators can be fabricated using an injection-molding process, but this is too expensive and time consuming for multiple design evaluations. Instead, a modified LOMS process has been used to rapidly fabricate functional components for direct evaluative testing. Griffin et al. [1994] document some of the early efforts to adapt the LOMS technique for fabricating ceramic (alumina) components.

The telescoping actuators are built by integrating the lamination of thin lead-zirconate-titanate (PZT) embedded polymer sheets [Bender et al., 2000] with precise laser cutting by the LOMS. Engineering of the ceramic-polymer sheet stock, referred to as ceramic tape, is critical to the success of the process. The ideal ceramic tape is stiff enough to avoid excessive distortion during handling, amenable to laser cutting, and suitable for lamination via solvent welding, while possessing appropriate firing properties [Cawley and Liu, 1998].

PZT tapes formulated with a polymer binder system optimized for alumina tapes were tried first. These tapes were very flexible due to the large amount of plasticizer that was added to allow mixing with the high specific gravity PZT. Microstructural characterization of the tape using scanning electron microscopy (SEM) showed non-uniform distributions of binder and PZT with PZT-free regions and a vertical density gradient (porous to dense going from top to bottom). Actuators made with these tapes were badly cracked and deformed (Figure 2A). The cracking and deformation were greatly reduced (Figure 2B) using tapes with PZT-optimized binder, which facilitates more uniform PZT powder and binder distributions within the tape.

Selection of an appropriate solvent for lamination welding is vital to achieving a good bond between the tape layers. The solvent must act as a tackifier, enabling bonding between the layers, and it must have a relatively low vapor pressure so that it doesn't evaporate before affecting the lamination process. Also, its action must be limited to the interface region. Otherwise it can diffuse to the laser-cuts and cause partial rebonding, which makes decubing of unwanted material from the build more difficult.

Previous research indicated that a light spray of propanol led to satisfactory lamination [Bender et al., 2000]. On closer examination, however, small interlaminar debonds were observed scattered throughout the actuator. One reason for the presence of these defects was uneven evaporation of the propanol. Longer spray times were tried in an attempt to prevent uneven distribution of the propanol, but the presence of too much solvent created small pockets of liquid that could not be eliminated during lamination leading to even larger interlaminar defects. A low vapor pressure solvent, iso-amyl alcohol, was tried as a laminating solvent. Uniform distribution of the solvent was observed, and after firing, fewer defects were observed. However, the iso-amyl alcohol softened the ceramic tape binder too much making decubing difficult. A solution was found that required adding 10% polyethylene glycol (PEG- MW 200) to the propanol to retard the evaporation, leaving behind a thin tacky interlaminar film. SEM characterization revealed a continuous interlaminar film ~1 μ m in width was left behind with no evidence of interlaminar defects. The PEG has time to dissipate away from the interfaces during binder burnout leading to low defect actuators after firing (Figure 2B).

Understanding the important SFF process parameters related to the PZT tapes and solvent lamination has allowed us to develop adequate process control, which leads to dimensional control and property reproducibility. As a result, this LOMS-based SFF process will facilitate more rapid R&D of novel ceramic piezoelectric actuators.

Rapid Tooling for Multifunctional Materials Fabrication

The LOMS machine has also been used to make molds and patterns for use in fabricating multifunctional fuselage prototypes for a micro air vehicle (MAV). We are integrating the MAV's structure and battery functions into one material to reduce weight and increase flight-time [Thomas et al., 2001]. The novel structure-battery materials being developed for this application are comprised of a thin-layer, polymeric lithium-ion battery material with structural additives and a barrier-layer packaging[1]. Molds and patterns are needed to form the composite structure-battery material "package" into the complex, 3-D curved fuselage shell shape.

A LOMS pattern of the MAV fuselage and the corresponding molds for the upper and lower fuselage halves are shown in Figure 3. These "tooling" components are made from standard Helisys paper (LPH 042). After decubing, they are sanded smooth and then epoxy coated for stiffening and strengthening at structure-battery fabrication temperatures ($80°C$ max). The tooling will be used in a vacuum-bag-forming operation to mold the structure-battery materials into the MAV fuselage form. Three types of structural enhancement are being considered. The first involves adding polypropylene (PP) or polyethylene (PE) films internally and bonding with the battery material. The second will increase the thickness of the PP or PE in the barrier-layer packaging to provide the required shape stiffness. The third type uses an epoxy-fiber shell. All three concepts require MAV fuselage molds/patterns for vacuum-forming at elevated temperatures ($80°C$ max) to affect interlayer bonding and shaping of the thermoplastics and curing of the thermosets. LOMS technology allows for rapid creation of complex tooling for this advanced development demonstration of multifunctional structure-power materials concepts.

Anatomical Prototyping for Surgical Visualization

Recently, we used the LOMS to create a very detailed anatomical prototype of a human spine with severe scoliosis from CT-scan digital data (Figure 4). SFF models are routinely used in medicine today for visualization and planning of complex surgical procedures, physician training, and informing/educating the patient, and that is the intended purpose of this model. Several fractional-scale models of the spine were made at the National Naval Medical Center using their Stratasys Fused-Deposition Modeler (FDM). Due to the complexity of the deformed spine structure, a full-scale model was desired, but model sizes are limited to 10 inches for this particular FDM machine. The build envelope for the NRL LOMS was large enough to fabricate the full-scale model of the spine, and it exhibited an added advantage of providing outstanding contrast on the various detailed skeletal features.

The spine prototype, shown in Figure 4, was fabricated as a solid block $18\times7\times5$ inches in dimension created with approximately 1070 layers of Helisys LPH 042 paper stacked in the 5 inch dimension. The build process took about 70 hours due to the fine-scale features in the model and the small crosshatching size (0.25×0.50 inch). Several days were spent on pre- and post-build tasks and *.StL file manipulations, and decubing took approximately 30 hours spread-out over several weeks.

The software MIMICS[2] was used to create the *.StL file from the CT-scan data. The data was filtered using triangle reduction, but the resulting *.StL file was still too large at 68.8 Mb for

---

[1] The battery is ~ 0.5 mm thick in the bicell configuration [Thomas et al., 2001], and was developed in the early 1990's by Telcordia Technologies [Gozdz & Warren, 1997]. The packaging is a multilayer polymer-aluminum heat-sealing laminate (~0.1 to 0.5mm thick) that serves as a chemical/moisture barrier layer.

[2] http://www.materialise.be/mimics/

the LOMSlice software. We used Cyberware's Decimate Polygon Reduction Software[3] to reduce the *.StL file ~50% to 37.7 Mb, which was manageable by LOMSlice. The software works by coalescing polygons of "little importance" for accurate model representation via elimination of select vertices.

Matrix Assisted Pulsed Laser Evaporation Direct Write (MAPLE DW)

A laser-based direct material writing technique known as: "matrix assisted pulsed laser evaporation: direct write" (MAPLE DW) has been developed here at the NRL. This system, which builds on recent developments in materials and laser-based materials processing, provides a radically different method of fabricating mesoscale inorganic structures for electronic and sensor device applications and organic structures for unique biological systems applications [Piqué et al., 1999; Fitz-Gerald et al., 2000; Chrisey et al., 2000a]. An individual electronic component or an array of sensors can be built conformally over the surface of almost any substrate in air and at room temperature using MAPLE DW. This capability opens the door for the rapid prototyping and testing of customized designs.

The material deposition process begins in MAPLE DW when a high-repetition-rate, 355 nm UV laser beam is focused on a material "ribbon." Upon heating from the laser pulse, the build material transfers to the receiving substrate where it forms an adherent coating. The ribbon is a transparent tape that supports a 1-10μm thick layer of build material on one side, analogous to a conventional ink typewriter ribbon. A schematic of the process is shown in Figure 5.

Using MAPLE DW, we can fabricate electronic circuit patterns with feature resolutions on the order of 10μm by synchronously moving the ribbon to a fresh, unexposed region, and the receiving substrate approximately one beam diameter. The individual mesoscopic 3-D pixels or voxels of electronic material, one voxel transferred per laser shot, are assembled into the desired 3-D pattern. Alternating the ribbon material between a metal and a dielectric, for example, allows us to fabricate three-dimensional multilayer structures like parallel-plate capacitors.

The MAPLE DW system can also be operated in a laser micromachining mode or a laser sintering mode by removing the ribbon. This provides the capability for etching grooves or vias in the substrate, or surface annealing, sintering, or etching of individual components to improve their performance or dimensional accuracy. See, for example, Pique et al. [2000] and Chrisey et al. [2000b] for improvements to the electronic properties of oxide ceramics. For infrared (IR) laser wavelengths (1 to 10μm), the penetration depth is on the order of microns for a variety of materials allowing the benefits of higher-temperature processing on thermally sensitive substrates. Ultimately, laser annealing might allow the decomposition and reaction of organometallic precursors for transfers onto substrates that cannot tolerate processing at temperatures above the boiling point of water, (e.g., biomaterials). It might also allow some degree of bulk diffusion and sintering of ceramics for transfers onto substrates that can tolerate heating to a few hundred degrees for a short period of time (e.g., polyimide).

Advances in the research community's understanding of new materials and laser-material interactions have driven the progress evident in direct writing of electronic materials. On the other hand, recent advances in the direct writing of biomaterials have been driven by progress in UV-laser based transfer technology. MAPLE DW in particular can be an extremely gentle process. Using ribbons made of an aqueous composite mixture, we have been able to transfer patterns of viable bacteria such as E. coli onto various substrates [Ringeisen et al., 2001].

[3] http://www.cyberware.com/products/decimate.html

The capabilities offered by the MAPLE DW technique have opened up the possibility of integrating bio-structures with electronic devices on the same substrate for rapidly prototyping unique cell-based biosensors and bio-electronic interfaces. Clearly, the ability to generate components on demand, any place, on any substrate, and in a matter of minutes instead of weeks, provides us with a unique opportunity for bringing new designs to life that can only be dreamed of with today's manufacturing techniques.

Fused Deposition Modeling for Microstructure Visualization

An SFF model for the microstructure of a steel alloy is shown in Figure 6A. This model was fabricated using the Stratasys Fused Deposition Modeling (FDM) process[4]. It depicts a 3-D austenite grain within the alloy where the white solid represents the cementite decorated grain boundary and cementite precipitates and the empty space represents the austenite phase. The material is a Fe-1.3%C-13%Mn model steel alloy that was isothermally heat-treated at 650°C for 50 sec. A series of 128 images of the grain was taken by optical microscopy from serial sections at 0.2μm depth increments (Figure 6B). They were read into a Solid Model Builder program developed by the University of Michigan [Marsan and Dutta, 1996]. Each image was used to generate one slice for the FDM of the solid model.

The microstructures were generated and analyzed by Kral et al. [2000] at the NRL. This work was performed to develop better understanding of the true 3-D morphology and distribution of the solid-state precipitates in structural metal alloys. This understanding is important for the control of microstructure features that have a direct influence on the mechanical properties of components. Microstructural characterization via conventional microscopy provides only 2-D views from which 3-D information can be inferred, often erroneously. Three-dimensional analysis of microstructures gives accurate information on the nature of the grain boundaries, the origin of the precipitates, and the shape, dimensions and distribution of the precipitates. This information makes quantification of microstructure and its relation to material behavior more meaningful.

Three-dimensional microstructures have been mathematically reconstructed using the serial sections and can be viewed in 3D using a Silicon Graphics Imaging system. The image can be rotated and translated as it is studied. However, 3D microstructures are best studied when viewed as solid models. Microstructures inherently have complex geometries and their solid models can only be reproduced by SFF techniques thus highlighting a significant benefit of the technology.

Future Work at the NRL

Continued research on the MAPLE DW process and capabilities and use of the LOMS for rapid fabrication of ceramic-based components is planned. The anticipated addition of a tape-casting machine for creating ceramic-polymer precursor materials for the LOMS will lead to a number of new materials related investigations. There is also potential interest in investigating the use of SFF related techniques for creating hierarchically structured materials with enhanced and multifunctional performance. Examples might include: tailoring the fracture resistance of ceramic-polymer composites and the dielectric properties of capacitor ceramics through hierarchical patterning.

---

[4] In collaboration with the University of Michigan-Ann Arbor.

Acknowledgements

Support for this work from DARPA, Office of Naval Research, and the Naval Research Laboratory Core Research Program is gratefully acknowledged.

References

Bender, B., Rayne, R., and Wu, C., "Solid Freeform Fabrication of a Telescoping Actuator Via Laminated Object Manufacturing", *Ceram. Eng. Soc. Proc.,* Vol. 21, pp. 143-150, (2000).

Cawley, J. D., and Liu, Z., "Applying Tape Casting to Layered Manufacturing Processes", *Ceram. Ind.,* Vol. 128, pp. 42-48, (1998).

Chrisey, D., Piqué, A., Fitz-Gerald, J., Auyeung, R., Wu, H., and Duignan, M., "New Approach to Laser Direct Writing Active and Passive Mesoscopic Circuit Elements", *Appl. Surf. Sci.*, Vol. 154-155, pp. 593-600, (2000a).

Chrisey, D., Pique, A., Modi, R., Wu, H., Auyeung, R., and Young, H., "Direct writing of conformal mesoscopic electronic devices by MAPLE DW", *Appl. Surf. Sci.*, Vol. 168, pp. 345-352, (2000b).

Fitz-Gerald, J., Piqué, A., Chrisey, D., Rack, P., Zeleznik, M., Auyeung, R., and Lakeou, S., "Laser Direct Writing of Phosphor Screens for High-Definition Display", *Appl. Phys. Let.*, Vol. 76, pp. 1386- , (2000).

Gozdz, A., and Warren, P., "Method for Making Laminated Rechargeable Battery Cells", US Patent Number 5,840,087, November 24, 1998.

Griffin, C., Daufenbach, J., and McMillin, S., "Desktop Manufacturing: LOM vs Pressing", *Amer. Ceram. Soc. Bull.,* Vol. 73, pp. 109-1113, (1994).

Kral, M., Mangan, M., Spanos, G., and Rosenberg, R., *Materials Characterization*, Vol. 45, pp. 17-23, (2000).

Lewis, D., and Kahn, M., "High Authority Telescoping Actuators", US Patent pending, Navy Case #77862, May 1997.

Marsan, A., and Dutta, D., *J. Mech. Design*, Vol. 118, pp. 412-418, (1996).

Piqué, A., Chrisey, D., Auyeung, R., Fitz-Gerald, J., Wu, H., McGill, R., Lakeou, S., Wu, P., Nguyen, N., and Duignan, M., "A Novel Laser Transfer Process for Direct Writing of Electronic and Sensor Materials", *Appl. Phys. A-Mat. Sci. & Proc.*, Vol. 69, pp. S279-284, (1999).

Piqué, A., Fitz-Gerald, J., Chrisey, D., Auyeung, R., Wu, H., Lakeou, S., and McGill, R., "Direct Writing of Electronic Materials Using a New Laser Assisted Transfer/Annealing Technique", *Proc. SPIE*, Vol. 3933, pp. 105- , (2000).

Ringeisen, B. et al., *Biomaterials*, accepted for publication.

Thomas, J., Qidwai, M., Matic, P., Everett, R., Gozdz, A., Culver, D., Keennon, M., and Grasmeyer, J., "Composite Materials with Multifunctional Structure-Power Capabilities", in *Proc. 16th Amer. Soc. Comp.*, Virginia Tech, Sept. 2001, to appear.

Wu, C., Lewis, D., Kahn, M., and Chase, M., "High Authority, Telescoping Actuators", *Proc. SPIE*, Vol. 3674, pp. 212-219, (1999).

Figures

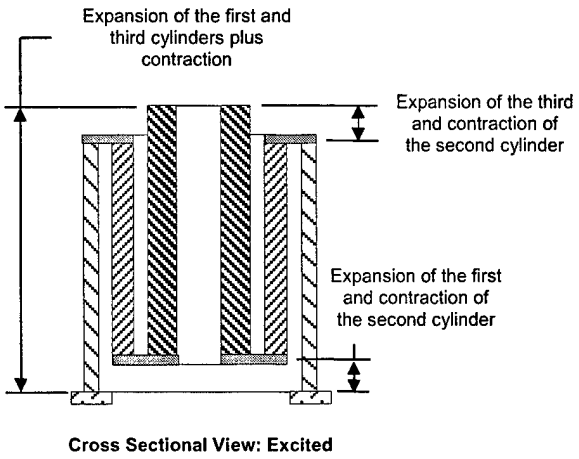


Figure 1: Schematic cross-sectional view of the telescoping actuator.

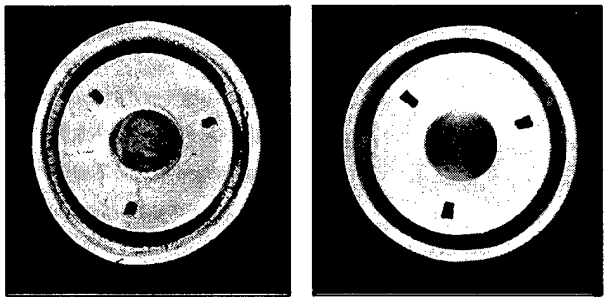


Figure 2A and 2B: Optical micrographs showing a bottom view of the consolidated telescoping actuators made with an unsatisfactory tape formulation (A) and a satisfactory tape formulation (B). Note that the outer cylinder diameter is 2.5 cm.

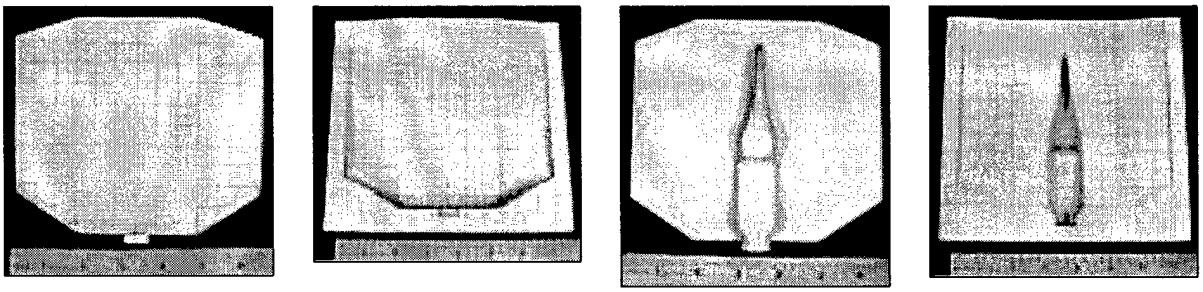


Figure 3. LOMS pattern and molds for a micro-air vehicle fuselage.

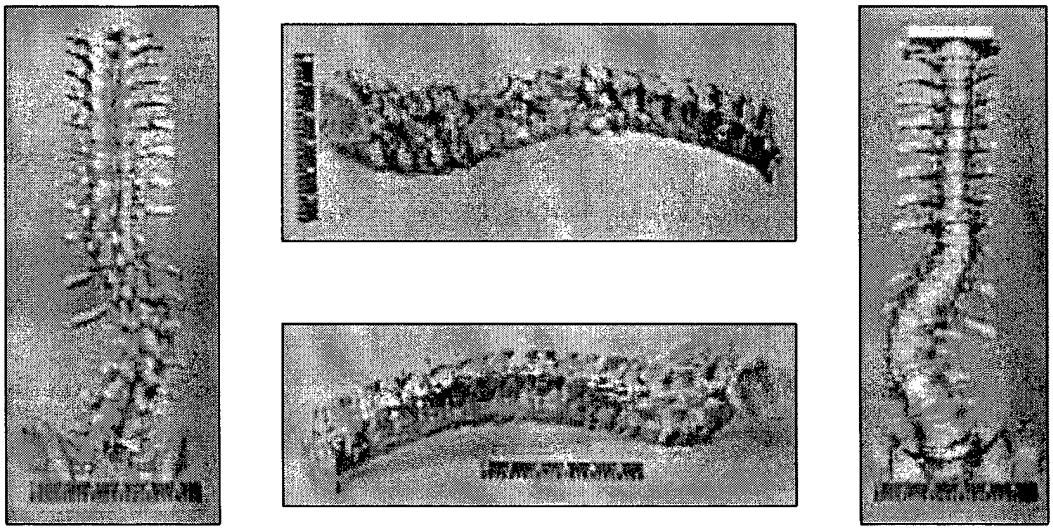


Figure 4. Human spine model created with the LOMS from the CT-scan data.

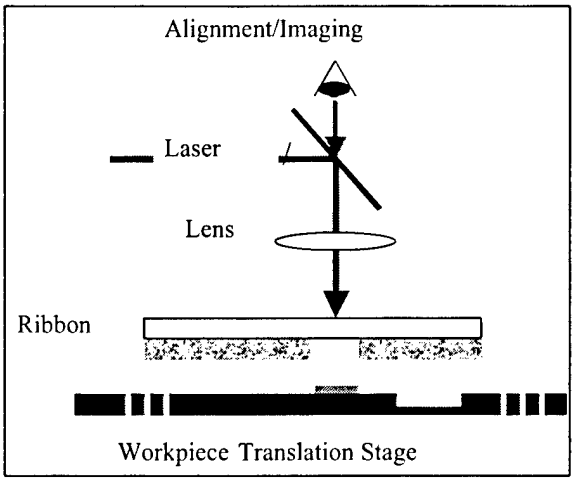


Figure 5: Schematic diagram of the MAPLE DW process.

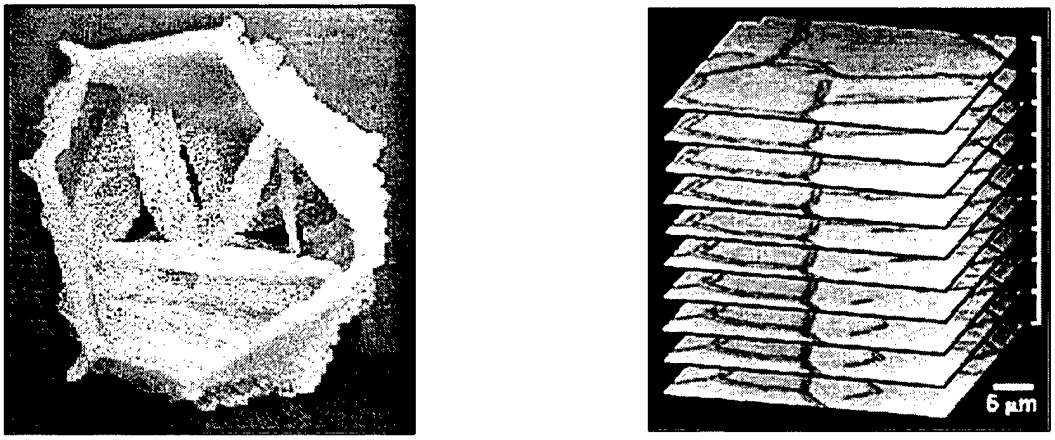


Figure 6A and 6B: (A) FDM model of cementite precipitates and austenite grain in a high carbon steel, and (B) a portion of the stack of 250 images of optical microstructures used as slices for the FDM process.

Solid Freeform Fabrication:

An Historical Perspective

Joseph J. Beaman

The University of Texas

Austin, Texas

Today, several new technologies are capable of producing complex freeform solid objects directly from a computer model of an object without part-specific tooling or knowledge. They are, for the most part, additive processes and have been termed *Solid Freeform Fabrication.* In this paper, an historical perspective is given for this relatively new field.

Symposium History

The name Solid Freeform Fabrication (SFF) grew out of the name for a symposium at the University of Texas at Austin (UT). This group was composed largely of representatives from companies forming beta sites for the SLS machines being designed and built by DTM. In 1987 and 1988, meetings of the group were held both on the UT campus and at host industrial sites, including Ford and United Technologies Research Center. Based on the successful discussions and presentations at these meetings, under the leadership of Harris Marcus of UT, a formal SFF Workshop of researchers in the area was held in 1989 at UT. Held in a conference room in the College of Engineering, approximately 20 researchers presented 7 formal presentations of research and development in the area of SLS were given by the academic participants over 1.5 days. The formal presentation format of the Workshop was well received by the small group. Encouraged by this, an organizing committee was formed to offer in 1990 an open research conference on SFF. This meeting was the first SFF Symposium, held in Austin on August 6-8, 1990. Seventeen talks were presented with 54 participants at the meeting. Ten presentations were by the UT group with external representation by notable researchers including Ely Sachs, Mike Cima, Paul Fussell, Lee Weiss, Fritz Prinz and Dick Chartoff. The first proceedings of the meeting were hardbound published and were 187 pages long. At this meeting, and as what turned out to be the operating guideline for all the following SFF Symposium, no explicit commercial talks or presentations were given. The spirit of the meeting was for open exchange to promote the research and development of the many SFF approaches that were being investigated.

The meeting grew each year to a steady state attendance of about 150 people over the next seven years. In that period, the diversity of topics expanded considerably to a wide variety of techniques and processes. Harris Marcus chaired the organizing committee for the 1990 through 1995 meeting. Since 1996, David Bourell has chaired the organizing committee. The focus of the meeting has been on reporting of current research in the field.

The SFF Symposium is the longest continuous annual meeting in the field of freeform fabrication and is one of the oldest such forums. In 2001, the 12th Annual SFF Symposium hosted almost 130 participants from 13 countries. Approximately one third of the meeting attendees are students. The remaining participants represented foreign and domestic universities (50%) and industry (35%), with the balance from national and government laboratories. The 2001 proceedings contains almost 70 papers.

Prehistory of Solid Freeform Fabrication

Of course, Solid Freeform Fabrication did not magically appear in the 1980's. It grew out of at least two early roots: topography and photosculpture.

Topography

As early as 1890, Blanther (Blanther, 1892) suggested a layered method for making a mold for topographical relief maps. The method consisted of impressing topographical contour lines on a series of wax plates and cutting these wax plates on these lines. After stacking and smoothing these wax sections, one obtains both a positive and negative three-dimensional surfaces that correspond to the terrain indicated by the contour lines. After suitable backing of these surfaces, a paper map is then pressed between the positive and negative forms to create a raised relief map. This is shown in Figure 1.

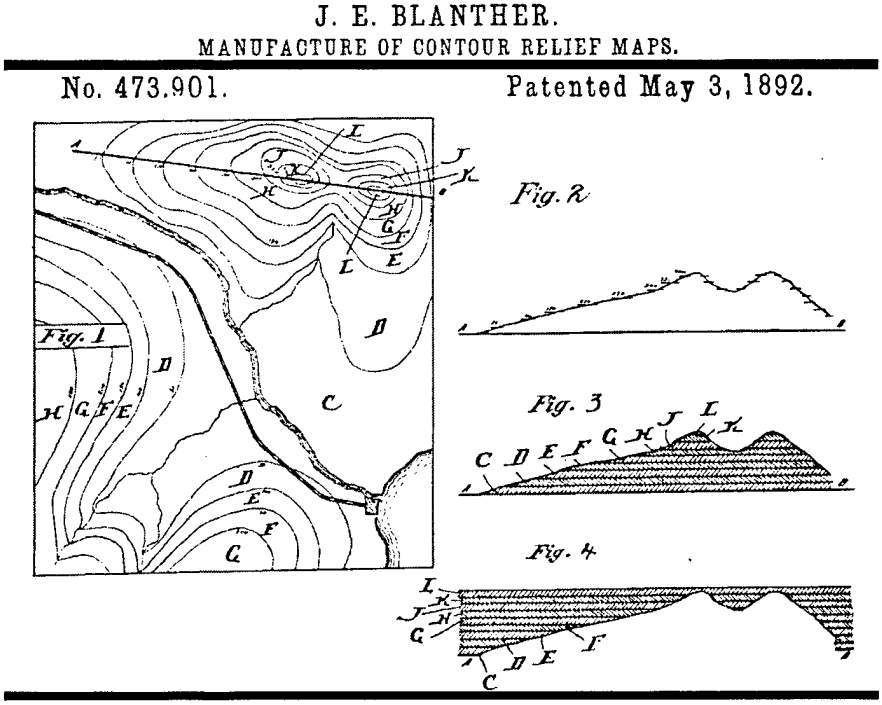


Figure 1: Blanther patent to fabricate 3-D relief map with layered method.

In a similar fashion, Perera (Perera, 1940) proposed a method for making a relief map by cutting contour lines on sheets (cardboard) and then stacking and pasting these sheets to form a three-dimensional map. Further refinements of this approach are found in Zang (Zang, 1964) who suggested using transparent plates with topographical detail inscribed on each plate and Gaskin (Gaskin, 1973) who described a three dimensional geological teaching device. In 1972, Matsubara of Mitsubishi Motors (Matsubara, 1974) proposed a topographical process that uses photo-hardening materials. In this process, a photopolymer resin is coated onto refractory particles (e.g., graphite powder or sand). These coated particles are then spread into a layer and heated to form a coherent sheet. Light (e.g., Mercury vapor lamp) is then selectively projected or scanned onto this sheet to harden a defined portion of it. The unscanned, unhardened portion is dissolved away by a solvent. The thin layers formed in this way are subsequently stacked together to form a casting mold. In 1974, DiMatteo (DiMatteo, 1976) recognized that these same stacking techniques could be used to produce surfaces that are particularly difficult to fabricate by

standard machining operations. Examples he mentions include propellers, airfoils, three-dimensional cams, and forming of dies for punch presses. In one embodiment, a milling cutter contours metallic sheets, these sheets are then joined in layered fashion by adhesion, bolts, or tapered rods as depicted in figure 2. This process has obvious similarity to the earlier 19th century work.

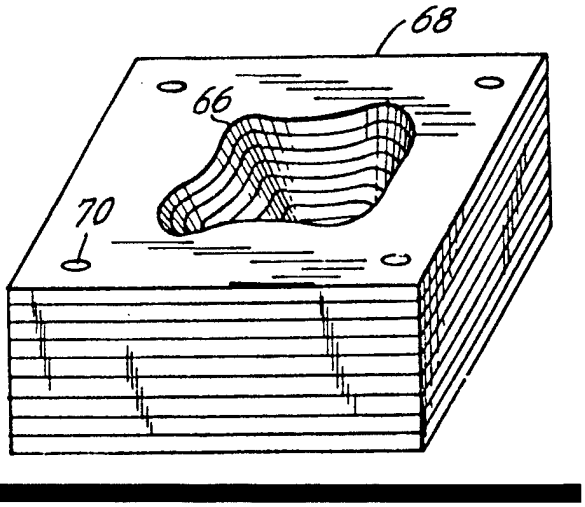


Figure 2: Layered mold by DiMatteo (1974).

In 1979, Professor Nakagawa of Tokyo University began to use lamination techniques to produce actual tools such as blanking tools (Nakagawa, *et al* 1979), press forming tools (Kunieda and Nakagawa 1984), and injection molding tools (Nakagawa, *et al* 1985). A laminated punch tool and the resultant part are shown in Figure 3.

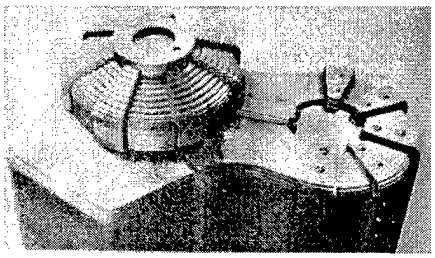


Figure 3: Laminated tool (unfinished) by Nakagawa (1984)

Work continues in this area today, with the recent formation of Solidica (2000), which combines lamination with ultrasonic welding and milling to create a tool.

Photosculpture

Photosculpture arose in the 19th century as an attempt to create exact three-dimensional replicas of any object - including human forms (Bogart, 1979). One, somewhat successful realization of this technology, was designed by Frenchman François Willème in 1860. As shown in Figure 4, a subject or object was placed in a circular room and simultaneously photographed by 24 cameras placed equally about the circumference of the room. An artisan then carved a $1/24^{th}$ cylindrical

portion of the figure using a silhouette of each photograph as seen in Figure 5.



Figure 4: 1860's photosculpture

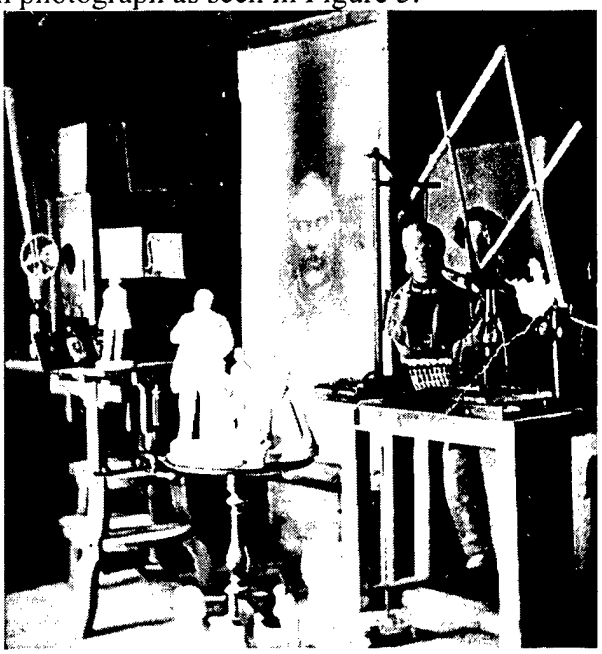


Figure 5: Solid reproduction from Willème's photosulpture

In an attempt to alleviate the labor-intensive carving step of Willème's photosculpture, Baese (Baese, 1904) described a technique using graduated light to expose photosensitive gelatin that expands in proportion to exposure when treated with water. Annular rings of this treated gelatin could then be fixed on a support to make a replica of an object as shown in Figure 6.

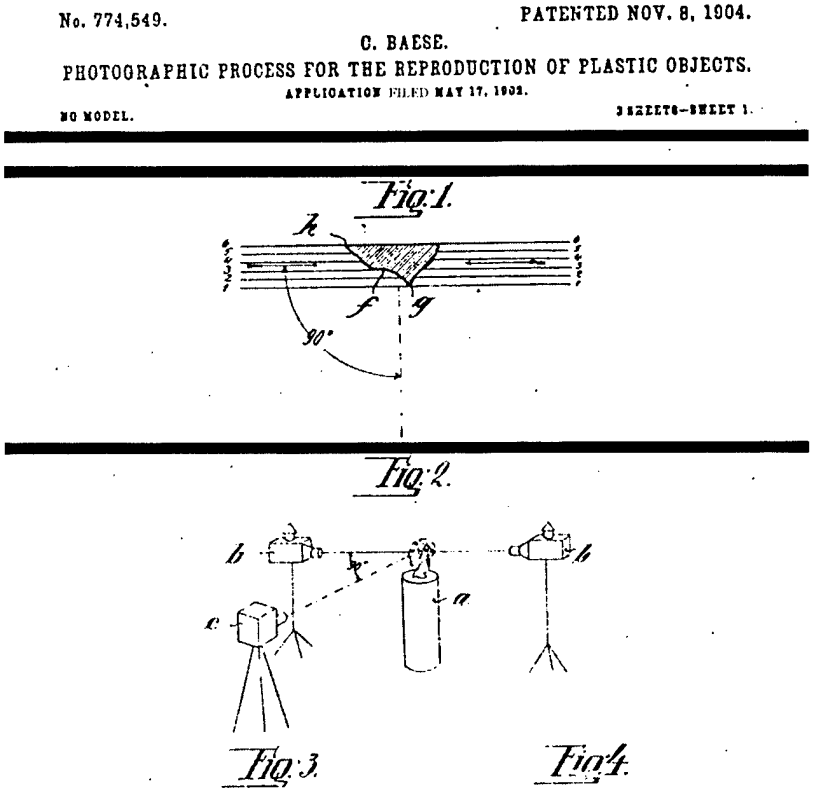


Figure 6: Baese photosculpture technique.

Monteah developed similar techniques (Monteah, 1924). In some of the earliest work in Japan, Morioka (Morioka, 1935,1944) developed a hybrid process between photosculpture and topography. This method uses structured light (black and white bands of light) to photographically create contour lines of an object. These lines could then be developed into sheets and then cut and stacked or projected onto stock material for carving.

In 1951, Munz (Munz, 1956) proposed a system that has features of present day stereolithography techniques. He disclosed a system for selectively exposing a transparent photo emulsion in a layerwise fashion where each layer comes from a cross section of a scanned object. Lowering a piston in a cylinder and adding appropriate amounts of photo emulsion and fixing agent create these layers. After exposing and fixing, the resulting solid transparent cylinder contains an image of the object. Subsequently this object can be manually carved or photochemically etched out to create a three-dimensional object. This system is shown in figure 7.

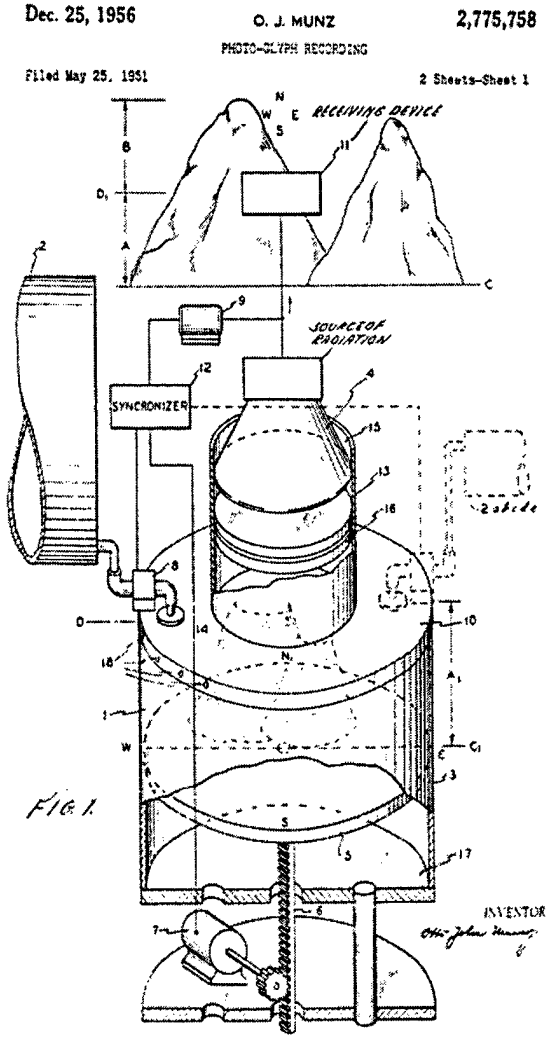


Figure 7: Photopolymer technique of Munz

Early Solid Freeform Fabrication

In 1968, Swainson (Swainson, 1977) proposed a process to directly fabricate a plastic pattern by selective, three dimensional polymerization of a photosensitive polymer at the intersection of two laser beams. Parallel work was conducted at Battelle Laboratories (Schwerzel, 1984). The essential features of this process, termed Photochemical Machining, are depicted in Figure 8.The object is formed by either photochemically crosslinking or degrading a polymer by simultaneous exposure to intersecting laser beams. Although laboratory hardware was constructed, it is not believed that a commercially viable process was achieved.

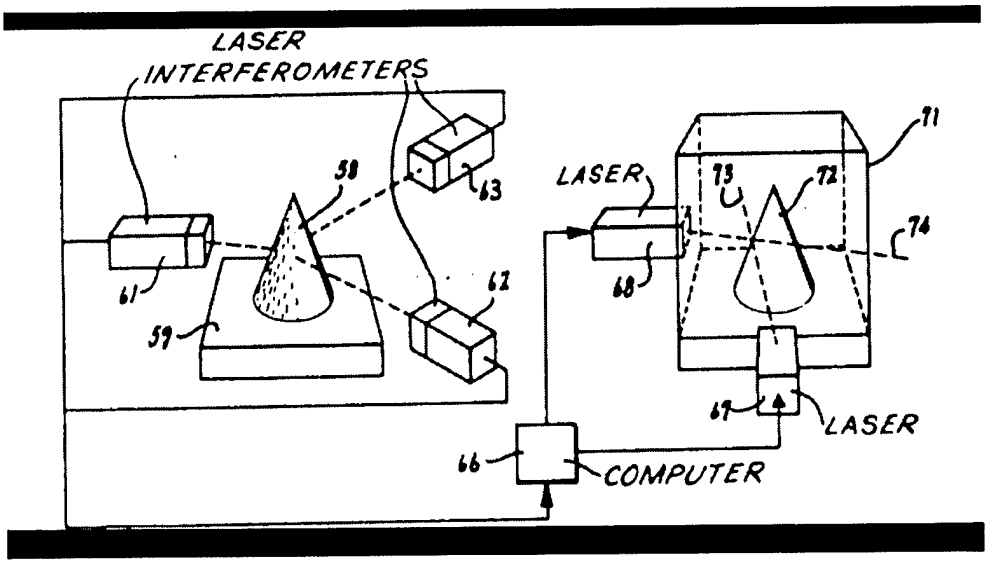


Figure 8: Photochemical SFF system of Swainson

Ciraud proposed a powder process that has all the features of modern direct deposition SFF techniques in 1971 (Ciraud, 1972). This disclosure describes a process for the manufacture of objects from a variety of materials that are at least partially able to melt. In order to produce an object, small particles are applied to a matrix by gravity, magnetostatics, electrostatics, or positioned by a nozzle located near the matrix. A laser, electron beam, or plasma beam then heats the particles locally. As a consequence of this heating, the particles adhere to each other to form a continuous layer. As shown in Figure 9, more than one laser beam can be used to increase the strength of the union between the particles.

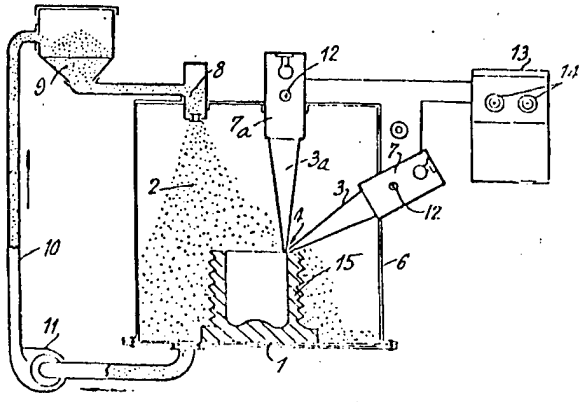


Figure 9: Powder SFF process of Ciraud.

Housholder (1979) presented the earliest description of a powder laser sintering process in a patent. He discussed sequentially depositing planar layers and solidifying a portion of each layer selectively. The solidification can be achieved by using heat and a selected mask or by using a controlled heat scanning process (Figure 10).

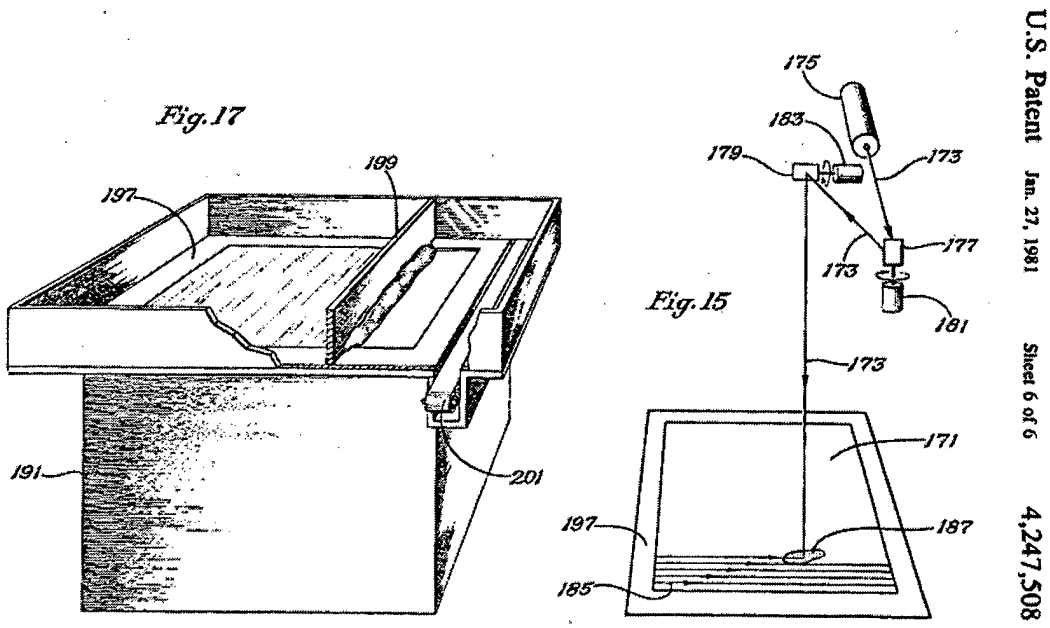


Figure 10: Powder process of Housholder.

Hideo Kodama of Nagoya Municipal Industrial Research Institute was the first to publish an account of a functional photopolymer rapid prototyping system (Kodama, 1981). In his method, a solid model is fabricated by building up a part in layers where exposed areas correspond to a cross-section in the model. He studied three different methods for achieving this:

(a) Using a mask to control exposure of UV source and immersing the model downward into a liquid photopolymer vat to create new layers.
(b) Using a mask, as in (1), but the mask and exposure is positioned on the bottom of the vat and the model is drawn upward to create a new layer.
(c) Immersing the model, as in (1), but using an x-y plotter and an optical fiber to expose the new layer. (See Figure 11).

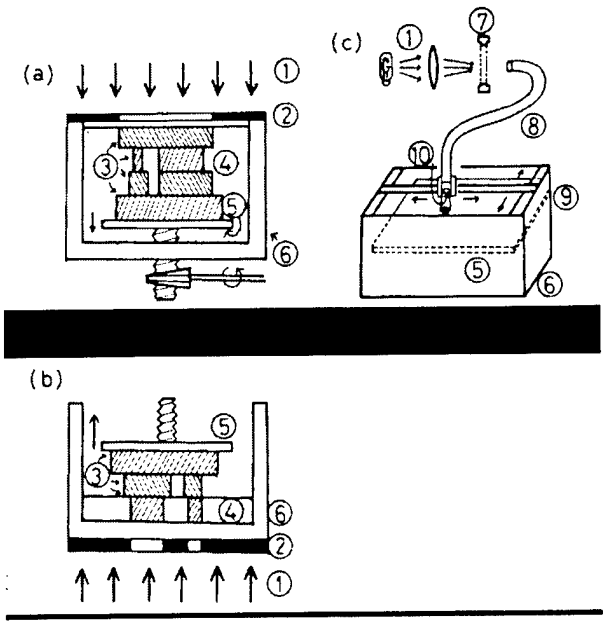


Figure 11: Stereolithigraphy systems of Kodama

Herbert conducted a second, parallel but independent, effort at 3M (Herbert, 1982). Herbert describes a system that directs a UV laser beam to a photopolymer layer by means of a mirror system on an x-y plotter. (See Figure 12) In Herbert's experimental technique, a computer was used to command a laser beam across a layer, the photopolymer vessel was then lowered (1mm), and additional liquid photopolymer was then added to create a new layer.

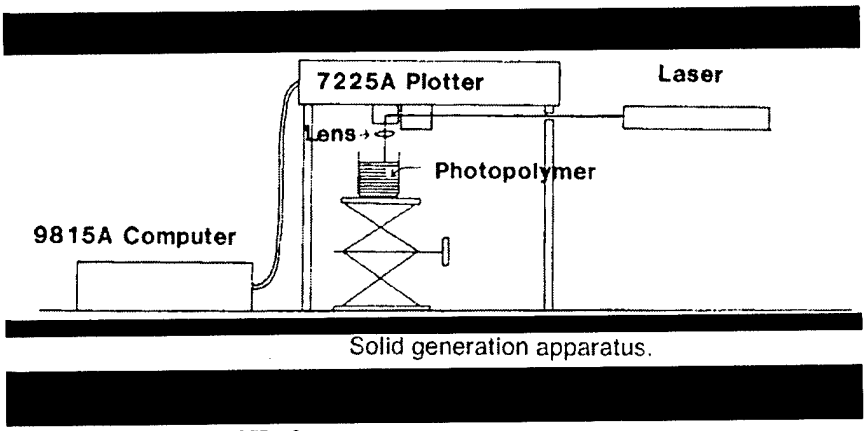
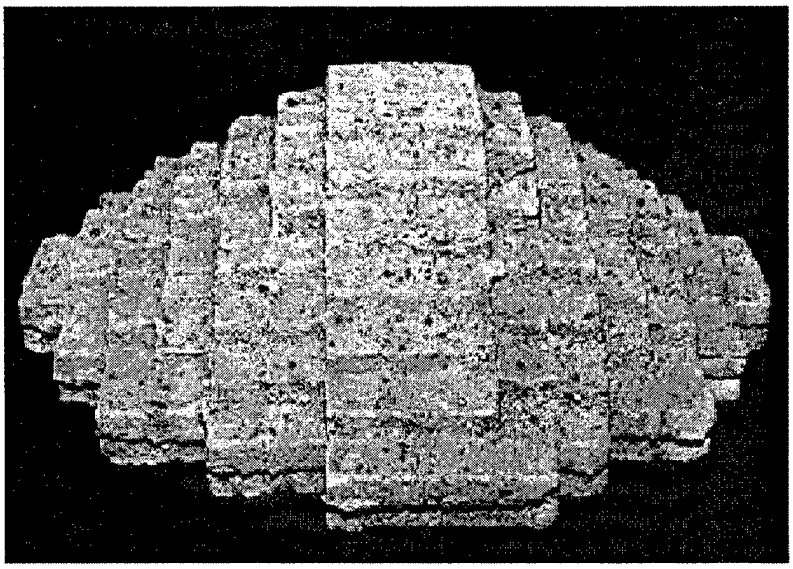
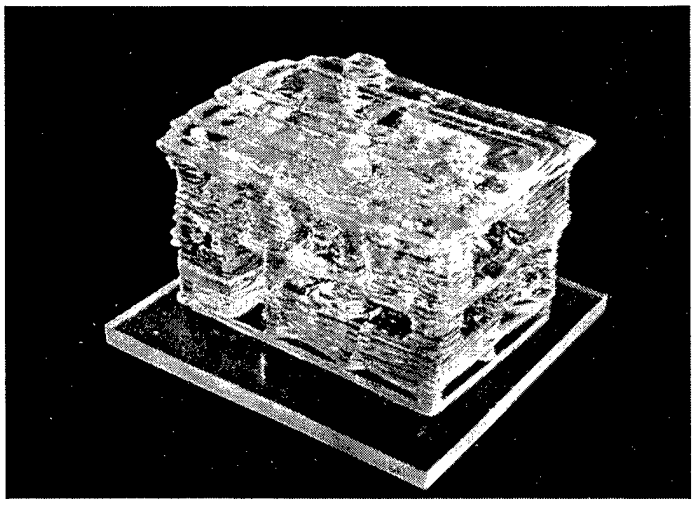


Figure 12: Stereolithography system of Herbert

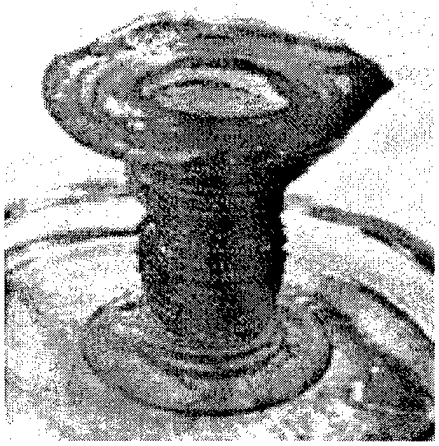
Although we are now accustomed to very intricate parts produced by freeform fabrication equipment, the first parts out of these types of systems required a good deal of faith that improvements would occur. Shown in Figure 13 are three early parts from different systems. The Housholder part was made from an embodiment that includes a grid for separating mold material (concrete and water) from casting material (dry concrete). The Herbert part was created in August 1979. The author does not know exactly when the Kodama and Housholder parts were created.



Housholder



Kodama



Herbert

Figure 13: Early parts by Housholder, Kodama, and Herbert

Commercial Development

In the earliest commercial development, Willème's photosculpture studio was commercially successful from 1861 to 1868 but eventually closed, probably due to the labor involved in hand sculpting with a pantographic (tracing) instrument. The next known commercial attempt was the formation of Formagraphic Engine Co. in 1977 by Swainson. Formagraphic later formed an alliance with Battelle Laboratories and changed its name to Omtec Replication. It appears that this effort was abandoned before a commercial process was developed. Also in 1977, DiMatteo formed a company called Solid Photography, which was spun out of Dynell Electronics Corporation when Dynell merged with United Technologies. As a result, an affiliated retail outlet called Sculpture by Solid Photography was opened in New York City. In this commercial endeavor, a subject was first photographed with structured lighting. From this photograph, a computer was used to create layered cutting paths in order to carve out a rough rendition of the subject which was subsequently smoothed to create a three dimensional likeness. In 1981, Solid Photography changed its name to Robotic Vision. Solid Photography and another company, Solid Copier, operated as subsidiaries of Robotic Vision until 1989 (Lightman, 1996). The following photographs show the process steps.

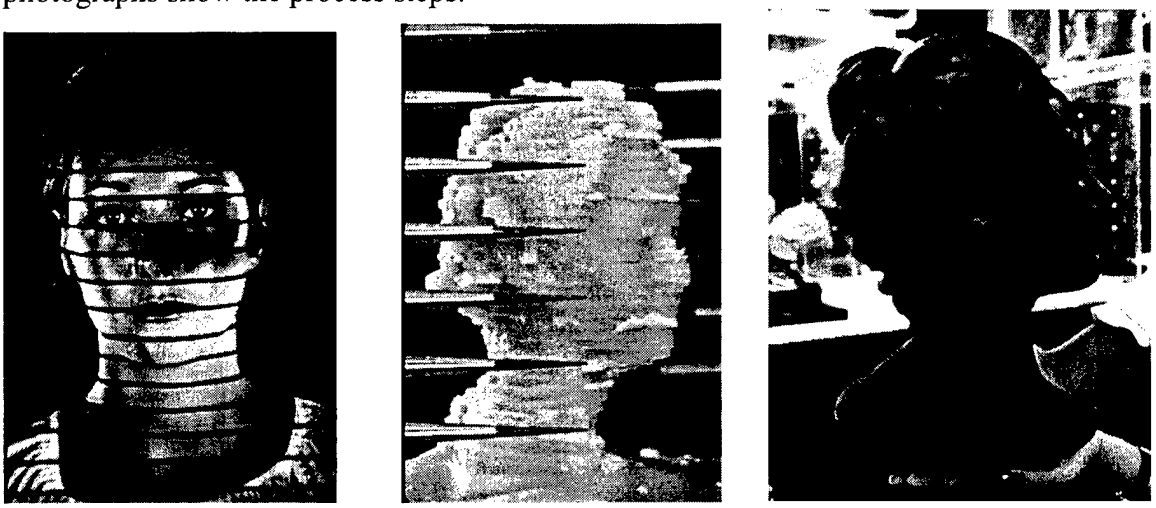


Figure 14: Sculpture by Solid Photography process (No longer in business) (Photos courtesy of SOHO Image Works)

The most important commercial development was the 1st shipment of a stereolithography machine by 3D Systems in 1988. This was the first SFF system that was widely used by customers in a commercial setting.

Summary

Figure 15 displays the overall chronology of Solid Freeform Fabrication. This chronology should not be considered complete; it indicates some (but not all) of the major time events in this rapidly changing field. One glaring omission is the extremely important government funding that was a catalyst for much of the growth in SFF. Of special note were programs at NSF like the Strategic Manufacturing Initiative in 1989, the programs of Dr. Ralph Wachter and Dr. Steve Fishman at ONR and the initiatives of Dr. Bill Coblenz and Dr. Robert Crowe at DARPA.

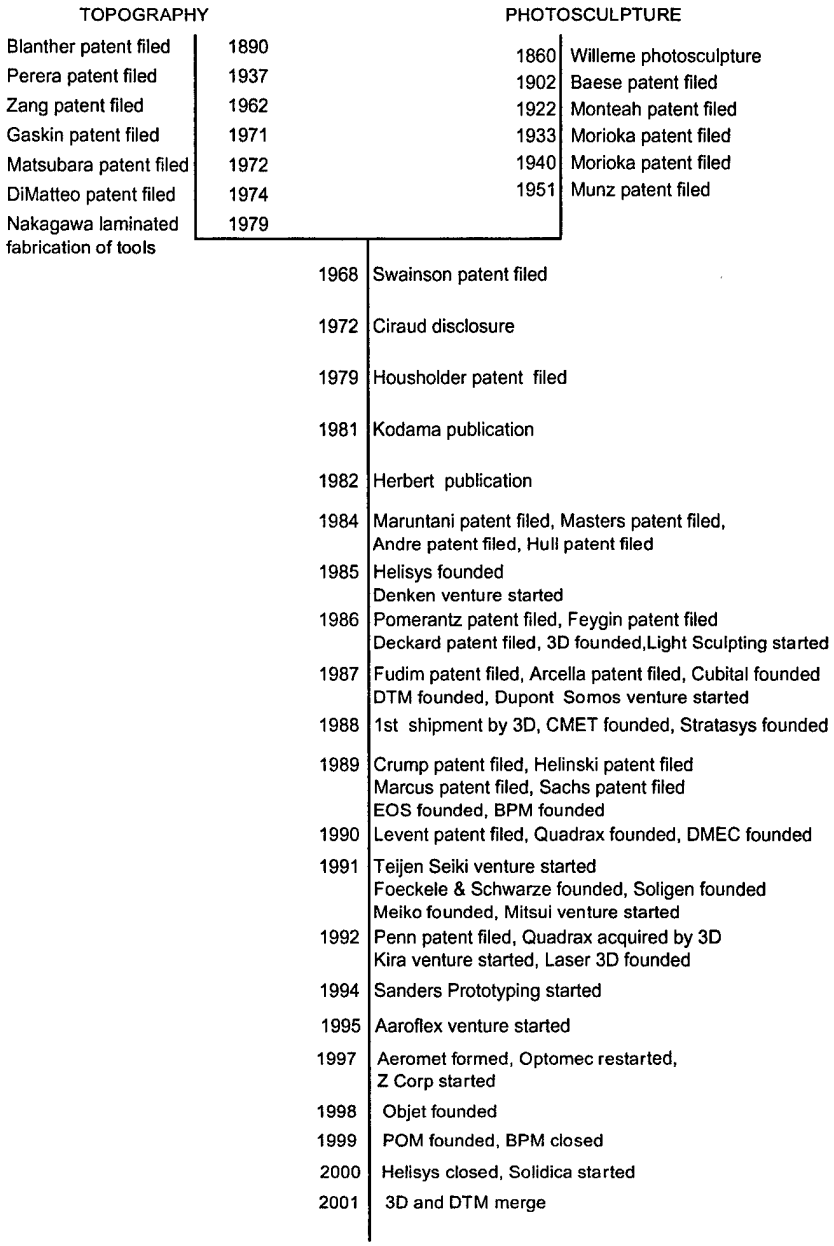


Figure 15: SFF Chronology

REFERENCES

Baese, C., "Photographic process for the reproduction of plastic objects", US Patent 774,549, 1904.

Blanther, J.E., "Manufacture of contour relief maps", US Patent 473,901, 1892.

Bogart, M., "In art the end don't always justify means", *Smithsonian*, 1979 , pp. 104-110.

Ciraud, P.A., "Process and device for the manufacture of any objects desired from any meltable material", FRG Disclosure Publication 2263777, 1972.

DiMatteo, P.L., "Method of generating and constructing three-dimensional bodies", US Patent 3,932,923, 1976.

Gaskin, T.A., "Earth science teaching device", US Patent 3,751,827, 1973.

Herbert, A.J., "Solid object generation", *Jour Appl Photo Eng*, vol 8, num 4, August, 1982 , pp. 185-88.

Housholder, R.F., "Molding Process", US Patent 4,247,508, 1981.

Kunieda, M. and T. Nakagawa, "Development of laminated drawing dies by laser cutting", *Bull of JSPE*, 1984, pp. 353-54.

Kodama, H., "Automatic method for fabricating a three-dimensional plastic model with photo hardening polymer", *Rev Sci Instrum*, 1981, pp. 1770-73.

Lightman, A., personal communication, 1996.

Matsubara, K., "Molding method of casting using photocurable substance", Japanese Kokai Patent Application, Sho 51[1976]-10813, 1974.

Monteah, F.H., "Photochemical process for producing BAS reliefs", US Patent 1,516,199, 1924.

Morioka, I., "Process for manufacturing a relief by the aid of photography", US Patent 2,015,457, 1935.

Morioka, I., "Process for plastically reproducing objects", US Patent 2,350,796, 1944.

Munz, O.J., "Photo-glyph recording", US Patent 2,775,758, 1956.

Nakagawa, T. , Et al, "Blanking tool by stacked bainite steel plates", *Press Technique*, 93-101, 1979.

Nakagawa, T., *et al*, "Laser cut sheet laminated forming dies by diffusion bonding", *Proc 25th MTDR Conf*, 1985 , pp. 505-510.

Nelson, J.C., "Selective laser sintering: a definition of the process and an empirical sintering model", *PhD Dissertation*, University of Texas, May, 1993.

Perera, B.V., "Process of making relief maps", US Patent 2,189,592, 1940.

Swainson, W.K., "Method, medium and apparatus for producing three-dimensional figure product", US Patent 4,041,476, 1977.

Schwerzel, R.E., *et al*, "Three-dimensional photochemical machining with lasers", *Appl of Lasers to Ind Chem, SPIE,1984 , pp. 90-97.*

Solidica, http://www.solidica.com/.

Manufacturing by Solid Freeform Fabrication

Emanuel Sachs
Professor of Mechanical Engineering
sachs@mit.edu

Department of Mechanical Engineering, Massachusetts Institute of Technology, Cambridge, MA

ABSTRACT

The SFF/RP industry has grown steadily with the most significant gains made in the number of models produced per year – three million in the year 2000. Future growth is most likely to be in manufacturing applications of SFF where even a single application can double the number of models/parts produced annually. There are a number of factors or drivers which can motivate a manufacturing application of SFF either individually or in combination. These drivers include: *i.* avoid conventional tooling, *ii.* minimizing hand work, *iii.* mass customization, *iv.* geometric flexibility, *v.* local control of composition. The most intriguing of these drivers is that of mass customization – the manufacture of highly individual products, but on a mass scale. SFF offers the possibility of mass customization of components with complex 3D geometry. A prominent current example is that of Align Technology of Santa Clara, CA which produces unique plastic aligners for orthodontic applications.

There already are manufacturing applications where the advantages offered by SFF are so compelling as to overcome any barriers. However, widespread impact of SFF on manufacturing will depend on overcoming several barriers. The essence of these barriers lies in the distinction between prototyping and manufacturing. Manufacturing applications are far more demanding in terms of build rate and associated cost, demands on dimensional control and tolerances, properties of materials, and ease of use and serviceability of equipment.

INTRODUCTION

Intent of Paper

This paper will examine the impact of SFF on manufacturing and the importance of manufacturing applications to the future growth of the SFF industry. It must be said at the outset that this paper is not an exhaustive review of manufacturing applications. Rather, the goal is to gain a sense of:

- *The drivers for manufacturing* – factors which make an application well suited to manufacturing by SFF.

- *Barriers to manufacturing by SFF* – generic issues that arise when attempting to manufacture by SFF.

A great deal of the information and the thoughts for this paper were derived through discussions with leaders in the industries. These discussions are acknowledged as reference citations.

Industry Status

The recent growth of the SFF industry may be represented in a variety of ways including by dollar volume, number of participating machine suppliers, and number of machines sold. Perhaps the metric which is most relevant to the role of SFF in manufacturing is the number of models made across the entire SFF industry as a function of time. Fig. 1 presents data on the number of models made over the past three years [1]. The SFF industry has experienced steady and significant growth in the number of models made with three million models per year having been made during the most recent fully reported year - 2000. In fact, while the SFF industry has grown in both total revenue and in machine sales, the growth in the number of models made per year has been the fastest aspect of the growth of the industry.

Fig. 2 shows the breakdown of SFF applications by industry [1]. What is significant about this pie chart is that two industries (motor vehicles and consumer products) together account for more than half of SFF applications. Note, however, that medical, government/military, and aerospace together account for only 23% of total applications at the present time.

Forecast

Fig. 3 shows, in a rough way, a forecast for the future growth for the SFF industry [1]. As can be seen, Wohlers has divided the field into three categories. "Prototyping" refers to the classic applications which provided the foundation for the rapid prototyping industry. A second category is referred to as "3D printing". In this figure, Wohlers uses the term 3D printing to refer to the lower cost machines which have become available in the past few years and which are often referred to as "office modeling machines". These machines include the 3D Systems Thermojet, the Prodigy from Stratasys and the machines from Z Corp. (The Z Corp. machines are based on MIT's Three Dimensional Printing process, which is itself referred to as 3D Printing. Thus, the terminology used in fig. 3 from Wohlers might be subject to confusion. Wohlers is referring to the entire field of office modelers when he uses the term 3D printing.) The third category in fig. 3 is called "Rapid Manufacturing" – the subject of this paper.

The first message from fig. 3 is that the total need for prototypes is forecast to remain roughly flat. However, there is forecast a significant realignment within the industry as the low cost "officer modelers" or "3D printers" assume a larger market share of these prototyping applications. This is already taking place as the speed, accuracy, and materials properties of the office modelers, continue to improve.

The second key point from fig. 3 is that the anticipated future growth of the SFF industry will be provided by manufacturing applications. That this is likely the case can be understood by referring back to fig. 1 and noting that in the most recent year three million models were made by SFF. While three million prototypes has a very significant impact on the design process and the quality of the final designs, it is a small number in the context of manufacturing. As we will see, a single manufacturing application can double the number of models made per year. Thus, the forecast that the growth of the industry vies with manufacturing seems quite sensible. If this is to be the case, we will also expect that in the future, the distribution of applications by industry will be quite different than that shown in fig. 2. As noted, the medical, aerospace and military applications total less than a quarter of the applications. However, as we will see, these are the industries that have the greatest near term potential for manufacturing by SFF. Accordingly, we would expect this pie chart to change over time to reflect the increased importance of these three application areas.

It should be noted that the author is not quite as pessimistic as Wohlers as to the flat forecast for prototyping applications. Indeed, a substantial reduction in machine cost might result in some significant growth in prototyping applications. Nonetheless, the key points of the importance of the office modelers to prototyping and especially of the importance of manufacturing applications to the growth of SFF are undoubtedly on target.

DRIVERS FOR MANUFACTURING BY SFF

In the growing number of cases where SFF is used to manufacture components, the competitive advantage of SFF can be traced to one or more of the following "drivers":

- Avoid conventional tooling
- Minimizing hand work
- Mass customization
- Geometric flexibility
- Local control of composition

A given application may gain its competitive advantage from a single one of these drivers. However, often, two or more of these drivers are acting simultaneously. Each of these drivers will be examined and some applications presented.

Avoiding Conventional Tooling

The manufacture of hard tooling is notoriously time consuming and expensive. For this reason, the use of SFF to avoid the fabrication of conventional tooling has been the most common driver for manufacturing by SFF. Indeed, such tooling avoidance has also played a large role in the prototyping implications of the RP field. As tooling avoidance is perhaps the best documented of the drivers for manufacture by SFF, this paper will provide only a representative discussion.

SFF can be used to avoid conventional tooling either by using tooling made by SFF or by making parts directly with no tooling at all. One example of each of these approaches will be presented.

Castings – An Example of Tooling Made by SFF

According to Wohlers, castings (prototypes and manufacturing) account for 6.3% of today's SFF market. Indeed, castings were one of the first major areas of application of SFF.

The impact of SFF on castings has been almost exclusively in the fabrication of castings of complex geometry including complex sand castings and especially investment castings. In this regard there is a strong interplay between two drivers – avoiding conventional tooling and geometric complexity (see later section on geometric complexity.) As an example, let us consider the use of SFF for castings at Bell Helicopter [2]. Bell Helicopter makes extensive use of stereolithography "Quickcast" patterns primarily for aluminum investment castings. When Bell is designing a new aircraft, they need a batch of four to six pieces which are often made from Quickcast patterns. They destructively test one and the others go into test vehicles. As the aircraft moves into preproduction, they might make another two pieces, again, using Quickcast patterns. The next stage is a ramp up to production. If one were to look purely at the economics (without regard to timing issues) the choice would be to make conventional tooling and make wax patterns. This would be the economic choice because at this point the number of patterns needed would justify the cost of the tooling, especially given the fact that foundries charge a premium for making a casting from a Quickcast pattern (this premium presumably derives from two factors: 1. the fact that extra steps are required to burn out the Quickcast pattern and 2. the fact that Quickcast patterns are normally associated with expedited delivery times.) *However*, Bell often enters the ramp up phase with stereolithography patterns due to timing considerations. In some cases, there is insufficient lead time for conventional tooling while in other cases an oversight meant that tooling was not ordered even when there was time to do so. For these reasons, it is now common for aluminum castings derived from Quickcast patterns to be used in production vehicles. In some cases, such castings can account for a "large percentage" of the total castings in a vehicle.

Plastic Parts – Avoiding Tooling

SFF is used to avoid conventional tooling by the direct fabrication of parts which would be normally made through tooling. An intriguing example is the fabrication of plastic parts which would normally be made by injection molding. Fig. 4 shows cost projections for a small plastic handle which is pictured as both a stereolithography part and a part made by selective laser sintering on an EOS machine. As this information comes from Phil Dickens and Neil Hopkinson at De Montfort University [3] the price per piece is presented in Euros. The price for the injection molded parts is based on quotations. The price for the sintered part is based on a capital cost of 340,000 Euros with eight year straight line depreciation, a yearly maintenance cost of 30,000 Euros, a build rate of 17.7 parts per hour based on building 1,056 parts in a 60 hour build, and 7,884 hours of production per year. This projection shows that the cost for the

sintered part has a break even with the injection molded part at about 30,000 pieces. Thus, if one expects to manufacture fewer than 30,000 pieces, one would be ahead economically with the sintered part while the expectation of more than 30,000 pieces would drive one toward injection molding. The interesting point is that this break even quantity of 30,000 is encouragingly high as there might be quite a lot of plastic components which one would desire to manufacture in quantities smaller than this. It should be noted that this is a small part and the break even quantity would decrease quickly with increase in part size. Further, this economic analysis assumes that no finishing is required of the sintered part in order to perform acceptably in the application.

There are indeed now a number of efforts underway to make direct use of sintered plastic parts. An example is the intended use of Duraform polyamide parts by Boeing for nonload bearing applications in military aircraft. According to DTM's website, such applications are now under study for certification.

Driver: Mass Customization

Perhaps the most intriguing single driver for manufacture by SFF is that of mass customization. In its cover article of July 14, 2001, the Economist Magazine (see fig. 5) defines mass customization as "the manufacture of highly individual products, but on a mass scale". The Economist draws an analogy between "built to order" approaches to manufacturing systems and mass customization. Indeed, one can consider mass customization to be a logical extension of "pool" or "just in time" or "lean" manufacturing systems. The limiting case of mass customization is that a single unit of a unique product is made to order.

The application of SFF to mass customization is intriguing because mass customization is the founding cornerstone of a number of companies which are leaders in their respective markets. For example:

- Dell Computer. Dell Computer functions by defining platforms and configuring these platforms (especially the software aspect) at assembly. As is well known, Dell Computer is now the market leader in PCs.
- Swatch. Swatch provides a huge variety of watches starting from platforms which are configured at assembly and with the addition of small amounts of custom fabrication. For example, fig. 6 shows Swatch watches built to order for the Museum of Modern Art (note the MOMA insignia on the watch face hands).
- Lenscrafters. Lenscrafters is a leader in eyewear and this leadership position is based on a stock of platforms (frames) and custom fabrication of the lenses using specialized equipment located in a distributed fashion at the stores.

In one perspective, SFF offers the key to mass customization opportunities which are based primarily on 3D geometry. There are now several intriguing examples which illustrate the potential of SFF for mass customization.

Align Technology of Santa Clara, California [4, 5]. Align Technology represents a new approach to orthodontics where a sequence of plastic aligners is used to move the teeth (rather

than the method of attachment of brackets and wires). Fig. 7 shows one of these plastic aligners. Align Technology is also an excellent example of mass customization. This mass customization is accomplished by five sequential steps: *i.* a physical model is made, *ii.* a virtual model is created from the physical model, *iii.* the virtual model is edited, *iv.* a tool is made from the virtual model using SFF, *v.* aligners are formed using the unique and disposable tool. An orthodontic treatment would require a patient to wear a sequence of approximately 15 pairs (upper and lower, of aligners) each for approximately two weeks. Each of these approximately 30 aligners is unique.

Fig. 8 shows the plaster physical model which is made by casting into the rubber impression taken in the orthodontist's office. Up to this point, the technology is quite identical to that in use for a long time by dentists and orthodontists. Fig. 9 shows a sequence of images depicting the steps required to create a point cloud of data which can be turned into a virtual model of the plaster model seen in fig. 8. First the plaster models are coated with an epoxy. They are then imbedded in a solid block of polyurethane. Multiple plaster models are imbedded in a single block. The block is placed on equipment produced by CGI Corporation which uses a destructive scanning technique to produce a point cloud. The block is milled with a fly cutter, and then a scanner is used to create a 2D pixel image of that layer. The fly cutter then removes another layer and the process continues to deconstruct the physical model and construct a point cloud. Software provided by Geomagic of Research Triangle, NC is used to create the virtual model from this point cloud. In the next step depicted in fig. 10, the virtual model is sliced into individual teeth which can then be individually manipulated. As shown in fig. 11, software operators begin from the arrangement of the teeth in the patient and manipulate the physical model and progressively reorient the teeth in small amounts until they are in the final desired position (in the virtual model). This is a time consuming process which is performed using custom software. At the present time, over 700 software operators in Pakistan perform this operation for Align Technology.

In the next step, stereolithography is used to form tools which will later be used for thermoforming. At the present time, Align Technology has 16 SLA 7000 machine with approximately 39 more on order. Present production is 8,000 aligners per day (accommodating approximately 230 patients per day). As an estimate, 500 aligners are made per machine per day with each build having many aligners in it as can be seen in fig. 12.

The final step is to thermoform plastic sheet around the one time use stereolithography tool as shown in fig. 13 and then to hand trim this formed part. Fig. 14 shows aligners in bubble pack about to be sent to the orthodontist. This forming and trimming step is the most expensive step, primarily due to the hand labor of trimming. This step is performed in Mexico. Align Technology is clearly an example of mass customization in the limiting case of single part made to unique custom order (each customer actually gets about 30 unique parts). In addition, Align Technology demonstrates the importance of geometric flexibility as a driver for solid freeform fabrication. Indeed, Align might have considered milling of the disposal thermoforming tools, but favored SFF because of the need for detail in the regions where the teeth meet.

It is interesting to note that SFF is not the most expensive step of the Align process but rather is "in the middle". Most interesting to note is that even at the young stage of the company, at

their current rate of fabrication, Align Technologies will make three million SFF models in the coming year. This single manufacturing application will double the number of SFF models over those made in the year 2000. This cogently demonstrates the importance of manufacturing applications to the future of SFF.

Another example of mass customization, again the medical field, is that of hearing aids [6]. In this application, being developed by Siemens Corporation (others are pursuing similar goals), a physical model, in this case, a rubber model molded into the ear and ear canal of the patient as illustrated in fig. 15, is the first step. This model is then nondestructively digitized using a laser scanning system and a virtual model is created as shown in fig. 16. This virtual model is then rendered as a shell and engineering detail such as the auditory channel shown in fig. 17 is added. Selective laser sintering is then used to create a shell. Fig. 18 shows an SLS shell on the right and a conventionally fabricated shell on the left. The electronics is added creating the finished hearing aid as shown in fig. 19.

This application is not only an example of mass customization but is also an example where the driver is the elimination of hand work. In the conventional practice of making hearing aids, a great deal of hand fabrication is used to go from the rubber physical model to the final hearing aid. While it is unlikely that SFF will yield a near term cost reduction over the conventional methods of fabrication, hearing aid companies are quite concerned about their continued ability to access the skill pool of hand work required in the conventional method. SFF answers that concern.

Another class of medical mass customization is the intriguing area of body parts. Perhaps the most likely early examples are bone replacement/reconstruction components. Fig. 20 shows a scan taken by MRI of a patient in need of reconstructive surgery of an eye socket. Fig. 21 shows bioceramic eye sockets made by Therics Inc. using Three Dimensional Printing [7]. Therics is currently in animal trials with bone replacement parts that will be produced in "shoe sizes". While this is not quite customization, it is a step in that direction.

The military has a tremendous need to provide units or small quantities of spare parts on demand. In some cases, the original design is available, however, in many cases an existing physical component must be reversed engineered. Fig. 22 shows a sequence of mass customization which would pertain to the case where a component must be reverse engineered. The original component is subjected to an industrial CT scan. The metallic replacement part is then made by SFF, for example, by 3D Printing. The ProMetal division of ExtrudeHone is engaged in such spare parts mass customization under a program funded by the Navy [8].

Driver: Geometric Flexibility

In some cases, the ability to fabricate geometries, not practically possible by other methods can drive a manufacturing application. Two examples will be examined: *i.* conformal cooling and tooling, and *ii.* complex internal geometry in castings.

Quite a number of organizations are pursuing the concept of fabricating tooling, especially injection molding tooling, using SFF techniques. Participants in this area include ExtrudeHone/DME, POM Corporation, Express Tool, and others. Figures 23 and 24 show a case study of the application of conformal cooling provided by ExtrudeHone and DME which are partnered in an enterprise called "Mold Fusion" [8,9]. A relatively simple geometry plastic part was selected that the mold could be made with a number of conventional cooling approaches for comparison. The part is a capacitor cup made of polypropylene. The part is basically a cylindrical component with a wall thickness of 0.60 inch, a diameter of 2.5 inch and a length of 8 inches. Fig. 23a shows a mold core using a conventional baffle to flow the coolant through the core. Fig. 23b shows a mold which takes advantage of the simple geometry and provides seven cooling rings to bring the water near to the core surface. Fig. 23c shows the "mold fusion" core made by 3D Printing where a helical cooling channel was created and extra coils were packed in the regions felt to be most sensitive to cooling. Fig. 24 shows the cycle times broken down into Injection/Hold/Eject and Cooling Times. Note that the Mold Fusion core with conformal cooling shows a 49% improvement in productivity over the conventional baffle (parts per hour is plotted on the right.) The bronze insert with cooling rings is significantly better than the conventional baffle but not nearly as good as the conformally cooled core. Note, that with a more complex geometry, this bronze insert with cooling ring approach would not be feasible and thus the improvement of conformal cooling would be even more dramatic over the alternative. Such improvements of 20-50% in cycle time have been seen in quite a number of case studies.

The plastics mold making industry produces 200,000 to 300,000 molds annually on a world wide basis at a cost of 15 to 20 billion dollars. The possible future penetration of conformal cooling may be up to 15% of molds made, or 30,000 to 50,000 molds annually, a significant impact. However, it should be noted that the plastics molding industry is quite conservative and it will take some time for this penetration to take place. As a reference point, it has taken 30 years for Hot Runner technology to penetrate to 30% of all applications [9].

Another class of applications which is motivated by the ability to fabricate complex internal geometry is that of complex castings, especially those for pumps, valves and other fluid control elements. Fig. 25 shows a sand core made on an EOS SLS machine for a fluid manifold. Fig. 26 shows a mold and casting for a fuel cross over for Rocketdyne made by Soligen, Inc. using 3D Printing [10].

Driver: Local Control of Material Composition

One of the intriguing possibilities associated with some SFF technologies is that of controlling the local composition of the fabricated component. Fig. 27 shows two cell phone covers made by 3D Printing on a Z Corp. machine. One component is printed in "monochrome" while the other component has color printed in. The color part is a three dimensional representation of the output of a mold filling finite element simulation [11].

Fig. 28 shows some "flash dosage" oral dosage forms from Therics, Inc. These pills have drugs printed in an interior core with flavor masking on the exterior of the pill. Example

applications are under study which would be based on the production of 50 million per machine per year [7].

While in many cases, the use of SFF technology to control the local composition can be enabling of new products, it is also true that these applications require a significant "stretch" from current practice as the products being considered may have no precedent and therefore no track record.

BARRIERS TO MANUFACTURING BY SFF

There are a number of issues or barriers which SFF must overcome if it is to have a large impact on manufacturing. These include:

- Speed/part cost
- Accuracy, tolerances, surface finish, detail
- Application specific materials properties
- Application specific machine design
- Product support (centralized manufacturing)
- Ease of use (distributed manufacturing)

Barrier: Speed/Part Cost

A primary driver of part cost is the build speed in the SFF machine. As documented in the appendix to this paper, the build rates of the fastest SFF machines today are on the order of one liter of part per hour. However, "standard" forming processes can be much faster. Certainly, there is a wide range of speeds associated with standard forming processes depending on the material being formed, the size of the part, and the process itself. However, as a generalization, standard forming processes can be 10 to a 1,000 times faster than today's SFF technologies.

It is useful to speculate about an SFF machine which can build 100 liters per hour, as such a machine would be competitive with at least some of the standard forming processes. An example of a machine which could achieve this build rate would be a machine with a bed size of one meter by one meter, building in layers that are 100 microns thick and forming each layer in 3.6 seconds. While such a goal is challenging, it is also within the realm of possibility, at least with some of the technologies. (For example, the author believes that such a machine is possible using Three Dimensional Printing technology.)

Barrier: Accuracy, Tolerances, Surface Finish and Detail

On the issue of accuracy, tolerances, surface finish and detail, a clear distinction must be made between manufacturing applications and prototyping applications. In a prototyping application, it is often acceptable to do selective final machining on the part and even extensive hand finishing can be tolerated because the combination of SFF with these techniques still yields

a part much faster than available alternatives. However, in a manufacturing application, any secondary operation (other than mass processes like media finishing) is a threat to competitive advantage. Thus, there is a significant barrier to overcome in achieving the net shape component with the desired surface finish and tolerances by SFF [12].

Barrier: Application Specific Material Properties

As in the case of accuracy and tolerances, a clear distinction must be made between prototype applications and manufacturing applications in the context of material properties. For a prototype, a part is still of considerable use even if not all of the material properties are as good as those of the part which will be ultimately manufactured. When testing a prototype, the longevity of the test may not matter in some applications. One may be able to reduce the severity (for example, minimize the temperature exposure of the part) and still devise the required technical information. In general, one may be able to accommodate materials properties that are not quite up to standard by correcting the measured results in order to compensate for the expected improvement which will correspond to the final component materials properties. However, in the manufactured parts, all the material properties must exceed some minimum standards. It is quite possible, for example, that a given component could be acceptable in yield strength, tensile strength, impact strength, creep, coefficient of thermal expansion, and elastic modulus, but fail in its fatigue properties. Failure in one aspect will mean that the component cannot be used in the manufacturing application. This is a much higher standard than that which has to be satisfied for prototypes. The danger is that the SFF materials may have to be tailored for specific applications in order to satisfy many requirements simultaneously. This will be an extremely expensive proposition and could only be justified for high volume applications [12].

Barrier: Application Specific Machine Design

As noted if manufacturing applications are more demanding than prototyping applications and many applications will *simultaneously* push limits on: *i.* accuracy, surface finish and detail, *ii.* rate, and *iii.* material properties. In order to simultaneously satisfy these requirements, it may become necessary to design machines for specific applications. The most obvious example of the need for application specific machine design is the need to accommodate different part sizes and therefore to create machines with different build volumes. However, other considerations may be even more demanding. For example, in Three Dimensional Printing, fine ceramic powders are processed using slurries, while larger powders are processed dry. Fine featured small components such as those pictured in Fig. 29 are fabricated by traversing the printhead in a vector outline and then raster filling. Larger components, however, must be made using raster scanning methods only, due to considerations of rate. Thus, a particular application will be best satisfied by a particular combination of powder deposition, binder deposition, and machine architecture. While general machines can go a long way to satisfy the requirements of a specific application, application specific machine design may be required to gain the full benefits.

Barrier: Product Support (Centralized Manufacturing)

Manufacturing facilities demand "no" down time. If down time is encountered, they expect nearly instantaneous repair. Further, they expect the ability to make parts elsewhere while equipment is down. The net result is a very much higher standard of product support which must be satisfied for manufacturing applications, as opposed to prototyping applications [12].

Barrier: East of Use (Distributed Manufacturing)

Mass customization applications are best satisfied by having the manufacturing capacity distributed. As a model, consider the lens making equipment which is distributed at various LensCrafters facilities. Perhaps the closest analogy in today's manufacturing world is that of the machine shop. However, machine shops do not accomplish mass customization as the processes are not facile enough to interface directly to the end user. In a mass customization application, there will be far less tolerance of process quirks and software challenges as compared to today's machine shops. Thus, the software equivalent of "MasterCam" will not be good enough – it will be too hard to use. The software orientation will have to be toward the end use customer [13].

CONCLUSIONS

The SFF/RP industry has grown steadily with the most significant gains made in the number of models produced per year – three million in the year 2000. Future growth is most likely to be in manufacturing applications of SFF where even a single application can double the number of models/parts produced annually. There are a number of factors or drivers which can motivate a manufacturing application of SFF either individually or in combination. These drivers include: *i.* avoid conventional tooling, *ii.* minimizing hand work, *iii.* mass customization, *iv.* geometric flexibility, *v.* local control of composition. Avoidance of conventional tooling has been the most common driver today with prominent examples in the metals casting and injection molding areas. The most intriguing of the drivers is that of mass customization – the manufacture of highly individual products, but on a mass scale. SFF offers the possibility of mass customization of components with complex 3D geometry. A prominent current example is that of Align Technology of Santa Clara, CA which produces unique plastic aligners for orthodontic applications.

There already are manufacturing applications where the advantages offered by SFF are so compelling as to overcome any barriers. However, *widespread* impact of SFF on manufacturing will depend on overcoming several barriers including : *i.* increased build speed, *ii.* improved accuracy and surface finish, *iii.* improved and possibly application specific materials properties, *iv.* application specific machine designs, *v.* improved product support, and *vi.* greater ease of use. The essence of these barriers lies in the distinction between prototyping and manufacturing. Characteristics which can be tolerated in a prototyping environment become intolerable in a manufacturing environment. For example, the wide gulf in build speed between SFF and conventional forming processes will have to be at least partly bridged. Tolerances that are acceptable in a prototype are unacceptable in manufacturing as secondary operations are

economically unacceptable. Demands on materials properties are greater. Mass customization demands ease of use in a distributed fabrication environment. As these barriers are addressed, manufacturing applications will proliferate and are likely to become a primary impact of the SFF field.

APPENDIX

In order to get a sense of the build rates of the current SFF technologies, a benchmark was attained for a fast "office modeler" and a "high end" machine targeted at manufacturing. The Z Corp. Z406 machine was chosen as the office modeler and the Vanguard machine from DTM as the high end machine. Data for a specific geometry was attained as it was felt to be more meaningful. An STL file was sent to Z Corp. and DTM and data returned from their build time estimators (not models were made) [11,12]. The STL file is pictured in Fig. 30. The volume of this part is approximately one liter.

	Starch (175μ layers)	Plaster (100μ layers)
One Part	1.45 hrs	2.9 hrs
Four Parts	5.8 hrs	11.6 hrs

Table I

Table I shows the build times returned by Z Corp. for two materials – starch and plaster. Build time estimates for one part and four parts are given.

	Nylon (150μ layers)	Metal (75μ layers)
One Part	4.4 hrs (2.75 warm up/dn)	6.6 hrs (no warm up/dn)
Four Parts	6.7 hrs (2.75 warm up/dn)	26.4 hrs (no warm up/dn)

Table II

Table II comes from DTM and has build time estimates for nylon and metal materials again for one part and four parts. Note that in the case of the nylon material the estimate for four parts is less than four times the estimate for one part as the nylon materials require a warm up and cool down cycle and this warm up and cool down would be the same for four parts as for one part.

The most important conclusion from these build time estimates is that current build rates are on the order of 0.2 – 1.0 liter per hour. The upper end of this range is the rate estimate used in the rate section of this paper. It is also interesting to note, however, that there is overlap in build rates between the office modelers and the "high end machines", although, it must be noted that making a direct comparison is impossible because the end product and the costs are so different.

REFERENCES

[1] Terry Wohlers, Wohlers Report 2001, Wohlers Associates, Fort Collins, CO, 2001.

[2] Lance Weihmuller, Bell Helicopter, Fort Worth, TX, communication with author.

[3] Phil Dickens and Neil Hopkinson, De Montfort University, Leicester, United Kingdom, communication with author.

[4] Len Hedge, Vice President of Manufacturing, Align Technology, Santa Clara, CA, communication with author.

[5] Mervyn Rudgley, Senior Director of Business Development, Stereolithography, 3D Systems, Valencia, CA, communication with author.

[6] "*LasR*™ Hearing Instrument Shells...Let your patients experience the most comfortable hearing instruments", Siemens Hearing Instruments, 2001, videocassette.

[7] Chris Gaylo, VP of Engineering, Therics, Inc., Princeton, NJ, communication with author.

[8] Michael Rynerson, Business Unit Manager, ProMetal Division, ExtrudeHone Corporation, Irwin, PA, communication with author.

[9] Larry Navarre, DME Corporation, Madison Heights, MI, communication with author.

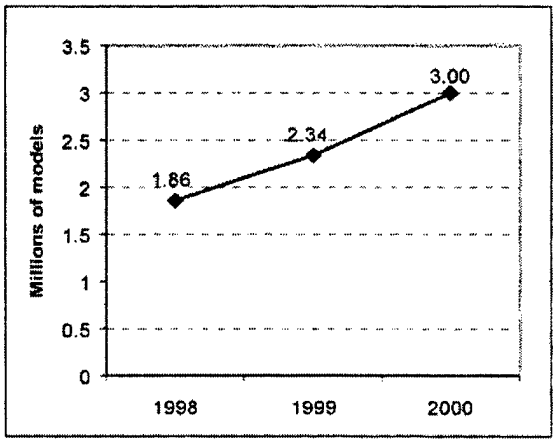
[10] Yehorem Uziel, President, Soligen, Inc., Northridge, CA, communication with author.

[11] Marina Hatsopolous, CEO, Z Corp., Burlington, MA, communication with author.

[12] Kevin McAlea, DTM Corporation, Austin, TX, communication with author.

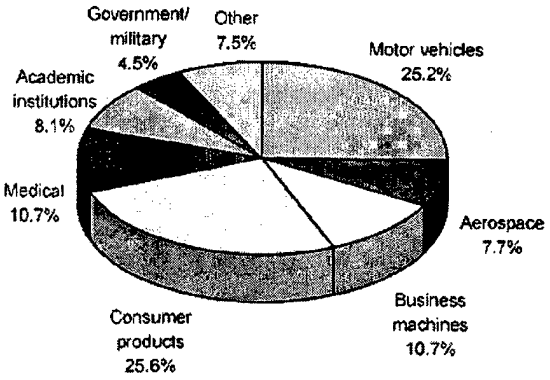
[13] Ping Fu. President, Geomagic, Research Triangle, NC, communication with author.

FIGURES



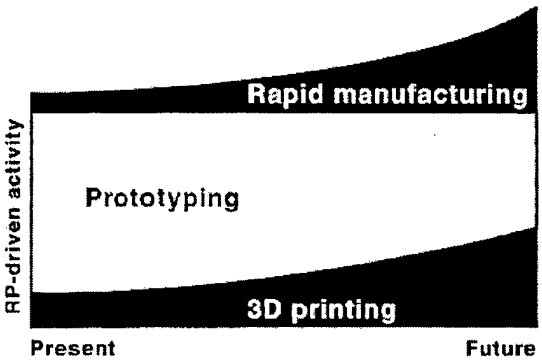
Source: Wohlers Associates, Inc.

Figure 1. The total number of models made annually by SFF for the past three years.



Source: Wohlers Associates, Inc.

Figure 2. The breakdown by industry of SFF applications.



Source: Wohlers Associates, Inc

Figure 3. A highly schematic anticipation of the future growth of SFF.

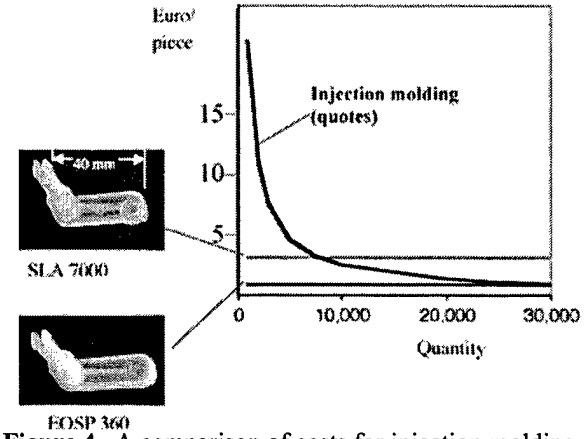


Figure 4. A comparison of costs for injection molding versus stereolithography and SFF for the small handle shown.



Figure 5. The cover of the Economist magazine from July 14, 2001 depicting mass customization.

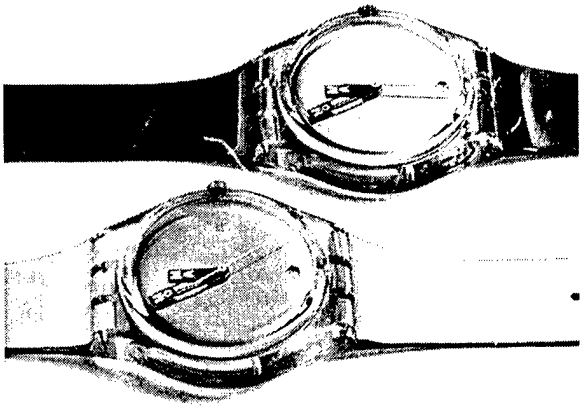


Figure 6. Swatch watches, an example of mass customization.

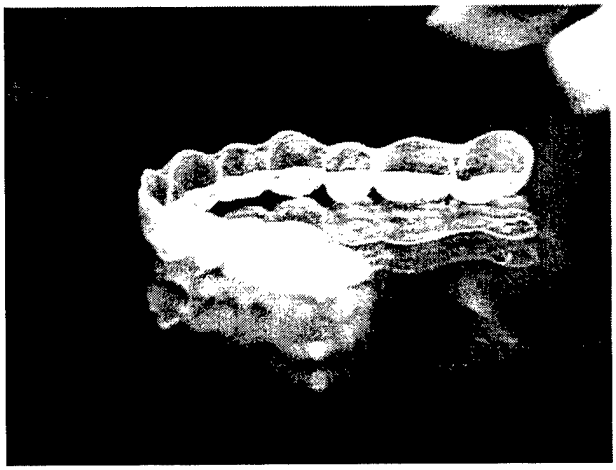


Figure 7. A plastic aligner made by Align Technology, Inc.

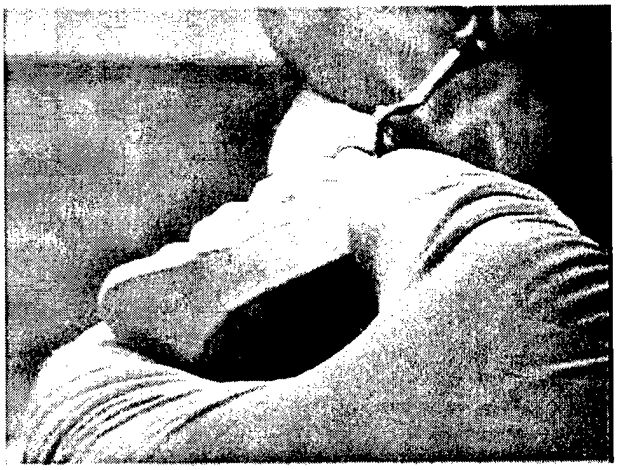


Figure 8. The plaster physical model taken from the rubber impression taken from the patient's teeth and gums.

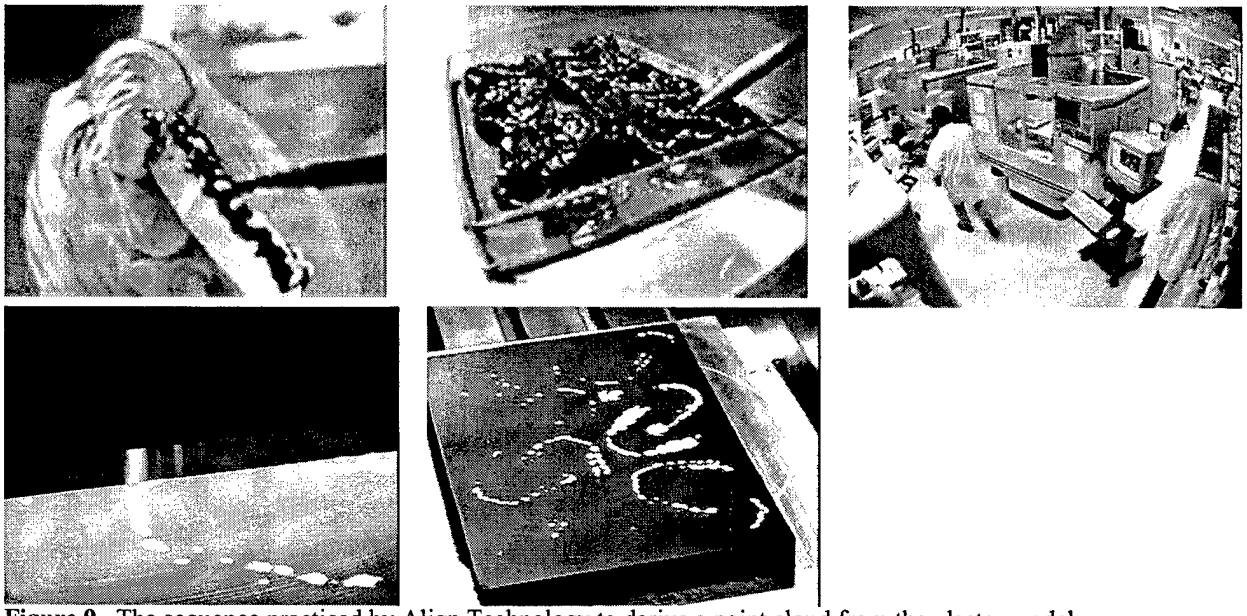


Figure 9. The sequence practiced by Align Technology to derive a point cloud from the plaster models.

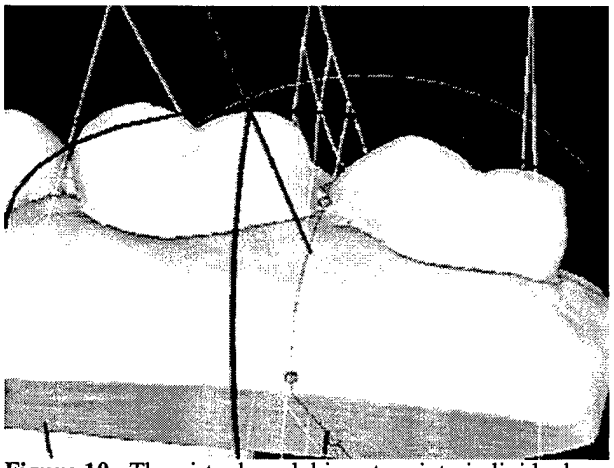


Figure 10. The virtual model is cut up into individual teeth.



Figure 11. Software operators move the virtual teeth to create the desired progression for the orthodontic treatment.

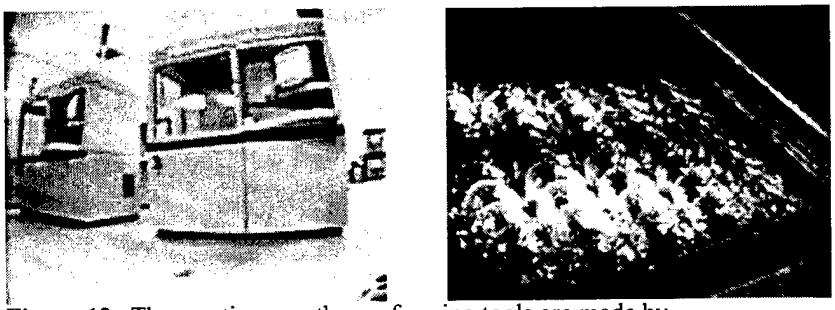


Figure 12. The one time use thermoforming tools are made by stereolithography using SLA 7000 machines.



Figure 13. The aligner is made by thermoforming a plastic sheet over the stereolithography tool.

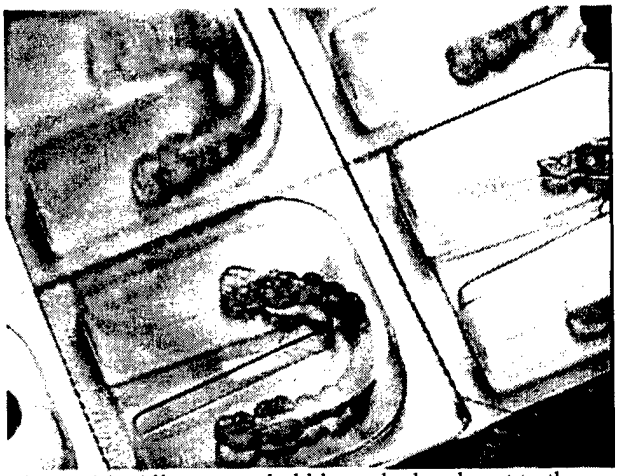


Figure 14. Aligners are bubble packed and sent to the orthodontist.

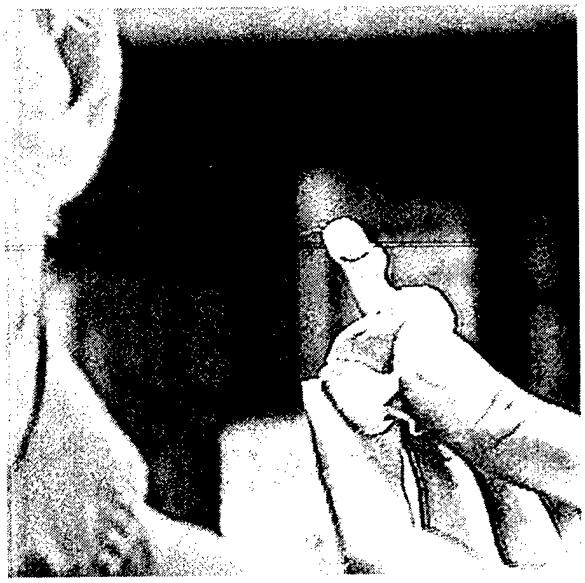


Figure 15. A rubber impression of the ear and ear canal is the first step in the manufacture of a hearing aid.

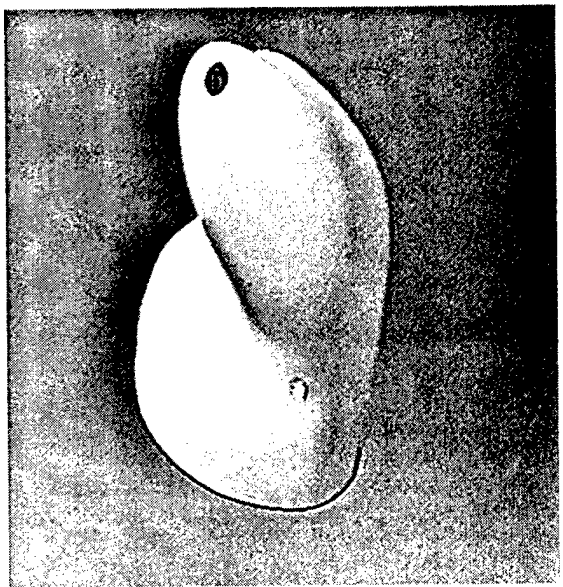


Figure 16. The rubber impression is scanned and turned into a virtual model.

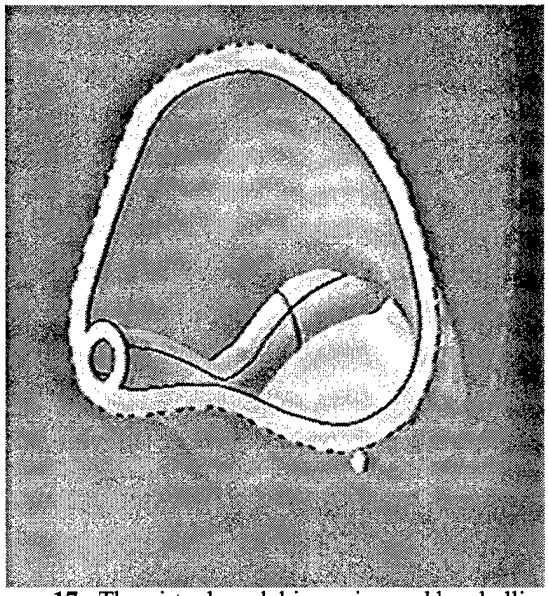


Figure 17. The virtual model is engineered by shelling and adding features.

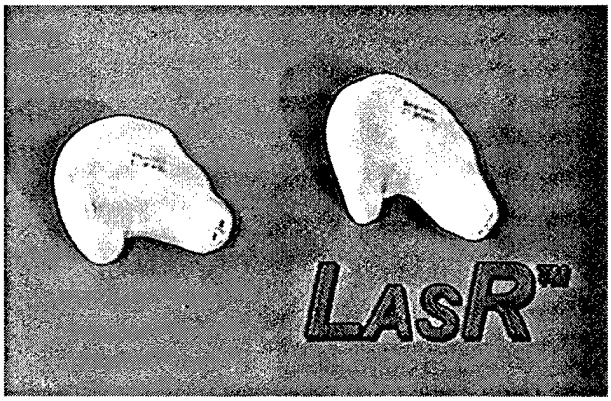


Figure 18. An SLS hearing aid is on the right while a conventionally fabricated one is one the left.

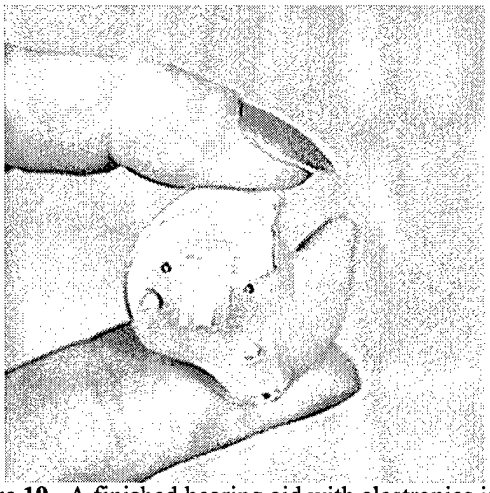


Figure 19. A finished hearing aid with electronics in place.

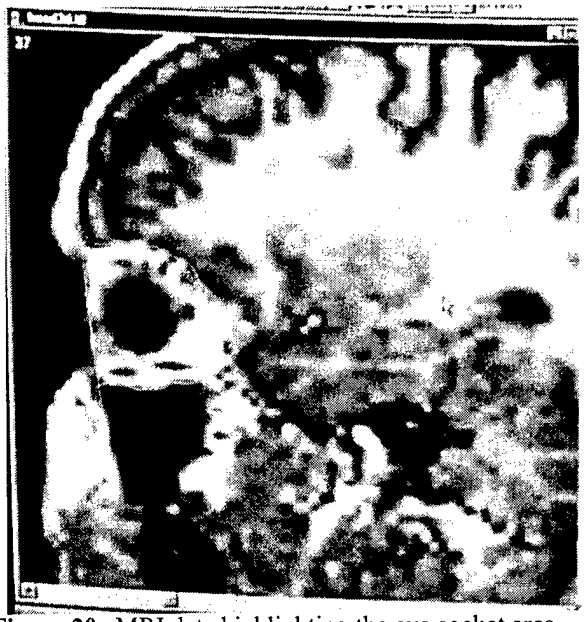


Figure 20. MRI data highlighting the eye socket area where reconstruction is needed.

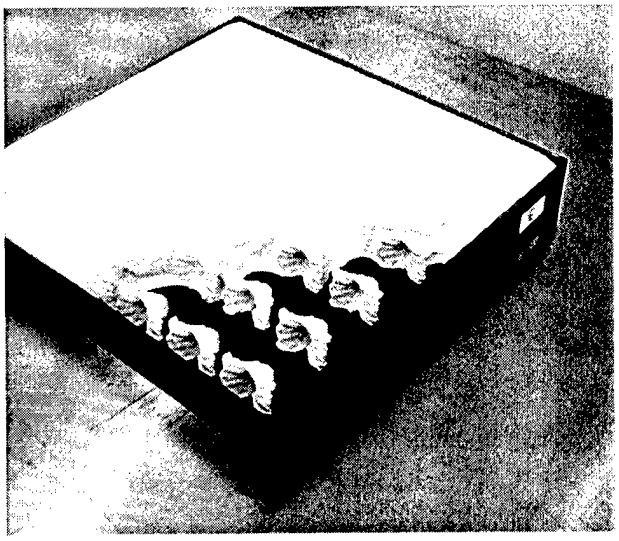


Figure 21. Bioceramic eye sockets made by 3D Printing.

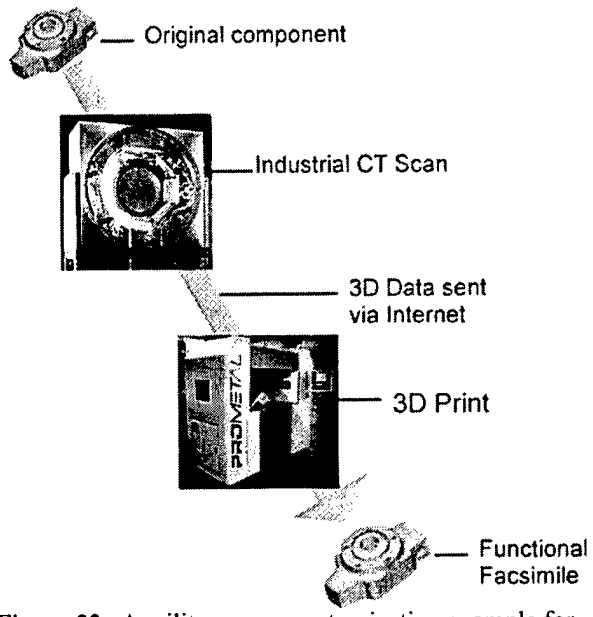


Figure 22. A military mass customization example for spare parts including reverse engineering and 3D Printing.

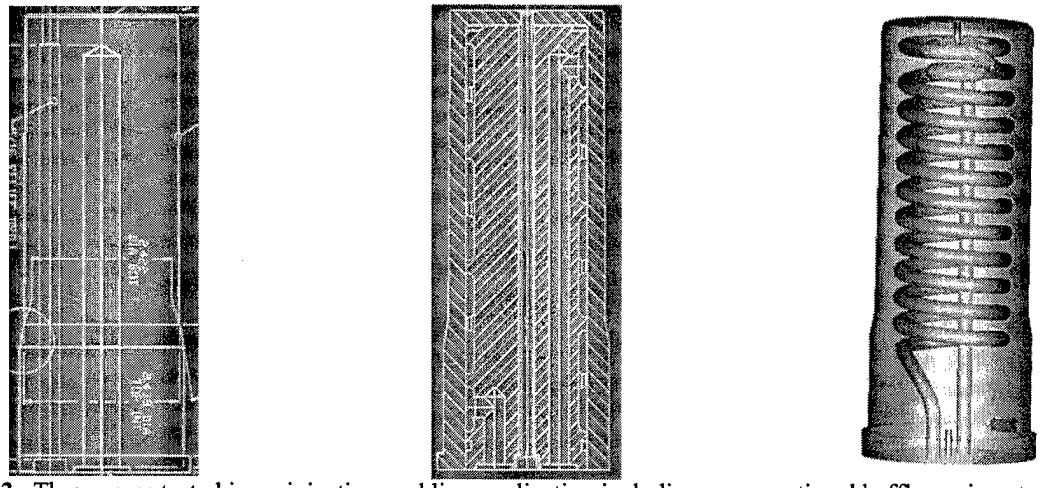


Figure 23. Three cores tested in an injection molding application including a conventional baffle, an insert with cooling rings and a 3D Printed conformally cooled core.

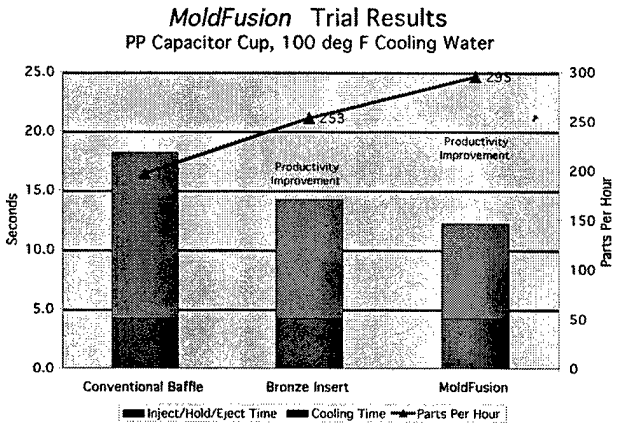


Figure 24. The cycle time in seconds (left) and the number of parts per hour (right) for the three cores shown in Figure 23. The green areas are the sum of injection, hold and eject times while the blue are the cooling times.

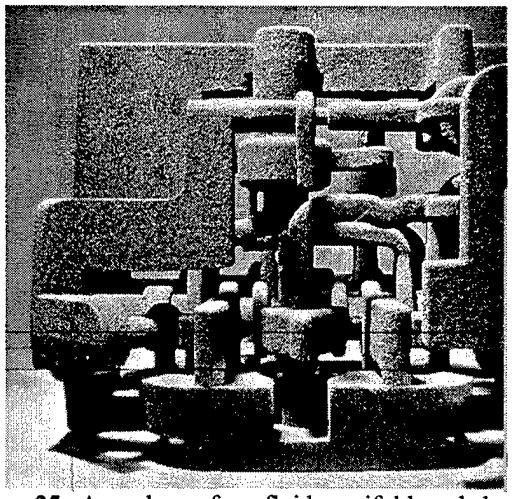


Figure 25. A sand core for a fluid manifold made by SLS on an EOS machine.

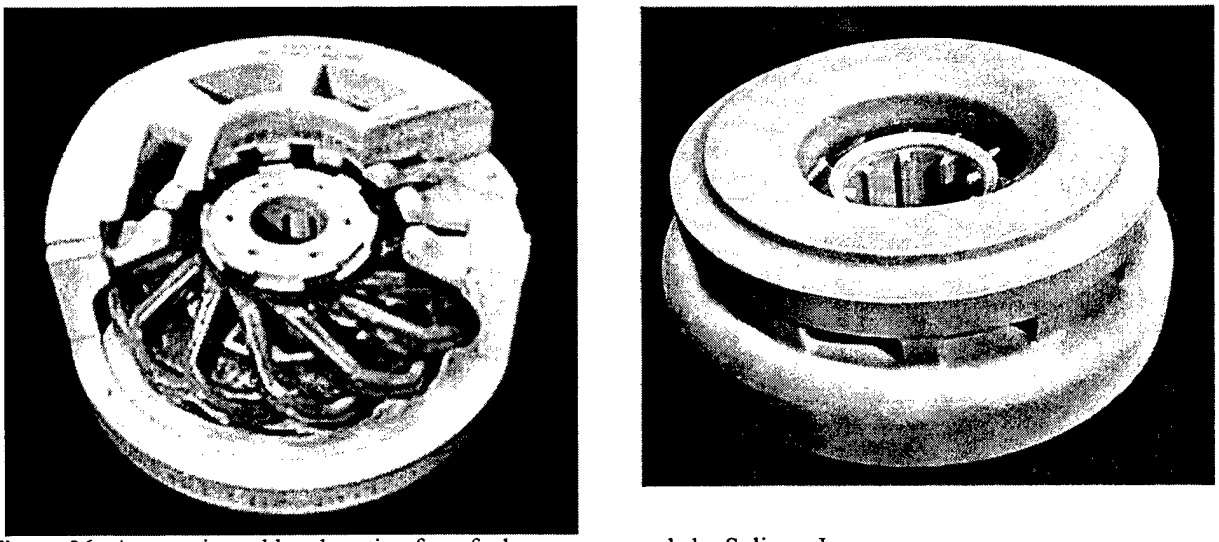


Figure 26. A ceramic mold and casting for a fuel cross over made by Soligen, Inc.



Figure 27. A monochrome and cover cell phone cover both made by 3D Printing by Z Corp.

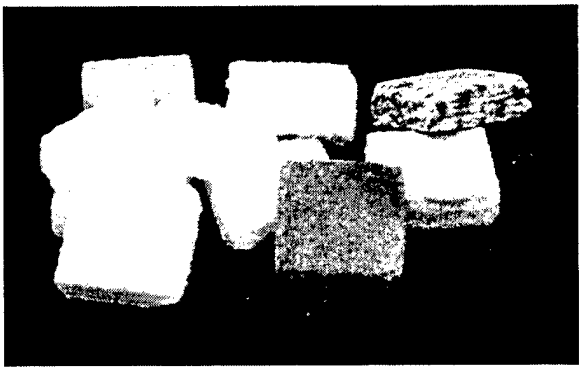


Figure 28. Pills for oral consumption made by 3D Printing by Therics, Inc.

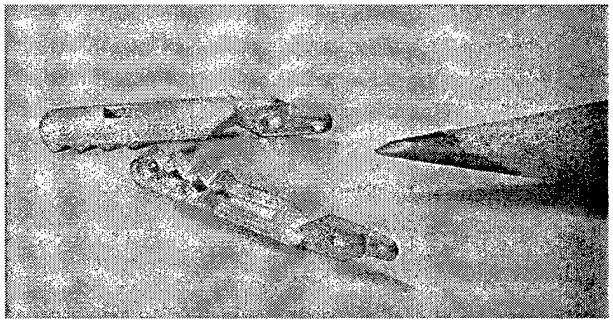


Figure 29. Sintered stainless steel components with fine features made by 3D Printing.

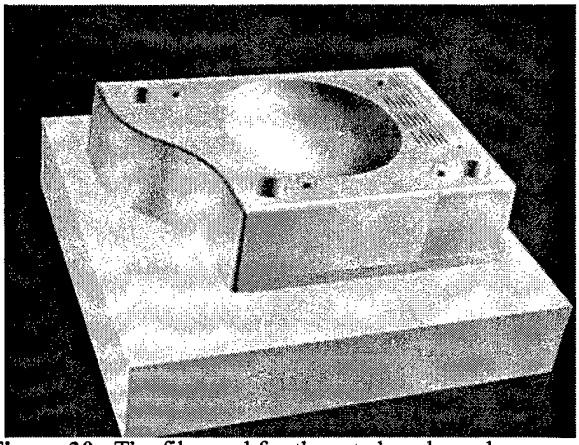


Figure 30. The file used for the rate bench mark. External dimensions are 140x135x57 mm.

this page intentionally blank

Integration of Solid Freeform Fabrication in Design

R. Hague*, I. Campbell**, P. Dickens*, P. Reeves***

*Department of Engineering & Technology, De Montfort University, Leicester, UK
**Department of Design and Technology, Loughborough University, UK
***Edward Mackenzie Ltd, UK

Abstract

During the last few decades, designers have been educated to develop designs with restricted geometry so that parts can be made easily. The revolutionary aspect of Rapid Manufacturing will be that geometry will no longer be a limiting factor. The introduction of Rapid Manufacturing will have a number of effects on *Design.* It will be possible to have re-entrant shapes without complicating manufacturing, no draft angles, variable wall thickness, no split lines and fewer parts leading to easier assembly and lower stock.

The individual designer's method of working will change with the introduction of Rapid Manufacturing and also there will be changes to the overall design process. Examples will be the elimination of prototype and pre-production stages, as end part manufacture will occur as soon as the CAD is finished. This will affect project management practices and sign-off procedures.

1 Introduction

The aim of this paper is to discuss the implications of the introduction of Rapid Manufacturing on design and on designers. As this is a new subject for discussion, the authors intend that this paper be viewed as a precursor to work that is needed. Many of the ideas discussed are the subject of much current research that is being performed into this area.

1.1 Definition of Rapid Manufacturing

First, it is important to give a definition of Rapid Manufacturing. The way that many things are manufactured in the future will change. The current use of moulds and dies to give items their form – be they parts for space shuttles, mobile phone covers or breakfast cereals – will be superseded by the emerging technologies that come under the Rapid Manufacturing banner.

Rapid Manufacturing is evolving from the now mature Rapid Prototyping (RP) technologies – such as stereolithography and laser sintering (amongst others). With Rapid Prototyping techniques, objects are created from a 3D CAD model without the use of either moulding or tooling. This is achieved by taking discrete 2D slices of the 3D CAD file and, either through the deposition of material, the sintering or binding of powder or by selectively changing the state of a UV sensitive liquid resin into a solid using a light source, objects are built-up layer-by-layer until the part is complete. Having been developed and commercialised over the last 15 years, layered manufacturing now plays an integral role in the modern product development cycle. RP processes are now routinely used for the production of functional and technical prototypes, visualisation and marketing models and even for the production of 'Rapid Tooling' cavities – although the value of some of these so-called Rapid Tooling techniques is questionable.

As the processes and materials improve over the next 10-years or so, much of this technology will develop into use within mainstream manufacturing.

2 Potential of Rapid Manufacturing on Design

For years, designers have been restricted in what they can produce as they have generally had to design-for-manufacture – that is, adjust their design intent to enable the component (or assembly) to be manufactured using a particular process or processes. In addition, if a mould is used to produce an item, there are therefore automatically inherent restrictions to the design imposed at the very beginning. Taking injection moulding as an example, in order to process a component successfully, at a minimum the following design elements need to be taken into account:

- Geometry
  - Draft angles
  - Non re-entrants shapes
  - Near constant wall thickness
  - Complexity
  - Split line location
  - Surface finish
- Material choice
- Rationalisation of components (reducing assemblies)
- Cost

With the advent of the Rapid Manufacturing techniques, there is the potential for many of the current obstacles to be removed. The following sections discuss the above points and also deal with some potential problems that are likely to occur with the on-set of Rapid Manufacturing in general.

2.1 Geometry for "Free"

One of the major benefits of some the additive manufacturing processes is that it is possible to make any complexity of geometry at no extra cost – this is virtually unheard of, as in every conventional manufacturing technique there is a direct link to the cost of a component to the complexity of its design. Therefore, for a given volume of component, it is effectively possible to get the geometry (or complexity) for "free", as the costs incurred for any given additive manufacturing technique are usually determined by the time to build a certain volume of part, that in turn is determined by the orientation that the component is built in.

2.2 Design Freedom

Additionally, the advent of Rapid Manufacturing will have profound implications for the way in which designers work. Generally, designers have been taught to design objects that can be made easily using current technologies – this being mainly due to the geometry limitations that exist with available manufacturing processes. For parts that are moulded, this means that draft angles, constant wall thickness, location of split line, etc, have to be considered in the design. However, with the additive manufacturing technologies, these limitations are removed as it is not necessary to withdraw the part

from the mould and therefore it would be possible to have re-entrant shapes without complicating manufacturing, no draft angles, variable wall thickness and no split lines. This new design freedom will place much more responsibility on the designer to think about the exact requirements of a part – with the unlimited geometry capability designers will therefore need to be much more imaginative to make full use of the new manufacturing processes. In the past, the processes have severely restricted designers and so they have become accustomed to designing relatively simple geometries.

The other main effect will be on the overall design process. At the moment a designer produces a rough CAD model and then a prototype is built, further design work is done until it is possible to manufacture a fully representative model. The next step may involve prototype tooling, functional testing and then production tooling and any final testing before large-scale manufacturing. If we are to have Rapid Manufacturing then the obvious question is what happens to these different stages because it will be possible to complete the CAD model and then directly manufacture the end use part?

2.2.1 Design Constraints

Although there will be the ability to manufacture whatever shape is required, this doesn't necessarily mean that there is complete design freedom. Recent work within a new UK funded EPSRC project on "Design for Rapid Manufacture" [1] has shown that even though, in theory, it is possible to design any shape that is desired, it is still necessary to consider the incorporation of existing components with the design process.

Products are generally a combination of many components that are assembled to produce the final article. Often "new" products incorporate components from existing proven designs and therefore the new products have to be designed accordingly to accommodate these components – this adds to the constraints in the products' design.

In addition, there is a clear need to design for assembly and maintenance. Even though there is the potential to reduce the part count by combining assemblies into fewer (more complex) individual parts, there will still be the need to assemble components such as electrical circuit boards, batteries, etc into the final article. It is recognised that, because the objects are being built additively, there is the potential to imbed components within the build, thus obviating the "design for assembly" issue. However, the machines required to perform these imbedding operations will be more complex and are likely to appear later than general Rapid Manufacturing machines and therefore the design requirements for general (single material) additive Rapid Manufacturing systems will need to be considered first. In addition, machines that imbed components as they build are likely to create other issues such as how they can be recycled – this is discussed in section 4.3.

2.3 Materials

When objects are formed in moulds, they are generally formed in one homogenous material. Even in the case of an over-moulded component where there can be two or more homogeneous materials in one finished part, there is a definitive boundary between one material and the other. With some of the additive manufacturing processes there is the potential to mix and grade materials in any combination that is desired, thus enabling materials with certain properties to be deposited where they are needed

The over-moulding technique is a classic example of how design can be influenced by the availability of a manufacturing technique. Over-moulding allows designers, within limits, the ability to produce parts that have added functionality and enhanced design. Indeed, the design of over-moulded components very often incorporates the different material combinations to accentuate the design to the extent that designers are able to exploit the delineation of the different materials used to produce design features as well as extra functionality. This is perfectly illustrated by the simple case of a toothbrush – an everyday item that will often include over-moulding to give a handle that is stiff, with an over-moulded grip and a different material at the neck to give a flexible head.

There are also issues when using different materials in a single product such as differences in thermal expansion or corrosion resistance. The ability to grade from one material to another could eliminate some of these problems.

Given that Rapid Manufacturing potentially allows the development of multiple materials to be deposited in any location or combination that the designer requires, this has potentially enormous implications for the functionality and aesthetics that can be designed into parts.

2.4 Custom Parts

There is a definite trend to "mass customisation" or even total customisation as people increasingly want to own items that are individual to themselves – wouldn't consumers all really like to have their own design of mobile phone (think of NOKIA Xpress-on™ covers), rather than one that looks like everyone else's? This last statement may or maybe not true, but most consumers have to have mass-produced items at the moment because all phones (or whatever) are made in moulds. The additive Rapid Manufacturing techniques are the enabling technologies to more cost-effective custom-made products.

One of the biggest advantages of Rapid Manufacturing will be the fact that tools will not be needed for many components as the products will be 'printed' directly. As it will not be necessary to mass produce parts to amortise the costs of the tooling into many thousands of components, this will lead to the potential for more custom made parts.

The potential to cheaply produce custom made products could prove to be lucrative to manufacturers who will be able to charge a premium for these so-called complex custom components that are, in effect, no more expensive to produce than simple parts. In the short term, this will present a tremendous profit making opportunities for manufacturers who pursue Rapid Manufacturing as an alternative to conventional techniques.

However, the ability to produce cost-effective custom made products will lead to the question of who will do the design work?

3 Who will do the Design Work?

It is thought that the Rapid Manufacturing technologies will split into home-based lower cost machines (akin to HP DeskJet's today) and more precise systems that will be company operated.

However, with the ability to produce custom-made products and the advances in web-enabled software, there is the potential to include the customer within the design process to enable them to produce their components either on their home-based systems or by the OEM (or third party supplier).

So far, this paper has described the implications on design by the advent of Rapid Manufacturing and has tended to concentrate on the implications to existing designers. If the end-user is to be involved in the design process, how can this be achieved? The following sections attempt to deal with how designs can be more custom-driven.

3.1 Customer-driven Design for Rapid Manufacturing

As discussed, Rapid Manufacturing potentially offers the end-customer the opportunity to design, order and receive a product without leaving their home. This vision of the future has been articulated by several people including Burns [2,3]. It is possible to imagine a situation where a home-based personal computer is used to design a three-dimensional (3D) object that is either produced on a 3D printer beside the operator or ordered over the Internet and delivered next day. But just how close are we to this vision today? Certainly, 3D CAD packages are readily available, ordering goods over the Internet has become an everyday activity for many and overnight production of physical models is on offer by Materialise [4]. However, there are issues that still need to be tackled. 3D printers are not yet readily available to home users. Multi-material models and "production quality" surface finishes are still the topics of much research. Intellectual property and product liability problems also need to be addressed.

Leaving these issues aside, there remains the critical matter of how deeply involved customers can become in the design of a product. Expecting a member of the general public to use a conventional 3D CAD system to create even simple shapes is not realistic. Even the most intuitive of menu-driven interfaces requires significant levels of training and knowledge of construction strategies. A number of options are available to overcome this constraint:

1. Restrict the design input of the user to selection from a pre-determined set of alternatives.
2. Use an innovative user-interface that requires little training and no construction strategy.
3. Enable the customer to work as part of the design team, e.g. in real-time collaboration with a designer.

Each of these will be discussed in turn and their potential contribution towards customer-driven Rapid Manufacturing will be assessed.

3.2 Restricted Input

Using parametric CAD and assembly modelling it is possible to create applications that use existing CAD models to create new product designs. The models are created by experienced designers and satisfy all the constraints of rapid manufacturing. Each model could represent a component within a particular product. An application can then be written that will allow the customer to select component options they wish to include in their "new design". Furthermore, some of the dimensions of the components can be varied within set limits to modify the design to meet customer

requirements. This makes use of knowledge relationships within the CAD model(s). A market where this technique has already been applied successfully is interior household design, e.g. DecoTech 3-D Design Software [5], Floor Plan 3D Design [6]. Applying this technique to products tailored specifically for Rapid Manufacturing is an area where much research is needed. An example of current research where designs are optimised to make full use of Rapid Manufacturing capabilities is the multi-material work at Clemson University [7]. The user can input design requirements and the optimum multi-material geometry is calculated automatically. CAD modelling capabilities need to be advanced to represent this type of information.

3.3 Innovative Interfaces

It may be feasible to give customers access to 3D design through innovative interfaces where little or no training is required. An example of this is the FreeForm™ system available from SenSable Technologies [8]. This technology enables the user to "sculpt" a "virtual clay" model inside a computer and in doing so can "touch & feel" the clay as they add or remove material. It uses a haptic feedback device that gives the impression of working with a resistive medium. The geometry that is created is truly freeform and in many cases can only be produced using Rapid Manufacturing. The method of operation has been designed to be intuitive to the user and reduces any computational or engineering skills necessary to operate the system to an absolute minimum. This approach ensures that not only are new users "up & running" and therefore productive within a very short period of time but they also feel far less inhibited and constrained by the technology. It can be easily envisaged that a customer could be allowed to generate new shapes, or at least modify existing designs, using this technology. An example of a novel design produced using Freeform and the 3D model produced using a Z-Corp machine are shown in Figure 1. The stippled effect on the surface of the model was produced using "virtual hammering".

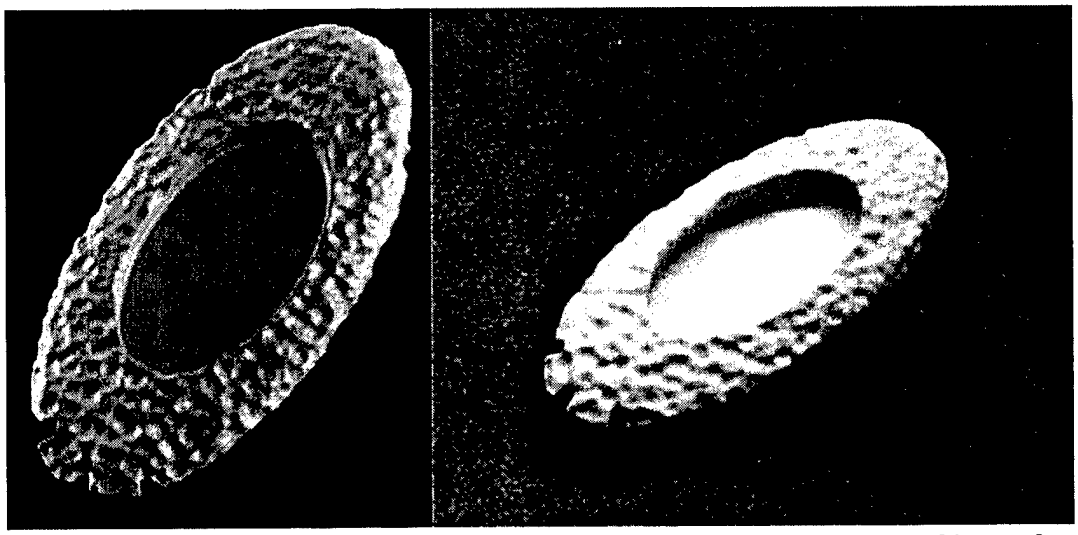


Figure 1: a) Virtual hammering effect created using haptic feedback, b) resultant physical model.

3.4 Collaborative Design

The third technique for involving customers in the design process is through partnership with a designer. This can be readily done when the customer is brought into direct contact with the designer, e.g. in a design studio. However, if the goal is to allow the customer to stay at home then an alternative strategy must be used. Using the Internet, it is possible to connect the customer and designer using virtual conferencing, real-time imaging software (e.g. Magics Communicator [9]) and collaborative CAD software. However, designers are not always available and international time-zones can cause serious difficulties. An alternative is to couple the user with a knowledge-based system that simulates an experienced designer. One such system is Cybercut™ developed at U. C. Berkeley. This is "a web based design-to-prototype service, allowing users to quickly design and manufacture prototypes for mechanical parts. A series of interactive web pages act as an on-line CAD tool linked to a 'computer machinist', which restricts the user to the design of 'manufacturable' parts. When the design is completed, the part specifications are sent directly to a computer controlled three axis milling machine, and fabrication can begin immediately" [10]. It is conceivable that a similar system could be developed specifically for Rapid Manufacturing.

Bringing the customer further into the design process is a desirable part of rapid product development that could lead to truly customised products. The unique characteristics of Rapid Manufacturing make it particularly suitable for this strategy. A number of alternative techniques offer this capability and the optimum solution will vary from one product to the next. Indeed, the optimum solution may well be a combination of those discussed here.

4 Potential problems with Rapid Manufacturing

4.1 CAD

One of the most important problems to be overcome in the future will be the limitation of existing CAD modelling systems. The new Rapid Manufacturing processes will be able to produce objects with different materials or microstructure throughout but existing CAD systems cannot represent this except with a very coarse resolution or on small parts only. A few researchers in Universities (Univ. of Michigan, Clemson) are investigating Voxel Modelling systems. Unless great progress is made in CAD development, the situation will arise that there will be the capability of manufacturing these complex structures but no way of representing them in CAD.

4.2 Materials

There are two fundamental problems with materials and they are both related to the global amount used. As the quantity used is very low compared to conventional processes then the production cost is very high and this is reflected in the sale price where for example Stereolithography resin costs around GBP160/kg whereas ABS plastic costs GBP0.40/kg. The other main problem is the limited variety of materials. As the quantity sold is low then it is more difficult to justify development of new materials.

Additionally, there is a dearth of information about even the limited number of materials that are available today – materials research is one of the keys areas at present. More reliable information is crucial to a greater uptake of Rapid Manufacturing as a mainstream technique.

4.3 Recycling

The potential to produce exotic graded materials and also to imbed components within a part as it is being built will present issues of recycling – how will the imbedded assemblies and exotic materials be separated for safe disposal or re-use?

At present this does not pose a particular problem as there is limited uptake of Rapid Manufacturing. However, if there is a larger uptake of Rapid Manufacturing technologies as expected, this will become an increasing issue as the volume of parts to be disposed of will increase.

4.4 Product Liability & IPR

With the potential for the consumer to be involved in the design of their components and also for them to be able to make them – or any other component that they download from the internet – at home on their own Rapid Manufacturing machine, there are major implications for product liability and intellectual property that need to be addressed.

5 Summary

The possibilities offered by Rapid Manufacturing are profound. Suddenly, designers will be able to manufacture any shape that they come up with and will no longer be constrained by the necessity to produce parts in moulds. In addition, using processes such as the laser sintering of dissimilar powders, RM will provide designers with new and exotic materials not available to other manufacturing processes

At the design phase, RM allows whatever shape is desired as the mould process will no longer limit design. This means objects can be designed with re-entrant features, no draft angles, unlimited wall thickness and increased complexity with none of the limitations imposed by either the moulding process or the tool making process – as neither will be required.

One of the most profound implications of RM on design will be that without the cost of tooling to amortise into the parts produced, each component can be different, potentially allowing for true mass-customisation of each and every product. With developments in web-enabled software, high levels of computer literacy and Internet connectivity in the home, the technologies are not far from giving the consumer the ability to modify the design of the product they desire for themselves. Although some way off, it is conceivable that the consumer may – for a price – want to influence the design of their new sun-glasses, mobile phone casing, steering wheel grip, surgical instrument, prosthetic part or favourite kitchen utensil, etc, and then send the data back to the manufacturer to be made for them.

Rapid Manufacturing will become more of a reality when the properties of the materials that are produced become more acceptable and consistent. This materials research is one of the main stumbling blocks to the adoption of these additive-manufacturing techniques for end-use parts and is the subject of much current research.

In addition, the potential changes in product design and the ability for consumers to potentially build parts for themselves also brings legal and management issues such as product liability, CE marking and quality concerns such as ISO9000-2000 conformance.

6 References

1 EPSRC Grant Reference GR/R13517/01, Design for Rapid Manufacture, P. Dickens, R. Hague.

2 Burns, M. *Automated fabrication: the future of manufacturing,* Rapid Prototyping Journal, vol 1, no 1, 1995, pp 37-38.

3 Burns, M. *The Freedom to Create,* Technology Management, vol 1, no 4, 1995, pp 157-163.

4 Materialise Next Day: http://www.materialise.com/NextDay/nextday.html?division=NextDay

5 DecoTech 3-D Design. http://www.pulsara.com/

6 Floor Plan 3D Design. http://www.imisoft.com/

7 Fadel, G. and Saminathan, M. *3-D Multi-Material Optimization using Developed Finite Element Code,* http://www.vr.clemson.edu/credo/

8 FreeForm Modeling System. http://www.sensable.com/

9 Magics Communicator. http://www.materialise.be/communicator/

10 Cybercut Network Manufacturing Service, http://kingkong.me.berkeley.edu/cybercut/

this page intentionally blank

Laser Fusion Coatings of Functional Parts

J.A. Ramos[1], D.L. Bourell[1], M.R. Govindaraju[2]

(1) Department of Mechanical Engineering, Laboratory for Freeform Fabrication
The University of Texas at Austin, Austin, Texas, 78712

(2) Karta Technologies, Inc., 5555 Northwest Parkway, San Antonio, Texas, 78249

ABSTRACT

Surface characteristics of functional parts made by Solid Freeform Fabrication techniques such as Selective Laser Sintering (SLS), Stereolitography Apparatus (SLA) or other fabrication techniques can be enhanced by the application of multi-element based laser fused coatings. Environmental protection and wear resistance, among other properties can be achieved by pre-depositing a slurry over the surface of the parts, followed by a high-speed scanning with a high power laser beam. Wetting of the part surface by the molten slurry is a main concern in this coating process. Wetting characteristics of molten slurry can be improved by the right combination of coating constituents, laser processing atmosphere, and laser processing parameters. Coating quality is also a critical issue to ensure good performance of the coatings especially for environmental protection. This paper presents results obtained for carbon-carbon composites coated with silicon-based slurries by laser fusion process. Criterion in selecting the coating constituents, laser process conditions, and oxidation test results are discussed.

Introduction

For more than two decades laser coatings have been successfully applied over metal substrates by several known techniques such as cladding, pre-deposited powders, foils or rods [1-3]. In all these laser processes, a bond is formed between the metal substrate and the coating as melting of the former facilitates the dilution of the coating elements into the substrate. On the other hand, when the substrate of the functional part is a ceramic material that decomposes rather than melts (e.g. carbon-carbon composite), coatings with good bonding characteristics and with overall wetting of the substrate are less likely to be obtained during laser fusion. Poor interfacial characteristics in laser fused samples can be attributed to lack of proper fusion temperature and inadequate dwell time as well as the presence of contaminants such as oxygen and moisture that alter the surface tension balance. Moreover, coating thickness, differences in coefficient of thermal expansion (CTE) between the coating and substrate have a major impact on the delamination or spalation behavior of the coatings [4]. Surface wetting by the chemical

slurry depends on the solubility, bonding compatibility, chemical reactivity of the substrate, and the coating constituents [5]. The degree of superheat of the molten slurry will also determine the viscosity of the coating as well as the reaction kinetics. The surface roughness of the samples may increase the interface area contributing to an increase in interfacial strength. However, a rough surface may have poor integrity because of poor wetting and sharp grooves [6]. Finally, the residence time of the molten slurry over the substrate will in turn control the thickness and evenness of the interface. Nonetheless, recent research on coating of ceramics using laser chemical decomposition and laser fusion has shown promising results [9].

Coating of Carbon-Carbon Composites

The surface of carbon-carbon (C/C) composite functional parts used in space vehicles (e.g. rocket nozzles and nose cones) requires environmental protection especially during atmosphere reentry maneuvers. Oxidation at high temperatures is deleterious to the performance of the C/C composites, which start oxidizing at 400 °C in air. For more than 30 years, single and multi-layer coating techniques have been investigated to enhance the performance of C/C composite materials at high temperatures. Chemical vapor deposition (CVD) is widely used to deposit SiC layers over C/C composites; however, this is a slow and cumbersome process and requires operation under high vacuum conditions. Diffusion-based processes such as pack cementation or fused slurry techniques are also being used to form oxidation resistant coatings. However, these processes require that all of the part surface must be coated and they too need several hours for processing [7, 8]. The purpose of the current ongoing research program is to develop a laser fusion methodology to deposit protective coatings to improve oxidation resistance of C/C composites. The laser fusion coating methodology is based on the principles of laser-induced chemical reduction of a carefully selected mixture of metals/elements to form complex phase coatings [9]. Metal salts can be reduced to their native states by the application of laser irradiation. For example, a metal salt such as nickel formate can be reduced to form nickel by laser energy. The elements then get fused in the surface layers of the C/C substrate. Laser fusion coating process involves formation of a chemical slurry consisting of the coating constituents and the deposition of slurry on the sample surface, followed by laser processing. In this paper, the effects of coating composition and laser process parameters on the coating quality are discussed.

The work presented here is a continuation of the investigation on laser fusion coatings; however, now it incorporates a laser beam delivery system similar to that used in Selective Laser Sintering. Galvanometer driven mirrors are used to raster scan the focused laser beam back and forth at speeds up to 5 times faster than used previously. Overlapping between scanned tracks of almost 90% is used to provide enough residence time so that a high temperature can be sustained to allow for a complete reaction between the substrate and the molten elements. Because of the faster scanning rate and high percentage of overlapping, the heat diffusion time is longer than the time it takes for the laser beam to raster scan one line. Thus, the material is subjected to a rectangular heat source rather than a single moving spot. Infrared thermal mapping of the surface confirmed observation of this rectangular heat distribution, which favors uniform and

continuous coatings. The process is carried out inside a sealed chamber under rough vacuum back-filled with an inert-reducing atmosphere.

Experimental

Samples of 3D C/C composites were obtained from BF Goodrich, Santa Fe Springs, CA. Coupons were machined having dimensions of 28 mm in length, 12 mm in width and 3 mm in thickness. Samples were cleaned with acetone to remove contaminants from the surface before laser processing. Slurries were prepared by mixing finely ground powders (mesh –325) with isopropyl alcohol to form a viscous paste that was then deposited manually over the surface of the composite by means of a spatula. After the slurry had dried, the samples were placed inside the processing chamber, which was evacuated to 200-mTorr vacuum level, and then back filled with argon-4% hydrogen.

Figure 1 shows a schematic of the laser process. A high power CO_2 laser beam focused down to 0.35+/-0.05 mm was scanned at a speed (V_s) up to 10 m/min using a scan density of 1000 raster lines/inch. To prevent heat accumulation due to the finite dimension of the sample and keeping a constant temperature during laser processing the laser power was linearly ramped down from 700 to 350 Watts. The traverse velocity (V_t) used was of the order of 55-80 mm/min. Figure 2 shows a thermal image of the area scanned by the laser beam obtained by using an infrared camera. The longer axis of the rectangle corresponds to the width of the composite (i.e.,12 mm); therefore the minor axis measures between 2-3 mm. The temperature inside the rectangular zone is relatively constant during the entire process. The temperature generated in the sample must be high enough to melt the coating elements and still cause some degree of superheat to allow for spreading of the slurry over the surface. A chemical reaction between the molten elements and the surface of the composite is expected to take place; however, the extent of this reaction depends on the laser dwell time.

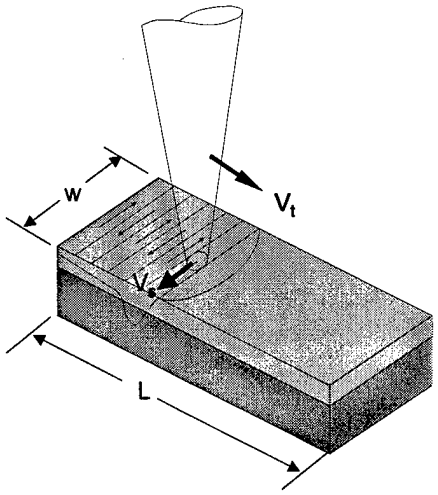


Figure 1. Schematic of the laser fusion coating process. The top layer is the coating on the composite surface.

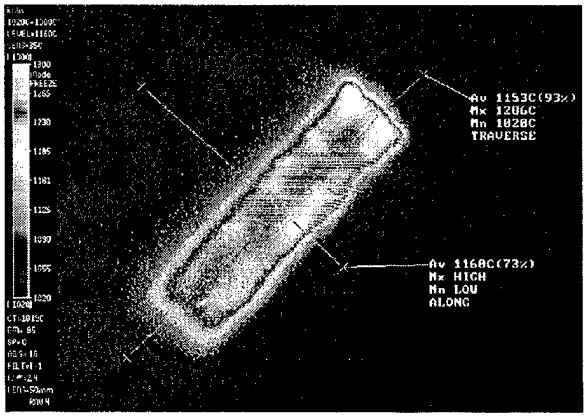


Figure 2. Infrared thermal image of raster scanned laser beam. The average temperature in the hot zone is 1160 °C.

All the samples were examined using light optical and scanning electron microscopy (SEM). Light and electron optic techniques were used to characterize the microstructural features of the surface and interfacial regions. Microchemical analysis of the coating and coating/substrate interface region was conducted by using the electron microprobe and energy dispersive x-ray analysis (EDAX). Oxidation behavior of the coated and uncoated samples was evaluated by heating the sample at 1000°C in a tube furnace in still air. The samples were removed from the furnace at intervals of 30 minutes, followed by weighing until the failure of the coated sample.

Results and Discussion

Microstructural Characterization

Figure 3 shows the microstructure of the as-received sample of a C/C composite. It is observed that the surface is inherently rough, providing a larger interface area for mechanical interlocking. However, surface roughness hinders wetting and formation of a continuous chemical bond due to the presence of sharp grooves. Figure 4 shows the microstructure of a C/C composite surface coated with a pure silicon layer by means of laser fusion. Complete wetting of the surface with pure silicon was not achieved, most probably due to the presence of oxygen resulting in the formation of silica (SiO_2) layer. Presence of silica layer on the surface also alters the surface tension balance and favors solidification with higher wetting angles. A SiC interfacial layer at the substrate is most likely to form as soon as the molten silicon wets the surface. The thickness and extent of this interfacial layer will be a function of the laser dwell time during which time the silicon remains at or above its melting temperature. Longer dwell times involve slower scanning speed and larger beam overlap. However, longer dwell times will lead to longer exposure times of the slurry to contaminants that hinder the wetting of the composite surface. This suggests that an optimum dwell time exist that minimizes the wetting angle caused by exposure to impurities and maximizes the reaction layer thickness which is controlled by atomic diffusion.

In order to improve wetting of the C/C composite surface by silicon the composition of the chemical slurry was changed by adding 10 wt.% of HfC. HfC is a refractory compound that melts at about 3900°C. The high heat capacity of this carbide thermally stabilizes the melting front and helps in even spreading of the molten slurry possibly by a dragging mechanism, as the melt region is stirred by Marangoni's type flow [1,2]. However, as seen in Figure 5, several long cracks can be seen on the surface most probably due to its high CTE relative to pure silicon and carbon. The formation of a eutectic-like pattern can be observed at higher magnification in Figure 6, the white microconstituents corresponding to HfC. This morphology may lower the melting point of the mixture and therefore increase the level of superheating, which in turn reduces the viscosity of the molten slurry allowing it to flow with less difficulty.

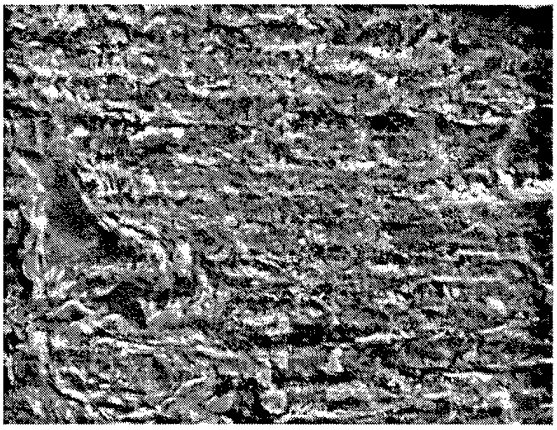


Figure 3. 3D C/C "shoe-brake" composite rough surface, 1000x.

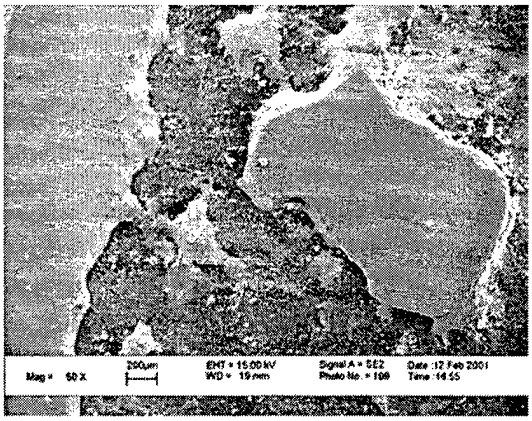


Figure 4. SEM image of Si coating indicating signs of incomplete wetting of the surface, 50x.

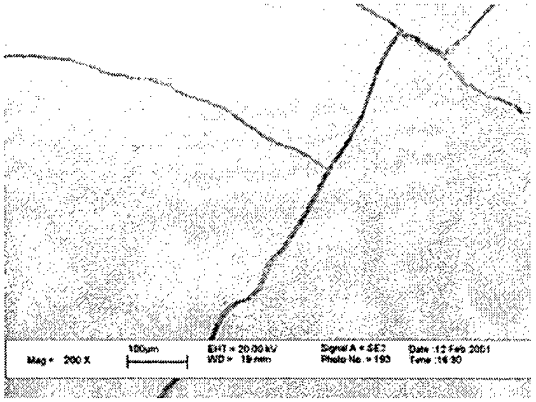


Figure 5. SEM image 200x of Si-10wt.%HfC coating showing signs of multiple cracks.

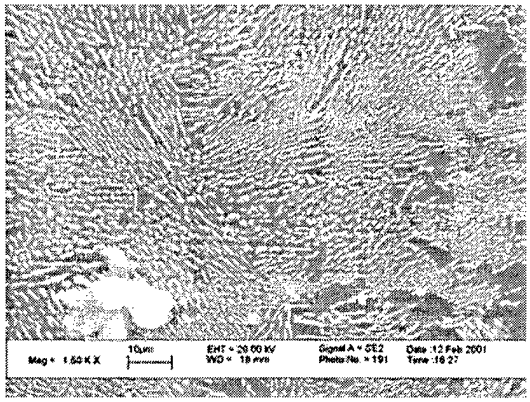


Figure 6. SEM image 1500x of Si-10wt.%HfC coating indicating a eutectic like morphology.

Figure 7 shows the microstructure of the primary laser fused CTE matching coating layer having the chemical composition of Si-20SiC-5Ti-5Al (all wt %.) EDAX analysis of the coating indicated the presence of aluminum and titanium silicates. Some cracks are observed on the surface caused by the CTE mismatch between the substrate and the coating. However, the sample showed improved wetting characteristics probably due to the addition of:

(a) Ti: which acts as an oxygen getter, helps to reduce the contamination by oxygen and thus enhance wetting
(b) Al: which lowers the melting point of the slurry thereby allowing for larger superheat that in turn lowers the viscosity of the melted slurry and enhanced wetting
(c) SiC: operates much in the same way as HfC by stabilizing the melt front due to its refractory properties, increasing drag on the melt and providing a dispersion of embedded particles that can help in arresting cracks.

Figure 8 shows the surface of the oxygen diffusion barrier coating - consisting of Si-15 HfC-10Ir-5Ti (wt.%). Iridium and HfC have been added to provide protection at temperatures where silicon can no longer provide sufficient oxidation protection.

Titanium was added to reduce oxygen contamination. However, severe cracking took place due to mismatch of the CTE between the diffusion barrier coating, the primary CTE matching layer and the substrate. It is possible that HfC and iridium can undergo a Lewis Acid-Base type exothermic reaction that creates a much more intermetallic compound which could lead to a further increase in the CTE mismatch [10]. The relative thickness of coatings can also lead to the formation of cracks. To mitigate the deleterious effect of the numerous cracks seen in Figure 8, a third coating was applied on the sample. This final coating step consisted of dipping the sample in a silica-based sealant agent (SILBOND^{TM}) for 10 minutes followed by drying in air for 24 hours. The sealant agent penetrated the cracks easily due to its extremely low viscosity and formed a glassy layer on the sample surface.

Figure 9 shows a cross-section of a coated C/C sample having a three-layer coating, namely: CTE matching layer of composition Si-20SiC-5Ti-5Al (wt %.), oxygen diffusion barrier layer of composition Si-15HfC-10Ir-5Ti (wt.%) and a SILBOND^{TM} layer. The coating thickness is clearly uneven, ranging from 5 to 20 μm. Good mechanical interlocking is observed. However, the thickness of the interfacial layer was not measured.

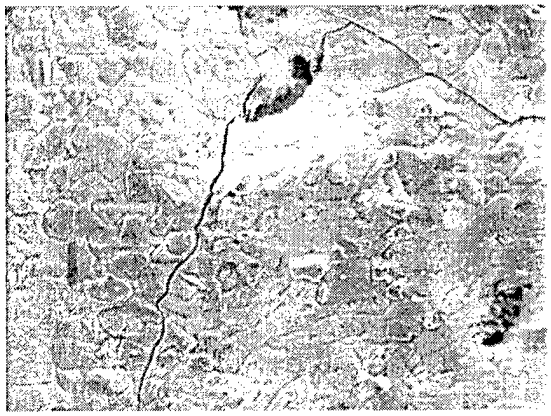


Figure 7. SEM image of Si-20SiC-5Ti-5Al (wt.%) CTE matching coating laser fused at 700 W and 55 mm/min over C/C composite surface, 500x.

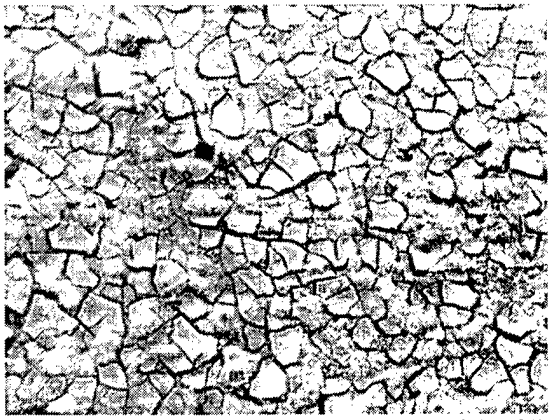


Figure 8. SEM image of Si-15HfC-10Ir-5Ti (wt.%) oxygen diffusion barrier coating laser fused at 560 W and 80 mm/min over previously deposited CTE matching coating, 200x.

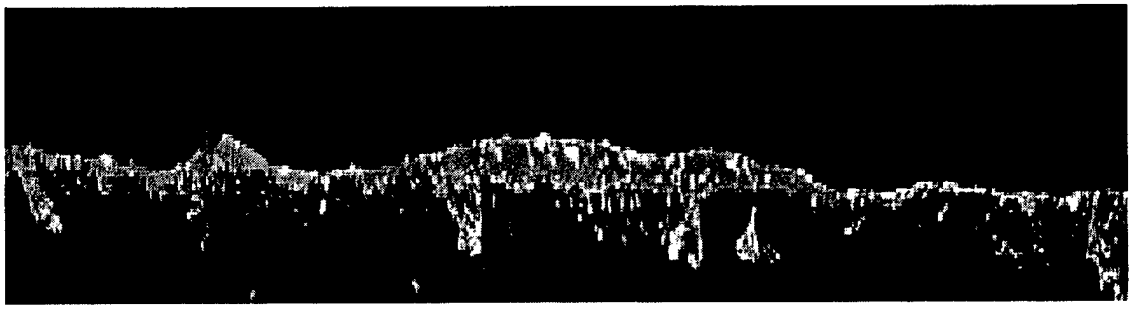


Figure 9. Scanning electron micrograph showing the cross-sectional view of the three-layer coating laser processed sample. Infiltration of the coating material into the voids or inter-fiber space is shown thereby providing mechanical interlocking of the coating to the substrate.

Oxidation Testing

Figure 10 shows a plot of the weight loss data for the coated and uncoated samples as functions of time at 1000°C in still air. Coated sample consisted of: Si-20SiC-5Ti-5Al (wt.%) CTE matching layer, Si-15HfC-10Ir-5Ti (wt.%) oxidation diffusion barrier layer and SILBOND^{TM} layer. After 1.6 hours of exposure the coated samples lost 57% of its original weight, whereas the uncoated sample was completely oxidized. Figure 11 shows a plot of the weight loss rate per unit area of sample surface for the coated and uncoated samples. These data points were obtained by computing discrete changes in weight loss with respect to time, normalized by the surface area of each sample. The coated sample maintained a weight loss rate of –0.012 gr/cm^2 for almost one hour, whereas for the uncoated samples it corresponded to –0.022 gr/cm^2, indicating a two-fold increase in oxidation.

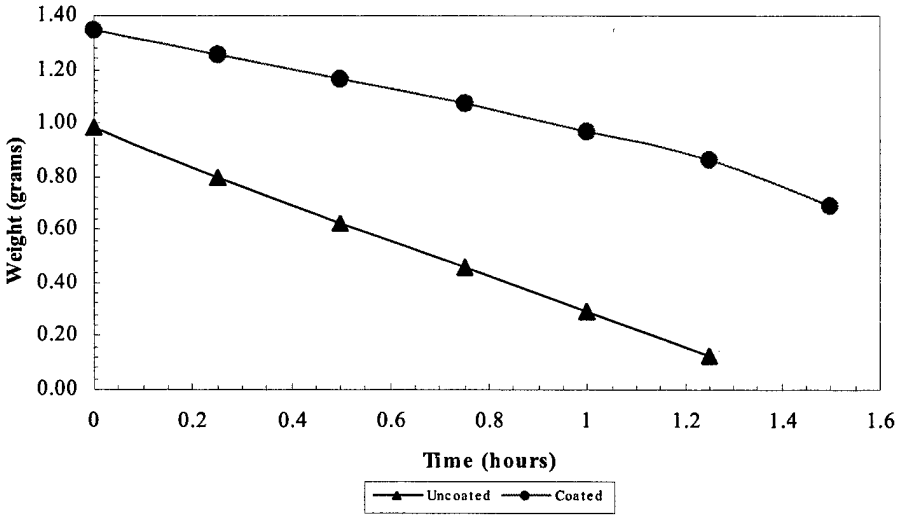


Figure 10. Weight loss data for coated and uncoated samples at 1000°C. Coated sample consisted of CTE matching layer (Si-20SiC-5Ti-5Al wt.%), oxidation diffusion barrier layer (Si-15HfC-10Ir-5Ti wt.%) and SILBOND^{TM} layer.

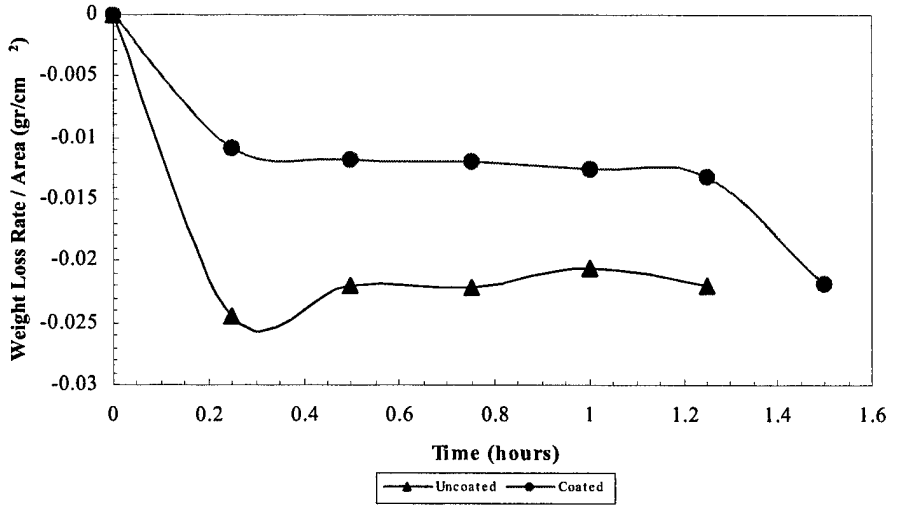


Figure 11. Weight loss rate versus time for coated and uncoated samples at 1000 °C in still air.

Conclusions

Laser fusion coating of functional parts can be achieved by means of high-speed raster scanning of a pre-deposited slurry with a high power CO_2 laser beam. Unlike in other conventional laser processes, the experimental procedure used in the laser fusion process uses a rectangular energy source rather than a single beam. This allows for a uniform fusion temperature during the process thereby resulting in a more uniform coating.

High scanning speed used in the process helps in overcoming the effect of surface tension dragging of coating regions ahead of the melt front and lowers the exposure time to contamination. Use of high scanning speeds however, reduces the dwell time necessary to grow a complete interface layer.

Under rough vacuum conditions an addition of 5 wt.% titanium powder to the coating helped reduce oxygen contamination. The study also indicated that addition of 5 wt.% aluminum to the coating lowers the melting point resulting in larger superheating that in turns lowers the viscosity of the melted slurry thereby enhancing wetting. Addition of Si and SiC to the coating composition provides oxidation protection to the C/C composite at temperatures below 1500°C due to the formation of a glassy SiO_2 layer, but at higher temperatures this coating layer delaminates. HfC and iridium are inherently refractory materials that provide oxidation protection at temperatures above 1500°C. Addition of SiC and HfC particles to the coating composition also seem to help in lowering the wetting angle by dragging the melt more uniformly over the surface of the composite. Applying a crack sealant coating could mitigate severe cracking due to the mismatch in CTE between coating layers and the substrate. The study indicates a two-fold increase in the oxidation resistance of the coated C/C composites at 1000°C in still air. Nonetheless, a crack free coating remains as the goal left to achieve by this laser fusion technique.

References

1. Steen, W.M.(1994) : Laser Material Processing, 2nd edition, Springer Verlag.
2. Schuocker, D. (1999): High Power Lasers in Production Engineering, Imperial College Press, World Scientific.
3. Dahotre, N.B.(1998) : Lasers in Surface Engineering: Surface Engineering Series, Vol 1. ASM International.
4. J.W. Hutchinson and Z. Suo, "Mixed Mode Cracking in Layered Materials"; pp. 64-191 in Vol. 29, *Advances in Applied Mechanics.* Edited by J.W. Hutchinson and T.Y. Wu. Academic Press, Inc., San Diego, CA, 1992.
5. J.V. Naidich, "The Wettability of Solids by Liquid Metals" *Prog. Surf. Memb. Sci.*, 14, pp. 353-484 (1981).

6. X.B. Zhou and J. Th.M. De Hosson, "Influence of Surface Roughness on the Wetting Angle", *J. Mater. Res.*, Vol.10, N° 8, pp. 1984-1992 (1995).
7. T. Morimoto, Y. Ogura, M. Kondo, and T. Ueda, "Multilayer Coating for Carbon-Carbon Composites"; *Carbon*, Vol. 33, No 4, pp. 351-357 (1995).
8. C. Isola, P.Appendino, F. Bosco, M. Ferraris, and M.Salvo, "Protective Glass Coating for Carbon-Carbon Composites." *Carbon*, Vol. 36, N° 7-8, pp. 1213-1218 (1998).
9. M.R. Govindaraju and J.A. Ramos, "Development of Laser Fusion Coatings for Improving Oxidation Resistance of Carbon-Carbon Composites"; Proceedings of the SAMPE Conference, Long Beach, CA, May 2001.
10. Leo Brewer, "Chemical Bonding Theory Applied to Metals", pp.1-128, *Alloying*, J.L. Walter, M.R. Jackson, and C.T. Sims (editors), ASM International, 1988.

Acknowledgements

The authors gratefully acknowledge the support of the Ballistic Missile Defense Organization (BMDO) for this work. The research is being funded under the Small Business Innovative Research (SBIR) Program and managed by the Wright-Patterson Air Force Base, Dayton, Ohio.

this page intentionally blank

Dave Alexander
Pratt & Whitney
MS 114-39
400 Main Street
East Hartford, CT 06108
USA
Phone: (860) 565-3665
Fax: (860) 755-4291
alexnder@pweh.com

Joel Barlow
The University of Texas at Austin
Dept. of Chemical Engineering
Austin, TX 78712
USA
Phone: (512) 471-1271
Fax: (512) 471-7060
barlow@che.utexas.edu

Joe Beaman (28, 296, 338, 468, 584)
The University of Texas at Austin
Mechanical Engineering Dept. C2200
Austin, TX 78712-1063
USA
Phone: (512) 471-3058
Fax: (512) 471-8727
jbeaman@mail.utexas.edu

Udo Behrendt
EOS GmbH
Haufllteilweg 14
85104 Pforring
Germany 85104
Germany
Phone: ++4984031430
Fax: ++4984031453

Jack Beuth (432)
Carnegie Mellon University
Department of Mechanical Engineering
5000 Forbes Avenue
Pittsburgh, PA 15213-3890
USA
Phone: (412) 268-3873
Fax: (412) 268-3348
beuth@andrew.cmu.edu

Amba Bhatt
Mechanical Engineering Dept.
Motilal Nehru Regional Engg. College
Allahabad
Allahabad (UP)
India-211004
adatt@lycos.com

Chris Bocking (486)
CRDM, Buckinghamshire Chilterns University College
Queen Alexandra Rd.
High Wycombe, Bucks Hp11 2JZ
UK
Phone: +44 1494 605085
Fax: +44 1494 538593
chris.bocking@bcuc.ac.uk

Mallikharjuna Rao Boddu (452, 460)
University of Missouri-Rolla
1300 North Oak St., Apt. #15
Rolla, MO 65401
USA
Phone: (573) 341-5335
Fax: (573) 341-6899
mallik@umr.edu

Klas Boivie (264)
Woxencentrum
Brinellvagen 68
10044 Stockholm
Sweden
Phone: +46 8 7906371
Fax: +46 8 210851
kbv@iip.kth.se

Scott Bondi (61, 373)
Georgia Institute of Technology
460 Marc Building, Mechanical Engineering
813 Ferst Drive
Atlanta, GA 30332
USA
Phone: (404) 894-1836
Fax: (404) 894-9342
scottbondi@hotmail.com

Dave Bourell (28, 296, 628)
The University of Texas at Austin
Mechanical Engineering Dept. C2200
Austin, TX 78712-1063
USA
Phone: (512) 471-3170
Fax: (512) 471-7681
dbourell@mail.utexas.edu

Henry J. Cataldo
The Gillette Company
37A Street
Needham, MA
USA
Phone: (781) 292-8351
Fax: (781) 292-8356
Henry_Cataldo@gillette.com

Joe Cesarano (175, 561)
Sandia National Labs
1001 University Blvd. SE
Albuquerque, NM 87106
Phone: (505) 272-7624
Fax: (505) 272-7663
jcesara@sandia.gov

Chan Mei Mei
The University of Hong Kong
Industrial & Mfg. Systems Engineering
Haking Wong Building
No. 1, Pokfulam Road
Hong Kong, Hong Kong
China
Phone: (852) 28597967
Fax: (852) 28586535
amychan@graduate.hku.hk

Paul Cherkas
Syneon
450 Cabot Road
S. San Francisco, CA 94080
USA
Phone: (650) 246-1226
Fax: (650) 246-1229
pcherkas@syneon.com

W. L. Cheung (1, 146)
The University of Hong Kong
Dept. of Mechanical Engineering
Pokfulam Road
Hong Kong
People's Republic of China
Phone: (852) 28592639
Fax: (852) 28585415
wlcheung@hkusc.hku.hk

Mark Chung
DTM Corporation
1611 Headway Circle
Building 1
Austin, TX 78754-5199
USA

Michael J. Cima (69, 216)
Massachusetts Institute of Technology
77 Massachusetts Avenue, Bldg. 12-011
Cambridge, MA 02139
USA
Phone: (617) 253-6877
Fax: (617) 258-6936
mjcima@mit.edu

William S. Coblenz
DARPA Visiting Scientist @ MIT
MIT Room 13-5057
77 Massachusetts Ave.
Cambridge, MA 02139
USA
Phone: (617) 452-3721
Fax: (617) 253-6201
wcoblenz@darpa.mil

Jim Comb
Stratasys Inc.
14950 Martin Drive
Eden Prairie, MN 55344-2020
Phone: (952)906-2234
Fax: (952)937-0070
jcomb@stratasys.com

Khershed P. Cooper (576)
Naval Research Laboratory
Materials Science & Tech. Div., Code 6324
4555 Overlook Ave., SW
Washington, DC 20375
Phone: (202) 767-0181
Fax: (202) 767-2621
cooper@anvil.nrl.navy.mil

Brian Cox
DTM Corporation
1611 Headway Circle
Building 2
Austin, TX 78754-5199
USA
Phone: (512) 425-2924
Brian_Cox@DTM-Corp.com

Rich Crawford (296, 338, 381, 505, 513)
The University of Texas at Austin
Mechanical Engineering Dept. C2200
Austin, TX 78712-1063
USA
Phone: (512) 471-3030
Fax: (512) 471-7682
rhc@mail.utexas.edu

Terry S. Creasy
Texas A&M University
100 ENPH
M.S. 3123
College Station, TX 77843-3123
USA
Phone: (979) 458-0118
Fax: (979) 862-3989
Tcreasy@mengr.tamu.edu

James Crocker (163, 170, 392)
University of Connecticut
U-136
97 North Eagleville Road
Storrs, CT 06269-3136
USA
Phone: (860) 486-4410
Fax: (860) 486-4745
james.e.crocker@uconn.edu

Jim Darrah
DTM Corporation
1611 Headway Circle
Building 2
Austin, TX 78754-5199
USA

Suman Das (85, 94, 102, 155, 357)
University of Michigan
Mechanical Engineering Dept.
2138 G. G. Brown
2350 Hayward St.
Ann Arbor, MI 48109-2125
USA
Phone: (734) 615-6646
Fax: (734) 647-3170
sumandas@umich.edu

Ken Davis
University of Louisville
Rapid Prototype Center
Vogt Building #101
3rd & Eastern Parkway
Louisville, KY 40292
USA
Phone: (502) 852-7599
Fax: (502) 852-8890
ken.davis@louisville.edu

Deepak Dcosta (203, 527)
Drexel University
2250 Holly Hall Dr., Apt. #255
Houston, TX 77054
USA
Phone: (281) 285-5240
Fax: (281) 285-5171
deepslb@hotmail.com

Carl Deckard
Deckard Engine Works
720 Bastrop Hwy. #108
Austin, TX 78741
USA
Phone: (512) 385-0388
Fax: (512) 385-0386
carld@deckardengine.com

Phill Dickens (441, 619)
De Montfort University
The Gateway
Queens Building
Leicester LE1 9BH
England
Phone: (+44 116) 257-7689
Fax: (+44 116) 257-7071
pdickens@dmu.ac.uk

Stefan Dreher (479)
Fraunhofer IPK Berlin
Pascalstr. 8-9
Berlin
Berlin 10587
Germany
Phone: (+49) 30 39006-111
Fax: (+49) 30 3930246
stefan.dreher@ipk.fhg.de

John N. DuPont (232)
Materials Science & Engineering Dept.
Lehigh University
5 East Packer Avenue
Bethlehem, PA 18015
USA
Phone: (610) 758-3942
Fax: (610) 758-4244
jnd1@lehigh.edu

Alan Dutson (296)
University of Texas at Austin
3104 Blazing Star Trail
Cedar Park, TX 78613
USA
Phone: (512) 918-1945
Fax: (512) 471-8727
adutson@mail.utexas.edu

Chad Duty (61, 373)
Georgia Institute of Technology
460 Marc Building, Mechanical Engineering
813 Ferst Drive
Atlanta, GA 30332
USA
Phone: (404) 894-1836
Fax: (404) 894-9342
gt4465a@prism.gatech.edu

Masami Eguchi
Toyota Tsusyo Corporation
128 Yamanote 5tyoume
Toyota City, Aichi Pref. 471-8512
Japan
Phone: +81-565-27-9428
Fax: +81-565-27-9483
Masami_Eguchi@gw.toyotsu.co.jp

Georges M. Fadel (553)
Clemson University
Box 340921
202 Fluor Daniel Building
Clemson, SC 29634-0921
USA
Phone: (864) 656-5620
Fax: (864) 656-4435
gfadel@ces.clemson.edu

Mario Faustini (381, 505)
The University of Texas at Austin
Mechanical Engineering Dept. C2200
Austin, TX 78712-1063
USA
faustini@mail.utexas.edu

Kent Firestone
DTM Corporation
1611 Headway Circle
Building 2
Austin, TX 78754-5199
USA
kentf@dtm-corp.com

Farid Fouchal (441)
De Montfort University
The Gateway
Leicester LE1 9BH
UK
Phone: (+44)116 250 6454
Fax: (+44)116 257 7071
farid@dmu.ac.uk

Matt Frey
3M Company
3M Advanced Materials Technology Center
3M center Bldg. 201-4N-01
St. Paul, MN 55144
USA
Phone: (651) 736-8968
Fax: (651) 737-4682
mhfrey@mmm.com

Slade Gardner
Lockheed Martin
PO Box 748
MZ 6834
Fort Worth, TX 76101
USA
Phone: (817) 777-4988
slade.h.gardner@lmco.com

Erik Geiss (170)
Uconn
U-136 97 N. Eagleville Rd.
Storrs, CT 06269
USA
geiss@main.phys.uconn.edu

Michel Gilio (46)
Katholieke Universiteit Leuven-PMA
Celestijnenlaan 300B
Heverlee 3001
Belgium
Phone: (+32) 16 32 2772
Fax: (+32) 16 32 2987
michel.gilio@mech.kuleuven.ac.be

Tim Gornet
University of Louisville
Rapid Prototype Center
Vogt Building #101
3rd & Eastern Parkway
Louisville, KY 40292
USA
Phone: (502)852-7599
Fax: (502)852-8890
tim.gornet@louisville.edu

Peihua Gu (187)
The University of Calgray
Dept. of Mechanical & Manufacturing Engg.
Calgary, Alberta T2N 1N4
Canada
Phone: (403) 220-7163
Fax: (403) 282-8406
gu@enme.ucalgary.ca

Richard Hague (619)
De Montfort University
The Gateway
Queens Building, Room D25
Leicester LE1 9BH
England
Phone: (+116) 257 7064
Fax: (+116) 257 7071
rhague@dmu.ac.uk

James Heidrich (567)
Milwaukee School of Engineering
1301 W. Jefferson, Apt. #27E
Morton, IL 61550
USA
Phone: (390) 675-0567
jheidrich@hotmail.com

Nicholas Herbert
Dept. of Design, Manufacture & Engg. Mgmt.
The University of Strathclyde
75 Montrose Street
Glasgow, Lanarkshire G1 1XJ
UK
Phone: (+141) 548 3486
Fax: (+141) 548 3309
nik_h@lineone.net

Diane Higgs
UTHSCA
202 Buckskin Drive
Boerne, TX 78006
USA
Phone: (830) 981-9185
usdiane@netscape.net

Neil Hopkinson
De Montfort University
Queens Building
The Gateway
Leicester LE1 9BH
UK
Phone: (+44) 116 2551551 x 8064
Fax: (+44) 116 2577071
nhopkins@dmu.ac.uk

Cheng Tiao Hsieh (313)
Rutgers University
Dept. of Mechanical & Aerospace Engg.
98 Brett Road
Piscataway, NJ 08854
USA
Phone: (732) 445-5769
Fax: (732) 445-3124
chsieh@caip.rutgers.edu

Michael Hutchison
3M
A141-1N-10
6801 River Place Blvd.
Austin, TX 78726
USA
Phone: (512) 984-6567
Fax: (512) 984-5064
mjhutchison@mmm.com

Zoran Jandric (110)
Southern Methodist University
1500 International Parkway
Richardson, TX 75081
USA
Phone: (214) 768-4873
zjandric@seas.smu.edu

Jeng Ywan Jeng (400)
University of California-Santa Barbara
Santa Barbara, CA 93117
USA
Phone: (805) 893-2723
Fax: (805) 893-4450
jeng@opto.ucsb.edu

Ryan Johnson (61, 373)
Georgia Institute of Technology
460 Marc Building
Mechanical Engineering
813 Ferst Drive
Atlanta, GA 30332
USA
Phone: (404) 894-1836
Fax: (404) 894-9342
gt2629b@prism.gatech.edu

Sheku Kamara (39)
Milwaukee School of Engineering
820 N. Milwaukee street
Milwaukee, WI 53202
USA
Phone: (414) 277-7189
Fax: (414) 277-7470
kamara@msoe.edu

Behrokh Khoshnevis (497)
University of Southern California
ISE Dept. USC
University Park
Los Angeles, CA 90089-0193
USA
Phone: (213) 740-4889
Fax: (213) 740-1120
khoshnev@usc.edu

Jonghyun Kim
Texas A&M University
2250 Dartmouth #1121
College Station, TX 77840
USA
Phone: (979) 458-0876
g9721021@hotmail.com

Carey King
University of Texas at Austin
Mechanical Engineering C2200
Austin, TX 78712-1063
USA
cking@ccwf.cc.utexas.edu

Pamela Kobryn (179)
Air Force Research Laboratory
AFRL/MLLM Bldg. 655
2230 Tenth St., Suite 1
Wright-Patterson AFB, OH 45433
USA
Phone: (937) 255-1313
Fax: (937) 255-3007
Pamela.Kobryn@afrl.af.mil

Ken Kornele
3M
A141-1N-10
6801 River Place Blvd.
Austin, TX 78726
USA
Phone: (512) 984-3985
Fax: (512) 984-5064
klkornele@mmm.com

Karina Krawczyk
Chemical Engineering Dept.
University of Louisville
106 Ernst Hall
2301 S. 3rd Street
Louisville, KY 40292
USA
Phone: (502) 852-2648
Fax: (502) 852-6355
kakraw01@yahoo.com

Ashok V. Kumar
University of Florida
237 MEB
Gainesville, FL 32611-6300
USA
Phone: (352) 392-0816
Fax: (352) 392-1071
akumar@ufl.edu

James Laeng (11)
Universiti Sains Malaysia
School of Mechanical Engineering
Engineering Campus
Nibong Tebal, Seberang Perai
Penang 14300
Malaysia
Phone: (604) 593-7788 x 3158
Fax: (604) 594-1025
jml111199@hotmail.com (temporary)

Wing K. Lau
Therics Inc.
115 Campus Drive
Princeton, NJ 08540
USA
Phone: (609) 514-7200 x 7249
Fax: (609) 514-7235
wlau@therics.com

Young Lim Lee
Kongju National University
Department of Mechanical Engineering
182 Shinkwan-dong
Kongju, Chungnam 314-701
South Korea
Phone: +82-41-850-8619
Fax: +82-41-854-1449
ylee@kongju.ac.kr

Longmei Li (187)
The University of Calgary
Dept. of Mechanical & Manufacturing Engg.
Calgary, Alberta t2N 1N4
Canada
Phone: (403) 220-5782
Fax: (403) 282-8406
longmei@enme.ucalgary.ca

Frank Liou (11, 20, 138, 452, 460)
University of Missouri-Rolla
121 ME Annex
1870 Miner Circle
Rolla, MO 65409-1350
USA
Phone: (573) 341-4603
Fax: (573) 341-4115
liou@umr.edu

Adam Lorenz (69)
Massachusetts Institute of Technology
Room 35-011
77 Massachusetts Ave.
Cambridge, MA 02139
USA
Phone: (617) 252-1591
Fax: (617) 253-0209
alorenz@mit.edu

Kevin Lyons
National Institute of Standards & Technology
100 Bureau Drive, MS8263
Bldg. 220/Room A127
Gaithersburg, MD 20899-8263
USA
Phone: (301) 975-6550
Fax: (301) 975-4482
klyons@cme.nist.gov

Guohua Ma
University of Texas at Austin
1630 West 6th Street, Apt. #P
Austin, TX 78703
USA
Phone: (512) 478-3313
maguohua@mail.utexas.edu

Karsten Manetsberger (346)
DaimlerChrysler
Postfach 2360
Ulm 89013
Germany
Phone: +49 7311 505-4194
Fax: +49 7311 505-4214
karsten.manetsberger@daimlerchrysler.com

Curtis W. Manning
NASA-Marshall Space Flight Center
MSFC, Bldg. 4707; Rm. 106E ED34
Huntsville, AL 35812
USA
Phone: (256) 544-7348
Fax: (256) 544-8970
curtis.manning@msfc.nasa.gov

Harris L. Marcus (163, 170, 195, 392, 546)
University of Connecticut
Institute of Materials Science
97 North Eagleville Road
Storrs, CT 06269-3136
USA
Phone: (860) 486-4623
Fax: (860) 486-4745
hmarcus@mail.ims.uconn.edu

Hanhua Mei (129)
Southern Methodist University
1500 International Parkway Suite 100
Dallas, TX 75231
USA
Phone: (214) 768-4873
Fax: (214) 768-0812
hmei@engr.smu.edu

Ibon Mitxelena
Inasmet Fundazioa
Mikeletegi Pasealekua
2 Teknologi Parkea
Donostia/San Sebastian
Gipuzkoa E-20009
Spain
Phone: +34 943 003700
Fax: +34 943 003800
imitxele@inasmet.es

Bina Modi
DSM Somos
2 Penn's Way, Suite 401
New Castle, DE 19711
USA
Phone: (302) 731-9752
bina.modi@dsm.com

Natalie Mohanty
University of Rhode Island
Rapid Manufacturing Center
Dept. of Ind. & Mfg. Engr.
Kingston, RI 02881
USA
Phone: (401) 874-5196
Fax: (401) 874-5540
natalie_mohanty@hotmail.com

Dwight Morejohn
Syneon
450 Cabot Road
S. San Francisco, CA 94080
USA
Phone: (650) 246-1224
Fax: (650) 246-1229
dmorejohn@syneon.com

Rhys Morgan (276, 283)
The University of Liverpool
Manufacturing Engineering
Ashton Building
Liverpool, Merseyside L69 3GH
UK
Phone: +44 151 794 4910
Fax: +44 151 794 4675
r.morgan@liverpool.ac.uk

Stephane Morvan (553)
Optomec Design Inc.
3911 Singer Blvd.
Albuquerque, NM 87120
USA
Phone: (505) 781-8250
smorvan@optomec.com

Jeremy Murphy (28, 468)
The University of Texas at Austin
Mechanical Engineering Dept. C2200
Austin, TX 78712-1063
USA
jmurphy101@hotmail.com

Srinivas Musti (452)
University of Missouri-Rolla
1300 N. Oak, Apt. #15
Rolla, MO 65401
USA
Phone: (573) 341-5335
Fax: (573) 341-6899
srinivas@umr.edu

Rajiv Nambiar (539)
The University of Texas-Pan American
1201 West University Drive
Engineering Department
Edinburg, TX 78539
USA
Phone: (956) 316-7056
Fax: (956) 381-3527
nambiar@panam.edu

Olli Nyrhila
Electro Optical Systems Finland
Aholantie 17
Rusko FIN-21290
Finland
Phone: +358-2-4365611
Fax: +358-2-4399620
olli.nyrhila@eos-finland.com

Seyi Onagoruwa (224)
Washington State University
Mechanical and Materials Engineering
P.O. Box 642920, Spokane Street
Pullman, WA 99164-2920
USA
Phone: (509) 335-5973
Fax: (509) 335-4662
seyi@mme.wsu.edu

Richard Ornelaz
DTM Corporation
1611 Headway Circle
Building 2
Austin, TX 78754-5199
USA

Ted Owens
DTM Corporation
1611 Headway Circle Bldg. 2
Austin, TX 78754
USA
Phone: (512) 425-2922
Fax: (512) 339-0634

Nachiket Patwardhan (338)
University of Texas at Austin
3401 Red River #253
Austin, TX 78705
USA
Phone: (512) 472-4231
nachiket@mail.utexas.edu

Haiko Pohl (366)
Fraunhofer IFAM
Wiener Str. 12
Bremen 28359
Germany
Phone: +49 421 2246 226
Fax: +49 421 2246 300
pl@ifam.fhg.de

Fritz Prinz
Stanford University
Mechanical Engineering Department
Bldg. 530, Room 220 MC 3030
Stanford, CA 94305-3030
USA
Phone: (650) 723-0084
Fax: (650) 723-5034
fbp@cdr.stanford.edu

Xiuzhi Qu (304)
University of Rhode Island
Rapid Manufacturing Center
Dept. of Ind. & Mfg. Engr.
Kingston, RI 02881
USA
Phone: (401) 874-5187
Fax: (401) 874-5540
qux@egr.uri.edu

Jagan Rajan (242)
University of Texas at Austin
2810 Salado St. #208
Austin, TX 78705
USA
Phone: (512) 296-5997
jagan_rajan@hotmail.com

Jorge Ramos (28, 468, 628)
University of Texas at Austin
Mechanical Engineering Dept. C2200
Austin, TX 78712-1063
USA
Phone: (512) 471-6709
Fax: (512) 471-7681
jaramos@mail.utexas.edu

Allan E. W. Rennie
CRDM, Buckinghamshire Chilterns University College
Queen Alexandra Rd.
High Wycombe, Bucks HP11 2JZ
UK
Phone: +44 1494 605085
Fax: +44 1494 538593
allan.rennie@bcuc.ac.uk

Bill Rogers (381, 505)
The University of Texas Health Science Center at San Antonio
Rehab Med-7798
7703 Floyd Curl Drive
San Antonio, TX 78229-3900
USA
Phone: (210) 567-5345
Fax: (210) 567-5354
rogers@uthscsa.edu

David Rosen
Georgia Institute of Technology
School of Mechanical Engineering
813 Ferst Dr.
Atlanta, GA 30332-0405
USA
Phone: (404) 894-9668
Fax: (404) 894-9342
david.rosen@me.gatech.edu

Brian Rosenberger
Lockheed Martin
P.O. Box 748
MZ 6834
Fort Worth, TX 76101
USA
Phone: (817) 763-3133
Fax: (817) 762-2540
brian.t.rosenberger@lmco.com

Kevin C. Rotheroe
Freeform, Digital Design & Manufacturing Studio
One Stuyvesant Oval Unit 9D
New York, NY 10009
USA
Phone: (212) 673-6881
freeform@nyc.rr.com

Dave Russell
Z Corporation
20 North Ave.
Burlington, MA 01803
Phone: (781) 852-5031
Fax: (781) 852-5100
drussell@zcorp.com

Emanuel Sachs (69, 216, 596)
MIT
Room 35-136
77 Massachusetts Avenue
Cambridge, MA 02139
USA
Phone: (617) 253-5381
Fax: (617) 253-0209
sachs@mit.edu

Phanvan Sanders
UTHSCSA
1802 Paso Del Sur
San Antonio, TX 78207
USA
Phone: (210) 432-6068
vsanders3@netscape.net

Bill Schafer
Dow Chemical
MEC
1616 Bldg.
Midland, MI 48667
USA
Phone: (989) 636-9377
Fax: (989) 636-8813
wlschafer@dow.com

Leon Shaw (163, 195, 330, 392, 546)
University of Connecticut
Dept. of Metallurgy and Materials Eng.
Storrs, CT 06269
USA
Phone: (860) 486-2592
Fax: (860) 486-4745
lshaw@mail.ims.uconn.edu

Moss Shimek (338)
University of Texas at Austin
Mechanical Engineering Dept. C2200
Austin, TX 78712-1063
USA
orig.mossimo@mail.utexas.edu

Harpreet Singh (77)
Loyola Marymount University
6412 Orange Ave. #25
Cypress, CA 90630
USA
Phone: (714) 952-1499
Fax: (310) 338-6029
mrhsingh@ucla.edu

Geoff Smith-Moritz
Rapid Prototyping Report
1010 Turquoise Street, Suite 320
San Diego, CA 92109
USA
Phone: (858) 488-0533
Fax: (858) 488-6052
rpreport@cadcamnet.com

Rupert Soar
De Montfort University
The Gateway
Queens Building, Room 0.25
Leicester LE1 9BH
England
Phone: +116 257 7093
Fax: +116 257 7071
asmith@dmu.ac.uk

Yong-Ak Song (55)
Korea Institute of Science and Technology
CAD/CAM Research Center
P.O. Box 131 Cheongryang
Seoul 137-791
South Korea
Phone: +82-2-958-5638
Fax: +82-2-958-5649
yongak@kist.re.kr

Shik-cheung Soo (424)
Hong Kong Polytechnic University
Department of Manufacturing Engineering
Hong Kong Polytechnic University
Hong Kong
China
Phone: (852) 27666622
Fax: (852) 23625267
billysoo@yahoo.com

Thomas Starr
University of Louisville
Department of Chemical Engineering
Speed Scientific School
Louisville, KY 40292
USA
Phone: (502) 852-1073
Fax: (502) 852-6355
tom.starr@louisville.edu

Brent Stucker (304)
University of Rhode Island
Rapid Manufacturing Center
Dept. of Ind. & Mfg. Engr.
Kingston, RI 02881
USA
Phone: (401) 874-5187
Fax: (401) 874-5540
stucker@uri.edu

John Stuecker (175, 561)
Sandia National Labs
POB 5800 MS 1349
Albuquerque, NM 87185-1349
USA
Phone: (505) 272-7125
Fax: (505) 272-7336
jnstuec@sandia.gov

Wei Sun (203, 527)
Drexel University
MEM Department
32nd & Chestnut Street
Philadelphia, PA 19104
USA
Phone: (215) 895-5810
Fax: (215) 895-2094
sunwei@drexel.edu

Rames Sundaram (408)
University of Missouri-Rolla
228 ME Building
1870 Miner Circle
Rolla, MO 65409
USA
Phone: (573) 308-1542
rames@umr.edu

Masaki Terada
Toyota Motor Co.
1 Toyota tyou
Toyota City, Aichi Pref. 471-8571
Japan
Phone: +81-565-23-3846
Fax: +81-565-23-5734
masaki_terada@mail.toyota.co.jp

Charles Thomas
University of Utah
50 S. Central Campus Drive
Salt Lake City, UT 84112
USA
Phone: (801) 585-6939
Fax: (801) 585-9826
cthomas@eng.utah.edu

Jim Thomas (576)
Naval Research Lab
Code 6350; Multifunctional Materials Branch
4555 Overlook Ave. SW
Washington, DC 20375-5343
USA
Phone: (202) 404-8324
Fax: (202) 404-7176
jthomas5@anvil.nrl.navy.mil

Fanny Ting Pong Yau (1)
The University of Hong Kong
Flat A, 22F, Fu Dat Court
32 Fortress Hill Road
North Point, Hong Kong
Hong Kong
Phone: (852) 9226 9308
Fax: (852) 2234 6235
hkufanny@graduate.hku.hk
fanny_ting@hotmail.com

Jiwen Wang (195, 546)
IMS, University of Connecticut
97 N. Eagleville Rd. U-3136
Storrs, CT 06269
USA
Phone: (860) 486-4410
Fax: (801) 720-7201
jiwenwang@yahoo.com

Haoyan Wei (163)
University of Connecticut
97 N. Eagleville Rd., U-3136
Storrs, CT 06269
Phone: (860) 486-4410
Fax: (860) 486-4745
weihy@ims.uconn.edu

Harovel G. Wheat
University of Texas at Austin
Mechanical Engineering Dept. C2200
Austin, TX 78712-1063
USA
Phone: (512) 471-1451
Fax: (512) 471-7681
hwheat@mail.utexas.edu

Kristin L. Wood (28, 242, 296, 338)
University of Texas at Austin
Mechanical Engineering Dept. C2200
Austin, TX 78712-1063
USA
Phone: (512) 471-0095
Fax: (512) 471-7682
wood@mail.utexas.edu

Soonkyu Yim (416)
Rutgers, The State University of New Jersey
98 Brett Road, Engineering Building D-134
Piscataway, NJ 08854
USA
Phone: (732) 445-1299
Fax: (732) 445-3124
skyim@jove.rutgers.edu

Kai-ming Yu (322, 424)
Hong Kong Polytechnic University
Department of Manufacturing Engineering
Hong Kong Polytechnic University
Hong Kong
China
Phone: 85227666603
Fax: 85223625267
mfkmyu@polyu.edu.hk

Gene Zak (120)
Queen's University
Department of Mechanical Engineering
McLaughlin Hall
Kingston, Ontario K7L 3N6
Canada
Phone: (613) 533-2567
Fax: (613) 533-6489
zak@me.queensu.ca

Yuhan Zhenz
DTM Corporation
1611 Headway Circle
Building 2
Austin, TX 78754-5199
USA

Byron Ziegler
High End Systems
P.O. Box 81892
Austin, TX 78708
USA
Phone: (512) 832-0363 x 369
byron_ziegler@highend.com